NUREG/CP-0142
Vol. 1

Proceedings of the 7th International Meeting on Nuclear Reactor Thermal-Hydraulics NURETH-7

Sessions 1–5

Held at
Sheraton Hotel and Convention Center
Saratoga Springs, New York
September 10–15, 1995

Compiled by
R. C. Block, F. Feiner, ANS

Sponsored by
American Nuclear Society
American Institute of Chemical Engineers
American Society of Mechanical Engineers
Canadian Nuclear Society
European Nuclear Society
Atomic Energy Society of Japan
Japanese Society of Multiphase Flow
U.S. Nuclear Regulatory Commission

Proceedings prepared by
Northeastern New York Chapter
American Nuclear Society

9509110196 950930
PDR NUREG
CP-0142 R PDR

AVAILABILITY NOTICE

Availability of Reference Materials Cited in NRC Publications

Most documents cited in NRC publications will be available from one of the following sources:

1. The NRC Public Document Room, 2120 L Street, NW., Lower Level, Washington, DC 20555-0001
2. The Superintendent of Documents, U.S. Government Printing Office, P. O. Box 37082, Washington, DC 20402-9328
3. The National Technical Information Service, Springfield, VA 22161-0002

Although the listing that follows represents the majority of documents cited in NRC publications, it is not intended to be exhaustive.

Referenced documents available for inspection and copying for a fee from the NRC Public Document Room include NRC correspondence and internal NRC memoranda; NRC bulletins, circulars, information notices, inspection and investigation notices; licensee event reports; vendor reports and correspondence; Commission papers; and applicant and licensee documents and correspondence.

The following documents in the NUREG series are available for purchase from the Government Printing Office: formal NRC staff and contractor reports, NRC-sponsored conference proceedings, international agreement reports, grantee reports, and NRC booklets and brochures. Also available are regulatory guides, NRC regulations in the *Code of Federal Regulations*, and *Nuclear Regulatory Commission Issuances*.

Documents available from the National Technical Information Service include NUREG-series reports and technical reports prepared by other Federal agencies and reports prepared by the Atomic Energy Commission, forerunner agency to the Nuclear Regulatory Commission.

Documents available from public and special technical libraries include all open literature items, such as books, journal articles, and transactions. *Federal Register* notices, Federal and State legislation, and congressional reports can usually be obtained from these libraries.

Documents such as theses, dissertations, foreign reports and translations, and non-NRC conference proceedings are available for purchase from the organization sponsoring the publication cited.

Single copies of NRC draft reports are available free, to the extent of supply, upon written request to the Office of Administration, Distribution and Mail Services Section, U.S. Nuclear Regulatory Commission, Washington, DC 20555-0001.

Copies of industry codes and standards used in a substantive manner in the NRC regulatory process are maintained at the NRC Library, Two White Flint North, 11545 Rockville Pike, Rockville, MD 20852-2738, for use by the public. Codes and standards are usually copyrighted and may be purchased from the originating organization or, if they are American National Standards, from the American National Standards Institute, 1430 Broadway, New York, NY 10018-3308.

DISCLAIMER NOTICE

Where the papers in these proceedings have been authored by contractors of the United States Government, neither the United States Government nor any agency thereof, nor any of their employees, makes any warranty, expressed or implied, or assumes any legal liability or responsibility for any third party's use, or the results of such use, of any information, apparatus, product, or process disclosed in these proceedings, or represents that its use by such third party would not infringe privately owned rights. The views expressed in these proceedings are not necessarily those of the U.S. Nuclear Regulatory Commission.

NUREG/CP-0142
Vol. 1

Proceedings of the 7th International Meeting on Nuclear Reactor Thermal–Hydraulics NURETH–7

Sessions 1–5

Held at
Sheraton Hotel and Convention Center
Saratoga Springs, New York
September 10–15, 1995

Date Published: September 1995

Compiled by:
R. C. Block, F. Feiner, ANS

Sponsored by
American Nuclear Society
555 N. Kensington Avenue
La Grange Park, IL 60525

American Institute of Chemical Engineers
345 East 47th Street
New York, NY 10017-2392

American Society of Mechanical Engineers
345 East 47th Street
New York, NY 1007-2392

Canadian Nuclear Society
144 Font Street West
Suite 725
Toronto, Ontario, Canada M5J2L7

European Nuclear Society
Secretariat: Monbijoustrasse 5
P.O. Box 5032
CH-3001 Berne, Switzerland

Atomic Energy Society of Japan
No. 1-13, 1-chome
Shimbashi, Minato-ku
Tokyo 105, Japan

Japan Society of Multiphase Flow
Prof. Akimi Serizawa
Department of Nuclear Engineering
Yoshida, Sakyo, Kycto 606-01
Japan

Division of Systems Technology
Office of Nuclear Regulatory Research
U.S. Nuclear Regulatory Commission
Washington, DC 20555-0001

Proceedings prepared by
Northeastern New York Chapter
Amrican Nuclear Society

NUREG/CP–0142, Volume 1, has been reproduced from the best available copy.

ABSTRACT

Technical papers accepted for presentation at the Seventh International Topical Meeting on Nuclear Reactor Thermal-Hydraulics are included in the present Proceedings. Except for the invited papers in the plenary session, all other papers are contributed papers. The topics of the meeting encompass all major areas of nuclear thermal-hydraulics, including analytical and experimental works on the fundamental mechanisms of fluid flow and heat transfer, the development of advanced mathematical and numerical methods, and the application of advancements in the field in the development of novel reactor concepts. Because of the complex nature of nuclear reactors and power plants, several papers deal with the combined issues of thermal-hydraulics and reactor/power-plant safety, core neutronics and/or radiation.

The participation in the conference by the authors from several countries and four continents makes the Proceedings a comprehensive review of the recent progress in the field of nuclear reactor thermal-hydraulics worldwide.

PLANNING COMMITTEE MEMBERS

General Chairman: Richard T. Lahey, Jr.

Vice-Chairman: M. Richard Mendelson

Technical Program Chairman: Michael Z. Podowski

Registration: Thomas M. Sutton

Secretary: Ray G. Gamino

Finance: Hunter B. Currin

Fund Raising: Brian Bielecki and Norman Francis

Publications: Frank Feiner and Robert C. Block

Arrangements: Robert C. Rohr

Publicity: David F. McMullan

Special Events: Jeffrey G. Hoole

Spouse Events: Ann E. Kelly

SCIENTIFIC ADVISORY COMMITTEE

K. Akagawa	Japan
G.F. Hewitt	Great Britian
Y.Y. Hsu	R.C., Taiwan
J. H. Kim	USA
S. Levy	USA
F. Mayinger	Germany
G. Matsui	Japan
U. Mueller	Germany
V. Nakoriakov	Russia
R.I. Nigmatulin	Russia
W. Rohsenow	USA
T. Sakaguchi	Japan
V.E. Schrock	USA
N. Todreas	USA
L.S. Tong	USA

TECHNICAL PROGRAM COMMITTEE

M. Akiyama	Japan
K.H. Ardon	Great Britain
S. Antal	USA
M. Aritomi	Japan
B. Azzopardi	Great Britain
S. Banerjee	USA
F.R. Best	USA
B. Boyack	USA
N. Brauner	Israel
G.P. Celata	Italy
J.H. Cha	South Korea
A. Clausse	Argentina
M.L. Corradini	USA
J.M. Courtaud	France
M. Cumo	Italy
V.K. Dhir	USA
G.E. Dix	USA
J.J. Dorning, Jr.	USA
R.B. Duffey	USA
F. Eltawila	USA
M. Epstein	USA
M. Erdman	USA
S. Ettore	USA
W. Frid	Sweden
M. Golay	USA
Y.A. Hassan	USA
S. Sreepada	USA
A. Strupczewski	Poland
L. Szabados	Hungary
R. Taleyarkhan	USA
T.G. Theofanous	USA
R.E. Henry	USA
G. Hetsroni	Israel
L. Hochreiter	USA
M. Ishii	USA
H. Karwat	Germany
G. Kojasoy	USA
V.S. Krishnan	Canada
T. K. Larson	USA
H. Lemmonier	France
J. March-Leuba	USA
M. Merilo	USA
F. Moody	USA
H. Nariai	Japan
B. Nigmatulin	Russia
H. Ninokata	Japan
O. Nylund	Sweden
P.F. Peterson	USA
V. Ransom	USA
K. Rehme	Germany
D.S. Rowe	USA
Z. Rouhani	USA
K. Rust	Germany
B.R. Sehgal	Sweden
A. Serizawa	Japan
B.S. Shiralker	USA
L. Shotkin	USA
J. Weisman	USA
W. Wulff	USA
G. Yadigaroglu	SWITZERLAND
S.T. Yin	CANADA

SESSION ORGANIZERS

Almenas, K.
Aritomi, M.
Banerjee, S.
Baratta, A.J.
Best, F.R.
Boyack, B.
Brauner, N.
Catton, I.
Celata, G.P.
Cha, J.H.
Chabard, J.P.
Cheng, L.
Corradini, M.L.
Courtaud, J.M.
Dhir, V.K.
DiMarzo, M.
Dorning, Jr. , J.J.
Eltawila, F.
Frid, W.
Golay, M.W.
Grand, D.
Groeneveld, D.C.
Hassan, Y.A.
Hodge, S.
Hochreiter, L.
Ishii, M.
Karwat, H.
Kojasoy, G.
Krishnan, V.S.
Kuru!, N.
Larson, T.K.
Lemmonier, H.
March-Leuba, J.
McMullan, D.
Merilo, M.
Modro, M.
Moody, F.
Nariai, H.
Ninokata, H.
Nylund, O.
Peterson, P.F.
Pilch, M.M.
Ransom, V.H.
Rehme, I.K.
Rouhani, Z.
Rowe, D.S.
Serizawa, A.
Shotkin, L.
Sreepada, S.
Taleyarkhan, R.
Theofanous, T.G.
Todreas, N. E.
Weisman, J.
Wilson, G.
Wright, R.W.
Wulff, W.
Yadigaroglu, G.
Yin, S. T.
Yoder, G. L.

TABLE OF CONTENTS

VOLUME I

Plenary Session - NUCLEAR POWER REACTORS FOR THE 21st CENTURY

"Turning Points in Reactor Design"
E. Beckjord 1

"Resolution of Thermal-Hydraulic Safety and Licensing Issues for the System 80+"
F.L. Carpentino, S.E. Ritterbusch, R.E. Schneider and M.C. Jacob 21

"AP600 Design Certification Thermal Hydraulics Testing and Analysis"
L.E. Hochreiter and E.J. Piplica 43

"Prospects for Bubble Fusion"
R.I. Nigmatulin and R.T. Lahey, Jr. 49

Session 1 - ADVANCES IN TWO-PHASE FLOW MODELING

"A Mechanistic Determination of Horizontal Flow Regime Boundaries Using Void Wave Celerity"
J.-W. Park 76

"A Criterion for the Onset of Slugging in Horizontal Stratified Air-Water Countercurrent Flow"
M.-H. Chun, H.-Y. Nam, B.-R. Lee and Y.-S. Kim 93

"Characterization of Non Equilibrium Effects on High Quality Critical Flows"
E. Camelo, H. Lemonnier, J. Ochterbeck and S. Selmer-Olsen 111

"Local Pressure Gradients Due to Incipience of Boiling in Subcooled Flows"
J. McDuffey and A. Ruggles 131

"Drift Flux Model as Approximation of Two Fluid Model for Two Phase Dispersed and Slug Flow in Tube"
R.I. Nigmatulin 141

"Development, Implementation and Assessment of Specific, Two-Fluid Closure Laws for Inverted-Annular Film-Boiling"
F. de Cachard 166

"Analytical Solution of Laminar-Laminar Stratified Two-Phase Flows with Curved Interfaces"
N. Brauner, Y. Rovinsky and D. Moalem Maron 192

"Velocity of Large Bubble in Liquid-Solid Mixture in a Vertical Tube"
H. Hamaguchi and T. Sakaguchi 212

"About the Statistical Description of Gas-Liquid Flows"
D. Sanz, G. Guido-Lavalle, P. Carrica and A. Clausse 231

"Entropy Analysis on Non-Equilibrium Two-Phase Flow Models"
H. Karwat and Y.Q Ruan 248

"A General Unified Non-Equilibrium Model for Predicting Saturated and Subcooled Critical Two-Phase Flow Rates Through Short and Long Tubes"
D.W.H. Fraser and A.H. Abdelmessih 264

"Predictions of Bubbly Flows in Vertical Pipes Using Two-Fluid Models in CFDS-Flow 3D Code"
A.O. Banas, M.B. Carver and D. Unrau 284

Session 2 - ADVANCES IN BOILING AND CONDENSATION HEAT TRANSFER

"Condensation During Gravity Driven ECC: Experiments with PACTEL"
R. Munther, H. Kalli and J. Kouhia 299

"An Investigation of Condensation From Steam-Gas Mixtures Flowing Downward Inside a Vertical Tube"
S.Z. Kuhn, V.E. Schrock and P.F. Peterson 312

"Study of Condensation Heat Transfer Following a Main Steam Line Break Inside Containment"
J.H. Cho, F.A. Elia, Jr. and D.J. Lischer 336

"Effect of Subcooling and Wall Thickness on Pool Boiling From Downward-Facing Curved Surfaces in Water"
M.S. El-Genk and A.G. Glebov 353

"Numerical Model of Condensation from Vapor-Gas Mixtures for Forced Down Flow Inside a Tube"
R.Y. Yuann, V.E. Schrock and X.M. Chen 377

"A Model for the Performance of a Vertical Tube Condenser in the Presence of Noncondensable Gases"
A. Dehbi and S. Guentay 402

"UPTF-TRAM Experiments for SBLOCA: Evaluation of Condensation Processes in TRAM Tests A6 and A7"
H.G. Sonnenburg, J. Tuunanen and V.V. Palazov 423

"Condensation Heat Transfer Coefficient with Noncondensible Gases for Heat Transfer in Thermal Hydraulic Codes"
S. Banerjee and Y.A. Hassan 434

Session 3 - EXPERIMENTAL METHODS AND INSTRUMENTATION

"Experimental Study of Horizontal Annular Channels Under Non-Developed Conditions"
G. Delgadino, J. Balino and P.M. Carrica 462

"Interfacial Shear Stress in Stratified Flow in a Horizontal Rectangular Duct"
C. Lorencez, M. Kawaji, A. Ousaka and Y. Murao 478

"Quenching Phenomena in Natural Circulation Loop"
H. Umekawa, M. Ozawa and N. Ishida 487

"Measurement of the Interaction Between the Flow and the Free Surface of a Liquid"
K. Okamoto, W.D. Schmidl, O.G. Philip and Y.A. Hassan 497

"The Use of Waveguide Acoustic Probes for Void Fraction Measurement in the Evaporator of BN-350-Type Reactor"
V. Melnikov and B. Nigmatulin 508

"Buoyancy-Driven Flow Excursions in Fuel Assemblies"
J.E. Laurinat, P.K. Paul and J.D. Menna 514

"An Experimental Investigation of the Post CHF Enhancement Factor for a Prototypical ITER Divertor Plate with Water Coolant"
T.D. Marshall, R.D. Watson, J.M. McDonald and D.L. Youchison 532

"Transient Pool Boiling Heat Transfer Due to Increasing Heat Inputs in Subcooled Water at High Pressures"
K. Fukuda, M. Shiotsu and A. Sakurai 554

"Cross-Sectional Void Fraction Distribution Measurements in a Vertical Annulus Two-Phase Flow by High Speed X-Ray Computed Tomography and Real-Time Neutron Radiography Techniques"
G.D. Harvel, K. Hori, K. Kawanishi and J.S. Chang 574

"Two-Phase Velocity Measurements Around Cylinders Using Particle Image Velocimetry"
Y.A. Hassan, O.G. Philip, W.D. Schmidl and K. Okamoto 591

"Characteristics of Turbulent Velocity and Temperature in a Wall Channel of a Heated Rod Bundle"
T. Krauss and L. Meyer 603

"The Coolability Limits of a Reactor Pressure Vessel Lower Head"
T.G. Theofanous and S. Syri 627

Session 4 - MULTIDIMENSIONAL FLOW AND HEAT TRANSFER PHENOMENA

"Numerical Simulation of Multidimensional Two-Phase Flow Based on Flux Vector Splitting"
H. Stadtke, G. Franchello and B. Worth 648

"CFD Simulation of Flow and Phase Distribution in Fuel Assemblies with Spacers"
H. Anglart, O. Nylund, N. Kurul and M.Z. Podowski 673

"Computational Fluid Dynamic Analysis of a Closure Head Penetration in a Pressurized Water Reactor"
D.R. Forsyth and R.E. Schwirian 696

"THEHYCO-3DT: Thermal Hydrodynamic Code for the 3 Dimensional Transient Calculation of Advanced LMFBR Core"
S.G. Vitruk, A.S. Korsun, P.A. Ushakov and B.N. Gabrianovich 711

"Transition to Chaos In a Square Enclosure Containing Internal Heat Sources"
A. Cihat Baytas 720

"ASTRID: a 3D Eulerian Software for Subcooled Boiling Modelling Comparison with Experimental Results in Tubes and Annuli"
E. Briere, D. Larrauri and J. Olive 736

"The Multi-Dimensional Module of CATHARE 2 Description and Applications"
F. Barre, I. Dor and C. Sun 750

Session 5 - CCFL AND FLOODING PHENOMENA

"Reflooding and Boil-Off Experiments in a VVER-440 Like Rod Bundle and Analysis with the Cathare Code"
V. Korteniemi, T. Haapalehto and M. Puustinen 770

"Counter-Current Flow in a Vertical to Horizontal Tube with Obstructions"
P. Tye, A. Matuszkiewicz, A. Teyssedou, A. Tapucu and W. Midvidy 781

"Flooding Characteristics of Gas-Liquid Two-Phase Flow in a Horizontal U Bend Pipe"
T. Sakaguchi, N. Nakamori, T. Ueno, J. Kodama, S. Hosokawa, H. Minagawa and Y. Fujii 804

"CCFL in Hot Legs and Steam Generators and Its Prediction with the Cathare Code"
G. Geffraye, P. Bazin, P. Pichon and A. Bengaouer 815

VOLUME II

Session 6 - NATURAL CIRCULATION AND/OR CONVECTION

"On Heat Transfer Characteristics of Real and Simulant Melt Pool Experiments"
T.N. Dinh, R.R. Nourgaliev and B.R. Sehgal 827

"Passive Decay Heat Removal by Natural Air Convection After Severe Accidents"
F.J. Erbacher, X. Cheng, H.J. Neitzel 846

"Natural Circulation in a VVER Geometry: Experiments with the PACTEL Facility and Cathare Simulation"
P. Raussi S. Kainulainen and J. Kouhia 854

"Parametric Numerical Investigation of Natural Convection in a Heat-Generating Fluid with Phase Transitions"
A.E. Aksenova, V.V. Chudanov, V.F. Strizhov and P.N. Vabishchevich 865

Session 7 - INSTABILITY MECHANISMS, WAVES, AND NONLINEAR DYNAMICS

"Geysering in Boiling Channels"
M. Aritomi, T. Takemoto, J-H Chiang, M. Mori and H. Tabata 875

"Two-Phase Flow Stability Structure in a Natural Circulation System"
Z. Zhou 888

"FIBWR2 Evaluation of Fuel Thermal Limits During Density Wave Oscillations in BWRs"
N. Nik, S.R. Rajan and M. Karasulu 911

"Density Wave Oscillations of a Boiling Natural Circulation Loop Induced by Flashing"
M. Furuya, F. Inada and A. Yasuo 923

"Rayleigh-Taylor Instability of Cylindrical Jets With Radial Motion"
X.M. Chen, V.E. Schrock and P.F. Peterson 933

"Two-Phase Flow Instabilities in Vertical Annular Channel"
I. Babelli, S. Nair and M. Ishii 947

"Problems in Experimental and Mathematical Investigations of the Accidental Thermohydraulic Processes in RBMK Nuclear Reactors"
B.I. Nigmatulin, L.K. Tikhonenko, V.N. Blinkov and A.J. Kramerov 967

"An Investigation of the Stability of a Boiling Water Reactor Under Natural Circulation Conditions Using TRAC-BF-1"
S. Lider, G.E. Robinson, A.J. Baratta and J.G. Refling 978

"Analysis of the Void Wave Propagations: Wave Number Independent Characteristics"
C.H. Song, H.C. No and M.K. Chung 986

"Modeling and Numerical Simulation of Oscillatory Two-Phase Flows with Application to Boiling Water Nuclear Reactors"
M. Rosa and M.Z. Podowski 1003

"Thermal-Hydraulic Instabilities in Pressure Tube Graphite-Moderated Boiling Water Reactors"
G. Tsiklauri and B. Schmitt 1022

"Dynamics of Shock Wave Propagation and Interphase Process in Liquid-Vapour Medium"
B.G. Pokusaev and N.A. Pribaturin 1032

Session 8 - TRANSIENT ANALYSIS AND SIMULATION

"Evaluation of a Main Steam Line Break With Induced, Multiple Tube Ruptures: A Comparison of NUREG 1477 (Draft) and Transient Methodologies - Palo Verde Nuclear Generating Station"
K.R. Parrish 1046

"Application of UPTF Data for Modeling Liquid Draindown in the Downcomer Region of a PWR Using RELAP5/MOD2-B&W"
G. Wissinger and J. Klingenfus 1069

"Plant Data Comparisons for Comanche Peak 1/2 Main Feedwater Pump Trip Transient"
W.J. Boatwright, W.G. Choe, D.W. Hiltbrand, C.V. DeVore and J.F. Harrison 1083

"RBMK-LOCA-Analyses with the ATHLET-Code"
A. Petry, A. Domoradov, A. Finjakin and A. Moskalev 1090

"Small-Break Loss of Coolant Accident in the Updated Pius 600 Advanced Reactor Design"
B. E. Boyack, J.L. Steiner, S.C. Harmony, H.J. Stumpf, and J.F. Lime 1100

"Simulation of a Beyond Design-Basis-Accident With RELAP5/MOD3.1"
J. Banati 1116

"Rapid Depressurization Event Analysis in BWR/6 Using RELAP5 and Contain"
A.K. Muftuoglu and M.A. Feltus 1127

"A Thermal-Hydraulic Code for Transient Analysis in a Channel with a Rod Bundle"
I.D. Khodjaev 1139

Session 9 - ADVANCED WATER REACTOR THERMAL-HYDRAULICS

"Analysis of an AP600 Intermediate Size Loss-Of-Coolant Accident"
B.E. Boyack and J.F. Lime 1153

"A Concept of JAERI Passive Safety Light Water Reactor System (JPSR)"
Y. Murao, F. Araya and T. Iwamura 1169

"Assessment of the Advantages of a Residual Heat Removal System Inside the Reactor Pressure Vessel"
G.M. Gautier 1196

"NRC Review of Passive Reactor Design Certification Testing Programs: Overview, Progress, and Regulatory Perspective"
A.E. Levin 1231

"Flooding of a Large, Passive, Pressure-Tube LWR"
P. Hejzlar, N.E. Todreas and M.J. Driscoll 1224

"SBWR PCCS Vent Phenomena and Suppression Pool Mixing"
P. Coddington and M. Andreani 1249

"Scaling for Integral Simulation of Thermalhydraulic Phenomena in SBWR During LOCA"
M. Ishii, S.T. Revankar, R. Dowlati, I. Babelli, W. Wang, H. Pokharna, M.L. Bertodano, V.H. Ransom, R. Viskanta and J.T. Han 1272

"A Practical View of the Insights from Scaling Thermal-Hydraulic Tests"
A.E. Levin and G.D. McPherson 1291

Session 10 - LIQUID-METAL-COOLED REACTOR THERMAL-HYDRAULICS

"Analysis of Overflow-Induced Sloshing in an Elastic-Wall Vessel Using Physical Component BFC Method"
D. Lu, A. Takizawa and S. Kondo 1302

"Study of Mixed Convective Flow Penetration into Subassembly from Reactor Hot Plenum in FBRs"
J. Kobayashi, H. Ohshima, H. Kamide and Y. Ieda 1313

"Large Eddy Simulation of Mixing Between Hot and Cold Sodium Flows-Comparison with Experiments"
J.P. Simoneau, H. Noe and B. Menant 1324

"Natural Convection Heat Transfer on Two Horizontal Cylinders in Liquid Sodium"
K. Hata, M. Shiotsu, Y. Takeuchi, K. Hama and A. Sakurai 1333

"Evaluation of Wrapper Tube Temperatures of Fast Neutron Reactors Using the Transcoeur-2 Code"
B. Valentin, G. Chaigne and P. Brun 1351

"Simulation of Decay Heat Removal by Natural Convection in a Pool Type Fast Reactor Model - RAMONA with Coupled 1D/2D Thermal Hydraulic Code System"
N. Kasinathan, A. Rajakumar, G. Vaidyanathan and S.C. Chetal 1361

"Conjugate Heat Transfer Analysis of Multiple Enclosures in Prototype Fast Breeder Reactor"
K. Velusamy, V. Balasubramaniam, G. Vaidyanathan and S.C. Chetal 1380

"Computational Modeling for Hexcan Failure Under Core Disruptive Accidental Conditions"
T. Sawada, H. Nimokata and A. Shimizu 1398

Session 11 - CONTAINMENT THERMAL-HYDRAULICS

"Investigations on Sump Cooling After Core Melt Down"
J.U. Knebel 1407

"Containment Atmosphere Response to External Sprays"
J. Green and K. Almenas 1418

"Modelling of Local Steam Condensation on Walls in Presence of Noncondensable Gases. Application to a LOCA Calculation in Reactor Containment Using the Multidimensional GEYSER/TONUS Code"
L.V. Benet, C. Caroli, P. Cornet, N. Coulon and J.P. Magnaud 1443

"The Modelling of Wall Condensation with Noncondensable Gases for the Containment Codes"
C. Leduc, P. Cost, V. Barthel and H. Deslandes 1456

"An Interpretation of Passive Containment Cooling Phenomena"
B.J. Chung and C.S. Kang 1477

"Detailed Thermal-Hydraulic Computation into a Containment Building"
A. Caruso, I. Flour, O. Simonin and C. Cherbonnel 1489

"Free Convective Condensation in a Vertical Enclosure"
R.J. Fox, P.F. Peterson, M.L. Corradini and A.P. Pernsteiner 1501

"Condensation in the Presence of Noncondensible Gases: AP600 Containment Simulation"
M. Anderson and M.L. Corradini 1519

"Hydrogen Behavior in Ice Condenser Containments"
P. Lundstrom, P. Gango, H. Tuomisto, O. Hongisto and T.G. Theofanous 1535

"Aerodynamics, Heat and Mass Transfer in Steam-Aerosol Turbulent Flows in Containment"
B.I. Nigmatulin, V.A. Pershukov, V.V. Ris, E.M. Smirnov, L.I. Zaichik, A.A. Vinberg, D.V. Sidenkov and V.A. Belov 1555

"GEYSER/TONUS: A Coupled Multi-D Lumped Parameter Code for Reactor Thermal Hydraulics Analysis in Case of Severe Accident"
M. Petit, M. Durin, and J. Gauvain 1574

VOLUME III

Session 12 - FUEL/COOLANT INTERACTION

"On The Constitutive Description of the Microinteractions Concept in Steam Explosions"
X. Chen, W.W. Yuen and T.G. Theofanous 1586

"Correlations Between the Disintegration of Melt and the Measured Impulses in Steam Explosions"
G. Frohlich, A. Linca and M. Schindler 1607

"Analysis of Supercritical Vapor Explosions Using Thermal Detonation Wave Theory"
B.I. Shamoun and M.L. Corradini 1637

"The Numerical Methods for the Development of the Mixture Region in the Vapor Explosion Simulations"
Y.H. Yang, H. Ohashi, M. Akiyama and T. Morii 1653

"Thermal-Hydraulic Behaviors of Vapor-Liquid Interface Due to Arrival of a Pressure Wave"
A. Inoue, Y. Fujii, M. Matsuzaki and M. Takahashi 1663

"Boiling Characteristics of Dilute Polymer Solutions and Implications for the Suppression of Vapor Explosions"
K.H. Bang and M.H. Kim 1677

"Experimental Investigation of 150-KG-Scale Corium Melt Jet Quenching In Water"
D. Magallon and H. Hohmann 1688

"FCI Experiments in the Corium/Water System"
I.K. Huhtiniemi, H. Hohmann and D. Magallon 1712

"Experimental Studies of Thermal and Chemical Interactions Between Oxide and Silicide Nuclear Fuels with Water"
A. Farahani and M.L. Corradini 1728

"The Effect of Constraint on Fuel-Coolant Interactions in a Confined Geometry"
H.S. Park and M.L. Corradini 1743

"The Mixing of Particle Clouds Plunging into Water"
S. Angelini, T.G. Theofanous and W.W. Yuen 1754

"Experimental Studies of Thermal and Chemical Interactions between Molten Aluminum and Water"
A.A. Farahani and M.L. Corradini 1779

Session 13 - THERMAL-HYRAULICS OF SEVERE ACCIDENTS

"Interaction Between the Radiative Flux Emitted by a Corium Melt and Aerosols from Corium/Concrete/Interaction"
M. Zabiego, G. Cognet and P. Henderson 1797

"Modeling of Heat and Mass Transfer Processes During Core Melt Discharge From a Reactor Pressure Vessel"
T.N. Dinh, V.A. Bui, R.R. Nourgaliev, T. Okkonen and B.R. Sehgal 1809

"Results of International Standard Problem No. 36 Severe Fuel Damage Experiment of a VVER Fuel Bundle at the CORA Facility"
M. Firnhaber, L. Yegorova, U. Brockmeir, S. Hagen, P. Hofmann and K. Trambauer 1830

"Oxidation During Reflood of Reactor Core with Melting Cladding"
L.J. Siefken, C.M. Allison, K.L. Davis and J.K. Hohorst 1851

"Crust Formation and Its Effect on the Molten Pool Coolability"
R.J. Park, S.J. Lee, S.K. Sim and K.J. Yoo 1863

"Simulation of the Thermalhydraulic Behavior of a Molten Core Within a Structure, with the Three Dimensions Three Components TOLBIAC Code"
B. Spindler, G.-M. Moreau and S. Pigny 1881

"The Modelling of Core Melting and In-Vessel Corium Relocation in the APRIL Code"
S.W. Kim, M.Z. Podowski, R.T. Lahey, Jr. and N. Kurul 1889

"CODE PACKAGE "SVECHA: Modeling of Core Degradation Phenomena at Severe Accidents"
M.S. Veshchunov, A.E. Kisselev, A.V. Palagin, A.V. Lemekha, A.M. Volchek, N.V. Yamshchikov, A.V. Boldyrev and A.I. Deryugin 1914

Session 14 - HEAT TRANSFER WITH PHASE CHANGE; APPLICATIONS TO SEVERE ACCIDENT SITUATIONS

"Experimental Simulation of Water Cooling of Corium Spread Over the Floor of BWR Containment"
F. Moraga, R.T. Lahey, Jr. and M.Z. Podowski 1930

"SULTAN TEST FACILITY Large Scale Vessel Coolability in Natural Convection at Low Pressure"
S. Rouge 1949

"An Integral Model for the Calculation of Heat Flux Distribution in a Pool With Internal Heat Generation"
J.M. Bonnet 1958

Session 15 - COMPUTATIONAL AND MATHEMATICAL MODELING

"Numerical Simulation of Stratified Shear Flow Using a Higher Order Taylor Series Expansion Method"
K. Iwashige and T. Ikeda 1972

"Application of an Analytical Method for Solution of Thermal Hydraulic Conservation Equations"
M. R. Fakory 1982

"Numerical Investigation of Heat Transfer in High-Temperature Gas-Cooled Reactors"
G. Chen and S. Anghaie 1997

"Development of a Graphical User Interface for the TRAC Plant/ Safety Analysis Code"
A.E. Kelly, C.K. Harkins and R.J. Smith 2003

"A Comparison of the Effect of the First and Second Upwind Schemes on the Predictions of the Modified RELAP5/MOD3"
G. Th. Analytis 2011

"Local Mesh Refinement for Incompressible Fluid Flow With Free Surfaces"
H. Teresaka, H. Kajiwara, K. Ogura. H. Ueda and A. Takizawa 2021

"Level Tracking in Detailed Reactor Simulations"
B. Aktas and J. Mahaffy 2035

"The Sensitivity Analysis by Adjoint Method for the Uncertainty Evaluation of the CATHARE-2 Code"
F. Barre, A. de Crecy and C. Perret 2045

Session 16 - MODEL & COMPUTER CODE VALIDATION & ASSESSMENT

"Development and Assessment of a Modified Version of RELAP5/MOD3"
G. Th. Analytis 2067

"A Study of the Dispersed Flow Interfacial Heat Transfer Model of RELAP5/MOD2.5 and RELAP5/MOD3"
M. Andreani, G.Th. Analytis and S.N. Aksan 2079

"Assessment of Computer Codes for VVER-440/213-Type Nuclear Power Plants"
L. Szabados, Gy. Ezsol and L. Perneczky 2102

"VIPRE Modeling of VVER-1000 Reactor Core for DNB Analyses"
Y. Sung, T.Q. Nguyen and J. Cizek 2112

"CATHARE2 Calculations of SPE4 Test Small Break LOCA on PMK Facility"
E. Laugier and J. Radet 2119

"Quantitative Code Accuracy Evaluation of ISP 33"
H. Kalli, A. Miettinen, H. Purhonen, F. D'Auria, M. Frogheri and M. Leonardi 2146

"FARO Base Case Post-Test Analysis by COMETA Code"
A. Annunziato and C. Addabbo 2159

"The Analysis of SCS Return Momentum Effect on the RCS Water Level During the Mid-Loop Operations"
J.K. Seo, J.Y. Yang, S.T. Hwang, and G.C. Park 2169

"An Assessment of RELAP5 MOD3.1.1 Condensation Heat Transfer Modeling with GIRAFFE Heat Transfer Tests"
B.D. Boyer, Y. Parlatan, G.C. Solvik and U.S. Rohatgi 2185

"ATHLET Validation Using Accident Management Experiments"
V. Teschendorff, H. Glaeser and F. Steinhoff 2203

"A Simple Modelling of Mass Diffusion Effects on Condensation with Noncondensable Gases for the Cathare Code"
P. Coste and D. Bestion 2222

"INJECT, and the Modeling of Waste Recycling Processes"
E. Gracyalny and M.L. Corradini 2240

"Some Thermohydraulics of Closure Head Adapters in a 3 Loop PWR"
F. Hofmann, O. Daubert, C. Bertrand, M. Hecker, F. Arnoux-Guisse and O. Bonnin 2250

"Analysis of a Small Break Loss-Of-Coolant Accident of Pressurized Water Reactor by APROS"
S. Al-Falahi, M. Hanninen and K. Porkholm 2263

"Evaluation and Assessment of Reflooding Models in RELAP5/MOD 2.5 and RELAP5/MOD3 Codes Using Lehigh University and PSI-Neptune Bundle Experimental Data"
M. Sencar and N. Aksan 2280

"Overview on CSNI Separate Effects Tests Validation Matrix"
N. Aksan, F. D'Auria, H. Glaeser, R. Pochard, C. Richards and A. Sjoberg 2303

"RELAP5 Analyses of Two Hypothetical Flow Reversal Events for the Advanced Neutron Source Reactor"
N.C.J. Chen, M.W. Wendel and G.L. Yoder 2335

"MELCOR Benchmarking Against Integral Severe Fuel Damage Tests"
I.K. Madni 2349

"Validation of the THIRMAL-1 Melt-Water Interaction Code"
C.C. Chu, J.J. Sienicki and B.W. Spencer 2359

"Experimental Assessment of Computer Codes Used for Safety Analysis of Integral Reactors"
A.A. Falkov, V.S. Kuul, O.B. Samoilov, A.N. Lepekhin and G.N. Polyansky 2384

"Assessment of the SE2-ANL Code Using EBR-II Temperature Measurements"
W.S. Yang and A.M. Yacout 2394

"RELAP5 Model to Simulate the Thermal-Hydraulic Effects of Grid Spacers and Cladding Rupture During Reflood"
C.K. Nithianandan, J.A. Klingenfus and S.S. Reilly 2410

"Validation of Advanced NSSS Simulator Model for Loss-of-Coolant Accidents"
S.P. Kao, S.K. Chang and H.C. Huang 2428

"Severe Accident Simulation at Olkiluoto"
H. Tirkkonen, T. Saarenpaa and L-C Po 2438

VOLUME IV

Session 17 - CHF MODELING AND PREDICTIONS

"The Sudden Coalescence Model of the Boiling Crisis"
P.M. Carrica and A. Clausse 2453

"Role of Heater Thermal Response in Reactor Thermal Limits During Oscillatory Two-Phase Flows"
A.E. Ruggles, A.D. Vasil'ev, N.W. Brown and M.W. Wendel 2470

"Methodology For the Study of the Boiling Crisis in a Nuclear Fuel Bundle"
F. de Crecy and D. Juhel 2480

"An Investigation of Transition Boiling Mechanisms of Subcooled Water Under Forced Convective Conditions"
K-W Lee and S-Y Lee 2489

"A Formal Approach For the Prediction of the Critical Heat Flux in Subcooled Water"
C. Lombardi 2506

"A Comparison of CHF Between Tubes and Annuli Under PWR Thermal Hydraulic Conditions"
C. Herer, A. Souyri and J. Garnier 2519

"New Model for Burnout Prediction in Channels of Various Cross Section"
V.P. Bobkov, N.V. Kozina, V.N. Vinogradov and O.A. Zyatnina 2539

"On the Look-Up Tables For the Critical Heat Flux in Tubes (History and Problems)"
P.L. Kirillov and I.P. Smogalev 2558

"A Comparison of Critical Heat Flux in Tubes and Bilaterally Heated Annuli"
S. Doerffer, D.C. Groeneveld and S.C. Cheng 2583

"Experience Using Individually Supplied Heater Rods in Critical Power Testing of Advanced BWR Fuel"
M. Majed, G. Norback, P. Wiman, G.I. Hadaller, R.C. Hayes and F. Stern 2608

"CHF Considerations for Highly Moderated 100% MOX Fueled PWRs"
D. Saphier and P. Raymond 2621

"General Correlation for Prediction of Critical Heat Flux Ratio in Water Cooled Channels"
R. Pernica and J. Cizek 2636

Session 18 - THERMAL-HYDRAULIC COUPLING IN REACTOR SYSTEMS

"A Study of the Effect of Space-Dependent Neutronics on Stochastically-Induced Bifurcations in BWR Dynamics(*)"
G. Th. Analytis 2654

"Analysis of the Return to Power Scenario Following a LBLOCA in a PWR"
R. Macian T.N. Tyler and J.H. Mahaffy 2669

"Stability Analysis of BWR Nuclear-Coupled Thermal-Hydraulics Using a Simple Model"
A.A. Karve, Rizwan-uddin and J.J. Dorning 2677

"Coupled Calculation of the Radiological Release and the Thermal-Hydraulic Behaviour of a 3-Loop PWR After a SGTR by Means of the Code RELAP5"
W. Van Hove, K. Van Laeken, L. Bartsoen, B. Centner and L. Vanhoenacker 2704

Session 19 - SUBCHANNEL THERMAL-HYDRAULICS

"Analysis of Two-Phase Flow Inter-Subchannel Mass and Momentum Exchanges by the Two-Fluid Model Approach"
H. Ninokata, A. Deguchi and A. Kawahara 2721

"Large Scale Transport Across Narrow Gaps in Rod Bundles"
M.S. Guellouz and S. Tavoularis 2738

"Void Fraction Distribution in a Heated Rod Bundle Under Flow Stagnation Conditions"
V.A. Herrero, G. Guido-Lavalle and A. Clausse 2762

"Numerical Determination of the Lateral Loss Coefficients for Subchannel Analysis in Nuclear Fuel Bundles"
S. Kim and G-C Park 2773

Session 20 - THERMAL-HYDRAULICS OF REACTOR SYSTEMS AND COMPONENTS

"The Low-Power Low-Pressure Flow Resonance in a Natural Circulation Cooled BWR"
T.H.J.J. van der Hagen and A.J.C. Stekelenburg 2785

"Flow Characteristics of Korea Multi-Purpose Research Reactor"
H. Kim, H.T. Chae, B.J. Jun and J.B. Lee 2786

"Analysis of Steam Generator Loss-Of-Feedwater Experiments with APROS and RELAP5/MOD3.1 Computer Codes"
E. Virtanen, T. Haapelehto and J. Kouhia 2806

"Horizontal Steam Generator Thermal-Hydraulics"
O. Ubra and M. Doubek 2815

Session 21 - THERMAL-HYDRAULICS TEST FACILITIES

"ISP33 Standard Problem on the Pactel Facility"
H. Purhonen, J. Kouhia and H. Kalli 2834

"SPES-2, An Experimental Program to Support the AP600 Development"
M. Tarantini and C. Medich 2841

"PWR-Related Integral Safety Experiments in the PKL III Test Facility - SBLOCA Under Beyond-Design-Basis Accident Conditions"
P. Weber, K.J. Umminger and B. Schoen 2856

"SPES-2, AP600 Integral System Test S01007 2" CL to Core Make-Up Tank Pressure Balance Line Break"
M. Bacchiani, C. Medich, M. Rigamonti, O. Vescovi, A. Alemberti and L.E. Conway 2869

"Investigations on the Thermal-Hydraulics of a Natural Circulation Cooled BWR Fuel Assembly"
H.V. Kok, T.H.J.J. van der Hagen and R.F. Mudde 2884

"Physical Modelling of a Rapid Boron Dilution Transient"
N.G. Andersson, B. Hemstrom, R. Karlsson and S. Jacobson 2895

"Further Evaluation of the CSNI Separate Effect Test Activity"
F. D'Auria, S.N. Aksan, H. Glaeser, A. Sjoberg, R. Pochard and J. Lillington 2904

"Water Hammer Phenomena Occurring in Nuclear Power Installations While Filling Horizontal Pipe Containing Saturated Steam With Liquid"
Y.F. Selivanov, P.L. Kirillov and A.D. Yefanov 2916

Session 22 - THERMAL-HYDRAULICS AND SAFETY OF NONCOMMERCIAL REACTORS

"Natural Circulation Analysis for the Advanced Neutron Source Reactor Refueling Process II"
R.F. Tucker, S. Dasaradhi, Y. Elkassabgi and G.L. Yoder 2924

"Cold Source Vessel Development For the Advanced Neutron Source"
P.T. Williams and A.T. Lucas 2941

"Modeling and Analysis of Thermal-Hydraulic Response of U-Al Reactor Fuel Plates Under Transient Heatup Conditions"
S.N. Valenti, T. Fuketa, S.H. Kim, V. Georgevich, R.P. Taleyarkhan, K. Soyama, K. Ishijima and T. Kodaira 2957

"Study on Severe Accident Fuel Dispersion Behavior in the ANS Reactor at ORNL"
S.H. Kim, R.P. Taleyarkhan, S.N. Valenti, V. Georgevich and J. Y. Xiang 2977

"The Phebus FP Thermal-Hydraulic Analysis with MELCOR"
K. Akagane, Y. Kiso T. Fukahori and M. Yoshino 2994

"Flow Excursion Time Scales in the Advanced Neutron Source Reactor"
C.D. Sulfredge 3003

"Thermal-Hydraulics of Wave Propagation and Pressure Distribution Under Hypothetical Fuel-Coolant-Interaction Conditions in the ANS Reactor"
R.P. Taleyarkhan, V. Georgevich, S.N. Valenti and S.H. Kim 3028

"Modeling and Analysis Framework for Core Damage Propagation During Flow-Blockage Initiated Accidents in the ANS Reactor at ORNL"
S.H. Kim, R.P. Taleyarkhan, S.N. Valenti and V. Georgevich 3052

Session 23 - MIXING AND TURBULENCE

"Turbulent Mixed Convection in Vertical and Inclined Flat Channels with the Aiding Flows"
P. Poskas, J. Vilemas, E. Adomaitis, G. Bartkus 3073

"Mixing Phenomena of Interest to Boron Dilution During Small Break LOCAs in PWRs"
H.P. Nourbakhsh and Z. Cheng 3083

"Numerical Boron Mixing Studies for Loviisa Nuclear Power Plant "
P. Gango 3096

"Turbulence Prediction in Two-Dimensional Bundle Flows Using Large Eddy Simulation"
W.A. Ibrahim and Y.A. Hassan 3120

Session 24 - LOCAL FLOW AND HEAT TRANSFER PHENOMENA IN REACTOR CHANNELS

"Statistical Parameter Characteristics of Gas-Phase Fluctuations for Gas-Liquid Intermittent Flow
G. Matsui, H. Monji and M. Takaguchi 3142

"3-D Flow Analyses for Design of Nuclear Fuel Spacer"
Z. Karoutas, C-Y Gu and B. Scholin 3153

"Bubble Behaviour and Mean Diameter in Subcooled Flow Boiling"
O. Zeitoun and M. Shoukri 3175

"Correlation of Critical Heat Flux Data for Uniform Tubes"
T. Jafri, T.J. Dougherty and B.W. Yang 3197

* "A Model of Film Boiling in the Presence of Electric Fields"
P.M. Carrica, V. Masson, A. Clausse, P. DiMarco and W. Grassi 3218

** "A Simple Delay Model for Two-Phase Flow Dynamics"
A. Clausse, D.F. Delmastro and L.E. Juanico 3232

* Paper assigned to Session 14 in the Conference Program
** Paper assigned to Session 11-3 in the Conference Program

PREFACE

Welcome to Saratoga Springs, the place of the first of the NURETH meetings, held in 1980. Since this first meeting, the NURETH series have included: Santa Barbara, California in 1983, Newport, Rhode Island in 1985, Karlsruhe, Germany in 1989, Salt Lake City, Utah in 1992 and Grenoble, France in 1993. Now, after fifteen years, the seventh of the NURETH meetings is being held again in the birth place of the series.

As you probable know, the NURETH meetings have been initiated and sponsored or co-sponsored by the Thermal-Hydraulics Division of the American Nuclear Society. The TH Division has clearly become a leader in establishing and maintaining high technical standards regarding topical meetings in the field of nuclear thermal-hydraulics, paper acceptance criteria for such meetings, and promoting international cooperation and exchange. In particular, the papers accepted for presentation at NURETH-7 and published in these volumes have been thoroughly reviewed by leading experts in their respective fields. Their work, as well as the efforts of the session organizers, are the cornerstones of the high technical quality of this meeting.

The present conference has been organized by the Northeastern New York Section of the American Nuclear Society. In addition, the following organizations have agreed to join the ANS Thermal Hydraulics Division as co-sponsors of NURETH-7: American Institute of Chemical Engineers (AIChE), American Society of Mechanical Engineers (ASME), Canadian Nuclear Society (CNS), European Nuclear Society (ENS), Japanese Nuclear Society (JNS), Japanese Society of Multiphase Flow (JSMF) and the U.S. Nuclear Regulatory Commission.

Except for the invited papers in the plenary session, all the other papers are contributed. They have been divided into twenty-four major topics. These topics cover all major areas of nuclear thermal-hydraulics.

The theme of the NURETH-7 conference is ***Thermal-Hydraulics for the 21st Century***. This theme has been implemented in the program of the meeting through technical papers covering areas such as: progress in analytical and experimental work on the fundamentals of nuclear thermal-hydraulics, the development of advanced mathematical and numerical methods, and the application of advancements in the field in the development of novel reactor concepts. Because of the complex nature of nuclear reactors and power plants, several papers deal with the combined issues of thermal-hydraulics and reactor/power-plant safety, core neutronics and/or radiation.

I hope that both the conference participants and other future readers of this multi-volume edition of NURETH-7 Proceedings will find several new and innovative ideas as the results of the work by the authors representing an outstanding international community of experts from academia and industry.

On behalf of the organizing committee I invite you to actively participate in the conference and wish you a pleasant stay in Saratoga Springs.

Michael Z. Podowski
Technical Program Chairman

ACKNOWLEDGMENTS

The efforts of the authors of both invited and contributed papers included in this volume are gratefully acknowledged. Also acknowledged is the cooperation of the members of the Technical Program Committee and the Scientific Advisory Committee who helped to organize the technical program of the meeting and accomplish its scientific objectives. Special thanks are extended to the session organizers and paper reviewers.

Finally, appreciation is expressed to the U.S. Nuclear Regulatory Commission for their support of the publication of the Proceedings.

Turning Points in Reactor Design

Eric S. Beckjord

Introduction

It is an honor and a pleasure for me to speak to you at the Plenary Session of the 7th International Meeting On Nuclear Reactor Thermal-Hydraulics. I greatly appreciate Professor Richard T. Lahey's invitation to give this lecture. He asked me to talk about key safety problems, where we have come from, and where we are going. I do, indeed, appreciate your invitation, Dick: this is a splendid opportunity to say what is on my mind.

I am going to talk about five turning points in reactor design and some safety problems associated with them. They are: Stability of the Dresden I Boiling Water Reactor; Emergency Core Cooling Systems; Probabilistic Risk Assessment; the Three Mile Island Unit 2 Accident; and Advanced Passive Light Water Reactors. I have selected the five based on personal involvement one way or another. They are not the only turning points, but I think they are important ones.

I will be talking about thermal-hydraulics, because I cannot think of an important safety problem that does not, at some point, involve thermal-hydraulics, but I will also be talking about systems. I hope you will bear with me on the systems part.

The Pressurized Water Reactor[1] (PWR) was proposed in 1948 for Naval Propulsion, and was the successful one of two candidates for development, following a study in depth of several systems, their merits and the state of technical knowledge needed to realize them. The other was the Submarine Intermediate Reactor, liquid metal-cooled, developed by the General Electric Company, but discontinued after the success of the Nautilus. Westinghouse Electric Corporation was the primary Naval PWR contractor, and chose the PWR with Yankee Atomic Electric Co. for the first round demonstration power plant,which was completed in 1960 at Rowe, Massachusetts. General Electric's response was the Boiling Water Reactor (BWR) built for Commonwealth Edison at Dresden, Illinois, and completed in 1961. Bruce Prentiss, a leader of the G. E. team, told me at the time that there was no way that G. E. would follow the Westinghouse lead in the choice of their first commercial nuclear plant. He said, "G. E. builds impulse turbines, Westinghouse builds reaction turbines, and that's the way things are!"

---

[1] The Atomic Submarine Clay Blair, Jr. Henry Holt & Co. 1954 p.114

I. Dresden I Reactor Stability

G. E. proposed Dresden 1, knowing the risk it was taking, with many questions of design and performance unanswered. It did, however, hedge its bet in the dual cycle, which produced about half of the turbine steam flow directly in the reactor core, but the other half indirectly in steam generators, thus assuring that the plant would be able to make at least half power based on PWR experience. In the light of the past 35 years, the G. E. decision says something today about the value of a competition that produced two viable reactor designs for the marketplace.

The Spert and Borax Reactor experiments[2] showed the effects of reactivity insertion and the shutdown mechanisms, including "chugging" as water moderator was cyclically expelled from the core, and in the extreme, core destruction. There was little concern early in the Dresden Project that the reactor would be unstable. Bill Muntz, an electronics engineer, was in charge of I&C, and he recognized the BWR as an analogue of a feedback amplifer, which can be unstable if the phase of the feedback signal reaches 180 degrees at a gain of 1: the feedback would become regenerative, and instability would be the result. He asked me to work on this question. We visited Argonne in 1956 when construction of EBWR was nearing completion, and he persuaded John West, the Project Director, to accept me on loan to study stability. I began an analysis of BWR dynamics, and worked with Argonne people on the EBWR rod oscillation tests, as part of my preparation for testing Dresden 3 years later.

The analysis[3] and experiments[4] for EBWR were in reasonable agreement. Accounting for the differences between Dresden and EBWR, the analysis predicted that Dresden would be far more stable than EBWR. However, there were two questions: (1) was the analysis of the Dresden reactor correct, and (2) was there a possibility of flow pulsations in the riser pipes conducting two-phase flow from the reactor vessel to the steam drum 90 feet above? Such pulsations could cause the core reactivity and power to resonate in tune with the riser pulsations. That could be troublesome, to say the least.

1

[2] The Technology of Reactor Safety Thompson and Beckerley MIT Press 1964 Chapter 11

1

[3] Dynamic Analysis Natural Circulation BWRs ANL-5799 1957

1

[4] J. A. De Shong Power Transfer Functions of EBWR ANL-5798 1957

The stability tests at Dresden[5] were conducted in March and June 1960 at half power and at full power, by oscillation of a control rod at constant frequency, measuring the response, and performing the test across a range of frequencies. The tests showed that the power-to-reactivity loop feedback was exceedingly stable, as predicted. The key factor was the oxide pellet fuel, having a long thermal time constant that served to attenuate the void reactivity feedback, preventing it from becoming regenerative.

There were tests conducted to detect riser flow pulsations and any response in the core. Shielded ion chambers were placed along a riser, detecting nitrogen 16 in the two-phase mixture rising from the reactor vessel. In the event of a flow pulsation, the water fraction passing an ion chamber would change, and likewise the N16 flowing with it. So too would the ion chamber signals, in coincidence with the changing water fraction. For measurements of core response, the reactor neutron flux instrument signals were used.

The tests gave interesting results. There were small flow pulsations related to the transit time of the two-phase fluid up the riser. The pulsation magnitude was a few % of the signal average value: 2 to 3% at half power and about 5% at full power. The frequency spectra of signal was measured with a variable frequency narrow bandpass filter, and it was found to correspond to the natural frequency of the riser carrying the two-phase flow mixture. This frequency increased from about 1 cycle in 10 seconds to 1 cycle in 7 seconds going from 50% power to 100% power, as expected due to the higher steam void fraction at full power. Similar measurements of core neutron flux were taken and analyzed, and the frequency spectra of neutron flux coincided with that of the riser. The measurements proved that the source of the riser pulsations was in the riser and not the core. If the core itself were the source, then the rod oscillation tests would have shown the core to be susceptible to excitation at the same frequency as measured in the riser, but they did not.

The most important conclusions drawn from these tests were, as stated in the Report, that Dresden was "exceedingly stable under normal operating conditions through design full power"; that "the power distribution in the core is fixed without side to side fluctuation, and finally external disturbances are well regulated." It was then clear that General Electric could design a larger BWR without concern about stability, and further, concentrate on the single cycle design, eliminating the dual cycle steam generators. General Electric formed a task force

---

1

[5] Dresden Reactor Stability Tests E. S. Beckjord GEAP-3550 1960

under Howard Cook to sift through all of the Dresden performance test results to guide future development. My recollection is that the general conclusion was much the same as the stability conclusion.

I note here that the stability conclusion was based on the assumption that future BWRs would use forced circulation, because stability analyses showed that forced circulation, and in particular designing pressure drop at the core inlet is stabilizing. This requirement is more difficult to fill in a natural circulation design, and for this as well as heat transfer reasons, the forced circulation doctrine stood for more than 30 years. Experience showed that there could be problems with natural circulation under some conditions, e.g., the power oscillations at LaSalle and several other foreign reactors.

Designers had thought about loss of recirculation in the 1960s, and protected for it, but had not thought about ATWS. If the pumps tripped and the reactor were unstable in natural circulation, and then an ATWS occurred, there could be a problem. Evidently a forced circulation BWR should be designed to accomodate ATWS regardless of whether it is operating in forced or natural circulation. A natural circulation BWR has just the one mode. In a choice between these two approaches, plant capital cost would be the deciding factor.

I return to the Dresden Reactor Stability Test for a moment to conclude this section. The people involved at the time were aware that these tests, and the various other reactor and plant performance tests, would frame the decisions on the next generation plants. The context as I recall it was capacity increase by 50% to 100%. It was not clear at the time, but is in hindsight, that the decisions leading not only to 600 Mwe plants, but to the much larger 1200 Mwe plants were based on the performance at Dresden for BWRs, and Yankee Rowe for PWRs. The Dresden tests, of which stability testing was a part are thus a true turning point in reactor development and design. How did the turning point decisions turn out? Despite the current U. S. outlook, I think they were a success in terms of the capacity installed and the energy generated world wide from U. S. LWR technology.

Of course, there were problems. Were there any actions in hindsight that could have made a difference? I think the answer is yes. More resources went to fuel development than to component development, excepting reactor vessel technology. However, the design life of components is much longer than fuel residence time in the reactor. I think it is possible that some more engineering attention to component designs could have improved them. As an example, thermal-hydraulic analysis and testing of steam generator tubing geometries and support configurations might have helped to reduce crevice corrosion

cracking near the tube sheet, and tube denting at support plates.

II. Emergency Core Cooling

Controversy over Emergency Core Cooling Systems (ECCS) erupted in 1966 during the Advisory Committee on Reactor Safeguards[6] review of the Dresden 3 and Indian Point 2 Applications for Construction Permits. Both sites were considered to be located in heavily populated areas. The trigger for this event was the conclusion of ACRS that "full-scale core melting must be strongly correlated with a loss of containment integrity--". In the course of hearings, Phil Bray of G. E. was asked what would happen to the core if ECCS failed. He said, "It would melt through and go to China." That remark was the origin of the "China Syndrome".

Zircaloy cladding, recently introduced in Construction Permit Applications of the time was a second factor, because the loss-of-coolant accident (LOCA), if uncontrolled, would lead to cladding temperatures approaching the average temperature of fuel pellets rather quickly. Metal-water reaction, heat release, hydrogen production, more release of heat, and possibly detonation would ensue. Although the amount of hydrogen generated was about the same as in the case of stainless steel clad, the heat of reaction for zirconium is considerably greater.

In this issue the most controversial points were (1) the ECCS design basis, and (2) the potential consequences of a LOCA that, if uncontrolled, would lead to core meltdown. As to the ECCS design basis accident (DBA), the practice, until the time of the Dresden 3 and Indian Point 2 Applications, was that the ECCS design would respond and provide adequate cooling for a break of the largest piping line connected the primary system, e.g., the pressurizer surge line for the PWR. For breaks smaller than the DBA LOCA, the AEC Division of Licensing required calculations showing that the charging system and the high head injection pumps if needed would maintain core cooling. The calculations showed that this was not a problem in general, although for a cold leg break in a PWR, it in fact was a problem. For pipe breaks exceeding the DBA LOCA, the Division of Licensing required calculation of heat release and pressure loads on containment, but the potential course of a molten core and its consequences were not considered.

As a consequence of decisions taken in these applications, the DBA LOCA became a double-ended rupture of the primary system piping, and this was a major turning point in reactor design. I

1

[6] Nuclear Reactor Safety David Okrent U. of Wisconsin Press 1981 Chapter 8

think it would take a number of lectures just to summarize the engineering and plant consequences of this decision. The conventional emergency cooling systems were greatly augmented with more sprays in the BWR, greater low pressure injection system capacity in both BWR and PWR, and in the PWR, accumulators connected to the reactor coolant piping through check valves, and designed to refill the reactor vessel in a few tens of seconds. The accumulators contained nitrogen gas at pressure, providing stored energy for passive pumping. New problems were discovered in the course of engineering, such as the loop seal, formed by a section of reactor coolant pipe having a loop at an elevation below the core, and leading to the possibility that water pumped from accumulators could pour out of the break instead of into the reactor vessel. There were other major engineering changes and design evolutions, including separation of ECCS trains, numbers of trains, and their connecting points. The larger dynamic loads of the DBA pipe breaks also had to be considered, and this led to very rigid piping supports and snubbers installed at great expense. Later research in the 1980s showed that rigid piping systems were more likely to fail than the flexible systems. The Leak-Before-Break concept made possible relaxation of the original requirements, and removal of pipe restraints that caused excessive rigidity. Sensitive leak detection systems made it possible to detect primary system leaks and thus give early warning to shut down.

Another consequence of the ECCS turning point was a world wide expansion in nuclear reactor thermal-hydraulics, in which the sum of nearly two billion dollars[7] was spent for the purpose of proving the effectiveness of the new DBA ECCS, a monumental effort which brings this community together, even today. Much of the work was carried out in the U. S., a large part of it by the U. S. Nuclear Regulatory Commission[8]. Although it is true as Levy notes "--that the original ECCS designs were satisfactory and underwent only minimal changes after all the results were in", this does not detract from the accomplishments, including the data that became available, the codes, multidimensional thermal-hydraulics, flow patterns, and scaling methodology. There is an impressive measure of this accomplishment, and also the conservatism of the early calculations. When the decisions were first made, the Regulatory Staff reviewed all the data and established a peak clad temperature limit of 2400 degrees Fahrenheit for the accident, with no exceptions granted. I

---

[7] The Important Role of Thermal Hydraulics in 50 Years of Nuclear Power Applications Salomon Levy NE&D 149 (1994) p. 4

[8] Compendium of ECCS Research for Realistic LOCA Analysis NUREG 1230 USNRC December 1988

believe the ACRS reviewed and concurred in this limit. My recollection is that the reactor designer had to show a credible margin. In other words, if he came with a best estimate of 2399 degrees, he would have to sharpen his pencil, and come up with a more convincing analysis, or as an alternative, increase ECCS capacity. After completion of the thermal-hydraulic research, including loop experiments, code validation and verification, statistical analysis of errors and all, best estimate calculations of peak clad temperatures for the accident gave values of 700 degrees. That is an impressive reduction. I do not recall the best estimate peak temperatures at that time, but if I split the difference, it is still impressive.

I turn now to the second issue of ECCS failure, given a LOCA, and core meltdown. Dr. Okrent gives his account of events in Chapter 11 of his book cited above. In the introduction to this Chapter, he states that three ACRS members believed that ACRS had agreed in August 1966 that it would recommend to the AEC Commissioners, as written in a draft letter that ACRS discussed with but did not send to the Commission, "development and implementation, in about two years, of safety features to protect against a loss-of-coolant accident in which the emergency core-cooling system did not work." However, in September 1966 the ACRS met with the Commissioners, and stated after the meeting in the ACRS monthly summary letter: "During the discussion between the Committee (the ACRS) and the Commission and members of the Commission staff on this subject, that the Commission suggested that a technically competent task force, including personnel from the AEC staff, Commission laboratories, industry, universities, etc., be formed to gather pertinent information. The Committee endorsed this suggestion, urged rapid convening of such task force, and recommended that the topics to be assigned to the task force include the following: 'The degree to which core cooling systems could be augmented for additional assurance that substantial meltdown does not take place; the potential history of large molten masses of fuel following a hypothetical accident; the engineering problems associated with possible 'core catcher' systems; and the build-up of excessive pressures or an explosive atmosphere in the containment.'" Evidently the commitment of the ACRS members other than the three named by Dr. Okrent to the position in the August letter was not as strong as he thought, or they preferred the Commission's suggestion when it was presented to them in September.

This, then, was the beginning of the AEC Advisory Task Force on Power Reactor Emergency Cooling, which was appointed on October 27, 1966. The announcement of release of the Task Force Report[9] was issued nearly a year later on October 23, 1967.

1

[9] Emergency Core Cooling U. S. Atomic Energy Commission

Although signed by the members, of which I was one, the report itself, 226 pages in length including 8 appendices, surprisingly has no AEC identifying number, and no date, making it difficult to find in any library. I have a copy. The report presents a discussion and 12 conclusions. I quote from a brief summary:

"The Task Force has concluded that within the framework if existing types of systems, sufficient reliance can be placed on emergency core cooling following loss-of-coolant and additional steps can be taken 'to provide additional assurance that substantial meltdown can be prevented.'"

"The effectiveness and adequacy of cooling systems requires that the core be maintained in place and essentially intact."

"A systematized approach to emergency core-cooling system design and evaluation would provide futher assurance that these systems will be capable of performing their intended function."

"Any assessment of emergency core cooling and core meltdown problems requires consideration of primary system integrity."

Core Meltdown: "---the description of events that could take place subsequent to a postulated meltdown of large portions of a core is at present indeterminate and quite speculative."

"While with present technology the integrity of the containment cannot be assured in the event of a postulated core meltdown, there is likelihood that a length of time will elapse before breachment of the containment might occur. It may be possible to develop preventive measures which are effective during this period and which could significantly reduce the hazards resulting from subsequent failure of the containment."

"The Task Force considered also the design and development problems associated with systems whose objective is the consequences of core meltdown---. We recommend for the near future a small-scale, tempered effort on those problems."

The ACRS gave the Commission its opinion of the Task Force Report in its February 1968 letter (Okrent, p.169), agreeing with recommendations for improvement of ECCS systems and technology and for improvement of Primary systems integrity, but taking issue with fact that the Task Force "---did not provide recommendations on design approaches to cope with large molten masses of fuel, or on the particular research and development problems related to these approaches."

To put the issue succinctly, the ACRS advocated development of designs to protect against ECCS failure, i.e., coping with molten fuel, while the Task Force believed that goal to be a mission impossible, given the state of knowledge of core meltdown

phenomena of the time.

With respect to ECCS augmentation and improvement, changes were accomplished quickly in all new plants, and backfitted to some of the earlier plants. The "core catcher" for Indian Point 2, a crucible lined with magnesium-oxide brick and located under the reactor vessel, remained in the Final Safety Analysis Report draft until June 1969, when the ACRS, the AEC Staff, and Consolidated Edison agreed to remove it. Despite the indecisive appearance of proceedings on the issue of ECCS failure at the time, I think that there was a clear de facto decision to focus on the objective of major improvement of ECCS systems, in design, in reliability, and in developing the technological base for ECCS systems, particularly in experimental thermal hydraulic validation and computer code development for both design and regulatory purposes.

My perspective on this whole matter is that the ACRS deserves credit for raising the issue, and the designers, researchers, and regulators deserve credit for development and implementation of vastly improved ECCS systems. They achieved a broad consensus in the nuclear engineering community in the U. S., and the result is accepted throughout the world today. The ECCS events of 1966-68 were indeed a major turning point in reactor design. I also believe that the decision taken on ECCS failure was the right one. The Commission made it in broad consultation with people from industry and laboratories as well as with the regulatory staff and the ACRS. The consequence of this decision was the full concentration of talent and resources on reliable ECCS development, an essential and realizable safety objective. The design basis capability of the ECCS was greatly augmented, and this provided margins for accomodating severe accidents. The design basis is important, but it is necessary to look at the individual plant configuration to see if the system will work as it is designed to do, as discussed below.

III. Probabilistic Risk Assessment

Probabilistic Risk Assessment (PRA) of nuclear power plants is a method of analysis that aims to identify performance faults, or initiating events, that can lead to damage to components or systems. In turn the damage may lead to release of radioactive material, leakage from containments, and exposure of workers and the public. The analysis also aims to determine the frequency of the damage states, given the frequency of initiating events. Risk in an interval of time is defined as the product of the consequence, e.g., exposure to radioactivity, and the frequency for that interval of time. PRA has two important roots. The

original idea stems from a paper by Farmer[10] in which he proposes the essential structure of PRA. The Reactor Safety Study[11], or Rasmussen Report(RSS), takes departure from the former and develops a comprehensive and detailed study of risk at two plants, Surry and Peach Bottom. The ECCS Hearings and Rule-making were in fact the stimulus for the AEC to undertake the study, in order to answer questions that came up frequently in the course of the hearings about how reliable the ECCS would be.

There was good news and bad news in the RSS findings. The good news was that the risk of large break LOCAs was small. Although the reactor core damage frequenies derived were higher than expected, the consequences of core damage were less than previously thought. The bad news was that the dominant risks were the small break LOCAs and plant transients, because these could lead to core damage with significant frequencies. Operator errors contributed about half the risk. Taken as a whole the RSS results were surprising, and nuclear opponents, incredulous of the results giving low the risk for large LOCAs, quickly attacked the report, and especially its summary. The result of the controversy was that the report was set aside for several years, until after peer review. The peer review concluded that the method of analysis was sound, but the uncertainties were greater than stated, and parts of the report were found to be "inscrutable". Unfortunately, the bad news, i.e., the findings about small breaks, plant transients and operator errors, were lost to view during this time, and they did not get the attention they deserved. One can only speculate on whether or not pursuit of the findings would have made any difference to Three Mile Island Unit 2 (TMI 2). Today I think that PRA bad news gets prompt and energetic attention.

I will tell you a true story about TMI 2. About a week after the accident I went to the office of Sol Levine, who was then Director of Research at the NRC, and who also had been the AEC Project Director and an important contributor to the RSS. I asked him, before getting to the business at hand, what did the RSS say about the TMI 2 accident. He took a large scroll of paper leaning against the office wall, unrolled it, and placed it on the table in front of his desk. The scrolls were the Surry event tree diagrams, and the one on top was loss of main feedwater evemt. "You know", he said, "the whole story is here and it hits you right in the eye, but we studied the event for Surry, where it's no problem, and we did not look at a Babcock

---

1

[10] Reactor Safety and Siting: a proposed risk criterion Farmer, R. J. Nuclear Safety 8(1967) 539-48

1

[11] Reactor Safety Study WASH-1400, US NRC, October 1975

OWilcox plant; the difference is that the saturated steam generators in Wesinghouse plants have about 30 minutes supply of water before they boil dry, whereas TMI 2 had about a minute and a half. That makes all the difference. The core damage frequency for this event is much higher at TMI 2." If the B&W design had been studied before the accident, analysis would have shown the crucial importance of the Auxiliary Feedwater System for the this type of plant, and a notably high core damage frequency.

PRA use and development revived quickly after TMI 2, but problems of large uncertainties, and variability of results when different people do the analysis have been persistent problems. NRC undertook a new study[12] in order to reassess the RSS risk estimates in the light of the latest knowledge, to provide a current estimate of severe accident risks, and to improve the state of the art. NUREG-1150 comprised 5 plant PRAs: Peach Bottom, Surry, Grand Gulf, Sequoyah, and Zion; Peach Bottom and Surry were analyzed in the RSS. In general the risk estimates of NUREG-1150 were lower than the RSS estimates, but a direct comparison would be misleading, because safety improvements were made to the plants after the RSS, and, in fact during the NUREG-1150 program. As vulnerabilities were discovered, the plant owners fixed them, and the final estimates reported reflected the fixes. NUREG-1150 underwent several peer reviews and revisions before final publication, and represented the state-of-the-art world wide when published, and it still does.

The applications of PRA have expanded gradually as techniques have been improved and confidence in results has increased. PRA became the centerpiece in the U. S. Individual Plant Examination (IPE), requested by the Commission in order to identify severe accident vulnerabilities at every plant in the U. S. Each plant owner performs the analysis for his plant, and submits a report to the NRC for review, with findings and actions that the owner plans to carry out as a result. The IPE has proved to be very important, because each plant has involved its own staff in performing the analysis and gaining experience with the process. Consequently operators have a better knowledge of the plant and develop a more critical and analytic approach to safety. Every plant has discovered vulnerabilities and fixed them with the result of palpable improvements in safety performance. The IPE PRAs have helped to reduce accident initiating frequencies, to reduce the failure rates of safety systems, and to improve mitigative measures.

Until a few years ago PRAs had been done for plants only in

1

[12] Severe Accident Risks: an assessment for five U. S. nuclear power plants NUREG-1150, December 1990

normal power operation. The French Safety Istitute (IPSN) decided to do PRA for plant shutdown conditions. At first glance surprisingly big core damage frequencies were found. On second glance the results are not so surprising, considering that during shutdowns a number of conditions occur that do not occur at power: for example, ECCS trains out of service for maintenance, containment hatches open for movement of equipment and spare parts, normally assigned personnel doing other jobs, and numbers of service personnel assigned for maintenance who do not have training in operations. In addition, some operating modes, such as PWR mid loop operation during steam generator tube inspection or repair proved to be very sensitive to loss of decay heat removal. As the results became known, the U. S. and other countries undertook their own studies, and found similar results.

Licensees have expressed interest in risk-based regulation, whereby they would allocate the resources at their disposal according to risk. The Station Blackout Rule is risk-based, and the Maintenance Rule promotes use of reliability goals. There is movement in that direction now, and more to come. Regulators are understandably uneasy at the prospect, because of familiarity with conventional, deterministic rules that establish fixed "speed limits". I think that several things are needed to make progress toward risk-based regulation. One is PRA analyses that do not vary when done by a different person or group. Another is better component failure rate data. The former requires an industry standard that gives minimum requirements for PRA analysis that is acceptable for regulatory purposes. The latter requires impetus to collect and maintain a data base of component failure rates for regulatory purposes. A third is further improvement of human reliabity analysis.

The fact is that PRA, despite some shortcomings, has earned its place of importance in reactor safety. It has provided generic insights into safety problems. It has also made safety determination plant specific, making it possible to focus attention on the systems and equipment actually built in the plant, and thereby to find errors and identify vulnerabilities that would otherwise be overlooked. The application of PRA to plant specific safety evaluation after the TMI 2 accident is an important turning point.

V. Three Mile Island Unit 2 Accident

Early in the morning of March 28, 1979, beginning with tripping of the condensate feedwater pumps, there followed rapidly main feedwater pump and then turbine trip. Protective signals started the auxiliary feedwater pumps, but the system block valve was closed, a serious human error. With no primary sytem heat removal, the primary pressure increased beyond the set point, and the power-operated pressurizer relief valve (PORV) opened automatically. After pressure was relieved, the PORV

failed to close, but the control room PORV indicator erroneously showed "closed". A small break LOCA had begun. In response to protective signals the high pressure safety injection pump activated to maintain water iventory in the primary system. The reactor operator was confused by the high pressurizer level and thought he had a solid water system. Therefore he throttled the valve, cutting off safety injection flow. At that point TMI 2 was on the path to a severe accident, as the consequence of an anticipated event (pump trips), an electromechanical fault (PORV stuck open), 2 human errors (AFWS block valve closed contrary to Technical Specifications; throttling the safety injection system that had properly activated); and 2 design weaknesses (misleading pressurizer level; poor instrument indication to operator of downstream temperature of PORV relief line). These are the very types of transients and faults identified in the Rassmussen Report of 1975, nearly four years before TMI 2, that can lead to a severe accident.

I think it is clear that special training is necessary to prepare operators for unexpected situations can vary in detail from one occurrence to the next. The TMI 2 operators amd their training were severely criticized at the time. I have a different view. The conclusion of the study of the accident in the months after TMI 2[13], confirmed by the post accident recovery and research, is that the operators had about 100 minutes after the accident began to recover and avoid the later, extensive core damage. They failed to regain control in this first period, because they did not respond effectively to what was occurring, were confused by pressurizer level and other signals, and were not able to diagnose what was happening and to develop a coherent strategy for moving in a direction toward recovery. However, they did discover the blocked AFWS valve early in this period and unblock it, which was a necessary condition to the later recovery. After the 100 minute mark, there was no way that they could prevent core damage, because that is when it started and then became progressively worse. The problem of recovery was more difficult in this second period, but the operators, though halting and inexperienced, were nevertheless able to achieve stabilization and recovery. They isolated the stuck open PORV; they restored high pressure safety injection thereby enabling heat removal from the primary system. They had emergency power and cooling water, and they used them. They have not received the credit due to them for the recovery. If they had not been successful at this stage, the situation would have been far more serious that it was. At TMI 2 we saw the beginnings of accident management, though it was years before it was recognized. Accident management is now a part of the training and Emergency

---

1

[13] (TMI 2) Technical Blow-by-Blow IEEE Spectrum Vol. 16, No. 11, p. 40, November 1979

Operating Procedures at U. S. nuclear plants, and, I believe, throughout the world.

I would like to present now a brief discussion of the final research task on TMI 2 that was completed and the technical papers were presented and discussed in Boston nearly two years ago, The TMI 2 Reactor Pressure Investigation Project[14]. The background of this work was the research sponsored by the U. S. Department of Energy during the recovery operations carried out by GPU Nuclear Corporation to remove the damaged core and to seal off the Containment and contaminated parts of the plant. By 1987 investigators had developed a clear picture and description of the course of events, including core melting and relocation of 20 tons of material to the bottom head of the reactor vessel. The work up to this point stopped short of investigation of the condition of the reactor vessel bottom head. Because the reactor vessel did not fail in the accident, it was very important to find out why it did not. The U.S. NRC Office of Research undertook this effort and formed a cooperative research project of 11 countries, members of the OECD Nuclear Energy Agency. The Project succeeded in removing 15 boat samples of the inside surface of the pressure vessel selected from the area of the vessel located adjacent to the known position of the core material that had flowed to and solidified on the bottom head. Metallurgical investigation of these samples established the existence of a "hot spot" about 1 meter in diameter on the bottom head, which reached a temperature of about 1150 degrees Centigrade after the molten core poured to the bottom head for 20 minutes before it quenched. This remarkable finding has important implications for severe accidents, accident management, and possible application to advanced reactor design.

An experiment called RASPLAV, performed by the Kurchatov Institute of Moscow and sponsored by the OECD Nuclear Energy Agency, including the U. S., is underway. RASPLAV is a test of external reactor vessel cooling after an accident. The idea is to help assure retention of molten core material within a reactor vessel, as at TMI 2.

TMI 2 was a traumatic event for everyone concerned. A review of the report[15] of the Kemeny Commission issued six months after the accident supports this statement. Its Findings were

---

1 [14] Three Mile Island - New Findings 15 Years After the Accident A. M. Rubin and E. S. Beckjord Nuclear Safety, Vol. 35, No. 2

1 [15] Report of the President's Commission on the Accident at Three Mile Island (aka The Kemeny Commission) USGPO October 1979

comprehensive and broad, covering 7 major topics: (1) Assessment of Significant Events; (2) Health Effects; (3) Public Health; (4) Emergency Response; (5) The Utility and Its Suppliers; (6) Training of Operating Personnel; and (7) The Nuclear Regulatory Commission. I quote here the overall conclusion: "To prevent nuclear accidents as serious as Three Mile Island, fundamental changes will be necessary in the organization, procedures, and practices -- and above all -- in the attitudes of the Nuclear Regulatory Commission and, to the extent that the institutions we investigated are typical, of the nuclear industry."

That is a challenging statement. What happened after the Kemeny Report? Ten years after the accident, the NRC issued a review[16] of the Kemeny Commission recommendations. The report describes the actions taken by NRC and the industry in response to the Kemeny Commission, indicating that significant modifications and improvements have been made. To summarize a few of the important changes, the NRC has made major revisions to its management structure,organization, and assigned responsibilities, e.g., creation of an office for evaluating and determining the significance of operating events at plants (AEOD). NRC has required major modifications and backfitting of new systems and equipment, and adding a new safety parameter display system to operating plants. The total cost of TMI 2 related fixes has been estimated to cost an average of about $400M per plant. Operator training and qualifications have become more demanding. The industry has made many changes, including plant improvements beyond what was called for in the TMI 2 fixes. It formed the Institute of Nuclear Power Operations (INPO), and the National Training Academy for training plant operators and supervisory personnel. Plant safety performance in the U. S. has increased significantly since the early 1980s. There is clearly a correlation between the actions taken by industry and the NRC, and the safety performance of the plants taken as a whole, but it would be difficult to identify the improvenents with a specific programs or actions.

TMI 2 was a turning point in the nuclear enterprise. That is not news, but I think it is worth looking back today to see what has been learned. There is still things to learn from completion of the research on the reactor vessel bottom head, and from the RASPLAV experiments. These could have exremely important consequences for the safety and defense-in-depth of the Advanced Reactors.

Advanced Passive Light Water Reactors

1

[16] The Status of Recommendations of the President's Commission on the Accident at Three Mile Island NUREG-1355 US NRC March 1989

Standard Design Certification under 10CFR Part 52 Subpart B was approved by the Commission about five years ago, has been carried out on the General Electric ABWR and the ABB Combustion Engineering System 80 Plus, and is underway on the Westinghouse AP600, and possibly will start again on the G. E. SBWR. The first two are so-called evolutionary plants, being improved versions of existing technology, and the last two are innovations in which emergency diesel generators are not required for operation of safety systems immediately after an accident. The concept of design standardization was borrowed from the experience of France in its nuclear program, although for somewhat different purposes. The purpose in the U. S. is to achieve a small number of reactor and plant designs that might be replicated many times, that would assure the applicability of experience and learning in one standard plant to all others of the same class, without the single supplier manufacturing economy that exists in France. The benefits are expected to include cost savings in design, manufacturing, construction, and operation and maintenance, through plant life and decommissioning, provided that a number of plants of the standard design are purchased. When a design is "cerified" under Part 52, the Certification is good for 15 years.

There will be costs associated with standard designs under this regime, that hopefully will be outweighed by the benefits. In the first thirty years of nuclear power in the U. S. innovations and improvements followed rather quickly on the heels of the last plant sold in a highly competitive market. A plant was sold, and then it was developed and designed. That is only small exaggeration. The 15 year certification period will slow down the development cycle and technological innovation, as will the high cost of certification to the parties who sponsor it: the licensing process is very thorough and detailed in its design review. The process provides for review of the functional design of the system at the certification review, and establishment of Inspection, Tests, Analysis, and Acceptance Criteria (ITAAC). The ITAAC accompanying the application indicate the specific inspections, tests, analysis, and the criteria that equipment must meet to assure the safety of the actual plant. ITAAC provides the method for approval of equipment to build the plant, at any time while the certification is valid. The process does not permit substitution of components or systems that do not meet specifications incorporated in the certification. To do that would require a modification or new certification. However, there is provision for introducing improved control systems technology that does not alter the plant basic design at a later time during the 15 year period of the certification. Digital control systems are developing rapidly, and there is no way to foresee the digital system that might be provided in a plant 10-15 years from now. To accomodate this need there are also Design Acceptance Criteria (DAC) for this kind of equipment. DAC is intended to make way for new control systems, provided that they

meet the DAC criteria. It will be important to the success of the design certification concept that such technological improvements can successfully be incorporated into detailed design without having to start the process all over again. I hope that the process will remain flexible enough to permit introduction of better technology, such as pumps and valves, without haveing to repeat the entire process. The Design Evaluation Report for the AP600 is expected in 1996, and Certification 1 1/2 years later.

The review process for the passive designs has evolved over the past five years, and is presented in a series of Commission Papers that define positions recommended by the staff for Commissionm approval on policy and technical issues related to the advanced reactor designs, and in the Commission's decisions on these papers. The most important Papers (together with the Commission's decisions) are:

1. SECY-90-016; 1/12/90 Topics: public safety goals; source term; ATWS; Mid-Loop operation; Station Blackout; Fire Protection; Inter-System LOCA; Hydrogen Generation and Control; Core-Concrete Interaction; Containment Performance; (ABWR Vent Design); Equipment Survivability; Operating Basis Earthquake; In-ervice Testing of Pumps and Valves.

2. SECY-93-087; 4/2/93 Topics: SECY-90-016 (above), plus Other Evolutionary and Passive Design Issues which are in part: -Evolutionary and Passive Designs-: Seismic Hazard Curves; LBB; Prototyping; Inspections, Tests, and Acceptance Criteria; PRAs; Severe Accident Mitigation Alternatives; Generic Rulemaking; Defense against Common Mode Failures in Digital Control and I&C Systems; Steam Generator Tube Ruptures; -Passive Designs only-: Definition of Passive Failure; SBWR Stability; Role of Passive Plant Operator.

3. SECY-94-084; 3/29/94 Topics: Regulatory Treatment of Non-Safety Systems; Definition of Passive Failure; Safe Shutdown Requirements; Control Room Habitability; Reliability Assurance Program; Station Blackout; Electrical Distribution; Inservice Testing of Pumps and Valves.

Note that where the same topic appears in a later document, the requirements have evolved. I have included these lists to make a point about the detail involved in the process. The stack of requirements I have abstracted from are mostly two-sided and about an inch thick. I would estimate that responses would to perhaps two decades greater in paper volume. These reviews are very detailed.

EPRI has established Requirements Documents for the Evolutionary Designs, and the Advanced Passive LWRs. These are broad in scope, and aim to present clear and complete statements of utility desires for the next generation of power plants

expected from vendors, architect-engineers, and constructors. EPRI has reviewed these documents with the NRC since beginning preparation in the late 1980s, and has resolved many licensing issues with only a short list of outstanding items remaining to be resolved. Volume I is a policy document and a summary of top-down requirements; Volume II contains the detailed Evolutionary ALWR requirements; and Volume III contains the Passive ALWR requirememts. The latter two are both multi-volume sets. It is apparent that the vendors have their work cut out for them to respond to the utilities and to the Regulator. I conclude that this dual regime, a new experience for the design teams, requires that concepts be thoroughly worked, so that construction drawings can be made quickly.

The Nuclear Energy Institute and the Nuclear Power Oversight Committee before it have issued a Strategic Plan[17] for new plants with annual revisions totalling four in all, with the latest issued in November 1994. The purpose of the Plan is to present an integrated effort to address the institutional and technical issues that must be resolved to make nuclear energy a viable choice for the utilities in the coming decade. The Plan identifies 14 building blocks (Current Nuclear Plant Performance, Low-Level Waste, High-Level Waste, Fuel Supply, Stable Regulations, ALWR Requirements, NRC Cerfication, Siting, First-of-a-Kind Engineering, Standardization, Public Awareness, Financing, Economic Regulatory Issues, and Enhanced Government Support) requiring coordination and action. The Plan outlines actions needed and shows which organization is responsible. These plans are unique, I think, from the point of view of the utilities, taking a comprehensive look at the total task to get a new plant designed, approved, financed, built, and put into operation, and they indicate a seriousness of intent that it happen.

The advanced passive plants, the AP600 and the SBWR offer the most important innovations of safety features to reactor design in more than 30 years. The important features are gravity powered emergency core cooling systems, by which cooling water drains into the reactor coolant systems frrom elevated tanks for core cooling purposes, and natural circulation containment cooling. Water reservoirs would require replenishment several days after an accident. These systems replace the high-head and low-head pumping systems in conventional nuclear plants that depend , in the event of loss of offsite power, on startup and operation of large, many-thousand horsepower diesel engines. In effect the passive systems nullify the station blackout problem, a low frequency but high consequence nuclear power plant hazard.

1

[17] Strategic Plan for Building New Nuclear Power Plants Nuclear Energy Institute December 1994

Although simple in concept, the design realization of passive systems are complex, because gravity driving pressure heads require venting to function, and are low compared to hydraulic heads for motor driven pumps. Extensive testing of these systems is underway by the vendors, and in NRC's confirmatory research program. These tests establish proof-of principle, and provide confidence in the performance of the systems to achieve design objectives.

The NRC initiated planning for confirmatory research on the AP600 and SBWR about 1990, because both designs were highly innovative and there was little experience available for making judgements about the performance of these systems. AP600 was ahead in schedule, and it was first in research planning. A full height, full pressure facility permitting the largest scale model that could be practically tested was desirable. A survey showed that the LSTF at Tokai in Japan could meet the top level requirement at a scale ratio of about 30:1 in volume. There was no comparable facility in size in the U. S., and to carry out the test here a new facility would have been required. The cost would have been in excess of $50M, and it could not have been funded. Negotiations with the Japan Atomic Energy Research Institute showed that an agreement to modify the LSTF would be acceptable, and after Commission approval, the project got underway. The NRC paid for the modification of the test facility to make the appropriate model of AP600, and JAERI funded the tests. These have been underway since early in 1994. The cost to NRC has been a fraction of what the cost would have been to build a U. S. facility, and the results came sooner. Many tests have been performed, some with expected results, and some with surprising results. I understand that there will be a paper at this conference describing the tests and analysis of some results. Taking into account the tests conducted by Westinghouse at Oregon State University, Piacenza in Italy, and the NRC tests at ROSA, I think that AP600 has had the most thorough and searching thermal-hydraulic testing of any commercial reactor scale model testing ever performed. If this assertion turns out to be true, there should be few surprises in regard to AP600 performance.

For SBWR testing the NRC decided to build a scale model facility, called PUMA, at Purdue University. Construction has been completed, but startup testing disclosed problems with insrumentation, and the test schedule has been delayed until September. Testing should be starting soon.

As I said earlier, the Advanced Passive LWRs are the most innovative development in the nuclear industry in 30 years, and they are the answer to the problem of Station Blackout in LWR NPPs. More generally, a long standing technical criticism of water reactors is that the cores, having relatively low heat capacity, tend to heat up rapidly after a LOCA (in a few hours).

In principle the passive designs, if they work as designed to do, fundamentally change the situation, by providing a combination of the core and a water reservoir that has very high heat capacity, preventing overheating for a day or more, during which long term cooling can be restored.

The question is, of course, can the passive plant compete economically? I do not know what the market will be for 600 Mwe. plants. If the market calls for larger plants, are larger passive plants technically and economically feasible? To what size can the passive concepts be scaled up? The vendors might be able to provide some answers to these questions. But there is another possibility, the hybrid. What are the passive features that one might try to graft to the 1200-1350 Mwe. size of plant? How would a hybrid compare with the current passive concept in its performance? And how would the hybrid compare in cost with the conventional design? These are interesting questions.

Summary: Turning Points

Dresden and Yankee performance testing led the way to far larger reactors.

The ECCS design basis increase was an excellent decision, and the decision was carried out well.

PRA focuses on the individual plant the way it actually is, helping to find vulnerabilities and thus to fix them.

Changes after TMI 2 have greatly improved reactor safety and performance.

Advanced Passive LWRs, like Paris, look so good, how can you ever go back to the same old model?

RESOLUTION OF THERMAL-HYDRAULIC SAFETY AND LICENSING ISSUES FOR THE SYSTEM 80+™ DESIGN

F. L. Carpentino, S. E. Ritterbusch, R. E. Schneider, M. C. Jacob

ABB-Combustion Engineering
A Business Unit of Combustion Engineering, Inc.
1000 Prospect Hill Road
Windsor, CT 06095

ABSTRACT

The System 80+™ Standard Plant Design is an evolutionary Advanced Light Water Reactor (ALWR) with a generating capacity of 3931 MWt (1350 MWe). The Final Design Approval (FDA) for this design was issued by the Nuclear Regulatory Commission (NRC) in July 1994. The design certification by the NRC is anticipated by the end of 1995 or early 1996.

NRC review of the System 80+ design has involved several new safety issues never before addressed in a regulatory atmosphere. In addition, conformance with the Electric Power Research Institute (EPRI) ALWR Utility Requirements Document (URD) required that the System 80+ plant address nuclear industry concerns with regard to design, construction, operation and maintenance of nuclear power plants. A large number of these issues/concerns deals with previously unresolved generic thermal-hydraulic safety issues and severe accident prevention and mitigation.

This paper discusses the thermal-hydraulic analyses and evaluations performed for the System 80+ design to resolve safety and licensing issues relevant to both the Nuclear Steam Supply System (NSSS) and containment designs. For the NSSS design, the Safety Depressurization System mitigation capability and resolution of the boron dilution concern are described. Examples of containment design issues dealing with containment shell strength, robustness of the reactor cavity walls and hydrogen mixing under severe accident conditions are also provided. Finally, the overall approach used in the application of NRC's new (NUREG-1465) radiological source term for System 80+ evaluation is described.

The robustness of the System 80+ containment design to withstand severe accident consequences was demonstrated through detailed thermal-hydraulic analyses and evaluations. This advanced design is shown to meet NRC severe accident policy goals and ALWR URD requirements without any special design features and unnecessary costs.

© 1995 Combustion Engineering, Inc.
All rights reserved

INTRODUCTION

The System 80+™ Standard Plant design with a generating capacity of 3931 MWt (1350 MWe) is an evolutionary advancement based upon the proven System 80® Pressurized Water Reactor (PWR) design currently employed at the Palo Verde site and in the Republic of Korea. It incorporates design enhancements to increase availability and improve safety margins. A Probabilistic Safety Assessment (PSA) initiated using System 80 as a reference plant design has been employed as an evaluation and confirmation tool throughout the design process.

The U. S. Nuclear Regulatory Commission (NRC) has completed its review of the System 80+ design by approving its advanced design features and closing out previously unresolved safety issues as well as the most recent severe accident licensing issues. The Final Design Approval (FDA) for this design was issued by the NRC in July 1994. With the design certification anticipated by the end of 1995 or early 1996, the System 80+ design is available now to meet the electric power needs of the 21st Century.

The System 80+ plant was designed in conformance with the EPRI ALWR Utility Requirements Document[1] (URD). In addition, the design enhancements considered the impact of the U.S. NRC's Severe Accident Policy goals specified in SECY-90-016[2] and SECY-93-087[3].

The advanced design features of the System 80+ design, in addition to providing higher thermal margin for full power operation and improved stability during plant transients, significantly contribute to reduced core damage frequency and resolution of all new safety issues. Of prime importance, the safety systems have been upgraded to provide more redundancy and diversity. As a result, the core damage frequency (CDF) associated with internal events for the System 80+ design is more than 100 times smaller than for the original System 80 design. The total CDF (including internal, external and shutdown events) is only 2.9×10^{-6} events/year. This result has full regulatory acceptance and surpasses both the NRC CDF goal of 1×10^{-4} events/year and the ALWR URD goal of 1×10^{-5} events/year.

The process of licensing the System 80+ design required that all known safety issues be addressed and resolved before the NRC would issue the FDA. Thus, many new issues never before addressed in a regulatory setting were resolved as part of this licensing process. Many of these required thermal-hydraulic analyses and evaluations using new methods to arrive at acceptable solutions. These included: (1) evaluation of possible containment bypass via single or multiple steam generator tube ruptures (SGTRs) based on best estimate models and assumptions, (2) investigation of potential boron dilution during a small break LOCA using computational fluid dynamics (CFD) methodology, (3) deterministic analysis of a full spectrum of severe accident sequences based on best estimate methods and assumptions, and (4) estimates of offsite radiological releases using a new, physically based source term.

The thermal-hydraulic analyses identified certain procedure changes and a few design features with attractive cost-benefit-ratios, which resolved the concerns. Some of the most significant of these included the following. A Nitrogen-16 monitor added to one steam line of each steam

generator (SG) provides fast and unambiguous indication of a steam generator tube rupture event. Modified emergency operations guidelines avoid the potential for a reactor coolant pump restart following small break LOCAs. A Safety Depressurization System (SDS), In-containment Refueling Water Storage Tank (IRWST), Cavity Flooding System, well-vented containment subcompartments and strategically placed hydrogen igniters throughout the containment allow for adequate hydrogen control and containment of radiation during severe accidents. The analyses/evaluations employed to resolve these issues/concerns are described below.

1. STEAM GENERATOR TUBE RUPTURE CONTAINMENT BYPASS

The issue of containment bypass following a steam generator tube rupture (SGTR) event was a concern because of the potential that the rupture flow would overfill the steam generator with primary coolant and force water through the Main Steam Safety Valves (MSSVs), causing them to fail open. In this containment bypass scenario, reactor coolant system (RCS) fluid, as well as radiation, would be discharged to the atmosphere depleting the IRWST water supply and eventually causing core damage. Operating experience has proven that adequate instrumentation and procedures can cope with the SGTR event. This issue was addressed for the System 80+ plant by conducting a thorough review of its instrumentation, emergency operations guidelines and system design alternatives.

The review was supported by analyses of various SGTR scenarios including the simultaneous double-ended ruptures of up to five tubes in one steam generator. These analyses used a best estimate plant transient analysis computer code. The choice of a maximum of 5 tubes ruptured is based on probabilistic assessments which indicated that accidents involving the simultaneous rupture of more than five tubes is extremely low. The results of the analyses showed that the System 80+ design allows a significant time for operator intervention to avoid safety valve actuation and SG overfill. For example, as shown in Figure 1, one ruptured tube allows more than four hours before MSSV actuation and five ruptured tubes allow more than thirty minutes. These significant times are due to the large steam generator size and the automatic SG level control capability of the System 80+ design. Nitrogen-16 (N-16) radiation alarms were added to provide a more rapid and unambiguous indication of early SG tube leakage. Additionally, the emergency operations guidelines were improved to reflect the use of N-16 alarms, the lessons learned from actual plant operations and the thorough knowledge gained through these special SGTR analyses.

2. SMALL BREAK LOCA BORON DILUTION

The small break LOCA boron dilution issue is a concern for the potential large accumulation of unborated condensate in the RCS piping following a SBLOCA which can then be suddenly introduced into the core by restarting the reactor coolant pumps (RCPs) or by regaining natural circulation. The unborated condensate is assumed to occur by boiling in the core and condensing in the SG tubes. This condensate collects in the RCP suction line and may then be subsequently

pushed into the reactor vessel. This issue required a detailed survey of SBLOCA analyses to determine which cases could produce a significant amount of condensate. The survey identified that, as a result of the System 80+ four train safety injection system (SIS) design, a very narrow range of break sizes have this potential (equivalent break diameters of one to three inches). Smaller breaks regain inventory too quickly to accumulate much condensate and larger breaks remove the steam to the containment with little condensation in the SGs. The reactivity response of the core was addressed for this range of breaks by assuming a conservative amount of condensate for these cases and analyzing two basic scenarios.

One scenario assumed that the condensate exceeds the core volume, remains completely unborated and is introduced to the core at a rate associated with regaining RCS natural circulation. This conservative analysis demonstrated that the shutdown margin of the System 80+ design is sufficient to minimize the return to power and preserve adequate core cooling. Figure 2 illustrates the resulting core power. Figure 3 shows that the fuel cladding temperatures remain well below acceptable limits. Separate mixing calculations showed that there is significant mixing between the unborated water and the highly borated water in the vessel such that, in reality, the core would remain subcritical.

A second scenario was assessed in which the condensate volume associated with the RCP piping is rapidly injected into the reactor vessel. Although RCP restart was already prohibited by the System 80+ Emergency Operations Guidelines (EOGs), the EOGs were revised by plant operations and human factors experts to substantially reduce the probability of a restart. A detailed multi-dimensional analysis of mixing was performed, assuming one RCP was restarted, to determine the lowest local boron concentration that could occur in the core. This analysis used the FLUENT[4] general purpose computational fluid dynamics computer program for the modeling of fluid flow, heat transfer, and chemical reaction.

A two-dimensional axisymmetric FLUENT model of the reactor vessel from the top of the fuel alignment plate to the bottom of lower head is used to model the turbulent chemical species mixing. The radial grid of the downcomer annulus is chosen to be fine enough to facilitate direct simulation of the annulus downflow pressure drop and radial mixing. In the lower head region, the grid structure is also fine enough to allow the prediction of turning losses and associated shear-generated turbulence and mixing.

Figure 4 graphically illustrates the reactor vessel boron concentration predicted by FLUENT at 13.5 seconds for one pump restart. It shows that as the mixing slug enters the core, boron concentration first decreases at the base and outer radius of the core, and the minimum concentration during the transient occurs at this location. Afterwards, the minimum concentration sweeps radially inward and then upward through the core as the highly borated water which follows flushes the mixing slug out of the core.

Figure 5 shows the results of assuming sweep-out of unborated water in one and two RCP suction legs. Even for the bounding assessment of sweep-out of two RCP suction leg volumes, the lowest concentration calculated (1850 ppm) exceeds the minimum required to maintain

subcriticality (550 ppm). Therefore, although RCP restart is very unlikely, the core will remain subcritical and adequately cooled even if it occurred.

3. SEVERE ACCIDENT RELATED ISSUES

The severe accident related issues involved a significant amount of deterministic analysis to support the Probabilistic Safety Assessment (PSA) for the System 80+ plant. These analyses were used to evaluate the ability of the plant design to prevent or mitigate severe accidents. The System 80+ design enhancements addressing severe accident mitigation include:

(a) large spherical steel containment with a concrete shield building (Figure 6),
(b) a Cavity Flooding System,
(c) a Hydrogen Mitigation System,
(d) a reactor cavity designed for corium disentrainment and debris cooling,
(e) a Safety Depressurization System,
(f) missile protection features, and
(g) an external connection for a backup water supply to the Containment Spray System.

The large open volume enhances mixing and avoids local, potentially explosive concentrations of hydrogen. The robust concrete supports below the reactor, which are designed with adequate reinforcement, are shown to withstand significant steam explosion loading based on deterministic analyses.

(a) Containment Performance

Deterministic analyses were used to demonstrate that a number of alternative methods are available to recover from scenarios which progress to partial core damage (in-vessel recovery) as well as complete molten core conditions (ex-vessel recovery). The analyses were performed using the PWR version of the MAAP 3[5] severe accident analysis computer code.

The four train Safety Injection System (SIS), the IRWST and the Safety Depressurization System (SDS) in conjunction with the normal emergency diesel generators and the alternate AC power source, i.e., gas turbine generator, provide highly reliable means of coping with the consequences of in-vessel recovery severe accident scenarios. Analyses were also performed to quantify the behavior for ex-vessel recovery scenarios. Several structural analyses were completed to confirm the containment strength since the more challenging severe accident scenarios could exceed the normal design limit of 53 psig. The containment pressure corresponding to the ASME service level "C" stress limit was determined to be 145 psig at a temperature of 290°F. The level "C" limit is still below the point of tensile failure of the steel containment and also corresponds to acceptable deflections of the containment penetrations. MAAP analyses of several severe accident sequences, including a station blackout, LOCA, and total loss of feedwater sequences, were performed. The results of these analyses demonstrate

that the containment pressure remains below the ASME Service Level "C" limit for significantly longer than 24 hours. The containment pressure and temperature transients for the most limiting case of the station blackout sequence are presented in Figures 7 and 8, respectively.

(b) Hydrogen Control

The Hydrogen Mitigation System (HMS) is a control-room-actuated system of 80 igniters that allow controlled burning of hydrogen at low concentrations. The number and placement of igniters were determined using a detailed review of the System 80+ containment layout and analyses using the MAAP 4[6] computer code. The generalized containment model of MAAP 4 code was used to quantify the distribution of hydrogen within the containment. The study assessed the potential for hydrogen build-up in the containment and determined the best-estimate response of the HMS.

MAAP 4 contains a lumped parameter model for the containment thermal-hydraulics. The model was especially constructed to simulate natural circulation in ALWR containments. Key elements of the model used for hydrogen distribution calculations are as follows:

a. Mechanistic, semi-implicit models for gas, water, and energy transport between control volumes;

b. Models for both unidirectional and counter-current flow through containment junctions,;

c. Stable treatment of water-solid regions; these can develop in System 80+ calculations; if the IRWST pool is sub-nodalized or if the cavity flooding system is actuated;

d. Flexible modeling of containment heat sinks; and

e. Advanced modeling of hydrogen combustion. Both non-global burns initiated by hydrogen igniters and global burns are treated using a single unified framework.

A detailed containment model using 23 control volumes, 35 junctions and 37 heat sinks (Figure 9) was constructed. The MAAP 3 predicted hydrogen and steam flow rates and energy transfer rates were fed into the MAAP 4 containment model. Hydrogen generation from reacting 100% of the active fuel cladding was included in the calculation to maximize the hydrogen concentration in each control volume.

Two limiting severe accident sequences were analyzed. These were a small break LOCA and a Station Blackout (SBO). The results of the analyses are presented in Table 1. It shows that the average hydrogen concentrations outside the IRWST remained below 10% by volume at all times, if the igniters were used. As expected, hydrogen concentrations are lower than this away from the control volumes containing the IRWST pressure relief dampers and the primary system break, if any. If sprays are in operation the hydrogen concentration were limited to 9% by

volume. This is attributed to the increase in effectiveness of the igniters at low steam concentrations and the more effective inter-node mixing promoted by the operation of the sprays and local combustion.

Table 1
System 80+™ Containment Hydrogen Distribution
Peak Hydrogen Concentrations

Case	Peak H_2 Fraction				
	Cavity	Dome	Lower Compt. 2	Steam Generator (low)	IRWST
SLOCA, No Igniters	0.09	0.10	0.10	0.12	0.10
SBLOCA, Igniters	0.06	0.06	0.06	0.09[a] 0.07[b]	0.06
SBLOCA, Igniters, Spray	0.06	0.05	0.06	0.06	0.06
SBO+SDS, No Igniters	0.11	0.11	0.15	0.14	0.31
SBO+SDS, Igniters	0.05	0.05	0.05	0.05	0.15[a] 0.10[b]
SBO+SDS, Igniters, Spray	0.05	0.04	0.05	0.05	0.09

SLOCA: Small Break LOCA
SBO: Station Blackout
SDS: Safety Depressurization System

[a]: Spikes
[b]: Average Values

Igniter effectiveness in the IRWST is sensitive to both steam and oxygen concentrations. Both are considered somewhat uncertain, but the uncertainties act in a direction that would make the mixture non-flammable so as not to present a threat. Hydrogen combustion in the IRWST was limited by oxygen availability. The calculated flow rates of oxygen were sufficiently large enough to maintain hydrogen combustion at a level that would limit the hydrogen concentrations to below 10% by volume.

(c) Cavity Strength

Analyses were performed to determine the strength of the cavity wall to withstand ex-vessel steam explosion (EVSE) loadings. The explosion is postulated to occur due to the generation of steam at a rate faster than can be acoustically or inertially relieved by the surrounding medium

following the discharge of corium into the reactor cavity that is filled with water. The initiation of explosion, if any, would occur either when the core debris initially contacts the water or when the debris penetrates the water and contacts the concrete surface at the bottom of the reactor cavity. The results of a potential steam explosion would be to generate impulse loads on the cavity walls and in-cavity structures.

Although the damage due to EVSE was considered negligible in NUREG-1150[7], analyses were performed for the System 80+ design to quantify the loads on the cavity walls and structures. This analysis used a "TNT equivalent" methodology (consistent with the methodology used in NUREG-1150) to calculate the impulse loads on the System 80+™ cavity walls by assuming that the stored thermal energy within a superheated mass of corium can be related to a charge of TNT. The results of the analysis indicated that the cavity impulse loads range between 0.25 to 1.5 psi-sec for corium mass discharges of between 500 and 5,000 lbms. The 5,000 lbms corresponds to discharge of corium via one instrument tube located in the lower head of the reactor vessel. This impulse loading has negligible impact on the System 80+ reactor cavity walls, since the walls are designed with a significant amount of reinforcement. For example, the concrete corbels (Figure 10) supporting the vessel have an impulse capability of 4.65 psi-sec.

(d) Core-Concrete Interaction

One of the concerns with regard to containment integrity is the potential for basemat concrete erosion due to core-concrete interaction (CCI) subsequent to reactor vessel failure and discharge of corium on to the cavity floor. The cavity is provided with adequate floor area for corium spreading. In addition, the Cavity Flooding System, the components of which include the IRWST, Holdup Volume Tank, the reactor cavity, and piping and valves, supplies water to the cavity for quenching the corium. Despite all of these features, CCI is conservatively postulated to occur subsequent to vessel failure with the resulting erosion of the cavity floor.

Argonne National Laboratory (ANL), under the sponsorship of the DOE Advanced Reactor Severe Accident Program (ARSAP), performed a core-concrete erosion calculation for the System 80+ design using the CORCON-MOD 3 Version 2.26[8]. This code has been developed by the NRC for the explicit purpose of computing core-concrete erosion rates and profiles during severe accidents. The CORCON-MOD3 study computed heat transfer to the upper crust via mechanistic heat transfer models which allowed for consideration of growth and depletion of the crust. These models allowed the code to select the most appropriate upper surface heat flux based on the thickness and surface temperature of the corium crust. It was assumed that the corium crust and the corium melt are in contact, and that the melt is impermeable to water ingression. The melt composition was based on basemat attack involving 100% of the molten core with a 75% equivalent zircaloy oxidation prior to concrete attack.

The ANL study considered core-concrete erosion in limestone, limestone/common sand, and basaltic concretes. Results of the study indicated that the average basemat depth will not erode

by significantly more than 3 feet in a 24 hour period following initiation of CCI for all concrete compositions. The erosion profile for a representative CCI transient is shown in Figure 11.

MAAP 3 calculations were also performed to corroborate the CORCON-MOD3 calculations. This was done by parametrically varying the corium upward heat flux, which is controlled by the MAAP pool boiling heat flux multiplier. These calculations confirmed that the erosion profiles were a strong function of the corium upward heat flux.

4. NEW RADIOLOGICAL SOURCE TERM

The significantly improved and more current technology reflected in the NRC's new radiological source term, as described in NUREG-1465[9] has been applied to the System 80+ design. For this new source term, radioactive fission products are released over a period of approximately 1.8 hours in comparison to the instantaneous release assumed for the old source term documented in TID-14844[10]. The new source term releases are mainly particulate as opposed to gaseous releases for the old source term. Also, the new source term consists of nine radionuclide groups in relation to consideration of only iodine and noble gases for the old source term.

Based on the new source term, a new model for containment spray effectiveness was developed to more accurately predict mixing between sprayed and unsprayed regions during an accident and cleanup of fission products from the containment atmosphere. Figure 12 shows a comparison of the containment spray particulate cleanup coefficient (spray lambda) for the old and new models. The new source term also required a more detailed analysis of the containment sump water chemistry, resulting in a switch to trisodium phosphate dodecahydrate for pH control.

The use of the new source term also necessitated an assessment of equipment survivability inside the containment. This included a review of the containment layout, the hydrogen igniter system, and material properties for severe accident temperature, pressure, and radiation conditions.

The new source term also impacted the prediction of the control room and offsite radiological releases. It involved a detailed safety analysis, review of ventilation systems, and use of a new model for site meteorology. As a result, the requirement for safety grade charcoal filters was eliminated from the plant, except for the control room, and the allowable containment leak rate was increased from 0.1% volume/day to 0.5% volume/day, easing containment integrity testing. Use of the new source term resulted in (1) a reduction in the design basis accident (DBA) doses by a factor of two to three, and (2) the best-estimate site boundary dose for a severe accident being less than the U.S. Environmental Protection Agency's Protective Action Guidelines (PAGs). It was determined from PAG analysis that the core melt scenarios would not exceed the PAG 16-km radius limits at the site boundary. For the System 80+ design, the worst scenario resulted in a site-boundary committed effective dose equivalent (CEDE) of 0.33 rem in comparison to the criterion of 1 rem. The best-estimate thyroid dose was 2.7 rems compared to the criterion of 5 rems. This analysis demonstrated the technical feasibility of simplified emergency planning for the System 80+ evolutionary design.

CONCLUSIONS

The System 80+ design is available now for the 21st Century. It adequately addresses all new unresolved safety issues and concerns with regard to severe accident mitigation capability. It was demonstrated via thermal-hydraulic analyses and evaluations of NSSS and containment design capabilities that the System 80+ design represents a robust containment design that can withstand severe accident consequences and meet NRC severe accident policy goals and EPRI URD requirements without any special design features and unnecessary costs. It is further concluded that best estimate severe accident evaluations are appropriate with the results interpreted within relevant uncertainties. The System 80+ containment design with the proven active containment spray system has significant beneficial impacts in terms of public health and safety.

REFERENCES

1. NP-6780-L, Advanced Light Water Reactor (ALWR) Utility Requirements Document, Rev. 3, Electric Power Research Institute, 1992.

2. SECY-90-016, "Evolutionary Light Water Reactor (LWR) Certification Issues and Their Relationship to Current Regulatory Requirements", USNRC, January 12, 1990.

3. SECY-93-087, "Policy, Technical and Licensing Issues Pertaining to Evolutionary and Advanced Light water Reactor (ALWR) Designs", USNRC, April 2, 1993.

4. Fluent User's Guide Version 4.0, Fluent, Inc., December 1991.

5. MAAP 3.0 B User's Manual, Fauske and Associates Inc., March 1990.

6. MAAP 4 User's Manual (Draft), Fauske and Associates Inc., March 1992.

7. NUREG-1150, "Severe Accident Risks: An Assessment for Five U.S. Nuclear Power Plants", USNRC, December 1990.

8. NUREG/CR-5843, SAND92-0167, "CORCON-MOD3: An Integrated Computer Model for Analysis of Molten Core-Concrete Interactions (Draft)", USNRC, October 1992.

9. Draft NUREG-1465, "Accident Source Term for Light Water Nuclear Power Plants", USNRC, June 1992.

10. TID-14844, "Calculation of Distance Factors for Power and Test Reactor Sites", US Atomic Energy Commission, March 23, 1962.

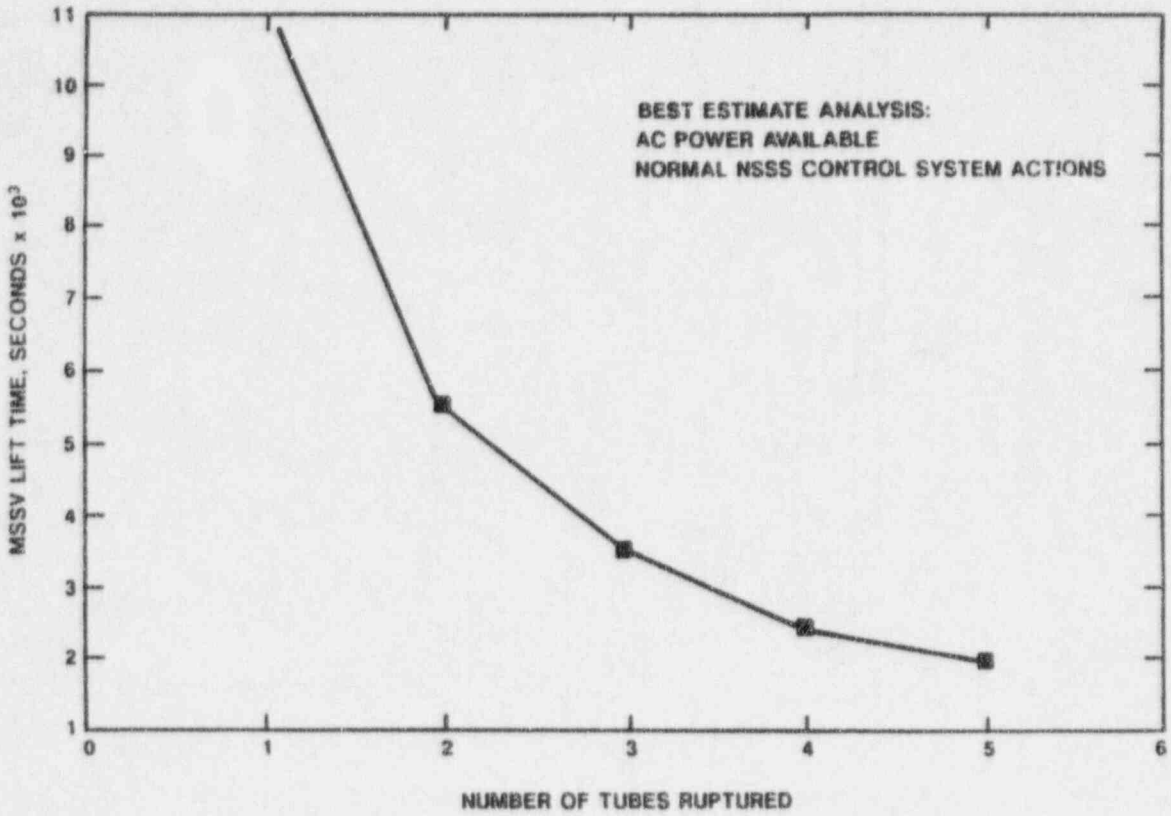

Figure 1
MSSV Lift Time vs. Number of Tubes Ruptured

© 1995 Combustion Engineering, Inc.
All rights reserved

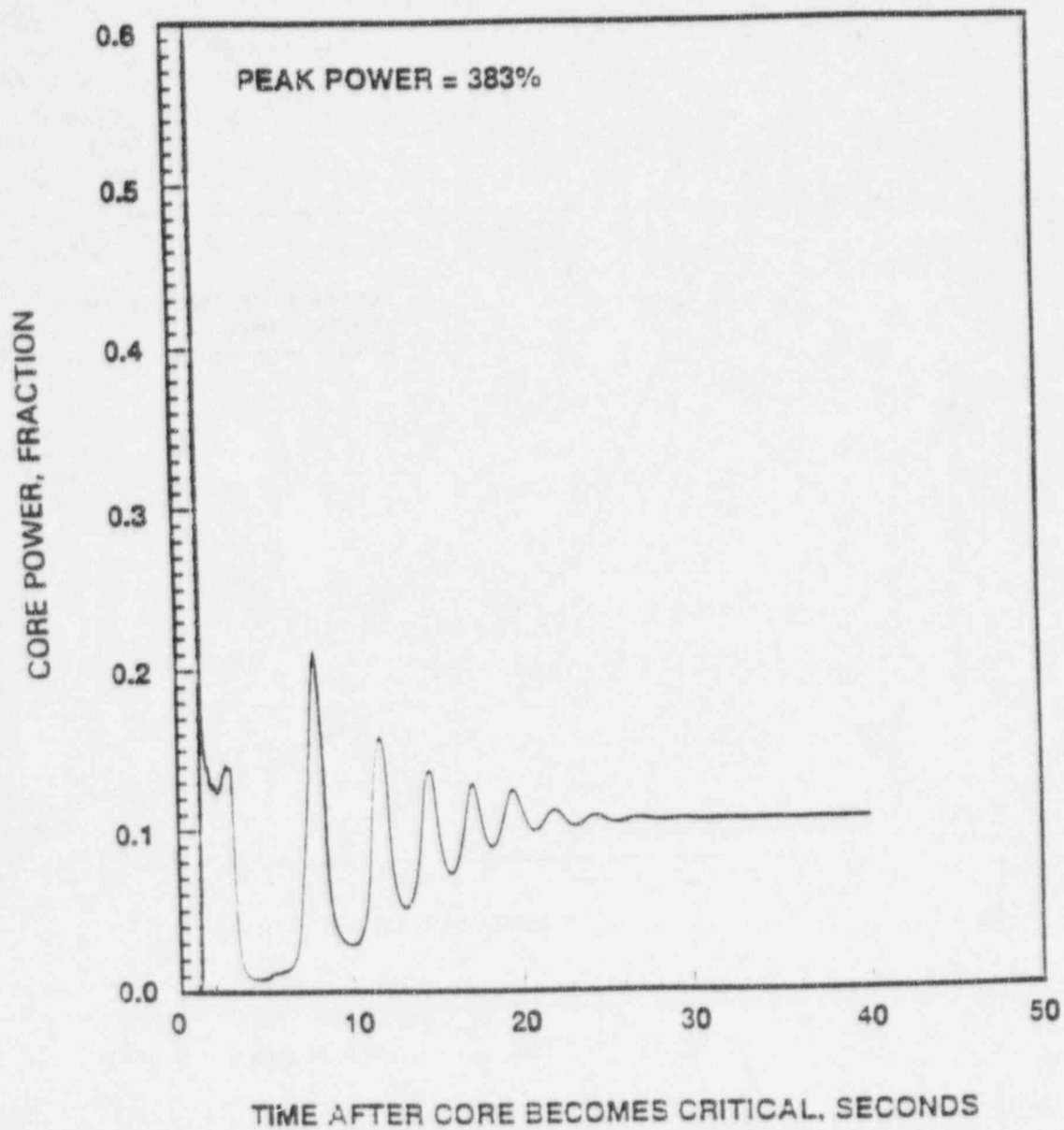

Figure 2
Normalized Power after Core Becomes Critical

© 1995 Combustion Engineering, Inc.
All rights reserved

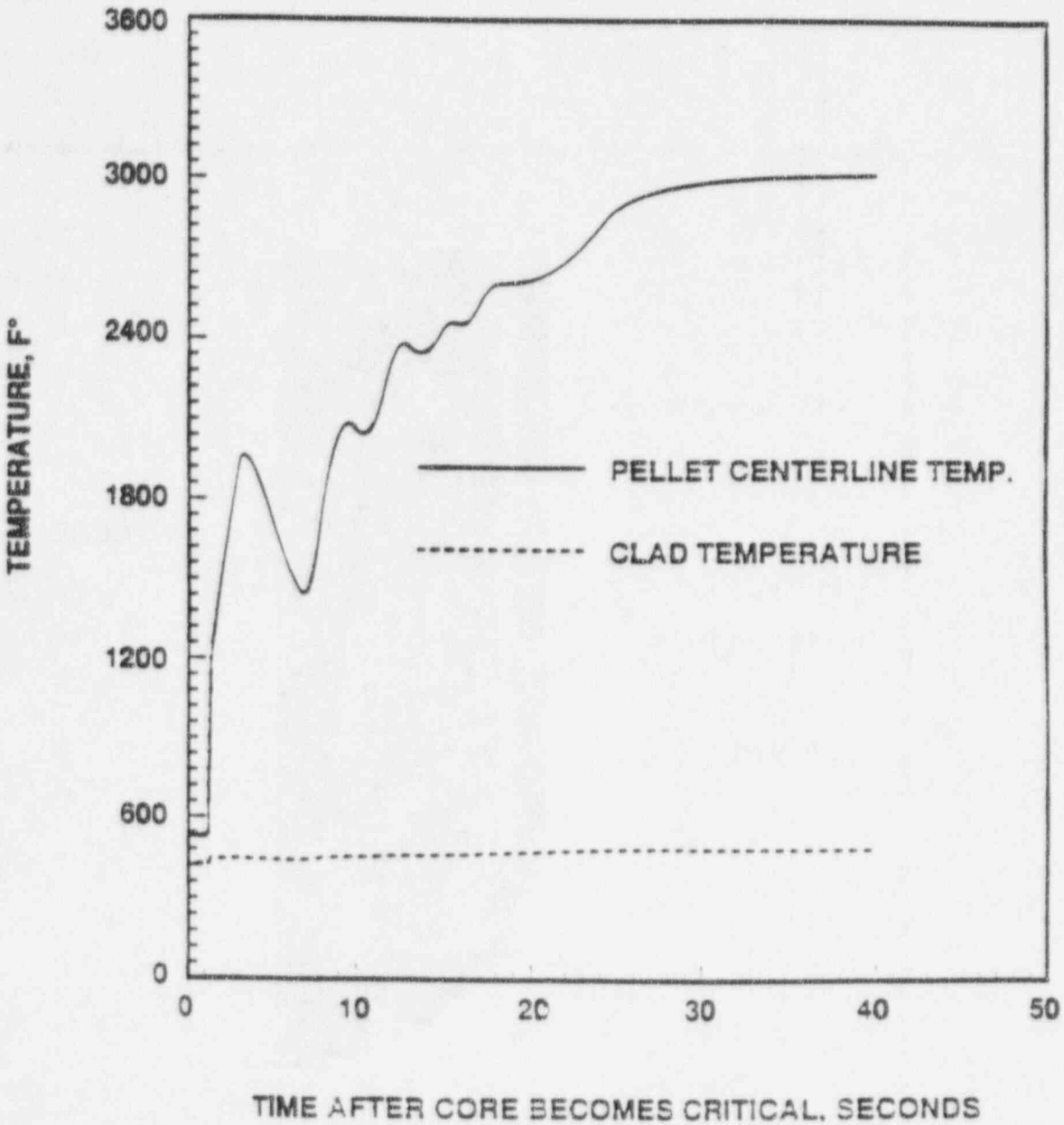

Figure 3
Hot Spot Temperature Transients

© 1995 Combustion Engineering, Inc.
All rights reserved

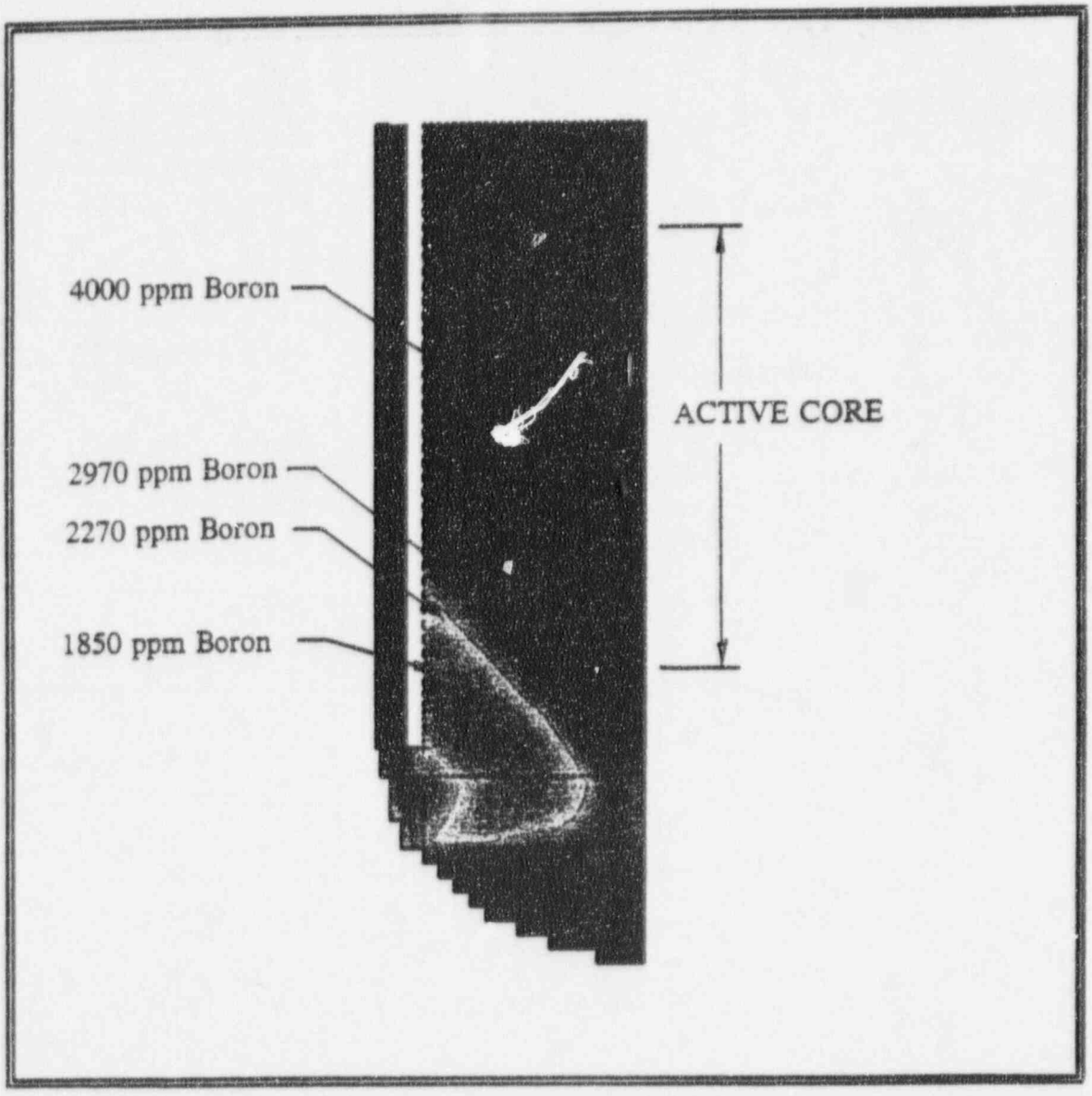

Figure 4
Boron Concentration at 13.5 Seconds with
RCP Restart

© 1995 Combustion Engineering, Inc.
All rights reserved

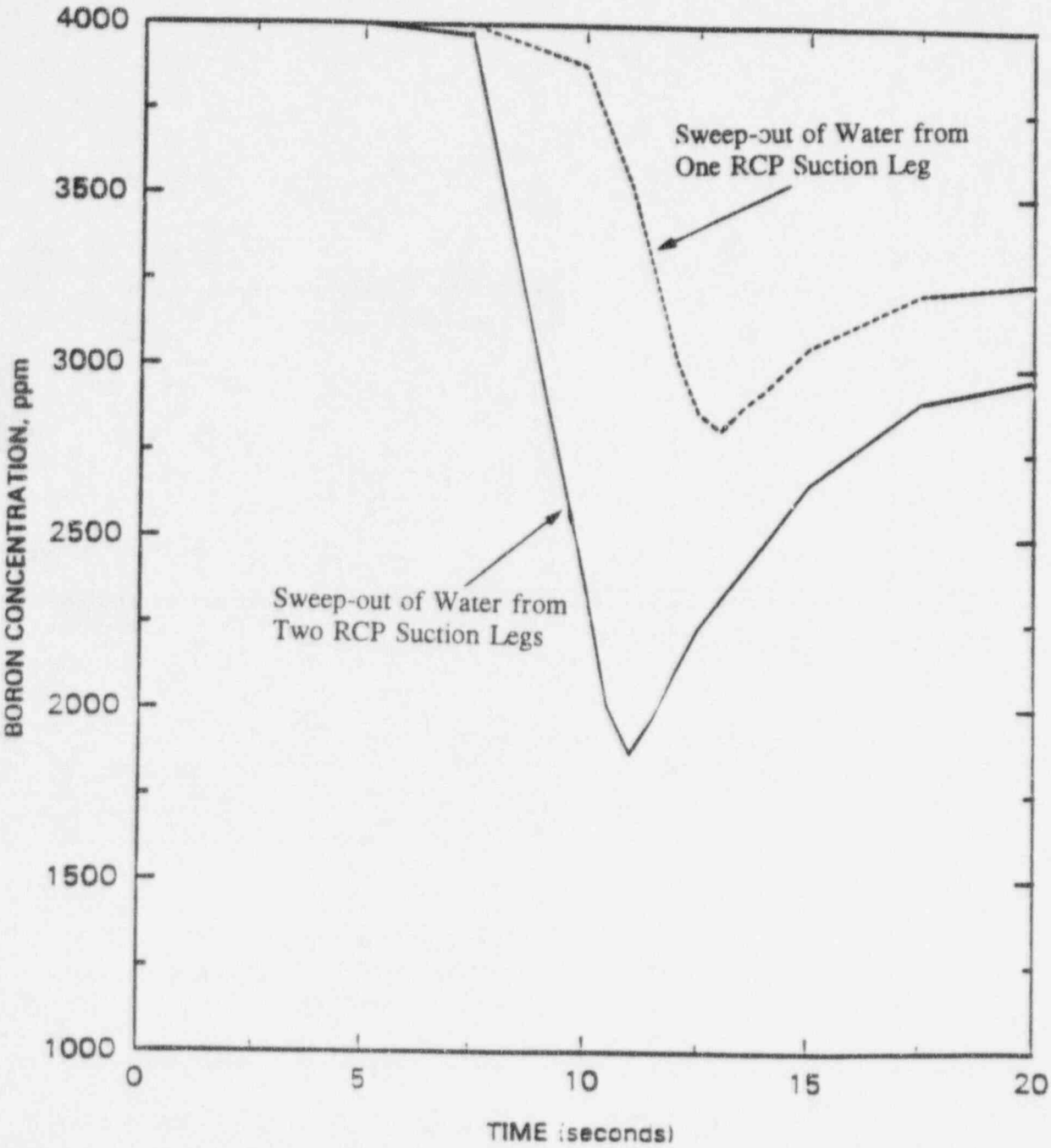

Figure 5
Minimum Boron Concentration with
RCP Restart

© 1995 Combustion Engineering, Inc.
All rights reserved

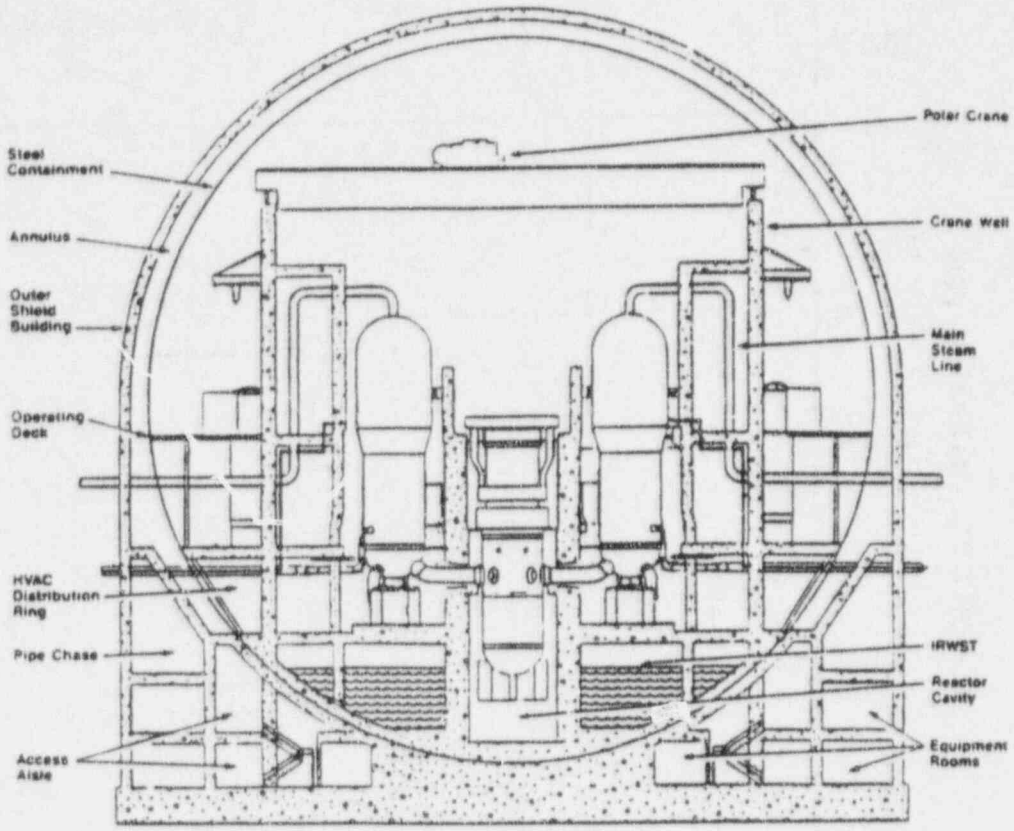

Figure 6
Elevation View of System 80+™ Containment
and Shield Building

© 1995 Combustion Engineering, Inc.
All rights reserved

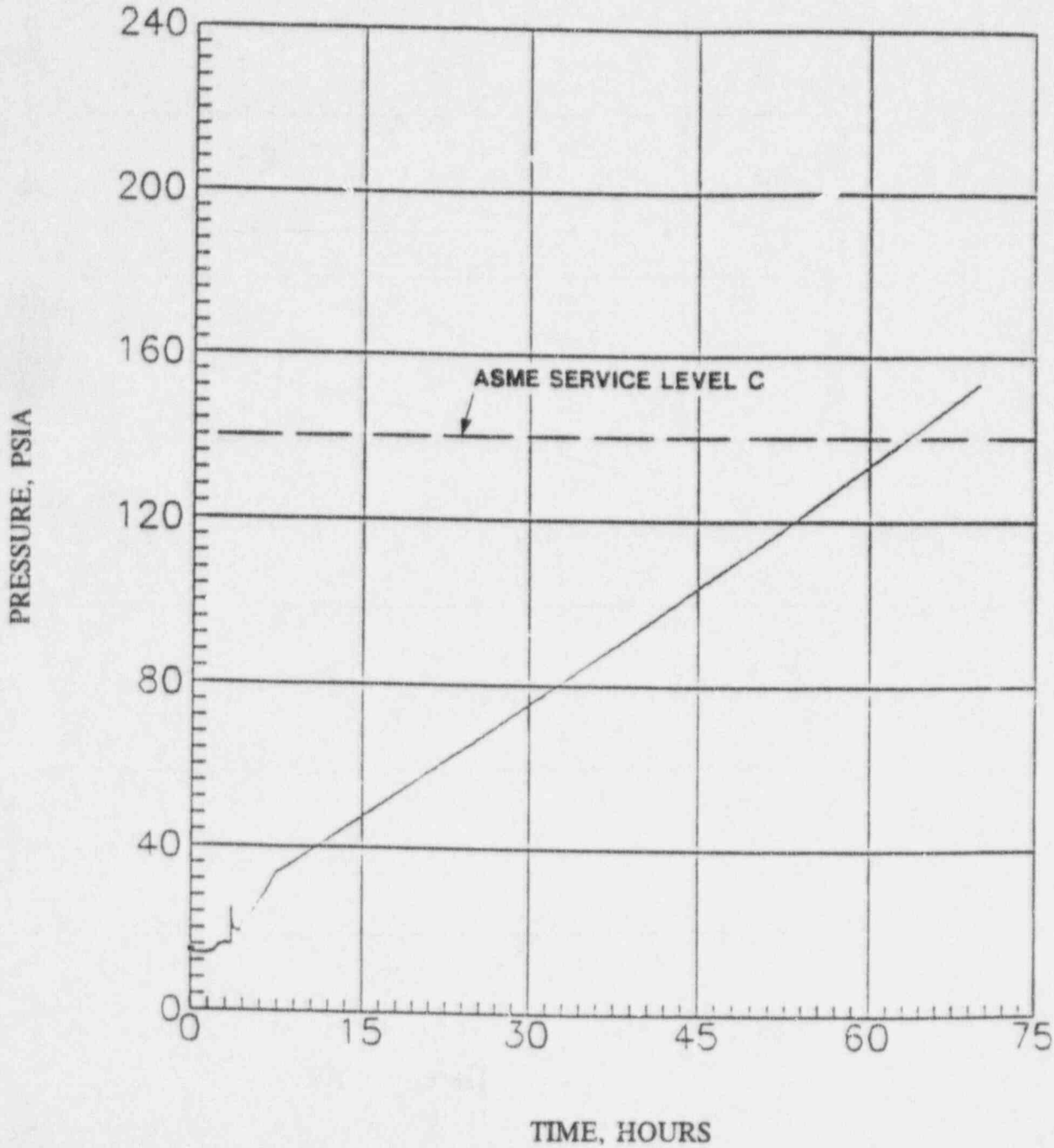

Figure 7
Station Blackout with Wet Cavity
Containment Pressure vs. Time

© 1995 Combustion Engineering, Inc.
All rights reserved

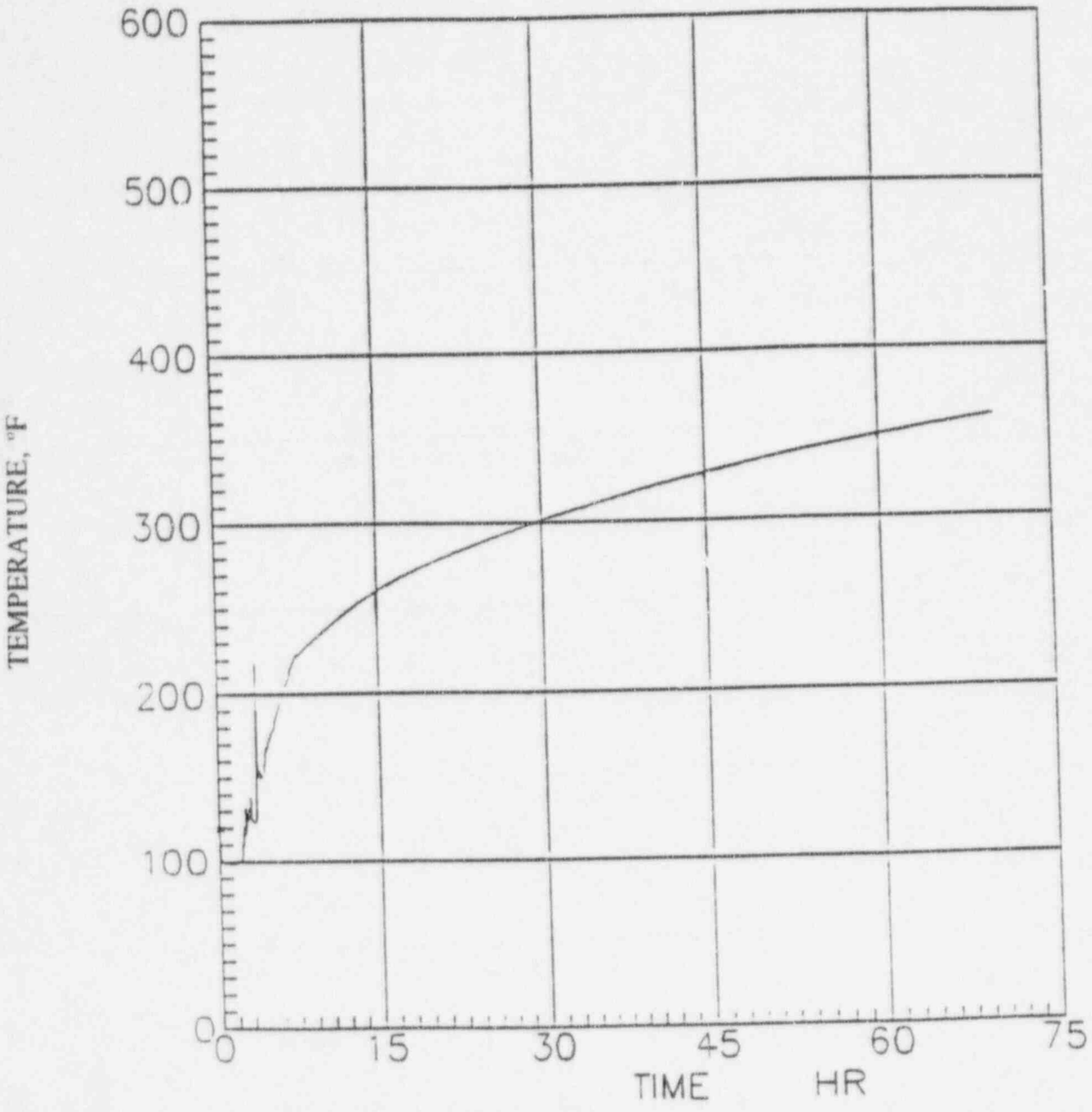

Figure 8
Station Blackout with Wet Cavity
Containment Temperature vs. Time

© 1995 Combustion Engineering, Inc.
All rights reserved

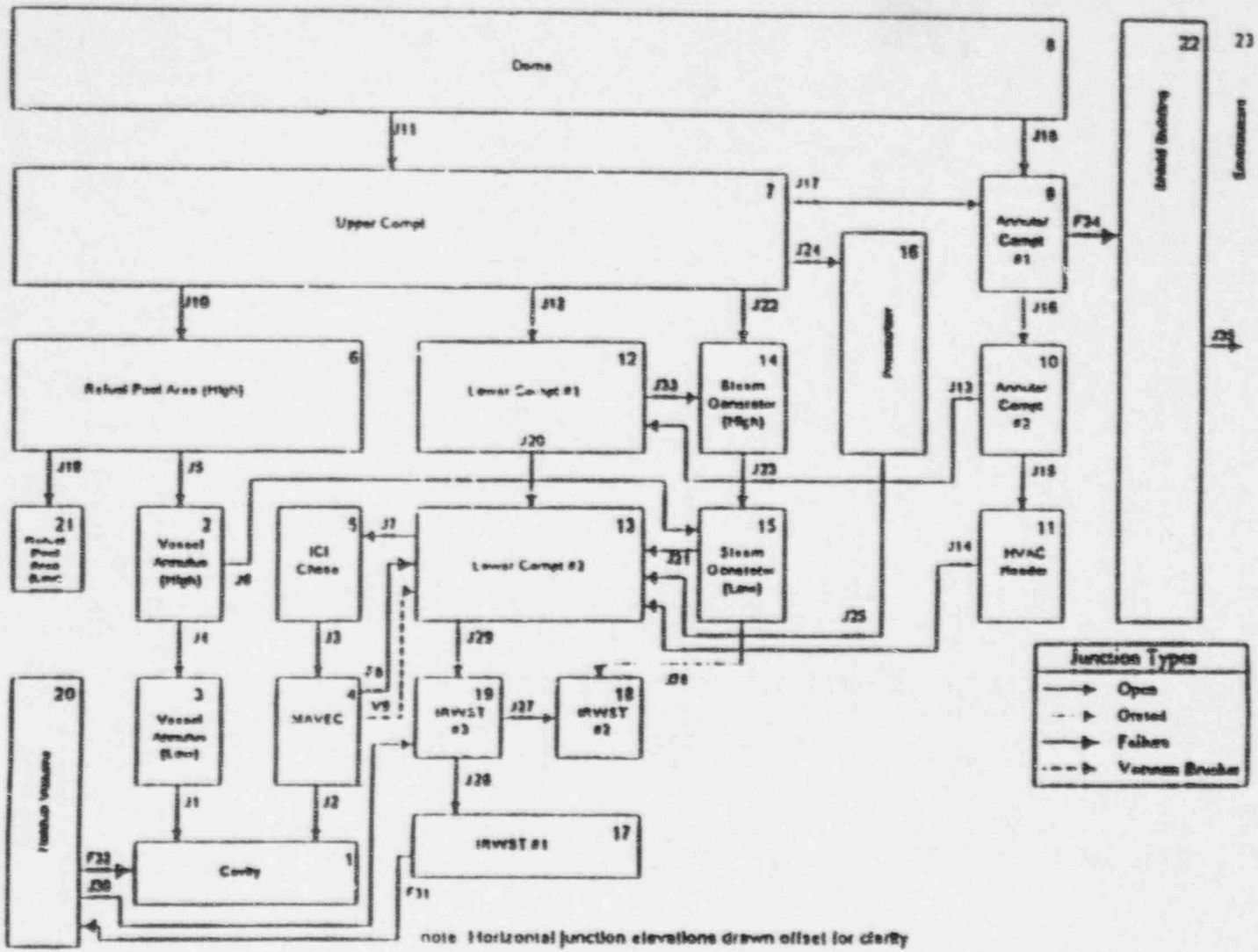

Figure 9
Containment Nodalization Using MAAP 4
Generalized Containment Model

© 1995 Combustion Engineering, Inc.
All rights reserved

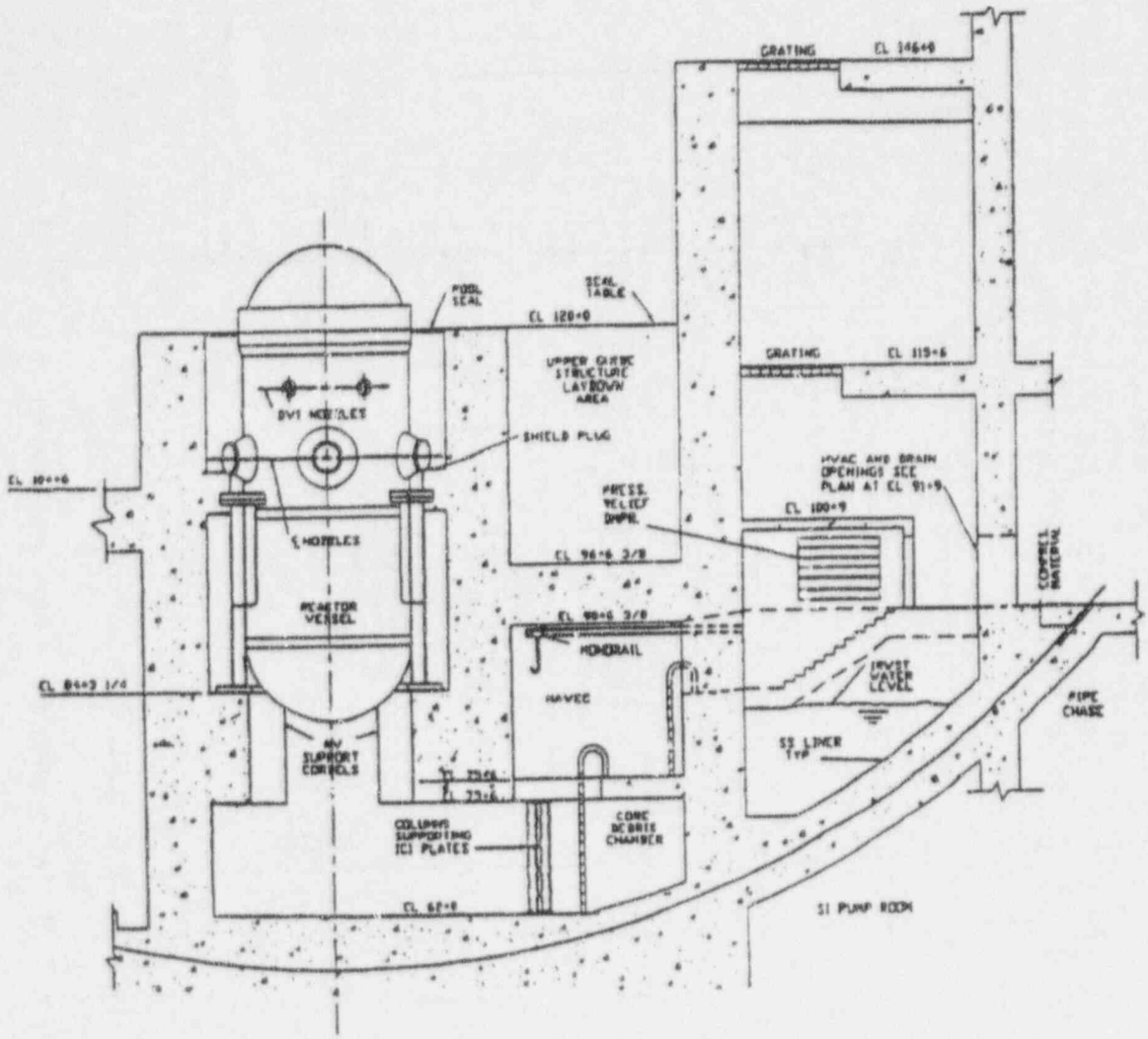

Figure 10
Elevation View of Reactor Cavity

© 1995 Combustion Engineering, Inc.
All rights reserved

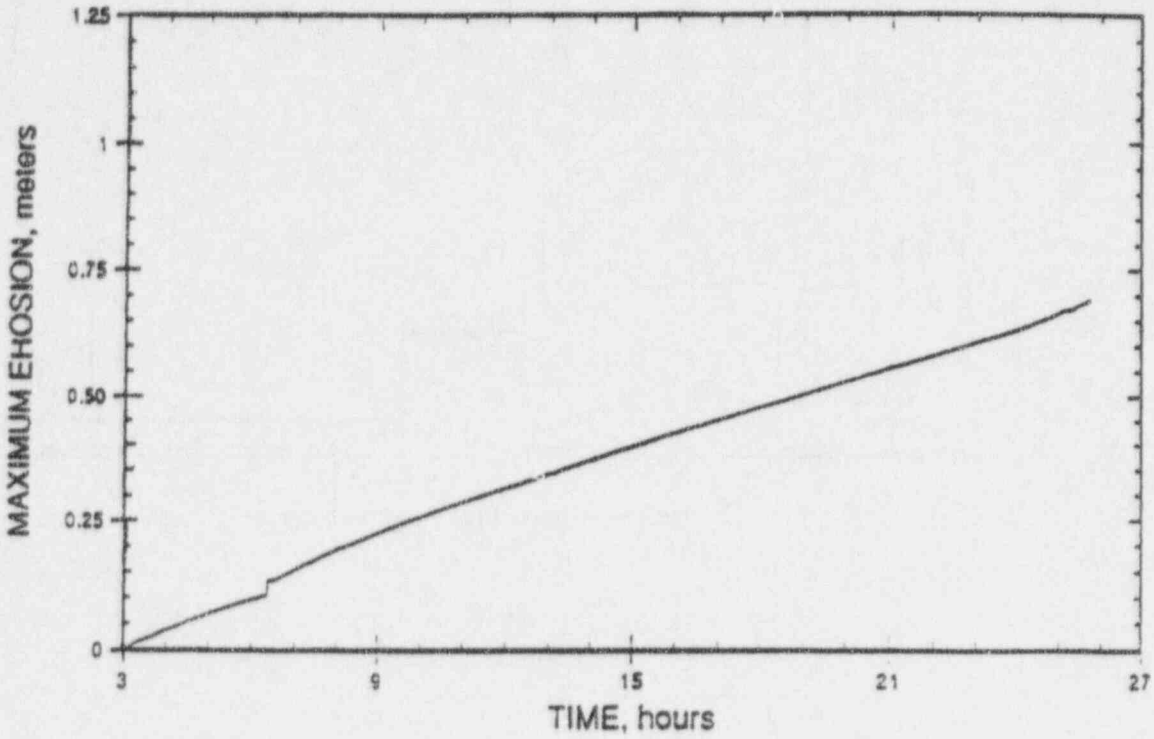

Figure 11
CORCON-MOD3 Prediction of Axial Erosion
Profile for the System 80+™ Basemat

© 1995 Combustion Engineering, Inc.
All rights reserved

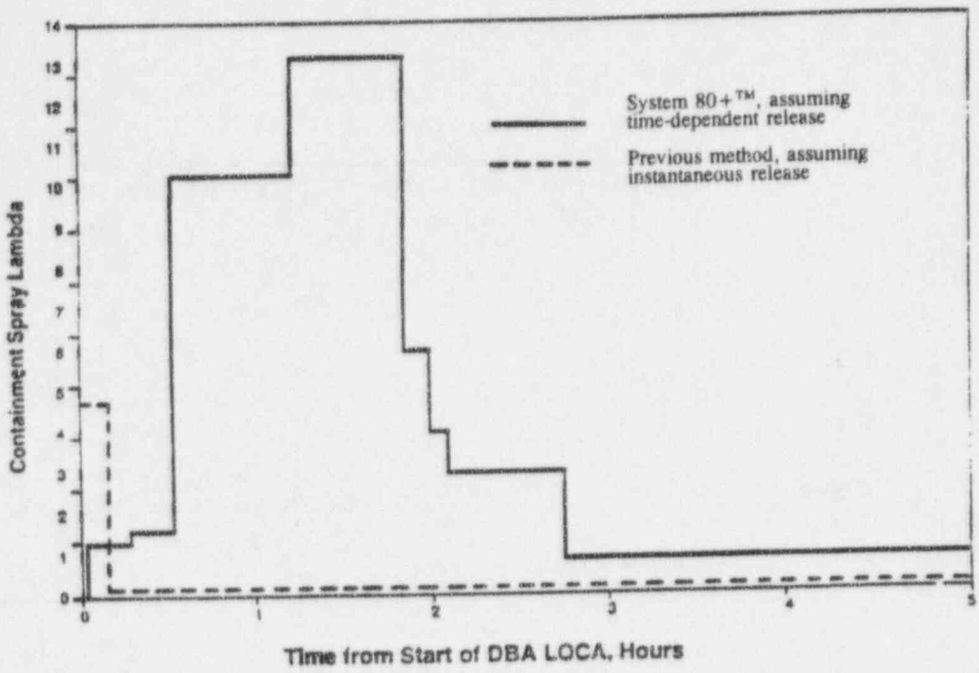

Figure 12
Containment Spray Lambda vs. Time

© 1995 Combustion Engineering, Inc.
All rights reserved

AP600 DESIGN CERTIFICATION

THERMAL HYDRAULICS TESTING AND ANALYSIS

L. E. HOCHREITER
CONSULTING ENGINEER

E. J. PIPLICA
MANAGER, AP600 TESTING

WESTINGHOUSE ELECTRIC CORPORATION
NURETH-7 CONFERENCE

INTRODUCTION/BACKGROUND

Westinghouse Electric Corporation, in conjunction with the Department of Energy and the Electric Power Research Institute, have been developing an advanced light water reactor design; the AP600. The AP600 is a 1940 Mwt, 600Mwe unit which is similar to a Westinghouse two-loop Pressurized Water Reactor. The accumulated knowledge on reactor design and plant operation has been factored into the AP600 design to reduce the capital costs, construction time, and the operational and maintenance cost of the unit once it begins to generate electrical power. The AP600 design goal is to maintain an overall cost advantage over fossil generated electrical power.

AP600 DESIGN FEATURES

The AP600 primary system, as shown in Figure 1, utilizes a four cold leg, two hot leg configuration with canned-motor primary reactor coolant pumps. The pressurizer used in the AP600 design has a volume of 1600 cu. ft, which is more than 30% larger then any operating two-loop PWR. The larger pressurizer allows the unit to tolerate operational transients with increased margin. There are 145 fuel assemblies in the AP600 core which, for the plant rating, reduces the average kw/ft by 20%. The lower kw/ft provides additional critical heat flux (DNB) margin for operational transients as well as margin for postulated design basis accidents such as the large break loss-of coolant-accident (LOCA). The two hot leg and four cold leg design also results in smaller cold legs for the AP600 compared to a current PWR, 0.559 m (22-inches) in diameter for the AP600 verses 0.686 m (27-inches) in diameter for current PWRs. As a result, the break flow is reduced for the postulated large LOCAs resulting in increased margin for the AP600.

The AP600 also uses direct vessel injection into the downcomer of the emergency core coolant (ECC) such that less cooling water is lost out the break making the ECCS more effective.

The most unique feature of the AP600 is the use of safety grade, passive core cooling systems to mitigate the consequences of postulated accidents. In addition to the passive core cooling systems, the AP600 also utilizes a safety grade passive containment cooling system which provides long term cooling water make-up for core cooling. The AP600 passive core cooling systems are shown in Figures 2 and 3 and include:

1) two large 56.63 cu. ft. (2000 cu. ft.) full system pressure core make-up tanks (CMT) which provide inventory to the primary system in the event of an uncontrolled loss of coolant.

2) an Automatic Depressurization System (ADS) which is located on the pressurizer and the reactor hot legs which acts to depressurize the primary system, into a Incontainment Refuelling Water Storage Tank (IRWST), in a controlled manner when the core make-up tanks have injected sufficient inventory. The ADS valve package is attached to the top of the pressurizer and consists of a two independent trains of valves for depressurization. Each valve package separately discharges into the Incontainment Refueling Water Storage Tank (IRWST) through an individual sparger. A fourth stage twelve-inch ADS valve is attached to the top of the hot legs of the primary loop. These valves discharge directly in the containment and are sized to insure that the primary system will depressurized to the containment pressure.

3) Passive Residual Heat Removal system (PRHR) which is a large primary system C-tube heat exchanger located in the IRWST and provide decay heat removal in the event of loss of steam generator secondary side inventory. The PRHR also provides additional depressurization capability for the AP600 since it provides a direct method of energy release to the containment.

4) incontainment refueling water storage tank (IRWST) which collects the discharge from the ADS and, once the primary system is depressurized, provides a gravity-fed cooling path to the reactor vessel through isolation check-valves for long term cooling. The condensate from the condensed steam on the inside of the containment is directed back to the IRWST such that a reflux cooling loop is established within the containment.

5) large 56.63 cu m (2000 cu ft) gas driven accumulators which are connected to the direct vessel injection lines which provide high flow for rapid core recovery for postulated large-break LOCAs.

6) a especially constructed reactor sump volume into which the liquid break flow collects as well as residual condensate

for the containment which does not collect into the IRWST. This sump can flood-up above the reactor loops such that a sufficient gravity head of water exists which can drive core cooling flow through the isolation check-valves into the reactor downcomer through the direct vessel injection lines once the IRWST liquid level is low.

The AP600 passive safety systems accomplish the same safety function as the active systems, used in current plants, by using natural gravitational forces instead of active components such as pumps, heat exchangers, fan coolers, and sprays, and their supporting electrical, HVAC, and cooling water support systems.

The safety strategy of the AP600 is to provide for a controlled, automatic primary system depressurization in the event that an unrecoverable loss of coolant accident would occur, and the normal support systems are not available. As the primary system depressurizes, core cooling is provided at high pressure by the core make-up tanks and at intermediate pressures by the accumulators. Once the primary system is depressurized to the containment pressure, core cooling is provided by the gravity flow from the IRWST into the reactor vessel. The long term cooling for the core is provided from the IRWST and the reactor sump. The passive safety systems are sized to provide ample flow such that the reactor core remains covered for all but the most limiting LOCA situations.

In addition to the passive core cooling systems, the AP600 uses a passive containment cooling system as shown in Figure 4. A large refillable water storage tank is located on the top of the containment structure. On receipt of a high containment pressure signal or a high containment radiation level, the water form the storage tank begins to flow on to the steel containment structure in a controlled manner. The cooling water flows down along the outside of the containment steel shell and is evaporated as it removes heat from the containment. The containment design also incorporates a shield building with an annular space and air entrances at the top of the structure. Air flow is drawn down the annulus and flows upward counter-current to the downward falling liquid film flow on the steel shell outer surface. The air flow is naturally driven by the buoyant differences between the inlet and the annular region adjacent to the containment steel shell and provides the heat flow path to the environment. The combination of the thin film evaporation and the upward air flow is very effective in removing the containment energy for postulated accident situations. Therefore, the containment shell acts as the heat transfer surface for the exterior cooling as well as the interior cooling where the steam/air atmosphere condenses and the condensate is recycled back to the IRWST to provide continuous core cooling.

AP600 TEST PROGRAM

A comprehensive test and analysis program has been developed to confirm the passive safety features of the AP600 design . The program consists of Basic research experiments to develop an understanding of the key thermal-hydraulic phenomena, large-scale separate effects tests on the major components such as the core make-up tank; the ADS valves, piping and sparger, the PRHR heat exchanger and the passive containment heat removal, and integral effects experiments in which the effects of the different phenomena are present.

The test program has also been designed to specifically respond to USNRC questions and issues on the performance of the passive safety systems; as well as capability of the Westinghouse safety analysis methods to predict the performance of the passive systems. Some of the NRC issues include:

1.) ability of the safety analysis codes to predict the natural circulation flows accurately

2.) possible interactions between passive and active systems

3.) prediction of specific thermal-hydraulic phenomena related to the passive systems such as condensation in the core make up tanks and IRWST; as well as heat transfer in the PRHR.

The AP600 program has been structured to address these issues and to provide data to validate the safety analysis computer codes.

Analysis has been performed on all these experiments using the safety analysis computer codes presented in the AP600 Standard Safety Analysis Report (SSAR).

In addition to the separate effects tests which examine the thermal-hydraulic behavior of a particular component, there are two integral systems experiments in-progress for the AP600 design which will examine systems interaction for the passive safety systems. While the data from the basic research and separate effects tests is used to develop and verify safety analysis component models, the integral systems effects tests are used to verify capability of the analysis methods to predict the integrated passive safety system behavior. The transients which challenge the passive safety system interactions are the small-break LOCA, Large streamline break and steam generator tube rupture.

The AP600 SSAR indicates that the large-break LOCA is very similar to existing PWRs excepting that more LOCA margin is available for the AP600 due to lower kw/ft values, improved blowdown performance of the reactor internals, and the smaller cold legs. The small-

break LOCA is more complex due to the interaction effects of the passive safety systems and the primary loop in determining the gravity driving forces which are do to small temperature, density, and elevational head differences.

The Three integral systems tests which have been performed include;

The full height,full pressure SPES-2 test, which simulated small-break LOCA, steamline break, and steam generator tube rupture experiments

The one-quarter scale low pressure Oregon State University integral systems test, which concentrated on small-break LOCA transients and the transition into passive long term cooling. response.

The large scale containment experiment for the containment analysis validation.

In the paper, each of the principle experiments will be discussed with the analysis of the data and comparisons to the safety analysis models will be provided.

AP600
Passive Safety Systems

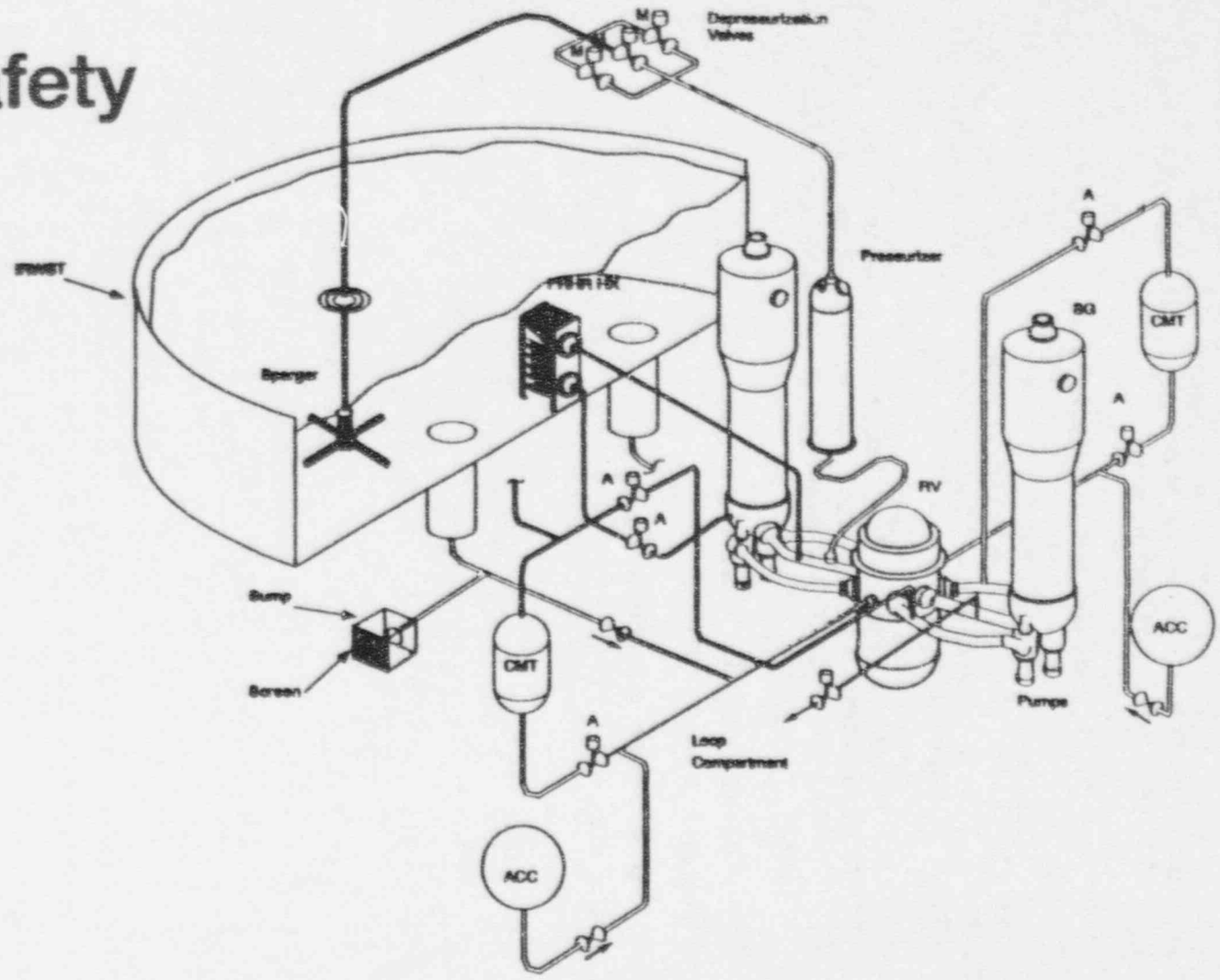

FIGURE 1

PROSPECTS FOR BUBBLE FUSION

R.I. Nigmatulin

Tyumen Institute of Mechanics of Multiphase Systems (TIMMS)

Ufa (Bashkortostan) Branch of Russian Academy of Sciences,

450025 Ufa-Bashkortostan, K. Marx 6, Russia

R.T. Lahey, Jr.

Center for Multiphase Research

Rensselaer Polytechnic Institute, Troy, NY, 12180-3590, USA

ABSTRACT

In this paper a new method for the realization of fusion energy is presented. This method is based on the superhigh compression of a gas bubble (deuterium or deuterium/thritium) in heavy water or another liquid. The superhigh compression of a gas bubble in a liquid is achieved through forced non-linear, non-periodic resonance oscillations using moderate amplitudes of forcing pressure. The key feature of this new method is a coordination of the forced liquid pressure change with the change of bubble volume. The corresponding regime of the bubble oscillation has been called "basketball dribbling (BD) regime" (Nigmatulin et al [1, 2]).

The analytical solution describing this process for spherically symmetric bubble oscillations, neglecting dissipation and compressibility of the liquid, has been obtained. This solution shows no limitation on the supercompression of the bubble and the corresponding maximum temperature. The various dissipation mechanisms, including viscous, conductive and radiation heat losses have been considered. It is shown that in spite of these losses it is possible to achieve very high gas bubble temperatures. This because the time duration of the gas bubble supercompression becomes very short when increasing the intensity of compression, thus limiting the energy losses. Significantly, the calculated maximum gas temperatures have shown that nuclear fusion may be possible (Nigmatulin et al [3]).

First estimations of the affect of liquid compressibility have been made to determine possible limitations on gas bubble compression. The next step will be to investigate the role of interfacial instability and breaking down of the bubble, shock wave phenomena around and in the bubble and mutual diffusion of the gas and the liquid.

1. INTRODUCTION

The forced oscillation of the liquid pressure in a bubbly mixture can cause bubble volume and gas pressure oscillations to take place. Due to the relatively large inertia of the liquid during gas bubble oscillations, very high gas compression and temperatures may occur. Indeed it is well known, that the bubble's gas temperature may be high enough to cause visible light radiation. This phenomena is called *sonoluminescence* (Susslik [4]; Gaitan et al [5]; Kamath et al [6]; Bradley et al [7]; Crum & Cordry [8]; Crum & Roy [9]; Hiller et al [10]).

Average gas temperatures of around 5000 K, which are close to the isentropic temperature of the gas, have been achieved in harmonically-forced sonoluminescence experiments. However, it appears that much higher local temperatures may have occurred. First of all, measurements of the time durations of the light flashes have shown that these durations are extremely short (i.e., less than 50 ps). Indeed, they are much shorter than the characteristic time of bubble compression. Secondly, measurement of the light emission spectrum indicates that a few orders of magnitude higher gas temperatures may have occurred. Thirdly, if one takes into account the shock waves initiated at the bubble's interface and spherical amplification (convergence and cumulation) and the reflection of these waves from the center of the bubble, extremely short time duration (0.1 ps) temperatures, which are much higher than 5000 K appear to be possible. This mechanism was numerically demonstrated in a paper by Wu & Roberts [11], who simulated the effect of an ideal spherically-symmetric shock wave in the bubble. More physically valid calculations of this effect using realistic equation of state for air were done by Moss et al [12]. It should be noted that ideal spherical cumulation gives infinite peak temperatures. Actually the upper limit of the peak temperature is determined by preliminary heating of the gas around the center of the bubble by radiation from the convergent shock wave before its rebound. Of course this radiation-induced heating is significant only when the shock wave becomes very strong. The preliminary heating of a small central region of the gas by radiation before shock compression causes the reflection and rebound of the shock wave not to be ideal.

It appears that it may be a possible to use this phenomena to obtain fusion in deuterium or deuterium/thritium bubbles (Margulis [13]; Bradley et al

[7]). However, for this to be feasible it is necessary to achieve very high compression-induced temperatures (i.e. ~ 10^8 K).

2. A NEW METHOD FOR GAS BUBBLE EXCITATION

Superhigh inertial compression of a gas bubble may be achieved by non-linear, non-periodic excitation of the kinetic energy of the liquid surrounding the bubble (Nigmatulin et al [1, 2]). This mode of excitation should allow one to reach very high gas bubble compression and temperature peaks using modest pressure perturbations (0.1 to 1 MPa) and excitation frequencies (~ 1 kHz).

This mode of excitation involves an initial stage of non-periodic liquid pressure forcing with increasing periods associated with the inertial expansion and compression of the bubble. This method is analogous to the method a basketball player uses for gradually increasing the ball's rebound off the floor during dribbling. Instead of periodic impacts by the player's hand on the ball of fixed frequency, the player coordinates his impacts with the ball's motion, not impeding the ball when it is rising and impulsively pushing the ball downward when it is falling. When the amplitude of rebound increases, the periods between the rebounds and the coordinated basketball player's impacts with the ball must increase too. What is happening is that the basketball player "pumps" kinetic energy into the ball which is moving between the floor and the player's hand. This coordination may be treated as a non-linear resonance forcing of the basketball.

When "pumping" kinetic energy into a gas-bubble/liquid system the method used by a basketball player can also be employed. The non-linear, non-periodic resonance excitation method for external liquid pressure forcing is as follows. At the moment of maximum gas bubble expansion, when the bubble's volume begins to decrease (because of the over-expansion of the bubble) the liquid pressure must be quickly increased to reinforce the liquid's compression of the gas bubble. This maximum pressure must be maintained until the moment of the maximum compression of the bubble, whereupon the bubble begins to expand because of over-compression of the bubble. At this moment the liquid pressure must be dropped sharply to its minimum so as not to impede the liquid being radially accelerated due to bubble expansion, and this low liquid pressure must be maintained until the subsequent end of bubble expansion. As the process continues the liquid pressure oscillation periods must also increase as the amplitude of the bubble's radius increases.

Thus the key feature of this method of bubble excitation is a coordination of the non-harmonic bubble oscillations, due to forced pressure in the liquid, with the periods of expansion and compression of the gas bubble.

This method of non-linear, non-periodic resonance excitation, which has been named the "basketball dribbling" (BD) regime, allows one to achieve successively increasing compressions and gas temperature peaks in the gas bubble. These temperature peaks greatly exceed the mean temperature peaks using traditional harmonic excitation with fixed frequency, which is based on the resonance response of the bubble for small amplitude oscillations.

The proposed method for obtaining superhigh gas temperatures may be achieved using feedback between the liquid pressure and bubble volume changes.

For the proposed regime, which has coordinated liquid pressure forcing with the oscillation of the bubble, the total dissipation (i.e., viscous dissipation mechanisms, conductive and radiation heat losses, compressibility of the liquid, etc.) may impose a limitation on the maximum temperature and pressure. Moreover, these losses may cause the establishment of a periodic regime. In addition, evaporation of the liquid at the bubble's interface (during subcritical conditions of the liquid), ionization, not only of the gas atoms but the liquid atoms too, mutual diffusion of the gas and liquid atoms across the interface, compressibility of the liquid, shock wave effects in the liquid and in the gas (Wu & Roberts [11]; Moss et al [12]), and instability of the bubble's interface, may have a significant influence on the maximum temperature and pressure of the gas bubble.

3. A MATHEMATICAL MODEL OF THE PROCESS

As a first step let us consider the mathematical analysis of the process neglecting liquid compressibility[1]. The mathematical description of this process is based on the Rayleigh-Lamb-Plesset equation (i.e., momentum equation for sphericaly-symmetric motion of incompressible liquid, Nigmatulin [14,15]):

$$a\frac{dw}{dt} = \frac{p_g - p_\infty - 2\sigma/a}{\rho_l} - \frac{3}{2}w^2 - \frac{4\mu_l w}{a\rho_l}, \qquad \frac{da}{dt} = w. \tag{3.1}$$

[1]Preliminary analysis of the liquid compressibility will be presented in Section 12.

where $a(t)$ is the instantaneous radius of the bubble, w is the radial velocity of the bubble's interface, ρ_l, μ_l and σ are the density, dynamic viscosity of the liquid and the surface tension, respectively, and p_∞ is the forced liquid pressure (i.e. the pressure impressed on the liquid far from the bubble).

As a first approximation for the equation-of-state of the gas in the bubble, the Van der Waals equation which takes into account the molecular volume for high compression, was used:

$$p_g = R_g T_g \rho_g \frac{\rho_*}{(\rho_* - \rho_g)}, \qquad e_g = c_g T + e_0, \qquad (\rho_* = 3\rho_{cr}). \tag{3.2}$$

Here p_g, T_g , ρ_g, and e_g, are the gas pressure, gas temperature, gas density, and R_g and c_g are the gas constant and constant volume heat capacity of the gas; while $1/\rho_g^*$ corresponds to specific volume of the gas molecules, which is constant and determined by the critical density of the gas, ρ_{cr}.

The Van der Waals gas model in Eq. (1.1) is characterized by a gas constant, R_g, heat capacity, c_g, and density, ρ_{cr}, at the critical point. For hydrogen we have:

$$\rho_{cr} = 31.2 \text{ kg/m}^3, \qquad \rho_* = 3\rho_{cr} = 93.6 \text{ kg/m}^3. \tag{3.3}$$

If the gas pressure is uniform throughout the bubble (i.e. $p_g = p_g(t)$), the internal energy equation for the gas bubble may be reduced to a gas pressure equation (Nigmatulin [14, 15]):

$$\left(1 - \frac{\tilde{\rho}_g}{\rho_g^*}\right)\frac{dp_g}{dt} = -\frac{3\gamma\, p_g}{a} w - \frac{3(\gamma - 1)}{4\pi a^3} q, \tag{3.4}$$

$$q = q_a + q_r, \quad q_r \equiv \int_{V_b} q_r''' dV, \qquad \tilde{\rho}_g \equiv \frac{1}{\frac{4}{3}\pi a^3} \int_{V_b} \rho_g \, dV, \quad \gamma = \frac{c_g}{(c_g + R_g)}.$$

Here q is the total heat loss from the bubble, consisting of heat transfer, q_a, due to the thermal conductivity through the bubble's interface and the energy losses due to radiation, q_r; $\tilde{\rho}_g$ is an averaged density of the gas and γ is the adiabatic exponent of the gas.

The mass conservation law for the gas in the bubble without phase change is,

$$\rho_g a^3 = \rho_{g0} a_0^3, \tag{3.5}$$

where ρ_{g0} and a_0 are the initial density and the initial radius of the bubble.

The system of equations (3.1) - (3.5) must be closed by the constitutive equations for the interfacial heat transfer, q_a, and q_r

Influences of the simplifications connected with spherically-symmetric motion, with incompressibility of the liquid, and the uniformity of the pressure in the gas bubble, will be analyzed and discussed separately.

4. NUMERICAL RESULTS

Figure 1 presents the non-linear oscillations of a hydrogen bubble in water (a_0 = 1 mm, p_0 = 0.1 MPa, Δp_0 = 1 MPa) that is forced harmonically at an angular frequency of $\omega = 10^5$ rad/s, which corresponds to the bubble's linear resonance frequency and is typical of traditional sonoluminescence experiments. The analysis assumes an adiabatic process in the gas (i.e., $q_a = q_r = 0$), and that the gas has a uniform pressure and temperature, and is undergoing an isentropic process. Until the moment $t = 0$ the bubble was assumed to be at rest and in equilibrium (i.e., $w = 0$, $p_\infty = p_g - 2\sigma/a$). In contrast, for $t > 0$ the pressure of the liquid far from the bubble, p_∞, is given by:

$$p_\infty = p_0 + \Delta p \sin\left(\omega t - \tfrac{\pi}{2}\right), \tag{4.1}$$

where p_0 and Δp are the initial liquid pressure and the pressure amplitude of the harmonic oscillations in the liquid far from the bubble. It is seen in Fig. 1 that even without dissipation there is no increase with time of the peak gas temperature. Variation of the forcing frequency, ω, or the period of the acoustic field oscillations, doesn't change the essential result, which is typical of the response seen in harmonically-forced sonoluminescence experiments.

Figure 2 shows the dependence of the various bubble parameters for non-linear, non-periodic resonance "BD" excitation. For the case under the consideration, during the time energy has been "pumped" into the bubble, dissipation, due to liquid viscosity, heat conductivity and radiation losses, have no significant influence.

For every period of compression (or expansion) two subperiods may be noted, as can be seen in Fig. 2. They are: a subperiod of slow compression (or expansion) and a subperiod of very fast compression (or expansion) with a "sharpening" of the temperature - time dependence. The superhigh

temperatures (i.e., $T > 10^4$ K) and pressures take place during a short time interval when the bubble is at it's minimum size.

The dissipation, because of the liquid viscosity, μ_l, thermal conduction, q_a, and radiation, q_r, and the transformation of part of the pumped kinetic energy not only into gas internal energy but also into the internal energy of the liquid due to its compressibility, must evolve asymptotically, after many non-harmonic oscillations, to a coordinated resonance regime of periodic oscillations with fixed frequency (depending of the pressure amplitude of the external forcing) where the amount of kinetic energy "pumped" into the system by external forcing during the period is equal to the quantity of the energy dissipated due to viscosity, thermal conductivity and radiation during the same period.

It is important that the appearance of this stabilized periodic oscillation regime, involving superhigh compression of the bubble, is possible only after non-periodic "basketball dribbling" regime which pumps-up the kinetic energy of the liquid in the oscillating system.

A practical realization of these periodic and non-periodic regimes may be associated with using feedback between the external driving pressure in the liquid, p_∞, and the bubble's transition from compression to expansion and back again. These transitions are determined by the change of the sign of radial velocity, w, on the bubble's interface: when $w < 0$, the pressure p_∞ must be a maximum, while when $w > 0$, the pressure p_∞ must be a minimum.

5. NON-DISSIPATIVE SOLUTION

For an ideal adiabatic behavior of the gas bubble ($q_a = q_r = 0$) and the absence of liquid viscosity ($\mu_l = 0$), one may obtain analytical estimations for the gas parameters at the moment of maximum bubble compression.

It is convenient to use the following non-dimensional variables for the radial velocity and the pressure:

$$A \equiv \frac{a}{a_0} \quad (A_*^3 = \frac{\rho_{g0}^\circ}{\rho_*} << 1), \qquad W \equiv \frac{w}{w_0} \quad (w_0 \equiv \sqrt{\frac{2p_0}{3(\gamma-1)\rho_l}}),$$

$$P \equiv \frac{p_g}{p_0}, \qquad P_\infty \equiv \frac{p_\infty}{p_0}, \qquad P_e \equiv \frac{p_e}{p_0}, \qquad \Theta = \frac{T}{T_0}. \tag{5.1}$$

The gas bubble's pressure and temperature for the reversible adiabatic regime when the gas at its initial state is rarefied (i.e., $\rho_{g0} << \rho_*$) are determined unequivocally by the radius of the bubble:

$$P \approx \left(A^3 - A_*^3\right)^{-\gamma}, \qquad \theta \approx \left(A^3 - A_*^3\right)^{-(\gamma-1)}. \tag{5.2}$$

After neglecting the liquid viscosity term the general solution of Rayleigh-Lamb-Plesset equation, Eq. (3.1), when the pressure at infinity is constant (p_∞ = const) is:

$$W^2A^3 = -\left(\frac{1}{A^3 - A_*^3}\right)^{\gamma-1} - (\gamma - 1)P_\infty A^3 + C, \tag{5.3}$$

$$P_\infty = \text{const}, \qquad C = \text{const}.$$

It is not difficult to show, using the condition of non-compressibility of the liquid for spherically-symmetric flow, that the value W^2A^3 determines the kinetic energy, K, of the liquid surrounding the bubble. That is,

$$K = \frac{1}{2}\rho_l^\circ \int_a^\infty 4\pi r^2 w^2(r)\, dr = 2\pi\rho_l^\circ w^2 a^3 = 2\pi p_0 a_0^3 W^2A^3, \tag{5.4}$$

Equation (5.3) may be interpreted as the energy conservation equation, where the sum of the kinetic energy of the liquid, the internal energy of the gas and the potential energy of the external field is constant.

Thus Eq. (5.3) may be used for a description of the liquid forcing steps (i.e., by step-wise forcing) if for each step we use a constant liquid pressure, p_∞, equal to a fixed p_e or p_0, as in Fig. 2.

Influence of the liquid-viscosity-induced dissipation of the energy in Eq. (3.1) is determined by the term $4\mu_l w/a\rho_l$, which after integration and translation to non-dimensional variables may, in accordance with Eq. (5.3), be characterized by the dissipation term related to the energy of the system given by the integration constant, C. Thus the influence of viscosity on the total energy is determined by the relative viscous dissipation deffect, $\delta\theta_\mu$:

$$\delta\theta_\mu = \frac{8\mu_l}{\rho_l a_0 w_0 C}\int W A\, dA. \tag{5.5}$$

6. ANALYTICAL SOLUTION FOR THE BASKETBALL DRIBBLING REGIME

The mathematical solution of this problem is connected with calculating the integration constant, C, in Eq. (5.3). Then, noting Fig. 3, for the (n - 1)-th expansion period, when the radius is increasing from the minimum value, $A_{(n-1)}$, till the maximum value, $B_{(n-1)}$, driving pressure $p_\infty = p_0$, and for n-th compression, when the radius is decreasing from $B_{(n-1)}$ to the minimum value $A_{(n)}$ at driving pressure $p_\infty = p_e$, we have respectively:

$$W^2A^3 = -\left\{\left(\frac{1}{A^3 - A_*^3}\right)^{\gamma-1} - \left(\frac{1}{A_{(n-1)}^3 - A_*^3}\right)^{\gamma-1}\right\} - (\gamma - 1)(A^3 - A_{(n-1)}^3). \quad (6.1)$$

$$W^2A^3 = -\left\{\left(\frac{1}{A^3 - A_*^3}\right)^{\gamma-1} - \frac{1}{B_{(n-1)}^{3(\gamma-1)}}\right\} - (\gamma - 1)P_e\,(A^3 - B_{(n-1)}^3). \quad (6.2)$$

There is a recurrence equation for subsequent compressions [Nigmatulin et al, 1995b]:

$$\frac{T_{(n)}}{T_0} = \frac{p_e}{p_0}\,\frac{T_{(n-1)}}{T_0}, \qquad \frac{p_{(n)}}{p_0} = \left(\frac{p_e}{p_0}\right)^{\frac{\gamma}{\gamma-1}}\frac{p_{(n-1)}}{p_0}. \quad (6.3)$$

It is useful to separate out the "fast" n-th compression and the following "fast" n-th expansion which are very short in time. For this situation the radius of the bubble is very small ($A << 1$) and the gas in the bubble is supercompressed and superheated. From Eqs (6.1) and (6.2) one may express a simplified equation for the radial velocity for these stages of the BD regime through the maximum temperature $T_{(n)}$:

$$W \approx \pm\sqrt{\frac{T_{(n)}}{T_0}\,\frac{1}{A^3}\left(1 - \frac{T}{T_{(n)}}\right)}, \quad (6.4)$$

$$\left(T = T_0\left(A^3 - A_*^3\right)^{-(\gamma-1)},\ T_{(n)} = T_0\left(A_{(n)}^3 - A_*^3\right)^{-(\gamma-1)},\ p_g = p_0\left(A^3 - A_*^3\right)^{-\gamma}\right).$$

Here the sign "+" corresponds to the n-th expansion, and "-" to the n-th compression.

The "slow" stages of the n-th compression and the preceding (n - 1)-th expansion, correspond to $A >> A_{(n)} > A_*$. These stages characterize the period between the following compressions. The expressions for the radial velocity during these stages follows from Eqs (6.1) and (6.3):

$$W \approx -\sqrt{(\gamma-1)\frac{p_e}{p_0}\frac{1}{A^3}\left(B_{(n-1)}^3 - A^3\right)} \qquad \text{(the n-th slow compression);}$$

$$W \approx \sqrt{(\gamma-1)\frac{1}{A^3}\left(B_{(n)}^3 - A^3\right)} \qquad \text{(the n-th slow expansion),} \tag{6.5}$$

where,

$$B_{(n-1)}^3 = \frac{p_0}{(\gamma-1)p_e}\frac{T_{(n)}}{T_0}, \qquad B_{(n)}^3 = \frac{1}{(\gamma-1)}\frac{T_{(n)}}{T_0}. \tag{6.6}$$

It is useful to introduce the characteristic velocity, $w_{(n)}$, determining the kinetic energy, $K_{(n)}$, of the liquid and equate it to the velocity of the liquid at the moment when the radius of the bubble, a, is equal to initial radius, a_0. The kinetic energy of the liquid, which causes bubble compression, is converted into the internal energy of the gas in the bubble with temperature $T_{(n)}$. This velocity is calculated from the following energy conservation equation:

$$E_{(n)} = K_{(n)}, \tag{6.7}$$

$$E_{(n)} = \tfrac{4}{3}\pi a_0^3 \rho_{g0} c_g T_{(n)}, \quad K_{(n)} = 2\pi a_0^3 \rho_l w_{(n)}^2.$$

After simple transformations we may write the following formula for the characteristic velocity of the liquid (when the initial bubble radius is: $a = a_0$) which is capable of compressing the bubble to temperature $T_{(n)}$:

$$w_{(n)} = \sqrt{\frac{2}{3(\gamma-1)}\frac{p_0}{\rho_l}\left(\frac{T_{(n)}}{T_0}\right)}. \tag{6.8}$$

It is interesting that this velocity does not depend of the value of the initial radius, a_0. At room conditions (p_0 = 0.1 MPa, T_0 = 300 K) for a hydrogen bubble in water, the velocity required to reach $T_{(n)} = 10^8$ K, neglecting the dissipation and liquid compressibility is:

$$w_{(n)} \approx 6000 \text{ m/s}.$$

It should be noted that to have "basketball dribbling" type resonance pumping of kinetic energy into the system it is not necessary to have exactly a

stepwise driving pressure p_∞, stopping and starting exactly at the moments of the maximum and minimum bubble radius. It is only important that the positive work, $W_{(c)}$, of the external forces during the compression ($w < 0$) time, $t_{(c)}$:

$$W_{(c)} = -4\pi \int_{t_{(c)}} p_\infty a^2 w \, dt \tag{6.9}$$

exceed the negative work, $W_{(e)}$, of the external forces during the expansion ($w > 0$) time, $t_{(e)}$:

$$W_{(e)} = -4\pi \int_{t_{(e)}} p_\infty a^2 w \, dt. \tag{6.10}$$

together with the energy dissipation and power losses during the time interval $t_{(c)} + t_{(e)}$.

7. THE TIME DURATIONS OF THE DIFFERENT STAGES

On the basis of the equations in the previous section one may obtain some estimations for the time durations of the slow (t_{sc}) and fast (t_{fc}) bubble compression stages, starting from the equation:

$$dt = \frac{da}{w}, \tag{7.1}$$

The time duration of the n-th period of the BD regime is practically equal to the sum of (n - 1)-th "slow" compression and n-th "slow" expansion as the time duration of the "fast" compression stages, $\delta t_{(n)}$, are negligibly small. Indeed (Nigmatulin [1, 2]),

$$t_s \approx t_{se} + t_{sc} = \frac{0.915\, a_0}{(\gamma - 1)^{1/3}} \sqrt{\frac{\rho_l}{p_0}} \left[1 + \left(\frac{p_0}{p_e} \right)^{5/6} \right] \left(\frac{T_{(n)}}{T_0} \right)^{1/3}. \tag{7.2}$$

The time duration of the "fast" bubble compression stages, $\delta t_{(n)}$, when the bubble is supercompressed, will be calculated as the time for the compression from the high temperature state of the gas, with temperature T' (which will be taken to be of the same order as $T_{(n)}$), to the maximum compression at temperature $T_{(n)}$, and then to expand to the state again having

temperature T'. Keeping in mind that the "fast" compression and expansion times are practically equal, it can be shown that:

$$\delta t_{(n)} \approx a_0 \sqrt{\frac{2\rho_l}{3(\gamma-1)p_0 A_*}} \left(\frac{T_0}{T_{(n)}}\right)^{\frac{\gamma+1}{2(\gamma-1)}} \sqrt{\frac{T_{(n)}-T'}{T_{(n)}}}. \tag{7.3}$$

In particular, for a bubble with an initial radius of $a_0 = 0.1$ mm in water ($\rho_l = 10^3$ kg/m^3), at with the standard room initial temperature and pressure ($T_0 = 300$ K, $p_0 = 0.1$ MPa), for the compression with a maximum temperature of $T_{(n)} \approx 3\times10^5$ K, the time duration of the compressed state with a temperature higher than $0.5T_{(n)}$ is only $\delta t_{(n)} \sim 10^{-11}$ s.

It is seen that a fundamental principle property of the "basketball dribbling" regime for bubble compression is: the higher the intensity of the compression, characterized by the temperature ratio ($T_{(n)}/T_0$), the shorter the time of the compressed state.

8. ESTIMATION OF VISCOUS DISSIPATION

The influence of viscosity, in the accordance with Eq. (5.5), is determined by the relative viscous dissipation defect, $\delta\theta_\mu$, for BD excitation:

$$\delta\theta_\mu = \frac{8\mu_l}{\rho_l a_0 w_0} \frac{\sqrt{8/3}}{\left[(\gamma-1)P_e\right]^{1/2}} \left(\frac{T_{(n)}}{T_0}\right)^{-1/2}. \tag{8.1}$$

For a bubble with an initial radius of $a_0 = 0.1$ mm in water at the standard initial room conditions $T_0 = 300$ K, $p_0 = 0.1$ MPa, for the compression with a maximum temperature $T_{(n)} > 3\times10^5$ K, the effect of viscous dissipation is relatively small, $\delta\theta_\mu < 10^{-6}$. It is important to note that the relative influence of viscous dissipation decreases with an increase of the intensity of the compression, which is characterized by $T_{(n)}/T_0$. Equation (8.1) for the dependence of dissipation defect, $\delta\theta_\mu$, on $T_{(n)}$ is also shown in Fig. 4.

9. HEAT LOSS ESTIMATIONS

Let us now estimate the thermal (q_a) and radiation (q_r) losses supposing that these losses ($q = q_a + q_r$) are governed by adiabatic temperatures.

There is a simplified model (Nigmatulin [14]) for thermal conductivity losses, q_a, which is related to the temperature driving potential, $T - T_0$, and the radial velocity w:

$$q_a = 4\pi a^2 \, \mathrm{Nu} \, k_g \frac{T - T_0}{2a}, \tag{9.1}$$

$$\mathrm{Nu} = \begin{cases} \sqrt{\mathrm{Pe}}, & \mathrm{Pe} \geq 100, \\ 10, & \mathrm{Pe} \leq 100. \end{cases} \qquad \mathrm{Pe} = 12(\gamma - 1)\frac{T_0}{|T - T_0|}\frac{a|w|}{\nu_g}, \quad \nu_g = \frac{k_g}{\rho_g c_g}.$$

Here k_g and ν_g are the heat conductivity and thermal diffusivity coefficients of the gas, and c_g is a constant volume heat capacity of the gas. For high temperature and a high velocity compression stage, one overestimates the heat losses using the correlation for Nu given by:

$$\mathrm{Nu} = 10 + \sqrt{\mathrm{Pe}}. \tag{9.2}$$

Assuming a temperature dependence of the gas heat conductivity for an ionized gas:

$$k_g = k_{g0}(T/T_0)^{\chi}, \quad (\chi \approx 0.5 \text{ to } 2.5), \tag{9.3}$$

we may use the following simplified expression for the thermal losses, q_a, which consists of two components:

$$q_a = q_s + q_w, \tag{9.4}$$

$$q_s = q_s^{\circ} A\left(\frac{T}{T_0}\right)^{1+\chi}, \qquad q_s^{\circ} = 20\pi a_0 k_{g0} T_0,$$

$$q_w = q_w^{\circ} |W|^{\frac{1}{2}}\left(\frac{T}{T_0}\right)^{\frac{1+\chi}{2}}, \qquad q_w^{\circ} = 4\pi a_0^{\frac{3}{2}}\sqrt{k_{g0}T_0 p_0}\sqrt{\frac{6p_0}{(\gamma - 1)\rho_l}}.$$

The radiation loss, q_r, is the equilibrium radiation from a hydrogen (i.e., deuterium or tritium/deuterium) plasma. It consists of four components:

$$q_r \leq q_\sigma + q_B + q_L + q_R, \tag{9.5}$$

where q_σ is thermal (i.e., black body) radiation heat transfer, q_B is the Bremsstrahlung radiation losses, q_L is the line losses, and q_R is the recombination losses. The last three components are associated with the plasma (ionization) state of the gas.

Thermal radiation heat transfer takes place through the gas/liquid interface and using the Stefan-Boltzmann constant, $\sigma = 5.7\times10^{-8}$ W/m^{2}K^4, is given by:

$$q_\sigma = 4\pi r^2 \sigma[T^4 - T_0^4]. \tag{9.6}$$

This expression may be simplified and approximated by:

$$q_\sigma \approx q_\sigma^\circ A^2 \left(\frac{T}{T_0}\right)^4, \qquad (q_\sigma^\circ = 4\pi a_0^2 \sigma T_0^4). \tag{9.7}$$

The other radiation terms are bounding by Eq. (9.6) and are connected with the amount of gas ionization and are distributed within the bubble's volume. For a hydrogen plasma they are approximated by the following formulas (Stacey [16]):

$$q_j = \tfrac{4}{3}\pi a^3 Q_j, \qquad j = B, L, R;$$

$$Q_B = C_B \kappa^2 n^2 \left(\frac{T}{T_{ev}}\right)^{1/4}, \quad Q_L = C_L \kappa^2 n^2 \left(\frac{T}{T_{ev}}\right)^{-1/2}, \quad Q_R = C_R \kappa^2 n^2 \left(\frac{T}{T_{ev}}\right)^{-3/2} \tag{9.8}$$

$$(C_B = 4.8\times10^{-37}\ \text{W}\cdot\text{m}^3,\ C_L = 1.8\times10^{-38}\ \text{W}\cdot\text{m}^3,\ C_R = 4.1\times10^{-38}\ \text{W}\cdot\text{m}^3,$$
$$T_{ev} = 11.6\times10^6\ \text{K}),$$

where n is the number of atoms per unit volume, κ is the ionized fraction of the atoms, which is determined by the gas temperature T, and atom density, n.

The conservation law for number of atoms implies:

$$na^3 = n_0 a_0^3, \ \text{or} \quad n = n_0 A^{-3}, \qquad n_0 = \frac{2p_0}{k_e T_0}. \tag{9.9}$$

Here n_0 is the atom density at the initial state (i.e., for a two atom gas such as for hydrogen) when the bubble radius is a_0, $k_e = 1.38\times10^{-23}$ J/K is the Boltzmann constant.

As a first approximation the ionization fraction, κ, may be estimated by the Saha equation:

$$\kappa(T, n) = \frac{2}{1+\sqrt{1+4/\kappa_*}} \qquad (0 < \kappa < 1), \tag{9.10}$$

$$\kappa_* = \frac{n_*}{n}, \qquad n_* = n_*^\circ \left(\frac{T}{T_*^\circ}\right)^{3/2} \exp\left[-\frac{T_*^\circ}{T}\right], \quad n = n_0 A^{-3}.$$

$$T_*^\circ = E_*/k = 1.578\times10^5\ \text{K}, \quad n_*^\circ = \frac{(2\pi m_e k T_*)^{3/2}}{h^3} = 1.507\times10^{29}\ \text{m}^{-3},,$$

$$(m_e = 9.1\times10^{-31}\ \text{kg}, \quad h = 6.63\times10^{-34}\ \text{J}\cdot\text{s}).$$

Here $E_* = 13.6$ eV is the ionization energy for hydrogen, h is the Planck constant, and m_e is the mass of an electron.

Using the Saha equation, which is appropriate for equilibrium ionization, we overestimate the plasma radiation. These radiation terms should overstate the actual energy losses because we have neglected the reflection of radiation from the interface.

Energy losses may be characterized by the relative temperature defects, $\delta\theta_j$ ($j = a, \sigma, B, L, R$), during the maximum compression for the period between t' and the final compression, having in mind only the "fast" stage of the compression (i.e. when $T >> T_0$ and $A << 1$):

$$\delta\theta_j = \frac{\delta\Theta_j}{\frac{4}{3}\pi r_0^3 \rho_{g0} c_g T_{(n)}}, \quad \delta\Theta_j = \int_{t'}^{t(a_{(n)})} q_j(t)\, dt, \quad j = a, \sigma, B, L, R. \tag{9.11}$$

The heat loss from the bubble, $\delta\Theta_j$, may be calculated supposing that the intensity of heat losses, q_j, is determined by an adiabatic gas bubble temperature, $T(A)$, which overestimates energy losses:

$$q_j = q_j(T(A)), \tag{9.12}$$

Using the expressions in Eq (6.4) for W (i.e., for the "fast" stages of gas bubble compression or expansion) and getting dA/dT, from Eq (5.2), one may write the temperature defect due to the different kind of heat losses.

Figure 4 are some typical results for calculations (Nigmatulin et al [3]) of relative energy losses, $\delta\theta_j$. Separately the energy defects $\delta\theta_j$ are calculated for the electron gas heat conductivity, $\delta\theta_e$ ($j = e$, see (9.3) for q_a when $\chi \approx 2.5$), and viscosity of the liquid, $\delta\theta_\mu$ ($j = \mu$, see (8.1)). It can be seen that the black body radiation temperature defect, $\delta\theta_\sigma$ ($j = \sigma$), due to q_σ, is always dominant at high gas temperatures.

10. NEUTRON PRODUCTION

The balance equation for the neutron production per unit volume and unit time due to fusion reactions in the gas bubble is given by:

$$\frac{dN'''}{dt} = n^2(t)\, \sigma_V(T). \tag{10.1}$$

Here N''' is the concentration of neutrons per unit volume; n is the concentration of hydrogen atoms (ions), and σ_V is a reaction rate parameter. For instance, for a tritium and a deuterium plasma at a temperature of $T = 10^8$ K, the reaction rate parameter, σ_V, equals 1.09×10^{-22} and 0.626×10^{-24}

m^3/s, correspondingly. Data for other temperatures (Miley et al [17]) are well approximated by the following Arrenius type formula (Nigmatulin et al [3]):

$$\sigma_V = z_0 \exp\left[-\frac{T_*}{T} + (-1)^i \frac{T^2}{T_{**}^2}\right] \qquad (T < 3\times10^{10}). \tag{10.2}$$

For spherical bubbles with radius $a(t)$, and assuming a uniform temperature in the gas bubble, we have:

$$\frac{dN}{dt} = J(T, n, a), \qquad J = \frac{4}{3}\pi\, a^3(t)\, n^{2\prime}(t)\, \sigma_V(T). \tag{10.3}$$

To calculate the neutron production for one compression, as in Eq. (9.12), it is necessary to integrate this equation in time, thus:

$$\delta N_{(n)} = 2\int_{t}^{t(a_{(n)})} J(T)\, dt = 2\int_{a}^{a_{(n)}} J(T)\, \frac{da}{w} = \frac{2a_0}{w_0}\int_{T}^{T_{(n)}} \frac{J(T)}{W}\frac{dA}{dT}dT. \tag{10.4}$$

Using Eqs (6.4) and (5.2) for W and dA/dT, one may write the expression for δN as:

$$\delta N = J_0\ I_N(T_{(n)}), \tag{10.5}$$

where,

$$I_N(T_{(n)}) = \left(\frac{T_{(n)}}{T_0}\right)^{-1/2} \int_{T}^{T_{(n)}} A^{-1/2} \exp\left[-\frac{T_*}{T} - \frac{T^2}{T_{**}^2}\right]\left(\frac{T}{T_n}\right)^{\vartheta}\left(1 - \frac{T}{T_{(n)}}\right)^{-1/2} \frac{dT}{T_{(n)}},$$

$$J_0 = \frac{8\pi a_0^4 n_0^2 z_0}{\vartheta(\gamma-1)w_0}, \qquad \vartheta = -\frac{\gamma}{\gamma-1} = -\,2/3.$$

For a simple estimation we may use the simplified formula for neutron production in the bubble during BD excitation:

$$\delta N \approx 6a_0^4 \left(\frac{\rho_* \mathcal{N}}{M_{mol}}\right)^{7/6} \frac{\rho_l^{1/2}}{k^{5/6}}\, \frac{p_0^{1/3}\, \sigma_V(T_{(n)})}{T_0^{1/3}\, T_{(n)}^{1/2}} \sqrt{1 - \frac{T_{ef}}{T_{(n)}}}, \tag{10.6}$$

where $\mathcal{N} = 6.022\times10^{26}$ (kmol)$^{-1}$ is the Avogadro number, M_{mol} is a molecular weight of the initial gas. Here it was supposed that for $T < T_{ef}$ the value of σ_V is very small and neutron production is negligible.

For a tritium or a deuterium bubble of $a_0 = 0.1$ mm in water, having initial room temperature conditions and compressed to a temperature of $T_{(n)} \approx 10^8$ K ($T_{ef} \approx 5\times10^7$ K), we obtain for tritium:

$$\delta N \approx 10^{12} \text{ to } 10^{13} \tag{10.7}$$

and for deuterium:

$$\delta N \approx 10^{10} \text{ to } 10^{11} \tag{10.8}$$

fusion reactions per bubble, per compression.

The number of nuclei of the two atomic gas in the bubble is:

$$N_0 = \tfrac{4}{3}\pi a_0^3 \rho_{g0} \frac{2\mathcal{N}}{M_{mol}}. \tag{10.9}$$

For the bubbles considered in Eqs (10.7) and (10.8) the number of nucleis was 2×10^{14}. Each nucleus of deuterium or tritium may produce one neutron. This means that the fusion resource will be exhausted after 10 to 10^2 oscillations of a deuterium-thritium bubble, and 10^3 to 10^4 oscillations of a deuterium bubble.

The expected frequency of the compressions is $\omega \sim 10^3$ s^{-1} but the supercompression process occurs in an extremely short period of time, $\delta t_{(n)} \sim 10^{-15}$ s for $a_0 = 0.1$ mm. This implies the possibility of additional dissipation processes and the need for new physical laws for a more proper consideration of the process. Indeed, more detailed bubble and plasma dynamics analyses are necessary and experimental confirmation is needed for these results. Nevertheless, they are very promising and very exciting.

11. ENERGY ESTIMATIONS (INCOMPRESSIBLE LIQUID)

The energy which is necessary to compress the gas bubble up to a superhigh temperature, $T_{(n)}$, is equal to:

$$E_{(n)} = \tfrac{4}{3}\pi a_0^3 \rho_{g0} c_g T_{(n)} = \tfrac{4}{3}\pi a_0^3 p_0 \frac{M_{mol}}{M_{at}(\gamma - 1)} \frac{T_{(n)}}{T_0}, \tag{11.1}$$

where M_{at} and M_{mol} are molecular weights of one atom and molecule (for a two atomic gas, $M_{mol}/M_{at} = 2$).

The number of possible fusion reactions is equal one half of all nuclei, and denoting by U the energy release of one fusion reaction, we may derive the possible total energy release due to fusion in one bubble as:

$$W = \tfrac{1}{3}\pi a_0^3\,\rho_{g0}\frac{\mathcal{N}}{M_{mol}}U, \qquad U = \begin{cases} 2.88\times10^{-12}\,\text{J}, & \text{for D + T;} \\ 5.85\times10^{-13}\,\text{J}, & \text{for D + D;} \end{cases} \tag{11.2}$$

The ratio of this fusion energy release to the energy required to compress the bubble is,

$$\frac{W}{E_{(n)}} = \frac{\mathcal{N}U}{M_{mol}\,c_g T_{(n)}} = \frac{\mathcal{N}M_{at}U(\gamma-1)}{\mathcal{R}M_{mol}T_{(n)}} = \frac{\gamma-1}{2}\frac{U}{kT_{(n)}}, \tag{11.3}$$

Recall, that as it was shown previously in this paper that the energy losses during the forcing of the bubble by the "basketball dribbling" regime are small compared with the "pumped" energy $E_{(n)}$. Thus,

$$\frac{W}{E_{(n)}} = \begin{cases} 700, & \text{for D + T;} \\ 140, & \text{for D + D;} \end{cases} \tag{11.4}$$

12. EFFECT OF THE LIQUID COMPRESSIBILITY

Due to the compressibility of the liquid during superhigh compression of the gas bubble, some part of the kinetic energy is transformed not only into the internal energy of the gas but also into the internal (thermal and elastic) energy of the liquid. In addition, at the moment of the maximum compression of the bubble, when,

$$\frac{da}{dt} = w = 0, \tag{12.1}$$

some part of the energy may be as kinetic energy of the liquid, because, for a compressible liquid, the condition $w = 0$ doesn't mean that all the liquid is at rest.

Full analysis of this problem must be done by solving a system of partial differential equation for the spherical-symmetric flow of an compressible liquid around and in a spherical bubble:

$$\frac{\partial\rho_l}{\partial t} + \frac{1}{r^2}\frac{\partial(\rho_l w r^2)}{\partial r} = 0, \qquad \rho_l\frac{dw}{dt} = -\frac{\partial p_l}{\partial r}, \tag{12.2}$$

$$\rho_l\frac{de_l}{dt} = -p_l\frac{d}{dt}\left(\frac{1}{\rho_l}\right) \qquad \left(\frac{d}{dt} \equiv \frac{\partial}{\partial t} + w\frac{\partial}{\partial r}\right).$$

Here an approximate analysis was done for a barotropic liquid where the pressure and the internal energy depend only on the density:

$$p_l - p_0 = B_0\left[\left(\frac{\rho_l}{\rho_{l0}}\right)^{\gamma_l} - 1\right], \qquad \left(C_{l0} = \sqrt{\frac{\gamma_l B_0}{\rho_{l0}}}\right), \tag{12.3}$$

$$e_l - e_{l0} = \frac{p_0}{\rho_{l0}}\left(1 - \frac{1}{x}\right) + \frac{B_0}{\rho_{l0}(\gamma_l - 1)}\left[\frac{x^{\gamma_l} - 1 + \gamma_l}{x} - \gamma_l\right], \tag{12.4}$$

$$\left(x = \frac{\rho_l}{\rho_{l0}} = \left[1 + \frac{p_l - p_0}{B_0}\right]^{1/\gamma_l}\right),$$

where B_0, γ_l, p_0, ρ_{l0} are constants that characterize liquid, in particular its compressibility; C_{l0} is a sound speed at the initial state: $p_l = p_0$, $\rho_l = \rho_0$.

Neglecting wave phenomena in the bubble and keeping the assumption of homogeneity in the bubble, the problem is closed if we take the boundary condition for the pressure far from the bubble and on it's interface:

$$r = \infty: \quad p_l = p_\infty(t); \qquad r = a(t): \quad p_l = p_g(a). \tag{12.5}$$

The initial conditions determining distributions of velocity, pressure and density were taken at the moment when the pressure around the bubble was not very high so that compressibility of the liquid could be neglected. Figure 5 shows the result for a numerical calculation of the problem made using the Godunov method[2] at moments close to the maximum compression of the gas bubble. The solution showed three very important features. First, for compressions corresponding to gas temperatures of more than 5000 K, liquid compressibility decreases the maximum compression and maximum temperature, $T_{(n)}$, of the gas. In other words, to reach a given gas bubble temperature, compressible liquids need more kinetic energy pumped into the liquid than for the case of incompressible liquid. Secondly, the time duration of high compression at the moments of maximum compression ($T \sim T_{(n)}$) is longer than for the case of incompressible liquid. Thirdly, the thickness, δ_{max}, of the zone of high compression of the liquid is less than, or the same order as, the minimum radius of the bubble:

$$\delta_{max} \leq a_{min}, \tag{12.6}$$

[2] The calculations were made by J. Kaghdan and T. Lutskaya (Keldish Institute of Applied Mathematics of Russian Academy of Sciences).

These solutions and conclusions should be checked using more precise equations-of-state for the liquid and for the gas (Zeldovich & Raizer [18], Moss et al [12]) at high pressures (more than 10^6 bar) and high temperatures (more than 10^6 K). For the liquid it is necessary to take into account the influence of the thermal components of the pressure and internal energy which are proportional to the liquid temperature, T_l. For the gas, for high pressure ($p > 10^3$ bar), the density of the gas, ρ_g, may be larger than $\rho_* = 3\rho_{cr}$. Then for the liquid at high temperatures ($T_l > 10^5$ K) it is necessary to take into account the internal energy and pressure of electronic "gas" which is proportional to T_g^2. Lastly, non-homogeneity of the pressure in the bubble must be considered because of shock wave phenomena. All these points may be very essential to quantify the effect of liquid compressibility.

The numerical calculations have given simplified estimations of the influence of liquid compressibility on the supercompression of the gas bubble, assuming that the liquid compressibility takes place only in a liquid "boundary layer", $a < r < a + \delta$, around the bubble. That is, the other part of the liquid, where the pressure is not so high, may be considered to be incompressible. Then, assuming that, the pressure of the liquid in the compressible "boundary layer" is homogeneous and equals to the gas pressure in the bubble, and the mass of this compressible liquid layer is fixed, the bubble, together with the compressible liquid "boundary layer", form a two-phase bubble surrounded by an incompressible liquid. The behavior of this pseudo-bubble is described by Rayleigh-Lamb-Plesset equation:

$$a_C \frac{dw_C}{dt} = \frac{p_g - p_\infty}{\rho_l} - \frac{3}{2} w_C^2 - \frac{4\mu_l w_C}{R\rho_l}, \qquad \frac{da_C}{dt} = w_C, \tag{12.7}$$

where, now,

$$a_C = a + \delta.$$

The pressure, p_g, in this pseudo-bubble may be expressed through the radius a_C. The variable thickness of the compressible liquid's "boundary layer", δ, and radius, a, may be expressed using the mass conservation equation and the equation-of-state for the liquid, taking into account that the pressure which determines the density of the compressed liquid, ρ_l, is determined by the pressure in the bubble:

$$\rho_l[a_C^3 - a^3] = \rho_{l0}[a_{C0}^3 - a_0^3], \qquad \frac{\rho_l}{\rho_{l0}} = \left[1 + \frac{p_g - p_0}{B_0}\right]^{1/\gamma_l}, \tag{12.8}$$

$$\rho_g a^3 = \rho_{g0} a_0^3.$$

The total internal energy of the bubble and the surrounding compressible liquid at the moment of maximum compression is,

$$E_{(n)} = \tfrac{4}{3}\pi a_0^3\, \rho_{g0}\, c_g\, (T_{(n,C)} - T_0) + \tfrac{4}{3}\pi\left[(a_0 + \delta_0)^3 - a_0^3\right]\rho_{l0}\left(e_{l(n)} - e_{l0}\right). \tag{12.9}$$

Here δ_0 ($\delta_0 << a_0$) is the initial thickness of the compressible liquid's "boundary layer", and $T_{(n,C)}$ is a more realistic estimate of the maximum average temperature of the gas. It will be lower than the temperature $T_{(n)}$, calculated in Sections 5 and 11, in which liquid compressibility was neglected, and the corresponding internal energy of the gas bubble at the moment of maximum compression was calculated by Eq. (11.11).

Equating Eqs (12.9) and (11.11) one may obtain the dependence of more realistic maximum temperature $T_{(n,C)}$ on the idealized temperature $T_{(n)}$.

This evaluation is presented in Fig. 6 for water ($\rho_{l0} = 10^3$ kg/m^3, $C_{l0} =$ 1500 m/s, $\gamma_l = 7.15$) for the same initial conditions[3] as in Fig. 2. and Fig. 4. It is seen that due to compressibility of the liquid a significant part of the pumped kinetic energy is converted into the internal (elastic) energy in the liquid, which causes the temperature of the gas, $T_{(n,C)}$, to be lower than for the case in which an incompressible liquid was assumed. Clearly more detailed calculations are needed to quantify this effect, however the basic conclusion should remain valid.

Figure 7 presents the calculations of the evolution of the process during times close to the maximum compression and maximum temperature of the bubble. The solid lines correspond to the calculation for a compressible liquid, Eqs. (12.8) - (12.12), the dashed lines correspond to an incompressible liquid with the same kinetic energy. It is seen that besides lowering the maximum gas temperature, liquid compressibility increases the time duration of the supercompression. This implies more time for energy losses, which again will reduce the peak gas temperature. Hence, more detailed analyses are needed to properly quantify the mean gas temperature.

---

[3] The calculations of Fig. 6 and 7 were made by V. Shagapov and N. Vakhitova (TIMMS, Ufa (Bashkortostan) Branch of Russian Academy of Sciences)

It necessary to keep in mind that the liquid compressibility effects occur only during short time intervals (< 10^{-11} s), thus they do not significantly influence the results for the basketball dribbling regime, in particular, for the forcing pressure, $p_\infty(t)$, and for the bubble radius, $a(t)$, presented in Fig. 2 for incompressible liquid. In fact, the principle effect will be on the temperature of the gas, $T_g(t)$. Liquid compressibility will lower the gas temperature peaks, as shown by the dashed envelopes of these peaks with and without compressibility in Fig. 2.

13. ON THE BASKETBALL REGIME FOR A BUBBLY MIXTURE

Practical realizations of bubble fusion will likely involve the use the "basketball regime" for a bubbly liquid with a finite void fraction, that is, a bubbly mixture rather than individual bubble (see Fig. 8)

In Fig. 9a is presented the initial stage[4] of the progressively intensifying compression of a bubbly two-phase mixture (glycerine and helium) occupying the cylindrical volume bounded by a solid wall and movable piston shown schematically in Fig. 8. At the initial (non-disturbed) uniform state the length of the cylinder was L_0 = 20 cm, the void fraction was α_{g0} = 0.01, the radius of the bubbles was, a_0 = 1 mm, the pressure was, p_0 = 0.1 MPa, and the temperature was, T_0 = 300 K. The piston produces the pressure, p_p, and velocity v_p disturbance in accordance with "basketball regime" feedback:

$$x = x_p: \quad p_p = \begin{cases} p_{max}, & if\ v_p > 0; \\ p_{min}, & if\ v_p < 0. \end{cases} \quad (p_{max} = 1.2\ p_0, \quad p_{min} = p_0) \qquad (13.1)$$

The state of the two-phase mixture is not homogeneous, but is characterized by waves propagating from the piston to the solid wall, wave reflection from the wall, waves returning to the piston, reflection, from the piston and so on. A calculation is based on the partial differential equations for non-steady, one-dimensional flow of a bubbly liquid (Nigmatulin [14]). In the Fig. 9a evolutions of the piston pressure, the piston velocity and the gas pressure in the bubble in the middle of the volume ($x = L/2$) are shown. It is seen that there is intensification of the bubble volume and pressure oscillations, compared with the simple shock compression of the mixture (p_p = 1.2 p_0 =

[4] The calculations were made by A. Gubaidullin (TIMMS, Siberian Branch of Russian Academy of Sciences)

const) presented on Fig. 9b. Thus it appears that "BD" excitation of superhigh compressions in bubbly mixtures is also possible.

14. SUMMARY AND CONCLUSION

A novel new non-linear method for non-periodic resonance liquid pressure forcing has been proposed for achieving superhigh gas pressures and temperatures in an oscillating gas bubble. It appears that it may be possible to achieve extremely high gas temperatures, including those of interest in fusion energy technology. Moreover, it has been shown that interesting simplified analyses are possible, however, more detailed numerical analysis and experimental confirmation of these results is needed. In particular, it is necessary to consider the influence of liquid compressibility, interfacial instabilities and breaking down of the bubble, and liquid/gas diffusion and mixing near the interface during very short times of extremely high temperature and pressure.

Nevertheless, it appears that bubble fusion may be possible. If so, this could lead to a whole new way or producing economical, safe and environmentally-friendly energy. Hopefully, the work presented herein will motivate the research needed to fully assess the enormous potential of bubble fusion.

REFERENCES

[1] R.I. Nigmatulin, V.Sh. Shagapov, N. Vakhitova, R.T. Lahey, Jr, "A method for superhigh compression of a bubble in liquid by non-periodic resonance vibration with moderate amplitudes," Dokl. Russian Acad. Sci. (1995)

[2] R.I. Nigmatulin, V.Sh. Shagapov, N. Vakhitova, R.T. Lahey, Jr, "A method for superhigh compression-induced temperatures in gas bubble using non-periodic resonance liquid pressure forcing," Chem. Engrg Comm. (to be published) (1995).

[3] R.I. Nigmatulin, V.Sh. Shagapov, N.K. Vakhitova, R.T. Lahey, Jr, M. Embrechts, D. Steiner, F. Bonetto, An analysis of nonlinear, nonperiodicaly forced bubble fusion, Nucl. Engrg Des (to be published) (1995).

[4] K.S. Suslik, "The Chemical Effects of Ultrasound", Scientific American 2, 80-86 (1989).

[5] D.F. Gaitan, L.A. Crum, C.C. Church, R.A. Roy J. Acoust. Soc. Am. 91, 3166 (1992).

[6] V. Kamath, A. Prosperetti, F.N. Egolfopulos "A theoretical study of sonoluminescence", J. Acoust. Soc. Am. 94, 1, 248 (1993).

[7] B.P. Bradley, C.C. Wu, R. Lofstadt, P.H. Roberts, S.J. Putterman, "Sensitivity of sonoluminescence to experimental parameters", Phys. Rev. Lett. 72, No. 9, 1380-1383 (1994).

[8] L.A. Crum, S. Cordry, "Single-bubble sonoluminescence", Bubble Dynamics and Interface Phenomena, (ed. J.R. Blake, J.M. Boulton-Stone & N.H. Thomas), Proc. IUTAM Symposium, Kluwer Academic Publisher (1994).

[9] L.A. Crum, R.A. Roy Sonoluminescence. Science 266, 14 233-234 (1994)

[10] R. Hiller, K. Weninger, S.J. Putterman, B.P. Barber "Effects of noble gas dopping in single-bubble sonoluminescence", Science 266, 14, 248-250 (1994).

[11] C.C. Wu, P.H. Roberts, "Shock-Wave Propagation in a Sonoluminescing Gas bubble," Phys. Rev. Lett. 70, 22, 3424-27 (1993).

[12] W.C. Moss, D.B. Clarke, J.W. White, D.A. Young "Hydrodynamic simulations of bubble collapse and picosecond sonoluminescence", Physics of Fluids 6, 9, 2979-2985 (1994).

[13] M.A. Margulis "Modern Views on the Nature of Acousto-Chemical Reactions", Russian Journal of Physcal Chemistry 50, 1, 1-11 (1976).

[14] R.I. Nigmatulin, Fundamentals of Mechanics of Heterogeneous Mixtures (in Russian), Nauka, Moscow (1978).

[15] R.I. Nigmatulin, Dynamics of multiphase media, Vol. 1, 2, Hemisphere Press (1991).

[16] W.M. Stacey, Fusion. An introduction to the Physics and Technology of Magnetic Confinement Fulion, John Wiley & Sons (1994).

[17] G.H. Miley, G.H., H. Towner, N. Ivich, University of Illinois Nuclear Engineering Report C000-2218-17 (1974).

[18] Ya.B. Zeldovich, Yu.P. Raizer, Physics of Shock Waves and High-Temperature Hydrodynamics Phenomena, Vol. 1, 2, Academic Press, NY, London (1966).

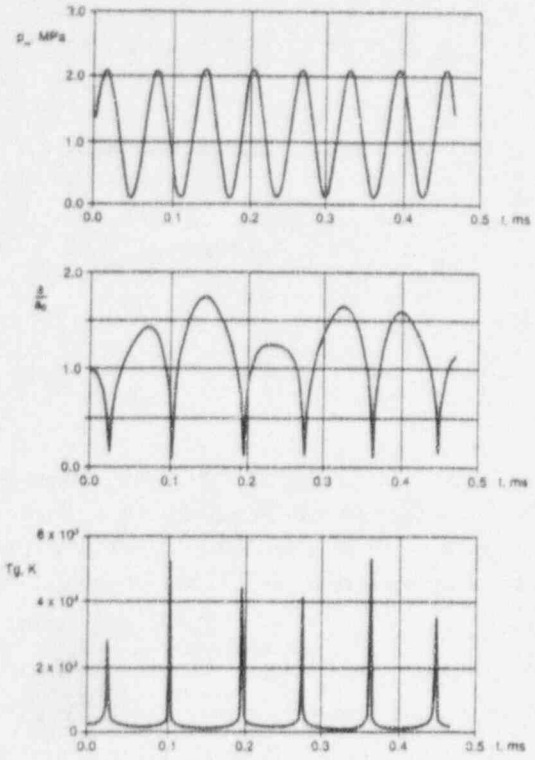

Fig. 1. Calculated results for the non-linear oscillations of a hydrogen bubble (a_0 = 1 mm) in water (p_0 = 0.1 MPa, T_0 = 300 K) driven by harmonic acoustic field with frequency $\omega = 10^5$ s^{-1} and pressure amplitude Δp = 1.0 MPa.

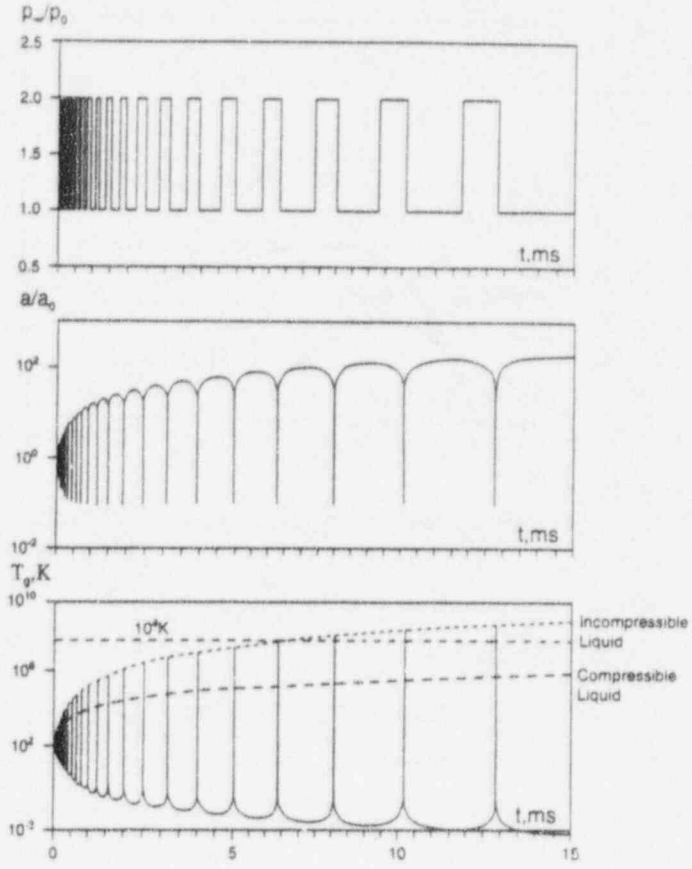

Fig. 2. Calculated results for the non-linear oscillations of a hydrogen bubble (a_0 = 1 mm) in water (p_0 = 0.1 MPa, T_0 = 300 K) driven by resonance pressure excitation, p_∞ (Δp = 1.0 MPa), coordinated with the change in the sign of the radial velocity. The dotted and dashed lines are envelopes of temperature maximums for incompressible and compressible liquids, respectively.

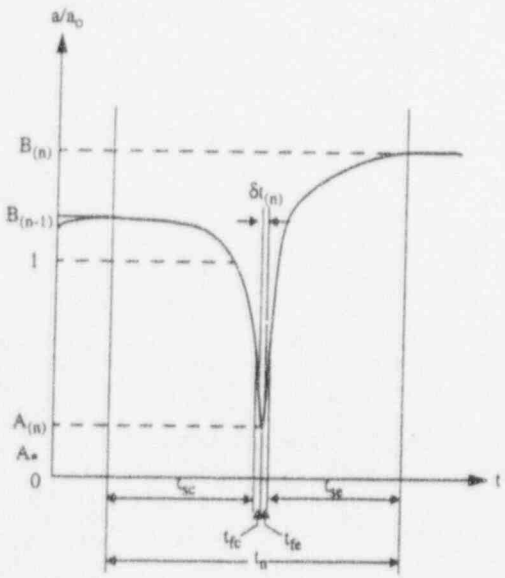

Fig. 3. A qualitative schematic of different stages in the n-th period of compression.

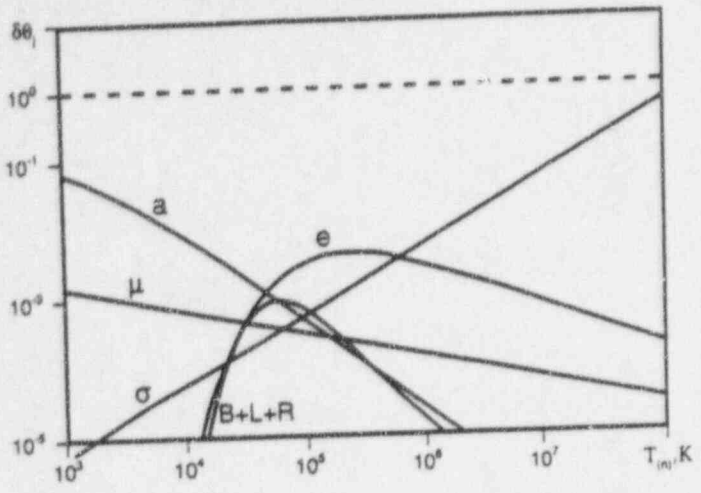

Fig. 4. Energy losses for a hydrogen bubble of radius a_0 = 0.1 mm in water having an initial temperature of T_0 = 300 K and an initial pressure of p_0 = 0.1 MPa. The labels $j = a, e, \sigma, B + L + R, \mu$ correspond to the different energy loss mechanisms or relative temperature defects, namely: $\delta\theta_a$, $\delta\theta_\sigma$, $\delta\theta_e$, $\delta\theta_B + \delta\theta_L + \delta\theta_R$, $\delta\theta_\mu$ respectively.

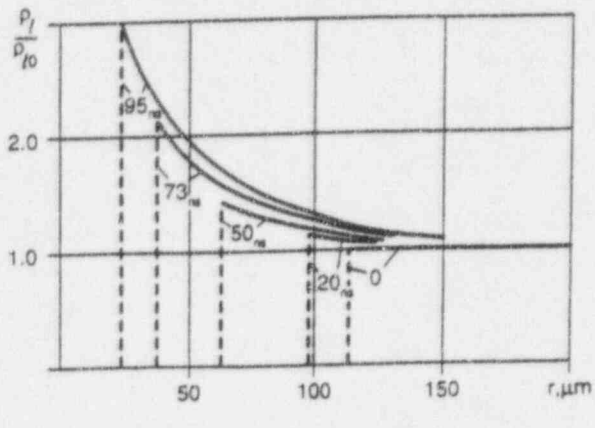

Fig. 5. Distributions of the liquid density around the bubble at the moments close to the maximum compression (i.e., minimum radius) for a hydrogen bubble of initial radius a_0 = 0.1 mm in water for an initial temperature of T_0 = 300 K and an initial pressure of p_0 = 0.1 MPa. The kinetic energy corresponds to $w_{(n)}$ = 1000 m/s (see (6.8), and the number labels correspond to the time moment in ns (10^{-9} s).

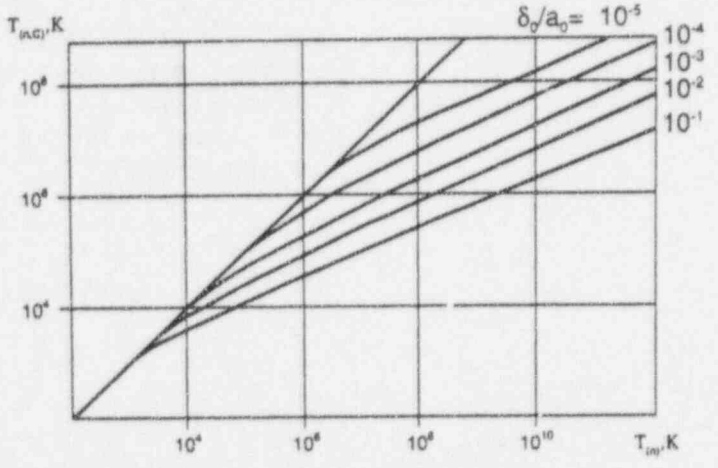

Fig. 6. Maximum temperature of the gas bubble, $T_{(n,C)}$, depending on the maximum temperature $T_{(n)}$ for incompressible liquid and on the relative thickness of the compressible liquid δ_0/a_0. Labels on the curves indicate the initial values of δ_0/a_0.

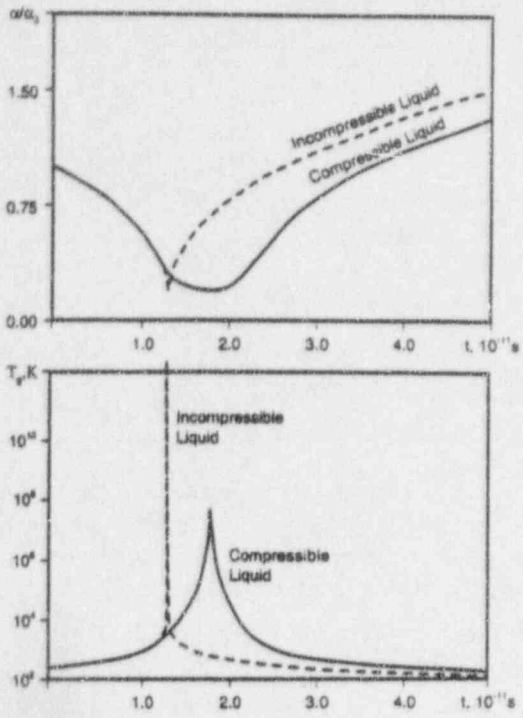

Fig. 7. Numerical calculation of the evolution of the process during the time close to the maximum compression of the bubble taking into account the influence of the liquid compressibility (solid lines) for a hydrogen bubble of initial radius a_0 = 0.1 mm in water for an initial temperature of T_0 = 300 K and an initial pressure of: p_0 = 1.0 MPa. The kinetic energy corresponds to $w_{(n)} = 3 \times 10^6$ m/s. The dashed line corresponds to incompressible liquid for the same kinetic energy.

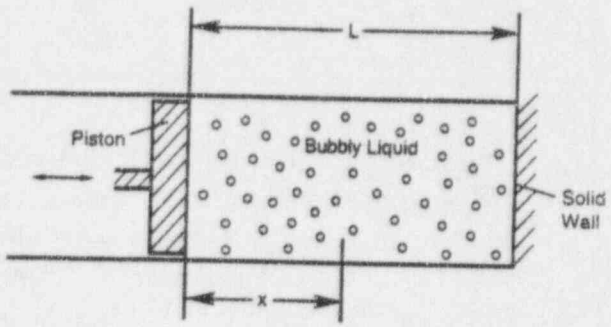

Fig. 8. Schematic of bubbly liquid excitation by a piston.

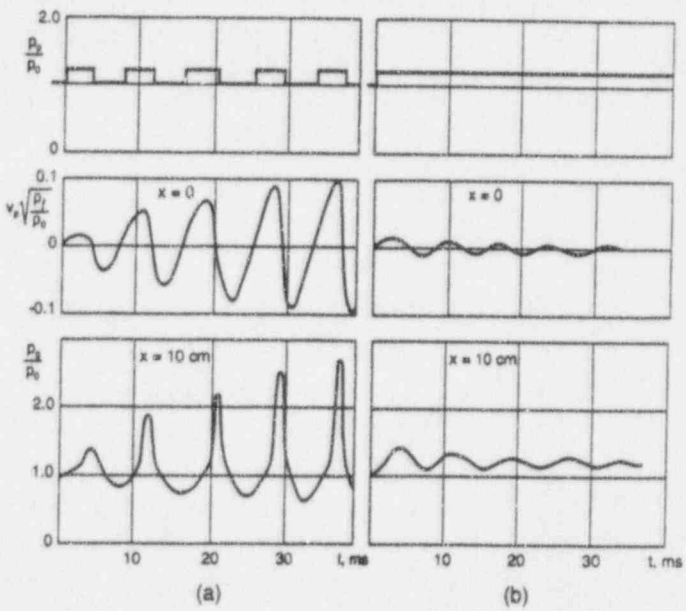

Fig. 9. The basketball regime (*a*), and shock (*b*) compression, of a bubbly liquid.

A MECHANISTIC DETERMINATION OF HORIZONTAL FLOW REGIME BOUNDARIES USING VOID WAVE CELERITY

Jee-Won Park
IAE-ESRC, Ajou University
Suwon, Korea
(Phone) 82-331-219-2669; (Fax) 82-331-216-2672

ABSTRACT

The two-phase flow regime boundaries in a horizontal channel has been investigated by using the behavior of the second order void wave celerities. The average two-fluid model has been constituted with closure relations for horizontally stratified and bubbly flows. A vapor phase turbulent stress model for a smooth interface geometry has been included. It is found that the second order waves (i.e., eigenvalues) propagate in opposite direction with almost the same speed when the liquid phase is stationary. Using the well-posedness limit of the two-phase system, the dispersed-stratified flow regime boundary has been modeled. Two-phase Froude number has been theoretically found to be a convenient parameter in quantifying the flow regime boundary as a function of the void fraction. It is found that interaction between void wave celerities become stronger as the two-phase Froude number is reduced. This result should be interpreted as that gravity and the relative velocity are key parameters in determining flow regime boundaries in a horizontal flow. The influence of the vapor phase turbulent stress found to stabilize the flow stratification.

This study clearly shows that the average two-fluid model is very effective for a mechanistic determination of horizontal flow regimes if appropriate closure relations are developed.

1. INTRODUCTION

Two-phase flow regime transition in a horizontal pipe has been theoretically investigated using the average two-fluid model.

The horizontal two-phase flow is often found in CANDU reactor coolant channel, the horizontal steam generator being used in Russian VVER type reactor, hot legs in PWR midloop operation and so on. Among many interesting phenomena in horizontal two-phase flows, there is a strong trend of each phase being separated due to gravity (i.e., the stratified flow) so that the heat transfer geometry dramatically changes correspondingly. There have been many works concerning flow regime determination in a horizontal pipe. The surface wave (e.g., the long wave) instability is known as one of important stratified/slug flow regime transition mechanisms. Significantly, Taitel & Dukler[1] determined stratified/slug flow regime boundary using inviscid Kelvin-Helmholtz theory. It should be noted that the state-of-the-art nuclear reactor system analysis codes (e.g., RELAP5/MOD3) contain this type of flow regime transition criteria either for stratified-to-dispersed or for dispersed-to-stratified flow transitions. On the other hand, the onset of slugging was also understood as a result of excessive energy (i.e., the kinetic energy and the potential energy) transfer from the mean gas phase to the liquid phase[2]. There also is a series of work which

indicates that the gas phase turbulent stress is very important in controlling stratified flow[3]. Recently, the interfacial shear may need to include the void fraction gradient term[4],[5] for realistic stability behavior in the stratified flows.

Even though much effort has been devoted to determination of the stratified/slug flow regime boundary, various thermal-hydraulic effects haven't been taken into account consistently to the two-phase system yet. Most significantly, the definitions of the phasic pressures for the stratified flow are different from each other in various models and sometimes are not consistently reduced to those of the dispersed two-phase flows. Therefore, we need to develop a model which has clear definition of two-fluid variables all over the flow regimes so that the modeled flow regime boundaries should represent consistent transitions between flow geometries when being used with the average two-fluid equations.

In this study, an average two-fluid model[6],[7] has been constituted with closure relations for horizontal flow. A vapor phase turbulent stress model for a smooth interface geometry has been included. Using the well-posedness limit of the two-phase system, the stratified/slug flow regime boundary has been found. Theoretically, two-phase Froude number has been found to be a convenient parameter in relating the dimensionless void wave celerities between the dispersed and the separated flow regimes. The flow regime transition criteria determined by using the void wave celerities in the separated flow can be consistently reduced to that obtained by previous worker[1] when the vapor phase turbulent stress is neglected. One of the interesting results is that since the two-phase system's eigenvalues of the separated two-phase flow (i.e., the void wave celerities [8],[9],[10],[11]) have almost an equal magnitude and the opposite sign, we find that the waves (i.e., the second order wave in the wave hierarchy) propagate in both direction with the same speed when the liquid phase is stationary.

2. THEORY

The one-dimensional phasic linear momentum equation can be written as[7],[12],[13]:

$$\frac{\partial(\alpha_k \rho_k v_k)}{\partial t} + \frac{\partial(\alpha_k \rho_k v_k^2)}{\partial z} = \alpha_k \rho_k g \cos\beta - \alpha_k \frac{\partial p_k}{\partial z}$$
$$+ \Delta p_{ki} \frac{\partial \alpha_k}{\partial z} + M_{ik} - \tau_i \frac{\partial \alpha_k}{\partial z} + \frac{\partial[\alpha_k (\tau_k + \tau_k^{Re})]}{\partial z} - M_{wk} + \Gamma_k v_{ki} \qquad (1)$$

where ρ_k, α_k, p_k, β, τ_i and τ_k are the phasic density, the volume fraction, the pressure, the angle of inclination of the pipe, the interfacial stress and the phase average viscous stress, respectively. Δp_{ki} is the difference between the phasic interface and the phasic average pressure. The liquid phase interfacial pressure difference (Δp_{fi}) for a dispersed two-phase flow can be given by[13],[14]

$$\Delta p_{fi} \equiv p_{fi} - p_f = -\eta \rho_f (v_g - v_f)^2, \qquad \text{with } \eta = \frac{1}{4} \tag{2}$$

The gas phase interfacial pressure difference is negligible for the dispersed flow. However, when the flow is separated, the gravity head across the channel cross section governs the interfacial pressure difference. The interfacial pressure differences for the stratified horizontal flow can be given by (see Appendix A):

$$\Delta p_{gi} \equiv p_{gi} - p_g = (\rho_g g D \sin\beta)\left(\frac{\sin^3\theta}{3\pi\alpha_g} - \frac{\cos\theta}{2}\right) \tag{3a}$$

$$\Delta p_{fi} \equiv p_{fi} - p_f = -(\rho_f g D \sin\beta)\left(\frac{\sin^3\theta}{3\pi\alpha_f} + \frac{\cos\theta}{2}\right) \tag{3b}$$

As shown in Eq.(3), the interfacial pressure difference for the separated flow has the void fraction dependency, which is quite different from the corresponding term for the dispersed two-phase flows.

M_{ik} is the interfacial momentum exchange which normally includes the interfacial drag and the virtual mass force, that is,

$$M_{ig} = -M_{if} = -\alpha_g (F_D + F_{vm}) \tag{4}$$

For the dispersed flows, the virtual mass force is known to have the form as[15]:

$$F_{vm} = C_{vm}\left(\frac{\partial v_g}{\partial t} + v_g \frac{\partial v_g}{\partial z} - \frac{\partial v_f}{\partial t} - v_f \frac{\partial v_f}{\partial z}\right) \tag{5}$$

The interfacial drag is the major algebraic force acting on the dispersed bubble which can be modeled as

$$F_D = \frac{C_D}{8\alpha_g} \rho_f A_i''' (v_g - v_f)|v_g - v_f \tag{6}$$

where the interfacial area density is given by[16]

$$A_i''' = \frac{3\alpha_g}{R_b} \tag{6a}$$

Harmathy[17] quantified the interfacial drag coefficient (C_D) for ordinary distorted bubbles. Significantly, it is recently found[13] that, for spherical vapor phase the interfacial force required to have the bubbles maintain a spherical shape is

$$m_i = \nabla_z \cdot [\alpha_{g=s} \sigma] = -\frac{3}{10} \frac{\partial}{\partial z} [\alpha_g \rho_f (v_g - v_f)^2] \tag{6b}$$

Since the spherical bubble formation in a horizontal flow is very unlikely except for very low global void fraction, the interfacial force given in Eq.(6b) is neglected in this study. However, for the separated flows, neither the virtual mass nor the interfacial forces can be observed.

M_{wk} is the phasic wall friction which can be modeled as:

$$M_{wk} = \frac{f_w}{2} v_k |v_k| \tag{7}$$

The phasic interfacial stress for the dispersed flows in normally small compared to the other interfacial forces such as the interfacial drag. However, for the separated flow, this is the major interfacial force. The phasic interfacial stress for the separated flow can be modeled as[7]:

$$\tau_i \frac{\partial \alpha_g}{\partial z} = \frac{\xi_i}{A_{x-s}} \tau_{gi} \tag{8}$$

where ξ_i is the wetted perimeter of the vapor phase. τ_{gi} in Eq.(1) should be understood as the interfacial shear force (i.e., the viscous shear) used by previous workers[1],[3].

In this study, the vapor phase turbulent stress, the so-called two-phase Reynolds stress, has been included in the two-fluid model. The source of this stress is clearly from the vapor phase velocity fluctuation from its averaged value in the frame of reference of the liquid phase velocity. It is found that the turbulent stress can be modeled[18] as

$$\tau_g^{Re} = -C_\tau \rho_g |v_g - v_f| (v_g - v_f) \tag{9}$$

It should be noted that the vapor phase Reynolds stress model given by Eq.(9) was derived for the gas flow over a stationary liquid phase. Therefore, this should be used as the first approximation of the turbulent stress effect. Further modeling effort is necessary to incorporate this effect accurately. Finally, the phase average viscous stresses, τ_g and τ_f are normally small for water and have been neglected in this study.

The constitutive relationships used in this study are summarized in Table 1.

Using the phasic continuity equations and the combined momentum equation, we obtain the equation of two-phase system as

$$\underline{\underline{A}}\frac{\partial \underline{\phi}}{\partial t}+\underline{\underline{B}}\frac{\partial \underline{\phi}}{\partial z}=\underline{c} \tag{10}$$

We obtain the dimensionless characteristics of the adiabatically separated two-phase system as (see Appendix B)

$$\lambda^*_{\pm,sep}=\frac{\lambda_{\pm,sep}}{\sqrt{gD}}=\frac{\rho^*_g(\alpha_f-C_\tau)}{(\rho^*_g\alpha_f+\alpha_g)}Fr_{2\varphi}\pm\sqrt{D^*_{sep}} \tag{11}$$

where

$$D^*_{sep}=\frac{\pi(1-\rho^*_g)\alpha_g\alpha_f\sin\beta}{4\sin\theta(\rho^*_g\alpha_f+\alpha_g)} -\rho^*_g Fr^2_{2\varphi}\left[\frac{\alpha_f\alpha_g-\alpha_f C_\tau(\rho^*_g\alpha_f+\alpha_g)-C_\tau{}^2\rho^*_g+2\alpha_f^2C_\tau(1-\rho^*_g)}{(\rho^*_g\alpha_f+\alpha_g)^2}\right] \tag{11a}$$

$$Fr_{2\varphi}=\frac{v_r}{\sqrt{gD}},\qquad v_r=v_g-v_f \tag{11b}$$

It should be noted that we assumed that the liquid phase is stationary in deriving the characteristics.

For the dispersed flow, the dimensionless characteristics can be found by using the same technique with the constitutive relations for the dispersed flow in Table 1.

$$\lambda^*_{\pm,dis}=\frac{\lambda_{\pm,dis}}{\sqrt{gD}}=\frac{(C_{vm}-\eta-k\alpha_g+\rho^*_g\alpha_f)\alpha_f}{(\alpha_g\alpha_f+C_{vm}+\rho^*_g\alpha_f^2)}Fr_{2\varphi}\pm\sqrt{D^*_{dis}} \tag{12}$$

where

$$D^*_{dis}=\frac{(C_{vm}-\eta-k\alpha_g+\rho^*_g\alpha_f)^2}{(\rho^*_g\alpha_f+\alpha_g+C_{vm}/\alpha_f)^2}Fr^2_{2\varphi} +\left[\frac{\alpha_g(\eta+k-C_{vm})+2\alpha_f(\eta-C_{vm}/2)-\rho^*_g\alpha_f^2}{(\rho^*_g\alpha_f+\alpha_g+C_{vm}/\alpha_f)}\right]Fr^2_{2\varphi} \tag{12a}$$

It should be noted that the characteristics for the vertical bubbly flow was found by previous author[10],[19], which are the same as those given by Eq.(12). It is important to note here that the nature of the dispersed flow (e.g., the bubbly flow) is the same for different directions of gravity (i.e., for the vertical flow, the horizontal flow, or etc.) *except* the void distribution across the cross section of the pipe (i.e., the

radial direction). Since the presented average two-fluid model does not allow to include the radial void distribution effect, we obtain the same characteristics for the dispersed flow regardless of the flow direction relative to gravity. One who is interested in the effect of the void distribution effect may look up previous works.

The separated two-phase flow system is hyperbolic when the eigenvalues are real or equivalently, the determinant of the quadratic equation is positive (i.e., $D_{sep}^* > 0$). Let us define a critical two-phase Froude number ($Fr_{2\varphi,crit}$) such that D_{sep}^* vanishes when $Fr_{2\varphi}=Fr_{2\varphi,crit}$. By setting $D_{sep}^* = 0$, we obtain the critical two-phase Froude number for a stratified flow as

$$Fr_{2\varphi,crit}^2 = \frac{\pi\alpha_g\alpha_f(1-\rho_g^*)(\rho_g^*\alpha_f+\alpha_g)\sin\beta/(4\rho_g^*\sin\theta)}{\alpha_f\alpha_g-\alpha_f C_\tau(\rho_g^*\alpha_f+\alpha_g)-C_\tau^2\rho_g^*+2\alpha_f^2 C_\tau(1-\rho_g^*)} \qquad (13)$$

Since the reality of eigenvalues implies that the two-phase system is stable against infinitesimal perturbations, we find the stable flow stratification is possible when $Fr_{2\varphi} < Fr_{2\varphi,crit}$. If we use the following assumptions in Eq.(13):

$$C_\tau = 0 \text{ and } \rho_g^*\alpha_f << \alpha_g, \qquad (14)$$

we obtain the critical relative velocity as:

$$|v_{r,crit}| = \sqrt{\frac{\pi\alpha_g(\rho_f-\rho_g)gD\sin\beta}{4\rho_g\sin\theta}} \qquad (15)$$

It should be noted that Eq.(16) is the same as the surface wave instability criteria previously used as a flow regime boundary[1]. In fact, the stratified-dispersed flow regime boundary is believed to have some hysterisis effect. However, the current state-of-the-art knowledge is not good enough to quantify such effect.

3. ESTIMATION OF VOID WAVE CELERITIES

The system's characteristics are actually the two-phase system's eigenvalues. Physically, the eigenvalues are the second order celerities of the void wave equation with which the high frequency void wave signals would propagate[10]. On the other hand, the reality of the eigenvalues is a necessary condition for the system's well-posedness. For example, we know stable bubbly flow in a horizontal pipe exists, therefore, the bubbly two-phase flow model should be well-posed to be a valid one. It was suspected that[19] a dramatic flow geometry change (e.g., the bubbly to slug flow

transition) could occur on the boundary between well-posedness and ill-posedness. As shown in Figure 1, if we plot the void wave celerities obtained in the previous section for a specified value of two-phase Froude number ($Fr_{2\varphi}$), we find the two-phase system is well-posed only within finite range of global void fraction. Both for the dispersed and the separated flows, the order of the two-phase system is two so that we obtain two distinct eigenvalues which disappear on the λ-α_g plane when those become complex numbers. When $Fr_{2\varphi}$=5.0 (the relative velocity is 25 m/s in 1 inch dia. pipe), the eigenvalues of the separated flow are real only when the global void fraction is very high, say, 0.75 as shown in Figure 1. For this large value of the relative velocity, the two-phase flow can hardly be separated except when the amount of the liquid in the flow field is very small. On the other hand, the horizontal dispersed flow is found to be stable when the global void fraction reaches up to 0.45 as shown in Figure 1. As will be shown later, the well-posedness boundary of the dispersed flow does not depend on global void fraction. The magnitude, however, of the celerities proportionally increase with the two-phase Froude number. If we decrease the Froude number to 3.5, we may find (Figure 2) the region of the well-posed separated flow is extended significantly. In other words, the stratified flow regime is possible for lower values of the global void fraction. This trend is physically right and is consistent with the previous works[1] which is being used in nuclear reactor system analysis codes, such as RELAP5/MOD3. The void wave celerities in horizontal bubbly flow are also shown with decreased value of two-phase Froude number. The magnitude of the faster characteristic is reduced proportionally. However, the limiting global void fraction (i.e., the well-posedness boundary) does not change. This result is somewhat embarrassing since it is normally believed that the flow geometry change quite strongly depends on the phasic relative velocity. One of the important reasons for this result is due to that the phase distribution along the cross section of the flow field is not included in the presented two-fluid model. However, for separated flow, the phase distribution effect has been tacitly incorporated since we constituted the conservation equation for the physically separated flow geometry (i.e., the stratified flow). In other words, we have found here that the radial void distribution model in a dispersed horizontal flow is crucial in quantifying the flow regime boundary mechanistically. In spite of some of decent experimental efforts[20] on steady and transient global void fraction measurement techniques, no significant relationships between local void distribution and the global two-phase flow phenomena have been found.

Further reduction of the two-phase Froude number enlarges the range of the separated two-phase flow as shown in Figure 3. If one realize the relative velocity is still high (v_r=10 m/s for $Fr_{2\varphi}$=2, D=1 inch), the result, shown in Figure 3, that the flow stratification occurs at global void fraction of, say, 0.1 does not make much sense. It is suspected that this result came from a wrong constitution of two-fluid model with separated flow geometry. In other words, for this low values of the void fraction, the void wave celerity would switch to those of the bubbly flow, that is, the faster void wave celerity would increase as the global void fraction decreases. Actually, this type of behavior is a dilemma of this type of approach since the accuracy of the physical constitutive relationships is not very high at this moment. However, it is believed that the very valuable result here is the sensitivity of the void celerity and the well-posedness of the two-fluid model which is frequently being used with the flow regime transition criteria.

One should be careful when interpreting the two-fluid system's characteristics. As discussed here, real to complex value transition of those may mean a catastrophic change in the flow field geometry. However, recent understanding of the flow regime transition is based on slower transition mechanism, such as the kinematic void wave shock phenomena in a inclined pipe [21]. Thus, the eigenvalues shown in this paper should be understood as a limiting indicator for the flow regime transition phenomena and the well-posedness of the two-fluid equation. There are only few experimental justifications concerning the relationship between the well-posedness and the flow regime change up to now.

4. SUMMARY AND CONCLUSION

The presented study is a theoretical investigation of the horizontal flow regime boundaries.

Result of this study shows that the flow regime boundary and the characteristics of the void wave celerities are strongly coupled so that a mechanistic determination of the flow regimes is possible by using the presented technique with the average two-fluid model. Some of unknown phenomena in horizontal flow can also be investigated by using the presented technique.

Horizontal flow regime boundaries shown in previous different flow regime maps are not completely validated. Therefore, the author hopes this work to stimulate such a research.

REFERENCES

[1] Y. Taitel and A.E. Dukler, "A Model for Predicting Flow Regime Transitions in Horizontal and Near Horizontal Gas-Liquid Flow", AIChE J., Vol. 22 (1976).

[2] G.C. Gardner, "Low and High Head Flooding for Countercurrent Flow in Short Horizontal Tubes", Int. J. Multiphase Flow, Vol.16 (1987).

[3] J. Abrams and T.J. Hanratty, "Relaxation Effects Observed for Turbulent Flow Over a Wavy Surface", J. Fluid Mechanics, Vol. 151 (1985).

[4] N. Brauner, and D.M. Maron, "Dynamic Model for the Interfacial Shear as a Closure Law in Two-Fluid Models", Nuclear Eng. & Dsn., Vol. 149 (1994).

[5] N. Brauner, and D.M. Maron, "Analysis of Stratified/Non-stratified Transition Boundaries in Inclined Gas-Liquid Flows", Int. J. Multiphase Flow, Vol. 18 (1994).

[6] D.A. Drew and R.T. Lahey, Jr., "Application of General Constitutive Principles to the Derivation of Multidimensional Two-Phase Flow Equations", Int. J. Multiphase Flow, Vol. 5 (1979).

[7] M. Ishii and K. Mishima, "Two-Fluid Model and Hydrodynamic Constitute Relations", Nuclear Eng. & Dsn., Vol. 82 (1984).

[8] J.A. Bouré, "Properties of Kinematic Waves in Two-Phase Pipe Flows. Consequences on the Modeling Strategy", Proc. Eur. Two-Phase Group Meet., Brussels (1988).

[9] A. Tournaire, Detéction et etudes des ondes de taux de vide en eécoulement diphasique a bulles jusqu'a la transition bulles-bouchons, Docteur-Ingenieur

Thèse, Université Scientifique et Medicale et Institut National Polytechnique de Grenoble (1987).

[10] J-W. Park, D.A. Drew and R.T. Lahey, Jr., "Void Wave Dispersion in Bubbly Flows", Nuclear Eng. & Dsn., Vol. 121 (1990).

[11] J-W. Park, D.A. Drew and R.T. Lahey, Jr., "The Measurement of Void Waves in Bubbly Two-Phase Flows", Nuclear Eng. & Dsn., Vol. 149 (1994).

[12] G. Arnold, Entropy and Objectivity as Constraints upon Constitutive Equations for Two-Fluid Modeling of Multiphase Flow, Ph.D. Thesis, Rensselaer Polytechnic Institute, Troy, New York (1988).

[13] J-W. Park, Void Wave Propagation in Two-Phase Flow, Ph.D. thesis (Nuclear Sci. & Eng.), Rensselaer Polytechnic Institute (1992).

[14] J.H. Stuhmuller, "The Influence of Interfacial Pressure Forces on the Character of Two-Phase Flow Model Equations", Int. J. Multiphase Flow, Vol. 3 (1977).

[15] D.A. Drew and R.T. Lahey, Jr., "Some Supplemental Analysis Concerning The Virtual Mass and Lift Force on a Sphere in Rotating and Straining Inviscid Flow", Int. J. Multiphase Flow, Vol. 16 (1989).

[16] S.T. Revankar and M. Ishii, "Theory and Measurement of Local Interfacial Area Using a Four Sensor Probe in Two-Phase Flow", Int. J. Heat Mass Transfer, Vol. 36 (1993).

[17] T.Z. Harmathy, "Velocity of Large Drops and Bubbles in Media of Infinite or Restricted Extent", AIChE Journal Vol. 6, No.2 (1960).

[18] R.H. Sabersky, A.J. Acosta and E.G. Hauptmann, Fluid Flow, The Macmillan Co. (1971)

[19] C. Pauchon and S. Banerjee, "Interphase Momentum Effects in the Averaged Multifield Model: II. Kinematic Waves and Interfacial Drag in Bubbly Flows", Int. J. Multiphase Flow, Vol. 14 (1988).

[20] M-H. Chun and C.K. Sung, "Parametric Effects on the Void Fraction Measurement by Capacitance Transducers", Int. J. Multiphase Flow, Vol.12 (1986).

[21] J-W. Park, "Nonlinear Void Wave Propagation In a Slightly Inclined Pipe Emptying Process", 2nd Int. Conf. Multiphase Flow, Kyoto, Japan (1995).

	Dispersed Flow (Bubbly Flow)	Separated Flow (Stratified Flow)
Δp_{fi}	$-\eta\rho_f(v_g - v_f)^2,\ \eta = \frac{1}{4}$	$-(\rho_f g D \sin\beta)\left(\frac{\sin^3\theta}{3\pi\alpha_f} + \frac{\cos\theta}{2}\right)$
Δp_{gi}	0	$(\rho_g g D \sin\beta)\left(\frac{\sin^3\theta}{3\pi\alpha_g} - \frac{\cos\theta}{2}\right)$
F_{vm}	$C_{vm}\left(\frac{\partial v_g}{\partial t} + v_g\frac{\partial v_g}{\partial z} - \frac{\partial v_f}{\partial t} - v_f\frac{\partial v_f}{\partial z}\right)$	0
F_D	$\frac{C_D}{8\alpha_g}\rho_f A_i'''(v_g - v_f)\lvert v_g - v_f\rvert$	0
$\tau_i\frac{\partial\alpha_g}{\partial z}$	0	$\frac{\xi_i}{A_{x-s}}\tau_{gi}$
τ_f^{Re}	$-k\rho_f(v_g - v_f)^2,\ \ k = \frac{1}{5}$	0
τ_g^{Re}	0	$-C_\tau\rho_f(v_g - v_f)\lvert v_g - v_f\rvert,\ C_\tau = \frac{1}{2}$
τ_g, τ_f	0	0

Table 1 Constitutive Relationships for Two-Phase Flow in an Inclined Pipe

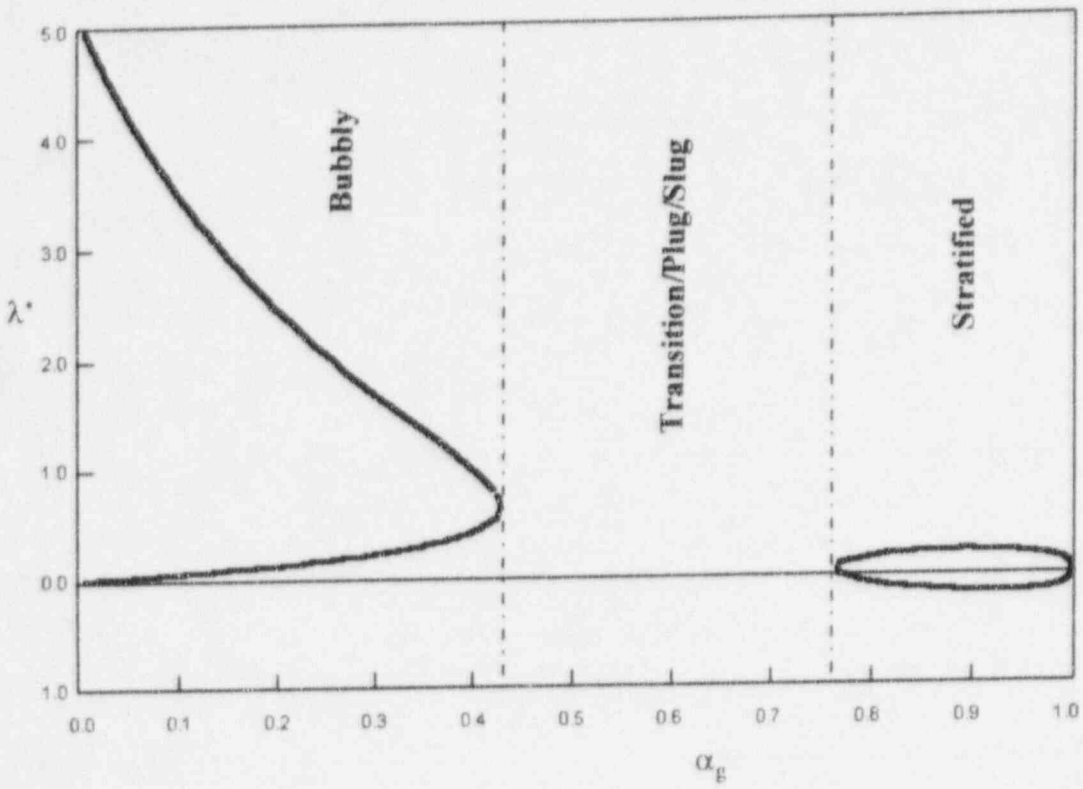

Figure 1. Second Order Void Wave Celerities for Horizontal Flow When $Fr_{2\varphi}$=5.0

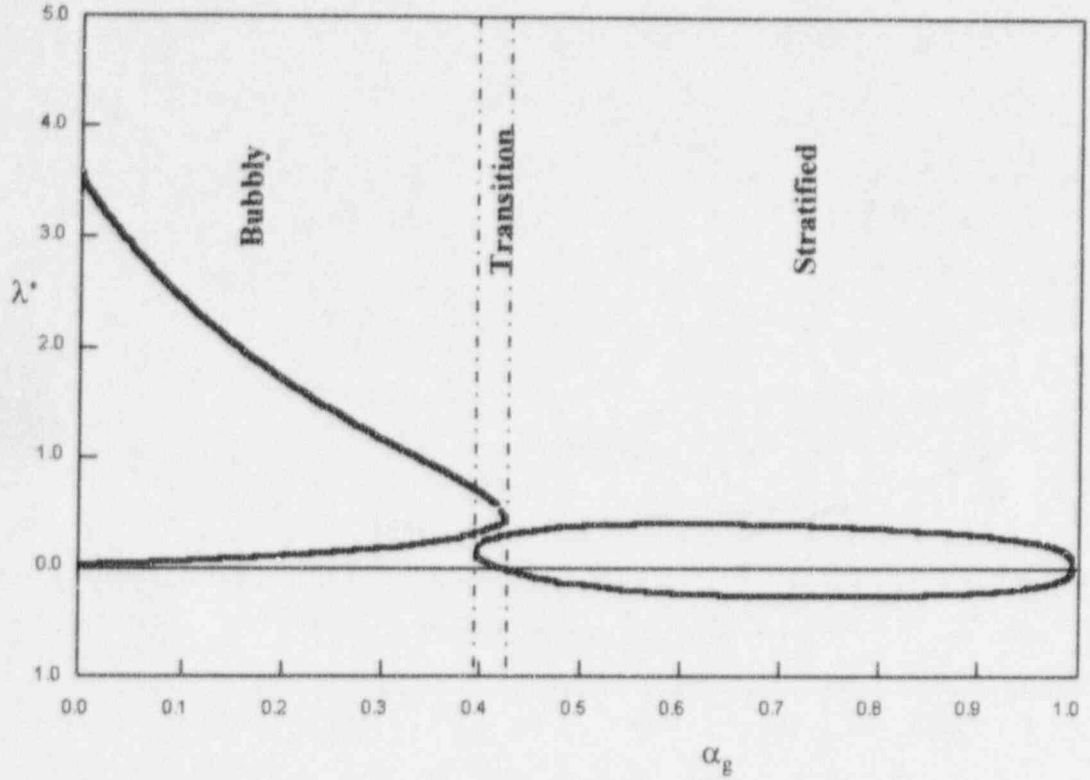

Figure 2. Second Order Void Wave Celerities for Horizontal Flow When $Fr_{2\varphi}$=3.5

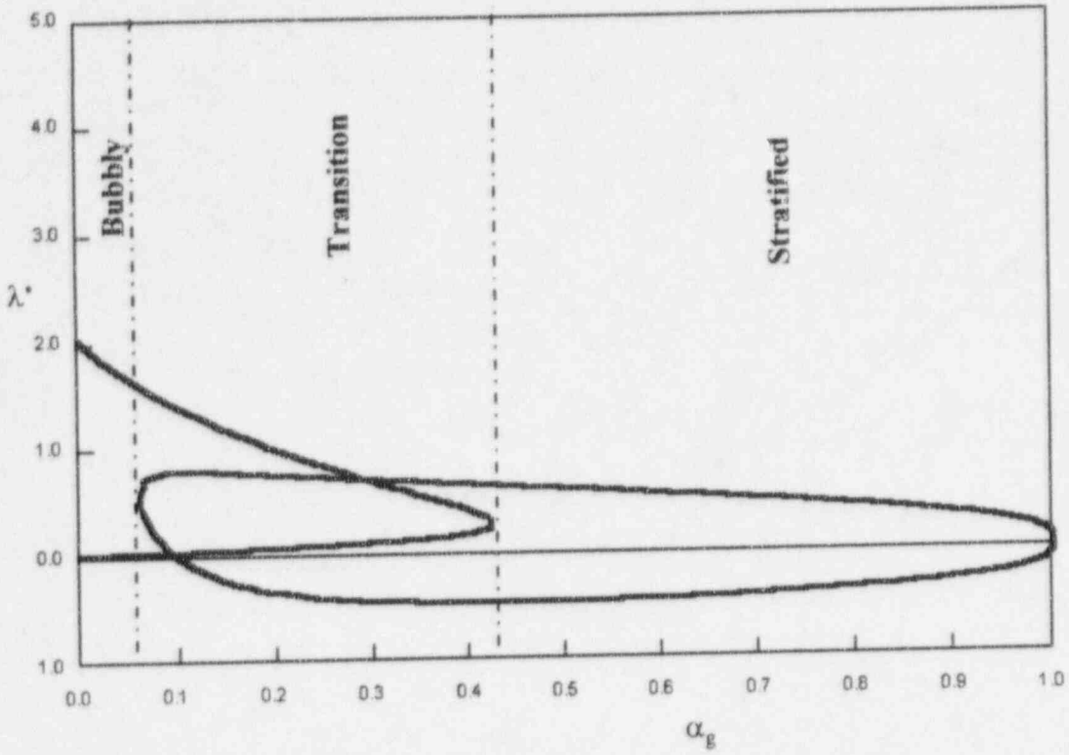

Figure 3. Second Order Void Wave Celerities for Horizontal Flow When $Fr_{2\varphi}$=2.0

APPENDIX A
THE INTERFACIAL PRESSURE DIFFERENCE FOR STRATIFIED FLOW

The local pressure in the pipe as shown in Figure A can be given by

$$p = p_{ki} - \rho_k g \sin\beta (h - H), \qquad k = \begin{cases} g & \text{for } h > H \\ f & \text{for } h < H \end{cases} \tag{a1}$$

The phasic interfacial pressures (i.e., p_{gi} and p_{fi}) are generally different from each other due to the surface tension.

The phase average pressure can be obtained by averaging the local pressure given by Eq.(a1) over each phase, that is:

$$p_k = \frac{1}{A_k} \iint_{A_k} p \, dA_k \tag{a2}$$

Evaluating the integral in Eq.(a2) for each phase, we obtain the phasic interfacial pressure differences as

$$\Delta p_{gi} \equiv p_{gi} - p_g = (\rho_g g D \sin\beta) \left(\frac{\sin^3\theta}{3\pi\alpha_g} - \frac{\cos\theta}{2} \right) \tag{a3}$$

$$\Delta p_{fi} \equiv p_{fi} - p_f = -(\rho_f g D \sin\beta) \left(\frac{\sin^3\theta}{3\pi\alpha_f} + \frac{\cos\theta}{2} \right) \tag{a4}$$

where the angle of stratification (θ) can be related to the void fraction as

$$\pi\alpha_g = \theta - \sin\theta\cos\theta \tag{a5}$$

Using Eq.(a4), we simplify the terms including the phasic pressure in the combined momentum equation (i.e., Eq.(7)) as:

$$\alpha_g \alpha_f \left(\frac{\partial p_g}{\partial z} - \frac{\partial p_f}{\partial z} \right) - \left(\alpha_g \Delta p_{fi} + \alpha_f \Delta p_{gi} \right) \frac{\partial \alpha_g}{\partial z} \equiv C_M \frac{\partial \alpha_g}{\partial z} \tag{a6}$$

where

$$C_M = \pi (g D \sin\beta)(\rho_f - \rho_g) \frac{\alpha_g \alpha_f}{4 \sin\theta} \tag{a7}$$

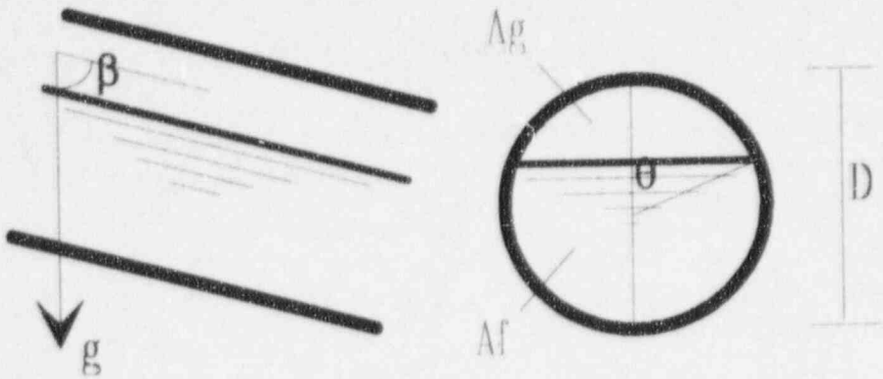

Figure 1. Stratified Flow In An Inclined Pipe

APPENDIX B
TWO-PHASE SYSTEM'S EQUATION

Multiplying $\alpha_{k'}$ (k'=g for k=f, k'=f for k=g) to the momentum equation of each phase (i.e., Eq.(1)) and subtracting one from the other, we obtain

$$\alpha_g\alpha_f\left(\rho_f\frac{\partial v_f}{\partial t}-\rho_g\frac{\partial v_g}{\partial t}\right)+\alpha_g\alpha_f\left(\rho_f v_f\frac{\partial v_f}{\partial z}-\rho_g v_g\frac{\partial v_g}{\partial z}\right)$$
$$=\alpha_g\alpha_f(\rho_f-\rho_g)g\cos\beta+\alpha_g\alpha_f\left(\frac{\partial p_g}{\partial z}-\frac{\partial p_f}{\partial z}\right)$$
$$-\left(\alpha_g\Delta p_{fi}+\alpha_f\Delta p_{gi}\right)\frac{\partial\alpha_g}{\partial z}-\tau_i\frac{\partial\alpha_g}{\partial z} \qquad \text{(b1)}$$
$$+\alpha_g\frac{\partial(\alpha_f\tau_f^{Re})}{\partial z}-\alpha_f\frac{\partial(\alpha_g\tau_g^{Re})}{\partial z}+\alpha_g M_{if}-\alpha_f M_{ig}$$
$$-\alpha_g M_{wf}+\alpha_f M_{iw}+\alpha_g\Gamma_f v_{fi}-\alpha_f\Gamma_g v_{gi}$$

If we cast the phasic continuity equation, that is,

$$\frac{\partial(\alpha_k\rho_k)}{\partial t}+\frac{\partial(\alpha_k\rho_k v_k)}{\partial z}=\Gamma_k \qquad (k=g,f) \qquad \text{(b2)}$$

with

$$\Gamma_g+\Gamma_f=0 \qquad \text{(b3)}$$

and the combined momentum equation (Eq.(b1)) into a matrix form, we obtain the system of equation as:

$$\underline{\underline{A}}\frac{\partial \underline{\phi}}{\partial t}+\underline{\underline{B}}\frac{\partial \underline{\phi}}{\partial z}=\underline{c} \tag{b4}$$

where

$$\underline{\underline{A}}=\begin{bmatrix} -\alpha_g\alpha_f\rho_g & \alpha_g\alpha_f\rho_f & 0 \\ 0 & 0 & 1 \\ 0 & 0 & -1 \end{bmatrix} \tag{b5}$$

$$\underline{\underline{B}}=\begin{bmatrix} -\alpha_g\alpha_f\rho_g[v_g-2C_\tau|v_r|] & \alpha_g\alpha_f\rho_f[v_f-2C_\tau\rho_g^*|v_r|] & -C_M+\alpha_f\tau_g^{Re} \\ \alpha_g & 0 & v_g \\ 0 & \alpha_f & -v_f \end{bmatrix} \tag{b6}$$

$$\underline{c}=\begin{bmatrix} c' \\ \Gamma_g/\rho_g \\ \Gamma_f/\rho_f \end{bmatrix}, \qquad \underline{\phi}=\begin{bmatrix} v_g \\ v_f \\ \alpha_g \end{bmatrix} \tag{b7}$$

$$\begin{aligned} c' \equiv\ & \alpha_g\alpha_f\Delta\rho g\cos\beta+\alpha_f M_{wg}-\alpha_g M_{wf} \\ & +\alpha_g\Gamma_f v_{fi}-\alpha_f\Gamma_g v_{gi}-\frac{\xi_i}{A_{x-s}}\tau_{gi}-M_{ig} \end{aligned} \tag{b8}$$

where the constitutive relations given by Eqs.(4) through (6) has been used.

The system's eigenvalues can be found by solving the characteristic equation, that is:

$$\det(\underline{\underline{B}}-\lambda\underline{\underline{A}})=0 \tag{b9}$$

where

$$\underline{\underline{B}}-\lambda\underline{\underline{A}}=\begin{bmatrix} \alpha_g\alpha_f\rho_g(\lambda-v_g+2C_\tau|v_r|) & -\alpha_g\alpha_f\rho_f(\lambda-v_f+2C_\tau\rho_g^*|v_r|) & -C_M+\alpha_f\tau_g^{Re} \\ \alpha_g & 0 & -(\lambda-v_g) \\ 0 & \alpha_f & \lambda-v_f \end{bmatrix} \tag{b10}$$

Rearranging Eq.(9), we obtain the system's characteristic equation as

$$\alpha_f \rho_g (\lambda - v_g)^2 + \alpha_g \rho_f (\lambda - v_f)^2 - C_M \qquad \text{(b11)}$$

$$+ \alpha_f \tau_g^{Re} + 2C_\tau \rho_g |v_r| (\lambda - \alpha_f v_g - \alpha_g v_f) = 0$$

A Criterion for the Onset of Slugging in Horizontal Stratified Air-Water Countercurrent Flow

Moon-Hyun Chun, Byung-Ryung Lee, and Yang-Seok Kim
Korea Advanced Institute of Science and Technology
Taejon, Korea

Ho-Yun Nam
Korea Atomic Energy Research Institute
Taejon, Korea

ABSTRACT

This paper presents an experimental and theoretical investigation of wave height and transition criterion from wavy to slug flow in horizontal air-water countercurrent stratified flow conditions. A theoretical formula for the wave height in a stratified wavy flow regime has been developed using the concept of total energy balance over a wave crest to consider the shear stress acting on the interface of two fluids. From the limiting condition of the formula for the wave height, a necessary criterion for transition from a stratified wavy flow to a slug flow has been derived. A series of experiments have been conducted changing the non-dimensional water depth and the flow rates of air in a horizontal pipe and a duct. Comparisons between the measured data and the predictions of the present theory show that the agreement is within ±8%.

1. INTRODUCTION

When a gas flows over a wavy liquid surface with sufficiently large relative velocity in a horizontal pipe or duct, the gas-liquid interface becomes disturbed and the suction effect due to the pressure difference over the wave becomes large and eventually the transition from a stratified wavy to a slug flow will occur. A number of experimental and theoretical studies have been performed[1-9] to investigate the phenomenon of transition to a slug flow over the last 25 years since Kordyban and Ranov[1] first analyzed the transition from a stratified to a slug flow for water and air between horizontal parallel plates.

The most typical models proposed by earlier workers are summarized in Table 1. Recently an excellent summary of existing theories of the transition to slug flow has been presented by Kordyban[10]. A review of literatures shows that the most widely used correlation to predict the initiation of slugs is the correction to the Kelvin-Helmholtz inviscid theory introduced by Taitel and Dukler[3]. Their model has been widely used as a criterion for the initiation of the flooding as well as the condensation-induced waterhammer. Improtant recent relevant investigations are also reported by Barnea and Taitel[11], Brauner and Maron[12, 13], Nydal et al.[14], Andreussi et al.[15], Ruder et al.[16], and Bendiksen and Espedal[17]. Barnea and Taitel[11] and Brauner and Maron[12,13], in particular, consider the complete non-linear dynamic one-dimensional, two-fluid equations in stability and well-posedness analyses to obtain complementary predictive tools for the stability of stratified gas-liquid flow and the departure to other bounding flow patterns. Bendiksen and Espedal[17], on the other hand, note that the transition to slug flow cannot be described in terms of wave formation alone and the slug front velocity must initially

Table 1. Analytical Correlations for Onset of Slug Flow

Author	Geometry & Wave Form	Theory (Key Concept)	Slug Flow Criterion
Wallis and Dobson [2]	Rectangular; DeepWater	Kelvin-Helmholtz theory; Bernoulli Eq.	$V_g \geq 0.5(gH_g\frac{\rho_l-\rho_g}{\rho_g})^{1/2}$
Taitel and Dukler [3]	Rectangular; Round Pipe; Solitary Wave	Kelvin-Helmholtz theory; Bernoulli Eq.	For Round Pipe Geometry $V_g \geq C(\frac{\rho_l-\rho_g}{\rho_g}\frac{gA_g\cos\theta}{dA_l/dH_l})^{1/2}$, $C=1-H_l/L$
Kordyban [4,5]	Rectangular; Deep Water	Kelvin-Helmholtz theory; Bernoulli Eq.	$1.35\frac{\rho_g}{\rho_l-\rho_g}\frac{V_c^2}{gH_c} = 1$
Gardener [6]	Pipe	Liquid phase energy flux difference	$V_r \geq 2(1-H_l^*)gH_g\frac{\rho_l-\rho_g}{\rho_g}$
Mishima and Ishii [7]	Rectangular; Deep Water	"Most dangerous" wave concept ; Potential & stream function ; Bernoulli Eq.	$V_r = V_g - V_t$, $V_r \geq 0.487(\frac{\rho_l-\rho_g}{\rho_g}gH_g)^{1/2}$
Lin and Hanratty [8]	Pipe; Film Wave	Viscous Kelvin-Helmholtz theory ; Perturbation method ; Semi-empirical equation	$\frac{V_{gs}}{(gD)^{1/2}}(\frac{\rho_g}{\rho_l-\rho_g})^{1/2} \geq K_2\,\alpha^{3/2}$, $K_2=K_1(\alpha,\nu,V_{gs})$K
Wang and Kondo [9]	Duct; Countercurrent	Viscous Kelvin-Helmholtz theory	$\frac{V_{gs}^2}{gD}(\frac{\rho_g}{\rho_l-\rho_g})^{1/2} \geq K_1\,\alpha^{3/2}$, $K_1=K_1(\tau_i/\tau_w,\alpha)$
Present Work	Pipe & Duct; Countercurrent	Total Energy Balance over a Wave Crest	$V_{g,cr} = \sqrt{\frac{\rho_g gH_g C_{p,cr}}{\rho_g}}\sqrt{\frac{4/\pi+f_i}{4/\pi+f_i}-1}$, $C_{p,cr}=1+\frac{32}{9\pi}\frac{D\eta_{cr}}{S_i^2}\left(\frac{D_{h,g}}{D_{h,l}}\right)^2\left(1-\frac{2H_l}{D}\right)$

exceed the tail velocity for some period of time. Based on this, they derived a simple criterion for the transition in terms of the average parameters of the previous stratified flow condition.

As recently pointed out by Kordyban[10], it appears that there are still important conceptual problems to be resolved in spite of many existing models: Most authors accept that the transition is due to Kelvin-Helmholtz instability of the waves, but if this is studied on the basis of wave motion equations, the transition is found to be dependent on wavelength which contradicts experimental data. A number of authors examined this instability by studying the Bernoulli equation, but this does not predict the wave height. The present study has been initiated to resolve the conceptual problem of the existing theory for transition to slug flow. That is, the main objective of this work is to develop a theoretical model that can predict the wave height and to derive a necessary but not sufficient condition for the transition from a wavy to a slug flow in a horizontal stratified flow. A series of experiments have been conducted to measure

the slug occurrence probability in a horizontal air-water countercurrent stratified pipe flow and to compare directly with the slug initiation criterion. In addition, measurements of the wave height of wavy flow in a horizontal countercurrent stratified duct flow are made. Both models for the wave height and the transition criterion for the slug flow are based on the total energy balance over the wave crest. In the present model, the shear stress acting on the gas-liquid interface, in particular, has been included.

2. EXPERIMENTAL METHOD

A schematic diagram of experimental apparatus is shown in Fig.1. It consists of an air-water fluid system where the water and air circuits are combined to form a countercurrent flow at the horizontal test section. Major components of the experimental facility are : (1) water surge tank, (2) air compressor, (3) two horizontal test sections, one is made of transparent acrylic pipe (0.05 m inside diameter and 8.28 m in length) and the other is a duct (0.1 $\times$ 0.1 m cross section and 7.98 m in length), and (4) associated sensors and devices to measure flow rates of air and water and the pressure drop.

The water surge tank is installed to provide enough head for water flowing by gravity. The inner vessel installed inside the water surge tank maintains constant head of water to prevent water from flowing in due to riffling. The two reservoirs located at both sides of the test section maintain steady state flow conditions and absorb waves generated in the test section.

The effect of vibrations in the experimental setup has been minimized by tightening the horizontal test sections with a number of level supports at 1 m interval. Also, the effects of flow fluctuations and water entrainment have been reduced by attaching a converging nozzle between the water reservoir and the horizontal test section as shown in Fig.1.

The volume flow rate of air was measured by two pitot tube type flowmeters (OMEGA models FPT-6310 and FPT-6320) with differential pressure transducers installed in series in the air line. The volume flow rate of water was calculated by measuring the time it takes to fill a 22.5 ℓ water receiver via a water outlet. The pressure drop of the air between both ends of the test section was measured by one of the two differential pressure transducers (3" H_2O and 10" H_2O) installed in parallel depending on the experimental range. The temperatures of water and air were also measured by means of two thermocouples installed at the water surge tank and the air reservoir, respectively. The measured temperature range was 9~16℃ in the present work. Measurements of wave heights and water depths were made by the rulers attached to the test section (at 7 locations for the pipe test and 11 locations for the duct test). For each preset experimental conditions, the measurements of the wave height and the water depth were repeated five times to obtain an average value. In the stratified wavy flow regime of the present work, the waves generated were long waves which traveled very slowly. The maximum measurement error of the wave height (i.e., the data shown in Fig.3), in particular, is ±16.7% when the wave height is low and ±10% when the wave height is high while the range of the measured wave height is from 0.6 mm to 10 mm. However, the average measurement error is within ±6.3% . The velocity of a surface wave, on the other hand, was obtained by measuring the average traveling time of the surface wave between the known distance of the present test sections.

A number of experiments have been conducted varying the nondimensional water depth ($H_l^* = H_l / D$) from 0.08 to 0.6 and for various combinations of air and water flow rates. The range of superficial water velocity was 0.012~0.12 m/s for the pipe test and 0.0053~0.14 m/s for the duct test. The range of superficial air velocity, on the other hand, was 1.0~7.5 m/s for the duct test. The actual air flow velocity was less than 13 m/s for the duct test, and all the flow regimes of air were fully turbulent flow.

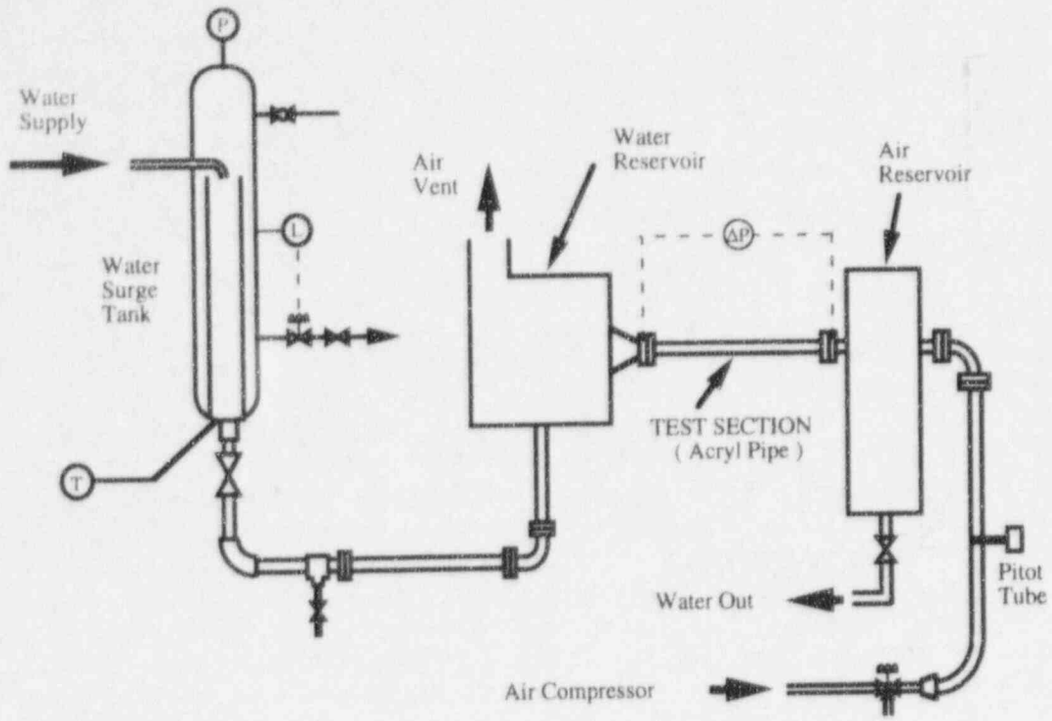

Fig. 1 Shcematic Diagram of Experimental Apparatus

The probability of occurrence of a slug flow has been experimentally determined by counting the number of actual occurrence of flow blockage of the whole test section(due to a complete slug flow) out of ten repeated experiments conducted under the same flow conditions. A total of 103 data for the slug occurrence probability in the pipe flow and a total of 23 data for the wave height in the duct flow are obtained in the present experiments, and the measured data are compared with theory.

3. DEVELOPMENT OF A MODEL FOR THE WAVE HEIGHT

When a gas flows over a liquid surface in a stratified flow at sufficiently large relative velocity in a horizontal pipe or a duct, the gas-liquid interface will become disturbed and a lump of water will be pushed up above the liquid surface by the combination of the gas stagnation pressure acting near its base and Bernoulli lift forces acting at its crest in addition to the shear stress acting on the front surface of the wave crest. Against these forces, there is an opposing and stabilzing force due to the gravity.

Therefore, the total energy balance near the wave crest(i.e. shaded area in Fig. 2a) can be expressed as follows :

Total potential energy of the wave crest (E_f)
= Net gas kinetic energy increase over the wave crest (ΔE_K)
+ Work done by the shear stress on the front surface of the wave crest (W_s) (1)

To derive the total energy balance equation over the wave crest, one may consider a control volume in the countercurrent stratified wavy flow as shown in Fig. 2(a). First, to analyze a gas flow which is confined between the surface wave of water and the rigid

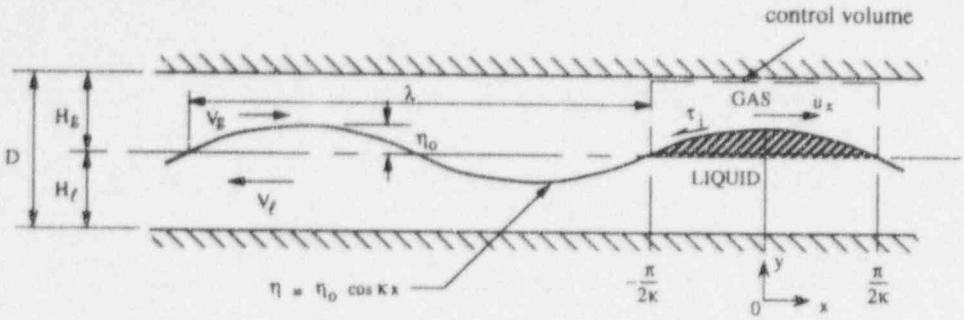

(a) Control Volume for Wavy Flow Analysis

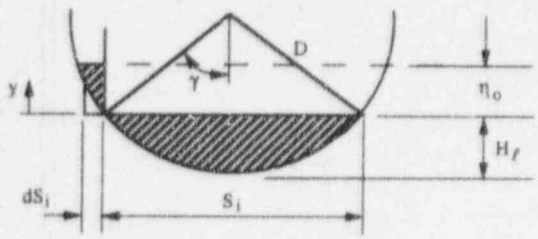

(b) Control Volume for Gravitational Energy

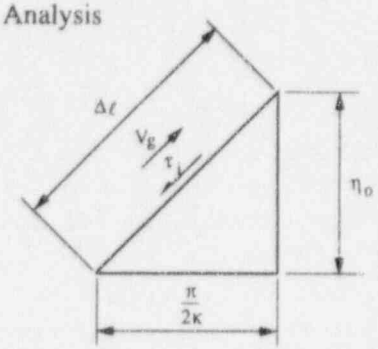

(c) Model for Frictional Work

Fig. 2 Models Used for Wavy Flow Analysis

horizontal plate, the gas velocity in the x-direction can be expressed in terms of the wave displacement η and the velocity potential function ϕ_v introduced by Lamb[18]. That is, to a first approximation, a steady wave motion which is periodic with respect to x, superposed on a uniform current of velocity V_g can be represented by the following equations:

$$\eta = \eta_o \cos \kappa x \tag{2}$$

$$\phi_v = -V_g x + c_g \cosh \kappa (y - H_g) \sin \kappa x \tag{3}$$

where c_g is an arbitrary constant. In the derivations of Eqs. (2) and (3), it is assumed that the amplitude of the disturbance is small compared with the wave-length.

The local gas velocity in the x-direction (u_x) is then given by

$$u_x = -\frac{\partial \phi_v}{\partial x} \tag{4}$$

Therefore,

$$u_x = V_g - c_g \kappa \cosh \kappa (y - H_g) \cos \kappa x \tag{5}$$

The mass balance equation over the wave crest on the other hand can be written as

$$V_g H_g = \int_{\eta_o}^{H_g} u_x|_{x=0}\, dy \tag{6}$$

Integration of Eq. (6) leads to the evaluation of constant c_g,

$$c_g = \frac{V_g \eta_o}{\sinh \kappa (\eta_o - H_g)} \tag{7}$$

The gas velocity, therefore, can be written as

$$u_x = V_g - \frac{V_g \eta_o \kappa}{\sinh \kappa (\eta_o - H_g)} \cosh \kappa (y - H_g) \cos \kappa x \tag{8}$$

3.1 Net Kinetic Energy Increase of the Gas-Phase (ΔE_K)

Referring to the control volume shown in Fig. 2(a), the net kinetic energy increase of the gas-phase over the wave crest, ΔE_K, may be considered to be the difference between the 'kinetic energy of the gas-phase in the control volume with the wave crest' and the 'kinetic energy of the gas-phase in the same control volume without the wave crest'. The ΔE_K can be expressed as

$$\Delta E_K = \frac{1}{2} \rho_g S_i \int_{-\frac{\pi}{2\kappa}}^{\frac{\pi}{2\kappa}} \int_{\eta}^{H_g} u_x^2 \, dy dx - \frac{1}{2} \rho_g S_i \int_{-\frac{\pi}{2\kappa}}^{\frac{\pi}{2\kappa}} V_g^2 H_g \, dx \tag{9}$$

Substitution of Eq. (8) into Eq. (9) and integrating with respect to y gives

$$\begin{aligned} \Delta E_K = \frac{1}{2} \rho_g V_g^2 S_i \int_{-\frac{\pi}{2\kappa}}^{\frac{\pi}{2\kappa}} \Bigg\{ & -\eta + \frac{2\eta_o \sinh \kappa (\eta - H_g)}{\sinh \kappa (\eta_o - H_g)} \cos \kappa x \\ & - \frac{\eta_o^2 \kappa [\, \sinh 2\kappa (\eta - H_g) + 2\kappa (\eta - H_g)]}{4 \sinh^2 \kappa (\eta_o - H_g)} \cos^2 \kappa x \Bigg\} dx \end{aligned} \tag{10}$$

For a gravitational long wave in a duct, i.e., when the amplitude of the wave η is small compared with the wave-length, $|\kappa (\eta_0 - H_g)| < 1$ and $\kappa H_g < 1$. In this case, one can approximate as $\sinh \kappa (\eta_0 - H_g) \simeq \kappa (\eta_o - H_g)$ and $\sinh \kappa (\eta - H_g) \simeq \kappa (\eta - H_g)$. Thus, Eq. (10) can be approximated as

$$\begin{aligned} \Delta E_K = \frac{1}{2} \rho_g V_g^2 S_i \int_{-\frac{\pi}{2\kappa}}^{\frac{\pi}{2\kappa}} \Bigg[& -\eta + \frac{2\eta_o}{H_g - \eta_o} (H_g - \eta) \cos \kappa x \\ & + \frac{\eta_o^2}{(H_g - \eta_o)^2} (H_g - \eta) \cos^2 \kappa x \Bigg] dx \end{aligned} \tag{11}$$

Substituting the relation $\eta = \eta_o \cos \kappa x$, i.e., Eq. (2) into above equation and carrying out the integration, the following equation can be obtained:

$$\Delta E_K = \frac{1}{2}\rho_g V_g^2 S_i \left[-\frac{2\eta_o}{\kappa} + \frac{4\eta_o}{\kappa(H_g-\eta_o)}\left(H_g - \frac{\pi}{4}\eta_o\right) + \frac{\pi\eta_o^2}{2\kappa(H_g-\eta_o)^2}\left(H_g - \frac{8}{3\pi}\eta_o\right)\right] \tag{12}$$

Since H_g is much larger than η_o ($H_g \gg \eta_o$),

$$\frac{H_g - \pi/4\ \eta_o}{H_g - \eta_o} \simeq 1 \tag{13}$$

$$\frac{H_g - 8/(3\pi)\ \eta_o}{H_g - \eta_o} \simeq 1 \tag{14}$$

Using Eqs. (13) and (14), Eq. (12) can be approximated as

$$\Delta E_K = \frac{1}{2}\rho_g V_g^2 S_i \left[\frac{2\eta_o}{\kappa} + \frac{\pi}{2\kappa}\frac{\eta_o^2}{(H_g-\eta_o)}\right] \tag{15}$$

3.2 Total Potential Energy of the wave crest (E_P)

The total potential energy of the wave crest(per unit thickness) is simply due to the elevated water from the undisturbed level in the control volume(i.e. the shaded area in Fig. 2a)

$$E_P = \int_{-\frac{\pi}{2\kappa}}^{\frac{\pi}{2\kappa}} \int_0^{\eta} y\rho_l g S_i dy dx + \int_{-\frac{\pi}{2\kappa}}^{\frac{\pi}{2\kappa}} \int_0^{\eta} y\rho_l g\, \Delta S_i dy dx \tag{16}$$

It should be noted here that Eq. (16) is expressed in such a way that it is directly applicable to the circular pipe flow geometry as shown in Fig. 2(b). The second term in Eq. (16) is a geometric term related only to a pipe flow and becomes zero for a rectangular duct. This term can be calculated by the geometric model shown in Fig. 2(b).

$$\Delta S_i = 2y\cot\gamma = 2y\left(1 - \frac{2H_l}{D}\right)\frac{D}{S_i} \tag{17}$$

Substituting Eq. (17) along with the relation $\eta = \eta_0 \cos\kappa x$ into Eq. (16) and carrying out the integration following equation for E_P can be derived :

$$E_P = \frac{\phi}{4\kappa}\rho_l g \eta_0^2 S_i C_F \tag{18}$$

where the geometric factor C_F for a pipe flow is given by

$$C_F = 1 + \frac{32}{9\pi}\frac{\eta_0}{S_i}\frac{D}{S_i}\left(1 - \frac{2H_l}{D}\right) \tag{19}$$

For a rectangular duct flow C_F is equal to 1. The expression for C_F involves η_0 but the second term in Eq. (19) is relatively small compared with 1 except when the water depth is very high or very low in the pipe.

3.3 Total Work Done by the Shear Stress on the Front Surface of the Wave Crest (W_r)

Figure 2(c) is the simplified representation of the front surface of wave crest to calculate the total work done on the wave surface by the gas-liquid interfacial shear. That is, the wave crest has been approximated by a triangle. The total work done on the front surface of wave crest due to the interfacial shear is given by

$$W_r = \int_l S_i \, \Delta l \, \tau_{i,y} \, V_g \, dl \tag{20}$$

where $\tau_{i,y}$ is the gas-liquid interfacial shear stress acting on the wave surface in the y-direction and Δl is the length of the wave crest. From the geometry shown in Fig. 2(c), $\tau_{i,y}$ and Δl can be obtained as

$$\tau_{i,y} = \frac{1}{2} \rho_g f_i V_g^2 \frac{\eta_0}{\sqrt{(\frac{\pi}{2\kappa})^2 + \eta_0^2}} \tag{21}$$

$$\Delta l = \sqrt{(\frac{\pi}{2\kappa})^2 + \eta_0^2} \tag{22}$$

In Eq.(20) $\tau_{i,x}$ is not included for calculating the work done on the wave front due to the interfacial shear stress, because $\tau_{i,x}$ acts in the same direction of the wave movement(i.e., in the x-direction) and, therefore, the contribution of $\tau_{i,x}$ component to push the wave height in y-direction is very small compared with the contribution of $\tau_{i,y}$ component.

The time interval Δl during which the interfacial shear stress is acting on the front surface of the wave crest is assumed to be equal to the time interval for the gas to travel the distance of $\frac{\pi}{2\kappa}$ in the x-direction with velocity V_g :

$$\Delta t = \frac{\pi/2\kappa}{V_g} \tag{23}$$

The total work done on the front surface of the wave crest by the interfacial shear stress can then be obtained by substituting Eqs. (21), (22), and (23) into Eq. (20) :

$$W_r = \frac{\pi}{4\kappa} \rho_g f_i S_i \eta_0 V_g^2 \tag{24}$$

3.4 Wave Height η_0 in a Horizontal Stratified Wavy Flow

Substitution of Eqs.(15), (18) and (24) into Eq.(1) leads to the following total energy balance equation :

$$\frac{\pi}{4\kappa} \rho_l g \eta_0^2 S_i C_P = \frac{\pi}{4\kappa} \rho_g V_g^2 S_i \eta_0 (\frac{4}{\pi} + \frac{\eta_0}{H_g - \eta_0} + f_i) \tag{25}$$

Defining the dimensionless wave height ($\eta_0^* \equiv \eta_0/H_g$) based on the mean gas depth (H_g), Eq.(25) can be rewritten as follows :

$$\eta_0^{*2} - [\,1 + C_\eta(\frac{4}{\pi} + f_i - 1)]\ \eta_0^* + C_\eta(\frac{4}{\pi} + f_i) = 0 \tag{26}$$

where

$$C_\eta \equiv \frac{\rho_g V_g^2}{\rho_l g H_g C_P} \tag{27}$$

In general, the wave height increases with increase in the gas velocity. Therefore, the physically meaningful solution of Eq. (26) for the wave height in a wavy flow is given by

$$\eta_0 = \frac{H_g}{2}\left\{1 + C_\eta(\frac{4}{\pi} + f_i - 1) - \sqrt{[\,1 + C_\eta(\frac{4}{\pi} + f_i - 1)]^{\,2} - 4C_\eta(\frac{4}{\pi} + f_i)}\ \right\} \tag{28}$$

where C_η is given by Eq. (27).

4. CRITERION FOR THE ONSET OF SLUG FLOW

The wave height increases with increase in the gas velocity. However, when the maximum wave height is reached by further increasing in the gas velocity, the flow may be forced to change from a stratified wavy to a slug flow. In view of the expression for the wave height, Eq. (28), the onset of slugging (i.e., a transition from a wavy to a slug flow) occurs when the terms in the square root in Eq. (28) becomes zero. This condition is given by

$$\left[\,1 + \frac{\rho_g V_g^2}{\rho_l g H_g C_P}(\frac{4}{\pi} + f_i - 1)\right]^{\,2} \le 4\frac{\rho_g V_g^2}{\rho_l g H_g C_P}(\frac{4}{\pi} + f_i) \tag{29}$$

The critical gas velocity ($V_{g,cr}$) at which the flow transition to a slug flow occurs can be obtained from Eq. (29) as follows :

$$V_{g,cr} = \sqrt{\frac{\rho_l g H_g C_P}{\rho_g}}\ \frac{\sqrt{4/\pi + f_i} - 1}{4/\pi + f_i - 1} \tag{30}$$

The maximum wave height (η_{cr}) in the wavy flow region is the wave height that occurs at the onset of slug flow. Therefore, the critical wave height can be obtained by substituting Eq. (30) into Eq. (28). In this case, the square root in Eq. (28) reduces to zero and the following expression can be obtained when η is replaced by η_{cr} :

$$\eta_{cr} = \frac{H_g}{2}\left[\,1 + \frac{(\sqrt{4/\pi + f_i} - 1)^2}{4/\pi + f_i - 1}\right] \tag{31}$$

The expression for C_F defined by Eq. (19) also includes the wave height η_0. Therefore, the critical value for C_F can be obtained by substituting Eq. (31) into Eq. (19) for η_0 :

$$C_{F,cr} = 1 + \frac{16}{9\pi}\frac{DH_g}{S_i^2}(1 - \frac{2H_l}{D})\left[1 + \frac{(\sqrt{4/\pi + f_i} - 1)^2}{4/\pi + f_i - 1}\right] \quad (32)$$

The final expression for critical gas velocity is obtained by replacing C_F in Eq. (30) by $C_{F,cr}$ as follows :

$$V_{g,cr} = \sqrt{\frac{\rho_l g H_g C_{F,cr}}{\rho_g}}\frac{\sqrt{4/\pi + f_i} - 1}{4/\pi + f_i - 1} \quad (33)$$

The criterion for the onset of slugging, Eq. (33), derived in the present work reduces to the same form obtained by Wallis and Dobson[2] and Mishima and Ishii[7] shown in Table 1 when the geometric factor $C_{F,cr}$ is taken as unity (as in the case of a rectangular duct flow) and the interfacial friction factor f_i is neglected. This fact becomes more clear when Eq. (33) is rewritten by taking into account of the buoyancy of the gas phase as follows :

$$V_{g,cr} = 0.470\sqrt{\frac{(\rho_l - \rho_g)gH_g}{\rho_g}} \quad (34)$$

It should be noted here that the numerical coefficient in Eq. (34) is 0.47 which is the result of theoretical derivation, whereas the numerical coefficients obtained by Wallis[2] and Mishima[7] are 0.5 and 0.487, respectively as can be seen in Table 1.

If it is assumed that the wave height η_0 in Eq. (19) is approximately proportional to the square of gas velocity according to the Bernoulli force, then η_0 can be expressed as

$$\eta_0 \simeq \eta_{cr}\left(\frac{V_g}{V_{g,cr}}\right)^2 \quad (35)$$

In this case, the geometric factor C_F given by Eq. (19) can be expressed as

$$C_F = 1 + \frac{32}{9\pi}\frac{D\eta_{cr}}{S_i^2}\left(\frac{V_g}{V_{g,cr}}\right)^2\left(1 - \frac{2H_l}{D}\right) \quad (36)$$

5. COMPARISON BETWEEN THEORY AND EXPERIMENTAL RESULTS AND DISCUSSION

5.1 Comparison of Present Theory with Experimental Results

For direct comparisons of the wave height (η_0) and the condition of onset of slugging ($V_{g,cr}$) predicted by present theory with those determined by experiments following procedures are used :

(1) To predict the wave height (η_0) for a given condition, Eq. (28) is used along with Eq. (27), whereas the condition of onset of slugging ($V_{g,cr}$) has been predicted by Eq. (33) along with Eqs. (32) and (39).

(2) The values of V_g and H_l used in Eqs. (28) and (32), respectively are the values determined at $x = L/8$ (from the inlet) where the slugging has occurred most

frequently in the present experiment.

(3) The gas-liquid interfacial friction factor (f_i) in Eqs.(28), (32), and (33) has been calculated from the following semi-empirical correlation developed recently by the present authors[19] :

$$f_i = 0.01(3X)^{(0.8+X)/4} \tag{37}$$

where

$$X = 0.02\left(\frac{V_r}{\sqrt{gD}}\right)^{2/3} Re_r^{1/3}\left(\frac{D_{h,l}}{D+D_{h,l}}\right)^2 \tag{38}$$

In Fig.3 the (η_0/D) values predicted by Eq.(28) are compared with experimental values obtained in the present duct tests. At the onset of slugging in the experiment, η_{cr}/H_g is 0.535 when the dimensionless water depth H_l^* is 0.208, and the η_{cr}/H_g value slightly decreases to 0.532 when H_l^* is increased to 0.714.

Figure 4 shows the probability of slug occurrence as a function of the relative velocity (V_r) for various superficial water velocities in a long horizontal pipe. From this figure, it can be observed that the relative velocity at which the transition to a slug flow occurs decreases with increase in the superficial water velocity, but it reaches a saturation value at about $V_r = 5\ m/s$ for the range of present experimental parameters used. Also, the probability of slug occurrence becomes 1.0 even for low suferficial water velicity (e.g., $0.037\ m/s$) when $V_r > 16\ m/s$.

Figure 5 shows, in particular, the result of reproducibility tests: A number of experiments have been conducted under the same experimental condition to examine the reproducibility of the present experiment. The same test has been run three times at different time interval between the tests, i.e., one day and one month after the first test. This figure shows that there is a reasonable reproducibility.

Figure 6 shows the probability of occurrence of the slugging in a pipe flow against the criterion of the onset of slugging. The $(V_{g,cr})_{th}$ values shown on the abscissa are obtained by substituting the various quantities obtained from the experiment into Eqs.(33) and (32). This figure shows that Eq.(33) tends to overpredict when the superficil water velocity is very low. This deviation may be partly due to the result of using the expression for the ΔE_x derived for a duct flow in the circular pipe flow geometry. When the water depth is low(i.e., $H_l^* < 0.2$) in a pipe flow, the area of the liquid phase is very small compared to that of the duct flow for a given width(i.e., S_i in Fig. 2b), whereas the reverse phenomenon occurs when the water depth is large. In the present work, this effect is taken into account in the geometric factor for the pipe flow using the ratio of hydraulic diameters defined by $(D_{h,g}/D_{h,l})^2$. That is, the geometric factors represented by $C_{P,cr}$ and C_P in Eqs.(32) and (36) are modified as follows :

$$C_{P,cr} = 1 + \frac{32}{9\pi}\frac{D\eta_{cr}}{S_i^2}\left(\frac{D_{h,g}}{D_{h,l}}\right)^2\left(1 - \frac{2H_l}{D}\right) \tag{39}$$

$$C_P = 1 + \frac{32}{9\pi}\frac{D\eta_{cr}}{S_i^2}\left(\frac{D_{h,g}}{D_{h,l}}\right)^2\left(\frac{V_g}{V_{g,cr}}\right)^2\left(1 - \frac{2H_l}{D}\right) \tag{40}$$

Figure 7 shows the probability of onset of slugging obtained from the substitution of the experimental parameters for the condition of onset of slugging into the present model, Eq.(33), using the geometric factor given by Eq.(39). All the experimental data

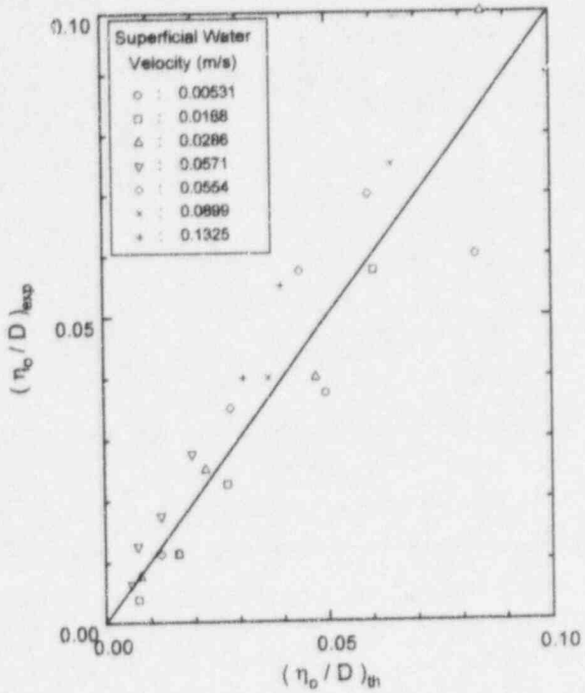

Fig. 3 Comparison Between Theoretical Dimensionless Wave Heights and Experimental Values Obtained in 0.1 × 0.1 *m* Duct Tests

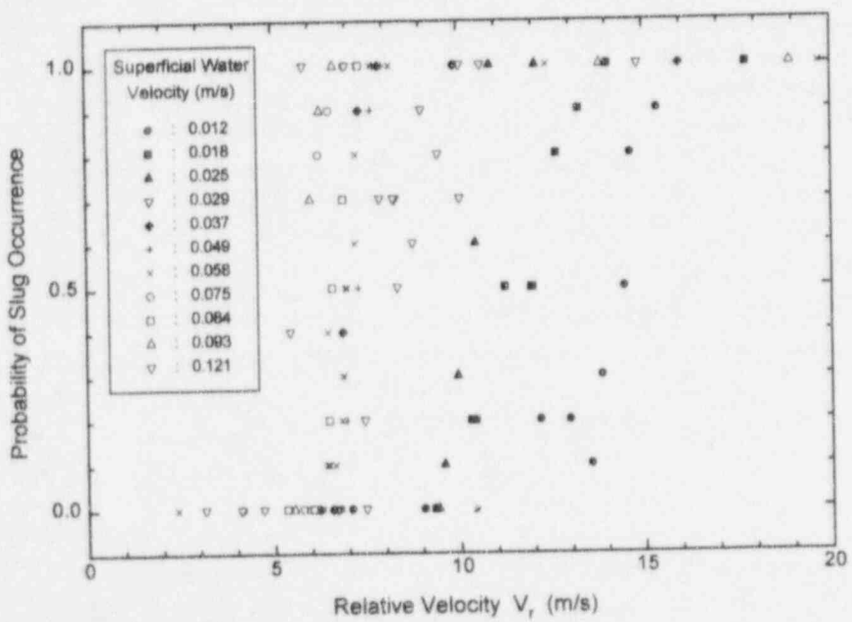

Fig. 4 Probability of Slug Occurrence versus Relative Velocity (V_r) for Various Water Flow Rates in a Long Horizontal Pipe.

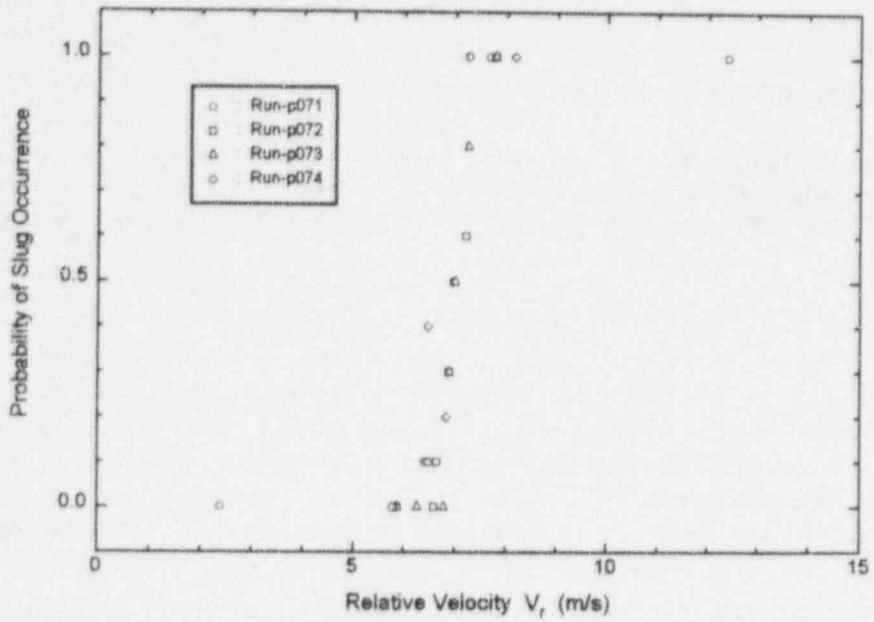

Fig. 5 Reproducibility Tests for the Probability of Slug Occurrenc with a Large Water Flow Rate (1.14×10^{-4} m^3/sec)

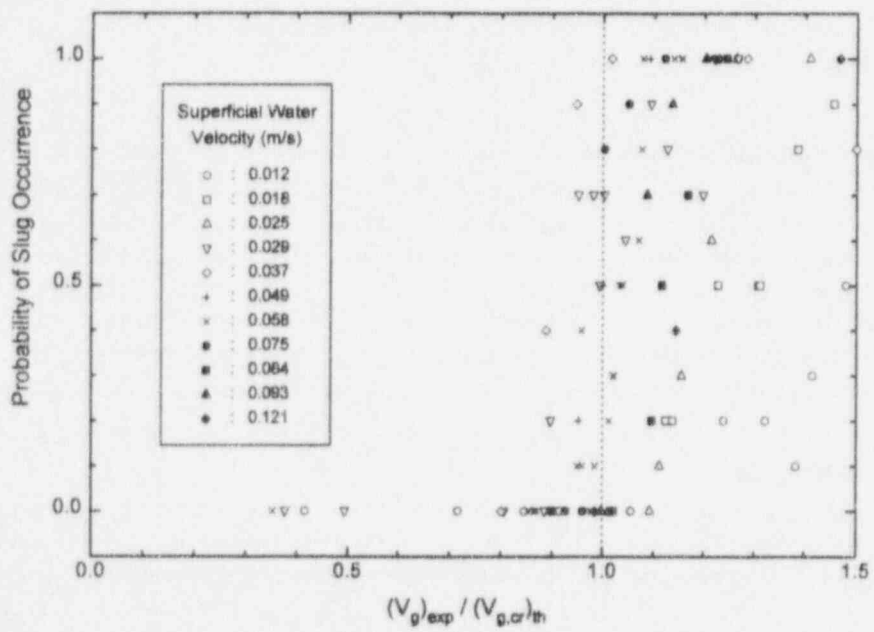

Fig. 6 Probability of Slug Occurrence (in a Pipe Flow) versus $(V_g)_{\exp} / (V_{g,cr})_{th}$ where $(V_{g,cr})_{th}$ is Obtained Using Eqs. (33) and (32)

are well clustered near the point of 1.0 which shows that the present criterion predicts the condition of the onset of slugging fairly well.

5.2 Comparison of Present Theory with Existing Models

In Fig.8, the dimensionless critical numbers for the onset of slugging obtained by present and existing models are compared with present experimental data. The dimensionless numbers shown on the abscissa in Fig.8 are obtained by the following expression:

$$(V_{g,cr})_{exp} \;/\; [\;(V_{g,cr})_{th} \text{ from each model}\;] \tag{41}$$

In Eq.(41), $(V_{g,cr})_{exp}$ is the critical gas velocity at which the onset of slugging occurred for a given test condition in the present experiment. The denominator in Eq.(41), on the other hand, is the critical gas velocity obtained from present and existing models listed in Table 1.

For a given water flow rate, the experimental relative velocity (V_r) at which the onset of slugging occurs corresponds to the point where the 'probability of slug occurrence versus V_r' curve intersects with the horizontal line of zero probability for a given superficial water velocity in Fig.4. For example, $(V_r)_{cr} \simeq 9.3\ m/s$ when the superficial water velocity is $0.018\ m/s$.

Figure 8 shows that when the dimensionless number given by Eq.(41) is equal to unity, then this means that the predictions made by a theory exactly agree with experimental data for the onset of slugging. As can be seen in Fig.8, the 'dimensionless critical values' predicted by present theory using Eq.(41) varies from 0.92 to 1.07 when dimensionless water depth is between 0.208 and 0.714. Also, it can be observed that the Taitel-Dukler criterion overpredicts in the case of low water depth, whereas it underpredicts for large water depth when it is compared with the present experimental data.

6. CONCLUSIONS

1. A theoretical formula for the wave height (η_0) in a horizontal stratified wavy flow, i.e., Eq.(28) has been derived employing the concept of total energy balance over a wave crest to include the shear stress acting on the gas-liquid interface.
2. A new, necessary but not sufficient condition for the onset of slugging, represented by Eqs.(33) and (39), has also been derived from the limiting condition of the formula derived for the wave height. The present criterion for the transition to a slug flow, Eq.(33), reduces to the same form obtained by Wallis and Dobson[2] and Mishima and Ishii[7] when the geometric factor $C_{F,cr}$ is taken as unity($C_{F,cr}$ = 1 for a rectangular duct flow) and the gas-liquid interfacial friction factor f_i is neglected.
3. A total of 103 data for the slug occurrence probability in the pipe flow and a total of 23 data for the wave height in the duct flow are obtained in the present experiment, and these experimental data are compared with present and existing theories.
4. A comparison between theoretical dimensionless wave heights and experimental values obtained in $0.1 \times 0.1\ m$ duct tests shows that the agreement is fairly close except for the case of low superficial water velocity can be seen in Fig.3.

Also, when the measured data are compared with the predictions of the present criterion for transition from a wavy to a slug flow, the agreement is within ±8% as can be deduced from the results shown in Fig.8.

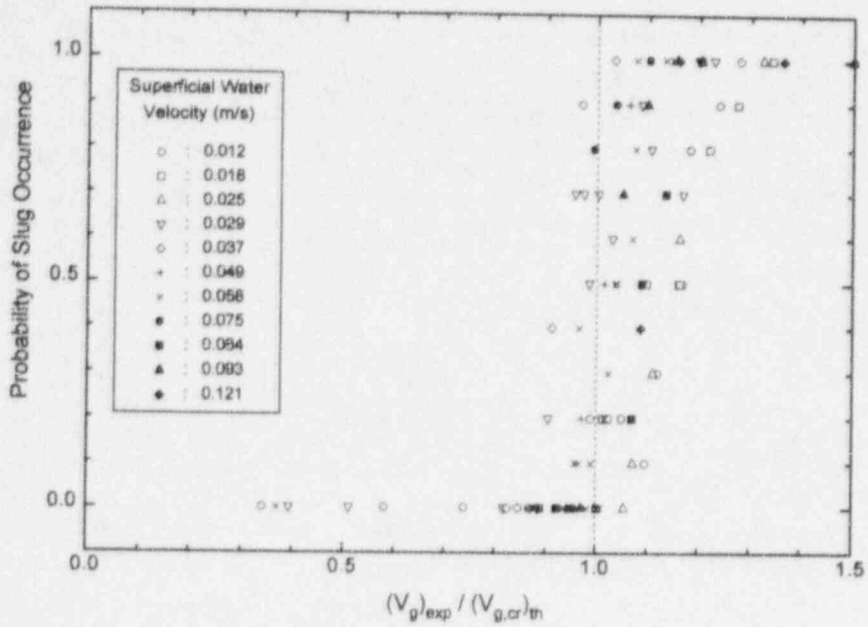

Fig. 7 Probability of Slug Occurrence (in a Pipe Flow) versus $(V_g)_{exp}/(V_{g,cr})_{th}$ where $(V_{g,cr})_{th}$ is Obtained Using Eqs. (33) and (39)

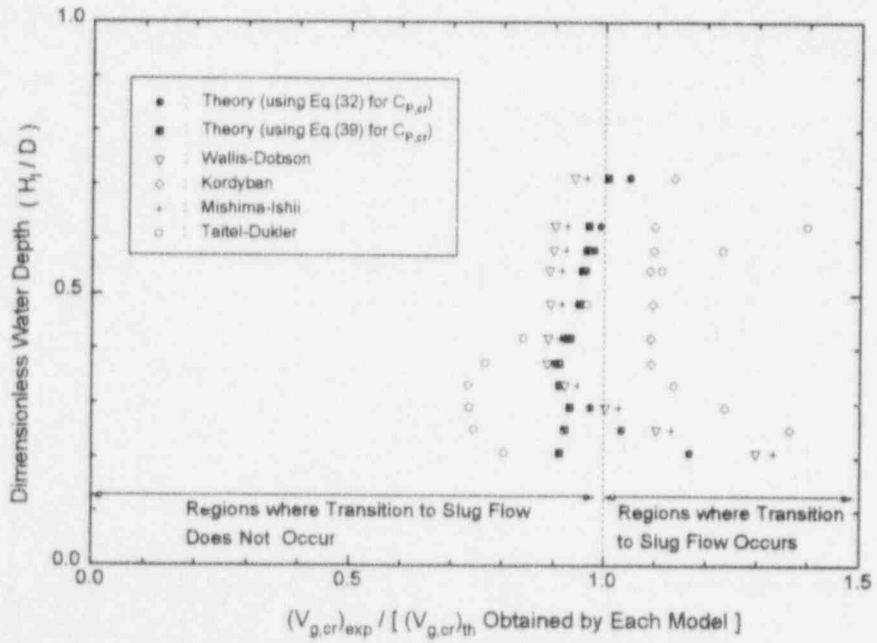

Fig. 8 Comparison of Present and Existing Model Predictions with Experimental Data for Onset of Slugging for Various Dimensionless Water Depths in a Horizontal Stratified Flow

NOMENCLATURE

c_g	constant of velocity potential function	m^2/s
C_f	geometric factor for a pipe flow	
C_y	dimensionless value, defined in text	
D	diameter	m
E_K	kinetic energy	Nm
E_f	potential energy	Nm
f	friction factor	
g	acceleration of gravity	m/s^2
H	depth	m
L	length of pipe	m
Δl	length of wave crest	m
N_f	dimensionless number	
Re	Reynolds number	
S	perimeter	m
ΔS_i	length defined in text for a pipe flow	m
t	time	sec
u_x	local gas velocity in the x-direction	m/s
V	velocity	m/s
V_r	relative velocity, $V_g - V_l$	m/s
W_i	work done by the interfacial shear	Nm
x	axial distance	m
X	dimensionless value, defined in text	
y	transverse distance	m

Greek Symbols

α	void fraction	
γ	angle	*radians*
η	interface displacement or wave profile	m
η_o	wave amplitude or height	m
κ	wave number	m^{-1}
ρ	density	kg/m^3
θ	pipe inclination	*radians*
τ	shear stress	N/m^2
ϕ_v	velocity potential function	m^2/s

Subscripts

c	at wave crest
cr	critical value
exp	experimental value
g	gas (or steam) phase
h	hydraulic
i	interfacial
l	liquid phase
th	theoretical value
x	x-direction
y	y-direction

Superscripts

* dimensionless quantities

ACKNOWLEDGEMENT

Authors gratefully acknowledge the financial support of the Ministry of Science and Technology.

REFERENCES

[1] E.S. Kordyban and T. Ranov, "Mechanism of Slug Formation in Horizontal Two-Phase Flow," ASME J. of Basic Engineering, 857-864 (1970).

[2] G.B. Wallis and J.E. Dobson, "The Onset of Slugging in Horizontal Stratified Air-Water Flow," Int. J. of Multiphase Flow , 1, 173-193 (1973).

[3] Y. Taitel and A.E. Dukler, "A Model for Predicting Flow Regime Transitions in Horizontal and Near Horizontal Gas-Liquid Flow," AIChE J., 22, 1, 47-55 (1976).

[4] E.S. Kordyban, "Some Characteristics of High Waves in Closed Channels Approaching Kelvin-Helmholtz Instability," ASME J. of Fluids Engineering, 339-342 (1977).

[5] E.S. Kordyban, "Some Details of Developing Slugs in Horizontal Two-Phase Flow," AIChE J., 31, 5, 802-806 (1985).

[6] G.C. Gardner, "Onset of Slugging in Horizontal Ducts," Int. J. of Multiphase Flow, 5, 201-209 (1979).

[7] K. Mishima and M. Ishii, "Theoretical Prediction of Onset of Horizontal Slug Flow," ASME J. of Fluid Engineering, 102, 441-445 (1980).

[8] P.Y. Lin and T.J. Hanratty, "Prediction of Slugs with Linear Stability Theory," Int. J. Multiphase Flow, 12, 1, 79-98 (1986).

[9] H. Wang and S. Kondo, "A Study on the Stratified Horizontal Counter-Current Two-Phase Flow," Nuclear Eng. and Design, 21, 45-52 (1990).

[10] E. Kordyban, "Horizontal Slug Flow: A Comparison of Existing Theories," ASME J. of Fluids Engineering, 112, 74-83 (1990).

[11] D. Barnea and Y. Taitel, "Transient Formulation Models and Stability of Steady-State Annular Flow," Chem. Eng. Sci., 44, 325-332 (1989).

[12] N. Brauner and D. Moalem Maron, "Analysis of Stratified/Nonstratified Transitional Boundaries in Horizontal Gas Flows," Chem. Eng. Sci., 46, 1849-1859 (1991).

[13] N. Brauner and D. Moalem Maron, "Analysis of Stratified/Non-Stratified Transitional Boundaries in Inclined Gas-Liquid Flow," Int. J. Multiphase Flow, 18, 541-557 (1992).

[14] O. J. Nydal, S. Pintus, and P. Andreussi, "Statistical Characterization of Slug Flow in Horizontal Pipes," Int. J. Multiphase Flow, 18, 439-453 (1992).

[15] P. Andreussi, K. Bendikson, and O. J. Nydal, "Void Distribution in Slug Flow," Int. J. Multiphase Flow, 19, 817-828 (1993).

[16] Z. Ruder, P. J. Hanratty, and T. J. Hanratty, "Necessary Conditions for the Existence of Stable Slugs," Int. J. Multiphase Flow, 15, 209-226 (1989).

[17] K. H. Bendiksen and M. Espedal, "Onset of Slugging in Horizontal Gas-Liquid Pipe Flow," Int. J. Multiphase Flow, 18, 237-247 (1992).

[18] H. Lamb, Hydrodynamics, Dover Pub. Co., Yew York, Art.231 and 232 (1945).

[19] M.H. Chun and H.Y. Nam, "An Experimental Investigation of the Adiabatic Interfacial Friction Factor in Horizontal Air-Water Countercurrent Stratified Flow," PVP-Vol.270, Transient Thermal Hydraulics, Heat Transfer, Fluid-Structure Interaction, and Structural Dynamics, ASME Book No.G00838 (1994).

CHARACTERIZATION OF NON EQUILIBRIUM EFFECTS ON HIGH QUALITY CRITICAL FLOWS

By E. Camelo, H. Lemonnier, J. Ochterbeck, S. Selmer-Olsen
Commissariat à l'Energie Atomique
Centre d'Etudes Nucléaires de Grenoble
Direction des Réacteurs Nucléaires
Département de Thermohydraulique et de Physique
Service de Thermohydraulique pour les Applications Industrielles

Mailing address: CENG/STI/LEF, 38054 GRENOBLE CEDEX 9, FRANCE
Phone: (33) 76 88 45 40, Fax: (33) 76 88 50 36

ABSTRACT

The appropriate design of various pieces of safety equipment such as relief systems, relies on the accurate description of critical flow phenomena. Most of the systems of industrial interest are willing to be described by one-dimensional area-averaged models and a large fraction of them involves multi-component high gas quality flows. Within these circumstances, the flow is very likely to be of an annular dispersed nature and its description by two-fluid models requires various closure relations. Among the most sensitive closures, there is the interfacial area and the liquid entrained fraction. The critical flowrate depends tremendously on the accurate description of the non equilibrium which results from the correctness of the closure equations. In this study, two-component flows are emphasized and non equilibrium results mainly from the differences in the phase velocities. It is therefore of the utmost importance to have reliable data to characterize non equilibrium phenomena and to assess the validity of the closure models. A comprehensive description of air-water nozzle flows, with emphasis on the effect of the nozzle geometry, has been undertaken and some of the results are presented here which helps understanding the overall flow dynamics. Besides the critical flowrate, the presented material includes pressure profiles, droplet size and velocity, liquid film flowrate and liquid film thickness.

1. INTRODUCTION

The safety of various industrial devices often relies on the appropriate design of relief or venting systems. There is no prototypical situation, as pressurized equipment may be found in almost any industrial field. The variability of the design problems may be exemplified by 2

simple cases: (i) on oil production platforms, several hundreds of safety valves must be sized to protect separators, catch tanks, etc., against fire or production line blockage; (ii) chemical reactors must be protected against thermal runaway by installing safety valves. They must be large enough to depressurize and generate boil off at a large enough rate such that tempering of the uncontrolled reactions occurs [1].

The validity of the sizing procedure relies on among other important parameters, on the appropriate description of the critical flowrate limitation. For given upstream conditions, there is a limit to the maximum flowrate which can be withdrawn from a given vessel through a given piping. Starting from rest, and by decreasing the back pressure, the flow velocity increases up to a point where it exceeds the propagation velocity of small perturbations. The decreasing back pressure information is blocked and the flow is choked. Reliable valve sizing procedure, derived from gas dynamics theory, exists for single-phase gas flows. Unfortunately, many applications require sizing for two-phase flows and conflicting procedures exist to tackle this difficult problem. Even with very high quality flows, relieving areas for two-phase flows may be 2 to 10 times larger than the corresponding single-phase gas situation.

It has been clearly identified in many instances that the flow cannot be considered as a homogenous mixture and that non equilibrium (thermal or mechanical) affects significantly the critical flowrate [2, 3]. Consistent theories have been elaborated to account for these phenomena. These theories are based on area-averaged models which comprise numerous closure relations and the mathematical aspects of critical flow calculations has been thoroughly explained by Bilicki and coworkers [4]. The assessment of these models requires data from well instrumented experiments. The critical flowrate data are not sufficient to validate a two-or three- fluid model. Local data and detailed flow structure information are also required. These parameters are generally predicted by the models, and must be also checked against experiments.

It is the purpose of this paper to describe the air-water high gas quality experiments which have been conducted in nozzles to characterize non equilibrium effects. In the presented experiments, the major source of non equilibrium is the difference in the phase averaged velocities and thermal non equilibrium plays a minor or even no role. Dedicated series of experiments highlight the effects on the critical flowrate of the entrained fraction of liquid at the inlet, of the nozzle throat length and convergence angle, of the upstream pressure and of the thermal non equilibrium at the inlet. Most of the interfacial transfer models require an interfacial area model. Droplet size have been measured in various conditions to validate these models. Size-velocity correlations analysis provide a deep insight into the entrainment and break up mechanisms. Pressure profiles, liquid film thickness and flowrates have also been

measured and these data are the basis of validation of a dispersed annular critical flow model outlined in [5].

2. EXPERIMENTAL FACILITY

Air-water experiments have been performed on the FOSSEGRIM flow loop. This equipment designed by Selmer-Olsen in Grenoble, has been described in [6]. It consists of an open circuit on the air side which can provide up to 400 kg/h at a maximum pressure of 8 bar. This flow capacity provides critical conditions for gas only up to 7 bar in nozzles with a 10 mm diameter throat. On the liquid side, a volumetric pump provides liquid flowrates up to 1000 kg/h which corresponds to a gas mass quality range of 100 - 5 %. The temperatures of both fluids are controlled from ambient to 60°C. The entrained fraction of the liquid upstream of the test section can be varied by admitting the water as annular film or by injecting the liquid centrally in the gas core. Both fluid are exhausted into a muffler which remains at the atmospheric pressure, though for some experiments a valve may be installed at the outlet of the test section to change the back pressure. The control parameters of the experiments on a given test section are therefore the upstream pressure, the liquid flowrate, the entrained fraction of the liquid, the fluids temperature and the back pressure. This is summarized by the following equation which also corresponds to the structure of the data base:

$$M_G = f\left(P_0, M_L, E, T_G, T_L, P_B\right) \qquad (1)$$

Several different test sections have been used to characterize the influence on the critical flowrate of the throat length, the converging angle and the diffuser section. These nozzles consist of successive conical or cylindrical sections connected by zones of gradual area change of known curvature. These sections are shown in Figure 1, where the pressure tap locations are also indicated. Table 1 provides a description of these nozzles. All but the first nozzle have a 10 mm throat diameter.

The liquid flowrate is measured by two electromagnetic flowmeters with staggered ranges. In both ranges 10-100 l/h and 100-1000 l/h the accuracy of the flowrate is ±1% of the reading. The pressure profile is measured by an absolute pressure transducer 0-11 bar, the uncertainty on the pressure measurement is ±0.1% of the full scale. The mass flowrate of gas is calculated from the readings of an absolute pressure transducer, a platinum temperature probe and a turbine flowmeter. The absolute pressure transducer has an accuracy of ±0.25 of the full scale whereas the volumetric flowrate is determined with an uncertainty of ±1% within the range of 6.5-65 m^3/h. The temperatures are measured with platinum probes within an uncertainty of ±0.5°C.

3. CRITICAL FLOWRATE DATA

The primary trend of the data is that the gas critical mass flowrate decreases when the liquid flowrate increases or in other words, when the gas mass quality decreases. Owing to this phenomenon, safety valves sized for gas only become severely undersized as soon as some liquid is entrained with the gas. The data of Figure 2 show a typical reduction by a factor of 6 of the critical gas flowrate for a mass quality greater than 5%.

Two-phase critical flowrate is much more sensitive to the nozzle geometry than it is for single-phase gas flows. The longer the throat, the smaller the critical flowrate. This effect is already present with pure gas flow where it does not however exceed 5%, whereas in two-phase flow this effect may affect the flowrate by more than 40%. Complementary data show that this trend is less pronounced when the pressure increases.

The sensitivity of the critical flowrate to the geometry is the consequence of the relaxation of the mechanical non equilibrium (unequal area averaged phase velocities). The longer the throat the longer the gas drags the liquid and the higher the liquid velocity at the exit. The momentum transferred to the liquid is regarded, from the gas side, as a loss of momentum very similar to the frictional pressure drop in pure gas flow but with a much larger magnitude. Momentum transfer in dispersed flows plays therefore the same role as friction in gas dynamics and hence decreases the critical flowrate. This can be rephrased as: the better the mixing of the phases the smaller the critical flowrate. These mechanisms are well reproduced by simple models [6, 7].

The effect of the entrained fraction at the inlet can be seen from Figures 2 and 3. For the 10 mm nozzle, the smallest critical flowrate is produced by the annular film injection conditions (circles) whereas the central liquid injection gives larger flowrates (triangles). In the former case, it has been observed [6] that the liquid film is squeezed in the convergent where it bulges and then was violently atomized at the throat inlet. In the latter case, the liquid jet formed upstream of the throat is only partly atomized and big lumps of liquid may cross the throat being only roughly broken up. When the liquid is finely dispersed the phases interaction is large and a smaller critical flowrate results. Figure 3 shows opposite trends for the 5 mm nozzle (black symbols). In this case, observation has shown [6] that due to the smaller perimeter reduction from the inlet to the throat, the liquid film remained partly on the wall and was not well atomized whereas for the central injection, the liquid jet diameter (8 mm) exceeds that of the throat and the atomization is strong at the throat inlet. For the 5 mm nozzle, the central injection generates a better mixing and a less critical flowrate results. It is therefore clear that critical flowrate depends on the liquid entrainment history as well as on the entrainment mechanisms. Only a dispersed annular flow model could reproduce this behavior.

4. PRESSURE PROFILE DATA

It has been shown that the flow was not necessarily critical even when the upstream to downstream pressure ratio was as high as 6 [7]. This conclusion has been drawn by analyzing pressure profile data similar to those of Figures 4, 5 and 6. These figures show pressure profiles for the 10 mm nozzle when the upstream pressure is 6 bar and for variable back pressures. For single-phase gas flow, the critical flowrate is reached as soon as the back pressure is less than 5 bar (Figure 4). It is clear that for lower back pressure values the mass flowrate does not increase further and the pressure profiles merge into a single one. From the expected saddle point pattern for the pressure profiles [3], a critical pressure value can easily be identified close to .5 times the upstream pressure. The critical section (location of the bifurcation point between subsonic and supersonic branches) is visibly located close to the throat end, as expected from theory. Next, Figure 5 shows data where liquid flowrate is 360 kg/h which corresponds to a quality of 37%. The flow is assuredly critical there when the back pressure is less than 2.8 bar (Table 2). The saddle pattern is clearly identifiable though the critical pressure ratio is certainly less than 0.4. For a higher liquid flowrate, 910 kg/h which corresponds to a gas quality of 13% (Figure 6), the saddle pattern is hardly visible and a further increase of the liquid flowrate would inevitably produce subcritical flow. Several hundreds of pressure profiles have been measured on the sections shown in Figure 1 and for various combinations of the parameter indicated in (1). A comprehensive report describing these experiments is in preparation.

5. LIQUID FILM FLOWRATE AND FILM THICKNESS DATA

The intensity of the momentum exchange between the phases depends on the entrained fraction of liquid in the vicinity of the critical section: the more entrained the liquid in the gas core, the less the critical flowrate. It is thus clear that if deposition exists, it must affect the critical flowrate in proportion to the amount of deposited liquid. This trend is predicted by annular dispersed flow models [5]. When deposition occurs, a liquid film is formed and determining the liquid film flowrate provides an indirect measure of the intensity of the deposition phenomena.

Using straight (truncated) nozzles is the simplest way to get data close to the critical section where it is useful for model assessment. For a cylindrical nozzle, the theory predicts [4] that critical conditions are reached at the end of the duct. Liquid film flowrate as well as droplet size and velocity have therefore been measured downstream of truncated nozzles (tests P, Q, R and S). The liquid film flowrate has been simply determined by separating the core from the film flow with a hollow cone of small angle located immediately (1 or 2 mm) downstream of the nozzle exit [9]. The internal diameter of this hollow cone was 9 mm and it has been considered that the 500 μm gap was large enough to collect any film that could flow along the

wall. The diverted liquid film flow has been metered separately by using a calibrated capacity. Data shown in Figure 7 suggest that the gap width is probably large enough for liquid flowrates smaller than 400 kg/h. For larger values of the liquid flowrate, the measured liquid film flowrate does not increase probably because some of the wave crests are larger than the gap width and are inefficiently collected. Figure 7 also shows that irrespective of the film diverter adjustments, the liquid entrained fraction is rather constant at the throat end and that the central injection of liquid generates slightly larger film flowrates. This is probably the consequence of the incomplete atomization of the centrally injected liquid. The partly atomized liquid (bigger droplets) may deposit faster under the action of the transversal momentum gained in the convergent section whereas well atomized liquid film may produce smaller droplets easily entrained in the flow and therefore less prone to deposit. Though the magnitude of this trend is barely larger than the data scatter it seems however significant. Data not shown here indicate that increasing the pressure does not change the overall pattern of the data but slightly increases the entrained liquid fraction.

Liquid film flowrate is slightly but significantly smaller at the outlet of a shorter nozzle (Figure 8). Similarly to the data from longer nozzles, increasing the pressure decreases slightly the liquid film flowrate. It seems however that no significant differences exist between the two injection modes. This is probably an artifact and rather the consequence of the particular experimental conditions. For practical reasons, the straight section separating the injection section (z=0) and the nozzle convergent section was 150 mm longer in these tests than what is shown in Figure 1. As a consequence, when the liquid is injected centrally, turbulence has more time to disperse the liquid and a significant film flow exists at the inlet of the convergent section. For most of the low values of the liquid flowrate the actual nozzle inlet conditions do not differ very much when the injection mode is varied.

By comparing Figure 7 and 8 where only the throat length differs, it seems reasonable to think that deposition occurs in the throat and that its magnitude is small. Droplet deposition is also suggested by the film thickness data shown in Figure 11 [6]. The film thickness grows clearly along the nozzle throat. Considering that the gas flow should accelerate and consequently drag and stretch the film, its thickening may only result from deposition. However, deposition in the throat is probably not the phenomenon which has the greatest impact on the critical flowrate and the analysis should focus on the interfacial area modeling.

6. DROPLET SIZE DATA

Droplet size and velocity measurements have been performed by using a Phase Doppler Anemometer. Due to space limitations, the measurements have been performed on the axis of the nozzle 15 mm downstream of its exit. Preliminary data have already been analyzed in [8]. These data have confirmed the model predictions that critical flow was impossible in

dispersed flow regime when the quality was less than a value ranging between 10 to 20%. In these conditions, the momentum lost by the gas is so large that reaching the sound velocity is no longer possible. The nature of the liquid entrainment mechanisms discussed in Section 3 and suggested by observation has also been confirmed by the analysis of the size-velocity correlations [8].

The Sauter Mean Diameter of the droplet decreases when the liquid flowrate increases (Figure 9). This is the mere consequence of the strong velocity decrease shown in Figure 10 which results from the decrease of critical flowrate shown in Figure 2. For the long nozzle, The Sauter Mean Diameter differs significantly from the mean diameter due to this two-peak distribution shown typically in Figure 12. The differences in the D_{SM} are not due to the overall drift of all the size distribution but rather to a change in the distribution of the droplets between the two peaks. This suggests that droplets are created by two different mechanisms. This is confirmed by the single peaked distributions shown in Figure 13 for short nozzles. The first peak close to 20 μm is present in both long and short nozzle data and may be assigned to the primary atomization mechanism at the inlet of the throat. On the other hand, the second peak may either correspond to either secondary atomization phenomena in the throat (from the liquid film) either be characteristic of the shattering of the liquid film downstream of the exit of the nozzle.

Figure 10 shows large differences in the droplet velocities between the long and the short nozzle. These differences are probably not the signature of a specific phenomenon but are rather mimicking the changes in the critical flowrate resulting from the already discussed mechanisms: the larger the critical flowrate the more energetic the break-up mechanisms.

7. FLOW VISUALIZATION

Some shadowgraphs were taken at the outlet of the long cylindrical nozzles in order provide a correct interpretation of the granulometry measurements at 4 and 6 bar upstream pressure. As already mentioned earlier in this text, the measurements have been taken downstream of the exit plane of the nozzle were the well known barrel shock and Mach disk patterns are clearly identifiable (Figure 13). These pictures indicate that at 4 and 6 bar the measuring volume is inside the supersonic jet which explain the supersonic droplet velocity measured at high quality. In two-phase flow, the shock structure remains unchanged (Figure 13) in spite of the presence of the second phase and a clear secondary atomization zone is shown immediately downstream of the Mach disk. Considering that parallel light absorption is proportional to the square of the droplet diameter, the atomization process downstream of the Mach disk is revealed by the darkening of the flow resulting from an increase of the interfacial area.

8. CONCLUSIONS

It was beyond the scope of this paper to present all the data that had been collected on nozzle flow experiments. A report describing them is in preparation and will serve as a basis for the development of a dispersed annular critical flowrate model and for code validation. It has rather been our intention here to show the kind of analysis and understanding on the flow processes that could be gained from the analysis of various sources of data. In particular, it has been shown that the critical flowrate was dependent on the flow history including different entrainment mechanisms and deposition processes.

REFERENCES

[1] Maddison N. & Rogers, R. L., «Understanding Chemical Reactions Hazards», **Chemical Technology Europe, 1**, 2, 13-19 (1994).

[2] Lemonnier, H., Selmer-Olsen, S., Aarvik, A. & Fjeld, M., 1991, «The effect of relaxed mechanical non equilibrium on gas-liquid critical flow modelling», **ANS Proceedings, 1991 National Heat Transfer Conference 5**, 57-65 (1991).

[3] Bilicki, Z. & Kestin, J., «Physical aspects of the relaxation model in two-phase flow », **Proc. Royal Society London 428 A,** 379-397 (1990)

[4] Bilicki, Z., Dafermos, C., Kestin, J., Majda, J. & Zeng, D. L, «Trajectories and singular points in steady state models of two-phase flow», **Int. J. Multiphase Flow 3**, 1-22 (1987).

[5] Camelo-Cavalcanti, S. E., Lemonnier H.,& Ochterbeck, J. M. , «Experimental and theoretical study of the thermal non equilibrium on two-phase two-component critical flow», to be submitted to Int. Journal Multiphase Flow and presented at European Two-Phase Flow Group Meeting, Piacenza, Italy, June 6-8 (1994).

[6] Selmer-Olsen, S., «Etude théorique et expérimentale des écoulements diphasiques en tuyère convergente divergente », Doctorat of Institut National Polytechnique de Grenoble, France (1991). Dissertation parlty in English, available on request from the second author.

[7] Lemonnier, H. & Selmer-Olsen, S., «Experimental investigation and physical modelling of two-phase two-component flow in a converging-diverging nozzle », **Int. J. Multiphase Flow 18**, 1-20 (1992).

[8] Lemonnier, H. & Camelo-Cavalcanti, E., S., «Droplet size and velocity at the exit of a nozzle with two-component near-critical and critical flow », **ANS Proceedings National Heat Transfer Conference 7**, 93-100 (1993).

[9] Camelo-Cavalcanti, E., S., «Caracterização de escoamento bifásico ar-água, disperso e critico, em bocal convergente-divergente», PhD thesis of the University of Rio de Janeiro, Brazil (1993).

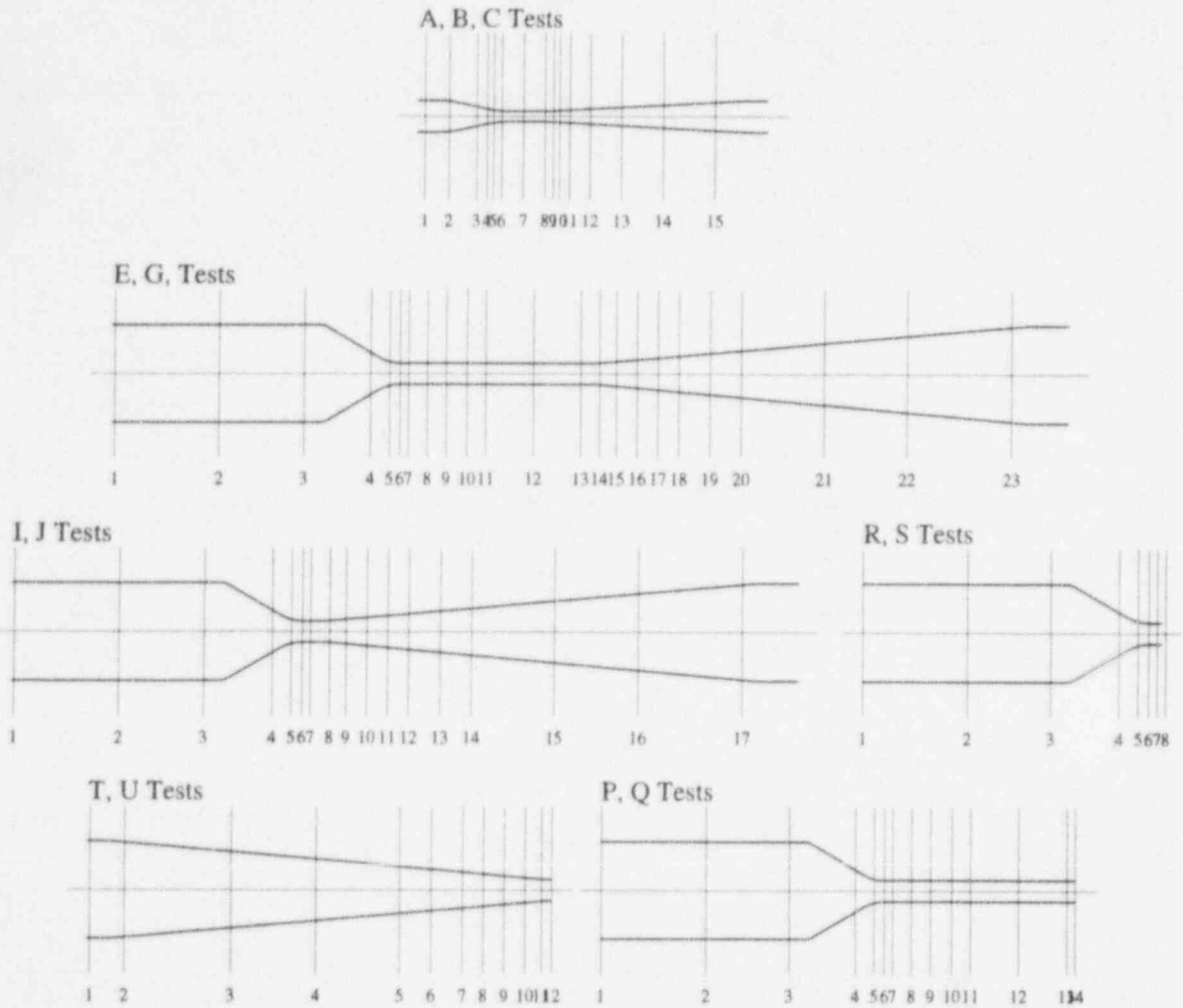

Figure 1: Nozzles utilized for the experiments. The numbers refer to the pressure tap locations. In the C, E, I, Q, S and U tests, the liquid is admitted in the test section as an annular film whereas in the A, G, J, P, R and T tests the liquid is injected centrally in the gas core.

Tests A, B, C, D		
Z (mm)	D (mm)	R_C (mm)
0	15	N. A.
15	15	38
38.5	5	38
63.5	5	76
158.5	15	152
168.5	15	N. A.

Tests E, F, G, H, M, N		
Z (mm)	D (mm)	R_C (mm)
0	46	N. A.
99.46	46	5
130.64	10	20
231.0	10	20
437.0	46	5
457.0	46	N. A.

Tests I, J, K, L		
Z (mm)	D (mm)	R_C (mm)
0	46	N. A.
99.46	46	5
130.64	10	20
148.0	10	20
354.0	46	5
374.0	46	N. A.

Tests P, Q		
Z (mm)	D (mm)	R_C (mm)
0	46	N. A.
99.46	46	5
130.64	10	20
225.0	10	N. A.

Tests R, S		
Z (mm)	D (mm)	R_C (mm)
0	46	N. A.
99.46	46	5
130.64	10	20
142.0	10	N. A.

Tests T, U		
Z (mm)	D (mm)	R_C (mm)
0	46	N. A.
10	46	5
217.0	10	20
220.0	10	N. A.

Table 1: Geometrical description of the nozzles of Figure 1.

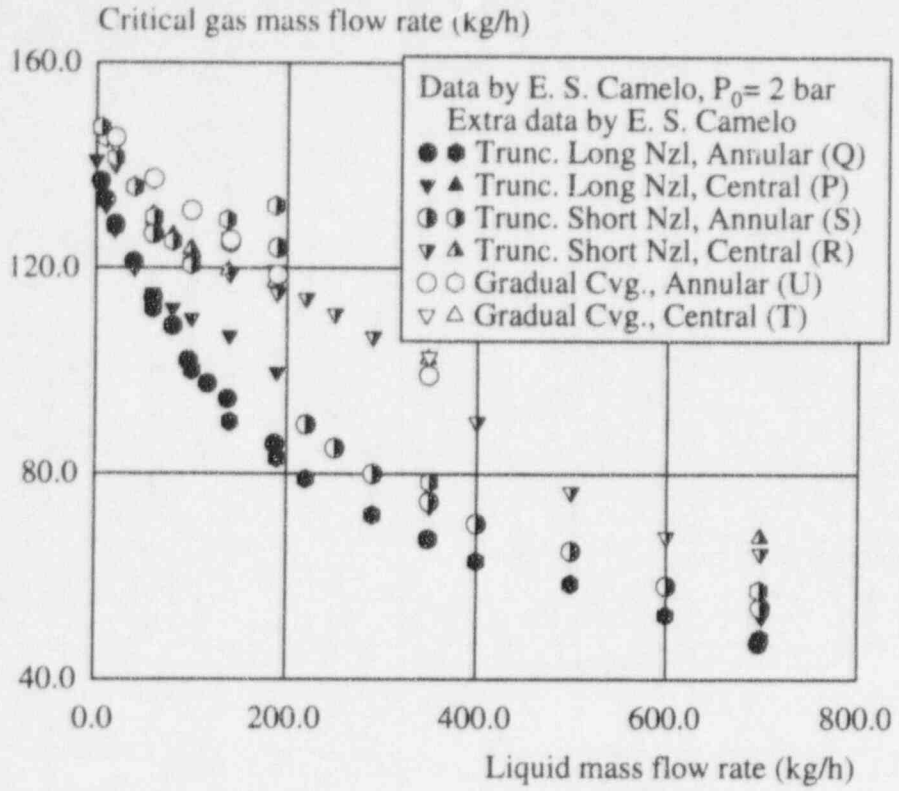

Figure 2: Effect of the nozzle throat length and convergence angle on the critical gas flowrate. This figure also shows the effect of the entrained liquid fraction at the inlet. Liquid film inlet conditions gives smaller gas critical flowrates.

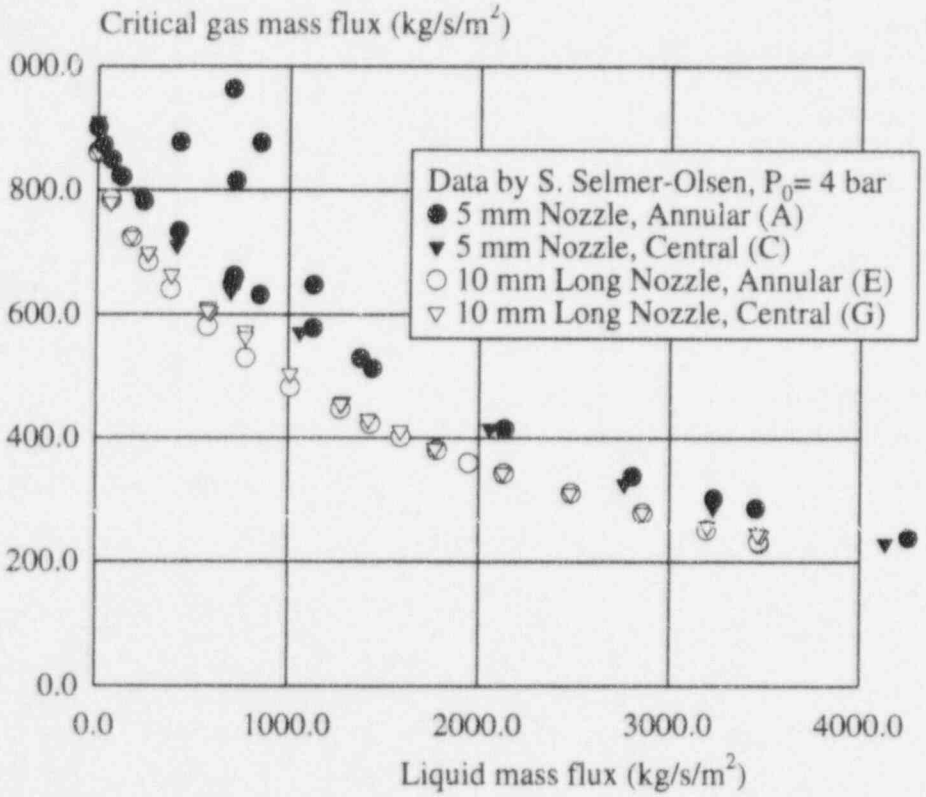

Figure 3: Critical gas mass flux for the 5 and 10 mm nozzles. This figure shows that varying the entrained fraction at the inlet may generate different results depending on the convergent geometry.

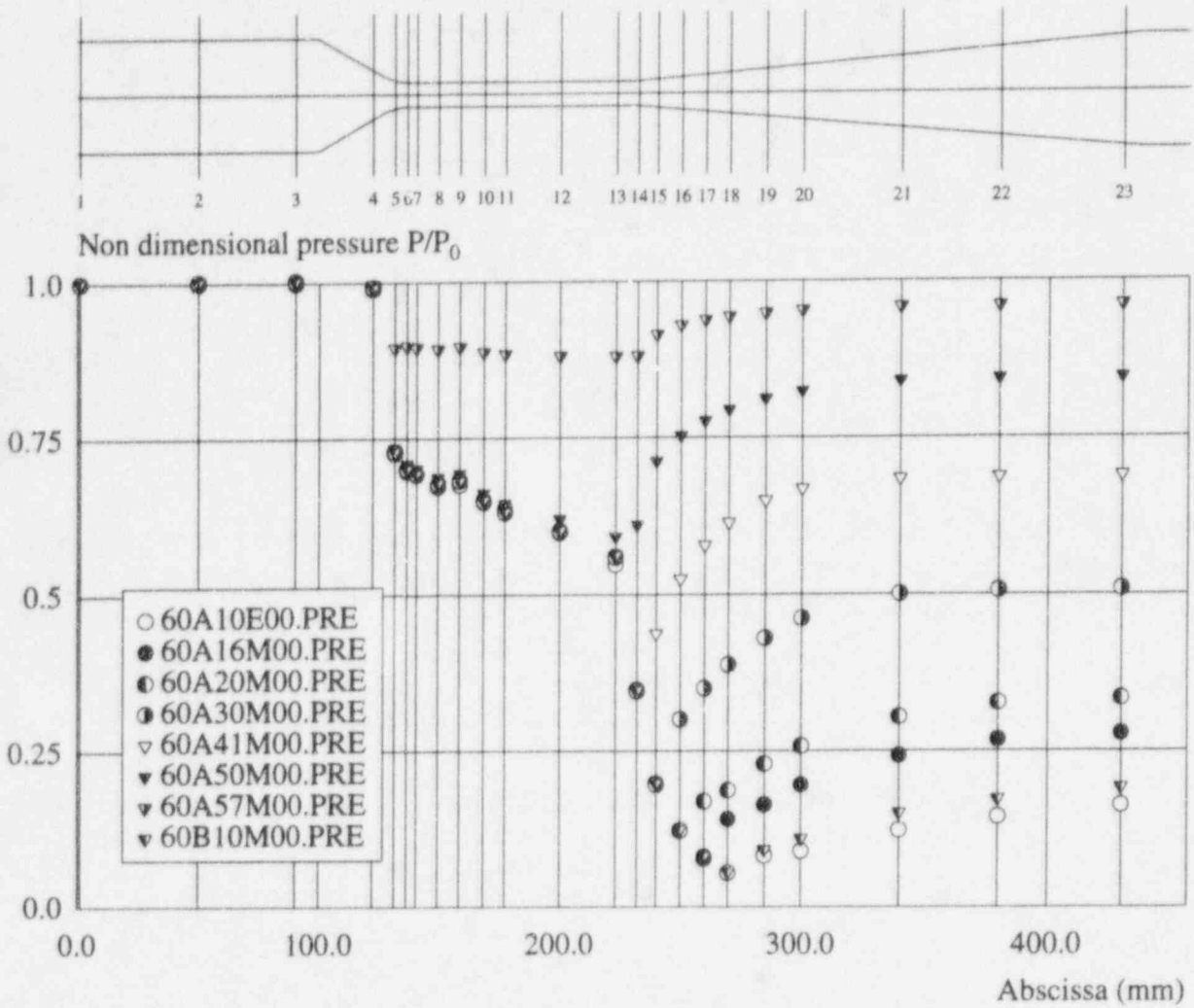

Figure 4: Pressure profiles in the 10 mm long throat nozzle for gas flow only, upstream pressure 6 bar and variable back pressures. The detailed flow parameters are given in Table 2.

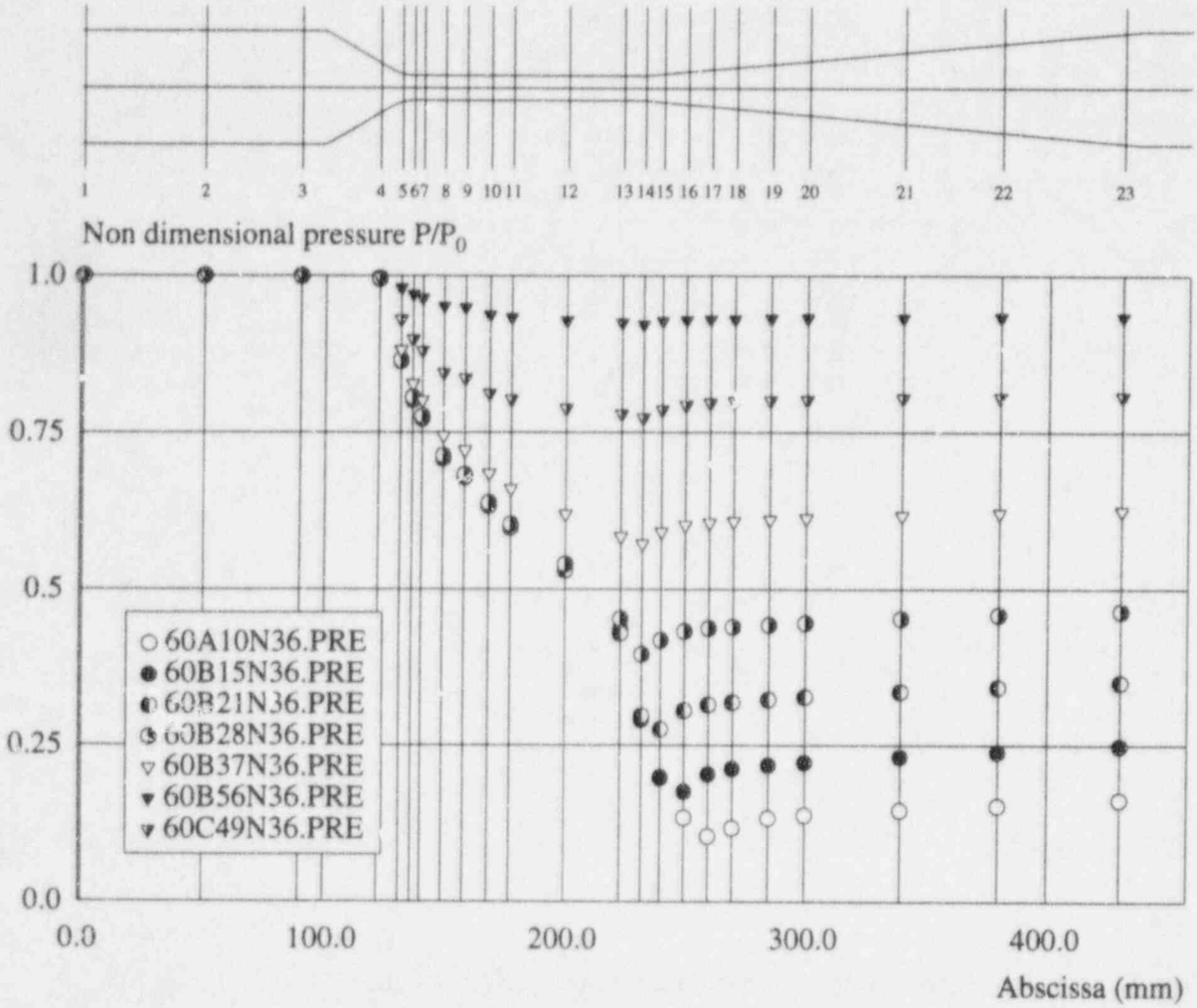

Figure 5: Pressure profiles in the 10 mm long throat nozzle for a liquid flowrate of 360 kg/h, 6 bar upstream pressure and variable back pressures. The detailed flow parameters are given in Table 2

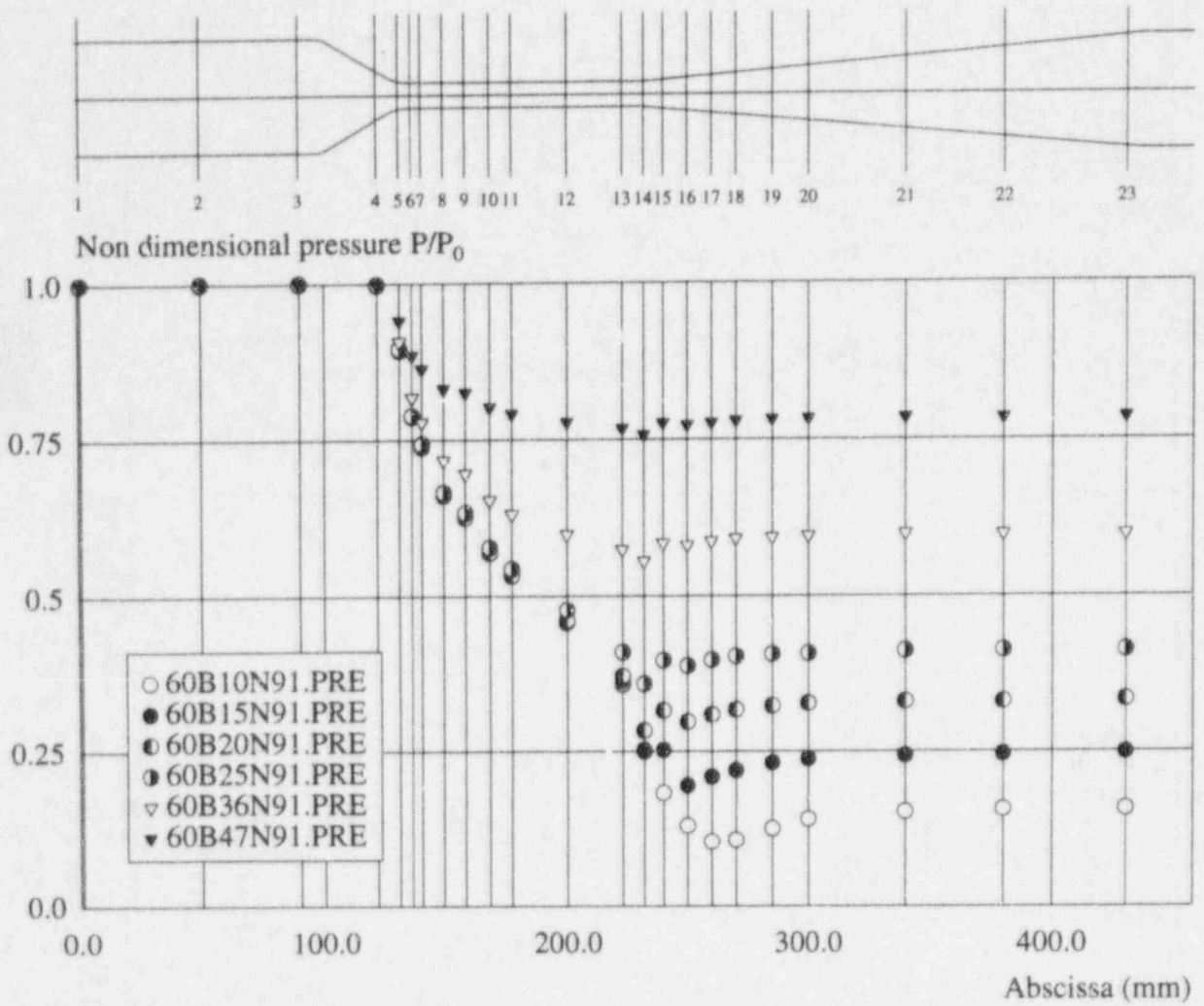

Figure 6: Pressure profiles in the 10 mm long throat nozzle for a liquid flowrate of 910 kg/h, 6 bar upstream pressure and variable back pressures. The detailed flow parameters are given in Table 2

Experiment	M_L (kg/h)	M_G (kg/h)	P_0 (bar)	T_L °C	T_G °C	P_{back} (bar)
60A10E00.PRE	0	363,938	5,9672	20,6	22,1	0,9725
60A10M00.PRE	0	364,258	5,9014	17,6	16,6	1,127
60A16M00.PRE	0	364,576	5,9402	17,6	17,9	1,6501
60A20M00.PRE	0	364,471	5,9386	17,7	17,9	1,9863
60A30M00.PRE	0	364,148	5,9431	17,7	18	3,0226
60A41M00.PRE	0	364,403	5,9372	17,9	18,2	4,0875
60A50M00.PRE	0	361,339	5,9437	18,2	18,6	5,022
60A57M00.PRE	0	246,597	5,9841	18,2	18,7	5,7486
60B10M00.PRE	0	362,885	5,9391	18	18,8	1,1351

Experiment	M_L (kg/h)	M_G (kg/h)	P_0 (bar)	T_L °C	T_G °C	P_{back} (bar)
60A10N36.PRE	358,369	221,231	5,9916	17	18,3	0,9744
60B15N36.PRE	358,639	221,291	5,9898	16,7	18,2	1,4886
60B21N36.PRE	357,563	220,651	5,9927	18,5	18,5	2,0975
60B28N36.PRE	358,152	219,964	5,9914	18	17,7	2,7835
60B37N36.PRE	358,269	208,442	5,9939	17,5	18,1	3,7512
60B49N36.DEB	357,06	160,743	6,004	18,5	18,3	4,8509
60B56N36.PRE	357,718	81,126	6,0137	18,5	19,7	5,6197
60C49N36.PRE	358,005	160,503	6,0013	18,4	18,8	4,8453

Experiment	M_L (kg/h)	M_G (kg/h)	P_0 (bar)	T_L °C	T_G °C	P_{back} (bar)
60B10N91.PRE	909,936	139,16	5,9915	19,6	19,2	0,9452
60B15N91.PRE	910,236	139,839	6,0066	20,2	20,6	1,4956
60B20N91.PRE	909,267	139,078	6,0052	19,7	20,6	2,0026
60B25N91.PRE	906,69	139,901	6,0023	19,3	20,7	2,4806
60B36N91.PRE	907,011	130,119	6,0036	19,1	19,5	3,5949
60B47N91.PRE	908,724	98,93	6,0072	19,2	19,2	4,7137

Table 2 : Detailed values of the control parameters of the experiments of Figures 4, 5 and 6.

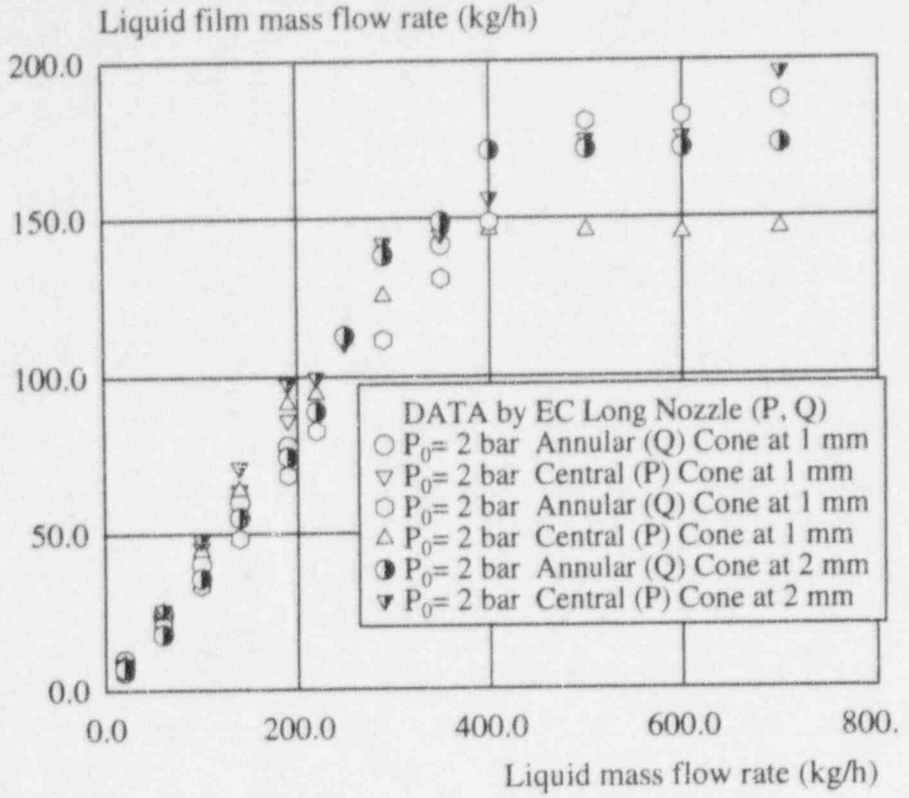

Figure 7: Liquid film flowrate as a function of the liquid flowrate for the 10 mm long nozzle. Upstream pressure 2 bar, for various conical diverter adjustments and the two liquid injection modes.

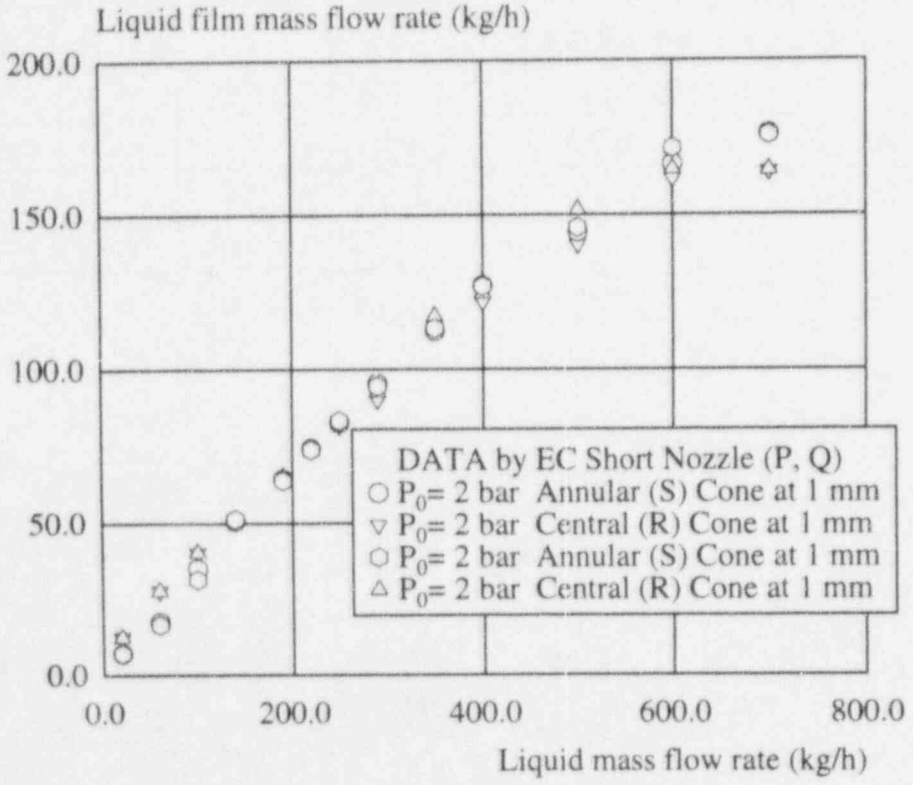

Figure 8: Liquid film flowrate as a function of the liquid flowrate for the 10 mm short nozzle. Upstream pressure 2 bar, for the two liquid injection modes.

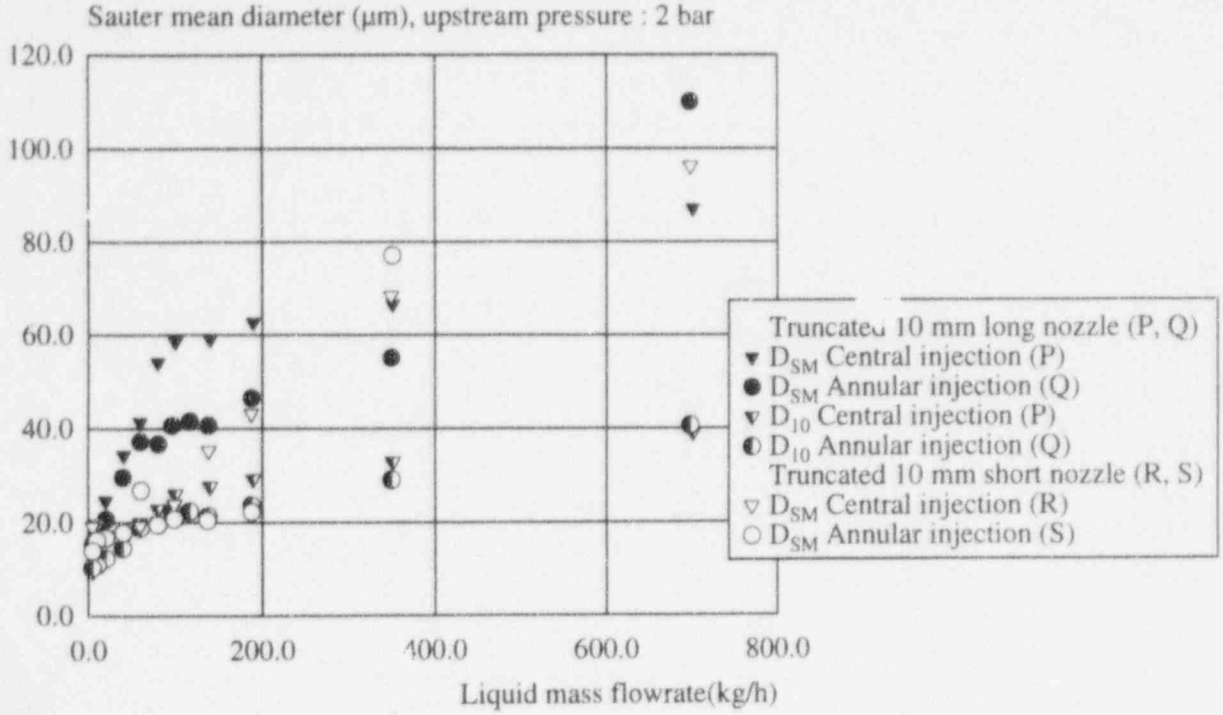

Figure 9: Droplet size as a function of the liquid flowrate at the exit of the two 10 mm throat diameter nozzles. Upstream pressure 2 bar, for the two liquid injection modes.

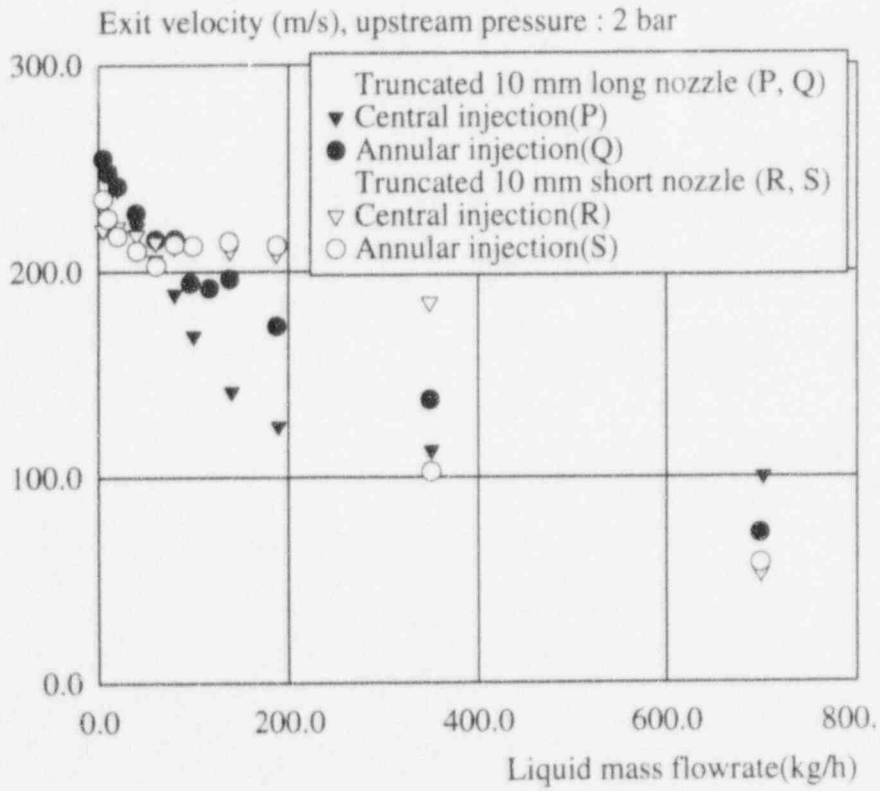

Figure 10: Droplet velocity as a function of the liquid flowrate at the exit of the two 10 mm throat diameter nozzles. Upstream pressure 2 bar, for the two liquid injection modes.

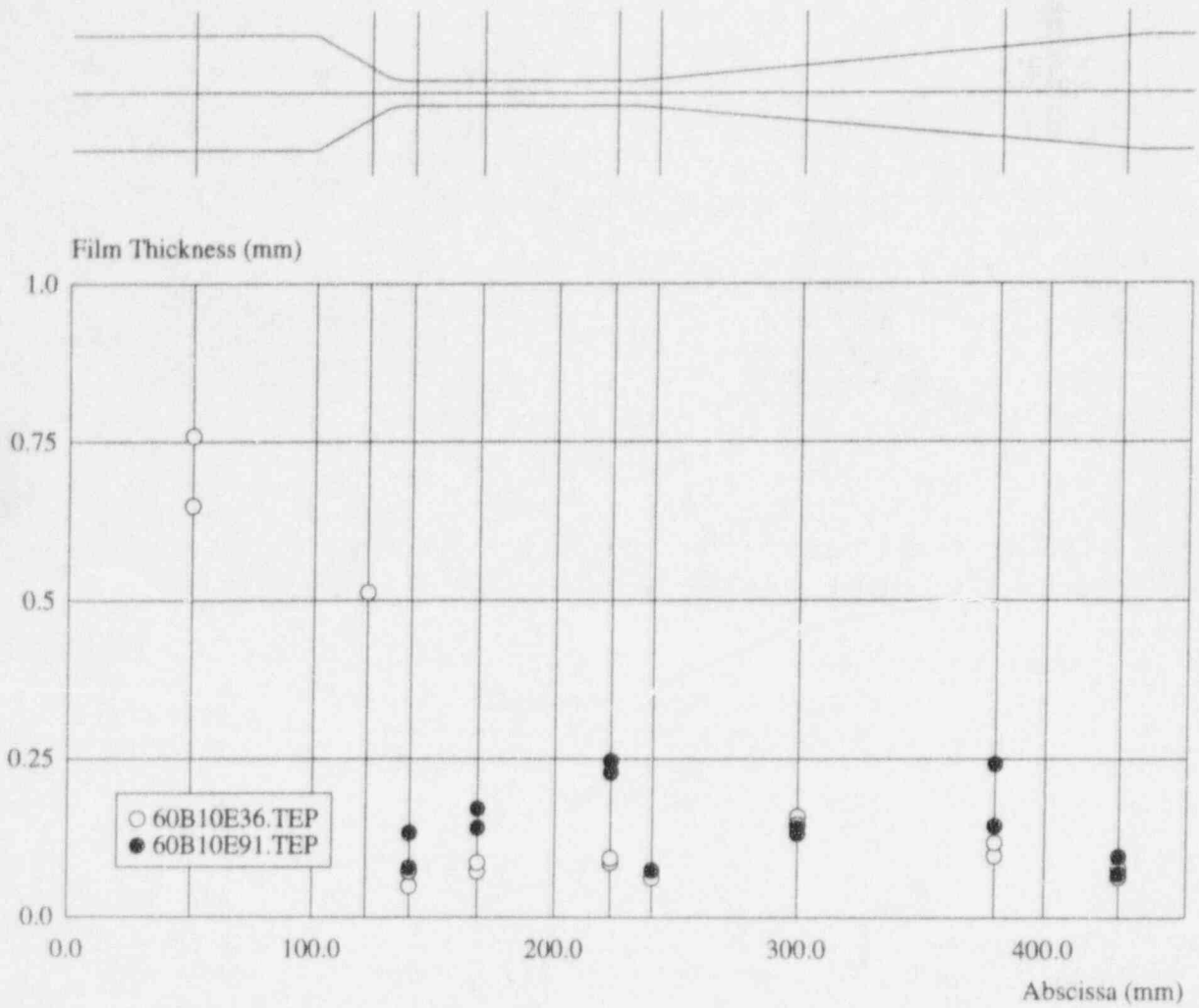

Figure 11: Film thickness measurements by impedance probes. Upstream pressure 6 bar, back pressure 1 bar, annular film inlet conditions, liquid flowrate 360 kg/h for run 60B10E36 and 910 kg/h for the run 60B10E91.

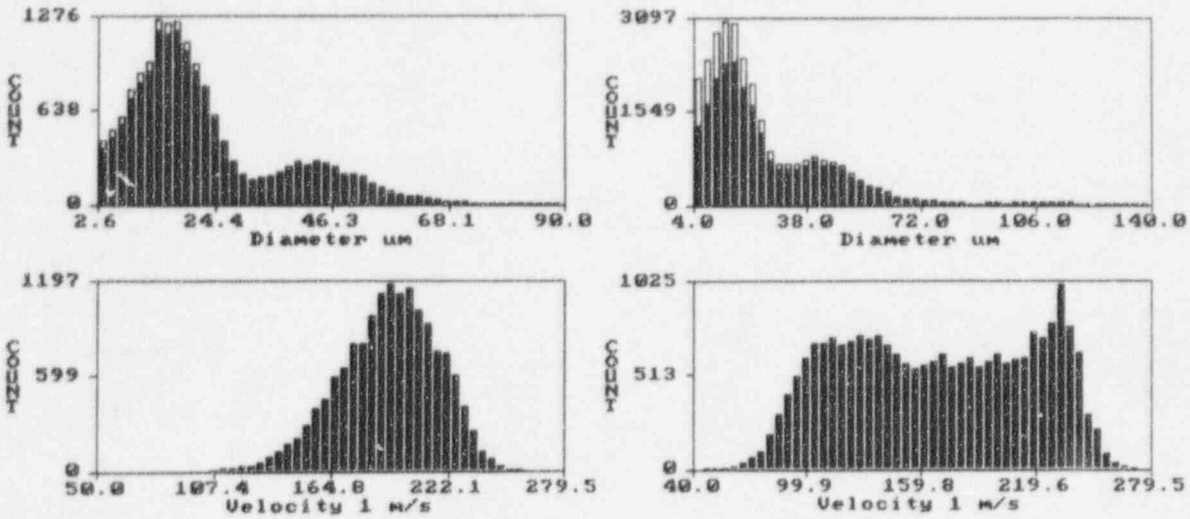

Figure 12: Droplet size and velocity at the exit of the 10 mm throat diameter nozzle (long throat). Upstream pressure 2 bar, liquid flowrate 100 kg/h. On the right hand: central injection, on the left hand: annular injection.

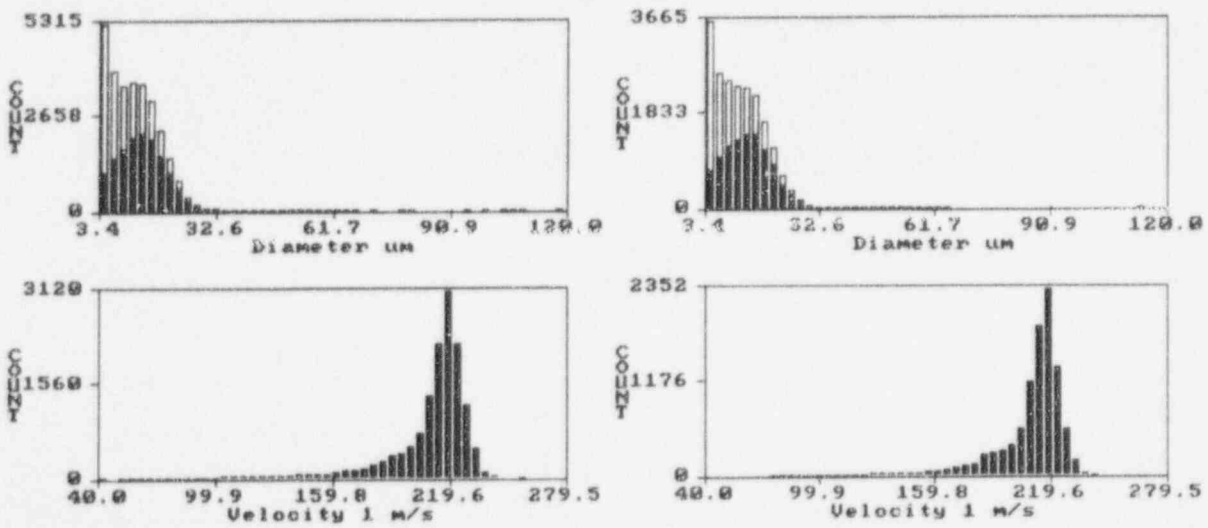

Figure 13: Droplet size and velocity at the exit of the 10 mm throat diameter nozzle (short throat). Upstream pressure 2 bar, liquid flowrate 100 kg/h. On the right hand: central injection, on the left hand: annular injection.

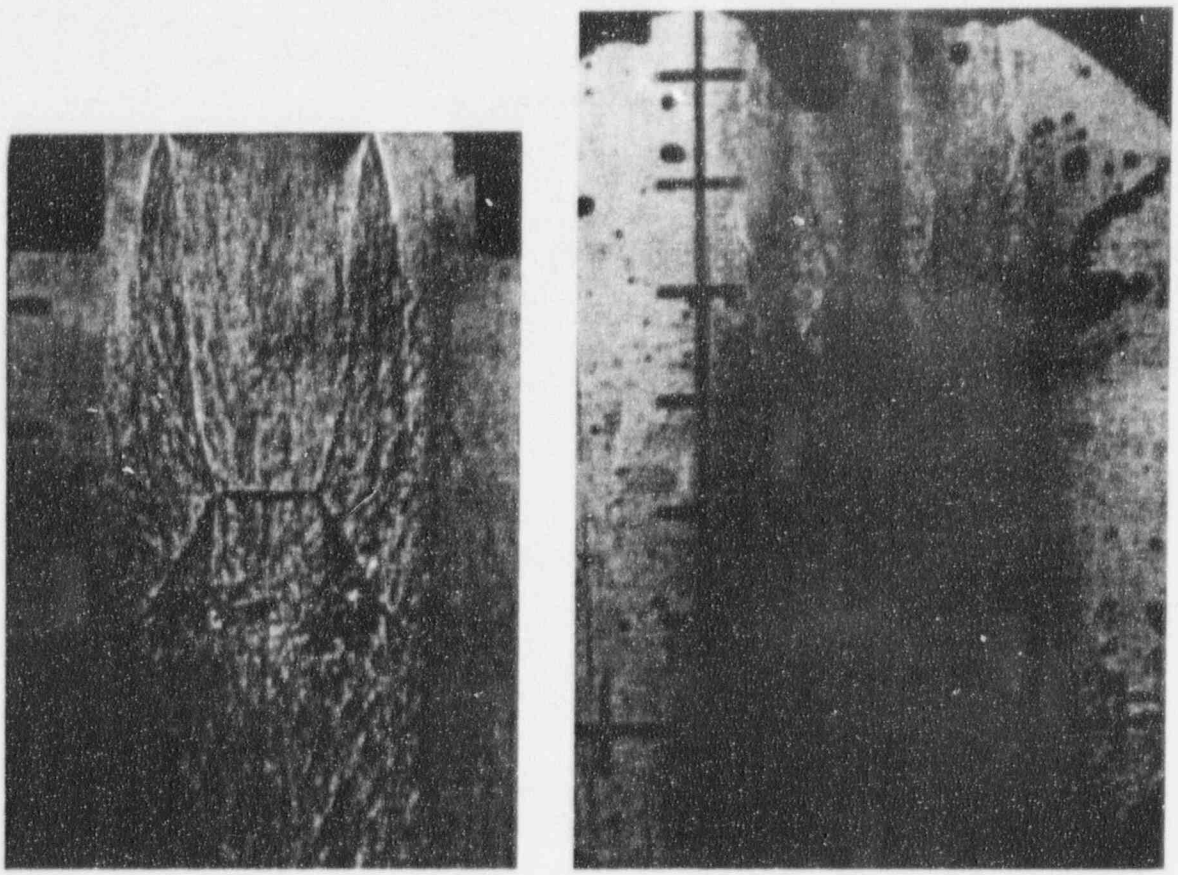

Figure 14: Shadowgraphs of the jet emerging from the 10 mm long throat nozzle. Upstream pressure 6 bar, single-phase flow on the right, the liquid flowrate is 31. kg/h on the right picture.

Local Pressure Gradients Due to Incipience of Boiling in Subcooled Flows

Arthur E. Ruggles
Nuclear Engineering
University of Tennessee
Knoxville, Tennessee

Joel L. McDuffee
Engineering Science & Mechanics
University of Tennessee
Knoxville, Tennessee

Abstract

Models for vapor bubble behavior and nucleation site density during subcooled boiling are integrated with boundary layer theory in order to predict the local pressure gradient and heat transfer coefficient. Models for bubble growth rate and bubble departure diameter are used to scale the movement of displaced liquid in the laminar sublayer. An added shear stress, analogous to a turbulent shear stress, is derived by considering the liquid movement normal to the heated surface. The resulting mechanistic model has plausible functional dependence on wall superheat, mass flow, and heat flux and agrees well with data available in the literature.

Nomenclature

A_{xs}	:	channel cross section area (m^2)
C_p	:	specific heat (J/kg °C)
C_{vm}	:	virtual mass coefficient
d	:	diameter (m)
E	:	Energy (J)
f	:	bubble growth frequency (s^{-1})
$f_{l\phi}$	:	single phase friction factor
G	:	mass flux (kg/m^2s)
h_{fg}	:	latent heat (J/kg)
IB	:	Incipience of Boiling
Ja	:	Jakob Number, $(T_w-T_{sat})C_p r_l/r_v h_{fg}$
k	:	conductivity, W/m°C
K	:	proportionality constant
l	:	length scale (m)
m	:	mass (kg)
n	:	area density of bubbles (m^{-2})
OSV	:	Onset of Significant Vapor
P_h	:	heated perimeter (m)
Pr	:	Prandtl Number, m C_p / k
q	:	heat flow (W)
r	:	radius (m)
t	:	time (s)
T	:	temperature (°C)
u	:	velocity (m/s)
u′, v′,	:	velocity perturbations (m/s)
α	:	thermal diffusivity (m^2/s)
α_w	:	wall void fraction
ε	:	eddy viscosity
ρ	:	density
τ	:	shear stress (Pa)
μ	:	dynamic viscosity (kg /m s)

Subcripts

b	:	bubble
H	:	property of heat transfer
l, v	:	liquid, vapor
life	:	bubble lifetime
M	:	property of momentum transfer
m, max	:	maximum value
o	:	initial or mean value
sat	:	saturation condition
t	:	turbulent
v	:	viscous
w	:	channel wall

Introduction

Highly subcooled flows are frequently used to remove high heat fluxes. These systems often operate at low to intermediate pressures (i.e., less than 5MPa) to reduce the conduction lengths associated with the pressure boundaries. Many heat removal systems use parallel flow paths connected between plenums. The design limit for systems of this type is associated with the minimum in the pressure demand characteristic of a heated channel. This minimum occurs when the production of void in the heated channel causes the total channel pressure drop to increase with decreasing mass flux rather than decrease, as is the case in single phase flow. The first channel in the system to encounter the minimum in the pressure demand characteristic is subjected to a Ledinegg [1932] flow excursion which leads to a rapid decrease in the channel mass flux and a corresponding increase in the channel exit enthalpy. The channel usually fails during the flow excursion due to a primary departure from nucleate boiling.

The position of the minimum in the pressure demand characteristic can be predicted if accurate models exist for the resistance to flow in the channel in the single phase and two phase regions. The position of the minimum in the pressure demand characteristic is closely connected with when significant void first appears at the channel exit in high mass flux and low pressure systems. Accurate prediction of when significant void first appears in the channel requires accurate models for the flow resistance in the channel for the single phase region and for the region from the Incipience of Boiling (IB) to the Onset of Significant Vapor (OSV). Otherwise, the mass flow in the heated channel and the exit enthalpy of the flow cannot be calculated, and the onset of significant void cannot be accurately known.

This situation is exacerbated in systems where the applied flux is tailored to provide a constant margin to the onset of significant void generation or to the incipience of boiling as is done in the Advanced Neutron Source (ANS) Reactor fuel design (Yoder et al [1994]). This approach peaks the applied flux at the inlet of the cooling channel in order to take advantage of the higher subcooling available there. This causes a large portion of the cooling channel to be beyond the incipience of boiling prior to the first occurrence of OSV when off-normal conditions are considered. The flow resistance in the region from IB to OSV is more significant to the evaluation of the thermal limits in such systems.

There exist several treatments of the void development and pressure gradient associated with subcooled flow boiling (e.g., Rouhani and Axelsson [1970; Larson and Tong [1969]; Saha and Zuber [1974]; Avdeev [1986]; Jai and Schrock [1986]; Levy [1967]). The mechanistic models for subcooled void development utilize models for vapor production and condensation. The difference between the vapor produced and that condensed results in vapor formation. Some of these models use a balance between the formation and condensation models to establish the position of the onset of significant vapor (Larson and Tong [1969]); Avdeev, [1986]). Others use separate models to establish when the onset of net vapor generation should occur and activate the vapor production and condensation models accordingly.

The augmentation in heat transfer is related to the augmentation in the wall shear associated with the presence of subcooled void on the wall by evoking the Reynold's analogy. The augmentation in wall shear is modeled by considering parameters such as the wall void or active nucleation site density along with the bubble departure diameter to establish an effective wall roughness. The augmentation in wall roughness is then related to the wall shear using conventional single phase flow modeling techniques. The Reynold's analogy then prescribes the augmentation in the heat transfer coefficient. This general strategy appears several times in the literature (e.g., Larson and Tong [1969]; Avdeev [1986]). This review is representative of previous work in this area but is not exhaustive.

It should be noted that the use of wall roughness implicitly assumes that the bubble growth rate is far slower than the mean fluid velocity near the wall. This condition is rarely met, especially in situations of high heat flux where the bubble departure frequencies are large.

Vapor bubbles form and collapse on and near the heater surface during subcooled boiling in the wall void region as is evidenced by several experimental studies (e.g., Gunther [1951]; Griffith et al [1958]; Bibeau and Salcudean [1994]). The observed behavior of the bubbles varies. Sometimes bubbles form and collapse at the nucleation site. Sometimes the bubbles are formed and slide along the heated surface before condensing on or near the wall. Other times the

bubbles form and depart from the wall into the flow where they condense rapidly. No generally accepted rules exist to determine when each type of behavior is to be expected. However, it is clear that bubbles form and collapse rapidly in the wall void region.

Many models are available for bubble growth and collapse, as can be found in Carey [1993]. The bubble growth and collapse near the surface is used in the mechanistic models for subcooled boiling to quantify the so-called pumping term associated with the convection of energy due to the water displaced by the bubbles near the surface. The liquid displaced by the vapor bubbles also convects momentum. Each bubble formation pushes liquid from a low velocity region near the wall into a higher velocity region away from the wall. Each bubble collapse draws water from the higher velocity region away from the wall to the lower velocity region near the wall. This transfer of momentum normal to the time averaged velocity of the flow produces additional resistance to flow and can be treated in a manner analogous to a turbulent shear stress.

The development that follows uses models for bubble formation, bubble departure diameter, and active nucleation site density to derive a bubble induced turbulent shear stress in the "laminar" sublayer. Both the pressure increase due to mechanical pumping and pressure losses due to turbulent shear are considered.

Direct Thermal to Mechanical Energy Conversion

An oscillating bubble may add energy or momentum to the fluid due to the acceleration of liquid surrounding a bubble during the growth process. The physics of this process can be captured by considering the work done to the surrounding media by a growing bubble.

$$E = \int_0^{r_{max}} \frac{d}{dt}\left(m_{vm} \frac{dr_b}{dt} \right) dr_b \qquad 1$$

Where the liquid virtual mass, m_{vm}, is approximated to first order using a virtual mass coefficient.

$$m_{vm} = C_{vm} \rho_l \frac{2}{3} \pi r_b^3 \qquad 2$$

The constant, C_{vm}, is used to model the liquid accelerated normal to the heater surface due to the formation and growth of the vapor bubble.

It remains to correlate both the bubble volume and growth equations. This development is focused on the thermal hydraulic conditions of the ANS reactor: high heat flux, moderate to high subcooling, high mass velocities, hydraulically smooth channel walls, and moderate to low system pressure. These conditions indicate that rapid, hemispherical bubble growth will occur, and that the growth regime will be inertially controlled. For such conditions Carey [1992] recommends a bubble growth formulation developed by van Stralen [1975] which matches microlayer conduction with the bubble growth rate.

$$r_b(t) = 0.470 Ja\, Pr^{-1/6} \alpha^{1/2} t^{1/2} \qquad 3$$

$$\frac{dr_b(t)}{dt} = 0.235 Ja\, Pr^{-1/6} \alpha^{1/2} t^{-1/2} \qquad 4$$

The relations given by Equation's 2-4 with Equation 1 yield a formula for the mechanical energy transferred to the liquid from the growing bubble.

$$E = 2.548(10^{-3}) C_{vm} \rho_l \pi Ja^5\, Pr^{-5/6} \alpha^{5/2} t_m^{3/2} \qquad 5$$

The maximum growth time, t_m, is related to the maximum bubble radius, $r_{b,m}$, by Equation 3.

$$t_m = \left(\frac{r_{b,m}}{0.470 Ja\, Pr^{-1/6}\, \alpha^{1/2}} \right)^2 \qquad 6$$

Combining this result with Equation 5 gives,

$$E = 0.0245 C_{vm} \rho_l \pi Ja^2\, Pr^{-1/3}\, \alpha r_{b,m}^3 \qquad 7$$

Although Equation 7 is convenient for determining mechanical energy, it is not obvious what effect this energy will have on the flow. Equation 7 can be converted to momentum, and then to a local pressure gradient prediction. If we introduce the area density of bubbles on the channel wall, n, the heated perimeter, P_h, and the bubble oscillatory frequency, f, Equation 7 can be converted to a 2nd order differential in space and time.

$$\frac{\partial^2 E}{\partial x \partial t} = n P_h f E \qquad 8$$

$$= 0.0245 C_{vm} n P_h f \rho_l \pi Ja^2\, Pr^{-1/3}\, \alpha r_{b,m}^3$$

Now dividing through by the mean flow velocity, $U_o = dx/dt$,

$$\frac{\partial^2 E}{\partial x^2} = \frac{0.0245 C_{vm} n P_h f \rho_l \pi Ja^2\, Pr^{-1/3}\, \alpha r_{b,m}^3}{U_o} \qquad 9$$

If it is assumed that all of the work done on the liquid by the bubbles is an isentropic process, then

$$\frac{\partial^2 E}{\partial x^2} = \frac{\partial}{\partial x}\left(\frac{\partial E}{\partial x} \right) = A_{xs} \frac{\partial P}{\partial x} \qquad 10$$

Combining Equations 9 and 10 and converting the bubble radius to the more commonly measured diameter yields

$$\frac{\partial P}{\partial x} = \frac{0.003 C_{vm} P_h n f \rho_l \pi Ja^2 \alpha d_b^3}{U_o A_{xs}\, Pr^{1/3}} \qquad 11$$

It can be shown that, for ANS nominal conditions, the pressure gradient described by Equation 11 is several orders of magnitude below the single phase viscous gradient. It is interesting to note that Equation 11 represents work done on the fluid which actually results in a positive dP/dx contribution. The bubbles will condense and thereby take energy from the fluid. However, the rate of condensation is less than the rate of formation, allowing for net work to be done on the liquid phase.

The bubble growth and collapse is accompanied with dissipative phenomena that increase the pressure gradient in the region from IB to OSV. These phenomena are considered in the three analyses that follow.

Eddy Viscosity due to Bubble Oscillations

In fully developed turbulent flow, the momentum equation must be modified to include the turbulent inertia, $\rho u'v'$. It is common practice to express the inertial terms as an apparent turbulent stress-tensor by redefining the shear stress, τ, as the summation of the Newtonian viscous stresses plus the apparent turbulent stress. For two-dimensional flow, this is approximately

$$\tau = \tau_{viscous} + \tau_{turbulent}$$

$$= \mu \frac{du}{dy} - \rho \overline{u'v'} \qquad 12$$

Many investigators have offered functional forms for the turbulent shear. This investigation presents three mechanistically based methods to formulate the shear due to dynamic bubbles in the region from IB to OSV.

Model 1. The Mixing Length

Prandtl postulated that u′ was of the same order as v′ and that u′ was proportional to the product of a mixing length, l, and the local velocity gradient. (Holman [1990])

$$u' \approx v' \approx l \frac{du}{dy} \qquad 13$$

For subcooled boiling, the length scale can be approximated by evaluating the distance that an arbitrary fluid "lump" would be moved by an expanding or contracting bubble,

$$l = K \left|\frac{dr_b}{dt}\right| \Delta t = K \left|\frac{dr_b}{dt}\right| \frac{2r_b}{u(r_b)} \qquad 14$$

Noting that $u(r_b)$ is related to the velocity gradient,

$$u(r_b) = r_b \frac{du}{dy} \qquad 15$$

Equation 15 leads directly to an approximation for the turbulent shear due to a single pulsating bubble.

$$\tau_{t,b} = 4\rho_l K^2 \left|\frac{dr_b}{dt}\right|^2 \qquad 16$$

A total flow turbulent shear is derived by introducing an area and time averaged nucleation site density. Defining α_w as the area void fraction of bubbles on the wall ($\alpha_w = n\ p\ r_b^2$) and multiplying by the product of the bubble frequency, f, and bubble lifetime, t_{life}, Equation 16 becomes

$$\tau_t = 4\rho_l \alpha_w f t_{life} K^2 \left|\frac{dr_b}{dt}\right|^2 \qquad 17$$

Model 2. The Shear Analogy

In this approach, the velocity perturbation in the direction of flow is modeled using the bubble radius as the characteristic length.

$$u' = r_b \frac{du}{dy} \qquad 18$$

Again assuming that rapid, hemispherical bubble growth occurs, the perturbations in the direction normal to the wall are taken proportional to the bubble growth rate.

$$v' = \frac{dr_b}{dt} \qquad 19$$

After including time and area averaging in a manner identical to that employed for Model 1, the turbulent shear becomes

$$\tau_t = Kft_{life}\rho_l \left|\frac{dr_b}{dt}\right| \left[r_b \frac{du}{dy}\right] \alpha_w \qquad 20$$

$$= Kft_{life}\rho_l \left|\frac{dr_b}{dt}\right| \frac{du}{dy} n\pi r_b^3$$

Vapor liquid exchange models similar to that proposed herein have been used to model the heat transfer augmentation due to pumping (Forster & Greif [1959]). It is generally acknowledged that additional subcooling decreases the bubble departure radius and increases the departure frequency such that the energy converted at a given nucleation site,

$$q_b = \rho_l C_{pl}\left(\frac{2\pi}{6}\right) r_b^3 (T_w - T_l) f \qquad 21$$

is approximately constant (Carey [1993]). If it is assumed this relationship, which was derived for pool boiling, applies for flow boiling then Equation 21 can be used to simplify Equation 20,

$$\tau_t = \frac{3Kq_b \left|\frac{dr_b}{dt}\right| \left[\frac{du}{dy}\right] nt_{life}}{C_{pl}(T_w - T_l)} \qquad 22$$

Model 3. Momentum Transfer

The momentum transfer due to bubble formation can be evaluated directly. Considering the liquid mass flux normal to the wall due to bubble formation

$$G_b = \rho_l nf \frac{4}{3}\pi r_b^3 \qquad 23$$

If the displaced liquid is inserted into the flow at position $y = r_b$, where the mean velocity is given by

$$u(r_b) = r_b \frac{du}{dy} \qquad 24$$

then the momentum per unit wall area provided to the liquid is given by

$$\tau_t = Kfr_b^4 n \frac{4}{3}\pi\rho_l \frac{du}{dy} \qquad 25$$

This model is simplified by making use of the constant nature of Equation 21, such that

$$\tau_t = \frac{4Kq_b r_b \frac{du}{dy} n}{C_{pl}(T_w - T_l)} \qquad 26$$

It is interesting to note that Models 2 and 3 are equivalent if

$$\frac{dr_b}{dt} \propto \frac{r_b}{t_{life}} \qquad 27$$

Extension to Heat Transfer

Since there is generally more data available for heat transfer in the IB to OSV region than for skin friction, it is natural to extend the above analysis to formulate a heat transfer coefficient. By dividing Fourier's law by $\rho_l C_p$ and adding an eddy viscosity term, ε_H, to the thermal diffusivity, the heat flow from the wall can be defined as

$$\frac{q''}{\rho C_p} = -(\alpha_l + \varepsilon_H)\frac{dT}{dy} \qquad 28$$

In addition, we can express the shear stress in terms of the wall velocity gradient.

$$\frac{\tau}{\rho} = -\left(\frac{\mu}{\rho} + \varepsilon_M\right)\frac{du}{dy} \qquad 29$$

Dividing Equation 28 by Equation 29, equating the diffusion coefficients, and integrating the result gives

$$q'' = \frac{\tau C_p}{\bar{u}}(T_w - T_b) \qquad 30$$

where

$$\tau = \frac{f_{l\phi}}{\frac{1}{2}\rho\bar{u}^2} + 0.195K^2 n\pi\rho Ja^4 Pr^{-2/3} \qquad 31$$

Model Results

The major difficulty in comparing these models is the large uncertainties associated with some of the parameters. The nucleation site density, for example, has been reported to vary with applied heat flux to some power, where the power ranges from 0.5 to 3. There is also large uncertainty associated with the wall velocity gradient since very little data exists for this parameter in subcooled boiling.

With these uncertainties in mind the following boundary conditions were assumed. 1) The exponent for nucleation site density was chosen to be 2 and the constant was adjusted to give a wall void fraction of about 50% at OSV. 2) The ratio of the bubble lifetime over the departure period was taken as constant at 50%. 3) The velocity profile was assumed to be equivalent to the single phase profile.

With these approximations, the three models were compared to each other and to a wall roughness model. The roughness model was developed by Avdeev [1986]) and was found to predict data well in subcooled boiling for ANS

conditions (McDuffee & Ruggles [1995]). The constant, K, was chosen to give reasonable results at ANS conditions. K values were found to be 81, 1.3×10^{-3}, and 5.7×10^{-7} for Models 1, 2, and 3, respectively. Figure 1 through Figure 3 show the results of the comparison for 6 MW/m² and for three different values of mass flux.

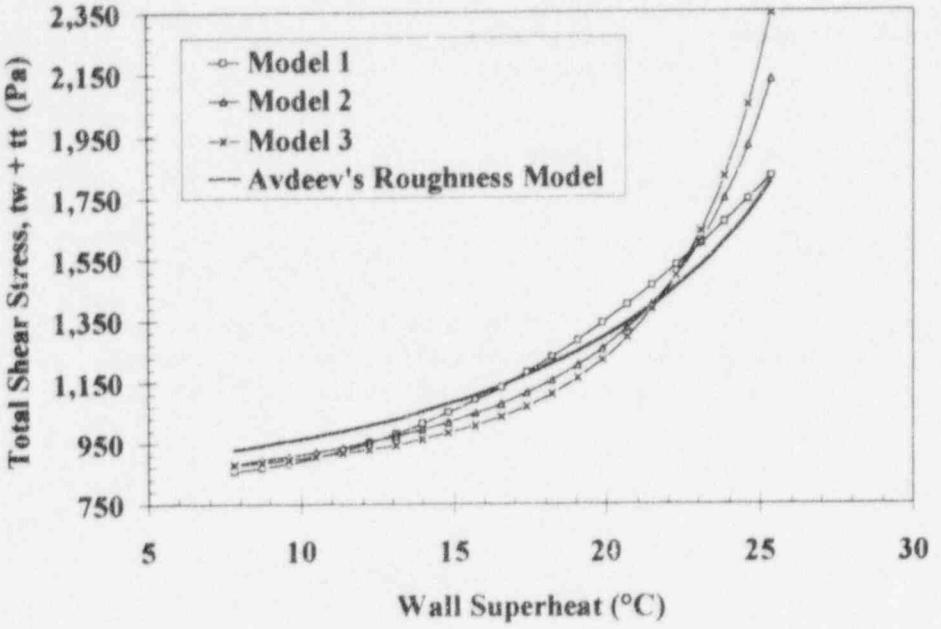

Figure 1. Model Comparison at 20 kg/m²s.

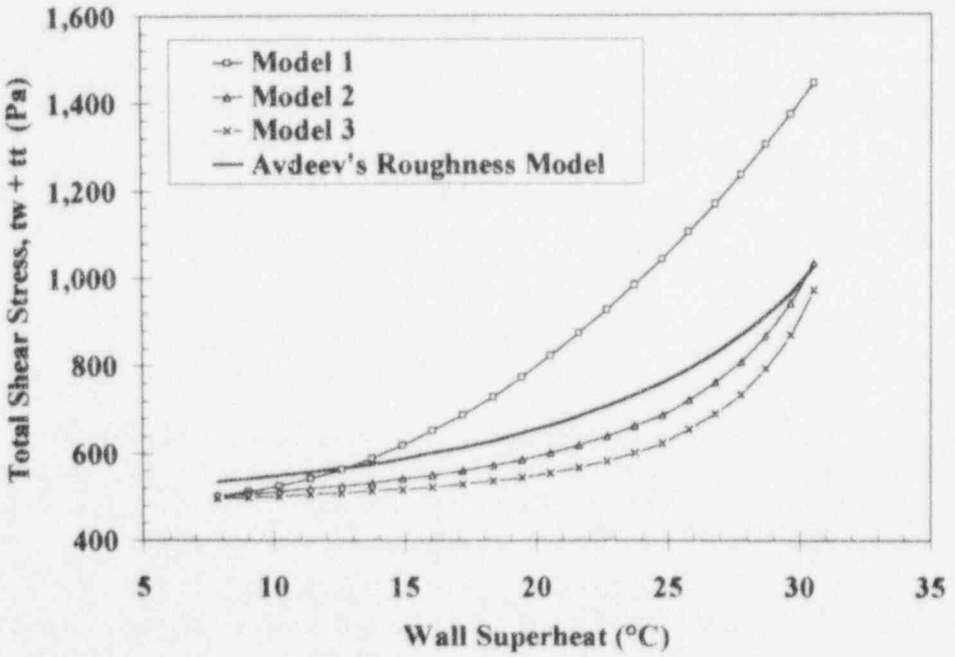

Figure 2. Model Comparison at 15 kg/m²s.

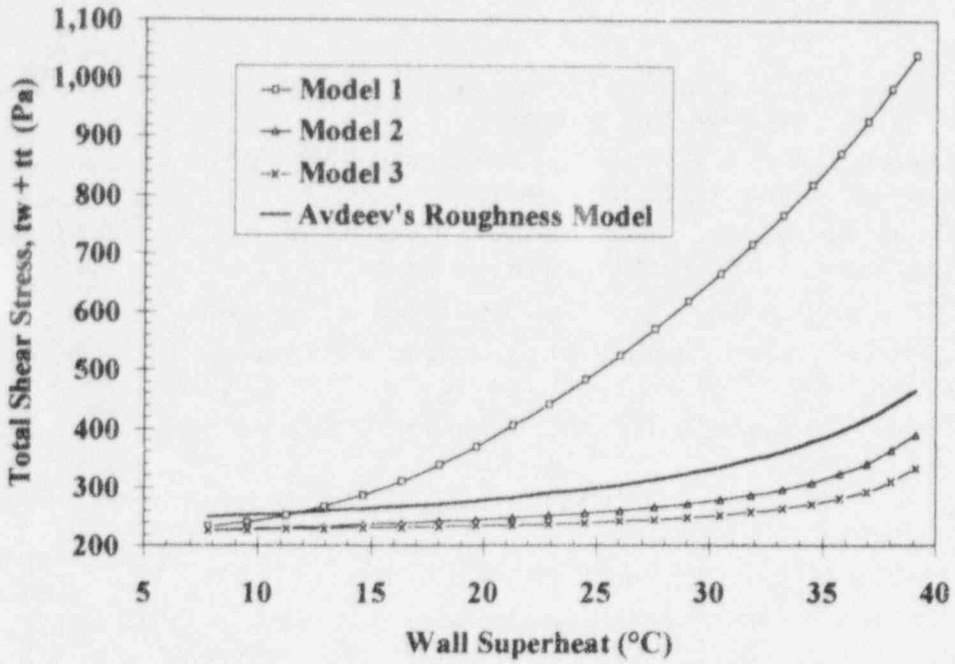

Figure 3. Model Comparison at 10 kg/m²s

In every case, Model 2 proved to be superior to the other two for wide ranges of mass flux and heat flux, assuming the model due to Avdeev is functionally correct over the range of states considered. Model 3, as expected, followed closely with Model 2, but tended to be more sensitive to changes in mass flux.

The heat transfer characteristics of the three models are consistent with that expected for highly subcooled flow. The predicted heat transfer coefficient at OSV for the model approaches 3 times that of the single phase heat transfer coefficient, depending on the model used. This is somewhat higher than predicted using the subcooled boiling model due to Bergles & Rohsenow [1964]. However, Griffith [1958] reported heat transfer coefficients of 5 times the single phase value at OSV.

Conclusions

The behavior of individual bubbles is related to the velocity gradient in the boundary layer to predict the pressure gradient and heat transfer coefficient in the attached void region (i.e., from the incipience of boiling to the onset of significant vapor). The model integrates modeling of the behavior of individual bubbles with boundary layer flow in a way that provides physical basis for many correlations existing in the literature.

The basis of the model requires further experimental verification. A careful study of vapor formation complemented with measurement of pressure gradient and heat transfer coefficient would allow verification of the model formulation in a disciplined and consistent way. Unfortunately, few data exist where all these parameters are measured simultaneously. Therefore, the model is presently constituted using models extracted from different places in the literature. The models selected are appropriate to high mass flux and low pressure situations wherever possible.

This model provides a treatment of subcooled boiling pressure losses and heat transfer that is mechanistic. It is hoped that this framework will lead to more accurate and robust engineering models for subcooled boiling.

References

1. Avdeev, A.A., 1986, "Application of the Reynold's Analogy to the Investigation of Surface Boiling in Conditions of Forced Motion," *High Temperature*, Vol. 24(1), pp. 111-119.
2. Bergles, A.E., and Rohsenow, W.M., 1964, "The Determination Of Forced Convection Surface Boiling Heat Transfer," *Journal Of Heat Transfer*, Vol. 86, pp 365-372.
3. Bibeau, E. L., and Salcudean, M., 1994, "A Study Of Bubble Ebullition In Forced-Convective Subcooled Nucleate Boiling At Low Pressure," *Int. J. Heat Mass Transfer*, Vol. 37, No. 15, pp. 2245-2259.
4. Carey, V., 1993, Liquid-Vapor Phase-Change Phenomena, Hemisphere, Washington.
5. Forster, H.K., and Greif, R., 1959, "Heat Transfer To A Boiling Liquid - Mechanisms And Correlations," *Journal Of Heat Transfer*, Vol. 81, pp 45-53.
6. Griffith, P., Clark, J. A., Rohsenow, W. M., 1958, "Void Volumes in Subcooled Boiling Systems," MIT Technical Report No. 12.
7. Gunther, F.C., 1951, "Photographic Study Of Surface Boiling Heat Transfer To Water With Forced Convection," *ASME Transactions*, Vol. 73, pp 115-123.
8. Holman, J.P., 1990, Heat Transfer, 7th Edition, McGraw Hill.
9. Jai, D. and Schrock, V. E., 1986, "A Generalized Procedure for Predicting the Pressure Drop in a Subcooled Boiling Channel," The 4th International Symposium on Multiphase Transport and Particulate Phenomena, Miami.
10. Larson, P.S., and Tong, L.S., 1969, "Void Fractions in Subcooled Flow Boiling," *Journal of Heat Transfer*, November, pp 471-476.
11. Ledinegg, M., 1938, "Instability of Flow During Natural and Forced Circulation," *Die Warme*, Vol. 61(8).
12. Levy, S., 1967, "Forced Convection Subcooled Boiling-Prediction of Vapor Volumetric Fraction," *Int. J. of Heat & Mass Transfer*, Vol. 10, pp. 951-965.
13. McDuffee, J.L., & Ruggles, A.E., 1995, "Prediction Of The Local Pressure Gradient In Partially Developed Subcooled Boiling For The ANSR", ASME Conference Paper, Maui, Hawaii.
14. Rouhani, S.Z., and Axelson, E., 1970, "Calculation of Void Volume Fraction in the Subcooled and Quality Boiling Regions," *Int. J. of Heat & Mass Transfer*, Vol. 13, pp. 383-393.
15. Saha, P. and Zuber, N., 1974, "Point of Net Vapor Generation and Vapor Void Fraction in Subcooled Boiling," Proc. of the 5th International Heat Transfer Conference, Japan, Vol. 4, pp. 175-179.
16. van Stralen, et al, 1975, "Bubble Growth Rates In Pure And Binary Systems: Combined Effect Of Relaxation And Evaporation Microlayers," *Int. J. Heat Mass Transfer*, vol. 18, pp. 453-467.
17. Yoder, G. L., with Dixon J. R., Elkassabgi, Y., Felde, D. K., Giles, G. E., Harrington, R. M., Morris, D. G., Nelson, W. R., Ruggles, A. E., Siman-Tov, M., Stovall, T. K., 1994, "Steady State Thermal-Hydraulic Design Analysis of the Advanced Neutron Source Reactor," ORNL/TM-12398.

DRIFT FLUX MODEL AS APPROXIMATION OF TWO FLUID MODEL FOR TWO PHASE DISPERSED AND SLUG FLOW IN TUBE

R.I. NIGMATULIN
Tyumen Institute of Mechanics of Multiphase Systems (TIMMS)
Ufa-Bashkortostan Branch of Russian Academy of Sciences[1]

The analysis of one-dimensional schematizing for non-steady two-phase dispersed and slug flow in tube is presented. Quasi-static approximation, when inertia forces because of the accelerations of the phases may be neglected, is considered.

Gas-liquid bubbly and slug vertical upward flows are analyzed. Non-trivial theoretical equations for slip velocity for these flows are derived.

Juxtaposition of the derived equations for slip velocity with the famous Zuber-Findlay correlation is presented. The widespread interpretation of the coefficients of the Zuber-Findlay correlation as cross correlation coefficients is criticized.

The generalization of non-steady drift flux Wallis theory taking into account influence of wall friction on the bubbly or slug flows for kinematical waves is considered.

1. Main assumptions

Let consider two phase flow of non-compressible phases[2], i.e. with fixed true densities ρ_1° and ρ_2° of the phases:

$$\rho_1^\circ = \text{const}, \quad \rho_2^\circ = \text{const} \tag{1.1}$$

in a pipe with a constant cross section[3]

$$A = \text{const}. \tag{1.2}$$

In particular for circular tube with diameter D

$$A = \tfrac{1}{4}\pi D^2. \tag{1.3}$$

It will be used averaged volume (cross sectional) concentrations of phases α_1 and α_2:

$$\alpha_1 = \frac{A_1}{A}, \quad \alpha_2 = \frac{A_2}{A}, \quad \alpha_1 + \alpha_2 = 1 \quad (A_1 + A_2 = A). \tag{1.4}$$

where A_i is a cross section occupied by i-th phase ($i = 1,2$) in the section A. The parameters corresponding to i-th phase will be marked as in (1.1) by subscripts $i = 1,2$.

Then it will be used averaged volumetric flux densities or superficial velocities of the phases j_i and of the mixture j (total volume flow rate density):

---

[1] The paper was written during the author's visting scholarship at Rensselaer Polytechnic Institute

[2] Generalization for compressible phases is possible.

[3] Generalization for smoothly variable crossection of the tube channel is possible

$$j_i = \frac{1}{A}\int_{A_i} v_i' \, ds \qquad (i = 1,2), \qquad j = j_1 + j_2 , \tag{1.5}$$

where v_i' is a longitudinal microvelocity of the i-th phase, fluctuating because of the relative motion of the phases and because of the turbulence.

The averaged velocities of the phases may be introduced by ratios:

$$v_i \equiv \frac{j_i}{\alpha_i} , \quad j \equiv \alpha_1 v_1 + \alpha_2 v_2 . \tag{1.6}$$

It is necessary to take into account that one dimensional approximation or schematizing will be used and all averaged variables, in particular α_i, v_i, j_i $(i = 1,2)$, will be considered as smoothly variable on time t and longitudinal coordinate x.

Then the dispersed flow will be considered. The carrier phase will be marked as the first phase $(i = 1)$, the dispersed phase will be marked as the second phase $(i = 2)$.

2. Mass conservation equations

Mass balance equations for the phases without phase transition[4], taking into account non-compressibility of the phases, may be written by the following:

$$\frac{\partial \alpha_1}{\partial t} + \frac{\partial \alpha_1 v_1}{\partial x} = 0, \qquad \frac{\partial \alpha_2}{\partial t} + \frac{\partial \alpha_2 v_2}{\partial x} = 0. \tag{2.1}$$

Summarizing these two equations we will have total volume flow rate integral of non-compressibility

$$\frac{\partial}{\partial x}(\alpha_1 v_1 + \alpha_2 v_2) = 0, \quad \text{or} \quad j \equiv \alpha_1 v_1 + \alpha_2 v_2 = j(t). \tag{2.2}$$

3. Momentum conservation equations

Two-fluid or two-velocity model for momentum conservation equations in one-dimensional approximation for dispersed flow without direct (not through the carrier phase) interaction (direct contacts, collisions, electromagnetic interaction, momentum transfer by random motion of the dispersed particles) between the dispersed particles (Nigmatulin [1], Lahey [2], Lahey & Moody [3]) may be presented as following:

$$\rho_1^\circ \alpha_1 \frac{d_1 v_1}{dt} = \frac{\partial \sigma_{1^\circ}}{\partial x} - M_{12} - F_{W1} + \rho_1 \alpha_1 g^x \qquad (M_{12} = n f_{12}), \tag{3.1}$$

$$\rho_2^\circ \alpha_2 \frac{d_2 v_2}{dt} = M_{12} - F_{W2} + \rho_2^\circ \alpha_2 g^x , \qquad \left(\frac{d_i}{dt} \equiv \frac{\partial}{\partial t} + v_i \frac{\partial}{\partial x}, \quad i = 1,2\right).$$

[4] Generalization for phase transition is possible.

On the left sides there are inertia forces due to acceleration (as temporal and as spatial (convective)) of the phases in the tube. On the right sides there are forces due to gradient of stresses σ_{1*} (including pressures p, shear stresses τ and Reynolds stresses τ_{Re} and practically coinciding with two-phase mixture stress), external interactions between the phases with the tube wall (F_{W1} and F_{W2}), external body forces, in particular, gravitational forces with the intensity g^x in the x-direction, and finally interface force M_{12}. The force M_{12} includes only some part of the full interface force, that is the sum of the forces from the dispersed particles (drops) which are fully in the macroscopic volume. The interface force M_{12} is determined by averaged force f_{12} from the carrier phase per one dispersed particle, multiplied on number of the dispersed particles n per unit volume. The other part of the interface force from the intersected particles by the boundary of the macroscopic volume is included in the stress σ_{1*} (see Nigmatulin [1], Nigmatulin et al [4]. All components of the equation (including F_{W1} and F_{W2}) are related for a unit volume of the two phase flow.

In the hydromechanics of turbulent flows stress σ_{1*} is usually determined only by pressure, and influence of the viscosity and turbulence manifests in the friction forces on the tube wall and on the interface. That is why it will be assumed

$$\sigma_{1*} = - p. \tag{3.2}$$

For dispersed flow there is a sense to detach the Archimedes force nf_A from the interface force, which is included in the first components in the right sides of the equations, and F_{12} may be expressed (Nigmatulin [1], Batchelor [5], Sedov [6]) as

$$M_{12} = M_A + M_*, \qquad f_{12} = f_A + f_*,$$

$$M_A \equiv nf_A = \rho_1^\circ \alpha_2 \left(\frac{d_1 v_1}{dt} - g^x \right), \quad M_* \equiv nf_* , \tag{3.3}$$

where n is number density of the dispersed particles (or drops or bubbles), f_* is an averaged force from the carrier phase per one dispersed particle due to viscosity (drag force) and added mass. Substituting (3.3) into the first equation of (3.1) we will have

$$\rho_1^\circ \frac{d_1 v_1}{dt} = - \frac{\partial p}{\partial x} - M_* - F_{W1} + \rho_1^\circ g^x. \tag{3.4}$$

Then the Archimedes force may be rewritten in the form

$$nf_A = - \alpha_2 \frac{\partial p}{\partial x} + \alpha_2 M_* - \alpha_2 F_{W1} . \tag{3.5}$$

Taking into account (3.2) and (3.3) we will have the momentum equations (3.1) in the following form

$$\rho_1^\circ \alpha_1 \frac{d_1 v_1}{dt} = -\alpha_1 \frac{\partial p}{\partial x} - \alpha_1 M_* - \alpha_1 F_{W1} + \rho_1^\circ \alpha_1 g^x , \tag{3.6}$$

$$\rho_2^\circ \alpha_2 \frac{d_2 v_2}{dt} = -\alpha_2 \frac{\partial p}{\partial x} + \alpha_1 M_* - \alpha_2 F_{W1} - F_{W2} + \rho_2^\circ \alpha_2 g^x .$$

Note, that in this form due to detaching Archimedes force from the interface force, expressing it through the gradient of pressure by formula (3.5), in the momentum equation *for the second (dispersed)* phase there is some part of the external force, acting *on the first phase* from the wall ($\alpha_2 F_{W1}$).

4. Inertia free flow

The main assumption of the drift flux approximation (Wallis [7], Nigmatulin [1],) is a *neglect by inertia forces* as due to temporal accelerations ($\rho_i^\circ \alpha_i (\partial v_i / \partial t)$) and as to spatial accelerations ($\rho_i^\circ \alpha_i v_i (\partial v_i / \partial x)$) compared with the other forces at the right sides of the equations (3.6). It means also that in the interface force f_* inertial added mass force component is small, and it is determined only by a drag component. The same is for the forces on the tube wall (F_{W1} and F_{W2}), which may be determined by quasi-static approximation.

Estimating the inertial forces due to acceleration and comparing them with the pressure drop forces we may write the necessary conditions for non inertia flow:

$$\rho_i^\circ \alpha_i \frac{\partial v_i}{\partial t} \sim \frac{\rho_i^\circ \alpha_{i0} \Delta v_0}{t_0} << \frac{\Delta p_0}{L_0}, \quad \rho_i^\circ \alpha_i v_i \frac{\partial v_i}{\partial x} \sim \frac{\rho_i^\circ \alpha_{i0} v_0 \Delta v_0}{L_0} << \frac{\Delta p_0}{L_0}. \tag{4.1}$$

Here α_{i0} and v_0, are characteristic values of the volume concentrations and velocities; Δv_0 and Δp_0 are characteristic values of the velocities changing and pressure drop for the case; t_0 is a characteristic value of time, when velocity changing Δv_0 takes place; L_0 is a characteristic tube length, where the pressure drop Δp_0 or velocity changing Δv_0 take place. The drift flux approximation is applicable for the case, if the estimations (4.1) are valid, i.e

$$\frac{\rho_i^\circ \alpha_{i0} v_0 \Delta v_0}{\Delta p_0} << 1, \qquad \frac{t_0}{L_0} >> \frac{\rho_i^\circ \alpha_{i0} \Delta v_0}{\Delta p_0} . \tag{4.2}$$

Note for the steady flow ($t_0 \to \infty$) only the second condition is non-trivial. Drift flux approximation may be used not only for steady and for non-steady flows too, but the characteristic time of the non-steadyness t_0 must be large enough to satisfy the second equation (4.2).

The Archimedes force for inertia free flow is determined only by the gravity acceleration.

Thus the momentum conservation equations for the dispersed flow, when the second phase is surrounded by the first phase and is acted by Archimedes force from the first phase, may be written in the quazi-static view:

$$-\alpha_1 \frac{\partial p}{\partial x} - \alpha_1 M_* - \alpha_1 F_{W1} + \rho_1^\circ \alpha_1 g^x = 0 , \tag{4.3}$$

$$-\alpha_2 \frac{\partial p}{\partial x} + \alpha_1 M_* - \alpha_2 F_{W1} - F_{W2} + \rho_2^\circ \alpha_2 g^x = 0, \qquad (M_* = nf_*).$$

Adding these equations and subtracting them after dividing on α_1 and α_2 correspondingly we have another *identical* form of these equations:

$$\frac{\partial p}{\partial x} - F_{W2} - F_{W1} + (\rho_1^\circ \alpha_1 + \rho_2^\circ \alpha_2) g^x = 0, \tag{4.4}$$

$$M_* - F_{W2} + (\rho_2^\circ - \rho_1^\circ)\alpha_2 g^x = 0,$$

To close the system of equations (2.1), (4.3) it is necessary to write the equations for the forces M_*, F_{W1}, F_{W2} through α_2, v_1, v_2, physical properties of the phases: true densities ρ_1° and ρ_2°, viscosities of the phases μ_1 and μ_2, surface tension σ, and characteristics of the tube: diameter D and roughness δ/D of its internal surface. This is a fundamental problem of using of the momentum equations that is distinguish mechanistic theory, in particular, two-fluid model.

5. Interaction forces on the interface surfaces

Interface force between the dispersed ($i = 2$) and the carrier ($i = 1$) phases may be written in the following form

$$f_* = \pi a^2 C_{12} \frac{\rho_1^\circ |v_1 - v_2|(v_1 - v_2)}{2}, \qquad n = \frac{3\alpha_2}{4\pi a^3}, \tag{5.1}$$

$$M_* \equiv nf_* = \frac{3C_{12}\alpha_2}{8a}|v_1 - v_2|(v_1 - v_2)$$

$$C_{12} = (\mathbf{Re}_{12}, \alpha_2, \mathbf{Lp}_{12}, \tilde{\rho}^\circ), \quad \mathbf{Re}_{12} = \frac{2a\rho_1^\circ |v_1 - v_2|}{\mu_1}, \quad \mathbf{Lp}_{12} = \frac{2a\rho_1^\circ \sigma}{\mu_1^2}, \quad \tilde{\rho}^\circ = \frac{\rho_2^\circ}{\rho_1^\circ}$$

Here C_{12} is a drag coefficient related to one dispersed particle (drop, bubble) considered as close to spherical by radius a, but taking into account influence of "collectivness" or finite volume concentration of the dispersed particles in the mixture unlike one sphere and influence of the shape and size change because of disintegration or coalescence for the case of drops or

bubbles. In general C_{12} may be dependant on Reynolds number $\mathbf{Re}_{12}$, volume concentration α_2, phase true density ratio $\tilde{\rho}^\circ$ and Laplace number $\mathbf{Lp}_{12}$, characterizing influence of the surface tension and viscosity on the drop or bubble shape change.

The drug coefficient dependence on Reynolds number may be presented by power function:

$$C_{12} = \frac{A^{(\gamma)}}{\mathbf{Re}_{12}^{1-\gamma}} \frac{1}{1-\psi_2(\alpha_2, \tilde{\rho}^\circ, \mathbf{Lp}_{12})}, \qquad (5.2)$$

$$A^{(\gamma)} = \text{const}, \quad 0 < \gamma < 1.$$

Here $\psi(\alpha_2)$ is a coefficient taking into account influence of "collectiveness" or finite volume concentration of the dispersed phase in the mixture unlike one sphere and influence of shape and dimension changing because of a disintegration or coalescence for the case of drops or bubbles; the exponent γ determines the interfacial force dependence on the slip velocity:

$$M_{12} = \alpha_2 K_{12}^{(\gamma)}(\alpha_2) \cdot |v_1 - v_2|^{\gamma}(v_1 - v_2), \qquad (5.3)$$

$$K_{12}^{(\gamma)}(\alpha_2) = \frac{3A^{(\gamma)}\rho_1^\circ}{8a}\left(\frac{\mu_1}{2a\rho_1^\circ}\right)^{1-\gamma} \frac{\alpha_1}{1-\psi_2(\alpha_2)}$$

There is a sense to emphasize two extreme cases in (5.1): creep flow ($\mathbf{Re}_{12} < 1$, $C_a = 24/\mathbf{Re}_{12}$, $\gamma = 0$, $A^{(\gamma)} = A^{(0)} = 24$), when the interfacial force is proportional to the slip velocity and dynamic viscosity of the carrier liquid and does not depends on the density of the carrier liquid:

$$M_{12} = \alpha_2 K_{12}^{(0)}(v_1 - v_2), \qquad K_{12}^{(0)}(\alpha_2) = \frac{9\mu_1}{2a^2}\frac{1}{1-\psi_2(\alpha_2)}, \qquad (5.4)$$

and when the interfacial force is proportional to the square of slip velocity ($\mathbf{Re}_{12} >> 1$, $\gamma = 1$, $A^{(\gamma)} = A^{(1)}$, $C_a = A^{(1)} = \text{const}$) and the density of the carrier liquid but does not depend on the its viscosity:

$$M_{12} = \alpha_2 K_{12}^{(1)} |v_1 - v_2|(v_1 - v_2), \qquad K_{12}^{(1)}(\alpha_2) = \frac{3A^{(1)}\rho_1^\circ}{8a}\frac{1}{1-\psi_2(\alpha_2)}. \qquad (5.5)$$

The wall interaction on the carrier phase by force F_{W1} (related per unit volume) is initiated be shear stress τ_{W1} along the perimeter of the tube wall and may be presented in the following form:

$$F_{W1} = \frac{\pi D \tau_{W1}}{\frac{1}{4}\pi D^2} = \frac{4\tau_{W1}}{D}, \qquad \tau_{W1} = C_D \frac{\rho_1^\circ |v_1| v_1}{2}\frac{1}{1-\psi_D(\alpha_2)}, \qquad (5.6)$$

$$C_D = C_D(\mathbf{Re}_1, \frac{\delta}{D}), \qquad \mathbf{Re}_1 = \frac{\rho_1^\circ v_1 D}{\mu_1}.$$

Here C_D is drag force coefficient on the tube wall, δ/D is a roughness of its internal surface, the last multiplier in the expression for τ_{W1} (determined by coefficient ψ_D) takes into account influence of disturbances because of the dispersed phase on the wall friction force with the carrier phase. The function $\psi_D(\alpha_2)$ as $\psi_2(\alpha_2)$ may be different in different diapasons of Reynolds numbers $\mathbf{Re}_1$, $\mathbf{Re}_{12}$ and Laplace number $\mathbf{Lp}_{12}$. Note that for practice the most typical is turbulent flow with the square dependence of wall friction on the carrier phase velocity v_1. Then by analogy (5.5), detaching the dependence on the velocity v_1 the expression for F_{W1} may be rewritten:

$$F_{W1} = K_1(\alpha_2)\cdot|v_1|\, v_1\,, \qquad K_1(\alpha_2) = \frac{2\rho_1^\circ}{D}\,\frac{C_D}{1-\psi_D(\alpha_2)}\,, \tag{5.7}$$

As to the interaction with the wall it seems quite natural from the first sight to neglect the direct wall interaction on dispersed phase

$$F_{W2} = 0, \tag{5.8}$$

supposing that contacts between the dispersed particles and the wall are absent. Nevertheless for the gas with liquid drops or solid particles flows such contacts due to collisions and reflections may occur ($F_{W2} \neq 0$) and influence on the process. But even for bubble up flows the investigations of distribution of the bubbles in the cross-section shows the anomalously high concentration of the bubbles *not only near* the wall (Nakoryakov et al [8], Serizava et al [9, 10], Heringe & Davis [11], Sekoguchi et al [12, 13]), but even *on and along* the wall (Fig. 1), where the bubbles *contact* with the wall and moves along the wall with the velocity v_{2W}, *differing* from the averaged on the tube cross section velocity v_2. The picture looks as the bubbles, moving on the wall, are pressed to the wall by a lateral hydrodynamic force from the liquid[5]. It means the contacts may initiate the direct force F_{W2} on the bubbles from the wall.

But even though the bubbles near the wall don't touch the wall they are surrounded by the liquid having smaller velocity than averaged velocity v_1. It leads that the wall brakes the near wall bubbles through the near wall liquid. This situation is analogous to the slug flow.

By analogy with (5.6) it is natural to assume this force is proportional to the perimeter of the tube and volume concentration of the bubbles and that is why it may be presented in the view

---

[5] This phenomena is seen explicitely on the movie made by colaborators of Dr. J. Bataille at the Laboratory of Fluid Mechanics and Acoustics of Central School in Lyon.

$$F_{W2} = \frac{\alpha_2 \pi D \tau^{\circ}_{W2}}{\frac{1}{4}\pi D^2} = \frac{4\alpha_2 \tau^{\circ}_{W2}}{D} \qquad (\tau^{\circ}_{W2} = K_2 v_{2W}). \tag{5.9}$$

where K_2 is a dispersed particle and wall interaction coefficient, and depending on the volume concentration α_{2W} of the dispersed particles on the wall, their dimension, velocities of the phases, physical properties of the phases:

$$K_2 = K_2(\alpha_{2W}, v_{2W}, a, \mu_1, \sigma). \tag{5.10}$$

6. Force equilibrium equations for the pressure gradient and for the slip velocity in dispersed flow.

Adding momentum conservation equations (4.3) for non-inertia force flow (drift flux flow) we have momentum balance for the two phase mixture (the first equation (4.4)):

$$-\frac{\partial p}{\partial x} - K_1 |v_1| v_1 - F_{W2} + (\rho^{\circ}_1 \alpha_1 + \rho^{\circ}_2 \alpha_2) g^x = 0, \tag{6.1}$$

The second momentum equation for relative motion may be derived from (4.3) dividing the first equation on α_1, the second equation on α_2 and subtracting them or taking the second equation(4.4):

$$- K^{(\gamma)}_{12}(\alpha_2) \cdot |v_2 - v_1|^{\gamma} (v_1 - v_2) + \frac{F_{W2}}{\alpha_2} + (\rho^{\circ}_1 - \rho^{\circ}_2) g^x = 0. \tag{6.2}$$

Here the equation (5.9) for F_{W2} was taken into account and for $K^{(\gamma)}_{12}$ only dependency on volume concentration α_2 is marked, because this dependency is more important for the consideration. The expression for the slip velocity from the equation has the following view

$$|v_2 - v_1|^{\gamma} (v_2 - v_1) = - \frac{(F_{W2} / \alpha_2) + (\rho^{\circ}_1 - \rho^{\circ}_2) g^x}{K^{(\gamma)}_{12}}. \tag{6.3}$$

One should mark that the slip velocity is not influenced directly by the external wall friction force (F_{W1}) on the first (carrier) phase. External wall force influence on the slip velocity only through the dispersed phase (F_{W2}). It is important to remember that this slip velocity equation fits only for the dispersed flows where one of the phase is surrounded by the other and is acted by Archimedes force from the carrier phase. This slip velocity equation doesn't fit for the annular flow but may be generalized for a slug flow (see below).

It is naturally to propose that the force, F_{W2}, connected with the interaction of the wall on the some part of the dispersed particles or bubbles, contacting with the wall much smaller then the interface force, $|M_{12}| =$

$\alpha_2 K_{12}^{(\gamma)} |v_1 - v_2|^{\gamma+1}$, connected with the carrier phase interaction on the all dispersed particles (see (3.1) or (4.3)). In this case the first component in the square bracket term is much smaller than the second component:

$$F_{W2}/\alpha_2 << \left(\rho_1^\circ - \rho_2^\circ\right) g \tag{6.4}$$

Then the slip velocity equation (6.3) may be presented in the simplified approximation for upward flow ($g^x = -g$)

$$v_2 - v_1 = \left[\frac{\left(\rho_1^\circ - \rho_2^\circ\right) g}{K_{12}^{(\gamma)}}\right]^{\frac{1}{\gamma+1}} \left(1 - \frac{F_{W2}/\alpha_2}{(\gamma+1)\left(\rho_1^\circ - \rho_2^\circ\right) g}\right). \tag{6.5}$$

The equations (6.3) (or its simplified version (6.5)) determines the slip velocity by the physical properties of the phases (ρ_1°, ρ_2°) and by the parameters of interphase ($K_{12}^{(\gamma)}$, γ) and external (g^x, F_{W2}/α_2) forces.

7. Two-fluid model for the vertical up slug flow

The slug upward vertical flow is characterized by as named "*Taylor bubble*" which has the shape of bullet (Fig. 2). Theory and experiment shows (Dumitriescu [14]) that the head surface of the Taylor bubble is close to spherical with radius

$$R_H \approx \tfrac{3}{8} D . \tag{7.1}$$

Then down the surface is turned asymptotically to cylindrical separated from the wall by a liquid *film*. Down the thickness of the film smoothly decreases from $\delta \approx \frac{1}{8} D$ till some fixed value $\delta \approx \delta_\infty$. The lateral surface of Taylor bubble S_{Bf} being at the same time by the interface surface of the film may be wavy. Macroscopically it may be considered as close to cylindrical with smoothly variable radius $R_B(x)$

$$R_H < R_B(x) < (\tfrac{1}{2} D - \delta_\infty), \quad (R_H \approx \tfrac{3}{8} D). \tag{7.2}$$

Very often the film separating Taylor bubble from the tube wall is thin and the length L_B of the Taylor bubble is long in compare with the diameter of the tube:

$$2\delta = D - 2R_B << D, \qquad L_B >> D. \tag{7.3}$$

That is why there is the sense to characterize the lateral surface of the Taylor bubble by the averaged diameter $\langle D_2 \rangle$ corresponding to averaged film thickness $\langle \delta_f \rangle$:

$$2\,(\tfrac{3}{8} D) < \langle D_2 \rangle < D - 2\delta_\infty , \qquad \delta_\infty < \langle \delta_f \rangle < \tfrac{1}{8} D . \tag{7.4}$$

The Taylor bubbles separated from each other by the liquid layers which are named as (liquid) *slugs*. The slugs may have small bubbles. But here we consider the case when the bubble volume content in the slugs is negligibly small. The slug is bordering with Taylor bubble by hemispherical surface S_{12H} and wavy down surface S_{Bd} which by analogy with S_{Bf} may be considered as plane.

For simplification let us suppose that all Taylor bubbles are identical and the distances between them are identical too or by other words we consider periodical slug flow. Having in mind mainly long slugs ($L_B >> D$) let us consider one period of the flow or one representative cell (see Fig. 2) with the volume V and length L bounded by up, S_u , and down, S_d, planes and cylindrical surface of the tube wall S_W having one Taylor bubble with the volume $V_2 \equiv V_B$:

$$V = \tfrac{1}{4}\pi D^2 L,$$

$$V_2 \equiv V_B = \tfrac{2}{3}\pi(\tfrac{3}{8}D)^3 + \tfrac{1}{4}\pi\langle D_2\rangle^2(L_2 - \tfrac{3}{8}D) \approx \tfrac{1}{4}\pi\langle D_2\rangle^2 L_2, \qquad (7.5)$$

$$S_u = S_d = \tfrac{1}{4}\pi D^2, \quad S_W = \pi DL.$$

For the given void fraction α_2 presented only by Taylor bubble volume $V_B \equiv V_2 \equiv \alpha_2 V$ the length of the Taylor bubble L_2 may be presented in the following view:

$$L_2 - R_H = \frac{(V_2/\pi) - \tfrac{2}{3}(\tfrac{3}{8}D)^3}{\tfrac{1}{4}\langle D_2\rangle^2} = \frac{1-\bar{d}}{(1-\bar{\delta})^2}\alpha_2 L, \qquad (R_H \approx \tfrac{3}{8}D) \qquad (7.6)$$

$$(\alpha_2 = \frac{V_2}{V}, \quad \bar{d} = \frac{9}{256}\frac{D}{L} << 1, \quad \bar{\delta} \equiv \frac{2\langle\delta_f\rangle}{D} << 1).$$

The liquid or carrier phase in the cell has three components: the first is the liquid in the up volume V_{1u} over the Taylor bubble having the averaged axial velocity v_{1u}, the second is in the down volume V_{1d} under the Taylor bubble having the averaged velocity v_{1d} and the third is in the film volume V_{1f} having the averaged axial velocity v_{1f}:

$$v_{1u} = \frac{1}{V_u}\int_{V_u} v_1' \, d'V, \quad v_{1d} = \frac{1}{V_d}\int_{V_d} v_1' \, d'V, \quad v_{1f} = \frac{1}{V_f}\int_{V_f} v_1' \, d'V. \qquad (7.7)$$

Below it is shown that

$$v_{1u} = v_{1d}, \qquad (7.8)$$

that is why there is a sense to use averaged velocity and length of the liquid slug

$$v_{1s} \equiv v_{1u} = v_{1d}, \qquad L_s = L - L_2, \qquad V_s = V - V_2 \qquad (7.9)$$

At that the averaged velocity of the carrier liquid v_1 and volume concentration α_1 together with the volume concentrations of the marked components are:

$$\alpha_1 = \frac{V_1}{V}, \quad \alpha_{1s} = \frac{V_{1s}}{V}, \quad \alpha_{1f} = \frac{V_{1f}}{V} \tag{7.10}$$

$$\alpha_1 = \alpha_{1s} + \alpha_{1f}$$

$$v_1 = \frac{1}{V_1}\int_{V_1} v_1' \, d'V = \frac{\alpha_{1s}v_{1s} + \alpha_{1f}v_{1f}}{\alpha_1},$$

$$(V = V_1 + V_2, \quad V_1 = V_{1s} + V_{1f}).$$

Due to periodicity the velocity distributions and corresponding averaged values on the up section S_u and down section S_d are the same:

$$v_1'\big|_{S_u} = v_1'\big|_{S_d}, \tag{7.11}$$

The velocity of the Taylor bubble is an averaged velocity of the gas phase:

$$v_2 = \frac{1}{V_2}\int_{V_2} v_2' \, d'V \qquad (\alpha_2 = 1 - \alpha_1). \tag{7.12}$$

The averaged mass conservation equations for this two fluid model is the same as (2.1).

Each cross section $S(z)$ of the tube consists of two parts: $S_1(z)$ and $S_2(z)$ occupied by liquid and gas correspondingly

$$S(z) = S_1(z) + S_2(z) = \text{const.} \tag{7.13}$$

Then there is a sense to use the surface average velocities on the sections:

$$v_1^{(S)}(z) = \frac{1}{S_1}\int_{S_1(z)} v_1' \, ds, \qquad (S_1(z) = \tfrac{1}{4}\pi D^2 - S_2(z)). \tag{7.14}$$

It is useful to consider the axial velocity field $w' = v_1' - v_2$ of the fluid in the coordinate system connected with the Taylor bubble and corresponding surface averaged axial velocities:

$$w_1^{(S)}(z) = \frac{1}{S_1}\int_{S_1(z)} w_1' \, ds = v_1^{(S)} - v_B. \tag{7.15}$$

This relative to the Taylor bubble velocity field in the cell is steady and corresponds to the non-compressible fluid. Then we have

$$\int_{S_1(z)} w_1'(z)\,dz = w_1^{(S)}(z)\;S_1(z) = (v_1^{(S)}(z) - v_B)\;S_1(z) = \text{const.} \qquad (7.16)$$

In particular introducing a specified slip velocity $w_1^\circ > 0$, determining the averaged relative velocity under or above the slug where $S_1(z) = S = \frac{1}{4}\pi D^2$ one may write

$$(v_1^{(S)}(z) - v_B)\;S_1(z) = -\,w_1^\circ\;S. \qquad (7.17)$$

From this equation it follows $v_{1u} = v_{1d}$ that was used in (7.9).

This equation may be used for an expression of the volume averaged velocity of the liquid:

$$v_1 = \frac{1}{V_1}\int_{V_1} v_1'\,dV = \frac{1}{V_1}\int_0^L dz \int_{S_1(z)} v_1'\,ds = \frac{1}{V_1}\int_0^L dz \int_{S_1(z)} (v_2 + w_1')\,ds. \qquad (7.18)$$

Taking into account that the velocity $v_B \equiv v_2$ is fixed for the cell we may write:

$$v_1 = v_B + \frac{1}{V_1}\int_0^L dz \int_{S_1(z)} w_1'\,ds = v_B - \frac{1}{V_1}\int_0^L w_1^\circ\,S\,dz = v_B - \frac{w_1^\circ}{\alpha_1}. \qquad (7.19)$$

By analogy using (7.16) one may write for the film when the thickness of the film $\delta(z)$ is small ($2\delta << D$)

$$\frac{1}{4}\pi D^2 w_{1s} = \pi D\,\delta(z)\,w_{1f}',$$

$$w_{1s} = v_{1s} - v_B, \qquad w_{1f}'(z) = v_{1f} - v_B. \qquad (7.20)$$

Then the expressions for the averaged velocities of the liquid slug (determined in (7.7) - (7.9)) and varying with the distance averaged velocity of the liquid in the near wall film (when it is thin) may be presented by the following

$$v_{1s} = v_B - w_1^\circ, \qquad v_{1f}(z) = v_B - w_1^\circ\frac{D}{4\delta(z)}. \qquad (7.21)$$

Momentum equation for the inertia free two-phase system follows from equilibrium equation for the cell

$$[p(L) - p(0)]S - [\tau_{Ws}(L - L_2) + \tau_{Wf} L_2]\pi D - [\rho_1^\circ\alpha_1 + \rho_2^\circ\alpha_2]g^x SL = 0, \qquad (7.22)$$

where τ_{Ws} and τ_{Wf} are averaged tangent viscous stresses on the tube wall corresponding to the slug and film parts of the cell. Dividing this equation on the volume of the cell $V = SL$ and taking into account that $[p(L) - p(0)]/L$ corresponds to $\partial p/\partial x$ one may write the equation analogous to (6.1)

$$\frac{\partial p}{\partial x} - F_{W1} - [\rho_1^\circ \alpha_1 + \rho_2^\circ \alpha_2] g^x = 0$$

$$F_{W1} = F_{Ws} + F_{Wf}, \tag{7.23}$$

$$F_{Ws} = \frac{4\tau_{Ws}}{D}\frac{L_s}{L}, \qquad F_{Wf} = \frac{4\tau_{Wf}}{D}\frac{L_f}{L} \qquad (L_s + L_f = L).$$

Equilibrium equation for the gas in the Taylor bubble related to the unit of the cell volume is determined by equilibrium of interface forces M_{12} on the surface $S_B = S_{Bf} + S_{Bu} + S_{Bd}$ and gravity force

$$M_{12} + \rho_2^\circ \alpha_2 g^x = 0. \tag{7.24}$$

The interface force M_{12} related to the unit of the cell volume $V = \frac{1}{4}\pi D^2 L$ consists of three components: Archimedes force M_A, viscous friction force M_f on the film surface, and drag or aerodynamical force M_s on the up, S_{Bu}, and down, S_{Bd}, interface surfaces of the Taylor bubble; these forces may be presented in the following view taking into account (7.6):

$$M_{12} = M_A + M_s + M_f, \tag{7.25}$$

$$M_A = -\rho_1^\circ \frac{V_2}{V}\left(g^x - \frac{d_1 v_1}{dt}\right) \approx -\rho_1^\circ \alpha_2 g^x,$$

$$M_s = -C_{Bs}\rho_1^\circ \frac{(v_{1s} - v_B)^2}{2}\frac{\frac{1}{4}\langle D_2\rangle^2}{\frac{1}{4}D^2 L} = -C_{Bs}\rho_1^\circ (w_1^\circ)^2 \frac{(1-\bar{\delta})^2}{2L}$$

$$C_{Bs} = \frac{A_{Bs}}{\mathbf{Re}_{Bs}^{1-\gamma_{Bs}}}, \qquad \mathbf{Re}_{Bs} = \frac{\rho_l^\circ w_1^\circ \langle D_2\rangle}{\mu_l} \qquad (A_{Bs} = \text{const}, \gamma_{Bs} = \text{const})$$

$$M_f = -\frac{\pi\langle D_2\rangle(L_2 - R_H)\tau_{Bf}}{\frac{1}{4}\pi D^2 L} = -\frac{4\tau_{Bf}}{D}\alpha_2 \frac{1-\bar{d}}{1-\bar{\delta}},$$

$$\tau_{Bf} = C_{Bf}\frac{\rho_g^\circ (v_B - v_\Sigma)^2}{2}, \qquad C_{Bf} = \frac{A_{Bf}}{\mathbf{Re}_{Bf}^{1-\gamma_{Bf}}}, \qquad \mathbf{Re}_{Bf} = \frac{\rho_g^\circ (v_B - v_\Sigma) D_2}{\mu_g}$$

$$(A_{Bf} = \text{const}, \gamma_{Bf} = \text{const})$$

The minus sign in the expression for M_f and M_s corresponds to the up direction of the x-axis when $g^x < 0$ and $M_A > 0$. In the Archimedes force expression the absence of inertia forces is taken into account. Then τ_{Bf} is an averaged tangent viscous stresses on the surface of the film S_{Bf} determined

by the velocity of the Taylor bubble v_B relatively to the velocity of the liquid v_Σ on this surface.

The multiplier $1/L$ (conforming to number of Taylor bubbles per unit length) in the expression for M_s corresponds to the decreasing of the drag force per unit volume for the longer Taylor bubble and fixed void fraction α_2 due to decreasing of the number of Taylor bubbles. At that the friction force M_f must not change very strongly with increasing of the averaged length L of the Taylor bubbles as the total length of the bubbles will be the same for fixed void fraction.

It is necessary to keep in mind that interface force M_s is determined by the wake flow near the bottom of the Taylor bubble and interface force M_f may strongly depend on intensity of waves on the near wall film surface that is determined by Reynolds and Weber numbers of the film:

$$\mathbf{Re}_f = \frac{\rho_l^\circ v_{1f}' \delta}{\mu_l} \qquad \mathbf{We}_f = \frac{\rho_l^\circ v_{1f}'^2 \delta}{\Sigma}.$$

The pressure of the gas into the Taylor bubble is homogeneous because of the small gas density and viscosity compared with the liquid density and viscosity. The pressure in the cross section of the flow is homogeneous too. It means that pressure drop along the film is zero. Then the equilibrium equation for the film related to the unit volume of the cell may be written by the following

$$F_{Wf} - M_{Bf} + \rho_1^\circ \alpha_{1f} g^x = 0. \tag{7.26}$$

The equations (7.24) and (7.25) give the possibility to derive the simple equation for slip velocity for the regime when interaction with liquid slug prevail the interaction with the film and the film is thin:

$$M_s >> M_f\,, \quad \bar{\delta} << 1 \tag{7.27}$$

that takes place for regimes far from flooding or from the transition to annular flow. The force M_s may be presented in the view analogical to (5.3):

$$M_s = K_{Bs}^{(\gamma)} \left(w_1^\circ\right)^{1+\gamma_{Bs}}, \quad \left(K_{Bs}^{(\gamma)} = \frac{A_{Bs}\rho_l^\circ}{2L}\left(\frac{\mu_l}{D\rho_l^\circ}\right)^{1-\gamma_{Bs}}\right) \tag{7.28}$$

Taking into account the last simplifications and the relation $v_2 - v_1 = w_1^\circ/\alpha_1$ following from (7.19) we have from the equation (7.24) :

$$K_{Bs}^{(\gamma)} \left(\frac{v_2 - v_1}{\alpha_1}\right)^{1+\gamma_{Bs}} = \alpha_2 \left(\rho_l^\circ - \rho_g^\circ\right) g. \tag{7.29}$$

Solving for the slip velocity one may write analogically to (6.5):

$$v_2 - v_1 = (1 - \alpha_2)\left[\frac{\alpha_2\left(\rho_l^\circ - \rho_g^\circ\right)g}{K_{Bs}^{(\gamma)}}\right]^{\frac{1}{1+\gamma_{Bs}}}. \qquad (7.30)$$

$$= (1 - \alpha_2)\left[2A_{Bs}\alpha_2\left(1 - \frac{\rho_g^\circ}{\rho_l^\circ}\right)gL\left(\frac{\rho_l^\circ D}{\mu_l}\right)^{1-\gamma_{Bs}}\right]^{\frac{1}{1+\gamma_{Bs}}}$$

It is necessary to keep in mind that even for long Taylor bubbles the near wall film may be not stabilized for essential part of the cell, i.e. the thickness of the film $\delta(z)$ along the axis and averaged velocity $v_{1f}(z)$ may be variable. It means that for long part of the flow stresses τ_{Bf} and τ_{Wf} may be variable along the film flow and calculation of the forces M_{Bf} and F_{Wf} may need more detailed consideration with integration of variable stresses along the flow. That essentially complicate the theory.

7. Zuber-Findlay drift flux law

Analysis of the experimental results for bubbly and slug upward vertical flows, attracting mass conservation equation and possible distributions of the volume concentrations and velocities of the phases in the cross section of the tube, allowed to Zuber and Findlay [15] to propose the famous and remarkable correlation for bubbly and slug flow regimes, usually named as Zuber-Findlay model, which corresponds *linear* dependency of v_2 on j:

$$v_2 = C_0\, j + V_{2j}. \qquad (8.1)$$

where the gas phase (dispersed bubbles or slugs) is marked as the second phase ($i = 2$), C_0 and V_{2j} are parameters, which must be determined from the experiments and which *do not depend* on j and may be considered as constants for the experimental set. But in general they may smoothly different for different regimes and diapasons of α_2, for different diameters of the tube, inlet and mixing devices and orientation of the flow relatively gravitation and physical properties of the phases. In particular, C_0 is smoothly decreasing with the increasing of the flow velocities and pressure. The non-trivial and even surprising sense of the Zuber-Findlay correlation is not only the formula itself but that the parameters C_0 and V_{2j} *are practically constant* in some sense.

It is not difficult to express the velocity of the liquid (first) phase using the Zuber-Findlay correlation (8.1):

$$v_1 = \frac{j - \alpha_2 v_2}{\alpha_1} = \frac{j - \alpha_2 C_0 j - \alpha_2 V_{2j}}{\alpha_1} = \frac{1 - \alpha_2 C_0}{\alpha_1} j - \frac{\alpha_2}{\alpha_1} V_{2j}, \qquad (8.2)$$

and then using for v_2 initial expression (8.1) to write the correlation for the slip velocity through the parameters of the Zuber-Findlay correlation

$$v_2 - v_1 = \frac{V_{2j}}{\alpha_1} + j\,\frac{C_0 - 1}{\alpha_1} \equiv \frac{V_{2j}}{\alpha_1}\,(1 + \frac{(C_0 - 1)j}{V_{2j}})\,. \tag{8.3}$$

The most principal physical sense of this correlation that for fixed void fraction α_2 the *slip or two velocity effect does depend on the total volume flux* j, if $C_0 \neq 1$, and this dependence is *linear*. It is very remarkable and non-trivial result and by author opinion the formula (8.2) may be named as *Zuber-Findlay law* for bubbly and slug flows in tube.

What physical processes govern by this phenomena?

It is amazing that beginning from the founder paper of Zuber and Findlay [13] in dozens of papers and books the coefficient C_0 was interpreted and in detail discussed as a correlation coefficient C_0^* of cross sectional distribution of the total volume microflux $j' \equiv \alpha_1' v_1' + \alpha_2' v_2'$ and void fraction α_2':

$$C_0^* \equiv \frac{\frac{1}{A}\int\limits_A j'\,\alpha_2'\,dA}{\left[\frac{1}{A}\int\limits_A j'\,dA\right]\left[\frac{1}{A}\int\limits_A \alpha_2'\,dA\right]} \equiv \frac{\langle \alpha_2' j' \rangle}{\langle \alpha_2' \rangle \langle j' \rangle}, \qquad \left(\langle \varphi' \rangle \equiv \frac{1}{A}\int\limits_A \varphi'\,dA\right). \tag{8.4}$$

For the interpretation they used identities:

$$v_2' - j' = v_2' - \alpha_1' v_1' - \alpha_2' v_2' = \alpha_1'(v_2' - v_1')$$

$$\alpha_2' j' \equiv \alpha_2' v_2' - \alpha_2'(v_2' - j') \equiv \alpha_2' v_2' - \alpha_1' \alpha_2'(v_2' - v_1'),$$

$$<\alpha_2'> \equiv \alpha_2, \quad <j'> \equiv j, \quad <\alpha_2' v_2'> \equiv \alpha_2 v_2. \tag{8.5}$$

Then it is not difficult to get from (8.4)

$$C_0^* \equiv \frac{\alpha_2 v_2 - \langle \alpha_1' \alpha_2' (v_2' - v_1') \rangle}{\alpha_2 j}\,. \tag{8.6}$$

Finally expressing this formula for v_2 one may write the *identity* (8.4) in the following view

$$v_2 \equiv C_0^*\, j + V_{2j}^*,$$

$$(V_{2j}^* \equiv \frac{\langle \alpha_2' V_{2j}' \rangle}{\alpha_2}, \quad V_{2j}' \equiv (v_2' - j') \equiv \alpha_1'(v_2' - v_1')). \tag{8.7}$$

This *identity* looks like Zuber-Findlay equation (8.1) with the correspondence $C_0 = C_0^*$ and $V_{2j} = V_{2j}^*$. But in reality only if the specified slip velocity V_{2j}^* (determined by the averaging of $\alpha_1'(v_2' - v_1')$ i.e. connected with the two velocity or slip velocity effect) does not depend on the total volume flux j one may write $C_0 = C_0^*$ and $V_{2j} = V_{2j}^*$. But for $C_0 \neq 1$ the term V_{2j}^*, connected with the two or slip velocity effect (i.e., v_2 - v_1) *does depend on* j (as it was shown in (8.3), starting from experimental Zuber-Findlay correlation itself). Really, if the averaged value

$$v_2 - v_1 = \int_A \left(\frac{\alpha_1' v_1'}{\alpha_1} - \frac{\alpha_2' v_2'}{\alpha_2} \right) dA = \frac{1}{\alpha_1 \alpha_2} \int_A (\alpha_1' \alpha_2 v_1' - \alpha_1 \alpha_2' v_2') dA$$

depends on j ($C_0 \neq 1$, see (8.3)) why very close to it the averaged value

$$\frac{V_{2j}^*}{\alpha_1} = \frac{1}{\alpha_1 \alpha_2} \int_A (\alpha_1' \alpha_2' v_1' - \alpha_1' \alpha_2' v_2') dA$$

must not depend on j? If one takes into account that V_{2j}^* must depend on j and if one compares the formula for v_2 in the form of identity (8.7) with the experimental linear dependency on j in the form (8.3) one may conclude that V_{2j}^* depends linearly on j, or the term must be written

$$V_{2j}^* = \Delta C_0 \cdot j + V_{2j}, \quad \Delta C_0 \neq 0. \tag{8.8}$$

where ΔC_0 is a constant coefficient. That is why

$$C_0 = C_0^* + \Delta C_0, \quad C_0 \neq C_0^*, \quad V_{2j} \neq V_{2j}^* \tag{8.9}$$

By the other words only if Zuber-Findlay experimental parameter $C_0 = 1$, when two or slip velocity effect does not depend on j (see (8.3)) it is possible (only possible, but not necessary) that C_0 coincides with C_0^* and V_{2j} coincides with V_{2j}^* or to write

$$C_0^* = C_0 = 1, \quad V_{2j} = V_{2j}^*. \tag{8.10}$$

But not reverse: even if $C_0^* = 1$, it is possible $C_0 \neq 1$. The coefficient C_0^* and specified slip velocity V_{2j}^* are determined by distribution of the microparameters for one regime characterized by j_1 and j_2. The coefficient C_0

and velocity V_{2j} correlate in (8.1) three relatively simply measurable averaged parameters: phase volume fluxes j_1 , j_2 ($j_1 + j_2 = j$) and void fraction α_2 ($v_2 = j_2/\alpha_2$). For determination C_0 it is necessary to make the measurement for many regimes, i.e. for different j_1 and j_2. All these three averaged and measured parameters may be realized by different distributions of the corresponding microparameters in the cross section A. The coefficient C_0 is a hydraulic coefficient and in the experimental correlation (8.1) it characterizes the force interaction between the phases and though it depends on distribution of α_2' and j' (characterized by C_0), in some sense it has no common with the correlational kinematical coefficient C_0^* and only in some cases ($C_0 = 1$) may coincide with $C_0^* = 1$.

Zuber-Findlay correlation and corresponding parameters C_0 and V_{2j} are governed by force interactions.

It is interesting that for mentioned above (before (5.9)) bubbly flows with the peaks of bubble concentration near the tube wall estimations show that the correlation coefficient $C_0^* < 1$, but for these conditions $C_0 > 1$ is characteristic.

The interpretation C_0 as cross sectional correlation parameter C_0^* is non-correct.

Comparing coefficients C_0 and C_0^* it is interesting to notice that for the determination C_0 it is necessary to measure three macroscopic or averaged (by the whole cross section) parameters (j_2, j, α_2) for a few regimes, but for determination C_0^* it is necessary to measure the distribution of the microscopic characteristics, namely: velocities of the both phases (v_1' and v_2') and volume concentration (α_2') in the cross section but for one regime. At that the measurement and the sense of α_2' is not unequivocal because in practice the ratio of the radius of the dispersed particles to the radius of the tube is not small. It is seen that the measurements for calculation C_0 are much easier than measurements necessary for calculation cross correlation parameter C_0^*.

It may be seemed all this considerations of differences between C_0 and C_0^* not to be essential because C_0 equal to values close to unit ($C_0 = 1 \div 1.2$) and only seldom it may reach $1.5 \div 1.6$. But the slip velocity, what all this play is making for, is determined just by $C_0 - 1$ and drift flux function V_{2j}. For one-velocity or "homogeneous model" ($v_1 = v_2$) one has $C_0 = 1$, $V_{2j} = 0$. That is why from methodological point of view it is better to use and to discuss the coefficient $C_0 - 1$ instead of C_0.

9. Solution of the reversed problem for determining of interaction coefficients from the Zuber-Findlay law equation

Comparing the Zuber-Findlay slip velocity equation (8.3) with the theoretical slip velocity equations (6.5) and (7.30), following from two velocity momentum balance equations for the inertia free *dispersed or slug* flow, we have that influence of the total flux j on the slip velocity ($C_0 > 1$) may be connected only with two factors: with the external (for the flow) friction force on the wall F_{W2}, acting on the dispersed phase, or with the bubble-liquid friction coefficient $K_{12}^{(\gamma)}(a)$ for dispersed flow or with Taylor bubble - liquid slug interaction coefficient $K_{Bs}^{(\gamma)}(L)$.

Firstly, increase of j decreases F_{W2} due to decrease of fraction of the bubbles near the tube wall. It may take place due to the turbulence intensification that tears near wall bubbles to the flow core. Then we may propose:

$$F_{W2} = F^{\circ} - kj$$

Secondly, increase of j decreases $K_{12}^{(\gamma)}(a)$ due to increasing of bubble diameter $2a$. It is possible due to inlet device influence on the forming of the bubble size.

For the slug flow where there is not contacts between the gas phase and tube wall ($F_{W2} = 0$) only the second factor is actual, namely increase of total volume flux j decreases $K_{Bs}^{(\gamma)}(L)$ due to increasing of Taylor bubble length L. It is also possible due to inlet device influence on the forming of the Taylor bubble length.

Effect of the wall interaction with the bubbles and slugs (F_{W2}) must decrease with the increasing the diameter of the tube D. It follows by three reasons:

1. F_{W1} and F_{W2} are related to the unit volume of the mixture

$$F_{W1}, F_{W2} \sim D^{-1}$$

2. Increase of D for a fixed flow velocity j or v_1 must decrease the concentration of the bubbles on the wall α_{2W}. It is explained by the decreasing of the cross-sectional velocity gradient $\partial v_1/\partial r \sim v_1/D$ which initiates the lateral "lift" force, pushing the bubbles to the wall.

An increase of the diameter of the tube D for a fixed flow velocity j or v_1 increases $\mathbf{Re}_1$ that testifies on an increase of turbulence intensity and spatial turbulence scale. This must intensify the mixing processes making the flow more uniform.

It is verified by the recent experiments of Johnson & White [16] with air-water flows in tube of $D = 200$ mm. In their experiment there was no any peak concentration of the bubbles near the wall and at the same time their measurements gave $C_0 = 1 \pm 0.02$. Though in many experiments mainly with the smaller diameters $C_0 = 1.1 \div 1.6$.

It is necessary to bear in mind a reasonable remark in Zuber & Findlay [15] paper that C_0 may depends on mode of gas injection in the inlet of the tube.

Experiments and present consideration would be more informative if together with the measurements of kinematical parameters j_1, j_2 and α_2 to make measurements of pressure gradient $\partial p / \partial x$, that allow to determine external force $F_{W1} + F_{W2}$ on the flow, using equation, and to have additional and independent information about forces. Formally after making the information on $\partial p / \partial x$ has to be used for determining coefficient K_1 in the formula for the force F_{W1}.

10. Comparison Zuber-Findlay law correlation with Armand and Miropol'skiy correlations

The first experimental correlation, determining the slip velocity in air-water gas-liquid flow in tube was Armand [17, 18] correlation, that may be presented as

$$\alpha_2 = 0.833\ \beta_2 \qquad (\beta_2 = \frac{j_2}{j}). \tag{10.1}$$

It is not difficult to write the sequence of this correlation

$$\alpha_2 = 0.833\ \frac{\alpha_2 v_2}{j},$$

and present it in the Zuber-Findlay correlation form (7.1) or (7.3)

$$v_2 = C_0 j\ , \quad C_0 = 1.2; \quad V_{2j} = 0. \tag{10.2}$$

$$v_2 - v_1 = \frac{0.2}{\alpha_1}\ j$$

It means that Armand correlation corresponds to the partial case of Zuber-Findlay law without acting Archimedes force along the flow ($g^x = 0$, $V_{2j} = 0$), for instance, for horizontal flow, when for $j = 0$ we have $v_2 - v_1 = 0$. Comparing this slip velocity equation with the (6.3) for the case $g^x \approx 0$ one may to get

$$\frac{F_{W2}}{\alpha_2} = 0.04\ K_{12}^{(1)} \frac{j^2}{\alpha_1^2}. \tag{10.3}$$

Thus for the horizontal flow described by Armand correlation this dependance on total volume flux j is quadratic as opposed to linear dependance for up bubbly or slug flow marked after (9.6). Apparently it is explained that for horizontal flow essential part of the gas flows as a turbulent gas layer directly contacting with the up part of the tube wall (without laminar liquid microlayers or thin films) and initiating the friction force F_{W2}.

Using the experimental data for vertical upward water steam flows ($g^x = g = 9{,}81$ m/s^2) Miropolskiy [19] proposed more complicated correlation

$$\frac{v_2}{v_1} = \frac{W_0}{v}, \tag{10.3}$$

$$W_0 = \frac{13{,}5(1-p/p_{cr})}{\mathrm{Fr}^{5/12}\,\mathrm{Re}^{1/6}} \equiv 13.5\frac{g^{5/12}D^{3/12}\mu^{1/6}}{(\rho_1^\circ)^{1/6}}\left(1-\frac{p}{p_{cr}}\right),$$

$$\left(\mathrm{Fr} = \frac{v^2}{gD},\ \mathrm{Re} = \frac{\rho_1^\circ v D}{\mu_1},\ v = \frac{\rho_1^\circ\alpha_1 v_1 + \rho_2^\circ\alpha_2 v_2}{\rho_1^\circ}\right),$$

where $p_{cr} = 22{,}1$ MPa is a critical pressure for water, g is gravity acceleration. This correlation was obtained using the experimental data in the diapason of mass averaged velocity $v = 0{,}3 \div 3{,}0$ m/s and diameter of tube $D = 5 \div 35$ mm. This correlation explicitly shows the influence of the diameter of the tube, the density and viscosity of the liquid phase on the slip velocity.

The dependence for not high pressures when $(\rho_2^\circ << \rho_1^\circ,\ v \approx \alpha_1 v_1)$ may be presented:

$$v_2 = \frac{W_0}{\alpha_1}\ ,\quad v_2 - v_1 = \frac{W_0}{\alpha_1^2} - \frac{j}{\alpha_1} \tag{10.4}$$

that corresponds to the coefficients $C_0 = 0$, $V_{2j} = W_0/\alpha_1$ but doesn't correspond to the linear Zuber-Findlay law with the fixed coefficients because of the dependency of V_{2j} on the void fraction $\alpha_2 = 1 - \alpha_1$. In spite of the explicit including the gravity force acceleration g, the formula apparently may correspond only for the earth condition ($g = 9.81$ m/s^2) because for the absence of the gravity ($g = 0$) it gives $v_2 = W_0 = 0$ that is not confirmed with the physical sense for the forced up flow. Then the Miropolskiy correlation (10.4) (as the Armand correlation (10.2)) doesn't take into account explicitly the influence of surface tensions. And finally because C_0 for Miropolskiy correlation (10.4) is not close to unit it is likely more appropriate for annular flow ($\alpha_2 > 0.8$) and there is no sense to use it for the interpretation by the slip velocity equation (6.3) or (6.5) which is proper only for bubbly or slug flow i.e. when the gas phase is dispersed phase.

10. Non-steady flows. Kinematical waves

Using the Zuber-Findley law equation (8.2) one may write

$$\alpha_2 v_2 = C_0\alpha_2 j + \alpha_2 V_{2j}, \tag{11.1}$$

Substituting this equation to the second equation (2.1) and taking into account that $j = j(t)$ one have the following quasi-linear partial differential equation for void fraction

$$\frac{\partial \alpha_2}{\partial t} + j'(t, \alpha_2) \frac{\partial \alpha_2}{\partial x} = 0 \qquad (11.2)$$

$$\left(j'(t, \alpha_2) = C_0\, j(t) + \frac{d}{d\alpha_2}\left(\alpha_2 V_{2j}\right) \right).$$

This equation generalizes the corresponding equation of Wallis drift flux theory (Wallis [7], Nigmatulin [1]) for taking into account the wall friction effects on slip velocity. At that the wall friction is manifested only by the coefficient C_0 instead 1 in the expression for $j'(t, \alpha_2)$. This difference is not principal for the mathematical procedure to get a solution of the equation, because the equation is transformed by the transformation of independent variables

$$x' = x - C_0 \int_0^t j(\tau)\, d\tau, \qquad t' = t\,. \qquad (11.3)$$

and finally has the following view

$$\frac{\partial \alpha_2}{\partial t'} + c(\alpha_2) \frac{\partial \alpha_2}{\partial x'} = 0 \qquad \left(c(\alpha_2) = \frac{d}{d\alpha_2}\left(\alpha_2 V_{2j}\right) \right),$$

that coincides with corresponding equation for drift flux theory without wall friction. It means that wall friction influence is easy to take into account.

Summary

1. Drift flux or quasi-static theory is an approximation when inertia forces because of the accelerations of the phases may be neglected. In this case momentum equations for the phases are equilibrium equations for friction and buoyancy interface forces between the carrier and the dispersed or slug phases together with the friction forces between the phases and the wall of the tube. For this case slip or relative velocity of the phases $v_2 - v_1$ may be expressed by simple algebraic equaton using the expressions for the mentioned friction forces in quasistatic approximation.

2. For the gas-liquid bubbly and slug vertical upward flows the famous Zuber-Findlay experimental linear law correlating the averaged velocity of the gas (dispersed or slug) phase v_2 and total volume flux j takes place: $v_2 = C_0\, j + V_{2j}$. Simple analys of this experimental law showed that if $C_0 > 1$, increase of total volume flux j with fixed void fraction α_2 increases slip velocity $v_2 - v_1$.

3. Juxtaposition of the derived theoretical equations for slip velocity with the Zuber-Findlay equation gives the idea of the physical mechanisms of the effect of the increasing of slip velocity with the increasing of total

volume flux for fixed void fraction. For a dispersed flow this is explained by two mechanisms: 1) by decreasing (due to intensification of turbulence by increasing j) concentration of the bubbles near the wall which may contact with wall and slowed down by the wall; 2) by increasing of an averaged diameter of the bubbles or averaged length of Taylor bubbles with the increasing j due to the specific influence of the inlet device.

4. It is shown inaccuracy of widespread idea, that the coefficient C_0 is a correlation coefficient for total volume flux and void fraction distribution in cross aasection of the tube. It is shown that C_0 is determined by interface force interactions (tube wall - near wall bubbles, bubbles - liquid, Taylor bubble - liquid slug and near wall liquid film). The fact that $C_0 > 1$ is connected with the influence of total volume flux on: 1) the bubble size (or Taylor bubble length) or 2) on the part of the bubble which may be braked by the tube wall.

5. The Zuber-Findlay law may be used as an additional experimental information for solving reversed problem: by kinematical experimental data to determine the friction force laws on interface between the gas, liquid and the tube wall.

6. The generalization of non-steady drift flux Wallis theory for kinematical waves connected with taking into account influence of wall friction on the bubbly or slug flows proved to be very simple.

Acknowledgments

The author is grateful for Dr. R.T. Lahey, Jr. from Renssellaer Polytechnic Institute for his very useful cooperation and discussions which gave the idea to make the analysis for the problem during the author's visiting scholarship at Renssellaer Polytechnic Institute.

REFERENCES

[1] R.I. Nigmatulin Dynamics of multiphase media, Vol. 1,2. Hemisphere, New York (1991).

[2] R. T. Lahey (Jr) "The relationship between drift correlations and interfacial shear in two-fluid models". Personal communications (1993).

[3] R.T. Lahey (Jr), F.J. Moody, The thermal-hydraulic of a boiling water nuclear reactor, American Nuclear Society Monograph (1993).

[4] R.I. Nigmatulin, R.T. Lahey (Jr), D.A. Drew, "Onthe different forms of momentumequations and on the intr- and interface interaction in the hydromechanics of a monodispersed mixture," Chem. Eng. Com., Memorial Issue devoted to Prof. A. Duckler (1995).

[5] G. Batchelor, An introduction to fluid dynamics. Cambridge, Univ. Press (1970).

[6] L.I. Sedov, Continua Mechanics, Vol. 1, 2., Moscow, Nauka (1984).

[7] G.B. Wallis, One-Dimensional Two-Phase Flows, McGraw-Hill (1969).

[8] V.E. Nakoryakov, A.P. Burdukov et al, "Investigation of turbulent two-phase flows". Ed. S. S. Kutateladze. Novosibirsk, ITPh (in Russian) (1973).

[9] A. Serizava, I. Kataoka, I. Michiyosi, "Turbulence structure of air-water bubbly flow - II. Local properties," Int. J. Multiphase Flow 2, 235-246 (1975).

[10] A. Serizava, I. Kataoka, "Phase distribution in two-phase flow," Proc. Transient Phenomena in Multiphase Flow, Ed. by N. Afgan, Hemisphere, 179-224 (1988).

[11] R.A. Heringe, M.R. Davis, "Structural development of gas-liquid flows," J. Fluid Mech. 73, 97-123 (1976).

[12] K. Sekoguchi, H. Fukui, S. Yoshifusa, "Flow characteristics and heat transfer in vertical bubble flow,". Proc. Two Phase Flow Dynamics, Ed. by A. E. Bergles & S. Ishigat, 59-74. Hemisphere, London (1981).

[13] T. Sekoguchi, H. Shakutsui, A. Tomiyama, H. Minagawa, S. Kitani, "Microscopic characteristics of multiphase flow using digital image processing," Proc 1st Int Conf. Multiphase Flows. - Tsukuba. Japan, 357-360 (1991).

[14] D.T. Dumitrescu, "Stromung an einer luftbase im senkreshter rohr," Z. Angew. Math. Mech. 23, 139-149, (1949).

[15] N. Zuber, J.A. Findlay, "Averaged volumetric concentration in two-phase flow systems," J. Heat Transfer 87, 453-468 (1965).

[16] A.B. Johnson, D.B. White, "Experimental determination of gas migration velocities with non-newtonianfluids," Int. J. Multiphase Flow 19, 6, 921-941 (1993).

[17] A.A. Armand, "Hydraulic resistance for two phase flow in horizontal tube," Izv. Vses. Teplotech. Inst. 1, 16-23 (in Russian) (1946). English Translation see AERE-Trans. 828, 1959.

[18] A.A. Armand, "Investigation of mechanism of two-phase flow in a vertical tube," Izv. Vses. Teplotech. Inst. 2 (in Russian) (1950).

[19] Z.L. Miropolskiy, R.I. Shneerova, A.I. Karamysheva, "Concentration of steam in forced flow of water-vapour mixture with heat influx and adiabatic conditions," Teploenergetika 5, 60-63 (in Russian) (1971).

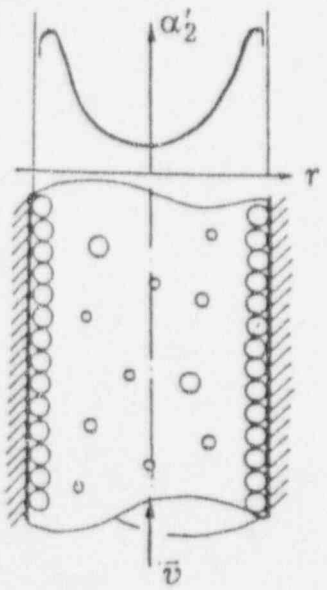

FIGURE 1. Anomalously high concentration of the bubbles along the tube wall in a vertical upward bubbly flow.

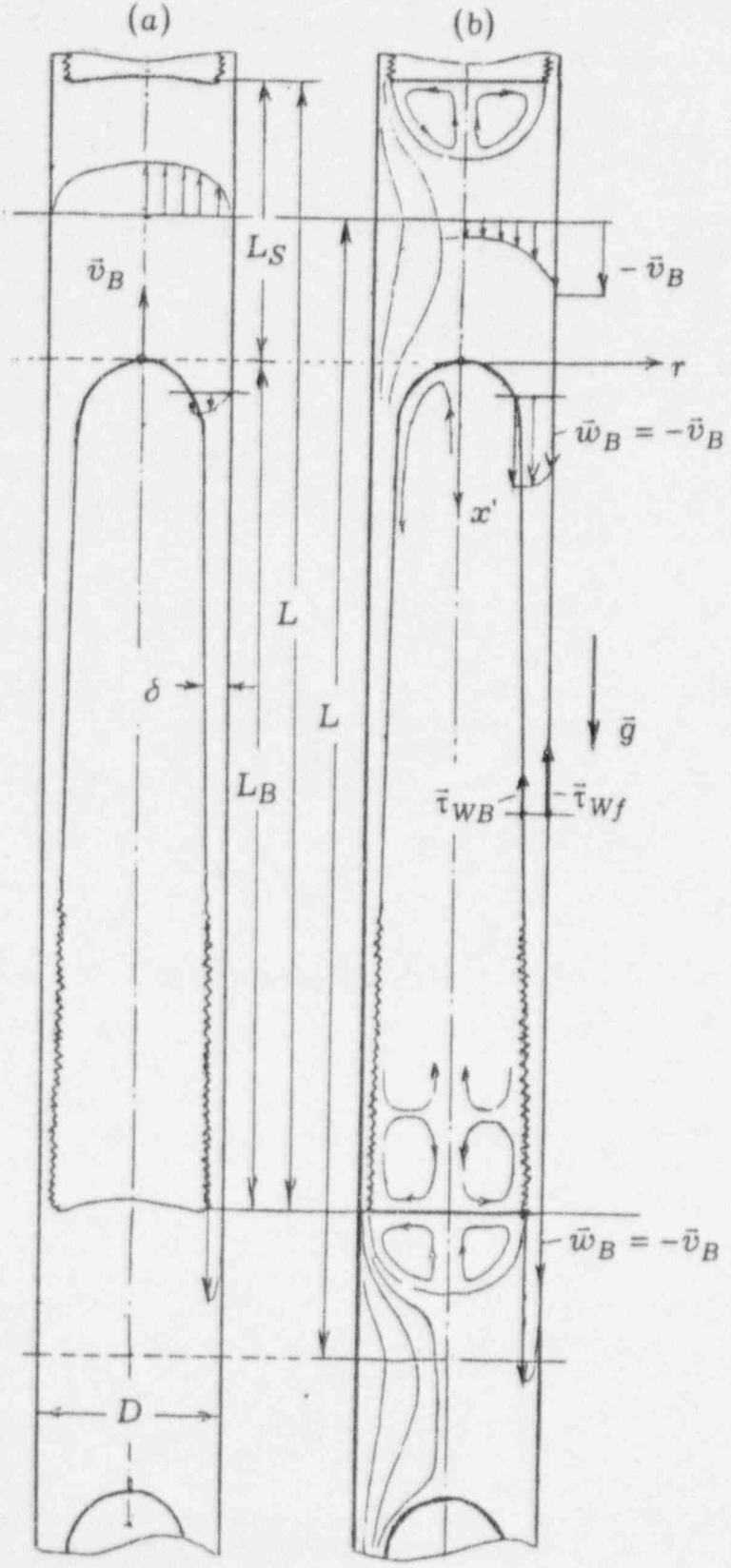

FIGURE 2. Scheme of a vertic1 slug flow.

DEVELOPMENT, IMPLEMENTATION AND ASSESSMENT OF SPECIFIC, TWO-FLUID CLOSURE LAWS FOR INVERTED-ANNULAR FILM-BOILING.

F. de Cachard

Laboratory for Thermal Hydraulics,
Paul Scherrer Institute (PSI),
CH-5232 Villigen PSI, Switzerland
Tel: 56 994143 / Fax: 56 992199

This work was supported by the *Bundesamt für Energiewirtschaft (BEW), Bern,* under contract ref. HSK-FIS(89)14.

Abstract

Inverted-Annular Film-Boiling (IAFB) is one of the post-burnout heat transfer modes taking place during the reflooding phase of the loss-of-coolant accident, when the liquid at the quench front is subcooled. Under IAFB conditions, a continuous liquid core is separated from the wall by a superheated vapour film.

The heat transfer rate in IAFB is influenced by the flooding rate, liquid subcooling, pressure, and the wall geometry and temperature. These influences can be accounted by a two-fluid model with physically sound closure laws for mass, momentum and heat transfers between the wall, the vapour film, the vapour-liquid interface, and the liquid core. Such closure laws have been developed and adjusted using IAFB-relevant experimental results, including heat flux, wall temperature and void fraction data.

The model is extensively assessed against data from three independent sources. A total of 46 experiments have been analysed. The overall predictions are good. The IAFB-specific closure laws proposed have also intrinsic value, and may be used in other two-fluid models. They should allow to improve the description of post-dryout, low quality heat transfer by the safety codes.

1 Analytical modeling of inverted-annular film-boiling

1.1 Introduction

Inverted-annular film-boiling (IAFB) is one of the modes of post-burnout heat transfer taking place in a number of situations and in particular during the reflooding phase of the Loss-of-Coolant Accident (LOCA).

IAFB takes place when the liquid at the quench front is subcooled. A thin vapour film develops on the wall, starting at the location of the quench front. Heat is transferred from the wall to the vapour and superheats it. The superheated vapour transfers heat to the vapour-liquid interface, where some vaporization takes place. The vapour generated at the interface thickens the vapour film and tends to decrease the rate of heat transfer.

IAFB resembles film boiling in a pool but only superficially. Indeed, the important influences of liquid flow and subcooling are absent in pool boiling of a saturated liquid. Thus, attempts to use classical film boiling correlations for modeling IAFB situations are in general not successful. On the contrary, approaches based on two-fluid modeling have shown promise (e.g. Chan and Yadigaroglu [5], Denham [8], Kawaji [17], Analytis and Yadigaroglu [3], Takenaka et al. [30]).

The work described here follows the general lines of the model of Analytis and Yadigaroglu [3]. Its purpose is to generalize it and make it applicable to both tubes and bundles; to remove certain global,

purely empirical correction factors that were used previously, as well as correlations that were applied outside their validity range, to further test and verify the model against data from tubes and bundles of different geometries (square and triangular lattices) and hydraulic diameters. Thus, certain closure laws in the model were modified to improve the physical representation of the phenomena. In particular, the formulation of the heat and momentum transfers within the liquid core has been changed, and IAFB specific, physically consistent correlations have been developed, using carefully checked, IAFB relevant, experimental data.

In a reflooding situation, the quench front progresses slowly along the bundle. Seen in a frame of reference moving with the quench front, the phenomena change very slowly. Thus, to easily test the model and to confront it to a large number of experimental data without having to use a large two-fluid code (such as the ones used for system analysis), a quasi-steady state approach and simple, ad-hoc two-fluid code were used: the equations are written, and both the calculations and the data reduction are performed in a frame of reference moving with the quench front. This, however, does not at all preclude a fully dynamic implementation of such a model in a two-fluid code; this indeed has already been done using a previous version of the model [2]. On the contrary, with the quasi-steady-state approach used here, one can investigate in great detail the influence of certain closure laws and assumptions and perform very detailed comparisons to the available experimental data.

1.2 Basic equations

The conservation equations already used by Analytis and Yadigaroglu [3] are also used here. These are the steady-state equations for mass, momentum and energy conservation for the liquid core and the vapour film, considered in a frame of reference moving with the quench front. The flow is assumed to be vertically upwards. U_l and U_v are the liquid and vapor velocities in the moving frame of reference.

$$\frac{d}{dz}\left[\rho_l\,\alpha_l\,U_l\right] = -\frac{M_{vap}}{A} \tag{1}$$

$$\frac{d}{dz}\left[\rho_v(1-\alpha_l)U_v\right] = \frac{M_{vap}}{A} \tag{2}$$

$$-\alpha_l\,\frac{dp}{dz} - \alpha_l\,\rho_l\,U_l\,\frac{dU_l}{dz} = \alpha_l\,\rho_l\,g - \frac{\tau_i\,P_i}{A} - \frac{M_{vap}(U_l - U_i)}{A} \tag{3}$$

$$-(1-\alpha_l)\,\frac{dp}{dz} - \rho_v(1-\alpha_l)U_v\,\frac{dU_v}{dz} = \rho_v(1-\alpha_l)g + \frac{\tau_i\,P_i}{A} + \frac{\tau_w\,P_w}{A} + \frac{M_{vap}(U_v - U_i)}{A} \tag{4}$$

$$\alpha_l\,U_l\,\frac{dT_l}{dz} = \frac{Q_{lh}}{c_{pl}\,\rho_l\,A} - \frac{M_{vap}(h_{ls} - h_l)}{c_{pl}\,\rho_l\,A} \tag{5}$$

$$(1-\alpha_l)U_v\,\frac{dT_v}{dz} = \frac{Q_{vh}}{c_{pv}\,\rho_v\,A} + \frac{M_{vap}(h_{vs} - h_v)}{c_{pv}\,\rho_v\,A} \tag{6}$$

where M_{vap} denotes the vaporization mass flowrate (per unit height), τ_i and τ_w the interfacial and wall shear stress, respectively, and Q_{lh} and Q_{vh} the liquid and vapour sensible heating rates (per unit height), respectively.

For a cylindrical tube of radius R, the relation between the liquid fraction α_l and the film thickness δ is

$$\alpha_l = \left[\frac{(R-\delta)}{R}\right]^2 \tag{7}$$

while, for a square lattice rod bundle,

$$\alpha_l = \frac{p'^2 - \pi(R+\delta)^2}{p'^2 - \pi R^2} \tag{8}$$

and for a triangular lattice rod bundle,

$$\alpha_l = \frac{(\sqrt{3}/2)p'^2 - \pi(R+\delta)^2}{(\sqrt{3}/2)p'^2 - \pi R^2} \tag{9}$$

R is the rod diameter and p' is the bundle pitch.

The interfacial perimeter P_i and the flow area A are given for a tube by

$$P_i = 2\pi(R-\delta) \tag{10}$$
$$A = \pi R^2 \tag{11}$$

and for a bundle by

$$P_i = 2\pi(R+\delta) \tag{12}$$
$$A = p'^2 - \pi R^2 \quad \text{(square lattice)} \tag{13}$$
$$A = (\sqrt{3}/2)p'^2 - \pi R^2 \quad \text{(triangular lattice)} \tag{14}$$

The wall perimeter is

$$P_w = 2\pi R \tag{15}$$

in both cases.

The remaining quantities, namely M_{vap}, U_i, τ_i, τ_w, Q_{lh} and Q_{vh} are expressed by the closure relationships given below.

1.3 Closure relationships

The various components of the heat and momentum transfers are represented in figure 1, together with the velocity profile.

The interfacial velocity U_i is implicity obtained by writing the interface equilibrium condition:

$$\tau_{vi} = \tau_{il} \tag{16}$$

where τ_{vi} and τ_{il} are the interfacial shear stress expressions on the vapour side and on the liquid side, respectively (equations 24, 48).

The vapour interfacial mass flowrate is given by

$$M_{vap} = \frac{Q_{vap}}{h_{vap}} \tag{17}$$

where the vaporization heat rate Q_{vap} is obtained from a heat balance for the interface, expressing the fact that the fraction of the heat rate from the wall and the vapour to the interface, that is not used to heat up the liquid, goes into vapor generation:

$$Q_{vap} = Q_{vi} + Q_r - Q_{lh} \tag{18}$$

where Q_{vi} and Q_r are the heat transfer rates from the vapour to the interface and the radiation heat transfer rate (per unit height), respectively.

The vapour sensible heating rate is given by the following balance

$$Q_{vh} = Q_{wv} - Q_{vi} \tag{19}$$

where Q_{wv} is the heat transfer rate from the wall to the vapour (per unit height).

Expressions for Q_{wv}, Q_{vi}, Q_r, Q_{lh}, τ_w, τ_{vi} and τ_{il} are provided by an analysis of the heat and momentum transfers in the vapour film and in the liquid core.

1.3.1 Vapour film

The vapour field is treated as a flow between two parallel plates, i.e., the wall and the liquid interface. The **wall shear stress** is expressed by

$$\tau_w = f_w \rho_v |U_v + V_{gf}| \frac{(U_v + V_{gf})}{2} \tag{20}$$

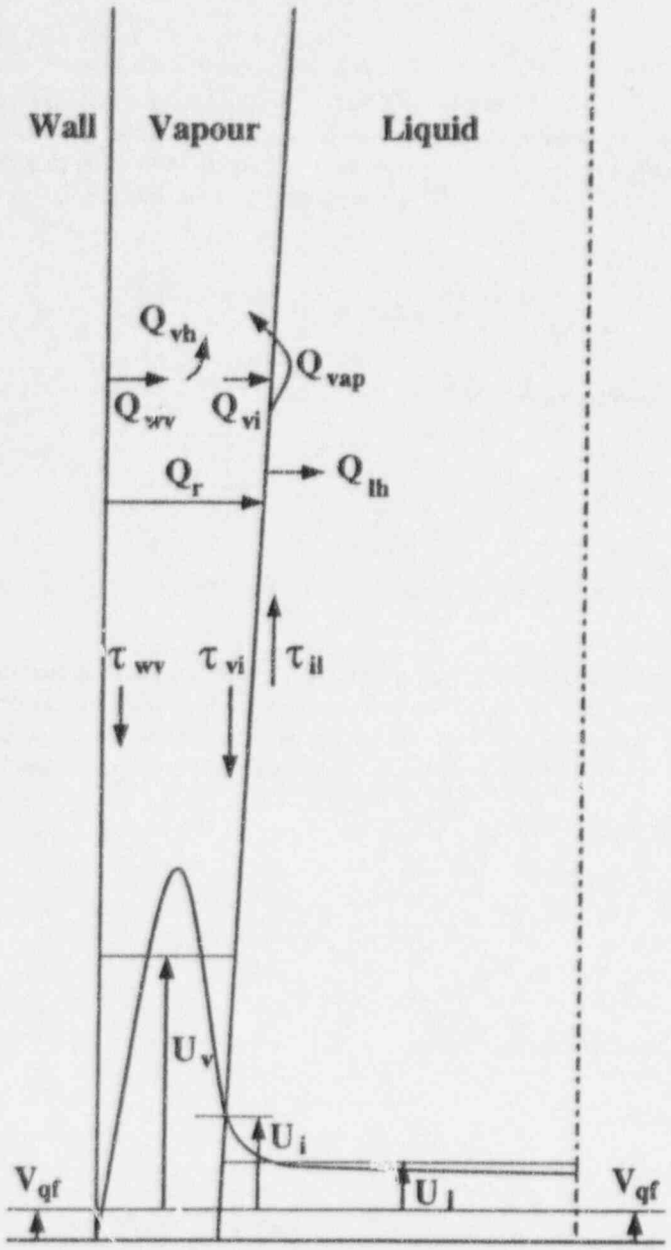

Figure 1: **Velocity profile in "ideal" IAFB; momentum and heat transfers.**
In fact the velocity profile is often strongly disturbed by some fluctuations of the vapour-liquid interface.

where V_{qf} is the quench front velocity. Indeed, the wall velocity relative to the moving frame is $-V_{qf}$.

The following expressions are used for the friction factor

$$f_w = \frac{24}{\mathrm{Re}_w} \quad \text{for} \quad \mathrm{Re}_w < 2000 \tag{21}$$

and

$$f_w = \frac{0.085}{\mathrm{Re}_w^{0.25}} \quad \text{for} \quad \mathrm{Re}_w > 2000 \tag{22}$$

The Reynolds number is defined by

$$\mathrm{Re}_w = \rho_v \, |U_v + V_{gf}| \, \frac{2\delta}{\mu_v} \tag{23}$$

Although it is often acknowledged that the flow regime in the vapour film is turbulent even for low Reynolds numbers (Kao et al. [16], Suryanarayana and Merte [29], Kawaji [17], Takenaka et al. [30]), the use of the usual turbulent flow correlations at low Reynolds numbers (often below 100) is questionable, since these correlations lead to unreasonably low values when extrapolated outside their intended range. Therefore, the turbulent flow friction law in the original model has been replaced by relations 21 and 22.

Similarly, the **interfacial shear stress** is expressed by

$$\tau_{vi} = f_{vi} \, \rho_v \, |U_v - U_i| \, \frac{(U_v - U_i)}{2} \tag{24}$$

where U_i is the interface velocity in the moving frame of reference,

with

$$f_{vi} = \lambda_{fv} \, \frac{24}{\mathrm{Re}_{vi}} \tag{25}$$

and

$$\mathrm{Re}_{vi} = \rho_v \, |U_v - U_i| \, \frac{2\delta}{\mu_v} \tag{26}$$

λ_{fv} is a factor accounting for the enhancement of the momentum transfer from the vapour to the interface, due to interfacial disturbances and turbulence. **The derivation of λ_{fv}, as well as of the similar quantities λ_{hv} (equation 36) and λ_l (equation 51) introduced later is a key point of the present study. It is described in details in section 1.5.** The expression proposed for λ_{fv} is

$$\lambda_{fv} = c_1 (\delta^*)^{c_2} \tag{27}$$

$$c_1 = 0.0362 \tag{28}$$

$$c_2 = 1.96 \tag{29}$$

where δ^* is a non-dimensional film thickness defined by

$$\delta^* \triangleq \delta \, [\frac{\rho_v \, (\rho_l - \rho_v) \, g}{\mu_v^2}]^{\frac{1}{3}} \tag{30}$$

whose introduction is also justified in section 1.5.

When δ^* is small, a minimal value $\lambda_{fv} = 1$ is used.

As turbulence effects on the interfacial shear stress are included in the factor λ_{fv}, equation 25 is used whithout restriction on the Reynolds number range.

The error made by not accounting for the cylindrical geometry (parallel plates) may be estimated, for laminar flow, from Shigechi and Lee [27]. In cylindrical geometry, the inner and the outer shear stress differ by 1.8 % for a surface area ratio (void fraction) of 10 %, and by 12% for a surface area ratio of 50%. The assumption of parallel plates is thus acceptable.

As in Kawaji [17], Kays' [19] formalism is applied to the **heat transfer in the vapour film**. Again, the approximation of parallel plates is made. The exchange perimeter is considered to be $(P_w + P_i)/2$ (mean perimeter). The resulting expressions of the heat transfer rates (per unit height) Q_{wv} and Q_{vi} from the wall to the vapour and from the vapour to the interface are

$$Q_{wv} = \frac{k_v \, \mathrm{Nu}_v}{2\delta} \, \frac{P_w + P_i}{2} \, \frac{(T_w - T_v)}{1 + (\frac{Q_{vi}}{Q_{wv}}) \, \Theta} \tag{31}$$

$$Q_{vi} = \frac{k_v \, \mathrm{Nu}_v}{2\delta} \, \frac{P_w + P_i}{2} \, \frac{(T_v - T_s)}{1 + (\frac{Q_{wv}}{Q_{vi}}) \, \Theta} \tag{32}$$

where Nu_v is the vapour Nusselt number, Θ the influence coefficient and T_s the vapour-liquid interface temperature, assumed to be the saturation temperature. This formulation has been modified to account for the heat transfer enhancement, due to interfacial disturbances and turbulence. The following expressions are proposed:

$$Q_{wv} = \lambda_{hv} \frac{k_v \mathrm{Nu}_v}{2\delta} \frac{P_w + P_i}{2} \frac{(T_w - T_v')}{1 + (\frac{Q_{wi}}{Q_{wv}})\Theta} \tag{33}$$

$$Q_{vi} = \lambda_{hv} \frac{k_v \mathrm{Nu}_v}{2\delta} \frac{P_w + P_i}{2} \frac{(T_v' - T_s)}{1 + (\frac{Q_{wi}}{Q_{vi}})\Theta} \tag{34}$$

$$\tag{35}$$

where λ_{hv} is a factor given by

$$\lambda_{hv} = c_3(\delta^*)^{c_4} \tag{36}$$

$$c_3 = 0.679 \tag{37}$$

$$c_4 = 0.509 \tag{38}$$

(when δ^* is small, a minimal value $\lambda_{hv} = 1$ is used) and T_v' is the mean vapour temperature in a postulated wall sublayer (cf. section 1.5), and is given by

$$T_v' = T_v + (\lambda_{hv} - 1)(T_v - T_s) \tag{39}$$

The vapour thermal conductivity k_v is evaluated at T_v' (the other physical properties are taken at T_v).

Equations 33 and 34 are solved for Q_{wv} and Q_{vi}, giving

$$Q_{wv} = \lambda_{hv} \frac{k_v \mathrm{Nu}_v}{2\delta(1 - \Theta^2)} \frac{P_w + P_i}{2} [(T_w - T_v') - \Theta(T_v' - T_s)] \tag{40}$$

$$Q_{vi} = \lambda_{hv} \frac{k_v \mathrm{Nu}_v}{2\delta(1 - \Theta^2)} \frac{P_w + P_i}{2} [(T_v' - T_s) - \Theta(T_w - T_v')] \tag{41}$$

For laminar flow and constant heat rate, Nu and Θ are given by Kays [19]

$$\mathrm{Nu}_v = 5.385 \tag{42}$$

$$\Theta = 0.346 \tag{43}$$

which we use without restriction on the Reynolds number range, turbulence effects beeing included in the factor λ_{hv}.

The error made by not accounting for the cylindrical geometry (parallel plates) may be estimated from a pure conduction calculation. For a film thickness-to-radius ratio of 1/3, i.e. a void fraction of 56 %, the relative error on the heat transfer rate is only 1 %.

For a tube, the radiation heat transfer rate is given by

$$Q_r = \frac{\sigma P_i (T_w^4 - T_s^4)}{\frac{1}{\epsilon_l} + \frac{P_i}{P_w}(\frac{1}{\epsilon_w} - 1)} \tag{44}$$

and for a bundle by

$$Q_r = \frac{\sigma P_w (T_w^4 - T_s^4)}{\frac{1}{\epsilon_w} + \frac{P_w}{P_i}(\frac{1}{\epsilon_l} - 1)} \tag{45}$$

The radiation absorption in the vapour film is neglected. A value $\varepsilon_l = 0.96$ is used for the water emittance (assumed to be equal to the absorbance), according to Eckert's recommendation for 0.1 mm or more thick water (in [22], pp. 15-23). For the wall emittance, the values recommended in the experimental data sources analysed are used. For Inconel 600, by default, the following relation is used:

$$\varepsilon_w = 1.979\,10^{-4} T_w + 0.5735 \tag{46}$$

where T_w is expressed in Kelvin.

It is a linear approximation, between 580 K and 1260 K, of the values recommended by Kawaji ([17], p. 31), based on a report from *The International Nickel Company, Inc.*

1.3.2 Liquid core

Proper modeling of the heat and momentum transfers from the vapour-liquid interface to the bulk of the liquid is of primary importance, as it describes how the wall heat flux is separated into a liquid heating term and a vaporization term. The approach here differs from the original model formulation, in that we consider, as the reference velocity for the transfers, the liquid velocity relative to the interface $U_l - U_i$, instead of U_l (figure 1). This requires use of one more closure equation, which is the liquid-interface friction law. Notice that $U_l - U_i$ is negative, as the vapour velocity is greater than the liquid velocity.

The liquid Reynolds number relative to the interface is defined as

$$\mathrm{Re}_{li} = \rho_l \, |U_l - U_i| \, \frac{D_{hl}}{\mu_l} \tag{47}$$

where D_{hl} denotes the hydraulic diameter of the liquid column.

Specific friction and heat transfer laws are used depending on the liquid core geometry. For inverted annular flow in a tube, the liquid flow relative to the interface is assumed to be equivalent to flow in a tube (radius $R - \delta$). For inverted annular flow in a rod bundle, the liquid flow is assumed to be equivalent to flow in a rod bundle (pitch p', rod radius $R + \delta$).

The **interfacial shear stress** is given by

$$\tau_{il} = -f_l \, \rho_l \, |U_l - U_i| \, \frac{U_l - U_i}{2} \tag{48}$$

with different expressions for the friction factor f_l, depending on the geometry and on the flow regime.

For laminar flow in a tube, we use

$$f_l = \lambda_l \, \frac{16}{\mathrm{Re}_{li}} \tag{49}$$

while for turbulent flow,

$$f_l = \lambda_l \, \frac{0.079}{\mathrm{Re}_{li}^{0.25}} \tag{50}$$

where λ_l is a factor given by

$$\lambda_l = c_5 (1 + c_6 \, \frac{D_h}{z}) \tag{51}$$

$$c_5 = 4.18 \tag{52}$$

$$c_6 = 0.7 \tag{53}$$

where D_h denotes the hydraulic diameter of the flow, and accounting for the enhancement of the transfers from the interface to the liquid, in particular due to interfacial disturbances, and for entrance length effects (section 1.5). When z is small, a maximal value $\lambda_l = 10$ is used.

For a rod bundle, we use the results of Cheng and Todreas [31], which depend on the flow regime and the bundle geometry. The friction factor is given by

$$f_l = \lambda_l \, \frac{c_l}{\mathrm{Re}_{li}^n} \tag{54}$$

with

$$4\, c_l = a + b \, (\frac{p'}{D'} - 1) + c \, (\frac{p'}{D'} - 1)^2 \tag{55}$$

and

$$D' = 2\,(R + \delta) \tag{56}$$

Values of the coefficients n, a, b and c, valid for pitch-to-diameter ratios between 1.1 and 1.5, are presented in table 1. λ_l is the IAFB-specific factor given by equations 51 to 53.

The liquid-to-interface friction factor is corrected for the influence of temperature dependent properties; this correction may be significant for high liquid subcooling. Denoting by f_l the value given by the above equations and f_{lc} the corrected value, the following relations are used [19].

Flow regime	laminar		turbulent	
Lattice	square	triangular	square	triangular
n	1		0.18	
a	35.55	62.97	0.1339	0.1458
b	263.7	216.9	0.09059	0.03632
c	-190.2	-190.2	-0.09926	-0.03333

Table 1: **Coefficients in equations 54 and 55.**

For laminar flow:

$$f_{lc} = f_l \left(\frac{\mu_s}{\mu_l}\right)^{0.58} \tag{57}$$

and for turbulent flow:

$$f_{lc} = f_l \left(\frac{\mu_s}{\mu_l}\right)^{0.25} \tag{58}$$

where μ_s is the liquid viscosity at the saturation temperature T_s and μ_l the liquid viscosity at the mean liquid temperature T_l.

The largest of the laminar or turbulent values of the friction coefficient is used. In practice, laminar flow is only predicted over very short lengths near the quench front: from some fractions of a millimeter for the largest hydraulic diameters in our data bank (about 14 mm), to some millimeters for the smallest (4 mm).

The **heat transfer from the interface** at T_s to the bulk of the liquid is expressed by

$$Q_{lh} = h_l P_i (T_s - T_l) \tag{59}$$

where T_l is the bulk liquid temperature and h_l the liquid-interface heat transfer coefficient.

For laminar flow, the liquid-interface Nusselt number

$$\mathrm{Nu}_l \triangleq \frac{h_l D_{hl}}{k_l} \tag{60}$$

for a tube at constant surface temperature is given by

$$\mathrm{Nu}_l = 3.66 \tag{61}$$

In a rod bundle, the results of Sparrow and Loeffler [31], based on constant axial heat flux, are used. For uniform circumferential temperature and a pitch-to-diameter ratio of 1.13,

$$\mathrm{Nu}_l = 6.0 \tag{62}$$

For a pitch-to-diameter ratio of 1.33,

$$\mathrm{Nu}_l = 9.4 \tag{63}$$

As these values correspond to a constant axial heat flux boundary condition and the modeled situation is for a constant (saturation) axial temperature, in an attempt to correct them, they are multiplied by the ratio

$$\frac{\mathrm{Nu}_t}{\mathrm{Nu}_f} \tag{64}$$

where Nu_t and Nu_f are the constant temperature and constant heat flux Nusselt numbers in a tube:

$$\mathrm{Nu}_t = 3.66 \tag{65}$$

$$\mathrm{Nu}_f = 4.364 \tag{66}$$

The laminar heat transfer coefficient is also corrected for the influence of temperature dependent properties according to Kays [19]. The corrected value is

$$h_{lc} = h_l \left(\frac{\mu_s}{\mu_l}\right)^{-0.14} \tag{67}$$

Finally, to account for interfacial disturbance effects, the same factor λ_l as for the friction coefficient is applied to h_{lc}.

For turbulent flow, the liquid-interface heat transfer coefficient is deduced from the interfacial shear stress through the Chilton-Colburn analogy:

$$h_l = \frac{|\tau_i|\, c_{pl}}{|U_l - U_i|\, \mathrm{Pr}_l^{2/3}} \tag{68}$$

The enhancement factor λ_l is implicitely applied to h_l through τ_i. Again, the largest of the two values of the heat transfer coefficient for laminar or turbulent flow is used.

1.4 Implementation

The initial values of the variables p, U_v, U_l, α_l, T_v and T_l at the quench front, the quench front velocity, and the wall temperature distribution in the dry region are given as input to the calculations. Equations 1 to 6, together with the closure laws 7 to 68 are solved by a standard Runge-Kutta method. As the computed variables may vary strongly near the quench front, a very small initial step (10^{-10} m) is used. This step is then exponentially increased.

The results allow us to derive the distribution of the wall heat flux, given by

$$q_w = \frac{Q_w}{P_w} = \frac{Q_{wv} + Q_r}{P_w} \tag{69}$$

and of a heat transfer coefficient defined by

$$h \triangleq \frac{q_w}{T_w - T_s} \tag{70}$$

where T_s is the saturation temperature.

1.5 Semi-empirical description of interfacial disturbance effects

1.5.1 Needs

Numerous reported observations of IAFB (De Jarlais and Ishii [7], Kawaji et al. [18], Costigan and Wade [6], Edelman et al. [10]) indicate that the vapour-liquid interface is irregular. In addition, liquid droplets may be entrained in the vapour film. It is generally agreed that the interfacial disturbances should increase the wall heat flux by locally thinning the vapour film and lowering the vapour temperature. The vapour-liquid momentum and heat transfer should also be enhanced, due to the hydrodynamic drag of interfacial waves, to the enlargement of the transfer area, and to the transfers between the vapour and liquid droplets. The interfacial disturbances also promote the appearance of turbulence in the vapour film, which further enhances heat and mass transfer. Finally, the interface-liquid bulk heat and momentum transfers should also be increased, due to roughness effects. The true boundary condition, i.e. a fluid-fluid instead of fluid-wall interface, should also play a role in that it affects the turbulence structure near the interface (e.g., Rashidi et al. [21]).

The way interfacial disturbance effects were accounted for in the original model is shown below to present some shortcomings. A new formulation of the momentum and heat transfer enhancements due to interfacial disturbances has since been developed and included in the IAFB model.

1.5.2 Physical background

The physical processes involved in heat and momentum transfer enhancement, i.e. waves, oscillations of the whole liquid core, droplet entrainment and redeposition, and turbulence, are very complex. As their modeling only represents one part of the IAFB model, which is in other respects already complex, any attempt of a fully analytical description of these effects seems hopeless. Therefore, these effects are accounted for in a global, semi-empirical manner. Four physical processes are specifically adressed, i.e. the momentum and heat transfers in the vapour and the liquid.

On the vapour side, a first enhancement factor λ_{fv} is applied to the **vapour-interface momentum transfer** (equation 25). It accounts for the hydrodynamic drag of interfacial waves, the equivalent roughness effect of ripples, and the momentum transfer between the vapour and liquid droplets. This factor will be correlated empirically.

The **vapour film heat transfer** description is modified, based on the following simple considerations and assumptions. The effective thermal conductivity in the vapour film may be much higher near the vapour-liquid interface than near the wall, due to interfacial waves, entrained droplets and turbulence. The temperature profile is then almost flat near the interface, and steep near the wall. The film is arbitrarily split into two sublayers (figure 2).

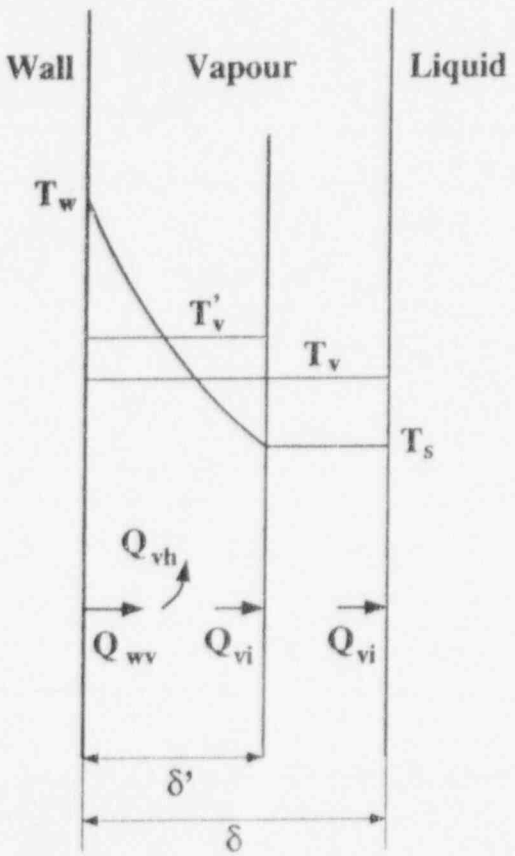

Figure 2: **Film heat transfer model.**

Near the interface, the vapour temperature is assumed to be uniform and equal to the saturation temperature. Near the wall, a laminar sublayer of thickness δ' is assumed to control heat transfer. The heat rates entering and leaving this sublayer are then given by (section 1.2, equations 31 and 32)

$$Q_{wv} = \frac{k_v \, \mathrm{Nu}_v}{2\delta'} \frac{P_w + P_i}{2} \frac{(T_w - T_v^v)}{1 + (\frac{Q_{vi}}{Q_{wv}})\Theta} \tag{71}$$

$$Q_{vi} = \frac{k_v \, \mathrm{Nu}_v}{2\delta'} \frac{P_w + P_i}{2} \frac{(T_v^v - T_s)}{1 + (\frac{Q_{wx}}{Q_{vi}})\Theta} \tag{72}$$

where T_v^v denotes the mean vapour temperature in the wall sublayer.

Introducing the factor λ_{hv} defined as

$$\lambda_{hv} \triangleq \frac{\delta}{\delta'} \tag{73}$$

where δ is the total film thickness, equations 71 and 72 become

$$Q_{wv} = \lambda_{hv} \frac{k_v \, \mathrm{Nu}_v}{2\delta} \frac{P_w + P_i}{2} \frac{(T_w - T_v^v)}{1 + (\frac{Q_{xi}}{Q_{wx}})\Theta} \tag{74}$$

$$Q_{vi} = \lambda_{hv} \frac{k_v \, \mathrm{Nu}_v}{2\delta} \frac{P_w + P_i}{2} \frac{(T_v^v - T_s)}{1 + (\frac{Q_{wx}}{Q_{vi}})\Theta} \tag{75}$$

Neglecting the vapour film curvature and the velocity profile effects, T_v (the mean bulk vapour temperature used in the 6 equation model), T_v^v, T_s (the saturation temperature), δ and δ' are related by

$$T_v = \frac{\delta'}{\delta} T_v^v + \frac{(\delta - \delta')}{\delta} T_s \tag{76}$$

or

$$T_v^v = T_v + (\lambda_{hv} - 1)(T_v - T_s) \tag{77}$$

The factor λ_{hv} will be correlated empirically.

The simple model proposed does not attempt a rigorous description of the heat transfer in the vapour film. It only provides a basis for a correlation.

It should be pointed out that, for realistic values of the variables involved, the predicted wall and interfacial heat transfer rates Q_{wv} and Q_{vi} are very close, and about equal to the pure conduction heat transfer rate through a vapour film of thickness δ, enhanced by a factor λ_{hv}. This is due to the low thermal capacity of the vapour film. Nevertheless, the use of equations 74, 75 and 77, rather than of a single conduction equation presents a major advantage. It allows to keep the frame of a full 6-equation model, whereas a single conduction equation would have fixed the vapour temperature at the average value between wall and saturation temperatures, making the vapour energy conservation equation obsolete. Moreover, the proposed model may predict a much lower value of the vapour temperature than the average between wall and saturation, which is realistic and significant, in that it influences the values of the steam physical properties.

As, according to the present model, the heat transfer is controlled by the wall sublayer, the vapour thermal conductivity k_v is evaluated at the temperature T_v^v, whereas the vapour physical properties which are involved in the hydrodynamic equations, i.e. density and viscosity, are evaluated at the mean bulk temperature T_v.

The expressions for the λ_{fv} and λ_{hv} factors, which characterize the momentum and heat transfer enhancement in the vapour film, have to rely on experimental data. Correlations have to be developed, which should, to the extent possible, involve the determining physical variables.

In the original model, the following enhancement factor,

$$\lambda = 1 + 150\,(\delta/R) \tag{78}$$

where δ denotes the film thickness and R the tube diameter, was applied to both the vapour-interface heat and momentum transfers. This correlation due to Wallis [32] [33] has also been applied to IAFB by Fung and Groeneveld [13]. However, it has originally been developed for the friction coefficient between the gas core and the gas-liquid interface in annular flow, which is quite a different situation. The correlating variable δ/R itself seems inadequate for IAFB in general. For example, this variable looses its significance in the ideal, limiting case of film boiling along a vertical flat plate, whereas the transfer enhancement mechanisms are still present in this case.

Another shortcoming of the original model is that the enhancement factor λ was only applied to the vapour-interface heat flux, and not to the wall-vapour heat flux. The wall heat flux was only indirectly modified, through the decrease in vapour temperature; as a consequence, for a given film thickness, it could not be increased by a factor greater than two (a factor two would correspond to an infinite value of the enhancement factor, and to a vapour temperature equal to the saturation temperature). This is clearly shown by experimental values of the wall heat flux enhancement factor (figure 4) to be insufficient.

The enhancement of the vapour-interface transfers may be attributed to two basic mechanisms, i.e. turbulence and continuity waves. These two mechanisms, which are mutually dependent, appear to be strongly related to the vapour Reynolds number. Evidence of the Reynolds number influence on the development of continuity waves may be found in linear stability analyses as the one by Kao et al. [16]. Shortly, inverted-annular flow (IAF) is always unstable with respect to long wavelengths (for short wavelengths, surface tension acts as a restoring force), and the rate of growth of instabilities strongly increases with the vapour Reynolds number.

The hydrodynamic stability of IAF is influenced by several other parameters than the vapour Reynolds number. However, it seems reasonable to leave these effects aside in this study, which mostly concerns the reflooding of nuclear reactor cores with water. The following qualitative justification may be given. As long as the liquid is water in a relatively narrow temperature range (i.e. with relatively constant physical properties), with a much larger hydraulic diameter than that of the vapour film and a much lower velocity, the hydrodynamic boundary conditions for the vapour film remain more or less the same. The vapour and interface hydrodynamics are thus largely specified by the vapour Reynolds number.

Thus, the vapour film Reynolds number appears to be a convenient correlating variable for λ_{fv} and λ_{hv}. Unfortunately, no vapour velocity measurements are available. A correlation based on the vapour Reynolds number would then have to rely on a computed vapour velocity, which seems precarious for further applications. Thus, use was made of a dimensionless film thickness, defined as follows:

$$\delta^* = \delta \left[\frac{\rho_v(\rho_l - \rho_v)\, g}{\mu_v^2}\right]^{\frac{1}{3}} \tag{79}$$

The link between the vapour Reynolds number and the non-dimensional film thickness δ^* appears by considering the momentum conservation equations in the IAFB two-fluid model (equations 3 and 4). A linear combination of these equations, with the factors $(1-\alpha_l)$ and $(-\alpha_l)$ respectively, neglecting the convective terms (which, according to the numerical results, is realistic, even with significant vaporization), gives

$$\frac{\tau_i\, P_i}{A} + \alpha_l \frac{\tau_w\, P_w}{A} = \alpha_l(1-\alpha_l)(\rho_l - \rho_v)g \tag{80}$$

Physically, relation 80 expresses that the vapour film buoyancy is entirely compensated by the wall and interfacial friction forces.

Assuming laminar vapour flow, a liquid fraction close to 1, and a liquid velocity much lower than the vapour velocity, and assimilating the vapour-liquid interface to a smooth wall, gives

$$P_i \simeq P_w \tag{81}$$

$$1-\alpha_l \simeq \frac{P_i\,\delta}{A} \tag{82}$$

$$\tau_i \simeq \tau_w \simeq \frac{24}{\mathrm{Re}_v}\,\rho_v\,\frac{U_v^2}{2} \tag{83}$$

where the vapour Reynolds number Re_v is given by

$$\mathrm{Re}_v \triangleq \frac{\rho_v\, U_v\, 2\delta}{\mu_v} \tag{84}$$

Substituting U_v (equation 84) in equation 83 yields

$$\tau_i = \frac{3\,\mu_v^2}{\rho_v\,\delta^2}\,\mathrm{Re}_v \tag{85}$$

Whith the above simplifications, equation 80 becomes

$$\tau_i = \frac{(\rho_l - \rho_v) g \delta}{2} \tag{86}$$

Combining equations 85 and 86 produces

$$\mathrm{Re}_v = \frac{(\delta^*)^3}{6} \tag{87}$$

which means that, under the assumptions made, δ^* may replace Re as the correlating variable. Real IAF approaches the "ideal" situation pictured by these assumptions near the quench front, and further up if the liquid sucooling remains high (in this case, the wall heat flux is high and goes almost entirely into the liquid core, the vapour film remaining thin). Indeed, very thin vapour films should remain laminar, and, according to the reported observations, relatively smooth. Relation 87 is no longer valid for very high flooding rates (of the order of 1 m/s or greater), where the liquid velocity may no longer be neglected.

A similar analysis with a turbulent friction law (constant friction coefficient) leads to a vapour Reynolds number proportional to $(\delta^*)^{3/2}$. Thus, the physical effects attributed to the Reynolds number may also be correlated with δ^* if some turbulence is present. Finally, it has been checked that the relation between Re_v and δ^* does not depend on the flow geometry (tube or rod bundle).

In summary, the quantity δ^* appears as a physically suited correlating parameter for the vapour-interface transfer enhancement during IAFB in reflooding situations.

A third enhancement factor, λ_l, is applied to the **interface-liquid momentum transfer** (equations 49 to 54). As the **heat transfer** is deduced from the momentum transfer using the Chilton-Colburn analogy (equation 68), it is also affected by this third coefficient.

The choice of correlating parameters for this factor is difficult. Indeed, the enhancement of the transfers within the liquid core may be attributed to several distinct effects. There is an increase of the transfers near the quench front due to the violent changes in the flow that take place there and cause a strong mixing. This effect should decrease downstream due do the development of a velocity profile in the liquid core. There is also a "roughness" effect due to the interfacial disturbances. This should increase along the flow, as the film Reynolds number and the wave amplitudes increase.

In the original model, the entrance-length effect was approximately accounted by applying the following enhancement factor,

$$F = 1 + 1.4\,(R/z) \tag{88}$$

to the interface-liquid heat transfer, where R denotes the tube diameter and z the distance from the quench front. This factor approximatively fits the thermal-entrance-length effect for turbulent flow in a circular tube, for constant heat rate and a Prandtl number of the order of 0.7 (the Reynolds number has little influence) (e.g. [19], figs. 13-8 and 13-9, pp. 264 and 265).

Still in the original model, another enhancement factor was required (a constant value of 2.5 was used), in some cases, in order to reach good agreement between the experimental and computed results. This was attributed to the "roughness" effect.

R/z or, rather, D_h/z (D_h: hydraulic diameter of the flow) seems a convenient correlating parameter with regards to the entrance-length effect, whereas the "roughness" effect could be accounted by using δ_l^*/D_h.

1.5.3 IAFB-specific correlations

The enhancement factors λ_{fv}, λ_{hv} and λ_l have been correlated using Fung's [12] experimental results. Fung obtained steady-state, post-dryout heat transfer data for vertical flow of water inside electrically heated inconel tubes of about 12 mm inside diameter and 800 mm length. The data were obtained using the "hot patch" technique in which an indirectly heated copper block brazed onto the inlet of the test section supplies the critical heat flux. This hot patch stabilizes the quench front upstream of the tube,

which may then be operated in post-dryout, down to relatively low heat fluxes and steam qualities. The wall temperature was measured at ten locations, and the heat transfer rates were derived from these measurements, taking into account axial conduction and heat losses. The void fraction was measured at five locations using γ-densitometry. The way input data for the present IAFB model are obtained from Fung's data, is described in [4], together with the processing of data from other sources.

Fung's results constitute a particularly well suited data base for IAFB-specific correlations since many of his experiments were performed in the IAFB-relevant parameter range (34 have been used for the new correlations) and they also include void fraction measurements. In addition to specifying a meaningful variable all along the flow, these measurements give access to the film thickness and thus to the correlating variable δ^* (equation 79).

Values of the three enhancement factors along the flow have been obtained, for each experiment, in the following way: All along the length of the flow, two experimental results are available, i.e. the wall heat flux and the void fraction. Near the quench front, the first enhancement factor (vapour friction) has little influence on the numerical results. The underlying physical reason is that, the liquid subcooling beeing high, most of the wall heat flux goes into the liquid core, and vapour generation is low. On the contrary, far away from the quench front, the third enhancement factor (transfers inside the liquid) becomes ineffective. The reason is that the liquid is close to saturation, and only absorbs a small part of the wall heat flux. Each experimental (heat flux and void fraction vs. distance from the quench front) curve was divided into two sections. In the first section, near the quench front, the second enhancement factor (vapour heat transfer) and the third one (transfers inside the liquid) were considered as dominant and stepwise computed, at each elevation, from the experimental results. In the second section, further downstream, the first enhancement factor(vapour friction) and the second one (vapour heat transfer) were computed. In each section, an extrapolation was used for the remaining enhancement factor. The results from each section depend to some extent on the results from the other. An iterative procedure was thus used until convergence was reached. The process was complex and partly interactive.

The results obtained for λ_{fv} (vapour-interface friction) differ to some extent from one experiment to another. Nevertheless, a common trend may clearly be detected, as may be seen in figure 3. The results obtained for λ_{hv} (heat transfer in the vapour film) correlate fairly well with δ^*, as shown in figure 4. It may be noted that no clear transition to turbulence (change in slope) appears in this curve.

The following laws are retained for the relations between the first two enhancement factors and δ^*:

$$\lambda_{fv} = c_1(\delta^*)^{c_2} \tag{89}$$
$$c_1 = 0.0362 \tag{90}$$
$$c_2 = 1.96 \tag{91}$$

$$\lambda_{hv} = c_3(\delta^*)^{c_4} \tag{92}$$
$$c_3 = 0.679 \tag{93}$$
$$c_4 = 0.509 \tag{94}$$

(When δ^* becomes small, λ_{fv} and λ_{hv} are not allowed to drop below 1, which would be physically meaningless).

The results obtained for λ_l (interface-liquid transfers, figure 5) are quite scattered, especially in the region downstream from the hot patches where, for some experiments, λ_l takes very large values. This might be due to a shortcoming of the present IAFB model, due e.g. to a physical phenomenon not beeing accounted for in this zone. However, it is believed that the hot patch technique is, at least partially, responsible for the effect observed. Indeed, the same trend (enhanced heat flux, in some cases, in the region downstream from the hot patch) may be directly observed in the wall heat flux profiles [4]. The hot patches beeing relatively long, i.e., 5.3 times the tube diameter in most cases and 2.1 in the remaining ones, and the quench front beeing most likely situated near the hot patch inlet, the zone concerned is already quite far from the quench front. Extrapolation of the measured heat flux up to

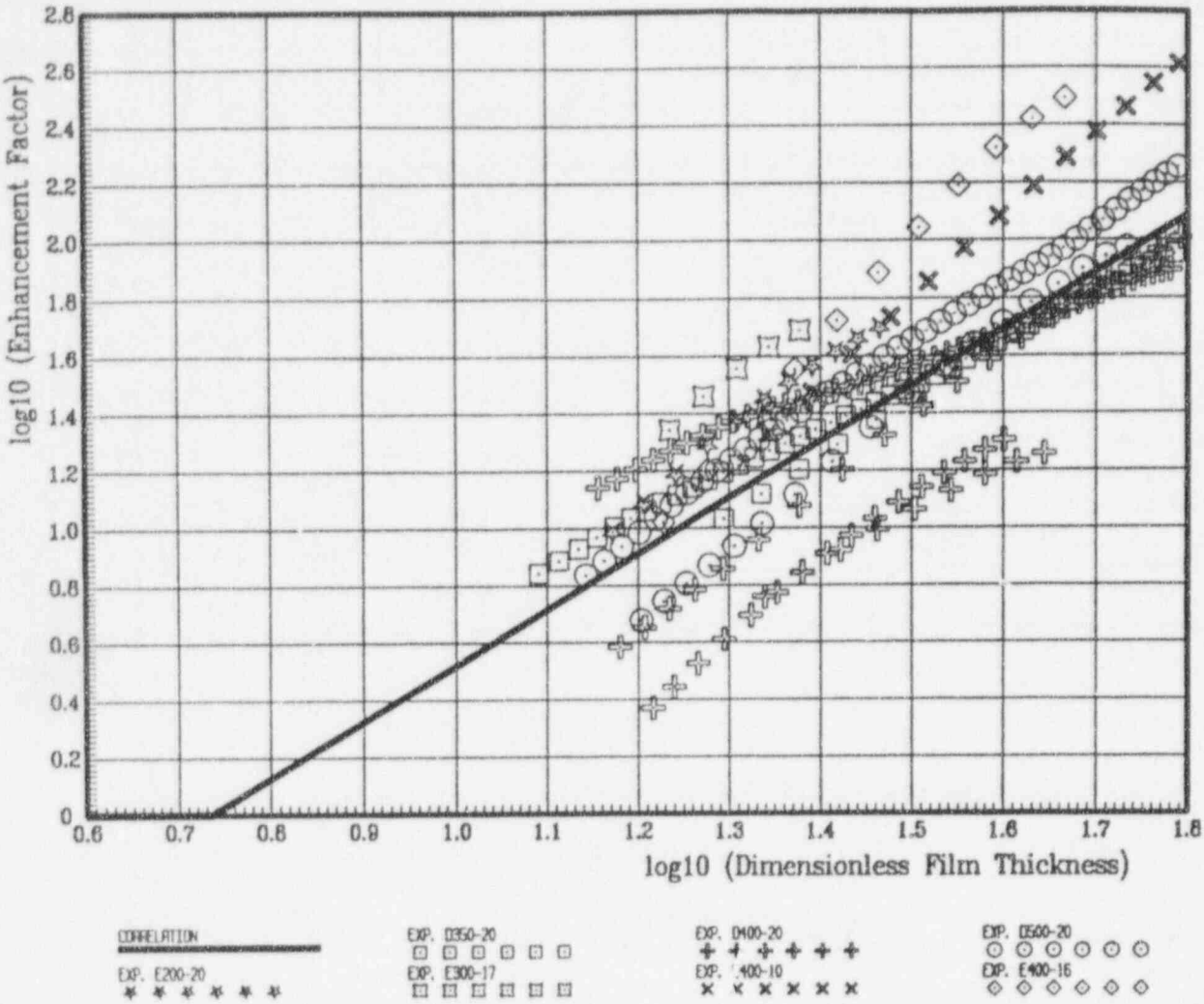

Figure 3: **Vapour-interface friction.**
Correlation of the vapour-interface friction enhancement factor λ_{fv} using Fung's [12] experimental data. The absence of experimental points in the left part of the graph is due to the low influence of the vapour-interface friction in this region (see text).
In the experiment designation, the first letter refers to the test section. The first three numbers represent the inlet velocity (in mm/s) and the last two represent the inlet subcooling (in °C).

the quench front region yields, in the cases concerned, to very high values, several times larger than for comparable reflooding experiments without hot patch. The high values of the wall heat flux downstream from the hot patch are encountered when the wall temperature is relatively low in this region (roughly, below 600 °C). The heat transfer enhancement might be due to partial and/or intermittent rewetting of the inconel tube downstream from the hot patch. Anyway, this effect, which seems to be hot-patch-related, is left aside in this study, which mostly concerns reflooding. However, this means that the values of λ_i obtained may only be used rather far from the hot patch.

For all experiments, at some point, λ_i reaches an approximatively constant value (figure 5). The average of the quasi-constant values obtained for the 14 experiments analysed is 4.18, with a standard deviation of 0.61, which gives, with a 95% probability threshold:

$$\lambda_i = 4.18 \pm 0.35 \tag{95}$$

The obtention of a constant value may be interpreted as follows: in a tube, according to Norris (in [19],

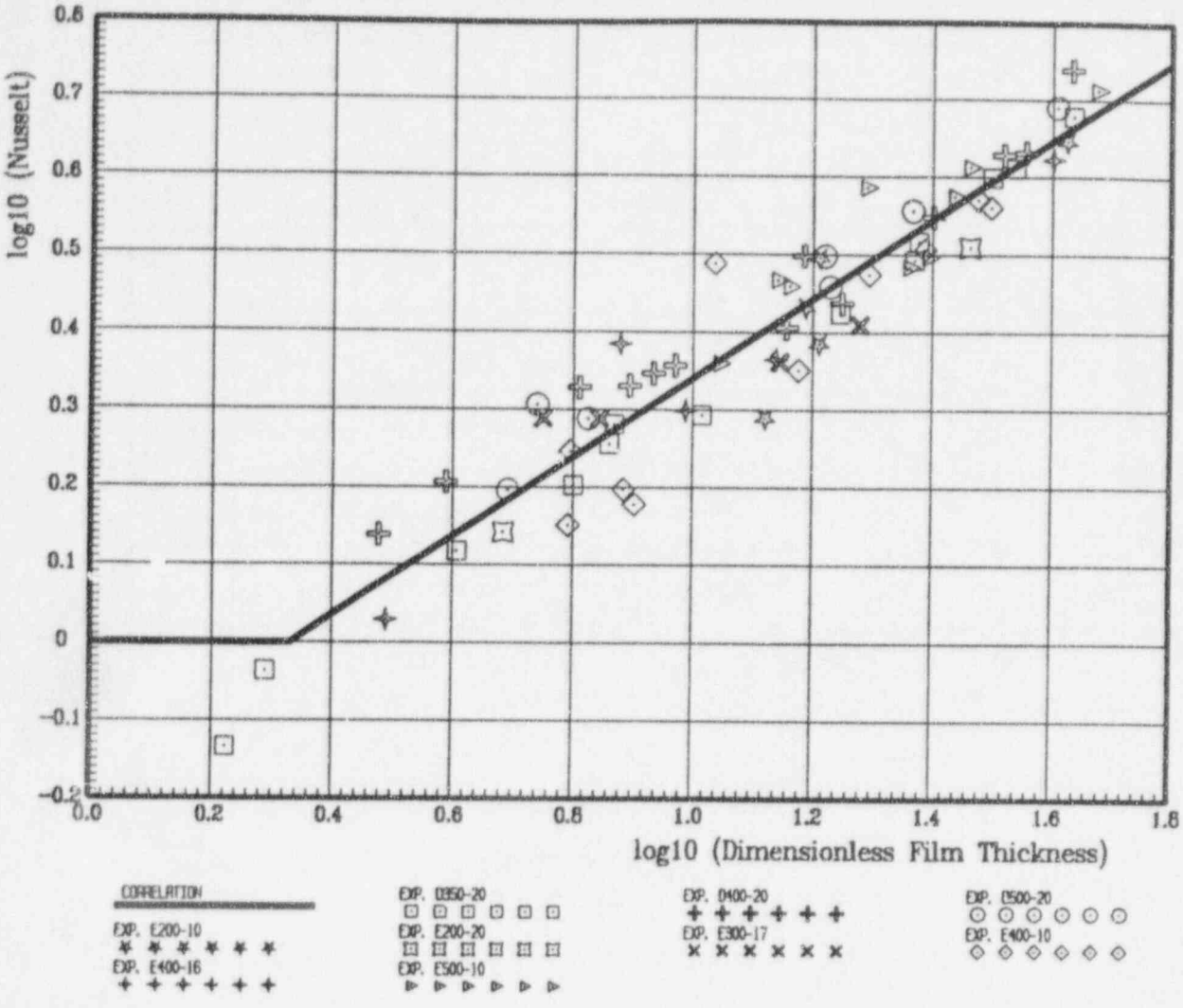

Figure 4: **Vapour film heat transfer.**
Correlation of the vapour film heat transfer enhancement factor λ_{hv} using Fung's [12] experimental data.
The basic model is very close to pure conduction; the enhancement factor may be interpreted as a Nusselt number.
Experiment designation as in figure 3.

p. 271), the heat transfer increases with the wall roughness up to a certain point only, and then remains unchanged. For the liquid core in IAFB, far from the quench front, the vapour-liquid interface would thus be equivalent to a very rough wall.

The constant value $\lambda_l = 4.18$ far from the quench front is retained in the present IAFB model. Entrance-length effects should also be accounted for in the quench front region. As the results derived from Fung's data may not be used in this region, the relation used in the original model (equation 88) is combined with the result obtained here in the following way:

$$\lambda_l = c_5(1 + c_6 \frac{D_h}{z}) \quad (96)$$

$$c_5 = 4.18 \quad (97)$$

$$c_6 = 0.7 \quad (98)$$

where D_h denotes the hydraulic diameter of the flow and z the distance from the quench front. When z is small, a maximal value $\lambda_l = 10$ is used.

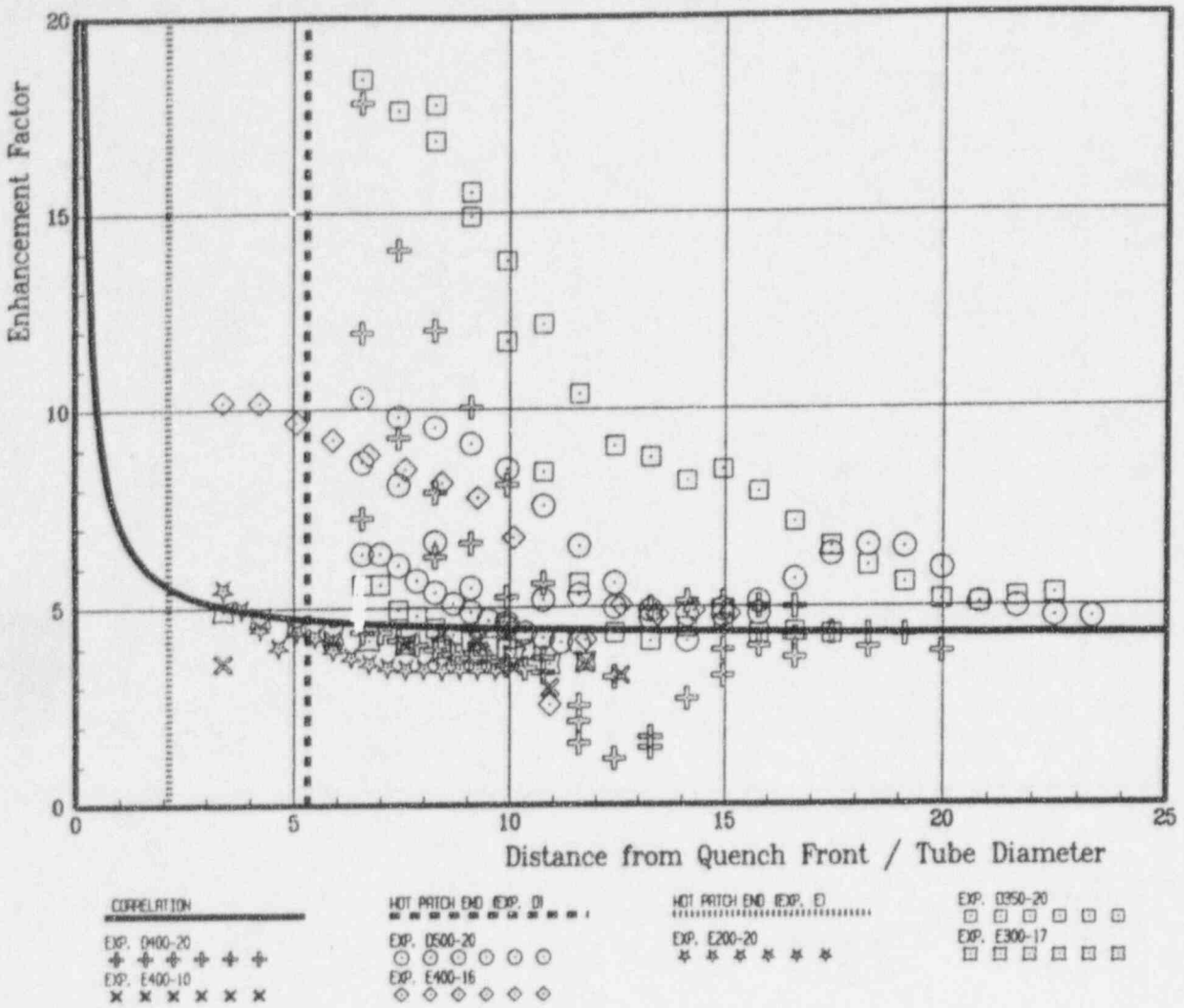

Figure 5: **Interface-liquid transfers.**
Correlation of the interface-liquid transfer enhancement factor λ_i using Fung's [12] experimental data. The quench front is assumed to be located at the hot patch inlet. The vertical lines represent the hot patch end, for each test section.
The large values of λ_i, in the left part of some curves, are attributed to a hot-patch-specific effect, and not accounted for in the correlation (see text).
Experiment designation as in figure 3.

As explained above, the empirical parameters appearing in the new correlations have been derived from Fung's results [12] only, whereas experimental data from other sources have been processed and analysed (section 2). A statistical analysis has been conducted [24] to try to optimize these parameters with respect to the entire data bank. Slightly better parameter sets could thus be obtained for each individual series of experiments (for example, for the NEPTUN tight lattice experiments), but the overall prediction could not be significantly improved. As Fung's experiments provide more experimental information than the others (i.e. void fraction measurements), it has been decided to keep the empirical coefficients unchanged.

Finally, it should be pointed out that the model results are very sensitive to the value of λ_{hv} (film heat transfer enhancement), the two other factors representing smaller corrections. The derivation of this factor from the experimental results is rather straightforward, and can be achieved independently from the IAFB model. Indeed, as mentioned above, λ_{hv} is very close to the ratio between the convection wall heat flux and the pure conduction heat flux (the small difference corresponding to the vapour sensible

heating rate):

$$\lambda_{hv} \simeq \frac{q_{wv}}{q_{cond}} \tag{99}$$

with

$$q_{wv} = q_w - q_r \tag{100}$$

(q_r is the radiation heat flux) and

$$q_{cond} = k_v \frac{T_w - T_s}{\delta} \tag{101}$$

The variables involved in equations 99 and 101, as well as in the correlating variable δ^* (equation 79), are directly derived from experimental results (provided void fraction or film thickness measurements are available). The correlation proposed for λ_{hv} (equation 92) has thus an intrinsic value and is very reliable, provided the experimental results used are precise.

Another advantage of this correlation (and also of the correlation proposed for λ_{fv}, equation 89) is that it is, to a large extent, independent of the flow channel geometry and of the parameter ranges. The reason for this is that the vapour film geometry remains the same, i.e. an annular geometry, in both a tube and a rod bundle. The tube or rod diameter should not much influence the results since the most determining parameter is the film thickness, which keeps the same order of magnitude in all cases. The only significant limitation of the correlation is at high liquid velocities (several m/s), where the interface velocity is no longer small in comparison with the vapour velocity; in this case, as mentioned above, δ^* is no more suited as a correlating variable. However, this situation is not likely to occur during reflooding.

2 Model assessment and conclusions

2.1 Experimental data

The model presented above has been assessed against experimental data from three independant sources. The first one is the NEPTUN rod bundle reflooding experiment at the Paul-Scherrer Institute [9] [14]. The second one is the University of California-Berkeley single tube, internally reflooded tube experiment [25] [26] [34]. The third one is the University of Ottawa [12] steady-state tube experiment using the hot patch technique. Among the available data, the most relevant to the IAFB regime have been selected, i.e. the experiments where the equilibrium quality above the quench front is still negative and the quench front velocity is much lower than the flooding rate. In fact, among the NEPTUN and UC-Berkeley data, these IAFB-relevant experiments constitute a minority. For the University of Ottawa data, the availability of void fraction measurements has also been a choice criterion.

2.1.1 Paul-Scherrer Institute data

The data analysed were obtained by forced-feed bottom reflooding of a simulated standard pressurized water reactor (PWR) bundle [11] [28] and a simulated light water high conversion reactor (LWHCR) bundle [23]. The heated length was 1.68 m. A continuously variable cosine profile with a peaking factor of 1.58 was used. The PWR bundle consisted of 33 electrically heated rods and 4 guide tubes, with a square lattice and a pitch-to-diameter ratio of 1.33 (13.6 mm hydraulic diameter), placed in an octagonal housing. The LWHCR bundle consisted of 37 heated rods, with a triangular lattice and a pitch-to diameter ratio of 1.13 (4.4 mm hydraulic diameter), placed in a hexagonal housing.

The test bundle was instrumented at 8 equally spaced levels. At these levels, the cladding temperature was measured, and the wall heat flux was derived by means of an inverse one-dimensional heat conduction computation [1] [15].

2.1.2 UC-Berkeley data

These data were obtained by forced reflooding of single electrically heated vertical tubes, about 14.3 mm in inside diameter and 3.7 m high. The wall temperature was measured at several points along the

tube. The wall heat flux was then estimated from a lumped-parameter heat balance for the heated wall, the heat losses being accounted for.

2.1.3 University of Ottawa data

These data (steady state, tubes of about 12 mm inside diameter), which have served as a basis for the three new correlations, have already been discussed in section 1.5.3.

2.2 Model assessment

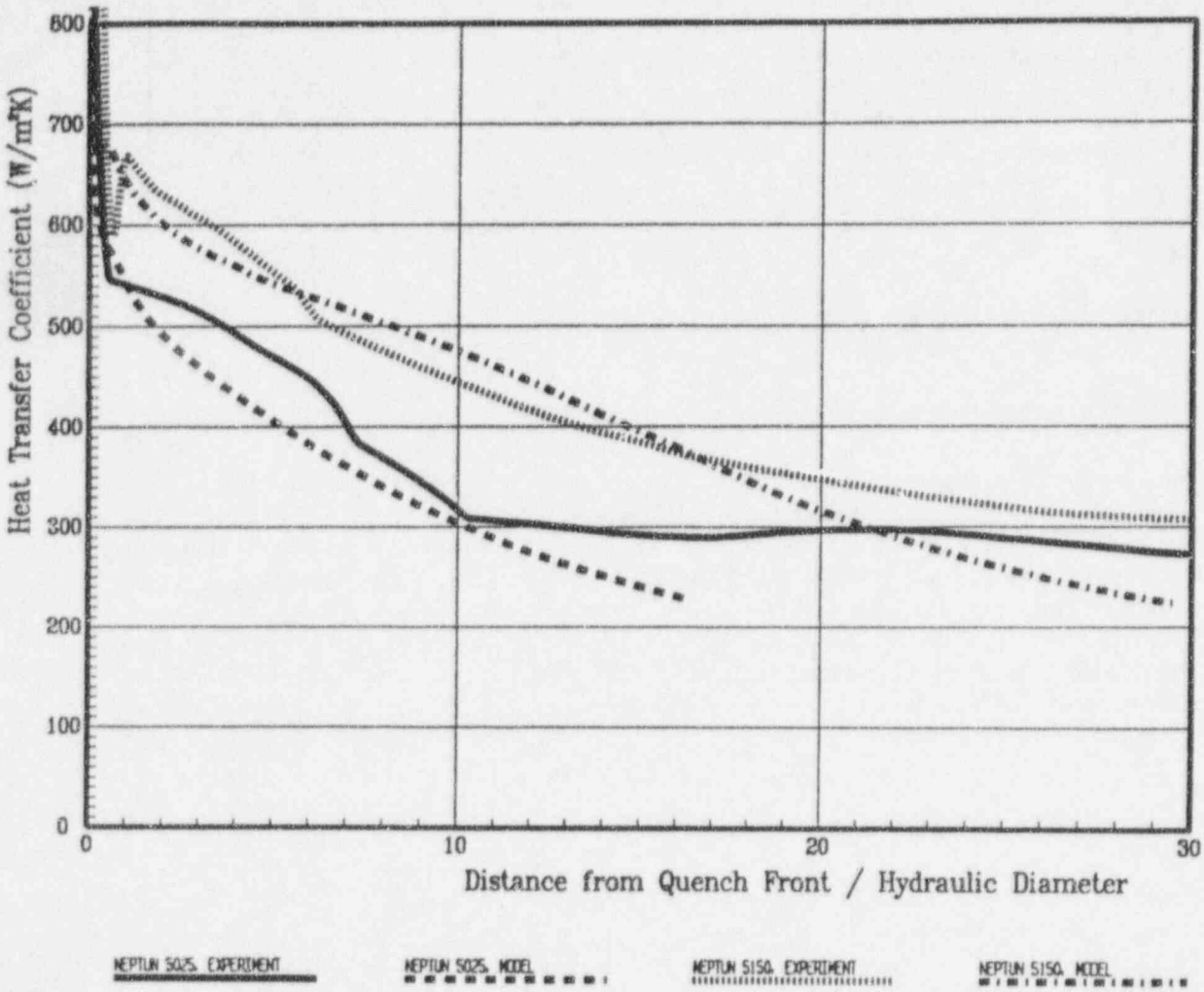

Figure 6: **Effect of subcooling at the quench front and flooding rate on IAFB heat transfer in a standard PWR bundle** (14 mm hydraulic diameter).
Comparison of experimental and predicted heat transfer coefficient distributions downstream from the quench front for NEPTUN reflooding experiment:
- Run 5025: 12 °C subcooling just above quench front, 10 cm/s flooding rate
1.5 cm/s quench front velocity, 487 °C wall temperature just above quench front, 472 °C at 30 cm
- Run 5150: 25 °C subcooling, 15 cm/s flooding rate
1.9 cm/s quench front velocity, 484 °C wall temperature just above quench front, 516 °C at 30 cm
(4.2 bar pressure and 95 cm quench front elevation in both cases).
Note. Calculations stopped at 60 % void fraction.

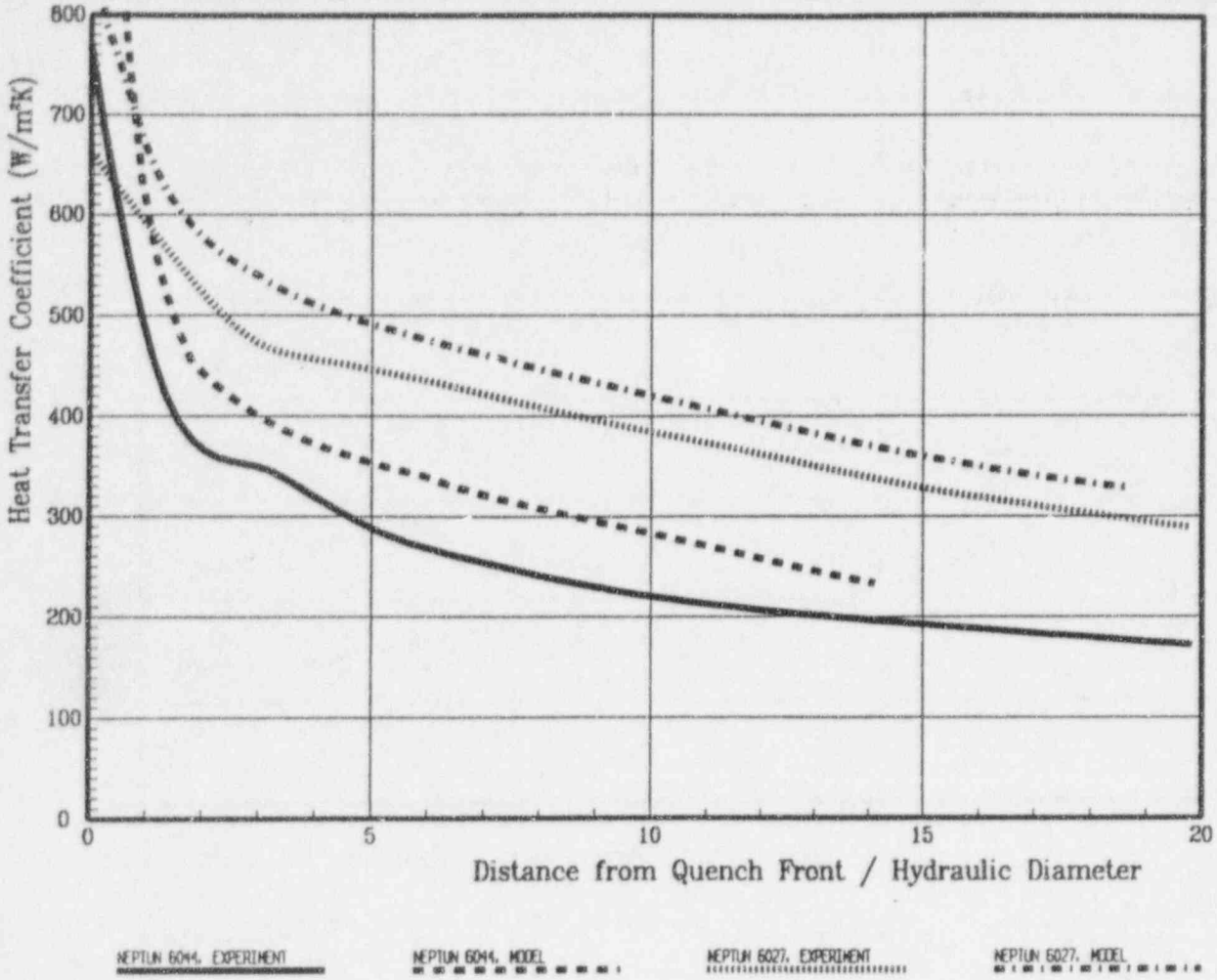

Figure 7: **Effect of flooding rate and pressure on IAFB heat transfer in a LWHCR bundle** (4.4 mm hydraulic diameter).
Comparison of experimental and predicted heat transfer coefficient distributions downstream from the quench front for NEPTUN reflooding experiment:
- **Run 6044: 10 cm/s flooding rate, 1.1 bar pressure**
0.8 cm/s quench front velocity, 374 °C wall temperature just above quench front, 585 °C at 30 cm
- **Run 6027: 16 cm/s flooding rate, 4.4 bar pressure**
1.3 cm/s quench front velocity, 438 °C wall temperature just above quench front, 637 °C at 30 cm
(48 cm quench front elevation, about 12 °C subcooling just above quench front in both cases).
Note. Calculations stopped at 60 % void fraction.

The model is implemented in the way described in section 1.4. The input data, i.e., the quench front velocity, the initial flow parameters just downstream from the quench front, and the wall temperature distribution in the dry region, have been carefully derived from the measurements [4]. The computational results are displayed as values of the heat transfer coefficient plotted against the distance from the quench front. In the cases where void fraction measurements are available, the predicted axial void fraction profiles are also plotted. The calculations are arbitrarily stopped when a void fraction of 50 % is reached. Indeed, it is unlikely that IAFB could persist beyond this value.

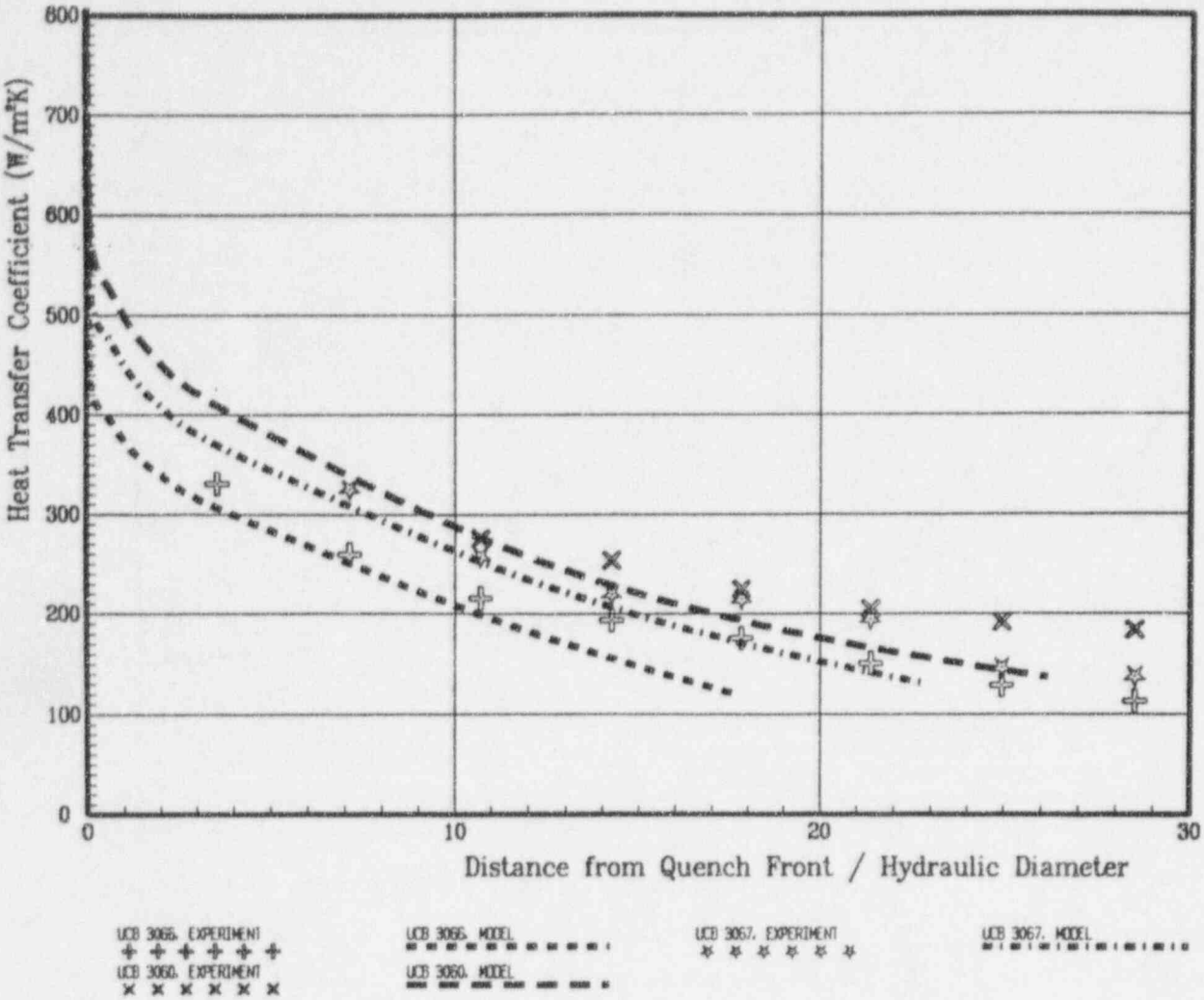

Figure 8: **Effect of pressure on IAFB heat transfer in a tube** (14 mm inside diameter).
Comparison of experimental and predicted heat transfer coefficient distributions downstream from the quench front for UC-Berkeley reflooding experiment:
- **Run 3066: 1.1 bar pressure**
424 °C wall temperature just above quench front, 576 °C at 30 cm
- **Run 3067: 2.1 bar pressure**
417 °C wall temperature just above quench front, 538 °C at 30 cm
- **Run 3060: 3.1 bar pressure**
411 °C wall temperature just above quench front, 516 °C at 30 cm
(13 cm/s flooding rate, 122 cm quench front elevation, 3.0 cm/s quench front velocity and about 11 °C subcooling just above quench front in all cases).
Note. Calculations stopped at 60 % void fraction.

2.2.1 Importance of the initial conditions

Lacking any experimental information, no vapour flow rate at the quench front is assumed as an initial condition. Anyway, the model is, to a certain extent, insensitive to the initial vapour flow rate: this was shown by computational tests performed assuming that half the heat release at the quench front served to vaporize some liquid. For these tests, an initial vapour temperature had to be specified for the model. Any realistic value (between the saturation temperature and the wall temperature) could in fact be used, without significantly affecting the results. An initial film thickness (or an initial vapour velocity) had also to be specified; this influence was also investigated using plausible values of the film

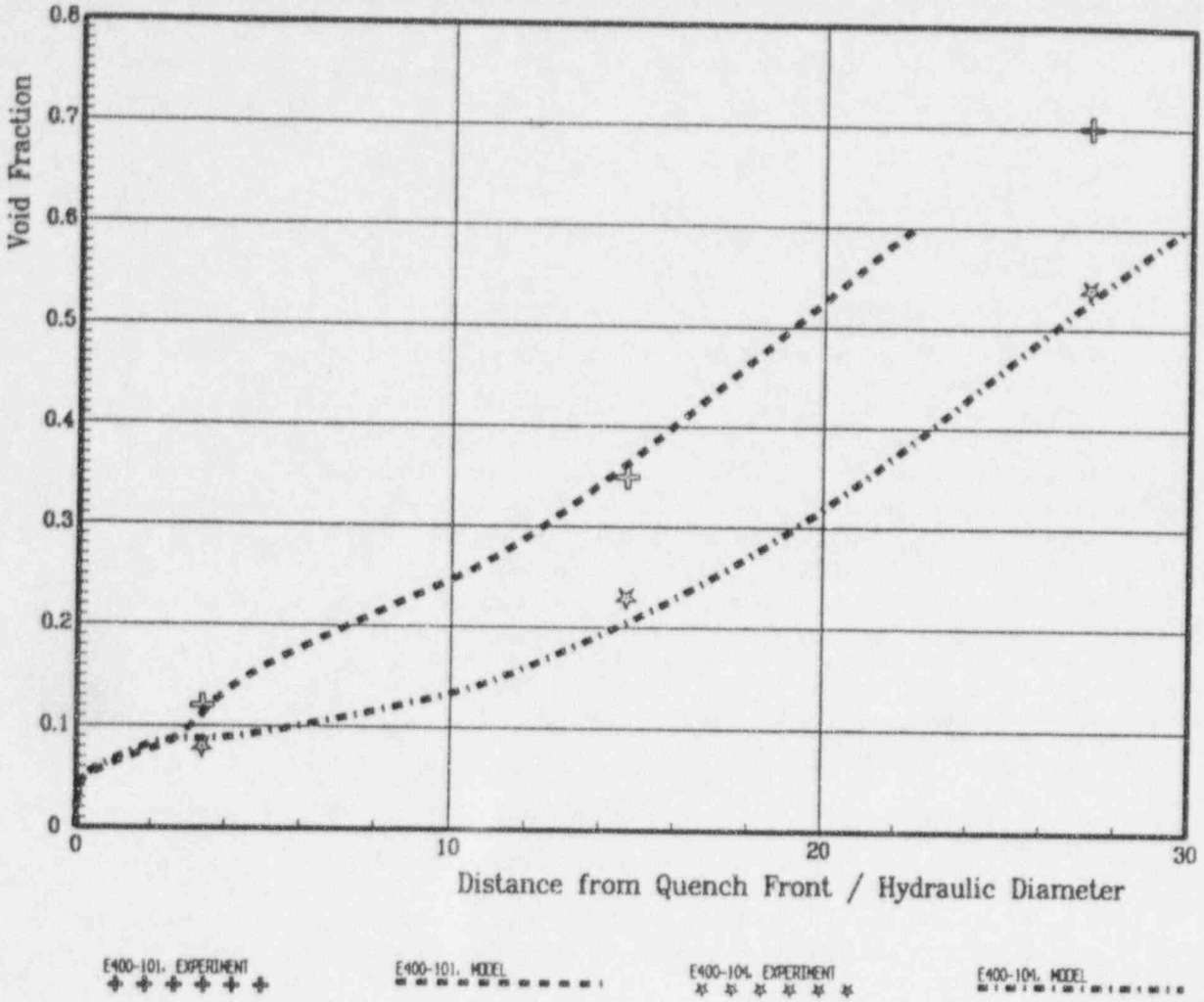

Figure 9: **Effect of wall temperature on IAFB void fraction in a tube** (12 mm inside diameter). Comparison of experimental and predicted void fraction distributions downstream from the quench front for University of Ottawa steady-state experiment:
- **Run E400-101: 579 °C wall temperature just above quench front, 988 °C at 30 cm**
- **Run E400-104: 574 °C wall temperature just above quench front, 810 °C at 30 cm**
(1.2 bar pressure, 41 cm/s flooding rate and about 13 °C subcooling just above quench front in both cases).
Note. Calculations stopped at 60 % void fraction.

thickness. In any case, beyond 1 mm from the quench front, the results were not significantly different from those obtained without initial vapour flow.

2.2.2 Results

46 experiments have been analysed. They correspond to very different geometries, i.e. tubes and rod bundles with hydraulic diameters ranging from 4 to 14 mm (section 2.1) and to large parameter ranges, i.e. 3 to 50 cm/s in flooding rate, 0 to 30 °C in subcooling, 1 to 4 bar in pressure, and 300 to 1000 °C in wall temperature. The experimental parameters and the computational results have been exhaustively displayed in [4].

The original model predictions are inadequate in many cases [4]. Fung's (University of Ottawa) experimental results have been used for the development of the new closure laws. The new model has been

assessed against the rest of the data bank, i.e., ten NEPTUN files (standard pressurized water reactor and light water high converter reactor rod bundle reflooding) and seven University of California-Berkeley files (tube reflooding). For these data, the overall predictions of the model are good. The root mean square (r.m.s.) error on the heat transfer coefficient, defined as

$$\text{r.m.s. error} = [\frac{1}{N-1}\sum_{1}^{N}(\frac{h_{\text{predicted}} - h_{\text{exp.}}}{h_{\text{exp.}}})^2]^{1/2}, \tag{102}$$

for the experimental points (all elevations) where the predicted void fraction was less than 60 %, was calculated to be 13%.

The main experimental trends, i.e. the favourable effects of system pressure, flooding rate and water subcooling just downstream from the quench front on heat transfer, are well described by the model. These main trends are illustrated by figures 6 to 9.

For standard PWR bundle reflooding, the effect of the flooding rate and of the water subcooling at the quench front may be seen in figure 6. The combined increases of water subcooling and flooding rate for Run 5150 in comparison to run 5025 result in increased heat transfer, in agreement with the experimental observations. The combined effects of flooding rate and system pressure are shown for the LWHCR bundle data in figure 7. Again the calculated trends agree with the experimental ones. The effect of system pressure alone is shown in figure 8 for tube reflooding data. The heat transfer coefficient increases with pressure; again the model predicts the experimental trend well.

The model also satisfactorily predicts some less obvious trends of the experimental data. For example, figure 9 illustrates the influence of the local wall temperature on the void fraction. A higher wall temperature leads to a significantly higher void fraction.

2.3 Conclusions

A six equation model was supplemented with closure laws specific to the IAFB regime. Closure laws applicable to tube and various bundle geometries were proposed; thus, all cases can be calculated with the same basic model.

The key point of the model proposed is the formulation of the heat and momentum transfers between the vapour-liquid interface and the liquid bulk, based on the liquid velocity relative to the interface. Indeed, the heat transfer rate in IAFB is strongly influenced by the heat transfer within the liquid core, which in turn is strongly coupled with the vapour film hydrodynamics. The formulation proposed in section 1.3.2 appears to be the only way to account for this coupling. Such a formulation does not seem to have been previously applied to IAFB.

The classical single-phase fluid dynamics and heat transfer laws have proven to be insufficient for describing IAFB. The interactions between the two phases, and, in particular, the irregular nature of the interface, have to be accounted for. As attempting a fully analytical description would have led to very complex developments, the use of, at least partially, empirical closure laws was required. In the previous models, some correlations were used that had been derived for other situations than IAFB, and whose applicability to IAFB was questionable. In the model proposed, some new correlations have been developed, based this time on measurements performed in IAFB. These new closure laws may be used outside the frame of the present model and thus have an intrinsic value.

Such specific closure laws are essential for accurate predictions of the heat fluxes or wall temperatures during IAFB. Indeed, the models actually implemented in the computer codes used for safety analysis can be shown to produce inadequate predictions [2].

Forced flow, subcooled film boiling experimental results from three different sources have been processed and analysed. The IAFB model has been successfully assessed against 46 experiments corresponding to very different geometries and parameter ranges (section 2.2, [4]). Although further assessment would be useful, particularly against void fraction data, this model seems now to represent an efficient analysis tool.

It seems useful to try and apply the results of the IAFB analysis to the safety codes in order to improve their description of post dryout, low-quality heat transfer .

Nomenclature

A	cross sectional flow area $[m^2]$
$c_1 ... c_6$	constants (eqs. 27, 36, 51) [–]
c_p	specific heat at constant pressure $[J/(kg\,K)]$
D_h	hydraulic diameter $[m]$
D_{hl}	hydraulic diameter of the liquid column $[m]$
f	friction factor [–]
g	gravitational constant $[m/(s^2)]$
h	specific enhalpy, heat transfer coefficient $[J/kg]$, $[W/m^2\,K]$
h_l	liquid-interface heat transfer coefficient (eq. 59) $[W/m^2\,K]$
h_{vap}	latent heat of vaporization $[J/kg]$
k	thermal conductivity $[W/(m\,K)]$
M	mass flowrate per unit height $[kg/(s\,m)]$
Nu_l	liquid core Nusselt number (eq. 60) [–]
Nu_v	vapour film Nusselt number (eq. 31, 32) [–]
P	perimeter $[m]$
p	pressure $[Pa]$
p'	rod bundle pitch $[m]$
Pr	Prandtl number [–]
Q	heat transfer rate per unit height $[W/m]$
q	heat flux $[W/m^2]$
Q_h	sensible heating rate (per unit height) (eqs. 5, 6) $[W/m]$
Q_r	radiation heat transfer rate (per unit height) $[W/m]$
Q_{vap}	vaporization heat rate (per unit height, eq. 17) $[W/m]$
R	tube (internal), rod (external) radius $[m]$
Re	Reynolds number [–]
T	temperature $[K]$
T_v^v	vapour temperature in the wall sublayer (eqs. 33, 34) $[K]$
U	velocity in a frame of reference moving with the quench front $[m/s]$
V	velocity in a fixed frame $[m/s]$
z	height $[m]$

Greek letters

α	area fraction [–]
δ	vapour film thickness $[m]$
δ^*	non-dimensional film thickness (eq. 30) [–]
δ'	wall sublayer thickness (eqs. 71, 72) $[m]$
ϵ	emissivity [–]
Θ	influence coefficient (eqs. 31, 32) [–]
λ_{fv}	enhancement factor (vapour-interface momentum transfer, eq. 25) [–]
λ_{hv}	enhancement factor (vapour film heat transfer, eqs. 33, 34) [–]
λ_l	enhancement factor (interface-liquid transfers, eqs. 49, 50) [–]
μ	viscosity $[Pa\,s]$
ρ	density $[kg/m^3]$
σ	Stefan-Boltzman constant $[W/(m^2\,K^4)]$
τ	shear stress $[Pa]$

Subscripts

i	interface
l	liquid
qf	quench front
s	saturation
v	vapour
w	wall

Additional nomenclature is defined locally in the text.

Acknowledgments

Many thanks are adressed to Prof. G. Yadigaroglu, who initiated, stimulated and reviewed this work.

References

[1] S.N. Aksan, G. Varadi and S. Güntay, "Properties of some materials for use in the analysis of light water reactor fuel rods and their simulators (e.g. LOFT, NEPTUN)," Swiss Federal Institute for Reactor Research (EIR) Report, TM-IN-816 (1979).

[2] G. Th. Analytis, "Implementation and assessment of an inverted annular flow model in RELAP5/MOD2," *ICAP Meeting, Madrid, Spain* (1990).

[3] G. Th. Analytis and G. Yadigaroglu, "Analytical modeling of inverted-annular film-boiling," *Nucl. Engrg. Des. 99*, 201-212 (1987).

[4] F. de Cachard, "Development, implementation and assessment of specific closure laws for inverted-annular film-boiling in a two-fluid model," Paul Scherrer Institute (PSI) Report 94-16 (1994).

[5] K.C. Chan and G. Yadigaroglu, "Calculations of film boiling heat transfer above the quench front during reflooding, exp. and anal. modeling of LWR safety experiments," *Proc. 19 th Nat. Heat Transfer Conf., Orlando, Florida*, 7, 65-72 (1980).

[6] G. Costigan and C. D. Wade, "Visualisation of the reflooding of a vertical tube by dynamic neutron radiography," *Proc. Int. Workshop on Post-Dryout Heat Transfer, Salt Lake City, Utah* (1984).

[7] G. De Jarlais and M. Ishii, "Inverted annular flow experimental study," Technical Report NUREG/CR-4277 (1985).

[8] M. K. Denham, "Inverted annular film boiling and the Bromley model," AEE-Winfrith Report 1590 (1983).

[9] J. Dreier, R. Chawla, N. Rouge and S. Yanar, "The NEPTUN experiments on LOCA thermal-hydraulics for tight-lattice PWRs," *Proc. IAEA Technical Committee on Technical and Economic Aspects of High Converters, Nürnberg* (1990).

[10] Z. Edelman, E. Elias and D. Naot, "Optical illustration of liquid penetration to the vapour film in inverted annular film boiling," *Int. J. Heat Mass Transfer 26-11*, 1715-1717 (1983).

[11] E. Frei and F. Stierli, "NEPTUN: Information about the reflood-experiments 5012-5056," Swiss Federal Institute for Reactor Research (EIR) Report, TM 32-83-6 (1984).

[12] K. K. Fung, "Subcooled and low quality film boiling of water in vertical flow at atmospheric pressure," Ph. D. Thesis, University of Ottawa (1981).

[13] K. K. Fung and D.C. Groeneveld, "A physical model of subcooled and low quality film boiling of water in vertical flow at atmospheric pressure," *Proc. 7 th Int. Heat Transfer Conf.* (1981).

[14] H. Grütter, F. Stierli, S.N. Aksan and G. Varadi, "NEPTUN bundle reflooding experiments: test facility description," Swiss Federal Institute for Reactor Research (EIR) Report 386 (1980).

[15] S. Güntay, "INCON, a computer program for the calculation of non-linear inverse heat conduction problem in cylindrical geometry using integral heat flux method," Swiss Federal Institute for Reactor Research (EIR) Report, TM 32-80-8 (1980).

[16] H. S. Kao, C. D. Morgan, M. Crawford and J.B. Jones, "Stability analysis of film boiling on vertical surfaces as a two-phase flow problem," *AIChE 118*, 147-155 (1972).

[17] M. Kawaji, "Transient non-equilibrium two-phase flow: Reflooding of a vertical flow channel," Ph.D. Thesis, UC-Berkeley (1984).

[18] M. Kawaji, Y.S. Ng, S. Banerjee and G. Yadigaroglu, "Reflooding with steady and oscillatory injection: Part1-Flow regimes, void fraction, and heat transfer," *Trans. ASME 670*, 107-121 (1985).

[19] W. M. Kays, Convective heat and mass transfer, McGraw-Hill (1980).

[20] N. Lee , S. Wong and L.E. Hochreiter, "Heat transfer mechanism during rod bundle reflooding in transient two-phase flow," *Proc. third CSNI Specialist Meeting*, Hemisphere Publishing Corporation, 243-260 (1983).

[21] M. Rashidi, G. Hetsroni and S. Banerjee, "Mechanisms of heat and mass transport at gas-liquid interfaces," *Int. J. Heat Mass Transfer 34-7*, 1799-1810 (1991).

[22] W.M. Rohsenow and J.P. Hartnett, Handbook of Heat Transfer, McGraw-Hill (1973).

[23] N. Rouge, J. Dreier, S. Yanar and R. Chawla, "Experimental comparisons for bottom reflooding in tight LWHCR and standard LWR geometries," *Nucl. Engrg. Des. 137*, 35-47 (1992).

[24] C. Schraeder, "Optimization of closure laws for the modeling of inverted-annular film-boiling," Diplomarbeit, Institut für Raumflug- und Reaktortechnik, Technische Universität Braunschweig (1992).

[25] R. A. Seban, "Reflooding of a vertical tube at 1, 2 and 3 atmospheres," EPRI Report, EPRI NP-3191 (1983).

[26] R. Seban, R. Grief, G. Yadigaroglu, E. Elias, K. Yu, D. Abdollahian and W. Peake, "UC-B reflood program: Experimental data report," EPRI Report, EPRI NP-743 (1978).

[27] T. Shigechi and Y. Lee, "An analysis on fully developed laminar fluid flow and heat transfer in concentric annuli with moving cores," *Int. J. Heat Mass Transfer 34-10*, 2593-2601 (1991).

[28] F. Stierli and S. Yanar, "Flutversuche NEPTUN 2: Übersicht, Unterlagen," Eidg. Institut für Reaktorforschung interner Bericht, TM-32-85-30 (1985).

[29] N. V. Suryanarayana and H. Merte, "Film boiling on vertical surfaces," *Trans. ASME* 377-384 (1972).

[30] N. Takenaka, T. Fujii, K. Akagawa and K. Nishida, "Flow pattern transition and heat transfer of inverted annular flow," *Int. J. Multiphase Flow 15*, 767-785 (1989).

[31] N. E. Todreas and M. S. Kazimi, Nuclear Systems, Hemisphere (1989).

[32] G. B. Wallis, "Annular two-phase flow, Part 1: A simple theory, Part 2: Additional effects," *J. of Basic Engrg. 59*, 59-72 (1970).

[33] G. B. Wallis, "Annular two-phase flow," *Trans. ASME 92*, D1 (1970).

[34] K.P. Yu, "An experimental investigation of the reflooding of a bare tubular test section," Ph.D. Thesis, UC-Berkeley (1987).

Analytical solution of laminar-laminar stratified two-phase flows with curved interfaces

Neima Brauner, Jakov Rovinsky and David Moalem Maron
Dept. of Fluid Mechanics & Heat Transfer
School of Engineering
Tel-Aviv University
Tel Aviv, 69978, Israel

Abstract

The present study represents a complete analytical solution for laminar two-phase flows with curved interfaces.

The solution of the Navier-Stokes equations for the two-phases in bipolar coordinates provides the 'flow monograms'. The 'flow monograms' describe the relation between the interface curvature and the insitu flow geometry when given the phases flow rates and viscosity ratios. Energy considerations are employed to construct the 'interface monograms', whereby the characteristic interfacial curvature is determined in terms of the phases insitu holdup, pipe diameter, surface tension, fluids/wall adhesion and gravitation. The two monograms are then combined to construct the system 'operational monogram'.

The 'operational monogram' enables the determination of the interface configuration, the local flow characteristics, such as velocity profiles, wall and interfacial shear stresses distribution as well as the integral characteristics of the two-phase flow: phases insitu holdup and pressure drop.

A. Introduction

Stratified two-phase flow has been the focus of a large volume of studies [1-8]. The stratified configuration represents a basic two-phase flow, thereby further insight into the other two-phase flow patterns is gained via stability analyses or mechanistic models, which are carried out based on a presumed stratified pattern and a corresponding model [1, 6, 9-11].

In a very general manner, most of the previous studies of stratified flow in pipes resorted to two-fluid models with a plane interface between the phases [1, 6, 7]. In a very recent work, the authors presented an attempt to relax these two basic simplifying features of modeling, whereby *analytical* solutions with plane or *lunar interfaces* have been considered. A general solution has been obtained with the interface curvature as an input parameter [12]. In a second phase of this study, an analytical tool for deriving the interface curvature has been proposed [13].

In general, when surface effects are significant, the interface configuration tends to attain a convex or concave configuration, depending on the relative wettability properties of the two fluids with the wall surface. On the other hand, when gravity is dominant, the interface approaches a plane configuration. Global energy considerations have been employed in order to tackle the problem of determining the interface configuration [13].

The consideration of interface curvature is usually related to capillary and small scale systems, where effects of surface tension become comparable with gravity. In large scale systems, however, the natural trend is to neglect surface phenomena. This is justified in high density differential systems, like gas-liquid systems under earth conditions. In high pressure vapor-liquid systems (approaching the critical point) or in liquid-liquid systems with small density difference, and in two-phase systems under reduced gravity conditions (even with high density difference), surface phenomena may dominate, resulting in a curved interface between the two stratified layers. In nuclear power plants, such occurrences may be encountered during transients, at states near the steam critical point or when two-streams of different temperatures come in contact (thermal stratification [14]). This curved interface may significantly affect the two-phase flow characteristics and associated transport phenomena. Previous studies on general two-fluid systems point out the need to account for the interfacial curvature in solving for the two-phase

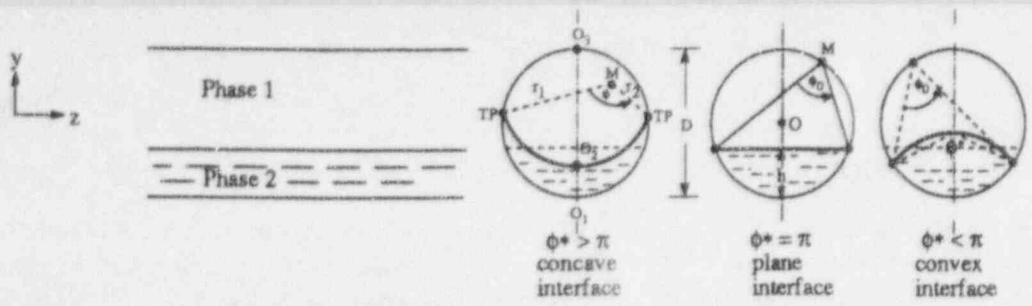

Figure 1a Physical domain (x,y,z) ; curved or plane interface.

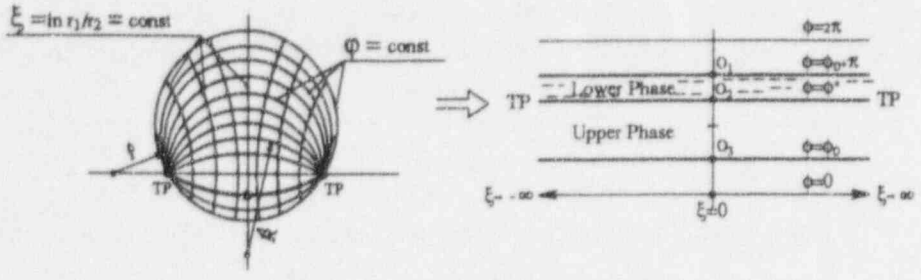

Figure 1b Bipolar coordinate system (ϕ,ξ)

Figure 1: Schematic description of the physical model and coordinate systems.

pressure-drop, insitu holdup and stability of the free interface [11, 15-17]. For instance, when the viscosity ratio is high, the interface curvature and its influence on the wetted areas may be of crucial effect on the flow pressure drop [18]. In thermal stratification, the evolution of thermal shear stresses in the piping lines and piping support structures are obviously dependent on the contact areas of the hot and cold phases with the pipe wall. As such, the consideration of the free interface configuration in gas-liquid and liquid-liquid systems is of importance in a variety of equipment and processes.

In order to initiate a solution of stratified flow with curved interfaces, an analytical tool for prescription of the interface curvature is required. Therefore, the present study proceeds first in deriving the characteristic interface curvature in terms of the system parameters. This solut is incorporated with the flow problem of two stratified layers, aiming at establishing the complete operational flow characteristics of stratified flow with curved interfaces for a variety of two-phase flow systems.

B. The physical model

Figure (1) describes a cross-section of fully-developed stratified flow in a circular tube of radius R with possible lunar (convex and concave) interface between the two fluids.

The bipolar coordinates (ϕ,ξ) are defined in Figure (1), where ϕ represents the view angle of the interface from an arbitrary point M in the flow field, while ξ relates to the ratio of the radius vectors r_1, r_2 ($\xi = \ell n(r_1/r_2)$, ϕ is counted in the same direction in both phases, from r_1 to r_2). The pipe perimeter and the interface between the fluids are isolines of coordinate ϕ, so that the upper section of the tube wall, which bounds the lighter phase is represented by ϕ_0, while the bottom of the tube, which bounds the denser phase, is represented by $\phi = \phi_0 + \pi$. The interface is defined by $\phi = \phi^*$ (convex interface for $\phi^* < \pi$ and concave interface for $\phi^* > \pi$). In particular, $\phi^* = \pi$ corresponds to the case of plane interface with a lower layer thickness $h/R = 1 - \cos\phi_0$. Hence, the two-phase domains are defined by:

$$\begin{aligned} \text{Upper phase}: \quad & -\infty < \xi < \infty \\ & \phi_0 < \phi < \phi^* \\ \text{Lower phase}: \quad & -\infty < \xi < \infty \\ & \phi^* < \phi < \phi_0 + \pi \end{aligned}$$

Thus, it is clear that in order to define the flow geometry and proceed in solving the flow problem, the interface curvature, ϕ^*, ought to be prescribed.

B.1. Prediction of interface configurations by energy considerations

In general, when surface effects are significant, the interface configuration attains a convex or concave configuration depending on the relative wettability properties of two fluids with the wall surface. On the other hand, when gravity is dominant (large density difference) the interface approaches a plane configuration (as in gas-liquid earth systems).

Utilizing an integral force balance for determining the meniscus elevation (as usually done in vertical capillary systems) is complicated for the system under consideration. It has been shown in Rovinsky et al [13] that the principle of minimal system energy (potential and surface energies), when applied to vertical capillary systems, yields the steady interface curvature identical to that obtained via force balance. Accordingly, the steady interface configuration in a horizontal conduit can be derived based on energy considerations as it corresponds to the minimum of the total system energy.

For the horizontal configuration under consideration, the potential and surface energies are [13]:

$$\frac{1}{L}\Delta E_p = \frac{1}{L} g\,(A_1\rho_1 + A_2\rho_2)\,(YG^*_{12} - YG^P_{12}) \qquad [1]$$

$$\Delta E_s = (\Delta E_s)_{1\omega} + (\Delta E_s)_{2\omega} + (\Delta E_s)_{12} = \sigma_{1\omega}\,\Delta S_{1\omega} + \sigma_{2\omega}\,\Delta S_{2\omega} + \sigma_{12}\,\Delta S_{12} \qquad [2]$$

$$(\sigma_{1\omega} - \sigma_{2\omega}) = \sigma_{12}\cos\alpha \;\; ; \quad \text{Young's relation} \qquad [3]$$

where, the variations of the potential and surface energy terms are calculated with respect to plane stratified interface (taken as a reference configuration). In equation [1], YG^P_{12}, YG^*_{12} denotes the centers of gravity of the two-phases with plane and curved interface, respectively.

Equation [2] represents the changes in surface energies involved due to variations of the corresponding contact areas of each phase with the solid wall $\Delta S_{1\omega}, \Delta S_{2\omega}$ and between themselves, ΔS_{12}, as the interface switches to its natural curved configuration (from the reference plane configuration). Accordingly, σ_{12} is the surface tension between the phases and $\sigma_{1\omega}, \sigma_{2\omega}$ are the surface tension coefficients between the two-phases and the solid wall, and these are related by Young's relation, eq. [3].

Utilizing YG^P_{12}, YG^*_{12} and the various geometrical wetting areas (as detailed in [13]), yields the expression for the change in the total system energy associated with the process of curving the interface from its otherwise plane shape;

$$\frac{\Delta E}{L} = \frac{1}{L}(\Delta E_p + \Delta E_s)\;; \quad \Delta\tilde{E} = \Delta E/[R^3(\rho_2 - \rho_1)g] \qquad [4]$$

$$\begin{aligned}\frac{\Delta\tilde{E}}{L} \;=\; & \left\{\left[\tfrac{\sin^3\phi_0}{\sin^2\phi^*}(ctg\phi^* - ctg\phi_0)(\pi - \phi^* + \sin(2\phi^*)/2) + \right.\right. \\ & \left.\left. + \tfrac{2}{3}\sin^3\phi_0^P\right] + \in_v \left[\sin\phi_0 \tfrac{\phi^* - \pi}{\sin\phi^*} - \sin\phi_0^P + \cos\alpha(\phi_0^P - \phi_0)\right]\right\}\end{aligned} \qquad [5]$$

where $\in_v$ is the Evöts number defined by:

$$\in_v = \frac{2\sigma_{12}}{(\rho_2 - \rho_1)g\,R^2} \qquad [6]$$

As shown in Figure (1), ϕ_0 is the view angle of the interface from the wall and it determines the distribution of the two-phases over the tube wall for a curved interface (at curvature ϕ^*), while ϕ_0^P corresponds to the phases distribution angle associated with a plane interface ($\phi^* = \pi$). For plane interface, the relation between the phases distribution angle (as represented by ϕ_0^P) and the phases holdup ratio is [13]:

$$a = \frac{A_1}{A_2} = \frac{\pi - \phi_0^P + \frac{1}{2}\sin(2\,\phi_0^P)}{\phi_0^P - \frac{1}{2}\sin(2\,\phi_0^P)} \;\; ; \;\; \phi^* = \pi \qquad [7]$$

whereas, for $\phi^* \neq \pi$ the phases holdup ratio, the phases distribution angle and the interface curvature are related by:

$$a = \frac{A_1}{A_2} = \frac{\pi - \phi_0 + \frac{1}{2}\sin(2\,\phi_0) - \left(\frac{\sin\phi_0}{\sin\phi^*}\right)^2[\pi - \phi^* + \frac{1}{2}\sin(2\,\phi^*)]}{\phi_0 - \frac{1}{2}\sin(2\,\phi_0) + \left(\frac{\sin\phi_0}{\sin\phi^*}\right)^2[\pi - \phi^* + \frac{1}{2}\sin(2\,\phi^*)]} \;\; ; \;\; \phi^* \neq \pi \qquad [8]$$

Hence, given the phases insitu holdup (specified $a = A_1/A_2$), the reference state of plane interface, ϕ_0^r, is determined by eq. [7]. When these phases form a curved interface with a specified curvature, ϕ^*, the corresponding ϕ_0 is determined by eq. [8]. Equation [5] then yields the change in the total system energy associated with curving the interface in terms of the interface curvature, $\Delta E(\phi^*)$. The ultimate interface configuration is obtained at a particular curvature, ϕ_m^*, for which the system total energy is at its minimum. Thus, by minimizing eq. [5], the steady interface curvature is predicted for a variety of two-fluid systems, of given density difference, surface tension, gravity conditions and tube diameter, which all are embodied in the single nondimensional Evöts number, ϵ_v, and in terms of the relative wettability of the phases with the tube wall, as represented by $\cos\alpha$.

In a recent study, the authors have explored in detail the particular behavior of the variations in the potential energy and surface energies associated with changing the phases interface curvature. Here, however, comprehensive monograms of the steady optimal interface curvature as function of phases distribution angle ϕ_0 and the phases relative wettability for various Evöts numbers are outlined in Figures (2) and (3).

It is worth noting again that solutions for $\phi^*(\phi_0)$ are bounded in the range of $\phi_0 \leq \phi^* \leq \phi_0 + \pi$ (see Figure 1). Thus, for $\phi_0 \to 0$, the maximal interface curvature is bounded by π while for $\phi_0 \to \pi$, the minimal curvature is π and its maximal value is 2π. These bounds are illustrated by the dashed lines in Figures (2) and (3), which define the envelope for the solutions to be obtained for ϕ_m^*.

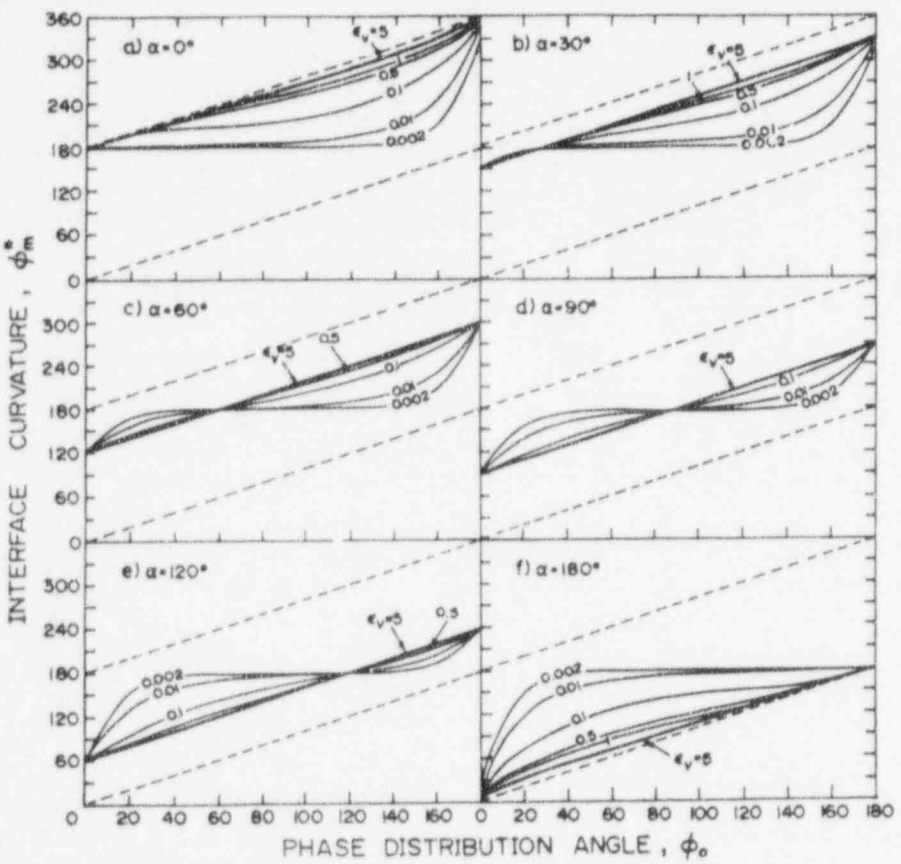

Figure 2: Interface monograms: effect of Evöts numbers for two-phase systems with various wettability angles.

In order to follow Figures (2,3), it is important to note that the Evöts number represents the ratio between the interfacial forces and gravity forces. As gravity forces dominate, $\epsilon_v \to 0$, the phases stabilize with a nearly plane interface, $\phi_m^* \to \pi$ over a wide range of ϕ_0 (except for thin layers of either the upper or lower phase, depending on the wettability angle, α). As the interfacial effects increase, a curved interface with either concave ($\phi_m^* > \pi$) or convex ($\phi_m^* < \pi$) configuration is obtained.

The other extreme of two-phase systems which are dominated by surface effects, $\epsilon_v \gg 1$ is given in Figure (2f). It is shown that for high Evöts number, the solution for the steady interface curvature

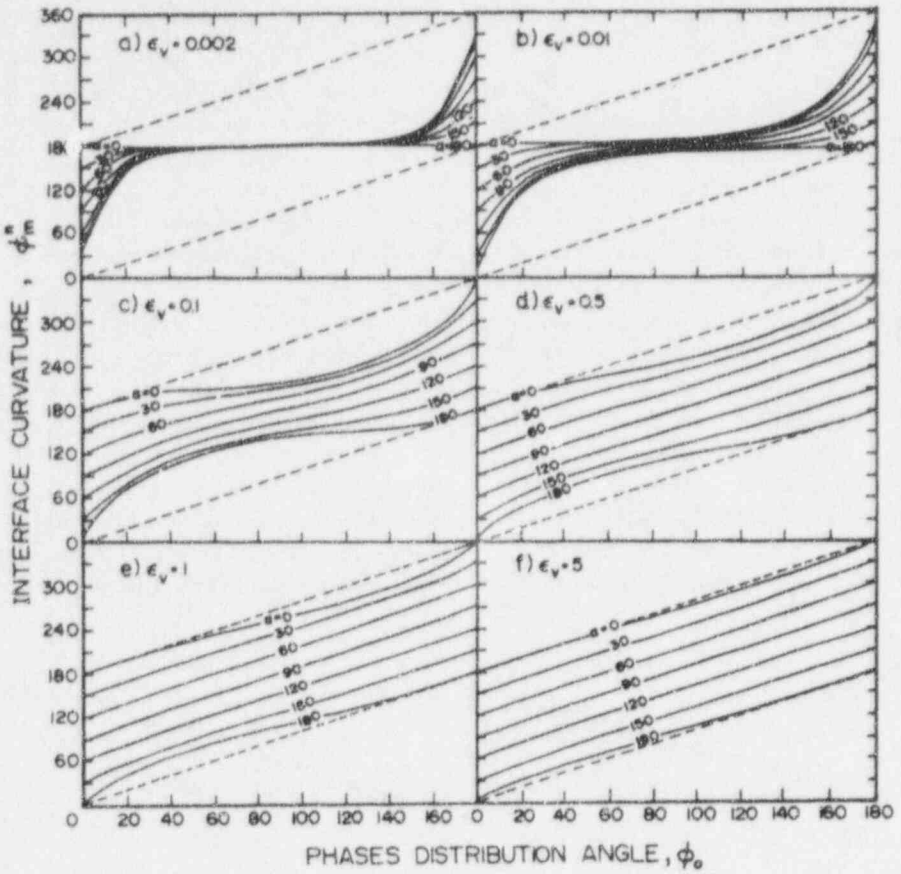

Figure 3: Interface monograms: effect of the wall/phase wettability for various Evöts numbers.

follows a straight line:

$$\phi_m^* = (180 - a) + \phi_0 \qquad [9]$$

Thus, when $\in_v \gg 1$ and $\alpha = 0$ (ideal wettability of the lower phase) the solution for ϕ_m^* coincides with the upper bound of the solution domain and for $\alpha = 180$ (ideal wettability of the upper phase) ϕ_m^* follows the lower bound of the solution domain.

Another point worth noting is the symmetrical properties of the solutions obtained for ϕ_m^*. This is demonstrated by comparing systems of identical $\in_v$ numbers in Figures (2) and (3). Given two systems A and B of identical $\in_v$ number, the interface curvature for system (B) with $\alpha > 90^\circ$ can be predicted from information obtained for systems (A) with $0 \leq \alpha \leq 90$, following the rule [13]:

$$\begin{array}{lll} \text{When} & (\in_v)_B & = \ (\in_v)_A \\ \text{and} & (\alpha)_B & = \ \pi - (\alpha)_A \end{array} \qquad [10.1]$$

Then for $(\phi_0)_B = \pi - (\phi_0)_A$ the interface curvature of system B is given by:

$$(\phi_m^*)_B = 2\pi - (\phi_m^*)_A \qquad [10.2]$$

The corresponding phases insitu holdup in systems A, B are also related whereby $(A_1/A_2)_B = (A_1/A_2)_A^{-1}$.

Figures (2) and (3) show that for ideal wettability of the lower phase ($\alpha = 0$), the interface is always concave. On the other hand, low wettability of the lower phase leads to convex interface. Recalling that each particular point of these monograms corresponds to a certain insitu holdup (A_1/A_2 as given in eq. [8] and Figure (4)), one may conclude that the shape of the interface (convex or concave) is independent of the insitu holdup for the extreme wettabilities ($\alpha \to \pi$ and $\alpha \to 0$). However, for a certain intermediate wettability (e.g. $\alpha = \pi/3$), a convex interface is predicted for relatively low ϕ_0 ($< 60^\circ$) whereas a concave interface is obtained for higher values of ϕ_0. Thus, the insitu holdup determines not only the extent of curvature but also whether a convex or a concave shape is obtained.

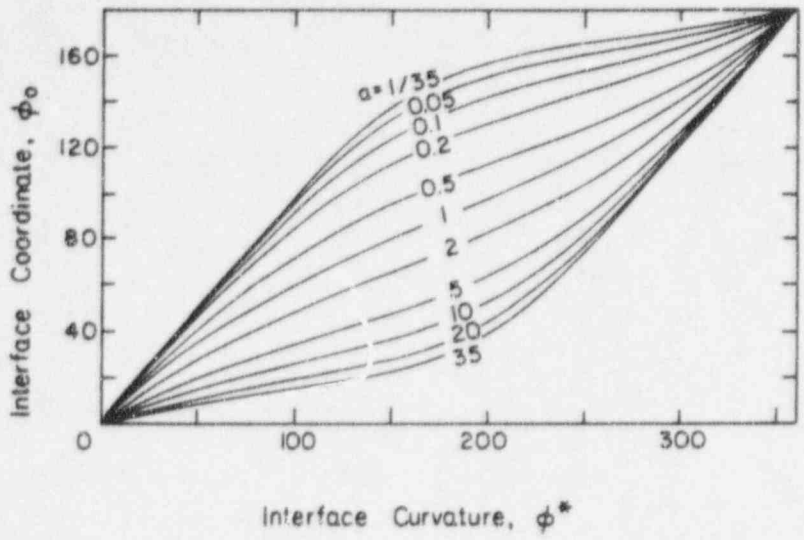

Figure 4: Insitu configurations: geometrical relation between interface curvature phases distribution angle and insitu holdup.

This will be further discussed below in the frame of the hydrodynamic problem, for which the interface curvature is required as a basic input. It is to be noted that combining Figures (2) or (3) with Figure (4) yields the *'interface monograms'* which relate the interfacial curvature with the phases insitu holdup.

B.2. The Flow Problem

Considering two-dimensional flow of the two phases in a circular conduit , the Navier-Stokes equations and boundary conditions in bipolar-coordinates are:

$$\frac{(\cosh\,\xi - \cos\,\phi)^2}{R^2\,\sin^2\,\phi_0}\left[\frac{\partial^2 V_1}{\partial\,\xi^2} + \frac{\partial^2 V_1}{\partial\,\phi^2}\right] = -\frac{1}{\mu_1}\,\frac{\partial\,p}{\partial\,z} \qquad [11.1]$$

$$\frac{(\cosh\,\xi - \cos\phi)^2}{R^2\,\sin^2\,\phi_0}\left[\frac{\partial^2 V_2}{\partial\,\xi^2} + \frac{\partial^2 V_2}{\partial\,\phi^2}\right] = -\frac{1}{\mu_2}\,\frac{\partial\,p}{\partial\,z} \qquad [11.2]$$

$$(V_1)_{\phi=\phi_0} = 0 \quad , \quad (V_2)_{\phi=\phi_0+\pi} = 0 \qquad [12.1]$$

$$(V_1)_{\xi=\pm\infty} = 0 \quad , \quad (V_2)_{\xi=\pm\infty} = 0 \qquad [12.2]$$

$$(V_1)_{\phi=\phi^*} = (V_2)_{\phi=\phi^*} \qquad [12.3]$$

$$\left(\mu_1\frac{\partial V_1}{\partial\phi}\right)_{\phi=\phi^*} = \left(\mu_2\frac{\partial V_2}{\partial\phi}\right)_{\phi=\phi^*} \qquad [12.4]$$

where V_1, V_2 are the phase velocities in the axial direction, μ_1, μ_2 are the dynamic viscosities of the fluids, and $\partial p/\partial z$ is the pressure gradient in the axial direction. Equations [12.1] to [12.2] represent the no-slip conditions at the tube wall and at the particular points where the interface intersects the wall ($\xi = \pm\infty$), while [12.3-12.4] stand for the continuity of velocities and shear stresses across the interface between the phases.

In a recent work [12], the authors presented and discussed in detail two routes for solving the mathematical system of equations [11] and [12]. One method is based on Fourier Series and the alternative one is via Fourier-Integrals. The later, however, has been found of an advantage as it provides the characteristics in the entire flow domain, including the two singular points where the interface intersects the tube wall (IP in Figure 1). In terms of Fourier-Integrals, the solution of the homogeneous Laplace equation (equations 11 with zero r.h.s) with the corresponding boundary conditions (as detailed in [12]) is:

$$V_{1h} = 2\gamma_1(1-\tilde{\mu})\frac{\sin(\phi^*-\phi_0)}{\sin(\phi^*)}\int_0^\infty H_{1v}(\omega)\cos(\omega\xi)d\omega \qquad [13.1]$$

$$V_{2h} = 2\tilde{\mu}\gamma_1(1-\tilde{\mu})\frac{\sin(\phi^*-\phi_0)}{\sin(\phi^*)}\int_0^\infty H_{2v}(\omega)\cos(\omega\xi)d\omega \qquad [13.2]$$

where:

$$H_{1v}(\omega) = \frac{\sinh[\omega(\phi^* - \pi)]}{\psi(\omega)\sinh(\pi\omega)} \; \frac{\sinh[\omega(\phi - \phi_0)]}{\cosh[\omega(\phi^* - \phi_0)]} \qquad [13.3]$$

$$H_{2v}(\omega) = \frac{\sinh[\omega(\phi^* - \pi)]}{\psi(\omega)\sinh(\pi\omega)} \; \frac{\sinh[\omega(\phi - \pi - \phi_0)]}{\cosh[\omega(\phi^* - \pi - \phi_0)]} \qquad [13.4]$$

and

$$\psi(\omega) = \tanh[\omega(\phi^* - \phi_0)] + \tilde{\mu}\tanh[\omega(\pi + \phi_0 - \phi^*)] \qquad [13.5]$$

This homogeneous solution is to be combined with a particular solution of the nonhomogeneous set of equations [11,12] which is:

$$V_{1p} = \gamma_1 \frac{\sin(\phi - \phi_0)}{\cosh\,\xi - \cos\,\phi} \; ; \quad \gamma_1 = \frac{R^2\,\sin\phi_0}{2\mu_1}\,\frac{\partial\,p}{\partial\,z} \qquad [14.1]$$

$$V_{2p} = \gamma_2 \frac{\sin(\phi - \phi_0)}{\cosh\,\xi - \cos\,\phi} \; ; \quad \gamma_2 = \frac{R^2\,\sin\phi_0}{2\mu_2}\,\frac{\partial\,p}{\partial\,z} = \tilde{\mu}\,\gamma_1 \; ; \quad \tilde{\mu} = \mu_1/\mu_2 \qquad [14.2]$$

Thus, the general solutions as obtained by combining equations [13] with [14] read:

$$\tilde{V}_1 = \frac{V_1}{V_R} = 2\sin\phi_0\{\frac{\sin(\phi - \phi_0)}{\cosh\,\xi - \cos\,\phi} + 2(1 - \tilde{\mu})\frac{\sin(\phi^* - \phi_0)}{\sin(\phi^*)}\int_0^\infty H_{1v}(\omega)\cos(\omega\xi)d\omega\} \qquad [15.1]$$

$$\tilde{V}_2 = \frac{V_2}{V_R} = 2\tilde{\mu}\sin\phi_0\{\frac{\sin(\phi - \phi_0)}{\cosh\,\xi - \cos\,\phi} + 2(1 - \tilde{\mu})\frac{\sin(\phi^* - \phi_0)}{\sin(\phi^*)}\int_0^\infty H_{2v}(\omega)\cos(\omega\xi)d\omega\} \qquad [15.2]$$

$$V_R = \frac{R^2}{4\mu_1}\,\frac{\partial\,p}{\partial\,z} \qquad [15.3]$$

Equations [15] provide the velocity profiles in the two-phases. The reference velocity, V_R, used for scaling the velocity profiles is the velocity at the pipe center in a single phase flow of the upper phase under a pressure drop identical to that obtained in the two-phase system.

The practical application of eqs. [15] involves integration over a finite frequency domain. For plane interface $\phi^* = \pi$, a cut-off frequency of $\omega_{max} > 10$ has been found to yield convergent results for all ϕ_0 and $\tilde{\mu}$ [12]. For curved interface, the cut-off frequency is of the same order of magnitude ($\omega_{max} = O(10)$), except when conditions of eccentric annular flow are approached, namely: $\phi_0 \to 0$, $\phi^* \to \phi_0 + \epsilon$ (eccentric core flow of the lower heavier phase) or $\phi_0 \to \pi$, $\phi^* \to 2\pi - \epsilon$ (eccentric core flow of the upper lighter phase). The cut-off frequencies for these two extremes and for plane interface configuration are evaluated in the Appendix.

Based on eqs. [15], the expression for the local shear stresses are derived. The general expression for the local shear stress over a surface defined by a normal $\hat{n}$, is;

$$\tau_n = \mu\frac{\partial\,V}{\partial\,n} = \mu\left(\frac{1}{H_\xi}\,\frac{\partial\,V}{\partial\,\xi}\cos\alpha_n + \frac{1}{H_\phi}\,\frac{\partial\,V}{\partial\,\phi}\sin\alpha_n\right) \qquad [16]$$

where, α_n denotes the direction of $\hat{n}$ with respect to the normal to isoline of ξ. Note that $H_\xi = H_\phi = H$, which is the Lamé coefficient for the bipolar transformation;

$$H = \left[\left(\frac{\partial x}{\partial\phi}\right)^2 + \left(\frac{\partial y}{\partial\phi}\right)^2\right]^{1/2} \qquad [17]$$

Of particular interest are the shear stresses along the upper tube wall, the lower tube wall and the interface between the phases, which are isolines of $\phi = \phi_0$, $\phi = \phi_0 + \pi$ and $\phi = \phi^*$, respectively. These are given by:

$$\begin{aligned}\tilde{\tau}_i = \frac{\tau_i}{\tau_R} = {} & \frac{\cos(\phi^* - \phi_0)\cosh\,\xi - \cos\phi_0}{\cosh\,\xi - \cos\,\phi^*} + \\ & 2(\tilde{\mu} - 1)\,\frac{\sin(\phi^* - \phi_0)}{\sin\phi^*}(\cosh\,\xi - \cos\,\phi^*)\int_0^\infty \omega\frac{\sinh[\omega(\phi^* - \pi)]}{\psi(\omega)\sinh(\pi\omega)}\cos(\omega\xi)\mathrm{d}\omega\end{aligned} \qquad [18.1]$$

$$\tilde{\tau}_{\omega 1} = \frac{\tau_{\omega 1}}{\tau_R} = 1 + 2(\tilde{\mu} - 1)\,\frac{\sin(\phi^* - \phi_0)}{\sin\phi^*}(\cosh\,\xi - \cos\,\phi_0)* \int_0^\infty \frac{\omega \sinh\,[\omega(\phi^* - \pi)]}{\psi(\omega)\sinh\,(\pi\omega)\cosh\,[\omega(\phi^* - \phi_0)]}\cos(\omega\xi)\mathrm{d}\omega \qquad [18.2]$$

$$\tilde{\tau}_{\omega 2} = \frac{\tau_{\omega 2}}{\tau_R} = -1 + 2(\tilde{\mu} - 1)\,\frac{\sin(\phi^* - \phi_0)}{\sin\phi^*}(\cosh\xi + \cos\phi_0)* \int_0^\infty \frac{\omega \sinh\,[\omega(\phi^* - \pi)]}{\psi(\omega)\sinh\,(\pi\omega)\cosh\,[\omega(\phi^* - \pi - \phi_0)]}\cos(\omega\xi)\mathrm{d}\omega \qquad [18.3]$$

$$\tau_R = \frac{R}{2}\,\frac{\partial p}{\partial z} \qquad [18.4]$$

The corresponding flow rates of the two fluids can be obtained by integrating the phase velocities, V_1, V_2, over the corresponding flows area, A_1, A_2 (defined in bipolar coordinate system):

$$Q_1 = \int_{A_1} V_1(\xi,\phi)J(\xi,\phi)d\xi d\phi = \frac{R^4\sin^3\phi_0}{2\mu_1}\,\frac{\partial p}{\partial z}\,F_1(\phi_0,\phi^*,\tilde{\mu}) \qquad [19.1]$$

$$Q_2 = \int_{A_2} V_2(\xi,\phi)J(\xi,\phi)d\xi d\phi = \frac{R^4\sin^3\phi_0}{2\mu_2}\,\frac{\partial p}{\partial z}\,F_2(\phi_0,\phi^*,\tilde{\mu}) \qquad [19.2]$$

$$J(\xi,\phi) = \frac{R^2\sin^2\phi_0}{(\cosh\,\xi - \cos\,\phi)^2} \qquad [19.3]$$

where, $J(\xi,\phi)$ is the transforming Jacobian from bipolar to Cartesian coordinates, and

$$F_1(\phi_0,\phi^*,\tilde{\mu}) = \int_{-\infty}^{\infty} d\xi \int_{\phi_0}^{\phi^*} \frac{1}{(\cosh\,\xi - \cos\,\phi)^2}\left\{\frac{\sin(\phi - \phi_0)}{\cosh\,\xi - \cos\,\phi} - 2(\tilde{\mu} - 1)\frac{\sin(\phi^* - \phi_0)}{\sin(\phi^*)}\int_0^\infty H_{1v}(\omega)\cos(\omega\xi)d\omega\right\}d\phi \qquad [19.4]$$

$$F_2(\phi_0,\phi^*,\tilde{\mu}) = \int_{-\infty}^{\infty} d\xi \int_{\phi^*}^{\pi+\phi_0} \frac{1}{(\cosh\,\xi - \cos\,\phi)^2}\left\{\frac{\sin(\phi - \phi_0)}{\cosh\,\xi - \cos\,\phi} - 2(\tilde{\mu} - 1)\frac{\sin(\phi^* - \phi_0)}{\sin(\phi^*)}\int_0^\infty H_{2v}(\omega)\cos(\omega\xi)d\omega\right\}d\phi \qquad [19.5]$$

Note that the ratio of the two fluid flow rates, is independent of the system pressure drop and is a function of ϕ_0, ϕ^* only. Thus, equations [19] can be rearranged to yield:

$$\frac{Q_1}{Q_2} = \tilde{Q}(\phi_0,\phi^*,\tilde{\mu}) \qquad [20]$$

The solution of equation [20] can be represented by monograms as in Figure (5). In view of Figure (5), knowing the flow rates ratio and given the interface curvature ϕ^*, the phases distribution angle ϕ_0, can be extracted , which together with ϕ^* determine the insitu holdup (see equation [8]). Clearly, for a given Q_1/Q_2 ratio, each point along the Q_1/Q_2 curve represents a possible combination of (ϕ^*, ϕ_0), corresponding to a certain interface curvature and insitu holdup combination.

Having obtained ϕ_0, the pressure drop can now be determined by either eq. [19.1] or eq. [19.2]. For instance, based on the upper phase plow rate;

$$\frac{\partial p}{\partial z} = \frac{2\mu_1 Q_1}{R^4\sin^3\phi_0 F_1(\phi_0,\phi^*,\tilde{\mu})} \qquad [21]$$

The corresponding nondimensional pressure drop (normalized with respect to the superficial pressure drop obtained for single-phase laminar flow of the upper fluid) reads:

$$\frac{\partial\tilde{p}}{\partial z} = \frac{\frac{\partial p}{\partial z}}{\left(\frac{\partial p}{\partial z}\right)_{1s}} = \frac{\pi}{4\sin^3\phi_0 F_1(\phi_0\,,\phi^*\,,\tilde{\mu})} = G(\phi_0\,,\phi^*\,,\tilde{\mu}) \qquad [22]$$

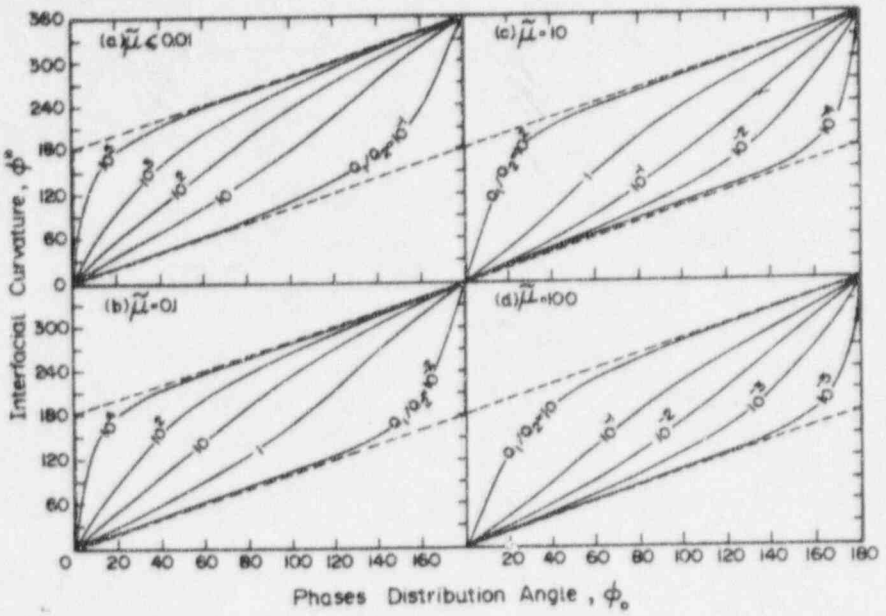

Figure 5: Flow monograms: effect of the phases flow rates ratio for two-phase systems with various viscosity ratios.

It is of particular interest to reevaluate – in view of the present exact model – some conclusions recently drawn from the analysis of averaged two-fluid models for stratified flow configuration with plane interfaces [7]. This analysis indicates that the insitu holdup is determined by two nondimensional parameters, the Lockhart-Martinelli parameter, χ^2, and the phases flow rate ratio, Q_1/Q_2. In the particular case of laminar-laminar flow, the Martinelli parameter becomes

$$\chi^2 = \frac{(\partial p/\partial z)_{2s}}{(\partial p/\partial z)_{1s}} = \left[\tilde{\mu}\frac{Q_1}{Q_2}\right]^{-1} \qquad [23]$$

The literature for gas-liquid systems, following the Lockhart & Martinelli approach, emphasizes the role of χ^2 as the sole parameter. Indeed, for horizontal gas-liquid flows, when the gas velocity is typically much greater than the liquid phase velocity, the two-fluid model equations reduce to a single parameter equation and the insitu holdup and pressure drop are determined by the Martinelli parameter. However, in general two-fluid systems, the velocities of the two-phases may be of comparable levels, and therefore the flow characteristics of the two-fluid system are dependent on the two parameters, χ^2 and Q_1/Q_2 (or the viscosity ratio and the flow rate ratio). Therefore, the flow monograms are rearranged in terms of $\tilde{\mu}\frac{Q_1}{Q_2}$ as in Figure (6), in which form the range of a single parameter solution shows up. In view of Figure (6), it is concluded that for the general case of two-fluid system of comparable viscosities, both parameters, $\tilde{\mu}$ and Q_1/Q_2 are required. However, in the extreme of $\tilde{\mu} > 100$ or $\tilde{\mu} < 0.01$ it can be observed that the flow monogram follows uniform curves of ϕ^* vs. ϕ_0 for each specified Martinelli parameter. Thus, Figure (5a) for $\tilde{\mu} = 0.01$ are valid practically for any $\tilde{\mu} \leq 0.01$ when curves of constant Q_1/Q_2 are considered in terms of the corresponding $\tilde{\mu}Q_1/Q_2$. Similarly, the results for $\tilde{\mu} \gg 1$ can be extracted from Figure (5d) for $\tilde{\mu} = 100$.

Another noteworthy point is the symmetry properties of the solutions to the hydrodynamic problem. Given two systems A and B for which

$$\begin{aligned} (\tilde{\mu})_A = (1/\tilde{\mu})_B \quad &; \quad (\phi_0)_A = (\pi - \phi_0)_B \\ \text{and} \qquad (Q_1/Q_2)_A \quad &= \quad (Q_2/Q_1)_B; \end{aligned} \qquad [24]$$

corresponds to:

$$\begin{aligned} \phi^*_A \quad &= \quad (2\pi - \phi^*)_B \\ (\partial\tilde{p}/\partial z)_A \quad &= \quad (\partial\tilde{p}/\partial z)_B \end{aligned} \qquad [25]$$

where the pressure drop in both systems is normalized with respect to the more viscous (or less viscous) phase.

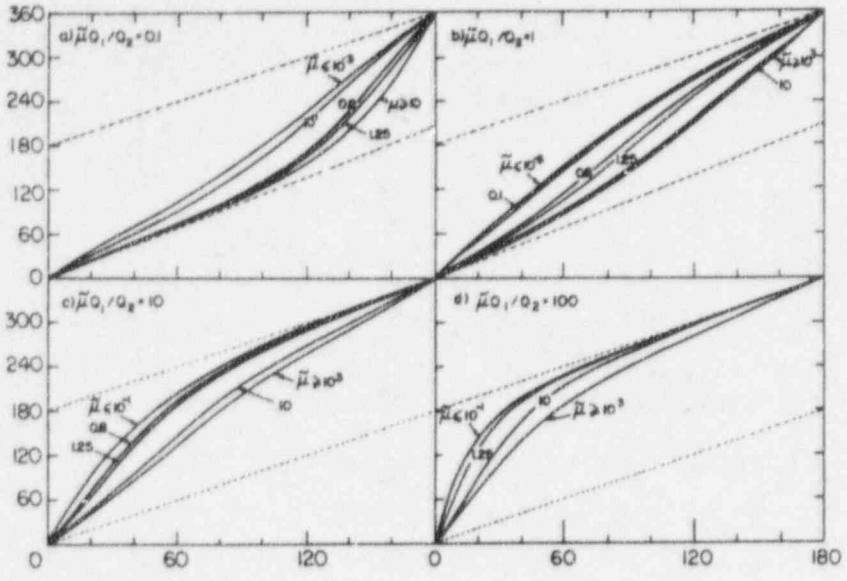

Figure 6: Unified flow monogram: effect of Martinelli parameter for systems of various viscosity ratios.

A comparison of Figure (6a) and (6c) shows that this symmetry is indeed met by the solutions. This symmetry can also be used to extend the results presented in Figure (6) to a wider range of $\tilde{\mu}Q_1/Q_2$. For instance, Figure (6d) for $\tilde{\mu}Q_1/Q_2 = 100$ with eqs. (24-25), can be used to produce the results for $\tilde{\mu}Q_1/Q_2 = 0.01$.

B.3. Combining the Energy Considerations with the Flow Problem

The prediction of the interface curvature, ϕ^*, ought to be an integral part of the complete stratified flow solution. Practically, the basic input for a stratified flow problem includes the two fluids properties and flow rates. Figures (2) and (5) represent independent relationships between the input parameters $(\tilde{\mu}, \alpha, \in_v, Q_1/Q_2)$ and the resulting insitu flow configuration (interface curvature, ϕ^* and phases distribution angle, ϕ_0). Based on the solution output ϕ^*, ϕ_0 all the rest of the flow characteristics can be obtained (insitu holdup, pressure drop, velocity profiles, shear stress, etc.)

Thus, having obtained the *'interface monogram'* as evolves from energy considerations (Figure 2), and independently the *'flow monogram'* via the hydrodynamic model (Figure 5), an *'operational monogram'* is now proposed, as demonstrated in Figure (7) for a particular set of $(\tilde{\mu}, \alpha, \in_v)$. The intersection between the 'interface' and 'flow' monograms represent all stratified flows solutions with curved interfaces obtained for varying Q_1/Q_2 ratios.

Figure (7) implies, that for a given physical system $(\tilde{\mu}, \alpha, \in_v)$ and operational condition Q_1/Q_2, there exists a single solution (ϕ^*, ϕ_0), which determines the resulting flow characteristics (o points). It is of interest to compare the corresponding solution obtained for plane interface (π, ϕ_0^P), denoted by $\times$ points. Figure (7) demonstrates that for $\alpha = 0$, the discrepancy between (ϕ^*, ϕ_0) and (π, ϕ_0^P) is fairly significant for high Q_1/Q_2 ratios and becomes more and more dramatic for lower Q_1/Q_2 ratios. Another noteworthy point demonstrated in Figure (7), is that for a given physical system, a wide range of interfacial curvatures may result with varying the phases input flow rates ratio.

In view of Figures (2) and (5), the 'interface monogram' varies due to $\in_v$ and α, while the 'flow monogram' varies due to $\tilde{\mu}$. Figure (8) demonstrates various 'operational monograms' obtained for different sets of $(\in_v, \alpha)$ and $\tilde{\mu}$. As is shown in Figure (8a), for the same two fluid system $(\tilde{\mu}, \in_v)$, the solutions may vary significantly due to wall/phases wettability; Not only in the curvature extent, but also the interface shape. For instance, for a given $Q_1/Q_2 = 1$, with $\alpha = 0$, the interface is concave with curvature of $\sim 250^\circ$ (Figure 7), while for $\alpha = 180$, a convex interface with 30° curvature is obtained (Figure 8a). For equal phases wettability, $\alpha = 90$, the interface is still convex, $\phi^* \approx 125$, for this particular operational condition $Q_1/Q_2 = 1$. However, there exists a particular α value ($< 90^\circ$) which for $Q_1/Q_2 = 1$, will result in a plane interface.

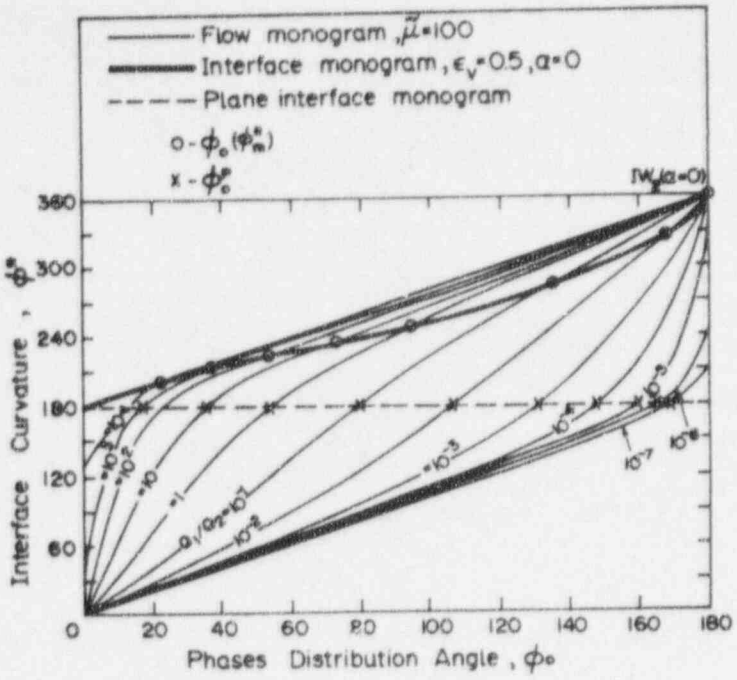

Figure 7: Construction of the system 'Operational monogram'.

Figure (8b) refers to a case of constant α and various ϵ_v numbers. For instance, various oil-water systems with practically constant viscosity ratio and varying density differential, or the same two-fluid system in various conduits or gravity conditions. For the case of Figure (8b) with $\alpha = 0$, the interface is always concave $\phi^* > \pi$, independently of the Q_1/Q_2 ratio. For $\epsilon_v \to 0$, the interface is almost plane for a wide range of flow rates ratio, while for $\epsilon_v \gg 1$, the interface curvature attains its maximum value of 2π, corresponding to an internal floating core enveloped by the peripheral heavier phase (fully eccentric annular configuration). The effect of the viscosity ratio is demonstrated in Figure (8c), indicating, again, a variability of the characteristic interfacial curvature due to this property.

It is interesting to note, in view of Figures (7) and (8), that for $\alpha \neq 0$ and $\alpha \neq \pi$, there exists a single solution for each Q_1/Q_2 ratio. For the extremes of $\alpha = 0$ or $\alpha = \pi$, however, there is always an additional trivial solution at $\phi^* = 2\pi$, $\phi_0 = \pi$ for $\alpha = 0$ or at $\phi^* = 0$, $\phi_0 = 0$ for $\alpha = \pi$. These two trivial solutions correspond to a fully eccentric annular configuration, whereby the ideal wetting phase envelopes a core of the second non-wetting phase.

C. Characteristics of stratified flow with curved interface

In view of section B.3, the combination of the interfacial parameters (α, ϵ_v) with the flow parameters $(\tilde{\mu}, Q_1/Q_2)$ for a given two-phase flow system yields the two geometrical parameters ϕ_0 and ϕ^*. With these two, all the other two-phase flow characteristics can be obtained.

Therefore, the complete data set for defining laminar-laminar stratified flow consists of the phases viscosity ratio, input flow rates ratio, the Evöts number and wettability angle. As demonstrated in Figures (7) and (8), the variability of the interface curvature for a specified set of flow parameters $(\tilde{\mu}, Q_1/Q_2)$ may expand over the entire range $0 \leq \phi^* \leq 360^\circ$ with varying the system interfacial parameters (α, ϵ_v). A comprehensive discussion on the effect of the interfacial curvature on the local two-phase characteristics is the focus of a separate study [19]. For instance, the effect of the interfacial curvature on local velocity distribution, wall and interfacial shear stresses profiles, etc. Here, however, the main focus is on the integral quantities, usually referred to as operational characteristics. The variation of the integral properties of the flow with ϕ^* is studied in Figures (9) to (11).

Figures (9a,b) demonstrates the effect of the interface curvature on the insitu holdup for various phases flow rate ratios when the lighter phase is the more viscous one ($\tilde{\mu} = 100$). For each specified interfacial curvature (e.g. plane interface, $\phi^* = 180^\circ$), the insitu holdup is determined by the phases

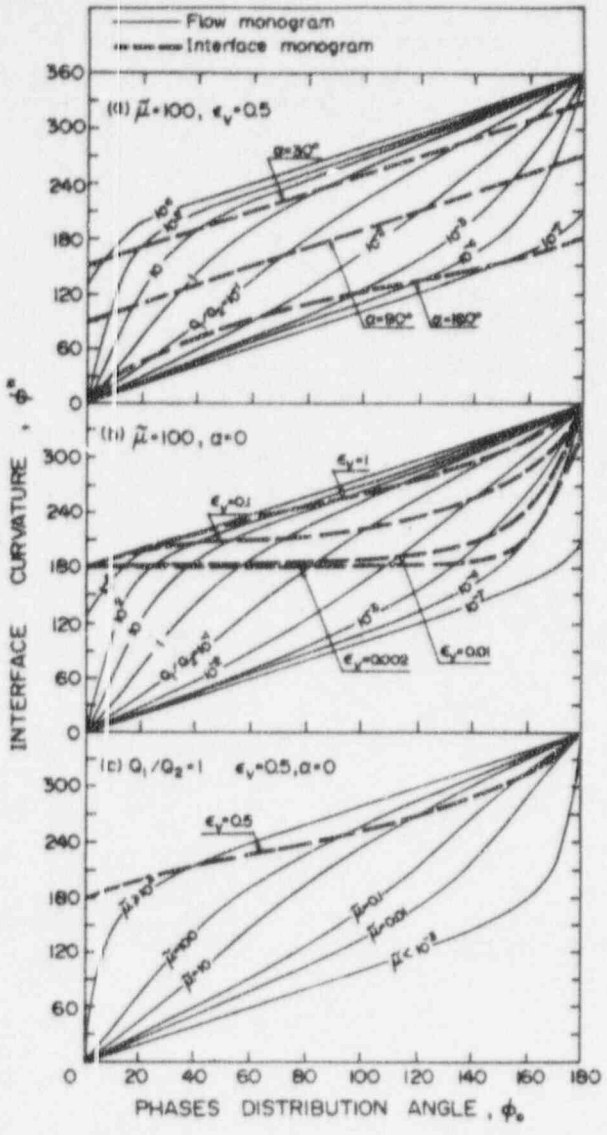

Figure 8: 'Operational monograms': effect of Evöts number, wettability angle and the phases viscosity ratio.

flow rate ratios. The corresponding ϕ_0 is determined by eq. [7] or [8]. Obviously, by increasing the phase flow rate ratios, the insitu holdup of the upper viscous phase increases. However, given the phases flow rates, it is shown in Figure (9) that large variations of the insitu holdup are affected by varying the interface curvature.

The effect of the interfacial curvature on the system pressure drop is shown in Figure (9c). The pressure drop is normalized with respect to the superficial pressure drop of the upper phase (eq. (22)). From the practical point of view, when the upper phase flow rate is maintained constant (and so $(\partial p/\partial z)_{1s}$) this nondimensional pressure drop yields the factor of pressure drop reduction (or enhancement) associated with introducing a second less viscous phase to the system.

Indeed, Figure (9c) demonstrates that for $\tilde{\mu} = 100$ a reduction of the system pressure drop can be achieved by adding small amounts of less viscous phase ($Q_1/Q_2 \leq 10^{-1}$, corresponding to the $\tilde{\mu}Q_1/Q_2 < 10$). The reduction is more significant as ϕ^* increases (hence ϕ_0 increases as well) and the interface attains a concave configuration, whereby the lower less viscous phase forms a thin film which spreads over an increasing portion of the tube wall. This film lubricates the flow of the viscous phase, yielding a reduction of the pressure drop up to a factor of 10 at $\phi^* \simeq 350^o$. Note that for plane interface, $\phi^* = \pi$, the maximal achievable pressure drop reduction is limited to about 25%, while in two-phase flow between parallel plates, it is about 75% [12]. With reducing Q_1/Q_2 (increasing the flow rate of the less viscous phase) the two-phase pressure drop eventually increases and for $Q_1/Q_2 < 10^{-2}$ ($\tilde{\mu}Q_1/Q_2 < 1$) an enhancement of the pressure drop results independently of the interface configuration. For low Q_1/Q_2

(high flow rates of lubricant fluid), the pressure drop shows a mild variation with the interface curvature over a wide range of ϕ^*. This mild sensitivity reflects the effect of two opposing trends affected by variation of ϕ^*. On one hand, increasing ϕ^* results in a lower insitu holdup (and higher velocity) of the viscous phase (Figure 9a), which is compensated, on the other hand, by the increased portion of the wall wetted by the less viscous phase. The main effect of the interfacial curvature on $\partial\tilde{p}/\partial z$ is shown in the extremes of $\phi^* \to 0$ and $\phi^* \to 360^o$. Starting with ϕ_0, $\phi^* \to 0$ (which corresponds to a fully eccentric core of the lubricant fluid situated at the bottom of the tube and surrounded by a viscous phase), a small increase of ϕ^* results in a steep increase of the lubricant fluid holdup and contact area with the tube wall which yields a pronounced lubrication effect. The increase of $\partial\tilde{p}/\partial z$ at the other extreme of $\phi^* \to 360^o$ (and $\phi_0 \to 180^o$), corresponding to fully eccentric viscous core (at the top of the tube) results from the fast decline of the insitu holdup and the associated escalation of the velocity of the viscous phase (Figure 9a). At this extreme, the average velocity of the viscous core, which is still in contact with the tube wall, exceeds the average velocity of the lubricating fluid phase, $\bar{V}_1/\bar{V}_2 = Q_1\bar{A}_2/(Q_2\bar{A}_1) > 1$. Thus, for specified fluids flow rates and $\tilde{\mu} > 1$, the minimal pressure drop of two stratified layers does not correspond to fully eccentric viscous core configuration but is obtained at $\phi^* < 360^o$.

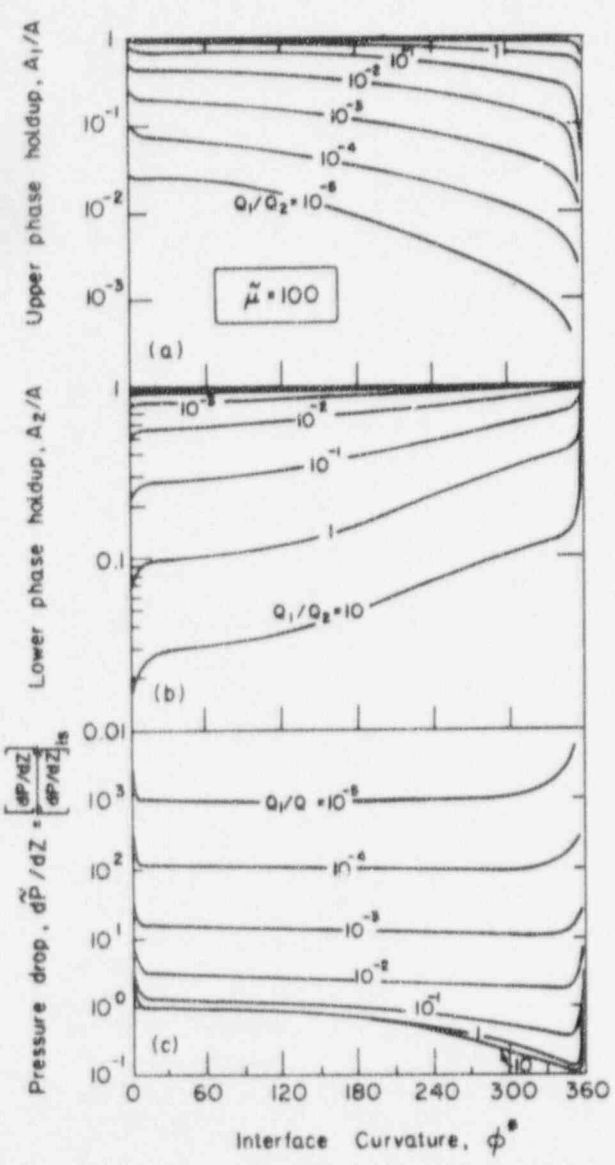

Figure 9: The effect of the interface curvature on the phases insitu holdup and the system pressure drop, $\tilde{\mu} \gg 1$.

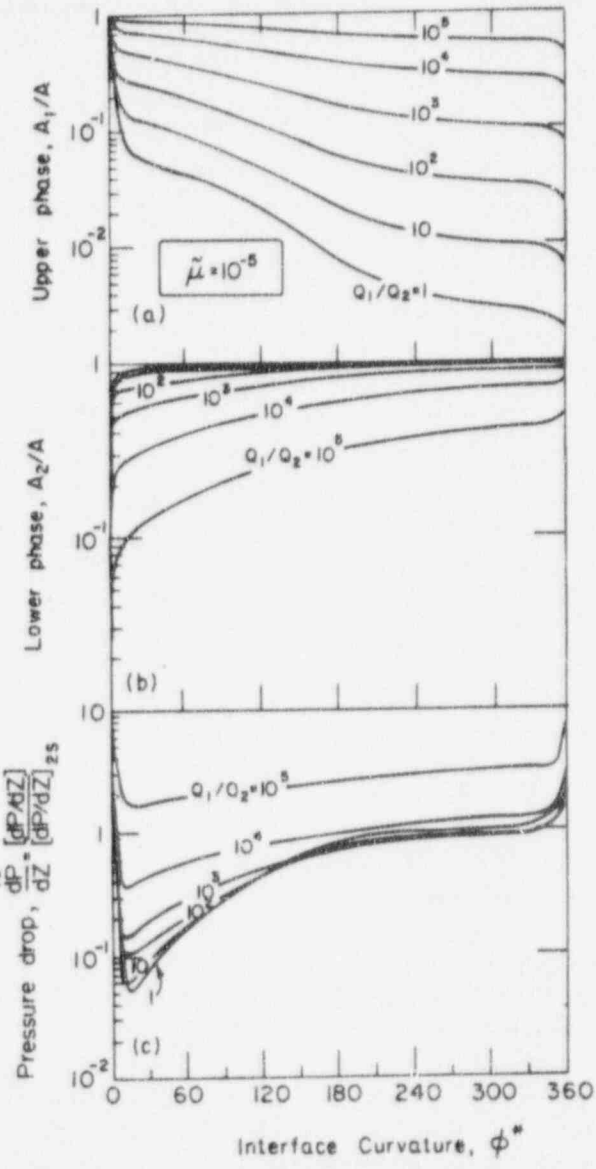

Figure 10: The effect of the interface curvature on the phase holdup and the system pressure drop, $\tilde{\mu} \ll 1$.

Similar effects of the interface curvature on the viscous phase holdup and system pressure drop are obtained for $\tilde{\mu} \ll 1$ (as in gas-liquid systems). Here, the system pressure drop is normalized with respect to the superficial pressure drop of the lower more viscous phase. These are demonstrated in Figures (10) for $\tilde{\mu} = 10^{-5}$. It is to be noted that the comparison of Figures (9) for $\tilde{\mu} \gg 1$ and Figure (10) for $\tilde{\mu} \ll 1$ is to be carried out in view of the definition of symmetrical two-phase systems as given in eqs. (24-25) and the unified solutions obtained for high $\tilde{\mu}Q_1/Q_2$ and low $\tilde{\mu}Q_1/Q_2$ (see Figures 6). For instance, $\bar{A}_1$ for $\tilde{\mu} = 100$, $Q_1/Q_2 = 10^{-2}$ and $\phi^* = 120^o$, is identical to the solution obtained for $\bar{A}_2$ with $\tilde{\mu} = 10^{-5}$, $Q_1/Q_2 = 10^5$ and $\phi^* = 240^o$, as these two solutions correspond to symmetrical two-phase systems with identical $\tilde{\mu}Q_1/Q_2$ values. Similarly, $\bar{A}_2$ for $\tilde{\mu} = 100$, $Q_1/Q_2 = 0.1$ and $\phi^* = 120^o$ is symmetrical to $\bar{A}_1$ for $\tilde{\mu} = 10^{-5}$, $Q_1/Q_2 = 10^4$ and $\phi^* = 240^o$. Introducing a lubricant fluid into the system affects a decrease of the pressure drop for $\tilde{\mu}Q_1/Q_2 \leq 0.1$ (symmetrical to $\tilde{\mu}Q_1/Q_2 > 10$ for $\tilde{\mu} \geq 1$), and the minimal pressure drop is obtained at $\phi^* \approx 10^o$. These properties of the solutions can be utilized in translating the results presented in Figures (9–10) for predicting the effect of the interface curvature on the insitu holdup and pressure drop in two-phase systems of any $\tilde{\mu} \gg 1$ or $\tilde{\mu} \ll 1$.

The two extremes of fully eccentric annular configuration corresponds to $\phi_0 = 0$, $\phi^* = 0$ and $\phi_0 = \pi$, $\phi^* = 2\pi$. For these two extremes, the solution domain of one of the phases degenerates in the bipolar coordinate system (see section B, Figure 1). Therefore, fully eccentric annular flow can not be calculated by the proposed solution procedure. The calculation presented in Figures 9 and 10 have been carried out up to $\phi_0 = 0.2^o$ (ϕ^* is obtained as part of the solution according to the specified flow rates ratio). For $\phi_0 = 0.2^o$, one obtains $\phi^* = \phi_0 + \epsilon$ while for $\phi_0 = \pi - 0.2^o$, $\phi^* = \phi_0 - \epsilon$.

The discussion presented so far, refer to the effects of the interface curvature on the flow characteristics in the framework of varying ϕ^* as an independent parameter. In view of Figures (7-8), for a specified phases flow rates ratio and viscosity ratio, all sets of (ϕ^*, ϕ_0) can in principle be realized in a two-phase system with corresponding combinations of Evöts number, $\in_v$ and wettability angle, α. It is therefore of interest to study the solutions obtained when given a complete data set which defines a specific two-phase system, namely: $\tilde{\mu}$, $\in_v$ and α. In this case, the interfacial curvature varies with the operational conditions Q_1/Q_2 and is determined from the system 'operational monogram' as part of the solution procedure.

Figure (11) presents the phases insitu holdup and the pressure drop obtained for $\tilde{\mu} = 100$ and ideal wettability of the lower phase, ($\alpha = 0$). The parameter in these figures is the $\in_v$ number, whereby the solutions for plane stratified flow correspond to $\in_v \to 0$. Note that a typical oil-water laboratory system with $\Delta\rho = 0.1\ gr/cm^3$; $D = 1''$ and $\sigma = 30\ dyne/cm$ corresponds to $\in_v \simeq 0.4$, but systems of lower density differential (higher $\in_v$) are common in liquid-liquid systems or vapor-liquid systems operating near the critical point.

Figures (11) shows that the characteristics of the stratified flow with the natural curved interface configuration are significantly different from those predicted by a model based on a plane interface configuration. Specifically, when the lower less viscous phase is the ideally wetting phase, its insitu holdup is underpredicted and the pressure drop overpredicted (by a factor of 4-5 for $\in_v = 5$). Also the maximal pressure drop reduction is obtained at lower flow rates of the less viscous phase (the minimum of $\partial\tilde{p}/\partial z$ is shifted towards a higher Q_1/Q_2). For the other extreme of ideal wettability of the upper viscous phase ($\tilde{\mu} = 100, \alpha = 180^0$, Figure 12) it is shown that a plane interface model underestimates the pressure drop and the upper phase holdup. The variation of the interface curvature and the phases distribution angle ϕ_0 corresponding to Figures (11–12) is shown in Figure (13).

The large effect of the phases/wall wettability properties in systems of finite $\in_v$ numbers indicates that the flow characteristics and the stability of the stratified configuration can be completely different just by switching the wall/phases wettability property. This switch may be affected not necessarily by changing the tube material, but just by changing the system start-up procedure. For instance, starting an oil-water system with oil flowing as single phase and later introducing water may yield an entirely different flow configuration than when starting the system with water flowing as a single phase.

To sum up, the relaxation of plane interface assumption on systems of finite $\in_v$ numbers results in large variations of the flow configuration, insitu holdup, pressure drop and the associated velocity profiles and shear stresses distribution.

Moreover, as stratified two-phase flow represents a basic flow pattern for exploring the transition to other bounding flow patterns, the present solution with curved interface may provide a new basis for stability analyses of stratified layers while accounting for surface tension and wall adhesion forces. The inclusion of interfacial forces as additional stabilizing (or destabilizing) terms may contribute to the understanding of the stability of the stratified configuration and flow patterns transitions in small

diameter two-phase systems, reduced gravity systems or low density differential systems.

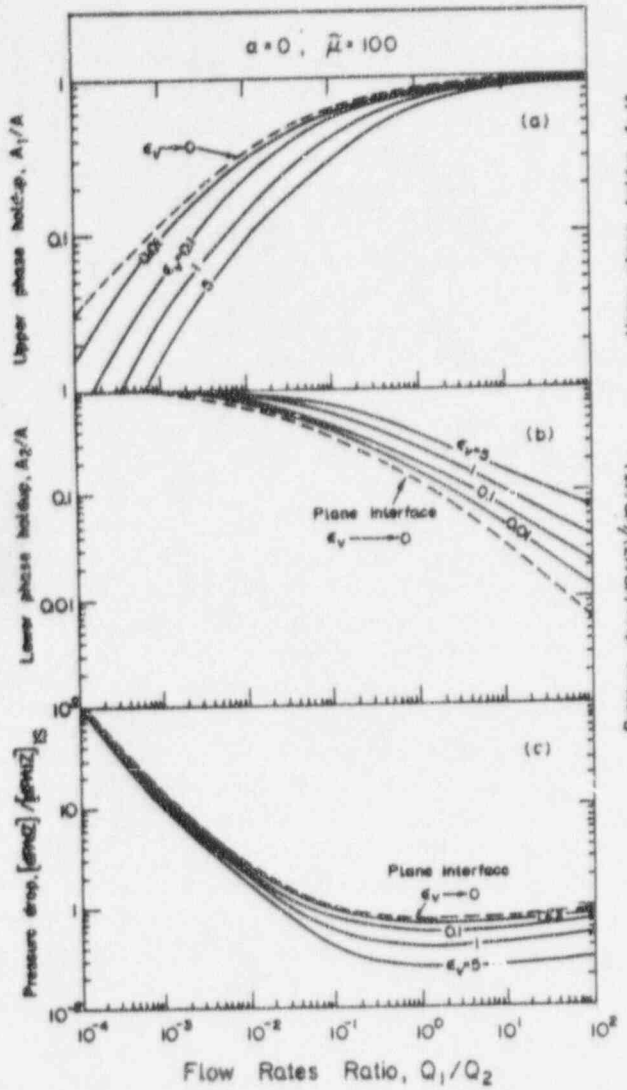

Figure 11: The effect of the Evöts number on the variation of the two-phase flow characteristics with the phases flow rates for ideal wettability of a lower less viscous phase ($\tilde{\mu} = 100,\ \alpha = 0$).

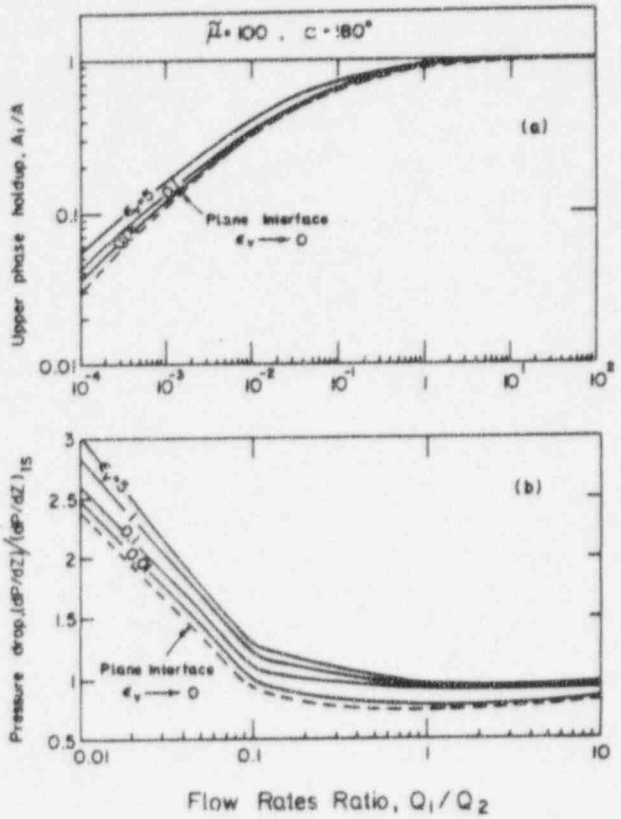

Figure 12: The effect of the Evöts number on the variation of the two-phase flow characteristics for ideal wettability of the upper more viscous phase ($\tilde{\mu} = 100,\ \alpha = 180°$).

Summary

Most of the studies on stratified two-phase flows relate to gas-liquid flows under earth gravitation. These flows are dominated by gravity, and therefore the basic flow configuration is stratified layers with a plane interface. The study is motivated by the need to develop an analytical tool for predicting the insitu flow configuration in a stratified two-phase flow of a general two-fluid system, for which the appropriate basic flow configuration is a stratified flow with a curved interface.

Apparently, the solution of laminar-laminar two-phase flow is determined in terms of two parameters: the phases flow rates ratio and the phases viscosity ratio and is independent of the density differential, surface tension effects, tube dimension or gravitation. This is indeed the case when the flow configuration is restricted to a plane interface between the phases. When this constraint is relaxed, the solution

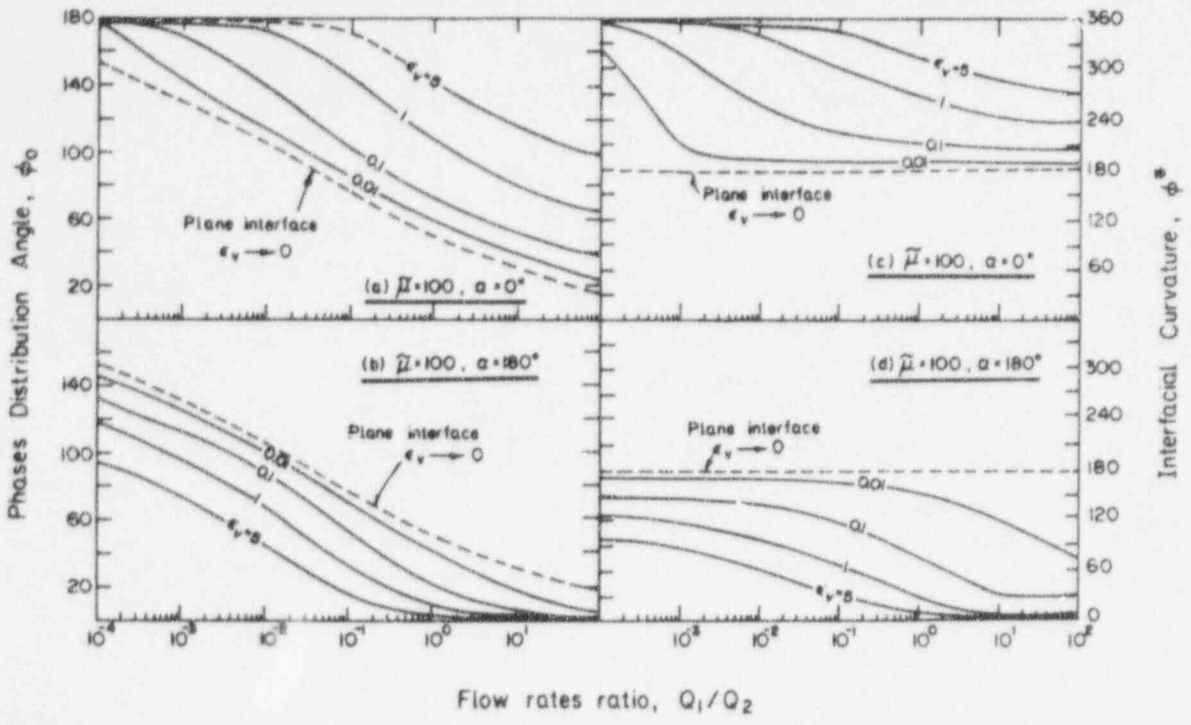

Figure 13: The effect of the Evöts number and the wettability angle on the interface configuration in stratified flow, $\tilde{\mu} = 100$.

of laminar two-phase flows is shown to be dependent on all of these, and is determined by four nondimensional parameters: phases viscosity ratio, flow rates ratio, wall/phases wettability angle and the Evöts number. The latter represents the ratio between surface tension and gravity forces.

Energy considerations are employed to predict the interface configuration. The characteristic interfacial curvature corresponds to the interface configuration for which the system total energy is at its minimum. Based on this principle, the interface monograms are constructed. Basically, these monograms relate the interface characteristic curvature to the phases insitu holdup, and are dependent on the Evöts number and wall/phases wettability angle. In parallel, the solution of the flow equations for the two-phases is carried out in bipolar coordinates, whereby the velocity and shear stresses profiles in the two-phases domains are obtained in terms of Fourier integrals. These are utilized to construct the 'flow monograms', which relate the interface curvature to the phases insitu holdup, given the phases viscosity and flow rates ratio. The interface monogram and the flow monogram are then combined to construct the system 'operational monogram' whereby a complete solution to the flow problem is obtained, including the insitu flow configuration (phases holdup and interface curvature), velocity and shear stresses distribution and the pressure drop.

Table of Nomenclature

a	- phases holdup ratio, dimensionless
A	- cross-sectional flow area, m^2
E	- energy, J
g	- gravity acceleration, m^2/s
H_v	- spectral function, eqs. [13.4, 13.5]
p	- pressure, N/m^2
Q	- input volumetric flow rate, m^3/s
R	- tube radius, m
V	- axial velocity, m/s
z	- coordinate in the downstream direction, m

Greek symbols

α	- wettability angle
$\in_v$	- Eötvös number $= \frac{2\sigma_{12}}{(\rho_2-\rho_1)gR^2}$, dimensionless
μ	- viscosity, $kg/m-s$
ν	- kinematic viscosity, m^2/s
ξ	- bipolar coordinate, dimensionless
ρ	- density, kg/m^3
σ	- surface tension, N/m
τ	- shear stress, N/m^2
ϕ	- bipolar coordinate
ϕ_0	- interface view angle
ϕ^*	- interface curvature
ϕ^*_m	- ϕ^* for minimum system energy
ψ	- function defined in Eq. [13.5]
ω	- spectral frequency, dimensionless
χ	- Martinelli parameter, eq. [23]

Subscripts

1	- upper fluid
2	- lower fluid
$1s$	- superficial, upper fluid
$2s$	- superficial, lower phase
i	- interfacial
p	- potential
R	- reference
s	- surface
w	- wall

Superscripts

$\sim$	dimensionless
p	- plane interface

References

[1] G.B.Wallis, One-dimensional two-phase flow, McGraw- Hill, New-York. (1969).

[2] M.E. Charles and L.U. Lilleleht, "Co-current stratified laminar flow of two immiscible liquids in a rectangular conduit," Can. J. Chem. Engng 43, 110 (1965).

[3] A.R. Gemmell N. Epstein, "Numerical analysis of stratified laminar flow of two immiscible Newtonian liquids in a circular pipe," Can. J. Chem. Engng. 40, 215–224 (1962).

[4] M.E. Charles and P.J. Redberger, "The reduction of pressure gradients in oil pipelines by the addition of water: Numerical analysis of stratified flow," Can. J. Chem. Engng. 40, 70–75 (1962).

[5] Y.P. Tang and D.M. Himmelblau, "Velocity distribution of isothermal two-phase co-current laminar flow in horizontal rectangular duct," Chem. Engng. Sci. 18, 143–144 (1963).

[6] Y. Taitel and A. E. Dukler, "A model for prediction flow regime transition in horizontal and near horizontal gas-liquid flow," A.I.Ch.E J. 22, 47–55 (1976).

[7] N. Brauner and D. Moalem Maron, "Two-phase liquid-liquid stratified flow," Physico-Chem. Hydrodynamics 11, 487–506 (1989).

[8] A.R. Hall and G.F. Hewitt, "Application of two-fluid analysis to laminar stratified oil-water flows," Int. J. Multiphase Flow 19 (4), 711–717 (1993).

[9] N. Brauner and D. Moalem Maron, "Analysis of stratified/nonstratified transitional boundaries in horizontal gas-liquid flows," Chem. Engng. Sci. 46, 1849–1859 (1991).

[10] N. Brauner and D. Moalem Maron, "Stability analysis of stratified liquid-liquid horizontal flow," Int. J. Multiphase Flow 18, 103–121 (1992).

[11] N. Brauner and D. Moalem Maron, "Flow pattern transitions in two phase liquid-liquid horizontal tubes," Int. J. Multiphase Flow 18, 123–140 (1992).

[12] N. Brauner, J. Rovinsky and D. Moalem Maron, "Analytical solution for laminar-laminar two-phase flow in circular conduits," accepted Special Issue, Chemical Engineering Communications (1995).

[13] J. Rovinsky, N. Brauner and D. Moalem Maron, "Determination of the interface curvature in stratified two-phase systems by energy considerations," Internal report, Faculty of engineering, Tel-Aviv University, sponsored by the Israeli Absorption Ministry (1995).

[14] R.M. Roidt and J.H. Kim, "Analytical and experimental studies of a stratified flow in a pipe," Proc. VI international topical meeting on nuclear reactor thermal hydraulics, edited by M. Courtaud and J.M. Delhaye, 1, 541-550 (1993).

[15] M. Bentwich, "Two-phase axial flow in pipe," Trans. of the ASME, Series D, 86 (4), 669–672 (1964).

[16] M. Bentwich, "Two-phase axial laminar flow in a pipe with naturally curved interface," Chem. Engng. Sci. 31, 71-76 (1976)

[17] D. Hasson, U. Mann and A. Nir, "Annular flow of two immiscible liquids: I. Mechanisms", Can. J. Chem. Engng. 48, 514-520 (1970).

[18] M.E. Charles, "The reduction of pressure gradients in oil pipelines: experimental results for the stratified flow of heavy crude oil and water," Can. Inst. Min. Metal. Trans. 63, 306–310 (1960).

[19] D. Moalem Maron, J. Rovinsky and N. Brauner, "Analytical prediction of the interface curvature and its effects on stratified flow characteristics," to be presented at the Int. Symp. on two-phase flow modeling and experimentation, October 9-11 Rome, Italy (1995)

APPENDIX A: Evaluation of the cut-off frequency

The cut-off frequency, ω_{max} which corresponds to a trancational error $Er_v \ll 1$ in the calculation of the velocity field via eqs. [15] is evaluated from the following criteria:

$$I_j = \frac{\int_{\omega_{max}}^{\infty} H_{jv}(\omega)d\omega}{\int_0^{\infty} H_{jv}(\omega)d\omega} < Er_v; \qquad j = 1,2 \qquad [A-1]$$

where $H_{jw}(\omega)$ is given in eqs. [13]. The maximal value of $H_{jv}(\omega)$ is obtained at the phases interface, $\phi = \phi^*$, therefore criteria [A-1] is applied at $\phi = \phi^*$.

The cut-off frequency varies with the flow parameters $\tilde{\mu}, \phi_0$ and ϕ^* and increases as the curved stratified configuration approaches the configuration of fully eccentric annular flow.

Fully eccentric core flow of the lower phase

This configuration is approached when $\phi_0 \to 0$ and $\phi^* = \phi_0 + \epsilon$, $\epsilon \to 0$ (see Figure A.1). For $\omega\epsilon \gg 1$, eq. [13.5] for $\psi(\omega)$ approaches a constant value:

$$\psi(\omega > 1/\epsilon) \to 1 + \beta \qquad [A-2]$$

and the spectral functions are given by:

$$H_{1v}(\omega > 1/\epsilon) = -\frac{2}{(\beta+1)} \frac{e^{\omega(\pi-\phi^*)}\sinh[\omega(\phi-\phi_0)]}{e^{\pi\omega}e^{\epsilon\omega}} \qquad [A-3]$$

$$H_{2v}(\omega > 1/\epsilon) = \frac{2}{(\beta+1)} \frac{e^{\omega(\pi-\phi^*)}\sinh[\omega(\phi-\pi-\phi_0)]}{e^{\pi\omega}e^{\omega(\pi-\epsilon)}} \qquad [A-4]$$

The maximal value of H_{jv} are obtained at $\phi = \phi^*$, whereby:

$$\mid Max\{H_{jv}(\omega)\} \mid = \frac{1}{(\beta+1)} e^{-\omega(\phi_0+\epsilon)} = \frac{1}{(\beta+1)} e^{-\omega\phi^*} \qquad [A-5]$$

Thus, the cut-off frequency can be evaluated from:

$$I < \frac{\int_{\omega_{max}}^{\infty} e^{-\omega\phi^*} d\omega}{\int_0^{\infty} e^{-\omega\phi^*} d\omega} = e^{-\omega_{max}\phi^*} \leq Er_v \qquad [A-6]$$

which yields:

$$\omega_{max} \simeq \frac{-lnEr_v}{\phi^*} \qquad [A-7]$$

Fully eccentric core flow of the upper phase

This configuration is approached when $\phi_0 \rightarrow \pi$ and $\phi^* = \phi_0 + \pi - \epsilon$, $\epsilon \rightarrow 0$. Considering $\omega\epsilon \gg 1$, whereby $\psi(\omega) \rightarrow (1+\beta)$, the spectral functions are given by:

$$H_{1v}(\omega > 1/\epsilon) = \frac{2e^{\omega(\phi_0-\epsilon)}\sinh[\omega(\phi-\phi_0)]}{(\beta+1)e^{\pi\omega}e^{\omega(\pi-\epsilon)}} \qquad [A-8]$$

$$H_{2v}(\omega > 1/\epsilon) = \frac{2}{(\beta+1)} \frac{e^{\omega(\phi_0-\epsilon)}\sinh[\omega(\phi-\pi-\phi_0)]}{e^{\pi\omega}e^{\epsilon\omega}} \qquad [A-9]$$

The maximal value of the spectral functions is, again, obtained at the phases interface:

$$\mid Max\{H_{j\omega}(\omega)\} \mid = \frac{1}{(\beta+1)} e^{-\omega(\pi-\phi_0+\epsilon)} \qquad [A-10]$$

For this case, criteria [A-1] are satisfied for:

$$\omega_{max} \simeq \frac{-lnEr_v}{(\pi-\phi_0+\epsilon)} = \frac{-inEr_v}{(2\pi-\phi^*)} \qquad [A-11]$$

Eqs. [A-7] and [A-11] indicate that when the flow configuration approaches that of fully eccentric annular flow, for either ϕ_0, $\phi^* \rightarrow 0$ or $\phi_0 \rightarrow \pi$, $\phi^* \rightarrow 2\pi$, the convergence of the Fourier integral is very slow and the cut-off frequency should be dramatically increased to meet the accuracy demands.

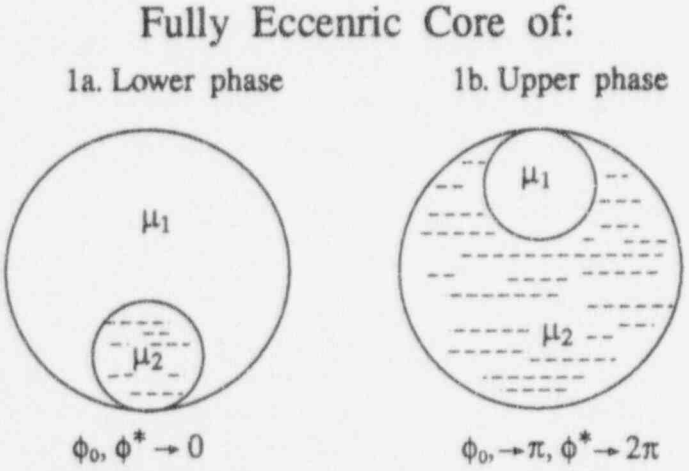

Figure A-1: Schematic description of fully eccentric core flow.

Plane interface, $\phi^* \rightarrow \pi$

For this case, the solution for $\tilde{V}_{1h}$, $\tilde{V}_{2h}$ (eqs. 13.1-13.4) reads:

$$V_{1h} = 2\gamma_1(\tilde{\mu}-1)\sin(\phi_0)\int_0^\infty \frac{\omega}{\sinh(\pi\omega)}\,\frac{\sinh[\omega(\phi-\phi_0)]}{\psi(\omega)\cosh[\omega(\pi-\phi_0)]}\cos(\omega\xi)d\omega \qquad [A-12]$$

$$V_{2h} = 2\tilde{\mu}\gamma_1(\tilde{\mu}-1)\sin(\phi_0)\int_0^\infty \frac{\omega}{\sinh(\pi\omega)}\,\frac{\sinh[\omega(\phi-\pi-\phi_0)]}{\psi(\omega)\cosh(\omega\phi_0)}\cos(\omega\xi)d\omega \qquad [A-13]$$

Considering $\omega \gg 1$, the spectral functions reduce to:

$$H_{1v} = \frac{2\omega}{\beta+1}e^{\omega(\phi-2\pi)} \qquad \phi_0 < \phi < \pi$$

$$H_{2v} = \frac{-2\omega}{\beta+1}e^{-\omega\phi} \qquad \pi < \phi < \pi+\phi_0$$

$$\text{Therefore:} \quad \text{Max}\{|\,H_{jv}\,|\} = \frac{2\omega}{\beta+1}e^{-\pi\omega}; \quad j = 1,2$$

Hence, the cut-off frequency is independent of ϕ_0 (or the phases insitu holdup). For this case, eq. [A.1] yields:

$$Er_v = (1+\pi\omega_{max})e^{-\pi\omega_{max}}$$

For instance, a cut-off frequency of $\omega_{max} = 3$ yields $Er_v \approx 10^{-3}$.

Velocity of Large Bubble in Liquid-Solid Mixture in a Vertical Tube

H.Hamaguchi
Faculty of Human Development
Kobe University
Tsurukabuto, Nada,Kobe
657 Japan
TEL +81-78-803-0934
FAX +81-78-803-0934

T.Sakaguchi
Faculty of Engineering
Kobe University
Rokkodaicho, Nada,Kobe
657 Japan

ABSTRACT

The upward movement of a large bubble in a stationary mixture of liquid and solid is one of the most fundamental phenomena of gas-liquid-solid three phase slug flow in a vertical tube. The purpose of this study is to make clear the characteristic of the rising velocity of this fundamental flow experimentally. The rising velocity of a large bubble V in a liquid-solid mixture was measured and compared with the velocity V_0 in a liquid (without solid). The experimental results were correlated using a non-dimensional velocity $V^*(=V/V_0)$, and the following results were obtained. It was found that the characteristic of the rising velocity differs according to the tube diameter and the liquid viscosity, or the Galileo number in the non-dimensional expression. It can be classified into two regimes. (i) When the liquid viscosity is large (or the tube diameter is small), V^* decreases linearly against the volumetric solid fraction ε of the mixture. (ii) When the viscosity is small, on the other hand, the relation between V^* and ε is not linear. This classification can be explained by the results in the previous papers by the authors[1,2] dealing with a large bubble in a liquid.

Nomenclature

D=Tube diameter, m or mm
d_s=Diameter of solid particle, m or mm
Eo=Eotvos number ($=\rho g D^2/\sigma$), -
Fr=Froude number ($=V/(gD)^{1/2}$), -
Fro=Froude number ($=V_0/(gD)^{1/2}$), -
g=gravitational acceleration, m/s^2
Ga=Galileo number (gD^3/ν^2), -
V=Velocity of large bubble in mixture, m/s
V_0=Velocity of large bubble in liquid, m/s
$V^*=V/V_0$, -
ε=Volumetric solid concentration, -
μ=Liquid viscosity, Ns/m^2
μ_e=Equivalent viscosity of mixture, Ns/m^2
ν=Kinematic viscosity of liquid, m^2/s
ρ=Density of liquid, kg/m^3

ρ_s=Density of solid, kg/m^3

σ=Surface tension, N/m

1. Introduction

Gas-liquid-solid three phase flow appears in many industrial plants such as air-lift pumps to transport manganese nodules from deep sea beds to ships. There are several reviews on gas-liquid-solid three phase flow[3]-[10]. Gas-liquid-solid three phase flow also appears in the field of the fluidized bed and have been reviewed[11]-[13]. Moreover, in the severe accident in a nuclear reactor such as the melt down of the fuel pellets or other structural materials, three phase flow is considered to appear, although information about it is limited because its research began a little more than ten years ago[14].

Therefore, a study of three phase flow is necessary in the design in these fields etc.

In gas-liquid two phase slug flow in a vertical tube, one of its fundamental phenomena is the upward movement of a large bubble rising in a stationary liquid, as shown in Fig.1(a). In gas-liquid-solid three phase slug flow, one of its fundamental phenomena is also the upward movement of a large bubble rising in a stationary liquid containing solid particles, as shown in Fig.1(b). In particular, the flow in which the density of solid particles is equal to that of a liquid is considered to be one of the most fundamental one. A study of this fundamental phenomenon is necessary to understand a general upward three phase flow, in which the solid phase may move slower than the liquid phase due to the difference between the densities of liquid and solid. However, this fundamental phenomenon has not been systematically studied.

On the other hand, the rising velocity of a large bubble moving in a liquid (without solid) has been studied by many researchers[15]. Some empirical equations and charts are proposed to obtain the rising velocity as a non-dimensional form[16] have been proposed.

It is also reported in the previous papers by the authors[1,2,17] that the flow of a large bubble can be divided from its characteristics into two regimes, i.e., the "boundary layer regime"(*) and the "viscous regime". In the "viscous regime", the viscous force is dominant and the inertial force is so small as to be neglected in this phenomenon. On the other hand, in the "boundary layer regime", the inertial force as well as the viscous force is important. The characteristic of a rising velocity differs according to the flow regime. Empirical equations for the rising velocity have been proposed for each flow regime[1]. A flow model has been also proposed, considering existence of a boundary layer in the "boundary layer regime"[2]. The boundary between the flow regimes was given by an empirical equation as a critical Galileo number which is a function of Eotvos number. The characteristic of the velocity of a large bubble rising in a liquid-solid mixture is also considered to be different according to the "flow regime".

It is, in general, expected that the rising velocity of a large bubble in a liquid-solid mixture is less than in a liquid (without solid particle), because the existence of solid may prevent the movement of the liquid when a large bubble rises in a tube. However, the effect of the existence of solid in a liquid on the rising velocity in the "viscous regime" will not be as same as in the "boundary layer regime". The purpose of this paper is to make clear the effect of the existence of solid on the rising velocity in each flow regime.

2. Experimental Apparatus and Procedure

A schematic diagram of the experimental apparatus is shown in Fig.2. An acrylic plastic tube 1 having a diameter D of 15 mm and 5mm was chosen as a test tube.

(*) The "boundary layer regime" was reffered to as the "inertial-viscous regime" in the previous papers. However, the word "boundary layer regime" is used in this paper to express more specifically.

Silicone oil (KF96) and styrol plastic particles were used to compose a liquid-solid mixture. The density ρ and the kinematic viscosity ν of silicone oil are 985 kg/m^3 and 50 to 350 mm^2/s, respectively, and the density ρ_s and the diameter d_s of the plastic particle are 1030 kg/m^3 and 0.63 to 2.5 mm, respectively.

The experimental conditions are shown in Table 1. In conditions 1 and 2 in the table, the tube diameter D and the solid particle diameter ds are both equal to each other, and only the liquid viscosity ν differs from each other. Condition 1 corresponds to the "viscous regime", and condition 2 to the "boundary layer regime" for a large bubble in a liquid (without solid)[1]. In condition 3, ν has the same value as in condition 2, but D is different from that in condition 2; and then, this condotion corresponds to the "viscous regime".

In carrying out the experiment, the test tube was filled with the liquid-solid mixture (i.e., the mixture of the silicone oil and the plastic particles) by operating the air pump 2, keeping the lower end of the tube under the surface of the liquid-solid mixture 3 as shown in Fig.2, and then the valve 4 was closed. After the preparation, the lower end of the tube was opened to the atmosphere by removing the container 5, then a large bubble was formed.

Pictures of the large bubble were taken, using a 35mm camera system 6 with a strobe light when it arrived at two points at the center of the tube. The rising velocity of the large bubble was obtained using its time interval and the distance between the two points along the tube length.

The rising velocity of a large bubble moving in a liquid (without solid) was also measured as a fundamental flow of a large bubble in a liquid-solid mixture to correlate the rising velocity in a liquid-solid mixture.

3. Expression of Experimental Results

The non-dimensional number such as the Froude number expressing the velocity of a large bubble rising in a liquid (without solid) is determined by two non-dimensional numbers such as the Eotvos number and the Morton number. In the previous papers[1,2] dealing with a large bubble in liquid, the Froude number Fr, the Eotvos number Eo, and the Galileo number Ga (or the Reynolds number instead of the Galileo number) were used to correlate the experimental data. In this paper, these three non-dimensional numbers will also be used. Then, the Froude number of a large bubble in a liquid is expressed by

$$Fr_o(=V_o/(gD)^{1/2})=f_1(Eo, Ga) \qquad (1)$$

where Eo is the Eotvos number ($=\rho gD^2/\sigma$), and Ga the Galileo number ($=gD^3/\nu^2$). The Eotvos number is also referred to as the Bond number.

In a large bubble rising in a liquid-solid mixture, additional non-dimensional numbers (i.e., ε, d_s/D, and ρ_s/ρ) exist, where ε is the volumetric solid concentration, and ρ_s and ρ are the densities of the solid and the liquid, respectively. Therefore, the Froude number Fr of a large bubble in a liquid-solid mixture is expressed by

$$Fr(=V/(gD)^{1/2})=f_2(Eo, Ga, \varepsilon, d_s/D, \rho_s/\rho) \qquad (2)$$

From these equations, a non-dimensional velocity V* or a ratio of the velocity in a liquid-solid mixture to that in a liquid is defined by

$$V^*(=V/V_o)=Fr/Fr_o$$
$$=f_3(Eo, Ga, \varepsilon, d_s/D, \rho_s/\rho) \qquad (3)$$

In this paper, since the condition $\rho_s/\rho=1$(const.) is assumed.

$$V^*(=V/V_0)=Fr/Fr_0=f_4(Eo, Ga, \varepsilon, d_s/D) \quad (4)$$

It is, therefore, concluded that the non-dimensional velocity V^* can be generally expressed by four non-dimensional numbers.

4. Experimental Results

4.1 Experimental results in the "viscous regime"

The experimental results of the ratio or the non-dimensional velocity V^* are shown against the volumetric solid concentration ε in Fig.3. These are the results in condition 1, and correspond to the "viscous regime".

As is seen in the figure, the relationship between V^* and ε is linear except for small ε ($\varepsilon<0.3$), i.e.,

$$V^*=A-B\varepsilon \quad (\varepsilon>0.3) \quad (5)$$

where B is the slope of the lines in the figure, and is not influenced by d_s/D, as expressed by

$$B=2.0 \quad (6)$$

On the other hand, the value A in Eq.(5) depends on d_s/D. More specifically, A is somewhat greater for greater d_s/D. The relation between them is shown in Fig.4. The following equation can be obtained from this figure.

$$A=1+0.4d_s/D \quad (7)$$

The above equation was obtained so that it would satisfy a condition that A was unity when d_s/D was 0. The meaning of this condition will be mentioned later. As a result, Eq(5) becomes

$$V^*=(1+0.4d_s/D)-2.0\varepsilon \quad (\varepsilon>0.3) \quad (8)$$

In the figure, the lines express Eq.(8). The experimental results agree well with the equation. When $\varepsilon=0$, the velocity V should be equal to the velocity V_0 in the liquid (without solid) or $V^*=1$. However, V^* is greater than unity by $0.4d_s/D$, if the equation is used for the calculation of V^* when $\varepsilon=0$. The reason of the disagreement will be mentioned later.

Now, some discussions about Eq.(8) will be made below.

(i) In the case of $d_s/D\rightarrow 0$

In this case, Eq.(8) becomes

$$V^*=1-2.0\varepsilon \quad (9)$$

The second term of the above equation shows the amount of the decrease in the velocity due to the existence of solid particles in the liquid. In the "viscous region", since the rising velocity of a large bubble in a liquid is reversely proportional to the liquid viscosity, the existence of solid makes an effect that as if the liquid viscosity increases or the equivalent viscosity of the mixture increases. Therefore, V^* is expressed by

$$V^*=\mu/\mu_e \qquad (10)$$

where μ is the liquid viscosity, and μ_e the equivalent viscosity of the mixture, and is expressed from Eq.(9) by

$$\mu_e/\mu=1/(1-2\varepsilon) \qquad (11)$$

If the Einstein's equation[18] is used in the liquid-solid mixture,

$$\mu_e/\mu=(1+2.5\varepsilon) \qquad (12)$$

This equation yields Eq.(13) instead of Eq.(9).

$$V^*=1/(1+2.5\varepsilon) \qquad (13)$$

When $\alpha \approx 0$, the Taylor expansion of the above equation yields

$$V^*=1-2.5\varepsilon \qquad (14)$$

This equation is qualitatively different from Eq.(9) in the multiplier in the second term on the right hand side. However, the value of V^* in Eq.(9) is equal to that in Eq.(13) when $\varepsilon=0.2$.

Considering that Eq.(9) (or Eq.(8)) expresses the experimental results well, the equivalent viscosity of the mixture can be said to be expressed by Eq.(11).

(ii) In the case of $d_s/D \neq 0$

In general, the value of d_s/D is not zero, and has a finite value in the actual flow. When ε tends to zero, Eq.(8) becomes

$$V^*=1+0.4d_s/D \qquad (16)$$

Therefore, V^* is greater than unity. In other words, when $\varepsilon>0$, the non dimensional velocity V^* has a greater value by $\Delta V(=0.4d_s/D)$ for a finite d_s/D as shown in Fig.5. This reason is considered to be as follows:

When $d_s/D \to 0$, the solid particles can distribute uniformly all over the cross section of the tube, i.e., the distribution of the volumetric solid concentration can be uniform in the r-direction as shown in Fig.6(a). However, when d_s has a finite value (See Fig.6(b)), the solid particles cannot distribute uniformly, i.e., the distribution of the volumetric solid concentration cannot be uniform all over the cross section, because the center of the particle cannot exist near the tube wall due to existence of the tube wall, as shown by the broken line. Therefore, the volumetric solid concentration is considered to be small near the tube wall as shown in the figure. That is to say, the equivalent viscosity is small in a area near the tube wall. This area has a width of $0.5d_s$, and is proportional to d_s/D.

Imagine a flow system of the upward movement of a large bubble in a liquid whose viscosity is small near the tube wall as shown in Fig.7. The flow resistance of the large bubble due to the viscosity is considered to be less than that in a liquid whose viscosity is uniformly distributed, because the shearing stress (i.e., the effect of the viscosity) is more important near the tube wall than in the center of the tube. As a results, the rising velocity of the large bubble will increase in this flow system. This is the reason why the non-dimensional velocity V^* increases by ΔV in Fig.5. It can also be qualitatively explained why ΔV increases in proportion to d_s/D in Eq.(16) (or Eq.(8)), if the effect of the reduction in the equivalent viscosity is proportional to its area.

When $d_s/D \to 0$, the amount of the increment of the velocity ΔV is considered to be 0, because the above-mentioned effect vanishes. This is the reason why the first term of the right-hand side of Eq.(7) is determined to be unity.

The experimental results for condition 3 are shown in Fig.8. This condition also corresponds to the "viscous regime". The values of Ga and Eo are different from that in Fig.3 for condition 1. However, the characteristic of V^* seems to be as same as in Fig.3. The straight line shows Eq.(8) obtained from Fig.3. This line also agrees well with the experimental values, and the equation is also useful in this condition, although the Eotvos number is changed from 110 to 12, and also Ga from 270 to 500. Therefore, Eq.(8) may be generally useful in the "viscous regime". However, it can be definitely concluded after more experiments are carried out in wider ranges of Eo and Ga that Eq.(8) is generally useful.

4.2 Experimental results for the "boundary layer regime"

The experimental results in condition 2 are shown in Fig.9. As shown in the figure, the characteristic of the non-dimensional velocity is different from those in Figs.3 and 8 in the "viscous regime" in the following three points:

(i) The relation between V^* and ε is not linear.
(ii) The value V^* significantly depends on d_s/D.
(iii) The amount of the reduction in V^* due to the existence of solid particles is smaller than that in the "viscous regime" when ε has the same value.

Discussion about the above three points will be made below.

For the point (i): in this flow regime (i.e., the "boundary layer regime"), it is known that the rising velocity of a large bubble in liquid is not inversely proportional to the liquid viscosity[1]. Therefore, it can be understood that V^* does not decrease linearly against ε even if the equivalent viscosity of the mixture is expressed by Eq.(11).

For the point (ii): in the "boundary layer regime", it is considered that a boundary layer exists near the tube wall within the liquid falling down around the nose of a large bubble[1,2]. The existence of the boudary layer seems to make the effect of d_s/D complex. For example, the solid particles will make the thickness of the boundary layer change. This effect will be influenced by the size of solid particles or d_s/D. Therefore, the phenomenon may depend on the diameter of solid particle even if the volumetric solid concentration is the same, because the relation between d_s and the thickness of the boudary layer δ or the ratio d_s/δ will significantly affect the flow system. Beside, the distribution of the volumetric solid concentration near the tube wall (or that in the boundary layer) is not uniform as shown in Fig.6(b). It can, therefore, be said that the effect of d_s/D in the "boundary layer regime" will be different from in the "viscous regime".

For the point (iii): in the "boundary layer regime", the movement of a large bubble will be influenced by the liquid viscosity only inside the boundary layer. It will be scarcely influenced by the viscosity outside the boundary layer or near the center of the tube. Therefore, the effect of the increase in the equivalent viscosity due to the existence of the solid particles on the rising velocity will be smaller than that in the "viscous regime", in which the movement of a large bubble is affected by the viscosity not only near the tube wall but also near the center of the tube. This is the reason why the amount of the reduction in the rising velocity in the "boundary layer regime" is smaller than that in the "viscous regime".

The lines in the figure show the following empirical equation.

$$V^* = 1 - C\varepsilon^2 \qquad (17)$$

where C is a function of d_s/D, and is expressed by the following equation from Fig.10.

$$C = 5.3\, e^{-6 d_s/D} \qquad (18)$$

The above equation was obtained for Eo=110 and Ga=13500. The value C is considered to be a function of Eo and Ga as shown in Eq.(4). Moreover, if Eo and/or Ga are changed, the power of ε in Eq.(17) may have a different value, although its value is 2.

Therefore, it is expected that much more experiments for various combinations of Eo, Ga, and ds/D are carried out by researchers in the future to establish a general equation or a chart to obtain the non-dimensional velocity.

5. Conclusions

The velocity of a large bubble rising in a liquid-solid mixture was measured, and its results were correlated using a non-dimensional velocity V^*. The following results were obtained.

(1) Two different characteristics of rising velocity were found according to the flow regime (i.e., the "viscous regime" and the "boundary layer regime").

(2) For small Ga(270 to 500) or in the "viscous regime", the non- dimensional velocity V^* decreases linearly against the volumetric solid concentration ε.

(3) In the "viscous region", the effect of the existence of solid particle is explained as an increase in the equivalent viscosity of the liquid-solid mixture.

(4) In the "viscous regime", V^* increases with increasing the ratio of the solid particle diameter d_s to the tube diameter D, although its effect is small. This result can be qualitatively explained by existence of the tube wall.

(5) For large Ga(13500) or in the "boundary layer regime", V^* decreases with increasing ε, but does not decrease linearly against ε.

(6) In the "boundary layer regime", V^* is affected by d_s/D. It increases with increasing d_s/D.

(7) In the "boundary layer regime", V^* is greater than that in the "viscous regime" when ε is the same.

Acknowledgments

The authors wish to express their thanks to H.Saito, a graduate student at Kobe University for his assistance in carrying out the experiments.

References

[1]Hamaguchi,H., Sakagichi,T. et al., Characteristic of Rising Velocity of Large Bubble in Vertical Tubes, Proc. of Japan-US Seminar, Berkeley (1992)

[2]Hamaguchi, H. and Sakaguchi,T., A Flow Model for Large Bubble in a Vertical Tube, Proc. of The 2nd International Conference of Multiphase Flow '95 Kyoto, Vol.1(1995)

[3]Sakaguchi,T., Present Situation of Study of Gas-Liquid-Solid Three Phase Flow, Text of Lecture Course, Jpn. Soc. Mech. Eng. 100th Lecture Course, p43(1982) (in Japanese)

[4]Giot,M., 7.2. Three-Phase Flow, in Hand book of Multiphase Systems (edit. by Hetsroni,G.), Hemisphere-Mcgraw-Hill, p7-29(1982)

[5]Sakaguchi,T, Present Situation of Study of Gas-Liquid-Solid Three Phase Flow (1), Science of Machine, 35-10, p.1113(1983)(in Japanese).

[6]Sakaguchi,T , Present Situation of Study of Gas-Liquid-Solid Three Phase Flow (2), Science of Machine, 35-11, p.1259(1983)(in Japanese).

[7]Sakaguchi,T., Flow Characteristics of Three Phase Flow, 2nd Symp. Multiphase Flow, by Academic Scence of Japan, p.171(1983)(in Japanese).

[8]Toda,M. and Konno,H., Fundamentals of Gas-Liquid-Solid Three Phase Flow, 1-2, 139-156, p.139(1987)(in Japanese)

[9]Sakaguchi,T., Gas-Liquid-Solid Three Phase Flow, Throw a fresh light on this dark field!, Trans. JSME., 54-503, p.1549 (1988)(in Japanese).
[10]Sakaguchi,T., Flow Characteristics of Gas-Liquid-Solid Three Phase Flow in Pipes, Proc. of Int. Conf. on Multiphase Flows '91 Tsukuba, Vol.3, p.61 (1991)
[11]Ostergaad,K., Chap.18, Three Phase Fluidization, in Fluidization (edit. by Davidson,J.F. and Harrison,D.), Academic Press, p.751 (1971)
[12]Shah,Y.T., Gas-Liquid-Solid Reactor Design, McGraw-Hill, (1977)
[13]Daeton,R.C., Chap.15, The Physical Behaviour of Three-Phase Fluidized Beds, in Fluidization (edit. by Davidson,J.F. and Harrison,D.), Academic Press, p.495 (1985).
[14]Theofanous,T.G., Multiphase Flows in Nuclear Reactor Sevier Accident, Proc. of The 2nd International Conference of Multiphase Flow, Vol.3(1995)
[15]For example, Clift et al., Bubble, Drops, and Particles, Academic Press (1978)
[16]White et al., The velocity of Rise of Single Cylindrical Air Bubbes through Liquids Contained in Vertical Tubes, Chem. Eng.Sci., 17 351-361 (1962)
[17]Hamaguchi,H. and Sakaguchi,T., Shape of Nose of Large Bubble Rising in Stationary Liquid in Vertical Tubes, Proc of the ASME-JSME Thermal Eng. Joint Conf. Vol.2, 69-74 (1995)
[18]Einstein,A., The Theory of Brownian Movement , New York, Dover, (1956)

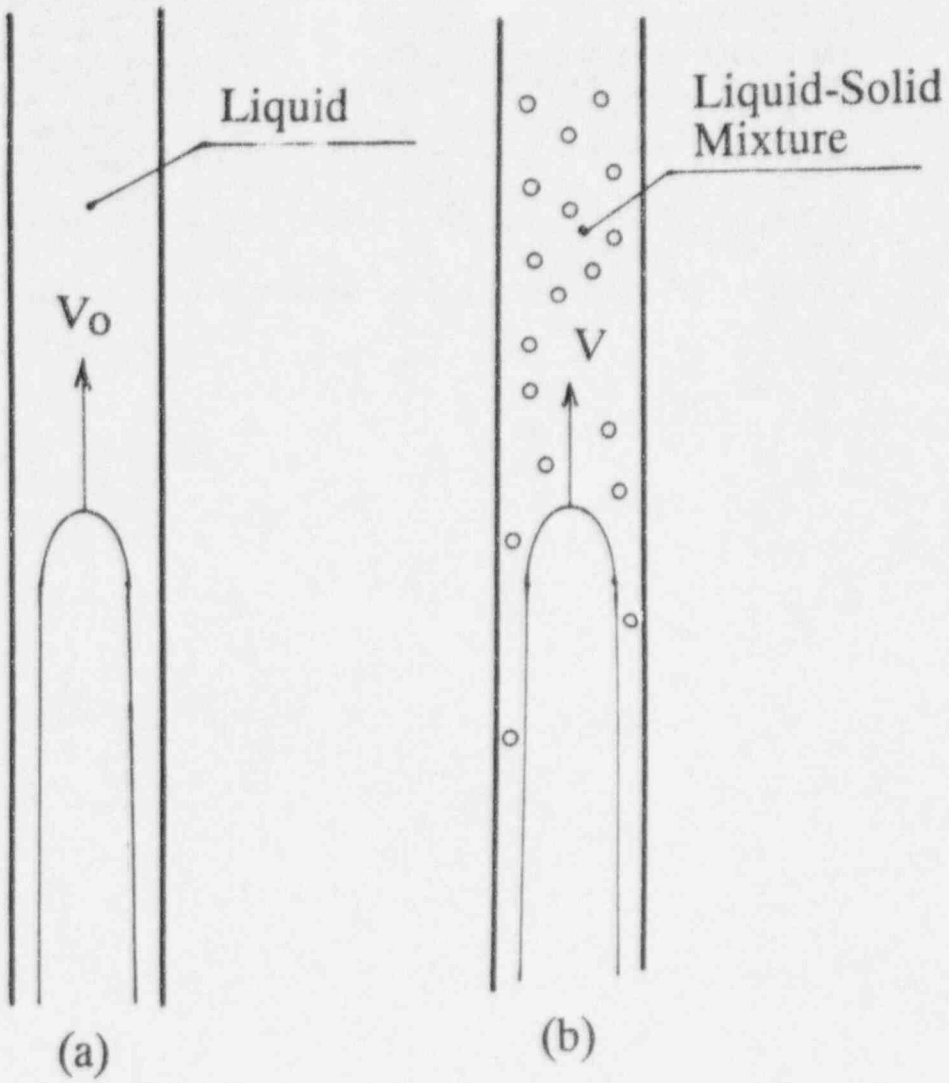

Fig.1 Large bubble

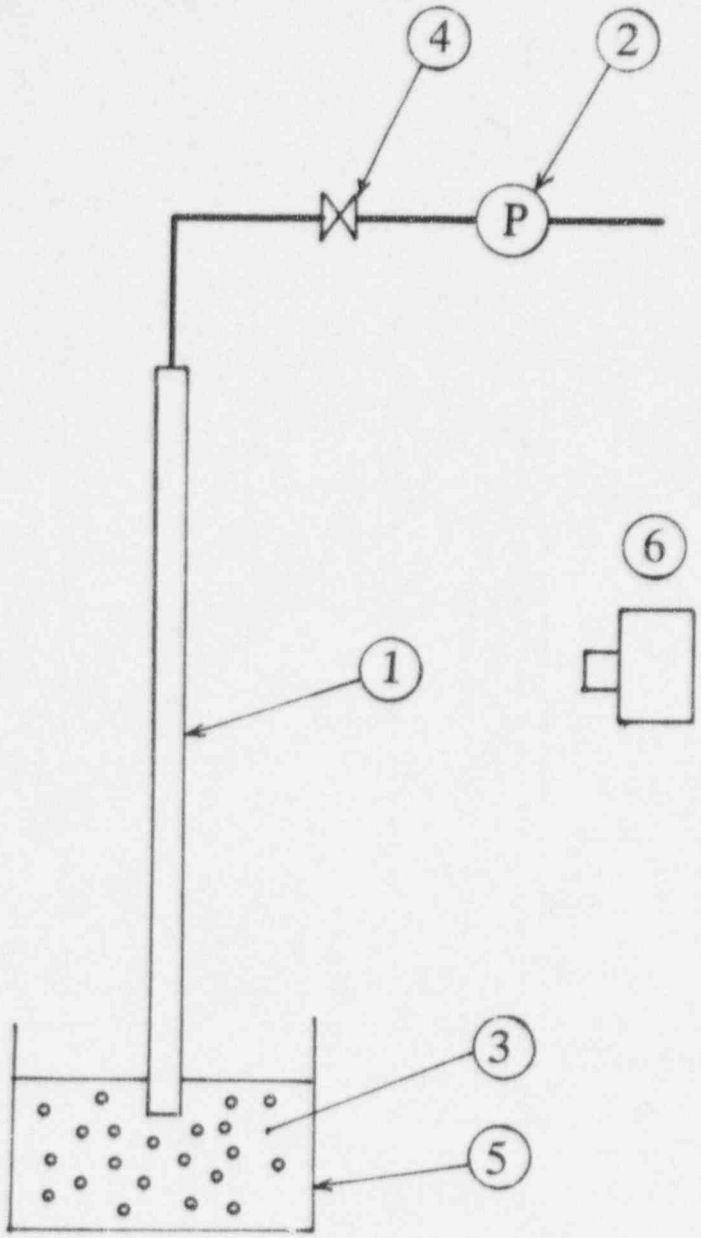

Fig.2 Experimental Appararus

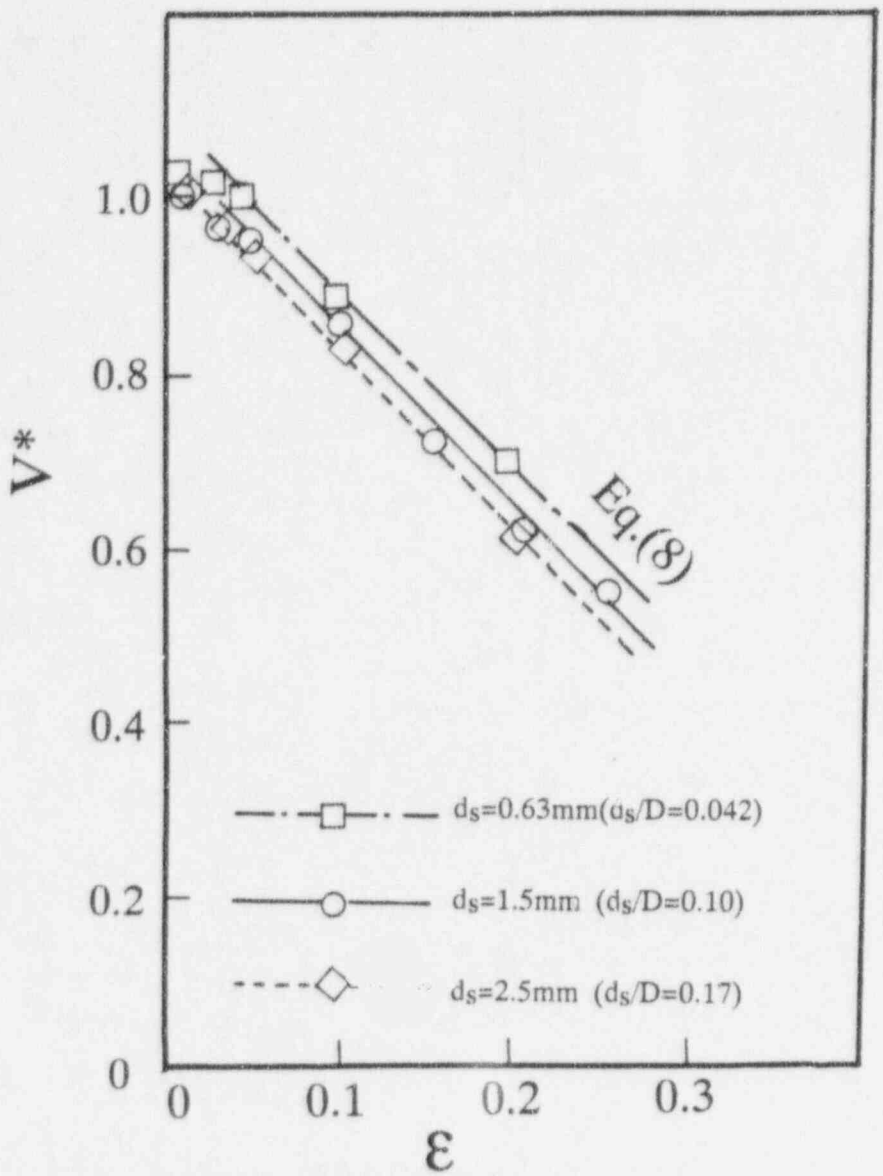

Fig.3 Experimental Results in condition 1

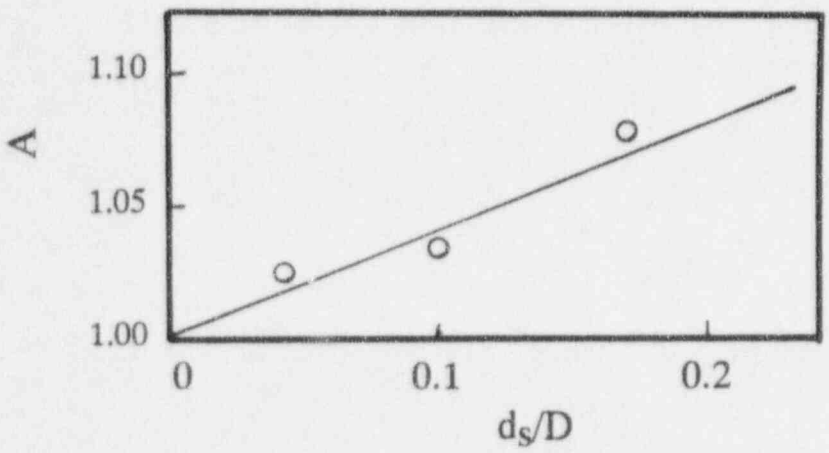

Fig.4 Relation between the value A and d_S/D

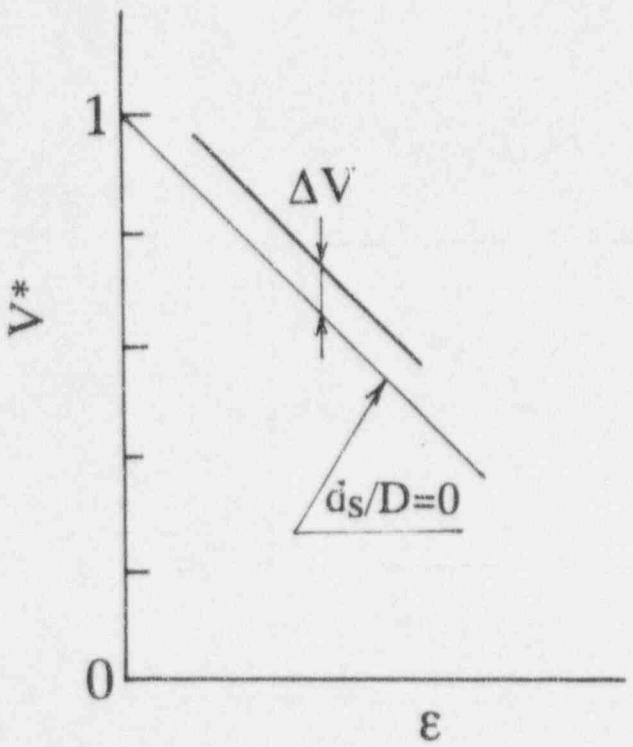

Fig.5 Increment ΔV in non - dimensional velocity

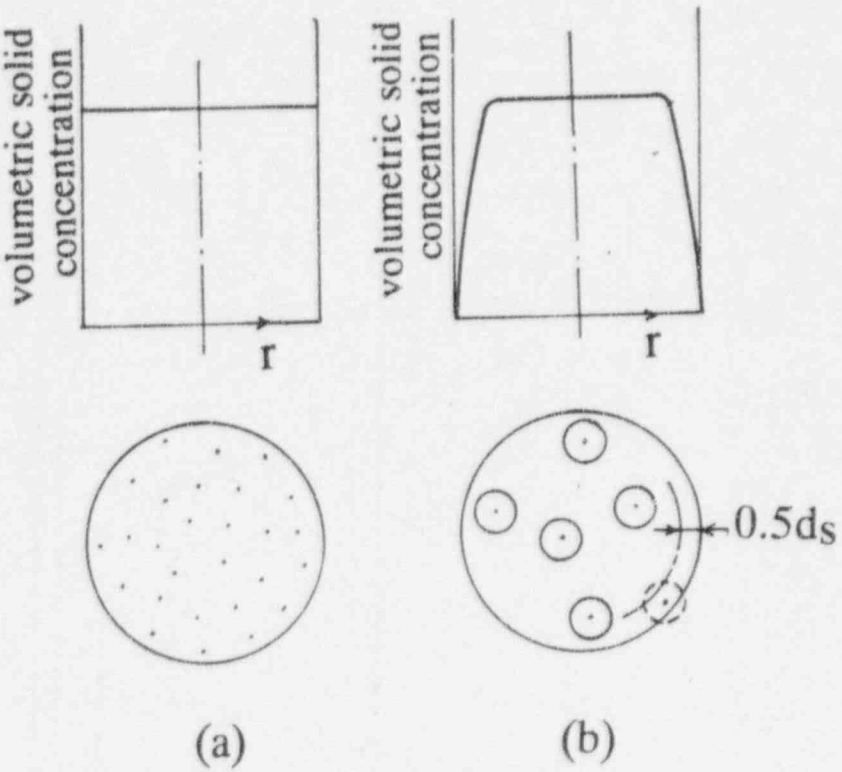

Fig.6 Distribution of particle

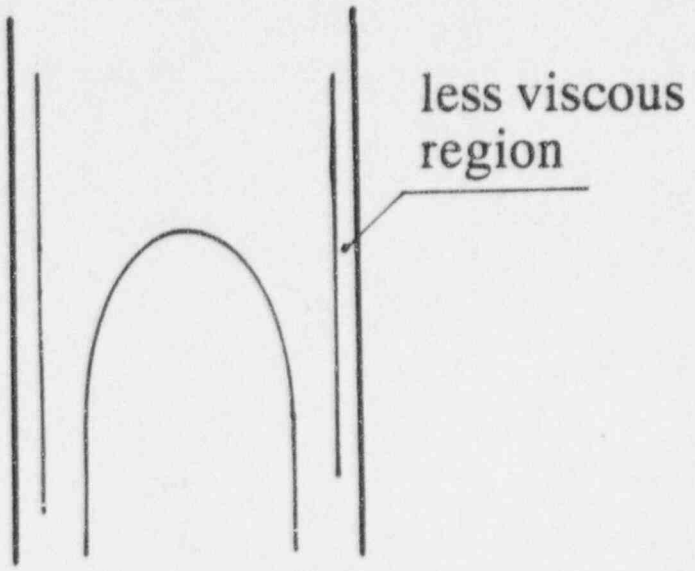

Fig.7 Movement of a large bubble in liquid whose viscosity is not uniform

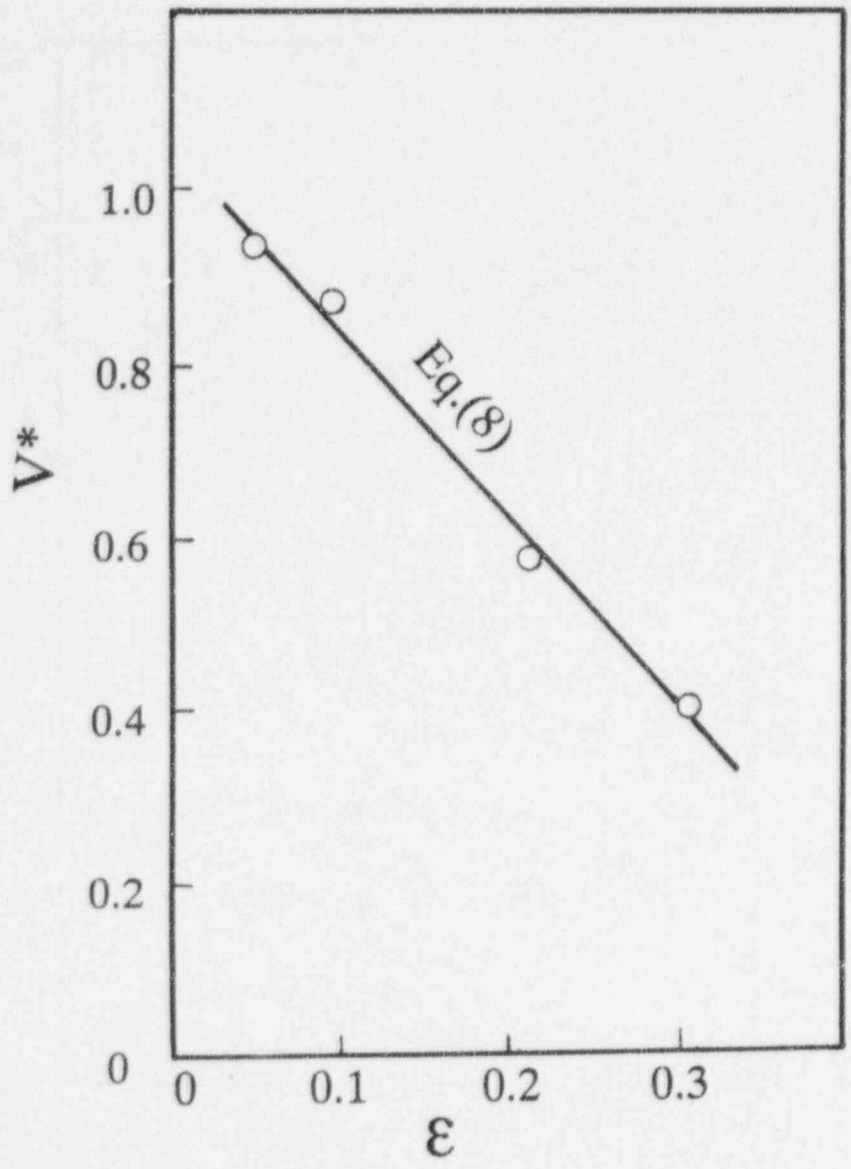

Fig.8 Experimental results in condition 3

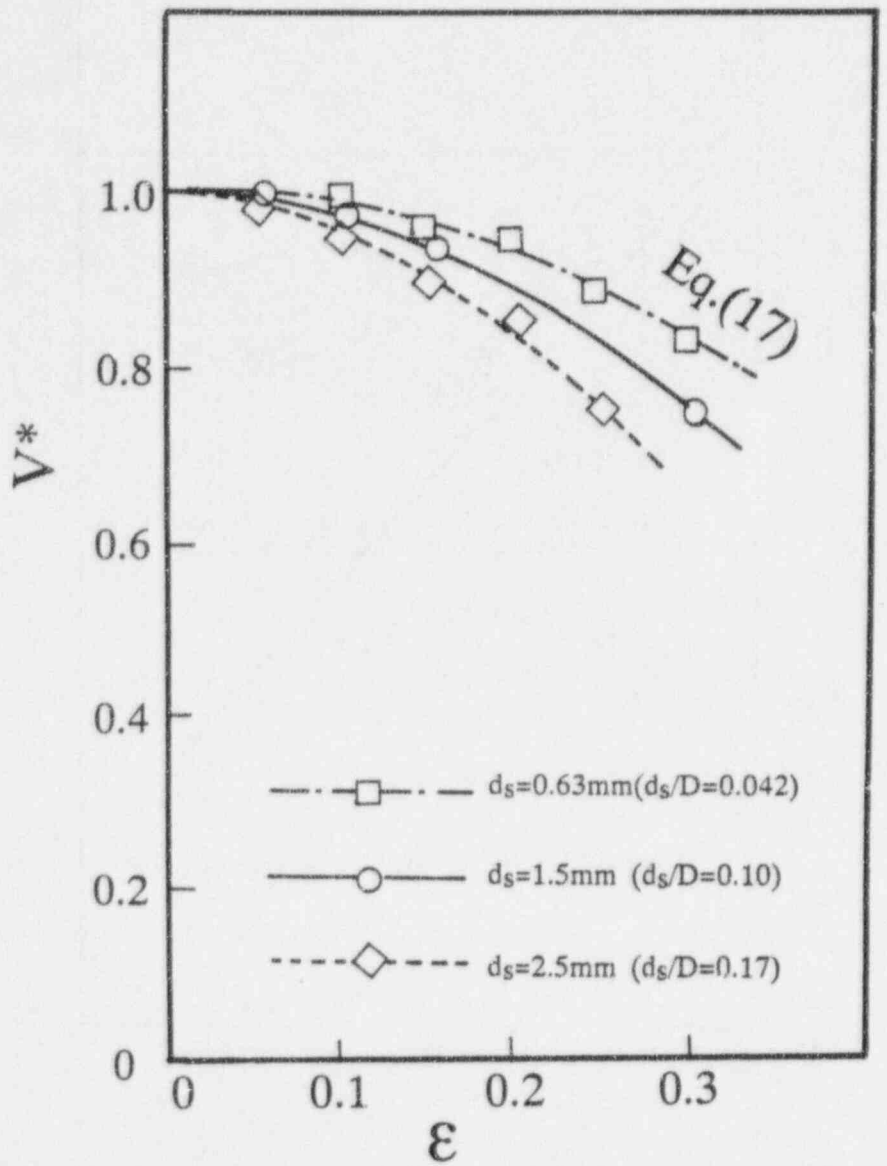

Fig.9 Experimental results in condition 2

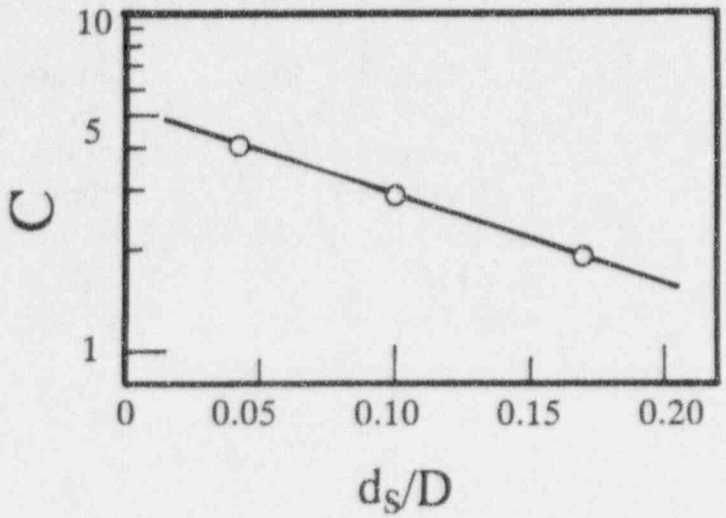

Fig.10 Relation between the value C and d_S/D

Table 1 Experimental condition

Condition 1	Condition 2	Condition 3
D=15mm	D=15mm	D=5mm
ν=350mm^2/s	ν=50mm^2/s	ν=50mm^2/s
d_S=0.63 to 2.5mm	d_S=0.63 to 2.5mm	d_S=0.63mm
Eo=110	Eo=110	Eo=12
Ga=270	Ga=13500	Ga=500

About the Statistical Description of Gas-Liquid Flows

D. Sanz, G. Guido-Lavalle, P. Carrica and A. Clausse[1]
Centro Atómico Bariloche and Instituto Balseiro
8400 Bariloche. ARGENTINA

Abstract

Elements of the probabilistic geometry are used to derive the bubble coalescence term of the statistical description of gas liquid flows. It is shown that the Boltzmann's hypothesis, that leads to the kinetic theory of dilute gases, is not appropriate for this kind of flows. The resulting integro-differential transport equation is numerically integrated to study the flow development in slender bubble columns. The solution remarkably predicts the transition from bubbly to slug flow pattern. Moreover, a bubbly bimodal size distribution is predicted, which has already been observed experimentally.

1. Introduction

The statistical description of two-phase flows is increasingly been used by different researchers [1-5]. It may be applied *per se* to some specific problems, or it may complement two-fluid models [6-8] by providing the urgently needed closure laws. In dispersed gas-liquid flows, it has been used to derive transport equations for bubble (or droplet) number density or interfacial area density. In most of the formulations within the statistical description, the concepts developed in the kinetic theory of gases —and used later in particulate flow technology— have been applied naively to gas-liquid flows. However, the description of this kind of flows poses some specific problems; namely, the non-negligible volume occupied by the dispersed phase and its deformable boundary. Another feature is that the flow regime determines whether the dispersed phase is liquid or gas, which may change considerably the properties of the flow [9-12].

[1] Author to whom correspondence should be addressed.

The purpose of this paper is to use the elements of probabilistic geometry to develop a consistent basis for a transport equation of two-phase flows. It will be shown that in doing so, some unexplained experimental results are clarified.

2. Theory

The statistical theory of two-phase flows is based upon the definition of the bubble volume distribution function $f(\mathcal{V}, \vec{x}, t)$. The definition is such that $f(\mathcal{V}, \vec{x}, t)\, d\mathcal{V}$ is the number of bubbles per unit volume, with volumes between $\mathcal{V}$ and $\mathcal{V} + d\mathcal{V}$, located in a volume $d\vec{x}$ around $\vec{x}$, at time t. This definition is convenient since the variables used to describe multiphase flows —such as void fraction or interfacial area density— are simply obtained as volume moments of the distribution function:

- *Number Density:*
$$N''' = \int_0^\infty f(\mathcal{V}, \vec{x}, t)\, d\mathcal{V}, \tag{1}$$

- *Void Fraction:*
$$\alpha = \int_0^\infty \mathcal{V}\, f(\mathcal{V}, \vec{x}, t)\, d\mathcal{V}\ , \text{ and} \tag{2}$$

- *Interfacial Area Density:*
$$A''' = \int_0^\infty s(\mathcal{V})\, f(\mathcal{V}, \vec{x}, t)\, d\mathcal{V}, \tag{3}$$

where $s(\mathcal{V})$ is a function that must be provided relating the individual volume and area of the dispersed phase. Finally, a derived quantity is the

- *Mean Volume:*
$$\hat{\mathcal{V}} = \frac{\int_0^\infty \mathcal{V}\, f(\mathcal{V}, \vec{x}, t)\, d\mathcal{V}}{\int_0^\infty f(\mathcal{V}, \vec{x}, t)\, d\mathcal{V}} = \frac{\alpha}{N'''}\ . \tag{4}$$

A transport equation can be written for the distribution function as [2,4]:

$$\frac{\partial}{\partial t} f(\mathcal{V}, \vec{x}, t) + \nabla \cdot \left(\vec{V}\, f(\mathcal{V}, \vec{x}, t)\right) = C(\mathcal{V}, \vec{x}, t) + B(\mathcal{V}, \vec{x}, t) + S(\mathcal{V}, \vec{x}, t) \tag{5}$$

The r.h.s. of Eq. (5) is composed of three terms: bubble breakup, coalescence and source, respectively. There is a wide agreement that the breakup term should be written as:

$$B(v,\vec{x},t)=\int_{v}^{\infty} b(v,u-v|u)\,f(u,\vec{x},t)\,du - \int_{0}^{v} b(u,v-u|v)\,f(v,\vec{x},t)\,du \tag{6}$$

where $b(v,u-v|u)$ is the breakup kernel function, which gives the probability per unit time that a bubble of volume u breaks into two bubbles of volumes v and $u-v$. The first term of the r.h.s. takes into account the production of bubbles having volume v due to the shattering of bigger bubbles, and the second removes bubbles due to the correspondent breakup.

The correct calculation of the coalescence term of the transport equation is one of the main objectives of this paper. It can be written as [13-15]:

$$C(v,\vec{x},t)=\frac{1}{2}\int_{0}^{v}\gamma(v-u,u)\,T(v-u,u,\vec{x},t)\,du - \int_{0}^{\infty}\gamma(u,v)\,T(v,u,\vec{x},t)\,du \tag{7}$$

where $T(v,u,\vec{x},t)$ gives the collision probability per unit time between bubbles of volume v and u, and $\gamma(v,u)$ is the probability that a collision of such bubbles results in a coalescence.

Most authors use Boltzmann hypothesis to express the collision probability [14,16]. The assumptions made are: uncorrelated particle positions (Boltzmann's *stosszahlansatz*), and that the volume occupied by the particles is negligible compared with the total volume. These assumptions lead to

$$T(v,u,\vec{x},t)=a\,f(v,\vec{x},t)\,f(u,\vec{x},t), \tag{8}$$

with a being a coefficient which may depend on v and u. Eq. (8) closes the system, but both assumptions are clearly non-realistic in gas-liquid two-phase flows.

To calculate the collision probability per unit time, let us use the concepts developed in the probabilistic geometrical theory [17]. Consider a space occupied by a spatially homogeneous distribution of fixed spheres, with their volumes randomly distributed according to the function $f(v)$.

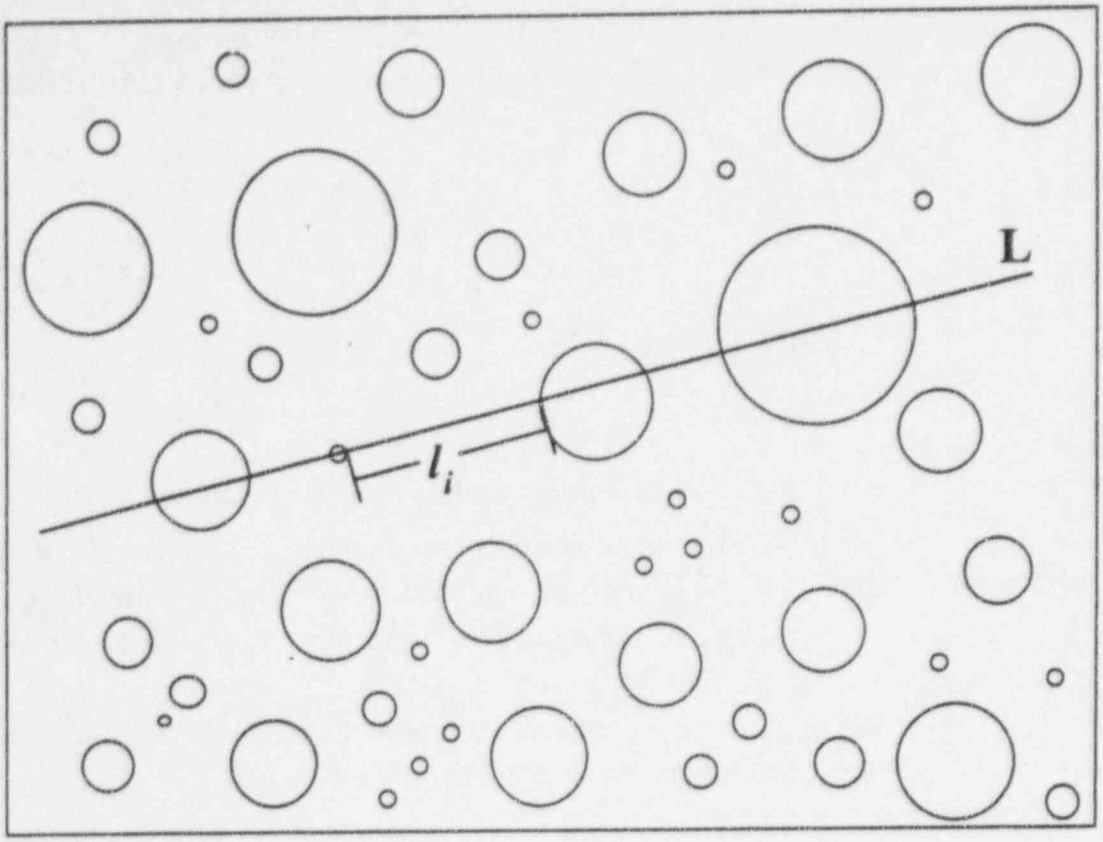

Fig. 1. The segment L intersects the gas of spheres, defining the external chords l_i.

Consider a straight line of length L, intersecting several spheres as shown in Fig. 1. The average external chord is defined as:

$$\langle l \rangle = \frac{\sum_{i=1}^{I(L)} l_i}{I(L)} \tag{9}$$

where $I(L)$ is the number of spheres intersected by the segment, and l_i is the *i-th* external chord.

The chordal void fraction is defined as the fractional part of a line touched by spheres, that is:

$$\alpha_L = \frac{L - \sum_{i=1}^{I(L)} l_i}{L}. \tag{10}$$

In homogenous media the chordal, area-averaged and volumetric void fractions are all the same, $\alpha_L = \alpha_A = \alpha_V = \alpha$.

A sphere will be penetrated by the line if its center lies in a cylinder of axis L, and radius equal to the sphere radius. Therefore, the number of intersected spheres with volumes between $\mathcal{V}$ and $\mathcal{V}+d\mathcal{V}$ is

$$I(\mathcal{V},L)\,d\mathcal{V} = \pi R^2(\mathcal{V})\,L\,f(\mathcal{V})\,d\mathcal{V}. \tag{11}$$

The total number of spheres intersected by the segment is:

$$I(L) = \int_0^\infty I(\mathcal{V},L)\,d\mathcal{V} = \frac{L\,A'''}{4}. \tag{12}$$

The mean external chord length may be calculated combining Eqs. (9), (10) and (12):

$$\langle l \rangle = \frac{4(1-\alpha)}{A'''}, \tag{13}$$

which does not depend on the arbitrary length L, as expected. This important result may also be generalized to a distribution of convex bodies, different than spheres [17].

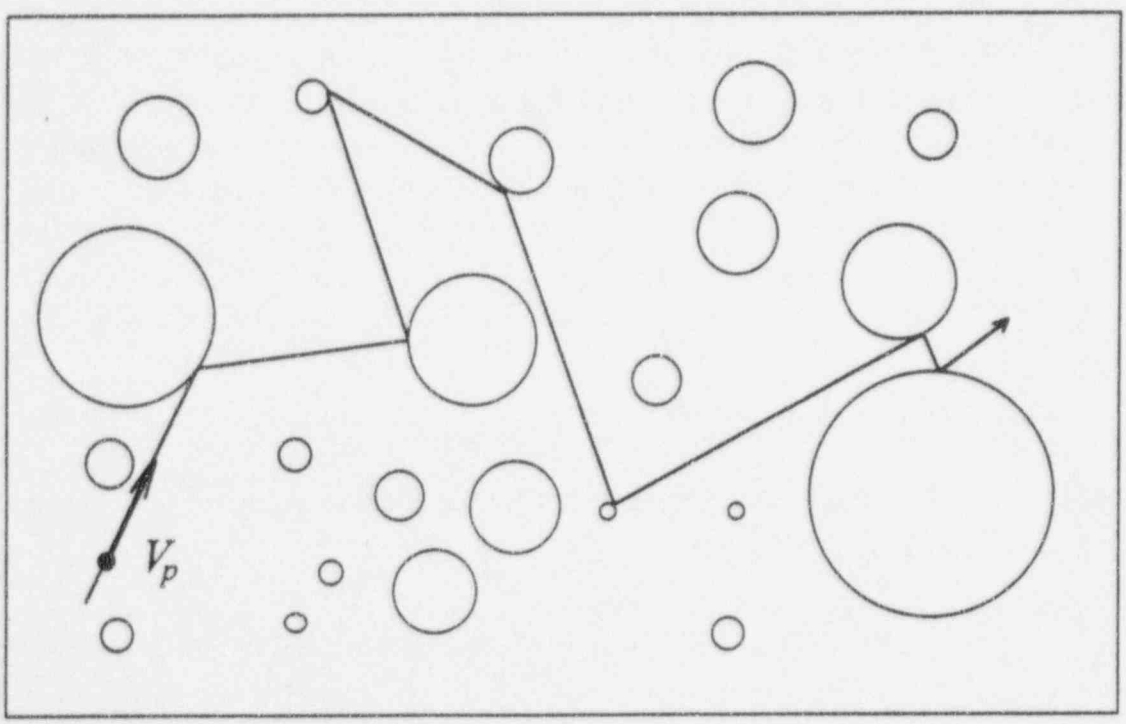

Fig. 2. Moving point within a gas of spheres reflecting at each collision with a random distribution of angles external to the spheres.

Now consider a point moving in this stationary gas of spheres with velocity V_P. Each time the point collides with a sphere it is reflected at any angle external to the sphere with the same probability, as shown in Fig. 2. The collision rate of the moving point against the spheres is given by:

$$T_P = \frac{V_P}{\langle l \rangle}. \tag{14}$$

The fraction of these clashes that corresponds to bubbles of volumes between $\mathcal{V}$ and $\mathcal{V}+d\mathcal{V}$ is given by

$$P(\mathcal{V})d\mathcal{V} = \frac{I(\mathcal{V},L)d\mathcal{V}}{\int_0^\infty I(\mathcal{V},L)d\mathcal{V}} = \frac{4\pi R^2(\mathcal{V})}{A'''} f(\mathcal{V})d\mathcal{V} . \tag{15}$$

Combining Eqs. (13) to (15), the collision rate of the point with bubbles of volumes in the interval $(\mathcal{V},\mathcal{V}+d\mathcal{V})$ results

$$T_P(\mathcal{V})d\mathcal{V} = T_P\, P(\mathcal{V})d\mathcal{V} = \frac{\pi V_P R^2(\mathcal{V})}{(1-\alpha)} f(\mathcal{V})d\mathcal{V} \tag{16}$$

Consider now a moving sphere of volume $\mathcal{U}$. The collision frequency with spheres of volume $\mathcal{V}$ is the same as that of a point interacting with the target spheres with their radii incremented to $R(\mathcal{V})+R(\mathcal{U})$ (see Fig. 3). Therefore, the double differential collision rate is obtained from Eq. (16) as:

$$T(\mathcal{U},\mathcal{V})d\mathcal{U}\,d\mathcal{V} = \frac{\pi V_r(\mathcal{U},\mathcal{V})[R(\mathcal{U})+R(\mathcal{V})]^2}{(1-\alpha)} f(\mathcal{U})f(\mathcal{V})\,d\mathcal{U}\,d\mathcal{V} \tag{17}$$

where the point velocity has been replaced by the relative velocity between bubbles of volumes $\mathcal{U}$ and $\mathcal{V}$, $V_r(\mathcal{U},\mathcal{V})$.

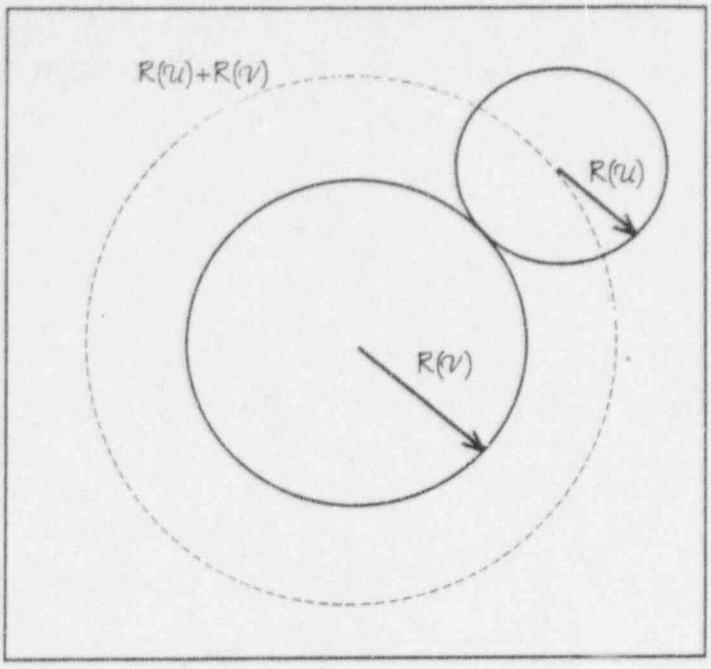

Fig. 3. The collision of a moving sphere of volume $\mathcal{U}$, with another of volume $\mathcal{V}$, is equivalent to consider the collision of a point with a sphere of radius $R(\mathcal{U})+R(\mathcal{V})$.

The collision rate, Eq. (17), closes the system composed of Eqs. (5), (6) and (7). Worth noting is the difference with the collision probability that results from Boltzmann's hypothesis, Eq. (8). The major difference is the factor $1/(1-\alpha)$, since the other volume-dependent parameters may be included in the coefficient a of Eq. (8). The factor is identical to that obtained by Enskog [16,18] for dense gases, and recently used in two-phase flow models [4,19]. The factor has a clear physical meaning: when the void fraction tends to unity, the collision rate tends to infinity. The bubbles are said to be "locked in place".

3. Bubble Columns

Let us apply the above-presented theory to predict bubble distributions in a bubble column; *i.e.*, a column of stagnant liquid with a free surface in which a gas is introduced at the bottom (see Fig. 4). The steady-state will be analyzed using a one-dimensional model, and negligible breakup will be assumed, which was observed in low turbulence flows.

To calculate the bubble velocities, experimental values of the terminal velocity in tubes [20] are used in conjunction with the drift-flux model [21] to account for

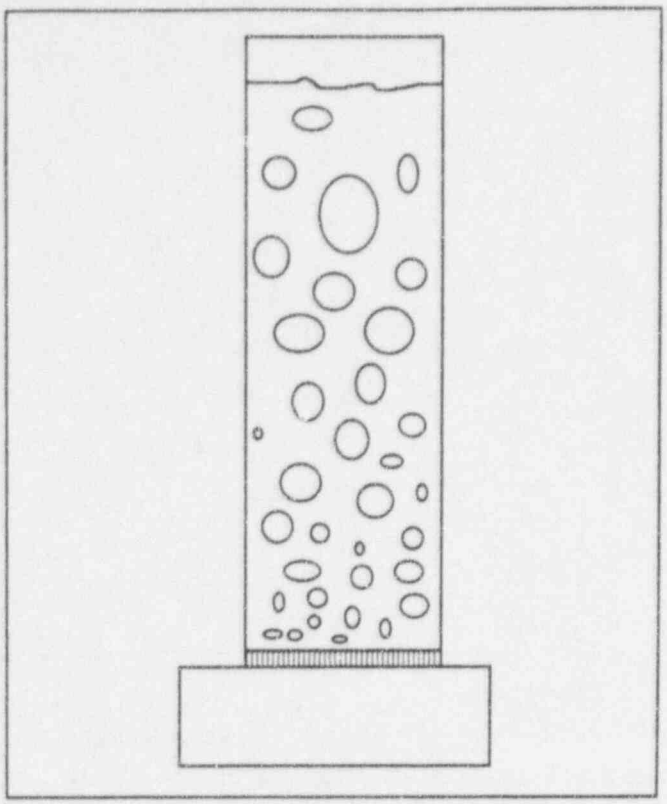

Fig. 4. Schematic diagram of a bubble column. Gas is injected through the bottom of tube containing a stagnant liquid.

bubble interactions; which results in

$$V(\mathcal{V},D) = V_{\infty}(\mathcal{V},D) + C_0(D)\, j, \tag{18}$$

where the left-hand side represents the actual velocity of bubbles of volume $\mathcal{V}$ in a tube of diameter D. It depends on the terminal velocity of such bubbles, $V_{\infty}(\mathcal{V},D)$, on the volumetric flux j, and on the so-called distribution parameter, C_0. A typical plot of the terminal velocity as a function of bubble volume is shown in Fig. 5.

Under the mentioned hypothesis, the transport equation of the distribution function at steady-state is given by:

$$\frac{\partial}{\partial z}\left[f(\mathcal{V},z)\; V(\mathcal{V},D)\right] = C^{+}(\mathcal{V},z) - C^{-}(\mathcal{V},z)\,, \tag{19}$$

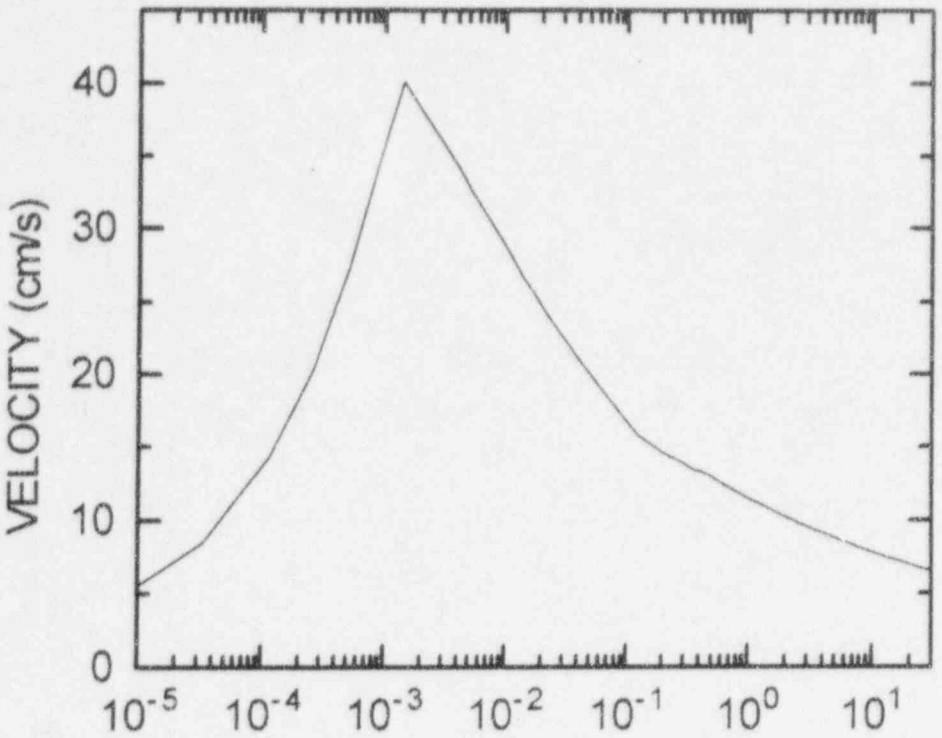

Fig. 5. Typical diagram of velocity *vs.* volume for rising gas bubbles in a liquid contained in a tube [20].

where the coalescence gain and loss are given by

$$C^{+}(v,z)=\frac{\pi\gamma}{2[1-\alpha(z)]}\int_{0}^{v}V_r(v-u,u)\left[R(v-u)+R(u)\right]^2 f(v-u,z)f(u,z)\,du \tag{20}$$

$$C^{-}(v,z)=\frac{\pi\gamma}{[1-\alpha(z)]}f(v,z)\int_{0}^{\infty}V_r(v,u)\left[R(v)+R(u)\right]^2 f(u,z)\,du \tag{21}$$

In Eqs. (20) and (21) a constant coalescence probability, $\gamma(v,u,u)=\gamma$, was assumed.

Taking the volume first-order moment of Eq. (19) results:

$$\frac{d}{dz} j(z) = \int_0^\infty v\, C^+(v,z)\, dv - \int_0^\infty v\, C^-(v,z)\, dv, \qquad (22)$$

where

$$j(z) = \int_0^\infty v\, f(v,z)\, V(v)\, dv. \qquad (23)$$

is the total volumetric flux since there is no net flow of liquid.

Note that j is directly related to the velocity of the center of volume, $\bar{V}$ that is:

$$\bar{V} = \frac{\int_0^\infty v\, f(v,z) V(v)\, dv}{\int_0^\infty v\, f(v,z)\, dv} = \frac{j}{\alpha} \qquad (24)$$

After some calculation, and due to the symmetry with respect to the volume variables of the integrands of Eqs. (20) and (21), it can be shown that:

$$\int_0^\infty v\, C^+(v,z)\, dv = \int_0^\infty v\, C^-(v,z)\, dv, \qquad (25)$$

and therefore

$$\frac{d}{dz} j(z) = 0, \qquad (26)$$

which indicates, as expected, that the coalescence process does not change the total gas volume, and that the gas flow at steady-state does not vary along the axial coordinate of the channel.

3.1 Numerical Solution

Only under very particular conditions the distribution function transport equation has an analytic solution [13]. In most cases, a numerical procedure should be applied to solve the equation.

The case under analysis constitutes a boundary-value problem; that is, the volume distribution should be specified at the inlet:

$$f(\mathcal{V}, z = 0) = f_0(\mathcal{V}), \tag{27}$$

which determines the volumetric flux as calculated by means of Eq. (23). To solve the transport equation, Eq. (19), an explicit finite-differences scheme was adopted for the spatial variable. Concerning the integral equation that results, at a given location, for the volume variable, a multigroup procedure was utilised. This combination gave a robust and efficient numerical scheme.

To obtain a whole picture of the different phenomena that occur in the bubble column, let us study the evolution that follows the injection of small bubbles. A square distribution function is assumed at the inlet as shown in Fig. 6a. The width and height of the distribution are such that the gas volumetric flux is of $j = 7.1\ cm/s$, the initial void fraction is $\alpha = 0.45$ and the correspondent number density $N''' = 6.10^3\ cm^{-3}$. These values are within the experimental range covered in Ref. [19], which will be used later for comparison.

The probability of coalescence, γ, was taken constant for simplicity (the extension to bubble volume dependencies may be the matter of future studies). Under this assumption, the effect of the coalescence probability, γ, is to change the length scale, provided that breakup terms are negligible, as can be seen in Eqs. (19) to (21). Therefore, in what follows the axial coordinate is taken as

$$\hat{z} = \gamma z. \tag{28}$$

The development of the distribution function along the tube is shown in Fig. 6. For the sake of clarity, the distribution is normalized to the same area below the curve. At the first stages of the coalescence process, a small peak appears to the right of the inlet bubbles (Fig. 6b, $\hat{z} = 0.3\ cm$). Downstream, the small peak grows developing a continuous distribution (Fig. 6c, $\hat{z} = 2.5\ cm$). These changes take place in a short distance as a consequence of the large number of bubbles present.

Further along the column a bimodal volume distribution function appears (Fig. 6d, $\hat{z} = 4.0\ cm$), which persists until about $\hat{z} = 30.0\ cm$ (Fig. 6e, $\hat{z} = 10.0\ cm$), with a progressive flattening of the large-volume peak. This is an important finding of the present theory, since such bimodal bubble volume distributions have been observed experimentally by different authors [19, 22], but remained unexplained. Its existence is related to the form of the velocity dependence shown in Fig. 5. The minimum of the volume distribution function coincides with the volume at which the velocity has a maximum. In fact, since bubble volume and velocity are related, the velocity distribution function, $g(V)$, may be constructed satisfying:

$$f(\mathcal{V})\, d\mathcal{V} = g(V)\, dV. \tag{29}$$

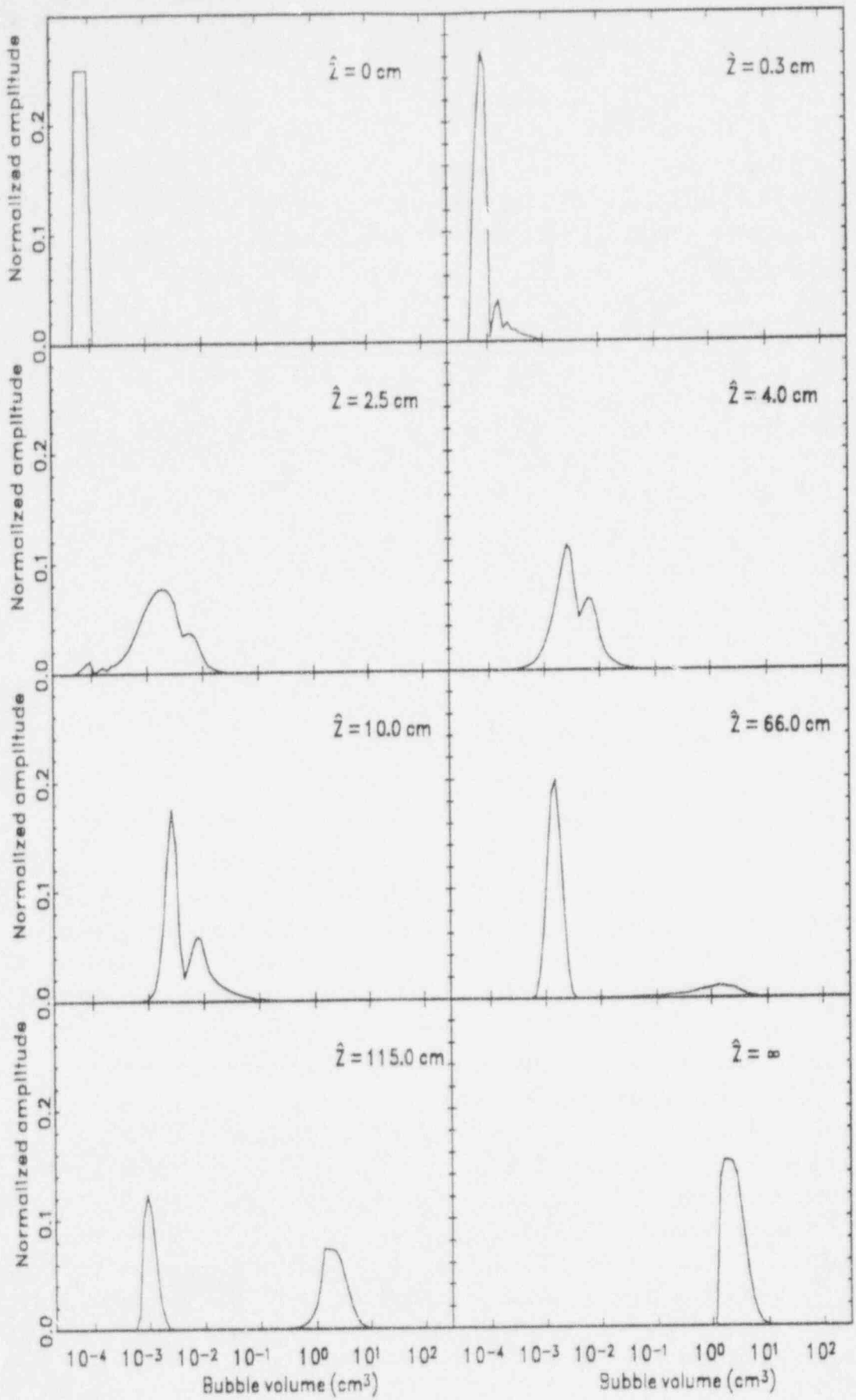

Fig. 6. Evolution of the bubble distribution function along the column.

Therefore, if the velocity distribution function does not go to infinity —which cannot occur if it is not a Dirac delta function—, the volume distribution has zeros where $dV/dv = 0$; *i.e.*, at the velocity maximum, which is the case shown.

Proceeding with the calculation, a new peak appears at bubble volumes between cm^3 and $0\ cm^3$ (Fig. 6f, $\hat{z} = 66\ cm$), which grows as the other shrinks (Fig. 6g, $\hat{z} = 115\ cm$). This second bimodality corresponds to the appearance of the slug flow pattern. The above-mentioned volumes correspond to Taylor bubbles, and the smaller ones are the typical satellite bubbles observed in this flow pattern [23]. As the velocity of the Taylor bubbles is independent of their volume ([20, 23], see figure 5), they do not coalesce with each other ($V_r = 0$, Eq. 17) and fully development is achieved (Fig. 6h, $\hat{z} = \infty$).

The global evolution of the distribution function can be observed in the 3-D plot showed in Fig. 7, keeping in mind that it was normalized at each axial location. The disappearance of the inlet bubbles gives rise to the bimodal bubbly flow for axial coordinates between $0.5cm$ and $15cm$. At $60cm$ Taylor bubbles appear, developing a slug flow pattern with satellite bubbles. The latter finally disappear —since breakup was precluded— resulting in a continuous train of plugs.

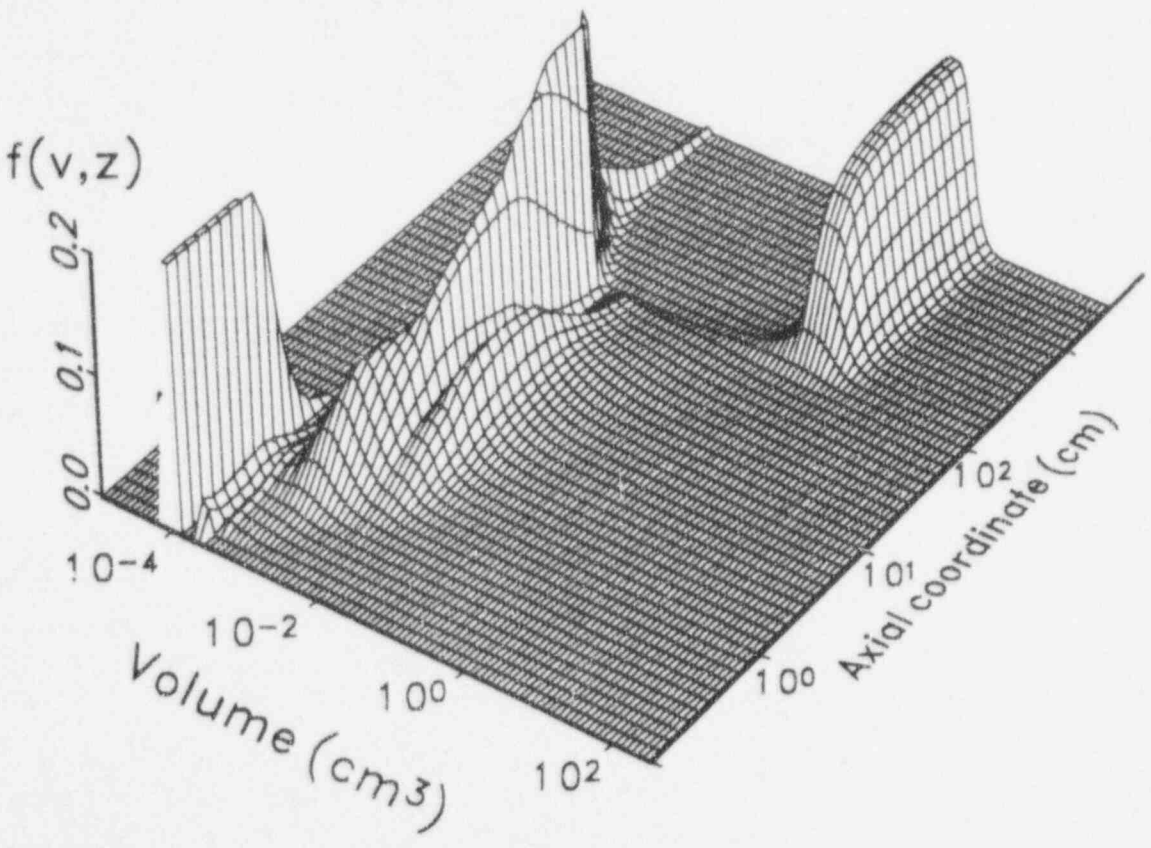

Fig. 7. The distribution function at each spatial location plotted in 3-D.

To complete the picture the void fraction occupied by each bubble volume, $v\,f(v)$, is shown in Fig. 8. The major contribution to the void fraction comes from the bigger bubbles, which dominate volume related phenomena such as neutron moderation. On the other hand, the smaller bubbles predominate in most of the development region, as can be seen in Fig. 9, where the partial number density profiles are depicted for comparison.

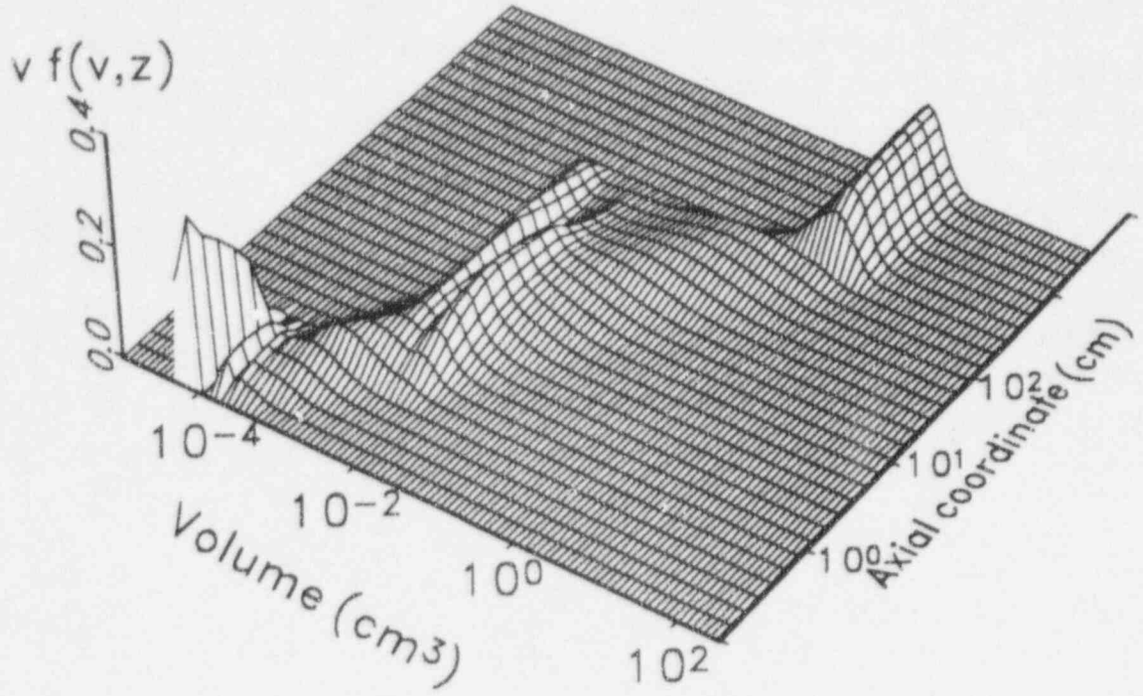

Fig. 8. Void fraction distribution occupied by bubbles of different volumes as a function of the axial positions.

4. Conclusions

The statistical description of gas-liquid two-phase flows is increasingly been used by different researchers to describe several relevant phenomena. However, there is a lack of agreement concerning primarily the mathematical form of the coalescence term of the bubble distribution function transport equation.

In this paper, elements of probabilistic geometry were used to derive the appropriate form of the coalescence kernel. It was shown that the collision frequency increases with the inverse of the liquid volume fraction, which agrees with its analogous in the kinetic theory of dense gases originally developed by Enskog.

The resulting integro-differential transport equation was integrated numerically to study the steady-state of a bubble column; *i.e.*, the evolution of gas bubbles in a tube containing stagnant liquid. The numerical scheme consisted of an

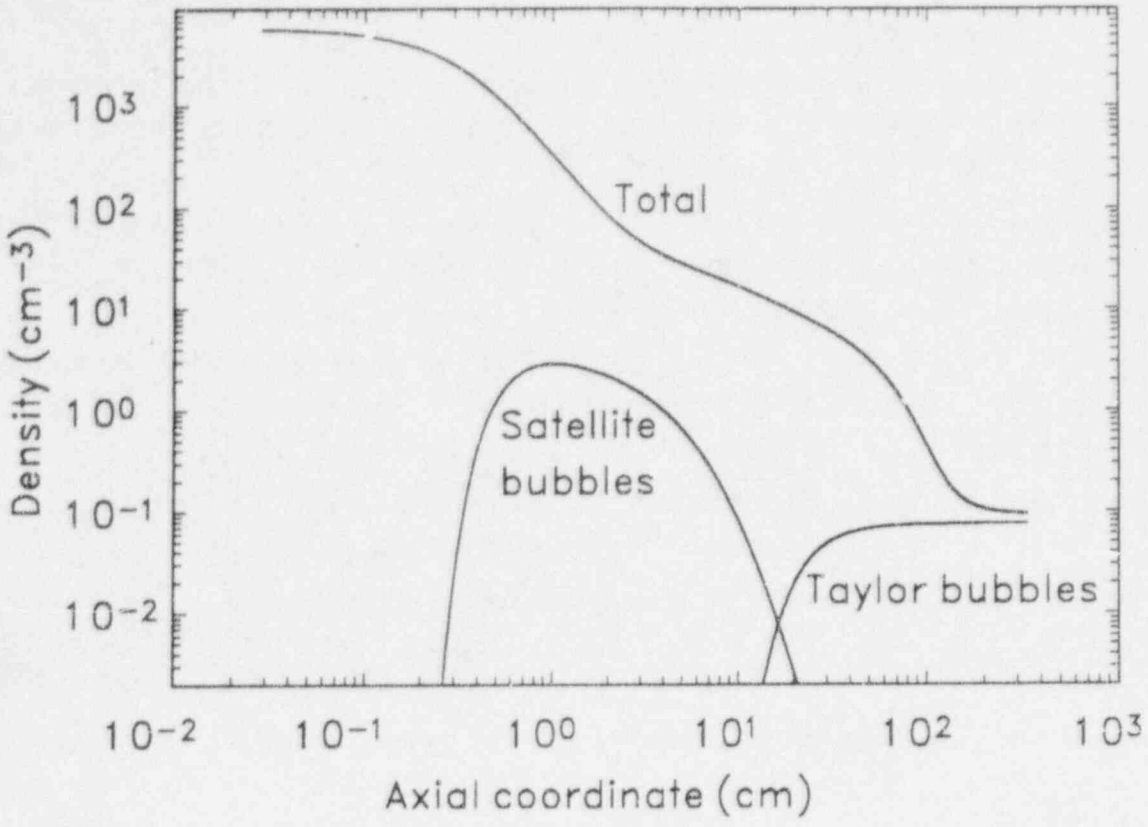

Fig. 9. Evolution of the bubble number density. Also shown is the fraction that corresponds to satellite and Taylor bubbles.

explicit method to solve for the axial location, and a multigroup calculation for the volume variable.

The results showed the formation of a bubbly flow with a bimodal distribution of bubble volumes. This is in accordance with previous experimental results, and it was shown that is due to the existence of a maximum in the bubble velocity as a function of their volume. Downstream along the tube a slug flow pattern, with Taylor and satellite bubbles, is developed. The large number of the smaller bubbles provides an important part of the total interfacial area density, which dominates area controlled phenomena such as mass exchange between phases, while the Taylor bubbles are responsible for almost all of the void fraction, which is the relevant quantity in volume dominated effects such as neutron thermalization.

Acknowledgements

The authors greatly appreciate the useful contributions of D. Zanette and G. Buscaglia.

5. References

[1] J.L. Achard, *Contribution à l'Étude Théorique des Écoulements Diphasiques en Régime Transitoire*. Ph.D. Thesis, Univ. Scientifique et Medicale et Institut National Polytechnique de Grenoble, Grenoble, 1978.

[2] S. Navarro-Valenti, A. Clausse, D.A. Drew and R.T. Lahey, Jr., *A Contribution to the Mathematical Modeling of Bubbly/slug flow regime transition. Chemical Engineering Communications* **102** (1991) 69.

[3] R.T. Lahey, Jr., D.A. Drew, S. Kalkach and J-W. Park, The Relationship Between Void Waves and Flow Regime Transition. *Int. Conf. on Multiphase Flow Instabilties*, Rouen, 1992.

[4] G. Guido-Lavalle, P. Carrica, M.K. Qazi and A. Clausse, A Bubble Number Density Constitutive Equation, *Nuclear Engineering and Design*, in press.

[5] G. Guido-Lavalle and A. Clausse, Application of the Statistical Description of Two-Phase Flows to Interfacial Area Assessment, *Proceedings VIII Brazilian Meeting on Reactor Physics and Thermal Hydraulics*, 143-146, São Paulo, 1991.

[6] M. Ishii, *Thermo-Fluid Dynamic Theory of Two-Phase Flows*, Eyrolles, Paris, 1972.

[7] J.M. Delhaye, Jump Conditions and Entropy Sources in Two-Phase Systems. Local Instant Formulation, *Int. J. Multiphase Flow* **1** (1974) 395-409.

[8] J.A. Bouré, Multiphase Flow Modeling. *Seminar on Multiphase Processes in LMFBR Safety Analysis*, Ispra, 1980.

[9] Y. Taitel, D. Bornea and A.E. Dukler, Modelling Flow Pattern Transitions for Steady Upward Gas-Liquid Flow. *AIChE Journal* **26** (1980) 345-354.

[10] S.Z. Rouhani and M.S. Sohal, Two-Phase Flow Patterns: A Review of Research Results. *Progress in Nuclear Energy* **11** (1983) 219-259.

[11] N.K. Tutu, Pressure Drop Fluctuations and Bubble-Slug Transition in a Vertical Two Phase Air-Water Flow. *Int. J. Multiphase Flow* **10** (1984) 211-216.

[12] C.N. Strizzolo and J. Converti, Capacitance Sensors for Measurement of Phase Volume Fraction in Two-Phase Pipelines. *IEEE Transactions of Instrumentation and Measurement* **42** (1993) 726-729.

[13] M. Ernst, Model Boltzmann Equations. *Physics Reports* **1** xx (1981).

[14] C. Cercignani, *The Boltzmann Equation and its Applications*. Springer-Verlag, New York (1988).

[15] D. Ramkrishna, The Status of Population Balances, *Reviews in Chemical Engineering* **3** (1985) 49-95.

[16] N. Bellomo, M. Lachowicz, J. Polewczak and G. Toscani, *Mathematical Topics in Nonlinear Kinetic Theory. II: The Enskog Equation*. World Scientific, Singapore (1991).

[17] L.A. Santaló, *Integral Geometry and Geometric Probability*, Addison-Wesley Pub. Co. (1976).

[18] J.H. Ferziger and H.G. Kaper, *Mathematical Theory of Transport Processes in Gases*, North-Holland Pub. Co., New York (1972).

[19] G. Guido-Lavalle, *Formulación Estadística de Flujos Bifásicos: Teoría y Experimentos*, Ph.D. Thesis, Instituto Balseiro, Bariloche (1992).

[20] G.B. Wallis, *One-Dimensional Two-Phase Flow*, McGraw-Hill, New York, 1969.

[21] N. Zuber and J.A. Findlay, Average Volumetric Concentration in Two-Phase Systems, *J. Heat Transfer* **87** (1965) 453-468.

[22] D.A. Peterson, R.S. Tankin, Holographic Measurements of Bubble Size and Velocity in a Three-Phase System, *Symposium on Measuring Techniques in Gas-Liquid Two-Phase Flows*, Nancy, 1983.

[23] J. Fabre and A. Liné, Modeling of Two-Phase Slug Flow, *Annu. Rev. Fluid Mech.* **24** (1992) 21-46.

Nomenclature

A''': interfacial area density
a: parameter of Eq. (8)
B: breakup integral
b: breakup kernel
C: coalescence integral
c: coalescence kernel
C_o: distribution parameter
D: diameter
f: bubble distribution function
N''': number density
I: number of intersected spheres
j: gas volumetric flux
L: length
l: chord length
R: radius
S: bubble source
s: bubble interfacial area
t: time
T: collision probability
V: velocity
$\mathcal{U}, \mathcal{V}$ volume
x: position
z: axial coordinate

Superscripts

$\hat{}$: mean, generalized
$+$: gain
$-$: loss

Subscripts

A: area-averaged
L: chordal
r: relative
V: volumetric
∞: fully-developed
0: boundary-value

Greeks

α: void fraction
γ: coalescence probability

ENTROPY ANALYSIS ON NON-EQUILIBRIUM TWO-PHASE FLOW MODELS

H. Karwat and Y.Q.Ruan
Lehrstuhl für Reaktordynamik und Reaktorsicherheit
Technische Universität München, 85748 Garching, Germany

Abstract

A method of entropy analysis according to the second law of thermodynamics is proposed for the assessment of a class of practical non-equilibrium two-phase flow models. Entropy conditions are derived directly from a local instantaneous formulation for an arbitrary control volume of a structural two-phase fluid, which are finally expressed in terms of the averaged thermodynamic independent variables and their time derivatives as well as the boundary conditions for the volume. On the basis of a widely used thermal-hydraulic system code it is demonstrated with practical examples that entropy production rates in control volumes can be numerically quantified by using the data from the output data files. Entropy analysis using the proposed method is useful in identifying some potential problems in two-phase flow models and predictions as well as in studying the effects of some free parameters in closure relationships.

1 Introduction

In numerical simulation of thermal-hydraulic transient processes the quantities to be calculated are usually pressure, temperature, enthalpy, mass and heat flow rates etc., but seldom involving entropy properties. It is also seldom to check whether such predictions do not violate the second law of thermodynamics in the sense that the entropy production rate in a thermodynamic system must be non-negative.

Theoretical modeling and numerical simulation of a two-phase flow are enormously complicated by the presence of interfaces and related interfacial interactions. As a matter of fact, two-phase flow engineering calculation is still highly dominated by empiricism. This is indicated in particular by the use and the implementation of a large number of empirical or semi-empirical correlations containing adjustable parameters. But the range of validity of such models, the influences of adjustable factors on the results of prediction are often not well understood and quantified. Although a modern thermal-hydraulic system code can usually provide a quite flexible framework for the analysis of a wide spectrum of two-phase problems, the bases of mathematical-physics of the code may not be reliable enough to cover all the situations which are intended to be analyzed. Moreover, a practical problem is that when a code is applied outside the range of validity of the models, the code user is often not provided with any warnings from the computer program, but the predictions may even violate some general physical principles, e.g., the second law of thermodynamics.

Recently an interesting work is done by Arnold et al [1]. An entropy inequality devoid of derivatives of phasic entropy is obtained by combining the ensemble-averaged entropy and thermal energy balance equations for each phase with a simplified Gibbs relation. The result is

then applied to the assessment of the basic balance equations and constitutive relations used in some United States computer codes. It is demonstrated specifically for bubbly flow conditions that the model equations in these codes violate the entropy condition. The investigation reported in [1] concentrates mainly on the partial differential forms of basic balance equations and on the related constitutive relations. Unfortunately, the final two-phase flow models actually implemented in a computer code are often quite different from the analytical forms which may appear in the manual. For example, when a model system of partial differential equations is transformed into a set of ordinary differential equations or a set of finite difference equations, all model equations must be finally expressed in terms of averaged quantities in some sense. Thus, additional physical and numerical assumptions are introduced inevitably into the intermediate or the final numerical model. Therefore, we should also consider such more practical models in order to explore the usefulness of the second law of thermodynamics in the assessment of thermal-hydraulic computer codes.

In this paper we concentrate on a specific class of two-phase flow models which can be finally formulated in terms of ordinary differential equations by using averaged properties in control volumes and along flow paths. The main purpose here is to propose a practical method of entropy analysis. In the next section we derive the general expressions for the entropy production rates in an arbitrary control volume of a structural two-phase fluid. In Section 3 a method of control volume averaging is suggested for the derivation of the general balance equations in terms of lumped-parameters. In Section 4 this method is also applied to the transformation of the general entropy conditions into practical forms. In the last two sections the method of entropy analysis is demonstrated with two numerical examples of depressurization experiments.

2 Two-Phase Flow Model and Entropy Production

Let us consider a control volume of a liquid-vapor two-phase flow with an arbitrary size V but a set of fixed bounding surfaces A. We assume that the closed bounding surface A can be split into three parts: the inlet boundary surface A_{in}, the exit boundary surface A_{ex}, and the wetted wall surface A_w. The entire set of interfaces in the control volume is collectively denoted by A_i, which divides the total volume and each part of the boundary surface into two parts occupied respectively by the liquid and the vapor phases. For example, V is split into V_ι and V_ν, A_{in} into $A_{\iota,in}$ and $A_{\nu,in}$, and so on. Note that $A_i + A_{k,w} + A_{k,in} + A_{k,ex}$ is a closed surface which encloses the phase-k in a volume V_k, where $k = \iota$ for the liquid phase, $k = \nu$ for the vapor phase .

We may consider the entire set of vapor phase subregions, e.g., all bubbles in the control volume, and the entire liquid phase in the control volume as two independent thermodynamic systems, which have the common boundary surface A_i. We assume that the standard set of balance equations of mass, linear momentum and total energy as well as the entropy inequality [2] is valid for the individual single-phase subregions

$$\frac{\partial \rho}{\partial t} + \nabla \cdot (\rho \vec{w}) = 0, \tag{1}$$

$$\frac{\partial}{\partial t}(\rho \vec{w}) + \nabla \cdot (\rho \vec{w}\vec{w}) = -\nabla p + \nabla \cdot \overrightarrow{\overrightarrow{\tau}} + \rho \vec{g}, \tag{2}$$

$$\frac{\partial}{\partial t}[\rho(u + \frac{1}{2}w^2)] + \nabla \cdot [\rho(u + \frac{1}{2}w^2)\vec{w}] = -\nabla \cdot \vec{q} - \nabla \cdot (p\vec{w}) + \nabla \cdot (\overrightarrow{\overrightarrow{\tau}} \cdot \vec{w}) + \rho \vec{g} \cdot \vec{w} + \rho Q, \tag{3}$$

$$\frac{\partial}{\partial t}(\rho s) + \nabla \cdot (\rho s \vec{w}) + \nabla \cdot (\vartheta \vec{q}) - \rho \vartheta Q = \psi\{s\} \geq 0 \tag{4}$$

where ρ is the mass density, $\vec{w}$ is the velocity vector, u is the specific internal energy, p is the pressure, s is the specific entropy, $\vec{\vec{\tau}}$ is the viscous stress tensor, $\vec{g}$ is the gravitational force field, $\vec{q}$ is the conduction heating flux vector, Q is the volumetric heating source. Here the symbol ϑ is used to denote the reciprocal of the temperature for a simplification of the expressions for entropy flows. The source term $\psi\{s\}$ has the meaning of a volumetric entropy production per unit time.

The Clausius-Duhem inequality (4) can be considered as a specific form of the second law of thermodynamics for the class of single-phase isotropic fluid under consideration [3]. As long as the postulate of local equilibrium [4, p.14] is valid, that is, the intrinsic relationship between the specific entropy, the internal energy and the density at each point in the fluid is expressed by the thermodynamic constitutive equations of the same forms as in an equilibrium state, an explicit expression can be obtained for the volumetric entropy production rate [2]. By substituting the expression back into (4) the Clausius-Duhem inequality becomes an entropy balance equation with a non-negative entropy source term $\psi\{s\}$. This differntial form of entropy balance equation is assumed to be valid for every point inside each single-phase subregion.

The entropy balance equation (4) can be integrated over $V_k(t)$, using the Leibniz rule and the Gauss theorem, to yield

$$\begin{aligned}
\dot{S}_{k,irr} &= \int_{V_k} \psi_k\{s\} dV \\
&= \dot{S}_k - \left\{ \int_{A_{k,in}} (\rho_k s_k \vec{w}_k + \vartheta_k \vec{q}_k) \cdot (-\vec{n}_k)\, dA \right. \\
&+ \int_{A_{k,ex}} (\rho_k s_k \vec{w}_k + \vartheta_k \vec{q}_k) \cdot (-\vec{n}_k) dA \\
&+ \int_{A_i} [\rho_k s_k (\vec{w}_k - \vec{w}_i) + \vartheta_k \vec{q}_k] \cdot (-\vec{n}_k) dA \\
&+ \left. \int_{A_{k,w}} \vartheta_k \vec{q}_k \cdot (-\vec{n}_k) dA + \int_{V_k} (\vartheta_k \rho_k Q_k) dV \right\} \geq 0,
\end{aligned} \tag{5}$$

where $\dot{S}_{k,irr}$ is the total entropy production rate inside the phase-k, S_k is the total entropy in the volume V_k, $\vec{n}_k$ denotes the unit normal vector directed outwardly from the phase-k, $\vec{w}_i \cdot \vec{n}_k$ is the speed of displacement of the interface with respect to the phase-k, the corresponding terms on the other parts of the boundary surface becomes zero since they are assumed to be fixed. The total entropy flow rate into the phase-k consists of the five terms within the braces in (5). They are respectively caused by the mass and/or heat transfer across the inlet, exit, interface, wall surface boundary as well as due to the volumetric heating source. The entropy condition requires that the change rate of the total entropy inside the phase-k must be larger or equal to the total entropy flow into this phase.

We assume that the effects of an interface can be macroscopically described by a two-dimensional continuum model [5, 6, 7]. If the storage and transport of mass, momentum, energy and entropy on the interfacial thin layer are negligible, the interfacial balance equations can be reduced to the following form [5, 6, 7]:

$$\sum_k \dot{m}_k = 0 \qquad \text{with} \qquad \dot{m}_k = \rho_k(\vec{w}_k - \vec{w}_i)\cdot\vec{n}_k, \tag{6}$$

$$\sum_k \{\dot{m}_k\vec{w}_k + (p_k\,\vec{\vec{I}} - \vec{\vec{\tau}}_k)\cdot\vec{n}_k\} = 0, \tag{7}$$

$$\sum_k \{\dot{m}_k(u_k + \frac{1}{2}w_k^2) + [p_k\vec{w}_k - (\vec{\vec{\tau}}_k)\cdot\vec{w}_k + \vec{q}_k]\cdot\vec{n}_k\} = 0, \tag{8}$$

$$-\sum_k \{\dot{m}_k s_k + \vartheta_k(\vec{q}_k\cdot\vec{n}_k)\} = \psi_i\{s\} \geq 0, \tag{9}$$

where $\dot{m}_k$ is the interfacial mass flow per unit area of interface, $\psi_i\{s\}$ is the interfacial entropy production rate caused by irreversible interfacial exchanges of mass, momentum, and energy across each unit area of interface. This entropy source can be expressed in terms of the properties of the bulk phases at interface as well as the surface properties of the interface [5, 6, 7].

The interfacial entropy balance equation can be integrated over the entire set of interfaces A_i to yield an global form

$$-\sum_k \int_{A_i} \{\dot{m}_k s_k + \vartheta_k(\vec{q}_k\cdot\vec{n}_k)\}\,dA = \int_{A_i} \psi_i\{s\}dA \geq 0. \tag{10}$$

If the entire two-phase mixture including the interfaces in a control volume is considered as a thermodynamic system, the total entropy production rate in the system is thus equal to the sum of those inside the liquid and the vapor systems plus the interfacial entropy production rate. Using the equations (5) and (10) we obtain

$$\begin{aligned}
\dot{S}_{irr} &= \sum_k \int_{V_k} \psi_k\{s\}dV + \int_{A_i} \psi_i\{s\}dA \\
&= \sum_k \dot{S}_k - \left\{ \int_{A_{k,in}} (\rho_k s_k \vec{w}_k + \vartheta_k\vec{q}_k)\cdot(-\vec{n}_k)dA \right. \\
&+ \int_{A_{k,ex}} (\rho_k s_k \vec{w}_k + \vartheta_k\vec{q}_k)\cdot(-\vec{n}_k)dA \\
&+ \left. \int_{A_{k,w}} \vartheta_k\vec{q}_k\cdot(-\vec{n}_k)dA + \int_{V_k} (\vartheta_k\rho_k Q_k)dV \right\} \geq 0.
\end{aligned} \tag{11}$$

It can be seen from (11) that the net sum of the interfacial entropy flows appears no longer within the braces after the second the equality sign as a part of the total entropy flow from the surroundings to the system, but it has become a part of the total internal entropy production of the system. Therefore, the total entropy production in a two-phase system must be larger than the sum of those inside each phase because of the presence of irreversible interfacial interactions.

3 Lumped-Parameter Modeling Approach

In numerical analysis of thermal-hydraulic problems a fluid system is usually subdivided into a set of control volumes which are connected by flow paths. The properties of interest here are those which are averaged over a volume, a surface, or a flow path with the characteristic length scale of a control volume. The model equations are finally expressed into the forms of a set of non-linear algebraic equations, e.g., as in the United States codes RELAP5 and TRAC, the French code CATHARE [8], or a set of ordinary differential equations, e.g., as in the German system code ATHLET and its predecessors [8, 9, 10]. Here we consider in particular the lumped-parameter approach in the second group, which has been successfully applied in the German codes.

The standard derivation of a lumped-parameter model for a control volume is usually to begin with the governing equations for averaged continua for each phase or for the two-phase mixture, which are supposed simultaneously exist at any position in a flow field. Alternatively we can begin directly with the local instantaneous equations by integrating them over a control volume of a structural two-phase fluid to yield a set of integral balance equations; these equations can be transformed into a set of ordinary differential equations in terms of the lumped-parameters defined by the following control volume averaging

$$\langle f_1 \rangle_V = \frac{1}{V} \int_V f_1 dV, \quad \langle f_2 \rangle_A = \frac{1}{A} \int_A f_2 dA, \tag{12}$$

where f_1 is a scalar, a vector or a tensor well defined in the volume V, which can be a single continuous region or a set of regions inside a control volume; f_2 is a scalar, a vector or a tensor well defined on the surface A, which can be a single continuous surface or a set of open or closed surfaces in association with a control volume. To show this method we derive in this section the general mass and energy balance equations for each phase in an arbitrary control volume. The same method will be applied to the transformation of the entropy conditions into practical forms.

3.1 Mass balances

By integrating the local mass balance equation (1) over the volume V_k, occupied by the phase-k, we can obtain the integral mass balance equation by using the Leibniz rule and the Gauss theorem

$$\frac{dM_k}{dt} = G_{k,in} - G_{k,ex} - G_{k,i} \tag{13}$$

where M_k is the total mass of the phase-k, $G_{k,in}$, $G_{k,ex}$ and $G_{k,i}$ are respectively the inlet, exit and interfacial mass flow rates. In particular, the total interfacial mass exchange rate $G_{k,i}$, is defined by

$$G_{k,i} = \int_{A_i} \rho_k (\vec{w}_k - \vec{w}_i) \cdot \vec{n}_k dA = A_i \langle \rho_k (\vec{w}_k - \vec{w}_i) \cdot \vec{n}_k \rangle_{A_i}. \tag{14}$$

The interfacial mass balance equation (6) requires

$$\sum_k G_{k,i} = 0, \qquad \text{or} \qquad G_{\iota,i} = -G_{\nu,i} = V\Gamma \tag{15}$$

where Γ is the volumetric vaporization rate.

3.2 Energy balances

The energy balance equation (3) can be integrated over V_k to yield

$$\frac{dE_k}{dt} = E_{k,in} - E_{k,ex} + E_{k,Q} - E_{k,i} \tag{16}$$

where E_k is the total energy of the phase-k inside V_k

$$E_k = \int_{V_k} [\rho_k e_k - p_k] dV = V_k \langle \rho_k e_k - p_k \rangle_{V_k}, \tag{17}$$

where $e_k = h_k + \frac{1}{2} w_k^2 + \psi_k$ is the total specific energy, ψ_k is the potential energy per unit of mass in the gravitational force field which is assumed to be uniform everywhere. As usually assumed in a lumped-parameter model, the average of a product of two or more properties is simply replaced by the product of the individual averaged properties. Using this assumption (17) can be written by omitting the angles into the following form:

$$E_k = M_k (h_k + \frac{1}{2} w_k^2 + \psi_k) - V_k p_k. \tag{18}$$

The terms $E_{k,in}$ and $E_{k,ex}$ are respectively the energy flow rate across the inlet and the exit boundary surface, $E_{k,Q}$ is the total energy flow rate from the wall to the fluid and due to the volumetric heating source. Finally, the last term on the right hand side of (16) is the total interfacial energy flow rate transferred from the phase-k to the interface, defined by

$$\begin{aligned} E_{k,i} &= \int_{A_i} [\rho_k e_k (\vec{w}_k - \vec{w}_i) + \vec{q}_k - \vec{\vec{\tau}}_k \cdot \vec{w}_k + p_k \vec{w}_i] \cdot \vec{n}_k dA \\ &\approx G_{k,i} (h_{k,i} + \frac{1}{2} w_{k,i}^2 + \psi_{k,i}) + Q_{k,i} + E_{\tau k,i} + L_{k,i}. \end{aligned} \tag{19}$$

Substituting the expressions for these therms into (16), and expanding the left hand side, yields the energy balance equation for the phase-k in terms of the lumped-parameters

$$\begin{aligned} M_k \left(\frac{dh_k}{dt} - \frac{1}{\rho_k} \frac{dp_k}{dt} \right) &= \{ G_k (h_k + \frac{1}{2} w_k^2 + \psi_k) + Q_k + E_{\tau,k} \}_{in} \\ &- \{ G_k (h_k + \frac{1}{2} w_k^2 + \psi_k) + Q_k + E_{\tau,k} \}_{ex} + \{ Q_{k,w} + Q_k \} \\ &- \{ G_{k,i} (h_{k,i} + \frac{1}{2} w_{k,i}^2 + \psi_{k,i}) + Q_{k,i} + E_{\tau k,i} + L_{k,i} \} \\ &- \{ M_k \frac{d}{dt} (\frac{1}{2} w_k^2 + \psi_k) + (h_k + \frac{1}{2} w_k^2 + \psi_k) \frac{dM_k}{dt} - p_k \frac{dV_k}{dt} \}. \end{aligned} \tag{20}$$

The phasic energy balance equations are coupled by the integral interfacial energy balance equations derived from (8)

$$\sum_k \{ G_{k,i} (h_{k,i} + \frac{1}{2} w_{k,i}^2 + \psi_{k,i}) + Q_{k,i} + E_{\tau k,i} + L_{k,i} \} = 0. \tag{21}$$

3.3 Interfacial mass and energy exchanges

In most thermal-hydraulic computer codes the effects of the interfacial kinetic energy ($w_{k,i}^2/2$), potential energy ($\psi_{k,i}$), work of viscosity ($E_{\tau k,i}$) and the interfacial work ($L_{k,i}$) are generally neglected [8]. This implies that the net sum of the heat flow rates transferred to the interface is exactly equal to the total amount of energy in association with the latent heat of vaporization or condensation [8, 10]:

$$\Gamma = (Q_{l,i} + Q_{v,i})/V\gamma = [C_l H_{l,i}(T_i - T_l) + C_v H_{v,i}(T_v - T_i)]/\gamma \tag{22}$$

where $Q_{k,i}$ is the heat flow rate from the phase-k to the interface with the dependence on the temperature difference of that phase with respect to the interface, $H_{k,i}$ is the volumetric heat transfer coefficient on the side of the phase-k, T_k is the averaged temperature of the phase-k, T_i is the averaged interface temperature, γ is the latent heat of vaporization or condensation. The flow regime dependent coeffiecients C_k take different values in different codes, but the interface temperature is generally assumed to be the saturation temperature corresponding to the averaged pressure in a control volume.

A typical example for the calculation of the interfacial heat transfer coefficients is the Wolfert's model [11, 12] which takes account of the effects of conductive and convective heat transfer as well as turbulent fluctuations. The constitutive relations for the heat transfer coefficients for the liquid and the vapor sides can be rewritten in the following forms

$$H_{l,i} = (H_{l,i})_a + (H_{l,i})_b, \quad H_{v,i} = (H_{v,i})_c \tag{23}$$

where

$$(H_{l,i})_a = K_a \lambda_l C_{pl} \rho_l n_b^{2/3} \alpha^{1/3} (T_i - T_{sat})/(\rho_v \gamma), \tag{24}$$

$$(H_{l,i})_b = K_b [(1 + \epsilon_l w_l) \lambda_l C_{pl} \rho_l n_b w_b \alpha]^{1/2}, \tag{25}$$

$$(H_{v,i})_c = K_c [(1 + \epsilon_v w_v) \lambda_v C_{pv} \rho_v n_d w_d (1 - \alpha)]^{1/2}. \tag{26}$$

Here K_a, K_b and K_c are positive constants, the meanings of other variables can be found in the references given above. The Wolfert's model has been applied in the German system code ATHLET and its predecessors [8, 9, 10].

4 Entropy Conditions for Practical Models

4.1 Phasic entropy production

Using the lumped-parameter approach on the basis of control volume averaging the entropy condition (5) for the phase-k can be integrated and averaged to yield the approximate form:

$$\begin{aligned} \dot{S}_{k,irr} &= \left\{ M_k \frac{ds_k}{dt} + s_k \frac{dM_k}{dt} \right\} \\ &\quad - \{(G_{k,in} s_{k,in} + \vartheta_{k,in} Q_{k,in}) - (G_{k,ex} s_{k,ex} + \vartheta_{k,ex} Q_{k,ex}) \\ &\quad - (G_{k,i} s_{k,i} + \vartheta_{k,i} Q_{k,i}) + (\vartheta_{k,w} Q_{k,w} + \vartheta_k Q_k)\} \geq 0 \end{aligned} \tag{27}$$

where $s_k, s_{k,in}, s_{k,ex}$ and $s_{k,i}$ are respectively the averaged specific entropy of the phase-k in the volume V_k, at the inlet and the exit, and on the interface; $\vartheta_k, \vartheta_{k,in}, \vartheta_{k,ex}$ and $\vartheta_{k,i}$ are respectively the averages of the reciprocal of the temperature of the phase-k in the volume V_k, at the inlet and the exit, and on the interface; $Q_{k,in}, Q_{k,ex}, Q_{k,i}, Q_{k,w}$ and Q_k are respectively the heat flow rates across the inlet, exit, interfacial and the wall boundary surface as well as due to the volumetric heating source. By assuming the usual form of the Gibbs relation to be valid for each phase

$$\frac{ds_k}{dt} = \vartheta_k \left(\frac{dh_k}{dt} - \frac{1}{\rho_k} \frac{dp_k}{dt} \right) \tag{28}$$

the entropy production rate inside the phase-k becomes

$$\begin{aligned}\dot{S}_{k,irr} &= \left\{\vartheta_k M_k\left(\frac{dh_k}{dt}-\frac{1}{\rho_k}\frac{dp_k}{dt}\right)+s_k\frac{dM_k}{dt}\right\}\\ &\quad-\{(G_{k,in}s_{k,in}+\vartheta_{k,in}Q_{k,in})-(G_{k,ex}s_{k,ex}+\vartheta_{k,ex}Q_{k,ex})\\ &\quad-(G_{k,i}s_{k,i}+\vartheta_{k,i}Q_{k,i})+(\vartheta_{k,w}Q_{k,w}+\vartheta_k Q_k)\}\geq 0. \end{aligned} \tag{29}$$

The derivative terms on the right hand side of the equality sign in the entropy condition (29) can be calculated by using the mass and energy balance equations obtained in the last section. The inlet and exit mass flow rates are calculated by the lumped-parameter momentum balance equations which are not shown here. The specific entropies can be calculated as the functions of the thermodynamic independent variables. To avoid the inaccuracy of a usual approximation method an accurate property package [13] should be used to calculate these quantities. In this way we can calculate quantitatively the entropy production rate according to the predictions of a lumped-parameter model.

4.2 Interfacial entropy production

Similarly, the interfacial entropy conditions (10) can be averaged and simplified using the usual assumption of a continuous interfacial temperature, i.e., $\vartheta_{\iota,i}=\vartheta_i=\vartheta_{\nu,i}$,

$$\dot{S}_{i,irr}=-\sum_k\{G_{k,i}s_{k,i}+\vartheta_{k,i}Q_{k,i}\}=\vartheta_i V\Gamma(g_{\iota,i}-g_{\nu,i})\geq 0 \tag{30}$$

where ϑ_i is the average of the reciprocal of the interface temperature in a control volume, $g_{\iota,i}$ and $g_{\nu,i}$ are respectively the averaged specific Gibbs free energy of the liquid and the vapor at interface.

For a vaporization process the mass exchange rate Γ is positive, thus the entropy condition requires the specific Gibbs free energy of the liquid phase at interface must be larger than that of the vapor phase:

$$g_{\iota,i}\geq g_{\nu,i}\quad\text{for vaporization process.} \tag{31}$$

The equality sign is valid only for the ideal conditions of an equilibrium or reversible two-phase flow system. The interfacial entropy condition implies that real vaporization process is possible when the liquid and the vapor phase are in non-equilibrium. Moreover, it can be shown by the examination of an isothermal line on the $g-p$ plane that the condition (31) can be satisfied only when both phases at interface are superheated. Therefore, we come to the important conclusion: In the case of a continuous interfacial temperature the interfacial vaporization of a pure liquid occurs only under a superheated condition. Similarly we can show according to the entropy condition (30) that the interfacial condensation of a pure steam is possible only when both phases at interface are in subcooled state. As will be shown later by numerical examples, these entropy conditions are not always satisfied by numerical predictions of some current non-equilibrium two-phase models.

4.3 Entropy production in two-phase mixture

Similarly, the total entropy production in two-phase mixture (11) can also be approximately written into the form:

$$\begin{aligned}\dot{S}_{irr} &= \sum_k\left\{\left[\vartheta_k M_k\left(\frac{dh_k}{dt}-\frac{1}{\rho_k}\frac{dp_k}{dt}\right)+s_k\frac{dM_k}{dt}\right]\right.\\ &\quad-[(G_{k,in}s_{k,in}+\vartheta_{k,in}Q_{k,in})-(G_{k,ex}s_{k,ex}+\vartheta_{k,ex}Q_{k,ex})\\ &\quad\left.+(\vartheta_{k,w}Q_{k,w}+\ {}^{\backprime}{}_kQ_k)]\right\}\geq 0. \end{aligned} \tag{32}$$

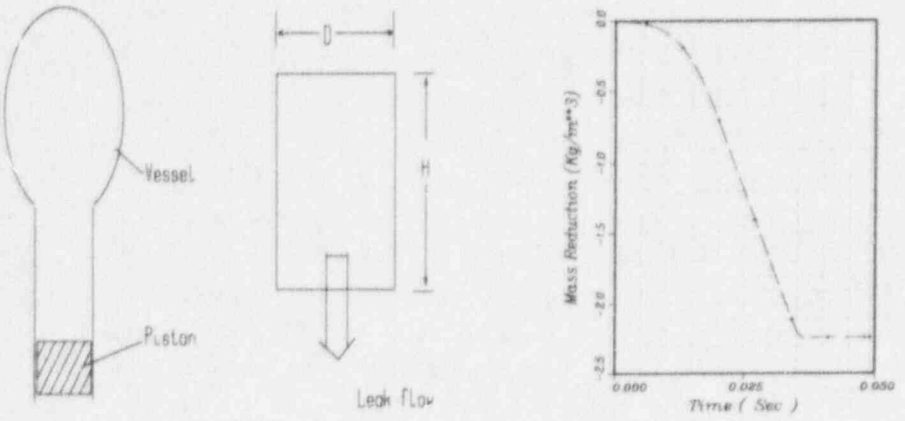

Figure 1: RS77 Experiment and an ATHLET simulation

The values of the terms on the right hand side of the equality sign in (32) are directly available or can be calculated by using the data from the output files of a two-phase flow computer code using lumped-parameter approach. Hence, we can also calculate the entropy production rate in the two-phase mixture in a control volume.

Simple examples will be given in the next two sections to show the application of the entropy conditions.

5 Entropy Analysis of RS77 Experiment

As the first example we consider a RS77 simple depressurization experiment (Figure 1). The vessel was filled with degased and demineralized water and it was put into a furnace to heat the fluid inside to a desired temperature. A depressurization was initiated by means of a quick opening valve which controlled the nitrogen pressure on the other side of the piston. During each experiment the initial liquid temperature, the transient fluid pressure as well as the piston displacement were measured. One of the test runs has been analyzed in detail in [11, 12] using a four equation non-equilibrium model. The experimental conditions are as following

-initial volume of subcooled water = 2.215E-3 m**3,
-initial pressure = 93.7 bar,
-initial temperature = 301.0 Celsius (P_{sat} = 87.1 bar),
-relative volume increase = 0.28 %.

This experiment is recalculated by using the five equation lumped-parameter model in the system code ATHLET MOD1.1 Cycle-A [10]. The final mass and energy balance equations have similar forms as shown in Section 3. For the calculation of interfacial mass and energy exchanges an extended form of the Wolfert's model is used [10]. The experiment is simulated by a constant control volume plus a leak flow with an equivalent rate of mass reducing per unit volume (Figure 1). As shown in [11] the pressure transient can be well predicted with an optimal value of bubble density ZB=1.0E+9 m^{-3}.

For the calculation of entropy production in each phase the interfacial energy transfer rates must be known, which can be calculated directly from the partial vaporization rates in

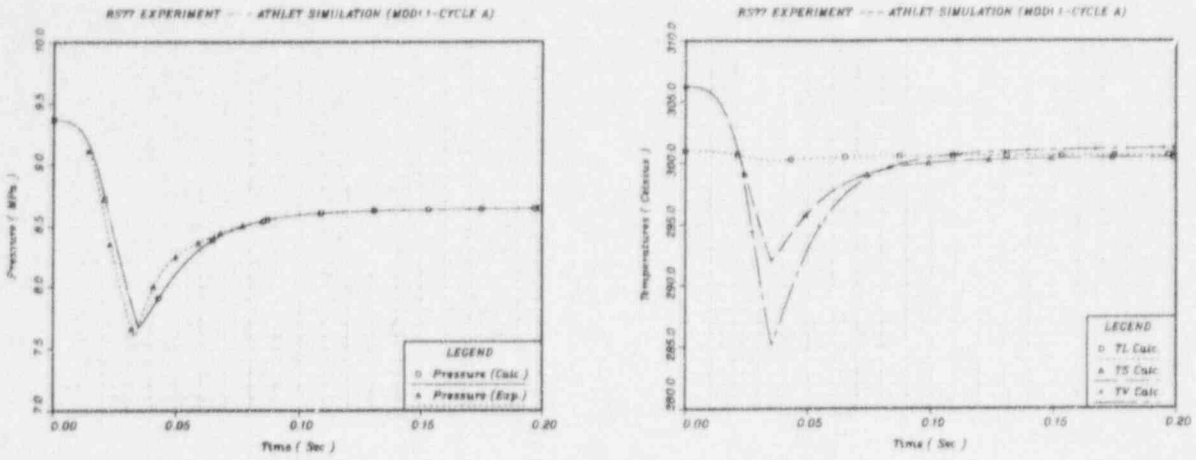

Figure 2: Predictions of pressure and temperatures

the Wolfert's model. The standard output data file for the five-equation model in ATHLET MOD1.1-Cycle A is extended to include also the time derivatives of the averaged pressure of the mixture, the enthalpies and the masses of each phase. The extended output file provides input data for the post-processor ATHPA (ATHlet Post-Analysis), which calculate the additional thermodynamic properties by using the IAPS property package [13] as well as the entropy production rates in a control volume according to the expressions given in the last section. The results of the ATHLET simulation and the ATHPA analysis of the RS77 experiment are shown in Figures 2 and 3. As can be seen from the diagram on the left of Figure 2, the non-equilibrium phenomenon of pressure undershoot is well predicted by the ATHLET model. The predicted pressure is well in agreement with the experimental data. Being consistent with the pressure undershoot there exits also a undershoot in the calculated saturation temperature (TS in the diagram on the right of Figure 2). This brings the liquid phase to a highly metastable state during the undershoot, although the liquid temperature remains almost constant during the transient.

According to the temperatures shown in Figure 2, the vapor phase is predicted to be in highly subcooled state during the period of pressure undershoot, but the vapor temperature becomes slightly higher than the liquid temperature in the second half of the transient (t>0.1 sec). The calculated maximal subcooling of the vapor occurs at the same time of the largest pressure undershoot. As will be shown later, the prediction of a highly subcooled vapor state and a higher temperature than the liquid phase may lead to the violation of entropy conditions.

The calculated volumetric entropy production in mixture, which is equal to the total amount of the production rate divided by the volume, is shown by the curve-A in the diagram on the left of Figure 3, implying a global irreversible process as expected. However, as can be seen from the curve-B in the same diagram with an amplified scale for the Y-axis, the entropy production indicates slight negative values after the point where the vapor temperature becomes higher than the liquid temperature. This violates the entropy condition (32) which requires a non-negative entropy production rate in the two-phase mixture. This violation is in fact also directly indicated by the calculated positive interfacial mass and heat transfer rates from the liquid phase with a lower temperature to the vapor phase with a higher temperature. It should be noted that the absolute value of this negative volumetric production rate is quite small in comparison with the positive peak value. In contrast, the negative volumetric entropy production rate in the vapor phase is stronger, as it can be seen

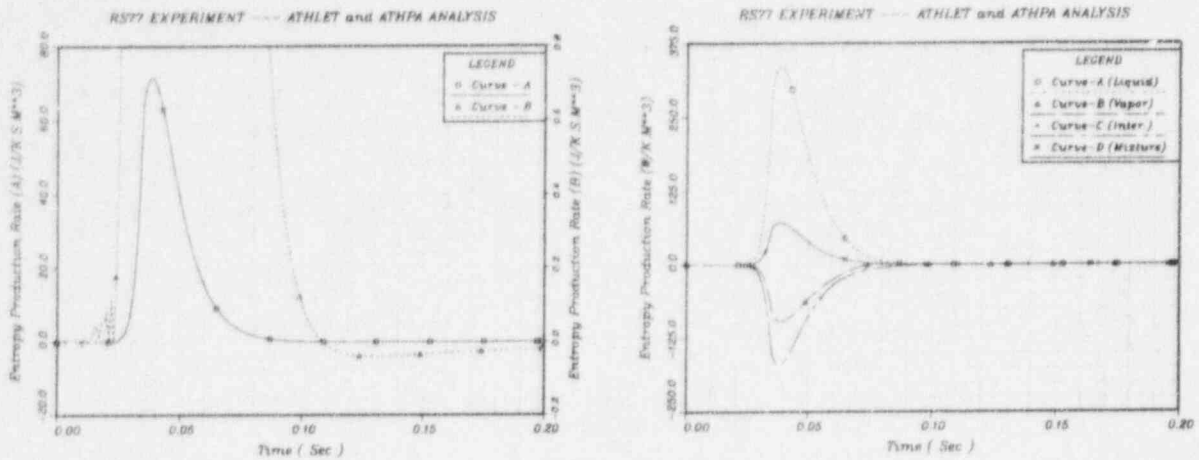

Figure 3: Volumetric entropy production rates

from the Curve-B in the digram on the right of Figure 3. The interfacial entropy production rate (Curve-C) is also negative but the absolute value is still larger. These violate the corresponding entropy conditions (29) for each phase and (30) for interfacial exchanges. In the both cases the negative peaks occur during the period of pressure undershoot. On the other hand, the entropy production rate in the liquid phase (Curve-A in the same diagram) is positive and the peak value is even larger than the sum of the absolute values of the two negative peaks. As a consequence, the negative interfacial entropy productions are compensated and this gives a positive total entropy production rate in the two-phase mixture (Curve-D) during the period of pressure undershoot. However, as can be seen from the broken line in the diagram on the left of Figure 3, the compensation is not strong enough in the later stage of the transient, showing a slightly negative entropy production in the two-phase mixture. Considering such compensation effects it is necessary to consider simultaneously the entropy conditions both for the two-phase mixture and for each phase. This conclusion supports the basic postulate that the second law should be applied not only to the two-phase mixture as a whole but also to each phase [1].

The appearance of negative entropy production rates is obviously related to the unsatisfactory prediction of the thermodynamic state of the vapor phase. Negative values of interfacial entropy production rates and in vapor phase are caused directly by the prediction of a too low vapor temperature. In comparison with the four equation model, in which the vapor phase under the condition of this example is always in saturation state, the thermodynamic state of the vapor phase in the five equation model is described by a differential energy balance equation instead of the saturation assumption for that phase. Thus, the departure of the vapor temperature from the saturation condition is strongly influenced by the constitutive relations for the calculation of interfacial mass and energy exchanges. In particular, as shown in Figure 1, after the leak flow is ended at t=0.035 second, the control volume becomes an isolated system without any mass or energy exchange with the surroundings. The evolution of fluid state is mainly controlled by interfacial mass and heat exchanges between the phases. Thus, the calculation of interfacial mass and energy transfer rates are the main reasons leading to the too low vapor temperature and thus the appearance of negative entropy production.

If the usual assumption of an averaged pressure for both phases is reasonable, the vapor pressure in this case is thus already well predicted as shown previously. Thus, the prediction of a too low vapor temparature and hence the violation of the entropy conditions are caused by a too small interfacial heat flow rate from the interface to the vapor phase, which depends

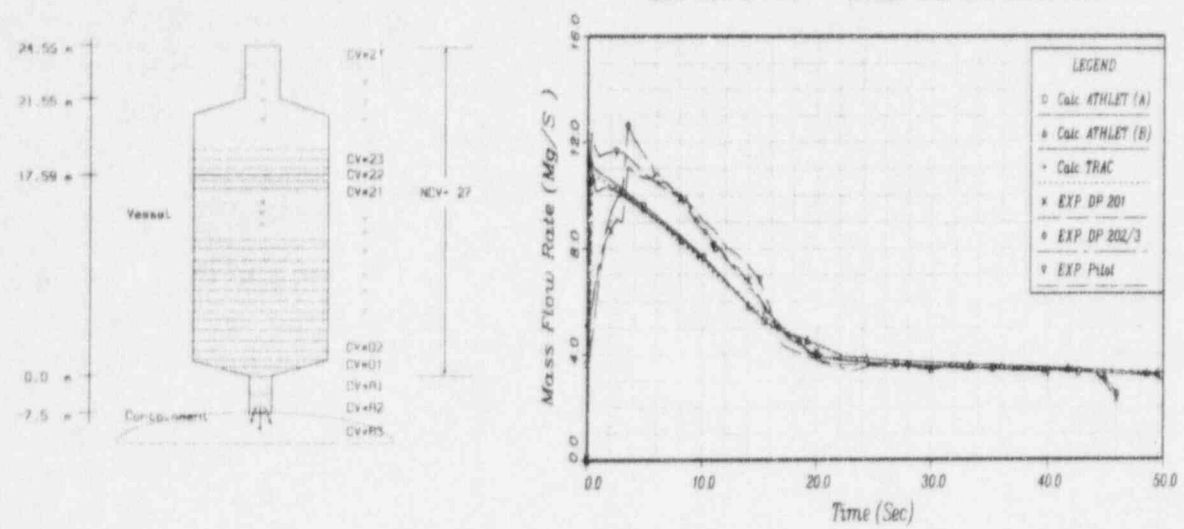

Figure 4: Marviken CFT No.4 and discharge flow rates

on the temperature difference bewteen the interface and the vapor phase. The neglect of interfacial work, viscosity work, kinetic energy and potential energy etc. may also influence the calculation of interfacial energy transfer rate. Otherwise, the assumption of a saturation interface temperature and the same pressure for both phases is a possible reason leading to the negative entropy produtcion rate. Without going into the details of the specific program we simply note that the re-examination of these commonally made assumptions in current thermal-hydraulic computer programs are of general interest.

6 Entropy Analysis of Marviken CFT No.4

As the second example of entropy analysis we consider the simulation of the Marviken full-scale Critical-Flow Test No.4 (CFT) [14]. The test was performed with a steam dome pressure 4.94 MPa above the initial water level which was at the elevation 17.59 m (Figure 4). A length of ca. 7 m below the water level was near saturation condition, and the water in the lower part of the vessel was subcooled down to a maximal subcooling 37 degrees at the exit of the pressure vessel. The test continued for ca. 50 seconds, the final collapsed liquid level was ca. 2 m.

Using the ATHLET system code [9, 10] the Marviken Test No.4 is simulated. A similar modeling approach as reported in [16] for another Marviken test is used: a fine nodalization for the vessel, a coarse nodalization for the discharge pipe and for the nozzle plus the use of the discharge flow model and the mixture level tracking model. To take into account the effects of the variable back pressure, the containment is also simulated as a time-dependent volume with the measured pressure as the boundary condition. A series of calculations are performd to achieve good predictions for the measured discharge mass flow rate and for the pressure in the steam dome with different combinations of the important adjustable parameters: the bubble and droplet density as well as the number of nodes for the vessel. Among the four nodalizations with different number of control volumes 54, 27, 9 and 2, it is found that the second one gives the similar good predictions but with relative less nodes than the first one. We use the second nodalization, as shown on the left of Figure 4, in the later analysis. The predictions of two ATHLET calculations are shown respectively on the right of Figure 4 and on the left of Figure 5 for the mass flow rate at the nozzle exit and the pressure in the

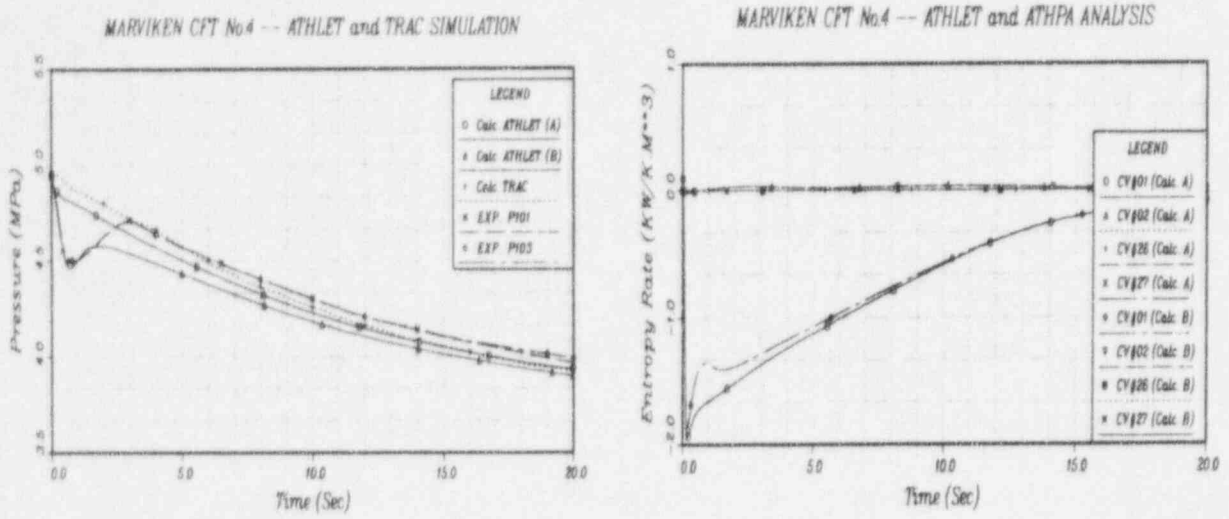

Figure 5: Steam dome pressure and entropy production

steam dome. The ATHLET calculation A is obtained using the default values for the bubble and droplet number density (5.0E+9 m^{-3}), the ATHLET calculation B is performed using reduced values for the bubble/droplet number (2.5E+6 m^{-3}).

For the purpose of comparison the measured data and the calculated results using the computer code TRAC-PF1/MOD1 as reported in [15] are also shown on the same diagrams. The mass flow rate evaluated by using pitot-static measurements are applicable to the whole test, but the data derived from the vessel differential-pressure measurements are not valid for the initial some seconds because of large oscillations in the differential pressure that occurred immediately after the initiation of the test. After the initial some seconds the two measurement methods show good agreement and the data are well within the error band ca. $\pm 10\%$ of the both methods. Taking this into account, both the ATHLET and the TRAC calculations well predicted the measured data except the initial 15 seconds. For this time period the both codes show the same tendency to underpredict the mass flow rate. As can seen from the diagram on the left of Figure 5, the phenomenon of the pressure undershoot is not predicted by the TRAC calculation, nor in the ATHLET calculation A with the default values for bubble/droplet number. The ATHLET calculation B with a reduced bubble density can well predict the phenomenon of the pressure undershoot, but it shows a underprediction of the pressure recovery after the point of the minimal pressure.

In summary, both the ATHLET and the TRAC calculations well predict the discharge mass flow rate and the pressure in the system for the near equilibrium region of the transient which are characterized by a less departure of the measured fluid temperatures from the saturation condition corresponding to the system pressure. In contrast, the predictions for the mass flow rate and the pressure during the initial strong non-equilibrium phase of the transient is less good which are complicated by the phenomenon of nucleation delay and bubble growth.

On the basis of the two ATHLET simulations entropy analyses are performed for some typical control volumes using the method discussed in the previous sections. During the transient the control volumes in the middle of the pressure vessel may contain single-phase liquid, single-phase vapor or two-phase mixture with or without mixture level. In order to achieve a comparable basis we consider here only the total entropy production rate in the two-phase mixture in a control volume and divide it with the geometric volume to get a

specific quantities per unit volume.

Typical results of the entropy analyses are shown on the right of Figure 5, where the volumetric entropy production rates are shown for four control volumes, two at the bottom and two at the top. Surprisingly, it is found that the most strong negative entropy production rate occurs in both cases in the control volume No.01 ! It is in fact a volume of subcooled water in the initial 20 seconds of the transient. Entropy production rates in other control volumes are relatively small in comparison with that in the first one. It is interesting to note that the global reducing tendency of the negative entropy production is consistent with the reduction of the discrepancies of the predicted pressure and discharge flow rate with respect to the experimental data. This tendency continues till the time point ca. 25 seconds, after that the entropy production rate in the control volume No.1 keeps at the level of about 8 % of the peak value. As can be seen from the diagram on the right of Figure 5, the reduction of the bubble/droplet density reduces only slightly the negative entropy production, but it do not change the sign and the global tendency.

To understand why the strongest negative entropy rate may occur in a control volume of single-phase liquid, we consider the expression (32). For a control volume of single-phase fluid it can be simplifed to the form

$$\begin{aligned} \dot{S}_{irr} &= \left\{ \vartheta_i M_i \left(\frac{dh_i}{dt} - \frac{1}{\rho_i} \frac{dp_i}{dt} \right) + s_i \frac{dM_i}{dt} \right\} \\ &\quad - \{ G_{i,in} s_{i,in} - G_{i,ex} s_{i,ex} \} \geq 0 \end{aligned} \tag{33}$$

where the effects of heat flows across the boundary surfaces of the volume have been neglected. The first large term within the braces is the time rate of change of the total entropy inside the control volume, the second is the net entropy flow rate into the volume. Therefore, the appearance of a negative entropy production rate implies that the storage rate of the entropy in the control volume is less than the net entropy flow into the volume. If the donor cell rule is applied to the determination of the specific entropy at the inlet and the exit boundary surfaces, the specific entropy $s_{i,in}$ and $s_{i,ex}$ take respectively the values in the present and in the upstream volume. Hence, the term of entropy flow to the control volume No.01 depends also on the fluid state in the immediate upstream volume. Generally, we can show that the fluid state in the last control volume depends also on the fluid states in all other control volumes because of the coupling effects of mass, momentum and energy transport in the system. The derivative terms can be analyzed in the same way. In particular, any change of pressure in the system is rapidly propogated to the volume No.01 depressurization because of the relative large propogation speed of pressure disturbance. Thus, the pressure rate in (33) is a global quantity which include also the influences of the vaporization or condensation rates in other control volumes. Therefore, the negative entropy production in the control volume No.01 is not a local phenomenon, but a consequence of complicated interactions of mass, momentum and energy in all control volumes in the two-phase system from the past up to the present time in question.

According to the expression (33), the underprediction of the rate of entropy storage or the net entropy flow rate out of the control volume can be significantly changed, e.g., by increasing the discharge mass flow rate. It is interesting to note that this is exactly the typical prediction discrepancy in this case. Therefore, there exist certain connection between the the appearance of the deficit of entropy in the first control volume and the underprediction of the discharge mass flow rate out of the volume.

In connection with the analysis in the last paragraph, some problems are also indicated in the predictions of fluid properties in the upstream volumes. For example, the calculated vapor temperatures in some liquid-dominant control volumes are much lower than the corresponding

saturation temperatures under the condition of vaporization. The predicted behavior of the vapor phase in such case is similar to the one as shown in the first example. In contrast, the calculated liquid temperature in some vapor-dominant control volumes are higher than the saturation value under the condition of condensation and the predicted vapor subcooling is obviously larger than the measured data. Since the discharge flow rate is mainly determined by the fluid states in the upstream control volumes when the boundary conditions are given as in this example, the unsatisfactory predictions for thermodynamic states in the upstream control volumes may have direct inflences on the calculation of discharge flow rate and also the balance of entropy.

7 Concluding Remarks

From the local instantaneous formulation for a structual two-phase fluid, the general integral entropy conditions are obtained respectively for the thermodynamic systems of the liquid, the vapor and the two-phase mixture as well as for the interfacial interactions in an arbitrary control volume.

By introducing the method of control volume averaging the general entropy conditions are transformed into practical forms in terms of quantities which are also used in a lumped-parameter two-phase flow model. On the basis of a widely used thermal-hydraulic system code it is shown that these entropy conditions can be implemented in the form of a post-processor to perform entropy analysis for practical two-phase flow models.

As examples of entropy analysis we have calculated the entropy production rates in the fluid systems of two depressurization experiments. In both cases strong negative entropy production rates occur during the initial phase of the transients with a large pressure undershoot. During this time period, in particular, the predicted thermodynamic state for a non-dominant phase in some control volumes may violate the interfacial entropy condition of non-equilibrium phase change. Preliminary analyses indicate that the most important reasons leading to the violation of the entropy conditions are closely related to some modeling assumptions which are usually used in current non-equilibrium two-phase flow computer codes for the calculation of interfacial mass and energy exchange rates.

As shown by the examples, the method of entropy analysis could be a useful means for the assessment of practical two-phase flow models to identify some potential problems in the calculation of mass, momentum and energy balances. The consideration of entropy conditions and entropy analysis may give a new perspective for the difficult issues of construction of interfacial constitutive relations for practical non-equilibrium two-phase flow models.

References

[1] Arnold, G.S., Drew, D.A. and Lahey, R.T. Jr., "An assessment of multiphase flow models using the second law of thermodynamics", Int. J. Multiphase Flow, Vol.16, 1990, pp.481-494.

[2] Whitaker, S., " Laws of continuum physics for single-phase, single-component systems ", Handbook of Multiphase Systems (ed. I. Hetsroni, P.), Hemisphere, New York, 1982, Chapter 1, pp.1-35.

[3] Truesdell, C., Rational Thermodynamics, McGraw-Hill Book Company, New York, 1969.

[4] Glansdorff, P. and Prigogine, I., Thermodynamics Theory of Structure, Stability and Fluctuations, Wiley-Interscience, London, 1971.

[5] Delhaye, J.M., "Jump conditions and entropy sources in two-phase systems, local instant formulation", Int. J. Multiphase Flow, Vol.1, 1974, pp.395-409.

[6] Ishii, M., Thermo-Fluid Dynamic Theory of Two-Phase Flows, Eyrolles, Paris, 1975.

[7] Ruan, Y.Q. and Karwat, H., "On entropy production in non-equilibrium two-phase fluids during depressurization processes", Proc. 3rd Int. Symposium on Multiphase Flow and Heat Transfer, Xi'an, China, September 19-21, 1994, pp.1179-1186.

[8] Forge,A., et al, Comparison of Thermal-Hydraulic Safety Codes for PWR Systems, Commision of the European Communities, Graham and Trotman, London, 1988.

[9] Wolfert,K., Lerchl, G., Miro, J. and Sonnenburg, H., "The GRS thermalhydraulic system code ATHLET for PWR and BWR analysis", Proc. 3rd. Int. Topical Meeting on Nuclear Power Plant Thermal-Hydraulics and Operation, Seoul, Korea, November 14-17, 1988.

[10] Bals,C., Lerchl, G. and Loy, D., Entwicklung einer ATHLET-Version mit zwei Energiegleichungen, Report GRS-A-1830, 1991.

[11] Wolfert, K., "The simulation of blowdown processes with consideration of thermodynamic nonequilibrium phenomena", Paper submitted to the Specialists' Meeting on Transient Two-Phase Flow, Toronto, Canada, August 3-4, 1976.

[12] Wolfert, K., et al, "Non-equilibrium mass transfer between liquid and vapor phases during depressurization processes", Proc. of the second CSNI Specialists Meeting on Transient Two-Phase Flow, Paris, June 12-14, 1978, pp.149-190.

[13] Haar, L., Gallagher , J.S. and G.S. Kell, NBS/NRC Wasserdampftafel, Thermodynamische und Transportgrössen mit Computerprogrammen für Dampf und Wasser in SI-Einheiten, Herausgegeben und aus dem englischen übersetzt von Ulrich Grigull, Springer-Verlag, Berlin, 1988.

[14] Joint Reactor Safety Experiments in the Marviken Power Station Sweden, The Marviken Full Scale Critical Flow Tests, Summary Report, NUREG/CR-2671, MXC-301, 1982.

[15] LANL (Los Alamos National Lab.), TRAC-PF1/MOD1 : An Advanced Best Estimate Computer Programm for Pressurized Water Thermal-Hydraulic Analysis, Report NUREG/CR-3858, 1986.

[16] Ringer,F.J., Nachrechnung des Marviken-Versuchs Nr.22 mit dem Rechenprogramm ATHLET, Report GRS-A-1361, 1987.

A General Unified Non-Equilibrium Model For Predicting Saturated and Subcooled Critical Two-Phase Flow Rates Through Short and Long Tubes

D.W.H. Fraser[*] and A.H. Abdelmessih[**]
[*]Research Associate
[**]Professor
Department of Mechanical Engineering
University of Toronto
Toronto, Ontario, Canada
[*]Currently Assistant Professor at the
University of British Columbia

ABSTRACT

A general unified model is developed to predict one-component critical two-phase pipe flow. Modelling of the two-phase flow is accomplished by describing the evolution of the flow between the location of flashing inception and the exit (critical) plane. The model approximates the nonequilibrium phase change process via thermodynamic equilibrium paths. Included are the relative effects of varying the location of flashing inception, pipe geometry, fluid properties and length to diameter ratio. The model predicts that a range of critical mass fluxes exist and is bound by a maximum and minimum value for a given thermodynamic state. This range is more pronounced at lower subcooled stagnation states and can be attributed to the variation in the location of flashing inception.

The model is based on the results of an experimental study of the critical two-phase flow of saturated and subcooled water through long tubes. In that study, the location of flashing inception was accurately controlled and adjusted through the use of a new device. The data obtained revealed that for fixed stagnation conditions, the maximum critical mass flux occurred with flashing inception located near the pipe exit; while minimum critical mass fluxes occurred with the flashing front located further upstream. Available data since 1970 for both short and long tubes over a wide range of conditions are compared with the model predictions. This includes test section L/D ratios from 25 to 300 and covers a temperature and pressure range of 110 to 280^{0}C and 0.16 to 6.9 MPa. respectively. The predicted maximum and minimum critical mass fluxes show an excellent agreement with the range observed in the experimental data.

TABLE OF NOMENCLATURE

A	Area, m^2
D	Diameter, m
e	Surface Roughness, m

f	Friction Factor,
g	Acceleration Due to Gravity, m/s^2
G	Mass Flux, $kg/m^2 \cdot s$
K_i	Tube Entrance Loss Coefficient
L	Tube Length, m
L_T	Total Tube Length, m
L_R	Ring Location Measured From The Exit, m
P	Pressure, N/m^2
P^*	Dimensionless Stagnation Pressure
P_s^*	Dimensionless Pressure at Flashing Inception
s	Specific Entropy, J/kg^0K
T	Temperature, ^0C
T^*	Dimensionless Temperature
v	Specific Volume, m^3/kg
x	Vapour Mass Quality
θ	Angle to Horizontal Plane, deg.
η	Critical Pressure Ratio
ρ	Density, kg/m^3

Subscripts

c	Critical (Choked) State
e	Exit
E	Thermodynamic Equilibrium
ENT	Entrance
f	Saturated Liquid Phase
F	Friction
Fi	Flashing Inception
g	Gas or Vapour Phase
H	Hydrostatic
l	Liquid Phase
m	Mixture
M	Momentum
0	Stagnation State
s	Isentropic
SAT	Saturation

INTRODUCTION

The critical flow rate of fluids is a common phenomenon that plays an important role in a number of situations which apply to the nuclear, chemical, and process industries. In particular, the prediction of the critical flow rate following a pipe rupture is of paramount importance in the safety analysis of nuclear reactors. Here, the ability to maintain adequate core cooling is highly dependant on the critical mass flux.

Generally, it has been accepted that non-equilibrium effects are important for nozzles and/or short pipes. For long pipes though, the relative effects of the flow length and diameter have not been adequately addressed. It has long been recognized that knowledge of the location

of flashing inception is crucial to the determination of the critical flow rate. The location of flashing inception within a pipe constitutes the origin of the time scale for bubble growth, thereby serving as the initial condition for the calculation of the vapour generation rate. Bubble growth rates in both constant and variable pressure fields are highly influenced by the initial degree of superheat (Jones and Zuber [24]). This, in turn, governs the void fraction development and consequently the critical flow rate. Furthermore, data from existing research indicate that a range rather than a single critical two-phase flow rate exists for a given thermodynamic state. Experiments conducted by Sozzi and Sutherland [35], Ardron and Ackerman [6], Alsahan [1], and Celata et al. [10], all revealed an unexplained range of critical flow rates in their experimental data. This range has formerly been attributed to effects such as experimental error, dissolved gases and impurities in the liquid, and more recently, possible cavitation effects (Jones [25]).

It is the purpose of this paper to present a unified model for the calculation of critical two-phase flow rates of initially saturated or subcooled liquids through short and long tubes. The model is based on the experimental results obtained by Fraser and Abdelmessih [16]. In that study, the location of flashing inception was carefully controlled and adjusted through the use of a new device. The results obtained revealed that a range in the critical mass flux does exist for a given upstream stagnation state. It will further be shown that the range in the critical mass flux can be modelled by including the effect of the location of flashing inception. Modelling of the critical flow is accomplished by describing the evolution of the flow from the location of flashing inception up to the exit (critical) plane. Nonequilibrium phase change is approximated by following thermodynamic equilibrium paths. The model is a useful analytical tool since it is based on and only requires a knowledge of the upstream stagnation state and pipe geometry. A comparison of the model predictions to available data since 1970, covering a wide range of test section geometries and thermodynamic states, are presented.

LITERATURE SURVEY

An extensive body of theoretical and experimental work on critical two-phase flow exists. This work has been thoroughly reviewed by Ellias and Lellouche [14], Giot [18], Wallis [36], Isbin [23], Saha [32], and Ardron [4], among others. There is, however, a scarcity of experimental work investigating the effects of the point of flashing inception on critical two-phase flow. Reocreux [29], Seynhaeve [33], and Ardron are Ackerman [6] all attempted to determine both the location and the superheat at flashing inception for critical two-phase flow in horizontal pipes. The results were quite scattered (the location of flashing inception was uncontrolled), and no relationship was found between the location of flashing inception and its effects on the degree of superheat and/or the critical flow rate. Flashing inception in nozzles, though, has received more attention. A thorough review of this phenomena can be found in Shin & Jones [34].

Theoretical models for critical two-phase flow range from the homogeneous equilibrium model (HEM), which is essentially a single-phase flow technique, to more elaborate mechanistic models that attempt to represent (approximately) all of the non-equilibrium phenomena. These will be briefly discussed in ascending order of complexity.

The Homogeneous Equilibrium Model (HEM), considers the two-phase fluid as a pseudo-single-phase flow with equal phasic velocities and temperatures. The evolution of the flow is taken to be isentropic. Other models attempted to incorporate non-equilibrium effects by introducing slip between the phases (Moody [28], Levy [27], Fauske [15], and Zivi [38]). Each

phase need not be in thermal equilibrium and methods were obtained to account for these effects in an empirical manner. Thermal non equilibrium models have been proposed by Henry [20] and Henry and Fauske [21]. Non-equilibrium vapour generation is handled entirely through an empirical coefficient that allows for only a fraction of the vapour generation rate to occur. All of these models are capable of predicting critical two-phase flow rates in a satisfactory manner only for well defined conditions. Furthermore, some of these models require knowledge of the conditions at the critical section, which becomes impractical in a design assessment. Numerous reviews can be consulted on the range of application of each of these models (e.g. Wallis [36], Henry [22], and Giot [18]).

The restricted use of the earlier models prompted the development of more elaborate mechanistic models in an attempt to provide a more general unified model. The advantage of mechanistic models is that both thermal and hydrodynamic non-equilibrium between the phases can be described by a large degree of complexity. Many of these models that attempt to follow the nucleation and growth of the vapour bubbles, however, require specification of the initial conditions at the onset of flashing in order to provide closure of the governing equations (e.g. Elias and Chambre [13], Richter [30], Dobran [12], Rohatgi and Reshotko [31], Ardron [5], and Alsahan [2]). Due to a lack of understanding regarding the onset of flashing, these models contain adjustable parameters such as the nucleation site density and the degree of superheat at flashing inception. The values of these parameters are often chosen to correlate the experimental critical flow data rather than representing measured characteristics. Current models which attempt to account for the physics of the flashing process include the modified kinetic theory of Alamgir and Lienhard [3], Jones [25] model which includes the effect of turbulent pressure fluctuations, and the wall nucleation model of Jones and Shin [26]. The assumptions used in the development of these models vary considerably and as yet, appear to lack experimental evidence to support them. At present there appears to be no general model for nonequilibrium vapour generation rates or for any of the three major factors which influence the subsequent void development: location and superheat at flashing inception, interfacial area available for vaporization, and rate of mass exchange per unit interfacial area. More recently, however, Bilicki et al. [9] have adopted the methodology of dynamical systems to solve the problem of choking during steady 1-D two-phase flows.

The Present Work

The experimental results obtained in the previous study by Fraser and Abdelmessih [16] provided considerable insight into the nature and the effects of flashing inception on critical two-phase flow. In that study, a new method of accurately controlling the location of flashing inception was developed. This allowed for a systematic investigation of the effects of the flashing process on the critical flow of saturated and subcooled water through long tubes. The effect of varying the location of flashing inception for different stagnation conditions and test section lengths were investigated. A range in the critical mass flux was observed for each stagnation condition. This range was more pronounced at lower subcooled stagnation states and can be attributed to the variation in the location of flashing inception. Maximum critical flow rates occurred with flashing inception located near the pipe exit; while minimum critical flow rates occurred with the flashing front located further upstream. It was also found that the superheat at flashing inception is strongly influenced by the critical flow rate and the flashing inception location. At highly subcooled stagnation states, flashing inception only occurred near the pipe exit, along with a negligible superheat. Furthermore, the visual observation of the flow

revealed that stable flashing inception nuclei were obtainable only through cavitation occurring at the tube wall. The nuclei formed were not uniformly distributed within the flow field, as commonly assumed in mechanistic models, and the initial bubble number densities appeared to vary considerably.

ANALYSIS

Instead of attempting to incorporate the additional theoretical complexities discussed above into more elaborate models, a reassessment of the earlier available models was performed by Fraser [17]. This resulted in identifying Henry's [19] and [20], and Henry and Fauske's [21] models as the basis for the formulation of the present model. These models were the only simplified approach that can be suitably modified to account for friction, the effect of the location of flashing inception, and the resultant non-equilibrium vapour generation rate. Furthermore, the assumption of an exponential relaxation of the phase change process assumed by Henry was consistent with the experimental results obtained in the previous study. The model was modified to predict both a minimum critical mass flux (for flashing inception located upstream of the exit) and a maximum critical mass flux with flashing inception located at the tube exit.

Henry's model is derived from considering the one-dimensional, steady-flow of an adiabatic, one-component two-phase system in a constant area duct. The model is based on considering the mixture mass, momentum and total energy balance equations. It was assumed that, in the vicinity of the exit plane, the momentum pressure drop is considerably larger than the sum of the frictional and elevational head losses. It was further assumed that flow was homogeneous (negligible slip) with an incompressible liquid phase. The following expression was then obtained for the critical mass flux

$$G_c^2 = -\left[x\left(\frac{dv_g}{dP} \right) + (v_g - v_{lo}) \left(\frac{dx}{dP} \right) \right]_e^{-1} \qquad (1)$$

Henry defined a non-equilibrium coefficient, N, that allows for a only a fraction of the equilibrium vapour generation to occur, $N = x/x_E$, where x_E is the equilibrium quality. By further assuming that the vapour expansion follows a polytropic process with an exponent n = 1.0, Equation (1) may be expressed as

$$G_c^2 = \left[\frac{x v_g}{P} - (v_g - v_{lo}) N \left(\frac{dx_E}{dP} \right) \right]_e^{-1} \qquad (2)$$

The parameter N was determined experimentally to be given by

$$\begin{aligned} N &= 20\, x_E \qquad & x < 0.05 \\ N &= 1.0 \qquad & x \geq 0.05 \end{aligned} \qquad (3)$$

The definition of the equilibrium quality is determined from an isentropic path,i.e.

$$x_E = \left(\frac{s_o - s_l}{s_g - s_l} \right) \qquad (4)$$

and the derivative of the mass fraction is given by

$$\frac{dx_E}{dP} = -\left[\frac{(1 - x)\frac{ds_l}{dP} + x\frac{ds_g}{dP}}{s_g - s_l} \right]_E \qquad (5)$$

where the subscript E indicates that all properties and derivatives are evaluated according to thermodynamic equilibrium at the exit local pressure.

The above equations may be combined to yield a transcendental equation for predicting the critical mass flux provided that the exit conditions, at the critical plane, are known. However, it is desirable to use a model which determines the conditions at the exit (critical) section based only on a knowledge of the input stagnation parameters. In order to fulfil this requirement, Henry proposed a solution for tubes with a sharp edged entrance geometry and length to diameter ratios within the range of 12 to 100. It was assumed that for an initially subcooled or saturated liquid flowing through a sharp edged entrance, a significant amount of vapour was not formed up to L/D = 12 (i.e. x = 0.0 at L/D = 12). After L/D = 12 the mixture would flash, and the two-phase mixture quality relaxed in an exponential manner towards the tube exit. The overall component of the entrance region and momentum pressure drop were added and a prediction of the critical mass flux was obtained based on the input stagnation state. The model, however, did not account for frictional losses (which become increasingly important for longer pipes), or for possible variations in the location of flashing inception. Comparisons between the prediction of Henry's model and available experimental results for nozzles and short pipes, which include water, nitrogen, potassium and carbon dioxide data, show that the model is in good agreement over a wide range of stagnation conditions. With longer pipes, however, the model has been found to overpredict the data and is therefore not recommended (Wallis [36], and Henry [22]).

Criteria for Minimum Critical Flow

The experimental results obtained by Fraser and Abdelmessih [16] have shown that the assumption of flashing inception occurring at a location of L/D = 12 from the entrance of the pipe is not universally valid. In that study, it was found that the location of flashing inception, for initially subcooled or saturated stagnation conditions, was always located further downstream from the entrance region. In fact, for highly subcooled stagnation conditions, flashing inception was observed to only occur within the exit region of the pipe. Data were obtained with the location of flashing inception accurately controlled through the use of a cavitating ring. This ring was located at a distance of L_R measured from the exit plane. The results have shown that under fixed stagnation conditions, moving the location of flashing inception upstream of the exit plane, by moving the cavitating ring, caused a reduction in both the critical mass flux and the flashing inception superheat. This effect can be attributed to the longer fluid residence time associated with an increase in the length of the two-phase region. Consequently, the two-phase mixture quality will tend to approach more of an equilibrium value at the pipe exit. The corresponding increase in the compressibility of the mixture approaching the exit will tend to minimize the critical flow rate. Consistent with these observations, the following modifications to Henry's model are proposed.

The nonequilibrium quality at the exit section, x_e, may be evaluated according to Henry, by assuming that the two-phase mixture quality relaxes in an exponential manner from the

location of flashing inception, $x = 0.0$ at L_R/D, towards the long tube value. Under these assumptions, the exit quality may be defined as

$$x_e = N x_E \left[1 - \exp\left(-B \frac{L_R}{D} \right) \right] \tag{6}$$

where N was defined previously by Equation (3). The constant B was determined to be representative of the decay of the degree of non-equilibrium with the length of the two-phase region. The constant B was found by Henry as $B = 0.0523$.

For a given exit pressure and thermodynamic state, the critical mass flux may be evaluated from Equation (2). The upstream stagnation conditions may then be calculated by considering the four components of the overall pressure drop as follows;

1) Entrance Region Pressure Drop

$$\Delta P_{ENT} = \frac{G_c^2 v_{l0}}{2} \left(1 + K_1 \right) \tag{7}$$

2) Momentum Pressure Drop

The homogeneous frictionless momentum pressure drop for flashing flow in a constant area duct is given by Wallis [37] as

$$\Delta P_M = G_c^2 x_e \left(v_{ge} - v_{l0} \right) \tag{8}$$

3) Frictional Pressure Drop

The overall frictional pressure drop is mainly dominated by the single-phase region. The frictional pressure loss for homogeneous two-phase flow may be represented by

$$-\left(\frac{dP}{dz} \right) = \frac{f G^2}{2 D} v_m \tag{9}$$

where the friction factor f has been assumed equal to that which would occur had the total flow been all liquid. The homogeneous fluid specific volume is given by

$$v_m = v_l + x v_{fg} \tag{10}$$

The exit quality predicted by Equation (6) is typically very low ($x_e < 0.004$) for the experimental range of the available data. Therefore, the mixture specific volume throughout the two-phase region may be approximated by

$$v_m = v_{l0} \tag{11}$$

Hence, the pressure drop due to friction is assumed to remain globally the same as in the single-phase liquid region. This approximation is also consistent with the results of Reocreux [29], and Senyhaeve [33]. Hence, the increase in the pressure drop represents mainly the accelerational term given by Equation (8). The frictional pressure gradient is given by

$$\Delta P_F = \frac{G_c^2 v_{l0}}{2} f \frac{L}{D} \tag{12}$$

4) Hydrostatic Pressure Gradient

For pipes at an inclination θ from the horizontal the hydrostatic pressure gradient for low quality flows may be approximated as

$$\Delta P_H = \rho_l g L \sin\theta \tag{13}$$

and the total pressure drop can then be written as

$$P_0 - P_e = G_c^2 \left[\frac{v_{l0}}{2} (1 + K_l) + \frac{v_{l0}}{2} f \frac{L}{D} + x_e (v_{ge} - v_{l0}) \right] + \Delta P_H \tag{14}$$

or in terms of the critical pressure ratio, η, as

$$\eta = 1 - \left(\frac{G_c^2}{P_0} \left[\frac{v_{l0}}{2} (1 + K_l) + \frac{v_{l0}}{2} f \frac{L}{D} + x_e (v_{ge} - v_{l0}) \right] + \frac{\Delta P_H}{P_0} \right) \tag{15}$$

where G_c is given by Equation (2).

Equations (2) through (15) may be combined to give a prediction of the critical flow rate based on a knowledge of the test section geometry and the upstream stagnation state.

For fixed stagnation conditions, increasing the value of L_R/D to greater than 50 was found to have a negligible effect on the critical mass flux. Although an increase in the length of the two-phase region caused a corresponding reduction in the critical mass flux, the magnitude of this effect decreased exponentially with an increase in the length of the two-phase region up to around $L_R/D = 50$. It is worthy to note that a similar relaxation of the vaporization process, as found by Henry, is given in Equation (6). Hence, for pipe length to diameter ratios greater than 50, the minimum critical mass flux may be found by setting $L_R/D = 50$ in Equation (6). For shorter pipes $L_R/D = L_T/D$, and the minimum critical mass flux is assumed to occur with flashing inception located at the entrance to the pipe.

Criteria for Maximum Critical Flow

The results of the experimental study have shown that the maximum critical mass flux was obtained with flashing inception located near the test section exit. For such cases $x_e = 0.0$ and the critical flow expression, Equation (2), is simplified to yield the limiting case

$$G_c^2 = -\left[(v_g - v_{l0}) N \left(\frac{dx_E}{dP} \right) \right]_e^{-1} \tag{16}$$

where N has the same functional dependence given previously by Equation (3). This equation is similar to that obtained by Henry and Fauske [21] to describe the critical flow rate through nozzles.

The derivative of the mass fraction in Equation (5) is dominated by the liquid phase in the low quality region. Therefore, the expression essentially describes the flashing of a

metastable liquid. Since $(1-x_e) \approx 1.0$ at the exit, the following expression is obtained

$$N\left(\frac{dx_E}{dP}\right) = -\left[\frac{N}{(s_g - s_l)}\left(\frac{ds_l}{dP}\right)\right]_E \qquad (17)$$

The upstream stagnation conditions may be determined by considering the single-phase region leading up to the exit plane. This may be expressed in terms of the critical pressure ratio by

$$\eta = 1 - \left(\frac{G_c^2 v_{l0}}{2 P_0}\left[(1 + K_l) + f\frac{L}{D}\right] + \frac{\Delta P_H}{P_0}\right) \qquad (18)$$

Equations (3), (4), (16), (17), and (18) may be solved simultaneously for the critical mass flux based on a given upstream stagnation state.

A computer program was developed, based on the above analysis, to calculate the maximum and minimum critical mass fluxes. Thermophysical properties and their derivatives were calculated using a cubic spline interpolating polynomial based on ASHRAE data [7]. Single phase friction factors were calculated by the Colebrook equation (Beatie, [8]). The program reads the input stagnation properties and pipe geometry. The program then coordinates the results from the various subroutines and tests for convergence of the solution. Following the solution, the degree of superheat (pressure undershoot) at flashing inception may also evaluated by considering the pressure at the location of flashing inception.

COMPARISON TO THE AVAILABLE DATA

The above maximum and minimum critical flow models can be utilized to produce a graph of the range in the critical mass flux versus the stagnation pressure, for a known pipe geometry, with stagnation temperature as the second independent variable. Hence, separate graphs are required for each choice of stagnation temperature. A more effective method of comparing the available data on a single graph, over a wide range of stagnation temperatures, was found by Fraser [17] through a dimensional analysis of the experimental data. In particular, the appropriate dimensionless parameters found are expressed as:

$$P^* = \frac{P_0}{P_{SAT,\,T_0}} \qquad (19)$$

where P^* is the dimensionless stagnation pressure. The dimensionless critical mass flux, G^*, is then given by

$$G^* = \frac{G_C^2}{2\,\rho_l\,P_{SAT,\,T_0}} \qquad (20)$$

The use of equation (19) is restricted to $P^* \geq 1$ since only stagnation pressures greater than or equal to P_{SAT} are considered.

The experimental results obtained in the previous study revealed that two-phase flow instabilities may occur during critical flow due to an absence of active nucleation sites along the

pipe length. In all experimental runs, unstable flow was observed (particularly for low values of L_R/D) when the stagnation pressure was near saturation. These instabilities were low frequency oscillations due to regenerative feedbacks between the flow rate, vapour generation rate and the corresponding pressure drop across the channel. Alternating single-phase and two-phase flow was observed due to periodic nucleation occurring within the entrance region of the test section. The analysis of the data resulted in the following expression to define the stable flow limit

$$P_S^* = 0.2 - \Delta P_S^* \tag{21}$$

where P_S^* is the dimensionless pressure undershoot at flashing inception and is defined as

$$P_S^* = \frac{\Delta P_{Fi}}{P_{SAT,\,T_0}} \tag{22}$$

Where ΔP_{Fi} is the pressure undershoot at flashing inception, it therefore represents the degree of thermal non-equilibrium. The second term in Equation (21) was found to be given as an exponential function of the dimensionless distance of the location of flashing inception

$$\Delta P_S^* = 0.103\ [1 - e^Y] \tag{23}$$

where $Y = -0.067 L_R/D$ and $0 \leq L_R/D \leq 50$. Equations (21) through (23) are only valid in predicting the stable flow limit (as will be shown later) and were found through an empirical fit to the pressure undershoot data obtained by Fraser [16] at the stable flow limit. Hence, it can be shown that these equations are not generally valid (outside of the narrow range where flow instablities occurred) for predicting the pressure undershoot at flashing inception during stable critical two-phase flow. The Dimensionless stagnation pressure, P^* given by Equation (19), corresponding to the stable flow limit given by Equations (21) to (23) was found by considering the single-phase flow from the location of flashing inception up to the stagnation conditions at the tube entrance.

The above equations may be used to construct a single graph to conveniently represent the data for a given test section geometry over a wide range of thermodynamic states. Figure 1 is an example of a graph of G^* versus P^*. Shown in this figure are sample predictions of the maximum and minimum Homogeneous Non-Equilibrium (HNE) critical flow model. Also shown is the line defining the stable flow limit as given by Equations (21) to (23). In addition the curve for the conditions where $P_{EXIT} = P_{SAT}$ is also shown. This curve is obtainable through a simple expression proposed by Celata et al. [11], for evaluating the critical mass flux at highly subcooled stagnation states. By assuming that the outlet critical pressure, P_C, is approximately equal to the saturation pressure at T_0, the critical mass flux is given by

$$G_C = \sqrt{\frac{2\,\rho_0\,[P_0 - P_{SAT,\,T_0}]}{1 + K_1 + f\,\frac{L}{D}}} \tag{24}$$

The curve for $P_{EXIT} = P_{SAT}$, therefore, represents a limiting condition where flashing inception would occur at the tube exit along with a negligible superheat.

Both the maximum and minimum critical flow models predict that for increasing subcooled stagnation states, the exit pressure approaches the saturation pressure corresponding to the inlet stagnation temperature. Hence, at highly subcooled stagnation states, the curve given by Equation (24) is asymptotically approached by the predictions of both the maximum and minimum HNE models. As the predicted exit pressure approaches saturation, the equilibrium quality, x_E, approaches zero. It can be shown that from Equations (2) and (16) the predicted critical flow rate increases with a decrease in the exit quality. In the limit, x_E approaches zero with increased subcooled stagnation states, and both predictions (maximum and minimum) approach an infinite flow rate. This is a consequence of the particular choice of the parameter N and the order of magnitude approximation that the liquid phase is incompressible. Such approximations used in developing the model results in discontinuous derivatives as the saturation line is approached (for a detailed discussion see Fraser [17] and Collins [11]). It is worthy to note, however, that the experimental results obtained in the present study have shown that the exit pressure does indeed approach saturation for highly subcooled stagnation states (i.e. when flashing inception occurs at the exit with a negligible superheat).

The predicted region of possible critical two-phase mass fluxes shown in Figure 1 is more pronounced at lower subcooled stagnation states (around 30 to 40 percent of the maximum) and decreases with increasing mass flux, gradually converging to the curve $P_{EXIT} = P_{SAT}$ at highly subcooled stagnation states. The two predictions (maximum and minimum) tend to convergence as the predicted exit quality approaches zero. This convergence is due to the corresponding reduction in the compressibility of the flow at vanishing quality (the first term in Equation (2) approaches zero) and both predictions reduce to the same expression for the maximum critical flow rate given by Equation (16). The critical mass fluxes for saturated stagnation conditions are predicted for the region $P^* = 1.0$. Furthermore, since $G^* \alpha G_C^2$, the apparent error in the prediction of G^* decreases with an increase in the critical mass flux as shown in Figure 1.

Figure 1 can be thought of as consisting of two regions; a) a lower bound region where a range of possible critical mass fluxes is predicted and, b) the highly subcooled region. The following is a brief discussion with respect to these two regions:

a) The Lower Bound Region

The maximum critical two-phase mass flux is predicted to occur with flashing inception located at the exit of a constant area duct ($L_R/D = 0$). The HNE maximum critical flow model asymptotically approaches the curve $P_{EXIT} = P_{SAT}$ with increased subcooled stagnation states. Data points that lie within the lower bound region are predicted to occur due to the flashing front moving upstream of the tube exit (i.e. increasing L_R/D). The predicted minimum critical mass flux occurs with $L_R/D \leq 50$ as the pressure approaches saturation conditions. The stable flow limit shown is given by Equation (21) and provides closure to the lower region of possible critical flow rates for near saturated stagnation conditions.

b) The Highly Subcooled Region

As discussed above, the curve identified as $P_{EXIT} = P_{SAT}$ is the limiting case for which flashing inception will occur at the tube exit along with a negligible superheat. Data that lie above this curve would be for flashing inception occurring upstream or at the tube exit with a certain degree of superheat. On the other hand, data that lie beneath the curve $P_{EXIT} = P_{SAT}$ are only possible if flashing inception occurs within the pipe at a negative superheat. Under those conditions, flow choking may occur due to the presence of a compressible phase within the

subcooled region of the pipe (the single-phase sonic velocity would be much larger). This may be possible when a large degree of dissolved gases are present in the fluid.

Available data for both short and long pipes since early 1970 were compared with the predictions of the maximum and minimum Homogeneous Non-Equilibrium critical flow model (HNE) described herein. The results of those comparisons are shown in Figures 2 to 8. In the figures where a large temperature range is shown, the predictions of the HNE varies slightly (± 3%) with the temperature. Hence, where a temperature range is specified, the average temperature was chosen as the input stagnation condition. Furthermore, the entrance loss coefficients, values of the pipe relative roughness e/D, and the relevant pipe geometry were obtained for each case from the published data. The only exception to this was the data of Sozzi and Sutherland [35] who failed to report on the relative roughness of the pipe. A brief discussion pertaining to each of the comparisons is given below:

Figure 2 shows the high pressure (2.0 - 3.4 MPa) and temperature (190-240°C) data of Dobran [12] for L/D = 97. These data were obtained only for saturated and highly subcooled stagnation states. The predictions of the HNE tend to converge at higher subcooled stagnation states, eventually following the curve $P_{EXIT} = P_{SAT}$. The data within the highly subcooled region are predicted well by the models as they approach the curve $P_{EXIT} = P_{SAT}$. The HNE predicts a slight superheat with flashing inception located at the tube exit. The experimentally obtained pressure profiles of Dobran for those highly subcooled stagnation states revealed the anticipated non-linearity of the axial pressure gradient profile (onset of flashing - developing two-phase flow) to occur near the exit with negligible superheat. Such an observation supports the prediction of the HNE. The data obtained for saturated stagnation conditions is also predicted well. For this case, the estimated length of the two-phase region (from the experimentally obtained axial pressure profiles) was around L_R/D = 50 from the exit, along with a moderate superheat. This was also predicted to occur by the HNE, hence resulting in the close agreement shown.

Also shown in Figure 2 is the effect of varying the value of the nonequilibrium coefficient, N, in the maximum critical flow model. Shown are two curves representing the predictions of the maximum critical flow model with $N = 10x_E$ (representing a higher non-equilibrium vapour generation rate) and $N = 30x_E$ (representing a closer approach to an equilibrium phase change at the critical plane). The following comparisons to the other available data make it clear that the choice of $N = 20x_E$ (for low quality flows) as proposed by Henry [20] is an appropriate choice.

The low pressure data of Ardron and Ackerman [6] for L/D = 38.6 are shown in Figure 3. Data taken at low to moderately subcooled stagnation conditions reflects the variation noted by most researchers and are well within the region bounded (maximum and minimum) by the HNE. As the static pressure near the tube inlet approached saturation, the flashing front was observed by Ardron and Ackerman to move upstream toward the location A shown (L_R/D = 30.6) as predicted to occur by the HNE for this region. Their experimentally obtained axial pressure profiles revealed that for higher critical mass fluxes (increased subcooling) the flashing front approached the exit along with a negligible superheat. This behaviour was also predicted to occur by the model. The close agreement between the predictions and the data within the highly subcooled region (within 6%) is clear.

The larger scale experimental results of Reocreux [29] and Senyhaeve [33] for L/D = 124 are shown in Figure 4. Figure 5 is the results obtained by Senyhaeve [33] for a shorter test section with L/D = 24.5. Both test sections were for vertical upflow. The data of Senyhaeve

for L/D = 124 shown in Figure 4 were obtained after that of Reocreux, utilizing the same test section installed in a different facility. As mentioned earlier, both Reocreux and Senyhaeve attempted to derive a relationship for the onset of flashing. They estimated the degree of superheat and the location of flashing inception from where the axial pressure profile deviated from linearity. Their data were quite scattered (the point of inception was uncontrollable), yet still revealed the superheat to behave inversely with respect to the critical mass flux. The superheat eventually decreased to around zero at higher flow rates, with flashing inception occurring near the exit (critical plane). Both of those observations were predicted to occur by the HNE. Reocreux and Senyhaeve also estimated the location of flashing inception L_R/D (the length of the two-phase region) from their experimental data. Those values are shown alongside the data points in Figure 4 and were in close agreement with the predictions of the model.

The high pressure data of Sozzi and Sutherland [35] for L/D = 50 and 140, P_0 = 6.2 to 6.9 MPa., are shown in Figure 6(a) and 6(b). The value of the relative roughness of the pipe was not obtainable from their data. Instead, the relative roughness was obtained by matching their highly subcooled data to the prediction for $P_{EXIT} = P_{SAT,T_0}$ (the validity of this assumption can be further supported by other data, notably Celata [10], for highly subcooled stagnation states). The data were again quite scattered in the low to moderately subcooled regions (≈ 30%). Saturated stagnation states were also well predicted. The decrease in the critical mass flux with the longer length test section (L/D = 140) due to flow friction was predicted to occur by the HNE. In both test sections, the relative roughness was the same (the shorter pipe was obtained by reducing the length of the longer pipe).

Also shown in Figures 6(a) and 6(b) are the predictions of the Homogeneous Equilibrium Model (HEM). This model dramatically overpredicts the data. As discussed earlier, the HEM is based on a single phase analogy and assumes the phases to be intimately mixed and to have equal velocities and temperatures. Although still widely used in many thermalhydraulic codes for nuclear reactor safety analysis, this model is a limiting case which neglects friction as well as thermal and hydrodynamic non-equilibrium effects.

The data of Alsahan [1] for L/D = 214 are shown in Figure 7. Again the data are all well within the region predicted by the HNE. The close agreement at highly subcooled and saturated stagnation states is also evident. Alsahan [2] later conducted a few experiments for saturated stagnation conditions only. His data are presented in dimensional form in Figure 8. The prediction of the critical two-phase mass flux based on the HNE (in dimensionless form) is shown in the inset graph. The prediction for $P^* \approx 1.0$ (corresponding to saturated stagnation states) is $G^* = 0.015$. From this, the plot of the critical mass flux versus the vessel stagnation pressure, P_0, was constructed as shown ($P_0 = P_{SAT,T_0}$). Excellent agreement between HNE and the experimental results are found. Furthermore, this example illustrates how the data is compressed through the dimensionless plot of G^* versus P^*. Similar results may be obtained for the data of Dobran, Ardron and Ackerman as well as Sozzi and Sutherland from the previous figures.

CONCLUSIONS

The one-component, critical two-phase flow of saturated and subcooled water in long pipes was investigated both analytically and experimentally. In the experimental investigation a new method of controlling the location of flashing inception during critical two-phase flow was developed. The method involved the use of a cavitating ring that could be easily positioned axially along the test section length thus allowing for a systematic study of the effect of flashing inception on critical two-phase flow. A review of the literature reveals that no prior studies

appear to exist on the effects of flashing inception on critical two-phase flow. This information led to the development of a computer model coupled with a dimensional analysis for predicting critical two-phase flow rates over a wide range of conditions.

The mathematical model was developed based on the nonequilibrium theories of Henry [20] and Henry and Fauske [21]. It was argued that for low quality flows, the mixture is homogeneous (i.e. no slip between the phases) and that the phase change is a nonequilibrium process. The critical flow prediction assumes neither a frozen nor a complete thermodynamic equilibrium phase change at the exit (critical plane). Instead, the models approximate the nonequilibrium phase change process by thermodynamic equilibrium paths. A criterion for predicting both the maximum and minimum critical mass flux were proposed. The prominent features of the proposed model are:

1. The solution is based on, and only requires, a knowledge of the upstream stagnation state and tube geometry.
2. The models include the relative effects of varying the location of flashing inception, the pipe geometry, fluid properties and length to diameter ratio.
3. The model predicts that a range of critical mass fluxes are possible for a given stagnation state. This range decreases with increased subcooling and is bounded from above by the maximum critical flow model and from below by the minimum critical flow model. A further criteria is proposed that defines the limit of stable flow for near saturated stagnation conditions. The maximum critical mass flux is predicted to occur with flashing inception located at the tube exit. The minimum mass flux is predicted to occur with the flashing front located further upstream.
4. Available data since early 1970 was compared with the model predictions in order to investigate the general predictive capability of the models. These data cover a wide range of test section geometries (length, diameter and geometry) over a wide range of thermodynamic states (pressures up to 6.9 Mpa and temperatures to 280^{0} C). The comparisons between the theoretical predictions and the available experimental results show an excellent agreement.

ACKNOWLEDGEMENTS

Financial assistance for this work, provided by the University of Toronto and the National Science and Engineering Research Council of Canada (grant #OGP-0004172), is gratefully acknowledged.

REFERENCES

[1] Alsahan, M.A., "Experimental Study of Two-Phase Critical Flow of Initially Subcooled Water in Long Tubes", M.Sc. Thesis, University of Toronto, Toronto, Canada, (1980).

[2] Alsahan, M.A., "On the Development of the Flow Regimes and the Formulation of a Mechanistic Model For Critical Two-Phase Flow", Ph.D. Thesis, University of Toronto, Toronto, Canada, (1987).

[3] Alamgir, Md. and Lienhard, J.H., "Correlation of Pressure Undershoot During Hot Water Depressurization", *ASME J. of Heat Transfer*, Vol. 103, pp. 52-55, (1981).

[4] Ardron, K.H. and Furness, R.A., "A Study of the Critical Flow Models Used in Reactor Blowdown Analysis", *Nuclear Eng. and Design*, Vol. 39, pp. 257-266, (1976).

[5] Ardron, K.H., "A Two-Fluid Model for critical Vapor-Liwuid Flow", *Int. J. Multiphase Flow*, Vol. 4, pp. 323-337, (1978).
[6] Ardron, K.H., and Ackerman, M.C., "Studies of the Critical Flow of Subcooled Water in a Pipe", CEGB Report RD/B/N4299, Berkely Nuclear Laboratories, (1978).
[7] ASHRAE Handbook, "Fundamentals", (1978).
[8] Beatie, D.R.H., "Friction Factors and Regime Transitions in High Presuure Steam-Water Flows", ASME Paper 75-WA/HT-4, (1975).
[9] Bilicki, Z., Dafermos, J., Kestin, J., Majda, G., Zeng, D.L., "Trajectories and Singular Points in Steady-State Models of Two-Phase Flows", *Int. J. Multiphase Flow*, Vol. 13, No. 4, pp. 511-533, (1987).
[10] Celata, C.P., Cuma, M., D'Annibale, F., and Farello, G.E., "The Influence of Non-Condensible Gas on Two-Phase Critical Flow", *Int. J. MultiPhase Flow*, Vol. 14, pp. 175-187, (1988).
[11] Collins, R.L., "Choked Expansion of Subcooled Water and the I.H.E. Flow Model", *ASME J. of Heat Transfer*, Vol. 100, pp. 275-279, (1978).
[12] Dobran, F., "Nonequilibrium Modeling of Two-Phase Critical Flow in Tubes", *ASME Journal of Heat Transfer*, Vol. 109, pp. 731-737, (1987).
[13] Elias, E., and Chambre, P.L., "A Mechanistic Non-Equilibrium Model For Two-Phase Critical Flow", *Int. J. MultiPhase Flow*, Vol.10, pp. 21-40, (1984).
[14] Elias, E., and Lellouche, G.S.,"Two-Phase Critical Flow", *Int. J. Multiphase Flow*, Vol. 20, Suppl. pp. 91-168, 1994.
[15] Fauske, H.K., "Contribution to the Theory of Two-Phase, One-Component Critical Flow", Tech. report No. ANL-6767, (1962).
[16] Fraser, D.W.H., and Abdelmessih, A.H., "A Study of the Effects of Flashing Inception on Maximum and Minimum Critical Two-Phase Flow Rates", Int. Symp. on Gas-Liquid Two-Phase Flows, ASME Spring Meeting, Washington, D.C., June 20-24, FED Vol. 165, (1993).
[17] Fraser, D.W.H., "A Study of the Effects of Flashing Inception and the Formulation of a Non-Equilibrium Model for Maximum and Minimum Critical Two-Phase Flow", Ph.D Thesis, University of Toronto, Toronto, Canada, (1993).
[18] Giot, M., "Experiments and Modelling of Choked Flow", *Proceedings, First World Conference on Experimental Heat Transfer, Fluid Mechanics, and Thermodynamics*, R.K. Shah et al., eds., Elsevier Publishing Co., New York, pp. 1105-1119, (1988).
[19] Henry, R.E., "A Study of One- and Two-Component, Two-Phase Critical Flow at Low Qualities", Tech. Report ANL-7430, (1968).
[20] Henry, R.E., "The Two-Phase Critical Discharge of Initially Saturated or Subcooled Liquid", *Nuclear Science and Eng.*, Vol. 41, pp. 336-342, (1970).
[21] Henry, R.E., and Fauske, H.K., "The two-Phase critical Flow of One-Component Mixtures in Nozzles; Orifices and Short Tubes", *ASME J. Heat Transfer*, (1971).
[22] Henry, R.E., "Caculational Techniques for Two-Phase Critical Flow", *Chem. Engg. Progress;*Symposium Series, No. 113, Vol. 67, (1979).
[23] Isbin, H.S., "Some Observations on the Status of Two-Phase Critical Flow Models", *Int. J. Multiphase Flow*, Vol. 6, pp. 131-137, (1980).
[24] Jones, O.C., and Zuber, N., "Bubble Growth Rates in Variable Pressure Fields", *Trans. ASME, J. of Heat Transfer*, 100 C, pp. 453-459, (1978).
[25] Jones, O.C., "Inception and Development of Voids in Flashing Liquids", *Two-Phase Flow Dynamics*, Hemisphere Publishing Co., Washington, D.C., pp. 437-469, (1981).

[26] Jones, O.C., and Shin, T.S., "A Distributed Nucleation Model for Critical Flows of Initially Subcooled Liquids", Transient Phenomena in Multiphase Flow, ed. Afgan, N.H., Hemisphere Pub. Co., New York, pp. 667-685, (1988).
[27] Levy, S., "Prediction of Two-Phase Critical Flow Rate", *ASME J. of Heat Transfer*, Vol. 8, (1965).
[28] Moody, F.J., "Maximum Discharge Rates of Liquid-Vapor Mixture From Vessels", ASME Symposium Non-Equilibrium Two-Phase Flows, eds., Lahey, R.T. and Wallis,G.B, (1975).
[29] Reocreux, M., "Contribution to the Study of Critical Flow Rates in Two-Phase Water Vapour Flow", Ph.D. Thesis, Universitie Scientifique et Medicale de Grenoble, Translated, NUREG-TR-0002, (1974).
[30] Richter, H.J., "Separated Two-Phase Flow Model: Application to Critical Two-Phase Flow", *Int. J. MultiPhase Flow*, Vol. 9, pp. 511-530, (1983).
[31] Rohatgi, U.S., and Reshotko, E., "Non-Equilibrium One-Dimensional Flow in Variable Area Channels", Non-Equilibrium Two-Phase Flows, Winter Annual Meeting ASME, Houston, Texas, pp. 47-54, (1975).
[32] Saha, P., "A Review of Two-Phase Steam-Water Critical Flow Models With Emphasis on Thermal Non-Equilibrium", NUREG/CR/0417, BNL-NUREG-50907 Report, (1978).
[33] Seynhaeve, J.M., "Etude Experimentale des Ecoulements Diaphasiques Critique a Faible Titre", Ph.D. Thesis, Universitie Catholique de Louvain, (1980).
[34] Shin, T.S., and Jones, O.C. , "Nucleation and Flashing in Nozzles", *Int. J. Multiphase Flow*, Vol. 19, No. 6, pp. 943-964, (1993).
[35] Sozzi,G.L., and Sutherland, W.A., "Critical Flow Of Saturated and Subcooled Water at High Pressures", General Electric Company., NEDO-13418, (1975).
[36] Wallis,G.B.,"Critical Two-Phase Flow", *Int. J. Multiphase Flow*, Vol. 6, pp. 97-112, (1980).
[37] Wallis, G.B., "One-Dimensional Two-Phase Flow", McGraw-Hill, (1969).
[38] Zivi, S.M., "Estimation of Steady-State Steam Void Fraction by Means of the Principle of Minimum Entropy Production", *J. of Heat Transfer*, May 1964, pp. 247, (1964).

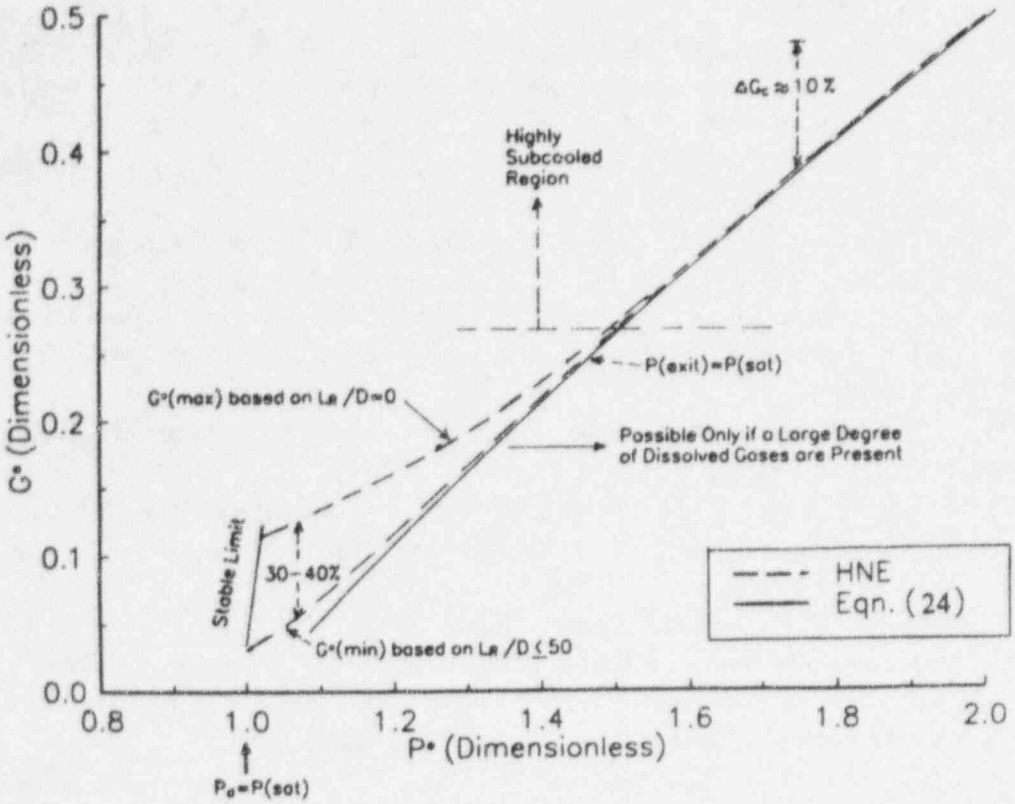

Fig. 1 Sample Graph of the Dimensionless Critical Mass Flux Versus Pressure

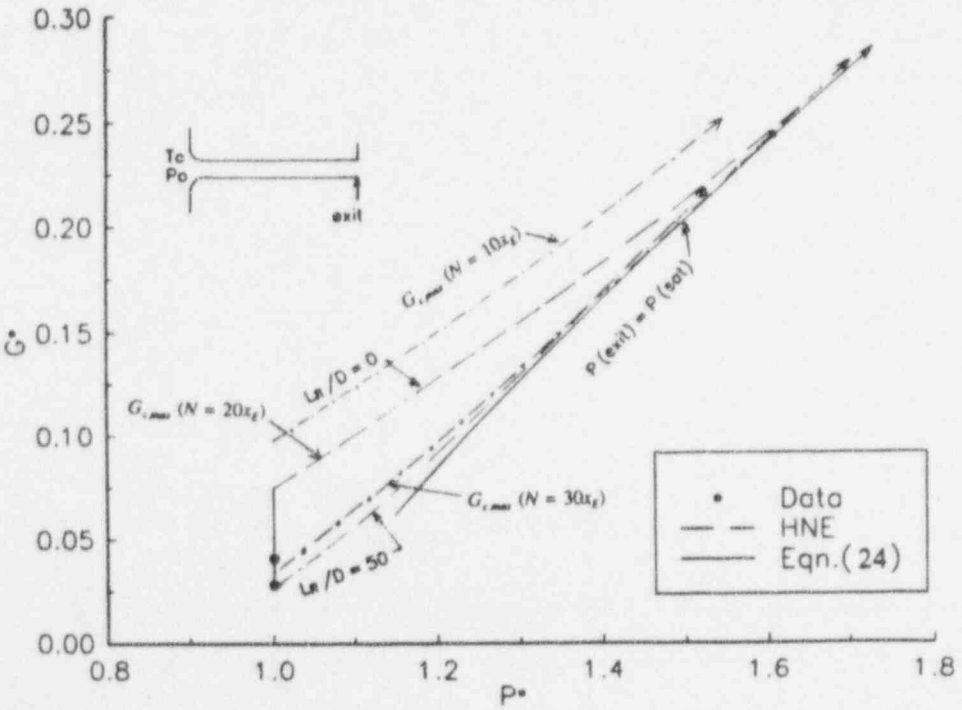

Fig. 2 Comparison to the Results of Dobran (T_0 = 190 - 240°C)
P_0 = 2.0 - 3.4 MPa, L/D = 97
K_i = 0.2, e/D = 0.0002, D = 0.0125 m.

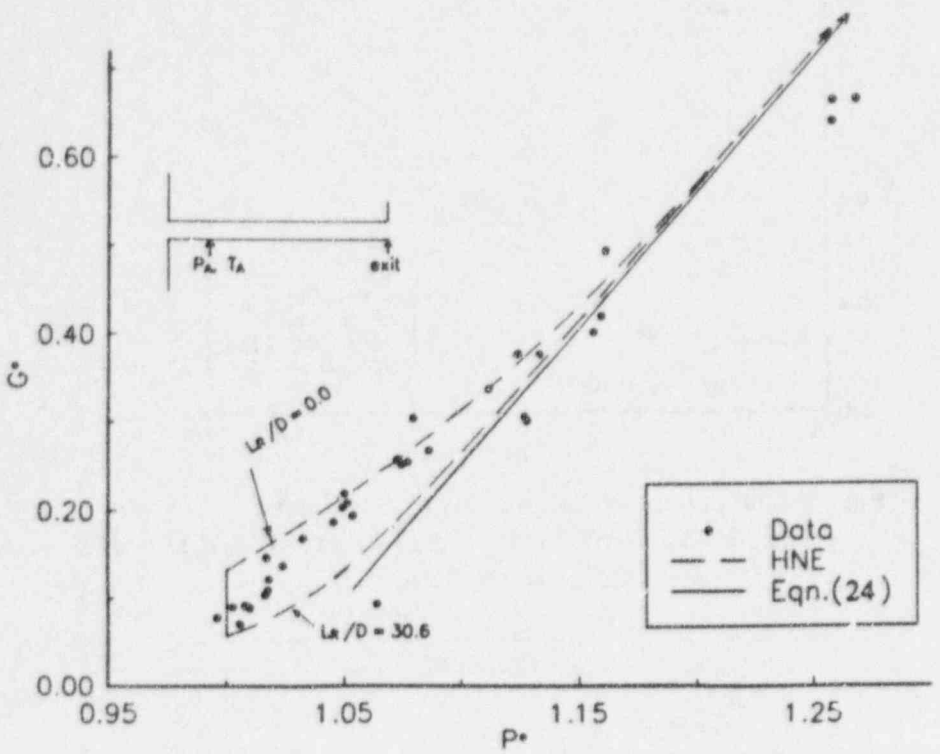

Fig. 3 Comparison to the Results of Ardron and Ackerma
(T_A = 110 - 140^{0}C), P_A = 0.16 - 0.37 MPa, L/D = 8.6
e/D = 0.00005, D = 0.02615 m.

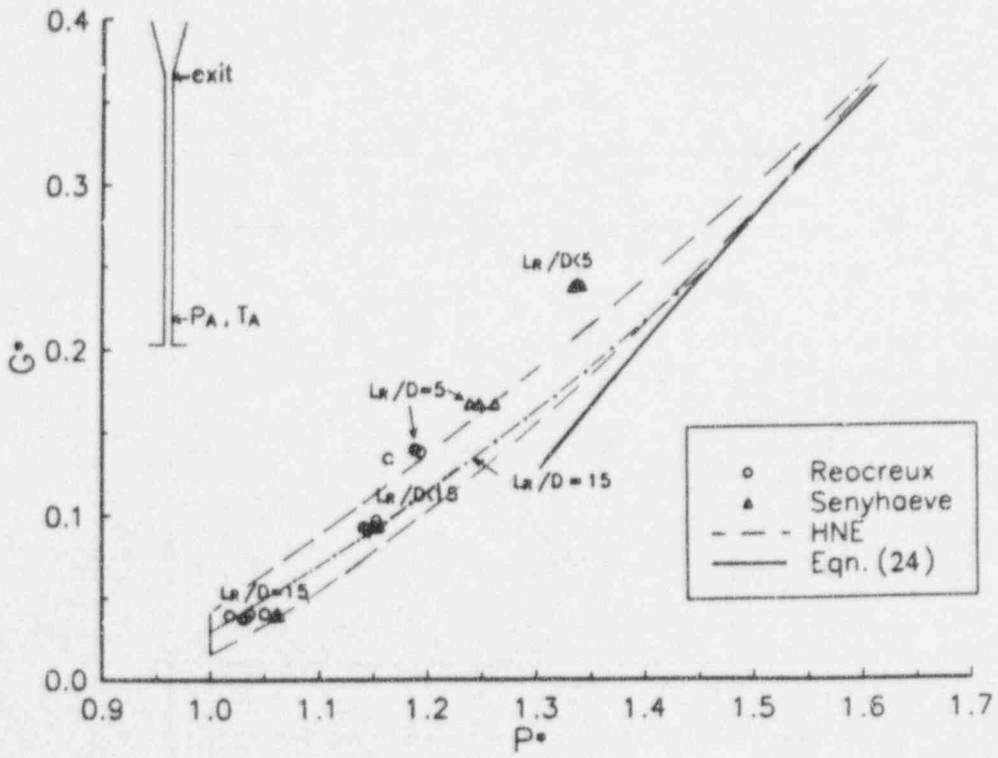

Fig. 4 Comparison to the Results of Reocreux and Seynhaeve
(T_A = 126 $\pm$ 0.1^{0}C), P_A = 0.24 - 0.30 MPa, L/D = 124
e/D = 0.00001, D = 0.02 m.

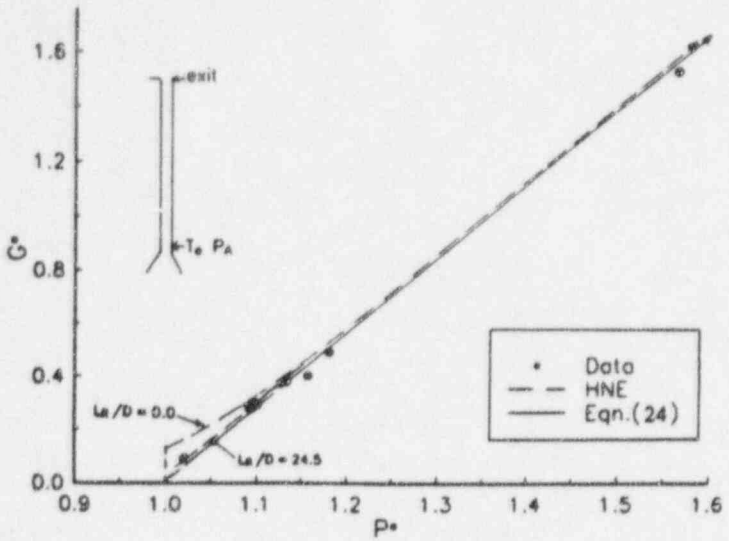

Fig. 5 Comparison to the Results of Seynhaeve
(T_A = 111 - 167^{0}C), P_A = 0.23 - 0.80 MPa, L/D = 24.5
e/D = 0.00022, D = 0.0125 m.

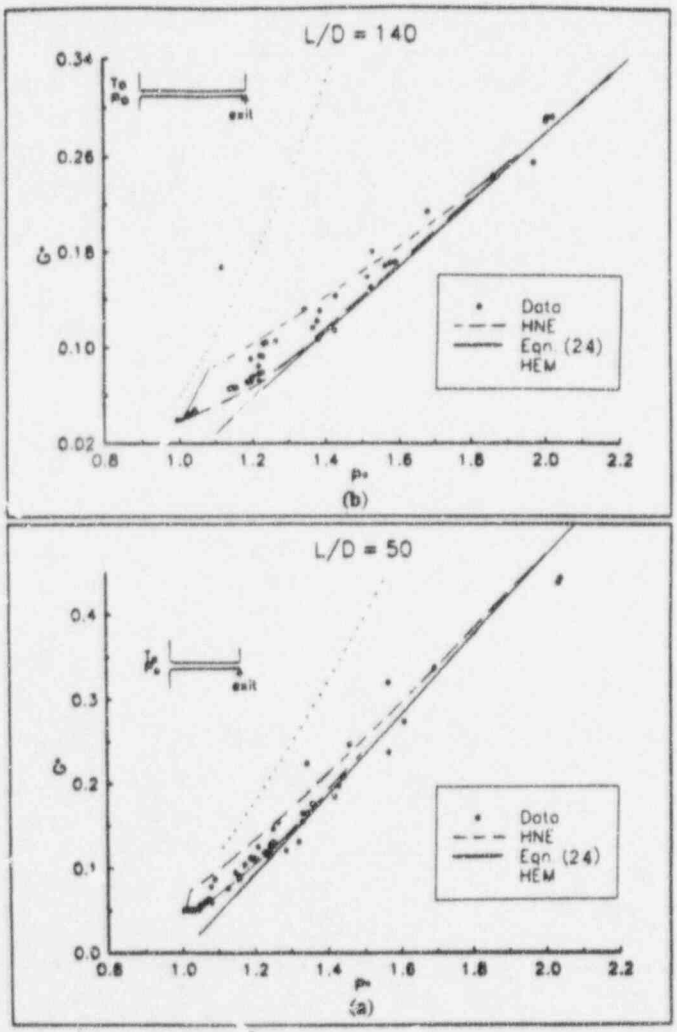

Fig. 6 Comparison to the Results of Sozzie and Sutherland
T_0 = 238 - 280^{0}C, P_0 = 6.2 - 6.9 MPa
K_i = 0.04, e/d = 0.001, D = 0.0127m.
(a) L/D = 50 and (b) L/D = 140

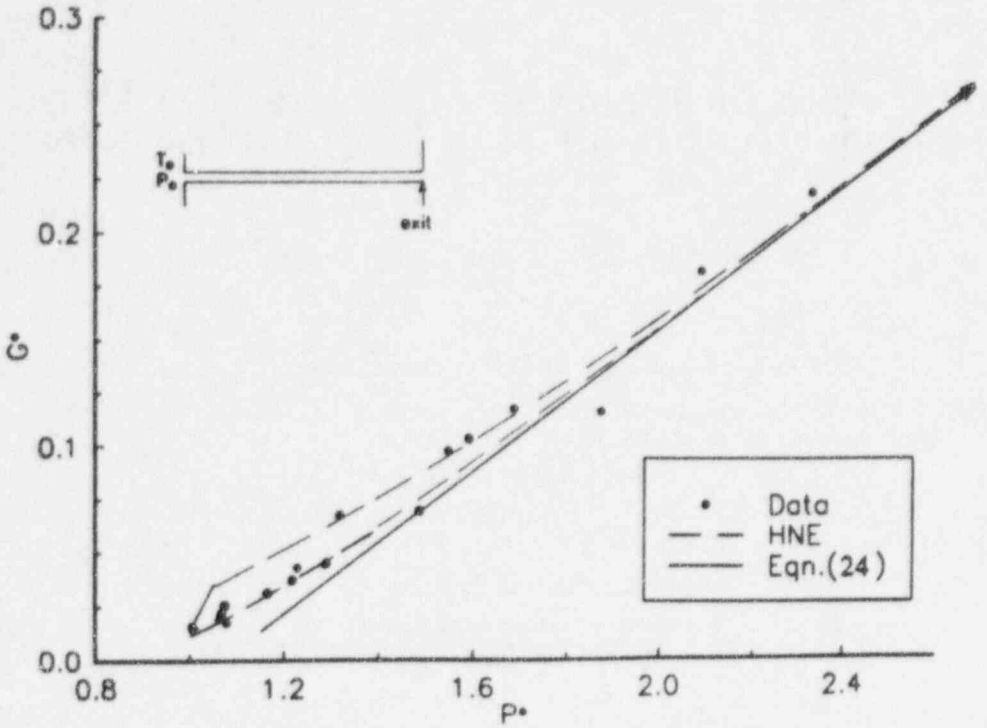

Fig. 7 Comparison to the Results of Alsahan (T_0 = 130 - 190^{0}C)
P_0 = 0.4 - 1.4 MPa, L/D = 214
K_i = 0.5, e/D = 0.0018, D = 0.0032 m.

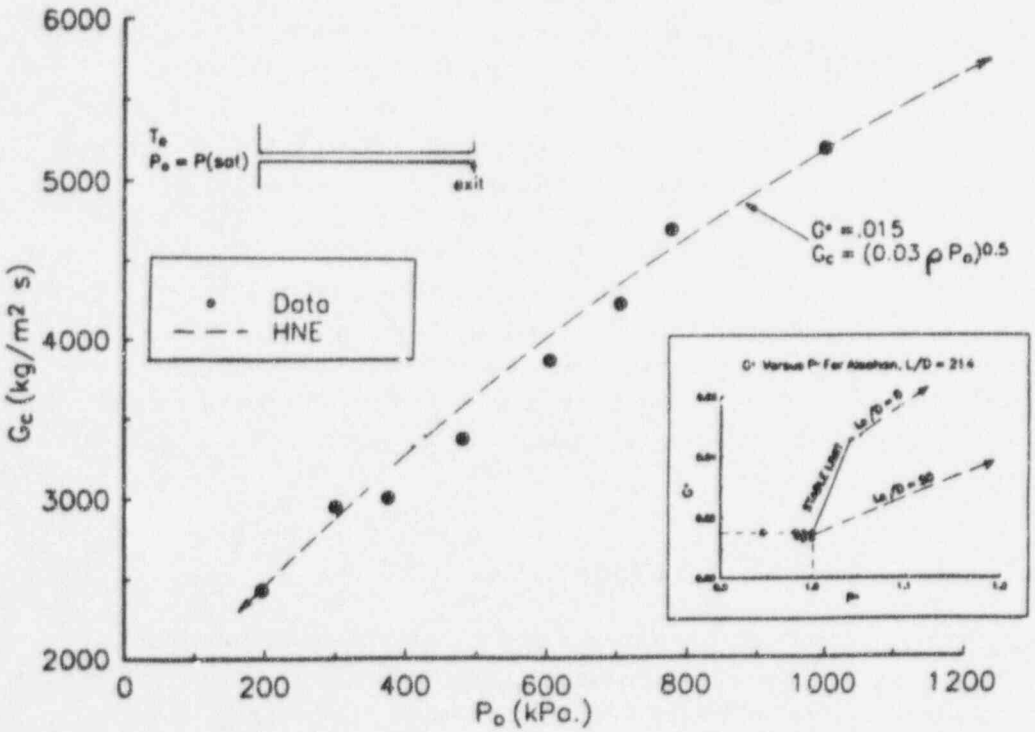

Fig. 8 Comparison to the Results of Alsahan, Saturated
(T_0 = 130 - 190^{0}C), P_0 = 0.19 - 1.0 MPa, L/D = 214
K_i = 0.5, e/D = 0.0015, D = 0.0032 m.

PREDICTIONS OF BUBBLY FLOWS IN VERTICAL PIPES USING TWO-FLUID MODELS IN CFDS-FLOW3D CODE

A.O. Banas[a], M.B. Carver[a] and D. Unrau[b]

[a]Fuel Channel Thermalhydraulics Branch
AECL
Chalk River Laboratories
Chalk River, Ontario
K0J 1J0

[b]University of Toronto
Institute of Aerospace Studies
4925 Dufferin Street
Downsview, Ontario
M3H 5T6

ABSTRACT

This paper reports the results of a preliminary study exploring the performance of two sets of two-fluid closure relationships applied to the simulation of turbulent air-water bubbly upflows through vertical pipes. Predictions obtained with the default CFDS-FLOW3D model for dispersed flows were compared with the predictions of a new model (based on the work of Lee), and with the experimental data of Liu. The new model, implemented in the CFDS-FLOW3D code, included additional source terms in the "standard" k–ϵ transport equations for the liquid phase, as well as modified model coefficients and wall functions. All simulations were carried out in a 2-D axisymmetric format, collapsing the general multifluid framework of CFDS-FLOW3D to the two-fluid (air-water) case. The newly implemented model consistently improved predictions of radial-velocity profiles of both phases, but failed to accurately reproduce the experimental phase-distribution data. This shortcoming was traced to the neglect of anisotropic effects in the modelling of liquid-phase turbulence. In this sense, the present investigation should be considered as the first step toward the ultimate goal of developing a theoretically sound and universal CFD-type two-fluid model for bubbly flows in channels.

1 INTRODUCTION

At present, thermalhydraulic computations of internal flows and heat transfer in nuclear-reactor components rely on porous-medium and subchannel approximations for capturing multidimensional effects. However, these approaches target only relatively crude resolution of flow details, and their underlying theoretical bases rest firmly on empirical *hydraulic* concepts. Methods of analysis rooted in Computational Fluid Dynamics (CFD) are steadily gaining in popularity and importance, but their acceptance as working tools of nuclear engineers is clearly tied to further development of their predictive capabilities for multiphase gas-liquid flows. Two-fluid formulation, with a long and successful track record as a basis of advanced computational methodologies in two-phase thermalhy-

draulics, is widely considered to be one of the most promising frameworks for modelling two-phase flows in CFD. Indeed, progress achieved in the development of general two- and multi-fluid numerical algorithms has enabled the realistic multidimensional simulations of many diverse types of two-phase flows. Nevertheless, the credible prediction of even the simplest gas-liquid flows by CFD methods continues to pose a significant challenge. If consistent reproductions of experimental data are to be achieved in two-fluid CFD simulations, more reliable *closure* relationships need to be formulated to complement the two-fluid formulation. To reduce the uncertainty regarding the appropriate *closure*, further insight into the microscopic physical mechanisms dominating various two-phase flow regimes must be developed and fed back into the modelling effort, while systematic numerical validations of new models continue.

In response to this need, a research project addressing the modelling and simulation of multiphase flows in the CFD context has been recently initiated at Chalk River Laboratories. Considering the paucity of experimental data appropriate for CFD validation of two-fluid models for boiling flows, we decided to focus our initial effort on assessing the two-fluid closures proposed for adiabatic air-water bubbly flows in pipes. Following the pioneering studies of Serizawa *et al.* [1], Nakoryakow *et al.* [2], and Theofanous and Sullivan [3], this class of two-phase flows has attracted the attention of many experimenters interested in the effects of the gas phase on the flow structure. Their measurements of local properties (liquid and bubble velocities, turbulent intensities, void, interfacial area and pressure) led to the accumulation of a sizeable data base that appears to be adequate for numerical validation of at least some two-fluid closure hypotheses. Serizawa and Kataoka [4] reviewed many of the bubbly-flow data available by 1987, and concluded that distinct lateral void profiles develop in upflows through vertical channels, depending on the superficial phasic velocities. On the basis of the observed void profiles, these authors distinguished three main subregimes of bubbly flows, which they termed the *wall-*, *intermeadiate-* and *core-peak* regions. They also discussed the phenomena that could contribute to the explanation of such phase distributions, calling attention to the close link between the mechanisms responsible for the development of phase distribution, turbulence and interfacial structures.

Because almost all of the bubbly-flow data available to date refer to fully developed turbulent flows, both the *interfacial* and *turbulence* components of the two-fluid closures are usually addressed in the two-fluid models attempting to replicate the trends observed in experiments. However, while it is now widely recognized that the turbulent structure in such bubbly flows arises as the combined outcome of the *shear-generated turbulence* in the liquid and the *bubble-induced pseudo-turbulence* [5], there is no consensus on how to represent these effects in the two-fluid formulations. In fact, a great variety of approaches have been proposed to model bubbly-flow turbulence (*e.g.*, [6, 7, 8, 9, 10, 11, 12, 13, 14, 15, 16, 17]), and their systematic, critical assessment is emerging as an urgent task for nuclear engineers. While the complete reconciliation among the distinct modelling approaches may be difficult to achieve, an unbiased evaluation may be expected to provide sufficient information about the strengths and limitations of individual models, enabling their gradual introduction into engineering practice.

This paper describes CFDS-FLOW3D simulations testing the performance of two sets of two-fluid closure relationships applied to turbulent bubbly flows in vertical pipes. The original CFDS-FLOW3D interfacial closure, "recommended" for dispersed two-fluid flows [18], was used in conjunction with the default set of k–ϵ transport equations for the carrier (liquid) phase. Predictions obtained with this model were compared with the predictions of a new model (based on the work of Lee [7]), and with the experimental data of Liu [19].

2 MULTIFLUID MODELLING OF MULTIPHASE TURBULENT FLOWS IN CFDS-FLOW3D

2.1 Multifluid Equations for Turbulent Flows in CFDS-FLOW3D

The multifluid *mean-flow* equations employed in CFDS-FLOW3D conform to rigorous standards of development [20, 21], consistently retaining correlational terms known as Reynolds stresses and Reynolds fluxes. All phases are assumed to be Newtonian fluids, and Fourier-type heat conduction is implied from the outset. The mean-flow balances incorporate other standard closure assumptions, including a single mean pressure field shared by all phases, diffusive modelling of all turbulent fluxes, and somewhat restricted forms of interfacial-transfer laws.

In the absence of an established "industrial standard" for turbulence modelling in multiphase flows, the phasic-turbulence model currently available in CFDS-FLOW3D (for use in conjunction with the multifluid mean-flow equations) is a straightforward generalization of the k–ϵ turbulence model for incompressible single-phase flows. Phasic turbulent kinetic energy (per unit mass), k_k, and phasic turbulent dissipation rate, ϵ_k, are selected as the relevant measures for turbulent behaviour of phase–k, and the turbulent diffusion of phasic momentum is governed by the *phasic eddy viscosity*,

$$\mu_k^{Re} = C_\mu \rho_k \frac{k_k^2}{\epsilon_k}, \tag{1}$$

with a single proportionality constant, $C_\mu = 0.09$, for all turbulent phases under consideration. The Reynolds stress associated with a given turbulent phase–k is specified according to a generalized eddy-viscosity hypothesis:

$$\boldsymbol{\sigma}_k^{Re} = -\frac{2}{3}\rho_k k_k \mathbf{I} + \mu_k^{Re}[\nabla\langle\mathbf{u}\rangle^{\theta_k} + \langle\mathbf{u}\rangle^{\theta_k}\nabla - \frac{2}{3}(\nabla\cdot\langle\mathbf{u}\rangle^{\theta_k})\,\mathbf{I}]. \tag{2}$$

For adiabatic multiphase flows of incompressible fluids (with constant densities, ρ_k), the relevant set of phasic balances includes mass-, momentum-, k_k- and ϵ_k-equations:

$$\frac{\partial(\alpha_k\rho_k)}{\partial t} + \nabla\cdot(\alpha_k\rho_k\langle\mathbf{u}\rangle^{\theta_k}) = 0, \tag{3}$$

$$\frac{\partial(\alpha_k\rho_k\langle\mathbf{u}\rangle^{\theta_k})}{\partial t} + \nabla\cdot(\alpha_k\rho_k\langle\mathbf{u}\rangle^{\theta_k}\langle\mathbf{u}\rangle^{\theta_k}) = \mu_k^t(\nabla\langle\mathbf{u}\rangle^{\theta_k} + \langle\mathbf{u}\rangle^{\theta_k}\nabla) + \alpha_k(\rho_k\mathbf{g} - \nabla\langle p\rangle) + \mathbf{M}_k \tag{4}$$

$$\frac{\partial(\alpha_k\rho_k k_k)}{\partial t} + \nabla\cdot(\alpha_k\rho_k k_k\langle\mathbf{u}\rangle^{\theta_k}) = \nabla\cdot(\alpha_k\mathbf{T}_k^k) + \alpha_k(P_k - \rho_k\epsilon_k) + I_k^k \tag{5}$$

$$\frac{\partial(\alpha_k\rho_k\epsilon_k)}{\partial t} + \nabla\cdot(\alpha_k\rho_k\epsilon_k\langle\mathbf{u}\rangle^{\theta_k}) = \nabla\cdot(\alpha_k\mathbf{T}_k^\epsilon) + \alpha_k\left(C_{\epsilon 1}\frac{\epsilon_k}{k_k}P_k - C_{\epsilon 2}\rho_k\frac{\epsilon_k^2}{k_k}\right) + I_k^\epsilon \tag{6}$$

In the above equations, the volume fractions arise as mean values of binary phasic distribution functions, $\alpha_k = \langle\theta_k\rangle$, while phasic velocities, $\langle\mathbf{u}\rangle^{\theta_k} = \langle\theta_k\mathbf{u}\rangle/\alpha_k$, result from conditional averaging over each of the phasic domains ($k = 1, \ldots, n$). The mean value of *modified* pressure, $\langle p\rangle$, includes the isotropic parts of the Reynolds-stress tensors, and the molecular and eddy phasic viscosities are

combined to yield the total viscosity, $\mu_k^t = \mu_k + \mu_k^{Re}$. In close analogy to single-phase turbulence modelling, the production rate of phasic turbulent energy due to mean shear,

$$P_k = \mu_k^t[\nabla\langle\mathbf{u}\rangle^{\theta_k}:(\nabla\langle\mathbf{u}\rangle^{\theta_k} + \langle\mathbf{u}\rangle^{\theta_k}\nabla)] - \frac{2}{3}(\nabla\cdot\langle\mathbf{u}\rangle^{\theta_k})[\,\mu_k^t(\nabla\cdot\langle\mathbf{u}\rangle^{\theta_k}) + \rho_k k\,], \tag{7}$$

is a term that does not require closure, and the production and dissipation rates of ϵ_k are scaled using the same constants, $C_{\epsilon 1} = 1.44$ and $C_{\epsilon 2} = 1.92$, as in the single-phase case. The diffusive fluxes of k_k and ϵ_k, which include both laminar and turbulent contributions, are closed in a traditional manner,

$$\mathbf{T}_k^k = -\frac{\mu_k^t}{\sigma^k}(\nabla k_k), \tag{8}$$

$$\mathbf{T}_k^\epsilon = -\frac{\mu_k^t}{\sigma^\epsilon}(\nabla \epsilon_k), \tag{9}$$

assuming that turbulent diffusion dominates. A single set of constant *effective Prandtl numbers*, $\sigma^k = 1.0$ and $\sigma^\epsilon = 1.3$, is used for all phases to quantify the turbulent diffusion of k_k and ϵ_k, respectively.

2.2 Interfacial-Transfer Models for Dispersed Two-Phase Flows

In the absence of interfacial mass transfer, the default formulation of the mean interfacial-momentum transfer in CFDS-FLOW3D accounts only for the *interfacial drag force*,

$$\mathbf{M}_k = \sum_j c_{k,j}^d(\langle\mathbf{u}\rangle^{\theta_j} - \langle\mathbf{u}\rangle^{\theta_k}) \tag{10}$$

where the summation extends over all phases in contact with phase–k, and $c_{k,j}^d$ denotes the *inter-phase drag coefficient*. The interfacial sources of k_k and ϵ_k can be modelled, respectively, as

$$I_k^k = \sum_j c_{k,j}^k(k_j - k_k) \tag{11}$$

$$I_k^\epsilon = \sum_j c_{k,j}^\epsilon(\epsilon_j - \epsilon_k). \tag{12}$$

where $c_{k,j}^k$ and $c_{k,j}^\epsilon$ are the *inter-phase turbulence transfer coefficients*. In CFDS-FLOW3D, their default values are $c_{k,j}^k = c_{k,j}^\epsilon \equiv 0$.

Since the study reported in this paper was concerned with two-fluid modelling only, the heavier fluid (water) and the lighter fluid (air) were assigned the roles of the carrier and dispersed phases, respectively ($k = 1 \equiv \ell$ and $k = 2 \equiv g$). The *particle-model* option [18] was applied to determine the inter-phase drag coefficients as

$$c_{k,3-k}^d = \frac{3}{4}\frac{C_d}{d}\alpha_{3-k}\rho_k|\langle\mathbf{u}\rangle^{\theta_{3-k}} - \langle\mathbf{u}\rangle^{\theta_k}| \quad \text{where} \quad k = 1, 2. \tag{13}$$

This model characterizes the interfacial drag force in terms of the drag coefficient, C_d, for a single particle (bubble), and the mean (effective) diameter, d, of the particulate phase. In CFDS-FLOW3D, the default version of the particle model provides for a variation of C_d with the local Reynolds number based on d, according to the *standard drag curve* [18].

In the study reported in this paper, the default values of inter-phase coefficients were used exclusively in all simulations testing the original two-fluid closure in CFDS-FLOW3D, as "recommended" for turbulent dispersed two-phase flows.

3 LEE'S MODEL FOR BUBBLY FLOWS AND ITS ADAPTATION TO CFDS-FLOW3D

3.1 Model Outline

Lee [7] was probably the first author to adapt the "standard" single-phase k–ϵ model to represent turbulence in bubbly liquids treated as two-fluid media. Lee's model, which was discussed in detail in a paper by Lee *et al.* [22], included new closure hypotheses for the interfacial sources in the k_ℓ- and ϵ_ℓ-transport equations, and a provision for adjustment of nearly all constants appearing in the "standard" k–ϵ closure.

The k_ℓ–ϵ_ℓ model of Lee formed an integral part of an iterati algorithm used by its author to predict radial profiles of flow properties in fully developed adiabatic air-water flows through vertical pipes. The formulation was derived from the standard two-fluid description, but the momentum balance for the gaseous phase was considered in a simplified form (assuming $\rho_g \approx 0$), and the k_ℓ–ϵ_ℓ model was used directly to constitute only a single shear component of the Reynolds stress $\boldsymbol{\sigma}_\ell^{Re}|_{rx}$, appearing in the axial x-momentum balance for the liquid. The radial-momentum balances for both phases were combined into a single equation, which was integrated across the pipe diameter to yield the radial distribution of void, α_g, as a function of axial relative velocity and turbulence anisotropy factors. The anisotropy factors were defined, in accordance with the earlier works by Drew and Lahey [23, 6], as

$$F_{\ell,\beta} = -\frac{\boldsymbol{\sigma}_\ell^{Re} : \mathbf{i}_\beta \mathbf{i}_\beta}{2\rho_\ell k_\ell} \tag{14}$$

where $\mathbf{i}_\beta$ denotes a unit vector along the β-coordinate line. Given the axial pressure gradient, $(\boldsymbol{\nabla}\langle p\rangle)\cdot\mathbf{i}_x$, the profiles of mean axial velocity and turbulent kinetic energy were then determined, along with the radial distribution of void, in a closed-loop iteration of all variables. Referring to the experimental data reported by Wang [24] and Wang *et al.* [25], the author assumed a constant value of the circumferential anisotropy factor, $F_{\ell,\varphi} = 0.25$, and empirically determined the anisotropy ratio, $F_{\ell,r}/F_{\ell,x}$, as a function of the liquid-phase Reynolds number and average void, optimized to provide the best fit to the observed void distributions.

3.2 Interfacial-Transfer Models

The k_ℓ- and ϵ_ℓ-transport equations adopted in the Lee model were formally identical to the corresponding CFDS-FLOW3D equations, except for their interfacial-source terms, which were postulated as

$$I_\ell^k = -C_{i1}\alpha_g(\boldsymbol{\nabla}\langle p\rangle)(\langle\mathbf{u}\rangle^{\theta_g} - \langle\mathbf{u}\rangle^{\theta_\ell}) : \mathbf{i}_x\mathbf{i}_x; \tag{15}$$

$$I_\ell^\epsilon = C_{i2}\frac{\epsilon_\ell}{k_\ell} I_\ell^k \tag{16}$$

to account for the *bubble-induced turbulence* in the liquid. The interfacial source of turbulent kinetic energy, I_ℓ^k, was derived from the consideration that gas bubbles induce turbulence as they rise through and displace liquid. When the low-density bubbles displace the same volume of high-density liquid from a low-pressure to a higher-pressure region, the turbulent kinetic energy of the liquid increases and its potential energy decreases. Since Lee's model was intended only for bubbly upflows in vertical pipes, I_ℓ^k was made proportional to the axial components of the pressure gradient and the relative mean velocity between phases, and it was not coordinte-invariant. An empirical correlation dependent on the liquid-phase Reynolds number, Re_ℓ, was derived for the proportionality factor,

$$C_{i1} = 0.03 + \frac{0.243 - 0.344 \times 10^{-5} Re_\ell}{1.0 + \exp\left[0.5 \times 10^{-3}\left(Re_\ell - 6.0 \times 10^4\right)\right]}, \tag{17}$$

to obtain a good agreement between the model predictions and the measured k_ℓ-profiles in various two-phase flows. The estimate of I_ℓ^ϵ, accounting for bubble-induced dissipation of liquid-phase turbulent kinetic energy, was patterned on considerations similar to those pursued for buoyant single-phase flows [26]. Considering the case of bubbles rising freely in a still tank, Lee [7] concluded that $C_{i2} \equiv C_{\epsilon 2} = 1.92$.

In addition to the novel modelling of interfacial transfer of turbulence, Lee's formulation of the interfacial-momentum transfer also differed from the "default" CFDS-FLOW3D model. Besides the *drag force*, characterized by the "dirty-water" drag coeficient,

$$C_d = \frac{2}{3}\sqrt{\frac{(\rho_\ell - \rho_g)g}{\sigma}}\left[\frac{1 + 17.67(\alpha_\ell)^{\frac{9}{7}}}{18.67(\alpha_\ell)^{\frac{3}{2}}}\right]^2, \tag{18}$$

dependent on the ratio of buoyancy and surface-tension forces as well as on the liquid-phase volume fraction, the momentum transfer included a *lift force* acting on the bubbles. During the implementation of Lee's model in the CFDS-FLOW3D code, several variants of momentum-transfer formulations were attempted, but in the end the interfacial lift forces were not included.

3.3 Modification of Coefficients in k-ϵ Equations

Lee [7] included simple empirical provisions for the increases of turbulent viscosity and k_ℓ-diffusivity in the liquid containing bubbles. The former was effected by significantly increasing the standard value of C_μ for the liquid phase. An empirical correlation with the channel cross-sectional average void, $\overline{\alpha_g}$,

$$C_\mu = 0.8 - [\,0.8 - 0.09\,]\exp(-100\overline{\alpha_g}), \tag{19}$$

made $C_\mu \gg 0.09$, and resulted in flatter liquid-velocity profiles, consistently observed in bubbly flows. The effective Prandtl number for the diffusion of k_ℓ was found to be dependent on Re_ℓ,

$$\sigma^k = 0.037 + 0.21 \times 10^{-5} Re_\ell + \frac{0.2}{1.0 + \exp\left[0.4 \times 10^{-7}\left(Re_\ell - 6.5 \times 10^4\right)^2\right]} \tag{20}$$

for the range $3.5 \times 10^4 \leq Re_\ell \leq 7.2 \times 10^4$.

3.4 Modifications of Wall Functions

In agreement with the assertion of Marié [27], Lee [7] assumed that the near-wall profile of liquid-phase velocity component parallel to the wall can be adequately approximated by the standard logarithmic profile used for single-phase flows [18]. As no gaseous-phase turbulence was considered in Lee's model, there was no need to tackle wall functions for the dispersed bubbles. The wall functions for k_ℓ and ϵ_ℓ, specified at the centre P of a near-wall control volume,

$$k_{\ell,P}^2 = \frac{u_* y_P}{2.5 C_\mu} \left(2.5 \frac{u_*^3}{y_P} - \frac{C_{i2}}{\rho_\ell} \frac{\alpha_{gP}}{\alpha_{\ell P}} (\langle \mathbf{u} \rangle^{\theta_g} - \langle \mathbf{u} \rangle^{\theta_\ell})(\nabla \langle p \rangle) : \mathbf{i}_x \mathbf{i}_x \right) \tag{21}$$

$$\epsilon_{\ell,P} = 2.5 \frac{u_*^3}{y_P} + \frac{C_{i2}}{\rho_\ell} \frac{\alpha_{gP}}{\alpha_{\ell P}} (\langle \mathbf{u} \rangle^{\theta_g} - \langle \mathbf{u} \rangle^{\theta_\ell})(\nabla \langle p \rangle) : \mathbf{i}_x \mathbf{i}_x \tag{22}$$

were derived from the assumptions that the production rates of k_ℓ and ϵ_ℓ balance out their respective dissipation rates in the buffer zone, and that the liquid-phase shear stress is nearly constant there. Here, y_P denotes the distance between the point P and the wall, $\alpha_{\ell P}$ and α_{gP} denote the respective volume fractions at this point, and u_* is the *friction velocity*. The original Lee's formulation used the friction velocity based on wall shear stress. In the CFDS-FLOW3D implementation of Lee's wall functions, this definition was changed to one based on the near-wall value of the liquid-phase turbulence kinetic energy, $k_{\ell,P}$.

3.5 Adaptation of Lee's Model to CFDS-FLOW3D

After close scrutiny, all of Lee's modifications to the "standard" k–ϵ model were adopted for the k_ℓ–ϵ_ℓ equations in CFDS-FLOW3D. More importantly, however, other changes to the original modelling procedure of Lee were introduced. They included:

- disregard of the void-distribution function derived by Lee through analytical integration of combined momentum-balance equations, and
- disregard of anisotropy-factor information and extending the use of eddy viscosity, defined in Eq. (1), to constitute all components of liquid-phase Reynolds stress, $\boldsymbol{\sigma}_\ell^{Re}$.

A similar approach has been followed by Golja *et al.* [28], who also adapted Lee's turbulence model in their work. In fact, the only major difference between Golja *et al.*'s adaptation of Lee's model and our adaptation was the rejection of Eq. (18) in the former approach, on the grounds that it showed little effect on radial profiles of liquid velocity in bubbly pipe flows. It must be stressed, however, that both the present and Golja *et al.*'s adaptations differ significantly from Lee's original, as they result in turbulence-transport models devoid of any ability to represent turbulence anisotropy in the liquid phase. Clearly, any adaptation of the Lee's model for use in a general-purpose CFD code would have to discard the analytically derived void-distribution function. However, the information about the anisotropy of liquid turbulence, contained in the empirically derived anisotropy factors, could be potentially incorporated into a closure formulated in terms of the *anisotropy tensor*,

$$\mathbf{b}_\ell = -\frac{\boldsymbol{\sigma}_\ell^{Re}}{2\rho_\ell k_\ell} - \frac{1}{3}\mathbf{I} \tag{23}$$

as is often done in the modelling of single-phase turbulence. We plan to explore this approach in our future work.

4 NUMERICAL SIMULATIONS

4.1 Test Problems

Both of the two-fluid models described in the previous sections were tested against the experimental data of Liu [19]. Liu's data were obtained for fully developed air-water bubbly upflow in a vertical pipe, and covered a range of superficial liquid flow rates, $0.376\,m/s \leq j_\ell \leq 1.391\,m/s$, and a range of superficial gas flow rates, $0.027\,m/s \leq j_g \leq 0.347\,m/s$. The data provided radial profiles of liquid velocity, bubble velocity, volume fractions and two components of liquid-phase Reynolds stress.

4.2 Problem Specification and Boundary Conditions

The two-fluid problem for bubbly air-water flow was formulated in the cylindrical system of (r, φ, x)-coordinates, assuming axisymmetric conditions. The 2-D rectangular domain, $0 \leq r \leq D/2$ and $0 \leq x \leq L$, representing circular-pipe geometry, was subdivided into $NI \times NJ = 30 \times 100$ identical finite volumes. The inner diameter of the pipe was $D = 0.0381\,m$, and the pipe's length was chosen as $L = 1\,m$. In all numerical simulations, the ratio $L/D = 26.25$ was found to assure developed-flow conditions close to the outlet, even though Liu's measurements were taken at the distance of $L = 1.3\,m$ apart from the pipe inlet (*i.e.*, at $L/D \approx 36$). The density ratio of the fluids was selected as $\rho_\ell/\rho_g = 10^3$.

At the inlet, uniform profiles of axial phasic velocities, $\langle \mathbf{u} \rangle^{\theta_\ell} \cdot \mathbf{i}_x = j_\ell/\alpha_\ell$ and $\langle \mathbf{u} \rangle^{\theta_g} \cdot \mathbf{i}_x = j_g/\alpha_g$, and of void, $\alpha_g = \overline{\alpha_g}|_{inlet}$, were specified according to Liu's measurements. The wall-functions discussed in section 3.4 were used to specify the near-wall profiles of all variables with the notable exception of volume fractions. In the original CFDS-FLOW3D treatment, the volume fractions in the near-wall control volumes remain unconstrained. In the new model, following Lee's development [7], the wall-point gas-volume fraction, α_{gP}, was correlated with the liquid-phase Reynolds number, Re_ℓ, and the global gas-volume fraction, $\overline{\alpha_g}$, using the relationship,

$$\frac{\alpha_{gP}}{\overline{\alpha_g}} = 5.3 \left(\frac{Re_\ell}{10^6} \right)^2 - 3.3 \left(\frac{Re_\ell}{10^6} \right) + 0.99 \tag{24}$$

4.3 Simulation Procedure

To avoid any detrimental effects on convergence rates, for each test case involving the newly implemented Lee's model, the first 500 iterations were run using an estimate of the pressure gradient in the source terms of the k_ℓ-ϵ_ℓ equations. False time steps of the size, $\Delta t = 1.0 \times 10^3\,s$, were used for all variables. Subsequently, the pressure-gradient value was replaced with that computed in 500 iterations, and the solution was carried out for another 500 iterations. In all cases, the pressure drop across the pipe was within 1% of the pressure drop predicted at 500 iterations.

4.4 Analysis of Simulation Results

In total, 28 sets of experimental conditions reported by Liu were simulated where k = 1, 2. with the newly implemented two-fluid model, and selected experiments by Liu were simulated invoking the "default" CFDS-FLOW3D model for dispersed flows. The results of all computations were compared along the radial slice at $x = 0.96\,m$, close to the pipe outlet.

Figures 1 and 2 show a typical comparison of predicted and measured profiles of radial velocity, corresponding to the inlet conditions of $j_\ell = 0.753\,m/s$, $j_g = 0.112\,m/s$ and $\alpha_g = 0.1091$. The two-fluid model based on Lee's development is clearly seen to better predict the shapes of velocity profiles of both phases, and the peak values of both phasic velocities. It also offers a better prediction of the liquid-phase velocity profile in the near-wall region, although a discrepancy with experimental data is apparent there. The flatter liquid-velocity profiles, consistently predicted with the new model, were confirmed to be the result of the increased constant, C_μ, in full agreement with Lee's assertion [7].

Figures 3 to 6 show other comparisons between the new-model predictions of radial profiles of velocity and the corresponding experimental data of Liu. These comparisons exemplify a general trend observed during our examination of velocity results: the accuracy of the velocity-profile predictions varied for different liquid-flow rates. The best predictions were usually obtained at a gas-flow rate of $0.112\,m/s$. This observation seems to indicate that the coefficients introduced for the purpose of bubbly-flow turbulence modelling require a volume-fraction as well as gas-flow-rate dependence. For instance, the modified values of $C_{\ell 1}$ and σ^k, as used in the new model, were dependent only on the liquid-phase Reynolds number, Re_ℓ, but not on the gas-phase Reynolds number. On physical grounds, there seems to be no valid reason why the Re_g–dependence of turbulence-model coefficients should be excluded.

The predicted gaseous-phase (bubble) velocity profiles were consistently off the experimental results by some amount. The corresponding experimental profiles are flatter. This effect could possibly be attributed to inadequately predicted volume-fraction profiles, or it could be an indication that a different set of turbulence-model coefficients should be assigned to the dispersed gas phase. The latter possibility is highly speculative, since in all computations reported here, liquid turbulence was assumed to dominate, and the gaseous phase was always declared laminar.

The spatial phase distributions (void profiles) were inadequately predicted by both the original CFDS-FLOW3D model and the adaptation of Lee's model. All void profiles were essentially flat, and showed no tendency for "near-wall peaking", which is a well-known phenomenon for low-void flows, dating back to the experimental studies by Serizawa *et al.* [1]. Despite this shortcoming, the void predictions obtained in the course of this study are consistent with the two-fluid analyses of Drew and Lahey [23, 6], valid for fully developed, turbulent, low-quality flows in vertical channels.

Under reasonable simplifying assumptions (including negligible inter-phase lift force), Drew and Lahey [6] derived an ordinary differential equation relating radial profiles of void, $\alpha_g(r)$, and phasic turbulent kinetic energies, $k_\ell(r)$ and $k_g(r)$, for two-phase flows in round pipes. In the case of negligible gas-phase turbulence, $k_g \equiv 0$, this equation reads:

$$-\alpha_g \frac{d}{dr}\left[(1-\alpha_g)\,F_{\ell,r}\,\rho_\ell\,k_\ell\right] + \frac{1}{r}(1-\alpha_g)\,\alpha_g\,(F_{\ell,\varphi} - F_{\ell,r})\,\rho_\ell\,k_\ell = 0 \tag{25}$$

When the turbulence in the liquid phase is isotropic, $F_{\ell,r} = F_{\ell,\varphi} = F_{\ell,x} \equiv 1/3$, a straightforward

integration of Eq. (25) yields:

$$[1 - \alpha_g(r)]\, k_\ell(r) = \text{const.} \tag{26}$$

Thus, in this case, the local values of α_g and k_ℓ should be inversely proportional to each other, irrespective of the details of the isotropic Reynolds-stress model used for the liquid phase.

Indeed, examination of the radial k_ℓ-profiles predicted by both k_ℓ–ϵ_ℓ models used in our study revealed predominantly flat distributions, with only occasional small variations in the near-wall regions. Comparisons of these profiles with the experimental data of Liu were not deemed meaningful, because complete reconstruction of k_ℓ (from the measurements of only two normal σ_ℓ^{Re}-components) was impossible.

The anisotropy of liquid-phase Reynolds stresses is also known to directly affect two-fluid predictions of mean-pressure profiles for vertical-pipe flows [23, 6]. In our study, all predicted mean-pressure profiles were flat, in agreement with Drew and Lahey's result for the isotropic-turbulence case [6].

5 CONCLUSION

A two-fluid model for turbulent, adiabatic bubbly flows has been assembled on the basis of the work of Lee [7] and Lee *et al.* [22]. Its implementation in the CFDS-FLOW3D code has been shown to improve the velocity-profile predictions for the entire range of conditions covered by the experimental work of Liu [19]. The spatial phase distributions (void profiles) in bubbly upflows are inadequately predicted by the new model, but the underlying reasons for this shortcoming have been identified. While our work has demonstrated the effective modification of the CFDS-FLOW3D code, and opens the path to new development, further effort is required to build confidence in the CFD-type two-fluid simulations of two-phase flows. Several other approaches to the two-fluid modelling of turbulent bubbly flows have already been identified as promising, and will be explored further. If suitable, they will be adapted to fit the multifluid modelling framework in CFDS-FLOW3D, and their numerical validation will proceed.

Acknowledgement. The work reported in this paper was partially supported by the AECL Centre of Mathematical Sciences through a research grant awarded to the first author.

REFERENCES

1. A. Serizawa, I. Kataoka, and I. Michiyoshi. Turbulence Structure of Air–Water Bubbly Flow – II. Local Properties. *Int. J. Multiphase Flow*, 2:221–259, 1975.

2. V.E. Nakoryakov, O.N. Kashinsky, A.P. Burdukov, and V.P. Odnoral. Local Characteristics of Upward Gas-Liquid Flows. *Int. J. Multiphase Flow*, 7:63–81, 1981.

3. T.G. Theofanous and J. Sullivan. Turbulence in Two–Phase Dispersed Flows. *J. Fluid Mech.*, 116:343–362, 1982.

4. A. Serizawa and I. Kataoka. Phase Distribution in Two-Phase Flow. In N.H. Afgan, editor, *Transient Phenomena in Multiphase Flow*, pages 179–224. Hemisphere Publ. Co., 1988. Proc. ICHMT Seminar, Dubrovnik, Yugoslavia, 1987 May 24–30.

5. Y. Sato, M. Sadatomi, and K. Sekoguchi. Momentum and Heat Transfer in Two–Phase Bubbly Flow. *Int. J. Multiphase Flow*, 7:167–177, 1981.

6. D.A. Drew and R.T. Lahey, Jr. Phase Distribution Mechanisms in Turbulent Low–Quality Two–Phase Flow in a Circular Pipe. *J. Fluid Mech.*, 117:91–106, 1982.

7. S.J. Lee. *Turbulence Modelling in Bubbly Two–Phase Flows.* PhD thesis, Rensselaer Polytechnic Institute, Troy, New York, 1986.

8. M. Lopez de Bertodano, M. Lee, R.T. Lahey, Jr., and D.A. Drew. The Prediction of Two–Phase Turbulence and Phase Distribution Phenomena Using a Reynolds Stress Model. *ASME J. Fluid Engng.*, 112:107–113, 1990.

9. M. Lopez de Bertodano, R.T. Lahey, Jr., and O.C. Jones, Jr. Development of k–ϵ Model for Bubbly Two–Phase Flow. *ASME J. Fluid Engng.*, 116:128–134, 1994.

10. A. Serizawa and I. Kataoka. Turbulence Suppression in Bubbly Two–Phase Flow. *Nucl. Engng. and Design*, 122:1–16, 1990.

11. I. Kataoka, A. Serizawa, and D.C. Besnard. Analyses of the Radial Distributions of Average Velocity and Turbulent Velocity of the Liquid Phase in Bubbly Two–Phase Flow. *JSME Trans. B*, 36:404–411, 1993.

12. I. Kataoka, A. Serizawa, and D.C. Besnard. Prediction of Turbulence Suppression and Turbulence Modeling. *Nucl. Engng. and Design*, 141:145–158, 1993.

13. I. Žun. The Mechanism of Bubble Non–homogeneous Distribution in Two–Phase Shear Flow. *Nucl. Engng. and Design*, 118:155–162, 1990.

14. I. Žun, I. Kljenak, and S. Može. Space–Time Evolution of the Nonhomogenous Bubble Distribution in Upward Flow. *Int. J. Multiphase Flow*, 93:151–172, 1993.

15. O. Simonin and P.L. Viollet. Numerical Study of Phase Dispersion Mechanisms in Turbulent Bubbly Flows. HE 44/89-20, Electricite de France (Direction des Etudes et Recherches), 1989. Also published in Proc. Int. Conf. on Mechanics of Two-Phase Flow, 1989 June 12-15, Taipei, Taiwan.

16. P.L. Viollet and O. Simonin. Modelling Dispersed Two–Phase Flows: Closure, Validation and Software Development. *Appl. Mech. Review*, 47:S80–S84, 1994.

17. A.J.N. Vreenegoor and J.A. Geurst. Two–Phase Bubbly Flow through Vertical Tube: Void–Fraction Distribution and Velocity Profiles. *Physica A*, 192:410–442, 1993.

18. Computational Fluid Dynamics Services, Inc. *CFDS–FLOW3D User Guide*, 1992 October.

19. T.J. Liu. *Experimental Investigation of Turbulence Structure in Two–Phase Bubbly Flows.* PhD thesis, Northwestern University, Evanston, Illinois, 1989.

20. M. Ishii. *Thermo–Fluid Dynamic Theory of Two–Phase Flow.* Eyrolles. Paris, 1975.

21. D.A. Drew. Mathematical Modeling of Two–Phase Flow. *Ann. Rev. Fluid Mech.*, 15:261–291, 1983.

22. S.L. Lee, R.T. Lahey, Jr., and O.C. Jones, Jr. The Prediction of Two–Phase Turbulence and Phase Distribution Phenomena Using k–ϵ Model. *Jap. J. Multiphase Flow*, 3:335–368, 1986.

23. D.A. Drew and R.T. Lahey, Jr. Phase Distribution Mechanisms in Turbulent Two -Phase Flow in a Channel of Arbitrary Cross–Section. *ASME J. Fluid Engng.*, 103(4):583–589, 1981.

24. S.K. Wang. *Three–Dimensional Turbulence Structure Measurements in Air/Water Two–Phase Flows.* PhD thesis, Rensselaer Polytechnic Institute, Troy, New York, 1986.

25. S.K. Wang, S.J. Lee, O.C. Jones, Jr., and R.T. Lahey, Jr. Three–Dimensional Turbulence Structure and Phase Distribution Measurements in Bubbly Two–Phase Flows. *Int. J. Multiphase Flow*, 13:327–343, 1987.

26. W. Rodi. *Turbulence Models and Their Applications to Hydraulics.* IAHR, Delft, The Netherlands, 1984.

27. J.L. Marié. Modelling of the Skin Friction and Heat Transfer in Turbulent Two–Component Flow. *Int. J. Multiphase Flow*, 13:309–325, 1987.

28. G. Golja, I. Žun, and A.C.M. Sousa. An Assessment of k–ϵ Modeling of Turbulent Bubbly Flow. European Two–Phase Flow Group Meeting, Stockholm, Sweden, 1992 June 1–3, 1992.

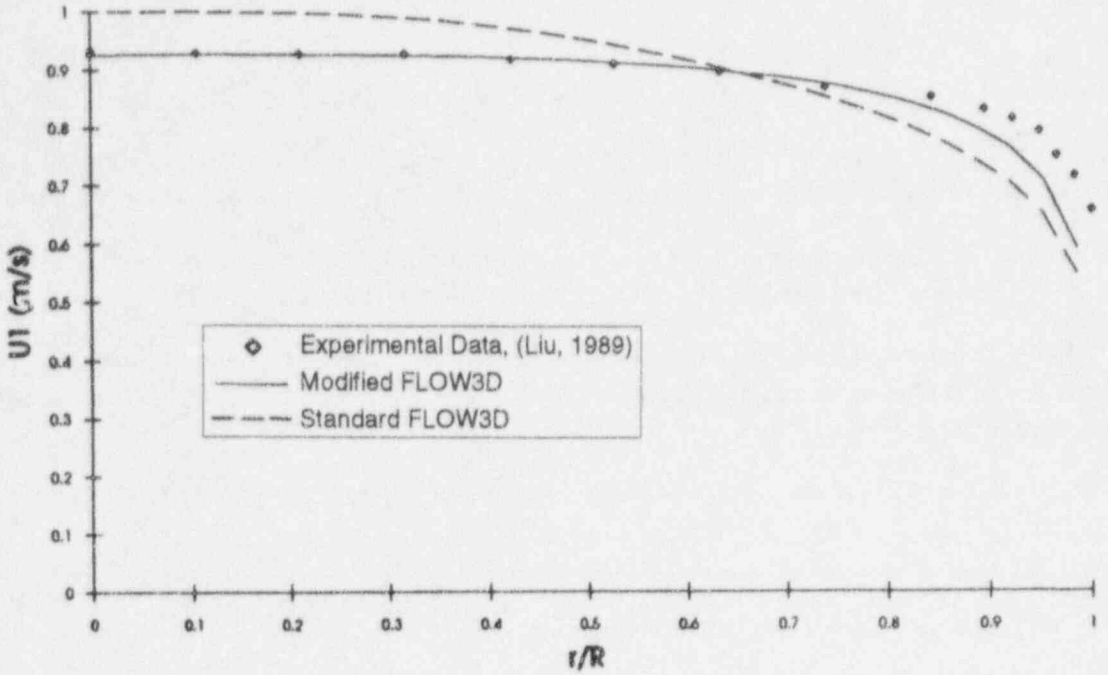

Figure 1. Comparison of Liquid-Velocity Predictions with Experimental Data: $j_\ell = 0.753\,m/s$; $j_g = 0.112\,m/s$; $\overline{\alpha_g}|_{inlet} = 0.1091$.

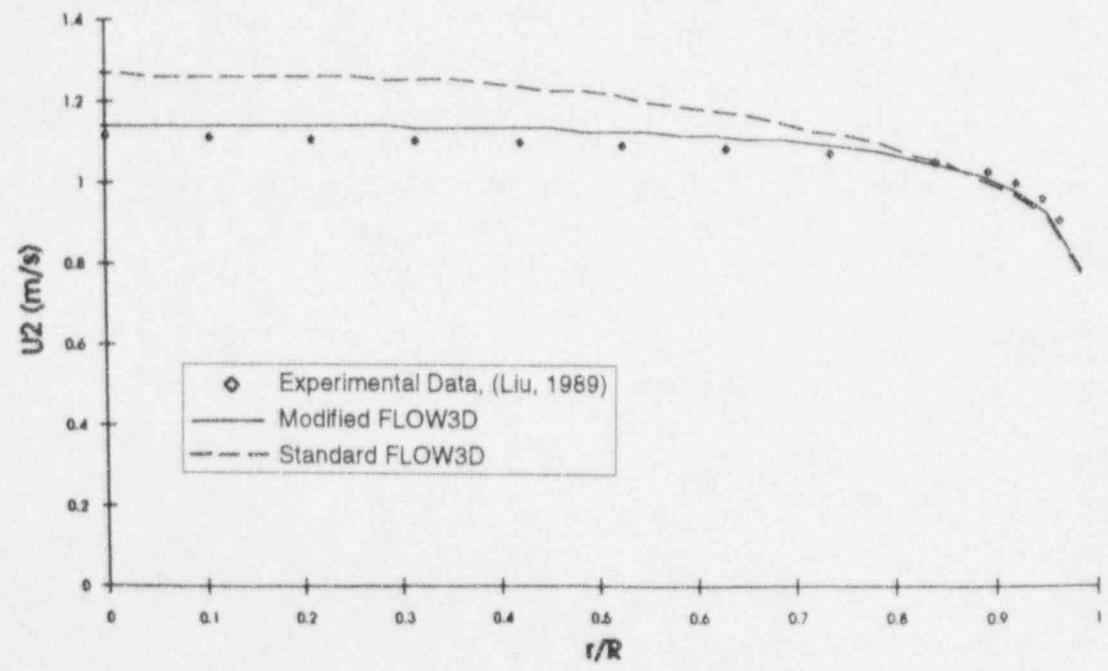

Figure 2. Comparison of Gas-Velocity Predictions with Experimental Data: $j_\ell = 0.753\,m/s$; $j_g = 0.112\,m/s$; $\overline{\alpha_g}|_{inlet} = 0.1091$.

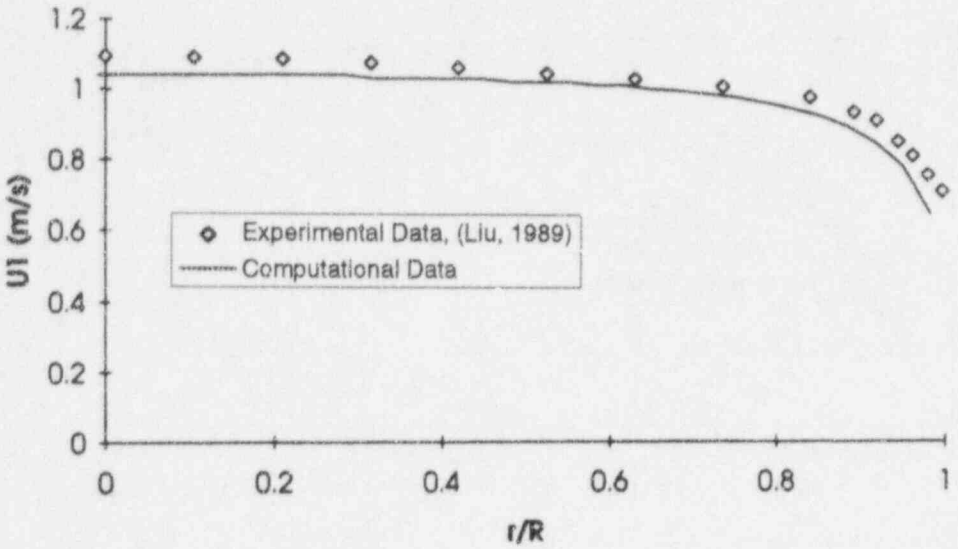

Figure 3. Comparison of Liquid-Velocity Predictions with Experimental Data: $j_\ell = 0.755\, m/s$; $j_g = 0.230\, m/s$; $\overline{\alpha_g}|_{inlet} = 0.1816$.

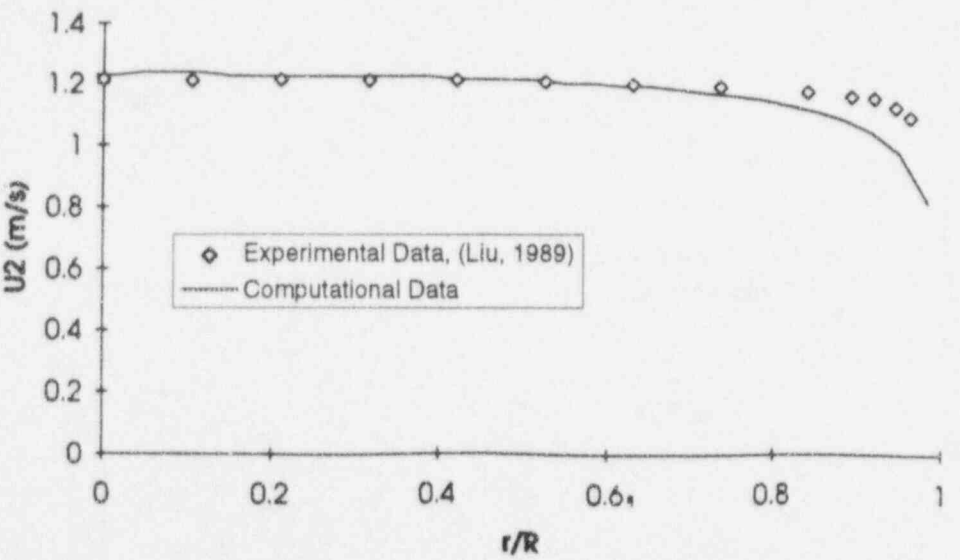

Figure 4. Comparison of Gas-Velocity Predictions with Experimental Data: $j_\ell = 0.753\, m/s$; $j_g = 0.230\, m/s$; $\overline{\alpha_g}|_{inlet} = 0.2381$.

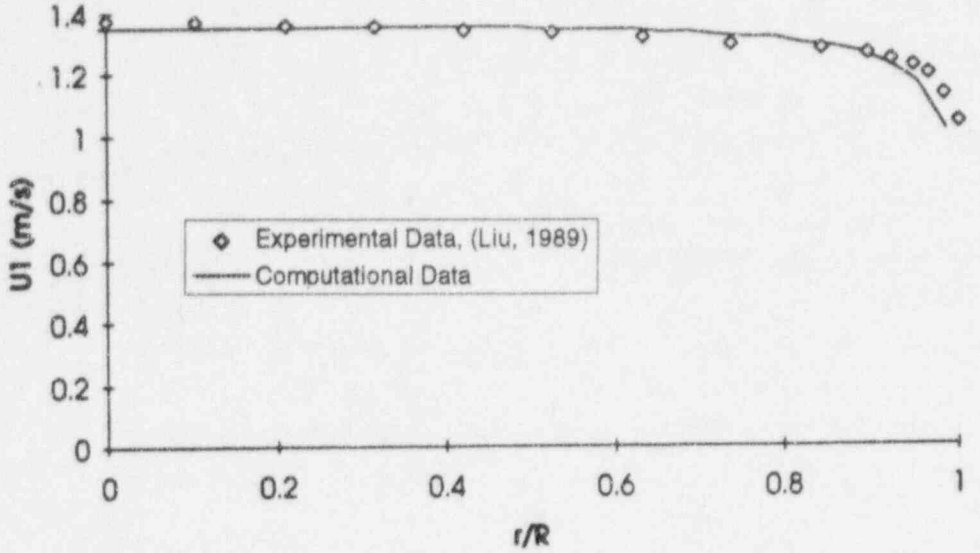

Figure 5. Comparison of Liquid-Velocity Predictions with Experimental Data: $j_\ell = 1.087\, m/s$; $j_g = 0.230\, m/s$; $\overline{\alpha_g}|_{inlet} = 0.1497$.

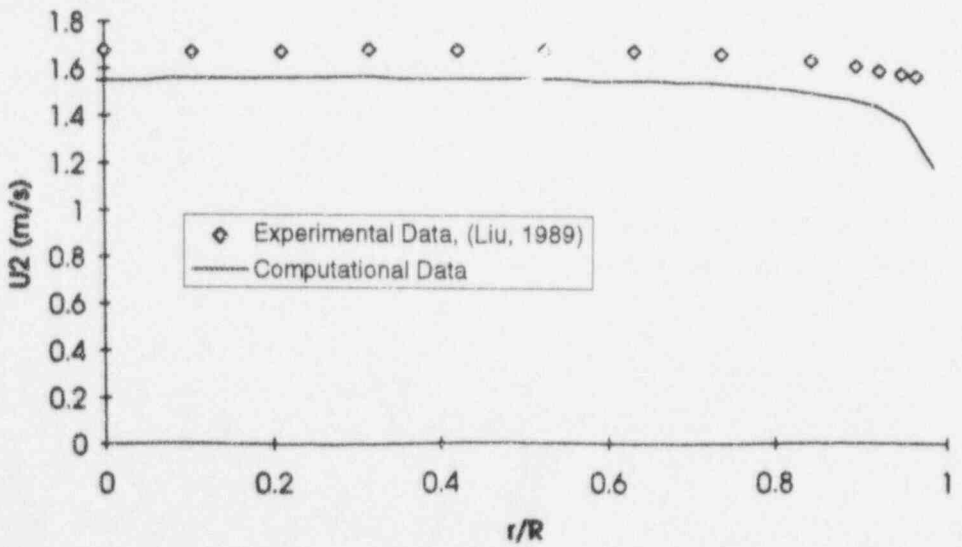

Figure 6. Comparison of Gas-Velocity Predictions with Experimental Data: $j_\ell = 1.087\, m/s$; $j_g = 0.230\, m/s$; $\overline{\alpha_g}|_{inlet} = 0.1497$.

Condensation during Gravity Driven ECC: Experiments with PACTEL

Reijo Munther, Heikki Kalli
Lappeenranta Univ. of Technology, PB 20, 53851, Lappeenranta, FINLAND

J. Kouhia
Technical Research Centre of Finland, PB 20, 53851, Lappeenranta, FINLAND

ABSTRACT

This paper provides the results of the second series of gravity driven emergency core cooling (ECC) experiments with PACTEL (Parallel Channel Test Loop). The simulated accident was a small break loss-of-coolant accident (SBLOCA) with a break in a cold leg. The ECC flow was provided from a core makeup tank (CMT) located at a higher elevation than the main part of the primary system. The CMT was pressurized with pipings from the pressurizer and a cold leg. The tests indicated that steam condensation in the CMT can prevent ECC and lead to core uncovery.

I. INTRODUCTION

A preliminary series of experiments with gravity driven core cooling was conducted with the PACTEL facility in November 1992 [1]. In these tests a rapid condensation of vapor interrupted the emergency core cooling flow several times. In order to investigate this behavior more precisely, a second series of experiments witn improved instrumentation of the facility was performed in November 1993. The second series of experiments consisted of four tests.

One of the applications, which utilize the gravity driven ECC as a main component of the early stage ECC, is the passive pressurized water reactor design AP-600 by Westinghouse. However, the tests presented here are not directly applicable to safety analyses of the AP-600 design, because of some major differences in the geometry between AP-600 and PACTEL. Our objective has been to simulate the gravity driven ECC and thus enhance the understanding of the physical phenomena important in passive safety systems working with low differential pressures and not directly to provide new ECC configurations to any existing or designed plants.

PACTEL is an experimental out-of-pile facility designed to simulate the major components and system behavior of a commercial Pressurized Water Reactor (PWR) during postulated small- and medium-size LOCAs [2]. Recently made modifications enable experiments to be conducted also on the passive core cooling.

Slight core uncovery was found in the first two tests as the ECC flow from the CMT was stopped when rapid condensation collapsed the CMT pressure. In these tests the CMT repressurized rather slowly and the ECC flow was provided just after the core uncovery started. In the third test with controlled repressurization of the system there were three short condensation phases during the test and no core uncovery was found. The last experiment was stopped straight after condensation initiation.

II. PACTEL FACILITY

PACTEL is a volumetrically scaled model of the 6-loop VVER-440 PWR with three separate loops and 144 full-length, electrically heated fuel rod simulators arranged in three parallel channels. The fuel rod simulators are heated indirectly. The scaling factor and some particular characteritics of the PACTEL facility are compared with some well-known facilities in Table I.

Table I PACTEL facility compared to other integral test facilities

Facility	Country/owner	Max Power (MW)	Pressure (MPa)	Number of Rods	Scaling factor Volume	Height	Reference Reactor
PWR-facilities							
CCTF	Japan/JAERI	10.0	0.6	2048	1: 21	1:1	1100 MWe PWR
LSTF	Japan/JAERI	10.0	16.0	1064	1: 48	1:1	3400 MWt PWR
LOFT	USA/INEL	50.0	15.5	1300	1: 60	1:2	-
BETHSY	France/CEMG	3.0	17.2	428	1: 100	1:1	2775 MWt PWR
PKL	FRG/KWU	1.5	4.0	337	1: 135	1:1	1300 MWe PWR
PACTEL	Finland/VTT	1.0	8.0	144	1: 305	1:1	VVER-440
FLECHT/SEASET	USA	1.5	0.4	161	1: 327	1:1	-
VEERA	Finland/VTT	0.12	0.5	126	1: 349	1:1	VVER-440
SPES	Italy/SIET	9.0	20.0	97	1: 420	1:1	-
UMCP	USA/Maryland	0.2	2.1	15	1: 500	1:6.6	-
LOBI-Mod 2	Italy/ISPRA	5.4	15.5	64	1: 700	1:1	1300 MWe PWR
MIST (2x4)	USA/B&W	0.34	15.6	45	1: 840	1:1	-
SEMISCALE	USA/INEL	2.0	15.0	25	1:1600	1:1	-
PMK-NHV	Hungary/KFKI	2.0	16.0	19	1:2070	1:1	VVER-440
REWET-III	Finland/VTT	0.09	1.0	19	1:2333	1:1	VVER-440
TPTF	Japan/JAERI	1.0	12.0	-	-	-	-
GIDROPRESS	USSR	-	15.0	-	-	-	VVER-1000
BWR-facilities							
TBL	Japan/Hitachi	10.0	7.2	128	1: 370	1:1	-
ROSA-III	Japan/JAERI	4.2	7.2	240	1: 424	1:1	3800 MWt GE BWR-6
BWR-FIST	USA/GE	4.6	7.4	64	1: 625	1:1	-
FIX-II	Sweden/Studsvik	3.3	7.4	36	1: 770	1:1	2700 MWt Asea Atom BWR
PIPER-ONE	Italy/PISA	0.28	7.4	16	1:2200	1:1	2650 MWt GE BWR

VVER-reactors are of Russian design with some major differences compared with Western PWRs there are six primary loops, horizontal steam generators (SGs) and loop seals in both hot and cold legs. One notable feature of the VVER-440 reactors is the large primary and secondary side water inventory, tending to slow down the progression of transients. Finland has two VVER-440 reactors at the Loviisa power plant.

Normally the facility consists of a three loop primary system, steam generators, and ECC systems. In these tests one of the loops was isolated and the tests were performed with a two loop primary system, Fig. 1. In PACTEL the peak operating pressures on the primary and secondary sides are 8.0 MPa and 4.6 MPa, respectively. The reactor vessel is simulated with a U-tube construction including separate downcomer and core sections. The core itself consists of 144 full-height, electrically heated fuel rod simulators with a chopped cosine axial power distribution and a maximum total power output of 1 MW, or 22 % of the scaled full power. The fuel rod pitch (12.2 mm) and diameter (9.1 mm) are identical to those of the reference reactor. The rods are divided into three triangular parallel channels describing a corner of three hexagonal fuel assemblies.

The heights and relative elevations of the components correspond to those of the full-scale reactor to match the natural circulation pressure heads in the reference system. The hot and cold leg elevations of the reference plant have been reproduced, including the loop seals. The hot leg loop seals are needed because the SGs are located at about an equal elevation with the hot leg connections to the upper plenum. The leg connections to a SG are under the collectors, thus a roughly U-shaped pipe is necessary to complete the connection to the pressure vessel without sharp bends. The cold leg loop seals are because of the elevation difference between the inlet and outlet of the reactor coolant pumps, just as in the other PWRs.

Three coolant loops with double capacity SGs are used to model the six loops of the reference power plant. The U-tube lengths (8.8 m) and diameters ($\varnothing_{out}$ = 16 mm) in the PACTEL SGs correspond to those of the full-scale SGs. The horizontal orientation of these SGs is one of the distinguishing features of the VVER design. One consequence of this geometry is a reduced driving head for natural circulation.

The gravity driven ECC system in the PACTEL facility consists of one CMT and pressure balancing lines (PBLs) from the pressurizer and from a cold leg connected to the top of the CMT in order to maintain the CMT in pressure equilibrium with the primary system during the injection. The cold leg PBL is connected to another loop than the break. More tests with different break locations are planned. The line from the pressurizer to the CMT is normally open. The PBL lines were insulated. Unfortunately there are no flow meters in the PBLs so it is impossible to give any measured result of the flow in these lines. The outlet pipe is connected from the side of the CMT to the downcomer and the line is equipped with flow and temperature meters. The available volume of ECC water in the CMT is 0.9 m^3, which is large compared with the total water volume of 0.881 m^3 in PACTEL. The CMT is located above the primary loops and SGs, so the motive force for ECC injection is the gravity head. The component elevations in the

PACTEL facility are shown in Fig. 2.

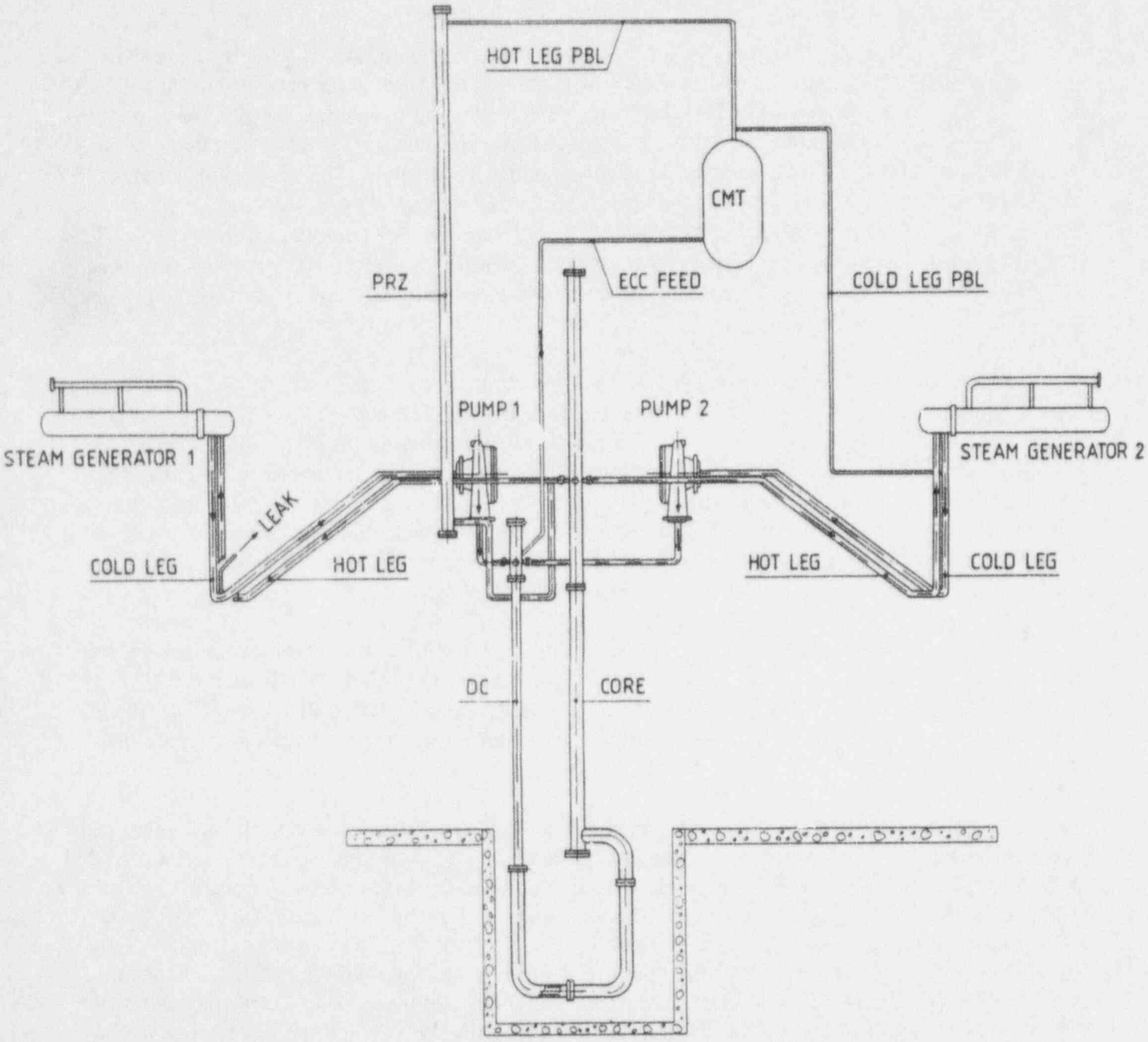

Fig. 1. PACTEL facility

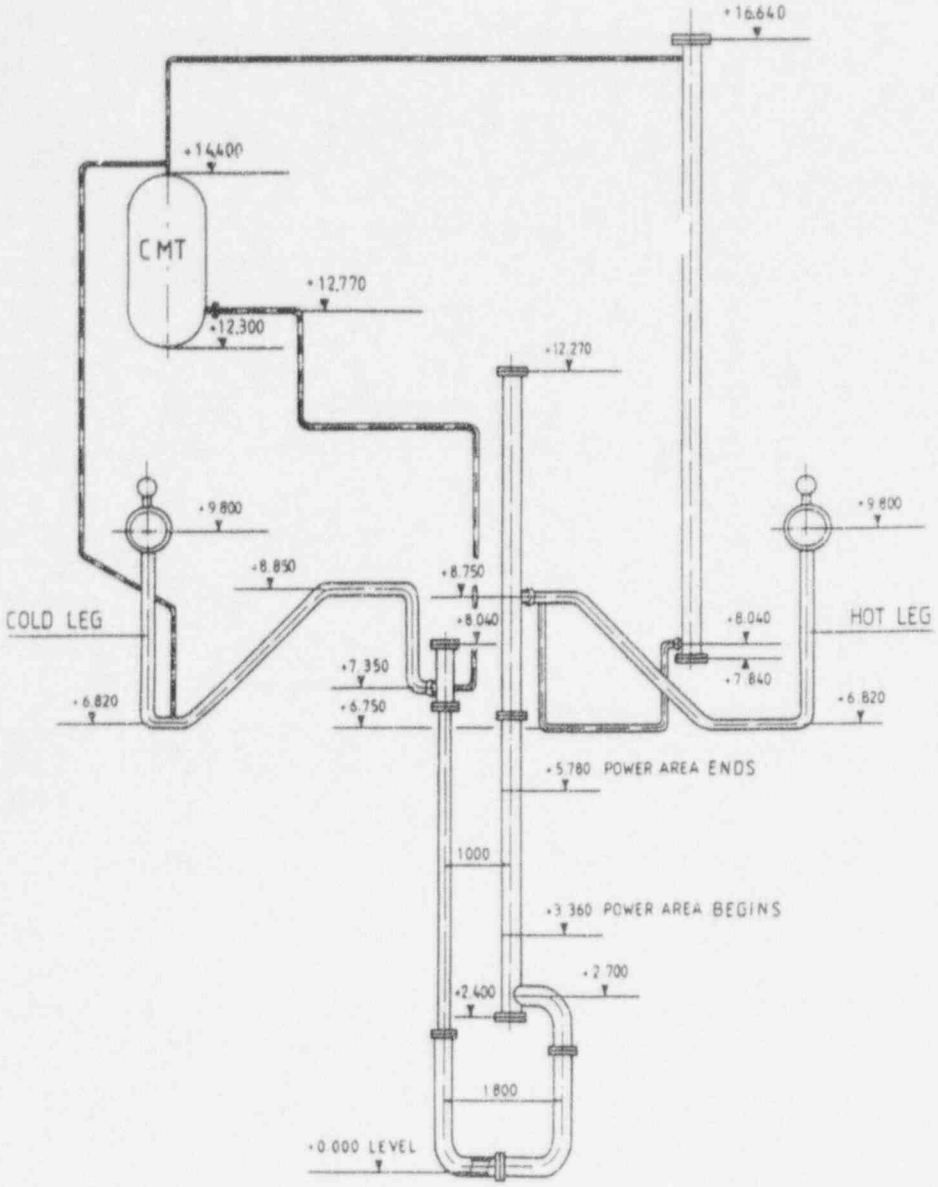

Fig. 2. Component elevations in the PACTEL facility

In order to investigate the temperature stratification in the CMT ten thermocouples were installed to the CMT. The thermocouples are located to the upper part of the CMT with distances as illustrated in the Fig. 3. The readout from the temperature measurement is clear during the ECC injection, but for analysing the temperature changes during the condensation faster measurements should be installed. The PBLs are connected to nozzle on the top of CMT and there is no distributor inside the CMT. The water level in the CMT was measured with a pressure difference transducer.

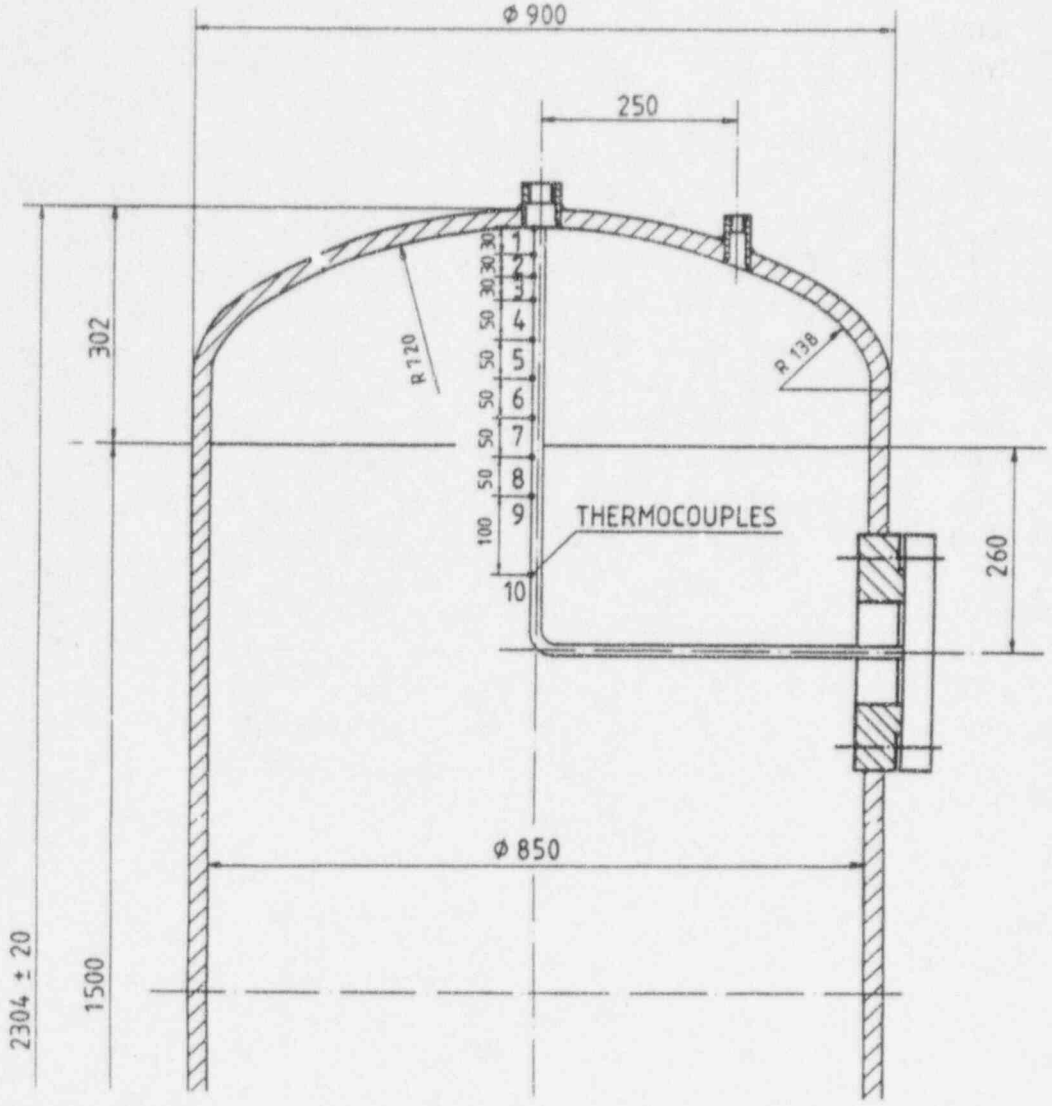

Fig. 3. The CMT temperature measurements.

III. EXPERIMENTAL PROCEDURE

The experimental procedure followed the routines used in preliminary tests. The core power was set to 80 kW corresponding to 1.8% of the 1375 MW thermal power of the Loviisa reactor. The fluid temperature and pressure in the primary system reached a quasi steady state near 220 °C and 38 bars. The secondary system pressure was set to 20 bars. The CMT was filled to the top with water at a temperature and pressure of about 40 °C and 38 bar, respectively. One loop of the three loop facility was isolated.

When compared to the first series of experiments the main differences were that the second series was carried out with two active loops, insulated PBLs and an improved instrumentation in the CMT.

The experiments were started by opening the break simulation valve in cold leg number 1 at time t = 0s. Two different break sizes (Ø 4 and 2mm) were used. Simultaneously with the break valve opening, the ECC line valve and the cold leg PBL valve were opened. The power of the pressurizer heaters was turned off. The first two tests, GDE11 and GDE12, were terminated by operator at t= 3000s. Neither the primary system nor the secondary system were depressurized by the operator in the GDE11 and GDE12 tests.

In test GDE13 the secondary side valve was also opened and the primary system was depressurized in stages through the pressurizer relief valve before the anticipated CMT flow interruption. This test was terminated at t=2000s by the operator.

For the small 2 mm (in dia.) break in the GDE14 test no depressurization was used. A high water level in the pressurizer was used in the initiation of the test in order to achieve circulation through the CMT in the early stage of the transient. The test was interrupted immediately after the condensation initiation at t=1170s.

The experiments can be summarized as follows:

1. GDE11
   - 2.0% (4 mm in dia.) cold leg break
   - no depressurization either on the primary or on the secondary side

2. GDE12
   - reproduction of the GDE11 test

3. GDE13
   - 2.0% (4 mm in dia.) cold leg break
   - depressurization of the primary system in stages
   - continuous depressurization of the secondary side

4. GDE14
   - 0.5% (2 mm in dia.) cold leg break
   - high water level in the pressurizer
   - no depressurization either on the primary or on the secondary side

IV. TEST RESULTS AND DISCUSSION

In all the tests the ECC flow rate from CMT was bigger than in the previous experiments. In the first test series the measured mass flow rates were below 0.1 kg/s, whereas now they were over 0.2 kg/s. A more detailed description of the preliminary experiments is given in Ref.[3].

Good reproducibility was achieved in the GDE11 and GDE12 test. The CMT pressures in GDE11 and GDE12 tests are shown in Fig. 1. In both experiments there was a condensation phase starting at about 1700s and lasting for 300s. The condensation behavior differed a lot from that observed in the preliminary tests. When the ECC flow in the first tests stopped totally several times because of rapid and very short condensations there was now only one condensation phase which lasted much longer. Due to the lack of proper instrumentation in the PBLs no information of flow conditions in the lines is obtainable.

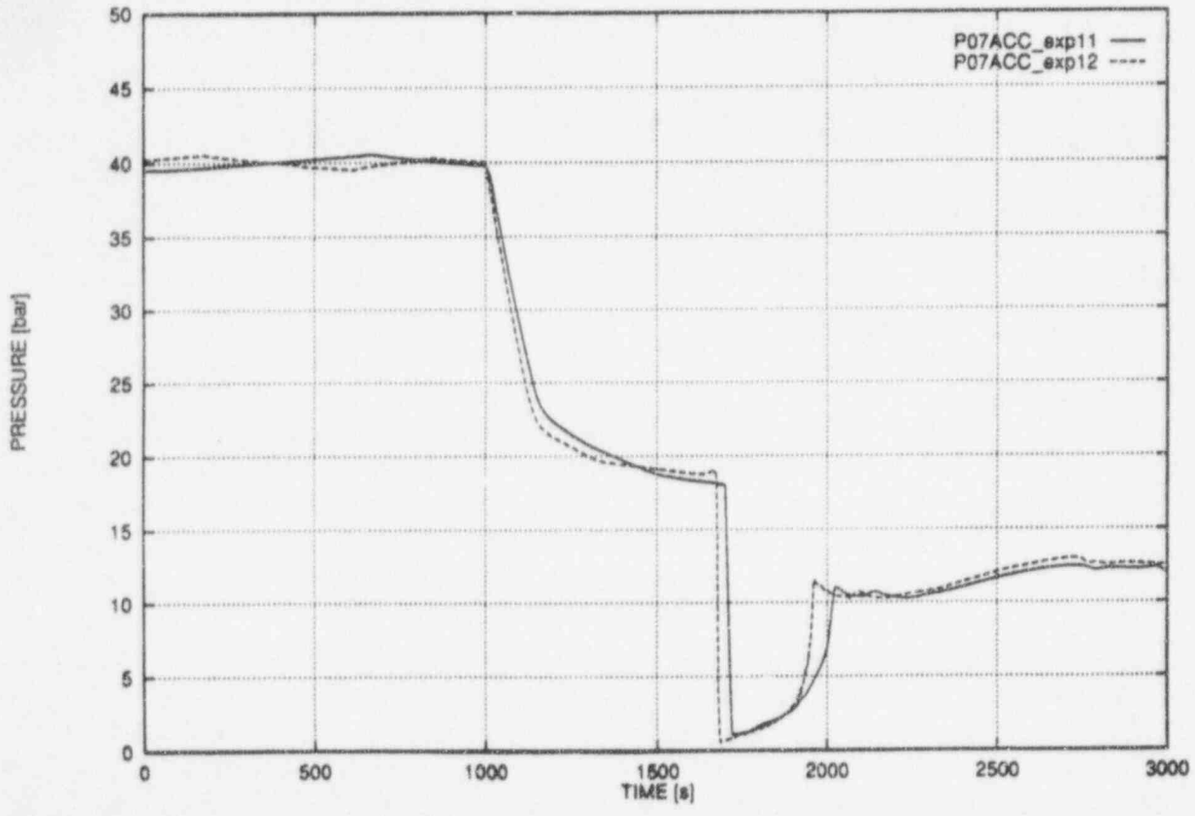

Fig. 4. The CMT pressures in GDE11 and GDE12 tests

However, the operator activated primary system depressurization stages affected to the total collapse of the vapor space, because in the GDE13 test there were three short condensations observed in the CMT, Fig. 5.

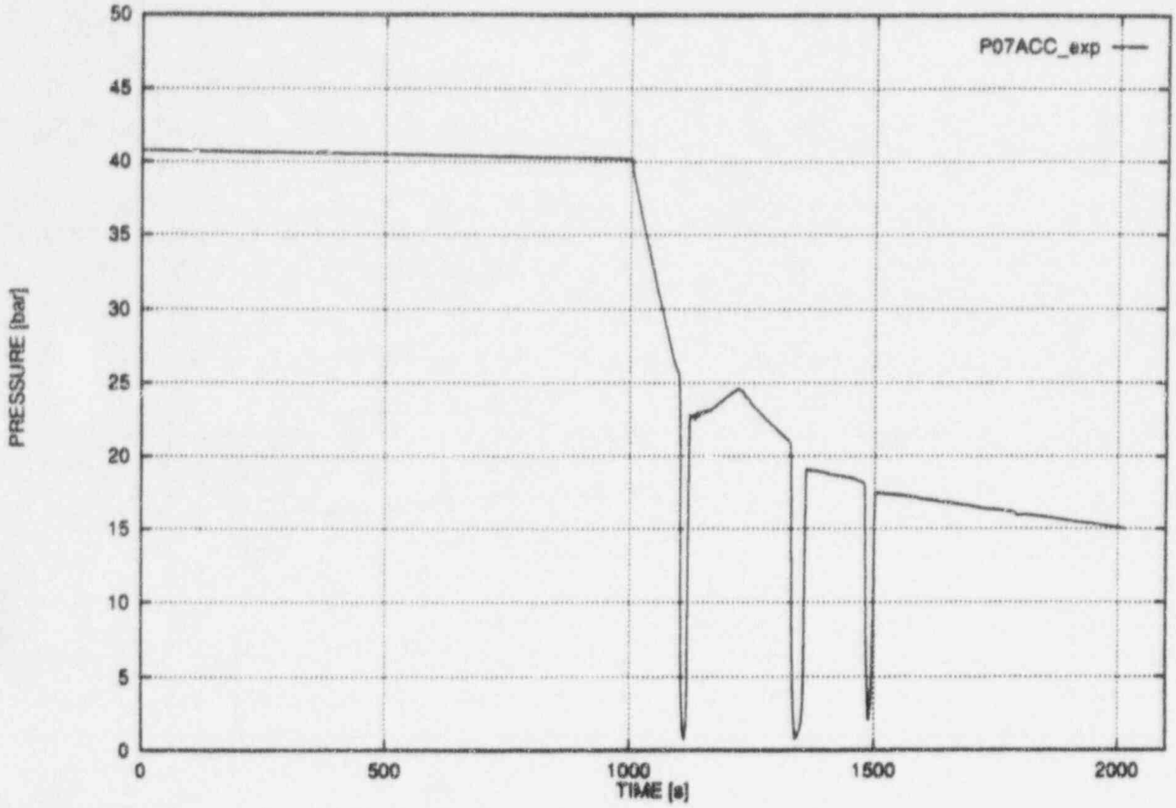

Fig. 5. The CMT pressure in GDE13

The first condensation was already at t= 1100 straight after the depressurization initiation. Similar periods of short condensations were observed in the experiments of the first series in both experiments with or without depressurizations. This behavior was found difficult to model in the RELAP5 analysis of the experiments of the first phase [4]. This is obvious, since the initiation of condensation is in reality a phenomenon in three dimensions and therefore the modelling capability of a one-dimensional computer code is not sufficient. It is not yet clear what is the initial phenomena behind the condensation: if it is the shattering of the stratification due to the flow from PBLs or steam condensation to the cold walls of the CMT or inner structures of the CMT causing cold water to get contacted with hot steam. A large degree of randomness is involved in the initiation of short and rapid condensations. However, in an integral system a rapid condensation of any kind may amplify perturbations and initiate different natural circulation modes and also have an impact on the energy transport capability of the system.

The rate of mixing and, hence, the length of the condensation period before CMT repressurizing was dependent on the momentum of the fluid injected to the tank. If only steam or a very small amount of water was injected, the repressurization was fast because only the temperature gradients in the uppermost water layers were mixed. This behavior was observed when the CMT temperature distributions in the GDE11 and the GDE13 tests were compared. The rate of condensation affected directly the time it took for new stratified layers to be formed in CMT. During the long condensation period in the GDE11 and GDE12 experiments the water level

dropped to the top of the core and even slightly below. The uncovery lasted only a short time and no significant heat-up in the core was found. In the GDE13 and GDE14 experiments no core uncovery was found.

A very steep vertical temperature gradient was formed inside the CMT in all the tests. Fig. 6. shows that the temperature difference just before the condensation in the GDE11 experiment was 180 K in a water layer 0.15 m thick.

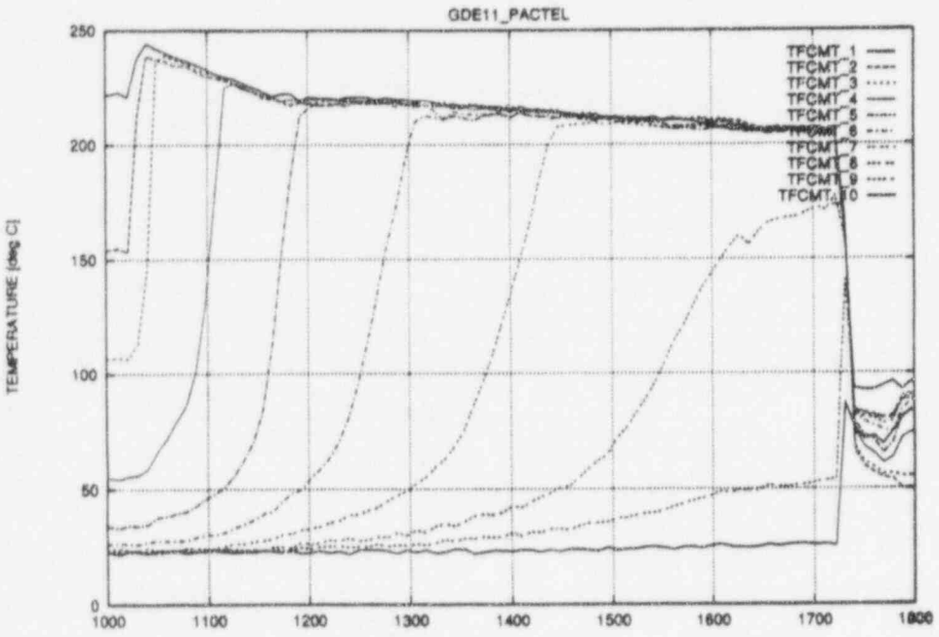

Fig. 6. Temperature distribution in the CMT

The thermocouples were located in a 0.05 m distance from each other except for number 10 which was 0.1 m lower than number 9 (the thermocouple numbering corresponds to that shown in Fig. 3.). When the hot uppermost layer of the CMT water space was shattered by the steam or water flow from the piping, the much colder water got to a direct contact with hot vapor and generated a scene of rapid condensation.

An effort to prevent the rapid condensation was done by carrying a thick, insulating level of hot water to the CMT with a natural circulation loop formed between the CMT and the primary system via the cold leg PBL and ECC line. For this reason the water level in the pressurizer was set high (to 7 m, when at 4 m normally) and a small break size was chosen at the GDE14 test initiation. This natural circulation phase of the CMT was also used in the ROSA-V/LSTF experiment [5]. With these preconditions a short natural circulation phase was then observed in the GDE14 experiment. However, this natural circulation phase was not effective

enough to form a sufficient layer of hot water in the CMT. In PACTEL the total water volume above the CMT is small since there are horizontal steam generators. The comparison of CMT water levels in the GDE12 and the GDE14 tests is shown in Fig. 7.

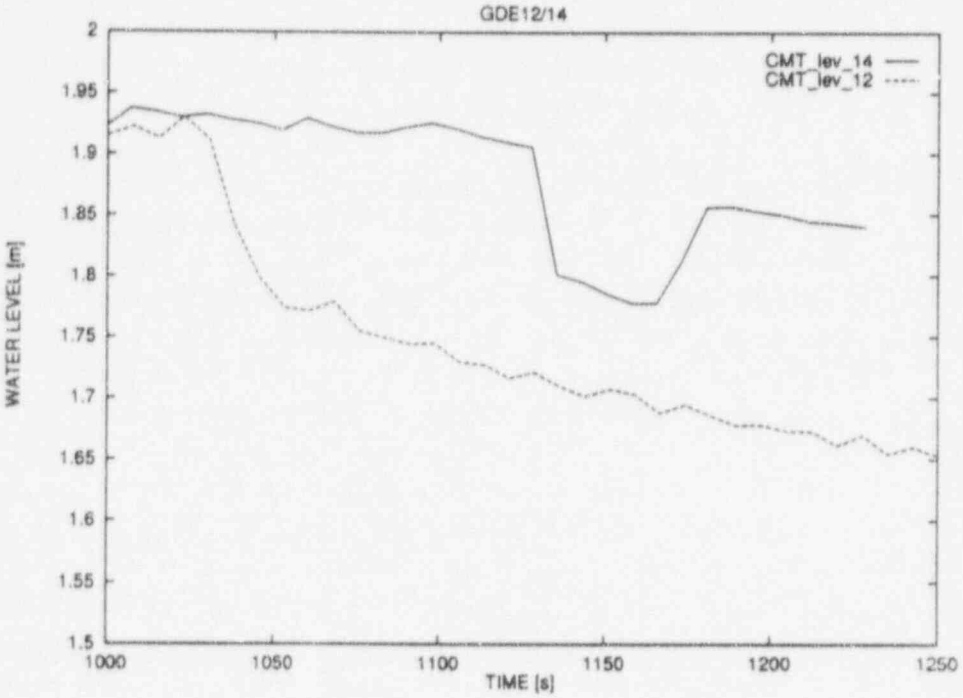

Fig. 7. CMT water level in GDE12 and GDE14 tests

V. CONCLUSIONS

A second series of experiments of gravity driven ECC was performed with the PACTEL. Only two of the three loops of the facility were used whereas in the first series of experiments all the loops were active. The break was now located in the cold leg and two different break sizes were used. In one of the tests both the primary system and the secondary system were depressurized.

In all the four experiments performed, steam was flowing into the CMT and then later condensed to the cold water of the CMT. There were striking changes in the vertical temperature gradient of the CMT. It was experienced that condensation was then initiated easily by steam or water flow from the PBLs as the steep stratification in the CMT was broken. Especially the changes in water level in the pressurizer seemed to be responsible for most of the condensation

periods. During the condensation period the pressure in the CMT decreased practically to zero and water was sucked from the primary system through PBLs. Two different types of mixing in the CMT were found:

1. A long lasting mixing, where the stratified layers inside the CMT were totally mixed

2. A period of short condensations where only the uppermost layers of the CMT were mixed.

In the first case the CMT repressurization and the continuation of ECC flow was prevented for a long period. In one of the tests the water level in the primary system sunk slightly under the core level. A period of short condensations was observed in the experiment with primary and secondary side depressurizations by the operator. The primary system water level was well above the core level during the experiment. Similar behavior was observed in the experiments of the first series in both experiments with or without depressurizations. However, it is obvious that having a possibility for powerful condensation in the primary system puts high demands on the strenght of materials.

The effort to carry a thick, isolating water layer to the CMT by using high pressurizer level at the test initiation was unsuccesful. However, a natural circulation loop through the cold leg PBL, CMT and the ECC line was formed but the flow interrupted soon. Despite these problems the energy transport was sufficient to provide core cooling and no core heatup was found.

Condensation of steam in the CMT could be avoided with some technical arrangements in the test facility like having a tall and slim tank, where the interfacial boundary layer is small. Also internal structures of the CMT like a honeycomb in the tank dividing it in "small tanks" would prevent or make condensation less possible. Abandoning the PBL between the pressurizer and the CMT would cut one way of interplay with the primary loop and at least prevent the pressurizer level changes from having an effect to the CMT. However, even though these kind of improvements were made to gravity driven ECC systems, we cannot guarantee that computational models will provide accurate answers. Therefore, to build this confidence more experimental data has to be obtained and new computational models developed.

References:

[1] Munther, R., Kalli, H., Kouhia, J., Kervinen, T. Passive core cooling experiments with PACTEL facility. Proc. of ENS TOPNUX'93, Haag, Netherlands, April 25-28, 1993.

[2] T. Kervinen, V. Riikonen, J. Kouhia, "PACTEL, Facility for Small and Medium Break LOCA Experiments," Proceedings of ENC'90 Conference. European Nuclear Society, Lyon, France,

September 23-28, 1990.

[3] Munther, R., Kalli, H., Kouhia, J., Kervinen, T. Passive core cooling experiments with PACTEL facility. EN A-18. LTKK 1993. ISBN 951-763-806-X.

[4] Munther, R., Vihavainen, J., Kalli, H., Kouhia, J., Riikonen, V., RELAP5 analysis of gravity driven core cooling experiments with PACTEL. Proc. ARS'94, INTL topical meeting on advanced reactor safety, Pittsburgh, USA, April 17-21, 1994. ISBN 0-89448-193-2.

[5] T. Yonomoto, Y. Kukita, Y. Anoda, "Passive Safety Injection Experiment at the ROSA-V Large Scale Test Facility," Proceedings of the ANS National Heat Transfer Conference, p. 393, American Nuclear Society, Atlanta, Georgia, August 8-11, 1993.

An Investigation of Condensation from Steam-Gas Mixtures Flowing Downward Inside a Vertical Tube

S. Z. Kuhn, V. E. Schrock and P. F. Peterson
Department of Nuclear Engineering
University of California, Berkeley
Berkeley, California 94720-1730, USA

Abstract

Previous experiments have been carried out by Vierow [1], Ogg [2], Kageyama [3] and Siddique[4] for condensation from steam/gas mixtures in vertical tubes. In each case the data scatter relative to the correlation was large and there was not close agreement among the three investigations. A new apparatus has been designed and built using the lessons learned from the earlier studies. Using the new apparatus, an extensive new data base has been obtained for pure steam, steam-air mixtures and steam-helium mixtures. Three different correlations, one implementing the degradation method initially proposed by Vierow and Schrock [5], a second diffusion layer theory initially proposed by Peterson et al. [6], and third mass transfer conductance model [25] are presented in this paper. The correlation using the simple degradation factor method has been shown, with some modification, to give satisfactory engineering accuracy when applied to the new data. However, this method is based on very simplified arguments that do not fully represent the complex physical phenomena involved. Better representation of the data has been found possible using modifications of the more complex and phenomenologically based method which treats the heat transfer conductance of the liquid film in series with the conductance on the vapor-gas side with the latter comprised of mass transfer and sensible heat transfer conductances acting in parallel. The mechanistic models [25], based on the modified diffusion layer theory or classical mass transfer theory for mass transfer conductance with transpiration successfully correlate the data for the heat transfer of vapor-gas side. Combined with the heat transfer of liquid film model proposed by Blangetti et al. [28], the overall heat transfer coefficients predicted by the correlations from mechanistic models are in close agreement with experimental values.

Background

Condensation from steam-gas mixtures inside tubes is an important technical problem in the design of passive containment cooling systems. The work reported in this paper was done in support of the Simplified Boiling Water Reactor (SBWR) in which decay heat is removed from containment passively by Passive Containment Cooling System (PCCS) condensers. These condensers utilize two-inch diameter vertical stainless steel tubes immersed in a pool of atmospheric pressure water outside the containment. In a hypothetical accident, the drywell contains a pressurized mixture of steam and nitrogen which flows into the PCCS condensers tubes driven by natural forces. The condensate drains by gravity into the Gravity Drain Cooling System tank while the residual steam gas mixture is vented into the pressure suppression pool located in the wetwell.

Film condensation in the presence of noncondensable gas has been studied rather extensively for condensation by free convection on isothermal vertical surfaces exposed to large gaseous volumes with or without imposed vertical gas velocities. For stationary pure vapor, Nusselt [7] modeled the problem as a smooth laminar draining liquid film through which heat flowed by pure conduction. He postulated that the local heat transfer coefficient is inversely proportional to the local film thickness which he found to vary as $x^{1/4}$ and the average heat transfer coefficient is therefore proportional to the height of the plate to the power -1/4. His

equation for average heat transfer coefficient agreed reasonably with data (it tended to be lower than data where waves were observed).

Othmer [8] did one of the earliest experiments which showed that presence of a small amount of noncondensable gas in vapor reduces the condensation rate significantly from that predicted by Nusselt. The reduction in heat transfer rate was attributed to the accumulation of gas near the condensing interface resulting in a reduction in the vapor partial pressure and corresponding saturation temperature at the interface. Some of the early work on the problem was summarized by Rohsenow [9]. Theoretical analyses for the free convection problem were carried out by Sparrow and Lin [10], Minkowycz and Sparrow [11], and Rose [12]. They modeled the problem using boundary layer theory for the condensate film and for the composition boundary layer on the vapor-gas side. Self similar solutions were obtained for the uniform wall temperature case. Rohsenow and Ling [13] analyzed the effect of vapor flow induced interfacial shear for pure vapor and considered the role of liquid film turbulence at high condensate flowrates. Denny et al. [14] carried out numerical studies that showed that in the case with noncondensable gas with flow is not self similar. Uchida et al. [15] carried out experiments that were the basis of early correlations for condensation on large vertical surfaces located inside reactor containment. The heat transfer coefficient was expressed as the Nusselt value times a "degradation factor". There have been a number of investigations to study the effect of noncondensable gas on forced convection condensation on external surfaces, e.g. , Rose [16], Sparrow et al. [17] and Acrivos [18]. Wang and Tu [19] developed a model for the effect of noncondensable gas on laminar film condensation inside a vertical tube. They noted that experimental data for this case are not available (except for a few rough data).

Rohsenow suggested that information developed for condensation on vertical plates may be applied to condensation inside tubes when the liquid film thickness is much smaller than the tube diameter. This is reasonable for condensation of pure vapor, however for the case with gas present the gaseous boundary layer will tend to fill tube and there is no longer a constant ambient vapor-gas reference state for the heat and mass transfer problem. The first experimental study for this case was carried out by Vierow [1]. It was recognized that the local heat transfer coefficient is needed for the present application because the wall temperature is not uniform, the wall heat flux does not follow the Nusselt prediction and the reference state for the heat transfer coefficient varies in the flow direction. It was further recognized that the heat transfer coefficient should be based on the difference between the saturation temperature at the local bulk vapor partial pressure and local wall temperature. Vierow used a one-inch diameter (OD) copper tube cooled by water in counter flow in an annular jacket. At several axial locations, thermocouples were placed downstream of mixers to measure local bulk cooling water temperatures. Local wall heat flux was calculated from the axial gradient of bulk temperature. Thermocouples were soldered to the outer tube surface to obtain the axial wall temperature distribution. The condensate flow rate and the bulk steam-gas composition at each axial location were obtained from energy and mass balances. Following the degradation factor concept, Vierow and Schrock [5] reasoned that the local heat transfer coefficient from the Nusselt hydrodynamic model would be enhanced by the interfacial shear and degraded by the presence of gas. They defined the degradation factor as $f = h_{exp}/h_{ref}$, where $h_{ref} = k/\delta$ and

$$\left(\frac{3\mu_f \Gamma}{g\rho_f(\rho_f - \rho_g)}\right)^{1/3} \qquad (1)$$

where μ_f is liquid viscosity, ρ_f is liquid density, ρ_g is mixture density, g is the gravitational constant and Γ is the condensate flowrate per unit tube inner circumference. The experimental data were correlated in the form

$$f = f_1 f_2 = (1 + Re_g^{\,a})(1 - Ma^b) \qquad (2)$$

where $f_1 = 1 + Re_g^a$, $f_2 = 1 - Ma^b$, Re_g is the local Reynolds number of the steam-gas mixture, Ma is the local bulk mass fraction of the gas in the mixture, and a and b are constants (piece wise). The form was chosen to produce the result $f_1 = 1$ for $Re_g = 0$ and $f_2 = 1$ for $Ma = 0$. Although this correlation method lacks the full representation of the complex physics, it has the advantage of simplicity when used in a large system computer code. The mechanistic correlations presented below require an additional interation procedure as described in the Appendix.

Later Ogg [2] and Siddique [3] did experiments using forced flow in two-inch diameter stainless steel tubes and Kageyama [3] did an experiment using a two-inch diameter glass tube. Ogg used the same experimental technique as Vierow to obtain bulk temperature of the coolant. Siddique placed thermocouples within the cooling annulus and injected air to promote mixing and give bulk temperature. His experimental technique was otherwise similar to Vierow's. Ogg did experiments with pure steam, steam-air mixtures and steam-helium mixtures. Siddique did experiments with steam-air and steam-helium. Ogg correlated his data in the form used by Vierow and Schrock while Siddique [4] assumed that the thermal resistance of the liquid film is negligible and correlated his data in terms of parameters deduced from the energy equation for the steam-gas mixture. Differences among the three data sets exceeded the experimental error estimates. Thermocouple and other experimental problems were identified for both the Ogg and Siddique experiments. In both experiments the observed tube wall temperatures did not vary smoothly along the tube. Certain thermocouples consistently gave readings higher or lower than expected from the general trend and gave the appearance of an effect like the one noted by Vierow. Hasanien et al. [20] suggested that this is caused by the heat transfer on the cooling jacket side. However, in Ogg's and Siddique's data the peaks and valleys consistently occurred at particular stations suggesting that the cause was thermocouple error rather than some physical phenomenon. These experiences were used to guide development of the improved experimental system described in the present paper.

Peterson et al. [6] developed an approximate correlation method which gave fair agreement with the data of Kageyama and Ogg. It was noted that the experimental data gave the overall heat transfer coefficient between the vapor-gas mixture (saturation temperature at the bulk vapor partial pressure) and the heat transfer surface temperature. So far, no experimental method has been developed to measure the interface temperature, so the resistances to heat transfer of the liquid film side and of the vapor-gas side are not separately measurable. To evaluate the vapor-gas side resistance from the data, it was necessary to choose a model for the liquid film thermal resistance. The liquid film resistance has been studied extensively [25] and is known to depend primarily upon the condensate flowrate but to be influenced by interfacial shear, waviness and turbulence. The experimental data indicate that for most, if not all, of PCCS operating conditions the condensate film is laminar. Appropriately, Peterson et al. used the same laminar film model as employed by Nusselt. To obtain a heat transfer coefficient between the bulk vapor-gas saturation temperature and the interface, the mass transfer and sensible heat transfer processes were represented by the standard correlation forms for single phase turbulent convection inside tubes (Dittus-Boelter form) without accounting for the effect of blowing (suction). The mass transfer problem was recast as a heat transfer problem by defining a "condensation thermal conductivity" to facilitate combining it with the parallel sensible heat transfer process. In a similar model, Kim and Corradini [22] suggested neglecting the thermal resistance of the liquid film and correlated their data for condensation on external surfaces in terms of mass transfer and sensible heat transfer in the vapor-gas flowing mixture. In the mass transfer literature, (Kays and Crawford [23], Mills [24]), a simplified model referred to as the Couette flow model has been used to obtain a theoretical prediction for the mass transfer conductance under the condition with transpiration (suction or blowing). The same concept used there to obtain the ratio of mass transfer conductance with and without transpiration was adopted in this paper but instead we obtain empirical correlations of this ratio from our experimental data.

Description of the Experiment

The experimental apparatus is shown schematically in Figure 1. It is an open loop comprised of metered steam and gas supplies, an instrumented test section with an annular cooling jacket, a separator to divide the test section effluent liquid and gaseous streams and a quench tank to condense any residual steam. Steam at a nominal pressure of 930 kPa (135 psia) was provided by the campus steam system. Steam was examined and noncondensable gas was less than 10^{-5} in mass fraction. A separator was provided to remove any residual moisture and supply dry steam to the test section. The steam flow rate was measured by calibrated orifices with differential pressure transducer installed. Compressed air from the building supply or helium from high pressure storage tanks was heated to the desired temperature for mixing. The gas flow rate was measured by high precision rotameters. The steam and gas streams were mixed downstream of the metering stations and then delivered to the top of the test section. The test section was a 5.08 cm (2.0 inch) O.D. type 304 stainless steel tube with a 1.65 mm wall thickness. The tube was 3.37m in length with an 81 cm adiabatic entrance followed by a 2.4 m long condensing section and a short adiabatic exit section. The condensing section was provided by an annular cooling jacket sealed at its two ends by O rings and held concentric around the condenser tube by small radial nylon spacers inserted through the jacket wall. Cooling water flowed upward in the annulus while the steam-gas mixture flowed downward inside the condenser tube. Cooling water could be supplied either from the city water supply or by a closed heat transfer loop coupled to the building cooling tower system. The latter system permitted operation with elevated mean coolant temperature.

The test section was fitted with thermocouples to measure the axial distribution of the tube wall temperature. These were 0.508 mm diameter sheathed thermocouples silver soldered into longitudinal grooves 0.7 mm wide, 0.58 mm deep and 12.7 mm long as illustrated in Figure 2. The sheath was then passed radially out through and sealed in the cooling jacket wall. This design was chosen to position the junction of the thermocouple wire at a well determined radial position within the condenser tube wall and to minimize the perturbation of the radial conduction within the wall. It also resulted in a minimum of thermocouple lead material to disturb the flow and heat transfer of the cooling water. This method of mounting condenser tube wall thermocouples was made possible by a unique cooling jacket design. The jacket was made from a 7.62 cm (3 inch schedule 80) pipe split longitudinally. After passing condenser tube thermocouples through the jacket seal fittings the two jacket halves were rejoined as a cylinder using strips of silicon rubber to compensate for the material lost in machining and to provide a seal. The two parts were held tightly together by metal strap clamps spaced axially at approximately 8 cm intervals. The reassembled jacket was then mounted and sealed in end fittings, themselves sealed to the condenser tube. After completing thermocouple installation by sealing the jacket penetrations, the sheaths passed through 10 cm thick fiber glass insulation applied over the entire length of condenser tube and cooling jacket. Figure 2 illustrates the jacket construction and positioning of thermocouples. Further detail of the cooling jacket and thermocouples may be found in the report by Kuhn et al. [25].

Rather than attempt to directly measure the local cooling water bulk temperature, the outer surface (adiabatic) temperature was measured at the same axial locations as the condenser tube wall temperature. This was done using 1.59 mm (1/16 inch) diameter sheathed thermocouples inserted through the jacket wall with the tip protruding about 1 mm into the water. Turbulent convective heat transfer theory was then used to obtain the local bulk coolant temperature from the temperatures of the two surfaces of the annulus. This method was not valid in the entrance and exit regions due to multidimensional effects at these locations. For this reason, data were used only from measurements made starting at the 17 cm (measured from the top of the condenser) station and no closer to the inlet (bottom of the condenser) than the 171.5 cm station. Thermocouple pairs were installed at 180 degree opposed circumferential positions at various axial locations to provide a check on the circumferential uniformity of the cooling.

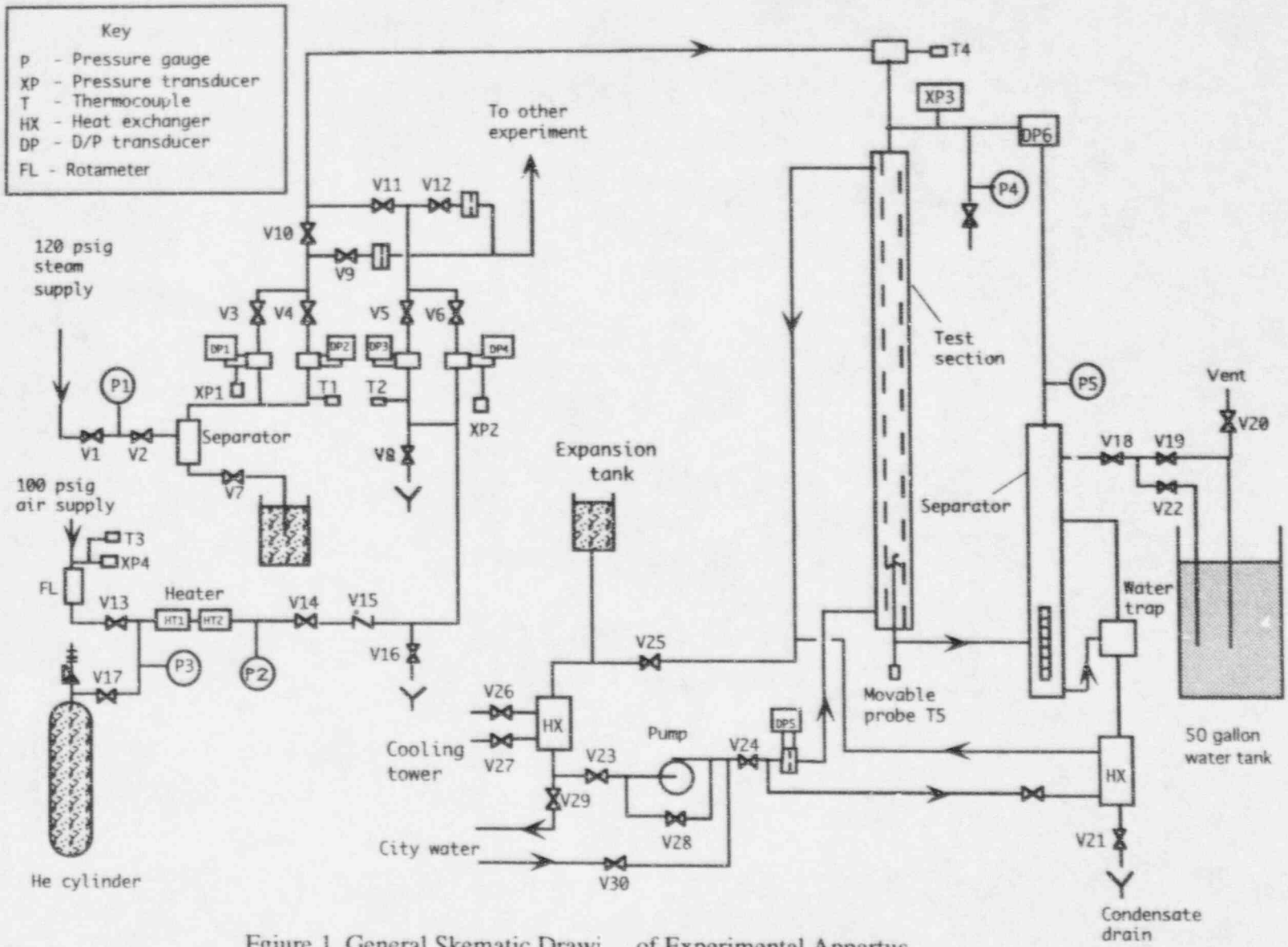

Fgiure 1 General Skematic Drawi _ of Experimental Appartus

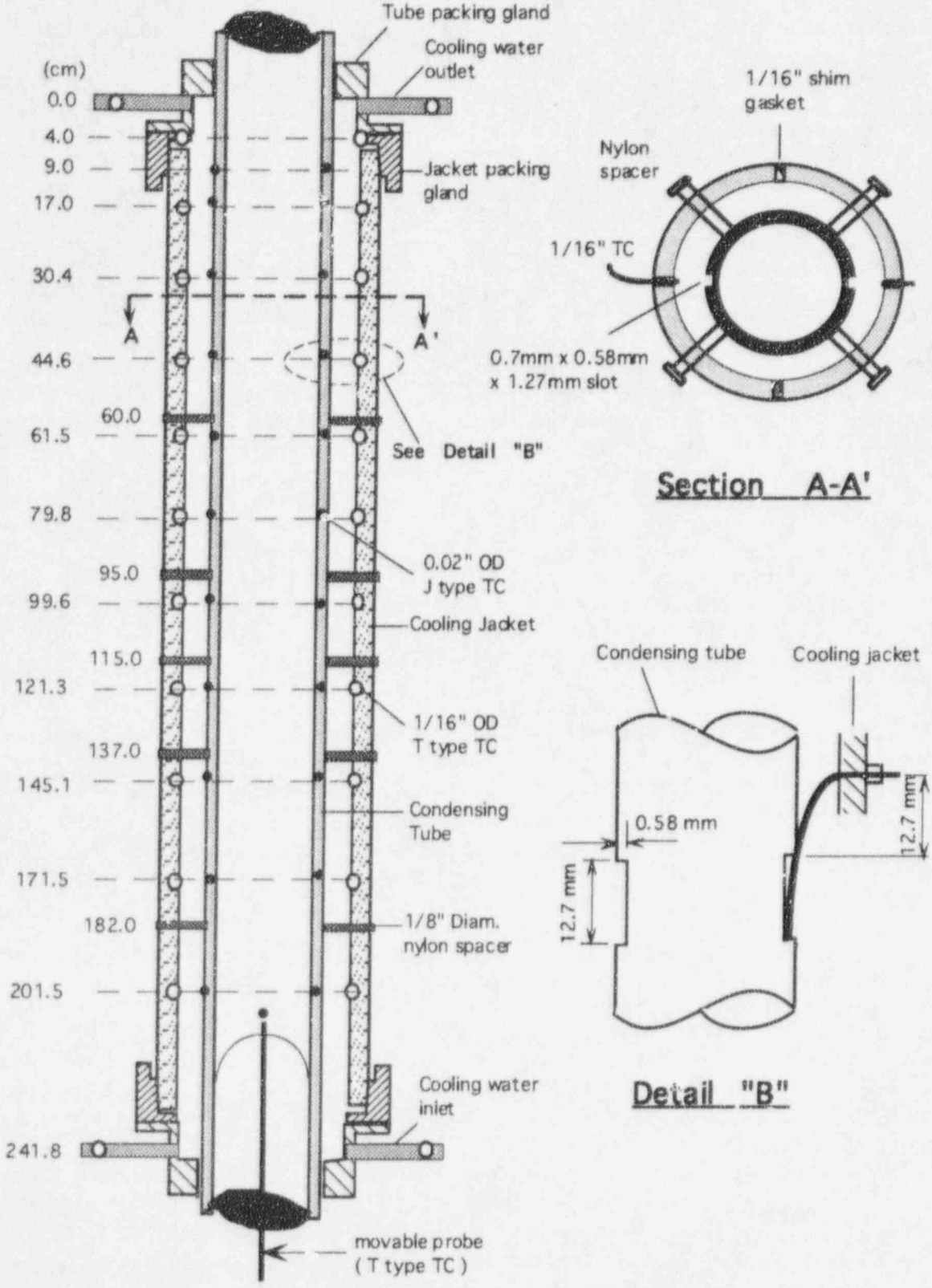

Figure 2 Detail of Test Section and Thermolcouple Installation

Cooling water was introduced at the bottom of the annulus through two radial pipes mounted on opposite sides and was discharged via four similar pipes mounted at 90 degree intervals around the top of the jacket. Thermocouples were also mounted in each of the discharge pipes far enough downstream from the jacket to assure complete mixing and a reliable measure of the exit bulk cooling water temperature. A concern about the previous experiments had been the lack of reliability of temperature measurements made close to the top of the cooling jacket. With four discharge pipes the problem was minimized. However, even with the present design, it was found that measurements at the 9 cm station were evidently influenced by multidimensional effects and these data were not used.

Pressure transducers were installed to measure the absolute pressure at the entrance of the test section and the pressure differential across the test section. Valves situated on the condensate and gaseous discharge lines allowed regulation of the test section pressure level and the level of condensate in the separator. A heat exchanger was installed in the condensate drain line so that condensate could be collected (without flashing) during tests or calibration runs. Data acquisition was accomplished using Strawberry ACM2-12-16 analog to digital convector cards installed on Macintosh computer and the software of Workbench to configurate, read, display and log data to disk in selected engineering units.

Extensive shakedown testing was performed to ensure the accuracy, reliability and reproducibility of the data. Isothermal checks of all test section mounted thermocouples at different temperature levels demonstrated consistency with a standard deviation 0.25 °C for the 49 thermocouples and a maximum deviation of 0.6 °C. Standard procedures were established for startup, testing and shutdown of the experiment. Data logging was started for each run only after monitoring showed that steady state was maintained.

Test Matrix

The test matrix included 42 runs with pure steam, 71 runs with steam-air mixtures and 24 runs with steam- helium mixtures, or 137 runs in all. The pure steam tests were run at pressures from approximately 100 kPa to 500 kPa (or 1-5 atm). and flowrates from approximately 30 kg/hr (8.3×10^{-3} kg/s) to 60 kg/hr (1.7×10^{-2} kg/s). The results were used to correlate the f_1 factor (Eqs. 7 and 9) used in the modified degradation factor method. Approximately half these tests were done to demonstrate reproducibility over the several month testing period. Lack of reproducibility had been a problem in the previous experiments.

The steam-air tests were divided into two series. In the first, 32 runs were conducted at a pressure of 400 kPa (4 atm) and steam flow rate of 50 kg/hr while varying the air flowrate to give air mass fraction of 1, 2, 3, 4, 6, 8, 10, 15, 20, 25, 30, 35, and 40 %. Again approximately an equal number of test were included to demonstrate reproducibility. For the second steam-air series two sub-matrices were selected using steam flow rates of 30 and 60 kg/hr and pressures of 200, 300 and 500 kPa, and gas mass fractions of 1, 5, 10, 20 and 40 % were the matrix parameters. The steam-helium tests were all run at a pressure of 400 kPa using steam flow rates of 30, 45 and 60 kg/hr and gas mass fractions of 0.3, 0.5, 1, 3, 5, 10, and 15 %.

Data Reduction

The local heat flux at the inside surface of the condenser tube was calculated from the energy equation for the cooling water, i. e. ,

$$q''_{wi}(x) = -\frac{W_{cw}c_p}{\pi d_i}\frac{dT_b(x)}{dx} \qquad (3)$$

The first step of the data reduction method was to calculate the axial distribution of bulk temperature. The data for each run were then fit using several analytic forms and a statistical analysis used to select the one that best fit the experimental data. The selected fit was then differentiated to obtain the local temperature gradient. As noted earlier, the bulk temperature was calculated from the two surface temperatures of the annulus. Temperature profile factors defined as

$$F = \frac{T_{wo} - T_b}{T_{wo} - T_a} \tag{4}$$

were obtained by turbulent flow analysis based on the k-ε turbulence model and assuming that the velocity and temperature profiles were fully developed at each axial location. These calculations took into account the radial variation of physical properties and were done parametricly for various wall temperatures to give a matrix of profile factors covering the experimental range. The factors were then used in the data reduction program. The variable wall boundary condition has only a minor effect on the value of F due to the characteristics of turbulent flow, which gives strong mixing and fast response to boundary condition change [23] and the data are reported only downstream of the cooling annulus thermal entry region. It is therefore reasonable to assume fully developed profiles. Bulk temperatures calculated by this method extrapolate in excellent agreement with the measured exit bulk temperature adding confidence to this method. Since the condenser tube thermocouples were embedded in the tube it was necessary to correct the measurements to obtain the outside wall temperature. This was done using an approximate heat flux as an initial guess, obtained by assuming that the axial gradient of the adiabatic wall temperature is the same as that of the coolant bulk temperature. This assumption is justified by the fact that the conduction correction is very small and therefore some error in the estimated heat flux is acceptable. The bulk temperature distributions so obtained are much smoother than had been the case in earlier experiments and they merged more accurately with bulk temperature data from the exit pipes.

Once the heat flux in the condenser tube was calculated (and corrected to the inner tube surface), it was used to calculate the experimental heat transfer coefficient from

$$h_{exp} = \frac{q''}{T_b^s - T_{wi}} \tag{5}$$

in which the bulk saturation temperature T_b^s is found from evaluation of the local bulk gas mass fraction. The mass fraction is found by subtracting the condensate flowrate from the inlet vapor flowrate to obtain the local vapor flowrate and noting that the gas flowrate remains unchanged along the condenser tube. In the data reduction, two models are used to obtain reference estimates of the condensate film thickness from solutions of the liquid momentum equation. For the case of zero interfacial shear, the Nusselt model, the film thickness can be calculated using Eq. 1, while for the case with interfacial shear we obtain the film thickness from the positive real root of the equation

$$\Gamma = \frac{g}{\mu_f}\rho_f(\rho_f - \rho_g)\frac{\delta_2^{\,3}}{3} + \frac{\rho_f \tau_i \delta_2^{\,2}}{2\mu_f} \tag{6a}$$

where $$\Gamma(x) = \frac{\int_0^x q_{wi}(x)dx}{h_{fg}'} \quad \text{with} \quad h_{fg}' = h_{fg} + \tfrac{3}{8}c_{p,f}\Delta T$$

τ_i is the interfacial shear stress calculated from the Darcy equation for smooth pipe flow times the enhancement factor $\beta_f / (\exp(\beta_f) - 1)$ due to condensation suction effect. β_f is the so-called blowing parameter for momentum transfer [23, 24, 25] and given by

$$\beta_f = \frac{m_c''}{\rho V_g \left(\frac{f_{i0}}{2}\right)} = \frac{m_c'' V_g}{\tau_{i0}} \qquad (6b)$$

where m_c'' is the condensation mass flux and f_{i0} and τ_{i0} is the friction factor and interfacial shear stress without suction effect.

Discussion of the Experimental Results

Examples of the experimental data are illustrated in Figures 3 through 6b. Figures 3, 4 and 5 are for pure steam runs. Figures 3 and 4, from experiments conducted 60 days apart show the quality of reproducibility of the data and are cases for which the steam was not fully condensed. The centerline temperature measurements obtained from the movable probe indicate a slight drop off in temperature along the condenser. This is partly attributed to the pressure drop which was measured to be only 2.4 kPa for this run and partly to the superheat of the steam at the entrance which was measured to be 35 °C. As seen for both the condenser tube wall and cooling jacket adiabatic wall, the data show very small circumferential asymmetry. Figure 5 shows a run at higher pressure and correspondingly higher temperature difference which resulted in condensation being completed at about the 160 cm position. Beyond that position the condenser tube was filled with condensate. The centerline thermocouple probe was able to provide a sharp delineation of the position of complete condensation. In such cases, only the data upstream of the position of complete condensation were used in fitting the coolant bulk temperature profile for calculation of the heat flux. Figures 6a and 6b present raw data for a steam-air case and again illustrate the quality of reproducibility of the data. In this case, the circumferential asymmetry of the condenser tube wall temperature is more noticeable, albeit small. The bulk coolant temperature calculated from the raw data of Figure 6a is shown in Figure 7. The results are very smooth and show very good agreement with the average outlet temperature measured by the thermocouples mounted in the discharge pipes.

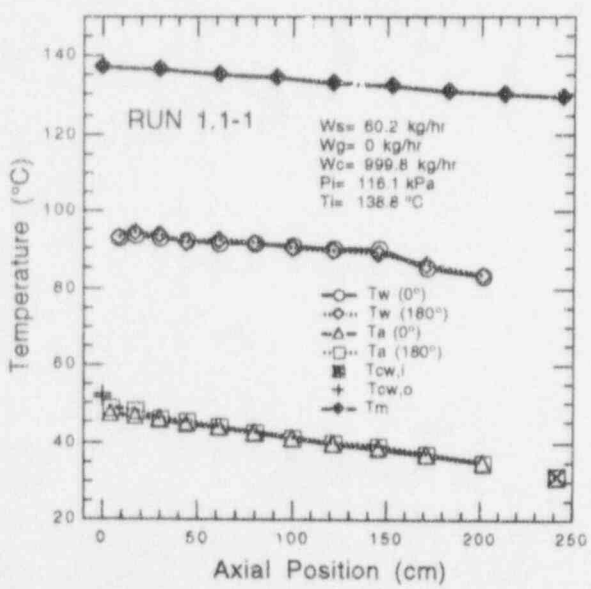

Figure 3 Temperature Distribution versus Axial Location for RUN 1.1-1

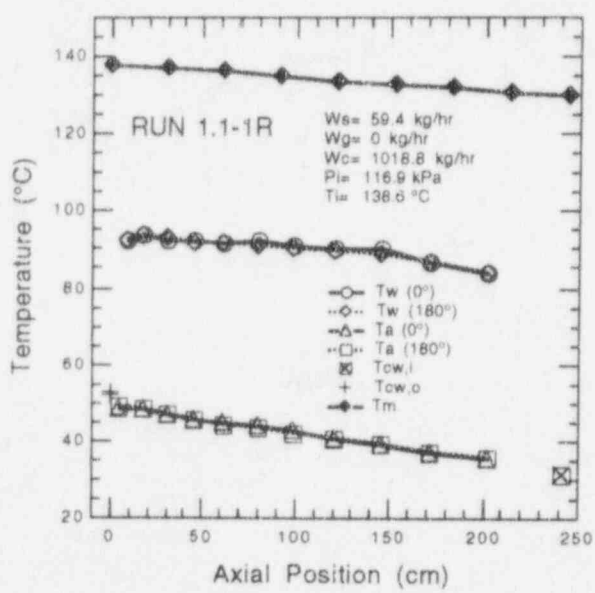

Figure 4 Temperature Distribution versus Axial Location for RUN 1.1-1R

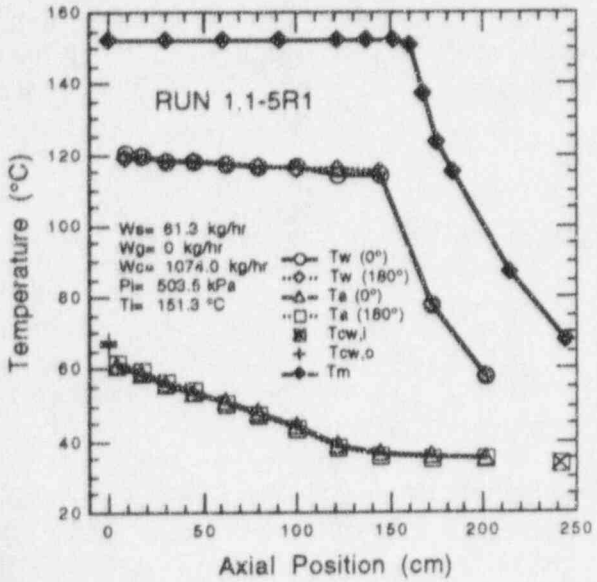

Figure 5 Temperature Distribution versus Axial Location for RUN 1.1-5R1

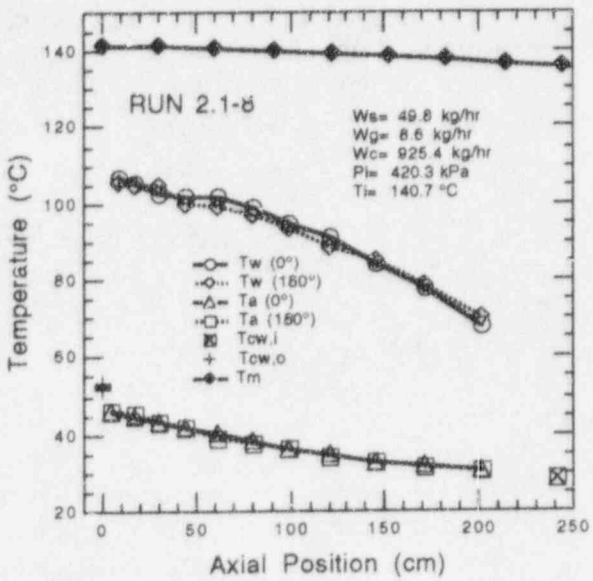

Figure 6a Temperature Distribution versus Axial Location for RUN 2.1-8

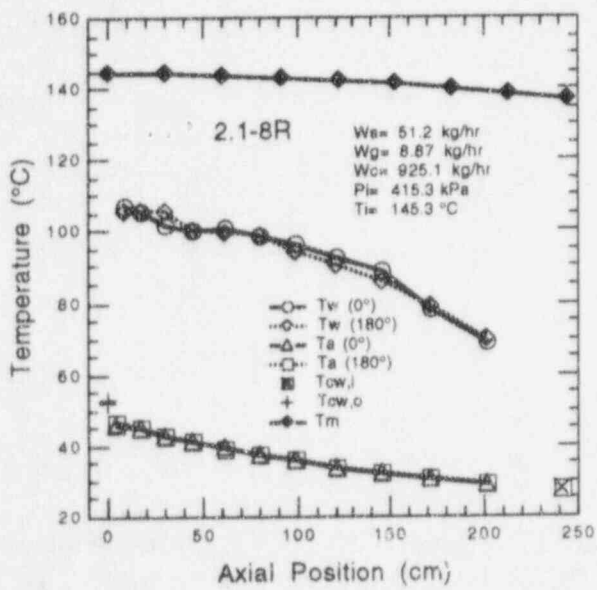

Figure 6b Temperature Distribution versus Axial Location for RUN 2.1-8R

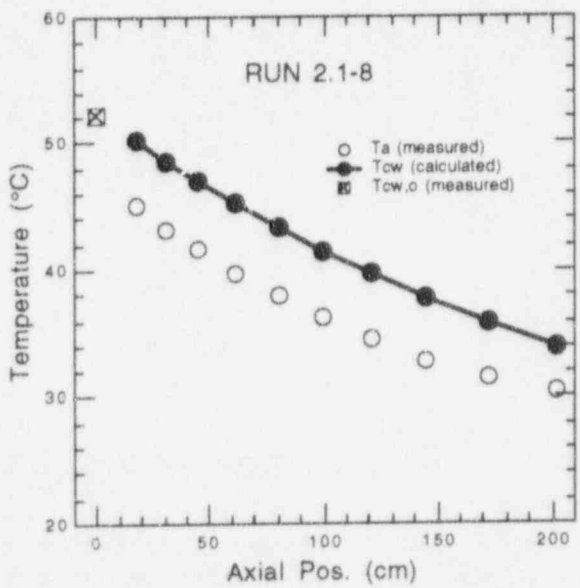

Figure 7 Determination of Cooling Water Bulk Temperature for RUN 2.1-8

Correlation of Data in Terms of Degradation Factor

The degradation factor was defined in the introduction. In the Vierow-Schrock correlation the degradation factor was not dependent upon the condensate flowrate. In the new correlation we have modified the shear enhancement factor, f_1, to include dependence on condensate flowrate. It is proposed that

$$f_1 = f_{1shear} \times f_{1other} \tag{7}$$

where $f_{1shear} = \delta_1/\delta_2$ represents the first order effect of interfacial shear obtained from the simple hydrodynamic theory while f_{1other} accounts for deviations from the simple theory (waves and other things) and is presumed to depend upon the condensate flowrate or the corresponding Reynolds number

$$Re_f = \frac{\Gamma}{\mu_f} \tag{8}$$

The factors f_1 and f_{1shear} were calculated from the experimental data for pure steam (note that $f_{exp} = f_1$ for the pure steam case, i.e., $f_2 = 1$) and f_{1other} was calculated from equation 7. The results were plotted against Re_f in Figure 8 to obtain the correlation

$$f_{1other} = 1 + 7.32 \times 10^{-4} Re_f \tag{9}$$

Correlation of the steam-gas data was then accomplished by plotting each data set (air and helium) in the form $(1 - f_{exp}/f_1)$ vs M_a. Piecewise fits were obtained as follows,

Steam - Air :

$$\begin{aligned} f_1 &= f_{1shear}(1 + 7.32 \times 10^{-4} Re_f) \\ f_2 &= (1 - 2.601 M_a^{0.708}) \quad \text{for} \quad M_a < 0.1 \\ f_2 &= (1 - M_a^{0.292}) \quad \text{for} \quad M_a > 0.1 \end{aligned} \tag{10}$$

Steam-Helium :

$$\begin{aligned} f_1 &= f_{1shear}(1 + 7.32 \times 10^{-4} Re_f) \\ f_2 &= (1 - 35.81 M_{He}^{1.074}) \quad \text{for} \quad 0.003 < M_{He} < 0.01 \\ f_2 &= (1 - 2.09 M_{He}^{0.457}) \quad \text{for} \quad 0.01 < M_{He} < 0.1 \\ f_2 &= (1 - M_{He}^{0.137}) \quad \text{for} \quad M_{He} > 0.1 \end{aligned} \tag{11}$$

Figure 9 shows the comparison of f_{exp} with the value of f obtained from the experimental parameters δ_1, δ_2, Re_f and M_a for steam-air mixtures. The standard deviation for this correlation is 0.176. A similar comparison for helium is shown in Figure 10 and the standard deviation for this correlation is 0.1297. These results represent a significant improvement over the Vierow - Schrock and Ogg correlations.

The experimental error analysis for the reduced data was performed by using the standard error propagation methods in Ref. [30]. The key uncertainties for typical experiment conditions were assessed to be the following [25] :

Heat Flux	10.4 %
Experimental Heat Transfer Coefficient	18.7 %
Reference Heat Transfer Coefficient	3.4 %
Degradation Factor	19.0 %

The new correlations were found to represent well the experimental data of Vierow [1] and Siddique [4] as well as the pure steam data of Goodykoontz [27]. The Vierow -Schrock correlation was found to considerably overpredict the f_1 factor when applied for Re_g beyond the range of Vierow's data base and at the higher range included in the new data base. These and other comparisons are discussed in greater detail in reference [25].

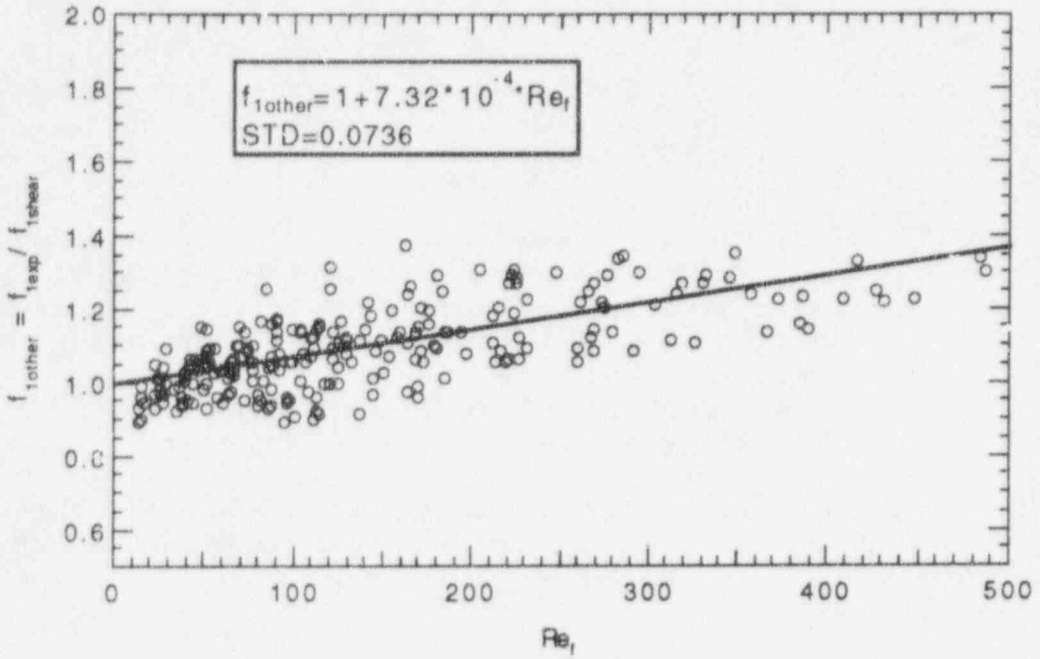

Figure 8 Plot of f_{1other} versus Film Reynolds Number for the Pure Steam Data

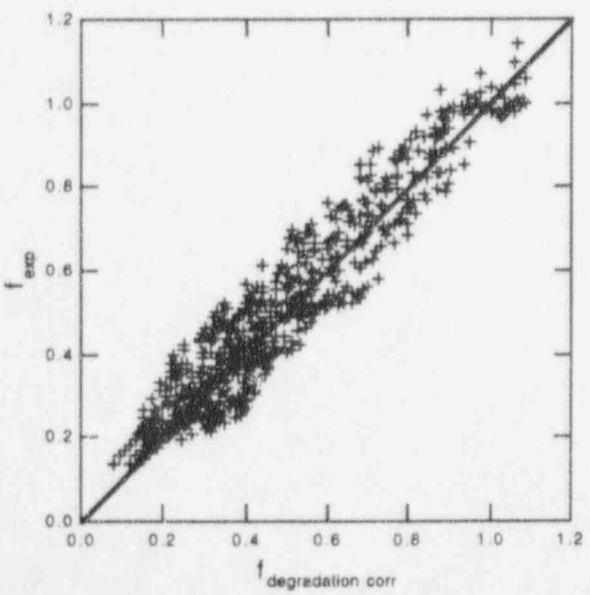

Figure 9 Comparison of Heat Transfer Coefficient for Steam/Air Mixture

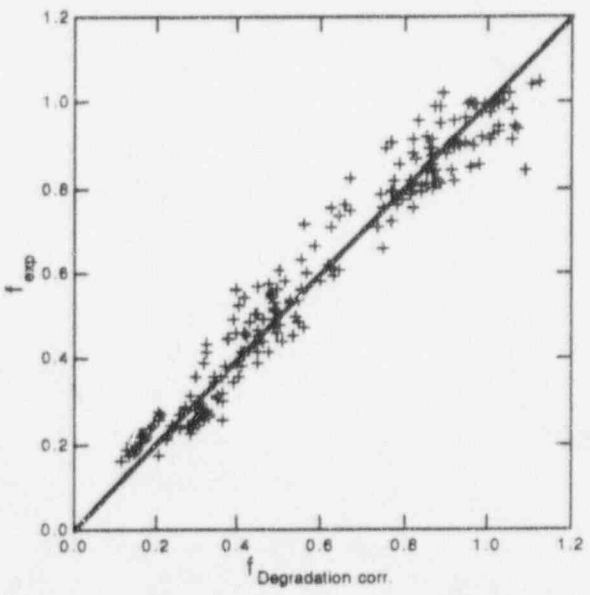

Figure 10 Comparison of Heat Transfer Coefficient for Steam/He Mixture

Correlation Based on Diffusion Layer Modeling with Blowing

The method of Peterson et al. has been modified and applied to the present data base. In this method the total wall heat flux (and overall heat transfer coefficient) may be written in terms of several contributing or component coefficients as

$$q_i'' = h_t\left(T_b^s - T_{wi}\right) = \frac{T_b^s - T_{wi}}{\dfrac{1}{h_c + h_s\left(\dfrac{T_b - T_i^s}{T_b^s - T_i^s}\right)} + \dfrac{1}{h_f}} \tag{12}$$

where h_t is the experimentally measured quantity

h_c is the condensing heat transfer coefficient between the bulk gas vapor saturation and interface temperatures

h_s is the sensible heat transfer coefficient between the bulk steam-gas and interface temperatures

h_f is the liquid film heat transfer coefficient between the interface and the tube inside surface temperatures

The equivalent thermal resistance circuit is shown in Figure 11. The component correlations are represented by correlations for turbulent convection without blowing recommended by Kays and Crawford [23]

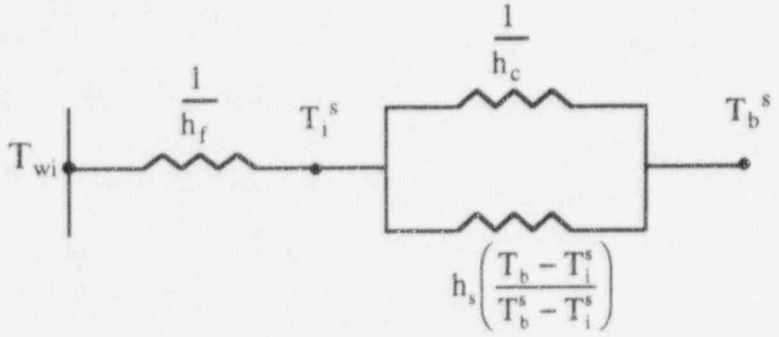

Figure 11 Equivalent Heat Transfer Resistance Circuit

$$Sh = 0.021 Re^{0.8} Sc^{0.5} \tag{13}$$

$$Nu = 0.021 Re^{0.8} Pr^{0.5} \tag{14}$$

or

$$h_c = 0.021 (k_c / d) Re^{0.8} Sc^{0.5} \tag{13a}$$

$$h_s = 0.021 (k_m / d) Re^{0.8} Pr^{0.5} \tag{14a}$$

where

$$k_c = -\frac{\ln\left[X_{gb}/X_{gi}\right]}{\ln\left[\left(1-X_{gb}\right)/\left(1-X_{gi}\right)\right]}\left(\frac{h_{fg}^2 p_t M_v^2 D}{R^2 T_{ave}^3}\right)$$

as derived by Peterson et al. [6]. The combined coefficient representing condensation and sensible heat transfer to the interface can then be written as

$$h_{gv} = h_c + h_s\left(\frac{T_b - T_i^s}{T_b^s - T_i^s}\right) \tag{15}$$

Substituting Eqs 13a and 14a into Eq. 15, h_{gv} becomes

$$\begin{aligned} h_{gv} &= 0.021\left[(k_c / d)Re^{0.8}Sc^{0.5} + (k_m / d)Re^{0.8}Pr^{0.5}\left(\frac{T_b - T_i^s}{T_b^s - T_i^s}\right)\right] \\ &= \left[k_c\left(T_b^s - T_i^s\right) + \left(\frac{Pr}{Sc}\right)^{0.5} k_m\left(T_b - T_i^s\right)\right] \times \frac{0.021\,Re^{0.8}Sc^{0.5}}{(T_b^s - T_i^s)d} \end{aligned} \tag{15a}$$

The effective Nusselt number for heat transfer to the interface is then defined as

$$Nu_{gv} = \frac{q_i'' d}{k_c\left(T_b^s - T_i^s\right) + \left(\frac{Pr}{Sc}\right)^{0.5} k_m\left(T_b - T_i^s\right)} \tag{16}$$

All the quantities appearing in Eq. 16 are obtained from the experimental data with the exception of the bulk temperature T_b and the interface temperature T_i^s. The measured centerline temperature was chosen as a reasonable approximation to T_b. After selecting a particular liquid film heat transfer model, T_i^s can be evaluated from the experimental data. The method of Blangetti [28] was adopted for the present model . In their model, the local Nusselt number Nu_z is written as

$$Nu_z = \frac{h_f L}{k_f} = \left(Nu_{z,la}^4 + Nu_{z,tu}^4\right)^{1/4} \tag{17}$$

The laminar Nusselt number $Nu_{z,la}$ is given by

$$Nu_{z,la} = \frac{L}{\delta_2} \quad \text{and} \quad L = \left(\frac{\nu_f^2}{g}\right)^{1/3} \text{ (characteristic length)} \tag{18a}$$

The turbulent Nusselt number $Nu_{z,tu}$ is given by

$$Nu_{z,tu} = a\,Re_f^b\,Pr^c\left(1 + e\,\tau_g^{*f}\right) \tag{18b}$$

where the coefficients a, b, c, e, f take on different values depending upon the range of the dimensionless interfacial shear [28].

Heat and mass transfer coefficients are lumped parameters characterizing the temperature and composition profiles. Equations 13 and 14 do not account for the influence of blowing (suction) effect on the enhancement of heat and mass transfer. Therefore it is now proposed that this effect be accounted for by correlating the experimental data in the form

$$\frac{Nu_{gv}}{0.021\,Re^{0.8}Sc^{0.5}} = \text{function to account for suction effect} \tag{19}$$

The effect of suction is often represented in terms of the "blowing parameter" which is defined as

$$\beta_m = \frac{m''}{g_m^*} = \frac{m''}{\rho u_\infty St_m^*} \quad \text{and} \quad g_m^* = \rho u_\infty St_m^* \tag{20}$$

Figure 12 shows the steam-air data plotted against β_m with a fit to the data represented by

$$\frac{Nu_{gv}}{0.021\,Re^{0.8}Sc^{0.5}} = 1 + 0.046\left(-\beta_m\right)^{2.48} \tag{21}$$

with a standard deviation of 13.1 % . Similar fitting of the steam-helium data as shown in Figure 13 gave

$$\frac{Nu_{gv}}{0.021\,Re^{0.8}\,Sc^{0.5}} = 1 + 0.126(-\beta_m)^{2.49} \qquad (22)$$

with a standard deviation of 11.8 %. These correlations were then combined with the liquid film heat transfer coefficients (equation 17) to calculate the total heat transfer coefficient h_t as illustrated in Figure 11. The overall agreement between the total heat transfer coefficients experimental determined and calculated using eqs. 17, 21, 22 is excellent with a standard deviation of 8.41 % for steam-air mixture and 6.07 % for steam-he mixture. Note that at low blowing parameters most of the data cluster around 1 and no adjustable constants are required for the correlation.

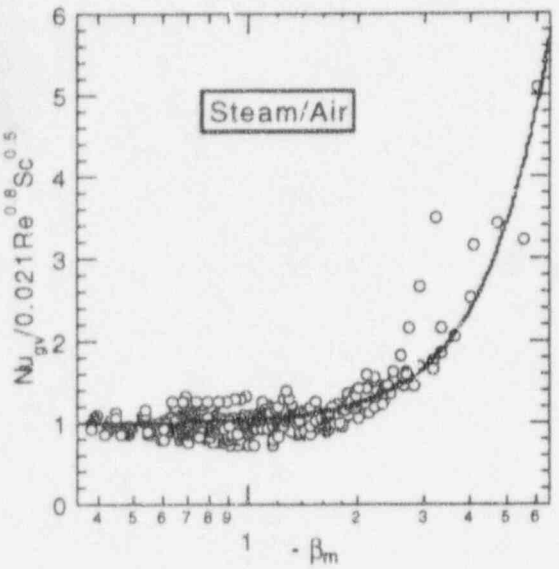

Figure 12 Ratio of Nu Versus Blowing Parameter for Steam/Air Mixture

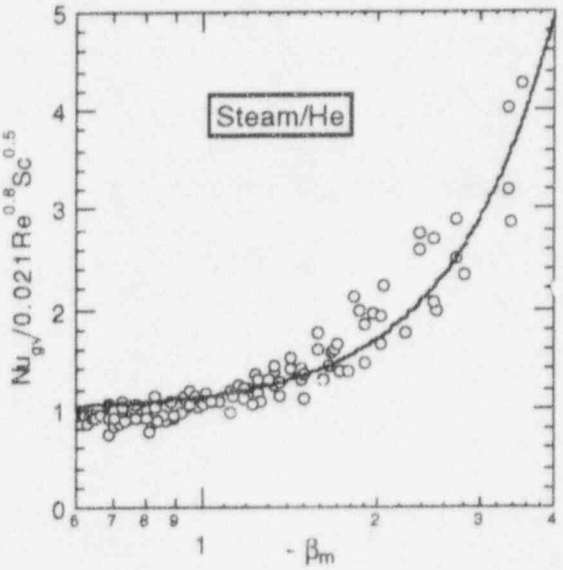

Figure 13 Ratio of Nu Versus Blowing Parameter for Steam/He Mixture

Correlation based on Mass Transfer Analysis

In this section we present an alternative approach to the diffusion layer modeling in which the condensation mass flux is represented in terms of mass transfer relations. This avoids the assumptions inherent in the "condensation thermal conductivity" and permits the use of the classical approach to analysis of mass transfer with blowing. Standard formulation for mass transfer is used following Kays and Crawford [23] and Mills [24]. In a general situation the local total mass flux due to convection and diffusion is

$$n_v = m_v n + j_v \qquad (23)$$

Since the condensation interface is impermeable to the gas, it has zero mass flux there in which case $n_i = n_{v,i} + n_{g,i} = n_{v,i} = m''$. Thus Eq. 23 becomes

$$m'' = m_{v,i} m'' + j_{v,i} \qquad (24)$$

The mass transfer conductance g_m is defined as

$$g_m = \frac{j_{v,i}}{m_{v,i} - m_{v,b}} \tag{25}$$

where $m_{v,b}$ is the mass concentration of water vapor in the bulk. Combining Eqs. 24 and 25 gives

$$m'' = g_m \frac{m_{v,b} - m_{v,i}}{m_{v,i} - 1} = g_m B_{md} \tag{26}$$

where $B_{md} = \frac{m_{v,b} - m_{v,i}}{m_{v,i} - 1}$ is the mass transfer driving force. The Couette flow model for transpiration (suction or blowing) at the surface of a flat plate ([23, 24]) leads to the predicted mass flux as

$$m'' = \frac{\rho D}{\delta} \frac{\ln(1 + B_{md})}{B_{md}} B_{md} \tag{27}$$

which combined with Eq. 26 gives

$$g_m = \frac{\rho D}{\delta} \frac{\ln(1 + B_{md})}{B_{md}} \tag{28}$$

In the limit of zero mass transfer this has been shown to be

$$\lim_{B_{md} \to 0} g_m = \frac{\rho D}{\delta} = g_m^* \tag{29}$$

and the mass flux becomes

$$m'' = g_m^* \frac{\ln(1 + B_{md})}{B_{md}} B_{md} = g_m^* \left(\frac{g_m}{g_m^*} \right) B_{md} \qquad \& \qquad \frac{g_m}{g_m^*} = \frac{\ln(1 + B_{md})}{B_{md}} \tag{30}$$

The "blowing parameter" is defined as

$$\beta_m = \frac{m''}{g_m^*} = \frac{m''}{\rho u_\infty St_m^*} \quad \text{and} \quad g_m^* = \rho u_\infty St_m^* \tag{31}$$

It can be used to replace the mass transfer driving force leading to

$$m'' = g_m^* \frac{\beta_m}{\exp(\beta_m) - 1} B_{md} = g_m^* \frac{g_m}{g_m^*} B_{md} \qquad \& \qquad \frac{g_m}{g_m^*} = \frac{\beta_m}{\exp(\beta_m) - 1} \tag{32}$$

The Couette flow model does not apply directly to the problem of condensation inside tubes. Instead we obtain an empirical correlation for g_m/g_m^* from our experimental data. The mass transfer Stanton number without transpiration can be written for the present problem as

$$St_m^* = \frac{Sh}{Re\, Sc} = \frac{0.021\, Re^{0.8}\, Sc^{0.5}}{Re\, Sc} = 0.021\, Re^{-0.2}\, Sc^{-0.5} \tag{33}$$

and therefore

$$g_m^* = \rho u_b \times 0.021\, Re^{-0.2}\, Sc^{-0.5} \tag{34}$$

and

$$\beta_m = \frac{m''}{\rho u_b \times 0.021\, Re^{-0.2}\, Sc^{-0.5}} \tag{35}$$

where the axial bulk velocity u_b has been substituted for the free stream velocity u_∞ in Eq. 31 of the Couette flow problem. The vapor mass flux at the interface is then given by

$$m'' = g_m^* \left(\frac{g_m}{g_m^*}\right) B_{md} = \left(\frac{g_m}{g_m^*}\right) \rho u_b \times 0.021\, Re_m^{-0.2}\, Sc^{-0.5} \left(\frac{m_{v,b} - m_{v,i}}{m_{v,i} - 1}\right) \tag{36}$$

As in the data processing for the diffusion layer model based correlation, the Blangetti liquid film model, Eqs 17 and 18, is employed here to obtain the interface temperature. The Couette flow theory was used as an initial guess to calculate the sensible heat transfer with transpiration. The vapor mass flux at the interface then becomes

$$m'' = \frac{q''_{wi} - \left(\frac{g_m}{g_m^*}\right)_{Couette} 0.021\, Re_m^{0.8}\, Pr^{0.5} \left(\frac{k_s}{d}\right)(T_b - T_i^s)}{h_{fg} + c_p(T_i^s - T_f)} \tag{37}$$

which combined with Eq. 36 leads to

$$\left(\frac{g_m}{g_m^*}\right) = \frac{m''}{g^* B_{md}} = \frac{q''_{wi} - \left(\frac{g_m}{g_m^*}\right)_{Couette} 0.021\, Re_m^{0.8}\, Pr^{0.5} \left(\frac{k_s}{d}\right)(T_b - T_i^s)}{\left(h_{fg} + c_p(T_i^s - T_f)\right) \times \rho u_b \times 0.021\, Re_m^{-0.2}\, Sc^{-0.5} \left(\frac{m_{v,b} - m_{v,i}}{m_{v,i} - 1}\right)} \tag{38}$$

The experimental data can then be used to determine the ratio g_m/g_m^*. The results, which are plotted against the blowing parameter in Figure 14 for steam-air and Figure 15 for steam-helium, were then correlated as

For air : $$\frac{g_m}{g_m^*} = 1 + 0.356(-\beta_m)^{1.43} \qquad \text{STD=8.67\%} \tag{39}$$

For helium : $$\frac{g_m}{g_m^*} = 1 + 0.484(-\beta_m)^{1.75} \qquad \text{STD=7.01 \%} \tag{40}$$

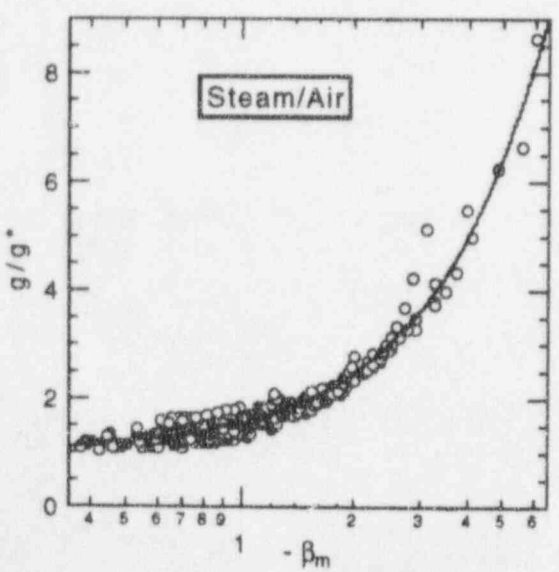

Figure 14 Ratio of Mass Transfer Conductance for Steam/Air Mixture

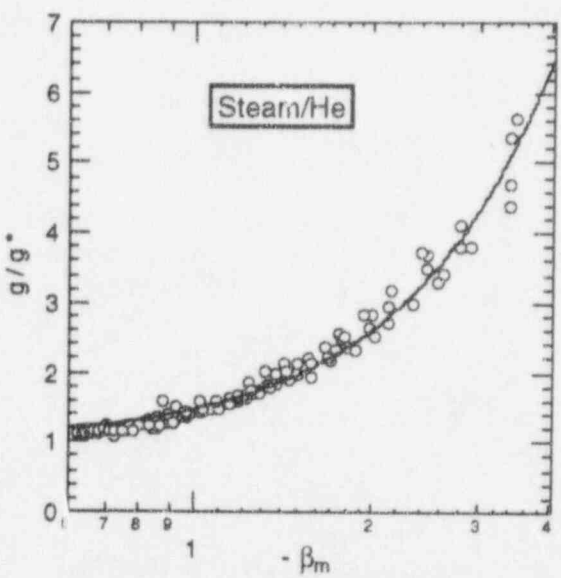

Figure 15 Ratio of Mass Transfer Conductance for Steam/He Mixture

To obtain the condensation heat transfer coefficient from these correlations we can write

$$m'' h_{fg} = g_m^* \left(\frac{g_m}{g_m^*} \right) B_{md} h_{fg} = h_c (T_b^s - T_i^s) \tag{41}$$

$$h_c = \frac{g_m^* \left(\frac{g_m}{g_m^*} \right) B_{md} h_{fg}}{(T_b^s - T_i^s)} \tag{42}$$

Equations 34, 39, 40 and 42 can then be used in an iterative process, starting with an initial guess of the interface temperature or steam mass concentration, to calculate the condensation heat transfer coefficient. The sensible heat transfer coefficient h_s with suction effect is taken to be

$$h_s = (g / g^*)\ 0.021 (k_m / d) Re^{0.8} Pr^{0.5} \tag{43}$$

and with the liquid film conductance given by the Blangetti method, all the conductances shown in Figure 11 are known from the correlations. By this method, the data parameters were then used to generate the correlation prediction of the total overall heat transfer coefficient h_t and the results are plotted against the experimental values for steam-air and steam-helium in Figures 16 and 17 respectively. The experimental data are seen to be represented with greater accuracy by this method with a standard deviation of 6.38 % for steam-air mixture and 3.24 % for steam-he mixture..

The Appendix to this paper presents a step by step procedure for implementing the method in a practical application. Reference [25] gives a similar detailed procedure for implementing the correlation based on diffusion layer modeling.

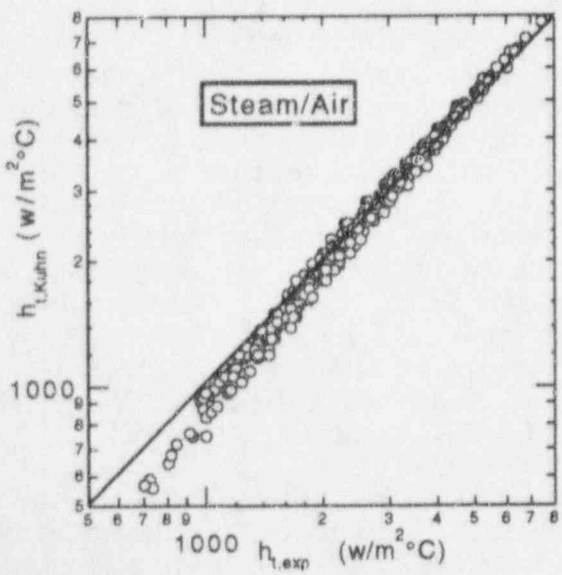

Figure 16 Comparison of Total Heat Transfer Coefficient for Steam/Air Mixture

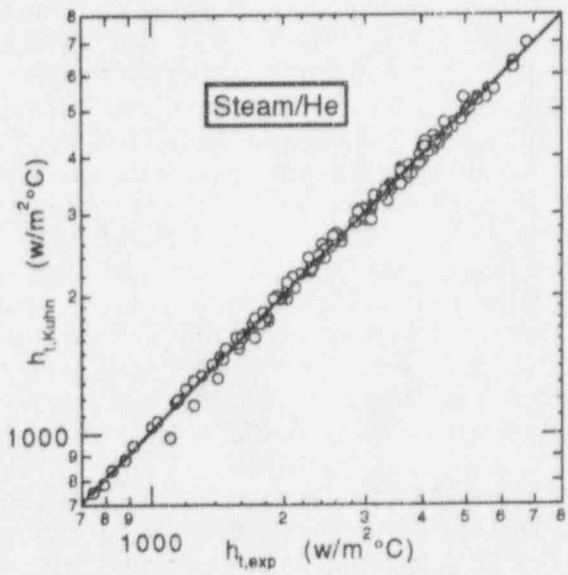

Figure 17 Comparison of Total Heat Transfer Coefficient for Steam/He Mixture

Summary and Concluding Remarks

The present experimental results constitute a highly comprehensive and accurate set of data for condensation of steam from mixtures (steam-air and steam-helium) flowing downward inside cooled vertical tubes. The stainless steel condenser tube used is of the same diameter as used in the PCCS condensers of the SBWR and the experimental conditions span the range of conditions expected for PCCS operation. The experimental design was the result of experience gained from previous experiments in our laboratory and others. Great care was taken to demonstrate the accuracy and consistency of temperature measurements and in fitting the bulk cooling water data to give accurate local wall heat fluxes. Many tests were repeated to demonstrate the level of reproducibility of the experimental data. Many pure steam tests were performed both to aid the correlation development and to compare the results with those of earlier experimenters.

Simple correlations were developed for each mixture case in a form similar to the Vierow-Schrock steam-air correlation which has been used in the TRAC-G code. In this method the degradation factor, defined as the ratio of the experimental heat transfer coefficient to a reference coefficient k/δ_l, is correlated in terms of the local gas phase mixture Reynolds number and gas mass fraction. Unlike the Vierow-Schrock correlation, the new form also includes a dependence upon the local liquid film Reynolds number. For pure steam, the two new correlations reduce to a single correlation which expresses the degradation factor ($f = f_l$) as a function of the gas phase Reynolds number. The pure steam data agree with the correlation with a standard deviation of 0.0736, the steam-air data agree with the new correlation with a standard deviation of 0.176 and the steam-helium data an correlation agree with a standard deviation of 0.130. These correlations do not distinguish between laminar and turbulent liquid film flow but the calculated Reynolds numbers indicate that in the preponderance of data within the data base the film flow is laminar. These correlations give good engineering accuracy and their simplicity makes them attractive for use in large computer codes such as TRAC-G. On the other hand the concept of degradation factor is not fully consistent with our understanding of the physical phenomena involved, i. e., it fails to represent the total resistance to condensation heat transfer as the sum of liquid and gas side resistances.

Two mechanistic correlation methods have been presented. The first is an improvement of the one proposed by Peterson et al. The second approach correlates the data to derive the empirical ratio of the mass transfer conductance with condensation suction effect to that without instead of implementing the analytical solution based on the mass transfer of Couette flow assumption on a flat plate. Both these approaches take account of the effect of transpiration (suction at the interface). Transpiration at the interface alters the structure of the turbulent boundary layer considerably, affecting the shear-stress distribution and the sublayer thickness as well as the temperature and concentration profiles which change the transfer coefficients. Prior to the present study, it had not been clear that detailed mechanistic models could produce correlations more accurate than the simple degradation factor method. This has now been demonstrated with the correlation from diffusion layer modeling giving standard deviations of the predicted overall heat transfer coefficient from the experimental data for steam-air of 0.084 and 0.061 for steam-helium. Using the mass transfer conductance approach, the comparable standard deviations are 0.064 for steam-air and 0.032 for steam helium.

In parallel with the experimental research, Yuann et al. have carried out numerical calculations based on the full set of conservation equations for the gaseous and liquid regions. Results of that work, including simulations of our experimental are reported in a companion paper [29]. The results show how dimensionless radial profiles of velocity, temperature and concentration evolve along the flow direction. Our mechanistic models used to correlate the data implicitly assume fully developed profiles locally (changes in the axial direction are still

possible). Further work is needed to fully assess the role and importance of the non uniform boundary condition inherent in the problem.

The present results indicate that the so-called temperature inversions, first noted in Vierow's natural circulation data, are not present for forced convection. The false effect in Ogg's data is explained as instrument error. We believe the same is true of Siddique's data. Our new data do not support the idea proposed by Hasanein et al. [20] that secondary side heat transfer characteristics can produce temperature inversions.

References

[1] K.M. Vierow, Behavior of Steam-Air Systems Condensing in Concurrent Vertical Downflow , MS Thesis, University of California at Berkeley (1990).

[2] D.G. Ogg, Vertical Downflow Condensation Heat Transfer in Gas-Steam Mixtures, MS Thesis, University of California at Berkeley (1991).

[3] T. Kageyama, Application of Diffusion Layer Theory to Vertical Downflow Condensation Heat Transfer, MS Thesis, University of California at Berkeley (1992).

[4] M. Siddique, The Effects of Noncondensable Gases on Steam Condensation under Forced Convection Conditions, PhD Dissertation, Massachusetts Institute of Technology (1992).

[5] K.M. Vierow and V.E. Schrock, Condensation in a Natural Circulation Loop With Noncondensable Gases Part I - Heat Transfer, Proc. Intl. Conf. on Multiphase Flows, Tsukuba, Japan, Sep. (1991), pp. 183-186.

[6] P.F. Peterson, V.E. Schrock, and T. Kageyama, Diffusion Layer Theory for Turbulent Vapor Condensation with Noncondensable Gases, ASME Journal of Heat Transfer, Vol. 115 (1993), pp. 998-1003.

[7] W. Nusselt, Die Oberflachenkondensation des Waserdampfes., Z. VDI, Vol. 60 (1916), pp. 541/546, 569/575.

[8] D.F. Othmer, The Condensation of Steam, Industrial and Engineering Chemistry, Vol. 21 (1929), No. 6, pp. 577-583.

[9] W.M. Rohsenow and J.P. Hartnett, Handbook of Heat Transfer, McGraw-Hill (1973).

[10] E.M. Sparrow and S.H. Lin, Condensation Heat Transfer in the Presence of noncondensable gas, J. Heat Transfer C86 (1964), pp. 430-486.

[11] W.J. Minkowycz and E.M. Sparrow, Condensation Heat Transfer in the Presence of Noncondensables, Interfacial Resistance, Superheating, Variable Properties, and Diffusion, Int. J. Heat Mass Transfer, Vol. 9 (1966), pp. 1125-1144.

[12] J.W. Rose, Condensation of a Vapor in the Presence of Noncondensing Gas, Int. J. Heat Mass Transfer, Vol. 12 (1969), p. 233.

[13] W.M. Rohsenow, J.H. Weber, and A.T. Ling, Effect of Vapor Velocity on Laminar and Turbulent Film Condensation, Trans. ASME, Vol.78 (1956), pp. 1637/1643.

[14] B.E. Denny, A.F. Mills, and V.J. Jusionis, Laminar Film Condensation From Steam-Air Mixture Undergoing Forced Flow Down a Vertical Surface, J. Heat Transfer Vol. 93 (1971), pp. 297.

[15] H.A. Uchida and Y. Togo, Evaluation of Post-incident Cooling Systems of Light-Water Power Reactors, Proc. from Int. Conf. on the Peaceful Uses of Atomic Energy, 3rd Conference, Geneva, Switzerland , Vol. 13 (1964), pp. 93-103.

[16] J.W. Rose, Approximate Equations for Forced-Convection Condensation in the Presence of a Non-condensing Gas on a Flat Plate and Horizontal Tube, Int. J. Heat Mass Transfer, Vol. 23 (1980), pp. 539-546.

[17] E.M. Sparrow, W.J. Minkowycz, and M. Saddy, Forced Convection Condensation in the Presence of Noncondensables and Interfacial Resistance, Int. J. Heat Mass Transfer, Vol. 10 (1967), pp. 1829-1845.

[18] A. Acrivos, Mass Transfer in Laminar-Boundary-Layer Flows with Finite Interfacial Velocities, AIChE Journal, Vol. 6 (1960), pp. 410-414.

[19] C.Y. Wang and C.J. Tu, Effects of Non-condensable Gas on Laminar Film Condensation in a Vertical Tube, Int. J. Heat Mass Transfer, Vol. 31 (1988), pp. 2239-2345.
[20] Hasanein, M. Golay, and M. Kazimi, The Effect of Cooling Water Conditions on in-Tube Condensation in the Presence of Noncondensables, Paper at ANS Winter Meeting (1993).
[21] Karl Stephan, Heat Transfer in Condensation and Boiling, Springer-Verlag Berlin Heidelberg (1992).
[22] M.H. Kim and M.L. Corradini, Modeling of Condensation Heat Transfer in a Reactor Containment, Nuclear Engineering and Design, Vol. 118 (1990).
[23] W.M. Kays, and M.E. Crawford, Convective Heat and Mass Transfer, Third Edition, McGraw-Hill, Inc.(1993), Chapter 14.
[24] A.F. Mills, Mass Transfer, Textbook in Draft (1994)
[25] S.Z.Kuhn, V.E. Schrock, and P.F. Peterson, Final Report on U. C. Berkeley Single Tube Condensation Studies , UCB-NE-4201, Rev.2, August (1994).
[25] R.B. Bird, W.E. Stewart and E.N. Lightfoot, Transport Phenomena, John Wiley & Sons, Inc. (1960).
[27] J.H. Goodykoontz and D.G. Dorsch, Local Heat-Transfer Coefficients for Condensation of Steam in Vertical Downflow Within a 5/8 Inch Diameter Tube, NASA TN D-3326 (1966).
[28] F. Blangetti, R. Krebs, and E.U. Schlunder, Condensation in Vertical Tubes - Experimental Results and Modeling, Chemical Engineering Fundamentals, Vol. 1/No. 2 (1982), ISSN 0723-0966, p20-63.
[29] R.Y. Yuann, V.E. Schrock and X.M. Chen, Numerical Modeling of Condensation from Vapor-Gas Mixtures for the Forced Downflow Inside a Tube, Proc. 7th Int'l Conf. on Nucl. Reactor Thermal Hydraulics, Saratogh Springs, NY., Sep. (1995).
[30] N.C. Barford, Experimental Measurements: Precision, Error and Truth, Second Edition, John Wiley and Sons, New York (1985).

Acknowledgment

The authors wish to acknowledge the contributions to the research made by Chen, X. M., Kageyama, T., Liu, J. C., Ogg, D., Vierow, K. M., and Yuann, R. Y.. Financial support for the research was provided by G. E. Nuclear Energy as part of the USDOE-EPRI-GE SBWR Project.

NOMENCLATURE

B_{md}	mass transfer driving potential
c	molar density
c_p	constant pressure specific heat
$c_{p,l}$	constant pressure specific heat of liquid
d_i	inside tube diameter
D	diffusion coefficient
f	degradation factor, friction factor
F	temperature profile shape factor
f_1	correlation factor for pure steam
f_2	correlation factor for noncondensable gas
f_{1shear}	f_1 subfactor due to interfacial shear stress
f_{1other}	f_1 subfactor due to other effects
g_m	mass transfer conductance
g_m^*	mass transfer conductance without suction
h	heat transfer coefficient
h_{fg}	latent heat of vaporization
h_{fg}'	pseudo heat of vaporization (= h_{fg} + 3/8 $c_p \Delta T$)
j	diffusive mass flux

k	thermal conductivity
M	molecular weight
M_a	air mass fraction
M_{He}	helium mass fraction
m	mass concentration
m"	mass flux
Nu	Nusselt number
n	mass flux
p	absolute pressure
q"	heat flux
R	universal gas constant
Pr	Prandtl number
Re	Reynolds number (refer to the text for specific definition when used)
Sc	Schmidt number
Sh	Sherwood number, $h_c d/k_c$
St_m	mass transfer Stanton number
STD	Standard deviation
T	absolute temperature
$\tilde{v}$	molar average velocity
V	velocity
W	mass flow rate
X	mole fraction
x	axial position
z	axial coordinate

Greek

β_m	blowing parameter for the mass transfer
δ	thickness
δ_1	film thickness without interfacial shear stress
δ_2	film thickness with interfacial shear stress
ϕ	gas/vapor log mean concentration ratio
Γ	mass flow per unit circumference
μ	dynamic viscosity
ρ	density
τ	shear stress

Subscripts

a	adiabatic and air
b	bulk
c	condensation
cw	cooling water
exp	experimental value
f	condensate
g	noncondensable gas species and acceleration due to gravity
gv	gas/vapor
i	liquid/vapor interface and inner wall of condenser tube
io	interfacial condition without suction effect
m	mixture and mass transfer
s	sensible heat
t	total
tu	turbulent

v vapor species
wi inner tube wall
wo outer tube wall

Superscripts
s saturation
* dimensionless form and condition without transpiration

Appendix Step by Step Procedure for Implementing Use of the Mass Transfer Based Correlation

The following section describes how to apply the correlations developed based on the diffusion layer modeling from Eq.39 to Eq. 43, to predict the local total heat fluxes in vertical tubes with noncondensable gases. The tube is divided into axial control volumes of size Δz_j and center position z_j. With the steam/gas inlet conditions and an initial approximation of the boundary condition (heat flux q") in the first control volume Δz_1, the calculation can be started from the beginning. The calculation procedure at each axial location z_j of the tube is comprised of 10 steps.

Step 1 - From the known total mass flow rate W_t and noncondensable gas flow rate W_g evaluate the local mass flow rate of condensate W_f, the local mass flow rate of the vapor/gas mixture W_m, and the local gas bulk mass fraction $m_{v,b}$.

$$W_f(z_j) = W_f(z_{j-1}) + \frac{q''(z_j)A(z_j)}{h_{fg}}$$

$$W_m(z_j) = W_t - W_f(z_j)$$

$$m_{v,b} = \frac{W_m(z_j) - W_g}{W_m(z_j)}$$

where $W_f(0) = 0$ and $A(z_j) = \pi d(\Delta z_{j-1} + \Delta z_j)/2$

Step 2 - Assume a local interface temperature T_i^s, its corresponding gas mole fraction gas, and condensation mass flux. As an initial guess for X_{gi} either the bulk gas mole fraction, or an interface value calculated immediately upstream, may be used. For condensation mass flux, the upstream value can be used as an initial guess. Evaluate the local mixture transport properties ρ_m, μ_m, D, k_m, and c_p, using an appropriate gas mixture model and tabular data or analytic expressions, at the arithmetic mean of the interface and bulk temperatures and gas concentrations.

Step 3 - Calculate the local steam/gas mixture Reynolds number Re_m and film Reynolds number Re_f,

$$Re_m(z_j) = \frac{4W_m(z_j)}{\pi d\mu_m} \qquad Re_f(z_j) = \frac{W_f(z_j)}{\pi d\mu_f}$$

Step 4 - Calculate the condensate film heat transfer coefficient h_f using the method proposed by Blangetti [28]. Also calculate the pipe wall resistance and secondary-side heat transfer coefficient.

Step 5 - Calculate the blowing parameter

$$\beta_m = \frac{m''}{\rho_m u_m \times 0.021\, Re_m^{-0.2}\, Sc^{-0.5}} \qquad \text{where} \quad u_m = \frac{W_m(z_j)}{\rho_m A_f(z_j)}$$

Step 6 - Calculate the ratio of mass transfer conductance and mass transfer driving force.

For air : $$\frac{g_m}{g_m^*} = 1 + 0.556(-\beta_m)^{1.43}$$

For helium $$\frac{g_m}{g_m^*} = 1 + 0.484(-\beta_m)^{1.75}$$

where $$B_{md} = \left(\frac{m_{v,b} - m_{v,i}}{m_{v,i} - 1} \right)$$

Step 7 - Calculate the condensation and sensible heat transfer coefficients,

$$h_c = \frac{g_m^* \left(\frac{g_m}{g_m^*} \right) B_{md} h_{fg}}{(T_b^s - T_i^s)} \qquad h_s = (g / g^*)\, 0.021 (k_m / d) Re^{0.8} Pr^{0.5}$$

Step 9 - Calculate the local heat flux based on the cooling medium temperature T_∞ and the bulk vapor saturation temperature, T_b^s.

$$q_t'' = \frac{T_b^s - T_\infty}{\frac{1}{h_c + h_s \left(\frac{T_b - T_i^s}{T_b^s - T_i^s} \right)} + \frac{1}{h_f} + \frac{1}{h_w}}$$

where h_w is the series combination of the condensate wall and secondary side heat transfer coefficients.

Step 10 - Calculate the interface temperature,

$$T_i^s = T_b^s - \frac{q_t''}{h_c + h_s \left(\frac{T_b - T_i^s}{T_b^s - T_i^s} \right)}$$

the interface gas mole fraction, and condensation mass flux

$$X_{gi} = 1 - \frac{P_i^s(T_i)}{P_t} \qquad m'' = \frac{q_c''}{h_{fg}} = \frac{h_c (T_b^s - T_i^s)}{h_{fg}}$$

and compare with the values assumed in Step 2. If different, iterate again through Steps 2 through 10 until convergence to the correct interface gas concentration is reached within $\pm 10^{-3}$.

Study of Condensation Heat Transfer Following a Main Steam Line Break Inside Containment

by
J.H. Cho, F.A. Elia, Jr, and D.J. Lischer

Stone & Webster Engineering Corporation
Boston, Massachusetts

ABSTRACT

An alternative model for calculating condensation heat transfer following a main steam line break (MSLB) accident is proposed. The proposed model predictions and the current regulatory model predictions are compared to the results of the Carolinas Virginia Tube Reactor (CVTR) test. The very conservative results predicted by the current regulatory model result from: (1) low estimate of the condensation heat transfer coefficient by the Uchida correlation and (2) neglecting the convective contribution to the overall heat transfer. Neglecting the convection overestimates the mass of steam being condensed and does not permit the calculation of additional convective heat transfer resulting from superheated conditions. In this study, the Uchida correlation is used, but correction factors for the effects of convection and superheat are derived. The proposed model uses heat and mass transfer analogy methods to estimate the convective fraction of the total heat transfer and bases the steam removal rate on the condensation heat transfer portion only. The results predicted by the proposed model are shown to be conservative and more accurate than those predicted by the current regulatory model when compared with the results of the CVTR test. Results for typical pressurized water reactors indicate that the proposed model provides a basis for lowering the equipment qualification temperature envelope, particularly at later times following the accident.

INTRODUCTION

Design criteria for nuclear power plants require that safety-related equipment be qualified to environments that may be encountered during postulated accidents. Such accidents include loss of coolant accidents (LOCAs) and main steam line break accidents (MSLBs).

The harshest peak temperature condition generally results from a MSLB, since the steam generator blowdown is saturated or superheated steam that is superheated at containment conditions. The current regulatory model for determining the containment temperature following a MSLB is set forth in NUREG-0588 [1]. This model bases the mass and energy removal during condensation on the Uchida [2] condensing heat transfer correlation. It assumes that the driving potential is the atmosphere saturation-to-wall (heat sink surface) temperature difference. All condensate formed on the heat sinks is transferred directly to the sump. When the atmosphere is superheated, a maximum of 8% of the condensate may be revaporized for Category II plants (i.e., those which are licensed after May 23, 1980 and whose Construction Permit SER is dated before July 1, 1974). The basis of 8% revaporization assumption is not provided in NUREG-0588. However, experience indicates it is based on conservative NRC benchmark calculations for the CVTR test data. For Category I plants (all other plants licensed after May 23, 1980), no condensate is allowed to remain in the vapor region.

The temperature predicted by the current regulatory model is compared with actual test data from the CVTR tests [3] and is shown to be very conservative. In this study, a more accurate but still conservative alternative to the current regulatory model is proposed for analysis of containment pressure/temperature transients following the MSLBs.

MODEL DEVELOPMENT

Heat is transferred from the hot air/steam mixture to the cold wall by three mechanisms: convection, radiation, and condensation. The temperature difference between the bulk atmosphere and the cold wall provides the driving potential for energy exchange by convective and radiative heat transfer. In the proposed model, radiation heat transfer is neglected since emission from the gases is confined to a few discrete wavelengths and is typically small. If the cold wall surface temperature is equal to or below the dew point of the air/steam mixture (i.e., the vapor saturation temperature at its partial pressure), then the vapor will diffuse through the noncondensable gas component and condense on the cold wall.

After condensation starts, a liquid film develops on the wall. Between the liquid film and the bulk atmosphere, an air/steam boundary layer develops in which the gas properties change from their bulk values to those at the surface of the liquid film. The temperature at this interface with the liquid film is different from the wall surface temperature. This interface temperature is determined by the heat and mass transfer processes that fix the steam partial pressure and concentration (and therefore the temperature) at the condensate surface. In general, the interface temperature is difficult to determine either analytically or experimentally. Therefore, the usual practice in correlating data for condensation heat transfer in the presence of noncondensable gas is to use a single overall heat transfer coefficient ($h_{overall}$) as defined by:

$$q'' = h_{overall} (T_B - T_W) \tag{1}$$

This was done, for example, in the experiments at CVTR, as well as those of Tagami [4] and Uchida. Such an approach simply reflects the fact that the coefficient is primarily a measure of the resistance to mass transfer of the vapor through the air-rich boundary layer to the condensate surface.

Peterson et al.[5] derived an expression for the total heat flux analytically by eliminating the interface temperature:

$$q'' = \frac{h_{cond}(T_B^s - T_W) + h_{conv}(T_B - T_W)}{1 + \dfrac{h_{cond} + h_{conv}}{h_{film}}} \tag{2}$$

where h_{cond} is the condensing heat transfer coefficient, h_{conv} is the sensible convective heat transfer coefficient, and h_{film} is the condensate film heat transfer coefficient to the surface. Note that the driving potential for the condensing heat transfer coefficient depends on the bulk saturation temperature, as this saturation temperature gives the driving potential for mass transfer. The driving potential for sensible convective heat transfer depends on the actual bulk temperature, which allows for additional heat transfer for superheated vapor conditions.

Recent works in the literature [5,6,7] have successfully used heat and mass transfer analogy methods to predict "best estimate" heat transfer coefficients. In this paper, the Uchida correlation is used to represent the overall heat transfer coefficient, as required by the NRC, but the recent theoretical developments are used as an analytical basis for determining the convective heat transfer fraction.

Since Uchida did not provide a curve fit of his data, the Uchida data were correlated as a function of ratio of steam partial pressure (P_s) to total atmospheric pressure (P_t) as follows:

$$h_u = AP_s/(3.25P_t) : \ for\ 0.01 \le P_s/P_t \le 0.19 \quad (3)$$

or

$$h_u = Ae^{-3.5(1-P_s/P_t)} : \ for\ \ P_s/P_t > 0.19 \quad (4)$$

where:

h_u = Uchida condensing heat transfer coefficient (W/m^2-°C)
A = Heat transfer coefficient for pure steam (1704 W/m^2-°C, 300 Btu/hr-ft^2-°F)
P_s = Partial pressure of the steam (MPa)
P_t = Total pressure of containment atmosphere (MPa)

This correlation is in good agreement with the actual Uchida experiment data. The Uchida correlation was derived for natural convection driven condensation on vertical flat surfaces so it will underpredict condensation rates for forced convection conditions such as that provided by forced jets and by large scale recirculating flows in enclosures. However, it is interesting to note that Peterson [8] has shown that the Uchida correlation is not appropriate if the initial air partial pressure departs significantly from the one atmosphere value that resulted in the experiments when ambient air was mixed with steam at constant volume. According to recent theory, the correlation will overpredict the actual heat transfer coefficient when the initial air pressure is over one atmosphere and underpredict the coefficient when the initial air pressure is under one atmosphere. Overall, the correlation is considered conservative for use following MSLBs inside containment because of the omission of forced convection.

CONVECTIVE HEAT TRANSFER FRACTION

If f is defined as the convective fraction of overall heat transfer, the total heat flux can be written as

$$q'' = q''_{cond} + q''_{conv} = (1-f)q'' + fq'' \quad (5)$$

and the condensate mass removal rate ($\dot{m}_c$) associated with energy absorption by the heat sinks is given by

$$\dot{m}_c = \frac{(1-f)q''A}{i_B - i_l} \quad (6)$$

where A is the total heat sink surface area and (i_B - i_l) is the enthalpy difference between the bulk vapor state and the liquid film. The term $fq''A$ reflects the removal of sensible energy from the bulk atmosphere by convective heat transfer without the removal of mass. As the value of f increases, the bulk temperature decreases because less steam is condensed and the specific internal energy of the bulk atmosphere is reduced. Thus, the convective heat transfer fraction (f) has a direct influence on calculated bulk atmosphere temperature.

Corradini [6] and Kim and Corradini [7] developed explicit expressions for evaluating the convection and condensation heat transfer coefficients for forced and natural convection for turbulent vapor condensation on a cold wall in the presence of a noncondensable gas. The magnitude of these coefficients is found to be strongly sensitive to gas velocity and geometry of heat sink. However, the ratio of these coefficients is independent of the gas velocity and geometry as shown below.

Forced Convection

For forced convection, by combining the approaches of Corradini [6] and Kim and Corradini [7], we observe that:

$$h_{conv} = \frac{0.037 Re_L^{0.8} Pr k_g}{(0.85 + 0.01/Pr) L} \tag{7}$$

$$h_{cond} = \frac{g \dfrac{X_B - X_I}{1 - X_I} (i_B - i_I)}{(T_B^s - T_I)} \tag{8}$$

where mass transfer conductance (g) is expressed as

$$g = \frac{0.037 \rho_g u_g}{0.85 + 0.01/Sc} \left(\frac{\rho_g u_g L}{\mu_g} \right)^{-0.2} \tag{9}$$

From Eqs. (7), (8), and (9), the ratio of these coefficients is found to be:

$$\frac{h_{conv}}{h_{cond}} = \frac{k_g Pr}{\mu_g} \frac{(0.85 + 0.01/Sc)}{(0.85 + 0.01/Pr)} \frac{(1 - X_I)}{(X_B - X_I)} \frac{(T_B^s - T_I)}{(i_B - i_I)} \tag{10}$$

Using $(0.85 + 0.01/Sc)/(0.85 + 0.01/Pr) \approx 1$ and $Pr = \mu_g c_{pg}/k_g$, Eq.(10) can be simplified to:

$$\frac{h_{conv}}{h_{cond}} = c_{pg} \frac{(1 - X_I)}{(X_B - X_I)} \frac{(T_B^s - T_I)}{(i_B - i_I)} \tag{11}$$

Natural Convection

For natural convection, again combining the approaches of Refs. 6 and 7, we find that:

$$h_{conv} = \frac{k_g C_1 (Gr Pr)^{C_2}}{L} \tag{12}$$

$$h_{cond} = \frac{g \dfrac{X_B - X_I}{1 - X_I} (i_B - i_I)}{(T_B^s - T_I)} \tag{13}$$

where mass transfer conductance (g) is expressed as

$$g = \frac{\rho_g u_g C_1 (GrSc)^{C_2}}{ReSc} \tag{14}$$

From Eqs. (12), (13) and (14), the ratio of these coefficients is simplified as

$$\frac{h_{conv}}{h_{cond}} = \frac{k_g Sc}{\mu_g} \left(\frac{Pr}{Sc}\right)^{C_2} \frac{(1 - X_I)}{(X_B - X_I)} \frac{(T_B^s - T_I)}{(i_B - i_I)} \tag{15}$$

Eqs. (10) and (15) indicate that the ratio of heat transfer coefficients for natural convection will be identical to the ratio for forced convection if Pr equals Sc. In current day PWRs, forced convection is expected due to the flow induced by steam blowdown and containment sprays. Since the peak temperature occurs during steam blowdown, forced convection heat transfer is investigated in this study. However, since Pr and Sc are not significantly different in the vapor-air mixture, the ratio of heat transfer coefficients for natural convection is considered to be about same magnitude as the ratio for forced convection.

When the mass of vapor becomes a relatively large fraction of the total mass of the air/steam mixture, the rate of condensation will increase. When the mass transfer rate increases, the momentum, thermal and mass transfer boundary layers are reduced in thickness because of the suction effect of the condensation process. This reduction in the boundary layer thickness increases the temperature and concentration gradients near the wall. The heat and mass transfer coefficients increase due to the lower resistance presented by the thinner boundary layer. To consider this effect, the correction factor for high mass transfer rates should be applied to the heat and mass transfer coefficients [6,7]. However, since the correction factors applied to the two transfer processes are roughly equal, the ratio of heat transfer coefficients in Eqs. (10) and (15) remains unchanged.

From Eqs. (2), (5), and (11), the ratio of convective heat transfer to condensing heat transfer (Ψ) for forced convection can be derived:

$$\Psi = \frac{f}{1 - f} = \frac{h_{conv}(T_B - T_W)}{h_{cond}(T_B^s - T_W)} = c_{pg} \frac{(1 - X_I)}{(X_B - X_I)} \frac{(T_B^s - T_I)}{(i_B - i_I)} \frac{(T_B - T_W)}{(T_B^s - T_W)} \tag{16}$$

where c_{pg} is the specific heat of gas and X_I and X_B are steam mass fractions at the interface and the bulk, respectively. Thus, from Eq. (16), a convective fraction of overall heat transfer, f, can be calculated:

$$f = \frac{\Psi}{\Psi + 1} \tag{17}$$

The specific heat of steam/air mixture (c_{pg}) in the steam-air boundary layer can be approximated based on the average steam mass fraction (X_R):

$$c_{pg} = X_R c_{pv} + (1 - X_R) c_{pa} \tag{18}$$

$$X_R = \frac{X_I + X_B}{2} \tag{19}$$

where c_{pv} is the specific heat of the steam and c_{pa} is the specific heat of air.

CORRECTION FACTOR FOR SUPERHEAT EFFECT

The convective heat flux term can be separated into two parts:

$$h_{conv}(T_B - T_W) = h_{conv}\,(T_B^s - T_W) + h_{conv}(T_B - T_B^s) \tag{20}$$

Then, Eq. (2) can be rearranged:

$$q'' = \frac{(h_{cond} + h_{conv})(T_B^s - T_W)}{1 + \dfrac{h_{cond} + h_{conv}}{h_{film}}} \left[1 + \frac{h_{conv}(T_B - T_B^s)}{(h_{cond} + h_{conv})(T_B^s - T_W)} \right] \tag{21}$$

The overall heat transfer coefficient in Eq. (1), which can be measured experimentally, is in general composed of two heat transfer resistances: the first due to energy transfer through the liquid condensate and the second due to energy transfer in the air/steam mixture. For saturated conditions, Eqs. (1) and (2) can be combined, yielding:

$$\frac{1}{h_{tot,sat}} = \frac{1}{h_{film}} + \frac{1}{h_{cond} + h_{conv}} \tag{22}$$

where $h_{tot,sat}$ is the overall heat transfer coefficient measured under the saturated condition.

Substituting this expression into Eq. (21) we find that

$$q'' = h_{tot,sat}(T_B^s - T_W) \left[1 + \frac{h_{conv}}{h_{cond} + h_{conv}} \frac{(T_B - T_B^s)}{(T_B^s - T_W)} \right] \tag{23}$$

If we define α to be:

$$\alpha = \frac{h_{conv}}{h_{cond} + h_{conv}} \frac{(T_B - T_B^s)}{(T_B^s - T_W)} \tag{24}$$

Eq. (23) can be rewritten as:

$$q'' = h_{tot,sat}(T_B^s - T_W)\,[1 + \alpha] \tag{25}$$

When the bulk mixture is saturated (i.e., $T_B = T_B^s$), α becomes 0 and when the bulk mixture is superheated, the term $\alpha h_{tot,sat}(T_B^s - T_W)$ reflects the additional heat flux transferred from the superheated atmosphere to the heat sink surfaces. Thus, α is a correction factor which adjusts for superheated conditions. The Uchida experiments were performed with saturated bulk conditions and thus measured $h_{tot,sat}$. The factor in Eq. (25) then corrects from the saturated conditions of the Uchida experiments to superheated conditions.

Combining Eqs (21) and (24), a final expression for α is obtained:

$$\alpha = \frac{1}{\left[\dfrac{(X_B - X_I)(i_B - i_I)}{c_{pg}(1 - X_I)(T_B^s - T_I)} + 1\right]} \frac{T_B - T_B^s}{T_B^s - T_W} \tag{26}$$

PROPOSED MODEL

Applying Eqs. (6) and (25), the proposed condensation heat transfer model can be related with the current regulatory model as follows:

$$\frac{q''_{PROPOSED}}{q''_{NUREG-0588}} = 1 + \alpha \tag{27}$$

$$\frac{\dot{m}_{c,PROPOSED}}{\dot{m}_{c,NUREG-0588}} = (1 + \alpha) \times (1 - f) \tag{28}$$

Since the direct use of the Uchida correlation for heat transfer to building heat sinks is an established licensing procedure, the proposed model employs the Uchida correlation for the overall heat transfer coefficient ($h_{tot,sat}$). However, if better empirical heat transfer coefficients measured under the saturated conditions are available, the proposed model can simply employ the coefficients and calculate the heat and mass removal rates whether the bulk mixture is saturated or superheated.

DETERMINATION OF THE INTERFACE TEMPERATURE

To determine the values of the correction factors α and f, the variables X_I and i_I should be evaluated at the unknown interface temperature. The noncondensable air accumulates near the condensate surface resulting in a much larger air partial pressure and, consequently, low steam partial pressure in this region. As a result, the condensate outer surface temperature (T_I) corresponding to the steam saturation temperature at this point is lower than the bulk region saturation temperature (T_B^s). In fact, for

noncondensable mass fractions greater than 50%, the difference between the wall and interface temperature is typically less than 0.5°C (1°F)[9]. Therefore, for bulk air mass fractions above 50%, we assume that the interface temperature equals the wall temperature.

Sensitivity studies indicate that for given values of T_B,T_B^s, and T_w, as the interface temperature increases both f and α decrease, which would result in higher predicted peak temperatures. Therefore, if the air mass fraction is less than 50%, we conservatively approximate T_i using:

$$T_i = \left[\frac{X_B - 0.5}{0.5}\right] T_B^s + \left[1 - \left(\frac{X_B - 0.5}{0.5}\right)\right] T_W \; : \; for \; X_B > 0.5 \qquad (29)$$

since $T_i = T_B^s$ for a pure steam atmosphere.

It is important to note that in the proposed model, the interface temperature T_i affects only the calculations of α and f; it does not affect the driving potential. Because we are using the empirical Uchida heat transfer coefficient, which was based on the temperature difference between the bulk atmosphere and the wall, it is correct to use the wall temperature directly when calculating the driving potential. In the literature, however, where the heat transfer coefficient is calculated analytically based on the interface temperature, the driving potential must be based on T_i [5,6,7].

COMPARISON WITH EXPERIMENTAL DATA

The proposed condensation heat transfer model is tested by implementing the model in the Stone & Webster computer program, LOCTIC (Loss of Coolant Transient Inside Containment) [10]. The results of the program are then compared to available experimental data. The LOCTIC program calculates the transient atmosphere pressure and temperature response of a dry containment subjected to postulated accident conditions.

The Carolinas Virginia Tube Reactor (CVTR) test series are large scale integral containment experiments that were performed in the United States. The CVTR containment is a reinforced concrete cylindrical structure with a hemispherical dome. The operating floor is also reinforced concrete. The most reliable experimental method for measuring the heat transfer coefficient through the containment wall utilized two heat transfer plugs. Heat Plug #1 was located at the elevation of the operating floor and Heat Plug #2 was approximately 5.5 m higher than the operating floor. The steam from a nearby fossil power plant was injected through a diffuser into the operating region.

The principal inputs to the LOCTIC code for the CVTR benchmark calculations were specifications of the initial containment environmental conditions, the composition of the heat conducting structures, including material types, dimensions and heat transfer coefficients, and the blowdown mass rate, energy rate and duration.

In Figure 1, the temperature profiles predicted by the current regulatory model and by the proposed model are compared with the measured maximum temperature profile. The data from the experiments exhibited significant stratification in containment (i.e. the temperature difference from top to bottom elevations of containment was approximately 55°C (100°F)), but because LOCTIC models containment as a single volume it cannot calculate this effect. The CVTR temperature transient shown in the figure is from the region near the dome, where the temperatures are highest.

As shown on Figure 1, the regulatory model overpredicts the peak temperature by 53°C (96°F) for Category I plants and by 21°C (38°F) for Category II plants. There are two major reasons for these extremely conservative predictions: all the heat transfer is considered to be due to condensation and the Uchida correlation is too low for the containment conditions following a MSLB, since forced convection will be observed. As shown in Figure 2, the measured heat transfer coefficients are at least three to four

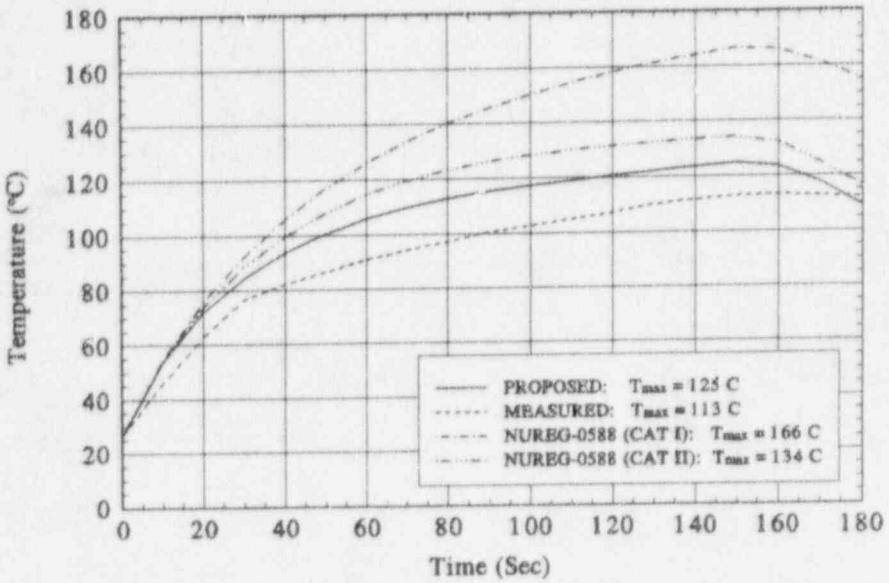

Figure 1: **Comparison of the calculated and measured temperature transients for the CVTR experiment.**

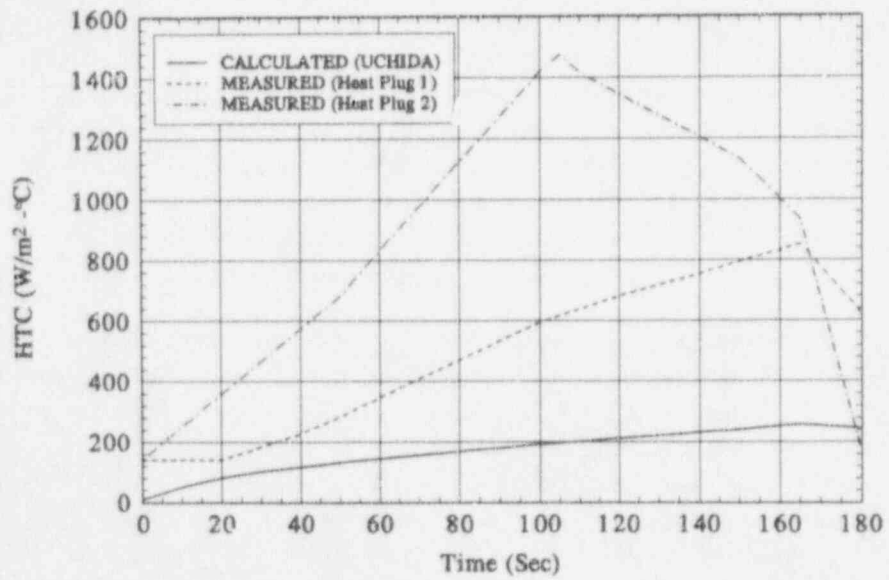

Figure 2: **Comparison of the calculated and measured overall heat transfer coefficients for the CVTR experiment.**

times higher than those that are predicted by the Uchida correlation.

By assuming only condensing heat transfer, the steam mass removal is overestimated because the amount of the heat transfer that is due to convection does not involve condensation. This excessive steam mass removal results in higher steam specific internal energy. As Figure 3 indicates, the proposed model predicts that the convective heat transfer fraction varies from 37% to 6% during the CVTR transient. Neglecting the convective heat transfer also prevents the additional heat transfer due to the superheated conditions from being calculated. Figure 4 indicates that the overall heat transfer coefficient (i.e., Uchida) increases by 3 to 4% as a result of the superheat condition. Although this amount may appear to be insignificant, the atmosphere temperature reduction resulting from it can be significant, since this increase is due to convective heat transfer. If the degree of superheat is increased, the role of this convective cooling is enhanced.

The proposed model predicts an average peak temperature 12°C (21°F) higher than the measured local peak temperature. The predicted temperature is an average temperature since the containment is represented by only a single volume.

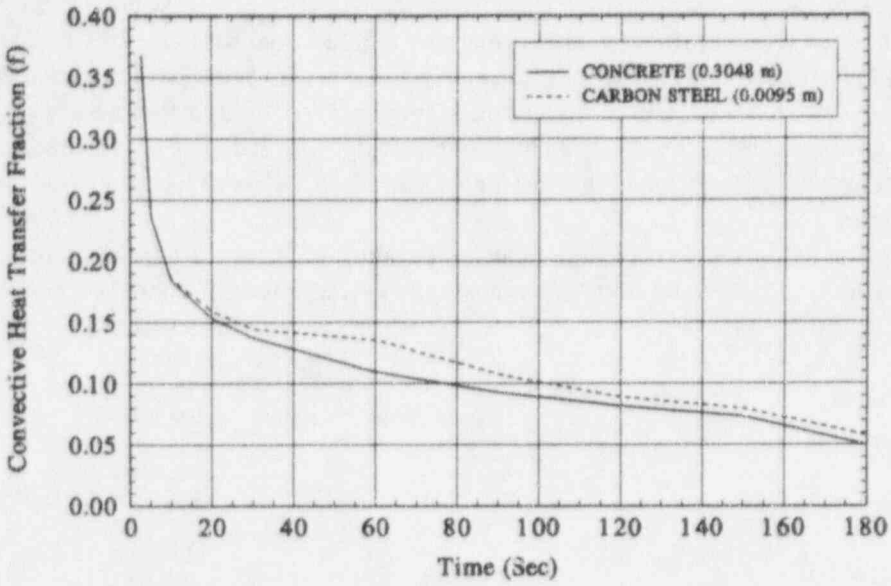

Figure 3: **Convective heat transfer fraction at the concrete and steel heat sinks for the CVTR experiment.**

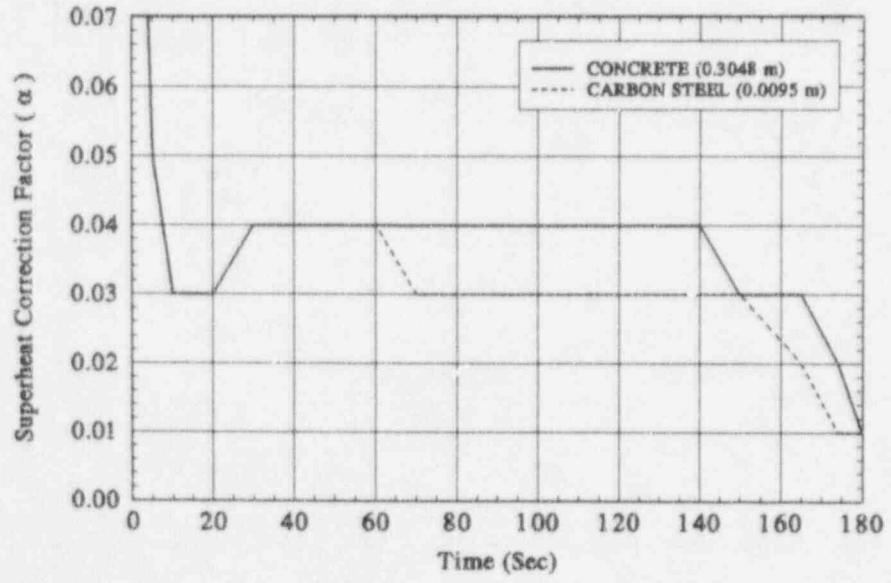

Figure 4: **Superheat correction factor at the concrete and steel heat sinks for the CVTR experiment.**

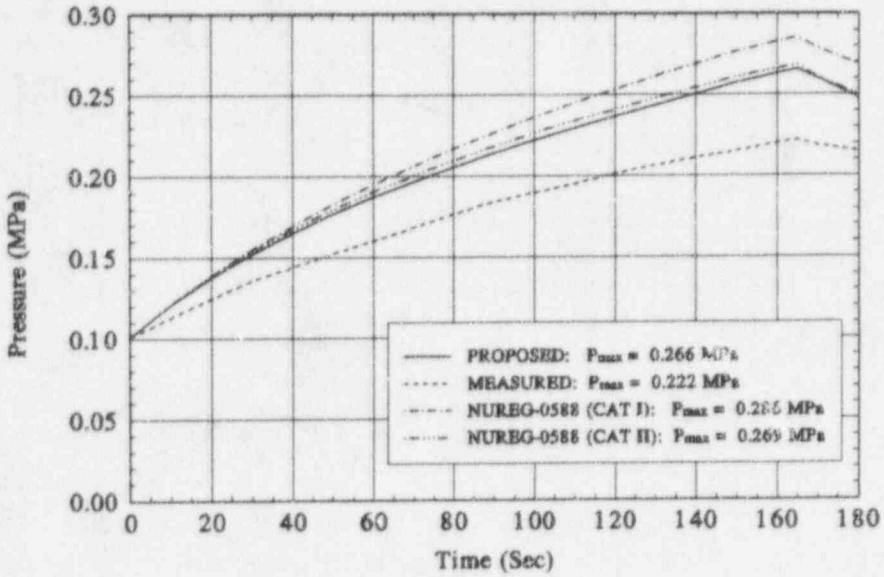

Figure 5: Comparison of the calculated and measured pressure transients for the CVTR experiment.

As shown in Figure 5, the regulatory model overpredicts the measured peak pressure by 0.064 MPa (9 psi) for Category I plants and by 0.047 MPa (7 psi) for Category II plants, while the proposed model overpredicts the pressure by 0.044 MPa (6 psi). In Figure 3, the convection heat transfer fraction transients for the 0.0095 m thick carbon steel and 0.3048 m thick concrete are presented. As shown in the figure, the convection heat transfer rates on both heat sink surfaces are significant early in the transient when the fractions of noncondensable gas (i.e., air) are large, and the condensing heat transfer becomes dominant as the steam mass fraction increases with time.

Since very conservative pressures and temperatures are predicted by the proposed model and since the Uchida correlation appears to be approximately 3 to 4 times smaller than the measured CVTR heat transfer coefficients (as shown in Figure 2), a sensitivity analysis is performed for twice the Uchida correlation. The temperature prediction of this "best-estimate" calculation, as shown in figure 6, is in excellent agreement with the measured temperature while the pressure prediction, as shown in figure 7, remains slightly higher (0.015 MPa, 2 psi) than the measured pressure. Further sensitivity studies revealed that the temperature and pressure predictions found using three or four times the Uchida correlation are not significantly different from the predictions found using two times the Uchida correlation.

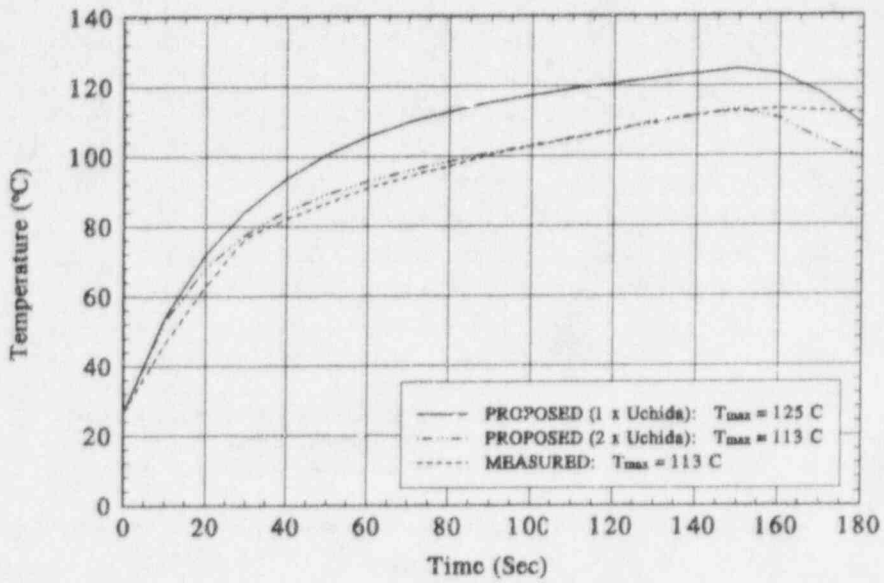

Figure 6: **Comparison of the calculated and measured temperature transients for the CVTR experiment. For the calculated transients, the effects of using two times the Uchida coefficient are examined.**

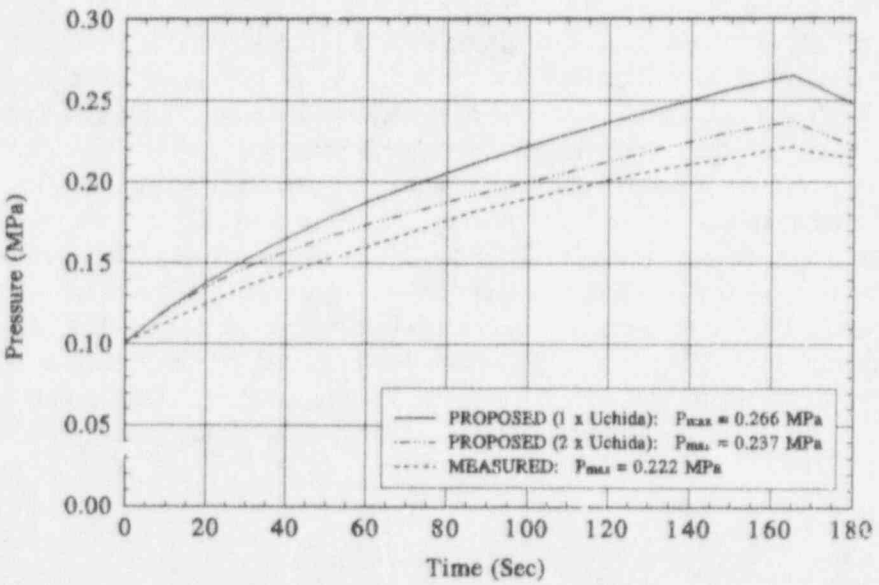

Figure 7: **Comparison of the calculated and measured pressure transients for the CVTR experiment. For the calculated transients, the effects of using two times the Uchida coefficient are examined.**

TYPICAL PWR RESULTS

The results of this paper indicate that the proposed model is more accurate than the regulatory mod In order to estimate the peak temperature reductions due to the proposed model in typical PWR pl high enthalpy and low enthalpy MSLB cases are investigated and the results are listed in Table 1. As shown in the table, the magnitudes of reduction vary for the different break sizes. The reductions for the large break size cases are less than those for the small break size cases since the heat sinks have less time to respond for the high blowdown mass and energy release rates. However, it is beneficial for establishing the environmental qualification (EQ) envelopes which consider time duration at elevated temperatures as well as the maximum temperature for a spectrum of break sizes. The magnitudes of reduction also depend on the plant specific containment volume, the total heat sink surface areas and heat sink material properties. In general, the proposed model is more effective in the temperature reductions for the small break sizes and the magnitudes of reduction will be enhanced as heat sink inventory increases.

Table 1: Peak temperatures resulting from a MSLB for a typical PWR

Blowdown Enthalpy Condition	Break Size (m^2)	NUREG-0588 (CAT I)		NUREG-0588 (CAT II)		Proposed Model	
		T(°C)	t(sec)	T(°C)	t(sec)	T(°C)	t(sec)
Saturated	Full DER	178	15	169	14	166	14
	0.078	184	105	157	55	143	51
	0.056	167	120	135	90	123	144
Superheated	Full DER	218	30	214	30	207	27
	0.221	212	43	207	43	200	40
	0.056	204	130	192	130	175	120

CONCLUSIONS

The current regulatory model for determining the containment peak pressure and temperature following an MSLB is benchmarked with the CVTR test data. The calculated peak pressure and temperature predictions are 0.047 to 0.064 MPa (7 to 9 psi) and 21 to 53°C (38 to 96°F) too high respectively. The very conservative results predicted by the current regulatory model results from: (1) the low estimate of the condensation heat transfer coefficient provided by the Uchida correlation, and (2) the omission of the convective heat transfer fraction. Neglecting convection results in a high estimate of the condensed mass and does not allow any additional heat transfer to be calculated for superheated conditions. Although the direct use of the Uchida correlation for large containments appears to have little basis, there is at present no other empirical correlation available. An underprediction of the heat transfer for actual containments leads to a high estimate of the atmosphere temperature, which is conservative for equipment qualification. In addition, the direct use of the Uchida correlation for building heat sinks is an established licensing procedure. Therefore, in the proposed model, only the effects resulting from convection are corrected by implementing the convective heat transfer fraction (f) and the correction factor for superheat effect (α). These correction factors are derived based on well-developed condensation theory which considers the presence of a noncondensable gas. The proposed condensation heat transfer model uses the Uchida correlation, calculates condensation and convection heat transfer fractions, and bases the steam removal rate on the condensation heat transfer portion only.

The results of the proposed model are significantly lower than those calculated with the current regulatory model, yet they are still very conservative when compared with the results of the CVTR test. For typical plant application, the magnitudes of reduction depend on the break sizes, plant specific containment volume, the total heat sink surface areas, and heat sink material properties. The proposed model has the following advantages:

- The reduction in calculated peak temperature for the MSLB accidents is expected to be beneficial for qualification of safety-related equipment in light water reactors (LWRs).
- The direct use of the Uchida correlation for heat transfer to building heat sinks is consistent with the current regulatory practice and is conservative.
- The sensible convective heat transfer fraction is based on the vapor-gas boundary layer conditions near the heat sink surface and does not rely on an arbitrary fixed revaporization fraction.
- Implementation of the proposed model into containment analysis computer programs can be accomplished easily.

The model developed here has significant advantages for the analysis of containment temperature transients following MSLB accidents. It is recommended that the regulatory requirements, as specified in NUREG-0588, be revised to consider the effects of superheat and convection heat transfer.

NOMENCLATURE

C_1	constant
C_2	constant
c_p	specific heat at constant pressure
f	convective heat transfer fraction of overall heat transfer
g	mass transfer conductance
Gr	Grashof number
h	heat transfer coefficient
i	enthalpy
k	thermal conductivity
L	length of plate
$\dot{m}_c$	condensate mass removal rate
P	pressure
Pr	Prandtl number
q"	heat flux
Re	Reynolds number
Sc	Schmidt number
T	temperature
X	vapor mass fraction
α	correction factor for superheat effect
ρ	density
u	velocity
μ	viscosity
Ψ	ratio of convective to condensing heat transfer

Subscripts

a	air
B	bulk
conv	convection
cond	condensation
g	gas
I	interface
R	average
v	vapor
W	wall

Superscripts

s	saturation

REFERENCES

[1] Szukewicz, A.J. , "Interim Staff Position on Environmental Qualification of Safety-Related Electrical Equipment," NUREG-0588 (July 1981).

[2] Uchida, H., Oyama, A., and Togo, Y., "Evaluation of Post-Incident Cooling Systems of LWR's," Proc. Int. Conf. Peaceful Use of Atomic Energy, Vol. 13,pp. 83-104,A/CONF.28/P436 (1965).

[3] Schmitt, R.C., Bingham, G.E., and Norberg, J.A., "Simulated Design Basis Accident Tests of the Carolinas Virginia Tube Reactor Containment Final Report," Idaho Nuclear Corporation report IN-1403 (December 1970).

[4] Tagami, T., "Interim Report on Safety Assessment and Facilities Establishment Project in Japan for Period Ending June 1965 (No. 1)," unpublished work (February 1966).

[5] Peterson, P.F, Schrock, V.E., and Kageyama, T., "Diffusion Layer Theory for Turbulent Vapor Condensation With Noncondensable Gases," Journal of Heat Transfer, Vol. 115, pp. 998-1003 (November 1993).

[6] Corradini, M.L., "Turbulent Condensation on a Cold Wall in the P[illegible]nce of a Noncondensable Gas," Nuclear Technology, Vol. 64, pp. 186-195 (February 1984)

[7] Kim, M.H., and Corradini, M.L., "Modeling of Condensation Heat Transfer," Nuclear Engineering and Design, Vol. 118, pp. 193-212 (1990).

[8] Peterson, P.F., personal communication (1995)

[9] Lampkin, D.E., Koestel, A., Gido, R.G., and Baranowsky, P.W., "Containment Main Steam Line Break Analysis for Equipment Qualification," NUREG/CR-1511, LA-8305-MS (June 1980).

[10] Hynek, S.J., "LOCTIC (Loss of Coolant Transient Inside Containment)," Stone & Webster Engineering Corporation NU-100 (July 1975)[Proprietary].

EFFECT OF SUBCOOLING AND WALL THICKNESS ON POOL BOILING FROM DOWNWARD-FACING CURVED SURFACES IN WATER

MOHAMED S. EL-GENK AND ALEXANDER G. GLEBOV
Institute for Space and Nuclear Power Studies/Chemical and Nuclear Engineering Dept.
University of New Mexico, Albuquerque, NM 87131, USA.

Abstract

Quenching experiments were performed to investigate the effects of water subcooling and wall thickness on pool boiling from a downward-facing curved surface. Experiments used three copper sections of the same diameter (50.8 mm) and surface radius (148 mm), but different thickness (12.8, 20 and 30 mm). Local and average pool boiling curves were obtained at saturation and 5 K, 10 K, and 14 K subcooling. Water subcooling increased the maximum heat flux, but decreased the corresponding wall superheat. The minimum film boiling heat flux and the corresponding wall superheat, however, increased with increased subcooling. The maximum and minimum film boiling heat fluxes were independent of wall thickness above 20 mm and Biot Number > 0.8, indicating that boiling curves for the 20 and 30 thick sections were representative of quasi steady-state, but not those for the 12.8 mm thick section. When compared with that for a flat surface section of the same thickness, the data for the 12.8 mm thick section showed significant increases in both the maximum heat flux (from 0.21 to 0.41 MW/m^2) and the minimum film boiling heat flux (from 2 to 13 kW/m^2) and about 11.5 K and 60 K increase in the corresponding wall superheats, respectively.

NOMENCLATURE

Cp	Specific heat (J/kg K)
Bi	Surface average Biot number, $\left(\bar{q} \cdot H / \left(\left(\overline{\Delta T_{sat}} + \Delta T_{sub}\right)\overline{k_{cu}}\right)\right)$
g	Acceleration of gravity (m/s^2)
h_{fg}	Latent heat of vaporization (kJ/kg)
H	Test section thickness (m)
l	Iteration number
k	Thermal conductivity (W/m K)
MHF	Local maximum heat flux (MW / m^2)
q	Local heat flux (MW / m^2)
r	Radial coordinate
R	Radius of curved surface (m)
T	Temperature (K)
t	Time (s)
z	Axial coordinates

Greek Letters

Δr	Control volume length in radial direction (m)
ΔT_{sat}	Local wall superheat ($T_w - T_{sat}$) (K)
ΔT_{sub}	Water subcooling ($T_{sat} - T_p$) (K)
Δz	Control volume length in axial direction (m)
ε	Convergence criterion
θ	Local inclination angle on the boiling surface (degree)
ρ	Density (kg/m^3)
σ	Surface tension (N/m)

Subscripts

cu	Copper

CHF	Critical Heat Flux
i	Index along r-coordinate
j	Index along z-coordinate
l	liquid
min	Minimum film boiling
p	Water pool
s	Convex surface of copper section
s.s.	Asymptotic
sat	Saturation
sub	Subcooling
v	vapor
w	Boiling surface

Superscripts

n	Temporal discretization number
-	Average, surface average

INTRODUCTION

Several experimental studies have been reported on pool boiling from inclined and downward-facing flat surfaces in saturated R-11, helium, nitrogen, isopropyl alcohol, and water [1-12] using steady-state heating. In these studies, the inclination angle, θ, was varied from 5° to 180° (upward-facing), no data, however, was reported for the downward position. Recently, Guo and El-Genk [13-15] and El-Genk and Guo [15,16] performed quenching experiments using a flat surface copper disk (50.8 mm in diameter and 12.8 mm thick) to investigate the effect of surface inclination on transient pool boiling in saturated and subcooled water at θ of 0° (downward-facing), 5°, 10°, 15°, 30°, 45°, and 90° (vertical). Their surface average nucleate boiling heat fluxes at low wall superheat agreed qualitatively with those of Nishikawa et al. [9] and Beduz et al. [2], and for the maximum heat flux (MHF) with those of Vishnev et al. [12] and Beduz et al. [2] for saturation boiling.

In these experiments [2,9,12,13-15], the maximum heat flux decreased as θ decreased. At low wall superheat, nucleate boiling heat flux increased as θ decreased, but decreased with decreased θ at high wall superheat close to the maximum heat flux. The increase in nucleate boiling heat flux with decreased inclination at high wall superheat could be attributed to the mixing induced in the boundary layer by sliding bubbles [16, 17]. Decreasing the inclination angle of the surface lowered the tangential component of gravity acting on the bubbles, thus increasing their travel time in the boundary layer before being released from the edge of the boiling surface. Visual observations and video images of the surface by Guo and El-Genk [13-16] confirmed the presence of small sliding bubbles, even for the downward facing position ($\theta = 0$). The results of Guo and El-Genk [13-16] also showed the maximum and the minimum film boiling heat fluxes, as well as the corresponding wall superheats, to decrease as the inclination angle was decreased. Both maximum and minimum film boiling heat fluxes increased with increased subcooling, nucleate boiling heat flux, however, decreased at small surface inclinations, but increased at large inclinations with increased subcooling [14,15]. The results of Guo and El-Genk as well as those of other investigators [1-16] are, however, not applicable to pool boiling from downward-facing curved surfaces, for which, to the best of the authors' knowledge, there is very little experimental data available [18-20].

Pool boiling from convex downward-facing surfaces in water is of interest to nuclear reactor safety for assessing the coolability of the bottom head of an Advanced Light Water Reactor (ALWR) pressure vessel, following a core meltdown accident [21-23]. In such an accident, molten fuel, cladding, and control material will flow downward under the influence of gravity, and may eventually collect in the bottom head of the reactor vessel. Once in the bottom head, the molten core materials will heat the structure and can eventually melt through the wall, unless adequate cooling can be provided. One of the accident management strategies under consideration for ALWRs is to passively cool the external surface of the reactor pressure bottom head by pool boiling of water in the underlying cavity. It is hoped that cooling the bottom head by pool boiling would preserve the structural integrity of the reactor vessel and cause the core debris to freeze on the concave side of the vessel bottom head wall [19-23].

The hemispherical and toroidal geometry of the reactor vessel bottom head provides continually increasing inclination and surface area for vapor generation and flow. Parameters which would influence pool boiling on

the outer surface of the vessel bottom head include: surface area, local curvature and inclination, water subcooling, and wall material and thickness. The effects of these parameters need to be understood in order to assess the coolability of a ALWR vessel bottom head by pool boiling. For example, the release of vapor bubbles at lower inclination positions may cause vapor accumulation at higher positions, lowering the pool boiling heat flux. However, on the other hand, an efficient release of vapor from the edge of the boiling surface can reduce vapor accumulation, hence enhancing surface coolability. Also, sliding bubbles generated at lower positions on the surface would cause mixing in the boundary layer, thus enhancing nucleate boiling heat transfer [13-17]. Another important point is that most pool boiling heat transfer data and boiling curves reported in the literature were based on the average surface heat flux and average surface superheat. The surface average pool boiling maximum heat flux, although useful for assessing overall heat removal rate, could underestimate the local heat flux for a portion of a convex surface. Therefore, data on both local and average heat fluxes for pool boiling from downward-facing convex surfaces in saturated and subcooled water are needed.

Quenching experiments were performed to investigate the effect of water subcooling and wall thickness on pool boiling from a small downward-facing convex surface in water. An important question in this work was whether the local and surface average values of the maximum and minimum film boiling heat fluxes were representative of quasi steady-state [24]. For an answer, experiments employed three copper sections of the same diameter (50.8 mm) and surface radius (R_S = 148 mm), but different thicknesses (12.8, 20 and 30 mm). Local pool boiling curves obtained at six different locations on the surface ($0^o \leq \theta \leq 8.26^o$) were compared with the surface average pool boiling curves at saturation and 5 K, 10 K, and 14 K subcooling. The effect of surface curvature was assessed by comparing the surface average pool boiling curve for the 12.8 mm thick section with that of Guo and El-Genk [14] for a flat surface section of the same material, diameter and thickness. A discussion of the applicability of the present results to the cooling of the bottom head of ALWR vessel is presented, despite the large differences in surface size and curvature and the difference in wall material (copper versus stainless-steel).

EXPERIMENTAL SETUP AND PROCEDURES

Each of the three test sections in the experiments had eight, K-type thermocouples (TC#1 through TC#8) placed ~ 0.5 mm from the boiling surface and three thermocouples placed near the back surface (TC#9 - TC#11). A cross-sectional view of an instrumented 20 mm thick section is shown in Figure 1a. The spacing and number of these thermocouples were selected such that to examine the symmetry of pool boiling on the curved surface and to provide sufficient temperature data for subsequent determination of the local and average pool boiling heat flux and surface temperature (see subsection on determination of pool boiling heat flux). The thermocouples were spaced horizontally relative to the centerline as follows: TC#1 and TC#10 at 0.0 mm, TC#2 at 4.25 mm, TC#3 and TC#7 at 8.5 mm, TC#4 at 12.75 mm, TC#5, TC#8, TC#9, and TC#11 at 17 mm, and TC#6 at 12.25 mm. Thermocouples TC#9, 10, and 11 were placed 4 mm and 5 mm from the back surface of the 12.8 mm and of both the 20 mm and 30 mm sections, respectively.

The near surface thermocouples (TC#1 - TC#8) were inserted all the way into the vertical, 1.5 mm diameter holes, which were drilled vertically to within 0.5 mm from the boiling surface; the holes for TC#9 - TC#11 were only 5 mm deep. The thermocouple wire was left insulated, but the junctions were exposed. After the fiber glass insulated thermocouples (0.8 mm in dia.) were placed fully into the holes, small pieces of silver solder were inserted at the bottom of the holes. The copper section was then heated to a high temperature (> 650 K) to melt the silver solder in the holes and establish metallic bond between the thermocouples junctions and copper. The section was then left to cool off slowly to allow the metal bond between the thermocouples and the inside surface of the copper in the holes to solidify. Thermocouple junctions were then tested separately by heating the surface in a water bath with a known temperature and comparing the signals given by the different thermocouples. Poor thermal bonds meant removing the thermocouples and repeating the process again. During experiments, the maximum surface temperature before quenching (~ 510 K) was well below the melting temperature of the silver solder.

Copper sections were thermally insulated on the back and sides using a water sealed mold of Marinite C (calcium silicate having a thermal conductivity, k = 0.2 W/m K). A 10 mm space was left between the back surface of the test section and the Marinite C, for routing the leads of the thermocouples to the data acquisition equipment. The test section and the Marinite mold were housed in a cylindrical Bakelite skull for

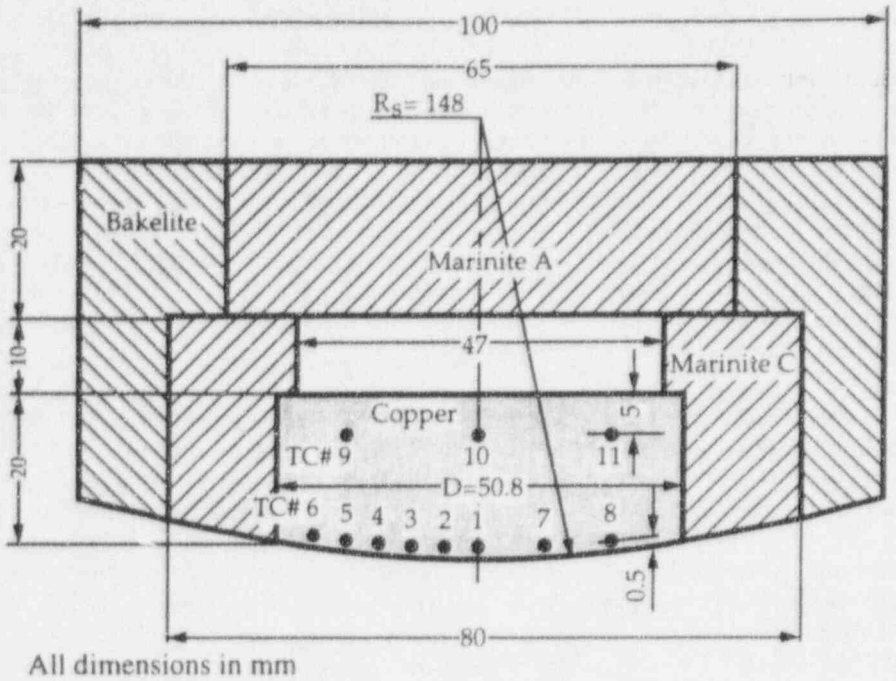

Fig. 1a. Cross-sectional view of the 20 mm thick instrumented test section.

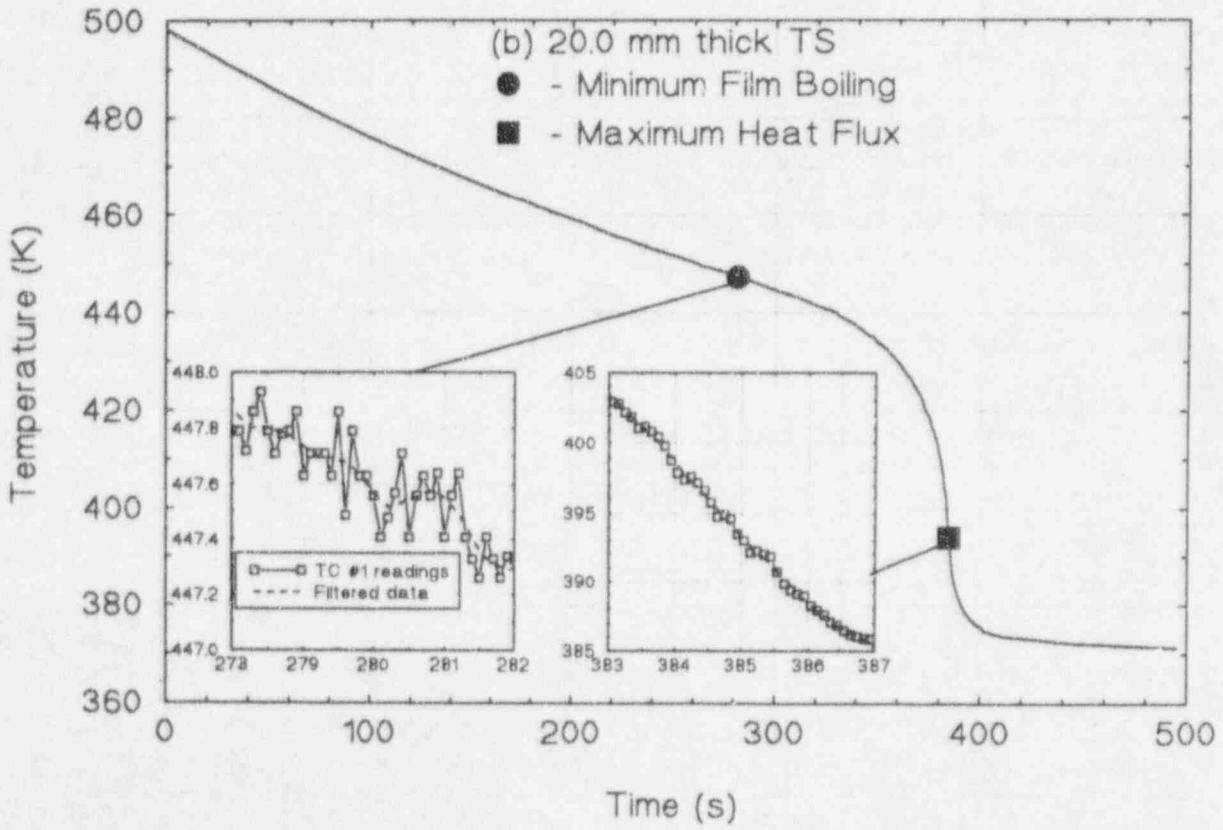

Fig. 1b. Effect of test section thickness and subcooling on the maximum pool boiling heat flux.

additional insulation and handling. The Marinite mold and the Bakelite skull were machined to the same curvature as the boiling surface in order to avoid edge effects influencing the release of vapor (Figure 1a).

The quenching tank, measuring 254 mm by 245 mm and 483 mm high in external dimension, was made of aluminum frame with large glass windows on four sides for visual observation and recording of pool boiling on the surface using a video camera. The dimensions of the tank were much larger than the diameter of the copper section (50.8 mm); no liquid entrainment around the surface and or disturbance of vapor release from the edge of the section was observed during experiments. The water in the tank was maintained at desired temperature during experiments using two, 2.0 kW, individually controlled immersion heaters [13-17]. A water sealed mirror was mounted at a 45° angle at the bottom of the tank for observing of the entire boiling surface during quenching.

Prior to each test, the distilled water in the tank was mixed thoroughly using an external circulation pump and degassed by boiling for about 15 minutes. After the surface was polished using #1200 Silicon Carbide sand paper and cleaned with acetone, the copper section was heated by placing its convex surface on top of a copper disk having a concave surface of the same curvature. The copper disk was then placed on top of a hot plate. The convex surface of copper section was tightly wrapped with aluminum foil before placing it on top of the copper disk to be heated. The aluminum wrap helped ensure good contact between the disk and the copper section surface and distributed the heat more uniformly along the surface, shortening the heating time and, hence, reducing potential oxidation. Surface oxidation was avoided by limiting the maximum temperature of the copper section to 510 K. When aluminum wrap was used, the surface maintained its shine while being heated. Wrapping the test section in aluminum foil while being heated and limiting the maximum surface temperature to 510 K, we were able to avoid surface oxidation before quenching. After being heated, the copper section was lowered into the pool, ~ 40 mm below the water surface in the quenching tank.

Data Recording and Processing

During quenching, all thermocouples in the copper section were scanned once every 100 ms using a high speed data acquisition unit connected to a 486-50 MHz PC. Because these thermocouples were scanned sequentially, recording time was adjusted for the time interval (~ 9 ms) between readings to obtain simultaneous temperature values at different thermocouple locations. While in film, transition and nucleate boiling, the high frequency, random oscillations in the recorded temperatures, due to electric equipment, had small amplitudes of less than $\pm$ 0.2 K (Figure 1b). Near the maximum heat flux, however, the amplitude of these random oscillations was as much as $\pm$ 0.5 K. In order to remove these high frequency, low magnitude random oscillations without unduly degrading the underlying information, numerical filtering (or smoothing) of raw temperature data was performed using a method similar to in [25].

The entire data array was scanned with a window containing a number of data points (3 to 11 points) and the data point in the middle of the window was replaced by a value determined from a second degree polynomial fit of the data points in the window. Next, the data point at one end of the window was dropped and the next point at the other end added, and the process was repeated. The width of the smoothing window was adjusted to reduce high-frequency noise without damping the low frequency desired signal. Best results were obtained when a 9-points window was used [18]. Figure 1b compares the raw and filtered temperature data for the lowermost thermocouple in saturation boiling experiments. As Figure 1b shows, numerical filtering did not disguise any important trend displayed by the raw data. The procedure used herein is standard [24], except that the number of points selected in the moving window to obtain the best results was determined by trial. The filtered temperatures in the test section were used, in conjunction with a numerical solution of direct transient heat conduction in the test section, to determine the local and surface average pool boiling heat fluxes and surface temperatures.

Determination of Pool Boiling Heat Flux

During quenching, the symmetry of heat transfer from the boiling surface, confirmed by the temperature measurements made near the boiling surface (see Figure 2a), justified the use of a two-dimensional (r, z) transient heat conduction analysis of the test section during quenching. As shown in Figure 1a , the test section is basically a right cylinder with a flat surface at the top (z = 0, r) and a slightly curved surface at the

bottom (z = H(r), r). The thickness of the copper section at any arbitrary radius from the centerline can be given by:

$$H(r) = H(R) + \sqrt{R_S^2 - r^2} - \sqrt{R_S^2 - R^2}. \tag{1}$$

The two-dimensional, transient heat conduction in the copper section during quenching can be described by the following equation in cylindrical coordinates:

$$\rho Cp\left(\frac{\partial T}{\partial t}\right) = \frac{1}{r}\frac{\partial}{\partial r}\left(k\,r\frac{\partial T}{\partial r}\right) + \frac{\partial}{\partial z}\left(k\,\frac{\partial T}{\partial z}\right), \tag{2}$$

subject to the following boundary and initial conditions:

$$T(r, z_C, t) = T_S(r,t),\; k\frac{dT}{dz}(r,0,t) = k\frac{dT}{dr}(R,z,t) = k\frac{dT}{dr}(0,z,t) = 0, \tag{3}$$

and,

$$T(r,z,0) = T_o, \tag{4}$$

where,

$$z_C(r) = (H(R) - 0.005) + \sqrt{\left((R^2+\delta^2)/2\delta\right)^2 - r^2} - \sqrt{\left((R^2+\delta^2)/2\delta\right)^2 - R^2}, \tag{5}$$

and,

$$\delta = \left(R_S - \sqrt{R_S^2 - R^2}\right)(H(R) - 0.005)/H(R). \tag{6}$$

The top surface and the sides of the copper section were assumed adiabatic (Eq. 3) and the physical properties of copper were taken to be temperature dependent. Because of the non-linearity of the governing equation and the relatively complex geometry of the test section, a closed form solution for determining the local temperature and heat flux on the boiling surface is not attainable. Instead, Eq.(3) was solved numerically using a fully implicit, control volume method.

In the experiment there were sufficient temperature measurements (TC#1 - TC#8) made in the copper section near the boiling surface (Fig. 2a) to establish a time dependent boundary condition, $T_S(r, t)$, (Eqs. 3 and 7). Although thermocouples TC#1 - TC#8 did not reside on the boiling surface, it was possible to use their measurements because they were located along the surface passing through the centers of control volumes bound by the boiling surface (Figures 2a and 2b). Thus, direct solution of equation (1) was used to determine the local surface temperatures and local pool boiling heat fluxes. The measured temperatures near the boiling surface as a function of time during quenching was given as:

$$T_s(r,t) = A_o(t)\cdot Cos\left[\pi\left(\frac{r}{R}\right)^{A_1(t)}\right] + A_2(t) \tag{7}$$

The coefficients $A_0(t)$, $A_1(t)$, $A_2(t)$ were obtained from the least square fit of Eq. (7) to the measured temperatures near the boiling surface at each time step. Figure 2a shows the curve fitted temperature measurements by TC#1 through TC#8 at different times during quenching; the solid lines were calculated by Eq. (7) and the symbols represent the measurements.

The solution of equation (1) employed a fully implicit alternating direction method [26], using a finite control volume (CV) discretization [27] to ensure stability of the solution and reduce the storage and computational time on a 486-50 MHz PC. A boundary fitted curvilinear coordinate system was used to represent the calculation domain within the test section, which was divided into a large number of finite control volumes (Fig. 2b). Each control volume was bound by two curved surfaces in the radial direction, two slightly curved surfaces in the axial direction. The curvature of the latter was gradually increased from 0 at the top surface, z = 0, to $(1/R_S)$ at the boiling surface, z = $H(R_S)$ (Figure 2b). For 20 mm thick section, Δr was taken constant and equal to 1.27 mm in a 20 x 20 grid size, while Δz, varied with radial location from

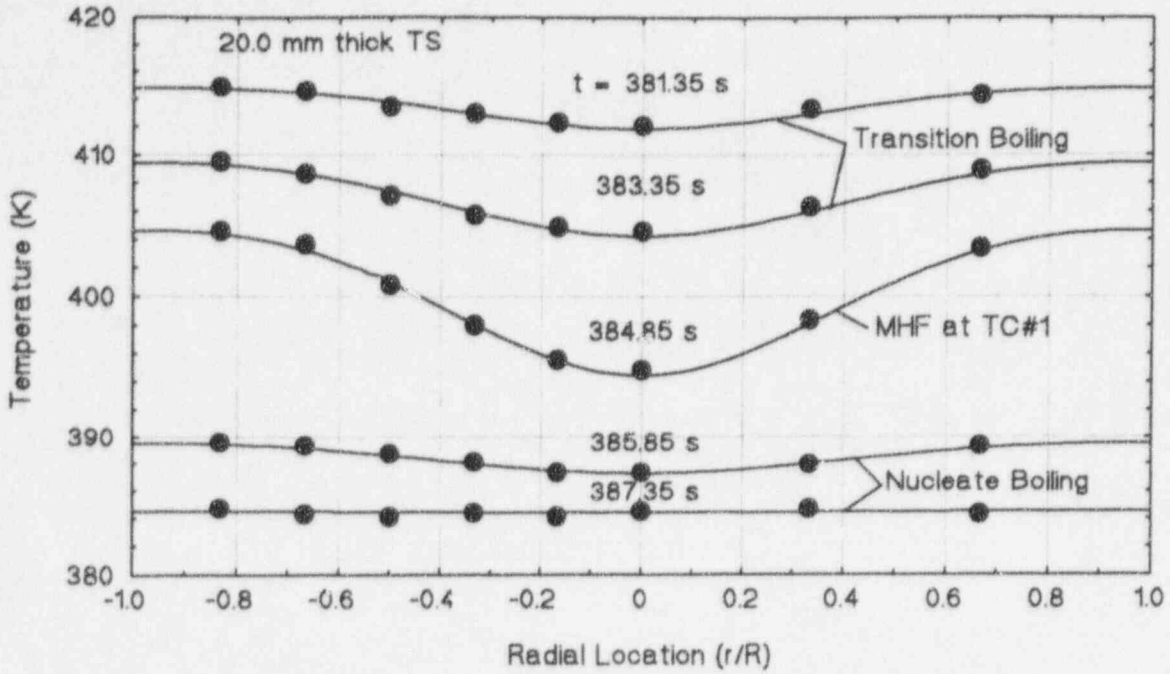

Fig. 2a. Curve fitting of temperatures measured in copper section near boiling surface.

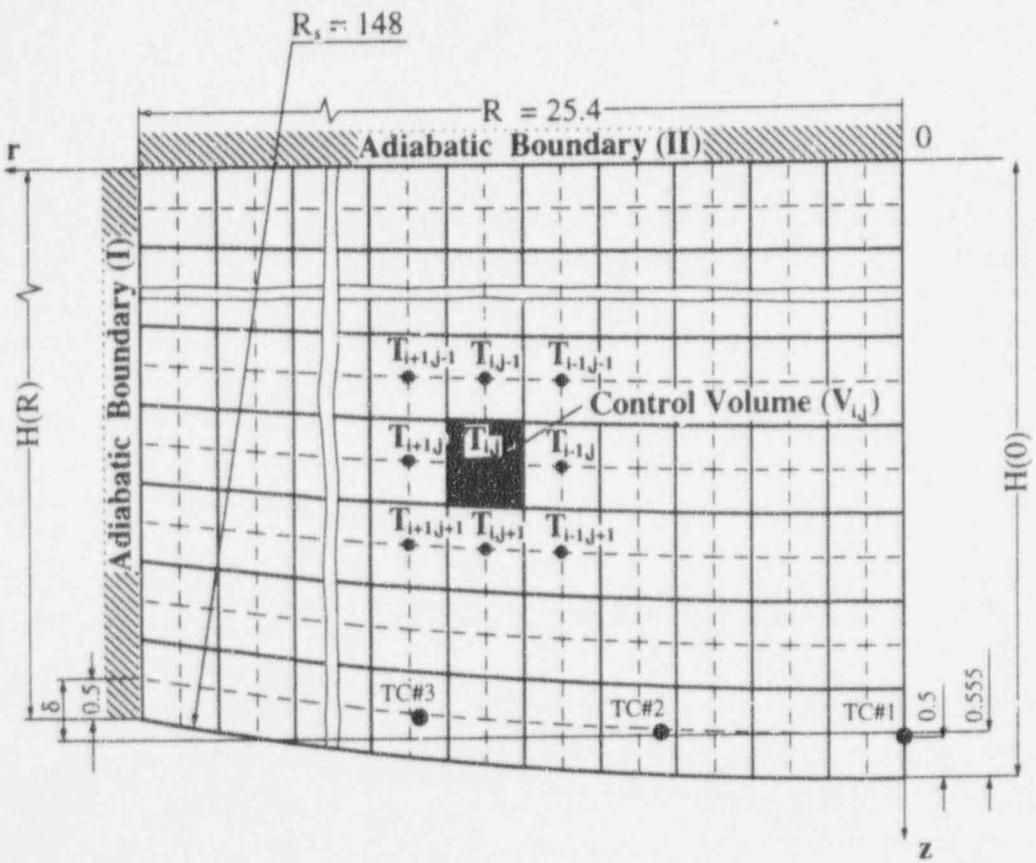

Fig. 2b. Calculation Numerical grid around arbitrary control volume inside domain.

1.11 mm at the center of the test section to ~ 1.0 mm at the side (r = R). The orthogonality of the heat flux with respect to the surfaces of CVs in the numerical grid was handled by calculating the temperature gradient from the derivative along the unit vector normal to the surface. The temperature derivatives were based on linear interpolation of temperatures along the lines passing through the centers of CVs.

At each time interval, the solution was obtained using iterative approach. The solution proceeded to the next time interval when calculated temperatures satisfied the convergence criterion, which was defined as: $\left|\left(T^n_{i,j}(I) - T^n_{i,j}(I-1)\right)\Big/ T^n_{i,j}(I)\right| < \varepsilon$. To ensure that the surface heat fluxes were correctly evaluated, several different grid sizes (10 x 10, 20 x 20, 30 x 30 and 40 x 40) and convergence criterion values ($\varepsilon = 10^{-4}$, 10^{-5}, 10^{-6}, 10^{-8}, 10^{-10}) were used. The accuracy of the numerical calculations was also confirmed by performing an overall energy balance after each time interval; calculations were accurate to within less than 0.1 %, and by comparing calculated and measured temperatures by TC#9-TC#11; the difference was of the same order of magnitude as the uncertainty in the thermocouples measurements, about ± 0.5 K. Results presented in this paper were obtained using (20 x 20) grid and convergence criterion value of 10^{-6}. When a (30 x 30) grid and/or a smaller convergence criterion were used, computation time increased significantly with a negligible change in calculated heat flux and surface temperature values.

The numerical solutions calculated the temperatures in the copper section at the center and the heat fluxes at the boundaries of the control volumes. The local heat flow at the boiling surface was determined from the heat balance in the control volumes (CVs) bound by the boiling surface. The local heat flux was determined by dividing the heat flow by the corresponding surface area of the control volume. The corresponding local surface temperatures were determined from the paraboiic extrapolation of the calculated temperatures at centers of the CVs near the boiling surface; using a linear extrapolation resulted in a negligible difference in calculated surface temperatures. The surface average pool boiling heat flux was determined from dividing the total heat flow by the total surface area. The corresponding average wall temperature was determined from the integral of the local wall temperatures over the entire boiling surface.

Sensitivity analyses were performed using the 2-D numerical solution to determine calculation uncertainties. The uncertainty in pool boiling heat flux was about ± 1.4% due to the uncertainty in the location of TCs near the boiling surface, ± 1.7% due to the uncertainty in TC readings, ± 3.4% due to numerical filtering of raw temperature data, and ± 1.7% due to curve fitting of measured temperatures near the boiling surface. Based on these values, the overall uncertainty in the maximum and the minimum film boiling heat fluxes, determined using the method outlined in [28], was ± 4.5% and ± 9%, respectively.

RESULTS AND ANALYSIS

Experimental results presented in the following sub-sections show the effects of water subcooling on both the local and surface average pool boiling curves and identify the proper test section thickness that ensures that boiling curves in quenching experiments are representative of quasi steady-state. The results also delineate the effect of local surface inclination on local pool boiling heat flux. In order to quantify the effect of surface curvature on pool boiling, the surface average saturation pool boiling data for the 12.8 mm thick section is compared with that of Guo and El-Genk [13] for a flat surface section of identical diameter, material, and thickness. At least two separate tests were performed at the same conditions to confirm the reproducibility of experimental results (Fig. 3); as demonstrated in this figure the experimental data was reproducible to within less than 5%. The local pool boiling curves presented in the following subsections are based on the average data of these two tests.

Effect of Wall Thickness

Figure 4 shows that for saturation and subcooling conditions, local and surface average maximum heat flux values increased with increased wall thickness, reaching asymptotic values, MHF_{ss} and $\overline{MHF}_{ss}$, respectively, at wall thickness > 20 mm; beyond this thickness the maximum heat flux was independent of wall thickness. The local and surface average values of the minimum film boiling heat flux, q_{min} and $\overline{q_{min}}$, respectively, however, decreased with increased wall thickness reaching asymptotic values, $(q_{min})_{ss}$ and

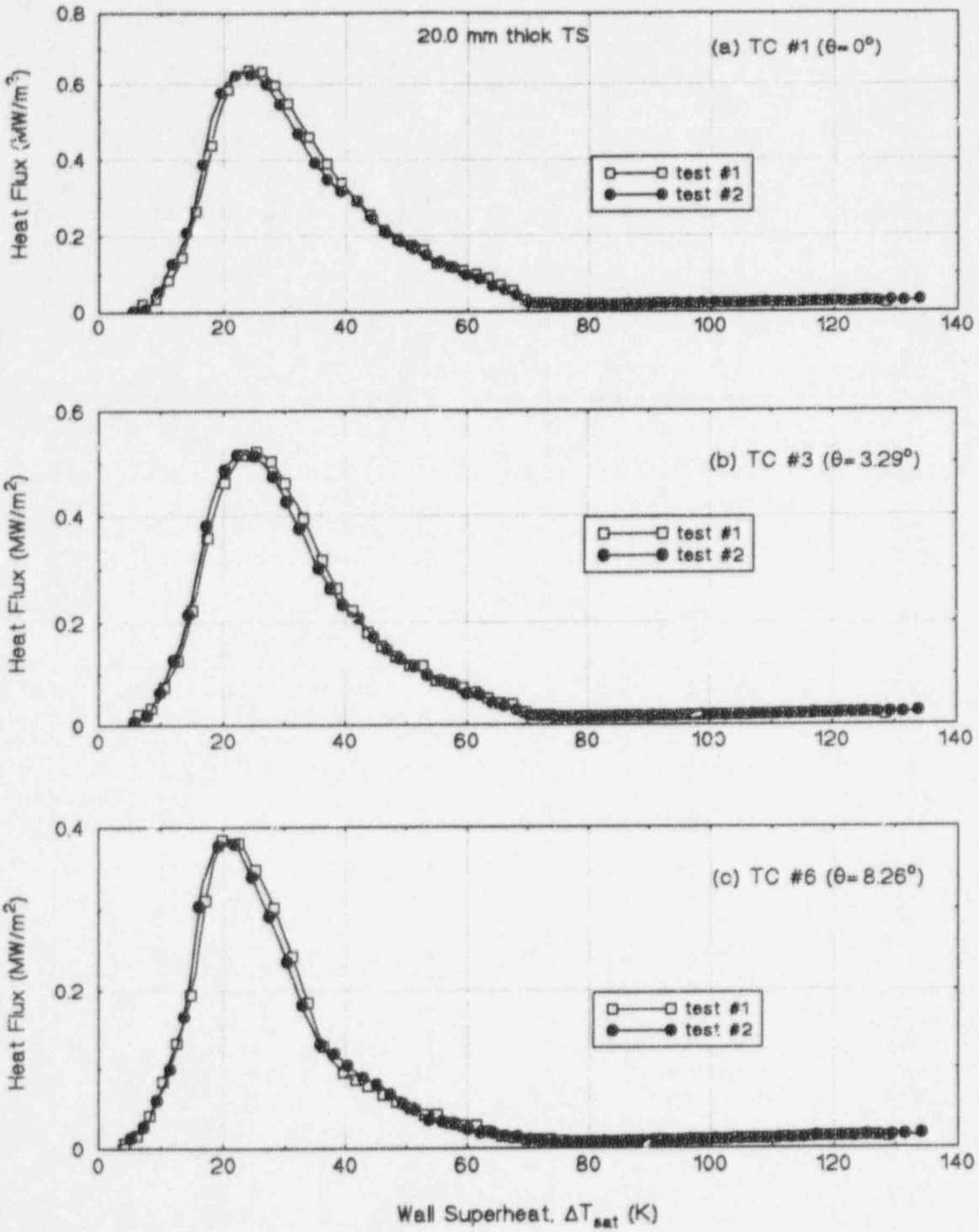

Fig. 3. Reproducibility of test data.

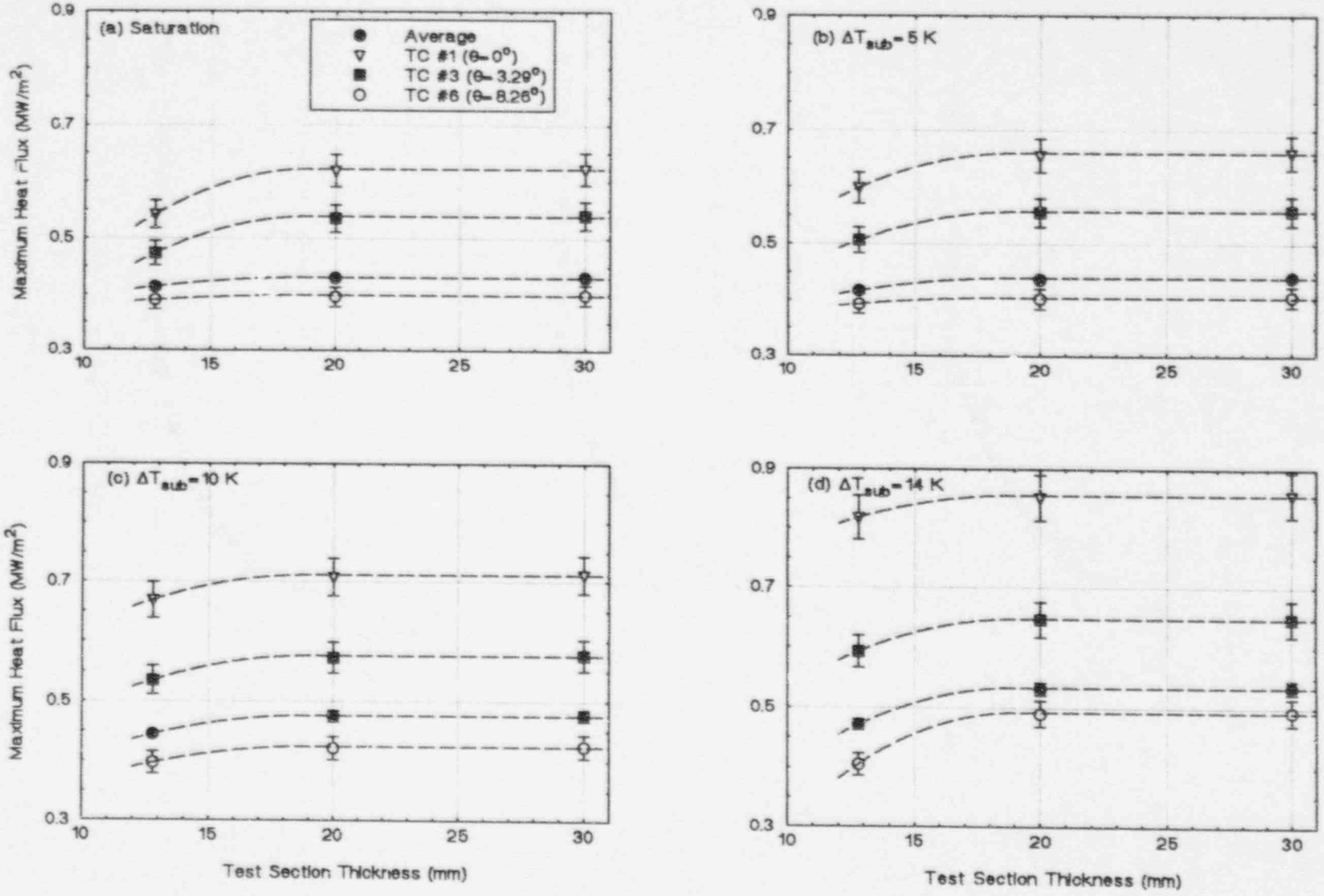

Fig. 4. Effect of test section thickness and water subcooling on the maximum heat flux.

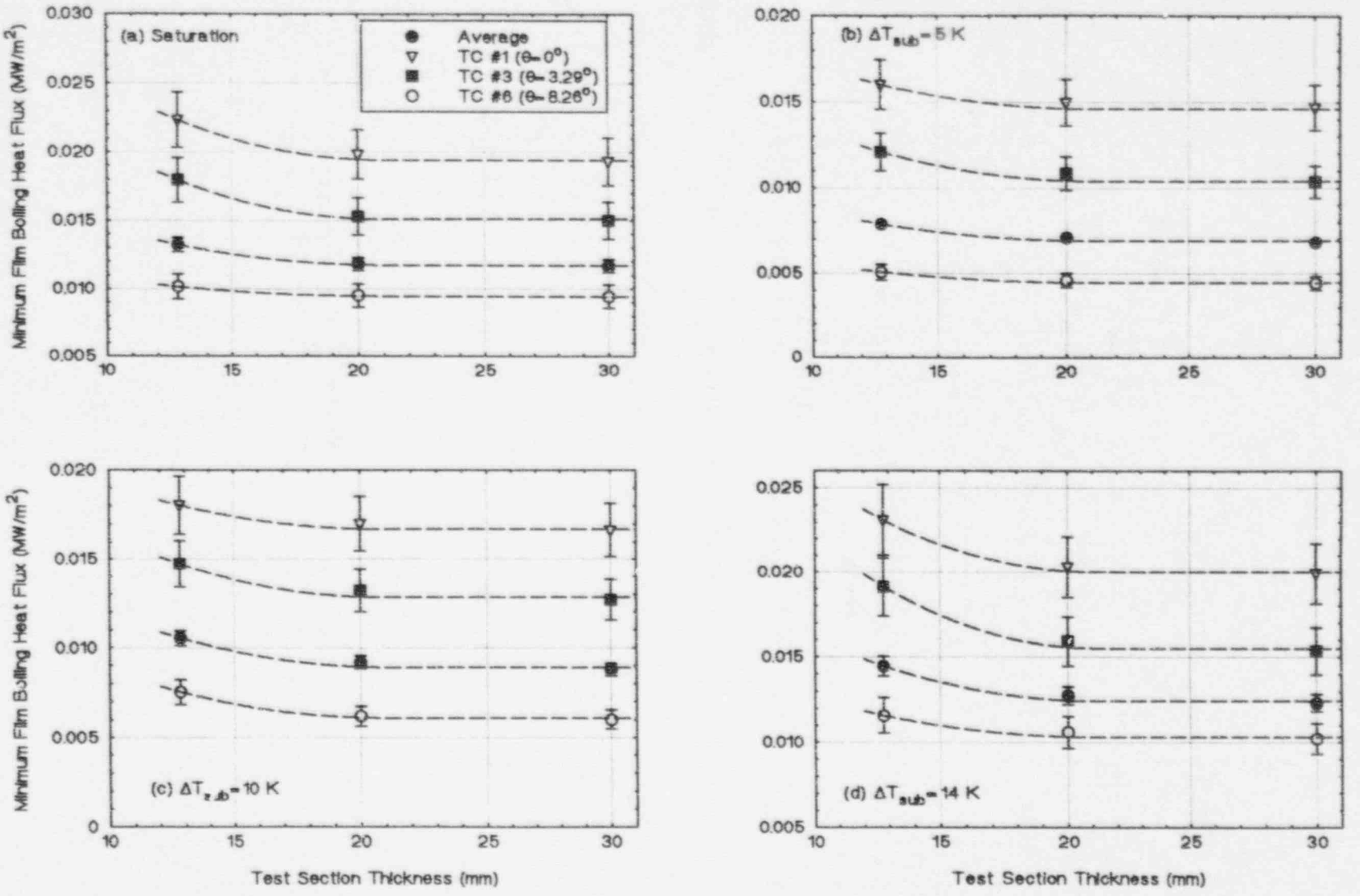

Fig. 5. Effect of test section thickness and subcooling on the minimum film boiling heat flux.

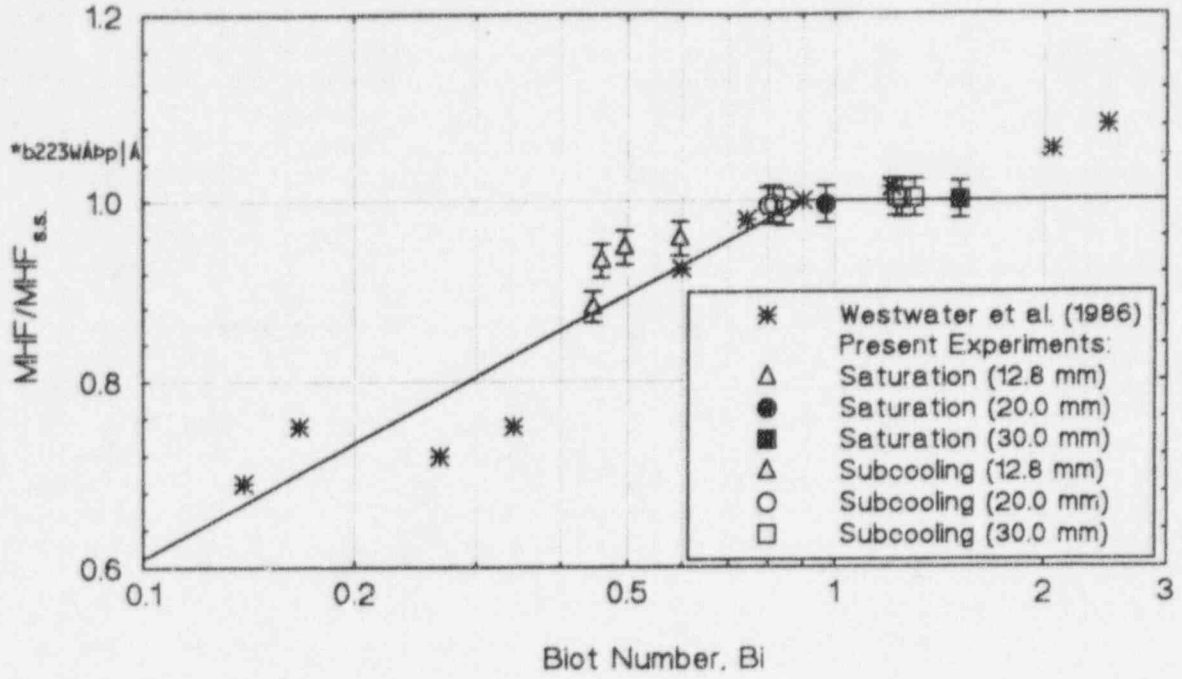

Fig. 6a. Biot nu.nber values corresponding to local and surface average maximum pool boiling heat fluxes.

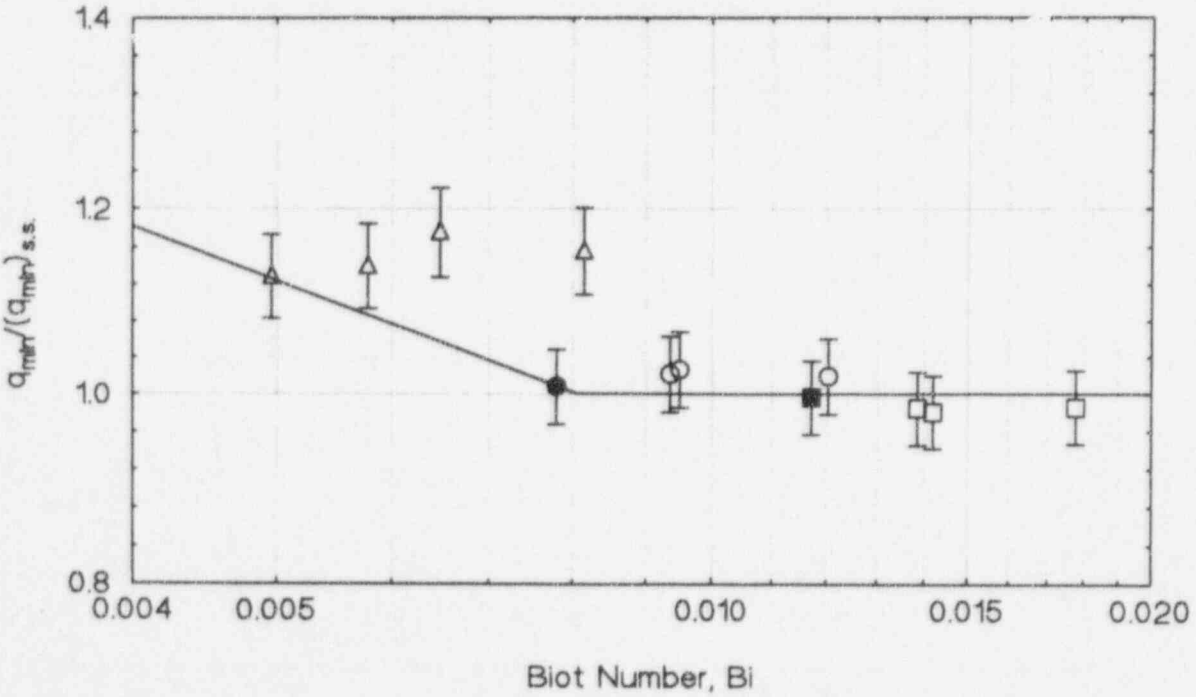

Fig. 6 b. Biot number values corresponding to local and surface average minimum film boiling heat fluxes.

$(\overline{q_{min}})_{ss}$, respectively, at approximately the same wall thickness of 20 mm (Fig. 5). The effect of test section thickness on the maximum heat flux is similar to that reported previously in [24, 29] in a series of quenching pool boiling on the face-up, horizontal flat surfaces of different materials. Their results showed that for test section ~ 25 mm in thickness, pool boiling curves were all quasi-steady state and equivalent to those obtained ... ady-state heating tests [29]. This wall thickness is about 25 % higher than that indicated by the present da ·n Figs. 4 and 5 for a convex downward-facing surface. Figures 4 and 5 show that in saturation boiling, b ..e maximum and the minimum heat fluxes increased with decreased surface inclination. These figures als ..ow that the dependence of both the local maximum and minimum film boiling heat fluxes for wall thicknesses < 20 mm was more pronounced at the lower inclination positions in saturation boiling, and at all inclinations in subcooled boiling.

In Figure 6 (a), the surface average maximum heat fluxes were divided by their asymptotic values and plotted versus the corresponding Biot number, Bi. As figure 6 (a) indicates, for Biot number $\geq$ 0.8 the average values of the normalized saturation and subcooling maximum heat fluxes for the 20 and 30 mm thick sections were equal to unity and independent of Biot number. This value of Biot number is also slightly lower than that reported by [24, 29] for saturation pool boiling from upward facing surfaces of different metals, including copper (Bi = 0.9). The normalized values in Figure 6 (a) for the 12.8 mm thick section, however, were less than unity and decreased with increased water subcooling (Figure 6 (a)). Similar results are delineated in Figure 6 (b), where for Biot number $\geq$ 0.008 the normalized saturation and subcooled surface average minimum film boiling heat fluxes of the 20 mm and 30 mm thick sections were equal to unity and independent of Biot number. For the 12.8 mm thick section, however, the normalized q_{min} values were higher than unity.

The results presented in Figs. 4 - 6, clearly demonstrate that the boiling curves of the 20 and 30 mm thick copper sections with a curved surface, and not those of the 12.8 mm thick section, were representative of quasi steady-state. Also, the maximum heat flux values for the two thicker sections were representative of the quasi steady-state critical heat flux.

Pool Boiling Curves

Figures 7(a) - 7(d) present the local pool boiling curves for the 20 mm thick section. The local inclination varied from $\theta = 0^{o}$ (lower most position, TC#1) to $\theta = 8.26^{o}$ (near the edge of the surface, TC#6). As shown in these figures, nucleate boiling can be divided into two distinct regions: (a) *a high wall superheat*, where nucleate boiling heat flux increased as local inclination decreased and (b) *a low wall superheat*, where nucleate boiling heat flux increases with increased inclination. As delineated in figures 7(a) - 7(d), nucleate boiling heat flux at high wall superheat and the maximum heat flux were highest at $\theta = 0^{o}$ (lower most position) and decreased as θ increased. The dependence of nucleate boiling heat flux on surface inclination was opposite to that reported for inclined flat surfaces by Beduz et al [2] and Nishikawa et al. [9] in their steady-state experiments and by Guo and El-Genk in their quenching experiments [15,16]. Figure 7a shows the transition from the high wall superheat to low wall superheat nucleate boiling region occurred at ΔT_{sat} ~ 13 K in saturation pool boiling and increased to 15 K and 15.5 K at 5 K and both 10 K, and 14 K subcooling, respectively.

The enhanced nucleate boiling at the low inclination positions on the curved surfaces at high wall superheat was due to the observed high nucleation density and efficient bubble release. The lower nucleate boiling heat fluxes at the higher inclination positions, however, were caused by the accumulation of vapor generated at the lower positions on the surface. In nucleate boiling at high wall superheat, visual observations and video images of the boiling surface in the experiments showed intense bubble nucleation and growth occurring in the middle portion of the surface, accompanied by a pulsating radial motion of bubbles and vapor release from the edge of the test section, as was recently reported in large scale tests [19].
In nucleate boiling at low wall superheat, the rate and density of bubble nucleation in the middle portion of the surface decreased, but intensified in the outer portion of the surface, causing the nucleate boiling heat flux to increase at higher location on the surface. The enhancement in nucleate boiling in the outer portion of the surface could be caused by sliding bubbles and mixing in the boundary layer near the lower locations on the surface. Because vapor bubbles released readily from the edge of the boiling surface, little vapor accumulated at higher locations. In the transition and film boiling regimes, the dependence of the boiling heat flux on θ was opposite to that in nucleate boiling at low wall superheat, but the same as for the maximum heat flux and in nucleate boiling at high wall superheat. Also, the transition from film to transition boiling was somewhat

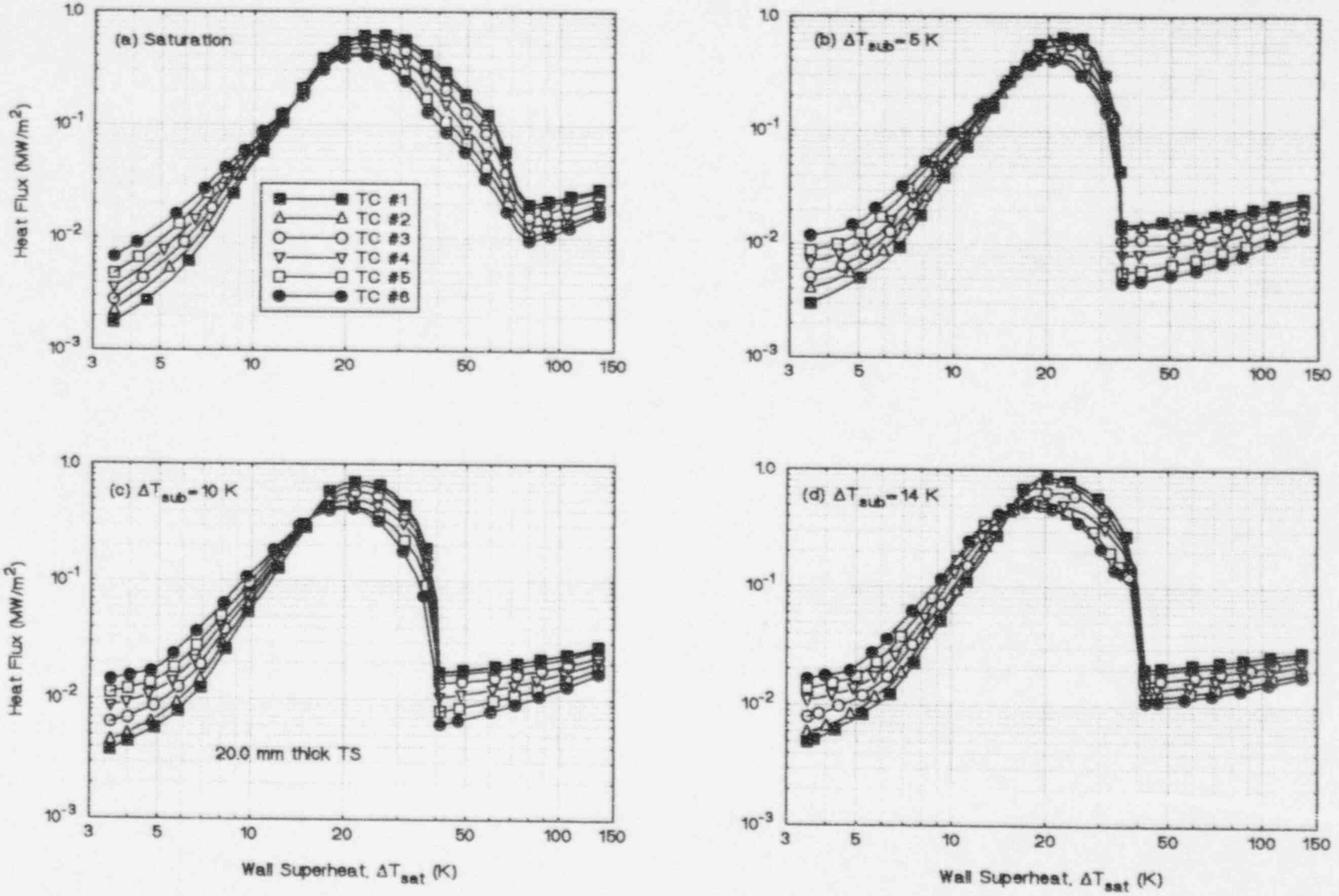

Fig. 7. Effect of water subcooling on local pool boiling curves for the 20 mm thick section.

sharper at the lowermost position ($\vartheta=0^{o}$) than at the higher inclinations and in subcooled boiling. The wall superheat corresponding to q_{min} was almost independent of local inclination, but increased with increased subcooling (Figs. 7(b) - 7(d)).

Effect of Water Subcooling

Figures 4 and 5 show the local maximum and minimum film boiling heat fluxes increased with decreased inclination and/or increased subcooling. Figure 8 also shows that the heat flux in all boiling regimes increased as water subcooling increased. However, at saturation, q_{min} and the corresponding wall superheat were significantly higher than those in subcooled boiling. The high q_{min} values for saturation boiling was caused by the quenching mechanism of film boiling. Visual observations and subsequent examination of the video images of the boiling surface showed the destabilization and collapse of the vapor film in saturation boiling experiments was hydrodynamic in nature, but thermally driven in subcooling boiling. In saturation film boiling, all heat released from the surface was consumed in the generation of vapor. The flow of vapor in the boundary layer caused the film thickness to be smaller at the lowermost position than near the edge of the test section surface [30]. At high wall superheat, the intermittent release of vapor slugs from the periphery of the swelled vapor film caused the vapor/liquid interface to oscillate repetitively, then fully stabilized as excess vapor in the film was released. Eventually, as the surface temperature decreased, induced film oscillations destabilized and collapsed the vapor film inducing surface rewetting [30] and, hence, marking the beginning of transition boiling. In both saturation and subcooled boiling, video images of the surface showed the destabilization front moving radially over the surface as film boiling gave the way to transition boiling; surface rewetting occurred first at the lowermost position and moved radially outward with time in transition boiling [30].

In subcooled film boiling, only a small fraction of the heat released from the surface was consumed by vapor generation; the largest fraction was conducted through the vapor film to the underlying water pool and removed by natural convection. Initially, vapor generated at the lower positions of the film accumulated and increased the film thickness at higher locations. No vapor, however, was seen released from the periphery of the vapor film, apparently due to condensation. As the surface temperature decreased, less vapor was generated, and the film thickness continued to decrease due to condensation. Eventually, the vapor film collapsed ensuing surface rewetting, where wall temperature corresponds to the minimum film boiling heat flux. Because of the different rewetting mechanisms, the values of q_{min} and of the corresponding wall superheat in saturation boiling were much higher than in subcooled boiling and the minimum film thickness prior to surface rewetting was significantly smaller (~ 50 μm versus ≥ 80 μm in subcooled boiling) [30]. The duration of film boiling in saturation boiling (~ 384 s) was also much shorter than in subcooled boiling. The film boiling duration for the latter decreased as water subcooling increased (713 s, 540 s, and 448 s for ΔT_{sub} of 5 K, 10 K, and 14 K, respectively), resulting in higher values for both q_{min} and the corresponding wall superheat.

Figure 9a delineates the effect of water subcooling on the surface average Biot number. In film boiling and in the lower portion of transition boiling (ΔT_{sat} > 33 - 48 K), Bi < 0.1, suggesting that the heat from the surface was easily removed by evaporation and convection in the water pool. In the upper portion of both transition boiling (ΔT_{sat} < 33 - 48 K) and in nucleate boiling at ΔT_{sat} < 5.2 - 7.2 K, Bi > 0.1, indicating the effectiveness of heat removal from the surface by boiling. Figure 9a also shows Bi corresponding to q_{MHF} was in excess of 1.0 in saturation pool boiling, but decreased with increased water subcooling.

Maximum Heat Flux

The local and surface average values of the maximum heat flux and the corresponding wall superheats, for saturation and subcooled boiling are presented in Figs. 9b and 9c, respectively. Figure 9b shows the maximum heat flux decreased with increased local inclination, but increases with increased water subcooling. Figure 9b indicates that the wall superheat corresponding to either the local or the average maximum heat flux generally decreased with increased surface inclination and/or increased subcooling. Figure 9b also shows that for a given pool temperature, the lower inclination positions on the surface were more coolable than indicated by $\overline{MHF}$. At higher inclination positions, however, $\overline{MHF}$ overestimated the local surface coolability, whereas

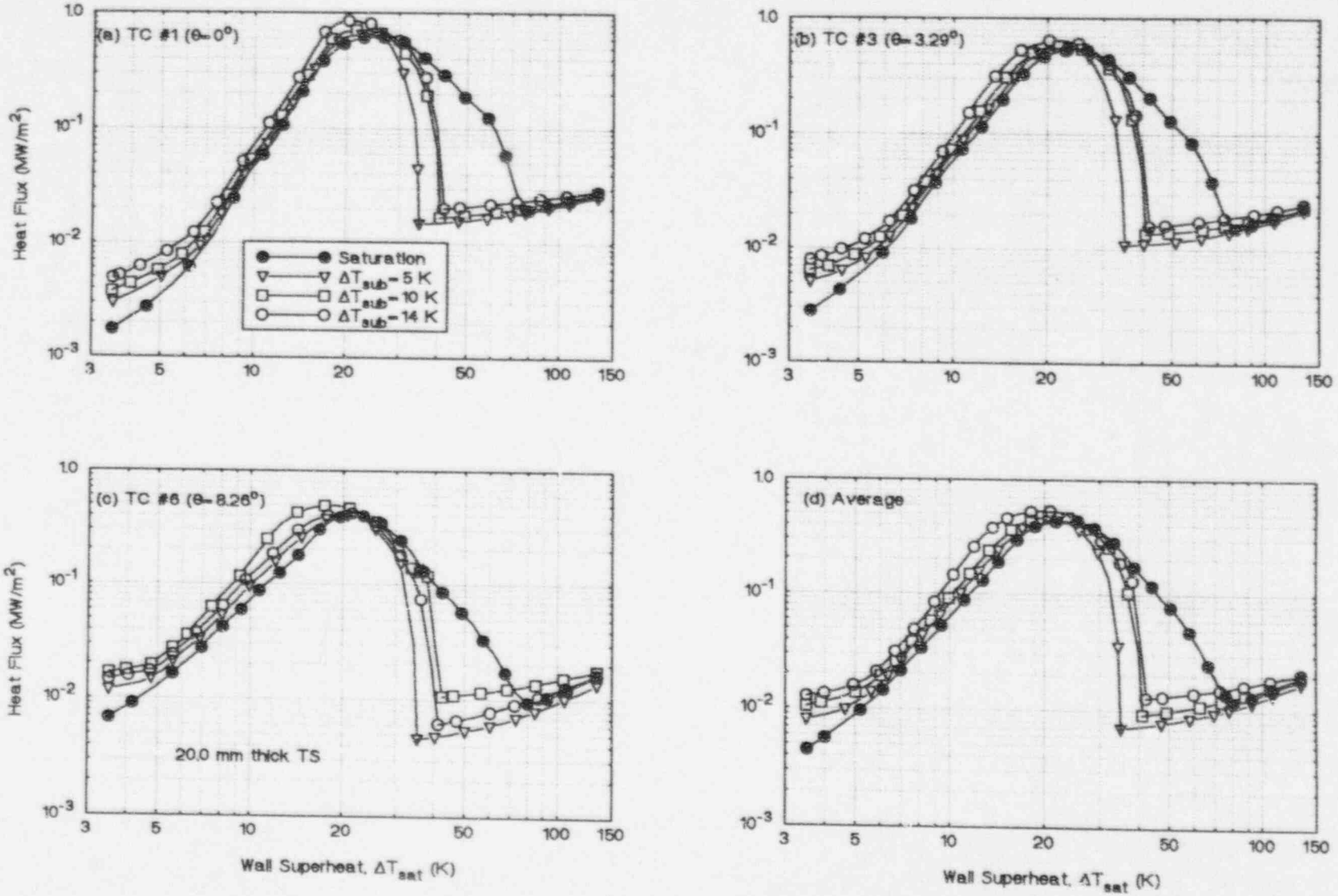

Fig. 8. Effect of water subcooling on local and surface average pool boiling for the 20 mm thick section.

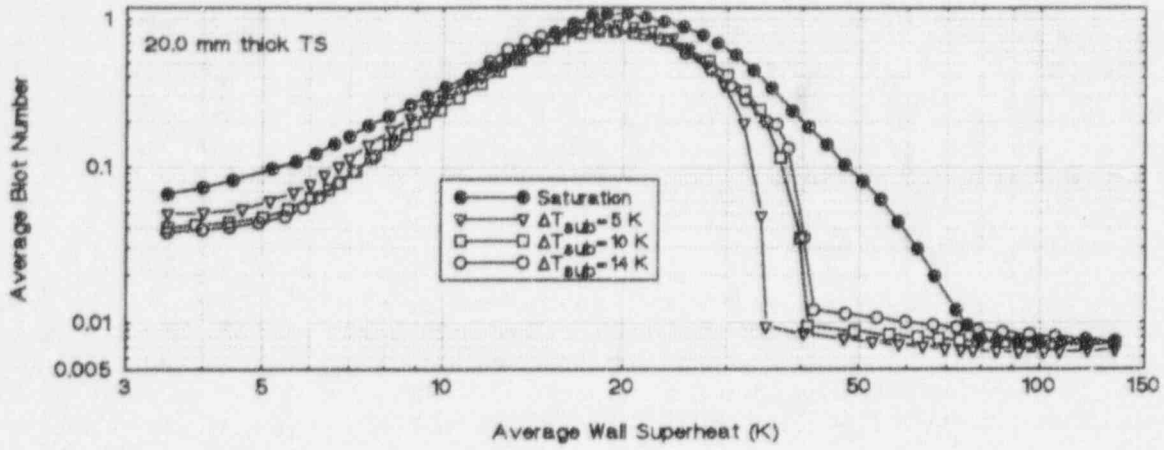

Fig. 9a. Effect of water subcooling on the average Biot numbers for the 20 mm thick section.

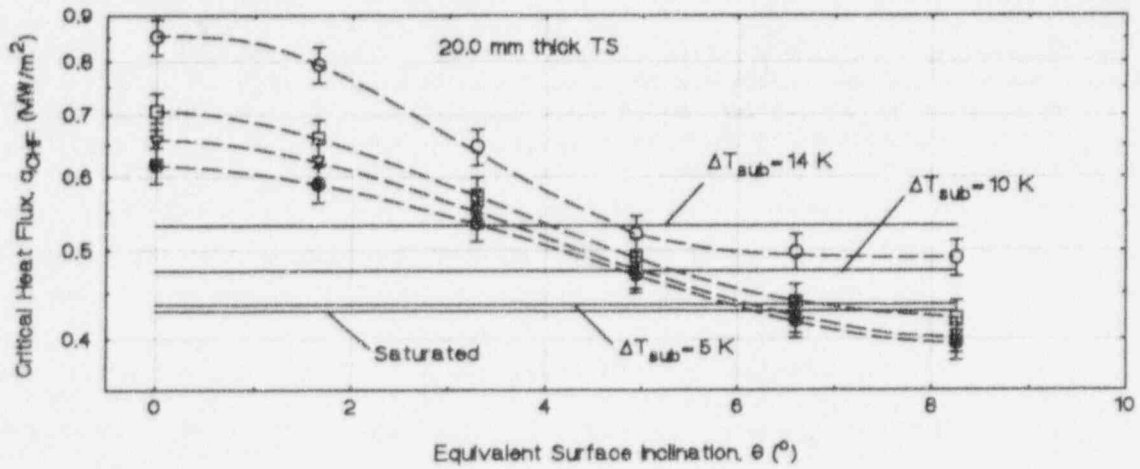

Fig. 9b. A Comparison of the local and surface average maximum pool boiling heat fluxes.

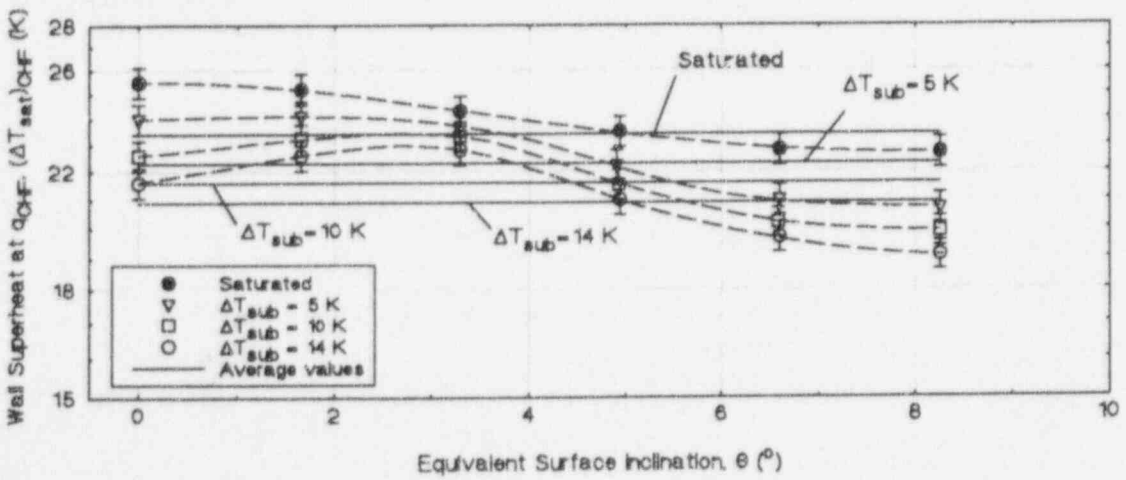

Fig. 9c. A Comparison of the wall superheats corresponding to the maximum heat fluxes.

the extent of the high and low coolability portions of the surface strongly depend on water subcooling. For example, at saturation $\overline{MHF}$ underestimated the coolability of the portion of the surface with $\theta \leq 6^{o}$, but overestimates the coolability of the outer portion of the surface with higher inclination. At 14 K water subcooling, the extent of the inner portion of the surface with MHF > $\overline{MHF}$ extends only to $\theta < 5^{o}$. Therefore, care should be taken when using the surface average maximum heat flux, $\overline{MHF}$, to assess the coolability of the entire curved surface.

Minimum Film Boiling Heat Flux

Figures 10a and 10b compare the local and the surface average values of the minimum film boiling heat flux and the corresponding wall superheats at different water subcooling. Figure 10a shows that the minimum film boiling heat flux decreases with increased inclination and/or decreased subcooling. At saturation, however, the minimum film boiling heat flux was significantly higher than that at 5 K subcooling, and only slightly lower than that for 14 K subcooling. Although independent of surface inclination, wall superheats corresponding to q_{min} in subcooling boiling increased with increased water subcooling (Fig. 10b).

Effect of surface curvature

As indicated earlier, the local and surface average pool boiling curves of the 12.8 mm thick section were not representative of the quasi steady-state phenomena. Nevertheless, a comparison of the surface average pool boiling curve for the 12.8 mm thick section with that of a flat surface section of the same dimensions and material [13], would quantify the effect of surface curvature on pool boiling (Fig. 10c). Figure 10c shows the pool boiling heat fluxes for the curved surface to be significantly higher in film boiling, transition boiling and nucleate boiling at high wall superheat. The $\overline{MHF}$ for the curved surface (0.43 MW/m^2) is almost twice that of the flat surface (0.21 MW/m^2) and the average the minimum film boiling heat flux, $\overline{q_{min}}$, (13 kW/m^2) is more than six times higher than that for the flat surface (2 kW/m^2). The wall superheat corresponding to $\overline{MHF}$ (23.5 K) and $\overline{q_{min}}$ (90 K) is 11.5 K and 60 K higher than those for the flat surface, respectively. In nucleate boiling at low wall superheat, however, the heat fluxes for the flat surface section are higher than those for the curved surface, at the same wall superheat. The high nucleate boiling heat flux for the flat surface section could be caused by the mixing induced in the boundary layer by the sliding vapor bubbles.

Critical Heat Flux Correlation

The local values of q_{CHF}, plotted in Figure 9b, were correlated using the general form suggested by Kutateladze [31], Leinhard and Dhir [32], and El-Genk and Guo [16] except that the coefficient $C_{CHF}(\theta)$ is a function of the inclination angle on the boiling surface and water subcooling:

$$q_{CHF}(\theta, \Delta T_{sub}) = C_{CHF}(\theta, \Delta T_{sub}) \sqrt{\rho_V}\, h_{fg} \left[\sigma g(\rho_l - \rho_V)\right]^{0.25}. \qquad (8)$$

The coefficient $C_{CHF}(\theta, \Delta T_{sub})$ is given as (Figure 11):

$$C_{CHF}(\theta, \Delta T_{sub}) = a \cdot \exp(-b \cdot \theta^2) + c. \qquad (9)$$

The coefficients a, b and c in Eq. (9) are functions of water subcooling (Figure 12a):

$$a(\Delta T_{sub}) = 7.86 \times 10^{-5} (\Delta T_{sub})^2 + 0.028, \qquad (9a)$$

$$b(\Delta T_{sub}) = -2.036 \times 10^{-4} (\Delta T_{sub})^2 - 0.039, \qquad (9b)$$

$$c(\Delta T_{sub}) = 6.15 \times 10^{-5} (\Delta T_{sub})^2 + 0.044. \qquad (9c)$$

As shown in Figure 11, the coefficient "C_{CHF}" (Eq. 8) decreased with increased inclination angle. The coefficients "a", "b", "c" are functions of water subcooling only. As delineated in Figure 12a, the coefficients "a" and "c" increased, but coefficient "b" decreased with increased subcooling. Figure 12b shows that the

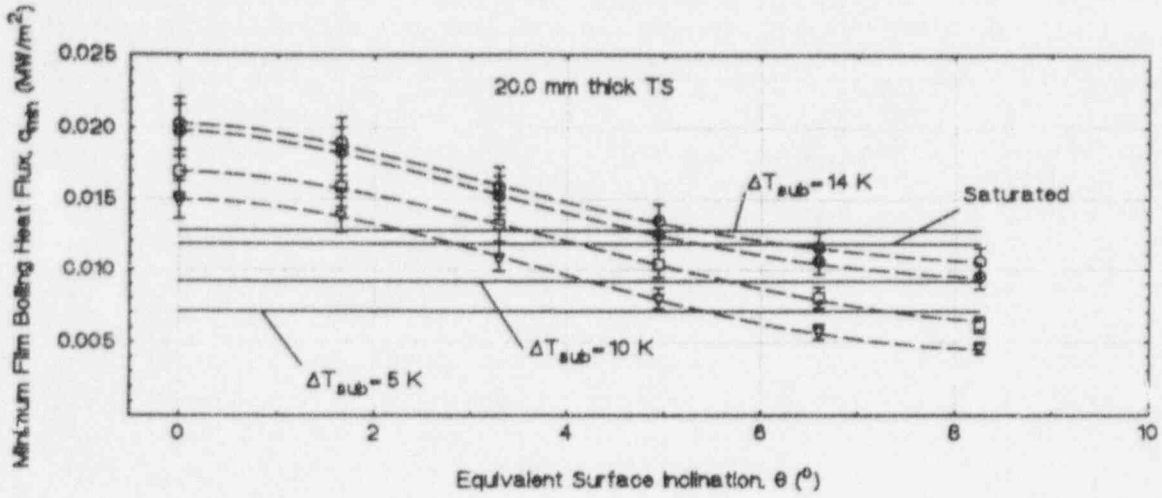

Fig. 10a. A Comparison of the local and surface average minimum film boiling heat fluxes.

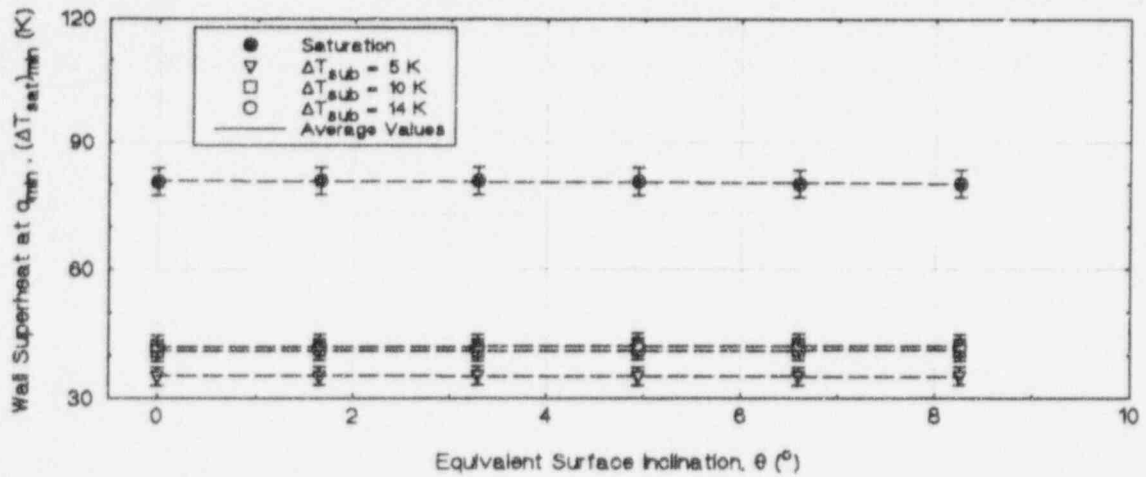

Fig. 10b. A Comparison of the wall superheats corresponding to the minimum film boiling heat fluxes.

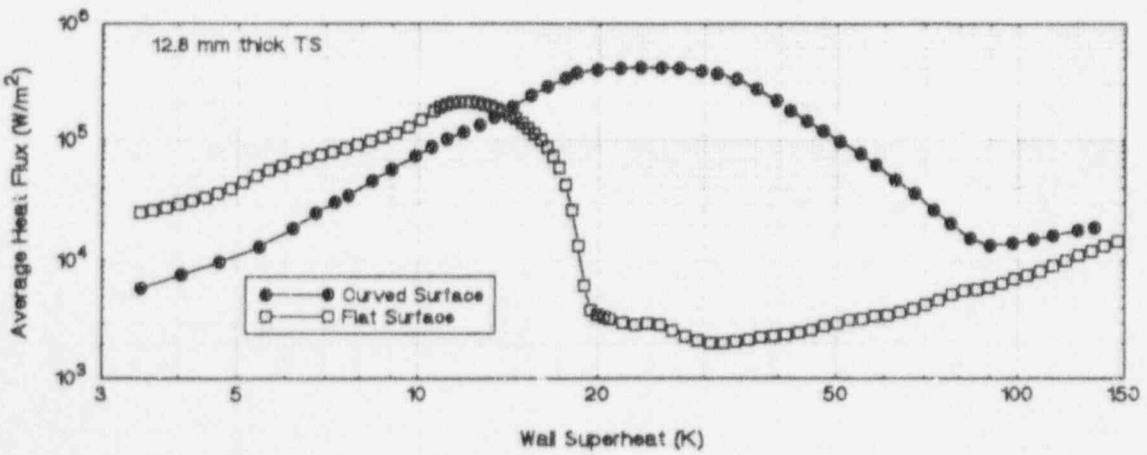

Fig. 10c. Effect of surface curvature on surface average pool boiling curves for the 12.8 mm thick section.

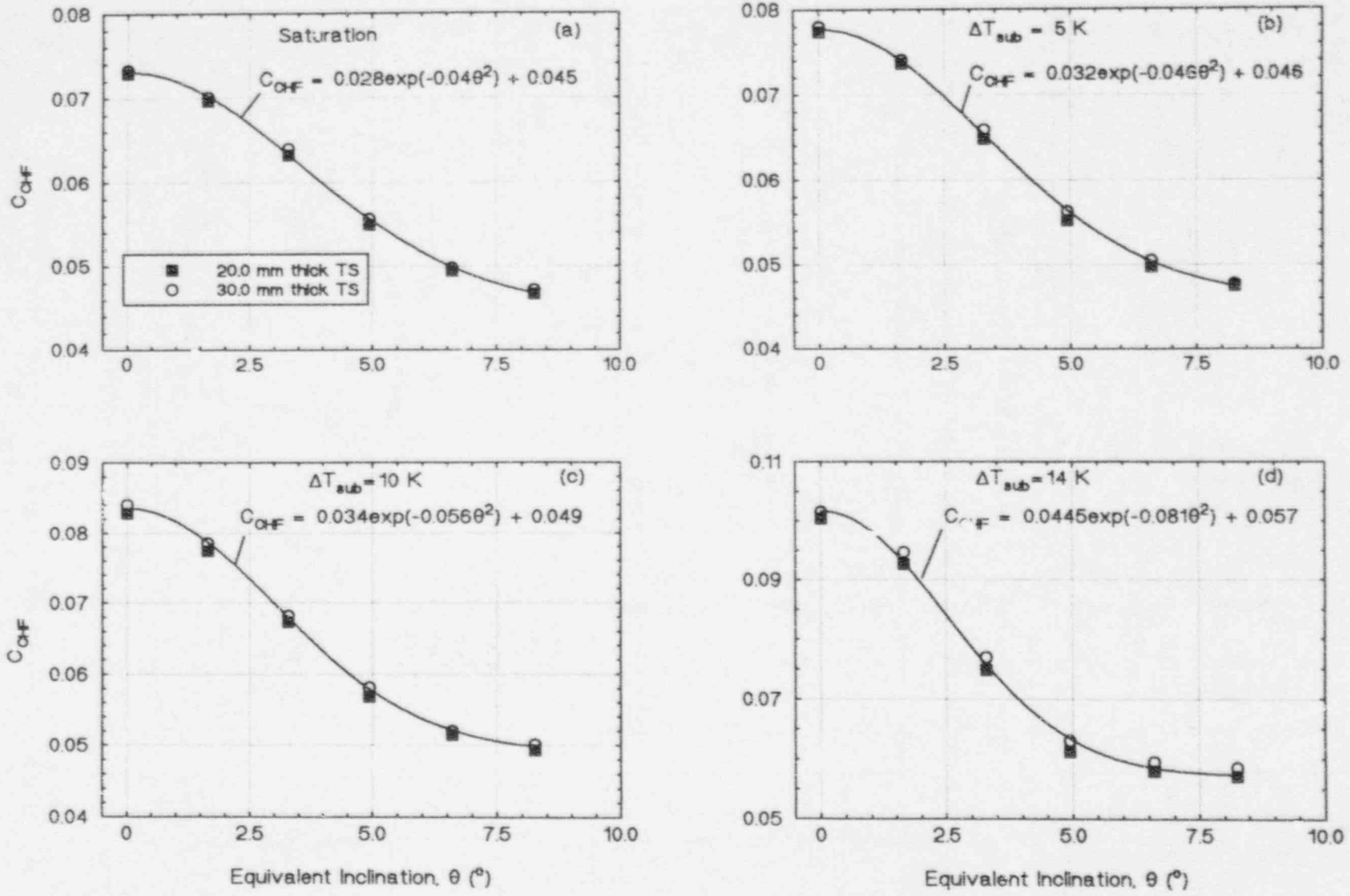

Fig. 11. Critical heat flux coefficients as functions of inclination.

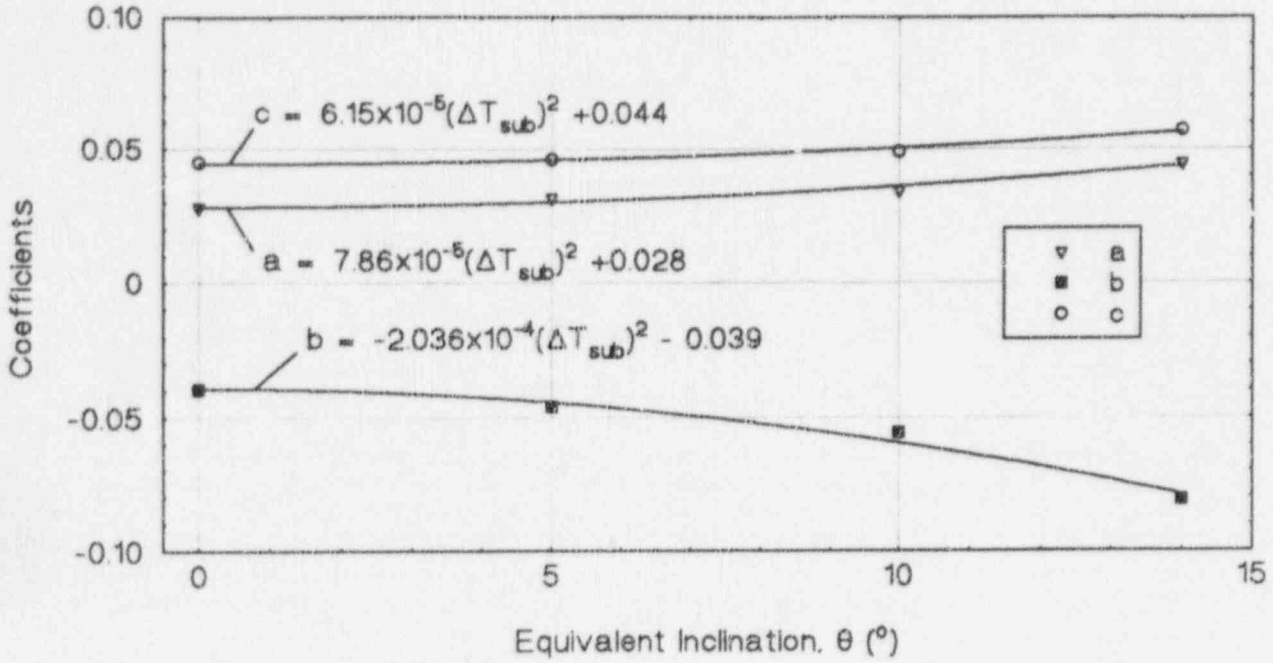

Fig. 12a. Critical heat flux coefficients as functions of water subcooling.

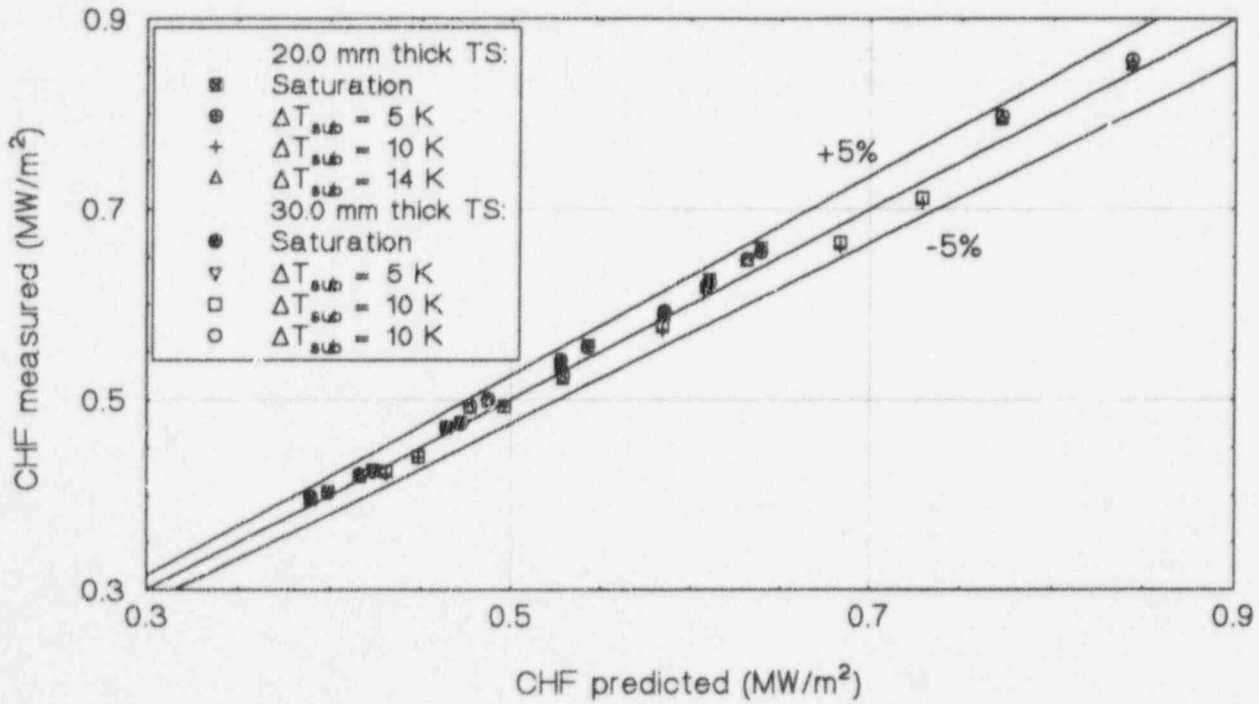

Fig. 12b. A comparison of measured and calculated critical heat flux values.

correlation for the local values of CHF (Eq. 8) was within ± 5 % of the data. Note that the validity of Eq. (8) is limited to the present data for which $\Delta T_{sub} < 14$ K.

DISCUSSION

The results of the present experiments for a small convex, downward-facing surfaces clearly demonstrate the important effect of surface curvature and water subcooling on pool boiling heat transfer. The flat surface nucleate boiling heat flux results at high wall superheat, which neglected upstream effects, were opposite to those obtained for convex surfaces, confirming that flat surface data are not applicable to convex surfaces. For convex surfaces, vapor generated at low locations accumulated at high positions, resulting in lower heat flux at these position, but the highest heat flux at the lowermost position. The effect of sliding bubbles on enhancing nucleate boiling heat transfer at low wall superheat as well as the accumulation of vapor on the surface at high wall superheat will greatly depend on the available surface area for both vapor generation and release, water subcooling, and the material of the wall, or Biot number. Some of the factors affecting the scalability of the present results to ALWR cooling of the vessel lower head are size and material properties. The results of the present small scale experiments showed incipient rewetting of the surface as well as the maximum heat flux to occur first at the lowermost position, conditions for larger size surface, however, could be different. For example, surface rewetting on the surface of ALWR vessel bottom head could occur randomly at more than one location owing to the vapor film thickness and presence of external hydrodynamic forces in the water pool. Also, the stainless-steel of the vessel wall has very poor thermal properties compared to those of copper, resulting in different, albeit lower, pool boiling heat fluxes. The surface conditions are also a major consideration in scaling up the results to ALWR vessel cooling.

In ALWR core meltdown accident, the heat removal from the outer surface of the vessel lower head will be mostly by nucleate boiling. The surface average heat flux has been estimated by Henry et al. [23] to be ~ 0.21 MW/m^2. This value is much smaller than the maximum heat flux values reported in this paper for copper. Finally, the insulation on the outer surface of the vessel lower head would also affect the boiling phenomena, which was not investigated in the presented work. Therefore, it is important to note that the present results are limited in scope and could not directly be applied to ALWR vessel cooling without developing the proper scaling law, which was outside the scope of this work. The results of the present experiments, however, may be viewed only as a very preliminary step in the physical modeling process. On an optimistic note, however, the present results showed that mixing caused by sliding bubbles could enhance heat transfer and increase pool boiling heat flux at low wall superheat; the measured values of the maximum heat flux were much higher than the highest surface high flux expected following a core meltdown accident in an ALWR [23]. Because of such lower surface heat flux, water subcooling in the lower cavity, and the large surface area of the vessel bottom head, vapor accumulation at higher locations on surface is not expected to significantly affect heat transfer.

SUMMARY AND CONCLUSIONS

Saturation and subcooled pool boiling data of the 20 and 30 mm thick sections, but not that of 12.8 mm thick section, was representative of quasi steady-state. Maximum and the minimum film boiling heat fluxes for saturation and subcooled boiling were independent of wall thickness > 20 mm. Local and average maximum heat fluxes increased, but the corresponding wall superheat decreased, with increased water subcooling, however, local values of both decreased with increased surface inclination. Local minimum film boiling heat flux also decreased with increased surface inclination, however, the corresponding wall superheat was independent of surface inclination, but increased with increased subcooling. The minimum film boiling heat flux and the corresponding wall superheat for saturation boiling were higher than those for subcooled boiling at $\Delta T_{sub} < 14$ K; surface rewetting was hydrodynamically driven while that in the latter was thermally driven. For the 12.8 mm thick sections, $\overline{MHF}$ for the convex surface (0.41 MW/m^2) was almost twice and $\overline{q_{min}}$ (13 kW/m^2) was more than six times higher than that of the flat surface section of the same dimensions.

Nucleate boiling from convex downward-facing surfaces can be divided into two distinct regions: *a high wall superheat*, where nucleate boiling heat flux decreased with increased local inclination, and *a low wall superheat*, where nucleate boiling heat flux increased with increased inclination. Wall superheat corresponding to the transition from the high wall superheat to low wall superheat nucleate boiling increased with increased water subcooling. The dependence of nucleate boiling heat flux on local surface inclination was opposite to that reported earlier by other investigators for flat surfaces. In nucleate boiling at low wall

superheat, however, pool boiling heat fluxes for the flat surface were higher than these for the curved surface because of the mixing caused by sliding bubbles. Thus, pool boiling heat transfer from flat surfaces is not directly applicable to convex surfaces, particularly in nucleate boiling.

Acknowledgments--This research is sponsored by the University of New Mexico's Institute for Space and Nuclear Power Studies.

REFERENCES

1. Anderson, R. P. and Bova, L., "The Role of Down facing Burnout in Post-accident Heat Removal," *Trans. Am. Nucl Soc.*, 14, 294-304 (1971).
2. Beduz, C., Scurlock, R. G. and Sousa, A. J., "Angular Dependence of Boiling Heat Transfer Mechanisms in Liquid Nitrogen," *Adv. in Cryogenic Eng.* (R. W. Fast, ed.), Plenum Press, New York, 33, 363-370 (1988).
3. Chen, L. T., "Heat Transfer to Pool Boiling Freon From Inclined Heating Plate," *Int. J. Heat Mass Trans.*, 5, 111-120 (1978).
4. Githinji, P. M. and Sabersky, R. H., "Some Effects on the Orientation of the Heating Surface in Nucleate Boiling," *J. Heat Trans.*, 85, 379 (1963).
5. Ishigai, S., Inoue, K., Kiwaki, Z. and Inai, T., "Boiling Heat Transfer From a Flat Surface Facing Downward," *Proc. Int. Heat Trans. Conf*, Paper No. 26 (1961).
6. Jung, D. S., Venart, J. E. S. and Sousa, A. C. M., "Effects of Enhanced Surfaces and Surface Orientation on Nucleate and Film Boiling Heat Transfer in R-11," *Int. J. Heat Mass Trans.*, 30 (12), 2627-2639 (1987).
7. Lyon, D. N., "Boiling Heat Transfer and Peak Nucleate Boiling Fluxes in Saturated Liquid Helium Between the λ and Critical Temperatures," *Int. Adv. in Cryogenic Eng.*, 19, 371-378 (1964).
8. Marcus, B. D. and Dropkin, D., "The Effect of Surface Configuration on Nucleate Boiling Heat Transfer," *Int. J. Heat Mass Trans.*, 6, 863-867 (1963).
9. Nishikawa, K., Fujita, Y., Uchida, S., and Ohta, H., "Effect of Heating Surface Orientation on Nucleate Boiling Heat Transfer," *ASME-JSME Thermal Engng Joint Conf*, 1, 129-136 (1983).
10. Nishio, S. and Chandratilleke, G. R., "Steady-State Pool Boiling Heat Transfer to Saturated Liquid Helium at Atmospheric Pressure," *JSME Int. J. Series I*, 32(4), 639-945 (1989).
11. Seki, N, Fukushako, S., and Torikoshi, K., "Experimental Study on the Effect of Orientation of Heating Circular Plate on Film Boiling Heat Transfer for Fluorocarbon Refrigerant R-11," *J. Heat Trans.*, 100, 624-628 (1978).
12. Vishnev, I. P., Filatov, I. A., Vinokur, Ya. G., Gorokhov, V. V., and Svalov, G. G., "Study of Heat Transfer in Boiling of Helium on Surfaces with Various Orientations," *Heat Trans.-Sov. Res.*, 8(4), 104-108 (1976).
13. Guo, Z. and El-Genk, M. S., "An Experimental Study of Saturated Pool Boiling from Downward Facing and Inclined Surfaces," *Int. J. Heat Mass Trans.*, 35(9), 2109-2117 (1992).
14. Guo. Z. and M. S. El-Genk , "Effects of Liquid Subcooling on the quenching of Inclined and Downward-Facing Flat Surfaces in Water," *AIChE Symp. Series No. 288*, 88, 241-248 (1992).
15. El-Genk, M. S. and Z. Guo, "Saturated and Subcooled Pool Boiling from Downward-Facing and Inclined Surfaces," *Flow and External Flow Boiling* (V. K. Dhir and A. E. Bergles, eds.), ASME, NY, 243-249 (1992).
16. El-Genk, M. S. and Z. Guo, "Transient Boiling from Inclined and Downward-Facing Surfaces in a Saturated Pool," *Int. J. Refrig.*, 16(6), 414-422 (1993).
17. Cornwell, K. and R. B. Schuller," A Study of Boiling Outside a Tube Bundle Using High Speed Photography," Int. J. Heat and Mass Transfer, 25 (5), 683 - 690 (1982).
18. El-Genk, M. S., A. G. Glebov and Z. Guo, "Pool Boiling from Downward-Facing Curved Surface in Saturated Water," *Proc. 10th Int. Heat Trans. Conf.*, Brighton, England, 5, 45 - 50 (1994).
19. Chu, T. Y., B. L. Bainbridge, J. H. Bents, and R. B. Simpson, *Observation of Quenching of Downward-Facing Surfaces*, SANDIA Report, SAND93-0688·UC-940, Sandia National Laboratories, Albuquerque, NM (January 1994)
20. Theofanous, T. G., Syri, S., Salmassi, T., Kymalainen, O. and Tuomisto, H., "Critical Heat Flux Through Curved, Downward Facing, Thick Walls", *Nuclear Engineering and Design*, 151, 247-258 (1994).
21. O'Brien, J. E. and G. L. Hawkes, "Thermal Analysis of a Reactor Lower Head with Core Relocation and External Boiling Heat Transfer," *AIChE Symp. Series No. 283*, 87, 159-168 (1991).
22. Park, H. and V. K. Dhir, "Steady-State Thermal Analysis of External Cooling of a PWR Vessel Lower Head," *AIChE Symp. Series No. 283*, 87, 1-7 (1991).
23. Henry, R. E., J. P. Burelbach, R. J. Hammersley, C. E. Henry, and G. T. Klopp, "Cooling of Core Debris Within the Reactor Vessel Lower Head," *J. Nucl. Tech.*, 101, 385-399 (1993).
24. Westwater, J. W., J. J. Hwalek, and M. E. Irving, "Suggested Standard Method for Obtaining Boiling Curves by Quenching," *J. Ind. Eng. Fundam.*, 25, 685-692 (1986).

25. Savitzky, A. and M. J. E. Golay, " Smoothing and Differentiation of Data by Simplified Least Square Procedures", *J. Eng. Anal. Chem.*, 36, 1627-1639 (1964).
26. Roache, P. J., *Computational Fluid Dynamics*, Hermosa Publishers, Albuquerque, NM (1982)
27. Patankar, S. V., *Numerical Heat Transfer and Fluid Flow*, Hemisphere Publishing Inc., Washington, DC. (1980).
28. Kline, M. and F. A. McClintock, "Describing uncertainties in single-sample experiments," *Mechanical Engineering* (January 3-8, 1953).
29. Peyayopanakul, W. and J. W. Westwater, "Evaluation of the Unsteady-State Quenching Method for Determining Boiling Curves," *Int. J. Heat and Mass Trans.*, 21, 1437-1445 (1978).
30. El-Genk, M. S. and A. G. Glebov, "Film Boiling from a Downward-Facing Curved Surface in Saturated and Subcooled Water", *Int. J. Heat and Mass Transfer*, in print, (1995).
31. Kutateladze, S. S., "Boiling Heat Transfer", *Int . J. Heat Mass Trans.*, 4, 31-45 (1961).
32. Lienhard, J. H. and V. K. Dhir, "Hydrodynamic prediction of peak pool-boiling heat fluxes from finite bodies", *Trans. ASME J. Heat Transfer*, 95, 152-158 (1973).

Numerical Modeling of Condensation from Vapor-Gas Mixtures for Forced Down flow Inside a Tube

Ruey Y. Yuann
Taiwan Power Company
242, Roosevelt Rd. Sec. 3
Taipei Taiwan R.O.C

Virgil E. Schrock
Department of Nuclear Engineering
University of California at Berkeley
Berkeley, CA 94720, U.S.A

Xiang M. Chen
GE Nuclear Energy
P.O. Box 780, M/C F21
Wilmington, NC 28402

ABSTRACT

Laminar film condensation is the dominant heat transfer mode inside tubes. In the present paper direct numerical simulation of the detailed transport process within the steam-gas core flow and in the condensate film is carried out. The problem was posed as an axisymmetric two dimensional (r, z) gas phase inside an annular condensate film flow with an assumed smooth interface. The fundamental conservation equations were written for mass, momentum, species concentration and energy in the gaseous phase with effective diffusion parameters characterizing the turbulent region. The low Reynolds number two equation k-ε model was employed to determine the eddy diffusion coefficients. The liquid film was described by similar formulation without the gas species equation. An empirical correlation was employed to correct for the effect of film waviness on the interfacial shear.

A computer code named COAPIT(Condensation Analysis Program Inside Tube) was developed to implement numerical solution of the fundamental equations. The equations were solved by a marching technique working downstream from the entrance of the condensing section. COAPIT was benchmarked against experimental data and overall reasonable agreement was found for the key parameters such as heat transfer coefficient and tube inner wall temperature. The predicted axial development of radial profiles of velocity, composition and temperature and occurrence of metastable vapor add insight to the physical phenomena.

INTRODUCTION

In the nuclear industry the Simplified Boiling Water Reactor (SBWR) is an advanced light water reactor being under development by a team led by General Electric. The main feature of its containment design is to provide passive removal of core decay heat and Reactor Coolant System sensible heat. This Passive Containment Cooling System (PCCS) is designed such that the vapor-gas mixture formed by the mixing of reactor steam and residual containment gas during accidents (such as the design basis accidents, etc.) will flow under the influence of natural forces (not by pumping) to PCCS condenser units which utilize vertical 2 inch diameter stainless tubes immersed in a pool of atmospheric pressure water outside containment. The heat will be rejected to the atmosphere through vaporization of pool water. The natural forces are due to the pressure difference between drywell and wetwell. Condensate drains by gravity back into the Gravity Drain Cooling System tank while the residual steam-gas mixture is vented into the pressure suppression pool located in the wetwell.

Since the presence of noncondensable gas will decrease the condensation heat transfer effectiveness and since the heat transfer coefficients vary greatly along the length of the condensing tube, a detailed knowledge of the local heat transfer characteristics is important to the successful design of the PCCS condensers. In support of the SBWR design effort on this aspect, single tube laboratory experiments have been carried out by Vierow [1], Ogg [2], Siddique [3] and Kuhn et al.[4] to develop working heat transfer correlations. In the present paper we have attempted to carry out direct numerical simulation of the detailed transport processes within the vapor-gas core and in the condensate film.

The classic Nusselt [5] integral analysis of laminar film condensation of a quiescent pure vapor on an isothermal vertical plate incorporated several simplifying idealizations. Theoretical

analyses subsequent to that of Nusselt have attempted to relax one or more of these assumptions. Rohsenow [6] considered the effects of subcooling in the condensate film and nonlinear temperature distributions. Sparrow and Gregg [7] presented a similarity solution of boundary-layer analysis for laminar film condensation on a vertical surface. Koh et al. [8] extended the similarity solution of Sparrow and Gregg and investigated the effect of interfacial drag on heat transfer under natural convection. The effect of waves on laminar film condensation was investigated by Hirshburg and Florschuetz [9]. They found that the experimental heat transfer coefficients are consistently above the Nusselt prediction and attributed this deficiency to the interfacial waves. Seban [10] proposed using known information about fully-developed turbulent pipe flow to calculate the eddy viscosities in a falling turbulent liquid film. Chun [11] and Chun and Seban [12] considered the condensation heat transfer for smooth liquid film, wavy laminar liquid film, and turbulent liquid film and proposed a general correlation for local heat transfer coefficient. Initial published work on the problem for condensation in the presence of noncondensable gases was concerned with laminar film condensation of vapor from a gas mixture undergoing natural convection on a vertical plate. Either the boundary layer analysis or the heat and mass transfer analogy was employed. Sparrow and Lin [13] considered the boundary-layer type conservation equations for both liquid phase and gaseous phase and obtained similiarity solutions for the case of a vertical isothermal surface assuming constant properties. Minkowycz et al. [14] carried the analysis further to include interfacial resistance, superheating, free convection due to both temperature gradient and concentration gradients, thermal diffusion, and variable properties. The results show that a small bulk concentration of noncondensable gas has a significant effect on the heat transfer rate.

The effect of molecular weight of the noncondensable gas was studied by Al-Diwany and Rose [15] experimentally. Recently Debbi et al. [16] conducted an experiment to investigate the effect of air on steam condensation under turbulent natural convection conditions and found that the heat transfer coefficient decreased slowly with wall subcooling and increased significantly with pressure.

The effects of forced vapor flow on falling film condensation on vertical plates or tubes were examined analytically in an early study by Rohsenow et al. [17]. They presented theoretical arguments and concluded that transition to turbulent film flow occurs at a transition Reynolds number $Re_{f,tr}$ which is dependent on the interfacial shear stress.

The effect of a noncondensable gas is still significant for film condensation under forced vapor-gas flow. Sparrow et al. [18] obtained similarity solutions of the differential conservation equations numerically and by an integral method. In fact the problem is quite nonsimilar in nature because the interface temperature varies along the condensing surface length and the system of boundary layer conservation equations can not be reduced to a set of ordinary differential equations. Denny et al. [19], noting this nonsimilar nature, obtained a solution using a finite-difference method to solve the governing differential equations. It was found that the mass transfer resistance decreases appreciably with increasing mixture velocity. Recently, Kim and Corradini [20] proposed a two-dimensional condensation model using a k - ε model for turbulent vapor-air flow and applied it for the heat transfer calculation inside a nuclear power plant containment in which vapor is condensing from a steam-air mixture on the containment wall.

Dobran and Thorsen [21] investigated forced down flow laminar film condensation of a pure saturated vapor in a vertical tube with fully developed vapor velocity profile at the tube inlet. It was found that the condensation process is governed by five parameters, ratio of vapor Froude number to Reynolds number, Buoyancy number, vapor to liquid viscosity ratio, liquid Prandtl number, and subcooling number. Seban and Hodgson [22] studied laminar film condensation inside a tube with upward vapor flow. Blangetti et al. [23] measured the local heat transfer coefficient for downward pure vapor condensation inside a vertical tube with moderate and high liquid Prandtl number. The experimental results indicate that the transition from laminar to turbulent liquid film is characterized by a minimum Nusselt number.

Borishanskiy et al. [24,25,26] carried out experimental investigations of condensation inside tubes, with and without noncondensable gas. An expression was developed relating the

reduction in the overall pure steam heat transfer coefficient to the inlet mole fraction of the noncondensable nitrogen. No results were obtained on a localized basis. Wang and Tu [27] developed a theory based on the analogy between condensation and the convective transport with boundary suction to reveal the effect of small amounts of noncondensable gas on laminar film condensation of a downward vapor-gas mixture flowing turbulently in a vertical tube. The results show that the effect of noncondensable gas on condensation heat transfer is more significant in tubes than in an unconfined space.

Vierow [1] carried out an experiment using a 22 mm ID vertical tube to study the behavior of a natural circulation condensation loop when operating with a noncondensable gas inventory. This experiment was intended to provide data on the effect of gas upon the local condensation heat transfer coefficient in support of the SBWR PCCS condenser design. A local heat transfer coefficient degradation factor f correlation, based on vapor-gas mixture Reynolds number and local air mass fraction, was obtained [1,28]. Ogg [2] continued the study using forced circulation within a 5.08 cm (2 inch) OD stainless tube similar to that used in SBWR PCCS condensers. Correlations of similar form were developed for bothe steam-air and steam-helium mixtures. Another experiment for condensation inside a Pyrex glass tube was performed by Kageyama [29] to measure radial gas concentration distribution using a miniature wet/dry bulb probe. The diffusion layer theory developed by Peterson et al. [30] was applied to correlate the data, with the driving potential for mass transfer treated as a difference in saturation temperature between the bulk vapor-gas mixture and the condensate interface.

Experiments similar to Ogg's were performed by Siddique [3] at MIT to examine the effect of noncondensable gases on steam condensation under forced convective conditions. Correlations of local Nusselt number were developed in terms of vapor-gas mixture Reynolds number, gas mass fractions in the bulk and at the interface, and Jakob number (based on gas specific heat) for condensation from steam-air and steam-helium mixtures, respectively. Vial [31] reviewed and compared the experimental data and results given by the correlations developed in the programs at UCB and MIT and found a significant difference among them.

Recently, Kuhn [4], using the experience of Vierow, Ogg, and Siddique, developed an improved experimental apparatus using several new and unique features and obtained an extensive new data base for steam-air and steam-helium mixtures. This work is reported by Kuhn, Schrock and Peterson [32] in a paper in the NURETH-7 conference.

In conjunction with these experimental works of Ogg, Kageyama and Kuhn, the present theoretical research work [33] has been undertaken in order to provide more detailed insight on the local condensation heat transfer characteristics for condensation from mixtures flowing downward inside vertical tubes. Figure 1 shows the schematics for the system under study. The vapor-gas mixture enters into the condensing tube at $z = 0$ with fully-developed velocity $V_{z,m}(0, r)$, uniform pressure P_0, uniform temperature $T_{m,0}$, and uniform noncondensable gas mass fraction $\omega_{g,0}$. The steam begins to condense on the tube inner wall of temperature $T_w(z)$ which is maintained below the steam saturation temperature by a forced cooling water flowing upward in an annular cooling jacket. A condensate film is formed at the tube inner wall and a mixture of uncondensed vapor and noncondensable gas flows as a core in the central part of the tube and constitutes a cocurrent annular film two phase flow.

The present paper discusses and presents the main results from this theoretical research work. .

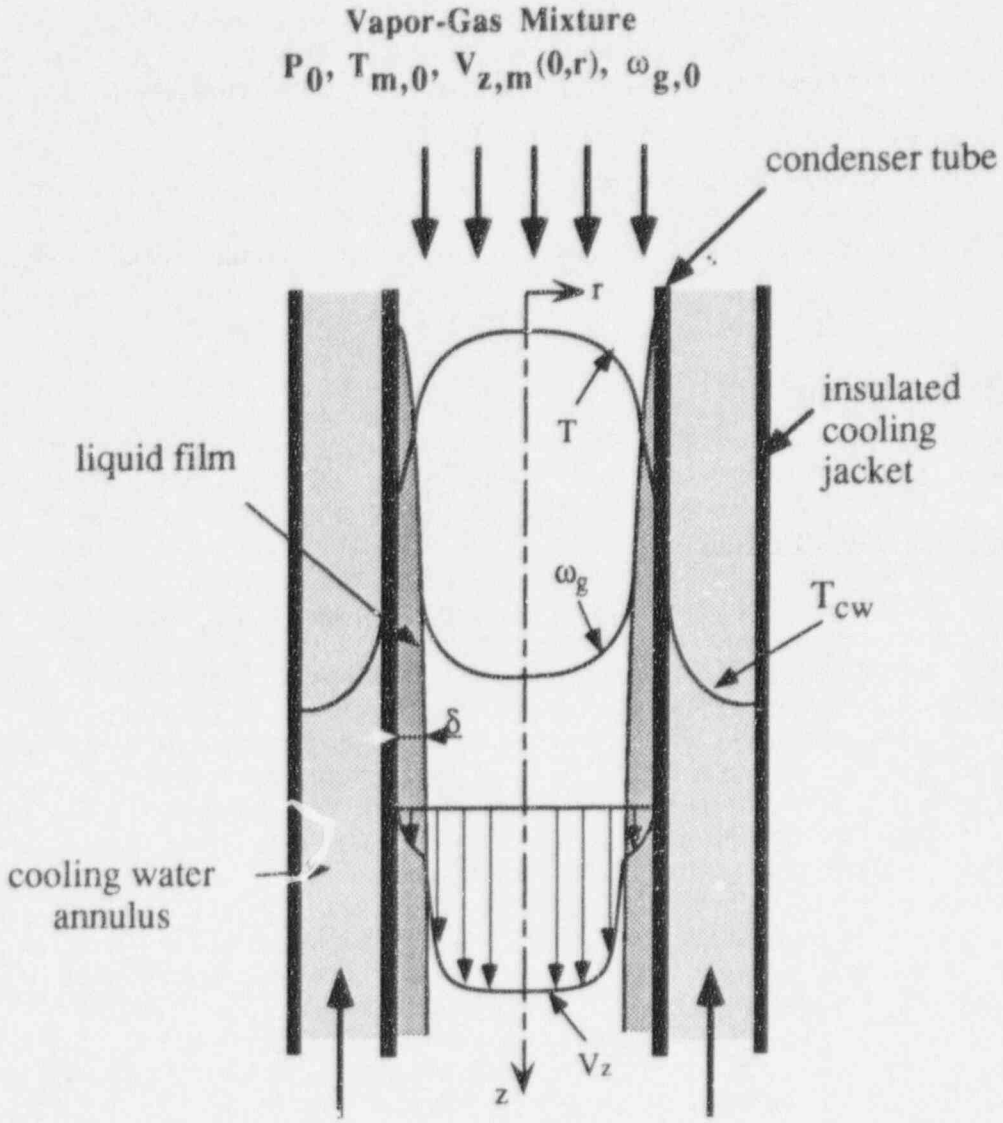

Fig. 1 System Schematics for Condensation Inside a Vertical Tube

MATHEMATICAL FORMULATION AND PHYSICAL MODELS

The problems in this study are approached through solution of the coupled fundamental conservation equations for mass, momentum, species concentration, and energy in the gaseous phase as well mass, momentum, and energy in the condensate film. For turbulent flow in liquid film or gaseous phase, additional low Reynolds number turbulence k - ε equations[34,35] are employed for the determination of eddy viscosity which is required when solving the momentum equations. The heat-momentum analogy is employed for the related eddy thermal conductivity.

Assuming the liquid film surface is smooth, steady state boundary layer type conservation equations in two-dimensional (r, z) coordinate system (Figure 1) are formulated. The waviness effects of liquid film surface are treated separately using the appropriate waviness effect model to be described later. The axial diffusion is neglected in the conservation equations. This is generally valid when Reynolds and Peclet numbers and the product Reeynolds and Schmidt numbers are sufficiently large. Also the radial momentum equations are eliminated by the assumption $\frac{\partial P}{\partial r} = 0$.

This results in a system of parabolic rather than elliptic equations thereby permitting calculation of the condensation heat transfer characteristics numerically using a forward-marching technique, starting from the tube inlet and advancing along the tube until full condensation is achieved or the end of tube is reached.

Liquid Phase Governing Equations

The conservation equations for the liquid film include continuity, axial momentum, and energy equations when the flow is laminar. If the liquid flow becomes turbulent an additional turbulence k - ε two-equation model is incorporated and the dependent variables denote the time smoothed variables. All properties in the equations are treated as temperature dependent variables.

Continuity Equation

$$\frac{\partial}{\partial z}\left(\rho_f v_{z,f}\right)+\frac{1}{r}\frac{\partial}{\partial r}\left(r\rho_f v_{r,f}\right)=0 \tag{1}$$

Axial Momentum Equation

$$\rho_f\left(v_{z,f}\frac{\partial v_{z,f}}{\partial z}+v_{r,f}\frac{\partial v_{z,f}}{\partial r}\right)=-\frac{dP}{dz}+\frac{1}{r}\frac{\partial}{\partial r}\left(r\mu_{eff,f}\frac{\partial v_{z,f}}{\partial r}\right)+\rho_f g \tag{2}$$

Energy Equation

$$\rho_f c_{p,f}\left(v_{z,f}\frac{\partial T_f}{\partial z}+v_{r,f}\frac{\partial T_f}{\partial r}\right)=\frac{1}{r}\frac{\partial}{\partial r}\left(r\kappa_{eff,f}\frac{\partial T_f}{\partial r}\right) \tag{3}$$

Turbulent Kinetic Energy k Equation

$$\rho_f\left(v_{z,f}\frac{\partial k_f}{\partial z}+v_{r,f}\frac{\partial k_f}{\partial r}\right)=\frac{1}{r}\frac{\partial}{\partial r}\left[r\left(\mu_f+\frac{\mu_f^{(t)}}{\sigma_{k,f}}\right)\frac{\partial k_f}{\partial r}\right]+G_f-\rho_f\varepsilon_f \tag{4}$$

Turbulent Dissipation Rate ε Equation

$$\rho_f\left(v_{z,f}\frac{\partial \varepsilon_f}{\partial z}+v_{r,f}\frac{\partial \varepsilon_f}{\partial r}\right)=\frac{1}{r}\frac{\partial}{\partial r}\left[r\left(\mu_f+\frac{\mu_f^{(t)}}{\sigma_{\varepsilon,f}}\right)\frac{\partial \varepsilon_f}{\partial r}\right]+c_{1,f}\frac{\varepsilon_f}{k_f}G_f-c_{2,f}\rho_f\frac{\varepsilon_f^2}{k_f} \tag{5}$$

In equations (2) and (3) $\mu_{eff,f}$ and $\kappa_{eff,f}$ are effective viscosity and effective thermal conductivity respectively, i.e., for laminar film flow, $\mu_{eff,f}=\mu_f$ and $\kappa_{eff,f}=\kappa_f$, and for turbulent film flow, $\mu_{eff,f}=\mu_f+\mu_f^{(t)}$ and $\kappa_{eff,f}=\kappa_f+\kappa_f^{(t)}$ where μ_f and κ_f are liquid molecular viscosity and molecular thermal conductivity respectively. The eddy viscosity $\mu_f^{(t)}$ is determined by solving the coupled turbulent k and ε equations (eqs.(4) and (5)). The eddy thermal conductivity $\kappa_f^{(t)}$ is determined by assuming the ratio $\nu^{(t)}/\alpha^{(t)}=1$, with $\alpha^{(t)}=\frac{\kappa_f^{(t)}}{\rho_f c_{p,f}}$ and $\nu^{(t)}=\frac{\mu_f^{(t)}}{\rho_f}$.

Equations (4) and (5) are the two-equation k - ε model of turbulence [33,34] in which the

local turbulent viscosity is determined from the solution of transport equations for turbulent kinetic energy k_f and the energy dissipation rate ε_f. Quantities k_f and ε_f are related by $\mu_f^{(t)} = c_D \rho_f \frac{k_f^2}{\varepsilon_f}$.

Also $G_f = \mu_f^{(t)} \left\{ 2\left[\left(\frac{\partial v_{z,f}}{\partial z} \right)^2 + \left(\frac{\partial v_{r,f}}{\partial r} \right)^2 + \left(\frac{v_{r,f}}{r} \right)^2 \right] + \left(\frac{\partial v_{z,f}}{\partial r} + \frac{\partial v_{r,f}}{\partial z} \right)^2 \right\}$ denotes the energy production rate per unit volume due to shear work of interaction between Reynolds stress and mean velocity gradient.

$\sigma_{k,f} = 1.4$

$\sigma_{\varepsilon,f} = 1.3$

$c_1 = 1.4$

$c_2 = 1.8\left[1 - 0.3\exp(-Re_{t,f}^2)\right]$

$c_D = 0.09\exp\left[-2.5/(1+Re_{t,f}^2)\right]$

$Re_{t,f}$ = turbulent Reynolds number at liquid film $\equiv \frac{k_f^2}{\nu_f \varepsilon_f}$

ν_f = kinematic viscosity of liquid

Gaseous Phase Governing Equations

In most condensation cases the vapor-gas mixture is in turbulent flow at the tube inlet, but it may revert to laminar flow at some location downstream in the tube because of decreasing mixture flowrate due to condensation. Four conservation equations (continuity, axial momentum, energy and species equations) are used to describe the gaseous phase when the flow is laminar. As in the liquid phase, additional turbulence k - ε equations are incorporated and all dependent variables represent time-smoothed variables when the flow is turbulent.

Continuity Equation

$$\frac{\partial}{\partial z}\left(\rho_m v_{z,m}\right) + \frac{1}{r}\frac{\partial}{\partial r}\left(r\rho_m v_{r,m}\right) = 0 \tag{6}$$

Axial Momentum Equation

$$\rho_m\left(v_{z,m}\frac{\partial v_{z,m}}{\partial z} + v_{r,m}\frac{\partial v_{z,m}}{\partial r} \right) = -\frac{dP}{dz} + \frac{1}{r}\frac{\partial}{\partial r}\left(r\mu_{eff,m}\frac{\partial v_{z,m}}{\partial r} \right) + \rho_m g \tag{7}$$

Energy Equation

$$\rho_m c_{p,m}\left(v_{z,m}\frac{\partial T_m}{\partial z} + v_{r,m}\frac{\partial T_m}{\partial r} \right) = \frac{1}{r}\frac{\partial}{\partial r}\left(r k_{eff,m}\frac{\partial T_m}{\partial r} \right) + \rho_m D\left(c_{p,g} - c_{p,v}\right)\frac{\partial \omega_g}{\partial r}\frac{\partial T_m}{\partial r} \tag{8}$$

Species Equation

$$\rho_m\left(v_{z,m}\frac{\partial\omega_g}{\partial z}+v_{r,m}\frac{\partial\omega_g}{\partial r}\right)=\frac{1}{r}\frac{\partial}{\partial r}\left(r\rho_m D_{eff}\frac{\partial\omega_g}{\partial r}\right) \tag{9}$$

Turbulent Kinetic Energy k Equation

$$\rho_f\left(v_{z,m}\frac{\partial k_m}{\partial z}+v_{r,m}\frac{\partial k_m}{\partial r}\right)=\frac{1}{r}\frac{\partial}{\partial r}\left[r\left(\mu_m+\frac{\mu_m^{(t)}}{\sigma_{k,m}}\right)\frac{\partial k_m}{\partial r}\right]+G_m-\rho_f\varepsilon_m \tag{10}$$

Turbulent Dissipation Rate ε Equation

$$\rho_m\left(v_{z,m}\frac{\partial\varepsilon_m}{\partial z}+v_{r,m}\frac{\partial\varepsilon_m}{\partial r}\right)=\frac{1}{r}\frac{\partial}{\partial r}\left[r\left(\mu_m+\frac{\mu_m^{(t)}}{\sigma_{\varepsilon,m}}\right)\frac{\partial\varepsilon_m}{\partial r}\right]+c_{1,m}\frac{\varepsilon_m}{k_m}G_m-c_{2,m}\rho_m\frac{\varepsilon_m^2}{k_m} \tag{11}$$

In equations (7) and (8), $\mu_{m,eff}$ and $\kappa_{m,eff}$ are defined in the same way as $\mu_{f,eff}$ and $\kappa_{f,eff}$ except they are evaluated for the vapor-gas mixture.

In equation (9), D_{eff} is effective diffusion coefficient which is defined as: for laminar flow, $D_{eff} = D$, and for turbulent flow, $D_{eff} = D + D^{(t)}$, where D is the binary diffusion coefficient for the vapor-gas mixture and $D^{(t)}$ is the eddy diffusion coefficient which is determined using the analogy between heat and mass transfer assuming $D^{(t)}/\alpha_m^{(t)} = 1$ and $\alpha_m^{(t)} \equiv \frac{\kappa_m^{(t)}}{\rho_m c_{p,m}}$.

The variables and coefficients in the mixture turbulent k - ε equations (eqs. (10) and (11)) have the same meanings as that in liquid turbulent k - ε equation except they are applied to the vapor-gas mixture.

Boundary Conditions

The governing equations in liquid and gaseous phases (eqs. (1) ~ (11)) are coupled and solved using the following boundary conditions which provide mathematical closure of the problem.

At Tube Inlet

$\delta = 0$	(liquid film thickness is 0)
$k_f = \varepsilon_f = 0$	(no turbulent kinetic energy and dissipation)
$T_f = T_w(0)$	(liquid film temperature equals to tube inner wall temperature)
$v_{z,m} = U_m(r)$	(fully developed mixture velocity)
$T_m = T_{m,0}$	(uniform mixture temperature)
$P = P_0$	(uniform mixture pressure)
$\omega_g = \omega_{g,0}$	(uniform gas mass fraction)

k_m and ε_m are determined through k - ε model for fully developed flow.

At Tube Inner wall

$v_{z,f} = v_{r,f} = 0$ (no slip conditions)

$T_f = T_w(z)$ or $q''_f = q''_w(z)$ (specify tube inner wall temperature or heat flux)

$k_f = \varepsilon_f = 0$ (turbulent kinetic energy and its dissipation equal to zero)

At Interface Between Liquid Phase and Gaseous Phase

$$v_{z,f} - v_i \frac{d\delta}{dz} = v_{z,m} - v_{r,m} \frac{d\delta}{dz}$$ (tangential velocities are equal)

$$\mu_f \frac{\partial v_{z,f}}{\partial r}\Big|_i = \mu_m \frac{\partial v_{z,m}}{\partial r}\Big|_i$$ (tangential shear stresses are equal)

$$\rho_f \left(v_{z,f} \frac{d\delta}{dz} + v_{r,f} \right) = \rho_m \left(v_{z,m} \frac{d\delta}{dz} + v_{r,m} \right)$$ (normal mass fluxes are equal)

$$\rho_g \left(v_{z,m} \frac{d\delta}{dz} + v_{r,m} \right) - \rho_m D \frac{\partial \omega_g}{\partial r}\Big|_i = 0$$ (interface is impermeable to noncondensable gas)

$T = T_{sat}(P_{v,i})$ interface temperature equal to the saturation temperature corresponding to vapor partial pressure $p_{v,i}$)

$$-\kappa_f \frac{\partial T_f}{\partial r}\Big|_i = -\kappa_m \frac{\partial T_m}{\partial r}\Big|_i + h_{fg} \frac{\rho_v D}{\omega_g} \frac{\partial \omega_g}{\partial r}\Big|_i$$ (energy balance at interface)

$k = \varepsilon = 0$ (turbulent kinetic energy and its dissipation is equal to zero)

Liquid Film Laminar-Turbulent Flow Transition Model

The liquid film is essentially laminar flow over the upper portion of the tube but it may become turbulent flow in the lower portion when the liquid film Reynolds number $Re_f = \Gamma / \mu_f$ becomes large enough. The transition Reynolds number $Re_{f,t}$ equations derived by Rohsenow et al.[17] was used in this study to determine when transition from laminar to turbulent flow occurs in the liquid film.

Liquid Film Waviness Effect Model

The transient equations are not solved to account for the waviness effect at the liquid film surface. Instead the effect of waviness is accounted for by incorporating an empirical correlation for correcting the friction factor and hence shear stress at the interface while still employing the steady state conservation equations. The correlation proposed by Wallis [35] is used, which states that for the case of no entrainment the friction factor f_δ at interface can be expressed as:

$$f_\delta = 0.005 \, (1 + 300 \, \delta / D) \tag{12}$$

where δ is the liquid film thickness for smooth film surface and D the tube inside diameter. This corrected friction factor is related to the interfacial shear stress by

$$\tau_\delta = \frac{\rho_{m,\delta}}{2} f_\delta (v_{z,m,avg} - v_{z,\delta})^2 \tag{13}$$

where $\rho_{m,\delta}$ is the mixture density at the interface, $v_{z,m,avg}$ the average mixture axial velocity and $v_{z,\delta}$ is interface velocity

The effect of waviness at the liquid film surface is then to increase the interfacial shear stress.

The increase of interfacial shear stress will cause the liquid film thickness to be thinner and increase the condensation heat transfer coefficient.

Thermophysical and Transport Properties

The liquid density ρ_f, viscosity μ_f, thermal conductivity κ_f, and specific heat c_f, are determined from ASME Steam Tables based on the calculated local pressure and temperature. The vapor-gas mixture density ρ_m is determined assuming ideal gas behavior for gas component while the water vapor is treated as real gas. The mixture viscosity is determined using the Wilke's method as described in Bird et al. [36]. The mixture thermal conductivity and binary mass diffusivity are determined using methods described in [37]. The mixture specific heat is determined assuming ideal gas mixture behavior.

NUMERICAL METHOD

The governing equations (2) ~ (11) can be cast into a general form of

$$\frac{\partial}{\partial z}(\rho v_z \Phi) + \frac{1}{r}\frac{\partial}{\partial r}(r\rho v_r \Phi) = \frac{1}{r}\frac{\partial}{\partial r}\left(r\Gamma_\Phi \frac{\partial \Phi}{\partial r}\right) + S_\Phi \tag{14}$$

where Φ stands for the dependent variable $v_{z,f}$, T_f, k_f, ε_f, $v_{z,m}$, T_m, ω_g, k_m or ε_m for which the equation is to be solved; Γ_Φ and S_Φ are the general diffusion coefficient and source terms, respectively, corresponding to the momentum equation, energy equation, species equation, k equation or ε equation; and ρ is liquid or vapor-gas mixture density.

Integrating eq. (14) over the general control volume shown in Fig. 2, assuming uniformity of the variables over the surface of the control volume, then we have

$$F_e\Phi_e - F_w\Phi_w + F_n\Phi_n - F_s\Phi_s = \int_w^e \left(r\Gamma\Phi\frac{\partial\Phi}{\partial r}\right)_n dz - \int_w^e \left(r\Gamma\Phi\frac{\partial\Phi}{\partial r}\right)_s dz + S_{\Phi,p}\left[\frac{r_n^2 - r_s^2}{2}\right]\Delta z_p \tag{15}$$

where

$$F_e = \int_s^n (\rho v_z)_e \, r dr = (\rho v_z)_e \frac{r_n + r_s}{2}\Delta r_p \tag{16}$$

$$F_w = \int_s^n (\rho v_z)_w \, r dr = (\rho v_z)_w \frac{r_n + r_s}{2}\Delta r_p \tag{17}$$

$$F_n = \int_w^e (r\rho v_r)_n \, z = (r\rho v_r)_n \Delta_{z,p} \tag{18}$$

$$F_s = \int_w^e (r\rho v_r)_s \, dz = (r\rho v_r)_s \Delta z_p \tag{19}$$

If the central difference scheme is applied to diffusion terms and the upwind scheme is applied to convection terms then eq. (15) becomes

$$a_P\Phi_P = a_W\Phi_W + a_E\Phi_E + a_S\Phi_S + a_N\Phi_N + S_{\Phi,P}\frac{r_n^2 - r_s^2}{2}\Delta z_P \tag{20}$$

where

$$a_W = \max(F_w, 0) \tag{21}$$

$$a_E = \max(-F_e, 0) \tag{22}$$

$$a_S = \max(F_s, 0) + \frac{r_s \Delta z_P}{\Delta r_s} \Gamma_{\Phi,s} \tag{23}$$

$$a_N = \max(-F_n, 0) + \frac{r_n \Delta z_P}{\Delta r_n} \Gamma_{\Phi,n} \tag{24}$$

$$a_P = a_W + a_E + a_S + a_N \tag{25}$$

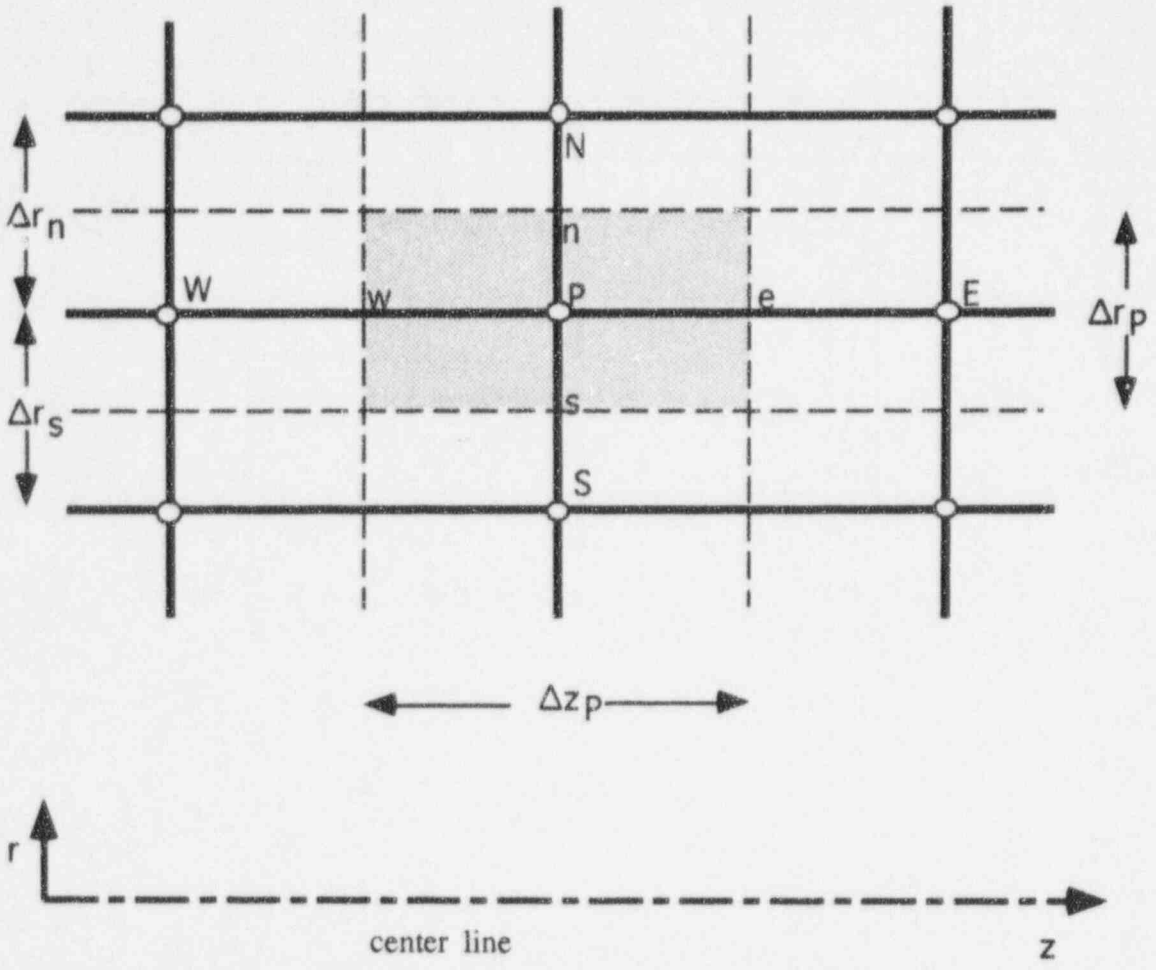

Fig. 2 Cylindrical Coordinate Grids for Finite-Difference Equations

Equation (20) is the final finite-difference form of the generalized differential equation (14).

If we limit the analyses to the non-reversed flow, then $a_E = 0$, and eq. (20) becomes

$$a_P \Phi_P = a_W \Phi_W + a_S \Phi_S + a_N \Phi_N + S_{\Phi,P} \frac{r_n^2 - r_s^2}{2} \Delta z_P \tag{26}$$

or

$$a_P\Phi_P = a_N\Phi_N + a_S\Phi_S + c \tag{27}$$

where

$$c = a_W\Phi_W + S_{\Phi,P}\frac{r_n^2 - r_s^2}{2}\Delta z_P \tag{28}$$

Equation (27) implies that the variable Φ_P can be calculated in terms of cross-stream neighbors (Φ_N and Φ_S) and the known value of c (consists of convection terms from upstream and source terms in the control volume). In other words, eq. (27) is parabolic and can be solved at each axial plane by marching downward from tube inlet.

SOLUTION ALGORITHM FOR CONDENSATION PROBLEMS

The grid structures for the present analyses are shown in Fig. 3.

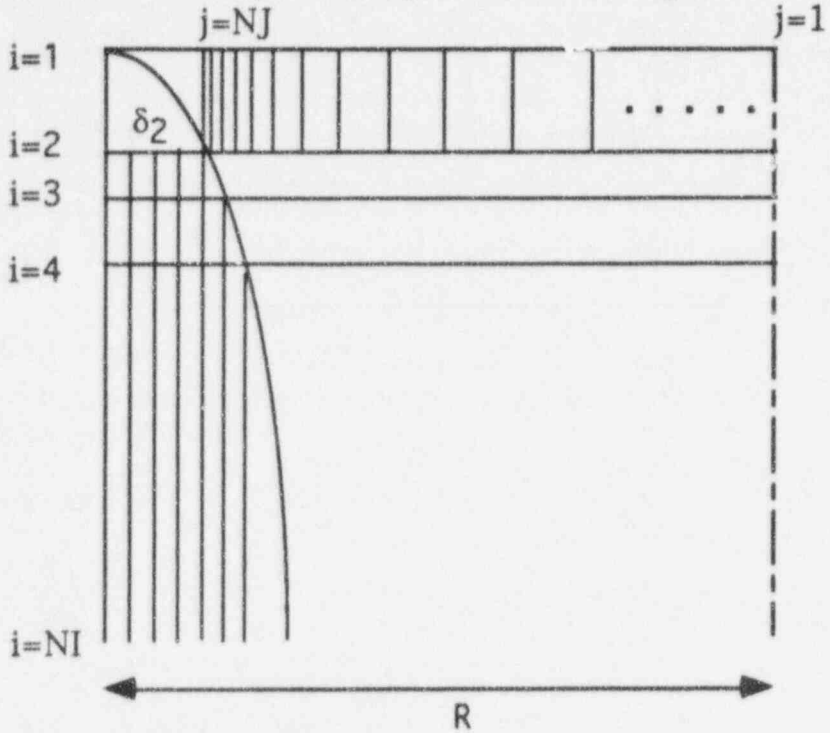

Fig. 3 Grid Structures for Liquid Film and Mixture Sides

The radial spacing of grid points for smooth liquid film is fixed in the following way:

(i) specify δ_2 and divide it into N_2 uniform radial spacing of $\Delta r = \delta_2 / N_2$.

(ii) set $\delta_i = \delta_{i-1} + \Delta r$ with $N_{i-1}+1$ uniform spacing for i = 3, 4,....NI.

The required axial spacing corresponding to δ_i is determined during the iterative calculation through the differential energy balance and adjusted according to the local condensation rate. The differential energy balance is as follows:

Total Heat Transfer at Wall = Energy gain from Condensation + Energy from Condensate Subcooling + Sensible Heat Transfer from Vapor/ Gas Mixture

or

$$q''_w 2\pi R dz = h_{fg}\frac{d\dot{m}_c}{dz}dz + \frac{dH}{dz}dz - \kappa_m \frac{\partial T_m}{\partial r}\Big|_{r=R-\delta} 2\pi(R-\delta)dz \tag{29}$$

where condensate flow rate $\dot{m}_c(z) = \int_{R-\delta}^{R} 2\pi\rho_f v_{z,f}(z,r)rdr$ and enthalpy of subcooling

$$H(z) = \int_{R-\delta}^{R} 2\pi c_f \rho_f v_{z,f}(z,r)[T_\delta(z) - T_f(z,r)]rdr$$

This differential energy balance equation is used to determine the required liquid film thickness δ at a certain axial position or the required dz for a certain liquid film thickness during the iteration calculation at each axial position. After the convergence of the solutions for smooth liquid film, the liquid film thickness is recalculated for wavy film, say δ_i', based on new interfacial shear stress with axial spacing dz_i remaining unchanged. We still use the same number of radial nodes for δ_i' as we use in δ_i. Since $\delta_i' \neq \delta_i$ the radial spacing is no longer equal to that of upstream and interpolations are needed for the calculations of convection terms.

For the gaseous phase, the radial spacing are non uniform at each axial position. The spacings are specified in such a way that there are more nodes in the region near the interface while less and less nodes are used in the region near the center because the profiles of the variables such as velocity, temperature, and concentration change rapidly in the region near the interface but change slowly near the center.

If the mixture is fully developed turbulent flow, then we can use the turbulent k - ε model to generate the velocity profile by solving the momentum equation, k equation and ε equation together through iteration. In order to solve the z-momentum equations for the liquid film and vapor-gas mixture, the pressure gradient dp/dz must be known first. This can be achieved through iteration using the constraint that total mass flow rate must be equal to the inlet mass flow rate for the adjustment of the pressure gradient during the iteration.

Based on above algorithm a FORTRAN computer code has been developed and is named as **COAPIT** (**Co**ndensation **A**nalysis **P**rogram- **I**nside **T**ube). The COAPIT code takes a generalized input deck for a downward flow condensation problem inside a tube. In the deck, users can specify problem grid structure, inlet mixture flow properties and also the boundary conditions along the condensing wall. Depending on the flag in the input deck, COAPIT code can take either wall temperature or wall heat flux as boundary conditions and predict the other quantity along the tube. The calculation is through downward-marching technique starting from tube inlet. At each axial position the convergence on interfacial parameters, such as velocity, temperature, shear stress, gas mass fraction, etc., are assured. The waviness effect is taken into account accordingly. The calculation is stopped when either full condensation or end of tube length is reached.

NUMERICAL CALCULATIONS OF EXPERIMENTAL CASES

Appropriate experimental cases were simulated to validate the computer code COAPIT developed in this study. Due to space limitations we have chosen two typical examples of Kuhn's data [4] for presentation here. Other simulations of data from Kuhn [4], Siddique [3] and Vierow [1] are presented by Yuann [32].

Kuhn's experimental apparatus was designed and used to simulate the conditions that might be encountered during postulated design basis accidents in the SBWR PCCS condensers. The condensing section consists of a stainless steel tube of the same size (OD = 5.08 cm, ID = 4.75 cm, length = 2.4m) as that used for the PCCS condenser design and an outer stainless steel tube forming a 10.9mm thick annulus for the cooling water which flows upward. The vapor-gas

mixture flows downward with fully developed velocity distribution and uniform temperature and gas mass fraction at the tube inlet.

The inlet conditions and tube inner wall heat flux distribution of Kuhn's experimental Run 2.2-2 and used as the input for the program COAPIT are presented in Table 1.

Table 1. Kuhn's Experiment Run 2.2-2 (with steam-air mixture)

Inlet conditions :	
Total pressure	119.9 kPa
Mixture temperature	134.6 ^{o}C
Mixture flow	18.5 x 10^{5} kg/s (51.5 kg/hr)
Gas mass fraction	0.023
Mixture Reynolds number	3.0 x 10^{4}
Velocity Profile	Fully Developed (calculated using k-e model)
Tube inner wall heat flux :	See Figure 4

Figures 5 ~ 7 show the changes along the tube length for the calculated radial profiles of mixture velocity, temperature, and noncondensable gas mass fraction respectively. The average mixture velocity which is fully developed at the tube inlet, decreases with distance along the tube due to the condensation. The velocity gradient at the interface will also decrease with the distance because the interfacial shear stress decreases as the total flowrate decreases. If the inlet mixture flow rate is low or the tube length is long enough the mixture may revert from turbulent flow to laminar flow. In the present case the mixture flow is still turbulent even at the end of tube length because the inlet mixture flow is high enough. The mixture temperature is uniform at the tube inlet and begins to develop a profile along the tube under the suction effect of the condensation. The average mixture temperature decreases with tube length because energy is being transported to the interface due to the depressed interface temperature. Since the interface is impermeable to the noncondensable gas, the gas accumulates there and causes the gas mass fraction and corresponding gas partial pressure to be higher there than in the bulk mixture. This then causes the vapor saturation temperature and mixture temperature to be lower at the interface.

Figure 8 shows the comparison of liquid film thickness between experiment and theory. Actually the liquid film thickness is not measured and the experimental film thickness curve shown in the figure is just the one determined using the simple one- dimensional hydrodynamic model which neglects the interfacial shear stress and convection terms and assumes constant properties in the momentum equation.

The liquid film thickness in the upper portion of the tube calculated using the present theory is thinner than the value determined by the simple hydrodynamic model because the interfacial shear stress is considered in the former while no interfacial shear stress is considered in the latter. The interfacial shear stress has the effect of thinning the liquid film (cocurrent downflow). In the lower portion of the tube, the effect is smaller due to the decreasing average mixture velocity. The liquid film thickness calculated using the smooth film model is thicker than that calculated using wavy film model because the waviness has the effect of increasing the interfacial shear stress.

Figure 9 shows the comparison of the heat transfer coefficient between the experiment and theoretical calculation. There is an overall agreement except except close to the tube entrance. At the axial position very close to the tube inlet, the liquid film is very thin and the temperature difference between the average saturation vapor temperature in the mixture and the tube inner wall temperature is very small. This causes the heat transfer coefficient to be particularly high in the numerical calculation. The heat transfer coefficient calculated taking account of the effect of liquid film surface waviness is higher than that calculated assuming smooth liquid film because the waviness effect is to increase the interfacial shear stress and make the film thinner which enhances the heat transfer coefficient.

Figure 10 shows the comparison of tube inner wall temperature between experiment and theoretical calculation. The tube inner wall temperature is calculated through the iteration until the calculated tube wall heat flux matches the input heat flux (heat flux from experiment). There is overall reasonable agreement. The tube inner wall temperature calculated taking account of the liquid film waviness effect is higher than that calculated assuming smooth liquid film because the liquid film is thinner in the former and has smaller temperature drop across the liquid film which results in higher tube inner wall temperature.

Figure 10 also shows the interface temperature from calculation. No interface temperature is measured in the experiment. The initial low interfacial temperature is the result of high mass fraction of non condensable at the interface which is induced by the larger condensation rate.

The second Kuhn run selected is Run 1.1-1, a pure steam run. The inlet conditions and tube inner wall heat flux distribution from Kuhn's experimental Run 1.1-1 and used as the input to COAPIT are listed in Table 2.

Table 2. Parameters for Kuhn's Run 1.1-1 (Pure Vapor)

Inlet conditions :	
Steam pressure	116.1 kPa
Steam temperature	138.8 ^{o}C
Steam flow	2.17 x 10^{5} kg/s (60.2 kg/hr)
Steam Reynolds number	3.6 x 10^{4}
Velocity profile	Fully Developed
tube inner wall heat flux :	See Figure 11

Figures 12 through 14 show the comparison of the liquid film thickness, heat transfer coefficient, and tube inner wall temperature between experiment and theoretical calculation respectively. The experimental values for liquid film thickness are determined in the same way as those used in the case of Kuhn's experiment Run 2.2-2. In general the same agreement and trends are obtained as in the case of Run 2.2-2 for those variables.

INSIGHT on the CALCULATED RESULTS

As condensation proceeds, the bulk gas concentration and hence the partial pressure profiles are changing along the tube length, and the vapor saturation temperature profile corresponding to the vapor partial pressure may not be equal to the actual vapor temperature and this will cause vapor to be either superheated or supercooled. If the supercooling of vapor is high enough such that the vapor spinodal line limit is reached then bulk condensation must occur in the gaseous phase and this may affect the condensation heat transfer. Experimental observation of mist formation has been reported in the literature [38]. Therefore the calculated supercooling is not unexpected. Run 72-1 of Kuhn's experiment is used as an illustration here. The experimental data used as input to COAPIT are listed in Table 3. Figure 15 gives the axial heat flux history deduced from the experiment. Figures 16 ~ 18. show the calculated profiles of mixture temperature and vapor saturation temperature at various positions along the tube length. The vapor is superheated in the upper part of the tube as seen in Figure 16 for the 25 cm location in the condenser. Figure 17 shows that at z = 0.72 cm the saturation temperature has changed little in the bulk but the local temperature has dropped considerably and is below saturation in most of the radius. This is evidently due to the depressed interface temperature driving sensible heat transfer which cools the mixture below local saturation. COAPIT has no bulk condensation model but it can calculate the metastable state in the absence of bulk condensation. Lower in the tube the predicted supercooling is still greater as seen in Figure 18. The experimental results are not detailed enough to to provide a check on these predictions. The calculated maximum supercooling of vapor for Run 72-1 is 28 ^{o}C. This is well below the spinodal limit of supercooling at the pressure (Shamsundar and Lienhard [39]) so homogeneous nucleation is not predicted. Bulk condensation may occur at this

degree of supercooling if sufficient condensation nuclei are present. It remains to analyze the effect that bulk condensation may have upon the condensation heat transfer problem. Also more detailed experimental data are needed to confirm the accuracy of the calculations.

Table 3. Kuhn's experiment Run 72-1 (with vapor-air mixture)

Inlet conditions :		
Total pressure	222.7	kPa
Mixture temperature	127.7	^{o}C
Mixture flowrate	36.2	kg/hr
Gas mass fraction	0.15	
Mixture Reynolds number	19,000	
Mixture velocity profiles	Fully developed	
tube inner wall heat flux :	See Figure 15	

CONCLUSIONS

In this study a FORTRAN computer code named COAPIT has been developed for the calculation of local heat transfer performance for condensation from vapor-gas mixtures for forced downflow inside a tube. The code was developed based on steady state boundary layer conservation equations in two-dimensional (r, z) cylindrical coordinate system for the liquid film and gaseous phase assuming a smooth liquid film surface. The effects of liquid film surface waviness are treated by incorporating an empirical correlation for correcting friction factor and hence the shear stress at interface. For turbulent flow the two-equation k- ε model is employed to solve for eddy diffusion coefficients. The code covers the pressure and temperature ranges of 0.6 ~ 8460 kPa and 0 ~ 300 ^{o}C respectively so that it can be used to simulate condensation heat transfer in experiments and actual SBWR Isolation Condensers and PCCS Condensers operations.

The code has been benchmarked against several experiments performed by Kuhn , Siddique and Vierow, including pure vapor condensation and condensation with noncondensable gas. A few of the comparisons are presented in this paper. Others are presented in the by dissertation Yuann [33]. Local key parameters such as liquid film thickness, heat transfer coefficient, tube inner wall temperature, interface temperature, etc. have been compared between experiment and simulation and reasonable agreements have been obtained. In general the code can provide many local flow and heat transfer characteristics, such as profiles of eddy viscosity, velocities, temperature, gas partial pressure and concentration; superheat, supercooling, liquid film thickness, interfacial shear stress, heat transfer coefficient, tube inner wall temperature, and interface temperature. Since the details of the analytical results go beyond the present experimental capability, to the extent that the code is validated by comparisons with some overall experimental results, it may also be used to gain better insight concerning the finer details such radial profiles of important variables. Prediction of the occurrence of the matastable vapor state and its distribution is an example of such details that are not usually measured. The code could also be used to evaluate the influence of nonuniform wall boundary conditions on the overall heat transfer coefficient.

The code COAPIT does not contain a bulk condensation model. A few models have been proposed (Fox [40]), however it did not seem desirable to include this added complexity at this early stage of the code development. This aspect of the problem does deserve further study to better understand the extent to which it influences the condensation heat transfer process.

Nomenclature

c_1, c_2, c_D	constants or functions of turbulence Reynolds number appearing in turbulence k-ε model.
c_p	specific heat
D	Tube inside diameter, binary diffusion coefficient
D_{eff}	effective diffusion coefficient, $D + D^{(t)}$
f	degradation factor for local heat transfer coefficient.
g	gravity constant
G	production term in turbulent k-ε equations
h_{fg}	heat of vaporization
k	turbulent kinetic energy per unit mass
$\dot{m}$	condensate mass flow rate
q"	heat flux
r	radial coordinate
R	tube inside radius
Re_f	liquid film Reynolds number $\equiv \frac{\Gamma}{\mu_f}$
Re_m	vapor-gas mixture Reynolds number
Re_t	turbulent Reynolds number, $\frac{k^2}{\nu\varepsilon}$
S_Φ	general source term in the generalized differential equation (3.1)
T	temperature
v_r	radial velocity
v_z	axial velocity
z	axial coordinate
$\dot{}$	differentiate with respect to time

Symbols

δ	liquid film thickness
ε	dissipation rate of turbulent kinetic energy per unit mass
Φ	denotes variable of V_z, T, ω_g, k, or ε
Γ_Φ	general diffusion coefficient in the generalized differential equation (3.1)
κ	thermal conductivity
κ_{eff}	effective thermal conductivity, $\kappa + \kappa^{(t)}$
σ_h	turbulent Prandtl number for enthalpy transport
σ_k	turbulent Prandtl number for turbulent kinetic energy (k)
σ_ε	turbulent Prandtl number for dissipation rate of turbulent kinetic energy (ε)
τ	shear stress
μ	dynamic viscosity
μ_{eff}	effective viscosity, $\mu + \mu^{(t)}$
ν	kinematic viscosity
ω_g	mass fraction of noncondensable gas

ρ	density

Subscripts

cw	cooling water
δ	value evaluated at interface
f	liquid phase
g	denotes pertaining to noncondensable gas
m	gaseous phase (mixture of vapor and noncondensable gas)
tr	transition from laminar film to turbulent film
v	vapor
w	tube inner wall
0	inlet

Superscripts

(t)	turbulent or eddy

REFERENCES

[1] Vierow, K.M., 1990, "Behavior of Steam-Air System Condensing in Cocurrent Vertical Downflow," MS Thesis, University of California, Berkeley.

[2] Ogg, D.G., 1991, "Vertical Downflow Condensation Heat Transfer in Gas-Steam Mixture," MS Thesis, Dep. of Nuclear Engineering; University of California, Berkeley.

[3] Siddique, M., 1992, "The Effect of Noncondensable Gases on Steam Condensation under Forced Convective Conditions," Ph.D. Thesis, Massachusetts Institute of Technology.

[4] Kuhn, S.Z., 1993, "Experimental Investigation of Downward Condensation in Vertical Tube with Noncondensable Gases," MS Thesis, University of California, Berkeley.

[5] Nusselt, W., 1916, "Die oberflachenkondensation des wasserdampfies," Z. Ver. Dt. Ing. 60, pp. 541- 546 and 569-575.

[6] Rohsenow, W.M., 1956, "Heat Transfer and Temperature Distribution in Laminar Film Condensation," Trans. ASME, vol. 78, pp. 1645-1648.

[7] Sparrow, E.M., and Gregg, J.L., 1959, "A Boundary-Layer Treatment of Laminar Film Condensation," J. Heat Transfer, vol. 81, pp. 13-23.

[8] Koh, J.C.Y., Sparrow, E.M., and Hartnett, J.P., 1961, "The Two Phase Boundary Layer in Laminar Film Condensation," Int. J. Heat Mass Transfer, vol. 2, pp. 69-82.

[9] Hirshburg, R.I. and Florschuetz, L.W., 1982, "Laminar Wavy Film Flow: Part I, Hydrodynamic Analysis," Trans. ASME, vol. 104, pp. 452-458.

[10] Seban, R.,1954 "Remarks on Film Condensation with Turbulent Flow," Trans. ASME, vol. 76, pp. 299-303.

[11] Chun, K.R., 1969, "Evaporation from Thin Liquid Films," Ph.D. Dissertation, University of California, Berkeley.

[12] Chun, K.R., and Seban, R.A., 1971, "Heat Transfer to Evaporating Liquid Film," Vol. 93, pp 391-396.

[13] Sparrow, E.M., and Lin S.H., 1964, "Condensation Heat Transfer in the Presence of Noncondensable Gas," J. Heat Transfer, vol. 86, pp. 430-436.

[14] Minkowycz, W.J., and Sparrow, E.M., 1966, "Condensation Heat Transfer in the Presence of Noncondensables, Interfacial Resistance, Superheating, Variable Properties and Diffusion," Int. J. Heat Mass Transfer, vol. 9, pp. 1125-1144.

[15] Al-Diwany, H.K., and Rose, J.W., 1973, "Free Convection Film Condensation of Steam in the Presence of Noncondensing Gases," Int. J. Heat Mass Transfer, vol. 16, pp. 1359-1369.

[16] Dehbi, A.A., 1990, "Analytical and Experimental Investigation of the Effects of Noncondensable Gases on Steam Condensation under Natural Convection Conditions," Ph.D. Dissertation, Dept. Nuclear Engineering, MIT.

[17] Rohsenow, W.M., Webber, J.H., and Ling, A.T., 1956, "Effect of Vapor Velocity on Laminar and Turbulent Film Condensation," Trans. ASME, vol. 78, pp. 1637-1643.

[18] Sparrow, E.M., Minkowycz, W.J., and Saddy, M., 1967, "Forced Convection Condensation in the Presence of Noncondensables and Interfacial Resistance," Int. J. Heat Mass Transfer, vol. 10, pp. 1829-1945.

[19] Denny, V.E., Mills, A.F., and Jusionis, V.J., 1971, "Laminar Film Condensation from a Steam-Air Mixture Undergoing Forced Flow Down a Vertical surface," J. Heat Transfer, pp. 297-304.

[20] Kim, M.H., and Corradini, M.L., 1990, "Modeling of condensation Heat Transfer in a reactor Containment," Nuclear Engineering and Design, vol. 118, pp. 193-212.

[21] Dobran, F., and Thorsen, R.S., 1980, "Forced Flow Laminar Filmwise Condensation of a Pure Saturated Vapor in a Vertical tube," Int. J.. Heat Mass Transfer, vol. 23, pp. 161-177.

[22] Seban, R.A., and Hodgson, J.A., 1982, "Laminar Film Condensation in a Tube with Upward Vapor Flow," Int. J. Heat Mass Transfer, vol. 25, pp. 1291-1300.

[23] Blangetti, F., Krebs, R., and Schlünder, E.U., 1982, "Condensation in Vertical Tube-Experimental Results and Modeling," Chemical Engineering Fundamental Vol. 1/ No. 2, pp.

20-62.
[24] Borishanskiy, V.M., Volkev, D.I., Ivashchenko, N.I., Vorontsova, L.A., Illarionov, Yu.T., Makarova, G.A., and Fishman, N.M., 1977, "Heat Tansfer from Steam Condensing Inside Vertical Pipes and coils," Heat Transfer- Soviet Research, Vol. 9, No. 2, pp. 35-42.
[25] Borishanskiy, V.M., Volkev, D.I., Ivashchenko, N.I., Vorontsova, L.A., Illarionov, Yu.T., Krektunov, O.P., Makarova, G.A., and Alekseyev, I.A., 1978 "Heat Tansfer from Steam Condensing Inside Vertical Pipes and coils," Heat Transfer- Soviet Research, Vol. 10, No. 4, pp. 44-57.
[26] Borishanskiy, V.M., Volkev, D.I., Ivashchenko, N.I., Krektunov, O.P., Fishman, N.M., and Chirkov, I.N., 1982, "Shell-Side Coefficient of Heat Transfer from Steam Contaminated with noncondensable Gases," Heat Transfer- Soviet Research, Vol. 14, No. 3, pp. 1-5.
[27] Wang, C.Y., and Tu, C.J., 1988, "Effects of Noncondensable Gas on Laminar Film Condensation in a Vertical Tube," Int. J. Heat Mass Transfer, vol. 31, pp. 2339-2345.
[28] Vierow, K.M., and Schrock, V.E., 1991, "Condensation in a Natural Circulation Loop with Noncondensable Gas Present Part I - Heat Transfer," and "Condensation in a Natural Circulation Loop with Noncondensable Gas Present Part II - Flow Instability," Proc. Int. Conf. on Multiphase Flow `91 Tsukuba, Tsukuba, Japan, Vol. 1, pp. 183-190.
[29] Kageyama, T., 1992, "Application of Diffusion Layer Theory to Vertical Downflow Condensation Heat Transfer," MS Thesis, University of California, Berkeley.
[30] Peterson, P.F., Schrock, V.E., and Kageyama, T., 1992 "Diffusion Layer Theory for Turbulent Vapor Condensation with Noncondensable Gases," Nat. Heat Transfer Conf., San Diego.
[31] Vial, E.and Schrock, 1992, "A Critical Review of the UCB and MIT Combined Data Base for Condensation from Steam Gas Mixtures in Forced Flow in Tubes", UCB-NE-4195.
[32] Yuann, R.Y., 1993, "Condensation from Vapor-Gas Mixture for Forced Downflow Inside a Tube," PhD Thesis, University of California at Berkeley.
[33] Jones, W.P., and Launder, B.E., 1972, "The Prediction of Laminarization with a 2-Equation Model of Turbulence," Int. J.. Heat Mass Transfer, vol. 15, PP. 301-313.
[34] Jones, W.P., and Launder, B.E., 1973, "The calculation of Low-Reynolds Number Phenomena with a Two-Equation Model of Turbulence," Int. J.. Heat Mass Transfer, vol. 16, PP. 1119-1130.
[35] Wallis, G.B., 1970, "Annular Two Phase Flow Part I: A Simple Theory," Trans. ASME, vol. 60, pp. 59-72.
[36] Bird, R. B., Stewart, W. E., and Lightfoot, E. N., 1960,**Transport Phenomena,** John Wiley & Sons, Inc., N.Y.
[37] Reid, R. C. and Sherwood, T. K., 1966, **The Properties of Liquids and Gases,** 2 nd. Ed.,McGraw-Hill Book Co., N.Y.
[38] Hijikata, K. and Mori, Y. 1973, "Forced Convection Condensation Heat Transfer with Noncondensable Gas on a Vertical Flat Plate", Int. J. Heat and Mass Transfer,Vol. 16, pp.2229-2240.
[39] Shamsundar, N. and Lienhard, J. H., 1993, "Equations of State and Spinodal Lines - a Review", Nuclear Eng. & Design, vol.141, pp.269-287.
[40] Fox, R. J., 1994, "Mixed Convective Condensation in Enclosures with Noncondensable Gases", Doctoral Disseration, University of California, Berkeley.

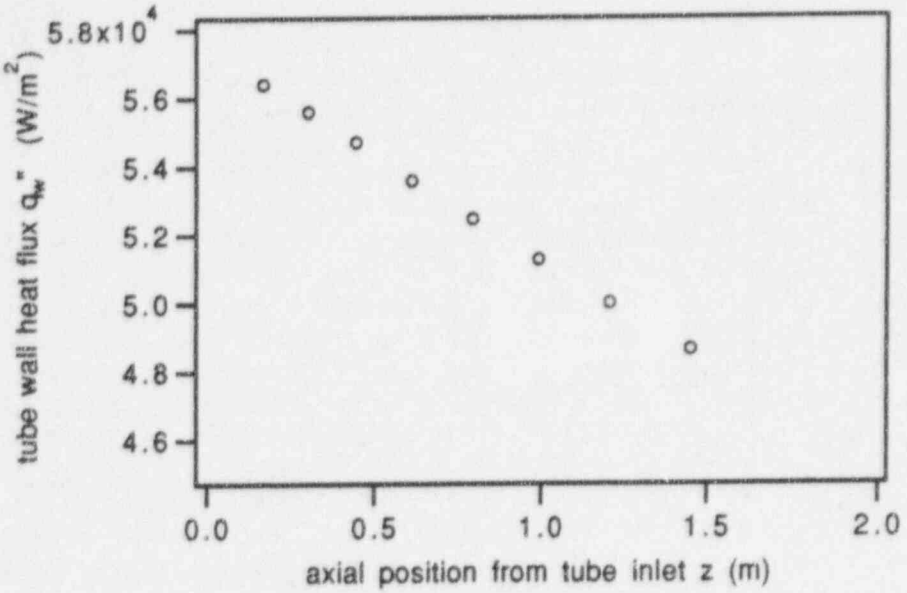

Fig. 4 Tube wall heat flux distribution for Kuhn's experiment Run 2.2-2
(Used as input for theoretical calculation)

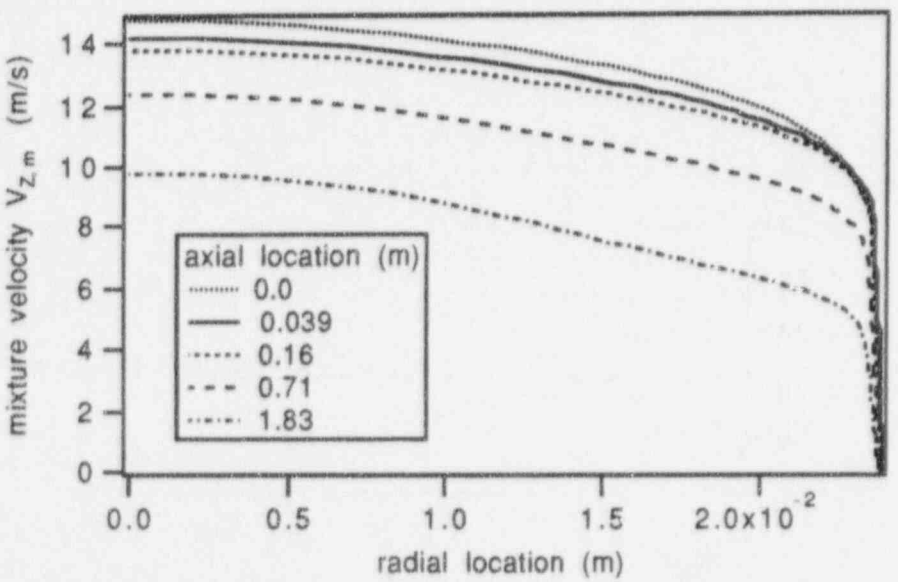

Fig. 5 Calculated mixture velocity profile along tube length for
Kuhn's experiment Run 2.2-2

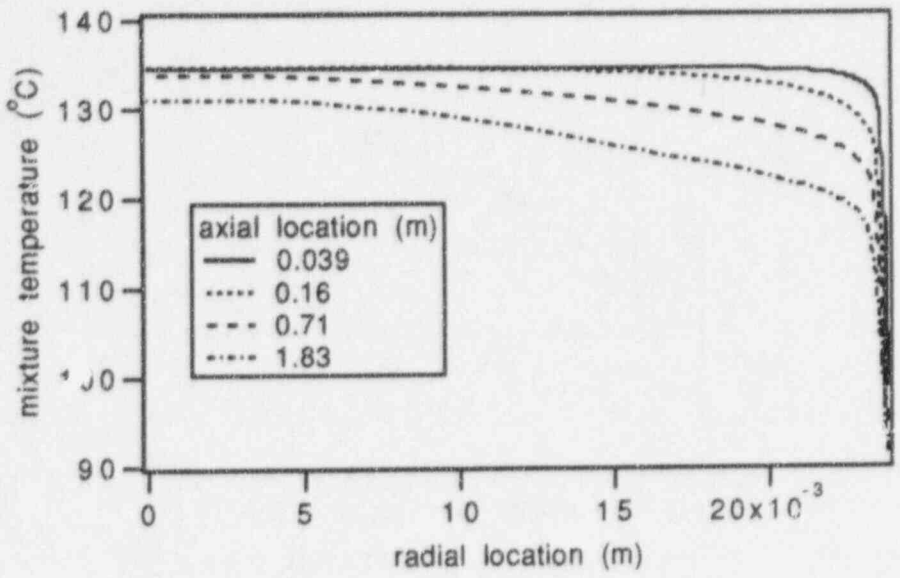

Fig. 6 Calculated mixture temperature profile along tube length for Kuhn's experiment Run 2.2-2

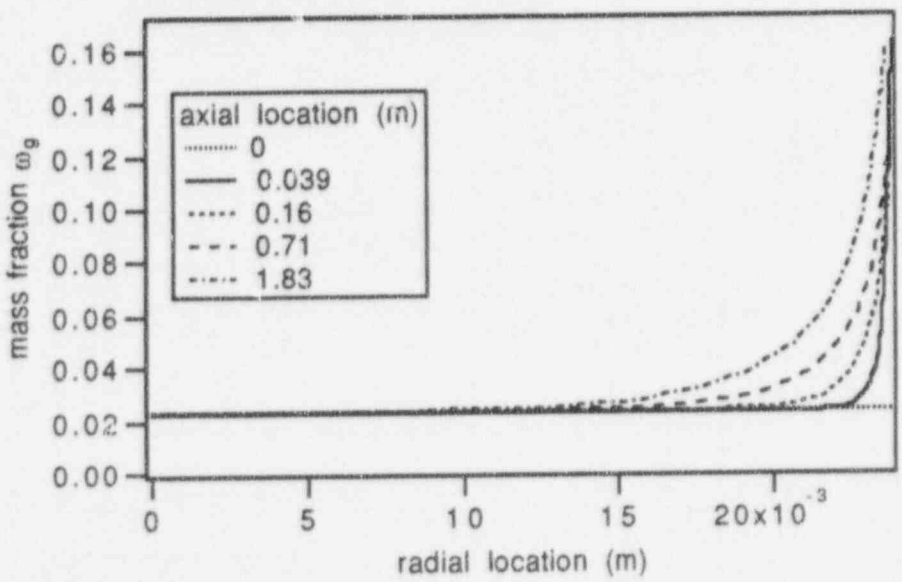

Fig. 7 Calculated gas mass fraction profile along tube length for Kuhn's experiment Run 2.2-2

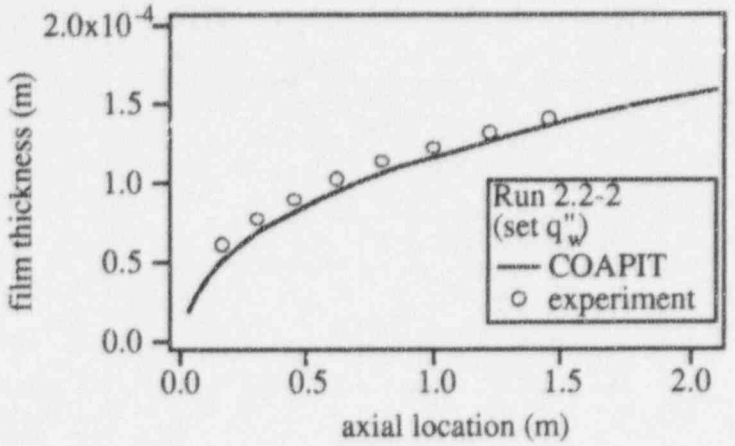

Fig. 8 Comparison of liquid film thickness between experiment and theory for Kuhn's experiment Run 1.1-1

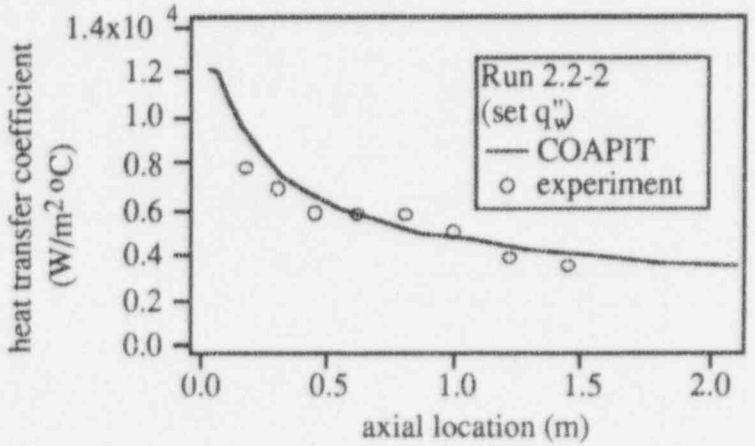

Fig. 9 Comparison of heat transfer coefficient between experiment and theory for Kuhn's experiment Run 1.1-1

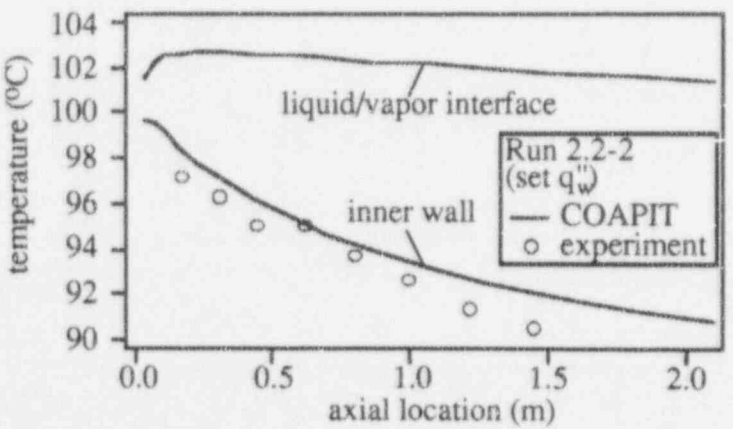

Fig. 10 Comparison of tube inner wall temperature between experiment and theory for Kuhn's experiment Run 1.1-1

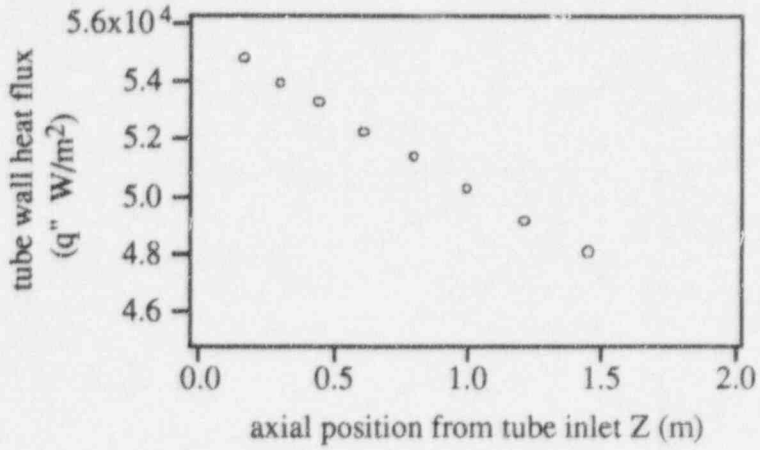

Fig. 11 Tube wall heat flux distribution for Kuhn's experiment Run 1.1-1
(Used as input for theoretical calculation)

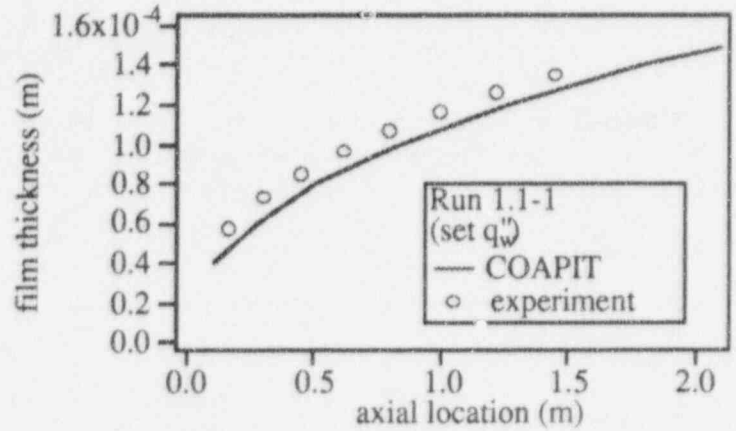

Fig. 12 Comparison of liquid film thickness between experiment and theory
for Kuhn's experiment Run 1.1-1

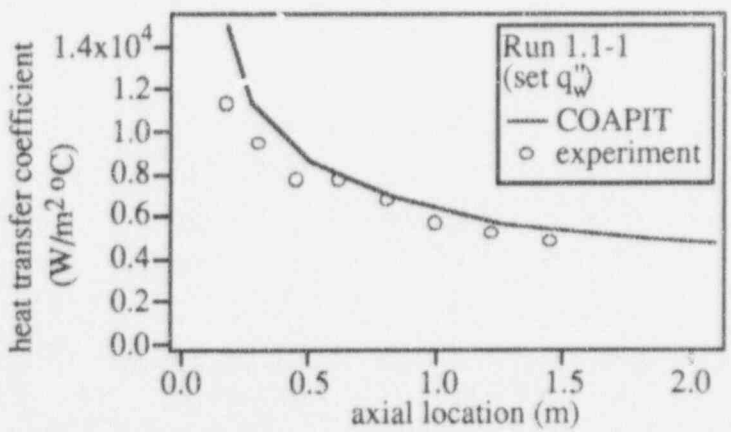

Fig. 13 Comparison of heat transfer coefficient between experiment and
theory for Kuhn's experiment Run 1.1-1

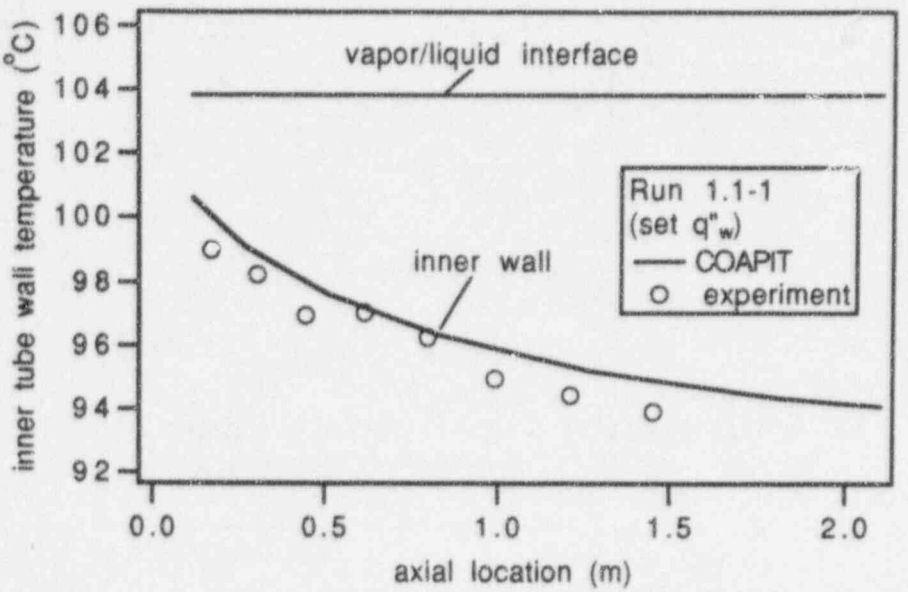

Fig. 14 Comparison for tube inner wall temperature between experiment and theory for Kuhn's experiment Run 1.1-1

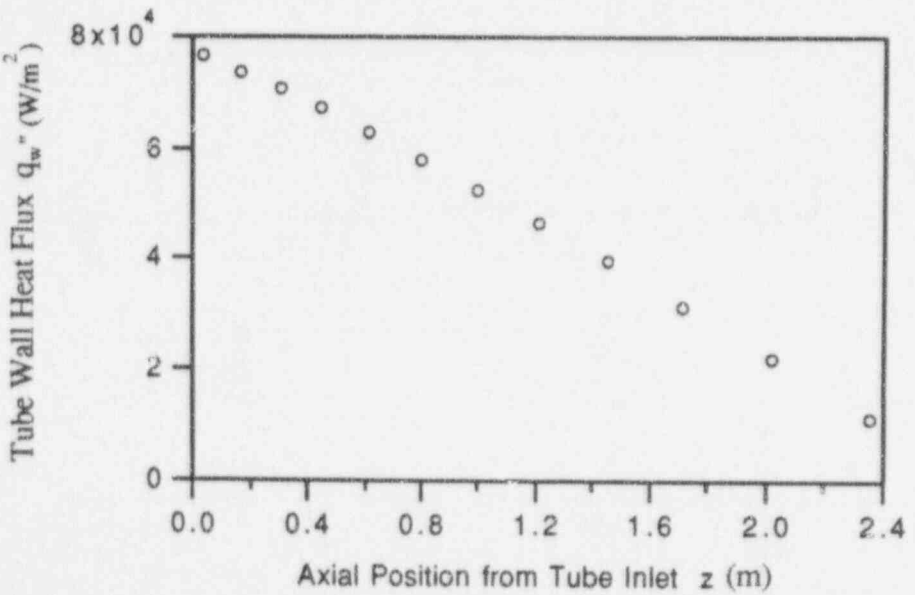

Fig. 15 Tube wall heat flux distribution for Kuhn's Experiment Run 72-1 (Used as input for theoretical calculation)

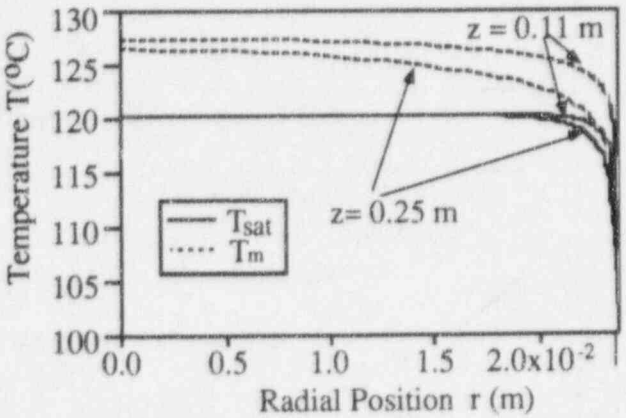

Fig. 16 Calculated vapor superheating/supercooling at axial positions of z = 0.11 m and z = 0.25 m for Kuhn's experiment Run 72-1

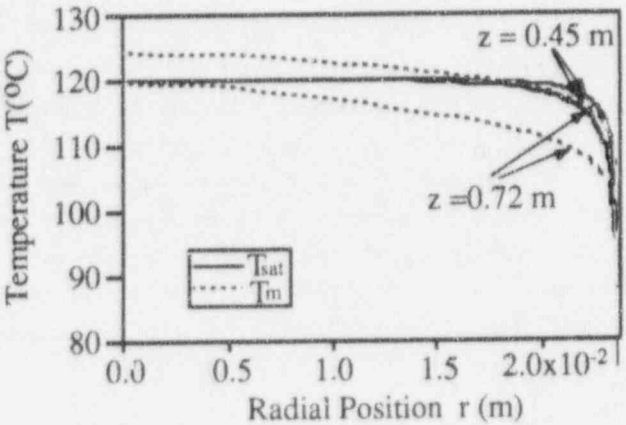

Fig. 17 Calculated vapor superheating/supercooling at axial position of z = 0.45 m and z = 0.72 m for Kuhn's experiment Run 72-1

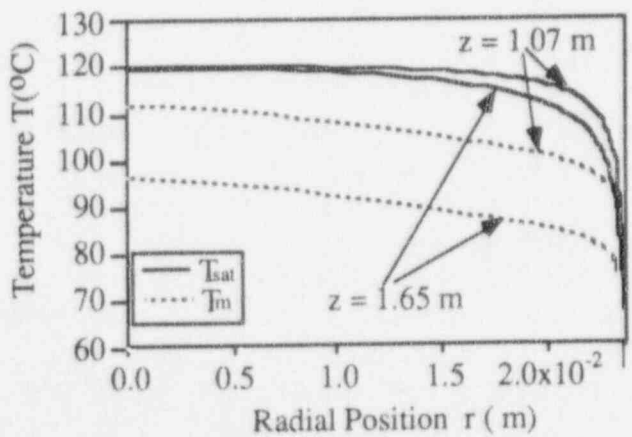

Fig. 18 Calculated vapor superheating/supercooling at axial positions of z = 1.07 m and z = 1.65 m for Kuhn's experiment Run 72-1

A Model for the Performance of a Vertical Tube Condenser in the Presence of Noncondensable Gases

A. Dehbi, S. Guentay
Paul Scherrer Institute
Switzerland

Abstract

Some proposed vertical tube condensers are designed to operate at high noncondensable fractions, which warrants a simple model to predict their performance. Models developed thus far are usually not self-contained as they require the specification of the wall temperature to predict the local condensation rate. The present model attempts to fill this gap by addressing the secondary side heat transfer as well.

Starting with a momentum balance which includes the effect of interfacial shear stress, a Nusselt-type algebraic equation is derived for the film thickness as a function of flow and geometry parameters. The heat and mass transfer analogy relations are then invoked to deduce the condensation rate of steam onto the tube wall. Lastly, the heat transfer to the secondary side is modelled to include cooling by forced, free or mixed convection flows. The model is used for parametric simulations to determine the impact on the condenser performance of important factors such as the inlet gas fraction, the mixture inlet flowrate, the total pressure, and the molecular weight of the noncondensable gas. The model performed simulations of some experiments with pure steam and air-steam mixtures flowing down a vertical tube. The model predicts the data quite well.

1 Introduction

Film condensation inside vertical tubes is an important engineering topic. The original work of Nusselt related to condensation on flat surfaces [1] has been extended to include such effects thermal advection in the film [2], vapor drag [3] and vapor superheat.

Some theoretical investigations tackled the problem of pure steam condensation in a vertical tube starting from the conservation equations for both the liquid and vapor phases. Dobran and Thorsen [4] simplified the governing equations and used an integral method to solve the problem. Bellinghausen and Renz [5] incorporated the the $k-\varepsilon$ turbulence model and solved the resulting equations using finite difference techniques.

It is important to note that most of the studies to date dealt with condensation in the absence noncondensable gases. In practice, small amounts of noncondensable gases are usually present in condensers due, among other things, to the sub-atmospheric operating conditions encountered in many of these applications. Moreover, some proposed condensers such as the Passive Containment Cooler (PCC) in the next generation Simplified Boiling Water Reactor (SBWR) are in fact designed to operate at high noncondensable fractions. Theoretical and experiment investigations have consistently shown that noncondensable gases have a strong impeding effect on steam condensation

in unconfined geometries such as on vertical flat plates [6],[7],[8], and on the outside of horizontal [9] or vertical [10] cylinders. In general, the greater the free stream gas fraction, the greater the resistance to condensation. For a given gas fraction, the impeding effect of noncondensable gases is more pronounced when the flow is naturally driven, or forced at small velocities.

Lately, the effect of noncondensable gases on vapor condensation inside tubes has been studied both theoretically and experimentally by a few authors.

Wang and Tu [11] studied the condensation of a turbulent vapor-gas mixture flowing down a vertical tube. The model uses the heat and mass transfer analogy relations to deduce the local condensation rate in a marching procedure. The model predicted nicely some experimental data; however it is not self-contained as it necessitates the specification of the tube wall temperature, while the latter is a by-product of the dynamics between the cold and hot sides of a condenser tube.

Siddique et. al. [12] presented a similar analysis as above, with the additional inclusion of film roughness, entrance length effects and property changes across the diffusion boundary layer. The model predicted reasonably well the data obtained by the authors earlier [13]. However, as with reference [11], the results of the model depend on the the specification of the experimentally determined wall temperature.

Kaiping and Renz [14] addressed the heat and mass transfer problem by solving the gas-phase mass, momentum, energy, and species equations in conjunction with a Nusselt-type treatment of the condensate film. The predictions fitted the authors' data reasonably well but the overall approach is too complicated for design purposes.

Recently, Ghiaasiaan et. al [23] proposed a two-fluid model for tube condensation in the presence of noncondensables. The model compares satisfactorily with some experimental data; nonetheless, the large number of equations and necessary closure relations make the model somewhat complicated. As with previous formulations, the channel boundary condition requires the specification of a wall temperature or a wall heat flux.

In the present paper, it is intended to develop a simple model to estimate the performance of a vertical condenser tube in the presence of noncondensable gases. The model is integral in nature. The secondary side is also taken into consideration so that the model is fully predictive and depends only on geometry and thermal hydraulic inlet conditions for the hot and cold sides of the condenser.

2 The Theoretical Model

2.1 The Governing Equations

Referring to the Figure 1, one can write the x-momentum balance for a small liquid element. With the assumption of a laminar film where advection effects are neglected, the statement of momentum conservation reads:

$$\mu_\ell \frac{\partial^2 u_\ell}{\partial y^2} = \frac{\partial p}{\partial x} - \rho_\ell g \tag{1}$$

Integrating twice with respect to y one obtains the velocity profile in the liquid film:

$$u_\ell(y) = \frac{1}{\mu_\ell}(\frac{\partial p}{\partial x} - \rho_\ell g)(\frac{1}{2}y^2 - \delta y) + \frac{\tau_i}{\mu_\ell}y \tag{2}$$

where τ_i is the shear stress exerted by the vapor on the condensate film. τ_i may be expressed as:

$$\tau_i = \frac{1}{2}\rho U^2 f \tag{3}$$

In the above expression, the mixture density and velocity are defined in the usual manner:

$$\rho = \rho_v + \rho_g = \rho_v \frac{1}{1-W}$$

$$\rho U A = m_m = m_v + m_g = m_v \frac{1}{1-W}$$

where W represents the noncondensable mass fraction defined as:

$$W = \frac{m_g}{m_v + m_g}$$

A momentum balance yields the following expression for the pressure gradient:

$$-\frac{\partial p}{\partial x} = \frac{4\tau_i}{d} + \frac{d(\rho U^2)}{dx} \tag{4}$$

At any vertical location x, one can readily find the condensate mass flowrate by simply integrating over the film thickness δ. Since δ is negligible compared to the tube diameter r, the condensate flow rate can be expressed as:

$$Q_\ell = \int_0^\delta \pi d \rho_\ell u_\ell dy \tag{5}$$

The latter integration yields:

$$Q_\ell = \frac{\pi d}{\nu_\ell}((\rho_\ell g - \frac{\partial p}{\partial x})\frac{\delta^3}{3} + \tau_i \frac{\delta^2}{2}) \tag{6}$$

Because condensation is a high mass-transfer phenomenon, the gradients near the liquid-gas interface are steeper than those predicted by low-mass transfer correlations, thus leading to greater friction factors and Sherwood numbers. To correct for friction, Kay and Moffat [15] have suggested the following expression:

$$f = f_o \frac{\phi e^\phi}{e^\phi - 1} \tag{7}$$

where ϕ is a dimensionless number defined by:

$$\phi = \frac{v_i/U}{f_o/2}$$

and f_o is the friction factor in the absence of suction. For a turbulent flow inside a smooth pipe, this friction factor is estimated from the following empirical relation:

$$f_o = 0.079 Re^{-1/4} \tag{8}$$

where the Reynolds number is based on the mixture-averaged properties.

$$Re = \frac{\rho U d}{\mu} \tag{9}$$

When the gas flow is laminar, the friction factor reduces to the analytically obtained expression:

$$f_o = \frac{16}{Re} \tag{10}$$

Because the condenser hot and cold side conditions vary along the vertical axis, one would need a step-wise procedure in order to solve the flow problem. With this in mind, one can write (6) as:

$$Q_\ell = \frac{\pi d}{\nu_\ell} F(\delta) \tag{11}$$

Differentiating with respect to the film thickness δ:

$$dQ_\ell = \frac{\pi d}{\nu_\ell} F'(\delta) d\delta \tag{12}$$

At steady state conditions, dQ_ℓ can be equated with the incremental vapor mass flow towards the wall:

$$dQ_\ell = \rho_v v_v dA = m_v'' dA = \frac{q_v'' \pi d}{h_{fg}} dx \tag{13}$$

If one assumes a laminar condensate film where conduction is the dominant heat transfer mechanism, then the heat flux across the film thickness may be expressed as:

$$q_v'' = \frac{k_\ell (T_i - T_w)}{\delta} \tag{14}$$

Combining equations (12) through (14), one arrives at the following relation:

$$\delta F'(\delta) d\delta = \frac{\nu_\ell k_\ell (T_i - T_w)}{h_{fg}} dx \tag{15}$$

where:

$$F'(\delta) = (\rho_\ell g - \frac{\partial p}{\partial x})\delta^2 + \tau_i \delta + \tau_i' \frac{\delta^2}{2} \tag{16}$$

The integration of equation (16) yields:

$$\int_{\delta(x)}^{\delta(x+\Delta x)} \delta F'(\delta) d\delta = \Bigg[\underbrace{(\rho_\ell g - \frac{\partial p}{\partial x})\frac{\delta^4}{4} + \tau_i \frac{\delta^3}{3} + \tau_i' \frac{\delta^4}{8}}_{\equiv G(\delta)} \Bigg]_{\delta(x)}^{\delta(x+\Delta x)} = \frac{\nu_\ell k_\ell (T_i - T_w)}{h_{fg}} \Delta x \tag{17}$$

The end result is the following non-linear equation in δ:

$$G(\delta(x+\Delta x)) = G(\delta(x)) + \frac{\nu_\ell k_\ell (T_i - T_w)}{h_{fg}} \Delta x \tag{18}$$

In the above equation, T_i represents the equilibrium temperature at the interface between the gas and the liquid phases. In the absence of noncondensable gases, T_i is simply the vapor bulk temperature T_∞. When noncondensable gases are present, a diffusion boundary layer is formed due to condensation at the wall, and hence the interface temperatures becomes lower then T_∞. Finding T_i requires addressing the mass transfer problem.

In the gaseous boundary layer, a bulk motion towards the wall is induced by vapor condensation (Stefan Flow). Superimposed on this bulk motion is a diffusion of the the noncondensable gas away from the wall. One can then write Fick's law for the noncondensable gas in the following way:

$$(\rho_g v_g)_i = (\rho_g v)_i - (\rho D \frac{\partial W}{\partial y})_i \tag{19}$$

Since the interface is impermeable to the noncondensable gas, $(v_g)_i$ is zero and the above equation reduces to:

$$(\rho_g v)_i = (\rho D \frac{\partial W}{\partial y})_i \tag{20}$$

At the interface, the noncondensable diffusive flux is:

$$\rho D (\frac{\partial W}{\partial y})_i = \rho H_g (W_\infty - W_i) \tag{21}$$

On the other hand, the mass conservation at the interface is given by:

$$(\rho v)_i = (\rho_v v_v)_i + (\rho_g v_g)_i = (\rho_v v_v)_i \tag{22}$$

After manipulation of these equations, and using the relation $(\rho_g v)_i = W_i (\rho v)_i$, the impermeability condition can be formulated as:

$$W_i = \frac{W_\infty}{1 - (Re_i Sc/Sh)} \tag{23}$$

where:

$$Sh = \frac{H_g d}{D}$$

and

$$Re_i = \frac{(\rho_v v_v)_i d}{\mu}$$

The diffusive mass transfer of the gas can be estimated by invoking the heat and mass transfer analogy. For low mass transfer conditions, the mass transfer rate can be estimated using the Gnielinski [16] correlation which fits quite well a variety of experimental data:

$$Sh_o = \frac{(f_o/2)(Re - 1000)Sc}{1 + 12.7(f_o/2)^{1/2}(Sc^{2/3} - 1)} \tag{24}$$

However, as with friction, one must correct the above relation for high mass transfer rates. As suggested by Kays and Moffat [15], the correction takes the following form:

$$Sh = Sh_o \frac{\Psi e^{\Psi}}{e^{\Psi} - 1} \tag{25}$$

where:

$$\Psi = \frac{Re_i Sc}{Sh_o}$$

If the wall temperature is kept constant by some external means, the preceding set of equations is sufficient to solve the heat transfer problem.

In actual condensers, the wall temperature is not known a-priori, and its local value depends on the flow dynamics and heat transfer conditions on the hot and cold sides. Therefore, for variable wall temperatures, the above equations must be supplemented with relations which express the heat balance between the condenser hot and cold sides. Referring to Figure 2, the steady-state heat flux can be written in three different forms, namely:

$$q'' = \frac{k_\ell}{\delta}(T_i - T_w) \tag{26}$$

$$q'' = \frac{k_w(T_w - T_{wo})}{r \ln(1 + \delta_w/r)} \tag{27}$$

$$q'' = \frac{r + \delta_w}{r} h_c(T_{wo} - T_c) \tag{28}$$

2.2 Solution Procedure

In order to predict the heat removal in the condenser, the following parameters are needed:

- The geometry of the condenser.
- The inlet mixture temperature, pressure, noncondensable fraction , and inlet vapor flowrate.
- The coolant flowrate and inlet temperature.

The solution algorithm depends on the direction of the gas and coolant flows. What follows is the procedure for the case when vapor flows from top to bottom while the coolant flows in the countercurrent direction:

1. Guess an exit coolant temperature $T_{c,out}$.
2. Guess an inside wall temperature T_w.

3. Guess an interface noncondensable mass fraction W_i.
4. Obtain the corresponding interface temperature T_i using the Gibbs- Dalton ideal gas mixture relation and the assumption that steam is at saturation conditions:

$$p_{v,i} = p\frac{1 - W_i}{1 - (1 - M_v/M_g)W_i}$$

$$T_i = T_{sat}(p_{v,i})$$

In the above expression, the relationship between T_i and $p_{v,i}$ is obtained following the recommendations in [17].

5. Calculate the friction correction factor as well as the interface shear stress.
6. Solve equation (18) for the film thickness $\delta(x + \Delta x)$.
7. Obtain an improved interface mass fraction W_i from equation (23).
8. Go back to step 4 until the W_i iteration converges.
9. When the W_i iteration has converged, then:
   (a) Compute the heat flux across the condensate film using equation (26).
   (b) Compute the outer wall temperature T_{wo} using equation (28). The coolant-side heat transfer coefficient h_c is obtained from different correlations depending on the flow regime.
   (c) Compute an improved inner wall temperature T_w using equation (27).
10. If the T_w iteration is not converged then go back to step 3.
11. When the T_w iteration has converged, prepare for the next axial location by calculating the new values for U, $p_{v,\infty}$, T_∞, W_∞, T_c, τ_i, τ_i' (calculated numerically) and go back to step 2.
12. Stop the calculation if, at the end of the tube, the predicted inlet coolant temperature is equal to the specified value $T_{c,inlet}$. If not:
    (a) Calculate the total heat removed $q_t = \int_0^L q'' dA$
    (b) Obtain an improved exit coolant temperature $T_{c,out} = T_{c,inlet} + (q_t)/(m_c c_p)$
    (c) Go back to step 2.

It should be noted that as long as no aerosol particles flow with the gas, the updated mixture velocity in step 11 is calculated in a straightforward manner by performing a mass balance on the vapor flow:

$$m_v(x) = m_{v,inlet} - Q_t(x) \tag{29}$$

and

$$U(x) = \frac{m_v(x)}{\rho A}\frac{1}{1 - W_\infty(x)} \tag{30}$$

However, when aerosols are present, a significant fraction of the steam can be removed by condensation on the insoluble particles or by suction due to the hygroscopic aerosols. A mass balance on the steam can then be written as:

$$dm_v = -dQ_\ell - dm_{insol} - dm_{hygro} \tag{31}$$

The impact of aerosols will be dealt with in a later investigation. dm_{insol} and dm_{hygro} are subsequently taken as zero in the present work.

3 Results and Discussion

3.1 Parametric Simulations

The model described previously was used for parametric studies to determine the impact on the tube performance of important factors such as the inlet gas fraction, the mixture flowrate, the total pressure, and the molecular weight of the noncondensable gas. The tube dimensions are taken to be the same as those in the design of the SBWR PCC tube, i.e. a length of 1.8 m, an inside diameter of 4.75 cm, and a thickness of 1.65 mm. In the simulations of this section, the wall temperature is assumed constant, and air was chosen as the noncondensable gas. The local heat transfer is given in terms of the Nusselt number which is defined as:

$$Nu(x) = \frac{h(x)d}{k_\ell} = \frac{d}{\delta(x)} \frac{T_i(x) - T_w}{T_\infty(x) - T_w} \tag{32}$$

3.1.1 Effect of the Inlet Noncondensable Gas Fraction

The effect of the inlet noncondensable mass fraction was studied by calculating the local Nusselt number for air mass fractions of 0, 0.05, and 0.1 while holding the other parameters constant. As shown in Figure 3, the performance of the condensing tube is strongly degraded as the inlet noncondensable fraction increases.

3.1.2 Effect of the Mixture Mass Flowrate

The effect of the mixture inlet flowrate is shown in Figure 4. As expected, the higher the inlet mass flowrate, the greater the heat transfer rate because as the velocity is increased, the shear stress on the film induces a higher condensate flowrate for the same film thickness (see equation (6)). Furthermore, the effect of the noncondensable gas is more pronounced for the low mixture flowrate case as displayed by the very different slopes of the two curves in Figure 4. The is readily explained by the greater rate of increase in the noncondensable gas fraction for the low mixture flowrate case.

3.1.3 Effect of the Mixture Inlet Temperature

The dependence of the heat transfer on the incoming mixture temperature is depicted in Figure 5. The wall temperature subcooling is kept constant at 20°C for both the

high (130°C) and the low (100°C) temperature cases. As can be seen from the plot, the average Nusselt number is almost independent of the inlet mixture temperature. Based on the Nusselt expression for stagnant steam, one would expect higher heat transfer values at higher temperatures because the heat heat transfer coefficient is inversely proportional to $\mu_\ell^{\frac{1}{4}}$. However, with flowing steam, the velocity is lower at higher temperatures for a given mass flowrate. This causes a reduction in the shear effect on the film, with a subsequent decrease in the condensation rate.

3.1.4 Effect of the Molecular Weight of the Noncondensable Gas

In the event of a severe accident in an SBWR, the noncondensable gas might be the hydrogen which would be released following fuel oxidation. It is therefore of interest to predict the degradation of the heat transfer which would occur if hydrogen replaces air as the noncondensable gas.

In the first calculation, the prediction is made for an inlet noncondensable mass fraction of 0.05. As seen in Figure 6, hydrogen causes a greater heat transfer degradation since it occupies more volume than air and hence acts as a efficient shield against condensation. The difference in the heat transfer coefficients for the two mixtures is especially pronounced at the beginning of the tube where the condensation rates are the largest. Towards the end of the tube, the heat transfer rates are of similar magnitude as the noncondensable fraction for for the air/steam mixture increases rapidly owing to the greater condensation rates in the first segment of the tube.

In the second calculation, the prediction is made for an inlet noncondensable mole fraction of 0.05. This corresponds to a mass fraction of 0.078 for air and 0.0058 for hydrogen. This time, the inlet mixtures have the same number of noncondensable moles. As a result, the heat transfer coefficients are of the same magnitude as shown in Figure 7. On a mole basis, air is a little bit more inhibitive to condensation because of its lower diffusion coefficient.

4 Comparison with Experimental Data

4.1 Comparison with Pure Steam Data

The model can readily be applied to pure steam cases by simply bypassing the T_i iteration in the solution procedure outlined earlier. Several experiments have been carried out for pure steam condensation inside vertical tubes. Two references [18], [19] are chosen here to serve as a test for the present model. In these investigations, the wall temperature were reported to be relatively constant owing to the high cooling rates used, and thus only an averaged value is given. The heat transfer results are given in terms of a mean Nusselt number for the entire tube. In the course of the calculation, the film physical properties were evaluated at $T_w + 0.31 * (T_i - T_w)$ in accordance with the recommendation in [7]. The agreement between the model and the data is satisfactory as shown in Table 1.

Reference	$U_{inlet}(m/s)$	$L(m)$	$D(cm)$	$T_\infty(°C)$,	$T_\infty - T_w(°C)$	Nu_{exp}	Nu_{theory}
1 (Fig.6)	20	1.21	0.04	100	28	325	325.7
1 (Fig.6)	40	1.21	0.04	100	11	475	414.3
1 (Fig.6)	20	1.21	0.04	100	28	369	441.3
1 (Fig.6)	40	1.21	0.04	100	11	491	571.4
1 (Fig.6)	20	1.21	0.04	100	4	460	590.7
1 (Fig.6)	10	1.21	0.04	100	6	363	453
1 (Fig.6)	10	1.21	0.04	100	12	340	371
1 (Fig.6)	20	1.21	0.04	100	20	353	365.7
2 (Run 5)	20	2.32	0.0148	130	23.5	112	112.4
2 (run 13)	26.5	1.86	0.0158	127	29.5	154	127.5

Table 1: Comparison between the model Predictions and Pure Steam Data

4.2 Comparison With Steam-Noncondensable Data

A number of experimental investigations ([13], [20]) have been conducted in support of the Passive Containment Cooling System (PCCS) condensers which are designed to transfer decay heat from the SBWR Drywell to a stagnant pool of water located outside the containment. In both experiments [13] and [20], the data scatter was quite large and the correlations obtained yielded significantly different values for the local heat transfer coefficient. A plausible explanation for these discrepancies is the unreliable method used for measuring the bulk coolant temperature. In both experiments, the coolant thermocouples were inserted in the narrow jacket channel where large temperature gradients existed. A more careful investigation was carried out lately by Kuhn et al. [21]. The set-up consisted of a vertical tube surrounded by a cooling water jacket. The condenser tube was a steel cylinder with a length of 2.4 m, an inside diameter of 4.75 cm, and a wall thickness of 1.65 mm. The cooling jacket had an inside diameter of 7.36 cm and was insulated from the outside to prevent heat losses to the environment. The steam-gas mixture ran from top to bottom while the cooling water ran in the countercurrent direction. The temperature distribution (and hence bulk temperature) in the cooling annulus was deduced by solving the turbulent flow equations in the coolant annulus subject to the experimentally measured temperatures at both boundaries of the flow channel. This method for determining the local heat flux was more accurate than in the preceding investigations, which explains the smaller scatter in the data.

The experimental runs were conducted with pure steam, steam-air, and steam-helium mixtures. The Kuhn investigation produced a set of correlations with represent the extensive experimental data quite accurately.

Five steam-air runs were chosen to test the theoretical model. The noncondensable mass fraction varies from 0 to 0.396. The experimental parameters are summarized in Table 2.

Since the coolant flowrate was quite small, and the temperature difference between the outer tube wall and the coolant quite high, turbulent mixed convection is the relevant flow regime for the annulus flow. Accordingly, the following correlation was used for the secondary side heat transfer [22]:

Parameter	Run 1-1-1	1-1-3R	Run 2-1-5	Run 2-1-8 R	Run 2-1-13
$T_{sat,inlet}$, $^{\circ}C$	104.0	136.0	143.5	141.4	131.8
$m_{v,inlet}$, kg/sec	0.01672	0.01653	0.01430	0.01422	0.01391
$W_{\infty,inlet}$	0	0	0.0589	0.148	0.396
m_c, kg/sec	0.278	0.308	0.343	0.257	0.2106
$T_{c,inlet}$, $^{\circ}C$	39.0	40.0	36.5	33.2	32.0

Table 2: Parameters in the Experimental Runs by Kuhn

$$Nu_c = (Nu_{nc}^3 + Nu_{fc}^3)^{\frac{1}{3}}$$

Nu_{nc} is given by the Bayly correlation for turbulent natural convection along a vertical wall, while Nu_{nc} is simply the well known Dittus-Boelter formula for turbulent forced internal flows:

$$Nu_{nc} = 0.1 Ra_c^{\frac{1}{3}}$$

$$Nu_{fc} = 0.023 Re_c^{0.8} Pr_c^{\frac{1}{3}}$$

The parameters in these correlations were evaluated at the average temperature between the wall and the coolant.

As shown in Figures 8 through 12, the model predicts quite accurately the various trends in the experimental data. The total heat removal rate was estimated with less than 5% error except for Run 1-1-1 where it is overpredicted by 15%.

5 Conclusion

A simple and self-contained model was presented for the prediction of heat transfer inside a condenser tube in the presence of noncondensable gases. The theoretical simulations agreed quite well with a variety of experimental data. The model can be easily extended to include the effect of hygroscopic aerosols flowing with the vapor-gas mixture.

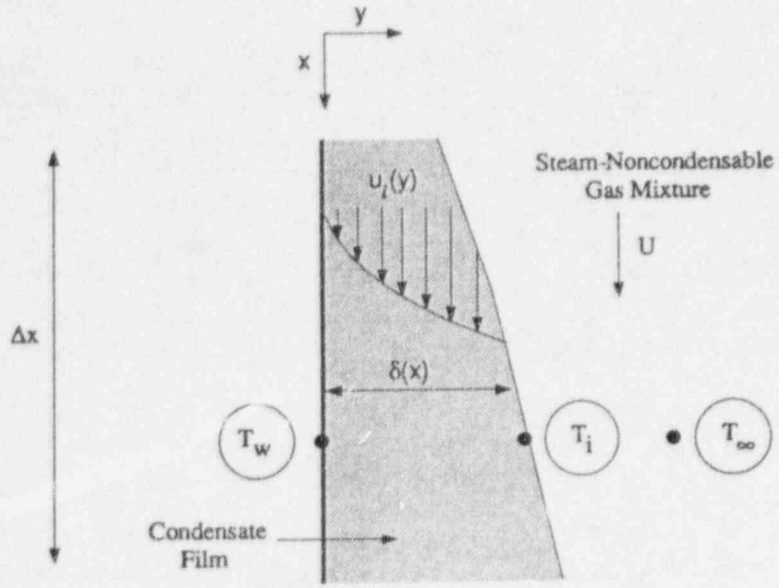

Figure 1: Illustration of the Film Condensation Model

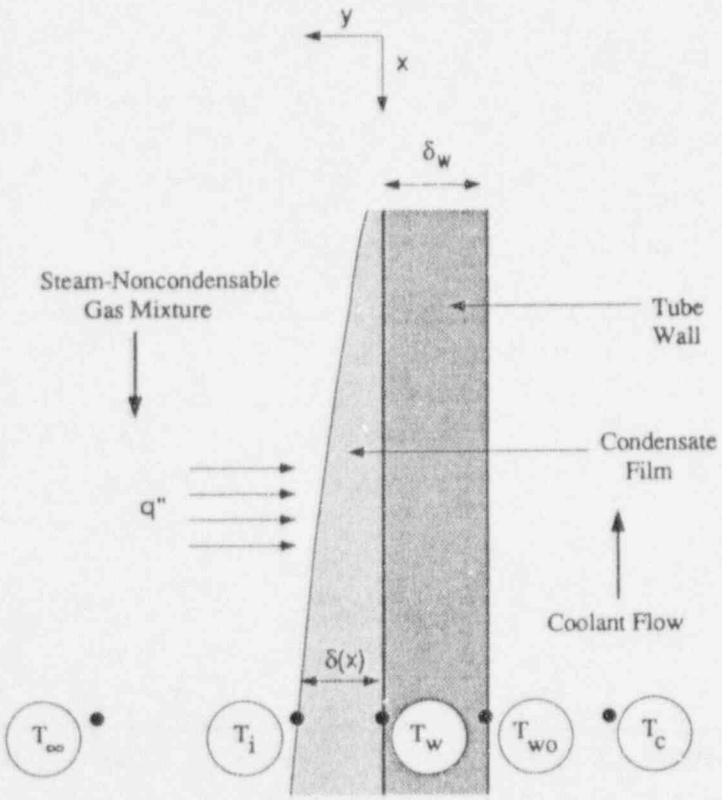

Figure 2: Illustration of the Heat Transfer in a Condenser Tube

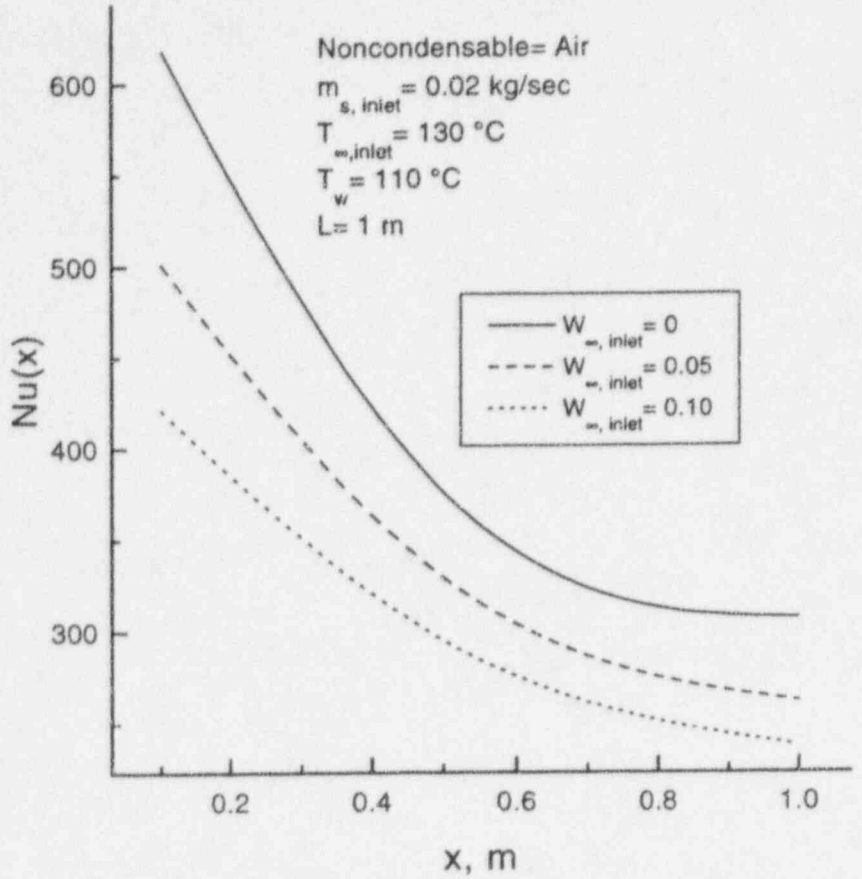

Figure 3: Effect of the Inlet Noncondensable Fraction on the Local Nusselt Number

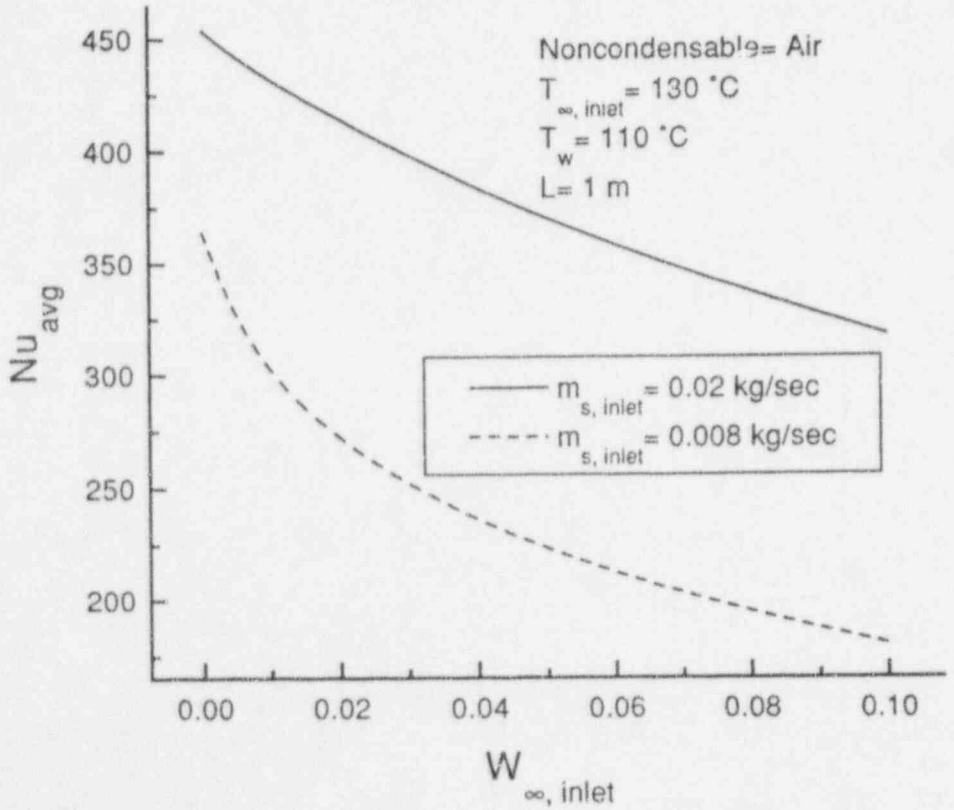

Figure 4: Effect of the Steam Flowrate on the Average Nusselt Number

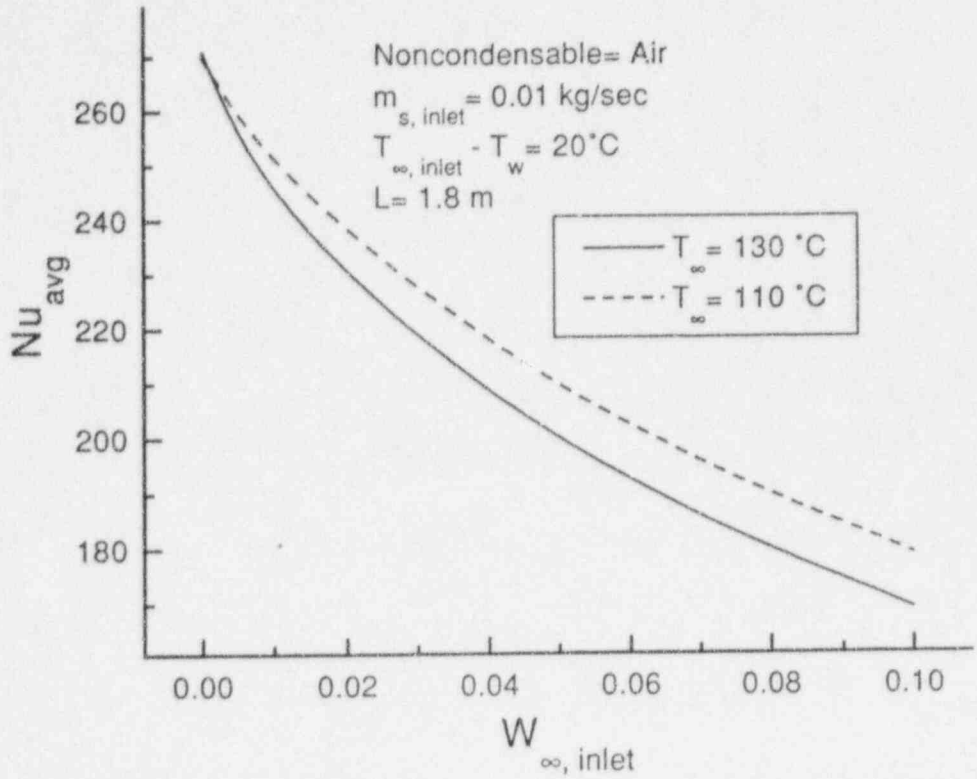

Figure 5: Effect of the Mixture Inlet Temperature on the Average Nusselt Number

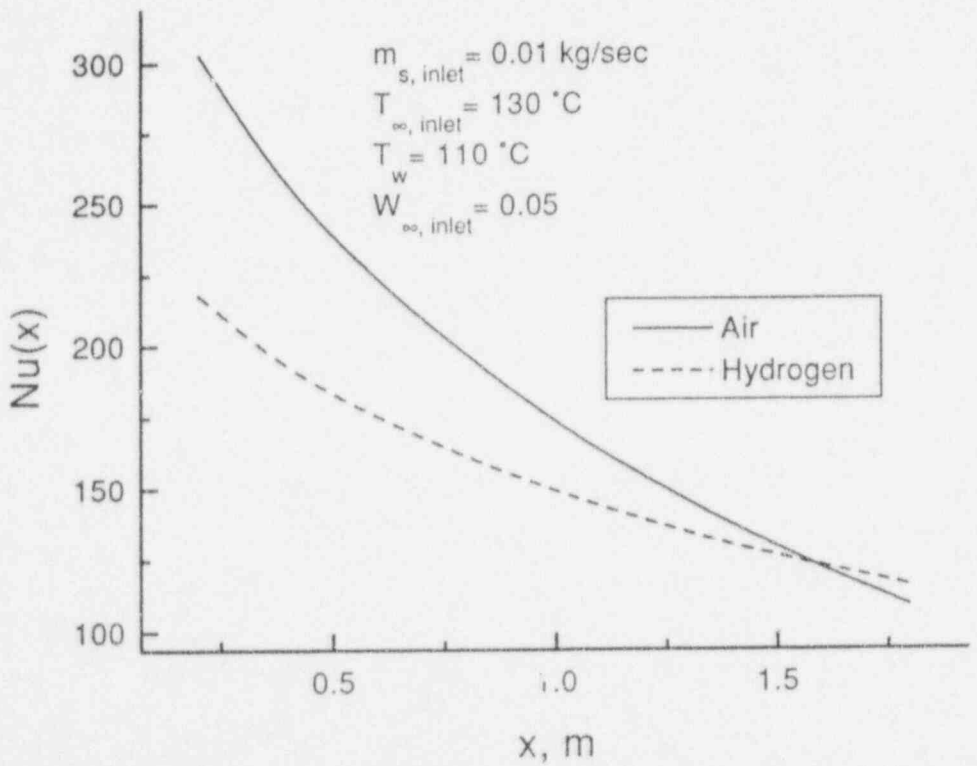

Figure 6: Effect of the Molecular Weight of the Noncondensable Gas on the Local Nusselt Number (Mass Fraction Basis)

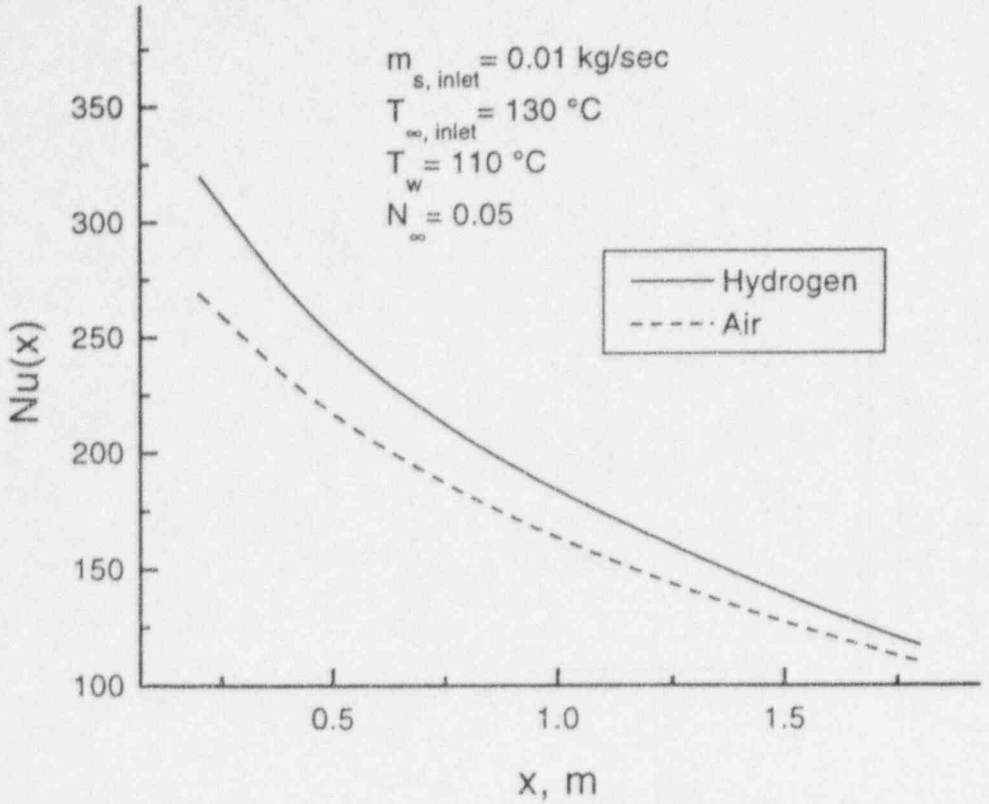

Figure 7: Effect of the Molecular Weight of the Noncondensable Gas on the Local Nusselt Number, (Mole Fraction Basis)

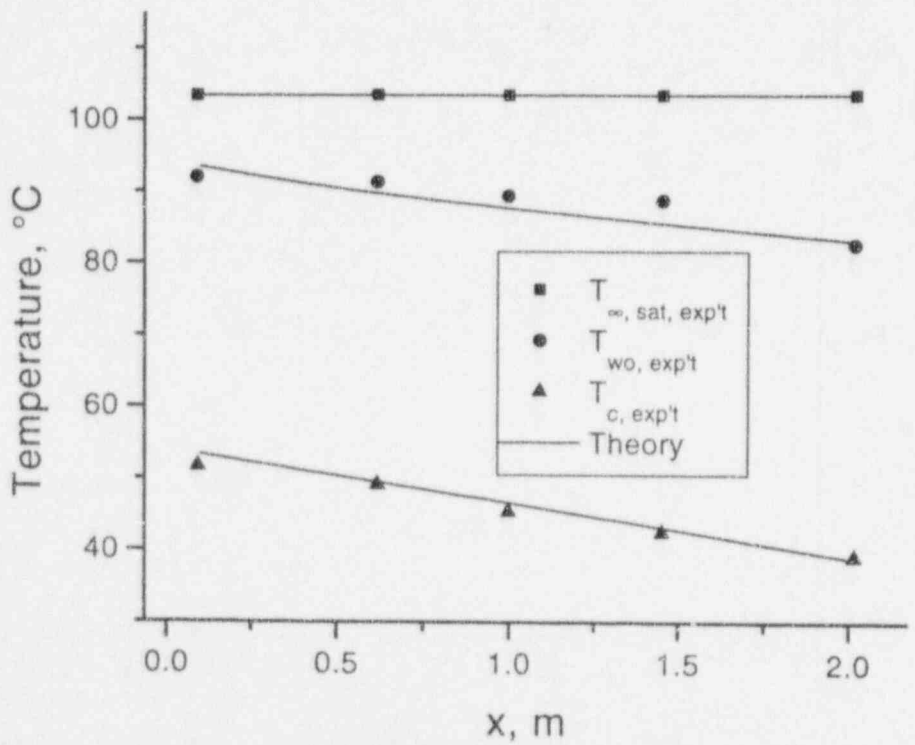

Figure 8: Comparison with Kuhn's Run 1-1-1

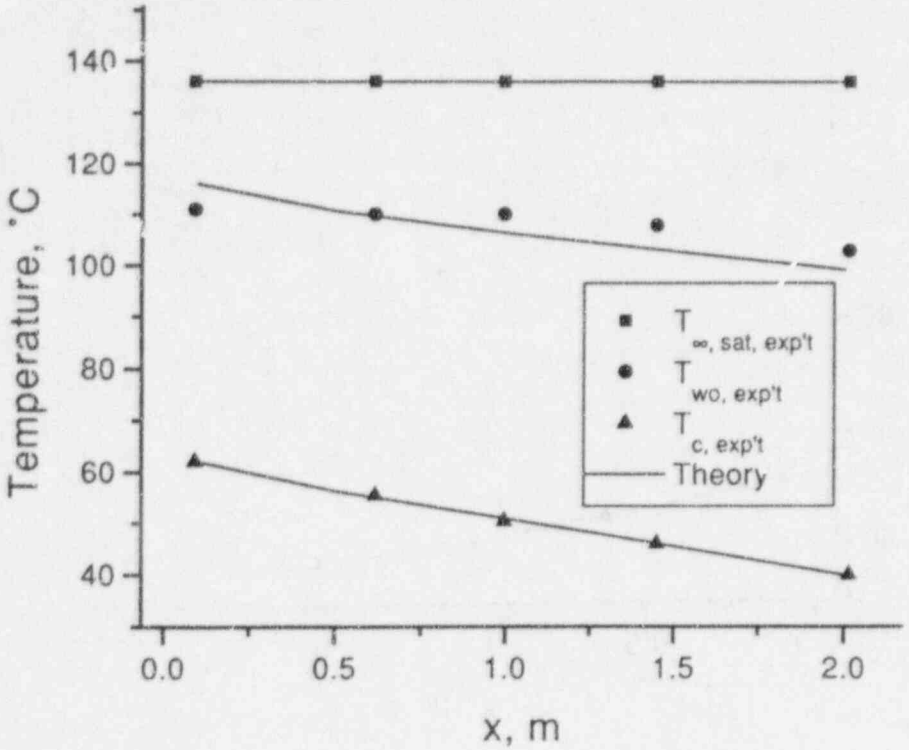

Figure 9: Comparison with Kuhn's Run 1-1-3R

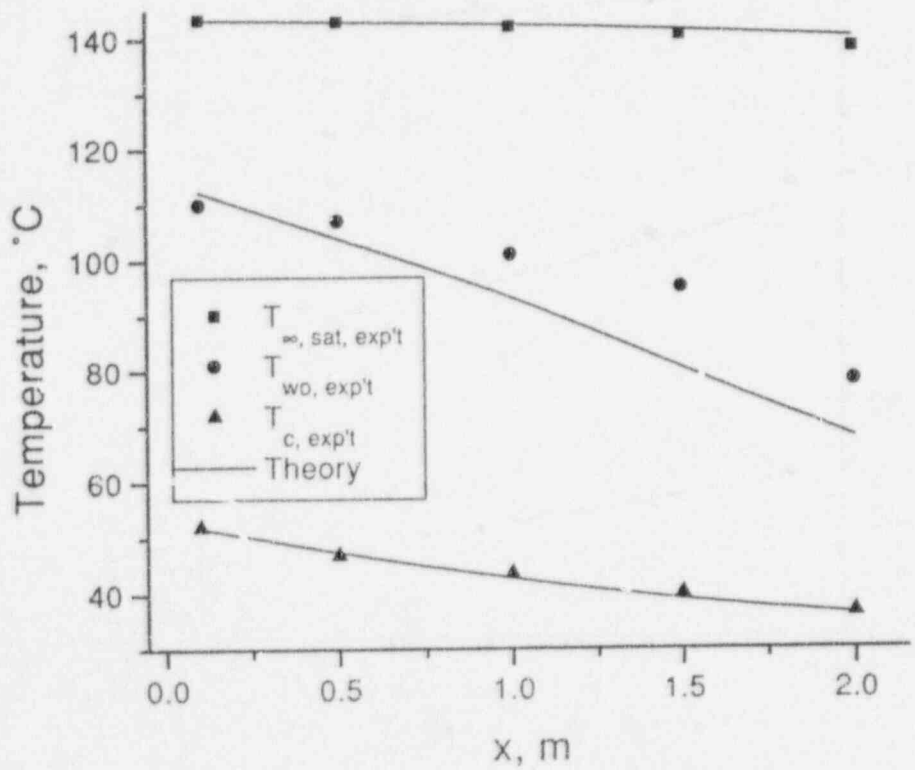

Figure 10: Comparison with Kuhn's Run 2-1-5

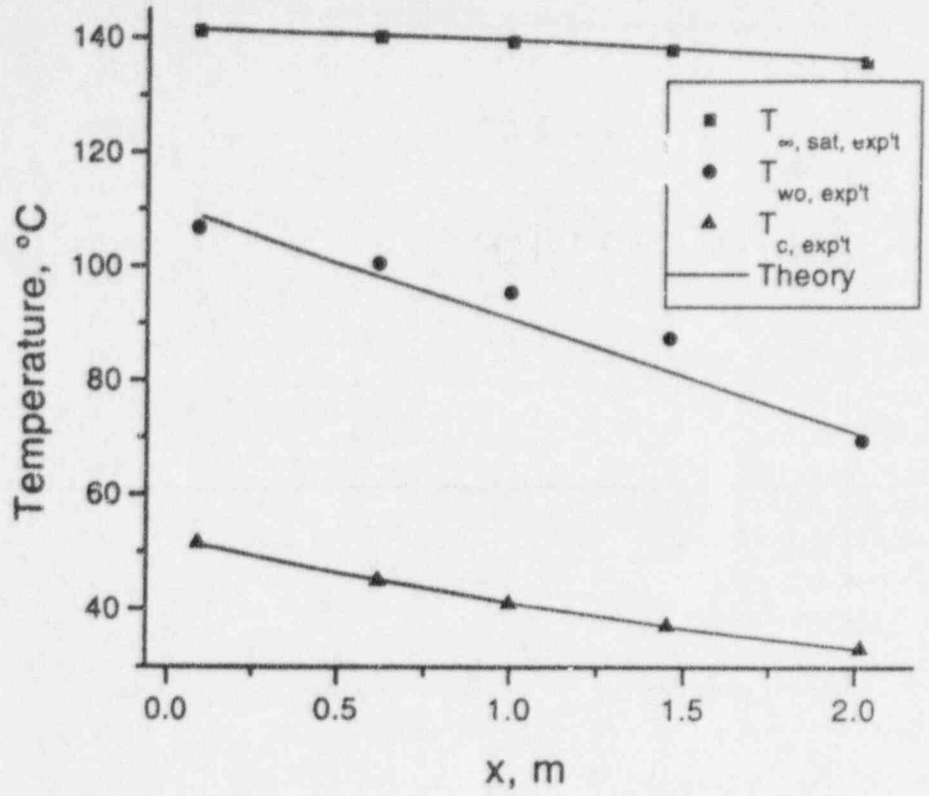

Figure 11: Comparison with Kuhn's Run 2-1-8 R

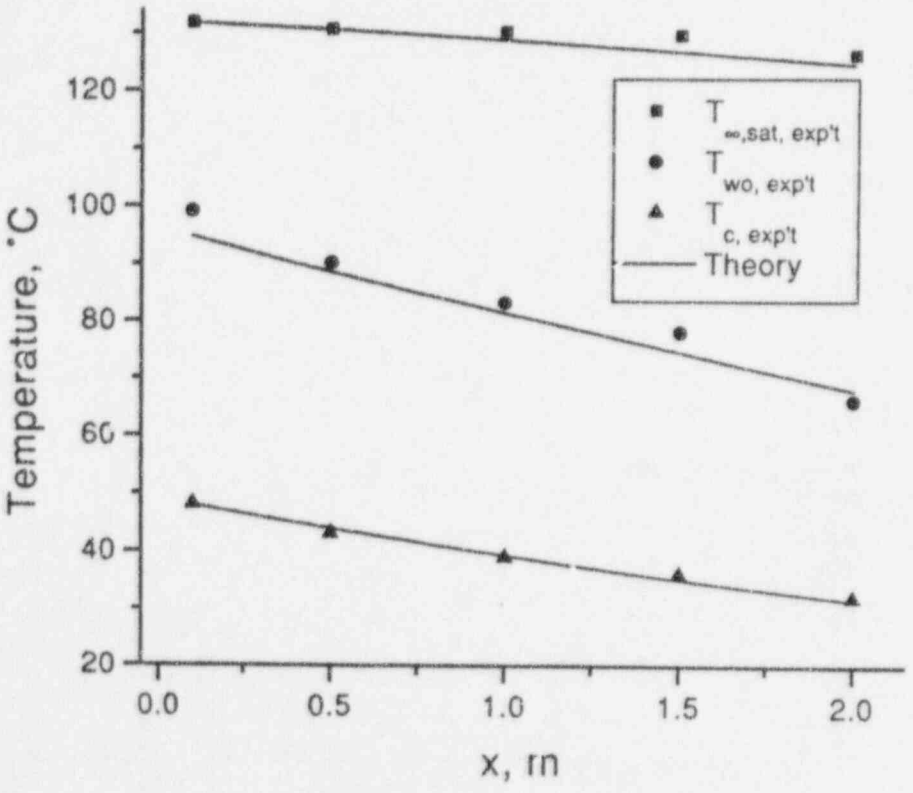

Figure 12: Comparison with Kuhn's Run 2-1-13

6 NOMENCLATURE

A : tube flow area
c_p : coolant heat capacity
D : diffusive coefficient
d : tube inner diameter
DF : degradation factor
f : friction factor
g : gravitational acceleration
H : mass transfer coefficient
h : heat transfer coefficient
h_{fg} : latent heat of steam
h_g : mass transfer coefficient
k : thermal conductivity
L : tube length
m : mass flowrate
m'' : mass flux
M : molecular weight of noncondensable
Nu : Nusselt number
N : noncondensable gas mole fraction
p : total pressure
Pr : Prandtl number
q_t : total heat removed by the coolant
q'' : heat flux
Q_ℓ : condensate film flowrate
r : tube inner radius
Ra : Rayleigh number
Re : Reynolds number
Sc : Schmidt number
T : Temperature
u_ℓ : liquid velocity
U : gas vertical velocity
v : velocity normal to the wall
W : noncondensable mass fraction
x : vertical distance
y : horizontal distance

Greek

ρ : gas mixture density
ρ_ℓ : liquid film density
μ : gas mixture dynamic viscosity
μ_ℓ : liquid dynamic viscosity
ν_ℓ : liquid kinematic viscosity

δ : liquid film thickness
ϕ : correction parameter for friction
Ψ : correction parameter for mass transfer
τ_i : shear stress at the gas-liquid interface
τ_i' : derivative of the shear stress with respect to δ

Subscripts

c : coolant
ℓ : liquid
f : film
fc : forced convection
g : noncondensable
i : liquid-gas interface
∞ : bulk gas mixture
$insol$: insoluble aerosol
$hygro$: hygroscopic aerosol
m : mixture
nc : natural convection
o : no-suction value
out : outlet
sat : saturation
v : vapor
w : inside wall
wo : outside wall

References

[1] W. Nusselt " Die Oberflachenkondensation des Wasserdampfes." Z. VDI, Vol. 60 (1916), pp. 541/546, 569/575.

[2] W.M. Rohsenow, J.H. Webber, A.T. Ling, Effect of Vapor Velocity on Laminar and Turbulent Film Condensation, Trans. Am. Soc. Mech. Engrs. 78, 1637-1643 (1956).

[3] J.C.Y. Koh, E.M. Sparrow and J.P. Hartnet, "The Two Phase Boundary Layer in Laminar film Condensation", Int. J. Heat Mass Transfer, 2 69-82(1961).

[4] F. Dobran and R. Thorsen, "Forced Flow Laminar Filmwise Condensation of a Pure Saturated Vapor in a Vertical Tube", Int. J Heat Mass Transfer, 23, 161-177(1979).

[5] R. Bellinghausen, U. Renz, " Heat Transfer and Film Thickness during Condensation of Steam Flowing at High Velocity in a Vertical Pipe", Int. J. Heat Mass Transfer, 35, No 3, 683-689(1992).

[6] E.M. Sparrow and S.H. Lin, "Condensation Heat Transfer in the Presence of a Noncondensable Gas", J. Heat Transfer, 9, 430, (1964).

[7] W. J. Minkowycz, and , E. M. Sparrow, " Condensation Heat Transfer in the Presence of Noncondensables. Interfacial Resistance, Superheating, Variable Properties, and Diffusion ", Int. J. Heat Mass Transfer, 9, pp. 1125-1144, 1966.

[8] H.K. Al Diwani, J.W. Rose, "Free Convection Film Condensation of Steam in the Presence of Noncondensable Gases", Int. J. Heat Mass Transfer, 16, 1359 (1972).

[9] J.W. Rose, "Approximate Equations for Forced Convection Condensation in the Presence of a Noncondensing Gas on a Flat Plate and Horizontal Tube", Int. J. Heat Mass Transfer, 23, 539 (1980).

[10] A. Dehbi, M.W. Golay, and M.S. Kazimi "Condensation Experiments in Steam-Air and Steam-Air-Helium Mixtures under Turbulent Natural Convection", National Heat Transfer Conference, AIchE Proceedings, Minneapolis, July 1991.

[11] C. Wang and C. Tu, "Effects of Non-condensable Gas on Laminar Film Condensation in a Vertical Tube", Int. J. Heat Mass Transfer, 31, 2339, (1988).

[12] M. Siddique, M.W. Golay, and M.S. Kazimi, "Local Heat Transfer Coefficients for Forced Convection Condensation of Steam in a Vertical Tube in the Presence of a Noncondensable Gas", Nucl. Technol., 102, 386, (1993).

[13] M. Siddique, M.W. Golay, and M.S. Kazimi, "Theoretical Modeling of Forced Convection Condensation of Steam in a Vertical Tube in the Presence of a Noncondensable Gas", Nucl. Technol., 106, 202, (1994).

[14] P. Kaiping and U. Renz, " Thermal Diffusion Effects in Turbulent Partial Condensation ",Int. J. Heat Mass Transfer, 34, No 10, 2629-2639(1991).

[15] W.M. Kays and R.J. Moffat "The Behavior of Transpired Turbulent Boundary Layers", Studies in Convection, Academic Press, New York (1975) Film Condensation in a Vertical Tube", Int. J. Heat Mass Transfer, 31, 2339, (1988).

[16] V. Gnielinski, "New Equations for Heat and Mass Transfer in Turbulent Pipe and Channel Flow", Int. Chem. Eng., 16, 359 (1976).

[17] UK Steam Tables in SI Units, Edward Arnold, 1970.

[18] M. Jacob, "Heat Transfer in Evaporation and Condensation -II", Mech. Engng 58, 729-740 (1936).

[19] , J. H. Goodykoontz, R. G. Dorsch.," Local Heat-Transfer Coefficients for Condensation of Steam in Vertical Downflow Within a 5/8 Inch Diameter Tube", NASA TN D-3326, 1966.

[20] K. M. Vierow and V. E. Schrock, " Condensation in a Natural Circulation Loop With Noncondensable Gases Part I - Heat Transfer ", Proc. Intl. Conf. on Multiphase Flows '91 Tsukuba, Tsukuba, Japan, pp. 183-186, September, 1991.

[21] S. Z Kuhn, V. E. Schrock and P. F. Peterson, " An Investigation of Condensation from Steam-Gas Mixtures Flowing Downward Inside a Vertical Tube ", To be presented to the NURETH-7 Conference.

[22] S.W. Churchill, " A Comprehensive Correlating Equation for Laminar, Assisted, Forced, and Free Convection", AIchE J., 23, 10, 1977.

[23] S.M. Ghiaasiaan, B.K. Kamboj, and S.I. Abdel-Khalik "Two-fluid Modeling of Condensation in the Presence of Noncondensables in Two-Phase Channel Flows ", Nuclear Science and Engineering, 119, 1-17 (1995).

UPTF-TRAM Experiments for SBLOCA:

Evaluation of Condensation Processes in TRAM Tests A6 and A7

Sonnenburg, H.G.; Tuunanen*, J.; Palazov, V.V.

Gesellschaft für Anlagen- und Reaktorsicherheit (GRS) mbH
Forschungsgelände, 85748 Garching b. München, Germany
Tel.: (089) 32004-259 Fax: (089) 32004 299

*) Resident Engineer from VTT, Finland

The paper is pertinent to the project RS 878 of the
German Ministry for Research and Technology (BMBF)

Abstract

The investigation of thermal-hydraulic phenomena related to reactor transients with accident management measures is the goal of the TRansient and Accident Management (TRAM) experimental programme being carried out at the Upper Plenum Test Facility (UPTF) at Mannheim (Germany). These experimental investigations and test analyses are funded by the German Federal Minister for Research and Technology (BMFT). The UPTF simulates these phenomena in a 1:1 scale relative to the dimension of a PWR.

Condensation of steam during Emergency Core Cooling (ECC) water injection from accumulators into the primary system is one of the phenomena studied within the TRAM programme. This phenomenon partly controls the efficiency of accumulator injection if the high pressure safety systems fail. Beside this, the condensation within the nitrogen inside the accumulator for a certain period controls the pressure development inside the accumulator. Thus, both condensation phenomena determine the ECC flow rate delivered to the primary system. Concerning the condensation inside the primary system, this is also of safety relevance in the case of Pressurized Thermal Shock (PTS) during cold leg injection.

Introduction

The investigation of thermal-hydraulic phenomena related to reactor transients with accident management measures is the goal of the TRansient and Accident Management (TRAM) experimental programme. The programme is carried out at the Upper Plenum Test Facility (UPTF) in Mannheim (Germany). The programme is funded by the German Federal Ministry for Research and Technology (BMFT). It is subdivided into 4 groups called A, B, C and D. While group A comprises the investigation of small leak related phenomena, group B contains tests devoted to the investigation of the thermal-hydraulics under the influence of steam venting from the pressurizer. The tests in the group C are dealing with the pressurized thermal-shock and boron dilution problems. In the group D the convective energy transport under severe accident conditions will be investigated. The experimental programme will end at the middle of 1995.

One of the results obtained from the test group A is the quantification of the condensation rate which may occur under a small leak transient during accumulator injection. This phenomenon has been investigated in the tests A6 and A7. Main findings from tests are presented in this paper.

Under small leak conditions (approximately 5%) combined with a failure of the high pressure safety injection system the injection of ECC water from accumulators may provide core cooling. Because only a decrease in primary pressure provides a certain ECC water injection from the accumulator, the development of the ECC flow rate depends on the effectiveness of the condensation process. When the sum of both the steam condensation due to ECC water injection and the discharge of steam at the leak is larger than the steam generation resulting from both the decay heat and flashing, the primary pressure decreases. Thus, the ECC injection is supported. In the opposite situation the ECC injection is reduced and even may stop.

In the case of cold leg injection the condensation rate within the cold leg determines the warming up of the ECC water flowing to the inlet of the downcomer. Therefore, this condensation rate is important in the context of the thermal shock problem, too.

The test A6 represents the system behavior for small leak transient with cold leg ECC injection and test A7 for hot leg injection. In both tests free falling water jets have been observed. While for the hot leg injection the jet is formed in the upper plenum, the water jet for the cold leg injection appears just at the injection port inside the cold leg.

While the pressure development in the primary system is controlled by the condensation processes in the vicinity of the ECC injection port, the pressure development in the accumulator is controlled to a large extent by a condensation process occurring inside the nitrogen of the accumulator. Steam dissolved in the nitrogen condenses here. By means of an energy balance for the nitrogen, it can be shown that this condensation process reduces significantly the depressurization of the nitrogen for a certain period. Therefore, the pressure development in the nitrogen significantly deviates from that one of an adiabatic nitrogen system.

1. Upper Plenum Test Facility

The Upper Plenum Test Facility (UPTF) is constructed and operated by Siemens [WEI 92] under the auspices of the German Federal Ministry for Research and Technology (BMBF). It simulates the following reactor components:

a) upper plenum with internals,
b) downcomer,
c) 4 connected loops,
d) parts of the core region

in a 1:1 scale relative to a PWR (see fig.1).

The flow behavior within the core region is simulated by a core simulator which allows injection of both steam and water. The pumps and steam generators within the primary loops are also represented by simulators. Leaks of different sizes can be alternatively realized in a cold leg or hot leg. The maximum operating system pressure of the UPTF is 2 MPa. For the tests under consideration (A6 and A7) the pressure transient starts at 1.8 MPa and the simulated ECC injection starts at 1.6 MPa.

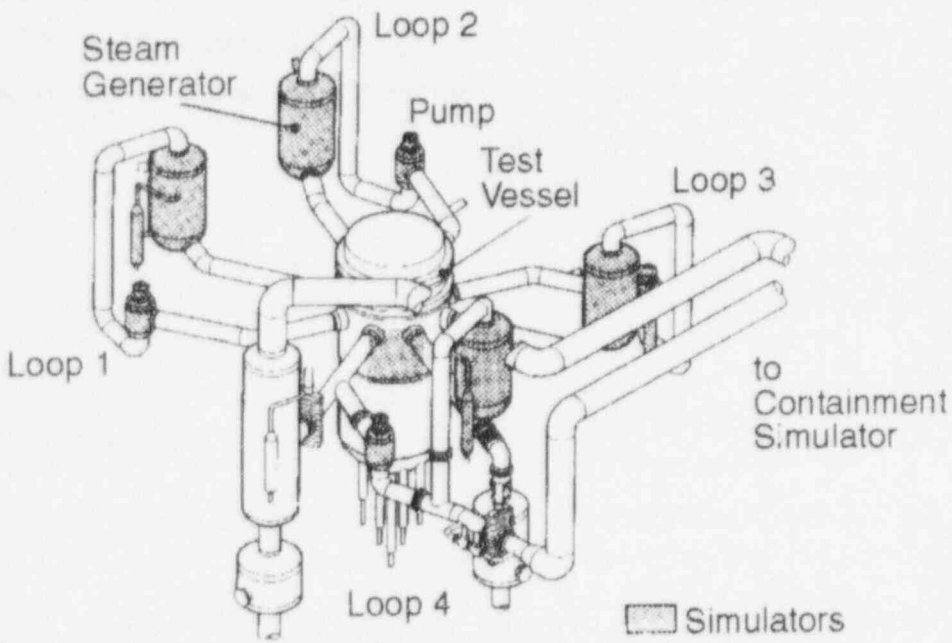

Fig. 1 Upper Plenum Test Facility (UPTF)

The UPTF is equipped with water storage tanks which are partially filled with water and nitrogen in order to simulate the behavior of the accumulators. The flow resistance occurring in an real injection line between accumulator and injection port is adjusted in the corresponding line of the UPTF.

2. Condensation in the cold leg during ECC injection

In the UPTF/TRAM test A6, ECC water was injected from the accumulators into the cold legs of the primary coolant loops. When the injection started the cold legs were full of steam and the water level in the downcomer was clearly below the cold leg pipe elevation.

The schematics of the situation in the cold legs and the downcomer during accumulator injection is presented in fig. 2. ECC water enters through a side pipe of 0.22 m inner-diameter into the cold leg pipe (∅ 0.75m). ECC water forms a jet of parabolic shape in the vicinity to the injection point and flows towards the downcomer where another jet is formed. Some mixing towards the pump simulator takes place but no flow of water to the pump seals appears. Flow regime in the cold legs is co-current stratified flow with water and steam flowing into the same direction towards the downcomer.

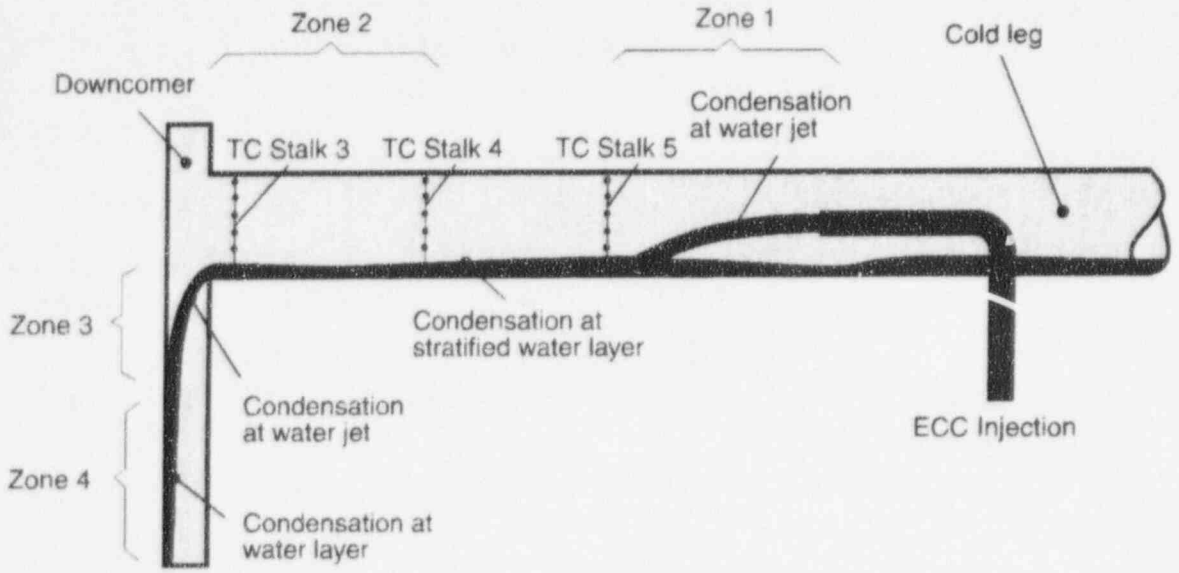

Fig. 2 Flow conditions in the cold legs and downcomer during ECC water injection from the accumulators.

Condensation process during ECC injection to the cold legs can be considered in four parts:

- condensation at the injection point (jet, zone 1 of fig. 2),
- condensation between the injection point and downcomer (co-current flow of steam and water, zone 2 of fig. 2),
- condensation in the upper part of the downcomer (water jet, zone 3 of fig. 2) and
- condensation at the water layer at the core barrel wall (water film at wall, zone 4 of fig. 2).

Because almost 2/3 of the total condensation was observed at the water jet this paper is restricted to this prevailing process.

3. Condensation at the water jet

The condensation rate of steam at the injection point of ECC water was determined from the energy and mass balance of the water jet [TUU 94]. The measurement data used to calculate the condensation rate included the temperature and flow rates of ECC water, pressure at the considered cold leg and the temperature of water downstream the ECC water injection point.

Using the condensation rate derived from this balance $\dot{m}_{cond}$ and assuming a jet of constant diameter along the length of this jet equal to the injection nozzle D_{jet}, the averaged heat transfer coefficient for the jet htc is:

$$htc = \frac{\dot{m}_{cond}\, r}{A_{jet}\, \Delta T} \quad \text{with} \quad \Delta T = T'' - \frac{T_{Accu} + Tm}{2} \quad \text{and} \quad A_{jet} = \pi D_{jet}\, L_{jet} \tag{1}$$

The length of the jet is derived from the mass flow rate of the jet:

$$L = \frac{1}{2} g T_y \sqrt{a^2 + T_y^2} + g\frac{a^2}{2} \ln \left| \frac{T_y + \sqrt{a^2 + T_y^2}}{a} \right| \tag{2}$$

$$\text{with} \quad a = \frac{v_{jet}}{g} \quad , \quad T_y = \sqrt{\frac{2H}{g}} \quad , \quad v_{jet} = \frac{4\dot{m}_{jet}}{D_{jet}^2\, \pi\, \rho_{ECC}} \quad \text{and} \quad g = 9.81 \frac{m}{s^2}$$

H is the measured vertical height of the water jet between injection port and entrance of the jet into the horizontal water layer at the bottom of the cold leg.

The overall energy and mass balance for the zone 1 reveals that about 30 to 40 % of the local condensation potential provided by the injected ECC water was used at the jet. The balance for the entire system shows a utilization of the total condensation potential of about 60%.

The results derived from the experiments have been compared with several correlations from different authors. Agreement with the experimental results was achieved by using Shklover's correlation [SHK 70]. This correlation is given by:

$$htc_{Shklover} = Nu \frac{\lambda_L}{D_{jet}} \tag{3}$$

$$\text{with} \quad Nu = 0.02\, Re_L^{1.2}\, Pr_L^{0.43}\, K^{0.1} \left[\frac{D_{jet}}{L_{jet}} \right]^{0.75} ,$$

$$Re_L = \frac{4\dot{m}_L}{\pi D_{jet}\, \eta_L} \quad , \quad Pr = \frac{\eta_L\, c_{PL}}{\lambda_L} \quad \text{and} \quad K = \frac{r}{c_{PL}\,(T' - T_{ECC})}$$

The correlation of Shklover [SHK 70] gives the averaged Nußelt number of the water jet as a function of the jet Reynolds, Prandl and subcooling numbers. In figure 3 the results of all test runs (run 1c, 2a, 3a and 4a) are plotted in related Nußelt number versus Reynolds number for liquid.

With the exception of test run 3a all test runs have been accomplished with nitrogen injection. The nitrogen injection rate at the test runs 1,2 and 4 is directly proportional to the ECC water mass flow rate. The proportionality is given by:

$$\dot{m}_{N2} = 3.44\ 10^{-4}\ \dot{m}_{jet} \qquad (4)$$

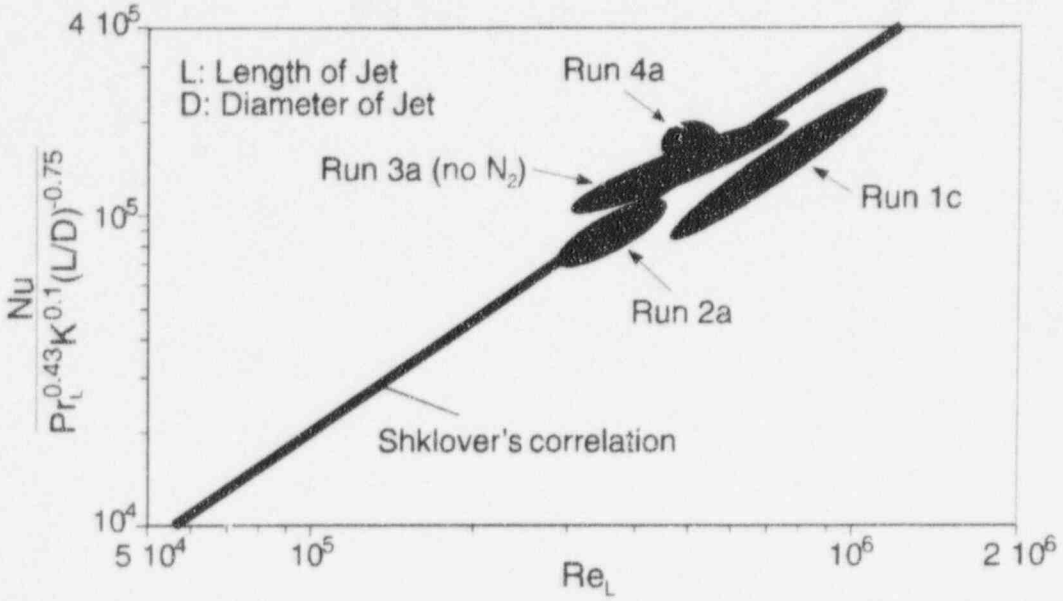

Fig. 3 The effects of nitrogen on the condensation heat transfer, TRAM test A6, test runs 1c, 2a, 3a and 4a.

Comparing results from TRAM test runs with nitrogen injection (test runs 1c, 2a and 4a) and without nitrogen injection (test run 3a), the effect of nitrogen on jet condensation appears to be not present (see fig. 3). Due to a permanent flow of steam free of nitrogen from the core region via upper plenum and steam generators towards the injection points, an accumulation of nitrogen in the system is prevented. It can be concluded that the amount of nitrogen provided to the system is insufficient in order to motivate a measurable reduction in the condensation at the water jet.

4. Condensation at the water fall during hot leg injection

In the UPTF/TRAM test A7, ECC water is injected from the accumulators into the hot legs. At the beginning of the test run the water level in the test vessel is far below primary legs. The phenomenological analysis of test A7 [SON 94] reveals that ECC water flows counter-currently to the steam flow toward the upper plenum. Because the ECC water flows in a stratified layer of approximately 1.5 m horizontal length towards the upper plenum, the condensation at the layer's surface is low. However, significant condensation occurs when the subcooled water enters into the upper

plenum. This water forms a water fall with a flat profile as shown in the figure 4. This water fall can be considered as a water jet, thus the phenomenon observed for the cold leg injection is comparable with this situation.

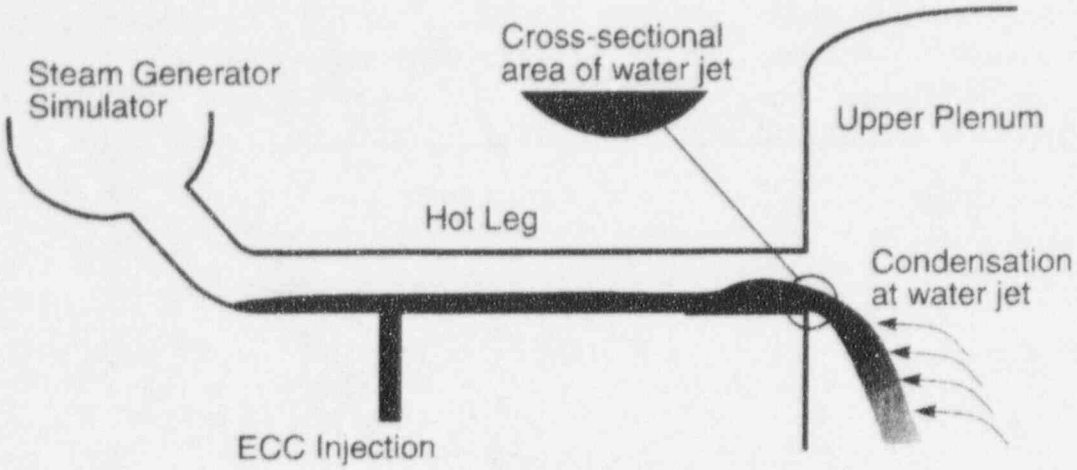

Fig. 4 Schematic view of the flow phenomenon

In the UPTF several thermocouples are mounted in the entrance region of the upper plenum which allow a quantification of the condensation rate. The figure 5 indicates the position of these thermocouples.

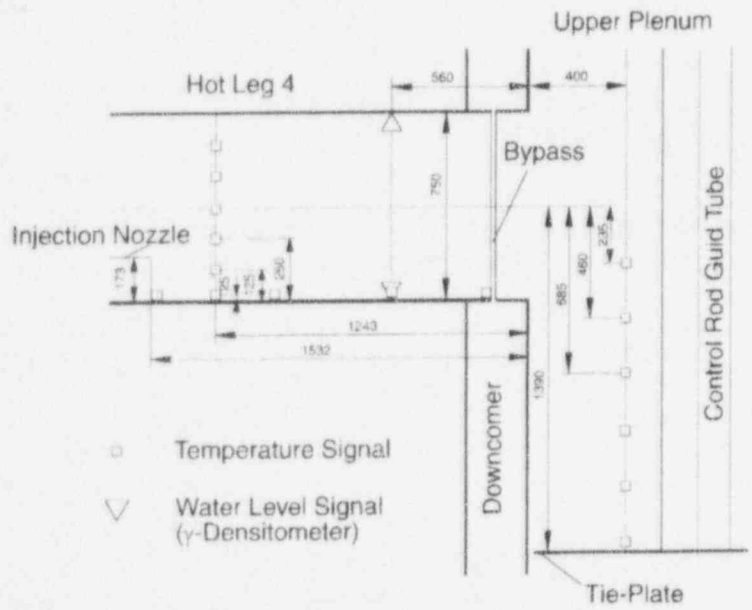

Fig. 5 Position of thermal couples in the upper plenum

Because no visualization of the flow in the upper plenum is available, the assumption of a gravity dominated parabolic shape of the water jet is used in order to provide all necessary geometric parameters (hydraulic diameter, active surface, length of jet). Using this assumption these parameters can be determined from the water mass flow rate and the water level signal at the hot leg entrance. The assumption made ignores the momentum exchange between the falling water jet and the

counter-currently flowing steam. Furthermore the change of the cross-sectional area as a result of the acceleration of the falling water is ignored, too. Under these simplifying assumptions the Nußelt numbers are evaluated and plotted in figure 6.

As it can be seen from the figure 6, the correlation of Shklover predicts again reasonable values in comparison with the evaluated data from the test A7 Run 1A.

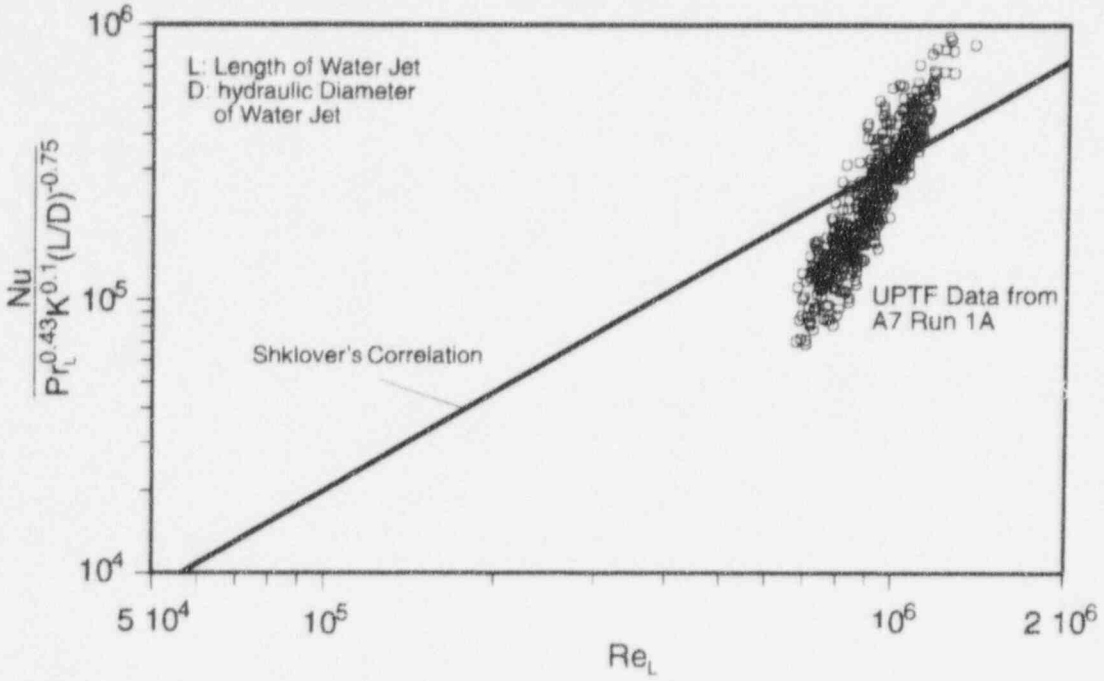

Fig. 6 Nußelt no. for condensation at the water jet in comparison with the Shklover's correlation

Also some scattering of the data is registered, this comparison suggests the applicability of Shklover's correlation [SHK 70] also for the water jets formed in the upper plenum.

Following the ECC water flow down to the core region the water jet will be disintegrated by structures in the upper plenum. An analysis of the condensation heat transfer becomes rather difficult. However, discussing the steam condensation efficiency and accumulator injection performance for hot and cold leg injection, it is found [SIE 93] that the hot leg injection leads to more intensive system depressurization. This results in significantly higher accumulator injection rates. Consequently the total condensation rate in the primary system for hot leg injection exceeds significantly that one for the cold leg injection.

5. Condensation of steam dissolved in the nitrogen of accumulators

The pressure development inside an accumulator depends on the pressure development in the primary system but also depends to some extent on the heat input to the nitrogen. The TRAM tests provide an opportunity to quantify the heat

input to the nitrogen [SON 94]. From temperature and pressure measurements inside the nitrogen, the total heat input $\frac{dQ}{dt}$ can be derived by:

$$\frac{dQ}{dt} = m_{N2}\, c_P \frac{dT}{dt} - V_{N2}\frac{dp}{dt} \qquad (4)$$

In TRAM test A7 run 2a the mass of nitrogen filled into the accumulator simulator was about 700 kg at 48.3°C and at 1.57 MPa. The depressurization due to accumulator injection leads to a decreasing temperature in the nitrogen. Assuming a constant temperature at the inner surface of the accumulator, the heat transfer coefficient for heat release from walls to fluid can be determined by:

$$\text{htcaccu} = \frac{\frac{dQ}{dt}}{A_{accu}(t)\,(48.3 - T(t))} \qquad (5)$$

$A_{accu}(t)$ is the present inner accumulator surface which is in contact with nitrogen and T(t) is the present temperature of the nitrogen. The resulting heat transfer coefficient is plotted in figure 7. The time point 0 s of figure 7 corresponds to the test situation which is shortly reached after the actuation of accumulator injection. The temperature difference between the structure of accumulator (48.3°C) and the nitrogen exceeds 5 K, thus the evaluation of equation (5) provides reliable htc values.

In the first period of accumulator injection the apparent heat transfer coefficient reaches values up to 200 W/m²K. For free convective heat transfer values of about 30 W/m²K are known. Thus, the test analysis reveals that there exists an additional source of energy which provides energy to the nitrogen atmosphere and therefore delays the depressurization of the nitrogen during accumulator injection.

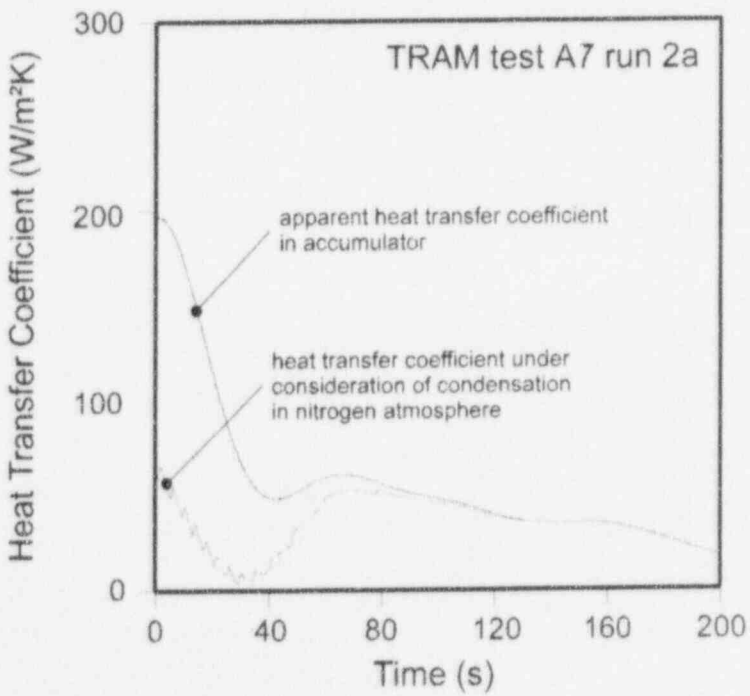

Fig. 7 Apparent heat transfer coefficient in TRAM test A7 run 2a

According to Daltons law 3.3 kg steam can be dissolved within the 700 kg nitrogen at 48.3°C and 1.57 MPa. Assuming that the condensation of steam follows the temperature decrease in the nitrogen, the heat release from steam to nitrogen can be calculated by:

$$\frac{dQ_{H2O}}{dt} = -r(T(t))\, m_{N2} \frac{M_{H2O}}{M_{N2}} \frac{d}{dt}\left[\frac{p'(T(t))}{p_{N2}(t)}\right] \qquad (6)$$

r(T(t)) is the latent heat of evaporation corresponding to the present temperature measured in the nitrogen. M_{H2O} and M_{N2} are molecule masses of water and nitrogen. p'(T(t)) is the saturation pressure for water corresponding to the present temperature measured in nitrogen. $p_{N2}(t)$ is considered as identical with the total pressure measured in the nitrogen atmosphere.

Subtracting the heat of condensation from the measured heat (equation 4), a reduced heat transfer coefficient can be calculated and plotted in figure 7. The value of the reduced heat transfer coefficient falls into the range of expected values for free convection. The comparison of both curves in figure 7 illustrates that for almost 80 s accumulator injection the temperature and pressure development is strongly influenced by condensing steam within the nitrogen atmosphere.

6. Conclusion

The effectiveness of accumulator injection under small leak conditions with additional failure of high pressure injection system depends on the condensation processes inside the primary system. This condensation has been studied in a 1:1 geometric scale in the UPTF facility separately for cold leg and hot leg accumulator injection. The phenomenological analysis of these tests reveals that close to the injection ports water jets are formed by the injected water. For cold leg injection the jet appears at the inlet nozzle within the cold leg whereas for the hot leg injection such a jet is formed in the upper plenum. In both cases the condensation rate of steam can be predicted by Shklover's correlation for jet condensation. The phenomenological analysis furthermore reveals that a condensation process within the nitrogen atmosphere of the accumulator significantly supports the injection over a period of 80 s from the beginning of the injection onward.

Literature

[SIE 93] Siemens AG, Power Generation Group (KWU):
UPTF-TRAM Test Group A - Test Results, Analysis, Working Group of Experts Meeting, Mannheim, December 6-8, 1993

[SON 94] Sonnenburg, H.G.; Palazov, V.V.:
Phänomenologische Analyse des TRAM-Versuchs A7 - Kondensation von Dampf im heißen Strang und oberen Plenum sowie Druckspeicher-Verhalten beim Einspeisen, GRS-A-2135, Februar, 1994

[TUU 94] Tuunanen, J.:
Phenomenological Analysis of TRAM Test A6 - Condensation of Steam in the Cold Legs and the Downcomer during ECC Water Injection from Accumulators, GRS-A-2113, Januar, 1994

[WEI 92] Weiss, P.:
2D/3D-Projekt Durchführung von Versuchen an der Versuchsanlage Upper Plenum Test Facility, Siemens Report, Siemens AG Bereich Energieerzeugung (KWU), R11/92/015, Dezember, 1992

Acknowledgements

This work has been performed in the frame of the BMBF (German Ministry for Research and Technology) sponsored project RS 878 (Analytische Begleitung des UPTF-TRAM Versuchsprogramms)

CONDENSATION HEAT TRANSFER COEFFICIENT WITH NONCONDENSIBLE GASES FOR HEAT TRANSFER IN THERMAL HYDRAULIC CODES

S. BANERJEE and Y.A. HASSAN
Texas A&M University
College Station, Tx-77843-3133

ABSTRACT

Condensation in the presence of noncondensible gases plays an important role in the nuclear industry. The RELAP5/MOD3 thermal hydraulic code was used to study the ability of the code to predict this phenomenon. Two separate effects experiments were simulated using this code. These were the Massachusetts Institute of Technology's (MIT) Pressurizer Experiment, the MIT Single Tube Experiment. A new iterative approach to calculate the interface temperature and the degraded heat transfer coefficient was developed and implemented in the RELAP5/MOD3 thermal hydraulic code. This model employs the heat and mass transfer analogy and considers the sensible and condensation heat transfer simultaneously. This model was found to perform much better than the reduction factor approach. The calculations using the new model were found to be in much better agreement with the experimental values.

INTRODUCTION

The condensation phenomenon plays an important role in the heat transfer process in many applications. This mode of heat transfer is often used in engineering because of the high heat transfer coefficients possible. However, condensation heat transfer is degraded when noncondensibles are present in the condensing vapor[1]. The presence of noncondensibles lowers the partial pressure of the vapor, thus reducing the saturation temperature at which condensation occurs. In the nuclear industry, condensation heat transfer is very important in many situations. In case of a loss of coolant accident, a large portion of the heat is removed by condensation of steam in the steam generators. The presence of noncondensibles such as nitrogen from the accumulator or from fission product gases hinders the heat removal process. The working of the pressurizer is dependent on the condensation of steam. Again, the presence of noncondensibles will hamper the performance of the pressurizer. In the next generation of nuclear reactors, there will be a greater emphasis on replacing the active systems with passive systems in

order to improve the reliability of operations. The 600 MWe Simplified Boiling Water Reactor designed by General Electric contains many passive safety systems. There are two Passive Containment Cooling Systems (PCCS) which have been introduced: the Isolation Condenser (IC), and the Water Wall. The PCCS are passive heat exchangers that allow the transfer of heat via steam condensation to the water pool or the suppression pool. The Westinghouse designed Advanced Passive 600 MWe (AP600) relies on condensation of vapor in the containment shell in order depressurize the containment following an accident. In order to ensure the reliability of these passive systems, the behavior of steam condensation in the presence of noncondensibles has to be studied and quantified.

Early work in the theoretical modeling of the condensation phenomenon in the presence of saturated steam-air mixture with constant fluid properties was done by Sparrow and Lin[2]. This analysis was based on conservation laws alone and did not utilize any empirical data. Minkowycz and Sparrow[3] conducted an analytical investigation of laminar film condensation in the presence of noncondensible gases to include the effect of interfacial resistance, variable properties and diffusion for both the liquid film and the steam-air mixture. A number of experiments have been conducted to study these phenomena. Vierow and Shrock[4] performed experiments to study the effects of air on the condensation of steam in a natural circulation loop. Reflux condensation and transition to natural circulation in the presence of noncondensibles in a vertical U-tube have been experimentally studied by Banerjee et al.[5] An experimental investigation of film condensation of steam-air mixture on the outside of a horizontal tube was performed by Vuono and Christensen[6].

The aim of the present study was to develop and implement a model for condensation in the presence of noncondensible gases. The model was tested by numerical simulation of two separate effects experiments. These experiments model physical phenomena encountered in the nuclear industry. These experiments were conducted at the Massachusetts Institute of Technology. The first was the MIT Pressurizer Experiment and the second was the MIT Single Tube Experiment.

The simulations were performed using the RELAP5/MOD3 thermal hydraulic code. The RELAP5 code is a best estimate transient analysis code sponsored by the U.S. Nuclear Regulatory Commission. The code is based on a one-dimensional, gas-liquid, two-fluid model which accounts for thermal and mechanical equilibrium between the phases. The code uses a six equation model for the calculations. The code has the capability to calculate the behavior of a system containing several types of noncondensible gases mixed with the steam. The simulations were initially performed

with the original condensation model. The modified model was based on the model by Peterson et al., and was suitably modified for implementation in RELAP. The calculations were then repeated with the modified model and the results compared.

II RELAP5/MOD3 CONDENSATION MODEL IN THE PRESENCE OF NONCONDENSIBLE GASES

The RELAP5/MOD3 code uses a six equation formulation to handle the phasic continuity, momentum and energy conservation equations (three equations for each phase). The two phase, single component model is extended to account for the presence of a noncondensible component in the gas phase. The noncondensible component is assumed to be in thermal and mechanical equilibrium with the vapor phase. The properties of the steam/ noncondensible mixture in the gas phase are calculated from the Gibbs-Dalton mixture properties.

The RELAP5 condensation heat transfer calculations consist of three correlations which were derived for the following specific situations: 1) laminar film condensation on an inclined plane, 2) laminar film condensation inside a horizontal tube with a stratified liquid surface , and 3) turbulent film condensation inside a vertical tube. The first correlation is the standard Nusselt film condensation correlation[7] and the second correlation is basically a modification to the original theory. The third correlation was given by Carpenter and Colburn[8].

The condensation heat transfer coefficient calculated from the above correlations is reduced when a noncondensible gas is present. The following reduction multiplier, FNC, is used:

$$FNC=\frac{[p_s-p_{min}]}{p^*(f[Re_g])}*F \qquad (1)$$

$$f[Re_g]=\frac{5}{1+0.0001*Re_g} \qquad (2)$$

$$F=\{1+f[Re_g]*\exp[-5*(\frac{p_g}{p})]\} \qquad (3)$$

where,

p_s = partial pressure of the steam

p_a = partial pressure of the air

p = total pressure of the steam/ noncondensible mixture

p_{min} = minimum pressure in the steam tables

Re_g = Reynolds number of the gas, such that, $0 < Re_g < 20000$

F is a function of the noncondensible gas concentration. It is also a weak function of wall subcooling which is not shown here. The definition of the minimum pressure, p_{min}, is not given anywhere in the RELAP5 documentation.

Thus the code accounts for the presence of noncondensible gases by reducing the heat transfer coefficient calculated without the presence of the noncondensibles by multiplying with a reduction factor. This reduction factor is a function of the noncondensible gas concentration and is used whenever the noncondensible gas concentration is greater than or equal to 0.0001.

A similar reduction factor approach was adopted by Grant in her investigation of the pressurizer response in the presence of nitrogen[9]. The reduction factor was obtained by curve fitting the experimental data. The reduction factor obtained was of the form given in Equation 3a:

$$FNC = 0.0151215 \left(\frac{\rho_n}{\rho_n + \rho_s} \right)^{-0.6006237} \qquad (3a)$$

where ρ_n and ρ_s are the densities of nitrogen and steam, respectively

The problem with the above formulations is that there is no theoretical basis to the reduction factor model. The reduction factor frequently overpredicts the heat transfer coefficients[10]. Moreover, the Nusselt heat transfer coefficient is based on very strict assumptions such as linear temperature profile in the liquid film and laminar fluid flow in the film. Both of these conditions are rarely encountered in practice. A need was therefore felt to develop a condensation model based on first principles rather than relying on simple correlations. Moreover, the new model should account for the physical phenomena under all ranges of gas concentrations, temperatures and pressures normally encountered in engineering practice.

III THE MODIFIED MODEL

The condensation model was modified to overcome the limitations of the original RELAP5/MOD3 model as pointed out above. This model was based on the

model proposed by Peterson et al[11]. Further modifications were made as necessary in order to make it suitable so that it could be implemented on RELAP which is a one-dimensional code. The model and the constitutive equations are discussed below.

When noncondensibles accumulate at the liquid vapor interface (Fig. 1), it reduces the interface saturation temperature T_i^s, below the bulk saturation temperature, T_b^s. The heat flux through the vapor-liquid interface is the sum of heat fluxes due to the latent and sensible heat transfer through the interface. This heat transfer should equal the heat transfer through the condensate film, the wall and the external resistance (the secondary side resistance). Sensible heat transfer becomes the dominant factor in case of large gas concentrations while at small gas concentrations the condensate film resistance becomes important.

As stated earlier, the heat flux through the condensate film should equal the sum of the latent heat flux and the sensible heat flux through the vapor liquid interface,

$$h_{cond}\,(T_i^s - T_w) = q_t'' = q_c'' + q_s'' = -h_{fg} c M_v \bar{v}_i + k_v \left(\frac{\partial T}{\partial y}\right)_i \qquad (4)$$

where h_{cond} is the effective condensation heat transfer coefficient, h_{fg} is the latent heat of vaporization, c is the total molar density, M_v is the molecular weight of the vapor, k_v is the vapor-gas mixture thermal conductivity, $\bar{v}_i$ is the average molar velocity away from the surface and y is the direction normal to the surface.

The Sherwood number for diffusion through the gas-vapor film of thickness δ_g can be obtained as,

$$Sh_d = \frac{d}{\delta_g} = \left(\frac{q_c''}{T_b^s - T_i^s}\right) d\Phi \left(\frac{R^2 T^3}{h_{fg}^2 P_t M_v^2 D}\right) \qquad (5)$$

The first term in the right hand side of the above equation is the condensation heat transfer coefficient h_C. The term Φ is the gas-vapor mean concentration ratio given by

$$\Phi = -\frac{\ln[(1-x_{gb})/(1-x_{gi})]}{\ln[x_{gb}/x_{gi}]} \qquad (6)$$

where x_{gb} and x_{gi} are the bulk and the interface gas concentrations. The last two terms can be regarded as the inverse of an effective condensation thermal conductivity $1/k_C$. This in turn can be calculated by the following relationship,

$$k_c = \frac{1}{\Phi T_{ave}} \left(\frac{h_{fg}^2 P_o M_v^2 D_o}{R^2 T_o^2} \right) \tag{7}$$

where the diffusion coefficient D is given in terms of D_O at a reference temperature T_O and a pressure P_O. The value T_{ave} is given by the following relationship,

$$T_{ave} = (T_b^s + T_i^s)/2 \tag{8}$$

which is the average temperature in the diffusion layer.
As mentioned earlier, the total heat flux can be obtained as,

$$h_{cond}(T_s^i - T_w) = h_l (T_b^s - T_s^i) + h_s (T_b - T_s^i) \tag{9a}$$

Eliminating the interface temperature, the total heat flux can be obtained as,

$$q_t'' = \frac{h_c(T_b^s - T_w) + h_s(T_b - T_w)}{1 + (h_c + h_s)/h_w} \tag{9b}$$

Of course, to solve for the heat transfer coefficient it is necessary to use an iterative technique successive substitution to find each of the heat transfer coefficients. The iterative technique outlined below is similar to the method suggested by Peterson and has been modified so that it can be implemented in RELAP5.

At the start of the calculation, the following values are available at each node: the gas and the liquid velocities, the gas and liquid temperatures, the bulk gas fraction, the temperature of the wall, and the partial pressure of the vapor at the center of the node.

The steps to solve the equations are outlined below:

1) Using the above information, the bulk partial pressure of the air is first calculated,

$$P_a = P_t - P_v \tag{10}$$

where P_t is the total pressure, P_a is the bulk partial pressure of the air and P_v is the bulk partial pressure of the vapor. Assuming that the steam and the air in the mixture are perfect gases, the number of moles of the gas and the vapor are calculated. From this the bulk mole fraction of the noncondensible, x_{gb}, is calculated.

2) The interface concentration, x_{gi}, is then assumed to be slightly greater than the bulk concentration, i.e.,

$$x_{gi} = x_{gb} + 0.001 \tag{11}$$

This step is necessary, otherwise the average concentration ratio as defined by Equation (5) will be undefined in the first iteration. The interface temperature is set equal to the bulk saturation gas temperature and the average temperature is calculated as indicated in Equation 7.

3) The next step is to calculate the necessary mixture properties using the appropriate gas mixture model. Here, the mixture properties are calculated using the formulation of Reid and Prausnitz [12]. The properties necessary are the local mixture density, the local mixture viscosity, the diffusion coefficient , the mixture thermal conductivity and the specific heat of the mixture. These properties are calculated at the arithmetic mean of the interface and the bulk concentrations and temperatures. The steps involved in this procedure is the calculation of the properties of the individual components of the phases followed by the calculation of the mixture properties. In the subroutine the properties were calculated using the relationships given below. The terms Φ_v and Φ_g are calculated by equations 12 and 13, respectively:

$$\Phi_v = \frac{\left[1+\left(\frac{\mu_g}{\mu_v}\right)^{0.5}\left(\frac{M_v}{M_g}\right)^{0.25}\right]^2}{\left[8\left(1+\frac{M_g}{M_v}\right)\right]^{0.5}} \tag{12}$$

$$\Phi_g = \frac{\left[1+\left(\frac{\mu_v}{\mu_g}\right)^{0.5}\left(\frac{M_g}{M_v}\right)^{0.25}\right]^2}{\left[8\left(1+\frac{M_v}{M_g}\right)\right]^{0.5}} \tag{13}$$

The mixture viscosity, mixture thermal conductivity and the mixture specific heat are then calculated using the following equations 13, 14 and 15 respectively.

$$\mu_m = \frac{x_g\mu_g}{x_g + (1-x_g)\Phi_v} + \frac{(1-x_g)\mu_v}{x_g\Phi_g + (1-x_g)} \tag{14}$$

$$k_m = \frac{x_g k_g}{x_g + (1-x_g)\Phi_v} + \frac{(1-x_g)k_v}{x_g\Phi_g + (1-x_g)} \quad (15)$$

$$c_{p,m} = x_g c_{p,g} + (1-x_g)c_{p,g} \quad (16)$$

4) The next step is to calculate the condensate film heat transfer coefficient. The film heat transfer resistance needs to take into account the fact that the temperature in the film is not necessarily linear, the flow may not necessarily be laminar and the film surface may be wavy due to the gas-vapor flow. Thus, the classical Nusselt formulation cannot be used for a wide variety of industrial situations. The correlation proposed by Tien et al.[13], was used to determine the film heat transfer coefficient. This method was chosen because it lends itself easily for implementation in RELAP5 and is applicable for a wide variety of situations.

The heat transfer coefficient for cocurrent vertical flow is given by the following correlation:

$$Nu_x = [(0.31 Re_{\delta,x}^{-1.32} + \frac{Re_{\delta,x}^{2.4} Pr^{3.9}}{2.37 \times 10^{14}})^{0.333} + \frac{Pr^{1.3}}{771.6}\tau_i^*]^{0.5} \quad (17)$$

where τ_i^* is the dimensionless form of the interfacial resistance. This is given by the following relationship:

$$\tau_i^* = A(Re_T - Re_{\delta,x})^{1.4} Re_{\delta,x}^{0.4} \quad (18)$$

$$A = \frac{0.252\,\mu_l^{1.177}\,\mu_g^{0.156}}{d^2 g^{0.667} \rho_l^{0.553} \rho_g^{0.78}} \quad (19)$$

For countercurrent flow, the appropriate proposed relationships are:

$$Nu_x = [(0.31 Re_{\delta,x}^{-1.32} + \frac{Re_{\delta,x}^{2.4} Pr^{3.9}}{2.37 \times 10^{14}})^{0.333} - \frac{C Pr^{1.3} Re_{\delta,x}^{1.8}}{771.6}]^{0.5} \quad (20)$$

$$C = \frac{0.023\,\mu_l^{1.133}\,\mu_g^{0.2}}{d^2 g^{0.667} \rho_l^{0.333} \rho_g} \quad (21)$$

In the above formulations, the Nu_x is the local Nusselt number, $Re_{\delta,x}$ is the local film Reynolds number and Re_T is the Reynolds number if all the vapor was condensed. The other symbols are defined at the end of the paper.

An alternative[14], though slightly complicated way of calculating the film heat transfer coefficient is to calculate the nondimensional film thickness from the following cubic equation:

$$\frac{Re_f}{1 - \rho_g/\rho_f} = \frac{\delta_f^{*3}}{3} + \frac{\tau_g^* \delta_f^{*2}}{2} \tag{22}$$

where the term τ_g^* is the nondimensional interfacial shear and δ_f^* is the nondimensional form of the film thickness. The interfacial shear is given by the following equation:

$$\tau_g = f \rho_f \frac{v_g^2}{2} \tag{23}$$

where v_g is the vapor velocity and f is the friction factor. This interfacial shear is then nondimensionalized using a characteristic length L defined by,

$$L = \left(\frac{\mu_f^2}{\rho_f^2 g} \right)^{1/3} \tag{24}$$

$$\tau_g^* = \frac{\tau_g}{g\rho_f (1-\rho_g/\rho_f)L} \tag{25}$$

Once the film thickness is determined, the local laminar film Nusselt number $Nu_{x,la}$ and the local turbulent film Nusselt number is given by:

$$Nu_{x,la} = 1/\delta_f^* \tag{26}$$

$$Nu_{x,tu} = aRe_f^b Pr^c (1 + e\tau_g^{*f1}) \tag{27}$$

The constants a,b,c,e,f1 are given in Table 1.

The local Nusselt number and the film heat transfer coefficient is then given by,

$$Nu_x = \frac{h_f L}{k_f} = \left(Nu_{x,la}^4 + Nu_{x,tu}^4\right)^{1/4} \quad (28)$$

5) The next step is the calculation of the Sherwood number for mass transfer and the Nusselt number for sensible heat transfer by,

$$C_c = 0.023\,(4.954 \times 10^{-4}\, Re_f + 0.905) \quad (29a)$$

$$C_s = 7.0 * C_c \quad (29b)$$

$$Sh_d = \min\,(C_c\, Re_g^{0.8}\, Sc^{0.6};10) \quad (30a)$$

$$Nu_d = \min\,(C_s\, Re_g^{0.8}\, Pr^{0.6};10) \quad (30b)$$

6) The condensation thermal conductivity is calculated using equation (7). Using this the condensation and the sensible heat transfer coefficients are calculated as:

$$h_c = Sh_d \frac{k_c}{d} \quad (31)$$

$$h_s = Nu_d \frac{k_s}{d} \quad (32)$$

7) The local heat flux based on the wall temperature T_w is and the assumed interface concentration and the temperature is then given by:

$$q_{it}'' = \frac{T_b^s - T_w}{1/(h_s + h_c) + 1/h_f} \quad (33)$$

8) From this, the interface temperature and interface concentration is then calculated as

$$T_i = T_b^s - \frac{q_{it}''}{(h_c + h_s)} \quad (34)$$

$$x_{gi} = 1 - \frac{P^s(T_i)}{P_{total}} \quad (35)$$

If this temperature and interface concentration are almost equal to the guessed values, then further iteration is stopped and the heat flux is calculated from the above equations. However, if the values of the interface concentration and temperature are not equal or differ greatly from the initial guesses, the whole process is repeated again using the values calculated in equations 34 & 35. The convergence criteria used was that the difference between the previous and new values of the interface temperatures and concentrations should be less than 10^{-3}. It was necessary for both the criteria to be satisfied simultaneously for convergence to be successful. It was found that a maximum of nine to ten iterations per time step were required for convergence to the order of 10^{-3}. Calculations indicated that this method of successive substitution for air fractions ranging from 0.03 to 0.9 achieved the required degree of convergence.

DISCUSSION OF THE SIMULATION RESULTS

As stated earlier, two experiments were simulated using RELAP5/MOD3. For each experiment the calculations were performed with the original model and the new condensation model discussed above. The results of the calculations are presented in the present section.

a) The MIT Pressurizer Experiment [15]

In accidents, nitrogen gas can be discharged into the reactor system from the accumulator after the water inventory is spent. The response of the pressurizer to transients plays an important role in determining the pressure history of the primary coolant system. This response is dependent on the condensation of steam on the vertical walls of the pressurizer. Several insurge tests were performed at MIT to determine the response of a pressurizer when the vapor region contained steam mixed with a noncondensible gas. The test facility (Fig. 2) essentially consisted of two stainless steel tanks, an insurge line and a gas injection system. One of the tanks modeled the pressurizer volume and the other served as a reservoir for the injection water. Two tests were performed using this test facility. In the first test, the pressurizer was initially filled with 3% nitrogen gas by weight along with steam. Electric heaters were used to bring the system to a steady state. Once the system reached steady state, the transient was initiated using the quick release valves that allowed water at 294.3 K to flow into the pressurizer from the storage tank. The primary pressure at the top of the pressure was the physical parameter of interest. The insurge was terminated when the water level in the pressurizer reached 0.86m. The second test involved the presence of 10% nitrogen in the pressurizer.

The calculations were performed using RELAP5/MOD3. The nodalization is shown in the Fig. 3. There were 11 volumes , 10 junctions and 10 heat structures. Thus the pressurizer was modeled as a pipe component with each subvolume having a length of 0.1143 m.

The RELAP5 calculations are shown in the Figs. 4 & 5 respectively. Figure 4 shows the results for 3% nitrogen and Fig. 5 shows the results for 10% nitrogen. The results indicate that the predictions using the original condensation model are significantly different from the experimental values. The figures also indicate that the modified condensation model performs much better and the predicted values and the experimental values agree with each other. The peak pressures are also well predicted.

The model does not take into account the direct contact condensation at the water/nitrogen interface. Indeed, this was not modeled at all. Thus the pressurizer test provides only a limited verification of the proposed model[16]. To verify the model further another set of simulations were performed which re described in the next section.

b) The MIT single tube experiment[17]

The MIT single tube experiment was another experiment performed at MIT to investigate the performance of the isolation condenser in the Passive Containment Cooling System (PCCS) design. The objective of the experiment was to measure the local heat transfer coefficients for steam condensing in the tube in the presence of air. The emphasis was to obtain data spanning the range of inlet noncondensible gas fractions, pressures, temperatures which would simulate the operating conditions of the isolation condenser in a LOCA.

The test apparatus (Fig. 6) essentially consisted of an open water cooling water circuit and an open noncondensible gas steam loop. Steam was generated in a vertical cylindrical stainless steel vessel by using four individually controlled electrical heaters. The heaters were rated at 7 kW each. Compressed air was supplied to the bottom of the steam generating vessel. This allowed for the thermal equilibrium between the gas and the steam. The steam/gas mixture was led to a condensing section which was 2.54 m long. The condenser tube had dimensions of 50.8 mm outside diameter, 46.0 mm inside diameter. A 62.7 mm inner diameter concentric jacket pipe surrounded the test condenser. The gas-vapor mixture flowed down through the tube while cooling water flowed counter currently through the annulus. The condensed liquid was collected in the condenser drum. The noncondensible was vented out through a throttle valve. The steam vessel, the test condenser and all the connecting piping were thoroughly insulated to prevent any heat losses to the atmosphere.

The RELAP5 nodalization of the experiment is shown in the Fig. 7. The nodalization consisted of 37 volumes and 36 junctions. The condenser section was nodalized using 16 volumes.

The results of run numbers 20 and 24 are shown in the Figs. 8 and 9, respectively. The results for run numbers 25 and 26 are shown in Figs. 10 and 11, respectively. The plots indicate that the heat transfer coefficients decrease down the length of the tube because the air fraction increases progressively as more vapor is condensed as we move downstream from the tube inlet. The RELAP5 calculations indicate that the unmodified RELAP performs very poorly when compared to the experimental values. The RELAP5 calculations with the modified subroutine show that the trends in drop in the heat transfer coefficient are captured very well. Moreover, the experimental and the calculated values agree very well with each other.

CONCLUSIONS

The RELAP5/MOD3 thermal hydraulic code was used to study the phenomena of steam condensation in the presence of noncondensible gases. The code was applied to simulate two experiments: the MIT pressurizer experiment and the MIT single tube experiment.

Each of the experiments were first simulated using the original formulation for calculating the degraded heat transfer coefficient in the presence of noncondensible gases. This original formulation is based on the reduction factor approach. It was found that in each of the cases simulated this model overpredicted the heat transfer coefficients. To overcome the deficiency of this model, an iterative method was employed to calculate the heat transfer coefficient. This method is based on a theoretical approach unlike the reduction factor approach. This model was implemented in RELAP5/MOD3 and each of the experiments were simulated again. It was found that the calculations using this model were much better and the predicted values of the heat transfer coefficients were in much better agreement with the experimental values.

Thus the new iterative approach was found to be far more suitable and accurate than the reduction factor approach for the experiments tested. The model is being tested on different separate effects and integral effects experiments to examine its performance and validity.

LIST OF SYMBOLS

d = diameter of the tube

c = total molar density (mole/m^3)

T = Temperature (K)

D = Diffusion coefficient (m^2/s)

δ_g = thickness of the gas-vapor boundary layer

P = pressure (N/m^2)

M = molecular weight (kg/mole)

x = mole fraction

k = thermal conductivity ($W/m/^oK$)

q" = heat flux (W/m^2)

h = heat transfer coefficient ($W/m^2/^oK$)

h_{fg} = latent heat of vaporization (J/kg/K)

μ = viscosity (Ns/m)

ρ = density (kg/m^3)

c_p = specific heat (J/kg/K)

R = Universal gas constant

Pr = Prandtl number

Re = Reynolds number

Nu = Nusselt number

Sh = Sherwood number

Sc = Schmidt Number

Subscripts

m = mixture

gb = bulk gas

gi = interface gas

b = bulk

i = interface

w = wall

c = condensation

s = sensible

v = vapor

g = gas

t =total

Superscripts

s = saturation

REFERENCES

1. J. G. COLLIER, "Convective Boiling and Heat Transfer," (2nd ed.), New York:McGraw-Hill, (1980)

2. E. M. SPARROW and S. H. LIN, "Condensation Heat Transfer in the Presence of Non-condensable Gas," Transactions of the ASME, vol. C86 pp 430-436 (August 1964).

3. W. J. MINKOWYCZ and E. M. SPARROW, "Condensation Heat Transfer in the Presence of Noncondensables, Interfacial Resistance, Superheating, Variable Properties, and Diffusion," International Journal of Heat and Mass Transfer, Vol. 9, p1125, (1966).

4. K. M. VIEROW and V. E. SCHROCK, "Condensation Heat Transfer in Natural Circulation with Noncondensable Gas," Report for General Electric Nuclear Energy UCB-NE 4170, Department of Nuclear Engineering, University of California at Berkeley (May 1990).

5. S. BANERJEE et al., "Reflux Condensation and Transition to Natural Circulation in a Vertical U-Tube," Journal of Heat Transfer, Vol. 105, pp719-727 (Nov. 1983).

6. De VUONO and R.N. CHRISTENSEN, "Experimental Investigation of the Pressure Effects on Film Condensation of Steam-Air Mixtures at Pressure Above Atmospheric", ASME, HTD, Vol. 38, pp 73-80, (December 1984)

7. V. H. RANSOM et al., "RELAP5/MOD3 Code Manual, Volumes 1 and 2," NUREG/CR-4312, EGG-2396, (Aug. and Dec. 1985).

8. E.F. CARPENTER and A.P. COLBURN, "The Effect of Vapor Velocity on Condensation Inside Tubes", Proc. of General Discussion on Heat Transfer, Institute of Mechanical Engineering/ American Society of Mechanical Engineers, pp. 20-26, 1951.

9. S.E. GRANT , " Modified Heat Transfer Coefficient in the Presence of Noncondensible Gas for RELAP5/MOD2 Computer Code", M.S. Thesis, Texas A&M University, (December 1990).

10. L. RAJA et al., "Analysis of Steam Condensation Experiments in the Presence of Noncondensible Gases using the RELAP5/MOD3 code.", Nuclear Technology, vol 104, No. 1, pp.76-88, (September 1993)

11. P. F. PETERSON et al., "Diffusion Layer Theory for Turbulent Vapor Condensation with Noncondensible Gases", Journal of Heat Transfer, Vol. 115, pp. 998-1003, 1993

12. R.C. REID et al., "The Properties of Gases and Liquids", Mc Graw-Hill, New York, 1988

13. C. L. TIEN et al., "General Film Condensation Correlations", Experimental Heat Transfer, vol. 1, pp 93-107, 1987

14. F. BLANGETTI et al., "Condensation in Vertical Tubes-Experimantal Results and Modelling", Chemical Engineering Fundamentals, 1, pp. 20-63, (1982)

15. A. A. DEHBI, M. W. GOLAY, and M. S. KAZIMI, "The Effects of Noncondensable Gases on the Steam Condensation Under Turbulent Natural Convection Conditions," Report No. MIT-ANP-TR-004, (June 1990).

16. S. W. KANG, P. GRIFFITH, "Pool Heat Transfer in a Simulated PWR Pressurizer", Transactions of the American Nuclear Society, Volume 46, pp. 845-847, 1984

17. M. SIDDIQUE , "The Effects of Noncondensible Gases on Steam Condensation Under Forced Convection Conditions", Ph. D Thesis, Massachussetts Institute of Technology, (January 1992)

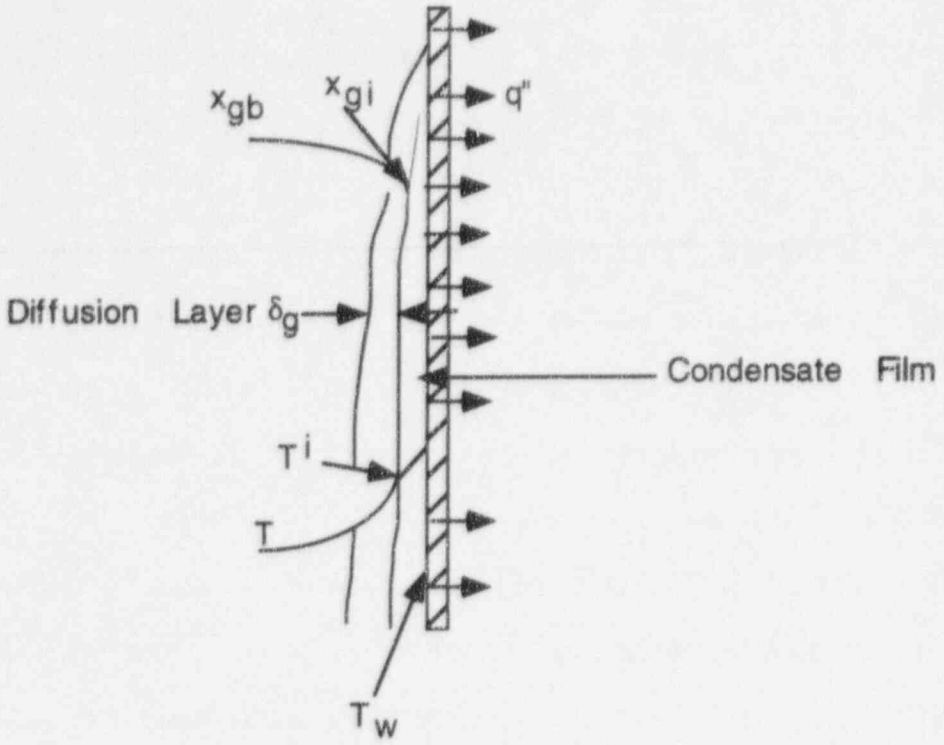

Fig. 1 Schematic Illustration of the Condensation Process

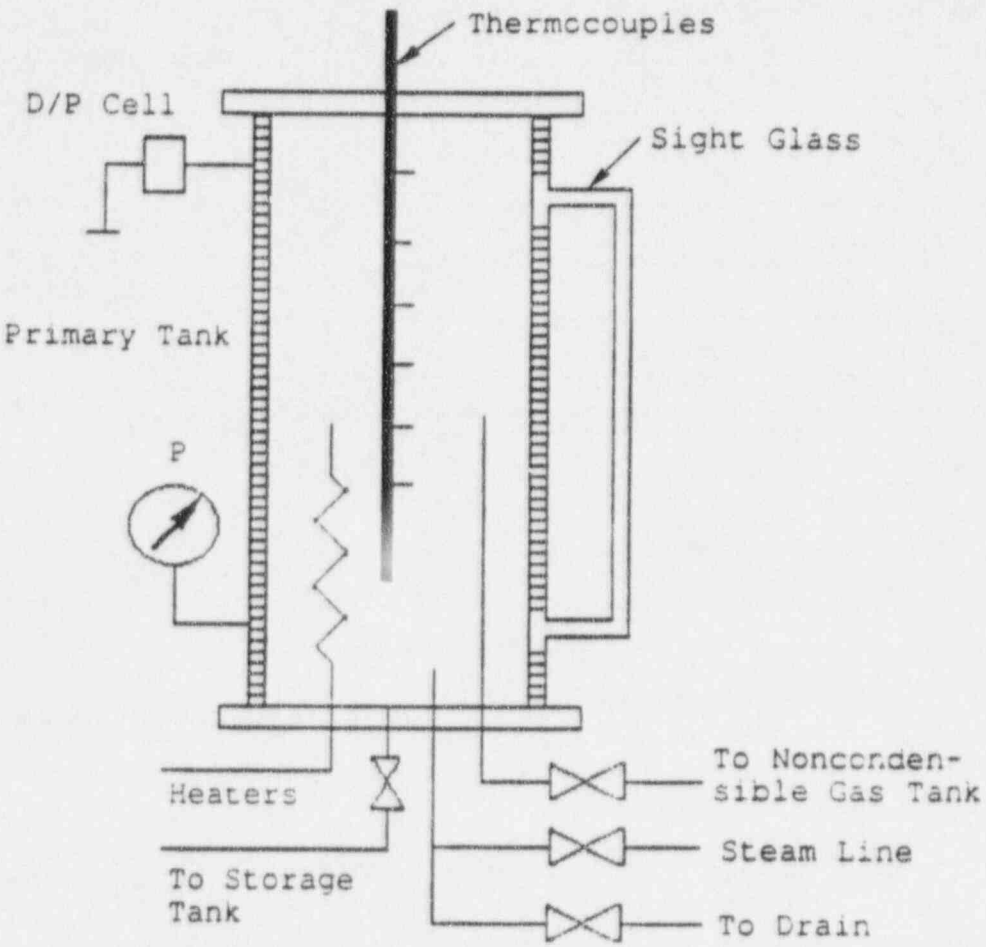

Fig. 2 Schematic of the MIT pressurizer Experiment

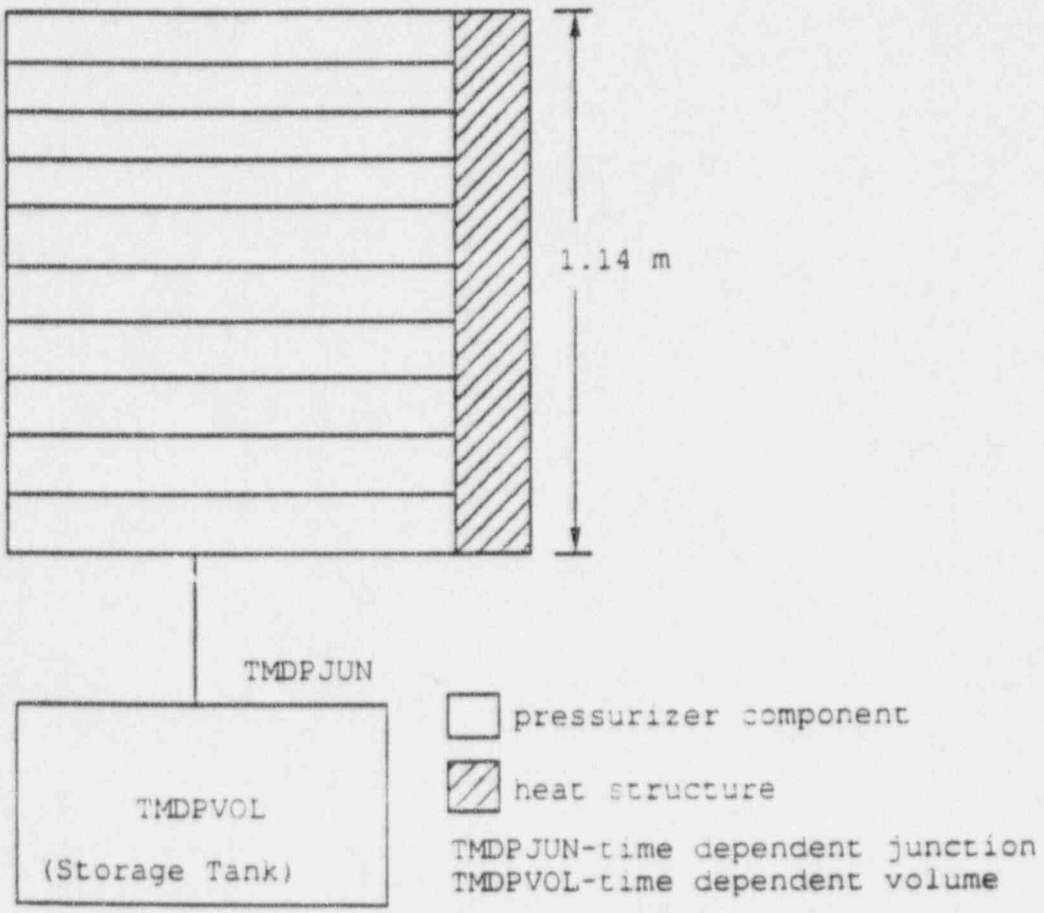

Fig. 3 RELAP5 Nodalization of the MIT pressurizer Experiment

Fig. 4 Pressure History for MIT Pressurizer Experiment (3% Nitrogen)

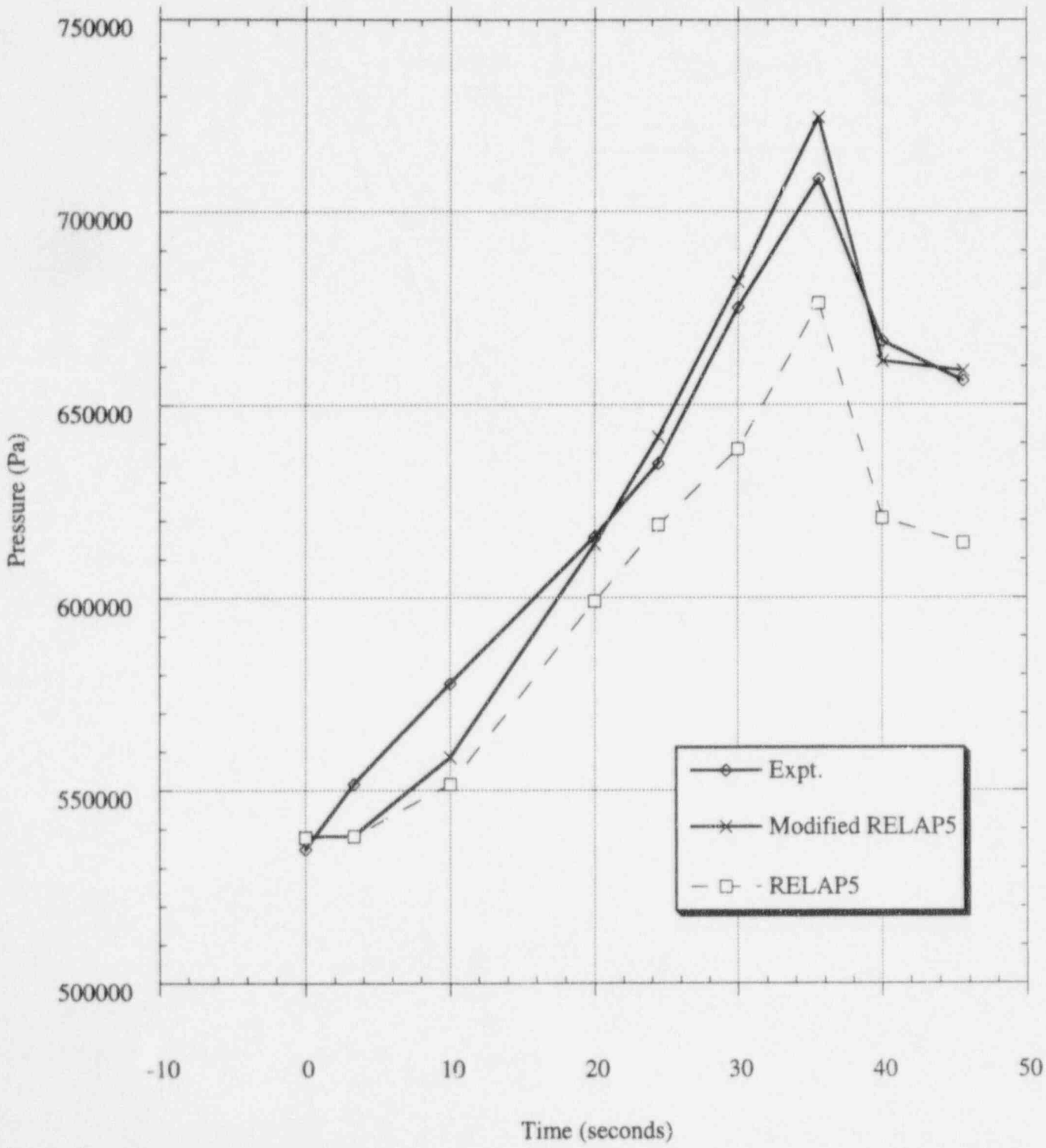

Fig. 5 Pressure History for MIT Presssurizer Experiment (10% Nitrogen)

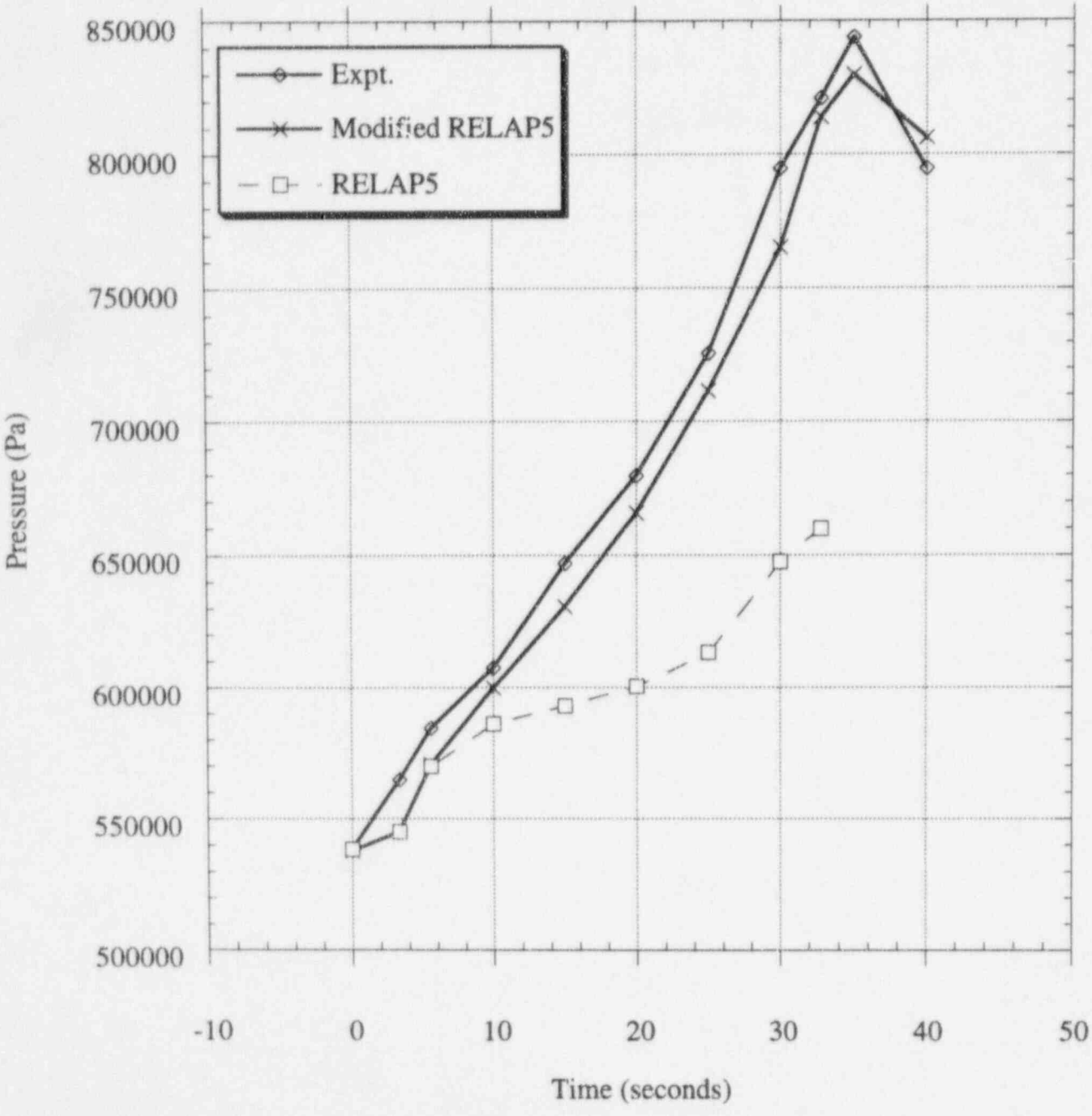

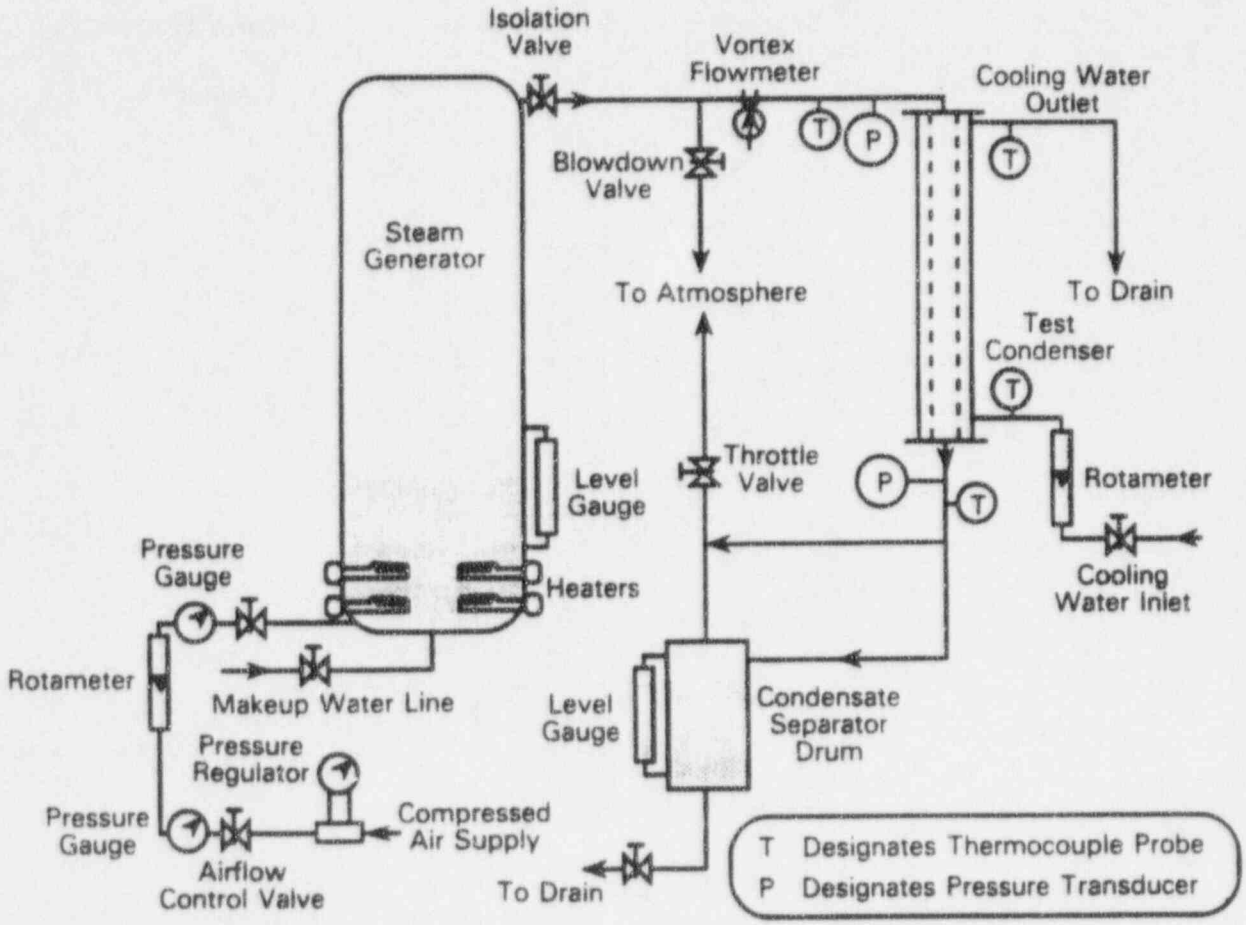

Fig. 6 Schematic of the MIT Single Tube Experiment

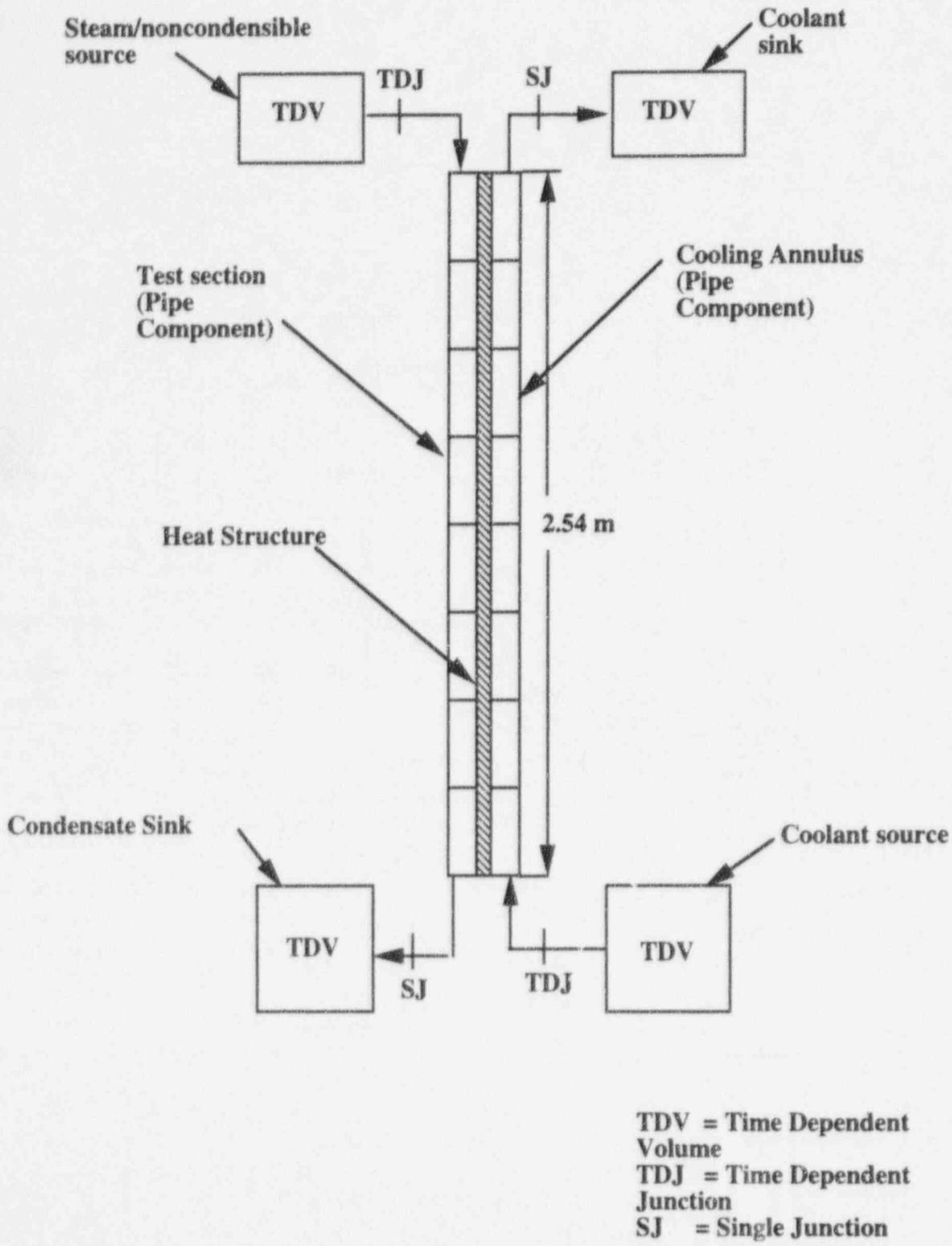

Fig. 7 RELAP5 Nodalization for the MIT Single Tube Experiment

Fig. 8 Heat Transfer Coefficients
(steam-air run #20) (MIT Expt #2)
Inlet Air Fraction: 0.206
Inlet Pressure:0.119 MPa

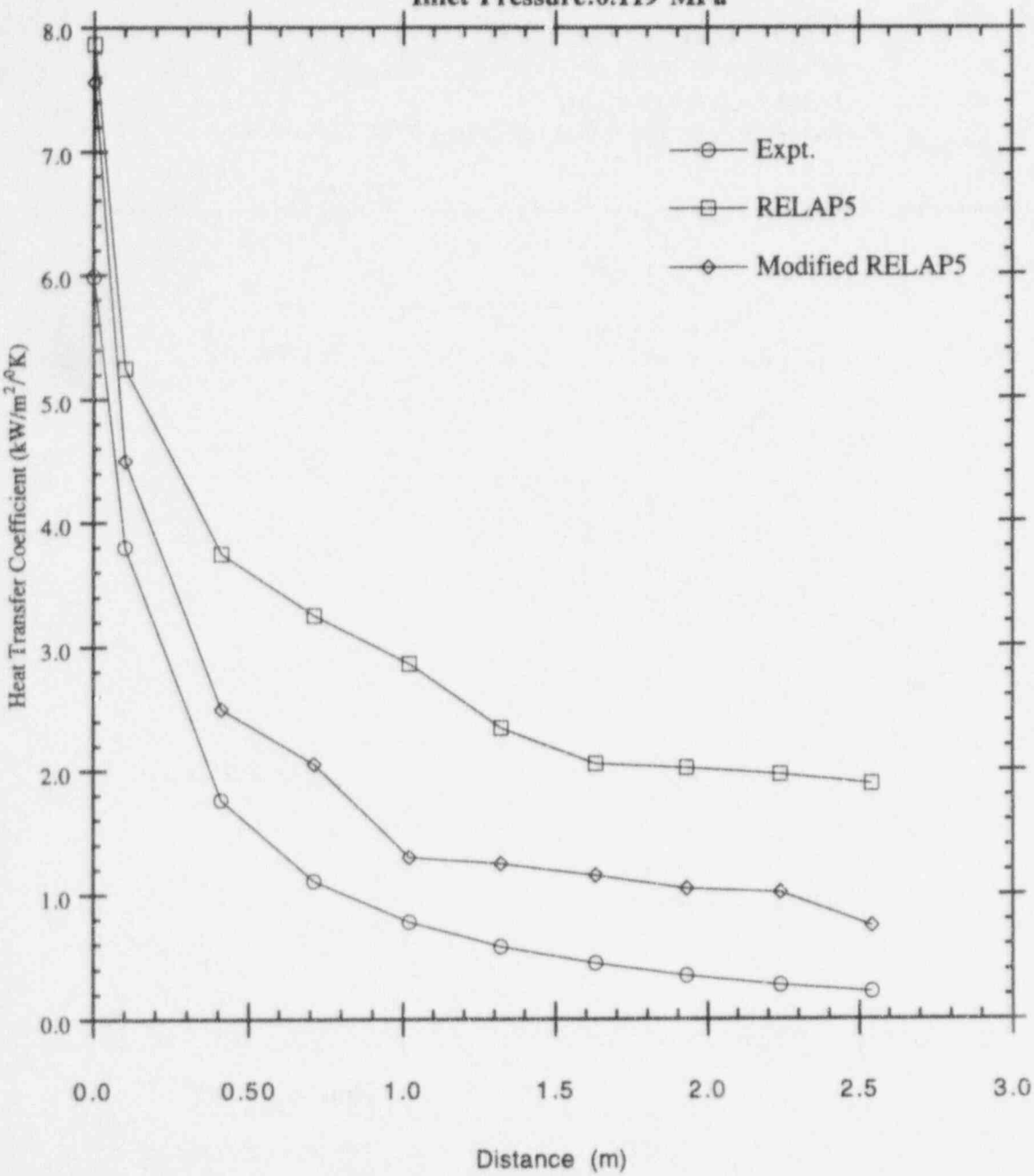

Fig.9 Heat Transfer Coefficients
(steam-air run #24) (MIT Expt #2)
Inlet Air Fraction: 0.113
Inlet Pressure: 0.214 MPa

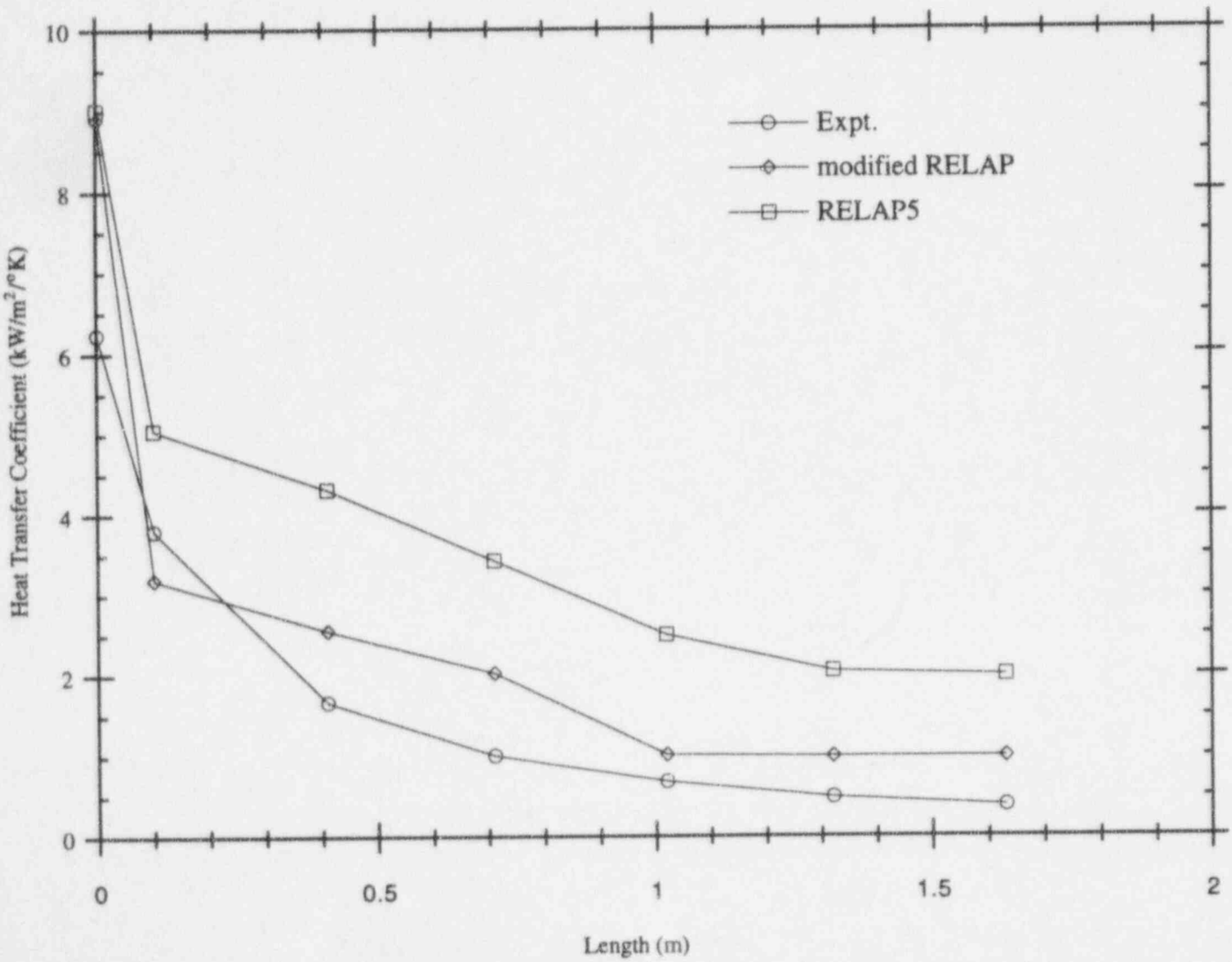

Fig. 10 Heat Transfer Coefficient vs. Distance (MIT Expt. #2) (Run#25)
Inlet Air Fraction: 0.155
Inlet Pressure : 0.221 MPa

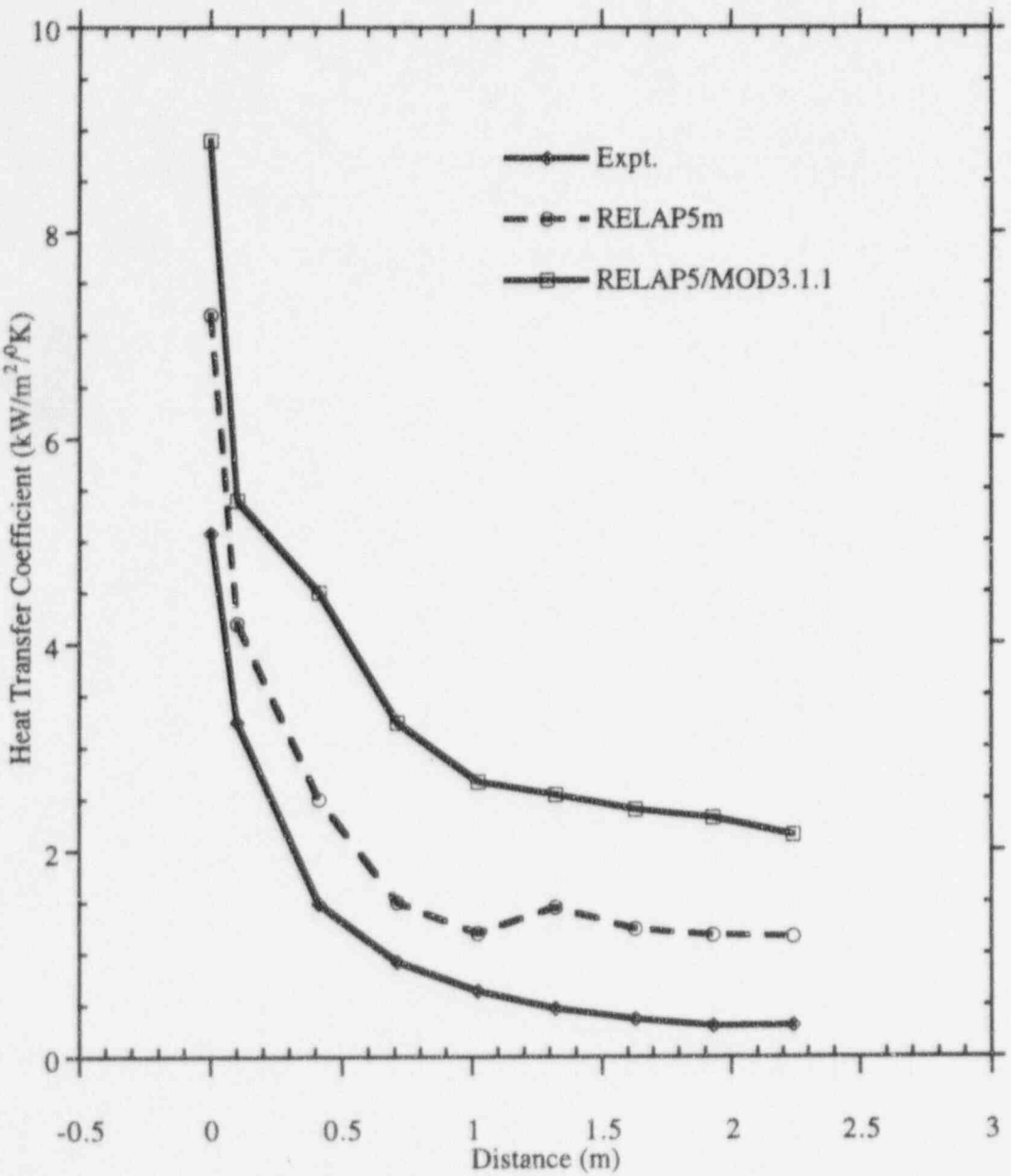

Fig. 11 Heat Transfer Coefficients (steam-air run #26) (MIT Expt #2) Inlet Air Fraction: 0.224 Inlet Pressure: 0.233 MPa

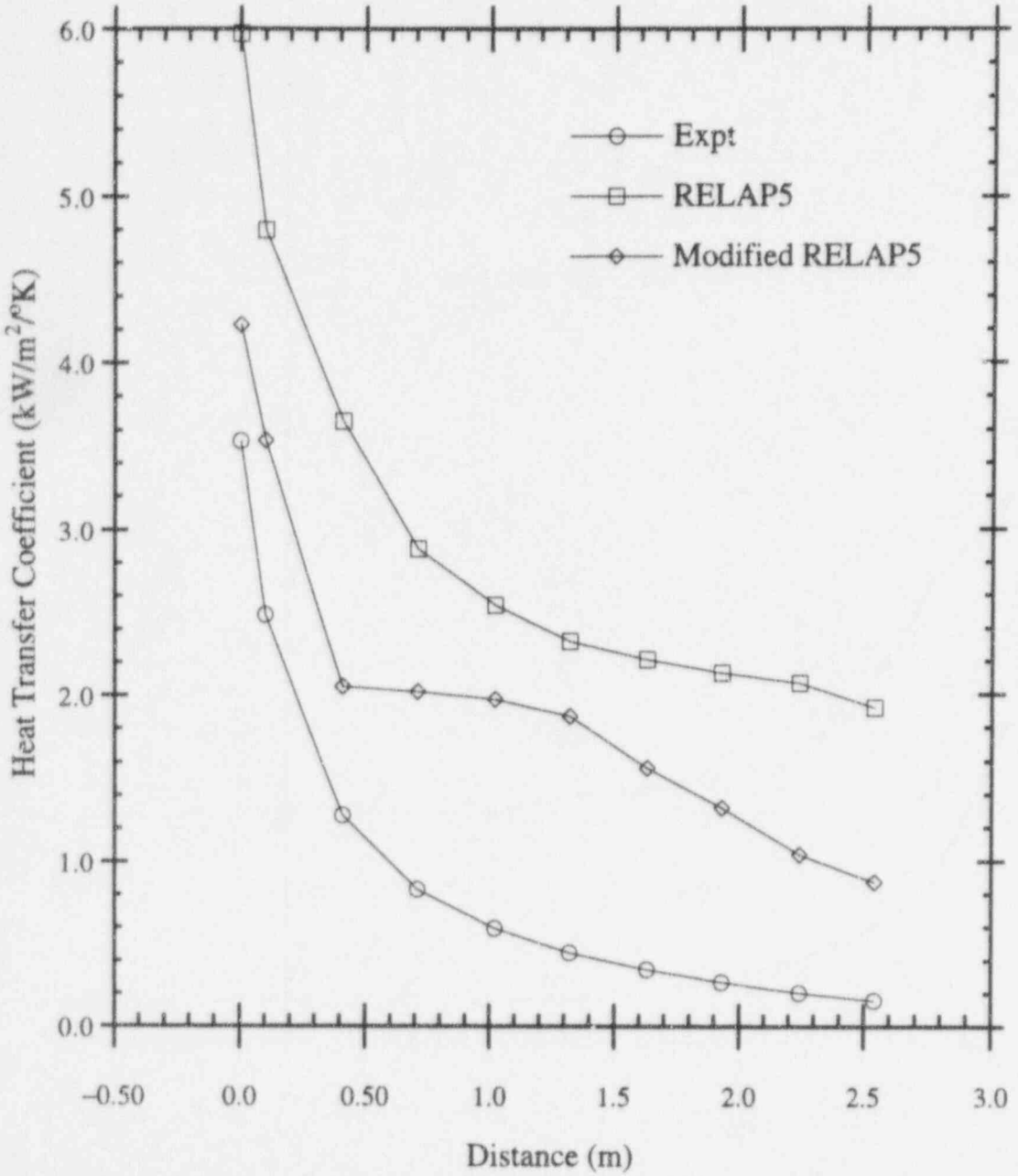

This page intentionally left blank.

Experimental Study of Horizontal Annular Channels Under Non-Developed Conditions

G. Delgadino[1] , J. Baliño and P. Carrica
Centro Atómico Bariloche e Instituto Balseiro
8400 - S. C. de Bariloche (R.N.)
Argentina

ABSTRACT

In this work an experimental study of the two–phase air-water flow in a horizontal annular channel under non–developed conditions is presented. A conductive local probe was placed at the end of the channel to measure the local phase indication function under a wide range of gas and water flow rates. The signal was processed to obtain the void fraction and statistical distributions of liquid and gas residence times. From these data the topology of the flow could be inferred. A laser intermittence detector was also located close to the channel exit, in order to measure statistical parameters for intermittent flows by means of a two–probe method.

1. INTRODUCTION

Gas and liquid flowing in a horizontal channel show a number of interfacial configurations, called flow patterns, which have received considerable attention in the literature. Due to the buoyancy force, particular flow patterns (namely stratified, wavy, elongated bubble and horizontal slug) appear in horizontal flows. When the gas or liquid superficial velocity is high enough, the importance of the buoyancy force decreases, resulting in similar flow patterns for horizontal and vertical flows. Most of the work in this area was done for adiabatic systems and developed conditions, *i.e.*, situations in which the flow patterns do not change noticeably along the channel; in these experiments, typically a length of the order of 200 diameters is left between the fluid injection and measuring locations. Nevertheless, these conditions are unlikely to occur in boilers or nuclear fuel channels because of the high and continuous vapor production rate and the interfacial heat and mass transfer.

It is well known that modelling of the CHF phenomenon and correlation of the experimental data has been focused on the different flow patterns which appear in the channel. Wong *et al.* [1] compiled CHF data from several sources and developed a generalized CHF prediction method for horizontal tubes, based on a modification of the vertical data by using a correction factor. This correction factor was determined semiempirically using the flow-pattern map developed by Taitel & Dukler [2].

---

[1] Currently at Rensselaer Polytechnic Institute, Troy, New York, USA.

A study was made by Baliño&Converti [3]; CHF measurements were performed for a horizontal annular channel (diameters 11.2 and 54 *mm*, approximately 1 *m* heated length), in which the eccentricity of the inner heater was varied. Measurements for low mass fluxes (up to 1600 $kg/m^2/s$) using freon-12 at a pressure of approximately 10.3 *bar* and saturation inlet conditions showed a strong influence of eccentricity on CHF. The data trend was discussed on a basis of the flow pattern under which the phenomenon occurred. A model based on the analysis of an intermittent flow pattern was developed, which explained satisfactorily the trend of the experimental data. The limitations of the model are due to the lack of basic knowledge about intermittent flow patterns under non-stable conditions and boiling.

The motivation for this work was to verify some of the assumptions made in the above mentioned model, concerning the non-developed condition. To do this, an experimental study of the two-phase flow on horizontal annular channels under non-developed conditions is presented (Delgadino [4]). Controlled and uniform air injection in water flow at normal pressure and room temperature was used to simulate saturated flow boiling conditions. A similar approach was used by Osamusali *et al.* [5] to determine the flow-pattern map in rod bundles.

2. EXPERIMENTAL SETUP

2.1 Flow loop

The experiments were made using an air-water loop, as shown schematically in figure 1. Tap water was circulated by a centrifugal pump through the test section; the water flow was manually controlled by a throttling valve and measured with a calibrated orifice plate. Clean air was supplied by a compressor at a controlled pressure of 6 *bar*; the air flow was manually controlled by precision valves and measured with a calibrated rotameter and a mass flow meter. The flow was essentially at standard conditions (1 *bar*, 20 ^oC). The range of liquid and gas superficial velocities covered in the experiments were j_L= 0.05 - 1.8 *m/s* and j_G= 0.3 - 2 *m/s*.

2.2 Test section

A 5 *cm* ID plexiglass test section was built, to allow for visualization of the different flow patterns and video recording. The test section is shown schematically in figure 2 and comprised an injector and positioners for the injector and the conductive probe. The injector was built by assembling 12 *mm* OD, 2 *mm* wall thickness, 6 *cm* long tubes made of sintered bronze. The total injector length was 1 *m* and the average particle size of the sintered material was 5 μm. The air flow was introduced through both ends of the injector, in order to obtain a uniform air distribution within the test section. The eccentricity of the injector could be varied by means of positioners, in order to study stratification effects. A positioner for the conductivity probe was designed to allow for radial and angular displacements of the probe; although the corresponding results are not presented in this

paper, in this way it was possible to measure the local void fraction distribution over the flow passage area.

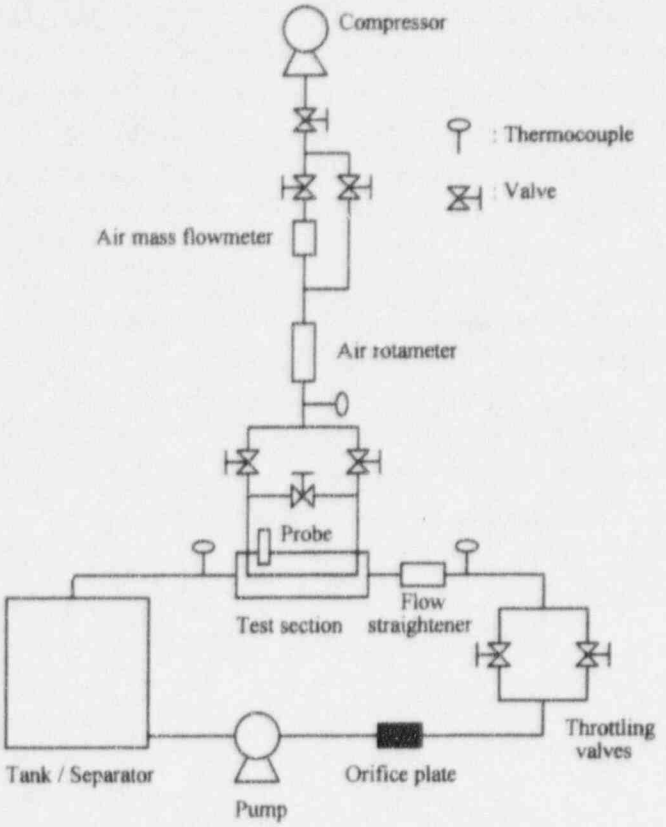

Figure 1. Schematic diagram of the air-water loop.

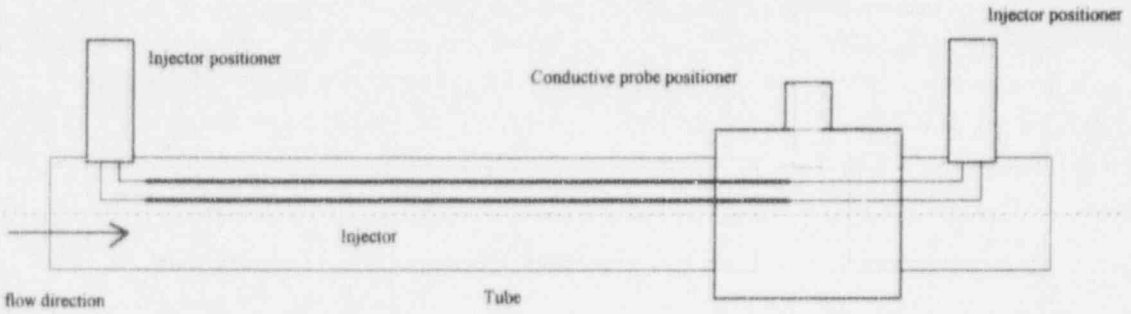

Figure 2. Schematic diagram of the test section

2.3 Conductivity probe and acquisition system for the phase indication function

The probe designed to measure the phase indication function is shown schematically in figure 3. The probe tip was made with a 2.5 μm diameter platinum wire soft-soldered to an electrically insulated wire. After this, the probe tip was covered with an electrical insulating painting and with a high temperature epoxy. The effective diameter of the probe tip was finally about 50 μm, as measured with a microscope. The second electrode was a

casing tube of stainless steel 2 *mm* in diameter. Both electrodes were soldered to a standard BNC connector through a support box.

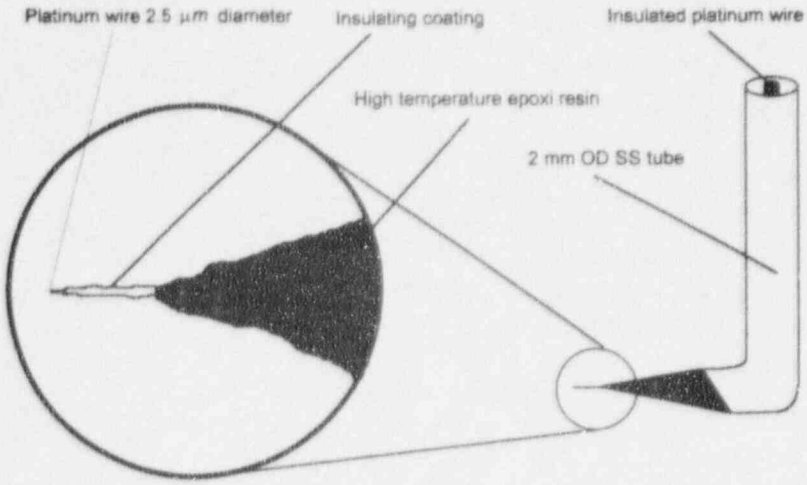

Figure 3. Schematic diagram of the conductive probe.

The probe was connected to an AC Wheatstone bridge fed by a high frequency sine-wave generator with variable amplitude and frequency. The bridge was adjusted and calibrated in order to obtain the optimum conditions for the signal coming from the probe. A schematic diagram of the data acquisition system is shown in figure 4, and further details can be seen in the work of Carrica *et al.* [6].

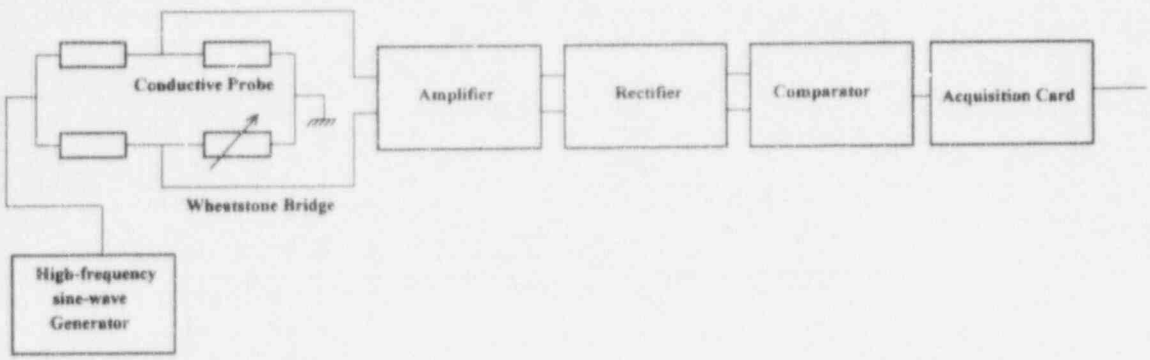

Figure 4. Schematic diagram of the data acquisition system.

2.4 Laser intermittence detector

A laser intermittence detector was located at a distance of 4.3 *mm* from the conductive probe measuring location. The operating principle is based on the deviation of a He-Ne laser beam due to refraction on the liquid and gas phases. In order to minimize the measuring chord, the laser beam was adjusted to cross the test section at a distance of 1 *mm* from the top surface. An LDR was put at the laser emergent direction when there was no liquid.

In order to build the flow-pattern map for non-developed conditions, the porous injector was kept in the concentric position. The liquid superficial velocities ranged from 0.05 and 1.8 *m/s*, while gas superficial velocities ranged from 0.3 and 2 *m/s*. Measurements were made by fixing the position of the air control valve and changing the liquid flow.

Determination of the flow pattern was achieved by analyzing the information obtained from the conductive probe and video films. It is important to notice that the determination of the flow-pattern map is more complicated than in experiments under developed conditions, because of the uniform air injection and the changing phase distribution along the channel. The flow-pattern map observed at the injector downstream end is shown in figure 5.

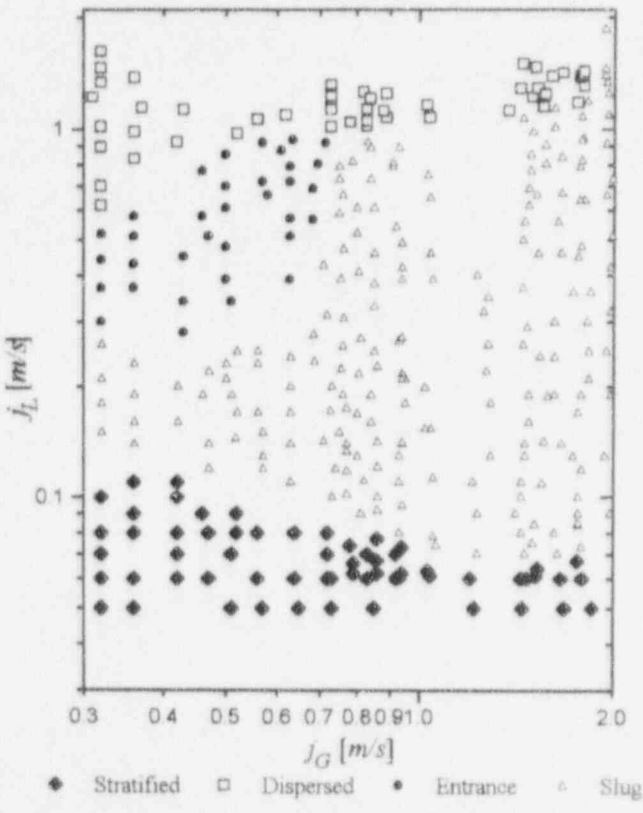

Figure 5. Flow-pattern map obtained from the experiments.

To determine the different flow patterns that appear at the end of the test section, it is important to describe the flow configuration along the channel resulting from the uniform air injection. For low liquid superficial velocities, air bubbles separated by very thin liquid

films form close to the upstream portion of the injector; these bubbles are fed by the air injected as they travel along the top of the test section. After a developing length, which depends on the superficial velocities, these bubbles eventually coalesce, originating a stratified or slug flow configuration.

For low liquid superficial velocities ($j_L < 0.1\ m/s$) a stratified flow pattern appears at the end of the test section, characterized by a relatively stable liquid level with some air bubbles on the surface, as shown in figure 6. Because of the aeration, no distinction was made between stratified and stratified-wavy flow patterns. As the liquid velocity is increased, the liquid level is higher and the developing length is increased, although the exit of the test section remains stratified.

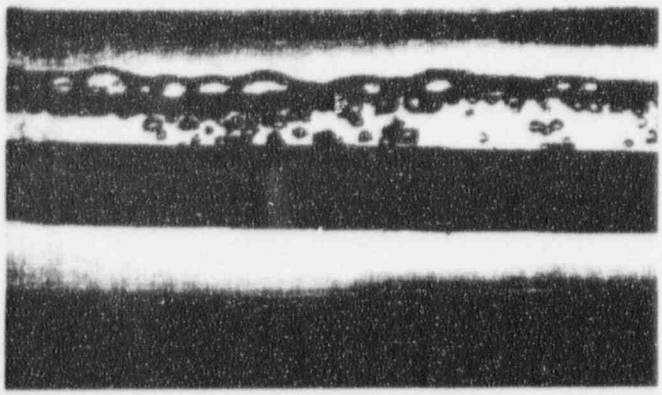

Figure 6. Stratified flow ($j_G = 0.51\ m/s, j_L = 0.09\ m/s$).

For relatively higher liquid superficial velocities, the small bubbles originate a slug flow pattern at some location located upstream the end of the test section, as shown in figure 7. The slugs show a strong aeration, because of the continuous air injection and the non-developed condition.

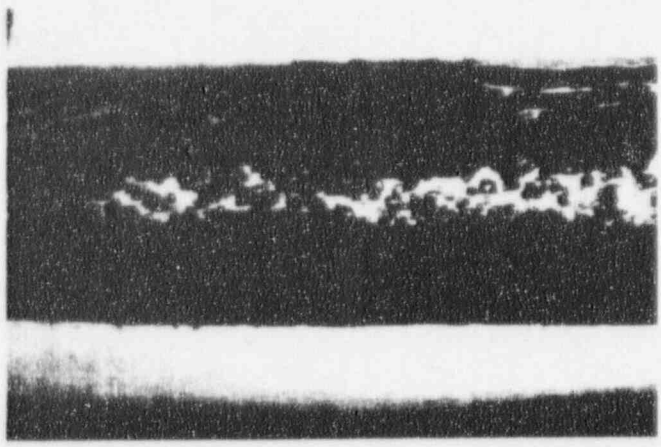

Figure 7. Slug flow ($j_G = 0.99\ m/s, j_L = 0.95\ m/s$).

As the liquid superficial velocity is increased, the location where the slugs are originated moves downstream, until it reaches the measuring location at the end of the test section. If the liquid superficial velocity is increased further, the slugs are originated

downstream the measuring point, and gas bubbles separated by very thin liquid films are observed along the entire test section, as shown in figure 8. This flow pattern is referred as *entrance* in figure 5. Thus, the entrance flow pattern can be regarded as a non-stable flow configuration related to the developing length to stratified or intermittent flow patterns.

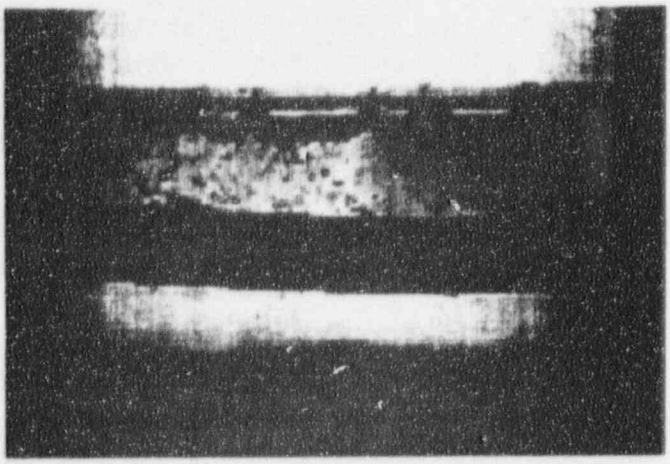

Figure 8. Entrance flow ($j_G = 0.49\ m/s, j_L = 0.34\ m/s$).

For high liquid superficial velocities ($j_L > 1\ m/s$) a dispersed flow pattern is observed, as shown in figure 9.

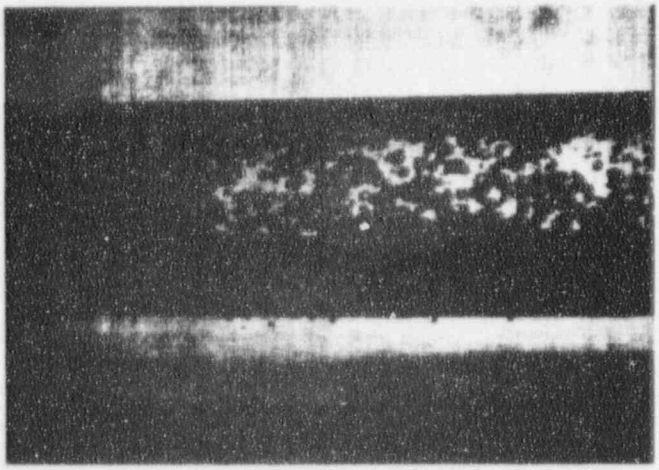

Figure 9. Dispersed flow ($j_G = 0.45\ m/s, j_L = 1.13\ m/s$).

For the range of explored superficial velocities, a strong influence of stratification is observed.

4. FLOW-PATTERN RECOGNITION USING THE INDICATION FUNCTION

For high superficial velocities, the flow-pattern recognition based on visualization became difficult; in these situations, the local indication function obtained from the conductive probe results a powerful tool to characterize the flow configuration.

From the local indication function, mean variables as void fraction and impact frequency can be calculated. On the other hand, normalized time histograms with the residence time for each phase can be built, as well as the liquid and gas fraction distributions obtained by multiplying the corresponding residence time times the relative quantity. The gas fraction is useful to show the contribution of the different bubble sizes to the void fraction. Typical liquid and gas fraction distribution are shown in figures 10, 11 and 12 for correspondingly dispersed, slug and entrance flow patterns. In these measurements, the probe tip was located over the downstream end of the injector, 1 *mm* apart from the top of the test section.

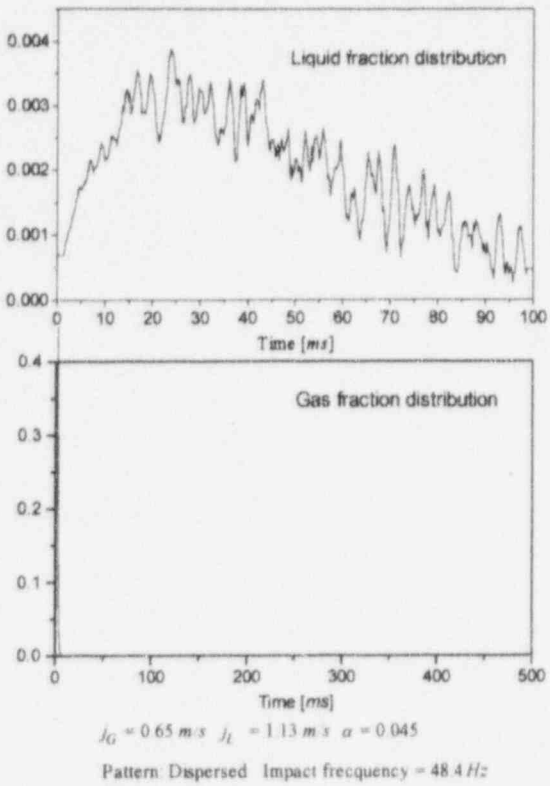

Figure 10. Liquid and gas fraction distribution for a dispersed flow pattern.

It is shown in figure 10 that the dispersed flow pattern is characterized by a contribution of gas bubbles with very short residence time (less than 5 *ms*) to the local void fraction, while the liquid fraction distribution has significant contributions for residence times greater than 100 *ms*.

It is shown in figure 11 that the slug flow pattern, on the other hand, shows significant contribution to the local void fraction from gas pockets with larger residence times (up to 500 *ms*), while the liquid fraction distribution reaches shorter residence times (up to 70 *ms*). The gas fraction distribution shows a local minimum (approximately at 50 *ms*) which roughly separates the contribution to the void fraction of the small bubbles within the slugs from the gas pockets with larger residence times.

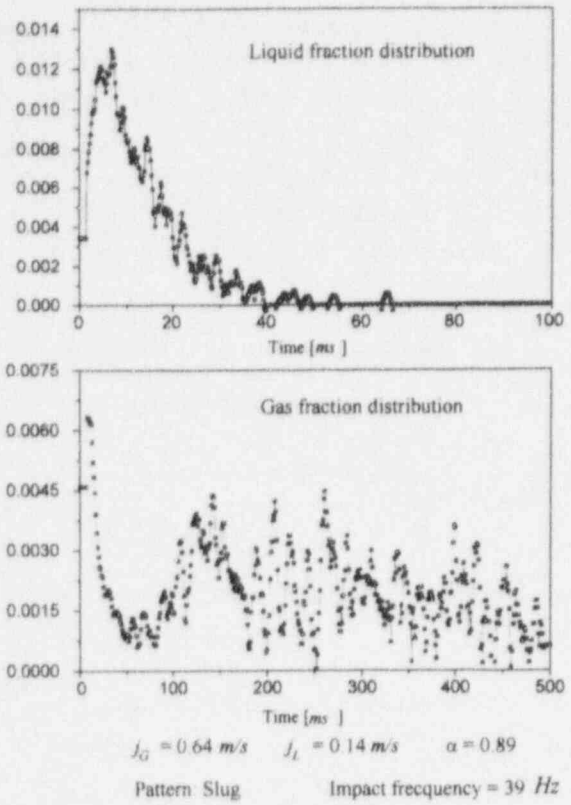

Figure 11. Liquid and gas fraction distribution for a slug flow pattern.

The structure of the entrance flow pattern is shown in figure 12. A peak for short residence times (less than 10 *ms*) can be observed in the liquid fraction, corresponding to the very thin liquid film separating the gas bubbles. Correspondingly, there is an absence of bubbles in the gas fraction distribution for short residence times.

5. STATISTICAL PARAMETERS FOR INTERMITTENT FLOW PATTERNS

Based on the information obtained from the signals coming from the conductance probe and the laser intermittence detector, it was possible to build the cross-correlation function, as well as velocity and length histograms for intermittent flow patterns. A processing procedure was necessary, in order to filter the influence of the small bubbles within the slugs in the indicating function coming from the laser intermittence detector. Besides, it was necessary to classify the slugs in time intervals according to their residence times. Typical results are shown for j_G = 1.07 *m/s* and j_L = 0.18 *m/s*. The cross-correlation function is shown in figure 13 for slugs with residence times ranging from 125 to 185 *ms*. The maximum was obtained for 36.5 *ms*; since the distance between detectors was 4.3 *mm*, the resulting slug speed for this time interval was 1.18 *m/s*.

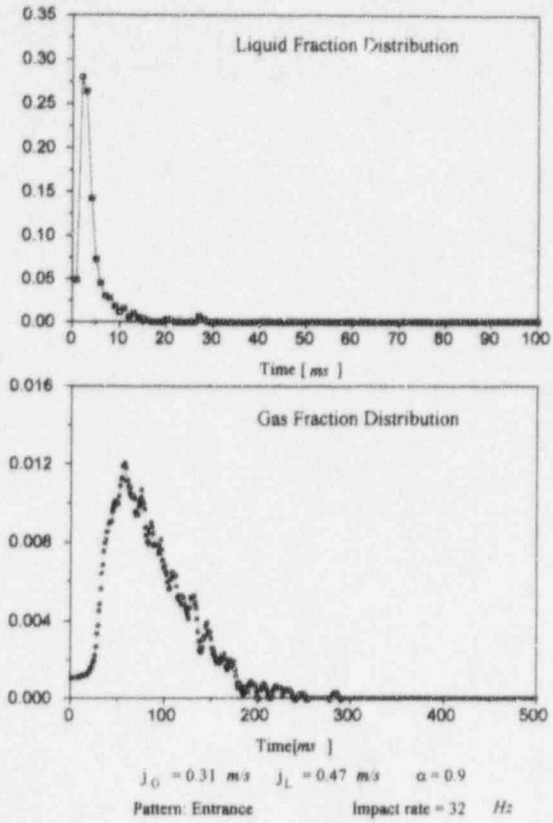

Figure 12. Liquid and gas fraction distribution for an entrance flow pattern.

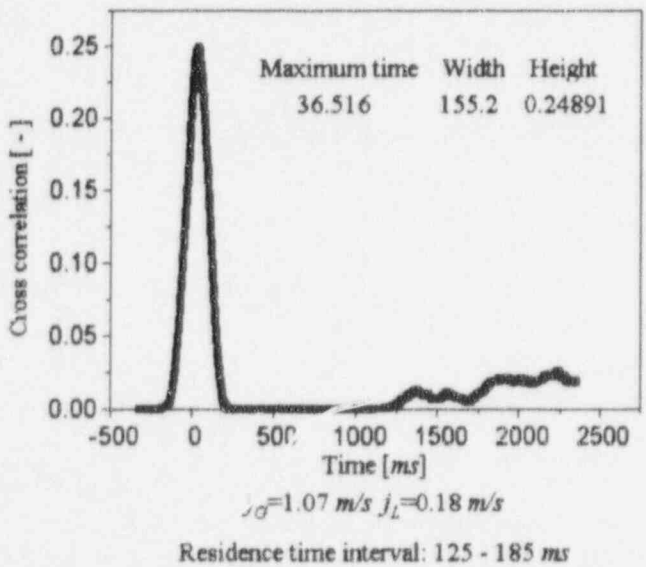

Figure 13. Cross-correlation function for an intermittent flow pattern.

The corresponding slug velocity histogram for j_G = 1.07 *m/s* and j_L = 0.18 *m/s* is shown in figure 14. The data obtained by Nydal *et al.* [7] for developed slugs predict slug velocities approximately 1.3 times the mixture superficial velocity; it can be seen that this value is very close to the mean velocity within the distribution. The relative standard

deviation resulted approximately ten times the corresponding measured value for developed conditions, probably because of the non-developed conditions.

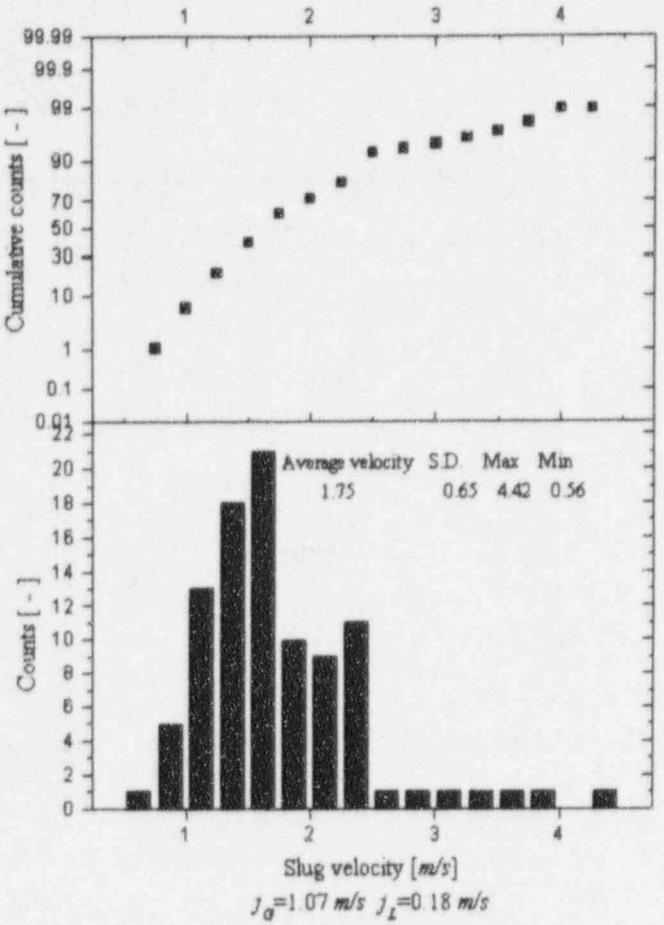

Figure 14. Slug velocity histogram for an intermittent flow pattern.

The corresponding slug length histogram for j_G = 1.07 *m/s* and j_L = 0.18 *m/s* is shown in figure 15. The mean slug length (216 *mm* or approximately 4 diameters) results smaller than the values obtained by Nydal *et al.* [7] under developed conditions (15 to 20 diameters). Correspondingly, the relative standard deviation resulted approximately two times the corresponding measured value for developed conditions.

From the information obtained in figures 14 and 15, the slug velocity as a function of the slug length can be displayed, as shown in figure 16. A trend for the developing slugs to move faster for larger lengths is observed, although more statistics would be necessary.

6. LOCAL VOID FRACTION AT THE INJECTOR TOP LEVEL

The motivation for this work was to verify some of assumptions made by Baliño&Converti [3] to explain the CHF mechanism in horizontal annular channels with variable eccentricity for low mass fluxes. According to measurements with freon-12 under

saturation inlet conditions, a strong influence of the position of the heater was found on CHF; on the other hand, the influence of mass flux was found to be moderate. A mechanistic model to explain the data trend was developed. According to this model, CHF occurs under an intermittent flow pattern, and the postulated CHF mechanism is dryout in a situation where the liquid level under the gas pockets reaches the heater top level at the channel exit.

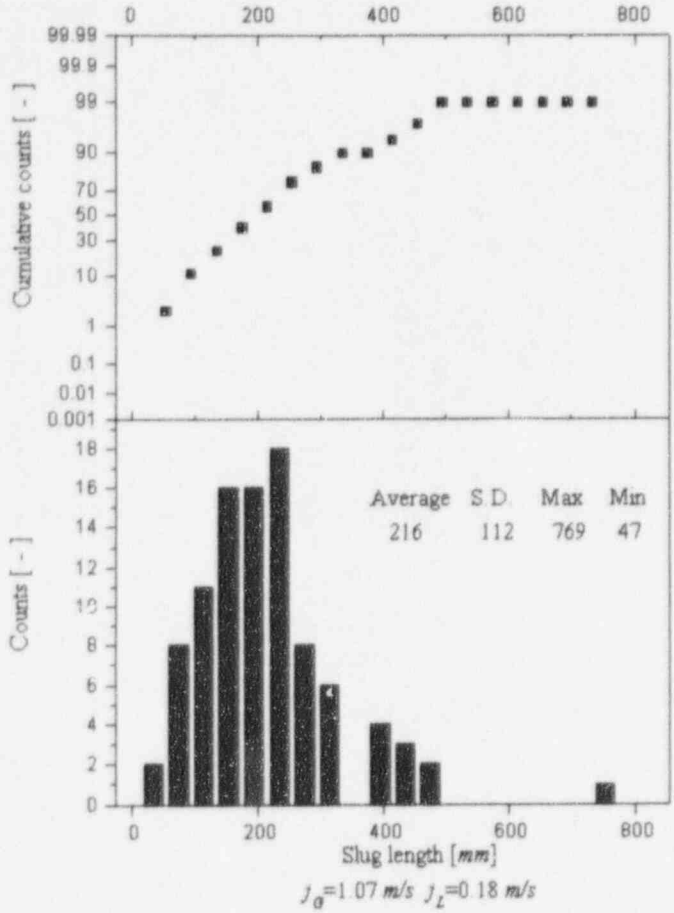

Figure 15. Slug length histogram for an intermittent flow pattern.

A series of measurements was made for situations in which the injector was located eccentrically. The eccentricity is measured in terms of the length the injector is displaced from its concentric position, eccentricity being positive when the heater is displaced upwards. For each position, the conductivity probe was placed 2 *mm* over the injector top level. For a fixed liquid superficial velocity, measurements of the indication function were made for different gas superficial velocities. The void fraction distribution was processed in order to obtain the local void fraction and the contribution of the big bubbles to the local void fraction.

Typical results are shown in figure 17 and 18 for j_L = 0.245 *m/s*. It can be observed that the local void fraction increases sharply as the gas superficial velocity is increased beyond a threshold value, for situations in which the injector is over the concentric position.

Besides, the local void fraction increment is due primarily to the bubbles with larger resident times (gas pockets) and not to the small bubbles within the slugs. Similar measurements were made for j_L = 0.423 and 0.597 *m/s*.

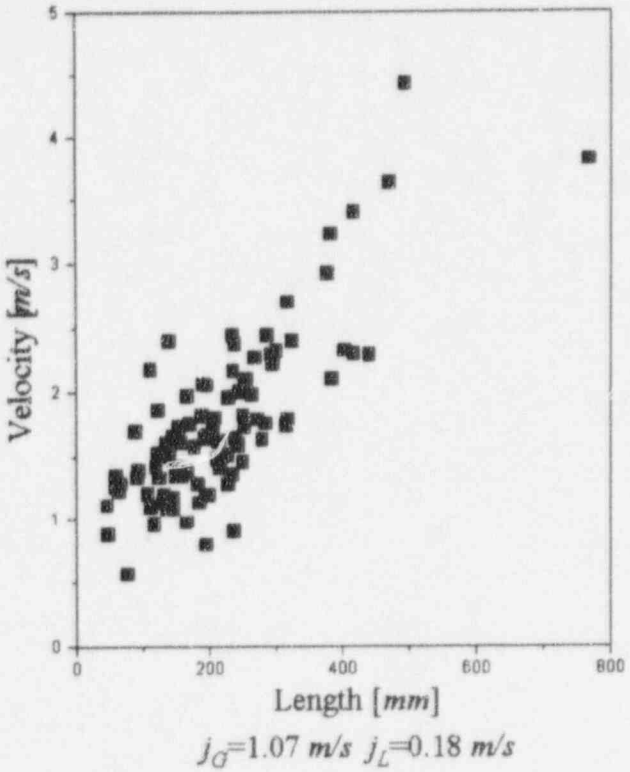

Figure 16. Velocity of the developing slugs as a function of the length.

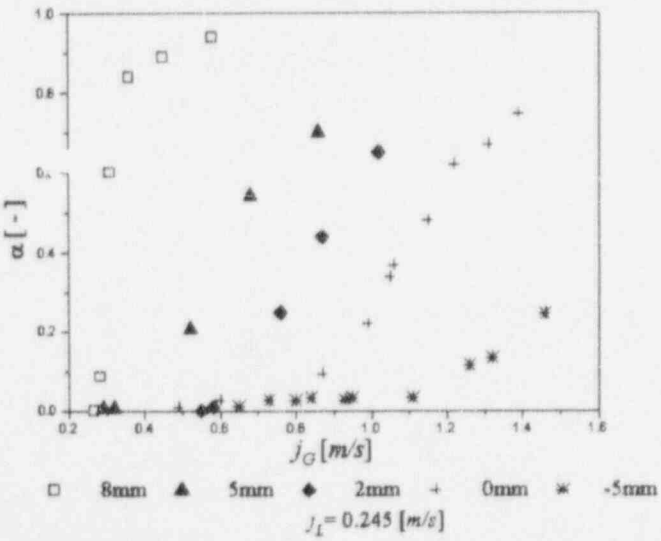

Figure 17. Void fraction at the injector top level as a function of eccentricity.

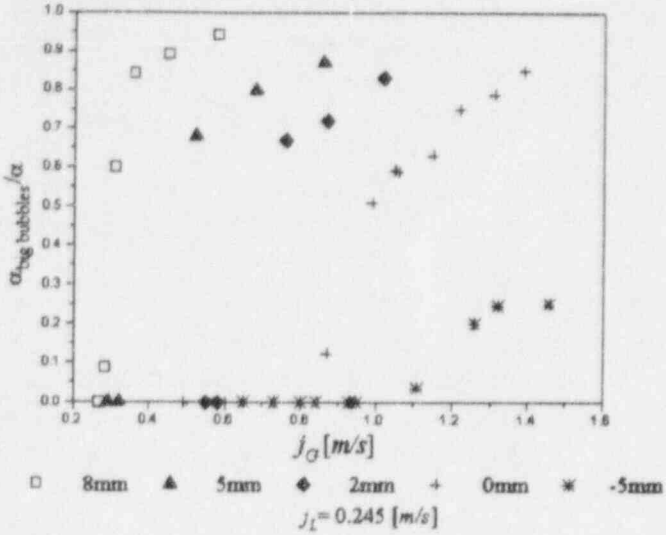

Figure 18. Contribution of the big bubbles to the void fraction at the injector top level.

With the arbitrary assumption that the dryout condition at the injector top level occurs when the contribution of the gas pockets to the local void fraction reach ~ 10 %, the dryout gas superficial velocity as a function of eccentricity is shown in figure 19 for different liquid superficial velocities. The qualitative trends agree with the dryout gas superficial velocities calculated from the CHF data obtained by Baliño&Converti [3] for the situations in which the heater was located over the concentric position.

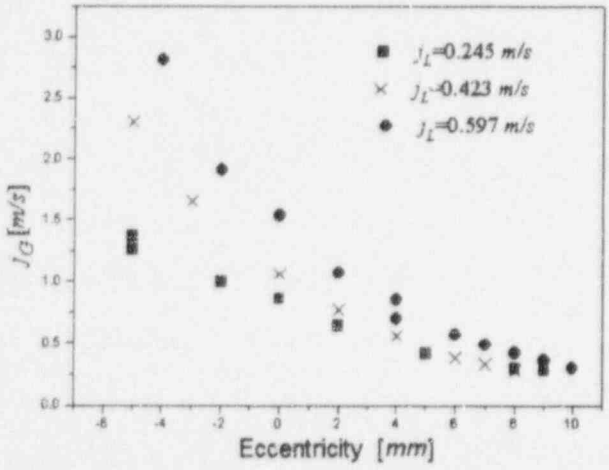

Figure 19. Dryout gas superficial velocity as a function of eccentricity.

7. CONCLUSIONS

In this work an experimental study of the two–phase air-water flow in a horizontal annular channel under non–developed conditions is presented. A flow-pattern map was

built, and different configurations were identified using a conductive local probe and video films. The signal coming from the conductive probe was processed to obtain the void fraction and statistical distributions of liquid and gas residence times. From these data the topology of the flow could be inferred. A flow topology was found, characterized by gas bubbles separated by very thin liquid films; this flow pattern can be regarded as a non-stable flow configuration related to the developing length to stratified or intermittent flow patterns.

A laser intermittence detector was also located close to the channel exit, in order to measure statistical parameters for intermittent flows by means of a two–probe method. In this way, it was possible to built the velocity and length histograms for the developing slugs. The mean value for the velocity distribution is very close to the corresponding value for developed slugs, while the standard deviation is larger. Concerning the length distribution, it was found that developing slugs are shorter than the developed ones. A trend for the developing slugs to move faster for larger lengths is observed, although more statistics should be necessary.

A series of measurements was made for situations in which the injector was located eccentrically. For each position and for a fixed liquid superficial velocity, measurements of the indication function at the injector top level were made for different gas superficial velocities. The void fraction distribution was processed in order to obtain the local void fraction and the contribution of the big bubbles to the local void fraction. It is observed that the local void fraction increased sharply as the gas superficial velocity is increased beyond a threshold value, for situations in which the injector is over the concentric position. Besides, the local void fraction increment is due primarily to the bubbles with larger residence times (gas pockets) and not to the small bubbles within the slugs.

ACKNOWLEDGEMENTS

The financial support for this work was provided by the Comisión Nacional de Energía Atómica and Combustibles Nucleares Argentinos S. A. (CONUAR).

The contribution of Mr. D. Mateos and Mr. M. Enevoldsen in building the test section is deeply acknowledged.

REFERENCES

[1] Wong, Y. L., Groeneveld, D. C., Cheng, S. C., "CHF prediction for horizontal tubes". Int. J. Multiphase Flow 16, pp. 123-138 (1990).

[2] Taitel Y., Dukler A. E., "Flow Pattern Transition in Gas-Liquid Systems: Measurement and Modelling", Multiphase Science and Technology, Vol. 2 (edited by Hewitt, G. F., Delhaye, J. M. and Zuber, N.), pp. 1-94, Hemisphere, Washington, D. C. (1986).

[3] Baliño, J. & Converti, J., "Saturated CHF in horizontal eccentric annuli for low mass fluxes: measurement and modelling". Int. J. Multiphase Flow 20, 5, pp. 901-913 (1994)

[4] Delgadino, G., "Distribución de una mezcla bifásica agua-aire en canales anulares horizontales", Final Report to obtain the degree of Nuclear Engineer, Instituto Balseiro, Universidad Nacional de Cuyo, Argentina (1994).

[5] Osamusali, S. I., Groeneveld, D. C., Schenk, J. R. & Cheng, S. C., "A technique for non-visual characterization of two-phase flow patterns in a horizontal 37-rod bundle", Proc. CNS Meeting (1991).

[6] P. M. Carrica, J. Achterberg, E. Taglialavore & S. Leonardi "A Conductive Acquisition System for the Local Phase Indication Function", Informe Técnico CNEA-CAB 93/012 (1993).

[7] Nydal O. J., Pintus, S., Andreussi, P., "Statistical Characterization of Slug Flow in Horizontal Pipes", Int. J. Multiphase Flow 13, 3, pp. 439-453 (1992).

INTERFACIAL SHEAR STRESS IN STRATIFIED FLOW IN A HORIZONTAL RECTANGULAR DUCT

C. Lorencez, M. Kawaji, A. Ousaka[1], Y. Murao[2]
Department of Chemical Engineering and Applied Chemistry
University of Toronto, Toronto, Ont., Canada M5S 1A4

1. Dept. of Mechanical Engineering
Tokushima University, Tokushima, Japan

2. Japan Atomic Energy Research Institute
Tokai, Ibaraki, 319-11, Japan

ABSTRACT - Interfacial shear stress has been experimentally examined for both cocurrent and countercurrent stratified wavy flows in a horizontal rectangular duct. Four different methods of evaluating the interfacial shear stress from the measurements were examined and the results have been compared with existing correlations. Some differences were found in the estimated interfacial shear stress values at high gas flow rates which could be attributed to the assumptions and procedures involved in each method. The interfacial waves and secondary motions were also found to have significant effects on the accuracy of Reynolds stress and turbulence kinetic energy extrapolation methods.

NOMENCLATURE

D	diameter [m]
C_f	friction factor
H	total channel height [m]
h	liquid height [m]
k	turbulence kinetic energy (TKE) [m^2/s^2]
k_s	surface roughness [m]
p	pressure [Pa]
Q	volumetric flow rate [m^3/s]
R	radius [m]
Re	Reynolds number (UD_h/ν)
U	mean streamwise velocity [m/s]
U^+	dimensionless mean streamwise velocity
u_*	friction velocity [m/s]
W	total channel width [m]
x	distance in the streamwise direction [m]
y	distance in the vertical direction [m]

Greek symbols

ε	dissipation of TKE [m^2/s^3]
κ	von Kármán constant
ν	kinematic viscosity [m^2/s]
ρ	density of fluid [kg/m^3]
τ	shear stress (Pa)
Δ	increment

Subscripts

h	hydraulic
i	interfacial
G	gas phase
L	liquid phase
W	wall
s	sand roughness
T	turbulent

INTRODUCTION

Stratified two-phase flow in pipes and ducts is widely encountered in many chemical and industrial processes, such as flow of steam and water in horizontal pipes during postulated nuclear reactor accidents, flow of oil and natural gas in pipelines, certain types of heat exchanger and mass transfer equipment. Generally, the prediction of the pressure drop and liquid holdup for this type of flow has been based on empirical correlations developed, for example, by Lockhart and Martinelli

(1949). However, significant differences between the experimental measurements and the predictions of these empirical correlations have been reported elsewhere.

A better approach was the analysis of Taitel and Dukler (1976), in which separate one-dimensional momentum equations for the gas and liquid phases were considered. This method requires an additional correlation for the shear stress at the gas-liquid interface to close the set of equations. Different correlations for interfacial shear stress or friction factor have been proposed for both cocurrent (Hanratty and Engen, 1957; Fukano et al., 1985; Kowalski, 1987; Fabre et al., 1987; Sadatomi et al., 1993, among many others) and countercurrent (Lee and Bankoff, 1983; Kaminaga et al., 1991) stratified two-phase flows. However, due to the different assumptions used by the researchers it is common to find disagreement among the values of the interfacial shear stress, τ_{iG}, predicted by different correlations.

Also, the accurate evaluation of the interfacial shear stress is important because it constitutes the driving force for the organized motion in the liquid phase (Rashidi et al., 1991; Komori et al., 1993; Lorencez, 1994). Turbulent bursts created as a result of the interfacial shear acting upon the upper layers of the liquid, carrying fluid from the interface towards the bulk of the liquid, are considered to be the main mechanism of the turbulent interfacial transport of heat and mass. Commonly, the frequency of appearance of interfacial turbulent bursts is expressed in terms of the interfacial friction velocity given by,

$$u_{*iG} = \sqrt{(\tau_{iG}/\rho_G)} \qquad (1)$$

Therefore, the objective of this study was to estimate the interfacial shear stress, τ_{iG}, in stratified two-phase flow by using different methods and compare those results with predictions of several existing correlations. Thus, τ_{iG} was evaluated from the measurements using the following methods: (1) a gas momentum balance which includes the interfacial level gradient term, (2) extrapolation of the gas Reynolds stress profile to the gas-liquid interface, (3) fitting the gas mean velocity profile to the velocity profile of flow over a rough surface, and (4) extrapolation of the turbulence kinetic energy (TKE) profile to the gas-liquid interface. Some of these methods have been employed previously to evaluate the interfacial shear stress, however, systematic evaluation of different methods and comparison with data have not been performed since Kowalski (1987). Here, the above methods will be evaluated by comparison with both cocurrent and countercurrent wavy-stratified flow data.

EXPERIMENTAL FACILITY

The present study was conducted using a flow loop which included a rectangular plexiglass flow channel and all the facilities required for cocurrent and countercurrent, gas/liquid stratified and wavy flows. The horizontal flow channel consisted of three sections: inlet chamber, test channel and outlet chamber (Figure 1). The chambers were designed to allow the cocurrent and countercurrent flows of gas/liquid in the same loop without modification. In the inlet chamber a floating element and a honey comb filter were inserted to minimize the effect of reflected waves.

The test channel was formed by three 240 cm long segments, which were joined end-to-end by flanges and assembled to ensure that the inside channel walls were flush. The inside dimensions of the test channel were 100 mm in width (W) and 50 mm in height (H). The test channel was engineered to ensure a constant geometry throughout its length and minimize deformation due to mechanical stresses. The lower and upper edges of the

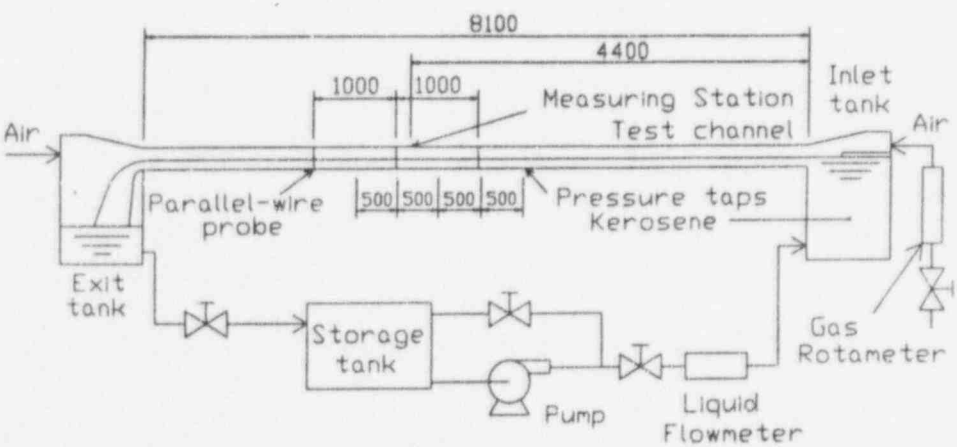

Figure 1: Schematic of the Test Facility

side walls were machined with a tolerance of 1 mm in 240 cm, and the top and bottom plates were glued and bolted down to the edges of the side walls to ensure flatness of the bottom (floor) and top (ceiling) of the channel and to prevent any sagging over time.

The working fluids were air and kerosene (Shell-Sol 715). Air was provided from the building supply through a pressure regulator/filter unit and the flow was monitored by a rotameter (Brooks model 1307D). The kerosene was circulated through the loop by a centrifugal pump and filtered to remove solid particles larger than 5 microns before entering the flow channel. The liquid flow rate was monitored by a turbine flow meter.

A two-channel hot-film anemometer (Dantec 5601 with 56C17 bridges) with a cross-wire film probe (Dantec 55R63) was used to measure the velocity profiles in the gas phase. Two differential input channels were simultaneously sampled at a rate of 1kHz/channel for 60 seconds. A separate air flow loop consisting of an inlet chamber and a 4.5 m long pipe with a 50.1 mm I.D. was used to calibrate the hot-film probe measurements for air. A Pitot tube was used to determine the center-line velocity at 60 pipe diameters from the inlet and a Baratron Type 223B variable capacitance differential pressure transducer with a full scale input range of 26.66 Pa and an accuracy of 0.5% of full scale was used to measure the dynamic head. Care was taken to ensure that the hot-film probe was placed exactly at the same position and in the same orientation as the Pitot tube. The signals from the differential transducer and anemometer were fed to the data acquisition system, and then the data were reduced by a microcomputer. The details of the experimental apparatus and the measurement methods can be found in Lorencez (1994) and Lorencez et al. (1991, 1993).

RESULTS AND ANALYSIS

To study the effect of the gas-liquid interface geometry on the interfacial shear, four different cases were examined: cocurrent and countercurrent flows with smooth and wavy interfaces. The experimental conditions are summarized in Tables I and II, where the liquid and gas volumetric flow rates, pressure drop, liquid height and wave amplitude, interfacial level gradient, wall shear stress and the Reynolds numbers are shown for each run. The wave amplitude was taken as the r.m.s. value of the liquid height. The Reynolds number was computed in terms of the hydraulic diameter for each phase. The gas-liquid interface was included in the computation of the hydraulic diameter for the gas but not for the liquid phase. In all the runs, the liquid flow was turbulent and the liquid Reynolds number was kept almost constant while the gas flow rate was varied. The profiles of mean liquid velocity and velocity fluctuations in both streamwise and vertical directions can be found elsewhere (Lorencez, 1994).

Hanratty and Engen (1957) developed a method to evaluate the interfacial shear by measuring the pressure drop, and the positions of the maximum gas velocity and the gas-liquid interface. This approach has been widely used (Cohen and Hanratty, 1968; Gayral et al., 1979; Fabre et al., 1987), under the assumptions that the stratified flow is fully developed and two-dimensional (a fact that strongly depends on the aspect ratio of the test section), and that the maximum in the velocity profile was a condition of zero stress. Today, it is known that the position of the maximum velocity does not necessarily match the position of the zero shear stress for flow over a rough surface, as it has been shown by Hanjalic and Launder (1972) for single-phase flow and Kowalski (1987)

Table I Experimental conditions for cocurrent flow

Run	$Q_L \times 10^4$ (m^3/s)	$Q_G \times 10^2$ (m^3/s)	$\Delta P/\Delta x$ (Pa)	h_L (mm)	Δh (mm)	$\Delta h/\Delta x \times 10^3$	τ_{wG} (Pa)	Re_L	Re_G
300	3.8	0.81	-2.05	17.1	0.25	-1.65	0.030	6620	8030
310	3.8	0.95	-2.63	16.9	0.45	-1.61	0.039	6770	9370
320	3.8	1.09	-3.16	16.7	0.67	-1.53	0.049	6800	10690
330	3.8	1.36	-6.51	15.9	1.30	-1.23	0.069	6900	13210
340	3.8	1.73	-9.77	14.5	1.54	-0.83	0.097	7190	16780

Table II Experimental conditions for countercurrent flow

Run	$Q_L \times 10^4$ (m^3/s)	$Q_G \times 10^3$ (m^3/s)	$\Delta P/\Delta x$ (Pa)	h_L (mm)	Δh (mm)	$\Delta h/\Delta x \times 10^3$	τ_{wG} (Pa)	Re_L	Re_G
500	3.8	3.4	-0.67	17.6	0.14	-2.5	0.007	7020	3330
510	3.8	5.2	-1.57	18.1	0.68	-3.0	0.014	6980	5020
520	3.8	7.4	-3.29	18.5	1.44	-4.1	0.027	6930	7170

for two-phase flow. Therefore, this method is not expected to yield good predictions of the data and tends to overestimate the interfacial shear as shown later.

A better approach was to perform a momentum balance in the gas phase. However, most of the previous derivations of the momentum equation ignored the contribution of the interfacial level gradient, which may be as much as 15% of the overall pressure gradient for countercurrent flow. In this work, the interfacial shear stress was evaluated by using Sadatomi et al.'s (1993) proposed momentum balance,

$$\frac{dP}{dx} - \frac{2(H-h)+W}{(H-h)W}\tau_{wG} - \frac{1}{H-h}\tau_{iG} + \frac{k_G\rho_G Q_G^2}{W^2(H-h)^3}\frac{dh}{dx} = 0, \qquad (2)$$

where $\partial P/\partial x$ is the measured pressure gradient in the gas phase, τ_{wG} is the wall shear stress calculated using a single-phase flow friction factor, and the last term includes the effects of the interfacial level gradient, $\partial h/\partial x$. Once all the terms in Equation (2) are known, the equation is solved for τ_{iG} assuming a smooth interface even in wavy flows. The smooth interface assumption is unique to this method and can result in overestimation of the interfacial shear stress if the interface is wavy and the actual interfacial area per unit volume is much greater than the smooth interface assumed. The results obtained using this first method for both cocurrent and countercurrent flows are denoted as τ_{iG1}, and are shown in Tables III and IV.

(2) Evaluation of τ_{iG} by extrapolation of the Reynolds stress profile.

In turbulent flows, the total shear stress is given by the sum of viscous and turbulent contributions. The viscous contribution is only significant near the solid/fluid boundaries and the turbulent contribution in the bulk of the flow. If the shear stress profile is linear as commonly assumed, extrapolation of the measured turbulent Reynolds stress profile, R_{XY}, to the gas-liquid interface would provide an estimate of the interfacial shear stress. In two-dimensional flows, that is to say, flows in test sections with a high aspect ratio where secondary motion is kept to a minimum, the profile of R_{XY} is linear, as shown by Laufer (1954) for flow over smooth walls, and Hanjalic and Launder (1972) for flow over a rough surface. However, in three-dimensional flows such as flow in pipes or in square and rectangular ducts with a smaller aspect ratio, the presence of secondary flow considerably distorts the linearity of R_{XY} (Gayral et al., 1979; Fabre et al., 1984; 1987a; 1987b; Kowalski, 1987; Lorencez, 1994). In these cases, the magnitude of the spanwise (R_{ZY}) and normal (R_{XZ}) stress gradients are not to be ignored, a fact that reduces the applicability of this method. Nevertheless, this method was used to obtain the interfacial shear stress from the measured Reynolds stress profile in this test section with an aspect ratio of 2.

Figures 2 and 3 show the R_{XY} profiles for cocurrent and countercurrent flows, respectively. The loss of linearity of R_{XY} increases with the gas volumetric flow rate since R_{XY} is linear in both cocurrent and countercurrent flows at low gas flow rates and deviation from linearity is noted at higher gas flow rates. This suggests that the magnitude and effects of the secondary flow increase with the gas flow rate. The results obtained using this method, τ_{iG2}, for both cocurrent and countercurrent flows are shown in Tables III and IV and later compared with the predictions of existing correlations.

(3) Evaluation of τ_{iG} by fitting the velocity profile to a universal profile.

(3.1) Smooth gas-liquid interface. Due to the difference in densities of the gas and liquid phases, the smooth

Table III Interfacial shear stress measured in cocurrent flow

Run	τ_{iG1} (Pa)	τ_{iG2} (Pa)	τ_{iG3} (Pa)	τ_{iG4} (Pa)
300	0.030	0.020	0.26	0.023
310	0.039	0.030	0.036	0.027
320	0.055	0.039	0.049	0.043
330	0.131	0.062	0.105	0.085
340	0.206	0.092	0.197	0.133

Table IV Interfacial shear stress measured in countercurrent flow

Run	τ_{iG1} (Pa)	τ_{iG2} (Pa)	τ_{iG3} (Pa)	τ_{iG4} (Pa)
500	0.007	0.006	0.005	0.009
510	0.016	0.013	0.013	0.016
520	0.029	0.025	0.034	0.031

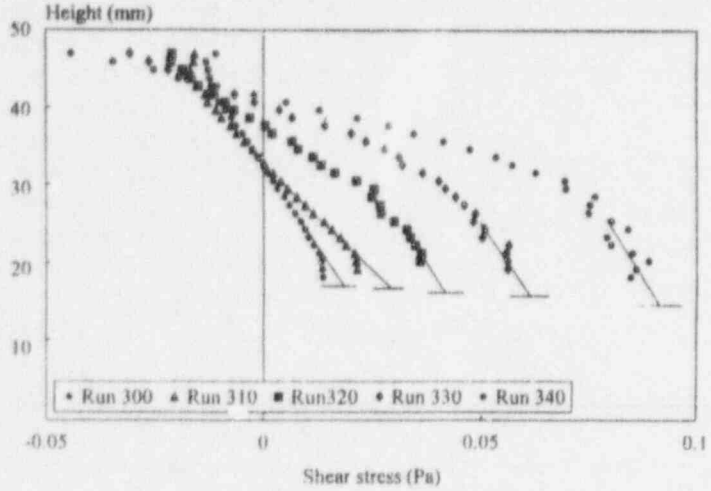

Fig. 2. Shear stress profiles for cocurrent flow.

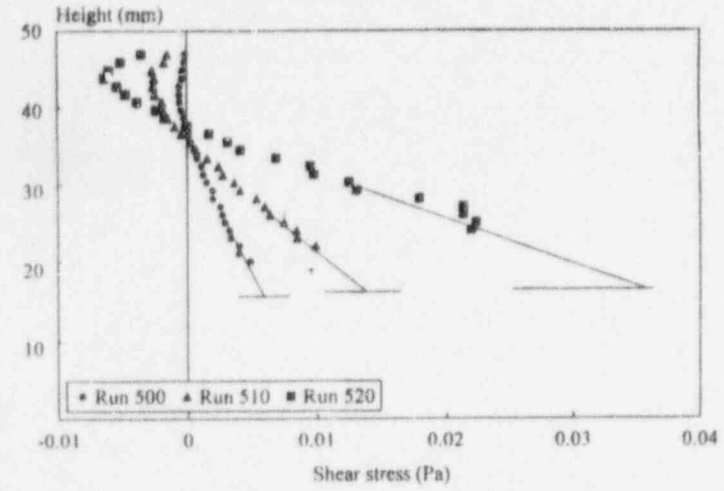

Fig. 3. Shear stress profiles for countercurrent flow.

interface can be generally considered as a solid wall for the gas flow. Therefore, the Law of the Wall was used to determine the interfacial friction velocity, u_{*iG}, and then $\tau_{iG} = \rho_G u_{*iG}^2$. This process was applied to Runs 300, 310 and 500, in which a symmetric velocity profile existed in the gas phase and the wave amplitude was small, $\Delta h < 0.5$ mm.

(3.2) Wavy gas-liquid interface. For a wavy gas-liquid interface in cocurrent flow, the measured mean velocity profile of the gas was fit to the universal velocity profile for flow over a rough surface,

$$u^+ = \frac{u - u_{iL}}{u_{*iG}} = \frac{1}{\kappa} \ln\left(\frac{y}{k_s}\right) + 8.5, \qquad (3)$$

where the interfacial friction velocity, u_{*iG}, and the equivalent sand roughness, k_s, are unknown. Here, the main assumptions are that the flow is in the completely rough regime ($k_s u_{*iG}/\nu > 70$) and fully developed. Under these conditions, the friction factor is given by,

$$C_f = [2 \log(R_H / k_s) + 1.74]^{-2} \qquad (4)$$

and the interfacial shear for cocurrent flow by,

$$\frac{\tau_{iG}}{\rho} = u_{*iG}^2 = \frac{1}{8} C_f (U_G - U_L)^2 \qquad (5)$$

For this case, an analytical solution is possible. Substitution of equation (4) into (5) yields

$$u_{*iG} = \frac{1}{\sqrt{8}} \frac{1}{[2 \log(R_H / k_s) + 1.74]} (U_G - U_L) \qquad (6)$$

If the mean velocities were measured at N points between the point of maximum velocity and the interface, Equation (3) can then be written as,

$$\frac{1}{u_{*iG}} \sum_{i=1}^{N} (u_i - u_{iL}) = \frac{1}{\kappa} \sum_{i=1}^{N} \ln\left(\frac{y_i}{k_s}\right) + N(8.5) \qquad (7)$$

to form a system of equations [(6) and (7)], which may be solved for the unknown, u_{*iG}, using a variety of methods. After some algebra, a simple elimination procedure yields,

$$k_s = \exp[(A + B - C - D)/E] \qquad (8)$$

where

$$A = 5.75 \sum_{i=1}^{N} \log y_i, \quad B = N(8.5), \quad C = \sqrt{8}\,(1.74) \sum_{i=1}^{N} (u_i - u_{iL}) / (U_G - U_L),$$

$$D = \frac{2}{1.74} \log R_H C, \quad E = N(5.75) - \frac{2}{1.74} C.$$

The corresponding value of u_{*iG} is obtained from Equation (6) or (7). By reversing the sign of the liquid velocity, this result may also be used for countercurrent flow as well.

The mean gas velocity profiles of cocurrent and countercurrent flows used in this method are shown in Figures 4 and 5, respectively. In Figure 4, the interfacial waves considerably modify the mean gas velocity profile for high gas flow rates, shifting the position of the maximum velocity closer to the upper wall. In countercurrent flow with lower gas flow rates shown in Fig. 5, the displacement of the plane of the maximum velocity is smaller.

The results obtained using this third method, τ_{iG3}, for both cocurrent and countercurrent flows are shown in Tables III and IV, respectively, and are later compared with the existing correlations.

(4) Evaluation of τ_{iG} by extrapolating the TKE profile. Another method to evaluate τ_{iG} requires the profile of the gas turbulence kinetic energy (TKE), k. This method is based on the experimental observation that in the inertial sublayer close to either the solid or fluid interface, the turbulence production is mainly balanced by the viscous dissipation (Hinze, 1975).

$$-\overline{uv} \frac{\partial U}{\partial y} = \varepsilon \qquad (9)$$

This has also been used in Computational Fluid Dynamics (CFD); in particular, in the "wall functions" for the k - ε

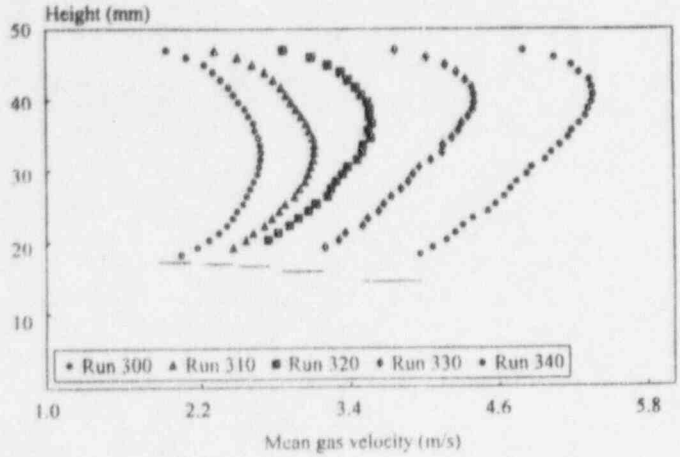

Fig. 4. Mean gas velocity profiles for cocurrent flow.

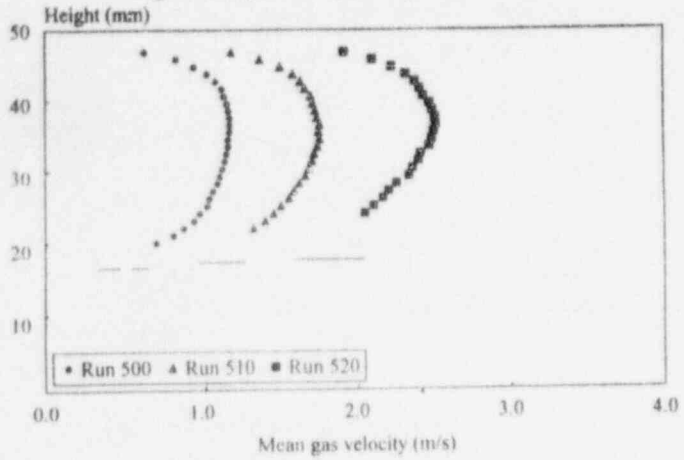

Fig. 5. Mean gas velocity profiles for countercurrent flow.

model. Here, the above assumption is also made for turbulence near a gas-liquid interface and the interfacial shear stress is estimated by using the equation of the turbulent viscosity from the k - ε model,

$$\nu_T = C_\mu \frac{k^2}{\varepsilon} \quad (10)$$

where $C_\mu = 0.09$ is a constant. In this model, the turbulent stress is given by,

$$\tau = -\rho \overline{uv} = \nu_T \overline{\left(\frac{\partial U}{\partial y}\right)} \quad (11)$$

Multiplying both sides of equation (9) by ν_T and simplifying yield,

$$\tau = \rho C_\mu^{1/2} k \quad (12)$$

Then, the extrapolation of the TKE profile to the gas-liquid interface provides an estimate of the interfacial shear stress. Needless to say, this method involves an assumption about the balance between turbulence production and dissipation rates, which may not be always correct near the gas-liquid interface as shown by Lam and Banerjee (1988). This method also demands a greater amount of experimental work to measure TKE. In the present work, only the streamwise (u) and vertical (v) velocity fluctuations were measured. So, to account for the contribution of the spanwise (w) velocity fluctuations, the vertical velocity fluctuations were assumed to be equal in amplitude to the spanwise velocity fluctuations. This, of course, is not valid for smooth interface cases where the vertical velocity fluctuations are damped by the interface as previously shown by Lorencez et al. (1993) and others. However, for many of the flow conditions examined in this work, the interface was wavy and the above assumption can result in overprediction of the total TKE since the vertical fluctuations increase more readily due to the vertical motion of the interfacial waves (Lorencez et al., 1993).

The profiles of TKE for cocurrent and countercurrent flows are shown in Figures 6 and 7, respectively. The results obtained using this fourth method, τ_{i04}, for both cocurrent and countercurrent flows are shown in Tables III and IV, respectively, and are later compared with the existing correlations.

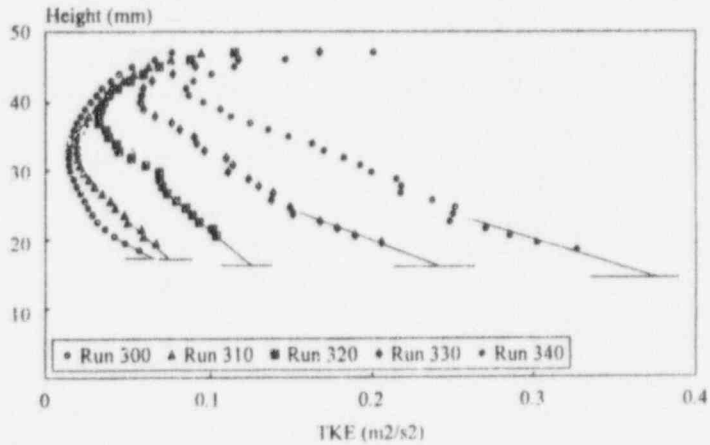

Fig. 6. Turbulence kinetic energy profiles for cocurrent flow.

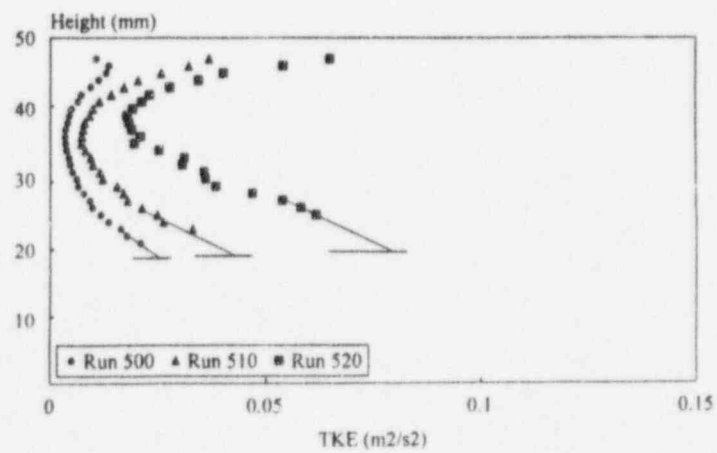

Fig. 7. Turbulence kinetic energy profiles for countercurrent flow.

DISCUSSION OF RESULTS

The interfacial shear stresses evaluated using four different methods are compared in Figures 8 and 9 for cocurrent and countercurrent flows, respectively. For cocurrent flow, all of the methods show good agreement at low gas flow rates (j_G < 2.2 m/s), where the amplitude of interfacial waves is still relatively small. At higher gas flow rates, the interfacial waves grow in amplitude and significant differences emerge among the values of interfacial shear stresses obtained by the four methods. In those runs, there are significant effects of the gas Reynolds number, wave amplitude, interfacial level gradient and secondary flow. Each of these factors can affect, in varying degrees, the interfacial shear stresses estimated using different methods.

The first method relying on the gas momentum balance yields the largest values, due possibly to the assumption of the smooth interface. The actual interfacial area for wavy flow should be considerably greater than that of the smooth interface, and this underprediction of the interfacial area can cause overprediction of the interfacial shear stress from the momentum balance equation.

Extrapolation methods (Reynolds stress and TKE profiles) yielded the lowest interfacial shear stress values, τ_{iG2} and τ_{iG4}, in this work. In both cases, the profiles are non-linear due to the presence of secondary flow and extrapolation to the interface involves a greater degree of uncertainty. Comparison of the two methods shows that the extrapolation of the TKE profile to the interface yields larger interfacial shear stress values than the extrapolation of the Reynolds stress profile. This could be due to the assumption of the spanwise velocity fluctuations to be of the same magnitude as the vertical fluctuations in the estimation of the TKE. As mentioned previously, the vertical velocity fluctuations are more likely to increase in amplitude than the spanwise velocity fluctuations in wavy flows, and the use of the vertical velocity fluctuations to estimate the spanwise fluctuations can lead to overestimation of the TKE, and thus the interfacial shear stress.

The third method involving fitting of the streamwise velocity profile to the universal velocity distribution yielded intermediate values of interfacial shear stress among the four methods examined, closer to the gas momentum equation results. This fitting procedure is simple and straight forward at low gas flow rates, however, it becomes more difficult as the interfacial wave amplitude increases with the gas flow rate and cause larger fluctuations in the local gas velocity near the interface.

Kowalski (1987) also compared the interfacial shear stress values obtained from the measurements in a

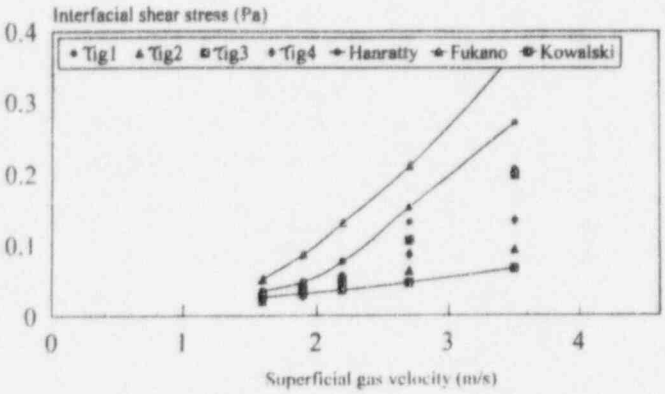

Fig. 8. Comparison of experimental results with correlations for cocurrent flow.

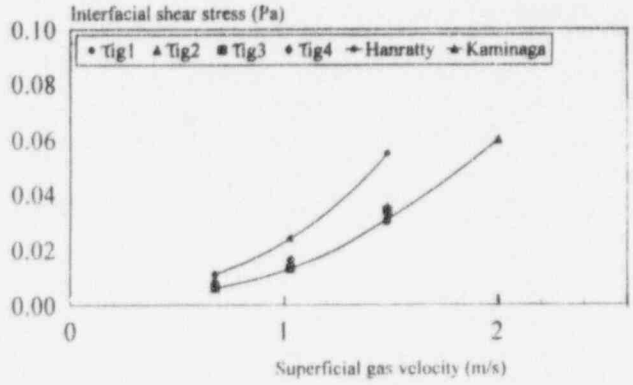

Fig. 9. Comparison of experimental results with correlations for countercurrent flow.

50.8 mm ID circular pipe using a gas momentum balance and extrapolation of the Reynolds stress profile. Although his momentum equation assumed zero interfacial level gradient since the flow was considered to be fully developed, and the experiments were conducted at substantially higher gas Reynolds numbers, he found that the momentum equation gave 13 to 20% greater values of interfacial shear stress than the Reynolds stress method, due to the underestimation of the interfacial area (Kowalski, 1987). The present results are consistent with his findings but the differences between the two methods are found to be even greater in this work. This could be because neglecting the interfacial level gradient can lead to significant underestimation of the interfacial shear stress in the gas momentum equation (Sadatomi et al., 1993).

For countercurrent flow, the results from the four methods were much closer to each other even for the highest gas flow rate tested where the interfacial wave amplitude was quite large. This relatively good agreement may be due to the limited gas flow rates used, since the maximum gas flow rate in countercurrent flow experiments was about the same as the lowest gas flow rate used in cocurrent flow. It is still somewhat surprising to see good agreement among the four results despite the

and Mass Transfer in Chemical, Process and Energy Engineering Systems, Vol. 2, Hemisphere (1979).

K. Hanjalic and B.E. Launder, "Fully developed asymmetric flow in a plane channel", J. Fluid Mech., 51, 301-335 (1972).

T. Hanratty and J. Engen, "Interaction between a turbulent air stream and a moving water surface", AIChE Journal, 3, No. 3, 299-304 (1957).

J.O. Hinze, Turbulence, 2nd. Edition, McGraw-Hill, Inc., (1975).

F. Kaminaga, K. Ogawa, Y. Okamoto, Y. Shibata and M. Osakabe, "Interfacial shear stress and flow characteristics of countercurrent stratified air-water flows in a horizontal channel", Proc. of ASME/JSME Thermal Engineering Conference, 2, 209-216 (1991).

S. Komori, R. Nagaosa and Y. Murakami, "Turbulence structure and mass transfer across a sheared air-water interface in wind-driven turbulence", J. Fluid Mech., 249, 161-183 (1993).

J.E. Kowalski, "Wall and interfacial shear stress in stratified flow in horizontal pipe", AIChE Journal, 33, No. 2, 274-281 (1987).

K. Lam and S. Banerjee, "Investigation of turbulent flow bounded by a wall and a free surface", in Fundamentals of Gas-Liquid Flows, ed. E. Michaelides and M. Sharma, ASME FED-Vol. 72, 29-38 (1988).

S.C. Lee and S.G. Bankoff, "Stability of steam-water countercurrent flow in an inclined channel: flooding", J. Heat Transfer, 105, 713-718 (1983).

R.W. Lockhart and R.C. Martinelli, "Proposed correlation of data for isothermal two-phase, two-component flow in pipes", Chem. Eng. Prog., 45, 39-48 (1949).

C. Lorencez, "Turbulent momentum transfer at a gas-liquid interface in horizontal stratified flow in a rectangular channel", Ph.D. thesis, Dept. of Chemical Engineering and Applied Chemistry, University of Toronto, Canada (1994).

C. Lorencez, M. Kawaji, Ojha, M., A. Ousaka and Y. Murao, "Application of a photochromic dye activation method to stratified flow with smooth and wavy gas/liquid interface", ANS Proc. 1993 National Heat Transfer Conference, ANS HTC-Vol. 7, 160-168 (1993).

C. Lorencez, T. Chang and M. Kawaji, "Investigation of turbulent momentum transfer at a gas-liquid interface in a horizontal counter-current stratified flow", in Turbulence modification in multiphase flows, ASME FED-Vol.110 97-102 (1991).

M. Rashidi, G. Hetsroni, and S. Banerjee, "Mechanisms of heat and mass transport at a gas-liquid interfaces", Int. J. Heat Mass Transfer, 34, No. 7, 1799-1810 (1991).

M. Sadatomi, M. Kawaji, C. Lorencez, and T. Chang, "Prediction of liquid level distribution in horizontal gas-liquid stratified flows with interfacial level gradient", Int. J. Multiphase Flow, 19, No. 6, 987-997 (1993).

Y. Taitel and A.E. Dukler, "A theoretical approach to the Lockhart-Martinelli correlation for stratified flow", Int. J. Multiphase Flow, 2, No. 5, 592-595 (1976).

large amplitude of interfacial waves and interfacial level gradient in the highest gas flow rate run. This means that the wave amplitude and level gradient do not contribute to the differences in the interfacial shear stress values obtained using different methods. Thus, the large differences seen in the shear stress values for cocurrent flow at high gas flow rates may be mainly due to the effect of the gas Reynolds number. A further investigation should be conducted at higher gas flow rates in countercurrent flow by slightly inclining the flow channel and preventing transition from wavy flow to slug flow.

Also shown in Figures 8 and 9 are the predictions of several existing correlations. For cocurrent flow (Fig. 8), Kowalski's correlation and Hanratty and Engen's method provided lower and upper bounds of the estimated values, respectively. The effects of the interfacial level gradient and the presence of a wavy interface and secondary flow become apparent from the comparison between the measured τ_{iG1} and predictions from Hanratty and Engen's method which assumes zero level gradient. Kowalski's predictions were close to the measured values of τ_{iG2}, but underpredicted all of the experimental results, due possibly to the difference in the channel geometry and ranges of flow rates tested. On the other hand, poor agreement with Fukano et al.'s (1985) correlation was found possibly due to the fact that their correlation was developed for gas flowing over thin liquid films at much higher velocities. Andritsos and Hanratty (1987) also proposed a new interfacial friction factor correlation based on the observation that the interfacial friction factor increases with the steepness of the waves (amplitude to wavelength ratio). However, their correlation postulated that the effect of the interfacial waves becomes significant at much higher superficial gas velocities (j_G > 5 m/s) than those tested in this work. Thus, a comparison of the present results with their correlation was not made.

For countercurrent flow, Hanratty and Engen's method overpredicted the interfacial shear stress data at high gas flow rates. In contrast, Kaminaga's predictions agreed very well with the measured values over the limited range of gas and liquid flow rates tested here.

CONCLUSIONS

Four different methods of evaluating the interfacial shear stress in wavy-stratified two-phase flows with smooth and wavy interfaces have been examined. There were systematic differences found in the estimated shear stress values due to certain assumptions or approximations involved in each method. The use of a gas momentum equation incorporating an interfacial level gradient term involves simple measurements and seems to give reasonable values, however, the assumption of a flat interface even in wavy flows can cause overestimation of the actual interfacial shear stresses. Methods that assume two-dimensional flow and no secondary motion require careful extrapolation of Reynolds stress or turbulent kinetic energy profiles, which are typically non-linear for flows in rectangular ducts and round pipes. Fitting the mean gas velocity profile to a universal velocity distribution is straight forward for smooth interfaces but can be difficult for wavy interfaces.

The existing correlations tend to show some agreement with a particular method of estimating the interfacial shear stress value from the measurements, due to the similar assumptions or procedures involved in the correlation development. Therefore, some care must be exercised when using a particular correlation in two-fluid models to predict the interfacial shear stress in stratified-wavy flows.

Acknowledgements - This work was financially supported by the Natural Sciences and Engineering Research Council of Canada and the Japan Atomic Energy Research Institute.

REFERENCES

N. Andritsos and T. Hanratty, "Influence of interfacial waves in stratified gas-liquid flows", AIChE Journal, 33, No. 3, 444-454 (1987).

L. Cohen and T. Hanratty, "Effects of waves at a gas-liquid interface on a turbulent air-flow", J. Fluid Mech., 31, part 3, 467-479 (1968).

J. Fabre, L. Masbernat and C. Suzanne, "New results on the structure of stratified gas-liquid flow", in Advances in Two-Phase Flow and Heat Transfer, Ed, S. Kakac and M. Ishii, Martinus Nijhoff, The Hague, Vol. 1, 135-150 (1984).

J. Fabre, L. Masbernat and C. Suzanne, "Stratified flow, Part 1: Local structure", Multiphase Science and Technology, 3, 285-301 (1987).

J. Fabre, L. Masbernat, R. Fernandez-Flores and C. Suzanne, "Stratified flow, Part II: Interfacial and wall shear stress", Multiphase Science and Technology, 3, 302-315 (1987).

T. Fukano, A. Itoh, H. Odawara, T. Kuriwaki and Y. Takamatsu, "Liquid films flowing concurrently with air in horizontal duct (5th Report, Interfacial shear stress)", Bulletin of JSME, 28, No. 244, 2294-2301 (1985).

L. Gayral, L. Masbernat and C. Suzanne, C., "Mean velocities and Reynolds stresses in cocurrent gas-liquid stratified channel flow", in Two-Phase Momentum, Heat

Quenching Phenomena in Natural Circulation Loop

Hisashi UMEKAWA[a], Mamoru OZAWA[a], and Naoki ISHIDA[b]

[a]Department of M hanical Engineering, Kansai University,
Yamatecho 3-3-3:, Suita, Osaka 564, JAPAN

[b]Daihatsu Motor Co.
Daihatsucho 1-1, Ikeda, Osaka 563, JAPAN

Quenching phenomena has been investigated experimentally using a natural circulation loop of liquid nitrogen. During the quenching under natural circulation, the heat transfer mode changes from film boiling to nucleate boiling, and at the same time mass flux changes with time depending on the vapor generation rate and related two-phase flow characteristics. Moreover, density wave oscillations occur under a certain operating condition, which is closely related to the dynamic behavior of the cooling curve. The experimental results indicates that the occurrence of the density wave oscillation induces the deterioration of effective cooling of the heat surface in the film and the transition boiling regions, which results in the decrease in the quenching velocity.

1. Introduction

Quenching is a very important phenomenon in numerous industrial equipments, such as metallurgy and cryogenics. Most serious example is found in the emergency core cooling system (ECCS) after postulated loss of coolant accidents (LOCAs), and many investigations in this field have been conducted in the past three decades (FLECHT[1,2], Nelson[3], JSME[4], Barnea[5], Ferng[6]).

In the quenching phenomena of a hot channel, the heat transfer mechanism changes from film boiling, transition boiling and to nucleate boiling. In relation to the film boiling in channels and/or subchannels of rod-bundles, inverted annular flow problems have been widely investigated mainly under steady state conditions (e.g. Ishii[7], Takenaka[8] and Fujii[9]). They classified flow patterns of the forced flow boiling and discussed the relationship between the flow pattern and the heat transfer characteristics.

The recent development of passive safety reactors have given rise to a great interest on the concept of the gravity reflooding (Dallman[10], McCandless[11]). During the gravity reflooding, the inlet mass flux is not constant against the time and depends on the driving force between the water accumulation vessel and the hot channel. During this transients, the flow oscillation was observed by Martini[12]. Erbacher[13] compared the quenching time by the gravity injection with that by the forced injection in the rodbundle system, and indicated that the former time is about three times longer than the latter. In addition, the experimental results by Erbacher clearly showed the existence of the flow oscillation during the gravity reflooding process. This fact suggests that the deterioration of heat transfer is closely related to the flow oscillation. Kawaji[14] and Oh[15] investigated the reflooding phenomena under the condition of forced flow oscillations. They reported valuable data and information about the heat transfer characteristics, but the transient behavior of the heat and flow characteristics under the gravity reflooding have not been fully understood, especially on the effect of the flow oscillation on the heat transfer deterioration, so far.

Thus in this present investigation, the experiment was conducted on the quenching phenomena in a natural circulation loop of liquid nitrogen (LN_2), and the effect of the occurrence of the density wave oscillation on the quenching phenomena was investigated in a simplified boiling channel system. Although the use of LN_2 as a working fluid has a merit for a small-scale laboratory experiments, the present results gives only the qualitative information on the quenching phenomena with reference to the nuclear reactor safety. In the field of cryogenics, however, the present paper may give not only qualitative but also quantitative information on the thermo-hydraulics during the quenching.

2. Experiment

Experimental apparatus and the detail of the test section are shown in Fig.1. The experimental apparatus is mainly composed of a head column, a test section, a subcooler and a liquid nitrogen (LN_2) tank. Most parts of these apparatus were thermally insulated from the ambient air. The head column was thermally insulated by using the vacuum insulation, and was filled with LN_2 supplied continuously from the LN_2 tank. The liquid level in the head column was monitored by measuring the pressure difference across the head column and was constant throughout the experiment. The inlet section were submerged in the subcooler. The subcooler was filled with LN_2 under the atmospheric pressure, so that LN_2 in the loop had the inlet subcooling given by the difference between the saturation temperatures of LN_2 in the test section and that in the subcooler. LN_2 from the head column flowed

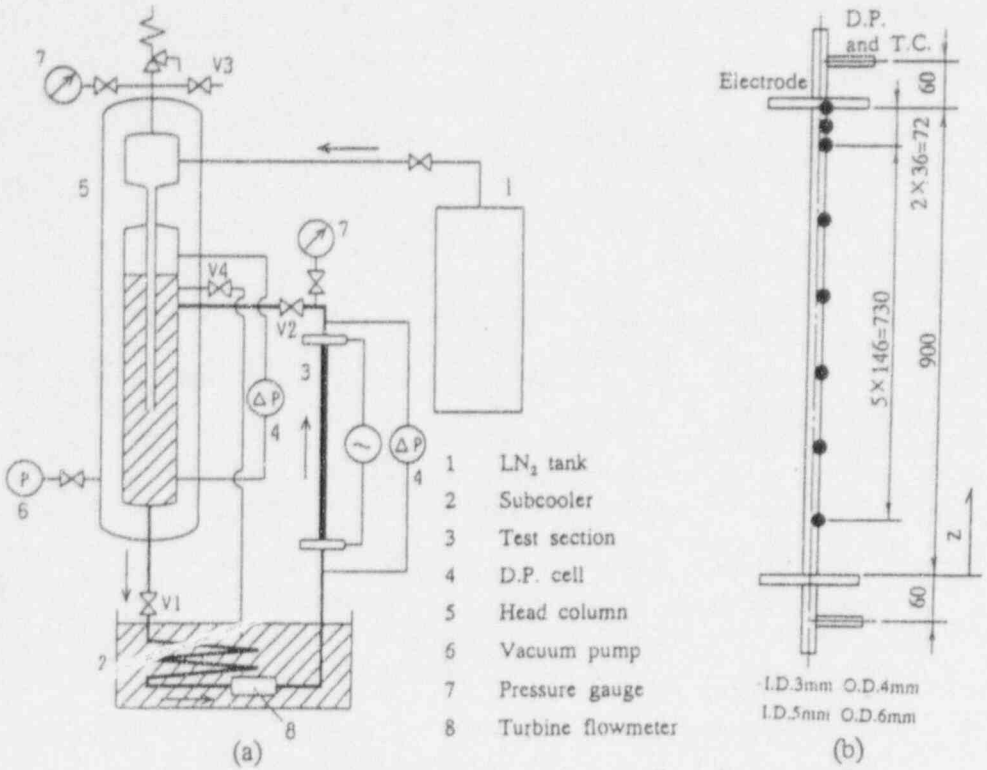

Fig.1 Experimental apparatus and detail of the test section.

through the inlet section and entered into the test section. Two-phase mixture of LN_2 formed in the test section returned to the head column, and the nitrogen gas separated from the liquid and the surplus LN_2 overflowed into the subcooler through the relief valve V4.

Experiment was conducted by using two different test sections. These test sections were SUS304 tubes with the heated length of 900mm and with the diameters 3.0mm I.D., 4.0mm O.D. and 5.0mm I.D., 6.0mm O.D. as shown in Fig.1(b). The test sections were heated by Joule heating of A.C. power.

The experimental procedures were as follows: Prior to the quenching experiment, the experimental apparatus was operated in the natural circulation mode under a predetermined constant heat flux and system pressure. The restriction of the inlet valve V1 was set to the predetermined values, but the exit valve of the test section, V2, was fully opened. Then the circulation characteristics were obtained in the relationship between the mass flux and the heat flux.

In the quenching experiment, firstly the exit valve of the test section, V2, was closed. Then, LN_2 in the test section was evaporated totally by heating, and the test section was filled with N_2 gas. The temperature of the test section started to increase. As soon as the outer wall temperature of the test section exceeded beyond the predetermined value, 100deg.C, the exit valve, V2, was opened quickly. Then LN_2 rushed into the test section from the head column trough the inlet section, and the quenching phenomena was observed. During the transients, the voltage of the input power imposed on the test section was kept constant. Therefore, the heating power increased with the time even for the constant voltage, as shown in Fig.2, because the electrical resistance of the tube material was affected by the tube temperature (In Fig.2 the horizontal axis represents the duration time from the beginning of the quenching experiment). The distribution of the heat flux was, of course, not uniform along the test section owing to the same reason. Thus in this investigation, the representative value of the heating power was defined as the measured value under the natural circulation mode after the transients, and the heat flux was calculated with assuming the uniform heat flux distribution along the test section.

The experimental apparatus was thermally insulated, as mentioned before, but the heat conduction through the

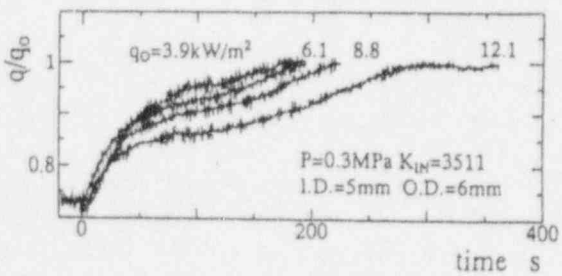

Fig.2 Power reduction rate during quenching experiment.

insulation material was still exist. The additional heat input was estimated from -0.4kW/m^2 to 1.2kW/m^2 during the quenching experiment (The positive heat flux means the heat input from the ambient air, and the negative one means the leak of the heat). Thus the total heat input to the fluid should be estimated by taking into account these additional ones as well as the heat flux from the wall heat capacity. However, this is not easy at the present state, so the heat flux value shown in this paper is the representative value mentioned above.

The typical examples of the distribution of the initial outer wall temperature are shown in Fig.3. The maximum difference between the inside and outside of the test section was estimated approximately at 0.5K. As shown in Fig.3, the initial temperature distributions are not uniform, especially the temperature at the inlet and the exit of the test section are lower than the other. It was mainly due to the heat release by conduction through the electrodes. The difference in the initial temperature distribution among experimental conditions were mainly owing to the human error. In this experimental procedures, such uncertainty of the initial conditions was hardly avoided, but was limited approximately within the range of ±10K by repeating experiments several times in the same run, which confirmed the generality of the discussions in this paper.

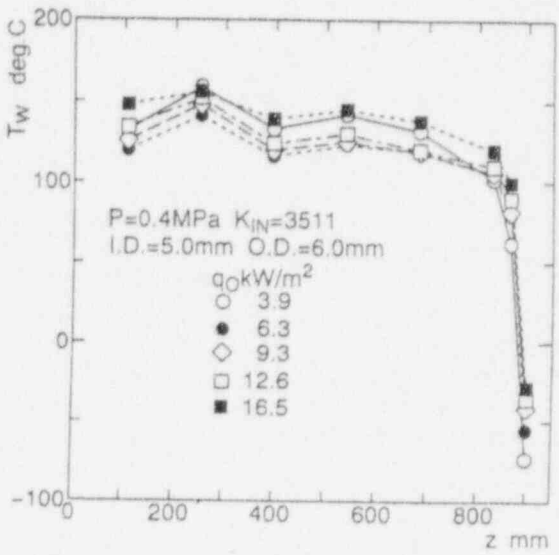

Fig.3 Initial temperature distribution.

The circulation flow rate was measured by using the turbine flowmeter, the pressure drop across the test section was measured by using the D.P. cell. The outer wall temperatures were measured by using bare type C-C thermocouples of the dimension of 0.1 mm in diameter welded directly to the tube wall. The location of these thermocouples are shown by solid dots in Fig.1(b). The inlet and the exit bulk temperatures of the fluid were measured by using sheathed C-C thermocouples with the dimensions of 0.5 mm in the sheath diameter installed into the test section. The system pressure was measured by using the Bourdone tube, and was controlled by throttling of the relief valve, V4. All data except the system pressure were monitored and recorded by pen-recorders and digital-data-recorder, respectively. Instrumentation accuracies are listed in Table.1.

Experimental range was as follows: The system pressures were 0.3 and 0.4MPa, the initial heat flux were in the range from 3.6 to 16.7kW/m^2. The inlet restriction, K_{IN}, including the valve V1 and the piping were in the range from 377 to 3511, where K_{IN} is defined by ;

$$\Delta P = K_{IN}\frac{G^2}{2\rho_L} \qquad (1)$$

3. Results and discussion

3.1 Natural circulation characteristics

Prior to the discussion on the quenching phenomena, the flow characteristics of this experimental loop under natural circulation mode are discussed. Experimental results of the natural circulation velocity are plotted against the heat flux in Fig.4. In this figure, the solid dot represents the time averaged velocity, and the triangles represent the minimum and the maximum values of the flow fluctuation. The negative value of the flow velocity

Table 1 Instrumentation accuracies.

Parameter	Instrument	Accuracy
Heating power	Wattmeter	±5W
Flow rate	Turbine flowmeter	±3cc/min
Temperature	C-C thermocouples	±0.5K

represents the flow reversal. The total heat flux q_T includes the heat input from the heating power and the heat input from the ambient air. The dryout heat flux condition is represented by the vertical solid line.

The circulation velocity increases with the increase in the heat flux under low heat flux condition. These tendency is due to the fact that the increase in the heat flux causes the increase in the void fraction which induces the increase in the driving force of the natural circulation loop. Further increase in the heat flux induces the increase in the frictional pressure drop which causes the decrease in the circulation velocity. In reality, this effect was relatively small in the present case, so that the circulation velocities was almost constant under relatively high heat flux condition. The increase in the inlet restriction results, of course, in the decrease in the circulation velocity.

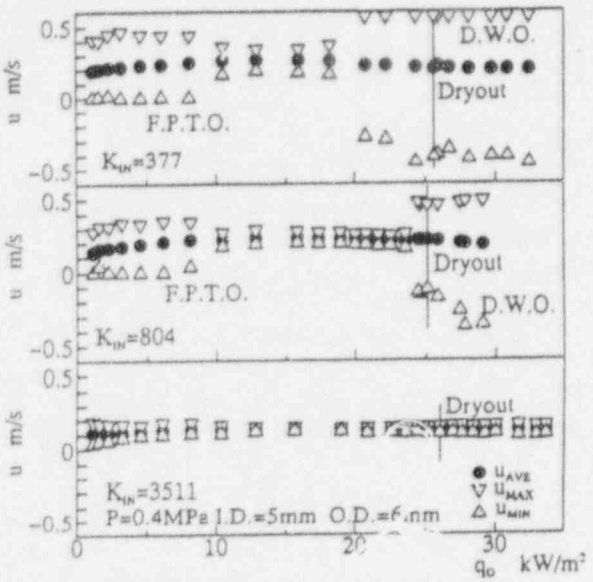

Fig.4 Natural circulation characteristics.

In this experiment, the density wave oscillation (D.W.O.) occurred under high heat flux condition, and the flow pattern transition oscillation (F.P.T.O) occurred under the low heat flux condition. The D.W.O showed the regular and large amplitude limit cycle oscillation as in the observation by Ozawa[16]. The numerical simulation based on the lumped-parameter model could well predicted the D.W.O. threshold (Ozawa[17]). The inlet restriction and the system pressure were stabilizing factors for both types of oscillation. These experiments conducted after sufficient pre-cooling of the system, and therefore, the flow oscillations observed in the transients of the quenching phenomena were slightly different in nature and also in the threshold condition from these results. The detailed discussion on the density wave oscillation will be reported in the separate paper.

3.2 Quenching phenomena

In this section, experimental results of the quenching phenomena are described mainly based on the data at 0.4MPa in 5.0mm I.D. tube. These data includes the stable and unstable flow conditions after the quenching, which makes the discussion understandable. In the case of 0.3MPa of I.D.5.0 mm tube, the oscillation region extended in the period of the transients, but the general characteristics were only slightly different from the results presented in this section. This was also true in the case of 3.0mm I.D. tube, while the flow oscillation was observed under almost all experimental condition.

Figure 5 shows the typical examples of the experimental recording traces; the wall and the fluid temperatures, the differential pressure across the test section and the circulation velocity. In Fig.5(a), the transient oscillation occurs immediately after the opening of the exit valve, V2, then the oscillation ceased after a while, and then the density wave oscillation appears. The oscillation period of the former oscillation is shorter than that of the latter density wave oscillation. The flow reversal condition cannot be detected, in general, only by using the turbine flowmeter signals. Judging based on the comparison with the trace of the pressure difference across the test tube, the small turns of the trace just above the 0-level of the velocity coordinate are considered to be the flow reversal. Thus, the density wave oscillation in the present case developed in the amplitude so as to include the flow reversal, but the transient oscillation at the initial stage does not. Owing to the relatively small amplitude and the short period of the flow oscillation, this transient oscillation seems to have less significant effect on the temperature history compared with the D.W.O. This phenomenon of the initial stage of the transients is referred to as the steam binding (White[18]). In this Fig.5(a), the stable flow region was observed between the transient oscillation and the D.W.O. In the case of the larger heat flux condition, this stable flow region disappeared, and the initial steam binding passed continuously into the stage of the D.W.O.

The wall temperature T_2 at z=864mm decreases rapidly immediately after the opening of the exit valve, and then have a plateau with the appearance of the D.W.O. This plateau of constant temperature condition continues almost 60s, and then quenching takes place. Even after the quenching, the oscillation continues, and thus the wall temperature fluctuates periodically. This fluctuation may be caused by the periodical dryout induced by the flow oscillation (Ozawa[19]). The wall temperature T_1 at the exit, z=900mm, of the test section, which is lower than the temperature T_2 at z=864mm at the initial state as mentioned before, does increase immediately after the start of the transients. After a short period, the temperature trace has the turn-around and then decreases gradually. Temperature traces upstream the position z=864mm showed the similar tendency to that at z=864mm. The

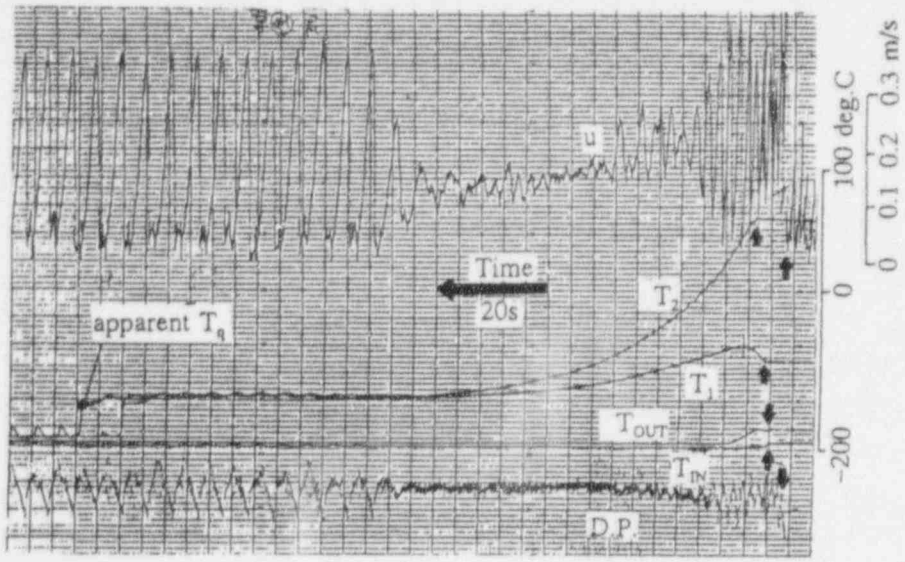

(a) K_{IN}=377 q_O=3.5kW/m^2 I.D.=5mm P=0.4MPa

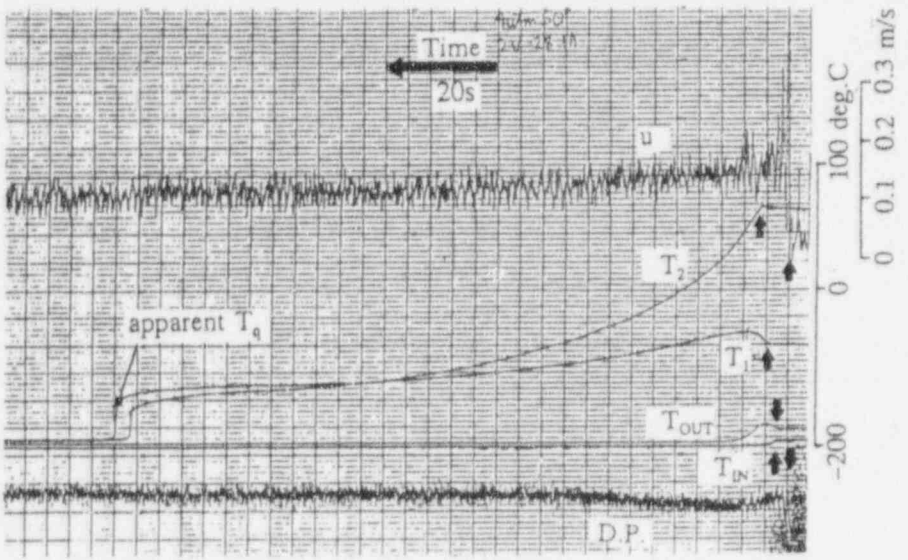

(b) K_{IN}=3511 q_O=3.9kW/m^2 I.D.=5mm P=0.4MPa

Fig.5 Typical recording traces during the quenching. u represents the circulation velocity measured by using the turbine flowmeter, T_1 and T_2 the wall temperatures at the distances of 900mm and 864mm from the tube inlet, respectively, T_{IN} and T_{OUT} the fluid temperatures at the inlet and the exit of the test tube, respectively, D.P. the differential pressure across the test section measured by using the D.P. cell, the solid dots examples of the apparent quenching temperature and arrows represent the beginning of the quenching experiment.

quenching propagated from the inlet to the exit with time. The inlet fluid temperature T_{IN} decreases immediately after the exit valve has been opened, and retains almost constant value throughout the transients. The exit fluid temperature T_{OUT} increases for a short period during the superheated vapor passing through, and then retains the constant value which depends on the saturation temperature.

Recording traces in the case of higher restriction, K_{IN}, is shown in Fig.5(b). The transient oscillation, i.e. the steam binding, is observed at the initial stage of transients but the density wave oscillation does not occur. The small fluctuation in the trace u is owing to the two-phase flow characteristics. Thus the recording traces of the

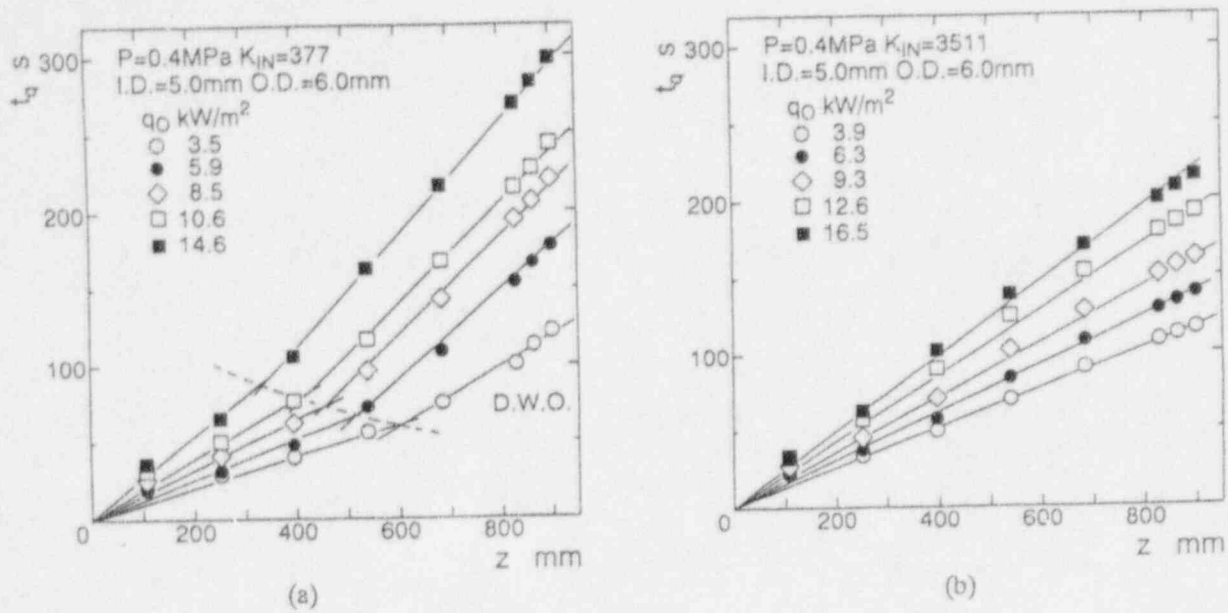

Fig.6 Quenching time.

wall temperatures show the smooth curves during the quenching phenomena.

Figure 6 shows the quenching time against the location of the measuring point. In Fig.6(a), the initiation times of the D.W.O. for the respective heat flux are shown by the broken line, and beyond this curve the D.W.O. is observed. On the other hand, the D.W.O. is not observed throughout the transients in the case of Fig.6(b).

The quenching velocities given by the gradient of these lines are almost constant along the test section in Fig.6(b), while in the case of Fig.6(a) the velocity is not constant but has two different values. In Fig.6(a), the quenching time-location diagrams are divided into two regions, and the boundaries between two regions almost coincide with the threshold of the density wave oscillation. The quenching velocities obtained from two successive thermocouples are plotted in Fig.7. The solid dots correspond to the quenching velocities during the D.W.O. The tendency mentioned in Fig.6 are clearly observed. There exist large variation along the test section, especially when the heat flux q_O is relatively low. The lower quenching velocity corresponds to the data obtained near the testsection exit. The quenching velocity decreases with increase in the heat flux until a certain level, and the scattering of data becomes small with the heat flux. The quenching velocities for the small restriction K_{IN}=377 are slightly faster than those for the large restriction K_{IN}=3511 under the stable flow condition. On the other hand, the quenching velocity of K_{IN}=377 under the D.W.O. are evidently lower than those of K_{IN}=3511. The former tendency is owing to the difference in the circulation flow rate which increases with the decrease in the inlet restriction as mentioned before, and the latter tendency depends on the flow oscillation.

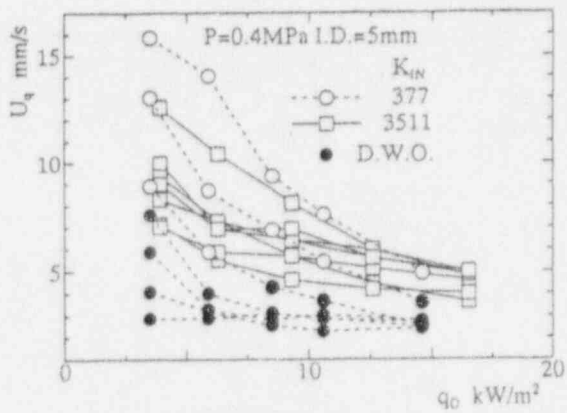

Fig.7 Quenching velocity.

The quenching temperature are plotted against the location of thermocouples in Fig.8. In this paper, the quenching temperature was defined as the apparent quenching temperature as is indicated by solid dot in Fig.5. In Fig.8(a), the threshold of D.W.O. is also drawn by the broken line based on the quenching time-location diagram shown in Fig.6. The quenching temperature are independent on the flow oscillation. The quenching temperature increases with the increase in the heat flux q_o, and is approximately uniform along the test section. The Leidenfrost temperature is estimated to be almost the same value of the foam limit (Baumeister[20]), and this foam limit temperature of LN_2 (Spiegler[21]) are also drawn by the dot-dash-line in Fig.8. The quenching temperature are higher than this foam limit temperature, and this may be owing to the flow agitation. The empirical correlation of Kim[22] are also drawn by the dashed line. This correlation was obtained on the basis of the data of atmospheric water experiment conducted under the forced flow condition. The decreasing tendency

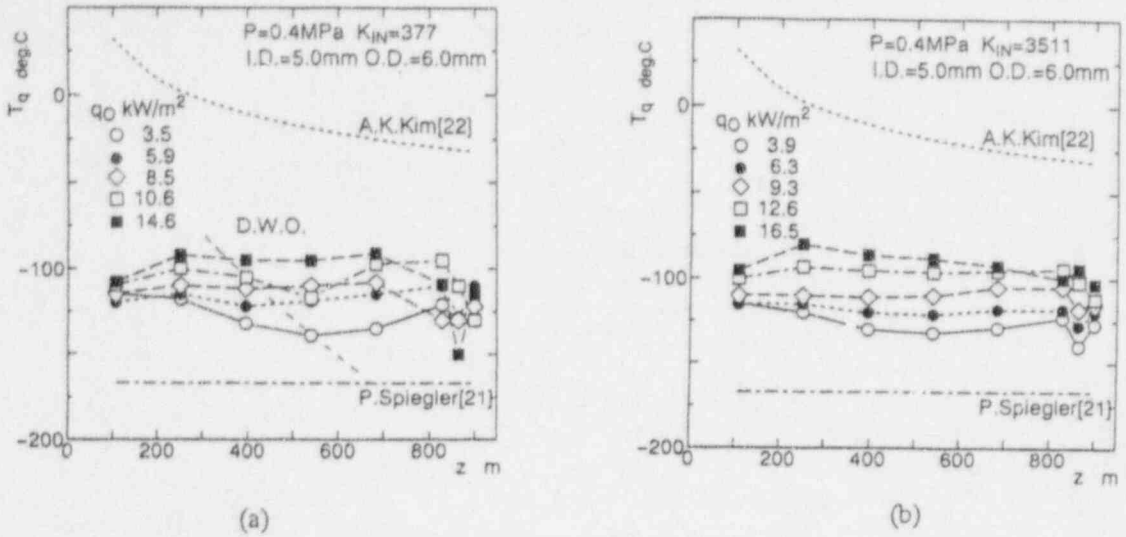

(a) (b)

Fig.8 Quenching temperature.

similar to the Kim's correlation was not observed in the present data.

For the more detailed discussion on the effect of the D.W.O. on the quenching phenomena, the wall temperature at z=864 mm and the inlet circulation velocity were recorded by using the digital-data-recorder with the sampling frequency 20 Hz.

Figure 9 shows wall temperature traces under the condition when the D.W.O. is observed and those under the stable flow conditions throughout the transients. The respective circulation-velocity traces are shown in Fig.10. The experimental apparatus used in these runs was almost the same one mentioned above except the inlet section, i.e. some minor changes were conducted about the inlet piping. Comparing the data sets with two-different inlet restrictions, the differences in the time-averaged behavior of circulation velocities are rather small. Until the flow oscillation developed into large-amplitude limit cycle oscillation, i.e. approximately until t=100s, the reduction speed of the wall temperature is almost the same in both cases of different restrictions. Beyond this time, the temperature histories show large difference depending on the inlet restriction, i.e. the wall temperature for the large inlet restriction

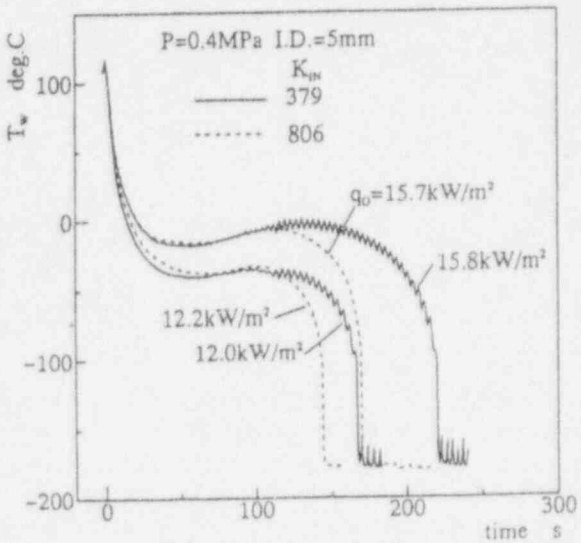

Fig.9 Recording trace of wall temperature.

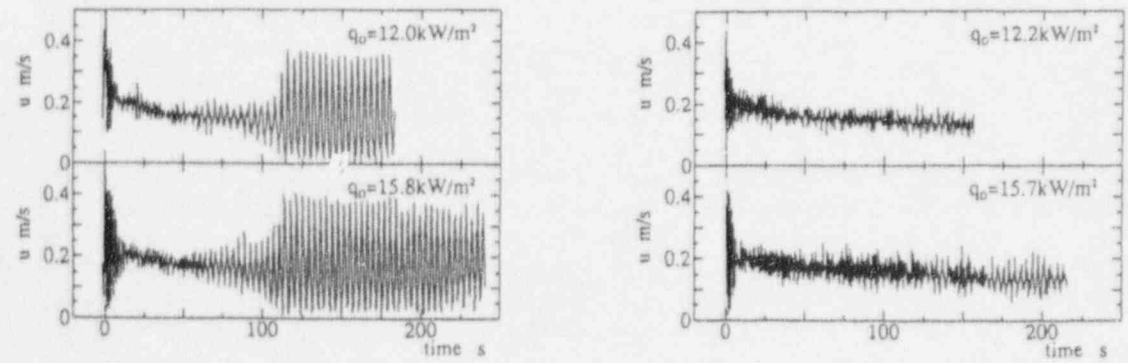

(a) K_{IN}=379 (b) K_{IN}=806

Fig.10 Recording trace of circulation velocity.

indicats quenching faster than those of the small inlet restriction.

In general, the large inlet restriction induces the decrease in the circulation rate of the cooling liquid, and small inlet restriction keeps the circulation rate at higher level. On the other hand, the heat transfer deterioration is induced by the flow oscillation, i.e. D.W.O. in the present case, which is caused by the insufficient inlet restriction of the loop. Depending on these two characteristics, the quenching time is determined. Thus, it is suggested that the optimum inlet restriction for gravity reflooding may exist.

Based on the data shown in Fig.9, the boiling curve, i.e. the relationship between the heat flux versus the wall superheat, are obtained as follows. The heat flux q was calculated by using the one-dimensional heat conduction equation along the tube axis as follows (Ueda[23]),

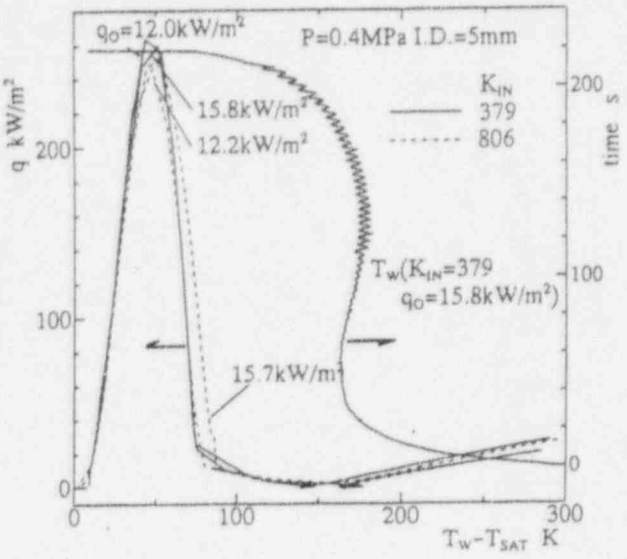

Fig.11 Boiling curve during transients.

$$\rho_W C_{PW} \delta \frac{\partial T}{\partial t} = k_W \delta \frac{\partial^2 T}{\partial z^2} - q + q_G \delta \quad . \tag{2}$$

Assuming that the temperature profile shifts by the quenching velocity, the next relationship is obtained,

$$\frac{\partial^2 T}{\partial z^2} = \frac{1}{U_q^2} \frac{\partial^2 T}{\partial t^2} \quad . \tag{3}$$

Substitution of Eq.(3) into Eq.(2) gives the heat flux under transient condition,

$$q = \delta \left[-\rho_W C_{PW} \frac{\partial T}{\partial t} + \frac{k_W}{U_q^2} \frac{\partial^2 T}{\partial t^2} + q_G \right] \quad . \tag{4}$$

It is necessary for the heat flux estimation to give the quenching velocity into Eq.(4). As the calculated results of q have relatively weak dependence on the quenching velocity in the present experimental range, the time-averaged value of the quenching velocity was used for calculation. The heat generation rate q_G was obtained from the recording data similar to that in Fig.2. Thus, the value q_G was not constant against the time, but was assumed to be uniform along the test section. The first and second order time derivatives of the wall temperature in Eq.(4) were obtained on the basis of 4th-order polynomial approximations fitted to the temperature trace. It is rather difficult to define the accuracy of these calculation owing to the above-mentioned assumptions, and therefore the detail discussion on the value of the heat flux may be meaningless. These calculation gives only qualitative tendency during the quenching. The obtained heat flux is rather low, at most 20kW/m², before the wall superheat beyond $T_W - T_{SAT}$=100 K in the film boiling region, and becomes extremely high, typically 250kW/m², after the quenching. The abrupt increase in the heat flux at about $T_W - T_{SAT}$=50 to 80K corresponds to the transition boiling. In the region corresponding to the plateau of the temperature trace, the heat flux variation is rather small compared with the other regions. Oh[15] suggested that the flow oscillation enhanced the heat transfer under subcooled condition and deteriorate the heat transfer under saturated condition. Thus the present results of the heat transfer deterioration verified the applicability of the Oh's latter case even in the gravity injection experiments.

Comparing the boiling curve for two different inlet restrictions, however, the q vs. $T_W - T_{SAT}$ relationships are almost the same in the film boiling region including the region corresponding to the above-mentioned plateau. This fact suggests that the heat transfer deterioration under the flow oscillation is not induced by the static relationship but by the transient effect of heat transfer. In the previous paper, the authors presented that the dryout heat flux reduces significantly by the flow oscillation (Ozawa[19] and Umekawa[24]). This is not the present case but the mechanism of the transient heat transfer may be similar. Thus, the dynamic interaction between the wall heat capacity and the two-phase flow dynamics, i.e. the dynamic behavior of the inverted annular flow including the agitation and/or droplet region, plays an important role in the heat transfer during the density wave oscillatory.

4. Conclusion

The experimental investigation was conducted on the quenching phenomena in the natural circulation loop of LN_2. The experimental results indicated that the occurrence of the density wave oscillation resulted in the decrease in the quenching velocity. This is closely related to the dynamic interaction between wall heat capacity and the two-phase flow dynamics. In order to deduce the general feature of this phenomena, the theoretical investigation on the dynamic behavior of thermodynamics and the experiment using the test section with the large heat capacity have to be conducted.

Acknowledgments-This work was partly supported by the Grant-in-Aid of the Ministry of Education, Science and Culture of Japan No.05750203(1993) and the Kansai University Research Grant. The authors wish to express their sincere thanks to Messrs. M.Ohyama, I.Kinoshita, Y.Shiba and T.Mitunaga. and Nippon Sanso Co. Ltd. for their support in carrying out the experiments.

Nomenclature

C_P	specific heat,
G	mass flux,
K_{IN}	resistance coefficient defined by Eq.(1),
k	thermal conductivity,
P	pressure,
q	heat flux,
q_G	volumetric heat generation rate,
T_W	wall temperature,
T_{IN}	fluid temperature at the tube inlet,
T_{OUT}	fluid temperature at the tube exit,
t	time,
U_q	quenching velocity,
u	flow velocity,
z	axial position along tube.

Greek symbols

δ	tube wall thickness,
ρ	density.

Subscripts

AVE	time-average value,
L	liquid phase,
MAX	maximum value,
MIN	minimum value,
O	representative value,
q	quenching state,
SAT	saturation state,
W	tube wall.

Reference

[1]J.D.Duncan and J.E.Leonard, "Emergency Cooling in Boiling Water Reactors under Simulated Loss-of-Coolant Conditions (BWR-FLECHT FINAL REPORT)", GEAP-13197(1971).
[2]L.E.Hochreiter, "FLECHT SEASET Program (FINAL REPORT)", EPRI NP-4112(1986).
[3]R.A.Nelson and K.O.Pasamechmetoglu, "Quenching Phenomena", Post-Dryout Heat Transfer, G.F.Hewitt, J.M.Delhaye and N.Zuber(eds.), CRC Press, Boca Raton, Florida(1992), 39-184.
[4]JSME, Film Boiling and Cooling, Nihonkougyou, Tokyo(1989), 283-309.
[5]Y.Barnea, E.Elias and I.Shai, "Flow and Heat Transfer Regime During Quenching of Hot Surfaces", Int. J. Heat Mass Transfer. 37-10, 1441-1453(1994).
[6]Y.M.Ferng, C.C.Chieng and Chin Pan, "Two Phase Flow and Heat Transfer Characteristics of Rewetting Process", Proc. 9th Int. Heat Transfer Conf., 3, 437-442(1990).
[7]M.Ishii and G.De Jarlais, "Flow Regime Transition and Interfacial Characteristics of Inverted Annula Flow", Proc. The Japan-U.S. Seminar on Two-Phase Flow Dynamics, B•7•1-B•7•9(1984).
[8]N.Takenaka, K.Akagawa, T.Fujii, K.Nishida, "Experimental Study on Flow Pattern and Heat Transfer of Inverted Annular Flow", Nucl. Engng Des. 120, 293(1990).
[9]T.Fujii, N.Takenaka, H.Asano and T.Yasuda, "Heat Transfer and Pressure Drop of Inverted Annular Flow", Proc. Int. Sympo. Heat Mass Transfer, Kyoto, 171-176(1994).
[10]R.J.Dallman and R.B.Duffey, "Heat Transfer Phenomena Relevant to Severe Accidents", Proc. 9th Int. Heat Transfer Conf., 1, 341-354(1990).
[11]R.J.McCandless and J.R.Redding, "Simplicity: The Key to Improved Safety, Performance and Economics", Nucl. Engng Int. 34-424, 20-24(1989).
[12]R.Martini and A.Premoli, "Bottom Flooding Experiments with Simple Geometries under Different E.C.C. Conditions", Energia Nucleare, 20-10, 540-553(1973).
[13]F.J.Erbacher and K.Wiehr, "Reflood Heat Transfer in Tight Lattice PWR Fuel Rod Bundles in a LOCA", Proc. 2nd Int. Sympo. Heat Transfer, 1-6(1988).
[14]M.Kawaji, Y.S.Ng, S.Banerjec and G.Yadigaroglu, "Reflooding with Steady and Oscillatory Injection", Trans. ASME J.Heat Transfer, 107, 670-678(1985).

[15]S.Oh, S.Banerjee and G.Yadigaroglu, "Reflooding with Steady and Oscillatory Coolant Injection", Trans. ASME J.Heat Transfer, 108, 448-456(1986).
[16]M.Ozawa, "Flow Instability in a Boiling Channel System", Doctor Thesis, Osaka University(1977).
[17]M.Ozawa, Y.Asao and N.Takenaka, "Density Wave Oscillation in a Natural Circulation Loop of Liquid Nitrogen", Instabilities in Multiphase Flow, G.Gouesbet and A.Berlemont(eds.), Plenum Press, New York(1993), 113-124.
[18]E.P.White and R.B.Duffey, "A Study of the Unsteady Flow and Heat Transfer in the Reflooding of Water Reactor Cores", Annals Nuclear Energy, 3, 197-210(1975).
[19]M.Ozawa and H.Umekawa, "Experimental Investigation on Dryout under Oscillatory Flow Condition in Vertical and Horizontal Tubes", Proc. the Germany-Japanese Symp. on Multiphase Flow, KfK5389(1994).
[20]K.J.Baumeister and F.F.Simon, "Leidenfrost Temperature - Its Correlation for Liquid Metals, Cryogens, Hydrocarbons and Water", Trans. ASME J. Heat Transfer, C-95, 166-173(1973).
[21]P.Spiegler, J.Hopenfeld, M.Silberberg, C.F.Bumpus Jr. and A.Norman, "Onset of Stable Film Boiling and the Foam Limit", Int. J. Heat Mass Transfer. 6, 987-994(1963).
[22]A.K.Kim and Y.Lee, "A Correlation of Rewetting Temperature", Letters in Heat Mass Transfer 6, 117-123(1979).
[23]T.Ueda, Two-phase flow, Youkendo, Tokyo(1989), 322-337.
[24]H.Umekawa, M.Ozawa and A.Miyazaki, "CHF in a Boiling Channel under Oscillatory Flow Condition", 2nd Int. Conf. Multiphase Flow '95, 3, CF•7-CF•14(1995), to be appeared in Advances in Multiphase Flow 1995, Elsevier, Amsterdam(1995).

Measurement of the interaction between the flow and the free surface of a liquid

Koji OKAMOTO*, William D. SCHMIDL, Olivier G. PHILIP
and Yassin A. HASSAN

Department of Nuclear Engineering
Texas A&M University
College Station, TX 77843

Abstract

The interaction between the flow and free surface was evaluated measuring the velocity distribution and surface movement simultaneously. The test section was a rectangular tank having a free surface. A rectangular nozzle was set near the free surface to form a quasi two-dimensional jet. The jet interacted with the free surface, causing the wavy free surface condition.

The flow under the free surface was visualized by a laser light sheet and small tracer particles. With image processing techniques, the movement of the free surface and the movement of the particles were simultaneously measured from the recorded images, resulting in the velocity distributions and surface locations. Then, the interactions between the flow and free surface were evaluated using the form of turbulent energy and surface-related turbulent values.

By increasing the turbulent energy near the free surface, the fluctuations of the free surface height and the inclination of the free surface were increased. The higher fluctuation of horizontal velocity was related to the higher surface position and negative inclination.

The image processing technique is found to be very useful to evaluate the interaction between free surface and flow.

1 Introduction

The sodium coolant in a reactor vessel of a liquid metal fast breeder reactor (LMFBR) has a free surface. The interaction between the free surface and the circulating flow under the free surface may cause undesirable surface phenomena, e.g., gas entrainment and surface oscillation. Since the core of the LMFBR has a positive void factor, the gas entrainment into coolant should be avoided. The surface oscillation may cause severe damage on the reactor vessel because of the relatively high thermal conductivity of sodium. In order to predict those free surface phenomena, the interaction between the flow and free surface should be evaluated.

Several studies have investigated the flow characteristics of the turbulence under near-flat surfaces using water as a test fluid. Nezu and Rodi [1] proposed the boundary condition of free surface turbulence in the non-wavy surface condition. They measured the turbulence in

* Nuclear Eng. Res. Lab , University of Tokyo, Tokai-mura, Ibaraki, 319-11 JAPAN

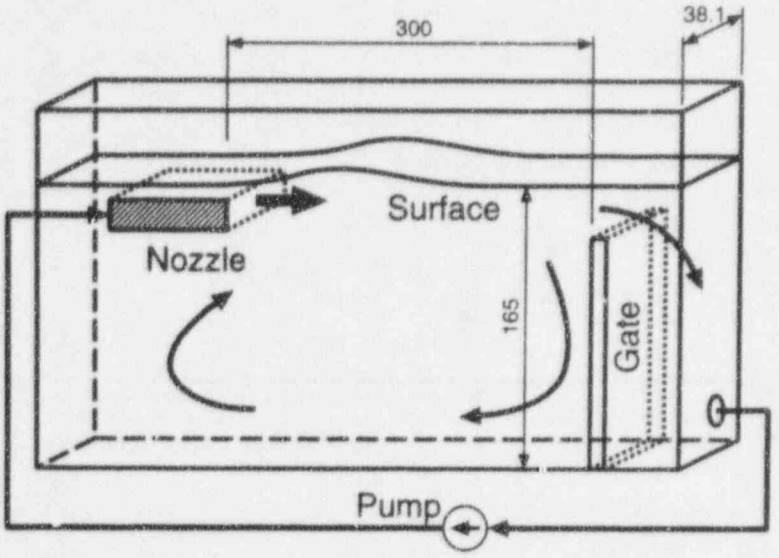

Figure 1: Schematic of test section

the rectangular open channel using a Laser Doppler Velocimeter (LDV), and proposed that the turbulent kinetic energy at the surface is about 0.8 times as large as that without surface.

Walker et al.[2] measured the three-dimensional velocity distribution beneath the surface using a three-dimensional LDV. The turbulent conditions were generated by the horizontal jet injected from a horizontal cylinder nozzle. At a lower Froude number, (calmer surface), the surface-normal velocity fluctuations decreases near the surface, and were transferred to the tangential velocity fluctuations. This relationship was similar to Nezu and Rodi's results. They reported that the tangential vorticity may interact with the 'image' above surface. At a higher Froude number, (very wavy surface), less energy was transferred from surface-normal to tangential velocity fluctuations near the surface.

In these studies, the characteristics of the free surface were not measured. However, the interaction between the flow and free surface can be directly evaluated by measuring the free surface and velocity simultaneously.

The turbulent boundary condition on the wavy free surface is very important in order to evaluate the free surface phenomena. However, no models for the surface turbulent boundary conditions in the wavy conditions were proposed, because of the higher non-linearity of the free surface. In order to investigate the interaction between the flow and the free surface, a new technique had been developed and applied to the measurement of the flow field. The flow velocity distribution and the free surface movement were measured simultaneously using the image processing technique. The interaction between the flow and the free surface could be evaluated with the measured data.

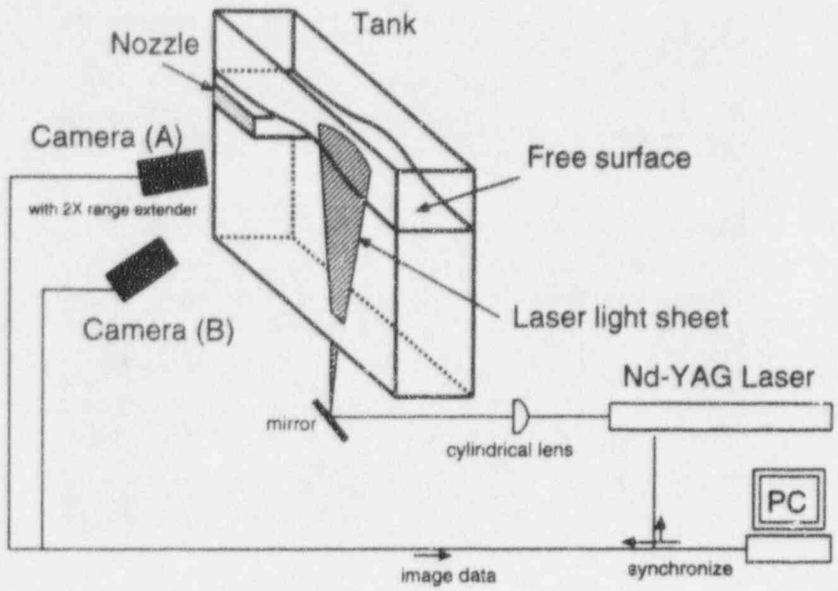

Figure 2: Measurement system

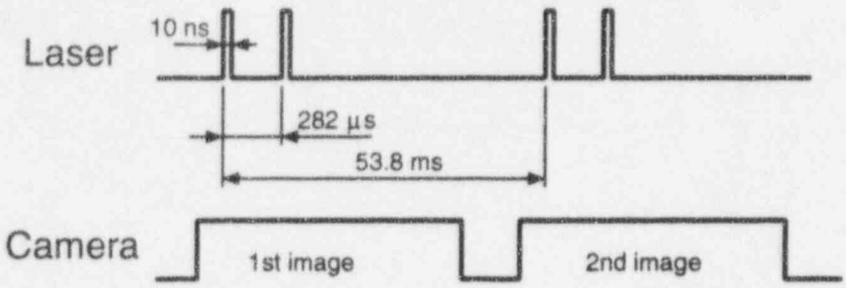

Figure 3: Timing chart of laser light

2 Experiment

In this study, the interaction between the free surface and the flow was measured by the image processing technique. Water served as a test fluid. The velocity distributions were measured by the Particle Image Velocimetry technique[3, 4, 5, 6]. The movement of the free surface was measured simultaneously by analyzing the image data.

In general, the interaction between the free surface and the flow is a three-dimensional phenomenon. However, the three-dimensional surface shape could not be measured using the two-dimensional image. In this study, the two-dimensional surface shape and the two-dimensional velocity distributions were measured simultaneously. Then, the interaction between the free surface and the flow was evaluated two-dimensionally.

In order to approximate the two-dimensional flow, a rectangular tank and a flat nozzle were used as a test section. Figure 1 shows the schematic view of the test section. The nozzle was

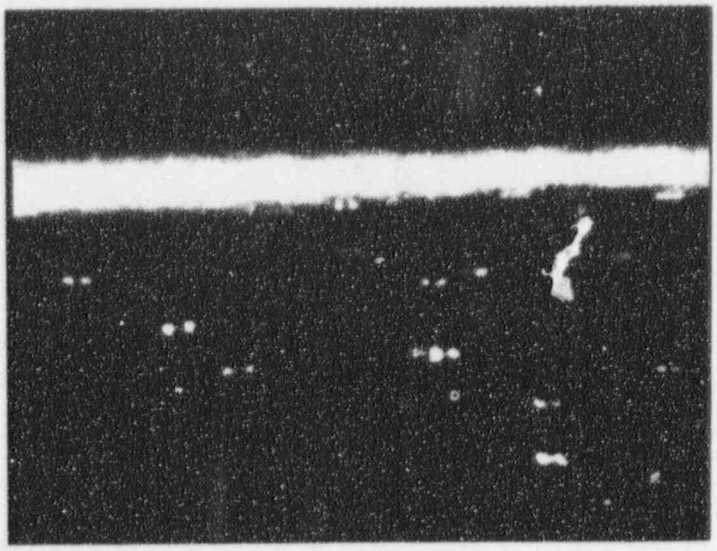

Figure 4: Example of captured image

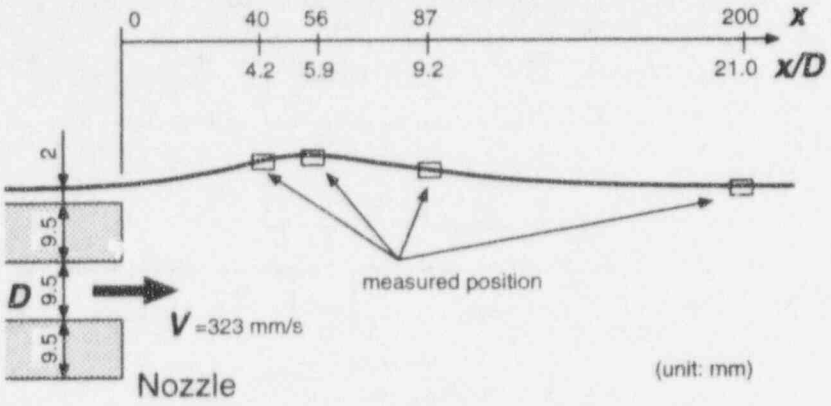

Figure 5: Measured position

horizontally set just beneath the free surface. The nozzle width was the same width as the tank, (38.1 mm). The flow was circulated by a centrifugal pump. The nozzle inlet height was 9.5 mm and the depth of the tank was 165 mm. The jet from the nozzle interacted with the free surface, causing the wavy free surface condition.

The nozzle inlet velocity was set to 323 mm/sec, i.e., Re=3070 and Fr=1.06, which is calculated by the nozzle height as the representative length and inlet velocity as the representative velocity.

The flow under the free surface was visualized by the laser light sheet and small tracer polystyrene particles, which were 6 μm in diameter and 1.01 in specific density. Figure 2 shows the measurement system. As a light source, an Nd-YAG laser was used, which can generate double pulses. The timing chart of the Nd-YAG laser is shown in Figure 3. Each pulse had a

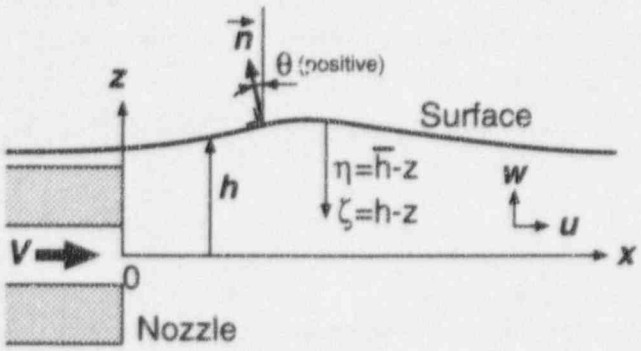

Figure 6: Coordinate system

10 nsec length and the time interval between two pulses was 282 μsec. The double pulses were repeated with 53.8 msec intervals. The CCD camera, which was synchronized to the laser pulse, recorded the double-pulsed images. The camera had a 640 $\times$ 480 spatial resolution. The image was digitized into 8-bit digital data.

In this study, two cameras were set to get the image. One camera (A) was focused on a small region to measure the velocity. The other camera (B) recorded relatively wide region to measure the movement and shape of the free surface. In order to measure the precise velocity data, the camera (A) was focused on very small area, i.e., 3mm $\times$ 2mm, with a 2X range extender between lens and camera. In this condition, the image resolution was 2mm/400pixel $\approx$ 5 μm/pixel.

Figure 4 shows an example of the obtained image. Because of the effects of the lens extender, the view depth of the camera was very thin, resulting in the relatively unfocused image. However, the particle location could be identified easily, since the image had high resolution, (5 μm/pixel), which was almost the same size of the particle diameter, 6 μm. In this image, two images of one particle were recorded with the double-pulse laser. The corresponding particle pair can also be determined easily. The direction of the flow was always from left to right because of the higher velocity of inlet jet and relatively small turbulence intensity. The velocity distributions can then be calculated.

The particle concentration ratio in the water was relatively high to get many particle images in a small region. Therefore, several particles floated on the free surface because of the effects of surface tension with the small particle diameter (6μm). Thus the free surface had a lot of contamination, causing the surface tension at the free surface to be much smaller than that without contamination. The measured condition was the condition with small surface tension.

Since the particles floating on the free surface reflected the laser light, it was easy to identify the surface location as shown in Figure 4. The surface location movement was relatively slow compared with the velocity. Even in the double-pulsed image, the free surface locations can be uniquely identified. From the image, the following surface parameters were measured: surface height, h, and surface inclination, $\vec{n}$.

Figure 5 shows the measured points, i.e., $x/D = 4.2$, 5.9, 9.2 and 21, where x is the distance from the nozzle outlet and D is the inlet height of the nozzle. The jet contacted with the free

surface around $x/D \approx 4$; therefore, the free surface was highly wavy around $x/D \approx 4$. On the other hand, the free surface was calm at the down stream, i.e., $x/D > 10$.

3 Results and Discussion

3.1 Velocity distributions

In this study, the instantaneous velocity distributions in a very small field near the surface were measured. The coordinate system near the surface was defined as shown in Figure 6. Surface height, h, is defined as the distance between surface and nozzle center line. The water depth, η, is defined as the distance from the mean surface height, namely,

$$\eta = \overline{h} - z, \tag{1}$$

where z denotes the vertical coordinate as shown in Figure 6. Therefore, the water depth η is defined in an Eulerian coordinate, (fixed coordinate). The mean surface height, $\overline{h}$ was calculated

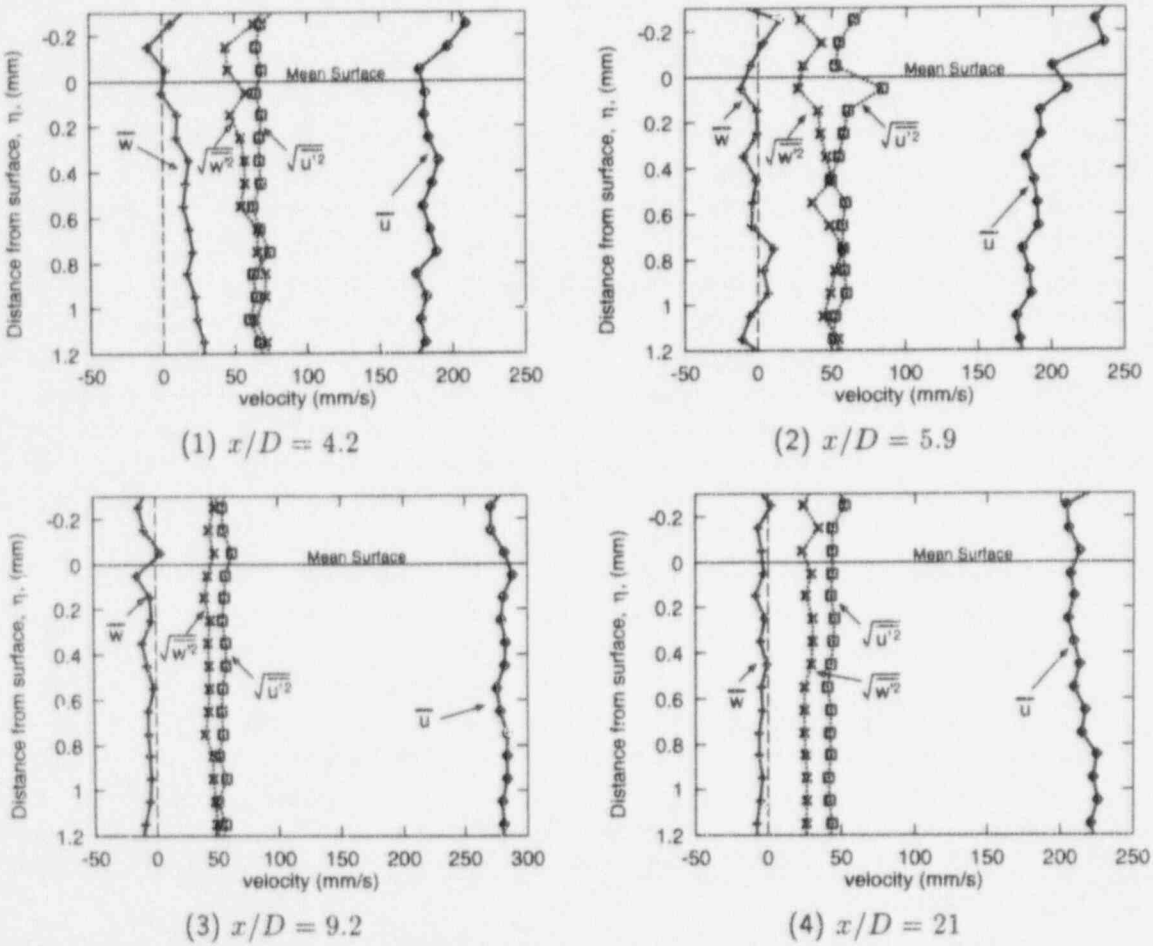

(1) $x/D = 4.2$ (2) $x/D = 5.9$

(3) $x/D = 9.2$ (4) $x/D = 21$

Figure 7: Velocity distribution

by averaging the surface height during the measuring period. Since the measured region was small, the effects of the x direction were assumed to be negligible. Then the average velocity distribution and fluctuation of velocity were calculated with the function of the z direction only. Figure 7 shows the relationship between the water depth, η, and velocity. In these figures, the root mean square values (RMS) of the velocity deviation are also plotted.

At the upstream region, Figures 7(1) and 7(2), the flow is accelerated by the main flow causing a highly turbulent condition. There is relatively large upward velocity, $\overline{w}$, beneath the free surface. However, it decreases to zero with decreasing the water depth, η. The RMS values of velocity components, $\sqrt{\overline{u'^2}}$, $\sqrt{\overline{w'^2}}$, depend a little on the water depth, η. At the downstream region, Figures 7(3) and 7(4), the average horizontal velocity, $\overline{u}$, is close to the nozzle outlet velocity, since the main flow contacted with the free surface. The vertical velocity, $\overline{w}$ is almost zero. The RMS values are almost constant with a different depth, η.

The actual free surface fluctuated around the average surface position. Therefore, the effects on the free surface were not evaluated directly using the fixed coordinate system. In this study

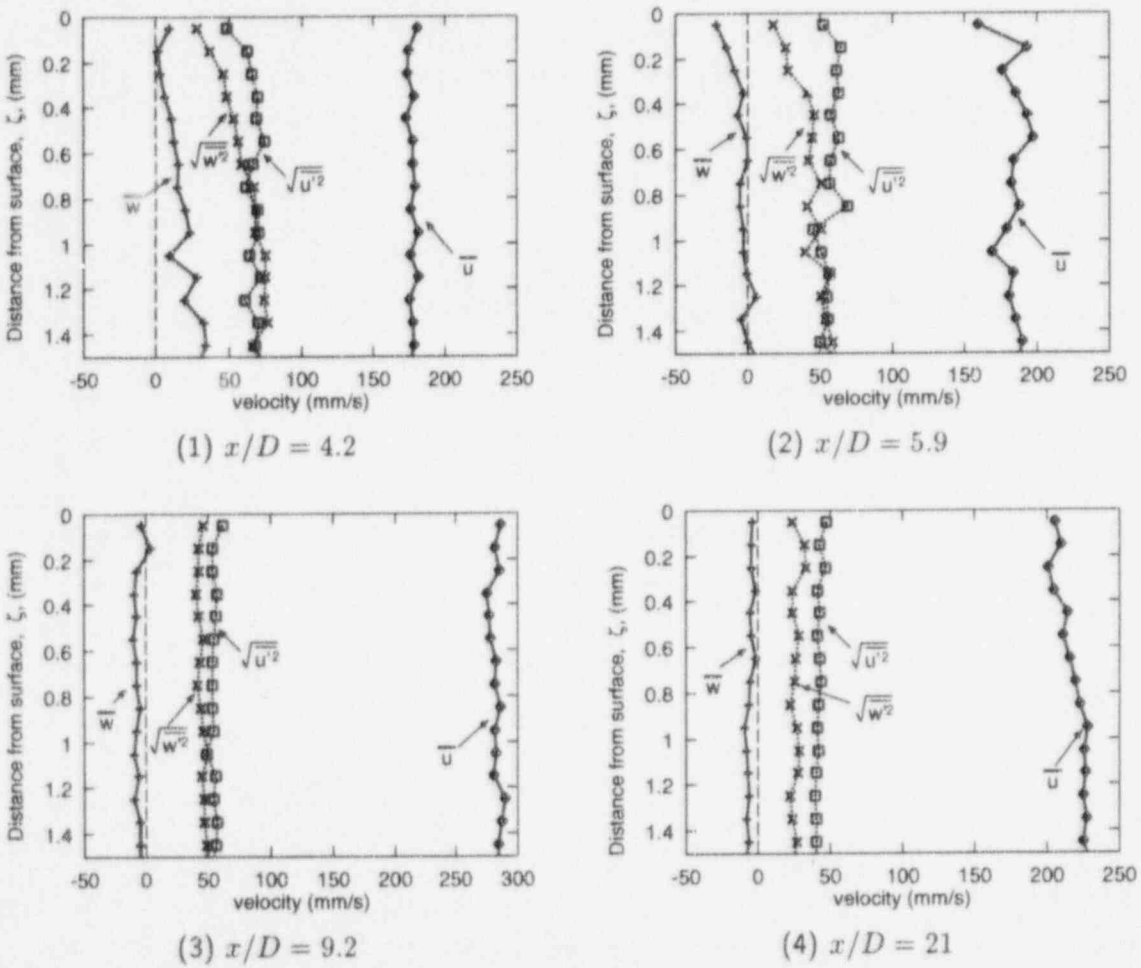

(1) $x/D = 4.2$ (2) $x/D = 5.9$

(3) $x/D = 9.2$ (4) $x/D = 21$

Figure 8: Velocity distribution in Lagrangian

the relative depth from the surface, ζ, is introduced to express the effects on the free surface directly.

$$\zeta = h - z. \tag{2}$$

where h is an instantaneous surface height. In order to correctly evaluate the surface effects in a Lagrangian coordinate system, the surface velocity, $\partial h/\partial t$, should be known. However, the time interval between two images, 53.8 msec, is too large to calculate the surface velocity correctly. Therefore, the surface velocity, $\partial h/\partial t$, is assumed to be zero in this study. The relationship between the velocity and relative depth, ζ, is shown in Figure 8.

At the upstream region (Figures 8(1) and 8(2)), the RMS for the upward velocity, $\sqrt{\overline{w'^2}}$, decreases as the relative depth, ζ, decreases. Because of the existence of the free surface, the vertical fluctuation is thought to be depressed. The same relationship was obtained by Nezu and Rodi[1] and Walker et al.[2]. However, at the downstream region (Figures 8(3) and 8(4)), the RMS for vertical velocity does not decrease near the surface. This result can be explained by the measurement error.

3.2 Digitized error

In this study, the velocity was measured by the digitized image, in which the resolution was limited to pixel. Here, the real value and measured value are expressed as a and $\widehat{a}$, respectively. The relationship between the two values is:

$$\widehat{a} = a + e, \tag{3}$$

where e is the measurement error which includes the digitized error caused by limited image resolution. The error, e, is considered to be distributed at random, therefore, the averaged value, $\overline{e}$ is zero. Therefore, the measured averaged value is equal to the real averaged value, i.e., $\overline{\widehat{a}} = \overline{a}$.

However, for the RMS value, the following relationship is obtained:

$$\sqrt{\overline{(\widehat{a} - \overline{a})^2}} \approx \sqrt{\overline{(a - \overline{a})^2} + \overline{e^2}} \tag{4}$$

Since the value $\overline{e^2}$ is not zero, the measured RMS is always greater than the real RMS.

In this study, when the order of e is assumed to be 1 pixel, the error, $\sqrt{\overline{e^2}}$ is about 20 mm/s in RMS for velocity. The error, $\sqrt{\overline{e^2}}$ is relatively large compared with the RMS values. In order to evaluate the turbulent value more precisely, an image with much higher resolution should be needed.

3.3 Turbulent value

As mentioned in the previous section, the measured RMS value contains a relatively large error term, $\sqrt{\overline{e^2}}$.

In order to evaluate the turbulent value, the effects of the error should be substituted. In this study, the turbulent kinetic energy is defined as follows:

$$k = \frac{1}{2}\left((\overline{u'^2} - \overline{e^2}) + (\overline{w'^2} - \overline{e^2})\right)\frac{3}{2}, \tag{5}$$

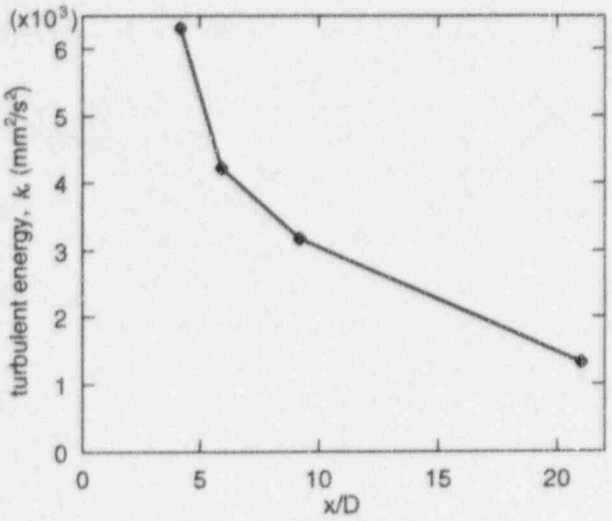

Figure 9: Turbulent kinetic energy near free surface

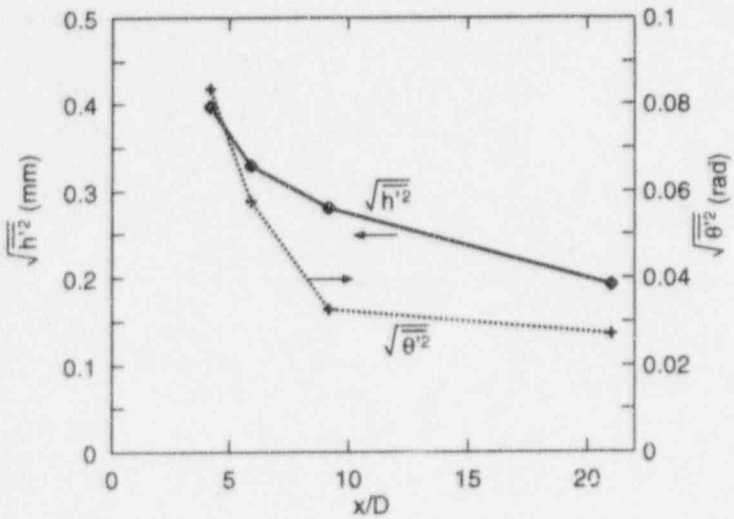

Figure 10: Distribution of free surface fluctuation

where e is assumed to be the order of 1 pixel, then $\sqrt{\overline{e^2}} = 20$ mm/s. Since the measurement is two-dimensional in this study, the isotropic turbulence is assumed to obtain the turbulent energy.

Figure 9 shows the distribution of turbulent kinetic energy near the free surface with the distance from the nozzle outlet. As expected, the turbulent energy, k, decreases with increasing the distance, x/D.

From the image data, the surface locations were also measured. Therefore, turbulent values related to the surface can be calculated. The RMS of the surface height fluctuation is expressed

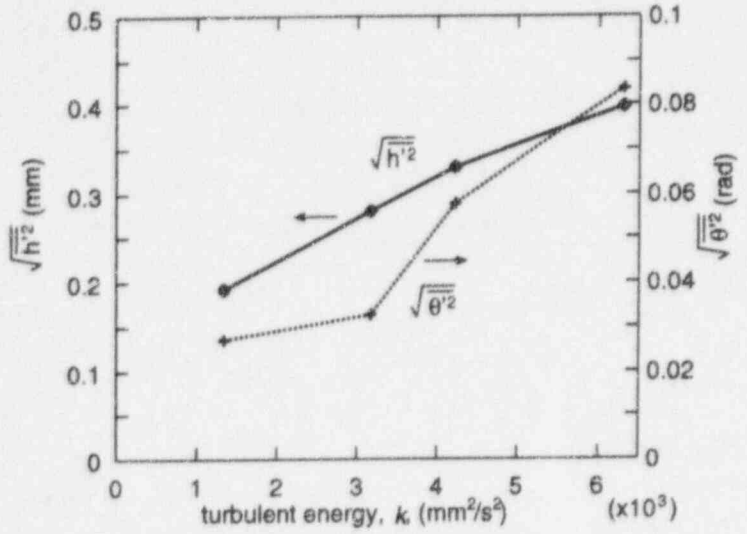

Figure 11: Relationship between turbulent energy and surface fluctuation

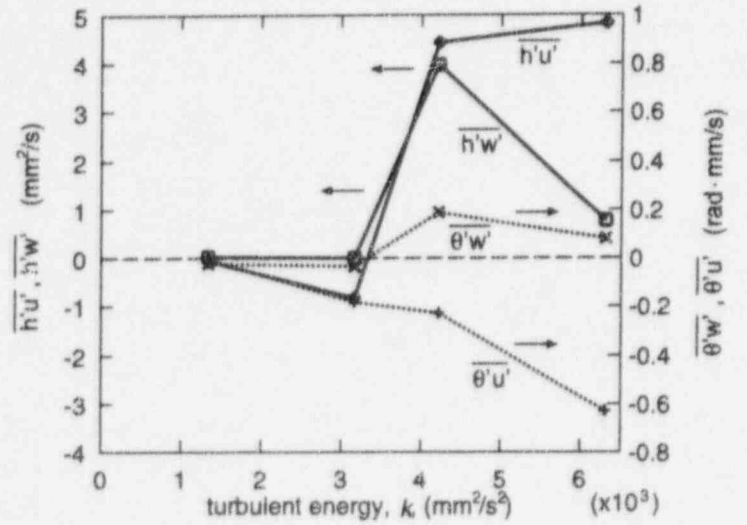

Figure 12: Interaction between free surface and turbulence

as $\sqrt{\overline{h'^2}}$. The surface inclination angle, θ is defined as shown in Figure 6, using the normal vector of free surface, $\vec{n}$. Then, the RMS of the surface inclination is expressed as $\sqrt{\overline{\theta'^2}}$. In these values, effects of the digitized error, e, is also included. When the error is on the order of 1 pixel, the error, $\sqrt{\overline{e^2}}$ is about 0.005 mm and 0.002 rad, for $\sqrt{\overline{h'^2}}$ and $\sqrt{\overline{\theta'^2}}$, respectively, which are very small compared with the RMS value. Therefore, in the calculation of surface-related turbulent values, the effects of the digitized error can be negligible.

Figure 10 shows the distribution of the surface-related turbulent values with the distance from the nozzle outlet. With increasing the distance, x/D, the surface-related turbulent values

decrease. This relationship is caused by the decreasing turbulent energy. Figure 11 shows the relationship between the surface-related turbulent values and turbulent kinetic energy. It is confirmed that the turbulence in the flow and that at the free surface are highly related to each other.

The interaction between the flow and the free surface can be evaluated with the cross term between them. Figure 12 shows the relationship between turbulent energy and the cross terms, i.e., $\overline{h'u'}, \overline{h'w'}, \overline{\theta'u'}$ and $\overline{\theta'u'}$. In the high turbulent energy conditions, the $\overline{h'u'}$ is positive and the $\overline{\theta'u'}$ is negative. The faster horizontal velocity is related to the higher surface height and negative inclination.

4 Conclusion

The interaction between the flow and the free surface was evaluated by measuring the velocity distribution and the surface movement simultaneously, using the image processing technique. The interactions between the flow and the free surface were evaluated using the form of turbulent energy and surface-related turbulent values.

With increasing turbulent energy near the free surface, the fluctuations of the free surface height and the inclination of the free surface were increased. The higher fluctuations of horizontal velocity were related to the higher surface height and negative inclination.

The image processing technique is found to be very useful in evaluating the interaction between free surface and flow.

References

[1] Nezu, I. and Rodi, W., 1986, "Open-Channel Flow Measurements with a Laser Doppler Anemometer," J. Hydraulic. Eng., ASCE, **112**, 335.

[2] Walker, D. T., Chen, C.-Y. and Willmarth, W. W., 1995, "Turbulent structure in free-surface jet flows," J. Fluid Mech., in print.

[3] Hassan Y. A., Blanchat, T. K., Seeley Jr., C. H. and Canaan, R. E., 1992, Simultaneous velocity measurements of both components of a two-phase flow using particle image velocimetry, Int. J. Multiphase Flow, **18**-3, 371.

[4] Uemura T., Yamamoto. F. and Koukawa, M., 1990, A High Speed Algorithm of Image for Particle Tracking Velocimetry Using Binary Picture Correlation, J. Visualization Soc. Japan, **10**-38, 196.

[5] Nishino, K., Kasagi, N. and Hirata, M., 1989, Three-dimensional particle tracking velocimetry based on automated digital image processing, Trans. ASME, J. Fluid Eng., **111**, 384.

[6] Okamoto, K., Madarame, H. and Shioya, R., 1991, Measurement of Velocity Distribution in a Tank by Velocity Vector Histogram, ASME, FLUCOME'91, 601.

THE USE OF WAVEGUIDE ACOUSTIC PROBES FOR VOID FRACTION MEASUREMENT IN THE EVAPORATOR OF BN-350-TYPE REACTOR

V.I.Melnikov, B.I.Nigmatulin

Research & Engineering Centre
of LWR Nuclear Plants Safety

Abstract

The present paper deals with some results of the experimental studies which have been carried out to investigate the steam generation dynamics in the Field tubes of sodium-water evaporators used in the BN-350 reactors.

The void fraction measurements have been taken with the aid of waveguide acoustic transducers manufactured in accordance with a specially designed technology (waveguide acoustic transducers - WAT technology). Presented in this paper are also the transducer design and calibration methods, as well as the diagram showing transducers arrengment in the evaporator. The transducers under test featured a waveguide of about 4 m in length and a 200-mm long sensitive element (probe).

Besides, this paper specifies the void fraction data obtained through measurements in diverse points of the evaporator. The studies revealed that the period of observed fluctuations in the void fraction amounted to few seconds and was largely dependent on the level of water in the evaporator.

1. Introduction

The sodium-heated steam generators (evaporators) employed in the fast breeder reactor are a unique type of heat exchange equipment with regard to the operation reliability and safety requirements. Acting essentially as an interface of chemically exlusive media-sodium and water, the steam generators must ensure total interloop leaktightness throughout the entire service life.

The evaporators of the BN-350 reactors make use of a multiple forced water circulation principle. The heating surface is made up of Field tubes wherein steam is generated under natural water circulation conditions. Steam separation takes place in the upper section of the shell, while the Field tubes are heated with sodium fed to the lower section of the evaporator shell (1). Some accidents evidenced in the course of operation of these evaporators were related to integrity failures of the Field tube heat-transfer areas and rendered the evaporator unserviceable. With the lapse of time after sealing of an affectd tube and returning the evaporator to service, the similar seal failure happened to the adjacent tube. Further on, this kind of trouble occurred over and over. Such an occurrence necessitated a reduction in the reactor power.

To inquire into the reason for the Field tubes rapture, appropriate steps have been taken to measure thermohydraulic parameters in the evaporator water section with the use of updated diagnostic devices with the reactor running at rated power. This work was accomplished with the aid of thermocouple sensors, conductivity probes and acoustic transducers fitted at the outlets of several Field tubes to monitor temperature and void fraction in the steam-water mixture flow.

2. Measurement Methods

The void fraction measurements were conducted with the utilization of an acoustic impedance method (2,3). This method is based on measuring attenuation of ultrasonic waves in the sensitive element (probe) submerged into the flow being checked.

The void fraction measurement acoustic transducer (Fig. 1) operates in the following manner. Acoustic pulses shaped by the converter are furnished via the waveguide to the sensitive element to be successively reflected thereon first from the waveguide-probe junction and then from the sensitive element free end.

The amplitude of the pulse reflected from the free end of the sensitive element is dependent on the degree of its damping by the passing flow and is minimum when the sensitive element is immersed into liquid.

The attenuation of the longitudinal wave in the sensitive element is represented as:

$$A = A_0 \exp(-k\rho c) \qquad (1)$$

where: k- proportionality factor depending on the sensitive element geometry and material, as well as on the operating frequency;

ρ - liquid density;

c - velocity of sound (ρ_c - shock-wave drag).

With the sensitive element dipped down into two-phase flow, a certain part of its surface is damped by coolant at any moment of time, while the other part is brought in contact with steam. The steam concentration is evaluated by the magnitude of ultrasonic pulse attenuation in the sensitive element.

The mean mixture quality on the sensitivy element surface is calculated by equation:

$$\varphi = \frac{\ln\left(\frac{A_1}{A_2}\right) - \ln\left(\frac{A_1}{A_2}\right)_l}{\ln\left(\frac{A_1}{A_2}\right)_v - \ln\left(\frac{A_1}{A_2}\right)_l} \qquad (2)$$

were A_1 and A_2 - amplitudes of pulses reflected from the sensitive ends;

v and l - Indices applicable to the instances when the sensitive element is submerged into steam (vapour) or liquid, respectively.

3. Design of Transducers

The transducers are manufactured from chromiun-nickel steel. The sensitive element is made of a thin-walled tube with dimensions of 1.5 mm in diameter, 0.2 mm in wall thickness and 200 mm in length. The waveguide coupling line comprises a waveguide of 0.8 mm in diameter and 4 m in length. It is enclosed in a protective sleeve of 6 mm in diameter and a mount incorporating ferrules with heat-resistant rubber and spacer wire pressed-in into the latter. The wave-guide is routed in a helically-shaped fashion with a helix lead 0.8 m to avoid its bending and assure a higher operational reliability in the event of thermal wobbling. The acoustic converter is manufactured from zirconium-titanium-lead ceramics and has a diameter of 2.5 mm.

The operating frequency of the transducers is rated at 580 kHz, and the acoustic pulse transmission ratio ranges from 0.01 to 0.012 in the emission-receipt mode.

Coupling between the transducers and the terminal electronic equipment is effected by means of a shielded double-conductor cable of 80 m in length and matching RF transformers which do a good job of suppressing man-made interference.

Arrangement of the transducers in the evaporator is illustrated in the Diagram in Fig.2. The transducers are tightly sealed in a special sealing assembly by welding applied to the protective sleeve. Welding technique is also utilized for attachment of the transducer senstive elements at the outlet of the Field tubes.

4.Transducer Calibration

The finished transducers have been tested and calibrated along with electronic monitoring instruments by immersing the sensitive element in model liquids (Ref.Fig.3,a). They simulated changes in water acoustic properties versus pressure and temperature. According to formula (1) the dependence of the ln - A_1/A_2 parameters on the shock-wave drag shall be regarded as linear in character.

With due account for effect of hydrodynamic factor associated with the two-phase flow passing over the sensitive element, the transducers were calibrated in a bubbler. The calibration procedure was monitored through the utilization of gamma-raying and dilatomery methods. The calibration results are specified in Fg.3,b. A correction to the data obtained was applied with empirical equation:

$$\varphi_n = \frac{\xi\varphi_s}{1+(\xi-1)\varphi_s} \qquad (3)$$

were: ξ=3.27:φ_s is the void fraction on the sensitive element surface (with no correction applied).

Besides, the temperature calibration was also perfomed on the acoustic transducer subjected to hot air environment in an oven.

5. Measurement Data

The void fraction measurements were taken within the reactor power range corresponding to 65-75% of its rated power.

The absolute values of the mean volumetric steam quality at the oultet of the Field tubes are within the following limits: at point A_1 - 40 to 65%, at point A_2 - 80 to 85%, and at point A_3 - 80 to 90 %. These data are in good agreement with the results of measurements obtained with conductivity probes located at the same reference test points.

In order to investigate the steam generation dynamic properties, an analyser was connected to the terminal void fraction measuring instruments.

In has been found that the pulse-height distribution of the signal being measured is normal, while the autocorrelation functions give evidence of a background component (Ref.Fig.4). The measurement time of one autocorrelation function varied from 200 to 400 sec

The autocorrelation function of the signals at the output of the A_2 and A_3 transducers featured background components with a period approximating 3 s and 1.8 s. The fluctuation amplitude constitutes 20 to 30 %. A 10-cm rise in the water level in the evaporator caused the oscillation period to increase by 10-15 %.

The autocorrelation function of the signal at the A_1 transducer output is indicative of an unsteady nature of the steam generation process as the test point concerned. Judging by the width of the autocorrelation function zero lobe the usual time of void fraction fluctuation is evaluated as 0.1-0.12 s.

The transducers have been operating in the evaporator for six months until they were removed for the scheduled preventive maintenance.

6. Data Analysis and Conclusions

Thermal load of the Field tubes across the evaporator section is far from being uniform and reaches its peak in its centre. The void fraction at the field tube outlets in the evaporator central part is below 100% (the maximum value comes to 85-90 %). As is clear from observations the void fraction fluctuations occur with a frequency of 0.3 to 10 Hz.
Moreover, the fluctuation frequence in the area of blanked-off Field tubes is maximum (about 10 Hz) and of irregular character. A high value of the mean volmetric mixture quality points out to the fact that the flow at points A_2 and A_3 containts drops and foam. At the same time the void fraction at point A_1 was noticeably lower (about 50%) which suggests a slugging flow.

Investigations performed earlier on the liquid metal-water steam generator model reveald that the tube wall temperature fluctuations went on at a frequency of 0.3 Hz with an amplitude of 18°C (4). The measurements were taken with the aid of a thermocouple fittied-in to a depth of 1.75 mm into the tube wall.

From this follows the conclusions that the reason for the Field tubes fracture is presumably an alterating water dampening and drying of the heat exchange surfaces which brings about fluctuations in the tube wall temperature. The slugging flow condition causes the local heat transfer coefficient to change from its lower to a higher value with a higher amplitude and frequency. This gives rise to high amplitudes of the wall temperature fluctuations. Thermal stresses developed under these conditions are responsable for precipitating the Field tubes fracture in the area of blancked-off defective tubes.

Figure 1. Design of Waveguide Impedance Transducer for Void Fraction measurement

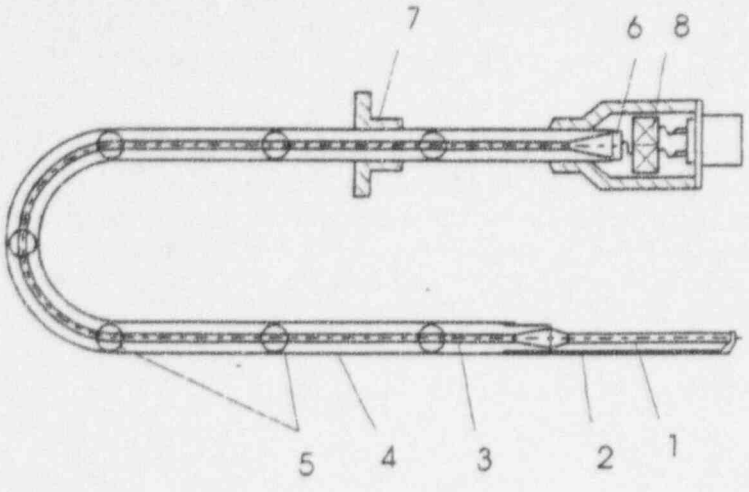

1.Sensitive Element
2.Supporting Fixture
3.WaveguideFigure
4.Proofing tube
5.Protective Sleeve
6.Acoustic Converter
7.Sealing Assembly
8.Matching Transformer

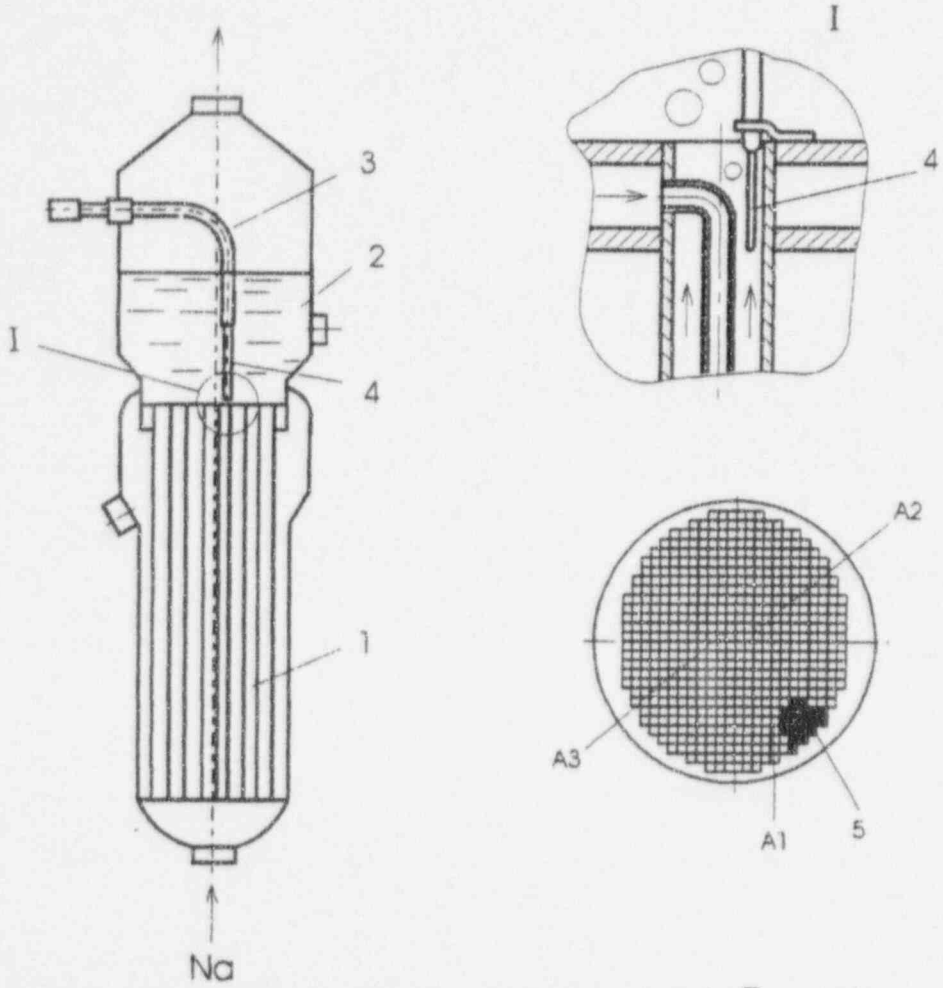

Figure 2.Transducer Arrangement in Evaporator. Schematic Diagram

') Field tubes
2) separation zone
3) transducer
4) sensitive element
5) Blanked-off tubes area A_1, A_2, A_3 - sensitive elements location

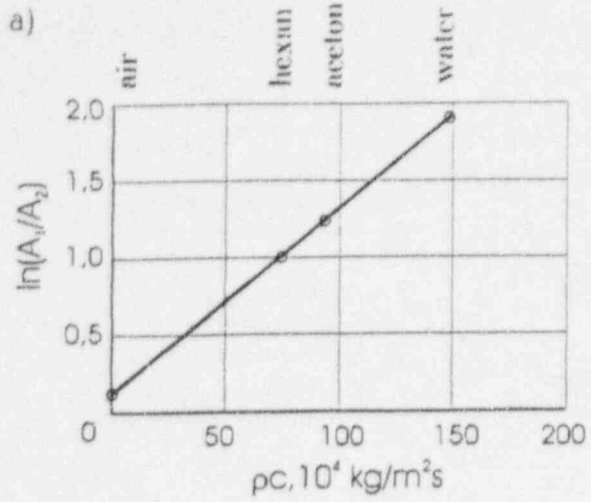

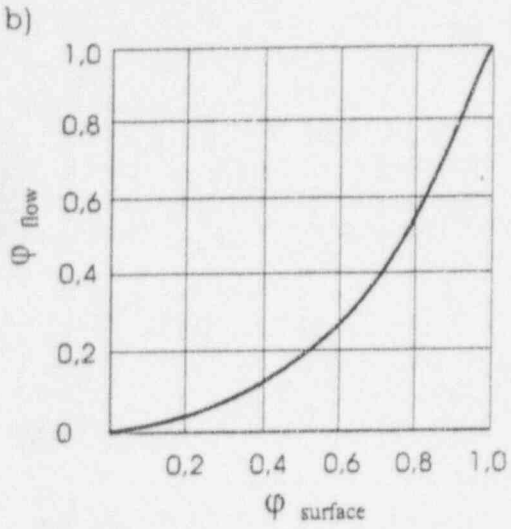

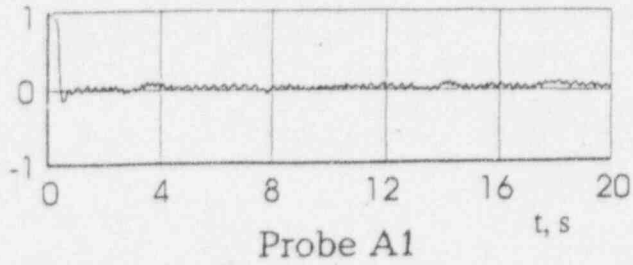

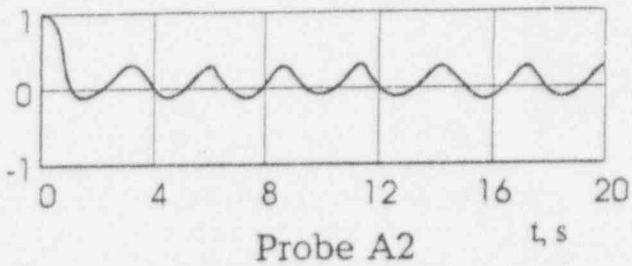

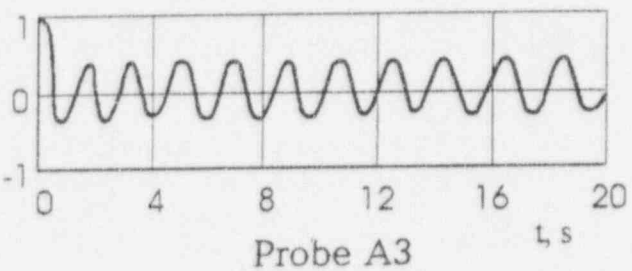

Fig. 3 (a) calibration chart for transducers Calibrated in model liquid
(b) transducers hydrodynamic calibration

Fig. 4 Autocorrelation function of void fraction fluctuations at Field tubes outlet

BUOYANCY-DRIVEN FLOW EXCURSIONS IN FUEL ASSEMBLIES

James E. Laurinat
Pran K. Paul
John D. Menna

Westinghouse Savannah River Company
Savannah River Technology Center
Aiken, SC 29802

Abstract

A power limit criterion was developed for a postulated Loss of Pumping Accident (LOPA) in one of the recently shut down heavy water production reactors at the Savannah River Site. These reactors were cooled by recirculating heavy water moderator downward through channels in cylindrical fuel tubes. Powers were limited to safeguard against a flow excursion in one or more of these parallel channels.

During full-power operation, limits safeguarded against a boiling flow excursion. At low flow rates, during the addition of emergency cooling water, buoyant forces reverse the flow in one of the coolant channels before boiling occurs. As power increases beyond the point of flow reversal, the maximum wall temperature approaches the fluid saturation temperature, and a thermal excursion occurs.

The power limit criterion for low flow rates was the onset of flow reversal. To determine conditions for flow reversal, tests were performed in a mock-up of a fuel assembly that contained two electrically heated concentric tubes surrounded by three flow channels. These tests were modeled using a finite difference thermal-hydraulic code. According to code calculations, flow reversed in the outer flow channel before the maximum wall temperature reached the local fluid saturation temperature. Thermal excursions occurred when the maximum wall temperature approximately equaled the saturation temperature.

For a postulated LOPA, the flow reversal criterion for emergency cooling water addition was more limiting than the boiling excursion criterion for full power operation. This criterion limited powers to 37% of the limiting power for previous long-term reactor operations.

Background

The production reactors at the Savannah River Site had several unique features that dictated a different approach to power limits analysis than is commonly used for commercial power reactors. The Savannah River reactors used heavy water as a moderator and coolant and operated at much lower temperatures and pressures than commercial reactors. In contrast with boiling water reactors, external heat exchangers connected to local surface water sources maintained core temperatures below the boiling point, so these reactors did not generate any steam. The Savannah River reactors also differed from commercial reactors in that the coolant was recirculated downward rather than upward through the fuel tubes. Because of their relatively low core pressures and the downward flow through the fuel tubes, the Savannah River reactors were much more

susceptible to parallel channel, bulk boiling flow instabilities than are commercial reactors.

Commercial reactor powers commonly are limited to avoid a critical heat flux on one of the fuel element surfaces or a dryout of the liquid film on a heated surface. By contrast, power limits for the Savannah River reactors were set to safeguard against a parallel channel, bulk boiling flow instability during a postulated design-basis Loss of Coolant Accident (LOCA) [1]. In the LOCA, a line break in one of the lines to or from the external heat exchangers interrupts the supply of primary coolant, causing the reactor to scram. Power limits were set to prevent a parallel channel flow excursion during the two to three seconds immediately following the scram. This flow excursion occurs when the pressure drop reaches a minimum in one flow channel due to boiling in that channel. If the coolant flow rate decreases further, the boiling diverts flow to adjacent channels, so that the affected channel dries out and undergoes a thermal excursion. The limiting criterion for a boiling excursion was a lower bound [1] to the Saha-Zuber correlation for onset of significant void generation [2]. The lower bound to the Saha-Zuber correlation, which accounts for uncertainties in the correlation, takes the form of a Stanton number, given by

$$St = \frac{q''}{Gc_p(T_{sat} - T_{bulk})} = 0.0065 \qquad (1)$$

By definition, the design-basis accident must be more limiting than other postulated accidents. One of these other accidents is the Loss of Pumping Accident (LOPA), in which a line break interrupts the supply of secondary cooling water to the heat exchangers. The secondary line break trips the power to the primary AC motors for the pumps that supply primary coolant. As a result, the primary pumps coast down and the coolant flow rate gradually drops, until the emergency cooling water supply is activated. This stabilizes the coolant flow rate until the backup DC pump motors become flooded with secondary cooling water. When these motors flood, the primary pumps eventually coast to a stop. A previous analysis indicated that the most limiting condition would probably occur during the coast down of the DC pump motors [3]. This analysis used a modified Stanton number criterion based on the results of flow excursion tests conducted in a single-channel test rig [4]:

$$St = 0.0025 \qquad (2)$$

The purpose of this study was to generate a low flow power limit criterion based on results of flow excursion tests performed in a multiple-channel test rig [5]. This test rig, called SPRIHTE, or SRS Prototypic Rig for Heat Transfer Experiments, was operated by the Savannah River Site heat transfer test facility.

Description of Test Facility and Tests

The SPRIHTE test rig, depicted in Figure 1, was built to be prototypic of a Savannah River fuel assembly. The test rig was operated by recirculating ordinary light water downward through a heated section using a centrifugal pump. This heated section consisted of concentric heated tubes separated by spacer ribs. In two of the concentric tubes, electrical resistance heat was added through wires embedded between an aluminum base tube and a plasma-sprayed aluminum coating. The heat was removed by passing the coolant through a heat exchanger. As in the fuel assemblies, coolant entered and exited the test rig through perforations in the sides of the outer housing.

Within the heated section, coolant flowed in the channels between pairs of adjacent concentric tubes. Spacer ribs divided each flow channel into four subchannels. Figure 2 shows the cross-sectional profile of the SPRIHTE rig. As this figure illustrates, the rig contained two heated tubes and two unheated tubes, which correspond to the fuel and target tubes of a fuel assembly. The rig differed from an actual fuel assembly, however, in that the there was no outer housing. The purge channel between the outer target tube and this outer housing was replaced by two external bypass tubes located on opposite sides of the heated section, as shown by Figure 1.

The test rig also differed from a fuel assembly in that only the middle two tubes of the test rig, corresponding to the inner and outer fuel tubes of the reactor assembly, were heated. In a fuel assembly, both the fuel and the target tubes generate heat. The outer heater tube of the test rig received 60% of the electrical power, and the inner heater tube received 40%. The heater tubes were constructed to give an axial power profile prototypic of a fuel assembly. The maximum power was located about three-quarters of the distance from the top of the heated section and was 1.43 times the average power.

As mentioned previously, the test rig was prototypic of a Savannah River reactor fuel assembly in that it had the same dimensions. Table 1 lists the dimensions of the test rig and compares the measured cross-sectional diameters rig with the design diameters of a Savannah River fuel assembly.

Overall flow rates to the SPRIHTE rig were measured using ultrasonic and turbine flow meters; the ultrasonic flow meters measured high flow rates and the turbine flow meters measured low flow rates. Individual channel and subchannel flow rates were not metered. The rig was fully instrumented to measure subchannel coolant and heater wall temperatures. Wall and subchannel coolant temperatures were measured using thermocouples; inlet and outlet fluid temperatures were measured using resistance temperature devices (RTD's). Inlet and outlet pressures also were measured. Measurement uncertainties were 2-3% for the ultrasonic flow meters, about 2% for the turbine flow meters, 1.0 K or less for the thermocouples, 0.5 K for the RTD's, and 1000 Pa or less for the pressure gauges [5]. In addition, the ultrasonic flow meter measurements were biased about 1% low, and the heater wall temperature measurements were biased about 1 K low [5]. No corrections were made to compensate for these biases.

During the tests, the flow rate and the inlet temperature were held constant, and the power was increased in increments until a thermal excursion was detected by wall thermocouples. A constant downward flow through the test section was maintained by a centrifugal pump with a high impedance. A standpipe connected to the test rig discharge kept pressures constant. The discharge was located just above the inlet plenum and was open to the atmosphere. Because pressure losses in the discharge line were small, it was assumed that the outlet from the heated section was under the static head of the discharge line.

Prior to thermal excursion, fluid thermocouple measurements indicated that there was unstable flow and flow reversal (upflow) in one of the outer subchannels. The thermal excursions always occurred in the outer channel. Unstable flow was detected by means of fluctuations of about 5 K in the effluent temperature. Flow reversal was said to occur when the inlet temperature exceeded any downstream temperature by 20 K or more. Finally, thermal excursions began when the maximum outer heater wall temperature reached 450 K. Power was shut off at this point to prevent damage to the rig.

Tests were conducted at flow rates of 0.000323, 0.000647, and 0.00097 m^3/s and at inlet temperatures of 298 K and 313 K. Only the 0.000647 and 0.00097 m^3/s tests were analyzed, since these flow rates were within the flow range at which the limit for the ECS addition phase of the LOPA was set [3]. Table 2 lists estimated individual channel flow rates, flow velocities, and Reynolds numbers for these tests.

Description and Evaluation of the Computational Model

The SPRIHTE tests were modeled using FLOPA, a finite difference thermal-hydraulic code developed at the Savannah River Site [6]. This code was an adaptation of another Savannah River code, FLOWTRAN, which was written to compute limits for the Loss of Coolant Accident [7]. Both codes combined a three-dimensional finite difference heat conduction model for the fuel assembly tubes with a one-dimensional donor cell model for flow and heat transfer in each subchannel. From comparisons with known analytical solutions, the codes' heat conduction calculations were accurate within about 0.6% [7]. Fluid temperatures calculated by the donor cell model were offset by one-half cell length. The heated length of the SPRIHTE test rig was divided into 40 axial cells for the calculations in this study. Thus, for a typical temperature increase of 60 K, the calculated temperatures were low by about 0.75 K. No correction was made for this offset.

The primary sources of uncertainty in the model calculations were fluid heat transfer coefficients and friction and form loss factors for subchannel flow. Fluid heat transfer was modeled using a modified Sieder-Tate forced convection correlation [7]:

$$\frac{hD_h}{k} = 0.023\left(\frac{D_h G\rho}{\mu}\right)^{0.8}\left(\frac{c_p\mu}{k}\right)^{1/3} \qquad (3)$$

Friction and form loss factors were obtained from constant temperature fuel assembly hydraulic test results. Differences between nominal fuel assembly and SPRIHTE rig tube diameters were small and were therefore ignored. It was assumed that the surface roughness of the test rig tubes was the same as that of reactor assemblies and that the heated section inlet and bottom end fittings were prototypic. The use of prototypic fuel assembly dimensions and friction and form loss factors from standard fuel assembly hydraulic tests was justified through comparisons of measured and calculated fluid and wall temperatures under stable flow conditions. These comparisons showed that the use of nominal dimensions and loss factors did not have a significant adverse effect on the ability of the FLOPA code to predict these temperatures. Neither heat transfer nor fluid flow models accounted for the presence of localized boiling where surface temperatures were higher than average, for instance, opposite spacer ribs.

The effect of thermocouple insertions on the flow in the inner and outer channels was assumed to be negligible, and corrections to fluid thermocouple measurements to account for fluid temperature gradients were not considered. Corrections to wall thermocouple measurements to account for thermal gradients in the heater tubes also were ignored. The wall thermocouples were centered within the heated walls. Subsequent calculations using the new limit criterion for the tests showed that the difference between the center wall and surface temperatures was 0.3 K at limit conditions. This difference was judged to be insignificant.

Finally, in calculations to determine a limit criterion, the test rig was modeled as a series of concentric annuli. Differences among subchannel fluid temperature measurements, particularly for the outer channel, indicated that the test rig cylinders may have been

eccentric. However, no credit was taken for this apparent eccentricity in the limit criterion analysis, since the eccentricity was not measured under heated conditions.

To determine the effect of eccentricity, three-dimensional, eccentric FLOPA models were used. Three models were created. In the first, designated Case 1 for ease of reference, the eccentricity of the outer channel was set to match the calculated difference between the hottest and coldest subchannel in the outer channel with the measured difference. In the second, designated Case 2, the eccentricity of the outer channel was set at its maximum value allowed by the rib tip clearance. Finally, in Case 3, a model was created in which the eccentricities in all three flow channels were set at the maximum values allowed by rib tip clearances. The eccentric channels were aligned in the same radial direction to maximize differences in subchannel heat transfer rates. Case 3 was used in LOPA limits calculations.

To verify that the FLOPA calculations accurately modeled flow and heat transfer in the test rig, calculated and measured values for subchannel fluid and heated wall temperatures were compared. In these comparisons, the Case 1 eccentricity model was used. A separate match was performed for a heated stable flow test at each test condition. Figure 3 compares typical fluid temperature profiles for the outer channel under stable flow conditions. This figure shows that FLOPA modeled flow and heat transfer to the coolant within a range of about 5 K. Figure 4 compares outer heater wall temperature profiles for the stable flow test condition at 0.00097 m^3/s and 313 K inlet. Again, the FLOPA model predicted measured temperatures within about 5 K. Figure 5 compares these wall temperatures at a higher power, where flow became unstable in the outer channel. In this case, measured wall temperatures for two of the outer subchannels are higher than the calculated temperatures, indicating that flow was diverted to the inner two channels.

Selection of a Limit Criterion

To bound the results of the tests, a criterion that the wall temperature not exceed the fluid saturation temperature was used. This wall saturation temperature criterion ensures that there is no boiling along the heated walls and, therefore, a thermal excursion cannot occur. A multiplier was added to account for differences between measured and calculated subchannel flow and heat transfer rates up to the point where unstable flow and possible flow reversal occur (see the discussion of wall temperature distributions in the preceding section). The limiting fluid temperature, in (degrees K - 273), is the product of this multiplier and the saturation temperature in (degrees K - 273).

Measured and computed maximum wall temperatures were compared to verify that FLOPA could accurately calculate the wall saturation temperature criterion. The maximum temperatures for these comparisons were located on the outer wall of the outer heater (the inner wall of the outer flow channel). Figure 6 illustrates these comparisons for the concentric flow model and for Cases 1, 2, and 3 eccentricity models. The Case 3 model was used to calculate LOPA limits. For Case 1, the FLOPA model accurately predicted the maximum wall temperature at low powers under steady flow conditions, but underestimated the maximum temperatures by as much as 10 K at higher powers.

Limits were computed for the concentric flow model and for Cases 1 and 2. For the eccentric cases at 0.000646 m^3/s, the FLOPA code predicted that flow reversal would occur in one subchannel of the outer channel. FLOPA did not predict that flow reversal would occur prior to measured thermal excursion conditions at 0.00097 m^3/s.

Figure 7 illustrates the comparisons between measured conditions and calculated limits. The powers where unstable flow and flow reversal were first detected in the outer channel are noted, as are the powers where the maximum measured wall temperature first exceeded the fluid saturation temperature and where thermal excursions took place. The onsets of unstable flow, flow reversal, and thermal excursion occurred somewhere between these power levels and the next lower powers. The powers at which the maximum wall temperature equaled the saturation temperature were determined by linear interpolation of measurements at different test conditions.

Figure 7 compares these measured conditions with calculated limits using the wall saturation temperature criterion with different multipliers and with the previously determined Stanton number limit for a LOPA (see Equation 2). Comparisons are made for the wall saturation temperature criterion with the concentric and Case 1 and 2 eccentric flow models.

Linear interpolations were performed to determine multipliers to match measured and calculated powers at which the maximum wall temperature first exceeded the saturation temperature. The powers for these interpolations were calculated based on both the concentric flow channel model and the Case 1 eccentric flow model.

The multiplier for the wall saturation temperature criterion was based on the calculated results for concentric channels. Table 3 lists the results of these calculations. A wall saturation temperature criterion multiplier of 0.885 was recommended for calculating LOPA ECS addition phase limits. For the four tests analyzed in this report, this is the average value of the multiplier that matches measured and calculated powers at which the maximum wall temperature equals the saturation temperature. The margin between the limiting power for this value of the multiplier and the power at thermal excursion is between 15% and 20%.

Table 4 gives the effect of the wall saturation temperature multiplier on the limit for the ECS addition phase of the LOPA. According to the results in this table, a multiplier of 0.885 would yield a limiting power that is 37% of the limiting power for previous long-term reactor operations.

Transition between High and Low Flow Rate Criterion

The wall saturation temperature criterion is applicable only at low flow rates, where the tests have demonstrated that buoyancy-induced flow reversal can occur prior to the onset of flow instability. A Stanton number criterion was retained for use at higher flow rates, where buoyancy effects are not significant. The wall saturation temperature criterion was restricted to Peclet numbers below 70,000, where the Peclet number is defined by

$$Pe = \frac{D_h c_p G}{k} \qquad (4)$$

This value corresponds to the lowest Peclet number tested in benchmarking the LOCA-FI Stanton number criterion (St = 0.00455) [8] and is considerably above the value where buoyancy effects are significant.

The structure of the FLOPA limits code made it easier to specify when to apply the wall saturation temperature criterion in terms of a transient time instead of a Peclet number. Figure 8 depicts variations in the Peclet numbers in the limiting subchannel (located outside the outer fuel tube of the fuel assembly) for a typical LOPA transient. As shown

in this figure, the wall saturation temperature criterion takes effect 344 seconds after the start of the LOPA transient, when the DC pump motors flood and the DC pumps begin to coast down. The Peclet number at this time is approximately 70,000.

Conclusion

Based on the results of the SPRIHTE rig tests, a wall saturation temperature criterion was recommended for calculating the limit for the ECS addition phase of the LOPA. An analysis of preliminary test results was used to set this limit criterion. This analysis shows that the maximum wall temperature inside the assembly should not exceed 0.878 times the local fluid saturation temperature in degrees C. Use of the criterion with this multiplier set the LOPA core power limit at 37% of the limiting power for previous long-term reactor operations.

References

[1] B. J. Hardy and A. M. White, "A Probabilistic Method for Determining Effluent Temperature Limits for Flow Instability in SRS Reactors (U)," Westinghouse Savannah River Company Report, WSRC-TM-90-5 (DPSTM-160) (1990).

[2] P. Saha and N. Zuber, "Point of Net Vapor Generation and Vapor Void Fraction in Subcooled Boiling," Proceedings, 5th International Heat Transfer Conference, Tokyo, Japan, Vol. 4 (1974).

[3] P. K. Paul and K. L. Barbour, "DEGB LOPA Limit Recommendation for the K-14.1 Subcycle," Westinghouse Savannah River Company Report, WSRC-RP-91-444, Rev. 1 (1992).

[4] B. S. Johnston, "Limits for Stable Downward Flow in a Single Heated Annulus at LOPA Conditions," Westinghouse Savannah River Company Report, NES-ETH-910190 (1991).

[5] H. N. Guerrero and C. M. Hart, "SPRIHTE Prototypic Assembly LOPA Test Data Report," Westinghouse Savannah River Company Report, WSRC-TR-93-012 (1993).

[6] S. E. Aleman, "Documentation of FLOWTRAN for Loss of Pumping Accident Analyses (FLOPA)," Westinghouse Savannah River Company Report, NES-CDG-910133 (1991).

[7] S. E. Aleman, M. V. Gregory, L. L. Hamm, L. D. Koffman, R. E. Pevey, W. H. Reed, and F. G. Smith, "FLOWTRAN: An Algorithm for Describing the Thermal-Hydraulic Behavior of SRP Assemblies (U)," Westinghouse Savannah River Company Report, DPSTM-140, Rev. 0 (1989).

[8] J. A. Block, C. J. Crowley, F. X. Dolan, R. G. Sam, and B. H. Stoedefalke, "Nucleate Boiling Pressure Drop in an Annulus," Creare, Inc., Technical Note, TN-499, Vol. 1 (1990).

Nomenclature

A_x	cross-sectional flow area
c_p	fluid heat capacity
D_h	hydraulic diameter of coolant channel
G	coolant mass flux
h	wall heat transfer coefficient
k	fluid thermal conductivity
Pe	Peclet number
q''	surface heat flux
St	Stanton number
T_{bulk}	bulk coolant temperature
T_{sat}	fluid saturation temperature
μ	fluid viscosity
ρ	fluid density

Table 1. Comparison of Savannah River Fuel Assembly Design and SPRIHTE Rig As-Built Dimensions

Dimension	Fuel Assembly Design	SPRIHTE Min.	SPRIHTE Max.
Inner Target OD	0.04039	0.04039	0.04041
Inner Target Rib Circle	0.04989	0.04983	0.04999
Inner Heater ID	0.05067	0.05057	0.05065
Inner Heater OD	0.05977	0.05977	0.05982
Inner Heater Rib Circle	0.07272	0.07264	0.07282
Outer Heater ID	0.07346	0.07353	0.07363
Outer Heater OD	0.08128	0.08136	0.08141
Outer Target Rib Circle	0.08204	0.08197	0.08242
Outer Target ID	0.08992	0.08954	0.08999
Distance from Inlet Plenum to Top of Fuel Assembly		1.72	
SPRIHTE Inner Heater Heated Length		3.76	
SPRIHTE Outer Heater Heated Length		3.91	
Fuel Assembly Design Overall Length		3.84	
Fuel Assembly Design Heated Length		3.78	

All dimensions are in m.

Table 2. Flow Conditions for Tests

Channel	Flow Rate (m^3/s)	Velocity (m/s)	Reynolds Number
Total	0.000647		
Inner	0.000134	0.19	3700
Middle	0.000308	0.22	6700
Outer	0.000205	0.18	4200
Total	0.00097		
Inner	0.000201	0.28	5500
Middle	0.000462	0.33	10000
Outer	0.000307	0.27	6300

Table 3. Measured Flow Reversal and Flow Instability Conditions

Flow Rate (m^3/s)	Inlet Temperature (K)	Condition	Power (W)
0.000647	298	Flow Reversal	106,800
		Wall Temp. = Sat'n Temp.*	130,800
		Thermal Excursion	160,600
0.000647	313	Unstable Flow	74,100
		Flow Reversal	80,700
		Wall Temp. = Sat'n Temp.*	92,400
		Thermal Excursion	127,100
0.00097	298	Unstable Flow	183,200
		Flow Reversal	197,300
		Wall Temp. = Sat'n Temp.*	199,100
		Thermal Excursion	231,400
0.00097	313	Unstable Flow	132,200
		Flow Reversal	151,800
		Wall Temp. = Sat'n Temp.*	164,100
		Thermal Excursion	188,200

*This power was estimated by linear interpolation of maximum measured wall temperatures at different test conditions.

Table 4. Comparison of Calculated and Measured Wall Saturation Temperatures

The wall saturation temperature criterion multipliers match measured and calculated powers at which the maximum wall temperatures first exceeded saturation temperatures, based on corrected wall temperature measurements.

Flow Rate (m^3/s)	Inlet Temperature (K)	Power when Max. Wall Temp. = Satn. Temp. (W)	Wall Saturation Temp. Criterion Multiplier
0.000647	298	130,800	0.881
0.000647	313	92,400	0.832
0.00097	298	199,100	0.905
0.00097	313	164,100	0.923
			0.885 = average

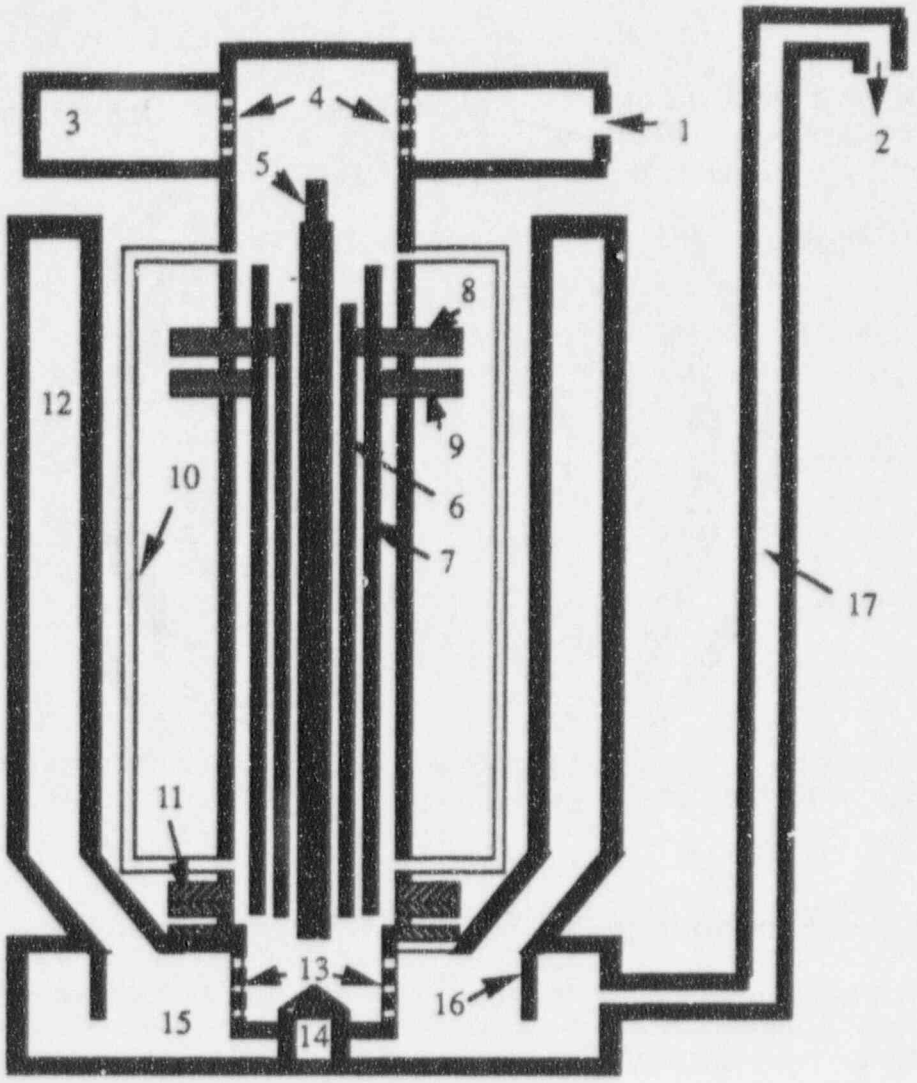

Figure 1. Test Apparatus Schematic. A key to figure captions follows.

1. Water Inlet from Flow Meters
2. Outlet to Catch Basin, Pump, and Heat Exchanger
3. Inlet Plenum
4. Perforated Tube Inlet to Heated Section
5. Center Pin (corresponds to Inner Target Tube)
6. Inner Heated Annulus
7. Outer Heated Annulus
8. Electrical Bus for Inner Heated Annulus
9. Electrical Bus for Outer Heated Annulus
10. Outer Bypass Tubes (one each side)
11. Bottom Flange
12. Unvented Air-Water Separators (one each side)
13. Perforated Tube Outlet from Heated Section
14. Monitor Pin
15. Outlet Plenum
16. Baffles
17. Outlet Standpipe

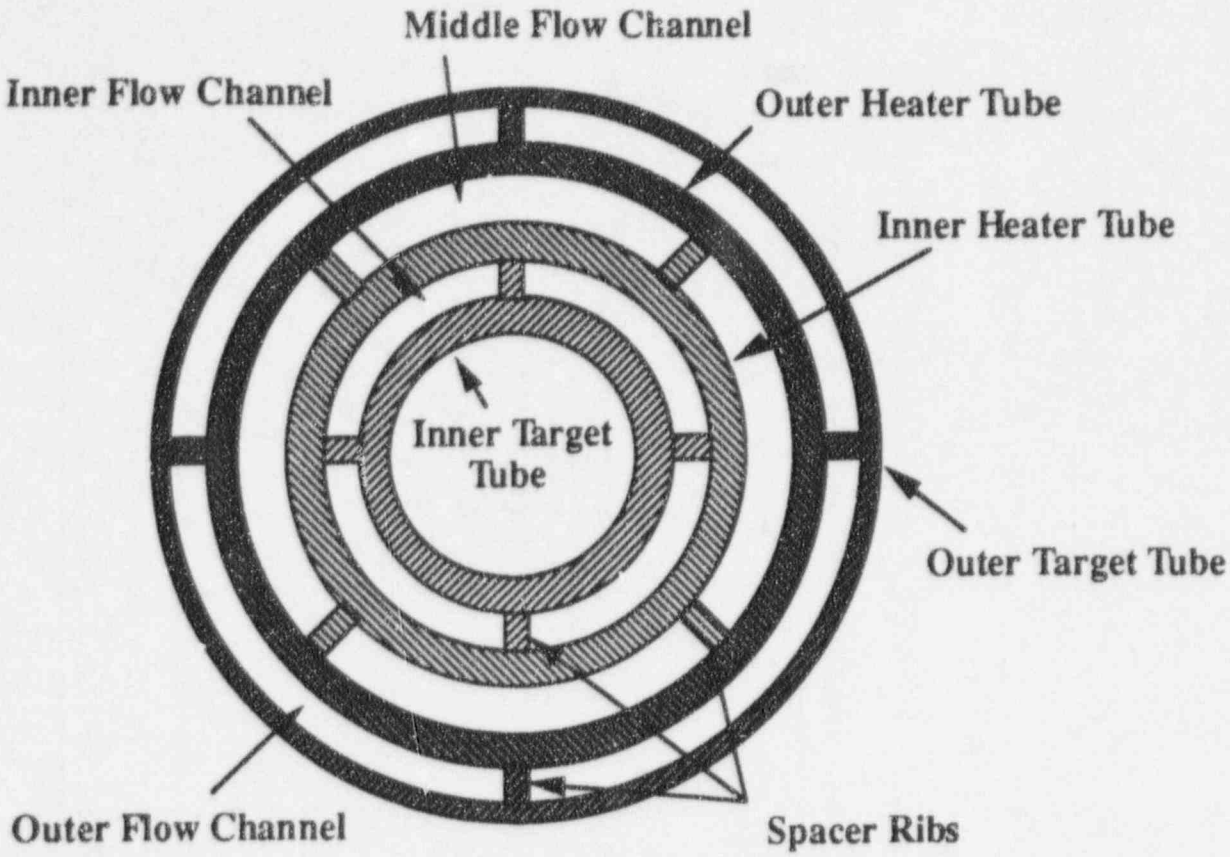

Figure 2. Cross-Sectional View of SPRIHTE Test Rig

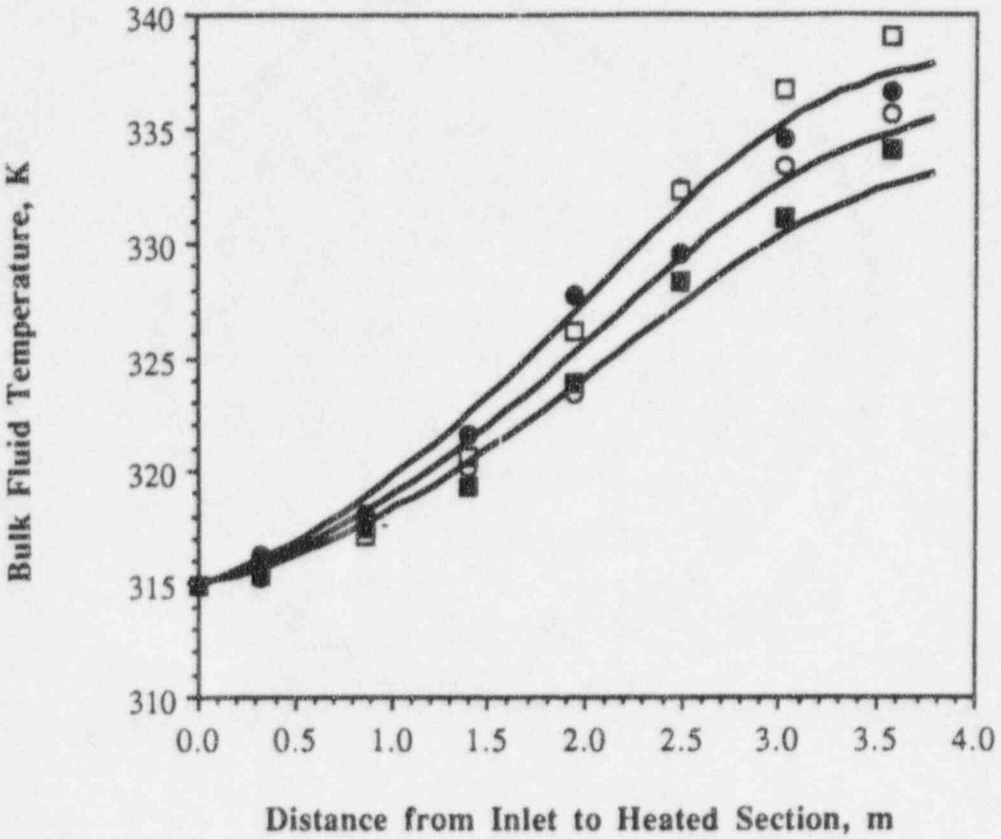

Figure 3. Comparison of Measured and Calculated Subchannel Fluid Temperatures for the Outer Channel at 0.00097 m^3/s, 40°C Inlet, 78,000 W

Symbols represent bulk fluid temperature measurements for the four outer subchannels. Lines represent calculated fluid temperatures for these four subchannels. (Calculated temperature profiles for two or more subchannels may coincide because of assumed symmetries in the model.) No correspondence between calculated temperature profiles and specific subchannel measurements is implied.

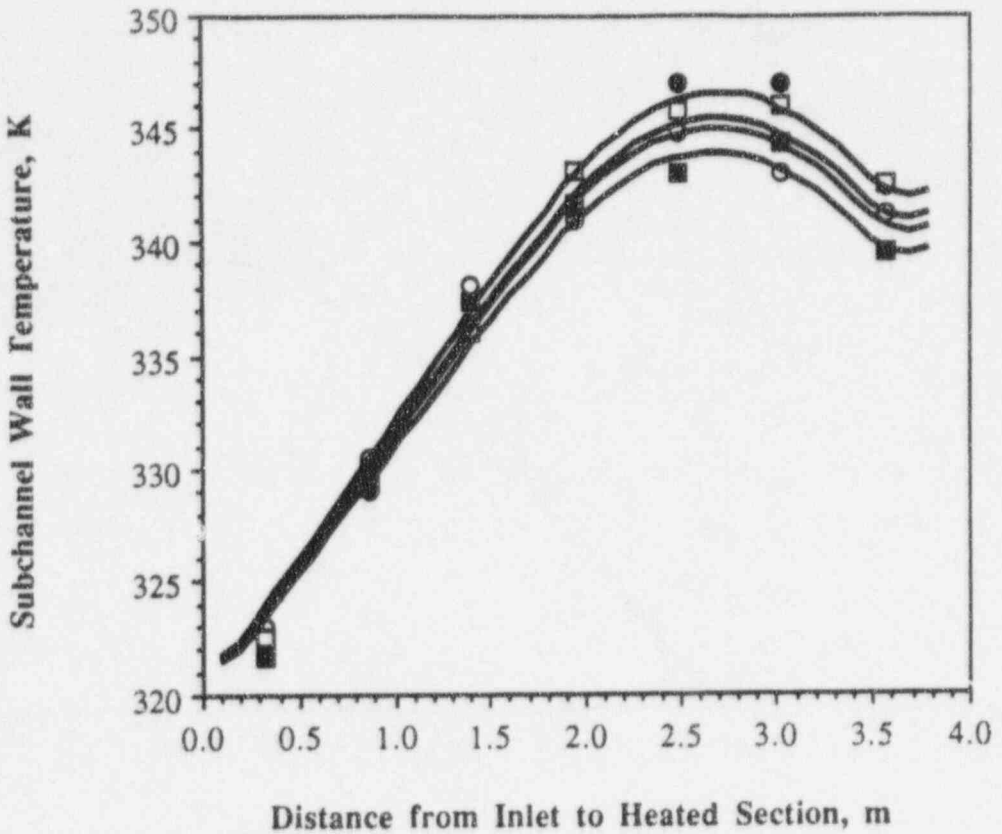

Figure 4. Comparison of Measured and Calculated Outer Heater Wall Temperatures at 0.00097 m^3/s, 40°C Inlet, 78,000 W

Symbols represent outer heater wall temperature measurements for the four subchannels. Lines represent calculated outer heater wall temperatures for the four subchannels. (Calculated temperature profiles for two or more subchannels may coincide because of assumed symmetries in the model.) No correspondence between calculated temperature profiles and specific subchannel measurements is implied.

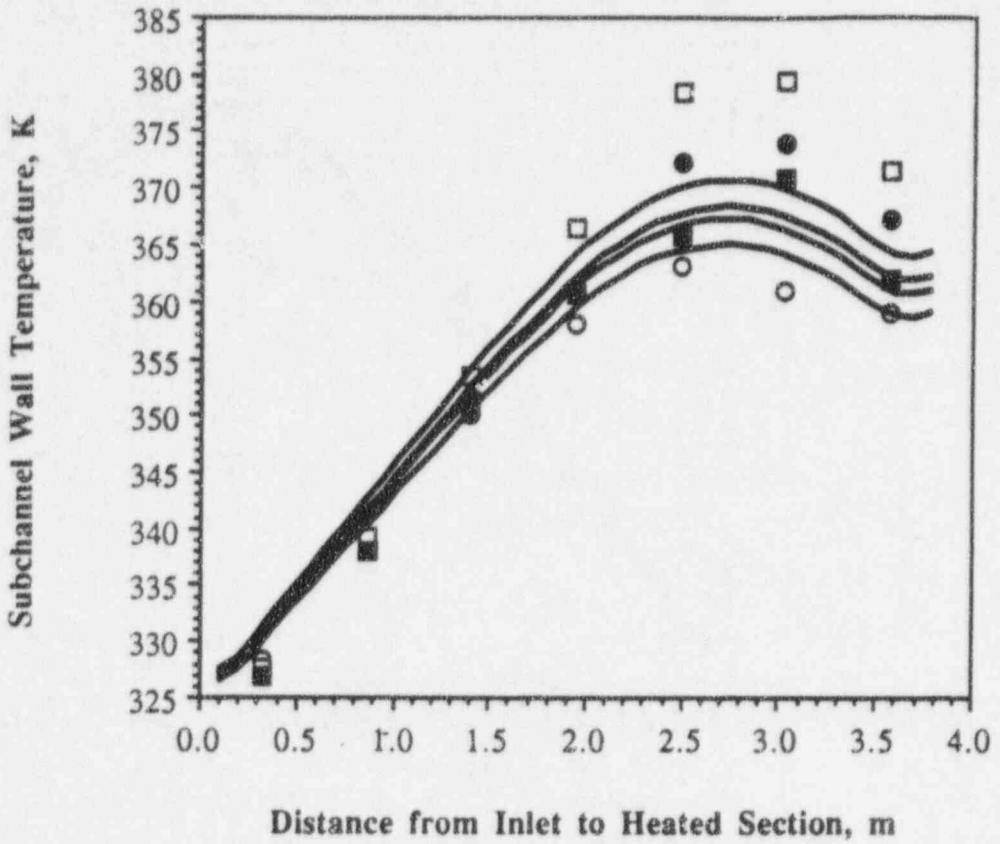

Figure 5. Comparison of Measured and Calculated Outer Heater Wall Temperatures at 0.00097 m^3/s, 313 K Inlet, 142,000 W

Symbols represent outer heater wall temperature measurements for the four subchannels. Lines represent calculated outer heater wall temperatures for the four subchannels. (Calculated temperature profiles for two or more subchannels may coincide because of assumed symmetries in the model.) No correspondence between calculated temperature profiles and specific subchannel measurements is implied.

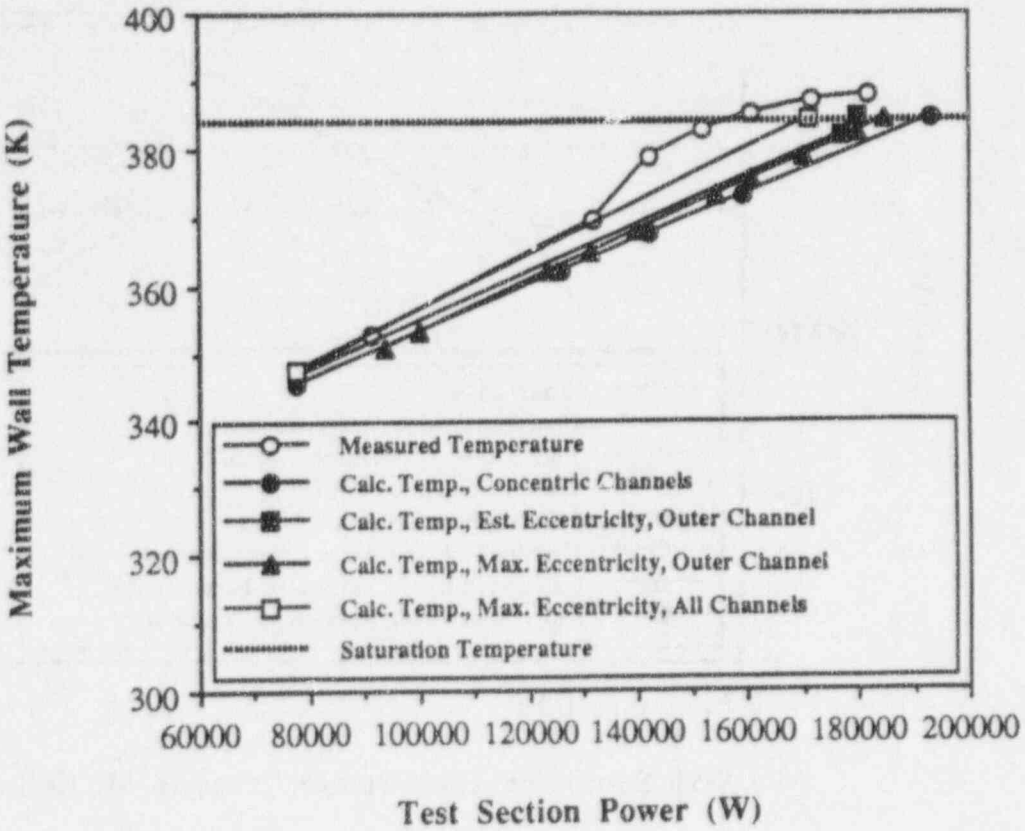

Figure 6. Comparison of Measured and Calculated Maximum Wall Temperatures for the SPRIHTE Tests at 0.00097 m^3/s and 313 K Inlet.

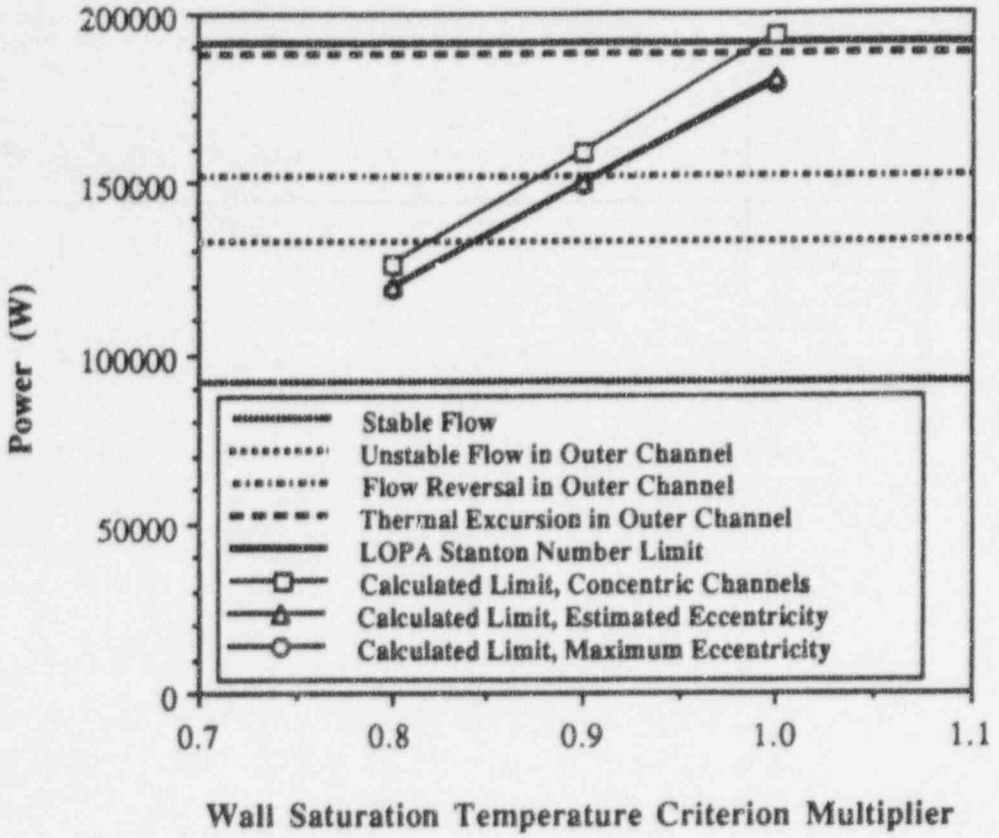

Figure 7. Comparison of Wall Saturation Temperature Criterion Limits with Measured Conditions for the SPRIHTE Tests at 0.00097 m^3/s and 313 K Inlet.

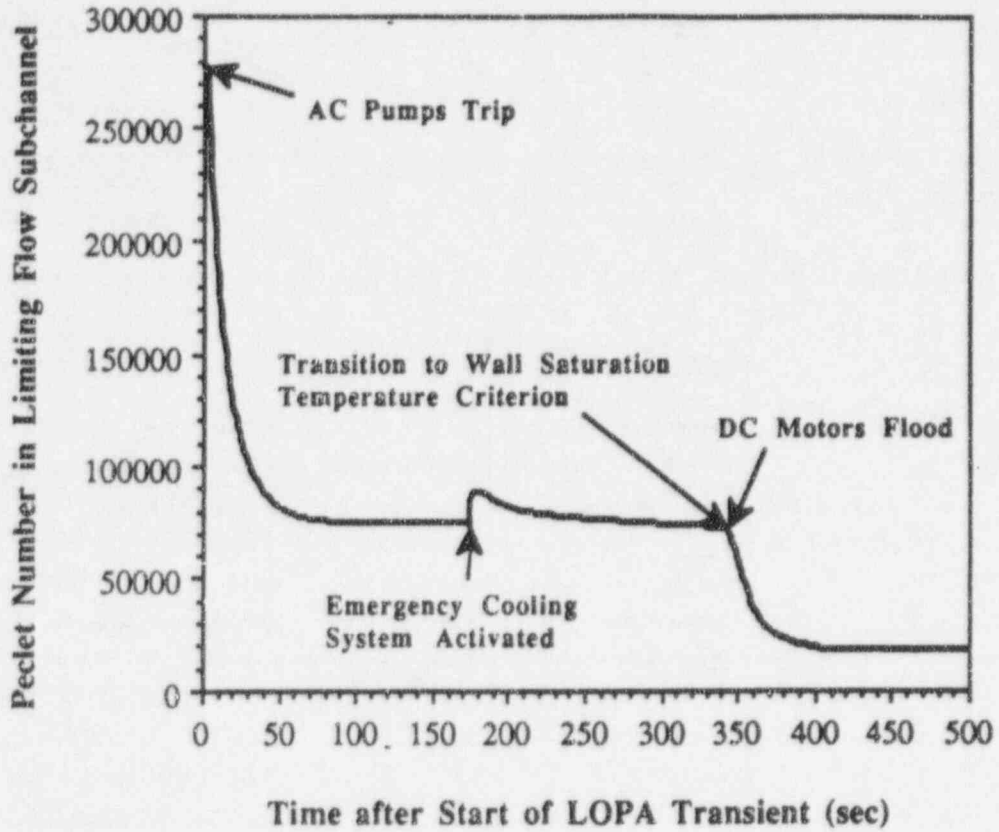

Figure 8. Variation of Peclet Numbers in the Limiting Subchannel during the LOPA Transient

An Experimental Investigation of the Post-CHF Enhancement Factor for a Prototypical ITER Divertor Plate with Water Coolant[1]

T. D. Marshall[a], R. D. Watson[b],
J. M. McDonald[b], D. L. Youchison[b]

[a]Department of Nuclear Engineering and Engineering Physics, Rensselaer Polytechnic Institute, Troy, New York 12180.

[b]Fusion Technology Department, Sandia National Laboratory, Albuquerque, New Mexico 87185.

ABSTRACT

In an off normal event, water-cooled copper divertor plates in the International Thermonuclear Experimental Reactor (ITER) may either experience heat loads beyond their design basis, or the normal heat loads may be accompanied by low coolant pressure and velocity. The purpose of this experiment was to illustrate that during one-sided heating, as in ITER, a copper divertor plate with the proper side wall thickness, at low system pressure and velocity can absorb without failing an incident heat flux, q_i, that significantly exceed the value, q_i^{CHF}, which is associated with local CHF at the wall of the coolant channel. The experiment was performed using a 30 kW electron beam test system for heating of a square cross-section divertor heat sink with a smooth circular channel of 7.6 mm diameter. The heated width, length, and wall thickness were 16, 40, and 3 mm, respectively. Stable surface temperatures were observed at incident heat fluxes greater than the local CHF point, presumably due to circumferential conduction around the thick tube walls when q_i^{CHF} was exceeded. The Post-CHF enhancement factor, η, is defined as the ratio of the incident burnout heat flux, q_i^{BO}, to q_i^{CHF}. For this experiment with water at inlet conditions of 70 °C, 1 m/s, and 1 MPa, q_i^{CHF} and q_i^{BO} were 600 and 1100 W/cm^2, respectively, which gave an η of 1.8.

1.0 INTRODUCTION

The next generation fusion reactor project is the International Thermonuclear Experimental Reactor (ITER), which is a joint effort by the U.S., Japan, European Community, and the Russian Federation to design, build, and operate a 1500 MW fusion machine. In fusion tokamak reactors, such as ITER, the plasma facing components (PFC) are exposed to one-sided heat fluxes that are created by energetically charged particles and photons striking the PFC surfaces. The divertor modules in a tokamak are used to remove exhaust from the burning plasma and, as such, receive the highest heat loads of the PFCs. To increase the heat removal capability of the divertor, the device may have several individual coolant channels, defined here as divertor plates, that run parallel to each other and are assembled as a unit. The divertor plates always have a protective armor, such as carbon fiber composite, beryllium, or tungsten tiles, to limit plasma damage to the copper heat sink.

During normal operations, ITER PFCs are expected to absorb an average heat load of 200 W/cm^2

[1]This work performed at Sandia National Laboratories is supported by the U.S. Department of Energy under Contract DE-AC04-76DP00789.

while the divertor plates will be designed to absorb average heat loads of 500 W/cm^2 [1]. To meet such design specifications, the divertor plates will be actively cooled by highly subcooled water (50 - 100 °C inlet) at moderate to high pressure (1 - 4 MPa) and velocity (5 - 10 m/s). It has been estimated that during an off-normal event, such as Edge Localized Modes (ELMS), the divertor plates may experience heat loads up to 2000 W/cm^2 for 10 seconds [2]. During the off-normal event, it is also possible that there may be decreases in the water coolant pressure and/or velocity. Thus, the reactor's cooling system needs to be designed to withstand the most probable and highest heat loads from the plasma, with a substantial margin of safety against heat sink burnout.

Traditional design practices suggest that tube destruction by melting will proceed rapidly when the local wall Critical Heat Flux (CHF) limit is reached. However, theoretical and experimental research by Tanchuk [3][4] at the Efremov Institute suggests that it is possible for a divertor plate's incident heat flux to exceed its local CHF, by as much as 80%, before causing global destruction of the plate. The region of stable surface temperatures beyond the local CHF has been termed by Tanchuk [4] as the "Post-CHF regime." According to Tanchuk's work, the phenomenon is a function of three variables: one-sided heating; tube wall thickness; and low values of coolant pressure, velocity, and degree of subcooling.

Boyd [5] has suggested that all regions of the boiling curve simultaneously exist within the coolant channel during one-sided heating with moderate to high surface heat fluxes. Figure 1 is a graphical representation of Boyd's [5] hypothesis. The most important observation in Figure 1 is that the vapor region, θ_{vapor}, is a function of the incident heat flux, q_i. For low values of q_i, where $q_i \le q_i^{CHF}$ and $\theta_{vapor} = 0$, only subcooled nucleate boiling and single phase heat transfer occur in the channel. As q_i exceeds q_i^{CHF}, θ_{vapor} increases and similarly increases the area of poor heat transfer due to film boiling. The Post-CHF vapor region, $\theta_{vapor} > 0$, continues to grow larger until channel failure via melting results because the vapor region has isolated too much of the tube wall to allow sufficient heat removal.

The methodology and nomenclature of Schlosser and Boscary [6] are used in this paper for the discussions on heat fluxes. Schlosser's [6] Incident Burnout Heat Flux (IBHF) and Wall Critical Heat Flux (WCHF) are equivalent to our q_i^{BO} and q_w^{CHF}, respectively. For a divertor plate with a square cross-section and circular coolant channel, the incident heat flux, q_i, differs from the heat flux at the tube wall-to-water interface, q_w, due to a geometric focusing effect. The difference arises from the fact that q_i is focused into a smaller heated area (upper region) at the tube wall-to-water interface. This results in q_w being greater than the corresponding q_i by typically 50%. Accordingly, it is paramount to specify the reference location (wall or surface) when discussing heat fluxes, since comparison should be made only between heat fluxes at the same location. In this paper, all comparisons are made at the heated, i.e., "incident," surface, as will be indicated by the subscript "i" for incident.

In the present problem, an experimental investigation of the Post-CHF phenomenon has been performed using a prototypical divertor plate cooled with water at low velocity, pressure, and moderate temperature. The experimental procedure was chosen to demonstrate stable temperatures beyond q_i^{CHF}.

2.0 EXPERIMENTAL PROCEDURE

2.1 Electron Beam Apparatus

The experiment was performed with the use of the Sandia Electron Beam Test System (EBTS), shown in Figure 2 [7]. The electron beam gun, rated at 30 kW (30 kV voltage at 1 A current), is mounted atop a 700 mm diameter by 1000 mm length stainless steel vacuum chamber. Electron beam heating is applied only to the top surface of the target, and this one-sided heating pattern simulates the heat fluxes received by PFCs. Pulse duration for the beam may be adjusted from two milliseconds to continuous irradiation of the target. Typical operating conditions are 25 kV acceleration voltage with a rise time of 1 milliseconds in a chamber pressure of 130 Pascal. At the specified acceleration voltage, the electrons have an approximate penetration depth of 1 micron in copper, which produces what is essentially a surface heat flux. For the experiment, the beam operated with a beam diameter of about 5 mm (full width, half maximum) and was rastered over a length of 40 mm at a frequency of 10 kHz. All beam control functions and data acquisition were processed by a VAX computer system.

2.2 Standard Diagnostics

Standard diagnostic equipment for the EBTS included infrared and video cameras, which were recorded with a standard video cassette recorder. For water calorimetry, differential temperature (ΔT) blocks and flow meters were logged 2 to 3 times per second during a beam pulse. Other routinely logged diagnostics were: one- and two-color pyrometers, for spot surface temperatures; Type-K thermocouples, for spot temperatures and infrared calibration; and pressure transducers, for measuring water inlet and exit pressures. Table 1 presents the operating ranges of the diagnostic sensors/transducers. All data were logged to the computer system via analog signals from the sensors/transducers, converted to digital signals by the data acquisition system, and then stored on the computer system disk drive. Estimated accuracy, the zeroth order error [8], of the diagnostics is shown in Table 2.

2.3 EBTS Water Loop

The EBTS water flow loop was designed to minimize the difficulties and inaccuracies due to phenomena such as flow instabilities and coolant electrical conductivity when measuring target CHF. The system cooling water is supplied by a deionized water loop, which has a maximum loop performance of 6.5 MPa pressure, 250 °C temperature, and 16 l/s flow rate. The schematic shown in Figure 3 describes the EBTS water flow loop. Tap water, at 0.41 MPa and 20 °C, is passed through degassing and deionizing particulate beds (not shown in the figure). After exiting the deionizing beds, the water has a resistivity greater than 18 mega ohm-cm. Immediately downstream of the deionizing beds, the water flows past an injection point where chemical streams can be added to maintain water pH. A turbine flowmeter is installed at the junction to measure the injected fluid's flow rate. Beyond the injection point the coolant passes through a quadraplex positive displacement pump system with each pump displaced in relative phase by ninety degrees. Since each pump's discharge is sinusoidal and out of phase by ninety degrees, the flow rate is relatively constant (±2.5%) with respect to time.

Table 1: Operating Ranges of EBTS Diagnostics

Diagnostics		Units	Range
ΔT blocks		°C	0 - 121
flow meter		m/s	0 - 10
1-color pyrometers	low λ	°C	150 - 550
	low-range	°C	300 - 1300
	mid-range	°C	1000 - 3000
	high-range	°C	3000 - 6000
2-color pyrometers	low-range	°C	700 - 1400
	high-range	°C	1500 - 3500
pressure transducers		MPa	0 - 7

Table 2: Accuracy of EBTS Diagnostics

Variable	Unit	Accuracy
Velocity	m/s	±0.1
Infrared camera surface temperature	°C	±5
Water temperature rise through heated section	°C	±0.1
Inlet/Exit Pressure	MPa	±0.01
Inlet/Exit Temperature	°C	±2
Thermocouples	°C	±2

Before the water enters the test section, steps are taken to assure that the water is fully mixed and that the flow is fully developed. The water first flows through a mixing chamber and then an extension tube (with a length-to-diameter ratio greater than 100). The water then flows through a turbine flowmeter and finally through the test section with bulk fluid temperatures upstream and downstream of the test section being measured by the ΔT blocks. In addition to the bulk temperatures, the upstream and downstream static pressures are measured using differential membrane pressure transducers.

2.4 Target Geometry

The experimental divertor plate is shown in Figures 4 and 5. The plate is an one piece assembly of oxygen free high conductivity (OFHC) copper bar stock and tubing. The square bar stock has a

length of 133.4 mm and a 15.7 mm by 15.7 mm square cross-section. A circular coolant channel of diameter 7.5 mm was axially, center drilled through the bar stock, see Figure 5. The bar stock's coolant channel entrance and exit were 3.175 mm counterbored to allow a slip fit of the 98.4 mm long copper tubes {9.5 mm (OD), 7.5 mm (ID)}, which were brazed in place and used to attach the plate to the EBTS water loop. On the two sides of the mockup are six (three each side) 13 mm long grooves, each with a 1 mm by 1 mm square cross-section. These grooves (positioned one centimeter from either end and in the center of the mockup) house the wires for the 0.5 mm Type-K thermocouples to prevent them from being damaged by the electron beam. As shown in Figure 5, the thermocouple sensor tips are mounted 0.5 mm from the top surface (heated surface) of the plate. The thermocouple wires are held in place by peening them against the wire channels in the sidewall.

The mockup has a total length of 133.4 mm, but the actual heated length was 40 mm. The heated length of the top surface is scribed on the mockup so that the heated length ends five millimeters beyond the two center thermocouples (TC2 and TC5), refer to Figure 6. Prior CHF experiments performed on the EBTS has shown that burnout of the target typically occurs just prior to the heated length exit. By having the heated length end five millimeters beyond the thermocouples (Figure 6), it was believed that the optical pyrometers should be looking at the most likely spot of burnout [9].

It has been noted by other experimenters [6], that the emissivity of copper divertor mockups changes as a result of electron beam heating and these changes directly influence the calibration of the optical pyrometers. To counteract this problem, we decided to create a highly uniform and emissive heated surface with the hope that this preparation would limit the emissivity changes during the testing campaign. To increase the copper emissivity, the top surface of the plate was sandblasted with 25 micron Al_2O_3 beads at 4.1 to 5.5 MPa for approximately 15 seconds. The mockup was then baked in air at 300 °C for two hours and placed in a relative humidity of 100% at 70 °C for 3 days. This procedure created an uniform layer of oxidation that increased the copper surface emissivity from less than 0.1 to approximately 0.4. The increased emissivity of the heated surface area correspondingly increased the efficiency of the low-wavelength pyrometer, and made a more uniformly emitting surface for the IR camera.

The plate was subsequently helium leak tested and passed a leak detection rate of 3×10^{-8} atm-cm^3/s at a vacuum of 1×10^{-2} Pascal. A dynamic water pressure test inside the EBTS chamber was also performed and the plate withstood a pressure of 1.38 MPa without visible signs of a leak or loss of chamber vacuum.

2.5 Test Conditions

Simulated ITER heat loads were applied to the divertor plate with the rastered electron beam. A uniform heat flux distribution across the width of the plate was established by achieving similar temperature readings by the two thermocouples (TC2 and TC5), see Figure 6, mounted on either sides of the plate in the heated area. Uniform heating in the axial direction was accomplished by using the thermal profile capabilities of the IR camera. Conditions of steady state heating were determined by analysis of the water calorimetry response for the electron beam pulses.

Water calorimetry calculations were performed using the ΔT blocks, one block in the water inlet tubing and the other block in the water outlet tubing. Each block has a thermocouple pile of

approximately twenty Type-T thermocouples that are positioned in the flow path of the water. The ΔT block circuitry averages the water temperature in the block's channel and calculates the absorbed power in the water using the equation: $Q = \dot{m} * c_p * \Delta T$. The ΔT blocks are not vacuum compatible and thus are mounted in the 25.4 mm diameter water loop tubing, approximately 300 mm outside the vacuum chamber. Review of the water calorimetry data during the initial stages of the experiment revealed that the chosen 90 second electron beam pulses were not giving steady state conditions, although bulk thermocouples TC2 and TC5 reached steady state temperatures in approximately 10 seconds. Several beam pulses were taken at a fixed power setting, but with increasing pulse lengths in order to determine a suitable pulse length. The calorimetry data for these pulses were reviewed, and pulse lengths greater than 180 seconds displayed the best steady state heating plots for the ΔT blocks thermal response. The improvement of the calorimetry data with longer pulse lengths is a result of the tubing between the divertor plate and ΔT block having sufficient time to achieve thermal equilibrium.

During the beam pulses, flow velocity through the plate was held constant at 1 ± 0.02 m/s. The inlet pressure to the divertor plate was set to 1 ± 0.01 MPa and the exit pressure allowed to fluctuate. Entrance water temperature of 70 ± 2 °C, providing an inlet subcooling of 110 °C, was used for all beam pulses. Typical exit subcooling during the experimental campaign was 96 °C, EBTS Shot 144288: T_{in} = 70 °C, V_{in} = 1 m/s, P_{in} = 1 MPa, and q_i = 924 W/cm^2.

The experimental procedure was chosen to demonstrate stable plate temperatures beyond q_i^{CHF}. Low power electron beam pulses were initially taken, with each subsequent pulse being a reasonable increase in power over the previous shot. The idea was to gradually step up the boiling curve so that the experimental data illustrated all regimes of the curve. A pressure of 100 Pascal was maintained in the vacuum chamber during the electron beam pulses, with each pulse being adjusted in the x-y (width-length) direction during the initial seconds of the pulse to insure an uniform heating pattern in the heated area. For all of the pulses, TC2 and TC5 were programmed to immediately shut off the electron beam upon a measured temperature of 750 °C; the spot pyrometer was programmed to immediately shut off the electron beam upon a measured temperature of 1000 °C. The higher pyrometer setting was used because the vapor blanket that forms in the center of the tube wall-water interface at q_i^{CHF} causes higher surface temperatures in the center of the heated width than at the corner edges (refer to Figure 1). This inverted temperature profile across the heated surface was observed experimentally with the IR camera at the higher incident heat flux levels.

3.0 EXPERIMENTAL RESULTS

3.1 Post-Critical Heat Flux Regime

In the experiment, q_i was step-wise increased until surface melting occurred. Surprisingly, although there was surface melting, the divertor plate did not develop a water leak. Nevertheless, the q_i that caused surface melting was defined as the incident burnout heat flux, q_i^{BO}. Figure 7 is a plot of the thermocouple temperature versus incident heat flux, q_i. In the figure, error bars for q_i, ± 10 %, and thermocouple temperature, ± 2 °C, have been added. The different regions of the boiling curve have also been identified on the plot. The data clearly shows the regions of single phase, fully developed nucleate boiling, and Post-CHF heat transfer. More importantly, the plot demonstrates that steady state surface temperatures were reached at incident heat fluxes beyond

q_i^{CHF}, providing direct evidence of the Post-CHF phenomenon.

Since the divertor plate was not intended to be destroyed in this experiment, true "burnout" was not achieved. However, it is believed that the q_i^{BO} measured in this experiment is very close to the true burnout heat flux for the specified inlet conditions. Electron beam pulse #144228 produced q_i^{BO} in which TC2 and TC5 measured a temperature of 750 °C and the pyrometer measured a temperature of 1000 °C. In Figure 7, q_i^{CHF} was determined as the inflection point in the data curve that follows fully developed nucleate boiling and indicates the beginning of the Post-CHF regime. This procedure gave a q_i^{CHF} of about 600 W/cm^2. The ratio of q_i^{BO}, 1100 W/cm^2, to q_i^{CHF}, 600 W/cm^2, (1100)/(800), gives a Post-CHF enhancement factor, η, of 1.8. In this case, the Post-CHF phenomenon allowed q_i^{CHF} to be exceeded by 80 % before melting the divertor plate's surface.

3.2 Error Analysis

The incident heat flux, q_i, during an electron beam pulse was calculated by dividing the steady-state water calorimetry data from the ΔT blocks by the heated area of the divertor plate. The accuracy of the incident heat flux calculations was determined using the methodology of Moffat [8]. The error in the water calorimetry was calculated as:

$$\frac{\delta Q}{Q} = \sqrt{\left(\frac{\delta \dot{m}}{\dot{m}}\right)^2 + \left(\frac{\delta \Delta T}{\Delta T}\right)^2} \qquad (1)$$

where $\dot{m}$ was replaced by the water velocity for first order approximations. Using the measurement accuracy data from Table 2 and the experimental inlet conditions, the following values were inserted into Equation 1: $\delta v/v$ = (0.02 m/s)/(1 m/s) and $\delta\Delta T/\Delta T$ = (0.1 °C)/(15 °C); which yielded an error of ± 2 % for the water calorimetry.

The error in the expected heated area measurement was calculated as:

$$\frac{\delta A}{A} = \sqrt{\left(\frac{\delta L_{heated}}{L_{heated}}\right)^2 + \left(\frac{\delta W_{heated}}{W_{heated}}\right)^2} \qquad (2)$$

The heated area for each pulse was estimated to be 624 mm^2 (40 mm heated length by 15.6 mm heated width). Graphite marks and scribes in the oxidation layer, both of which glowed brightly on the IR video during an electron beam pulse, were made on the divertor plate to help the EBTS operators setup the requested heated area. Since there was an intentional spillage of the electron beam beyond the width of the plate, there was very little uncertainty associated with the heated width (i.e., $\delta W_{heated} = 0$). However, determination of the heated length was not as precise so an uncertainty, δL_{heated}, of ± 4 mm was assumed. Using δW_{heated} = 0 mm and δL_{heated} = 4 mm in Equation 2 yielded an error of ± 10 % for the expected heated area.

The error in the calculated heat flux was calculated as:

$$\frac{\delta q_i}{q_i} = \sqrt{\left(\frac{\delta Q}{Q}\right)^2 + \left(\frac{\delta A}{A}\right)^2} \tag{3}$$

With a calculated accuracy of ± 10 % for the expected heated area and ± 2 % for the water calorimetry, Equation 3 yielded an error of ± 10 % in the calculated incident heat flux, q_i.

4.0 MODELING RESULTS

Steady-state temperature profiles for a two dimensional cross-section of the cooling channel were calculated using the finite element analysis code ABAQUS [10]. The mockup was meshed with eight-noded, isoparametric, quadrilateral elements (DC2D8) with 760 nodes and 200 elements, as shown in Figure 8. Heat transfer from the mockup to the coolant water via forced convection was computed by ABAQUS using a user supplied film subroutine, which calculated the heat transfer coefficient as a function of wall temperature. The film subroutine version used here contains the Sieder-Tate [11] correlation for single phase heat transfer and the Thom [12] correlation for fully developed nucleate boiling heat transfer. Currently there are no provisions in the subroutine to utilize the local CHF point or the Post-CHF heat transfer regime.

Figure 9 is a plot of temperature isocontours for the mockup, as calculated by ABAQUS with q_i equal to the experimental q_i^{CHF}, 600 W/cm^2, and inlet conditions of 70 °C, 1 m/s, and 1 MPa. Figure 9 also shows the wall heat flux distribution, q_w. From the figure, one sees that a uniform surface heat flux, q_i, 600 W/cm^2, essentially becomes a peaked wall heat flux, q_w, 789 W/cm^2. In Figure 9, one sees a peak copper temperature of 302 °C and a peak wall temperature of 237 °C. Figure 10 is a plot of wall temperature and q_w versus angle around the tube. As shown in the figure, the region of subcooled boiling was determined by ABAQUS to be $\theta \approx 100°$, which is essentially the entire upper half of the cooling channel.

We can define a heat flux peaking factor from the finite element analysis, FEPF, to be:

$$FEPF = \frac{q_w^{peak}}{q_w} \tag{4}$$

For this case, the FEPF is (789/600) = 1.3.

Recognizing that significant heat transfer beyond CHF occurs in the transition and film boiling regime, future modeling efforts will include adding the two features to the ABAQUS film subroutine. The Tong-75 correlation is generally considered to best agree (± 25%) with single sided heating CHF experimental data [13] and will be added to the ABAQUS film subroutine. The Post-CHF regime will be modeled by calculating the Leidenfrost point for the inlet conditions and then using a linear logarithmic interpolation from the wall temperature at local CHF to the wall temperature at the

Leidenfrost point. This modeling method, suggested by J. Gonzalez [4], has been studied by Groeneveld and Stewart [14][15], but not fitted to experimental data. Beyond the Leidenfrost point, the usual film boiling correlation by Berenson [16] will be used. Future modeling work will also include three dimensional finite element analyses, to account for axial conduction effects.

5.0 DISCUSSION

5.1 Temperature Measurements

Figure 7 shows the experimental data with an overlay of thermocouple temperature data points calculated by ABAQUS. It can be seen from the figure that there is very good agreement between the experimental and calculated thermocouple temperatures in the regions of single phase and fully developed nucleate boiling. However, near q_i^{CHF}, the calculated thermocouple temperatures begin to underpredict the experimental data and as the respective curves approach q_i^{BO}, their difference becomes quite substantial. The underprediction of the ABAQUS data can be attributed primarily to the inability of the ABAQUS film subroutine to recognize the local CHF and incorporate Post-CHF heat transfer behavior.

5.2 Critical Heat Flux

For comparison purposes, q_w^{CHF} was also calculated using the Tong-75 CHF correlation [17] as programmed in a Sandia FORTRAN code [18]. For a heated length of 40 mm and water at inlet conditions of 1 m/s, 70 °C, and 1 MPa, the Tong-75 CHF correlation gave a q_w^{CHF} of 796 W/cm^2. Note that the Tong-75 correlation predicts the CHF at the wall, q_w^{CHF}, which according to Equation 4, must be divided by the FEPF, 1.3, to get the incident CHF, q_i^{CHF}. Thus, the predicted q_i^{CHF} is (796/1.3) = 612 W/cm^2, which is within 2% of the experimental q_i^{CHF}, 600 W/cm^2.

5.3 Post-Critical Heat Flux Regime

For thick walled copper tubes with one-sided surface heating and active water cooling, only limited Post-CHF information was found in the literature. To date, Tanchuk's [3][4] data and calculations are the most extensive in this area. Tanchuk [4] has reported that η is a function of three variables: one-sided heating; tube wall thickness; and low values of coolant pressure, velocity, and degree of subcooling. The contributions of each factor to the stable Post-CHF surface temperatures can be explained as follows. During one-side heating, there can be considerable circumferential conduction around the tube. The good circumferential conduction allows the continued removal of heat by the tube sidewalls after a vapor blanket forms in the uppermost region of the tube when $q_i > q_i^{CHF}$ and vapor $\theta_{vapor} > 0$. Without the significant circumferential conduction, as in a thin walled tube, the vapor blanket created by q_i^{CHF} would quickly isolate the tube wall from the coolant and cause tube failure from melting via the lack of heat transfer.

Since circumferential conduction is responsible for the stable temperatures in the Post-CHF regime, tube wall thickness and material thermal conductivity are as equally important to the phenomenon as one-sided heating. It would be logical to assume that maintaining a constant coolant channel and using ever thicker tube walls, would infinitely increase the enhancement of the Post-CHF phenomenon. However, too thick of a tube wall will increase the peaking factor, FEPF, and cause

premature plate failure since even moderate values of q_t are concentrated into larger values of q_w at the tube wall-water interface. In his Post-CHF experiments and predictions with divertor plates, Tanchuk showed that the optimum thickness is greater than 1 mm and less than 4 mm [3].

The final variables influencing the Post-CHF regime are the inlet water conditions. At high values of coolant pressure, velocity, and degree of subcooling, a cooling system is very efficient in its removal of heat from the divertor plates. While beneficial for high heat flux applications, this aggressiveness is a disadvantage in the Post-CHF regime since it competes with circumferential heat conduction; making very high heat fluxes necessary to cause substantial circumferential conduction. However, these high heat fluxes produce surface temperatures near the material's melting point so that the Post-CHF enhancement effect is very small.

CONCLUSIONS

The Post-CHF regime is an interesting phenomenon from both an academic perspective of the heat transfer region and as a potentially added safety factor for ITER operations. What the Post-CHF phenomenon shows is that steady state surface temperatures are possible even when q_t exceeds q_t^{CHF}. This is an exciting development because it contests the popular belief that exceeding q_t^{CHF} is immediately followed by mockup destruction, i.e., burnout. Accurate understanding of the Post-CHF regime will be important during off-normal scenarios for ITER such as a Loss of Flow Accident (LOFA) or Loss of Coolant Accident (LOCA) where the surface heat flux remain constant, but the water pressure and/or velocity decrease.

The Post-CHF effect is enhanced with low coolant pressure, velocity, subcooling, and thick tube walls. The degree of enhancement is characterized by a Post-CHF enhancement factor, η, defined as the ratio of q_t^{BO} to q_t^{CHF}. In this experiment an η of 1.8 was achieved, which indicates q_t^{CHF} was exceeded by 80% without failing the target divertor plate. Currently, there is no established method for predicting temperatures in the Post-CHF regime, but an initial attempt will be to use the methodology suggested by Groeneveld and Stewart. The methodology involves a linear logarithmic interpolation from the wall temperature at local CHF to the wall temperature at the Leidenfrost point. Beyond the Leidenfrost point, the usual film boiling correlation by Berenson will be used.

More experimental data is required to further define the range of the Post-CHF regime. Parametric studies should include varying the: tube wall thickness, heated length, and coolant velocity, pressure, and subcooling. In addition, the Post-CHF prediction methodology suggested in this paper requires experimental data for statistical fit and optimization purposes. Subsequent to the verification of the correlation, three dimensional FEA is required to account for axial conduction.

Acknowledgment

The authors would like to thank M. Araki of JAERI, J. Schlosser of CEA, and L. Cadwallader of INEL for their valuable reviews, comments, and discussions. L. Wold, K. Troncosa, and F. Bauer are also thanked for their assistance in producing and verifying the experimental data. The authors would especially like to thank M. Ulrickison of SNL, M. Cohen of DOE, and D. Steiner of Rensselaer for their respective support. Finally, the authors issue a most heartfelt thank you to K. Myers-Lovato, T. Myers, and P. Stevens for their invaluable contributions toward the completion of this paper.

NOMENCLATURE

Acronyms

ABAQUS	finite element code
EBTS	Sandia's 30 kW Electron Beam Test System
ELMS	edge localized modes
FEA	finite element analysis
FEPF	finite element peaking factor
ITER	International Thermonuclear Experimental Reactor
LOFA	loss of coolant accident
LOFA	loss of flow accident
OFHC	oxygen free high-conductivity copper
PFC	plasma facing component
TC2	left side thermocouple in the mockup heated area
TC5	right side thermocouple in the mockup heated area

Greek Symbols

δ	variation in measurement
η	Post-CHF enhancement factor
Δ	difference in temperature

Subscripts

i	incident, at the heated surface
w	wall, in contact with the coolant

Units

A	ampere
C	Celsius
cm	centimeter
kV	kilovolts
kW	kilowatts
l/s	liter per second
m/s	meter per second
m	meter
mm	millimeter
MPa	megaPascal
MW	megawatts
MW/m^2	megawatts per meter squared
Pa	Pascal

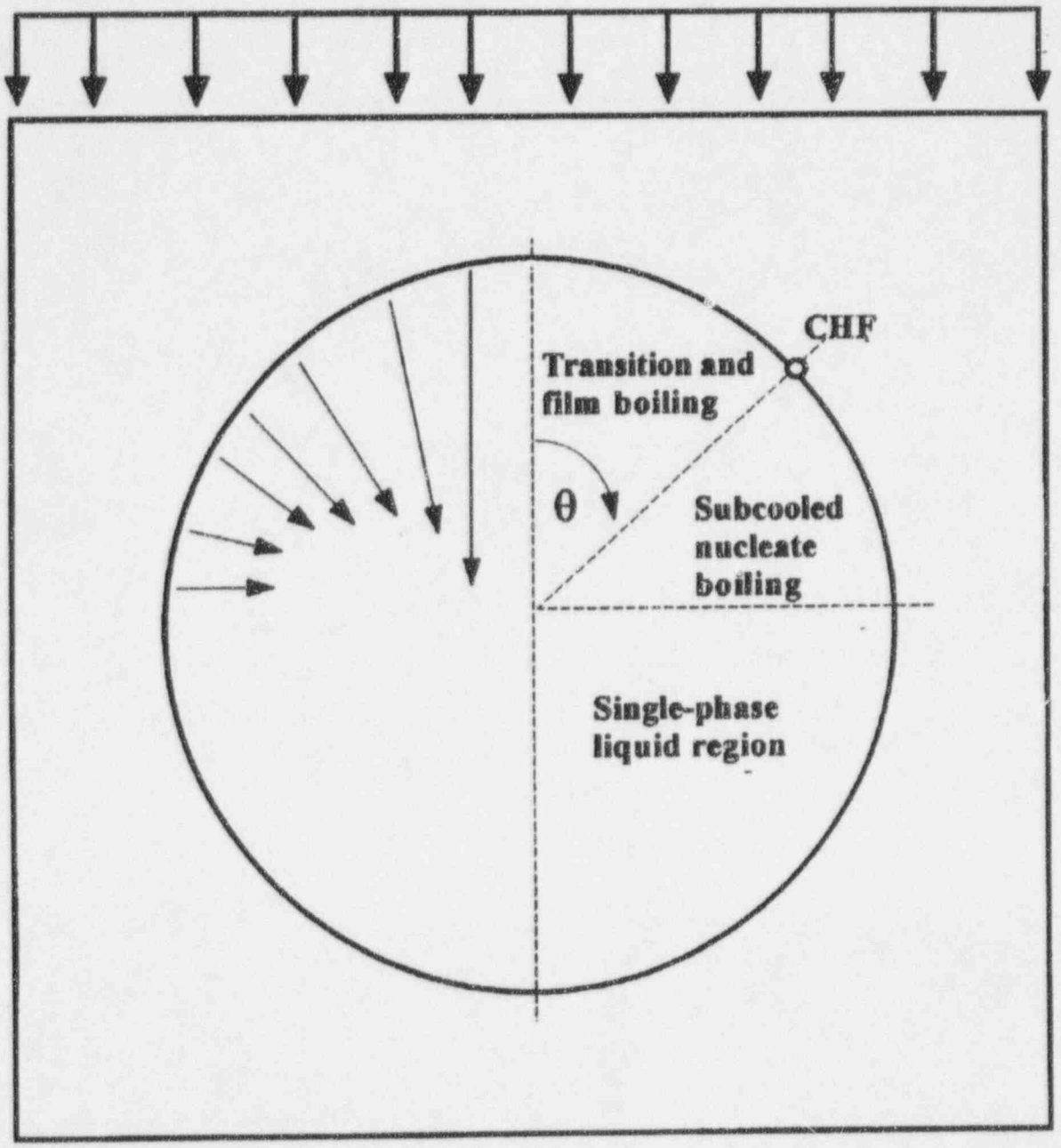

Figure 1: Heat Transfer Regions and Internal Heat Fluxes for One-Sided Heating

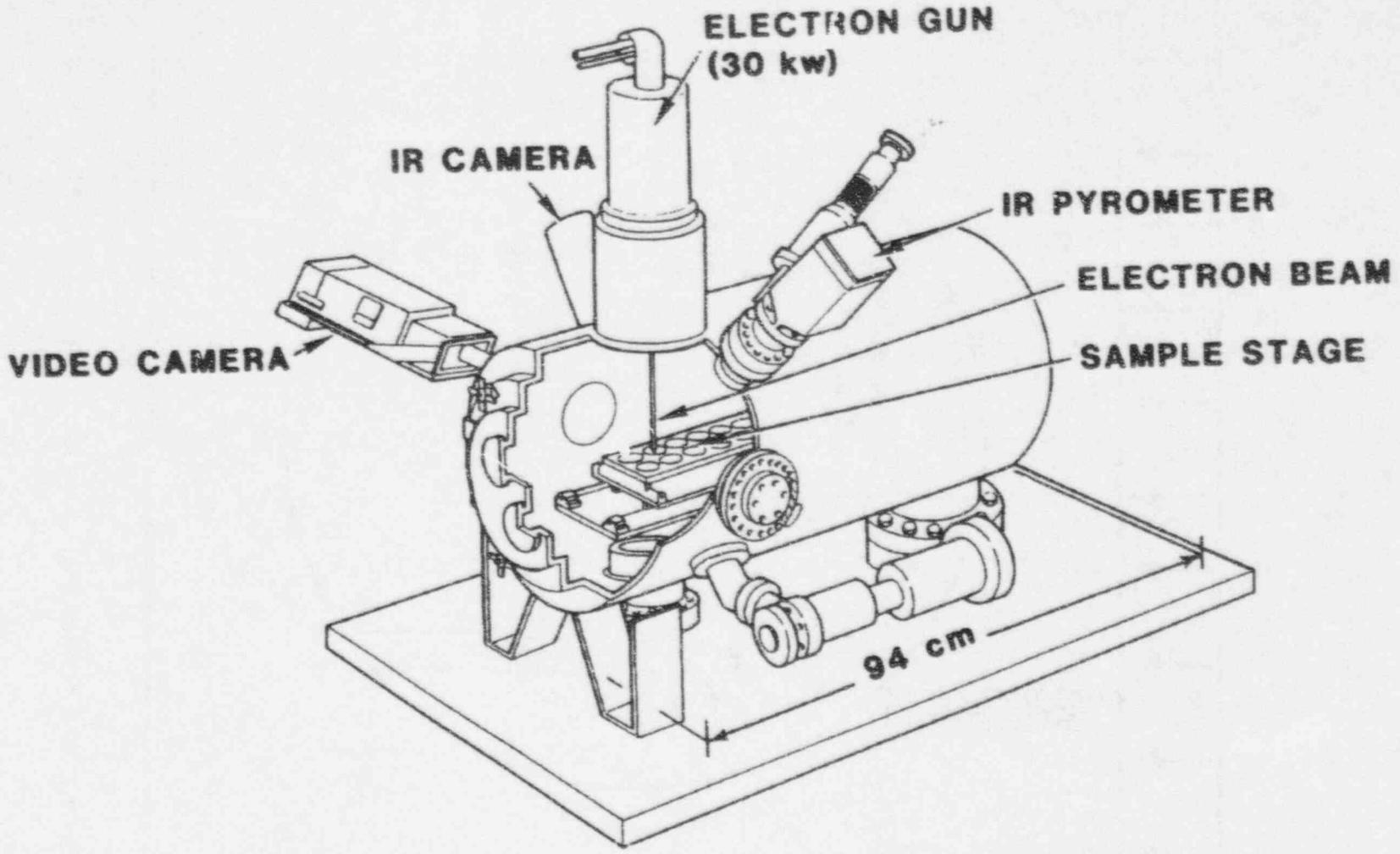

Sandia National Laboratories

Figure 2: Sandia 30 kW Electron Beam Test System

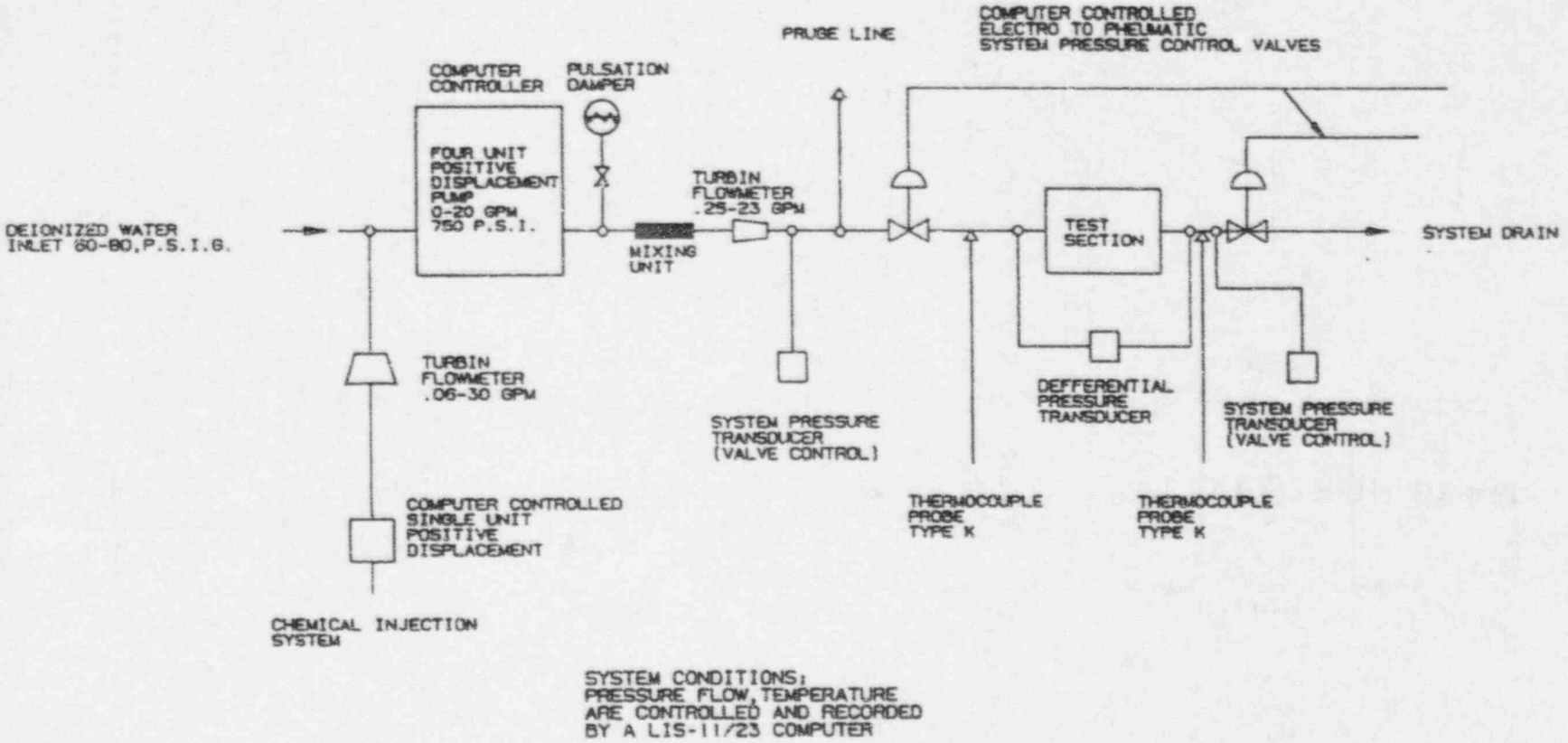

Figure 3: Schematic of Sandia EBTS Water Loop

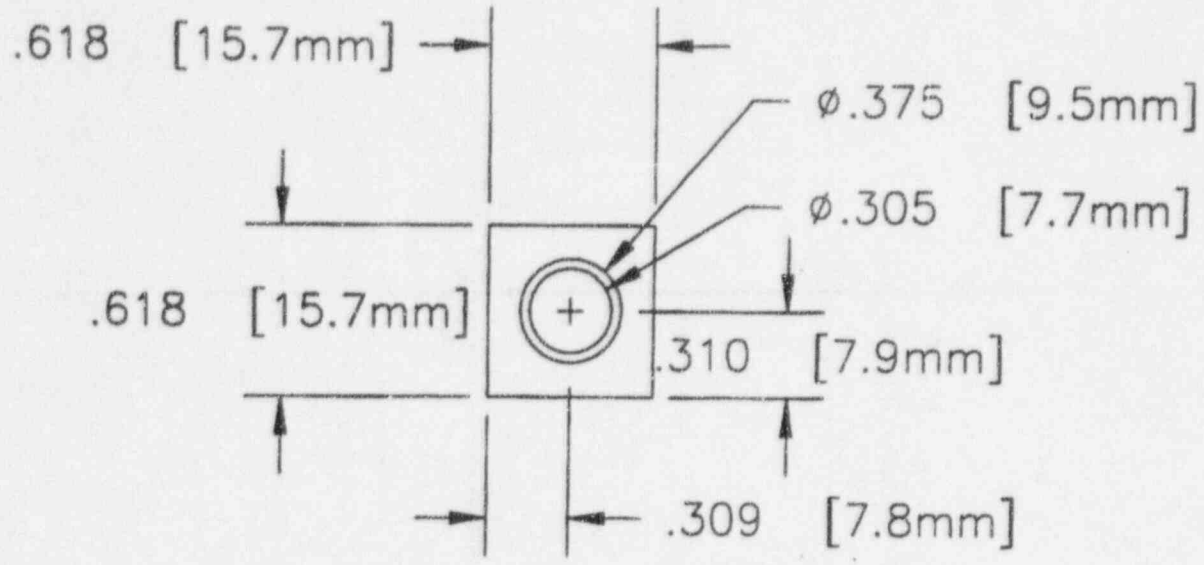

Figure 4: Face Dimensions of Mockup

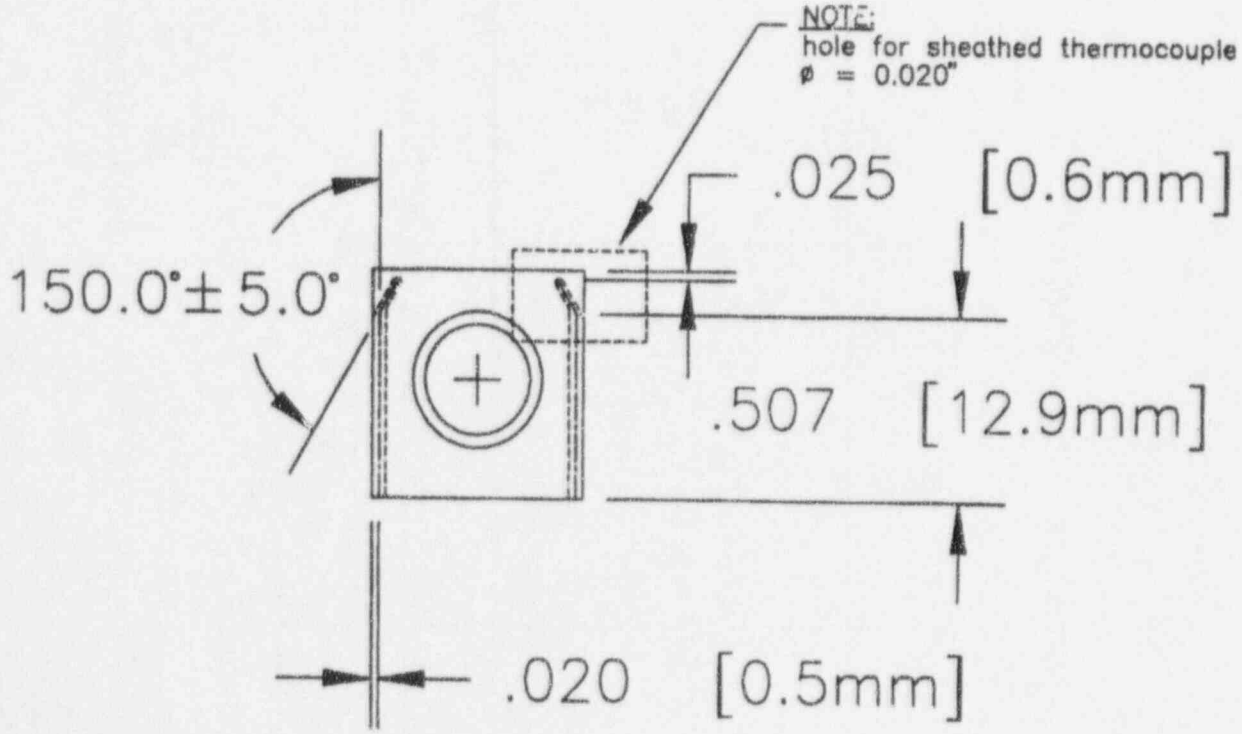

Figure 5: Thermocouple Positioning in Mockup

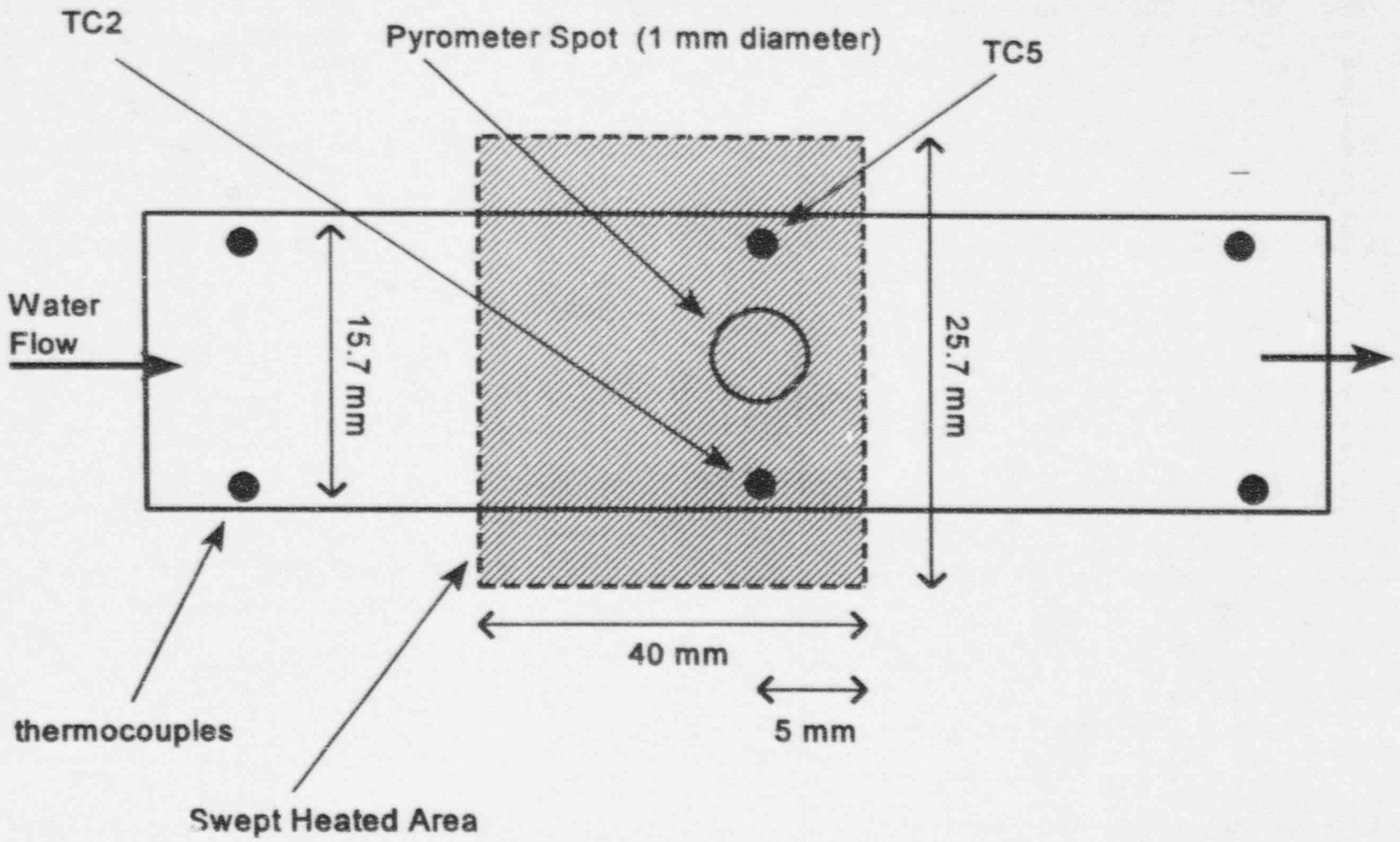

Figure 6: Heated Area of Mockup (Top View of Mockup) and Thermocouple positioning

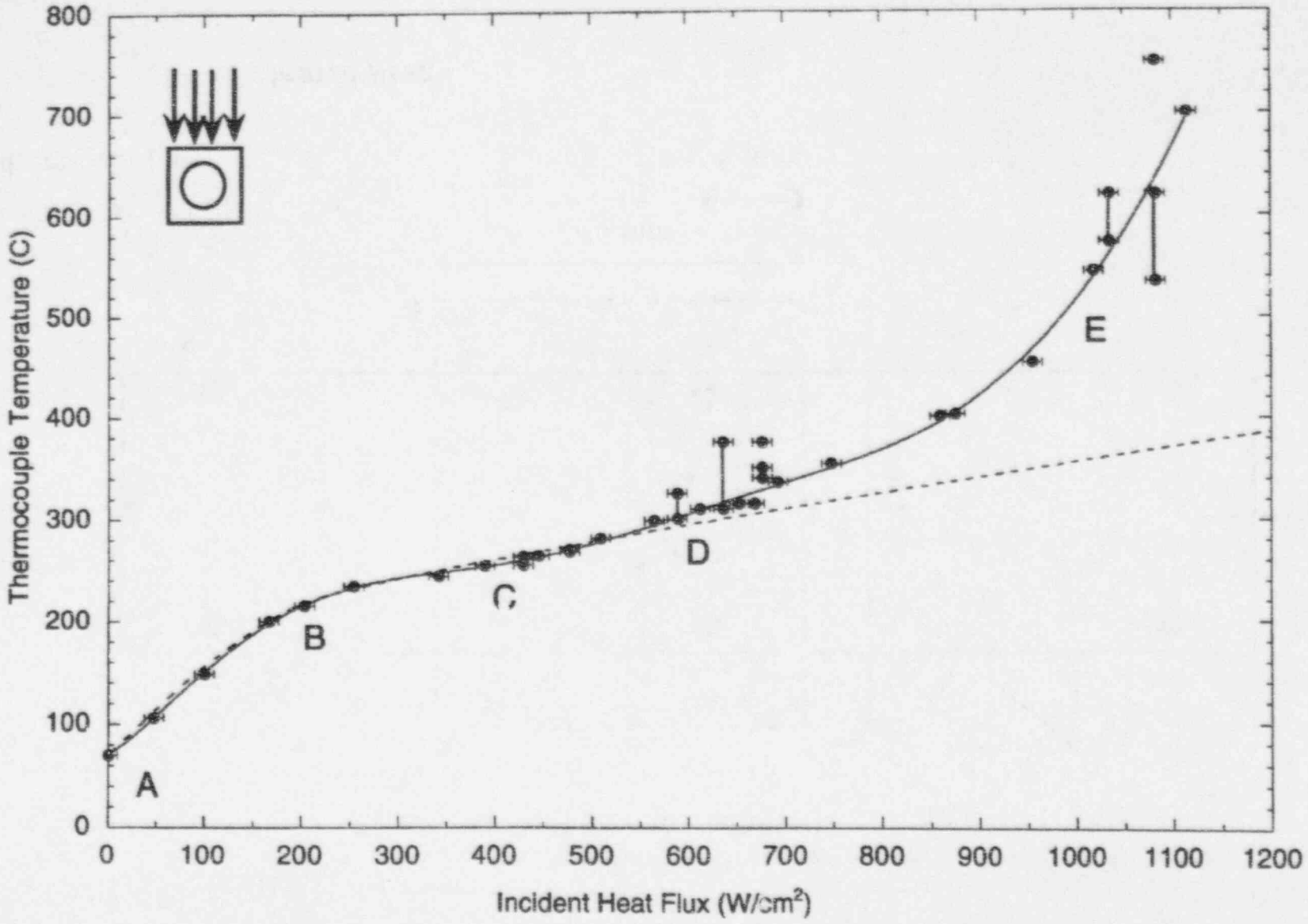

Figure 7: Thermocouple Temperature vs. Incident Heat Flux; Inlet Conditions = 1 MPa, 70 C, 1 m/s, 40 mm heated length; ID = 7.6 mm, heated width = 15.7 mm; ABAQUS Prediction represented by dashed line; A = Single Phase Liquid; B = Onset to Nucleate Boiling, C = Fully Developed Nucleate Boiling, D = Critical Heat Flux, E = Post-CHF Regime.

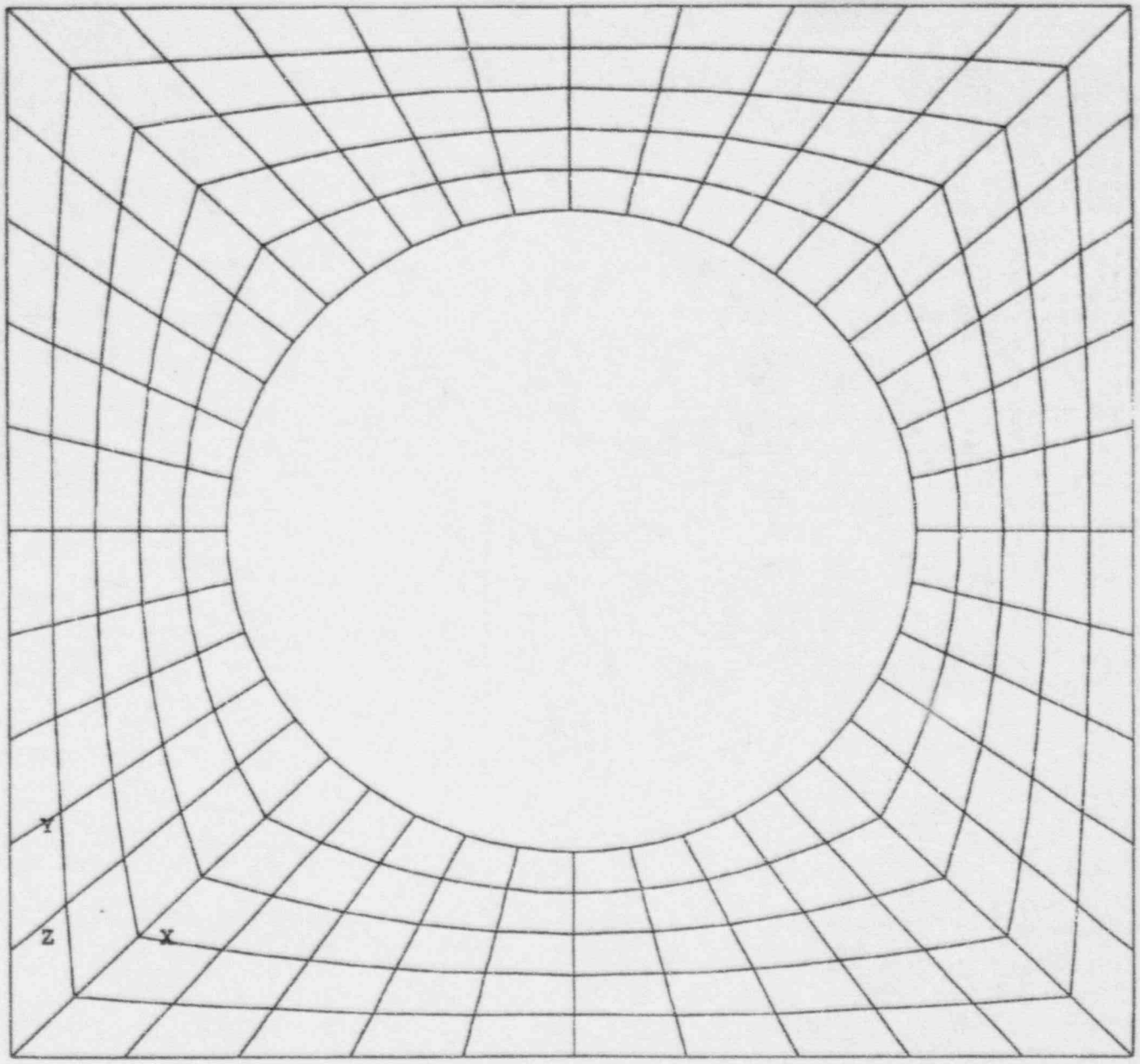

Figure 8: PATRAN Finite Element Mesh of Mockup - 200 Elements and 760 Nodes.

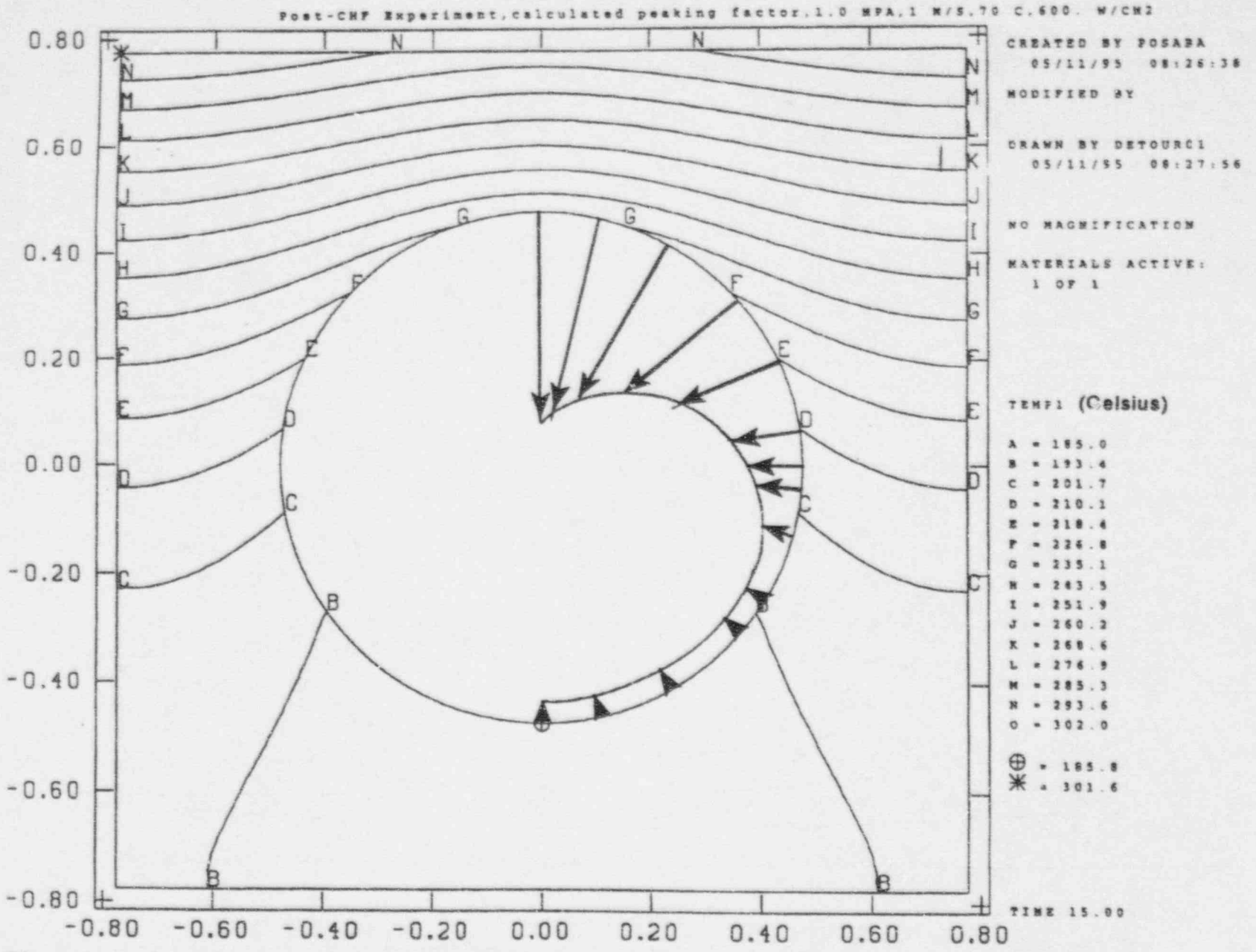

Figure 9: Isothermal Contours and Internal Heat Flux Distribution from ABAQUS FEA Calculations, Incident Heat Flux = 600 W/cm^2, Inlet Conditions = 1 MPa, 70 C, 1 m/s.

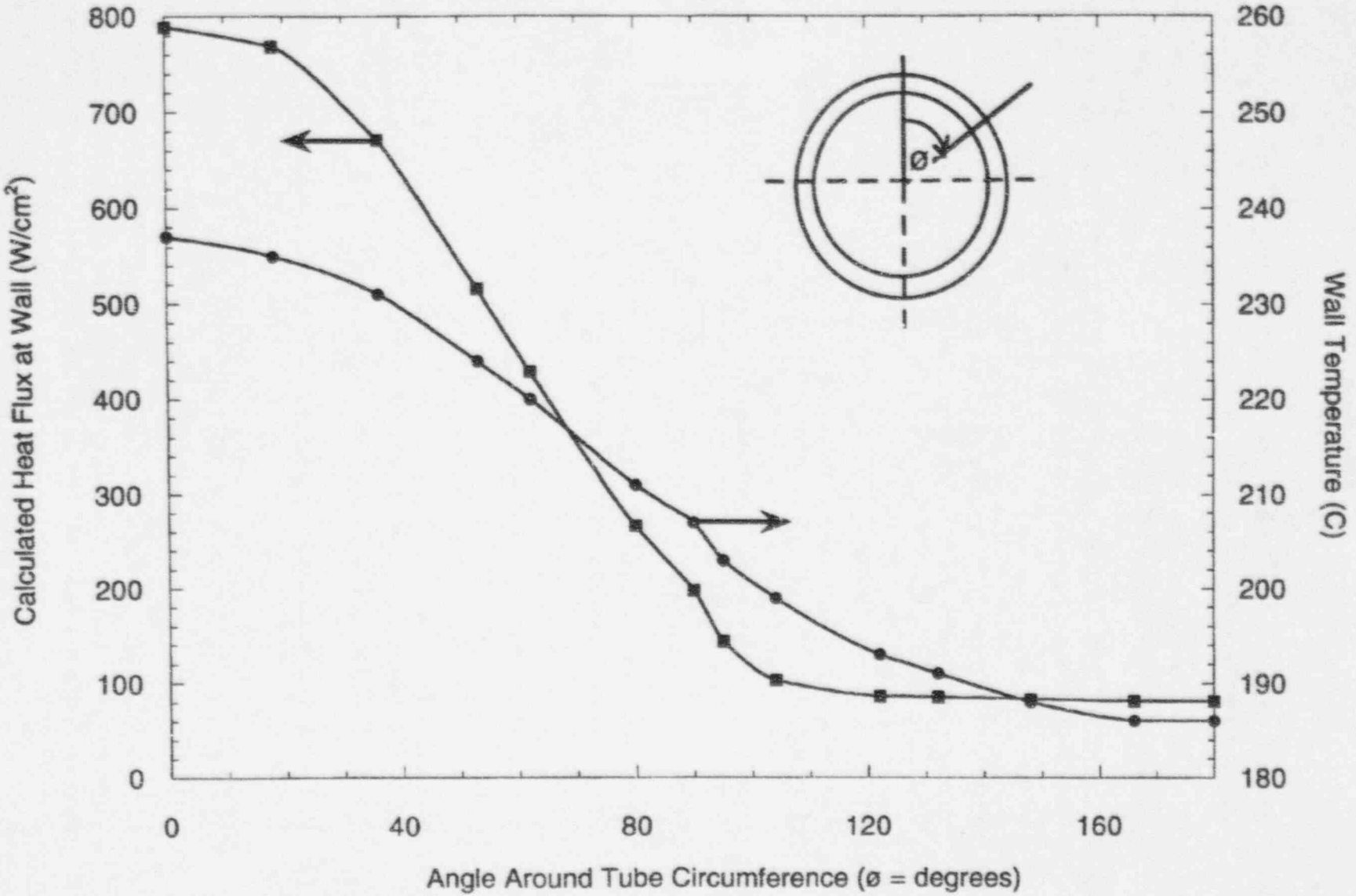

Figure 10: Temperature and Heat Flux Distributions Along the Circumference of the Tube at Experimental CHF calculated by ABAQUS.

REFERENCES

[1] T. Kuroda and G. Vieider, "ITER Plasma Facing Components," ITER Documentation Series, 30, IAEA, Vienna, (1990).

[2] G. Vieider, "Design Assessment of the ITER EDA Divertor," ITER Design Assessment Meeting, San Diego, (Oct 17-28, 1994).

[3] V. A. Divavin, V. N. Tanchuk, and A. E. Shrubok, "Limited Heat Loads and Burnout Heat Transfer in One-Sided Heated Channels," Heat Transfer Research, Vol. 24, No. 5, pp. 612-624, (1992).

[4] V. Divavin, V. Tanchuk, A. Shrubok, R. Watson, and J. Gonzalez, "An Experimental and Numerical Investigation of Post-CHF Heat Transfer for One-Sided Heat Load with Highly Sub-Cooled Flow Boiling," Accepted for publication in Fusion Engineering and Design, manuscript MS#94-07.

[5] R. D. Boyd, et. al., "Preliminary Design Analysis of ALT-II Limiter for TEXTOR," Journal of Nuclear Materials, Vol. 121, pp. 309-315, (1984).

[6] J. Schlosser, and J. Boscary, "Thermal Hydraulic Tests at NET/ITER Relevant Conditions On Divertor Targets Using Swirl Tubes," NURETH 6, Grenoble, France, pp. 815-824, (Oct 1993).

[7] J. Koski and C. Croessmann, "Critical Heat Flux Investigations for Fusion-Related Conditions with the Use of a Rastered Electron Beam Apparatus," ASME Winter Annual Meeting, 88-WA/NE-3, (1988).

[8] R. Moffat, "Describing the Uncertainties in Experimental Results," Experimental Thermal and Fluid Science, 1, pp. 3-17, (1988)

[9] M. Araki, R. D. Watson, T. D. Marshall, P. D. Rockett, and M. Akiba, "Effect of Subcooling on the Critical Heat Flux Under One-Sided Heating Conditions," Proceedings of the 18th Symposium on Fusion Technology, Karlsruhe, Germany, (August 22-26, 1994).

[10] Hibbitt, Karlsson, and Sorensen, Version 4-8 Finite Element Analysis Code, Pawtucket, RI, (1992).

[11] M. Ozisik, Heat Transfer - A Basic Approach, McGraw-Hill Book Company, pp. 300-340, (1985).

[12] R. Thom, W. Walker, W. Fallon, and G. Resing, "Boiling in Subcooled Water During Flow Up Heated Tubes in Annuli," Symposium on Boiling Heat Transfer in Steam Generating Units and Heat Exchangers, Institute of Mechanical Engineers Paper No. 6., Manchester, London, (1965).

[13] G. Celata, M. Cumo, and A. Mariani, "Assessment of Correlations and Models for the Prediction of CHF in Water Subcooled Flow Boiling," International Journal of Heat and Mass Transfer, Vol. 37, No. 2, pp. 237-255, (1994).

[14] D. Groeneveld, S. Cheng, L. Leung and C. Nguyen, "Computations of Single- and Two-Phase Heat Transfer Rates Suitable for Water-Cooled Tubes and Subchannels," Nuclear Engineering and Design, Vol. 114, pp. 61-77, (1989).

[15] D. Groeneveld and J. Stewart, "The Minimum Film Temperature for Water During Film Boiling Collapse," Proceedings of the 7th International Heat Transfer Conference, Munich, Germany, Vol. 4, pp. 393-398, (1982).

[16] P. Berenson, "Film-Boiling Heat Transfer From a Horizontal Surface, " Journal of Heat Transfer, Vol. 83, pp. 351-358, (1961).

[17] L. Tong, "A Phenomenological Study of Critical Heat Flux," ASME, 75-HT-68, (1975).

[18] J. Koski, R. Watson, A. Hassanein, P. Goranson, and J. Salmonson, "Thermal-hydraulic Design Issues and Analysis for the ITER Divertor," Fusion Technology, Vol. 19, pp. 1729-1735, (1991).

TRANSIENT POOL BOILING HEAT TRANSFER DUE TO INCREASING HEAT INPUTS IN SUBCOOLED WATER AT HIGH PRESSURES

K. Fukuda, M. Shiotsu* and A. Sakurai*
Kobe University of Mercantile Marine, Higashinada-Ku, Kobe, 658 Japan
*Institute of Atomic Energy, Kyoto University Uji, Kyoto, 611 Japan

ABSTRACT

Understanding of transient boiling phenomenon caused by increasing heat inputs in subcooled water at high pressures is necessary to predict correctly a severe accident due to a power burst in a water-cooled nuclear reactor. Transient maximum heat fluxes, q_{max}, on a 1.2 mm diameter horizontal cylinder in a pool of saturated and subcooled water for exponential heat inputs, $Q_0 e^{t/\tau}$, with periods, τ, ranging from about 2 ms to 20 s at pressures from atmospheric up to 2063 kPa for water subcoolings from 0 to about 80 K were measured to obtain the extended data base to investigate the effect of high subcoolings on steady-state and transient maximum heat fluxes, q_{max}. Two main mechanisms of q_{max} exist depending on the exponential periods at low subcoolings. One is due to the time lag of the hydrodynamic instability which starts at steady-state maximum heat flux on fully developed nucleate boiling (FDNB), and the other is due to the heterogeneous spontaneous nucleations (HSN) in flooded cavities which coexist with vapor bubbles growing up from active cavities. The shortest period corresponding to the maximum q_{max} for long period range belonging to the former mechanism becomes longer and the q_{max} mechanism for long period range shifts to that due the HSN on FDNB with the increase of subcooling and pressure. The longest period corresponding to the minimum q_{max} for the short period range belonging to the latter mechanism becomes shorter with the increase in saturated pressure. On the contrary, the longest period becomes longer with the increase in subcooling at high pressures. Correlations for steady-state and transient maximum heat fluxes were presented for a wide range of pressure and subcooling.

INTRODUCTION

Knowledge of transient boiling phenomenon including incipient boiling, transition to film boiling from nonboiling regime and etc. due to increasing heat inputs is important to understand correctly the severe nuclear reactor accidents such as rapid power burst and pressure reduction. Though many papers concerning with the experimental and theoretical studies on transient boiling phenomena were published by workers for about thirty years, the mechanisms of transient boiling for high subcooling and high pressure were not clear especially those for rapid ones till quite recently.

It was clearly observed by Sakurai and Shiotsu [1] that transient maximum heat flux, q_{max}, on a horizontal cylinder in saturated water at pressures around atmospheric due to exponential heat inputs with the periods, τ, over the range of 5 ms down to 10 s, firstly increased, then decreased and again increased with the decrease in periods: the maximum and minimum values of q_{max} at about 100 ms and 20 ms, were higher about 50 % and slightly lower than the steady-state value, q_{st}, respectively. The anomalous trend of q_{max} for τ shows that there exists three different mechanisms for q_{max} due to increasing heat inputs; it can be understood that the increasing mechanism of q_{max} for the periods longer than about 100 ms is due to the time lag of the hydrodynamic instability near the cylinder surface which causes the steady-state heat transfer crisis pointed out by Kutateladze[2] and Zuber[3]. However,

the mechanism of the trend of q_{max} which decreases and then increases with the decrease in period remain unsolved for a long time.

Recently, Sakurai et al.[4, 5] carried out detailed studies on transient boiling phenomenon on a horizontal cylinder in pressurized and subcooled liquid nitrogen due to exponential heat inputs for the wide ranges of period and pressure. They observed the anomalous trend of the q_{max} for τ at pressures higher than about atmospheric: the trend is just similar to that observed in water mentioned above. The q_{max} values for long exponential periods gradually increase with the decrease in the period: the heat transfer process is such that the transition from nonboiling regime to fully developed nucleate boiling (FDNB) regime firstly occurs at a certain wall superheat, and then the heat flux gradually increases along the steady-state FDNB curve and its extension up to the q_{max} point at which transition to film boiling occurs. The q_{max} values for short exponential periods increase with the decrease in the period: the heat transfer process is such that the transition from nonboiling regime to film boiling occurs without or with the increase of heat flux for a short period of time, depending on pressures and periods. The direct transition (the transition without increase of heat flux) occurs for the increasing heat inputs over the range from quasi-steady to rapid ones at pressures lower than atmospheric, and it also occurs for the periods shorter than a certain value dependent on pressure at pressures between that higher than atmospheric and about 1 MPa. The semi-direct transition (the transition with the increase of heat flux for a short period of time) occurs for periods shorter than a certain value dependent on pressure at pressures higher than about 1 MPa. The q_{max} values for the intermediate periods between those corresponding to maximum and minimum q_{max} decrease with the decrease in pressure. Sakurai et al. assumed that the direct and semi-direct transitions occurred due to the explosive heterogeneous spontaneous nucleation(HSN) in initially flooded cavities for initial boiling caused by the increasing heat inputs on the solid surface: all the cavities on the surface that could serve as nucleation sites would initially be flooded since surface tension is so low that vapor is not entrained in the surface cavities and no dissolved gas exists in the liquid except for possible trace amounts of helium, hydrogen and neon in liquid nitrogen.

The contribution of active cavities entrained vapor or gases on the test heater surface in water for boiling initiation due to a heat input can be eliminated by the pre-pressurization of test vessel with high pressure for a while; the boiling initiation mechanism becomes similar to that for liquid nitrogen. Sakurai et al.[5, 6] clearly observed, in water experiments caused by exponential heat inputs with initial pre-pressurizations, the direct and semi-direct transitions and the same trend of q_{max} for period (as that for liquid nitrogen). The q_{max} at the transition from nonboiling regime to film boiling with and without heat flux increase was observed at pressures ranging from 50 kPa to 1 MPa for liquid subcoolings over the range of zero to 30 K in water. They also observed that the q_{max} for short exponential periods at pressure around atmospheric in the cases without and with pre-pressurization (in other words, in the cases with and without the contribution of active cavity for initial boiling) agreed with each other, though the wall superheat at q_{max} for the former case was lower than that for the latter. They [5, 6] assumed that, for a short period in the case with the contribution of the active cavities for initial boiling, the q_{max} also occurred mainly due to the HSN in originally flooded cavities at a certain wall superheat, though the nucleate boiling from active cavities coexisted with it. A few vapor bubbles from active cavities on the cylinder surface growing up due to a rapid heat input for a short period of time lead to the occurrence of heterogeneous spontaneous nucleation at the wall superheat lower than that for the same period in the case with pre-pressurization. This is because the increasing rate of wall superheat on the local positions of the cylinder surface is decreased due to the bubbles. Semi-theoretical correlation of the lower limit of HSN temperature in flooded cavities has been presented based on experimental data of liquid nitrogen, liquid helium, ethanol and water[5, 7, 8].

The objective of this work is firstly to obtain an extended data of the q_{max} values due to exponential heat inputs in water for the exponential periods and subcoolings over the ranges of 2 ms to 20 s and zero to 80 K at pressures ranging from 101.3 to 2063 kPa in cases with and without pre-pressurization; and secondly to investigate the effect of high subcoolings at high pressures on the main two mechanisms of q_{max} depending on the exponential periods already presented [5,6]. The steady-state q_{max} values for high subcoolings at high pressures are also investigated experimentally to predict the experimental data obtained.

1. APPARATUS AND METHOD

1.1 Experimental apparatus

The schematic diagram of the experimental apparatus is shown in Fig. 1. It mainly consists of a boiling vessel (1), a pressurizer (5), and a liquid feed tank (8) with a booster pump (9). The boiling vessel is a cylindrical stainless steel pressure vessel of 20 cm inner diameter and 60 cm height capable of operating up to 5.0 MPa. The vessel has two sight ports and is equipped with a pressure transducer and a sheathed 1 mm diameter K type thermocouple that is used to measure the bulk liquid temperature. A cylinder test heater (2) is horizontally supported in the vessel. The vessel is connected via a valve and the booster pump to the liquid feed tank. The air driven booster pump (Haskel, Model DSF-25) was used for the pre-pressurization before the runs.

1.2 Test heater

A platinum cylinder test heater of 1.2 mm in diameter was used. The steady-state maximum heat flux for the heater agree with the constant value obtained by the cylinders with the diameters larger than 1.2 mm with larger heat capacities. The length of the horizontal section was about 90 mm. Two fine 30-μm-diam platinum wires were spot welded at around 20 mm from each end of the horizontal heater section. The effective length of the heater between the potential taps on which transient boiling heat transfer was measured was about 50 mm. The heater was annealed and its electrical resistance versus temperature relation was calibrated in water and glycerin baths before using it in the experiments. The calibration accuracy was estimated to be within $\pm$ 0.5 K.

1.3 Method and procedure

The test heater was heated by electric current from a power amplifier whose input signal was controlled by a digital computer so that the heat generation rate of the heater agrees with the desired time function. The input signal to the power amplifier is shut off to prevent the heater from melting as soon as the average temperature of the test heater rises up to a preset value.

The average temperature of the test heater was measured by resistance thermometry using the heater itself. A double bridge circuit with the test heater as a branch was first balanced at the bulk liquid temperature. The output voltages of the bridge circuit, together with the voltage drops across the potential taps of the test heater and across a standard resistance, were amplified and passed through analog-to-digital converters of the digital computer. The average temperature of the test heater was calculated by using the previously calibrated resistance-temperature relation. The surface temperature was obtained by solving transient conduction equation in the heater under the conditions of the average temperature and heat generation rate. The experimental error was estimated to be about $\pm$ 1 K in the heater surface temperature and $\pm$ 2 percent in the heat flux. A high speed video camera system (200 frames/sec with a rotary shutter exposure of 1/2000 sec) was used to observe the transient boiling behavior and to confirm the start of boiling on the whole test heater surface for each experimental run.

Distilled and demineralized water was boiled at least half an hour in the boiling vessel and liquid feed tank to remove dissolved gases. The water was fully filled in the boiling vessel with the free surface only in the pressurizer and liquid feed tank by using the booster pump. Water temperatures in the boiling vessel and in the pressurizer were separately controlled to realize the desired saturated or subcooled conditions. Pre-pressurization before a run was performed in the following way: the valve between the boiling vessel and the pressurizer was shut off, and the booster pump was used to raise the pressure in the boiling vessel up to the desired pre-pressure of 5.0 MPa (we refer to this procedure as pre-pressurization). The pressure value was kept for about 2 minutes and then it was released to a preset value by opening the valve between the boiling vessel and the pressurizer. High pre-pressurization can be achieved without increasing the amount of dissolved gases in water.

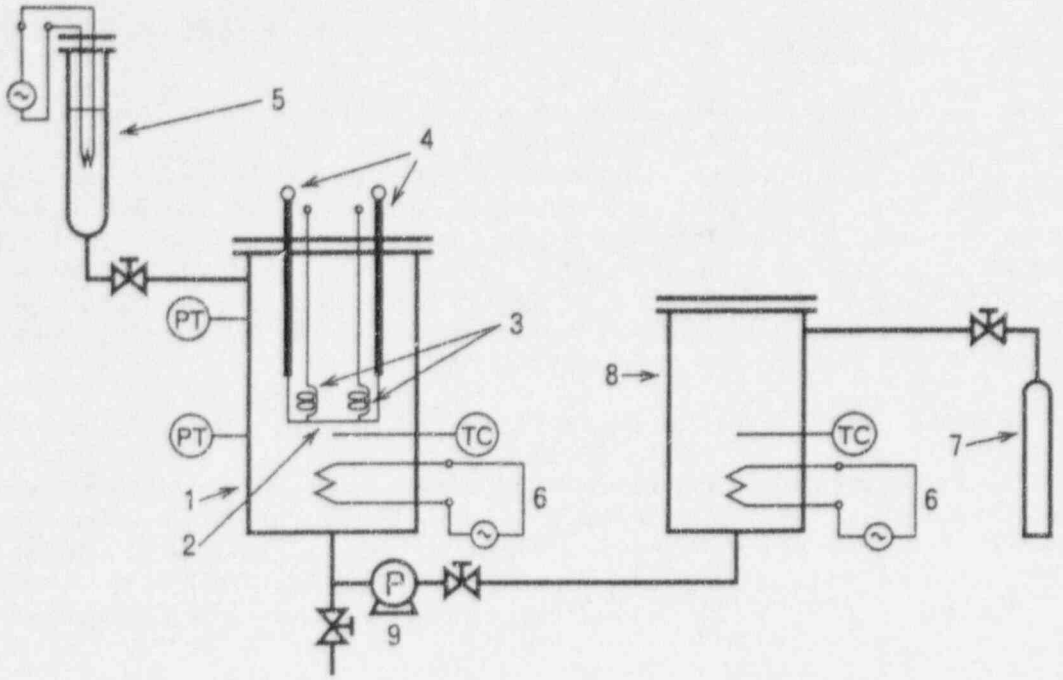

1 Boiling Vessel
2 Test Heater
3 Potential Taps
4 Electrodes
5 Pressurizer
6 Sheathed Heater
7 He Gas
8 Liquid Feed Tank
9 Booster Pump
(PT) Pressure Transducer
(TC) Thermocouple

Fig. 1 Schematic diagram of experimental apparatus.

Table 1 Experimental conditions.

Heater Dia.	1.2 mm
Pressure	101.3 kPa, 199 kPa, 297 kPa 494 kPa, 690 kPa, 1082 kPa 1474 kPa, 2063 kPa
Subcooling	0 K, 10 K, 20 K, 30 K 40 K, 50 K, 60 K, 80 K (100 K), (120 K), (140 K)
Exponential Period	2 ms to 20 s

( ):steady-state only

2. RESULTS AND DISCUSSION

2.1 Experimental conditions

Transient boiling heat transfer processes on a 1.2 mm diameter horizontal cylinder in water due to exponentially increasing heat inputs with periods ranging from around 2 ms to 20 s were measured at pressures ranging from 101.3 to 2063 kPa for liquid subcoolings over the ranges from 0 to 80 K at pressures higher than 199 kPa, and from 0 to 60 K at atmospheric pressure. The heat transfer processes for the periods of around 20 s, which were treated as steady-state ones, were measured for the subcoolings up to 80 K at pressures from 101.3 to 490 kPa, up to 120 K at 699 kPa, and up to 140 K at 1082 to 2063 kPa. Details are shown in Table 1. These experiments were performed for the cases without and with the pre-pressurization by the pressure of around 5 MPa.

2.2 Steady state maximum heat flux for pressurized and subcooled water

The ratio of the steady-state maximum heat flux under subcooled condition to that under saturated condition, $q_{st,sub}/q_{st,sat}$, is shown versus liquid subcooling with system pressure as a parameter in Fig. 2. The ratio increases with the increase in liquid subcooling at each pressure. The value of $q_{st,sub}/q_{st,sat}$ at each subcooling becomes lower with the increase in pressure. The values of $q_{st,sat}$ are well expressed by the following Kutateladze's correlation with the coefficient K of 0.17:

$$q_{st,sat} = K L \rho_v [\sigma g(\rho_l - \rho_v)/\rho_v^2]^{1/4} \tag{1}$$

Kutateladze presented the following correlation for subcooled steady-state maximum heat flux by introducing the recirculation coefficients, α and β.

$$q_{st,sub} = q_{st,sat}[1 + \alpha(\rho_l/\rho_v)^{\beta}(C_{pl}\Delta T_{sub}/L)] \tag{2}$$

where, the values of the coefficients α and β were fitted by him to be 0.065 and 0.8 respectively. The values of $q_{st,sub}/q_{st,sat}$ calculated from the Kutateladze's correlation for various subcoolings at each pressure are shown in the figure as a broken line for comparison. The experimental data are seen to be very much higher than the corresponding calculated values from the Kutateladze's correlation. On the other hand, the values for the subcoolings lower than around 50 K at each pressure are well expressed by the following correlation derived by modifying the Kutateladze's correlation:

$$q_{st,sub} = q_{st,sat}[1 + 0.87(\rho_l/\rho_v)^{0.69}(C_{pl}\Delta T_{sub}/L)^{1.5}] \tag{3}$$

where $q_{st,sat}$ is given by Eq. (1). The values predicted by this equation for each pressure are shown in the figure as a solid curve. The experimental data of $q_{st,sub}$ obtained here were compared in Fig. 3 with the corresponding values predicted by the correlation. The data for the subcoolings ranging from 0 to 50 K agree with the predicted values at all the pressures tested here. At atmospheric pressure, good agreement can be seen for the subcoolings up to about 80 K. However, the data at pressures higher than atmospheric do not agree with the predicted values for the subcoolings larger than 60 K; the data become almost independent of pressure for the pressures higher than around 690 kPa and gradually increase with the increase in subcooling. The following empirical correlation for $q_{st,sub}$ for pressures and subcoolings higher than about 690 kPa and 60 K was derived.

$$q_{st,sub} = 3.75 \times 10^6 + 7.3 \times 10^4 \Delta T_{sub} \tag{4}$$

The curve given by Eq.(4) is also shown in the figure as a broken line.

The fact mentioned above means that there exists another mechanism of $q_{st,sub}$ for the higher subcoolings at the pressures: the mechanism which is different from that due to the

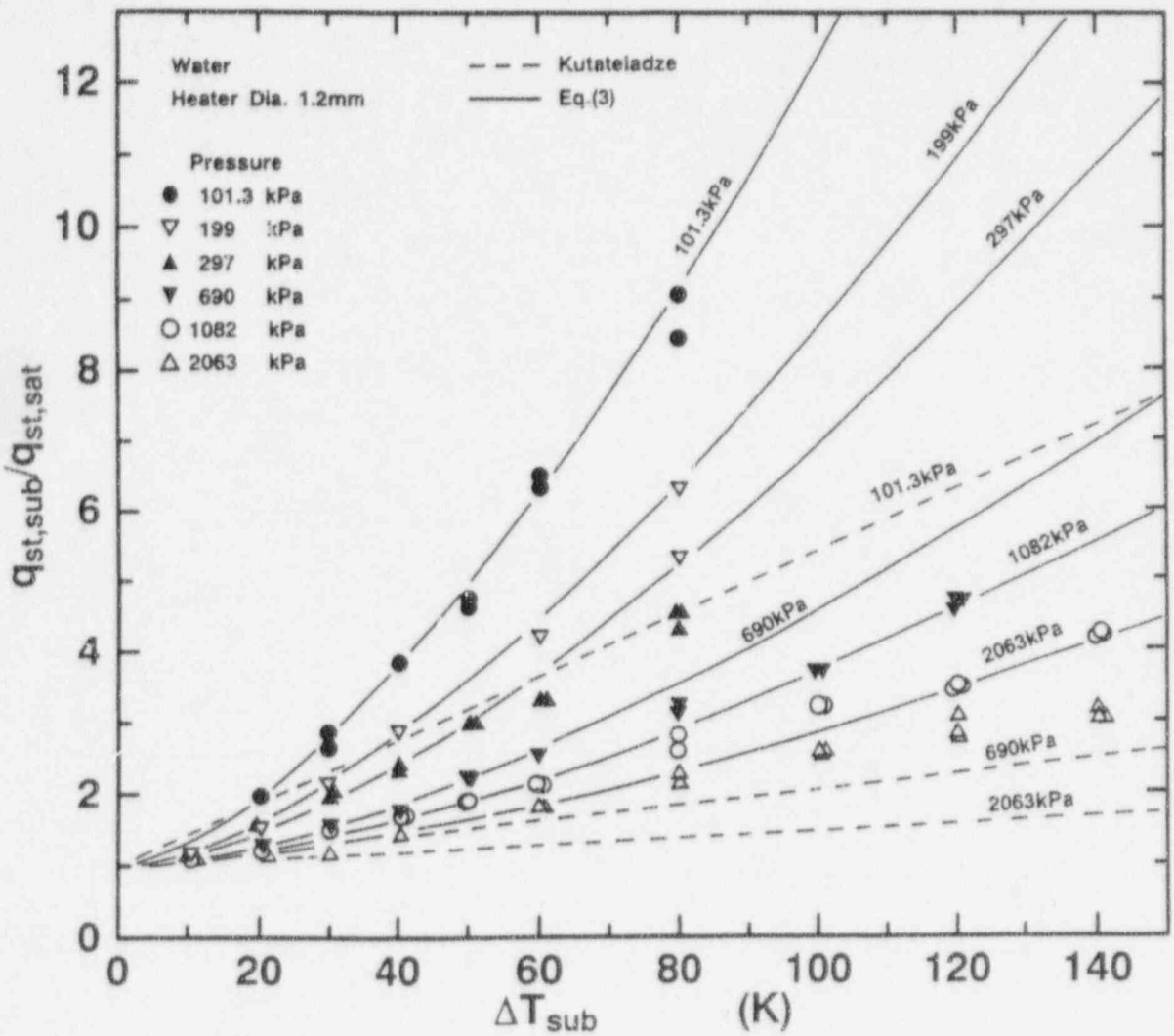

Fig. 2 Ratio of subcooled to saturated steady-state maximum heat flux, $q_{st,sub}/q_{st,sat}$, versus liquid subcooling at pressures ranging from 101.3 to 2063 kPa.

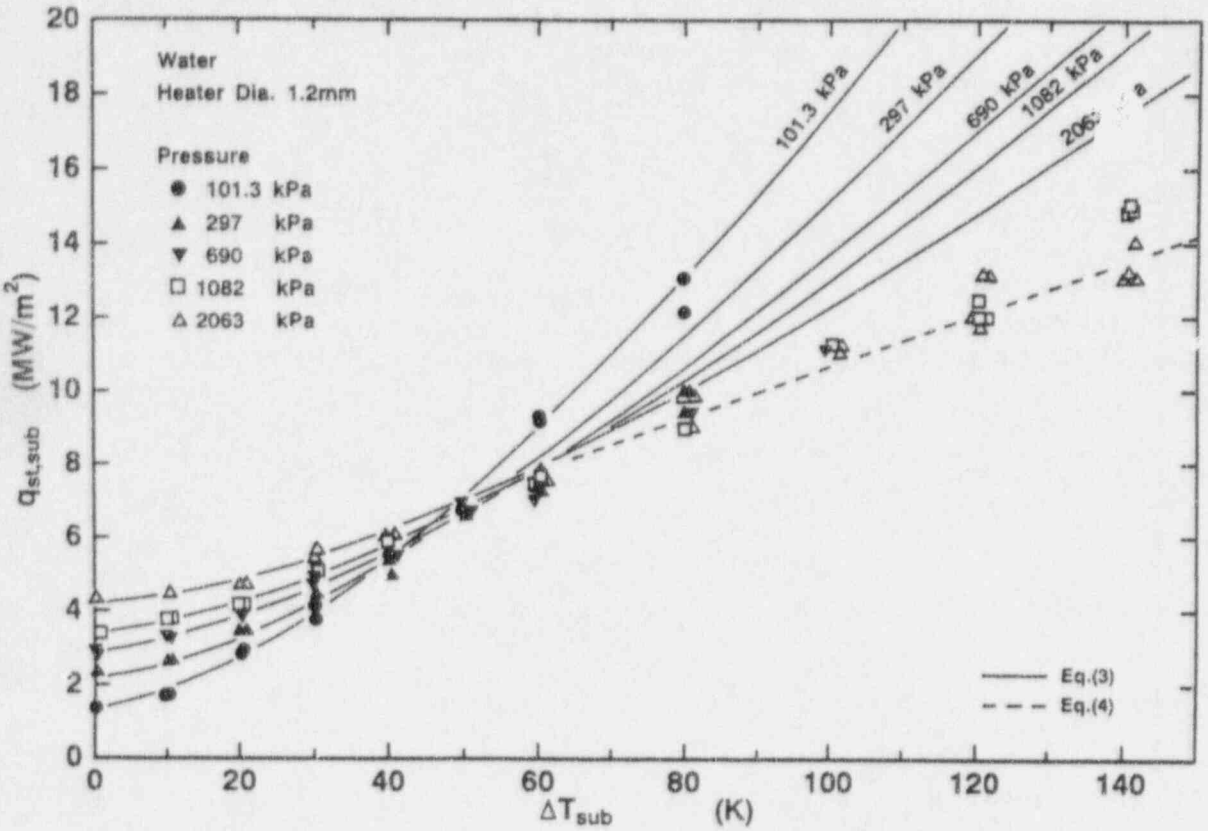

Fig. 3 Steady-state maximum heat flux versus liquid subcooling at pressures ranging from 101.3 to 2063 kPa.

hydrodynamic instability previously pointed out by Kutateladze[2] and Zuber[3]. It is assumed that the $q_{st,sub}$ for a high subcooling at a high pressure would occur on fully developed nucleate boiling at the lower limit of heterogeneous spontaneous nucleation(HSN) surface superheat, ΔT_{iLH} in originally flooded cavities on the cylinder surface. Figure 4 shows the heat transfer processes due to quasi-steadily increasing heat inputs for subcooling of 60 K at pressures of 101.3 and 1082 kPa with and without pre-pressurization. The surface superheat at the incipient boiling point in each pre-pressurized run (solid circle in the figure) corresponds to the lower limit of HSN surface superheat, ΔT_{iLH}. As assumed above, the surface superheat at the critical heat flux, ΔT_m, for the pressure of 1082 kPa almost agrees with ΔT_{iLH}. On the contrary, the value of ΔT_m at atmospheric pressure is far lower than the corresponding ΔT_{iLH}. The $q_{st,sub}$ for higher subcooling and pressure becomes lower than that expected by the hydrodynamic instability. Detailed study on the mechanism of $q_{st,sub}$ appears elsewhere.

2.3 Transient maximum heat fluxes for exponential heat inputs under saturated condition for the cases without and with pre-pressurization

Transient maximum heat fluxes due to exponential heat inputs to the horizontal test cylinder in a pool of water were obtained for wide ranges of exponential periods, pressures and subcoolings.

Figure 5 shows typical results of transient maximum heat flux q_{max} for the exponential heat inputs with the periods ranging from about 2 ms to 20 s at pressures of 101.3, 690, 1082 and 2063 kPa under saturated conditions for the cases without and with pre-pressurization which are called as the Case 1 and Case 2, respectively. The maximum heat fluxes for the periods at the pressures are separated into three groups for the periods as clearly seen in the data for the Case 1 at atmospheric pressure and for the Case 2 at pressures of 101.3, 690, 1082 and 2063 kPa. The three grups of q_{max} for periods at atmospheric pressure for the Case 1 are shown in Fig. 5 as a typical.

The first group of q_{max} at each pressure for the Cases 1 and 2 is for the periods longer than around 100 ms and around 3 s, respectively, at 101.3 kPa, and longer than around 200 ms at other pressures. The q_{max} values in the first group at each pressure for both cases agree with each other. The point of the q_{max} in the group at each pressure on the graph of log q vs. log ΔT_{sat} exist on the extrapolation of steady-state developed nucleate boiling curves as shown later in Fig. 8. Therefore, it can be assumed that the heat transfer crisis at the q_{max} which is larger than q_{st} is due to the time lag of the hydrodynamic instability which starts at the steady-state q_{max} expressed as q_{st}.

The curves representing the q_{max} values of the first group for periods at the pressures are expressed by the following empirical equation:

$$q_{max} = q_{st,sub}(1 + 0.21\tau^{-0.5}) \tag{5}$$

where $q_{st,sub}$ is given by Eq. (3). The curves for the pressures obtained from Eq.(5) are shown in Fig. 5 in comparison with the corresponding experimental data.

The second groups of q_{max} for the period shorter than the period of minimum q_{max} for the Case 1 at atmospheric pressure and for the Case 2 at pressures of 101.3, 690, 1082 and 2063 kPa were observed. The q_{max} for period at each pressure has a linear asymptotic line on a log-log graph. The q_{max} of second groups at pressures higher than 690 kPa for the Case 1 and at the pressure of 2063 kPa for the Case 2 were not observed for the periods tested here. However, it is supposed that the q_{max} values for the second group will be observed for the periods sufficiently shorter than the shortest one tested here and the q_{max} values for the Cases 1 and 2 agree with each other for the same period.

The asymptotes representing the q_{max} data for the shorter periods at a pressure for the Cases 1 and 2 are expressed by the following empirical equation obtained based on the data for the pressures ranging from 101.3 kPa to 1474 kPa and for the subcoolings up to 80 K.

$$q_{max} = [1.0 \times 10^5 (P/P^*)^{-0.21\exp(-0.025\Delta T_{sub})} + 600\Delta T_{sub}]\tau^{-0.6} \tag{6}$$

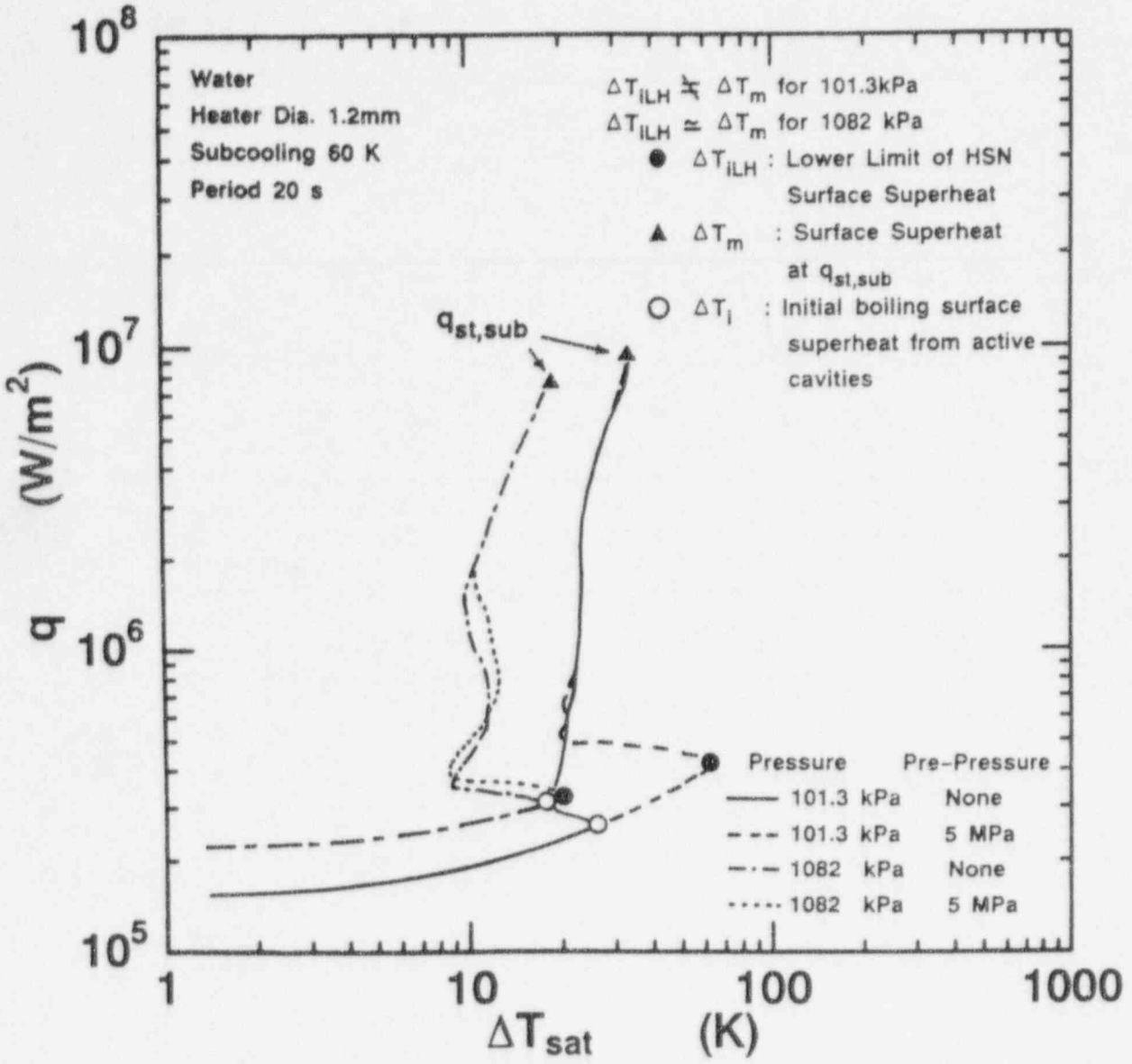

Fig. 4 Heat transfer processes for the period of 20 s for subcooling of 60 K at pressures of 101.3 and 1082 kPa without and with pre-pressurization.

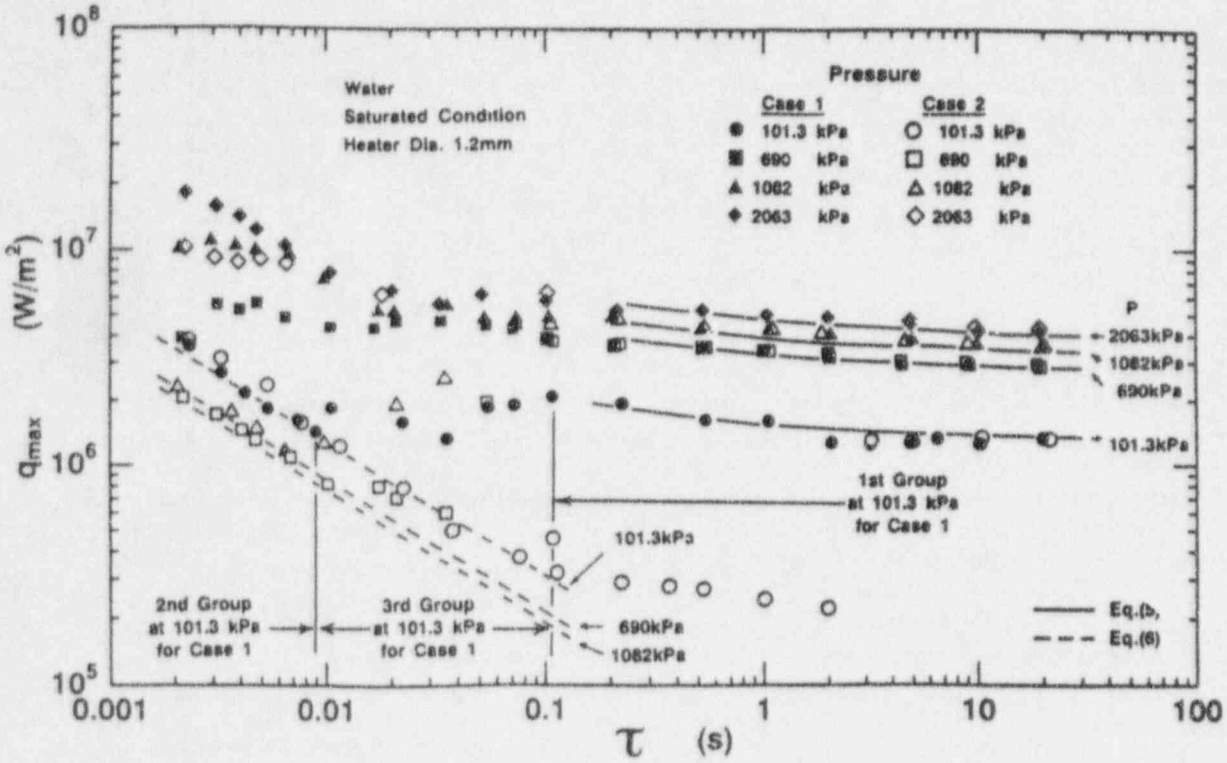

Fig. 5 Relation between q_{max} and τ at pressures ranging from 101.3 to 2063 kPa under saturated condition for the Cases 1 and 2.

where the reference pressure $P^* = 0.05$ MPa, and the dimensions of τ and P are (s) and (MPa). The curve for each pressure obtained from Eq. (6) is also shown in Fig. 5 for comparison with the corresponding experimental data. The asymptotes for lower pressures are representing the q_{max} data corresponding to the direct transition, namely the heat fluxes at incipient boiling whose values for the periods shorter than 100 ms are approximately expressed by the following equation[1].

$$q_{max} = h_c \Delta T_i(\tau) \tag{7}$$

$$h_c = (k_l \rho_l c_{pl}/\tau)^{\frac{1}{2}} K_1(\mu D/2)/K_0(\mu D/2) \simeq (k_l \rho_l c_{pl}/\tau)^{\frac{1}{2}} \tag{8}$$

where $\mu = [\rho_l c_{pl}/(k_l \tau)]^{1/2}$, K_0 and K_1 are the modified Bessel functions of the second kind of zero and first orders.

The lower limit of the period for the second group becomes shorter with the increase in pressure. It should be noted for the Case 2 that the direct or semi-direct transitions at the q_{max} occur from nonboiling regime to film boiling without or with the heat flux increase for a short period of time, and the minimum q_{max} values for the longest period for the second group at each pressure are extremely lower than corresponding q_{st}.

These transient heat transfer processes including direct and semi-direct transitions for the Case 2 in water correspond to those obtained by the Sakurai et al. for the liquid nitrogen experiments under the same conditions at pressures higher than atmospheric: there exist no contribution of active cavities on the solid surface in both liquids. It has been assumed [4, 5] that the initial boiling occurs due to HSN in originally flooded cavities.

On the other hand, as clearly shown in the figure, the q_{max} for short periods at atmospheric pressure in the Cases 1 and 2 (in other words, in the cases with and without the contribution of active cavity for initial boiling) agreed with each other, though the wall superheat at q_{max} for the former case is lower than that for the latter case. It has been assumed [5, 6] that the q_{max} for short periods with the contribution of active cavities for the Case 1 probably occur due to the HSN in originally flooded cavities, though the nucleate boiling from active cavities coexists with it. A few vapor bubbles growing up from active cavities on the cylinder surface remaining on the surface before the detachment lead to the occurrence of the heterogeneous spontaneous nucleation at the wall superheat lower than that for the same period for the Case 1; this is because the increasing rate of wall superheat on the local positions of the cylinder surface is decreased due to the increased heat flux by the bubbles. The wall superheat at initial boiling due to HSN decreases with the decrease in wall superheat increasing rate.

The third group of q_{max} is for the intermediate range of period between those corresponding to the maximum and minimum q_{max}: those are about 100 ms and 30 ms at atmospheric pressure for the Case 1. The q_{max} in the group decreases or gradually increases with the decrease in periods and then approaches the curve representing the q_{max} at which the direct or semi-direct transitions to film boiling occurs. The transition to film boiling at the q_{max} in the group occurs in incompletely developed nucleate boiling due to originally unflooded cavities with entrained vapor or gases, and vapor entrained cavities activated from flooded cavities by neighboring vapor bubbles: the q_{max} becomes lower than that supposed due to the hydrodynamic instability.

2.4 Transient maximum heat flux under subcooled condition

The values of q_{max} for periods at 1.08 MPa for the Case 1 and Case 2 are shown with liquid subcooling as a parameter in Fig. 6 as a typical for subcoolings at a high pressure. The q_{max} values of the first group are for the periods longer than around 200 ms for $\Delta T_{sub} = 0$ K, and longer than around 500 ms for $\Delta T_{sub} = 20$ K and longer than around 2 s for ΔT_{sub}=40 K for both cases; the heat transfer crisis for the subcoolings at the q_{max} which is larger than q_{st} is assumed to be occurred by the same mechanisms as that for the saturated condition. The periods for the maximum q_{max} become longer with the increase in pressure.

On the other hand, the q_{max} values of first group for the subcoolings of 60 and 80 K are for the periods longer than around 20 ms for both cases. As mentioned in the previous section, it was assumed that the heat transfer crisis at q_{st} (steady-state q_{max}) for the high subcoolings

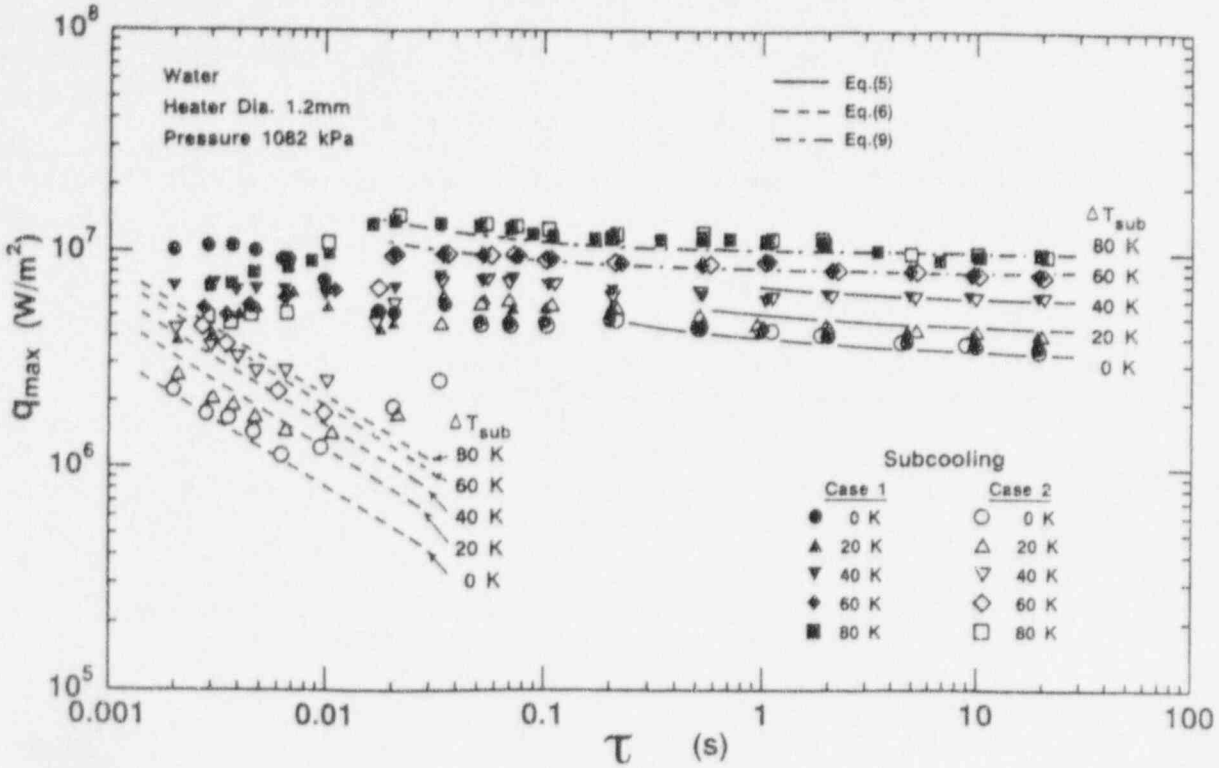

Fig. 6 Relation between q_{max} and τ for subcoolings ranging from 0 to 80 K at a pressure of 1082 kPa for the Cases 1 and 2.

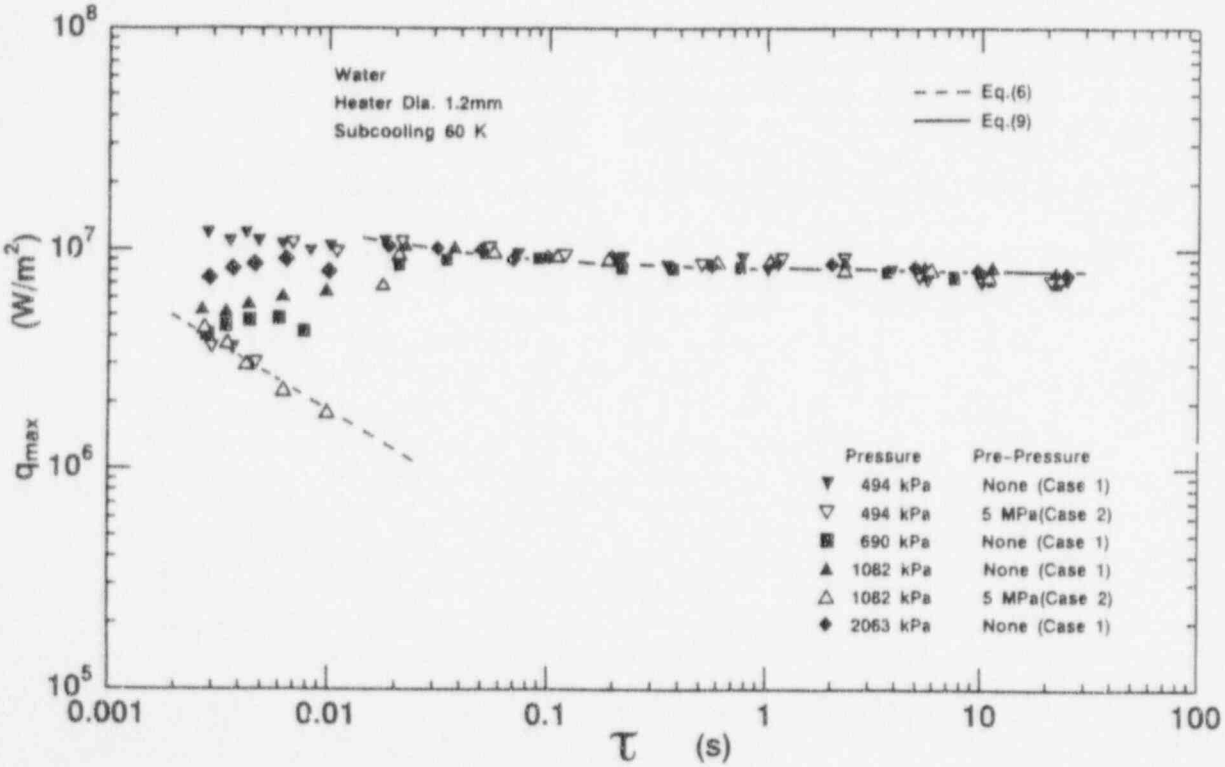

Fig. 7 Relation between q_{max} and τ for a subcooling of 60 K at pressures ranging from 494 to 2063 kPa for the Cases 1 and 2.

occurs by the HSN in originally flooded cavities on fully developed nucleate boiling at the heat flux lower than that supposed by the hydrodynamic instability. The q_{max} for period in the first group gradually increases with the decrease in the period. It should be noted that the q_{max} at the period of 20 ms is only about 140 % of the q_{st}. The curves representing the q_{max} for period are expressed by the following equation for the high subcooling at the high pressure.

$$q_{max} = q_{st,sub}[1 + 2.3 \times 10^{-2}\tau^{-0.7}] \tag{9}$$

The slight increase in q_{max} on fully developed nucleate boiling is due to the slight increase of the HSN surface superheat; it is not due to the time lag of the hydrodynamic instability which starts at the steady-state maximum heat flux. The curves obtained by Eq.(9) are shown in Figs.6 and 7 in comparison with the corresponding experimental data.

The second group q_{max} for the Case 1 are obtained only for the period of 2.1 ms at ΔT_{sub} = 20 K and 2.9 ms at ΔT_{sub} = 60 K; therefore the asymptotic lines of the maximum heat fluxes of the second group for the Case 1 were not obtained. However, the asymptotic lines for the Case 2 were obtained for all the subcoolings. The q_{max} in the second group for the Case 1 will be measured by using the exponential heat inputs with periods sufficiently shorter than the shortest one tested here; the q_{max} value will exist on the asymptotic line of corresponding subcooling for the Case 2. The asymptotic line for each subcooling has almost the same gradient on the graph and it moves upwards for higher liquid subcooling.

The maximum heat fluxes in third group are those for the intermediate range of period between those for the first and second groups. With the decrease of period in the range, the q_{max} slightly increases and then obviously decreases and finally approaches the asymptotic line for each subcooling.

The q_{max} for periods obtained for subcooling of 60 K at pressures of 494, 690, 1082 and 2063 kPa for the both cases are shown in Fig. 7. The q_{max} values for periods over the range from 30 ms to 20 s are independent of pressure: the q_{max} values for the period of 20 s correspond to steady-state values for the pressures. The q_{max} values for the pressures of 690 and 1082 kPa for the Case 1 decrease with the decrease in period from around 30 ms down to the values which are significantly lower than the corresponding steady-state maximum heat fluxes: these q_{max} values for periods around 3 ms for the both Cases 1 and 2 are on the asymptotic line representing the q_{max} values for periods in the second group on the graph of the figure. The values are equal to about 60 % and 70 %of the corresponding steady-state maximum heat fluxes, respectively. This means that both transitions are near direct ones to film boiling and the effect of vapor bubbles from active cavities for the Case 1 on the transition is negligibly small

2.5 Transient heat transfer processes for saturated and subcooled conditions

The heat transfer processes for the periods of 510 ms under saturated condition at 1.08 MPa for the Cases 1 and 2 are shown on the q vs. ΔT_{sat} graph in Fig. 8 as the typical ones in which the transition to film boiling occurs at the q_{max} of first group. The transition to fully developed nucleate boiling (FDNB) firstly occurs in quasi-steadily increasing natural convection regime for the period of 510 ms at points A and A′ for the Cases 1 and 2. Initial boiling at point A or A′ occurs due to nucleation from active cavities entrained vapor and gases or due to heterogeneous spontaneous nucleation (HSN) in initially flooded cavities: the surface superheats for the cases are 9 and 25 K, respectively. The lower limit of HSN surface superheat, ΔT_{iLH}, which was obtained as an initial boiling surface superheat for the period of 20 s for Case 2 under the same conditions is shown as an open circle. The surface superheat for the period of 510 ms at point A′ was almost in agreement with the value of ΔT_{iLH}. At the transition points A and A′, the wall superheat and the heat flux rapidly change through the processes of AB and A′B′ to FDNB: the decrease of surface superheat in each process is due to the activation of flooded cavities. The activation progresses for the slow increasing heat input such as that for the period of 510 ms. After that the heat flux increases along the fully developed nucleate boiling (FDNB) curve up to the heat flux (points C, C′) where the transition from FDNB to film boiling occurs. As shown in the figure, the q_{max} points exist on the extrapolation of the steady-state FDNB curve. The q_{max} values agree with each other and the surface superheats at q_{max} are lower than the value of ΔT_{iLH}. Little influence of

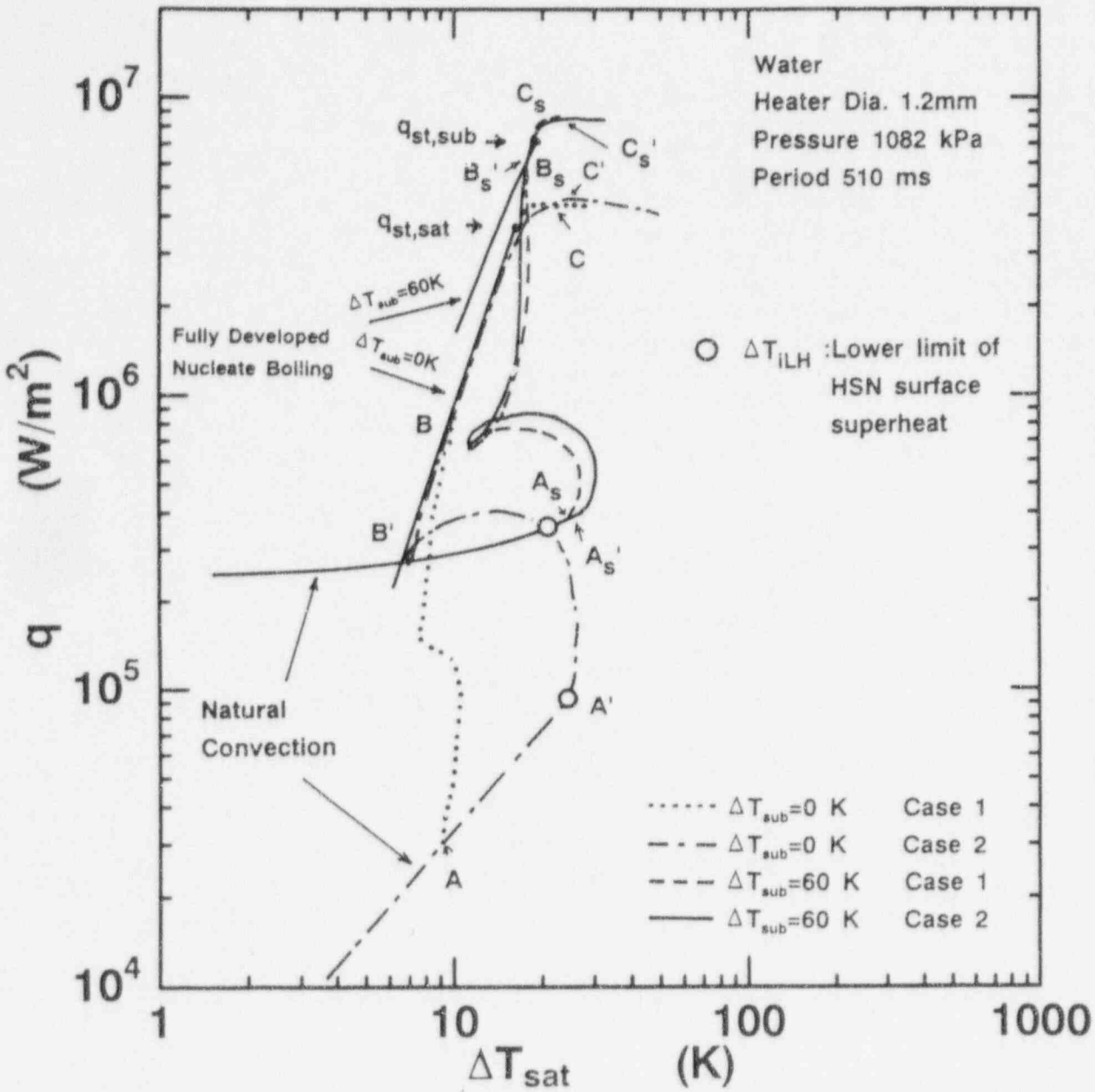

Fig. 8 Typical heat transfer processes with the q_{max} of 1st group at saturated and subcooled conditions for the period of 510 ms for the Cases 1 and 2.

the pre-pressurization on the FDNB heat transfer and on the transition from FDNB to film boiling can be seen, though the heat transfer processes from the boiling initiations to FDNB are considerably different each other. Therefore, it is assumed that the heat transfer crisis at the q_{max} in the first group which is larger than the q_{st} is due to the time lag of hydrodynamic instability which starts at the q_{st}.

The heat transfer processes for the subcooling of 60 K for the same period and pressure in both cases are also shown on the graph as typical ones under subcooled condition. The transition to FDNB occurs in quasi-steadily increasing natural convection regime for the subcooling at points A_s and A'_s for the Cases 1 and 2. The surface superheats for the cases are 23 and 26 K respectively: the former value for the Case 1 is far higher than that for the saturated condition at point A (about 9 K) though the latter value almost agrees with the value at point A'. The surface superheats are slightly higher than the lower limit of HSN surface superheat ΔT_{iLH} shown as an open circle on the solid curve. The wall superheat and heat flux change through the processes of A_sB_s and $A'_sB'_s$ to FDNB. The process A_sB_s for the Case 1 almost agrees with that for the Case 2, $A'_sB'_s$, though the wall superheat for the process soon after the initial boiling point is slightly lower than that for the Case 2. The heat fluxes at B_s and B'_s are as high as that slightly lower than the steady-state maximum heat flux $q_{st,sub}$: the activation of originally flooded cavities is relatively slow to progress under high subcooling for the increasing heat input with the period of 510 ms. The q_{max} points C_s and C'_s exist on the extrapolation of the steady-state FDNB curve and the maximum heat fluxes agree with each other. The wall superheats at the q_{max} points of C_s and C'_s almost agree with the ΔT_{iLH}; as mentioned before, the heat transfer crisis at the q_{max} occurs due to the heterogeneous spontaneous nucleation.

The heat transfer process for the period of 2.9 ms at 1.08 MPa under saturated condition for the Case 2 is shown in Fig. 9 as a typical one with the q_{max} of second group. The q_{max} for the Case 1 for the same period belongs to the third group, whose heat transfer process is shown in the next figure: the q_{max} in the second group under saturated condition is not obtained for the Case 1 even at the shortest period tested here. As shown in the figure, boiling firstly occurs in conduction regime for the period at the wall superheat of 60 K (point A') and then the heat flux and wall superheat rapidly decreases and increases, respectively, to film boiling. The q_{max} at point A' is the direct transition heat flux from nonboiling to film boiling.

The heat transfer processes for the subcooling of 60 K for the same period and pressure for the Cases 1 and 2 are also shown on the graph as typical ones under subcooled condition. The heat transfer processes after the initial boiling points A_s and A'_s are near direct transitions to film boiling. The wall superheats at the initial boiling points are 50 and 54 K, respectively. The values of q_{max} for both cases are almost in agreement with each other and are significantly lower than $q_{st,sub}$ as shown in the figure.

As typical ones with the q_{max} of third group, Fig. 10 shows the heat transfer process for the period of 2.9 ms under saturated condition at 1.08 MPa for the Case 1, and those for the period of 53.5 ms and liquid subcooling of 60 K for the Cases 1 and 2 at the same pressure . In the former heat transfer process under saturated condition, the heat flux rapidly increases with a slight decrease of wall superheat up to q_{max} after the boiling initiation at point A: the wall superheat at the q_{max} is 29 K. The heat flux reaches the maximum value at point C before reaching the FDNB regime with the decrease in surface superheat due to the activation of originally unflooded cavities. The explosive-like HSN occurs at point C, which has become possible to occur at the point due to the decrease of surface superheat increasing rate. In the latter heat transfer processes under subcooled condition, boiling initiates on conduction regime at points A_s and A'_s for the Cases 1 and 2. The wall superheats for the cases are 28 and 32 K, respectively. After the boiling inception, wall superheat first increases, then decreases and again increases with the increase in heat flux. The transient heat transfer process for the Case 1 almost agrees with that for the Case 2, though the wall superheat for the process just after the initial boiling is slightly lower than that for the Case 2. It should be noted that the heat flux for each case increases after the initial temperature overshoot and setback on the higher superheat side of the steady FDNB curve almost parallel to it and has a maximum value. Namely the maximum heat flux is reached before the originally flooded cavities are fully activated. However, it is supposed that the heat transfer crisis at the q_{max}

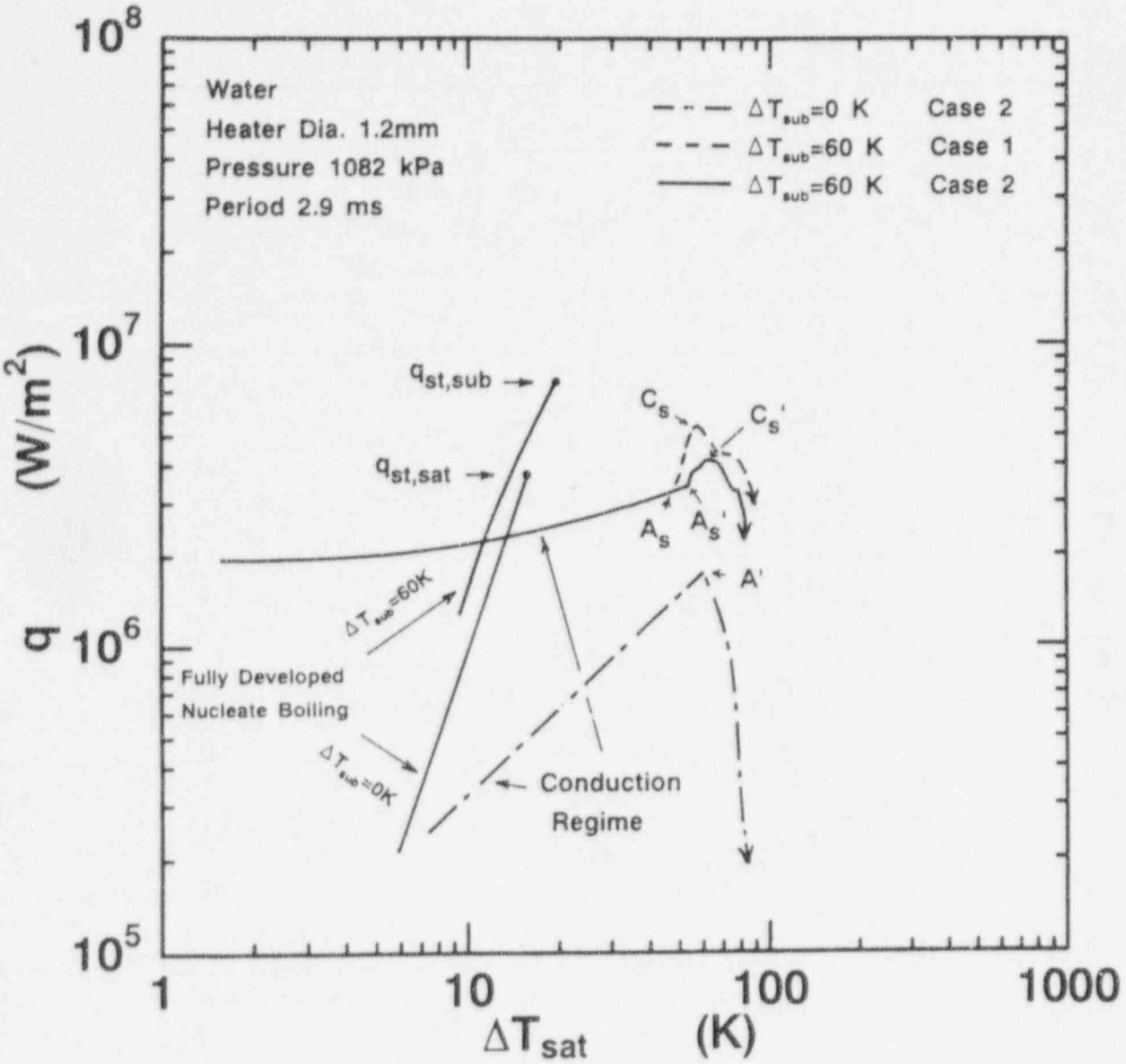

Fig. 9 Typical heat transfer processes with the q_{max} of 2nd group for the period of 2.9 ms at saturated condition for the Case 2 and at subcooled condition for the Cases 1 and 2.

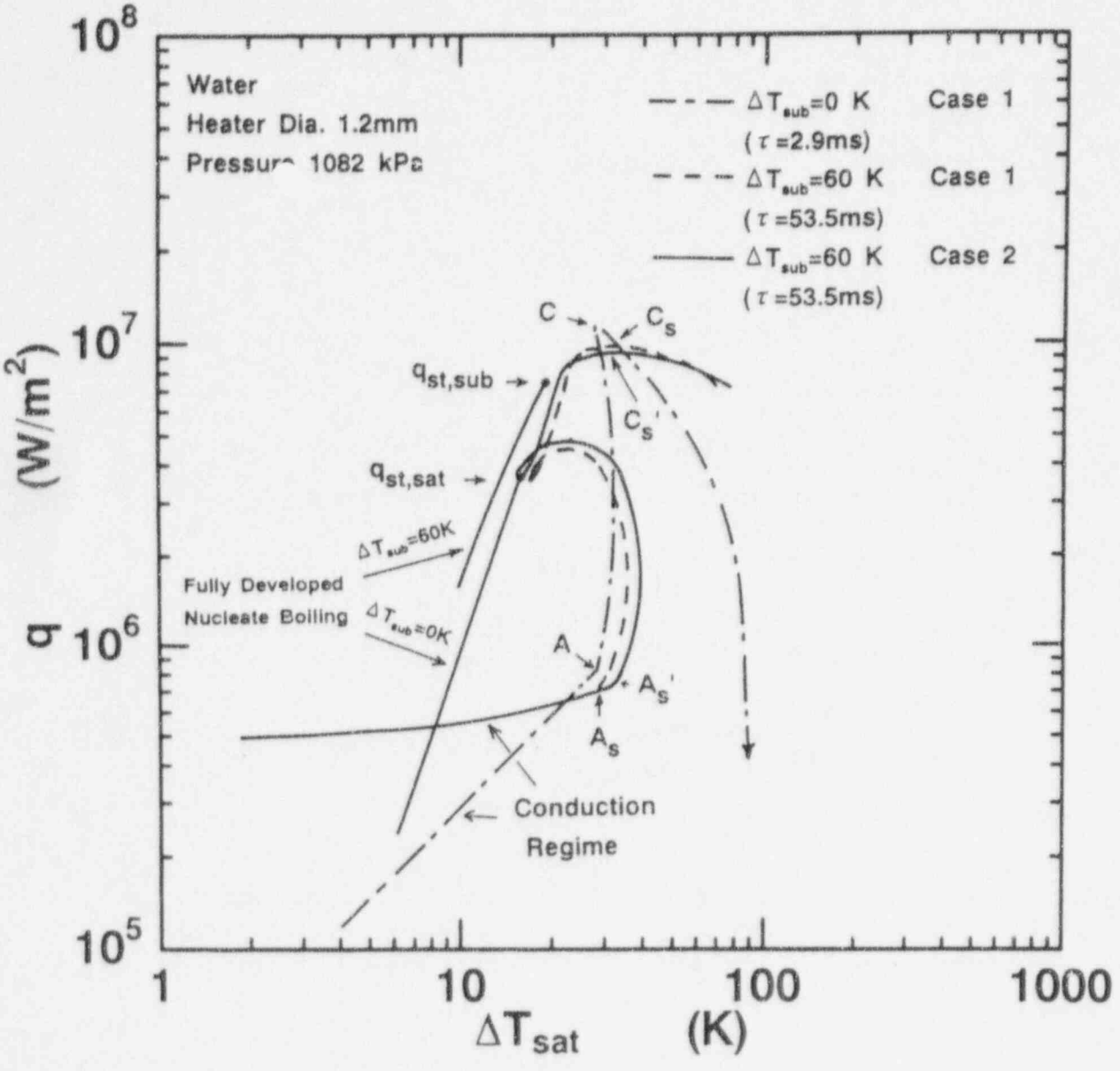

Fig. 10 Typical heat transfer processes with the q_{max} of 3rd group at saturated condition for the period of 2.9 ms for the Case 1 and at subcooled condition for the period of 53.5 ms for the Cases 1 and 2.

occurs due to the HSN in originally flooded cavities.

2.6 Comparison of experimental data with numerical results from a conventional correlation

Recently, Pasamehmetoglu and Nelson [9] presented a model of pool boiling maximum heat flux for power transients under saturated and subcooled conditions based on a macrolayer thinning model which is to be applicable for the q_{max} in the first group for a low subcooled condition. The data of q_{max} for periods for the subcoolings of 20 and 60 K at 1.08 Mpa are compared with those predicted by their model with their empirical coefficient of unity in Fig. 11. The q_{max} values obtained from Eq.(5) for the subcooling of 20 K and Eq.(9) for that of 60 K in the first group are also shown in the figure for comparison. The predicted values at the subcooling of 20 K are different in the trend of dependence on the period from the corresponding experimental data in the range of period longer than around 200 ms: the predicted value increases with a lower rate than that for the experimental data with the decrease in the period. As shown in the figure, the q_{max} values derived from their model for the subcooling of 60 K looks like agreeing with the corresponding experimental data of q_{max} for the period longer than around 100 ms. As mentioned before, the mechanism of heat transfer crisis at the q_{max} for high subcoolings at high pressures in the first group is different from that for the low subcoolings due to the hydrodynamic instability not only in transient state but also in steady state. For the periods shorter than the value, the predicted values for each subcooling by the model become several times higher than the experimental data. The experimental values of q_{max} significantly decrease with the decrease in period: the q_{max} approaches the asymptotic line of direct or semi-direct transition with the decrease in period. The asymptotic curves for the subcoolings derived from the empirical Eq. (6) with the corresponding experimental data of q_{max} for the Case 2 for short periods are also shown in the figure.

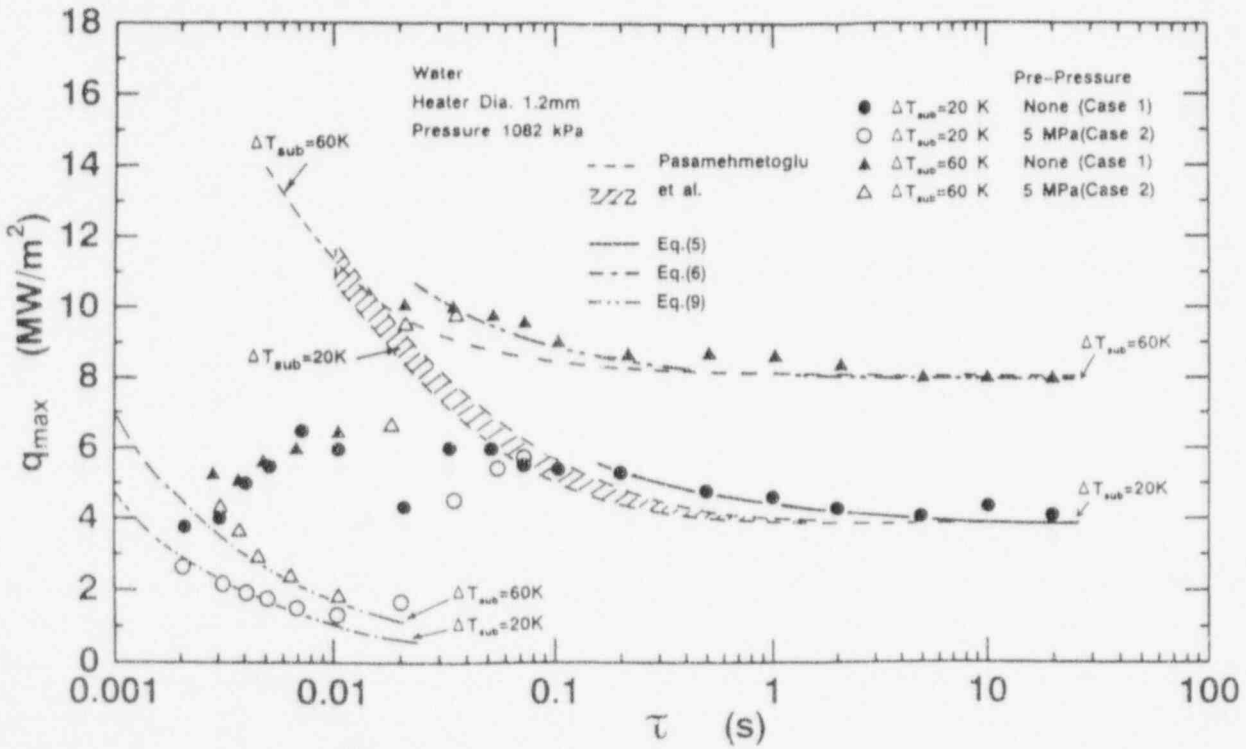

Fig. 11 Comparison of the authors' q_{max} data for subcoolings of 20 and 60 K at a pressure of 1082 kPa with predicted values by Pasamehmetoglu et al.'s and authors' correlations.

SUMMARY AND CONCLUSIONS

Experimental data of the steady-state and transient maximum heat fluxes, q_{st} and q_{max}, due to exponential heat inputs in water for the Cases 1 and 2 (without and with pre-pressurization) were obtained for the exponential periods ranging from 2 ms to 20 s and for the subcoolings from 0 to 80 K at the pressures ranging from 101.3 to 2063 kPa. Experimental results lead to the following conclusions.

1. The q_{st} correlations for the subcoolings lower or higher than around 50 K were given based on the experimental data obtained. There exist different mechanisms of heat transfer crisis at q_{st} for lower and higher subcoolings: the former mechanism of heat transfer crisis is due to the hydrodynamic instability and the latter one is due to the heterogeneous spontaneous nucleation.

2. The q_{max} data for the Case 2 with pre-pressurization for all the subcoolings and pressures tested here except those for the pressure of 2063 kPa can be clearly separated into three groups in their relation versus exponential period; the q_{max} values for the second group at which direct or semidirect transitions occur were obtained. The q_{max} in the second group for the Case 1 were observed for the subcoolings lower than 10 K at pressures lower than 494 kPa. The curves representing the q_{max} in the second group almost agree with those obtained for the Case 2 on the graph of q_{max} versus τ.

3. The q_{max} in the second group for the Case 1 without pre-pressurization will be obtained for the periods sufficiently shorter than the shortest one tested here for high subcoolings at high pressures; the q_{max} values will almost agree with those obtained for the Case 2 at the same conditions of subcoolings and pressures at the same period.

4. The correlations representing the q_{max} for periods in the first group for lower range of subcoolings from zero to around 50 K and for higher subcoolings were given; the former is due to the time lag of hydrodynamic instability which starts at steady-state maximum heat flux, and the latter is due to the occurrence of heterogeneous spontaneous nucleation, the surface superheat for which depends on the increasing rate of surface superheat. The q_{max} values for periods in the first group are independent of pressures at high subcoolings such as 60 and 80 K.

NOMENCLATURE

c_p = specific heat at constant pressure, $J/(kgK)$
D = cylinder diameter, m
FDNB = fully developed nucleate boiling
g = acceleration of gravity, m/s^2
HSN = heterogeneous spontaneous nucleation
h_c = conduction heat transfer coefficient, $W/(m^2\ K)$
K = constant
k = thermal conductivity, $W/(m\ K)$
L = latent heat of vaporization, J/kg
P = system pressure, MPa
P^* = reference pressure, MPa
Q = heat input, W/m^3
Q_0 = initial exponential heat input, W/m^3
q_{max} = transient maximum heat flux, W/m^2
q_{st} = steady-state maximum heat flux, W/m^2
$q_{st,sat}$ = steady-state maximum heat flux under saturated condition, W/m^2
$q_{st,sub}$ = q_{st} for subcooled condition, W/m^2

T_l = bulk liquid temperature, K

T_{sat} = saturation temperature, K

T_w = wall temperature, K

t = time, s

ΔT_i = surface superheat at the initiation of boiling, K

ΔT_{iLH} = lower limit of HSN surface superheat, K

ΔT_m = surface superheat at q_{max}, K

ΔT_{sat} = $T_w - T_{sat}$, surface superheat, K

ΔT_{sub} = $T_{sat} - T_l$, liquid subcooling, K

α = constant

β = constant

μ = $[\rho_l c_{pl}/(k_l \tau)]^{1/2}$, m^{-1}

ρ = density, kg/m^3

σ = surface tension, N/m

τ = exponential period, s

Subscripts

l = liquid

v = vapor

REFERENCES

[1] A. Sakurai and M. Shiotsu, "Transient Pool Boiling Heat Transfer, Part 1 and Part 2", J. Heat Transfer, Trans ASME,Ser. C., 99, 547-560(1977).

[2] S.S. Kutateladze, "Heat Transfer in Condensation and Boiling", AEC-tr-3770(1959).

[3] N. Zuber, "Hydrodynamic Aspects of Boiling Heat Transfer", USAEC Report, University of california, Los Angels, AECU-4439(June 1959).

[4] A. Sakurai, M. Shiotsu and K. Hata, "Boiling Heat Transfer from a Horizontal Cylinder in Liquid Nitrogen", Heat Transfer and Superconducting Magnetic Energy Storage, ASME HTD-Vol.211, 7-18(1992).

[5] A. Sakurai, M. Shiotsu and K. Hata, "New Transition Phenomena to Film Boiling due to Increasing Heat Inputs on a Solid Surface in Pressurized Liquids",Instability in Two-Phase Flow Systems, ASME HTD-Vol.260, 27-39(1993).

[6] A. Sakurai, M. Shiotsu, K. Hata and K. Fukuda, "Transient Pool Boiling Heat Transfer from a Horizontal Cylinder in Water at Pressures", Proc. 6th International Topical Meeting on Nuclear Reactor Thermal Hydraulics, 1, 231-239(1993).

[7] A. Sakurai, M. Shiotsu and K. Hata, "Mechanism of Nucleate Boiling on a Solid Surface in Liquid Helium I", Advances in Cryogenic Engineering, 39, 1759-1768 (1994). [8] A. Sakurai, M. Shiotsu and K. Hata, "Boiling Phenomenon due to Quasi-steadily and Rapidly Increasing Heat Inputs in LN2 and LHe I," Proc. International Symposium on Safety of Superconductors and Related Heat Transfer at Low Temperatures, 1A-2 (1994), or to appear in Cryogenics.

[9] K. O. Pasamehmetoglu, R. A. Nelson and F. S. Gunnerson, "Critical Heat Flux Modeling in Pool Boiling for Steady-State and Power Transients", J. Heat Transfer, Trans. ASME, Ser. C., 112, 1048-1057(1990).

Cross-Sectional Void Fraction Distribution Measurements in a Vertical Annulus Two-Phase Flow by High Speed X-ray Computed Tomography and Real-Time Neutron Radiography Techniques

G.D. Harvel[1,2], K. Hori[2], K. Kawanishi[2], and J.S. Chang[1]

[1]Department of Engineering Physics
McMaster University
Hamilton, Ontario, Canada

[2]Combustion and Heat Transfer Laboratory
Takasago Research and Development Centre
Mitsubishi Heavy Industries
Takasago, Hyogo Pref., Japan

Abstract

A Real-Time Neutron Radiography (RTNR) system and a high speed X-ray Computed Tomography (X-CT) system are compared for measurement of two-phase flow. Each system is used to determine the flow regime, and the void fraction distribution in a vertical annulus flow channel. A standard optical video system is also used to observe the flow regime. The annulus flow channel is operated as a bubble column and measurements obtained for gas flow rates from 0.0 to 30.0 l/min. The flow regimes observed by all three measurement systems through image analysis shows that the results agree well with each other. Both the RTNR and the X-CT systems show that the two-dimensional void fraction distribution can be obtained. The X-CT system is shown to have a superior temporal resolution capable of resolving the void fraction distribution in an (r,θ) plane in 4.0 ms. The RTNR system is shown to obtain void fraction distribution in a (r,z) plane in 33.0 ms. Void fraction distribution for bubbly flow and slug flow is determined.

1. Introduction

In order to understand the detail transient two-phase flow structure, more advanced two-phase flow instrumentation is required. Advanced radiation techniques are being seriously considered as one of the options, since we can obtain information about the void fraction distribution non-intrusively. The best applications for these new instruments will be opaque and metallic flow channels with highly complex structures.

The two advanced radiation techniques studied in this work are a Real-Time Neutron Radiography system (RTNR) and a high speed X-ray Computed Tomography system (high

speed X-CT) . Both techniques are non-intrusive since they use ionizing radiation. Water in the test section attenuates radiation without the radiation depositing significant amounts of energy. The void fraction is the percentage of the flow channel volume not occupied by the water phase. Therefore, measuring the attenuation of the radiation beam can detect the void fraction in the flow channel.

Real-Time Neutron Radiography (RTNR) is a complementary technique to X-ray radiography that allows for the measurement of local void fraction as a function of the spatial (x,r,z) and temporal (t) coordinates. Typically RTNR has less attenuation than X-rays for metal pipe systems. Early two-phase flow studies of Real-Time Radiography were performed by Narabayashi et al.[1] using an X-ray source. Robinson and Wang[2] used an image intensifier for visualization of two-phase flow. Mishima et al.[3] performed a quantitative analysis by examining two-phase flow in a narrow rectangular duct by RTNR. Chang et al.[4] examined two-phase interfaces for air-water and coal-water slurry flows in pipe and bundle geometries by an RTNR system. Cross-sectional averaged axial vmid fraction profiles have been measured for two-phase flow in both pipe [5] and bundle geometries [6].

Some investigators have studied the single beam X-ray densitometer. More recently though, investigators have applied multiple beam X-ray techniques for the measurement of void fraction and void distribution[1,7,8,9,10]. Narabayashi et al. discussed in detail a scanning X-ray system for measurement of void fraction in pipe flow[1,8]. Morooka et al. discussed application of computed tomography to the X-ray technique[7,9]. Each investigator improved the spatial measurement of void fraction using the X-ray technique, but usually at the expense of temporal resolution. Hori et al. [10] developed a high-speed X-ray CT system for measurement of void fraction in a pipe which has both good spatial and good temporal resolution that can scan a cross-sectional plane of a cylindrical flow channel. This system is considered high speed as it can acquire a void fraction distribution image across the cross-sectional plane of the cylindrical flow channel every 4.0 ms. This is achieved by using 122 X-ray detectors and 18 X-ray sources in a fixed array. With this system, Hori et al. [10] determined void fraction and void fraction distribution in bubbly flow and in slug flow for a vertical pipe flow channel.

With a basic understanding of how these instruments perform in pipe flow, we can now examine more complex flow structures. In this work, we apply these advanced techniques to a more complex flow structure; namely a vertical annulus flow channel for real-time cross-sectional void fraction distribution measurement.

2. Experimental Apparatus

This work uses three independent measurement techniques for two-phase flow parameters. They are the RTNR system, the X-CT system, and an Optical video system. The RTNR system is used at McMaster University in the McMaster Nuclear Reactor (MNR) facility[11]. The X-CT system and the optical video system are used at the Mitsubishi Heavy Industries Takasago Research and Development Centre[10]. The test apparatus studied in this work

is a vertical annulus flow channel.

2.1 X-CT System

The high speed X-ray CT scanner is shown in Figure 1[10]. A 100 kV grid accelerates an electron beam in a vacuum chamber to strike a target and produce 70 keV X-rays in a 24° fan beam. A detector array measures the X-ray beam strength in a cross-section of the channel using Cadmium Tungstenate ($CdWO_4$) scintillators and silicon photodiodes. To increase temporal resolution, 18 X-ray sources and 122 $CdWO_4$ detectors are arranged around the test channel. The sources and detectors are stationary and numerous enough to eliminate the need to rotate either source or detector array. Eliminating the rotation improves the temporal resolution; then the temporal resolution is limited by the photon decay time in the scintillation crystal, the number of X-ray sources, and the electronic timing circuit[10]. The current cross-section sampling time is 4.0 ms(250 cross-section/s). The spatial resolution is currently liited to 2.0 mm. Further details of the X-CT system including accuracies are given in previous work[10].

2.2 RTNR System

The RTNR system used in this work is shown in Figure 2[11]. An LTV Co., model NRTV-2 Real-Time Neutron Radiography Camera is used as the central component of the RTNR system. The other components in the system include a time code generator (Telcom Research Model T5010), a Mitsubishi video cassette recorder (VHS), an image processing board (Data Translation DT2861), and a personal computer (IBM-Compatible 486 AT). The details for this system including accuracies have been discussed in previous work [11].

The RTNR camera provides a standard RS-330 video signal to a VCR for video storage at a sample rate of 30 frames/second. The video can then be acquired by the Image Processing board for enhancement and analysis by computer. The RTNR Camera operates under relatively low thermal neutron fluxes; on the order from 10^4-$10^6 n/(cm^2 s)$[12]. The spatial resolution of the RTNR camera is approximately 1 mm for a high contrast image. The temporal resolution of the RTNR system is limited by the sampling rate of 30 frames/second or 33.0 ms. The exposure time for each image is also 33.0 ms as the camera uses a continuous exposure feature.

The image processing system allows for some key image manipulation such as frame averaging, filtering, image subtraction, and contrast imaging. By combining these image processing features in the correct manner, it is possible to clearly visualize various two-phase flow patterns[13]. Each image is acquired in such a way as to maximize the dynamic range of intensities providing the highest possible sensitivity. Each image is then corrected for target integration effects[11]. The corrected image is examined to determine the flow regime. Each pixel representing the flow channel field of view is analyzed by custom software and the local void fraction is determined. The cross-section is then averaged to obtain the cross-sectional averaged void fraction. The DT2861 image processing board

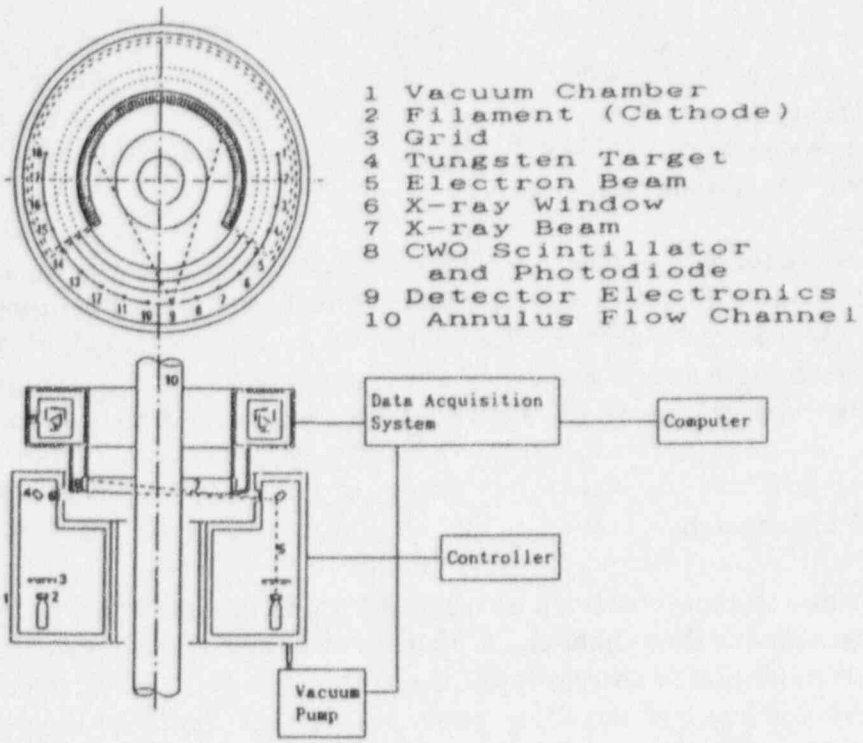

Figure 1: Schematic of the high speed X-ray computed tomography scanner

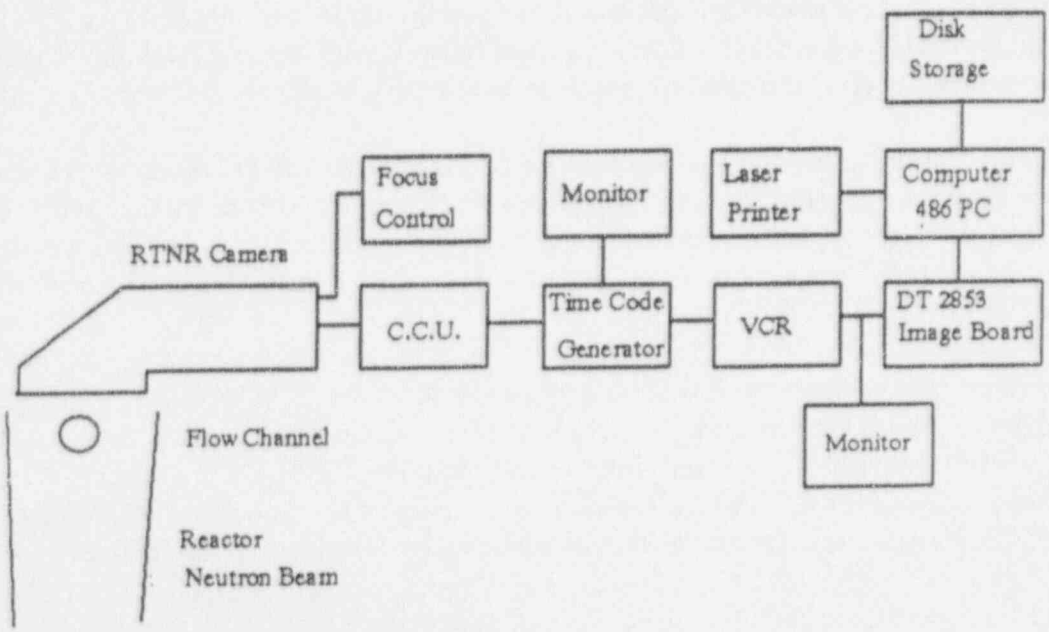

Figure 2: Schematic of the real-time neutron radiography system: CCU is the camera control unit, VCR is a S-VHS video cassette recorder

contains 16 image buffers numbering from 0 to 15. The custom software developed in this project was designed to take advantage of the 16 image buffers for temporal analysis of the images. Analysis of several images allows for determination of temporal behaviour and time averaged void fraction measurement.

Previous work compared the accuracy of cross-sectional averaged void fraction measurement between the X-ray CT system and the Real-Time Neutron Radiography system.[14] In general, the measurement accuracy for both techniques are dependent on several factors such as source strength and geometry. The previous work used identical factors to this work and found the cross-sectional averaged void fraction measurement accuracy to be within 4.0%.

2.3 Optical Video System

The optical video system records an image of the gas-liquid interface inside the flow volume of the vertical annulus flow channel. A high shutter speed (250 frames/ second) allows for the sharp determination of the gas-liquid interface. The recorded image is a planar image of the vertical axis and can show the shape and distribution of the bubbles in the image.

2.4 Experimental Flow Loop

The experimental apparatus consists of a gas injector, gas flow meters, and an annulus flow channel as shown in Figure 3. A packed bed glass bead mixer injects gas into the annulus. A rotameter (Osaka Flowmeter) measures the gas flow rate between 0.0 and 30.0 l/min and the static liquid level(i.e. no gas flow) is varied between 4.0 cm and 80.0 cm. Experimental measurements for void fraction are made between an elevation of 4.0 cm and 90.0 cm.

The gas used in these tests is atmospheric air and the liquid used in these tests is light water (H_2O) or heavy water (D_2O). Gas supply is provided by an air compressor and is regulated to 5.0 kg/cm^2. Two pressure gauges are used. The first gauge monitors the gas flow meter pressure to correct the gas flow rate and the second gauge monitors the system pressure at the inlet of the gas injector.

The annulus test section is constructed either from acrylic resin tubes, quartz tubes, or aluminium tubes. Acrylic resin tubes allow for visualization by X-rays, the optical video system, and the naked eye. Aluminium and Quartz are used for visualization by neutrons. Two boronated rubber shields are used on either side of the annulus test section to reduce neutron scattering components in the image and to eliminate high frequency electronic noise.

An overflow flange is used to ensure the instrumentation remains dry at high gas flow rates. Sponge supports are used to centre the test section inside the X-ray CT scanner. An adjustable stand is used to vary the measurement elevation.

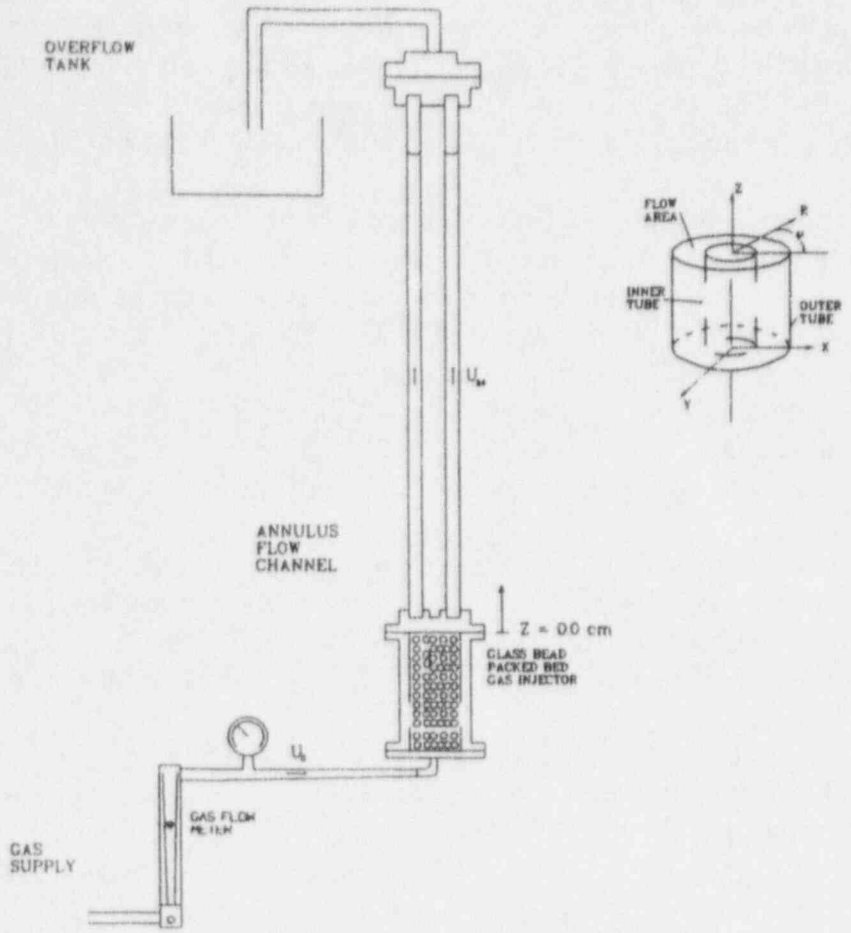

Figure 3: Experimental apparatus of the annulus flow channel

The length of the test section for the acrylic resin and Aluminium tubes is 1.0 m and is 0.50 m for the Quartz tubes. The inner diameter of the outer tube is approximately 4.75 cm and the outer diameter of the inner tube is approximately 1.9 cm which gives an annular flow area of 0.00133 m^2 and a hydraulic diameter of 2.63 cm for the acrylic resin tubes used in the high speed X-ray CT study and the optical video study. Slight variations in the diameters for each tube material exists such that the flow area and hydraulic diameters for the acrylic resin and Aluminium tubes are not exactly identical for each test. For the RTNR study, the flow area is 0.00145 mm^2 and the hydraulic diameter is 2.84 cm for the Aluminium tubes. For the Quartz tubes, the hydraulic diameters and flow areas are the same as for acrylic resin tubes.

3. Flow Regime Observations

Four possible flow regimes can exist in a vertical annulus flow channel. Bubbly flow is characterized by small bubbles that can be spherical or non-spherical in shape. Small diameter bubbles tend to be more stable and spherical and larger bubbles tend to be non-spherical. Each bubble does not surround the inner tube of the annulus flow channel but may coalesce into larger bubbles due to collisions with neighbouring bubbles.

As the gas flow rate increases, the bubbles will become larger and increasingly irregular in shape. The bubble collision frequency will increase and the probability of bubble coalescence will increase. As the gas flow rate increases further, large bubbles now coalesce and occupy a significant part of the flow area. These bubbles represent slug flow where a large packet of bubbles has coalesced into one large bubble followed by a liquid slug with a much lower void fraction. As the large bubble moves upwards along the flow channel, the interface becomes increasingly smooth and the bubble represents a donut-shaped Taylor bubble with the central core occupied by the inner tube of the flow channel.

With further increases in the gas flow rate, the void fraction in the liquid slug increases and the stability of the formed Taylor bubble decreases. At a certain point, the gas flow rate is too high and the Taylor bubble formation cannot be maintained. This flow regime is called churn flow Churn flow bubbles are highly irregular in size, shape, and distribution.

Large increases in the gas flow rate will push the liquid to the inner and outer walls of the annulus flow channel to form a thin film with a gaseous core. This flow regime is commonly called annular flow. However, the gas flow rates required for annular flow are too high for the present gas supply to measurably achieve. To simulate annular flow, an oscillatory film flow is produced by a high gas flow rate and low liquid inventory. This flow regime represents an entrained liquid flow in a gaseous core where droplets are deposited on the walls in the upper part of the annulus flow channel. The droplets fall downwards and produce an oscillating film in the imaging region due to the countercurrent nature of the two-phase flow.

Of the four flow regimes mentioned, only the first three experiments are observed under measurable conditions. Annular flow has been achieved as a simulated oscillatory film flow but the gas flow rate is unknown for this test.

Figure 4 shows the flow regime map obtained by all three observation techniques. The x-axis is the superficial gas Reynolds number as shown in Equation 1 as follows:

$$Re_{gs} = \frac{\rho_g U_{gs} D_h}{\mu} \qquad (1)$$

where U_{gs} is the superficial gas velocity, ρ is the gas density, D_h is the hydraulic diameter, and μ is the gas viscosity. The y-axis is the non-dimensional static liquid level from the sieve plate obtained by dividing by the hydraulic diameter(L/D_h).

Two non-dimensional static liquid levels are observed at 23 and 30 which correspond to liquid levels of 60.0 cm and 80.0 cm. Bubbly flow, Slug flow, and Churn flow are characterized by the high speed X-ray CT system. Figure 4 shows the transition from Bubbly flow to slug flow occurs close to a superficial gas Reynolds number of 120. The transition from slug flow to churn flow depends strongly on both the superficial gas Reynolds number and the non-dimensional static liquid level. The optical video system observes similar flow regimes as does the high speed X-ray CT system. Results for high non-dimensional static liquid levels (>16) show a small bubbly flow region, a slug flow region, and a churn flow region. At low non-dimensional static liquid levels(<16), the bubbly flow region extends to higher superficial gas Reynolds numbers and the churn flow region extends to lower superficial gas Reynolds numbers. Also, for low non-dimensional static liquid levels, the residence times of bubbles are short and hence the bubble collision frequency becomes small. Thus, at higher superficial gas Reynolds numbers($0<Re_{gs}<220$), the flow regime is still bubbly flow. As the superficial gas velocity increases further, the bubble collision frequency will increase to the point where large bubbles will be formed, however, at this point the bubbles will be unstable due to a high superficial gas Reynolds number and will develop into churn flow.

In general, the agreement among the three techniques is quite good. The transition from bubbly flow to slug flow is seen to occur at increasing superficial gas Reynolds numbers as the non-dimensional static liquid level decreases. The slug flow to churn flow transition occurs at a superficial gas Reynolds number near 400.

There is some difficulty with the transition between bubbly flow and slug flow at the higher liquid levels. This is caused by the interpretation of the images produced by each technique. For bubbly flow, agglomeration of the bubbles into larger bubbles occurs for lower flow rates than shown for the transition to slug flow. These bubbles cannot be considered as slug flow as they are still too small. However, this means the determination of the transition between bubbly flow and slug flow is quite difficult from observation of the images alone since the main criteria will be bubble size and shape.

4. Void Fraction Distribution

Figure 5 shows typical two-dimensional (r,θ) reconstructed images of a cross-sectional plane by the high speed XCT system for an initial static liquid level at L_0 = 60.0 cm (L/D_h=23) and a gas flow rate Q_g = 5.0 l/min (Re_{gs} = 110). The reconstructed images have been corrected for background and the presence of the tube walls. The light regions in the image represent the air or void fraction in the image. The dark regions represent all other materials common with the background image such as water, tube walls, and the air beyond the flow channel. Figure 5 shows binary images where white is the void fraction and black is the flow channel. The binary image is a clearer representation of the void fraction distribution. The top row is separated by 4.0 ms, the middle row is separated by 32.0 ms, and the bottom row is separated by 64.0 ms. Thus, Figure 5 shows the temporal variation in the void fraction distribution at one axial plane.

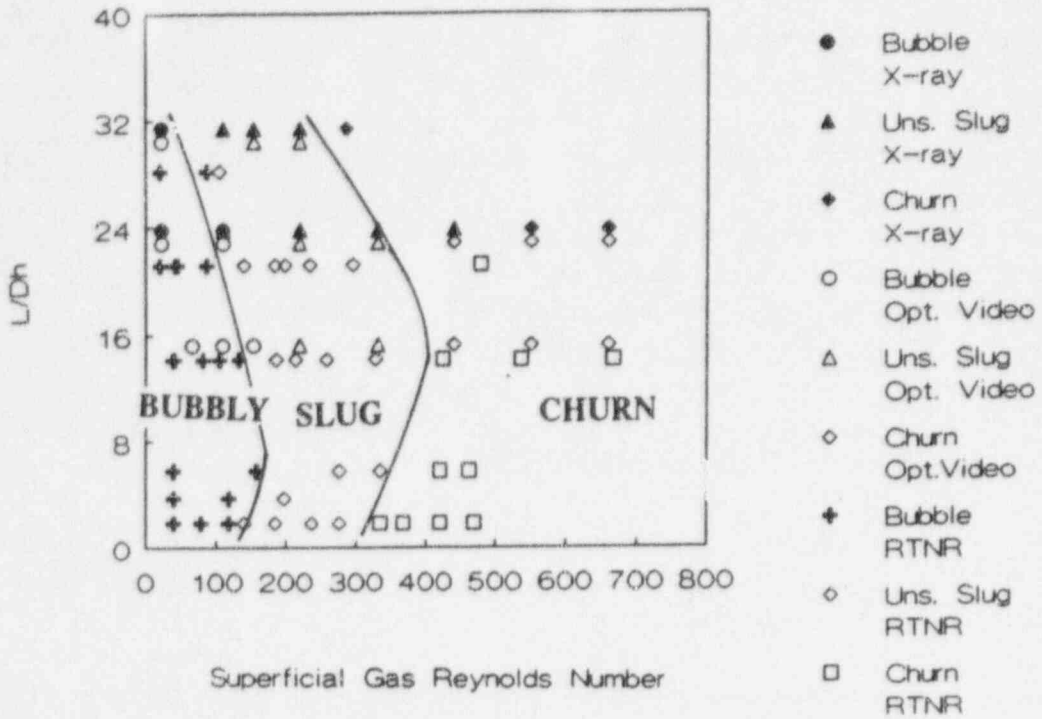

Figure 4: Flow regime map obtained for a vertical annulus flow channel as observed by the high speed X-CT system, RTNR system, and an optical video system

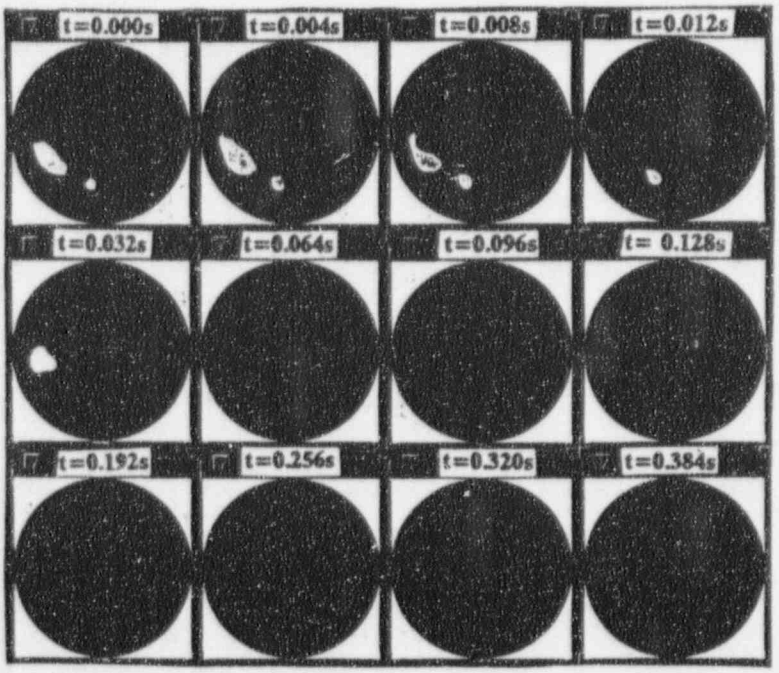

Figure 5: Reconstructed X-CT images of bubbly flow for a gas flow rate of 5.0 l/min(Re_{gs} = 110) and a static liquid level of 60.0 cm(L/D_h = 23)

Fig re 6 shows 2D (r,z) void fraction contour maps produced by the RTNR system and software. Figure 6(a) and 6(b) show results for a gas flow rate of 5.0 l/min (Re_{gs} = 105 and L/D_h=23) similar to Figure 5. These results are obtained using an Abel Inversion technique and represent the radial void fraction distribution at each axial elevation between 60.0 and 80.0 cm[11]. Figure 6(a) and 6(b) are observed 10.0 s apart. Both Figures 5 and 6 show that the flow regime is bubbly flow, and similar void fraction distributions are observed in a vertical annulus flow channel.

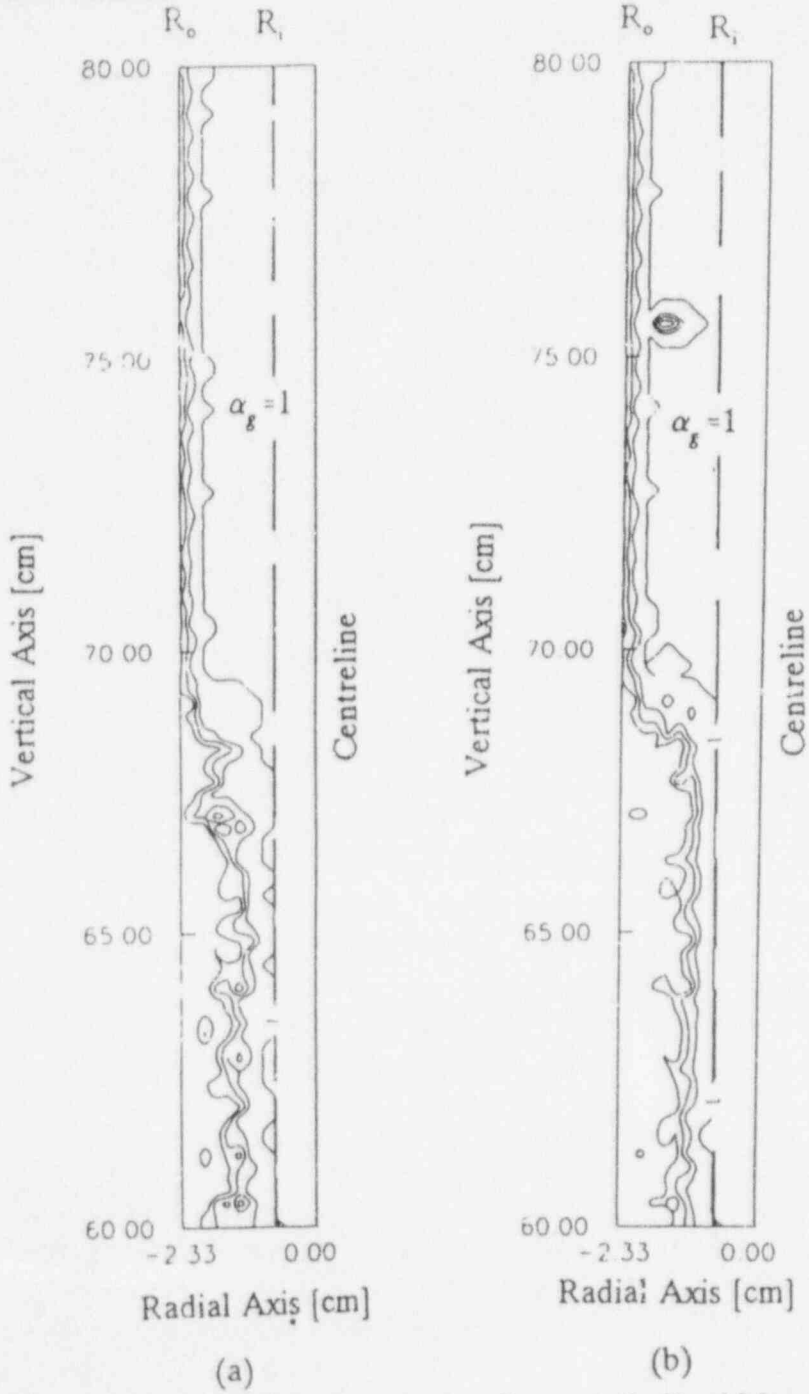

Figure 6: Two-dimensional void fraction contour maps for a static liquid level of 60.0 cm (L/D_h = 23) and a gas flow rate of 5.0 l/min(Re_{gs} = 105) by an RTNR method. Contour interval is 25% void fraction; (a) $t = t_0$; (b) $t = t_0 + 10.0$ s

Figure 7 shows the RTNR determined lateral void fraction (x-Coord.) in time as a contour map for a gas flow rate of 5.0 l/min at an elevation of 65.0 cm (same elevation for X-CT measurements) and is in the bubbly flow regime. The X-axis is the lateral position along the coordinate of the cross-section of the flow channel where 0.0 is the centre of the test section. The Y-axis is time in seconds times 10. The strange unit is due to limitations in the plotting software. Each contour represents a step in void fraction of 2.5%. The maximum local void fraction in this figure is 12.5%. Two immediate observations are apparent. First, there is a large grouping or cluster of void near x=1.1 cm similar to results observed from the X-CT system (Figure 5) and elsewhere in the figure is several small isolated voids. Simply, this figure confirms the flow regime is bubbly flow and that at a gas flow rate of 5.0 l/min, the bubbles will travel both isolated and in clusters. Another important observation is that the bubbles are not moving laterally across the flow channel. This suggests the flow is relatively smooth and without strong eddy currents as we can observe in Figure 5(X-CT). The X-CT images shown in Figure 5 cover a time span of 0.384 s. The data shown in Figure 7 covers a time span of 0.48 s.

Figure 8 shows the same data as Figure 7 but in a three-dimensional form. The magnitude of the void fraction and the void distribution is more clearly seen.

Figure 9 shows the two-dimensional (r,θ) void fraction distribution for an undeveloped slug flow as determined by the X-CT system. Twelve images are shown for a gas flow rate of 10.0 l/min (Re_{gs} = 220). The top row is separated by 4.0 ms, the middle row is separated by 32.0 ms, and the bottom row is separated by 64.0 ms. The top row of images show small bubbles entrained in a liquid slug. The middle row of images shows larger bubbles which have coalesced and will eventually be absorbed into the large bubbles typical of slug flow. The bottom row of images shows a large bubble preceded by a liquid slug and followed by entrained bubbles. The shape of the bubble is smooth along the outer edge but is still developing at the circumferential ends as the bubble traverses the flow channel.

Figure 10 shows the two-dimensional (r,z) void fraction distribution for an undeveloped slug flow as determined by the RTNR system for a gas flow rate of 10.0 l/min (Re_{gs} = 235). The two contour maps are for images acquired 10.0 s apart in time. In Figure 10 (a), we can see the end of a large agitated bubble in the neutron field of view followed by a liquid slug near an elevation of 64.0 cm. In Figure 10 (b), a liquid slug is shown between an elevation of 65.0 cm and 70.0 cm with a large bubble above 70.0 cm.

Figures 11 and 12 show the lateral void fraction as a function of time for a gas flow rate of 10.0 l/min(Re_{gs} = 235) at an elevation of 65.0 cm and is in the slug flow regime. Each contour represent 10% void fraction and the maximum void fraction in the figure is approximately 60%. Two large bubbles, indicating slug flow, are shown at a lateral position of 1.5 cm and times of 0.14s and 0.3s. The majority of the void fraction is situated for positions of x > 0.4 cm. Large bubbles are also seen in other regions of the figure but they are not as regularly shaped as the two slug like bubbles which strongly shows the flow is still developing. The shape of the two large bubbles is very distinct with a sharp void fraction front and an irregular void fraction tail as we can observe from the X-CT results (Figure 9).

Figure 11 also shows the large slug flow bubbles as wrapping around the inner tube. This

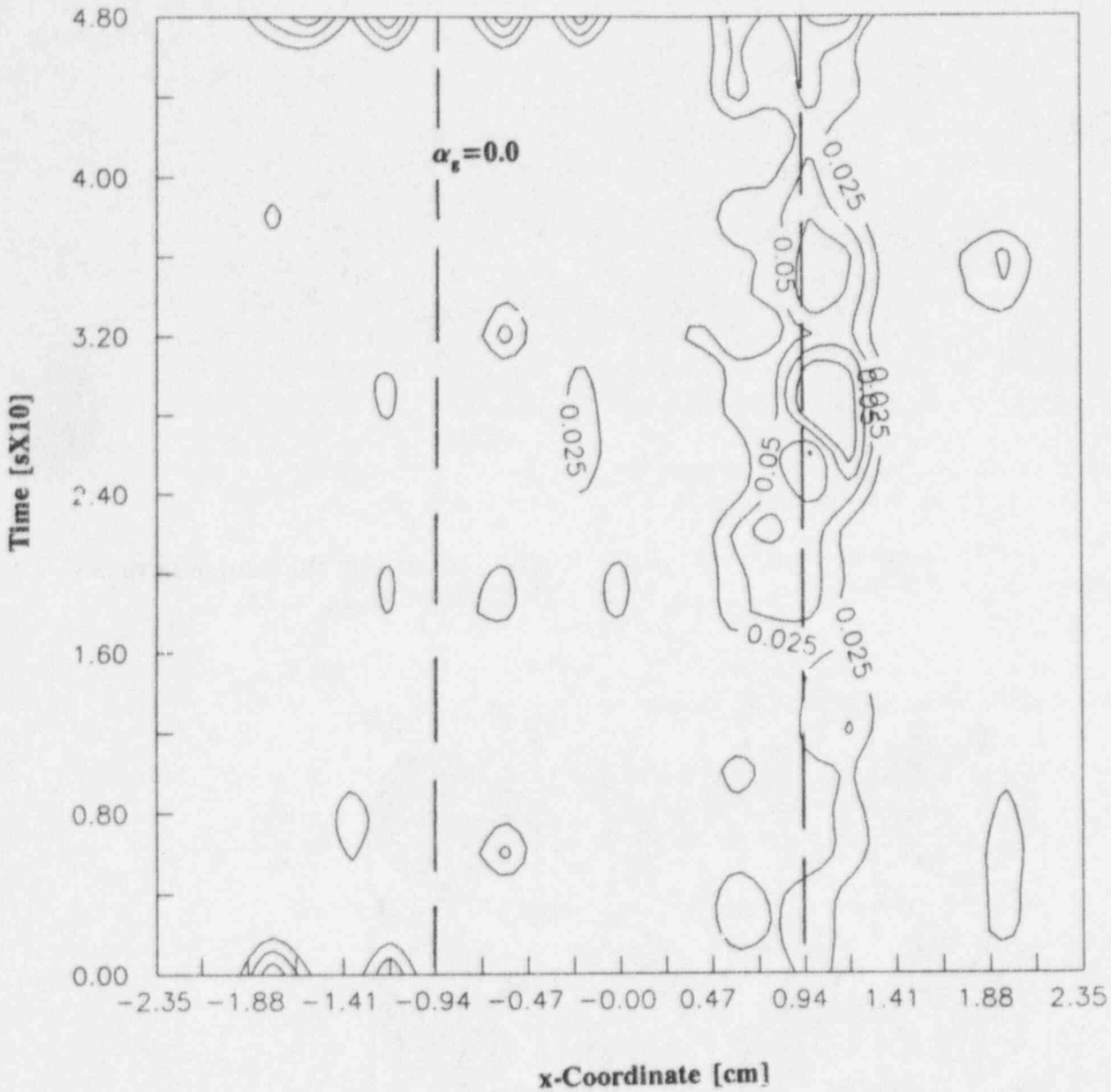

Figure 7: Contour map of the lateral void fraction in time for a gas flow rate of 5.0 l/min(Re_{gs} = 105) by an RTNR method(L/D_h = 23): Contour interval is 2.5% void fraction

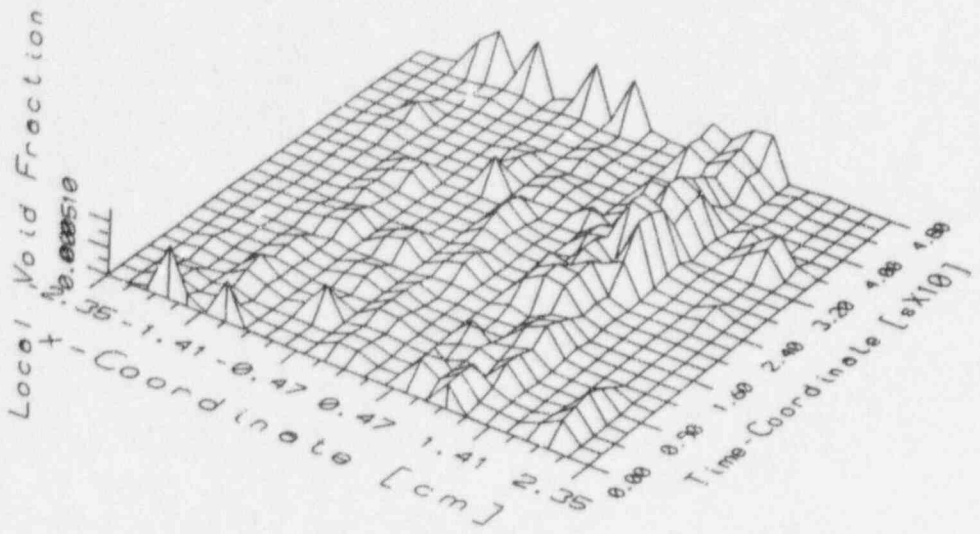

Figure 8: Three-dimensional representation of lateral void fraction fluctuation in time for a gas flow rate of 5.0 l/min (Re_{gs} = 105) by an RTNR method (L/D_h = 23)

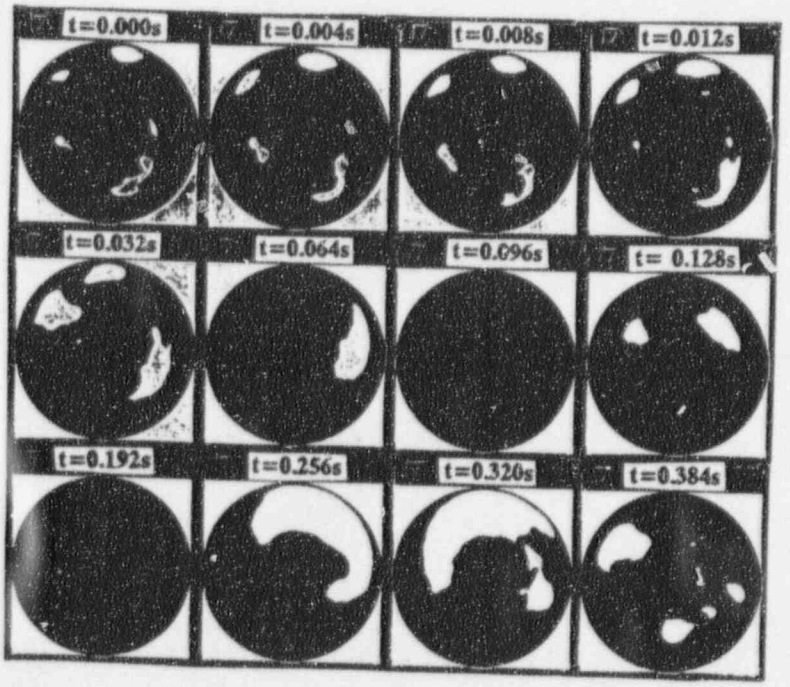

Figure 9: Real-time void distribution of developing slug flow for a gas flow rate of 10.0 l/min (Re_{gs} = 220) by an X-CT method(L/D_h = 23)

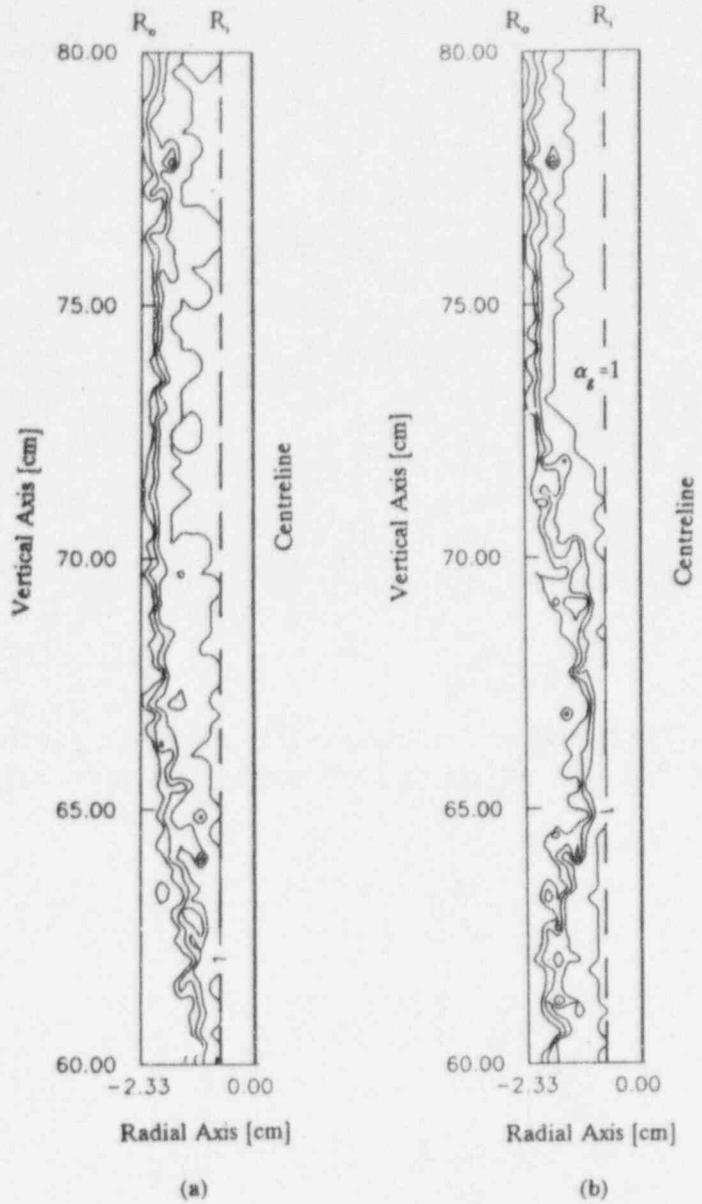

Figure 10: Real-time void distribution of developing slug flow for a gas flow rate of 10.0 l/min (Re_{g_s} = 235) by an RTNR method(L/D_h = 23). Contour interval is 25%; (a) $t = t_0$; (b) $t = t_0 + 10.0$ s

is shown by the bubble at 0.3 s, which has significant void fraction surrounding the tube, as well as the large bubbles in Figure 9 observed by the X-CT system. This suggests each bubble has significant entrainment typical of developing slug flow.

Figure 12 is the three-dimensional version of figure 11. The void fraction magnitude is clearly shown. Three very large bubbles exist along with several smaller ones. As in Figures 7 and 8, the lateral void fraction motion still does not exist even though we have entered the transition from bubbly flow to slug flow.

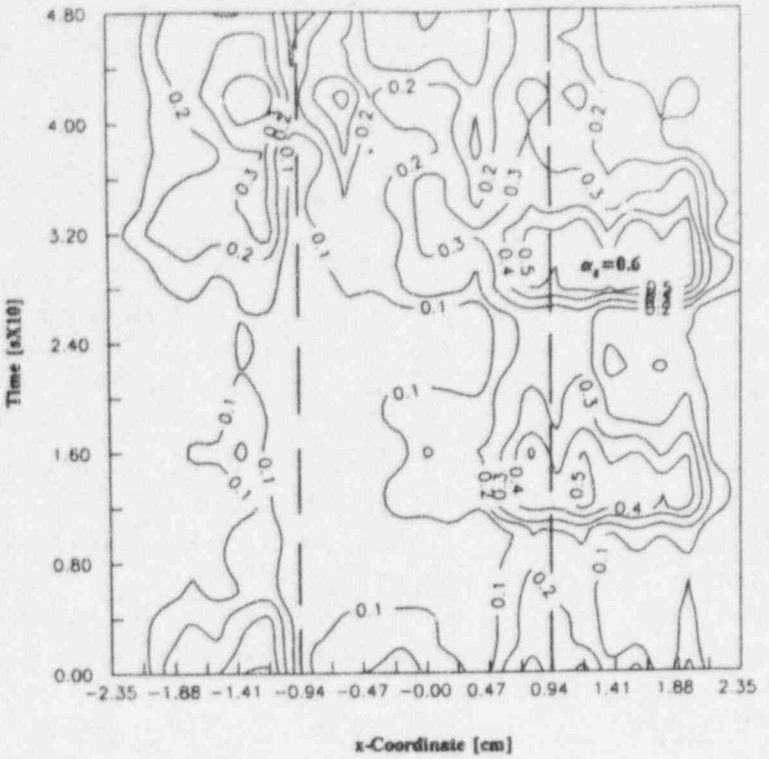

Figure 11: Contour map of the lateral void fraction (x,t) in time for a gas flow rate of 10.0 l/min (Re_{g_s} = 235) by an RTNR method(L/D_h = 23): Contour interval is 10% void fraction

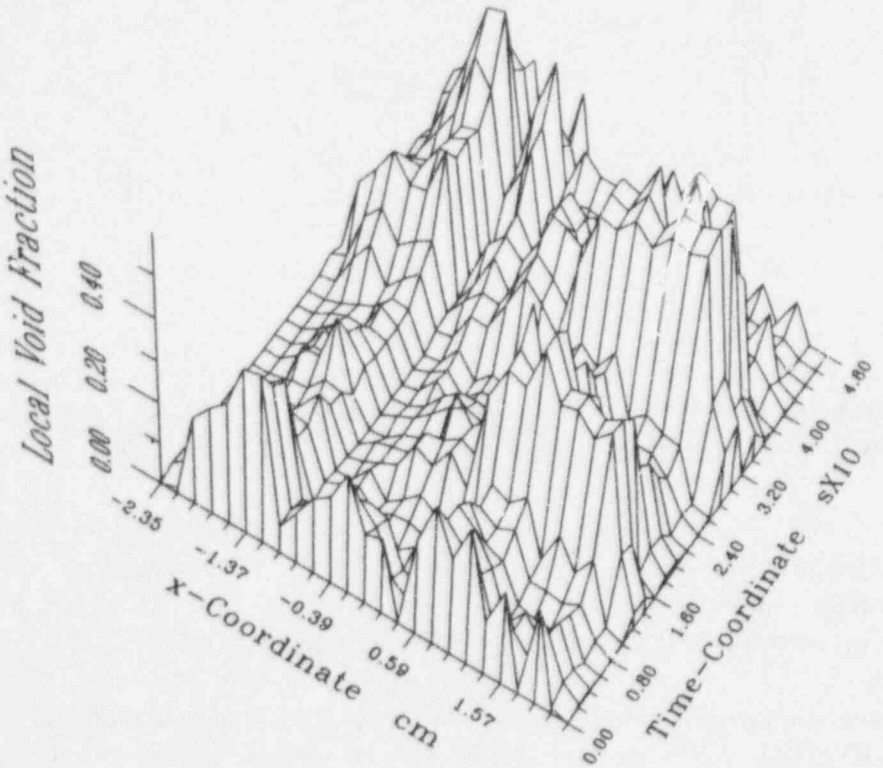

Figure 12: Three dimensional representation of lateral void fraction fluctuation in time for a gas flow rate of 10.0 l/min (Re_{g_s} = 235) by an RTNR method(L/D_h = 23).

5. Concluding Remarks and Future Work

A Real-Time Neutron Radiography system and a high speed X-ray CT system are shown to correctly determine the flow regimes of bubbly flow, slug flow, and churn flow in a vertical annulus flow channel. Two-dimensional void fraction distribution in (r,θ) coordinates are determined by the X-CT system and in (r,z) coordinates by the RTNR system. Circumferential bubble motion is easily observed in the X-CT system at high gas flow rates. Axial bubble motion is observed in the RTNR system as well as bubble development which cannot be observed by the X-CT system. The X-CT system has a much better temporal resolution than the RTNR system but the RTNR system can still provide good temporal analysis and measurement of void fraction distributions, since both systems show qualitatively similar behaviour for two-phase interfacial motions and void distributions. Temporal lateral void fraction (x,t) is measured by the RTNR system. Both the RTNR system and the X-CT system show that the lateral and circumferential void fraction motion does not occur for superficial gas Reynolds numbers less than 220 which shows a relatively low turbulence in the flow channel.

Future work should examine the bubbles in detail for information such as bubble velocity, bubble size and bubble shape.

Acknowledgements

The authors would like to thank NSERC (Natural Sciences and Engineering Council of Canada), and the Ontario Ministry of Universities and Colleges URIF program for supporting this work. We would like to thank Dr. V.S. Krishnan and Dr. A. Tsuge for their valuable discussions and comments.

References

1. T. Narabayashi, T. Tobimatsu, H. Nagasaka, and T. Kagawa. "Measurement of Transient Flow Pattern by High Speed Scanning X-ray Void Fraction Meter", J.M. Delhaye and G. Cognet, Eds. Measuring Techniques in Gas-Liquid Two-Phase Flows, 259-280. Springer-Verlag, (1984).

2. A.H. Robinson and S.L. Wang, "High Speed Motion Neutron Radiography of Two-Phase Flow", Neutron Radiography, 653-659, (1983).

3. K. Mishima, K. Yoneda, S. Fujine, K. Kanda, H. Nishihara, K. Yonebayashi, M. Sobajima, and S. Ohtomo, "An Application of Neutron Radiography and Image Processing Techniques to Gas-Liquid Two-Phase Flow in a Narrow Rectangular Duct",Annu. Rep. Res. Reactor Inst. Kyoto Univ., 22, 133-141, (1989).

4. J.S. Chang, J.C. Campeau, G.D. Harvel, S.I. Osamusali, S.H. Wang, and M.P. Butler, "Real-Time Neutron Radiography for Visualization of Interfacial Geometry and Phase

Distribution in Two-Phase Flow", U. Muller, K. Rehme, and K. Rust, Eds., Proceeding of Fourth International Topical Meeting on Nuclear Reactor Thermal-Hydraulics,413-417, Karlsruhe,NURETH-4, (1989).

5. J.S. Chang and G.D. Harvel, "Determination of Gas-Liquid Bubbly Column Instantaneous Interfacial Area and Void Fraction by a Real-Time Neutron Radiography Method," Chemical Engineering Science,47, (13/14):3639-3646, (1992).

6. G.D. Harvel and J.S. Chang, "Determination of Time Dependent Void Distributions using a Real-Time Neutron Radiography Method in Gas-Liquid Two-Phase Flow,"To be Published in Proceedings of 6th Miami Int. Heat Transfer Conference, December 12, (1990).

7. S. Morooka, T. Ishizuka, M. Iizuka, and K. Yoshimura, "Experimental Study on Void Fraction in a Simulated BWR Fuel Assembly", Nuclear Engineering and Design, 114, 91-98, (1989).

8. T. Narabayashi, T. Ishiyama, H. Miyano, and H. Nei, "Measurement of Void Distribution in High Pressure Steam-Water Two-Phase Flow using High-Speed X-ray Scanner", Proceedings of First International Conference on Multiphase Flows, Sept. 24-27, Tsukuba, Japan, (1991).

9. T. Mitsutake, S. Morooka, K. Suzuki, S. Tsunoyama, and K. YOSHIMURA, "Void Fraction Estimation within Rod Bundles based on Three-Fluid Model and Comparison with X-ray CT Void Data", Nuclear Engineering and Design, 120, 203-212, (1990).

10. K. Hori, K. Kawanishi, H. Hamamura, M. Ochi, and M. Akai, "A High Speed X-ray Computed Tomography Scanner for Multipurpose Flow Visualization and Measurement", Proceedings of Fourth International Topical Meeting on Nuclear Thermalhydraulics, Operations, and Safety, Taipei, Taiwan,43-D-1 - 43-D-6, April 6-8. (1994).

11. G.D. Harvel, J.S. Chang, and V.S. Krishnan, "Determination of Time Dependent Void Fraction Distribution in Bubbly Two-Phase Flow by a Real-Time Neutron Radiography Technique", Journal of Nuclear Technology, 109,(1):132-141, January, (1995).

12. W.E. Dance and S.F. Carollo, "High Sensitivity Electronic Imaging System for Reactor and Non-Reactor Neutron Radiography", Neutron Radiography, 2, 415-422, (1986).

13. S. Fujine, K. Yoneda, and K. Kanda, "Digital Processing to Improve Image Quality in Real-Time Neutron Radiography", Nuclear Instruments and Methods in Physics Research, 228, 541-548, (1985).

14. G.D. Harvel, K. Hori,, K. Kawanishi, and J.S. Chang, "Real-Time Cross-Sectional Averaged Void Fraction Measurements in Vertical Annulus Gas-Liquid Two-Phase Flow by Neutron Radiography and X-ray Tomography Techniques",(T. Fukano and J. Bataille, Eds.), Second International Conference on Multiphase Flow, Vol.2, P1-69-1, 1995.

TWO-PHASE VELOCITY MEASUREMENTS AROUND CYLINDERS USING PARTICLE IMAGE VELOCIMETRY

Y. A. Hassan, O. G. Philip, W. D. Schmidl, and K. Okamoto
Department of Nuclear Engineering
Texas A&M University
College Station, TX

ABSTRACT

The Particle Image Velocimetry flow measurement technique was used to study both single-phase flow and two-phase flow across a cylindrical rod inserted in a channel. First, a flow consisting of only a single-phase fluid was studied. The experiment consisted of running a laminar flow over four rods inserted in a channel. The water flow rate was 126 cm^3/s. Then a two-phase flow was studied. A mixture of water and small air bubbles was used. The water flow rate was 378 cm^3/s and the air flow rate was approximately 30 cm^3/s. The data are analyzed to obtain the velocity fields for both experiments. After interpretation of the velocity data, forces acting on a bubble entrained by the vortex were calculated successfully. The lift and drag coefficients were calculated using the velocity measurements and the force data.

INTRODUCTION

One of the major concerns with steam generator operation is the tube vibration caused by turbulent flow buffeting. This vibration can cause wear on the tube joints, where the steam generator tubes interface with their support plates. The tube support plates are shown in Fig. 1. This wear may eventually lead to ruptures and leaks between the primary and secondary side. When the cumulative leaks result in a major loss in the fluid, the plant needs to be shut down and the leaking tubes either plugged or removed. This repair procedure can be very costly. Figure 1 shows a typical U-tube steam generator. To help avoid this problem experimental data is needed to test the empirical correlations which predict the behavior of the turbulent flow around the cylinders [1], [2], [3], [4]. The Particle Image Velocimetry (PIV) flow measurement technique can be used to acquire that experimental data [5], [6], [7].

The PIV flow measurement technique has a unique feature over conventional single sensor methods, such as laser doppler anemometry or hot-wire anemometry, because it offers the opportunity of capturing all the in-plane velocities of a spatial velocity field simultaneously.

The objective of this study was to use the PIV technique to study the flow around cylinders in a channel by finding the velocity of each phase of a two-phase flow. This information will be useful for developing or improving computer models which simulate this type of flow field.

The development and improvement of models and computer simulations relies mainly on experimental data. There is a need for more experimental data about this type of flow induced vibrations. It may also be useful for understanding the structure of two-phase flows.

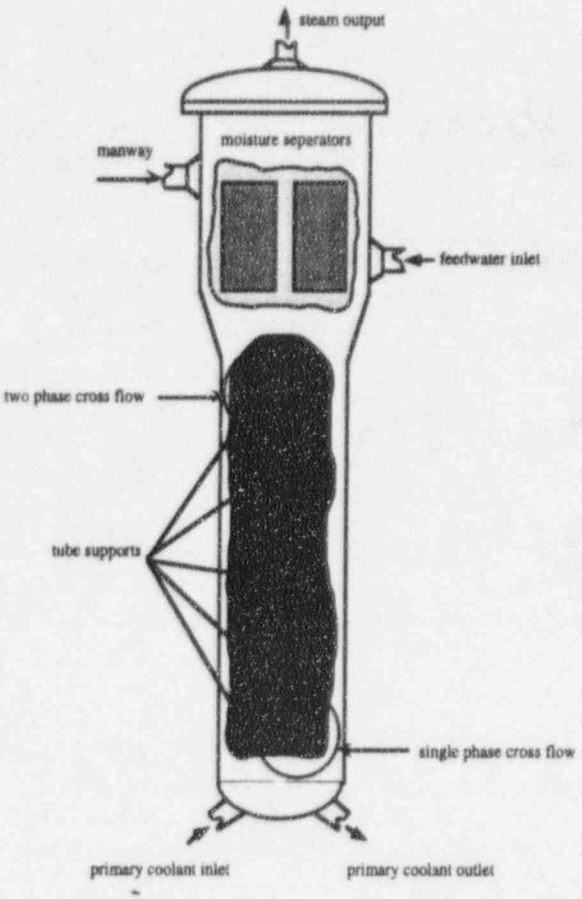

Figure 1. Typical U-tube Steam Generator

EXPERIMENTAL SETUP

Both the single-phase and two-phase experiments were conducted in a channel flow. The first experiment consisted of measuring the velocity of a single-phase, non-turbulent, parallel (horizontal and uniform) flow of water in the channel around four cylindrical rods which had been inserted in the flow path. The second experiment consisted of separately measuring the velocity of each phase of a two-phase, non-turbulent, parallel flow of water in the channel around a single cylindrical rod.

A PIV flow visualization technique requires clear optical visual access to the test section, so the channel used in the experiment is made entirely from 12.7 mm thick clear Plexiglas. Therefore any section along the channel can be studied. The channel is 3.05 m long. Its height is 8 cm and its width is 15 cm. A section of the channel approximately 2 m downstream of the inlet was selected for this experiment. The inlet nozzle of the channel was connected to the discharge from a pump. The discharge from the channel flowed back to a reservoir. The pump takes suction from this reservoir to complete the loop.

The PIV portion of the setup for this experiment included an Nd-YAG pulsed laser, two charged coupled device (CCD) cameras, an image intensifier, and two frame grabber boards. Figure 2 shows the experimental setup which was used to study the two-phase flow around the cylinder in the channel. The setup for the single-phase flow experiment is similar, however, only one camera is required. Figure 3 shows the two-phase flow experimental setup.

The light source used in the experiment is a frequency doubled Nd-YAG high energy, pulsed laser. It has a peak throughput energy of over 1.0 Joules per pulse for the primary wavelength of 1064 nm (infrared). The pulse width is approximately 8 ns, with a 7 mm circular, Gaussian distributed, beam of light. The light can be moved into position with high energy mirrors. The light is shaped from a circular beam into a planar sheet with a set of cylindrical lenses, and passed through the moving fluid under study. The lenses shrink the

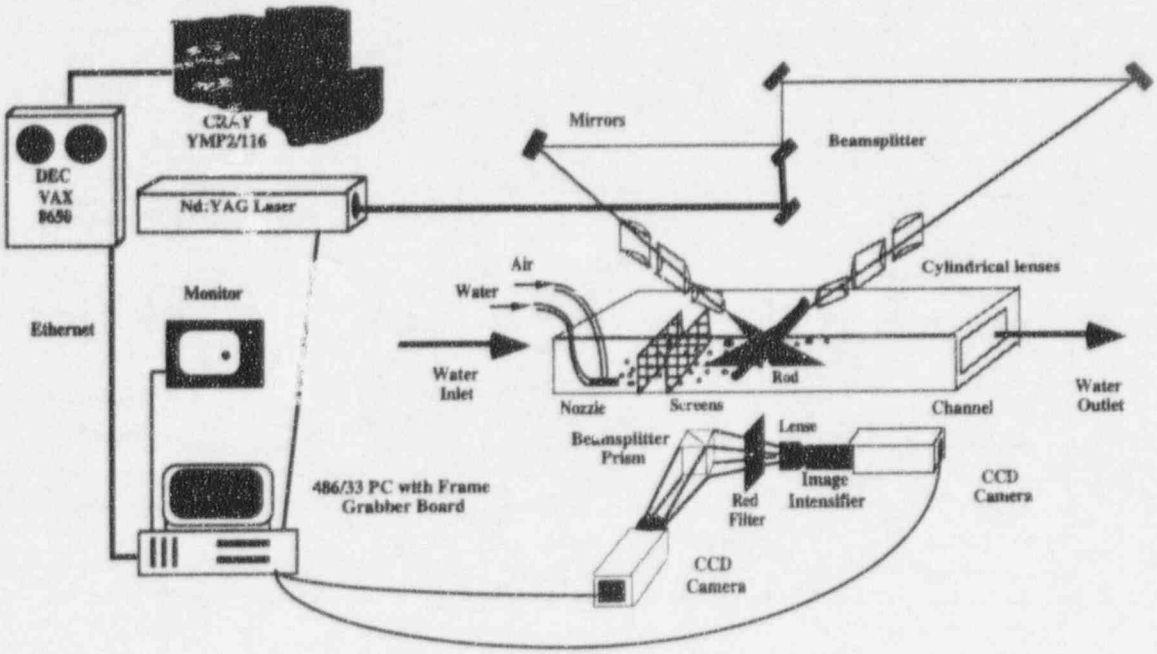

Figure 2. Experimental Setup

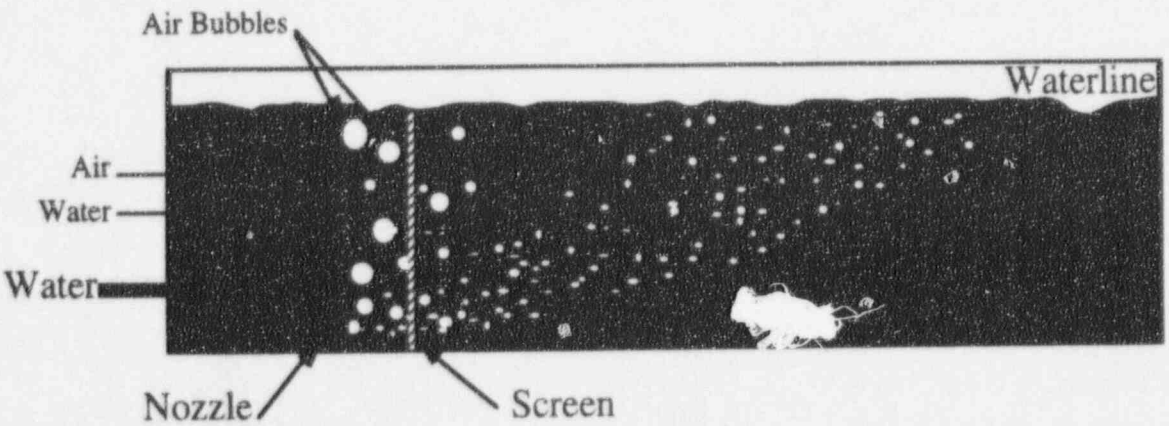

Figure 3. Bubbly Flow around a Cylinder

light from a 7 mm beam thickness into a sheet of light approximately 2 mm thick. The lenses also expand the length of the sheet to 5 cm. The near infrared laser light produced by the laser has an extremely high absorption cross-section in water. So a frequency doubling crystal is used to convert the 1064 nm (infrared) light to 532 nm (green) light. This results in a drop in the maximum energy output to 400 mJ. However, the extremely low absorption cross section at this wavelength makes up for the loss in energy.

Since an opaque cylindrical rod will not allow light to pass through it, creating a dark zone, two

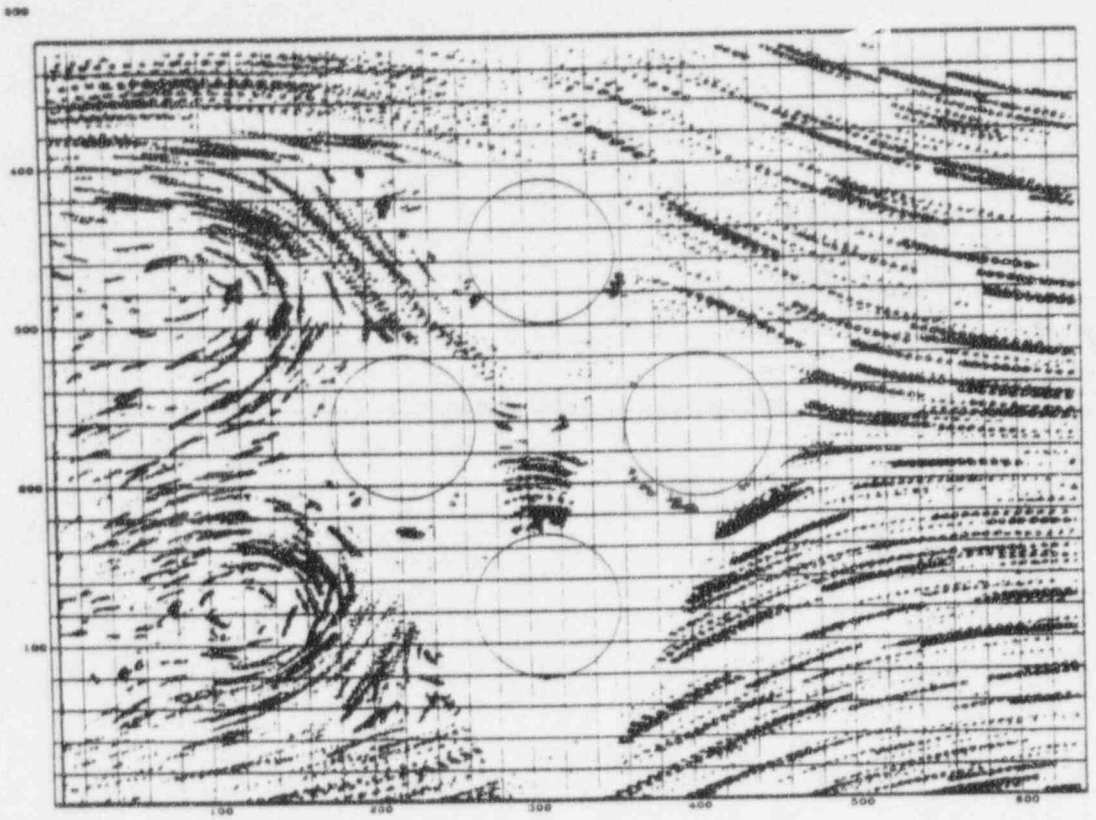

Figure 4. Single-Phase Flow Experiment Binary Overlay

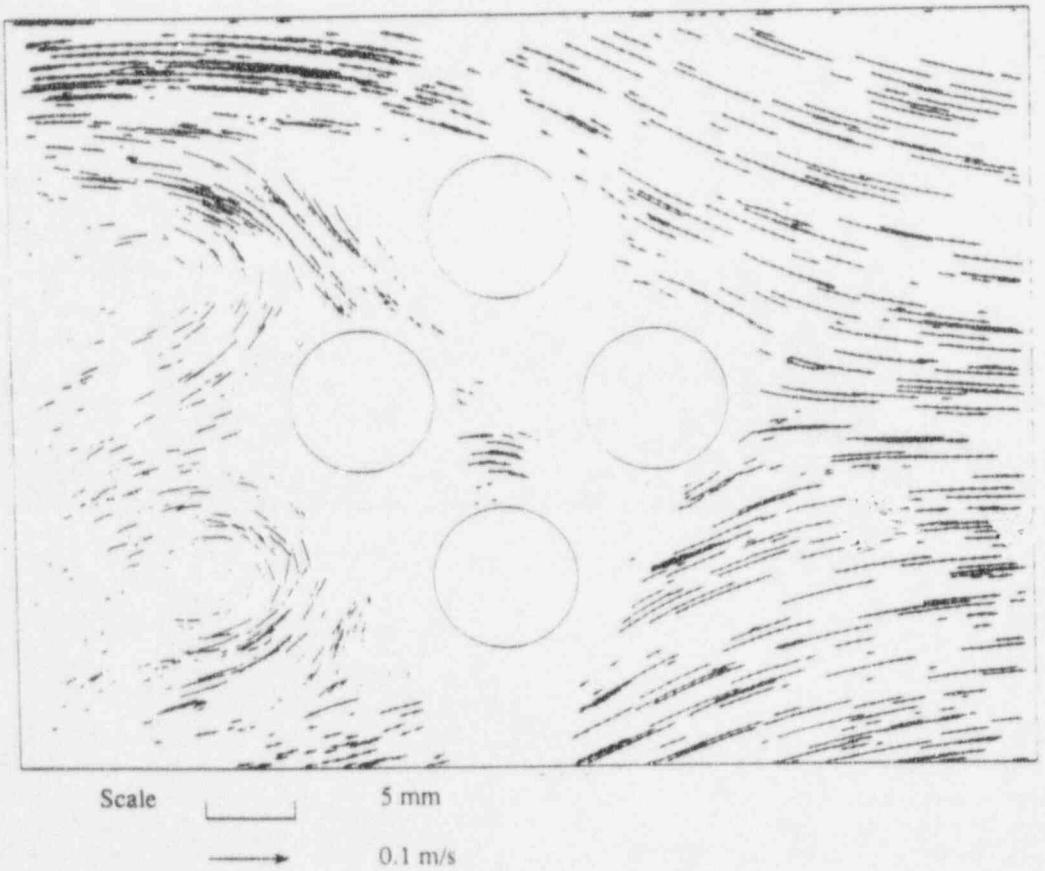

Figure 5. Velocity Vector Track for Single Phase Flow Experiment

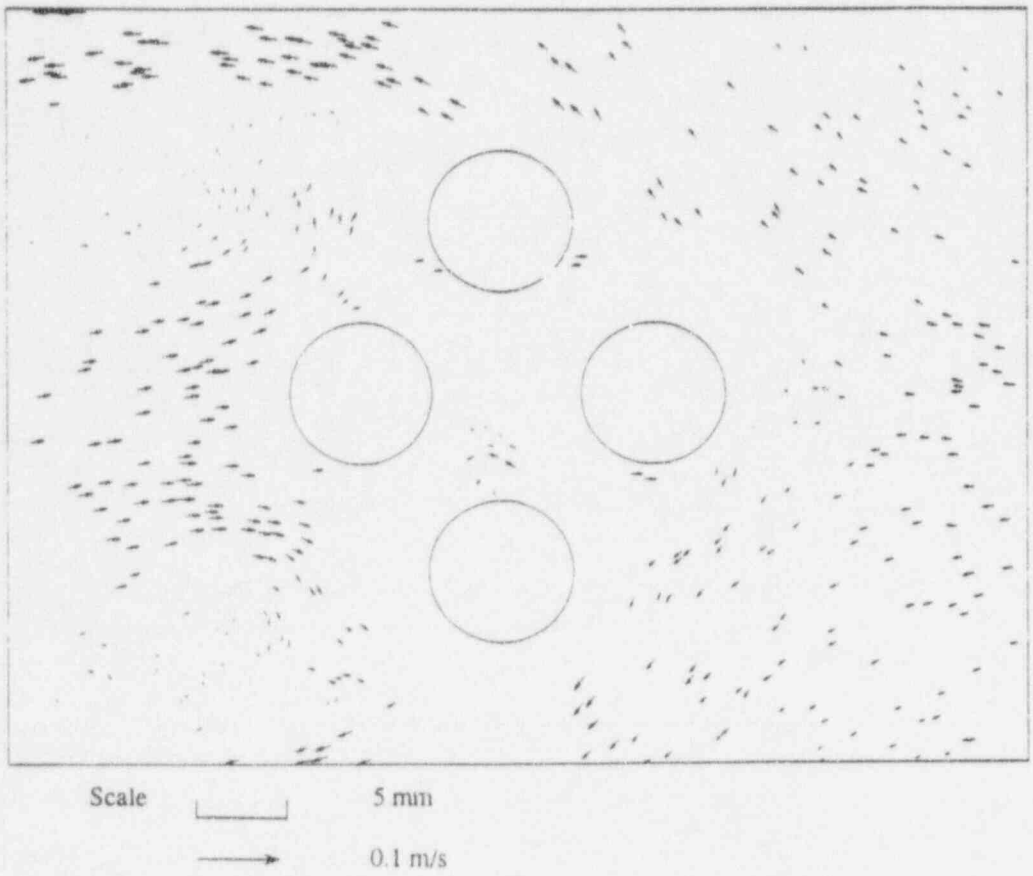

Figure 6. Velocity Vector Track for Single Phase Flow Experiment with 0.65 of Mean Velocity Subtracted

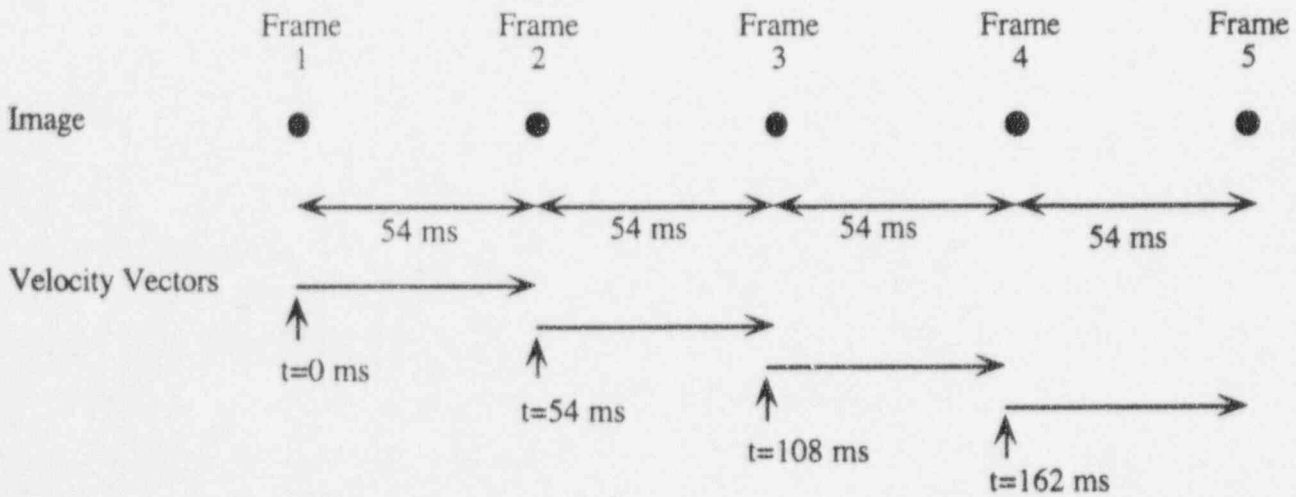

Figure 7. Velocity Vectors of Four Time Segments

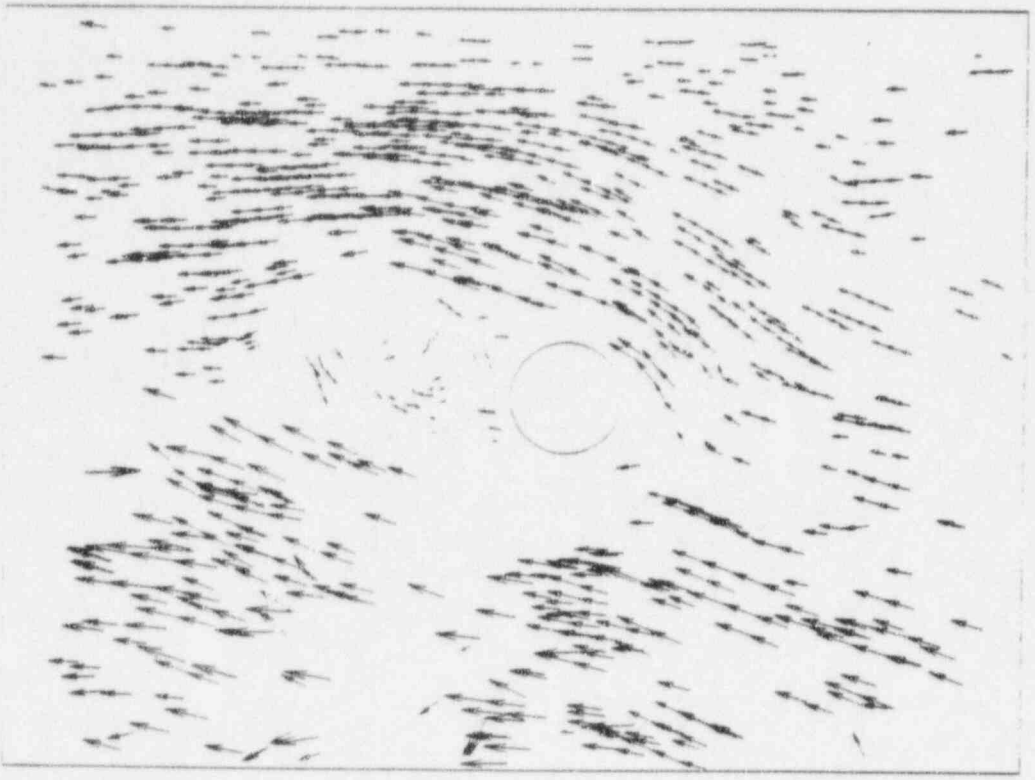

Figure 8. Two-Phase Flow Velocity Vector Track - Water, Conditional Time=0 ms

Figure 9. Two-Phase Flow Velocity Vector Track - Water, Conditional Time=162 ms

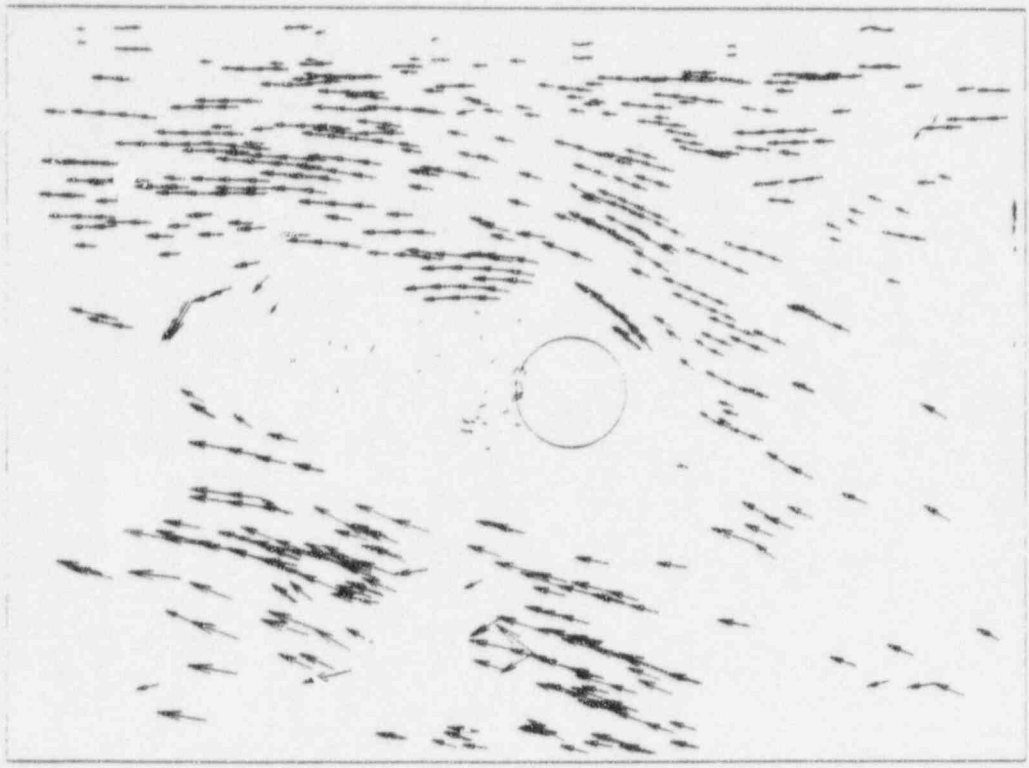

Figure 10. Two-Phase Flow Velocity Vector Track - Water, Conditional Time=324 ms

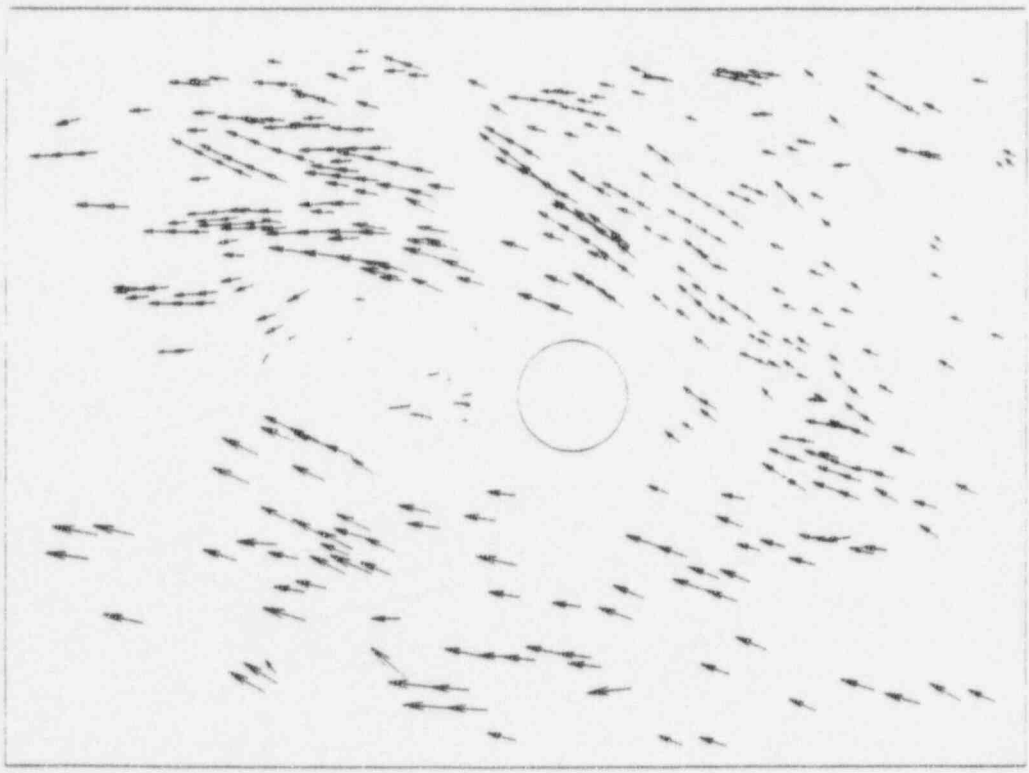

Figure 11. Two-Phase Flow Velocity Vector Track - Air Bubbles, Conditional Time=0 ms

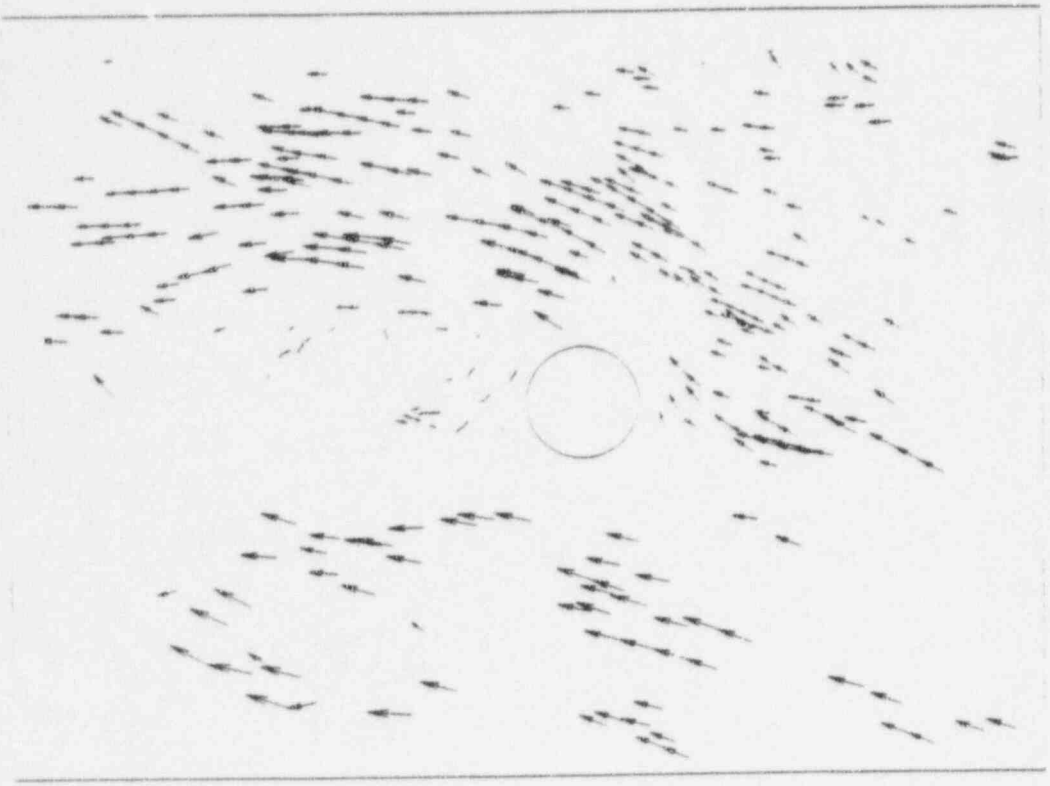

Figure 12. Two-Phase Flow Velocity Vector Track - Air Bubbles, Conditional Time=162 ms

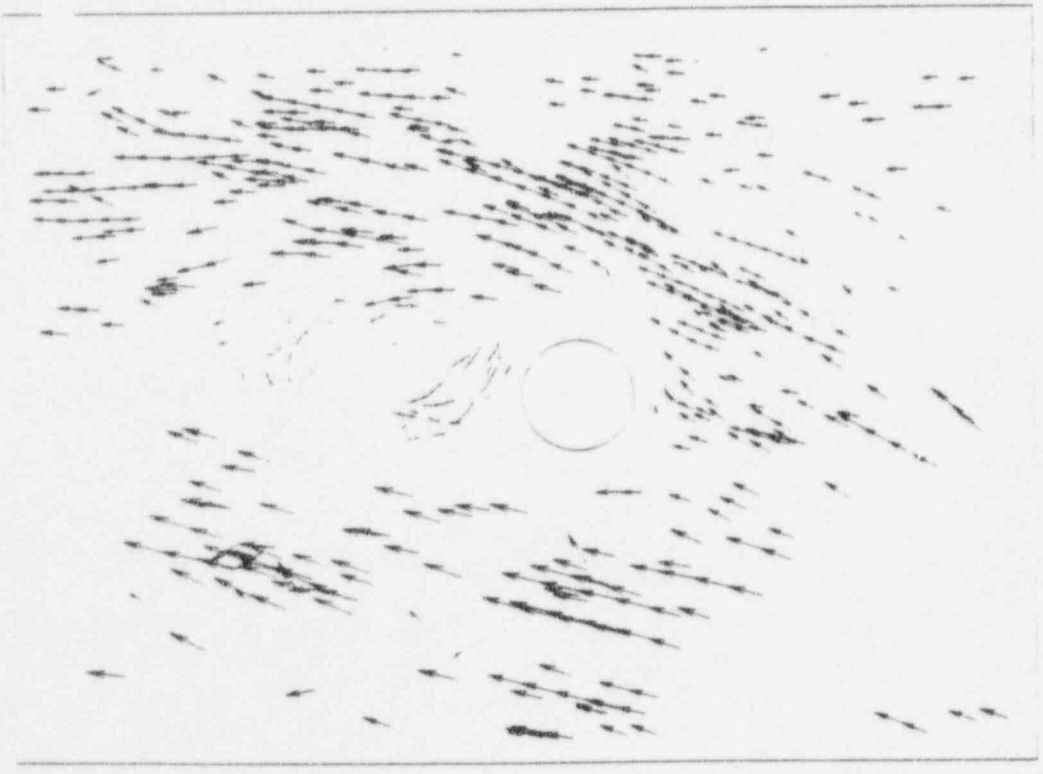

Figure 13. Two-Phase Flow Velocity Vector Track - Air Bubbles, Conditional Time=324 ms

planes of light are needed to capture the flow field on the dark side of the rod. Two beams were generated by inserting a beam splitter lens in the laser light's path. This was done before the cylindrical lenses.

To set up the light source, first the circular laser beams were positioned with a set of high energy mirrors. A system of three cylindrical lenses were inserted to expand each beam into a planar sheet of light larger than the view area captured by the cameras. Each beam hits the rod with an inclination angle of ~60 degrees as shown in Fig 2.

The next task was to set up the CCD cameras. The first camera was positioned perpendicular to the rod. The second camera was positioned perpendicular to the first camera. A beam splitter prism was used so that both cameras could focus on the same view plane simultaneously. Fluorescent seeds (emit red when struck by green light) were used in the two-phase flow experiment so the seed images could be discriminated from the air bubbles. A red filter was placed in front of the camera which was capturing the images of the seeds to block the green light reflected by the bubbles. Since the red light which was emitted by the fluorescent seeds was not very intense, an image intensifier had to be used. The camera which acquired images of the bubbles did not acquire images of the seeds because of the low intensity of the light emitted by the fluorescent seeds and the camera's aperture setting. The data from each CCD camera was stored on its respective frame grabber board, before being transferred to the computer's hard disk.

The cameras were operated in the asynchronous reset mode (a mode in which an electronic signal is used to reset the camera to acquire an image when desired). The maximum framing rate of each camera in this mode is limited to 54 ms or approximately 20 HZ. A pulse is required with these cameras because the cameras continue to acquire data once they are activated until the data is transferred off the CCD array. In this case the pulsed laser acts as the strobe.

The data from each CCD camera was stored on its own frame grabber board, before being transferred to the hard disk. The frame grabber board was also used to both trigger the laser and reset the cameras. The reliability of this tracking technique was tested by using a photodiode to measure the time between laser pulses on an oscilloscope. The timing of the laser pulses was also compared to the timing of the vertical resets of the cameras.

The sequence of events to acquire data consists of :

1. The computer sends a signal to the laser to fire it. The laser will take approximately 3 ms to actually fire after receiving this signal.
2. After a delay controlled by the computer (approximately 3 ms), the first computer sends a signal to both CCD cameras to reset them both asynchronously.
3. The laser fires and the image is captured by both CCD cameras.
4. The data is transferred from both cameras to the computer.
5. The sequence is repeated 13 times.

The small air bubbles were generated by positioning a nozzle at the bottom of the channel. The nozzle generated the bubbles by breaking up the inlet flow of air with a high speed stream of water. The flow through the channel consisting of water and entrained air bubbles was straightened by a set of two screens inserted in the channel. The screens also filtered out the larger air bubbles. Figure 3 shows the flow path of the air bubbles and water around the cylinder in the channel.

The seeds which were used to track the water flow were 6 μm diameter, neutral density (1.02 specific gravity), thermoplastic microspheres for the single-phase experiment. Red fluorescent, 30 μm, neutral density (1.02 specific gravity) microspheres were used for the two-phase flow experiment. The data for the experiment was acquired by first establishing a steady flow through the channel. Then the data acquisition sequence was triggered from the computer. The data set was stored to the hard drive of the computer. Then the next set of data was captured.

The data was stored on a vax computer which is also the interface for a Cray YMP computer. The Cray was used to perform the image analysis and the particle tracking procedure because of its fast computational capability.

DATA ANALYSIS

Once the data is acquired, the first step is to convert the gray scale data images to binary images. This was done with a local threshold. Figure 4 shows an overlay of 13 binary images (one dataset) from the single-phase flow experiment around 4 rods. The tracks of the seeds around the rod are clearly visible. There are two recirculation regions behind the rods (an upper and a lower). Then the binary image is converted into an array of tracers by combining the spots in the binary image. This array is input into a tracking algorithm,

to prod[illegible] velocity vectors, as described in details by Hassan [8].

A dynamic, particle tracking method can be quickly performed between two sequential, medium resolution (640 x 480 x 8 bit),single frame images, if the particle tracer information is first converted to binary data. The binary data conversion is a method where all the 8-bit (0-255 gray level) pixels defining a particle have been converted to 2-bit (value 0 or 1) pixels through image processing techniques, e.g, thresholding and connectivity algorithms. The particle velocity is found by determining the correspondence between particles in two consecutive video frames. Every particle belongs to a characteristic group which has a specific local distribution pattern. This correspondence is obtained through the calculation of a correlation coefficient between a referenced pattern in the first binary image and a possible candidate pattern in the second binary image, where the latter is shifted so that the centroids of the possible particle pair coincide, (Yamamoto [9],
Hassan [8]). One particle in the first image will correspond to the particle in the second image which keeps the most similar pattern, providing the local pattern of the distributed particles does not vary much between sequential video frames. The local pattern should be similar between the two frames if the frames were acquired with a very small time separation or the flow is slow.

The region directly behind the cylinder was difficult to track with the cross-correlation program because the vortex changed the pattern of the seeds between frames. The vortex rotated groups of seeds (compressing distances closer to the center of the vortex and expanding distances farther away). To solve this problem a multi-frame tracking technique which tracked individual particles between four frames was used.

An automated method was used which eliminates tedious, undesirable, manual, operator assistance in removing erroneous vectors [10]. This method was an iterative process involving an interpolated field produced from the most reliable vectors, which allowed fast analysis and presentation of sets of PIV image data. The interpolation method that was developed is based on the Hardy multiquadratic equations [11] as discussed by Narcowich [12].

Once the velocity field at any given point in the flow field is obtained, the vorticity and flow streamlines can be derived using the full-field equation for the interpolated vector field. For further details on this technique refer to Hassan [8] and Blanchat [10].

The figures presented in this paper are an overlay of several vector fields which were obtained by tracking between consecutive images in a single data set of 13 images.

There is a direct relationship between the frame rate of the cameras and the flow speed which the visualization system can measure. This is because the tracking algorithm is limited in its ability to follow patterns of tracer particles. If the seeds move too far apart and the pattern between them is distorted the algorithm has difficulty finding corresponding seeds in sequential frames. The algorithm works best for a separation of less than 20 pixels, for a non uniform flow (for a uniform, laminar, parallel flow, much larger separations are acceptable). For this experiment the frame rate was ~20 frames/sec, the horizontal view was length was ~5cm. So for a 20 pixel movement in a 640 pixel view length, flow speeds up to ~2.7 cm/s can be measured with this system (by double exposing the images, thereby achieving effective faster framing speeds, higher flow rates can be measured).

RESULTS AND DISCUSSION

Figure 5 shows the velocity vectors for a single-phase water flow around an array consisting of four cylinders. A recirculation region is obtained behind the cylinders. Figure 6 was produced by subtracting 0.65 of the mean entrance velocity vector (0.65 u) from all the vectors in the flow field. This procedure was used to scale down the mean component of the flow and to enhance the
features of interest which is the fluctuating components of the velocity vectors behind the cylinders. The water flow rate was 126 cm^3/s. The average velocity of the water was estimated to be 0.01 m/s.

For the two-phase flow experiment, the water flow rate was 378 cm^3/s and the air flow rate was estimated to be 30 cm^3/s. The following figures present the flow velocity vectors and vorticity plots for three time intervals. Each time interval is composed of 3 smaller time segments of 54 ms. For example, the velocity vectors shown in the interval are the sum of three sets of vectors computed from images between frames 1 and 2; 2 and 3; 3 and 4; and frames 4 and 5 (see Figure 7). These combined velocity vectors represent the conditional average of velocity fields for a time period of 162 ms. The conditional time is the time at which the sequence of vectors was acquired (0 ms for sequence 1, 162 ms for sequence 2, 324 ms for sequence 3 ...). The first combined velocity vectors plot (Figure 8) represents the velocity at starting

reference time zero (t=0).

Figure 9 represents the combined velocity vectors at reference time of 162 ms (t=162). Figure 10 depicts the velocity vector field for reference time of 324 ms. From these figures, it is clear there is a displacement of the recirculation zone.

With a similar approach, the velocity fields of air bubbles around the cylinder are plotted in Figures 11, 12, and 13, for reference time of 0, 162, and 324 ms, respectively.

The velocity vector plots were combined to obtain a reasonable number of velocity vectors directly behind the cylinder where they were difficult to obtain. The reason for the fairly sparse data directly behind the cylinder was a lack of seed particles and the difficulty of tracking the turbulent region directly behind the cylinder. This problem was solved by using the cross-correlation technique on the larger region surrounding the cylinder and a multi-frame tracking technique directly behind the cylinder and combining the results.

The vortex period was estimated to be 5 sec. It can be seen that the movement of the seed particles and the movement of the bubbles are different. From the calculated velocities of the seeds and the bubbles at the point indicated on these figures, the forces acting on the bubble and the drag and lift coefficients can be obtained. The bubble's radius is about 100 μm, the relative velocity between the bubble and the water is 1.5 cm/s and the local Reynolds number (for the bubble) is approximately 1.5.

$$R_e=\frac{U_r d_{bubble}}{\nu}=\frac{1.5e\text{-}2 \times 100e\text{-}6}{1e\text{-}6}=1.5 \quad (1)$$

Strouhal number=0.2 for a flow around a cylinder.

$$S_t=\frac{\omega L}{U}=\frac{2\pi f L}{U}=0.2 \quad (2)$$

$$f=\frac{0.2\ U}{2\pi L}=\frac{0.2 \times 5e\text{-}2}{2\pi \times 0.8e\text{-}2}=0.2=\frac{1}{5}\ \text{Hz} \quad (3)$$

CONCLUSIONS

In a first experiment the PIV technique was used to study a single-phase fluid flow around four cylinders. The results showed that there were two recirculation regions behind the cylinders. In a second experiment the PIV technique was also used to show that there was a displacement of the recirculation zone behind the single cylinder in the two-phase flow experiment. Plots of the velocity field were shown for both phases. Even though more data would be needed to verify the accuracy of the results, this study showed that a two-phase bubbly flow around a cylinder in a channel can be effectively studied using the PIV flow visualization technique.

REFERENCES

[1] J. Blake, and D. Gibson, "Cavitation Bubbles Near Boundaries," Ann. Rev. Fluid Mech., 19,97-123 (1987).

[2] Y. Hassan, and T. Blanchat, "Flow Velocity Measurements using Digital Image Pulsed Laser Velocimetry," Optical Engineering, 30, 8, 1220-1227 (1991a).

[3] L.M. Lourenco, A. Krothapalli, "Application of PIDV to the Study of the Temporal Evolution of the Flow Past a Circular Cylinder," Proceedings of the Third International Symposium on Applications of Laser Anemometry to Fluid Mechanics, Lisbon (1986).

[4] J. Wu, J. Sheridan, and J. Soria, "An Investigation of Unsteady Flow Behind A Circular Cylinder Using A Digital PIV Method," ASME FED Summer Meeting (1994).

[5] R.J. Adrian, "Particle-Imaging Techniques for Experimental Fluid Mechanics,"Ann. Rev. Fluid Mech.,23 (1991).

[6] Y.A. Hassan, and R.E. Canaan, "Full-field bubbly flow velocity measurements using a multiframe particle tracking technique," Experiments in Fluids, 12, 46-60 (1991b).

[7] E.R. Ramer, F.D. Shaffer, "Automated Analysis of Multiple-Pulse Particle Image Velocimetry Data", Applied Optics, 31, 6,.779-784 (1992).

[8] Y.A. Hassan, T.K. Blanchat, C.H. Seeley, "PIV Flow Visualization Using Particle Tracking

Techniques," Measurement Science and Technology, 3, 633-642 (1992).
[9] F. Yamamoto, T. Uemura, M. Koukawa, M. Itoh, and A.Teranishi, "Application of Flow Visualization and Digital Image Processing Techniques to Unsteady Viscous Diffusing Free Doublet Flow," Proceedings, 2nd International Symposium on Fluid-Control, Measurement, Mechanics- and Flow Visualization, 184-188 (1988).
[10] T.K. Blanchat, "Development of Pulsed Laser Velocimetry Techniques for Measurement of Two-Phase Interfacial Drag in a Horizontal Stratified Flow," Ph.D. Thesis, Texas A&M University, College Station, Texas (1991).
[11] R.L. Hardy, "Multiquadric Equations of Topography and Other Irregular Surfaces," Journal of Geophysics Research, 76, 1905 (1971).
[12] F.J. Narcowich, J.D. Ward, "Norms of Inverses and Condition Numbers for Matrices Associated with Scattered Data", Journal of Approximation Theory, 64, 1, January, 69-94 (1990).

Characteristics of Turbulent Velocity and Temperature in a Wall Channel of a Heated Rod Bundle

T. Krauss, L. Meyer
Forschungszentrum Karlsruhe, Institut für Neutronenphysik und Reaktortechnik,
Postfach 3640, D-76021 Karlsruhe, Germany

ABSTRACT

Turbulent air flow in a wall sub-channel of a heated 37-rod bundle (P/D = 1.12, W/D = 1.06) was investigated. Measurements were performed with a hot-wire probe with x-wires and a temperature wire. The mean velocity, the mean fluid temperature, the wall shear stress and wall temperature, the turbulent quantities such as the turbulent kinetic energy, the Reynolds-stresses and the turbulent heat fluxes were measured and are discussed with respect to data from isothermal flow in a wall channel and heated flow in a central channel of the same rod bundle. Also, data on the power spectral densities of the velocity and temperature fluctuations are presented. These data show the existence of large scale periodic fluctuations of velocity and temperature in the gap region of two adjacent rods or between rods and the wall. These fluctuations are responsible for the high intersubchannel heat and momentum exchange.

1. INTRODUCTION

The prediction of the temperature distribution within the rod bundle of a nuclear reactor is of major importance in nuclear reactor design. The thermal-hydraulic analysis is performed by solution of the conservation equation for mass, momentum and energy. Recently developed codes [1] applying a distributed parameter analysis need empirical information on turbulent transport properties of both momentum and energy transport.

A large number of experiments has been performed in various rod bundle geometries with isothermal flow (for a review see Ref. 2). It has been found that distributions of the turbulence intensities in rod bundles are unusual and different from those in tubes and parallel plates [3,4,5]. The highest turbulence intensities were observed at positions of greatest distance from the walls in the gap region. The eddy viscosities parallel to walls are considerably higher than those normal to walls and depend strongly on the pitch to diameter ratio of the rod bundle. The high mixing rates between subchannels of rod bundles have been explained by the effects of secondary flow for a long time, although Rowe [6,7] in 1973 had noticed that a non-gradient macroscopic flow process, possibly flow pulsation, affects the mixing between subchannels. Detailed turbulence measurements of the axial flow through closely-spaced rod bundles have confirmed the observations of Rowe and have shown that an energetic and almost periodic flow pulsation exists through the gaps between the rods and between rods and channel walls, respectively [8,9]. It was demonstrated that these flow pulsations are the reason for the high mixing rates between the subchannels of rod bundles [10,11] and secondary flows in subchannels do not contribute significantly to the mixing rates. In a recent investigation on turbulent flow through compound rectangular channels [12] it was shown that these large scale flow pulsations or vortices are a general phenomenon existing in any longitudinal slot or groove in a wall or a connecting gap between two flow channels, provided its depth is more than approximately twice its width. Thus, the momentum- and heat transfer proc-

esses in the rod-gap area for turbulent flow through closely spaced rod arrays are governed by a low frequency quasi-periodic fluctuation of the velocity component directed through the gap.

To model correctly the heated flow it is necessary to know the turbulent quantities of the velocity and those of the temperature such as the eddy diffusivity of heat in all directions. No such data were available for flow through rod bundles. In carrying on the 15 years of research on turbulent flow through rod bundles at Kernforschungszentrum Karlsruhe (KfK) the investigations were continued at a heated 37-rod bundle. The results of the measurements in a central channel have been published earlier [13]. Here we present the main results of the measurements in a wall subchannel and discuss them with respect to those results in the central channel and with isothermal flow in the wall channel [14].

2. EXPERIMENTAL APPARATUS AND PROCEDURE

A rod bundle of 37 parallel rods (O.D. D = 140 mm) arranged in triangular array in a hexagonal symmetric channel was built (Fig.1). The position of the channel is horizontal. The total length of the working section is L = 11.50 m with an unheated entrance length of L_{iso} = 4.60 m and a heated length of L_{heat} = 6.90 m. The pitch to diameter ratio of the rods is P/D = 1.12 (W/D = 1.06), which gives a length to hydraulic diameter of central channel ratio for the heated part of $L_{heat}/D_{h,c}$ = 128. The rods are made of epoxy reinforced with fiberglas, sheathed with a 50 µm foil of monel metal, which serves as resistance heating element. It is heated by low voltage, high direct current to temperatures in the range of 60° to 100 °C. Since the metal foil has a very accurate thickness the heat flux is uniform around the perimeter of the rods. The heat conduction is very small due to the small thickness of the metal foil and the low conductivity of the rod material. Thus, the circumferential temperature variations due to different heat transfer will not be eliminated by conduction. The wall heat flux was determined from the measurements of the current and the voltage drop along the rods with an estimated error of ±1.5 %.

The channel walls are made of aluminum covered with a thick insulation at the outside to minimize the heat losses. The whole bundle is made up from five sections, each 2.30 m long. The rod gap spacers were made of 4 mm thick and 15 mm wide (in axial direction) steel with rounded edges. Due to extremely small manufacturing tolerances the deviations from the nominal bundle geometry are less than 0.2 mm, including the bending of the rods. The fluid is air at atmospheric pressure and room temperature at the entrance. The air is driven by a centrifugal blower. Before entering the working section it passes through a filter to remove particles greater than 1 µm and an entrance section of 5 m length with a honeycomb grid and a number of fine grid screens.

The measurements are performed at a position 20 mm upstream of the outlet. The time-mean values of the axial velocity and the wall shear stresses are measured by Pitot and Preston tubes (O.D. d=0.6 mm), respectively, the mean temperatures are measured by sheathed thermocouples (O.D. d=0.25 mm). The wall temperatures are measured by an infrared pyrometer (Heimann KT 4), which has a range of 0°C-100°C and a target area of 5 mm diameter at 1 m distance. Mainly due to difficulties with calibration the uncertainty is ±1 K.

The turbulent quantities are measured by hot wire anemometry using a three-wire probe. This probe consists of an x-wire probe with an additional cold wire perpendicular to the x-wire plane for simultaneous measurement of two components of instantaneous velocity and temperature. The x-wires have a length of 1.1 mm, a diameter of 2.5 µm and a spacing of 0.35 mm. The cold wire has a diameter of 1 µm, a length of 0.9 mm and is positioned 0.1 mm upstream of the x-wire prong tips. The measuring volume is approximately 1 mm^3. The probe was fabricated in our laboratory. The calibration and evalua-

tion method uses look-up tables as described by Lueptow et al. [15], extended by the temperature dimension [16]. Since the cold wire is run in the Constant Current Anemometer-mode (CCA) the frequency response is not as good as that of the x-wires, which are run in the Constant Temperature Anemometer-mode (CTA). The attenuation and phase shift of the temperature signal leads to errors in all correlations of u, v and θ. A rough estimate for a 1μm wire gives the following maximum errors: $\overline{\theta^2}$ is 2%, $\overline{u\theta}$ is 4% and $\overline{v\theta}$ is 6% too small; $\overline{u}$ and $\overline{uv}$ are 4% too large and there is a negligible error in $\overline{v}$.

Apart from these errors there are several errors typical for x-probes, such as the error due to the velocity component normal to the x-plane and the errors due to the finite length of the wires and the distance between them. The velocity component normal to the x-plane will result in the evaluation of too high axial components $\overline{u}$, while the finite length of and the distance between the wires leads to errors in $\overline{v^2}$, $\overline{w^2}$ and in the correlations such as $\overline{uv}$. Those latter errors depend on the velocity and temperature gradient [16].

The performance of the measurements is fully automated; the mass flow rate, the heating power and the traversing of the measuring probe are controlled by a 486-PC. The triple wire probe is run by two CTA- and one CCA-bridge of an AN-1003 anemometer system. The signals were digitized at sample rates of 7 kHz per channel by a DT2829-card, which provided sample and hold digitization with 16-bit resolution. The total number of samples taken in a continuous stream were 49152 per channel, with a measuring time of 7 seconds. The raw data were loaded into extended memory of the computer by DMA. The evaluation of all correlations takes approximately 20 seconds. At each measuring point the probe is turned into eight positions to measure all six Reynolds stresses, three turbulent heat fluxes and ten triple products [17]. To evaluate the above correlations it is necessary to roll the probe about its axis to the positions 0°, 45°, 90° and 135° with respect to the start. The positions 180°, 225°, 270° and 315° are used to compute the average between two corresponding positions, 0° and 180° for example, in order to minimize possible errors in the radial or azimuthal components.

In a wall channel measurements at 636 positions (Fig. 2) were taken under non-isothermal conditions, which took approximately forty hours. The data of the heated experiment were: Reynolds number in the wall channel $Re = 6.5 \times 10^4$, hydraulic diameter $D_{h,w} = 0.0488$ m with a bulk velocity $U_b = 19.4$ m/s and a bulk temperature $T_b = 29.1$ °C. The rod wall heat flux in the present experiment was 1.39 kW/m^2.

3. RESULTS

3.1. Wall shear stress and wall temperature distribution

Fig.3 shows the measured wall shear stress distribution of the 37-rod bundle in comparison to the results of a 4-rod bundle. The shear stress was calculated by Preston's method. The properties of air were evaluated at the fluid temperature at y = 0.3 mm, which is the radius of the Preston tube. The wall shear stress reduced by the average wall shear stress of the wall and the rod ($\tau_{w,av} = 1.21$ N/m²) shows no relevant difference between the heated and isothermal data in a wall subchannel of the 37-rod bundle. Even the shear stress distribution in the 4-rod bundle shows good agreement with these results, which confirms the similarity of flow through wall channels of 4-rod- and 37-rod bundles. Compared to the data obtained in a heated central channel of the 37-rod bundle, the wall shear stress in the wall channel of the bundle is about 13% larger. The minimum value of τ_w occurs in the rod-to-wall gap region and the maximum value at the position of maximum channel width.

In Fig.4 local wall temperatures of the heated and unheated wall bounding the wall channel are plotted versus mean temperatures of each boundary. As expected, the temperature gradient along the unheated wall is very small due to excellent thermal conductance of the wall material. The values of this unheated wall show a maximum in the rod-to-wall gap and decrease gradually with increasing distance from the gap. In contrast to this the temperature distribution of the heated rod varies over a wider range with the minimum appearing at the position of maximum wall shear stress. The highest temperatures are reached in the rod-to-rod gap region.

3.2. Mean velocity and mean temperature distribution

Isoline plots of both, the time mean velocity and time mean temperature are shown in Figs. 5 and 6. Time mean velocities are related to the bulk velocity of the wall channel U_b = 19.4 m/s. The bulk temperature in the wall subchannel was T_b = 29.1 °C and the difference (T_w-T_b) was 19.55 °C. There is no relevant difference in the velocity data between the isothermal and the heated case. The temperature range in the wall channel is very large compared to a central channel, due to the proximity of an unheated wall. As expected, the temperature reaches its maximum value in the rod-to-rod gap region.

The logarithmic plots of the radial velocity distribution, computed with local friction velocities (Figs. 7 and 8) follow the law of the wall $u^+ = 2.5 \ln y^+ + 5$ with reasonable agreement at most positions. The logarithmic temperature profiles are shown in Figs. 9 and 10, together with the lines $T^+ = 2.5 \ln y^+$, displaced by 1 K every second angular position. Fig. 9 shows the logarithmic temperature profiles calculated with local friction velocities in accordance with the calculation of u^+. Previous measurements in a heated central channel of our 37-rod-bundle have shown that the logarithmic temperature profiles at different azimuthal positions would not collapse if local friction velocities were used. Therefore temperature profiles computed with the friction velocity averaged over the perimeter of the heated rod are presented in Fig. 10. The logarithmic profiles in Fig. 10 are slightly higher compared to Fig. 9, but the tendency to change its slope at different angular positions remains the same. The slope of the profiles is higher in the rod-to-wall gap and lower in the gap between two heated rods, the latter also being found in central channels. The temperature profiles, calculated with local friction velocities can be fitted by logarithmic laws that gradually change from $3.69 \ln y^+ - 6.21$ in the rod-to-wall gap to $2.32 \ln y^+ - 0.25$ in the gap between two heated rods. The reason for the deviation of these temperature profiles from a single logarithmic law is the extremely asymmetric temperature distribution in the wall channel.

3.3. Turbulent intensities and kinetic energy

All quantities displayed in isoline plots were scaled by values of the friction velocity and temperature that are averaged over the perimeter of the rod and along the wall. All data are shown for the heated case. The differences between the unheated case and the heated case were negligible. Compared to the data from measurements in central channels [13] the variation of all three velocity components in azimuthal direction is larger. All turbulent intensities except for the radial velocity component are higher in the wall channel.

The turbulent intensities in axial direction $\sqrt{\overline{u^2}} / u_{\tau,av}$, shown in Fig. 11, are much higher than in a central channel, where the maximum value of 1.9 was reached close to the wall. Here it reaches its maximum value of 2.6 near the line of maximum wall distance in the gap rod-to-wall at an angular position between 30° and 35°. The distribution of the turbulent intensities in radial direction (Fig. 12) close to the walls and at 0° and 90° is similar to that in central channels with $\sqrt{\overline{v^2}} / u_{\tau,av}$ = 0.9 near the wall and 0.6 at the sym-

metry line. With increasing distance from the gap region the radial distribution becomes flatter. The turbulent intensities in azimuthal direction $\sqrt{\overline{w^2}} / u_{\tau,av}$, shown in Fig. 13, are very high in the narrow rod-to-wall gap at the line of maximum wall distance (=1.9) and somewhat lower near the wall. This is due to the existence of large scale quasi-periodic velocity fluctuations in the rod gap regions. In the rest of the wall channel the wall-parallel turbulent intensities are highest near the wall. Because the rod-to-rod gap is twice as wide as the rod-to-wall gap, the large scale velocity fluctuations are less pronounced between the rods. The relative kinetic energy

$$k^+ = \frac{1}{2}(\overline{u^2} + \overline{v^2} + \overline{w^2}) / u_{\tau,av}^2 \qquad (1)$$

in Fig. 14 is mainly governed by the intensity in axial direction, being the largest contributor in all positions except for the rod-to-wall gap region, where the azimuthal intensities are largest. The intensities of the temperature fluctuation $\sqrt{\overline{\theta}} / T_{\tau,av}$ (Fig. 15) are larger than those of the central channel because of the asymmetric distribution of the temperature in wall channels. The maximum values are reached in the gap between two heated rods, independent of the wall distance. In this region the temperature gradient in azimuthal direction and the intensity of the azimuthal velocity component both are large, which leads to an intensive exchange of fluid of different temperature. In contrast to this, the smallest values of the temperature fluctuation are measured near the unheated wall. The variation of the temperature fluctuation in azimuthal direction is negligible near the unheated wall and becomes most significant close to the heated rod at an angular position between 35° and 75°, with its minimum value near 50°.

3.4. Reynolds shear stress

The scaled turbulent shear stresses normal to the wall $-\overline{uv} / u_{\tau,av}^2$ (Fig. 16) and in azimuthal direction $\overline{uw} / u_{\tau,av}^2$ show exactly the same distribution as for isothermal flow in wall channels. Near the wall $-\overline{uv} / u_{\tau,av}^2$ reaches the same values as in central channels and decreases linearly with increasing distance from the wall. The turbulent shear stress normal to the wall tends to zero at the line of maximum wall distance, where also the gradient of mean velocity in radial direction $\partial U / \partial y$ is equal to zero.

Values of the planar shear stress $\overline{vw} / u_{\tau,av}^2$ have rarely been measured in the past. With an X-wire probe aligned with the mean flow direction the planar shear stress cannot be measured directly because the heat transfer from a given wire of the probe is dependent only on the component of velocity normal to the wire. If the probe is rolled about its axis to the position 45° and 135° with respect to the start, $\overline{vw}$ can be determined as a difference between the obtained intensities normal to the probe axis [17]. As $\overline{vw} / u_{\tau,av}^2$ is very small and is determined as a difference between two quantities, it may be expected to have considerable scatter. Nevertheless the planar shear stress measured by Hooper [18] in a six-rod bundle and our present results (Fig. 17) show some similarity in magnitude and distribution. In the wall region values of about 0.2 are obtained for $\overline{vw} / u_{\tau,av}^2$, which decrease rapidly with increasing wall distance. At the line of maximum velocity, high values are reached at angular positions where $\overline{uw} / u_{\tau,av}^2$ is high, due to the influence of this component on the magnitude of $\overline{vw} / u_{\tau,av}^2$. The unsteadiness of the data at the line of maximum velocity is due to the choice of the coordinate system, which is not continual there.

The scaled azimuthal shear stress $\overline{uw} / u_{\tau,av}^2$, shown in Fig. 18, is close to zero near the symmetry line at 0° in the rod-to-wall gap region and between 60° and 90° in the rod-to-rod gap region, where the azi-

muthal gradient of mean velocity vanishes. The maximum values are reached at an angular position between 20° and 30° at the line of maximum wall distance, exactly in the region, where the highest values have been obtained for the axial intensity $\sqrt{\overline{u^2}}/u_{\tau,av}$. Compared to the results from measurements in central channels of this rod bundle the maximum values found in this wall channel are higher by a factor of about eight.

3.5. Turbulent heat flux

The distribution of the turbulent heat flux in azimuthal direction $\overline{w\theta}/u_{\tau,av}T_{\tau,av}$, shown in Fig. 19, has some similarity to the measured azimuthal shear stress. At the position of maximum azimuthal shear stress (φ = 20°-30°) $\overline{w\theta}/u_{\tau,av}T_{\tau,av}$ reaches its highest negative values of -1.2. The maximum positive values of 1.2 have been measured in the gap between two heated rods, where the intensity of the temperature fluctuation also has a maximum. At an angular position of 45°, $\overline{w\theta}/u_{\tau,av}T_{\tau,av}$ is equal to zero, due to a vanishing azimuthal gradient of mean temperature $\partial T/\partial\varphi$. In contrast to the data obtained in a heated central channel, the variation along the perimeter of the heated rod is very large, the maximum values of the azimuthal heat flux being about 3.5 times higher.

The scaled turbulent heat flux in axial direction, $\overline{u\theta}/u_{\tau,av}T_{\tau,av}$, shown in Fig. 20, has its absolute maximum close to the wall at an angular position of 25°-30°, where both the intensity of the temperature and the axial velocity fluctuation reach high values. Additionally there is a local maximum near 75°-80° in the region of highest temperature fluctuations. On approaching the unheated wall the axial heat flux decreases to zero at the symmetry line. Compared to the results of a heated central channel $\overline{u\theta}/u_{\tau,av}T_{\tau,av}$ is higher by a factor of about 1.7.

At the heated wall the scaled turbulent heat flux in radial direction $\overline{v\theta}/u_{\tau,av}T_{\tau,av}$ (Fig. 21) is of the same magnitude as in central channels. It has its maximum at φ = 30°-50° near the heated rod. From the line of maximum velocity towards the unheated wall $\overline{v\theta}/u_{\tau,av}T_{\tau,av}$ decreases almost linearly to zero. The variation of the radial turbulent heat flux along the perimeter of the rod is small.

3.6. Eddy diffusivities of heat and momentum

The eddy diffusivity of momentum or eddy viscosity normal to the wall is defined by

$$\varepsilon_{mr} = \frac{-\overline{uv}}{\partial U/\partial y} \tag{2}$$

Shown in Fig. 22 is the non-dimensional eddy viscosity

$$\varepsilon^{+}_{mr} = \varepsilon_{mr}/(\hat{y}_{max}u_{\tau,av}), \tag{3}$$

i.e. it is scaled by the average value of the friction velocity and the maximum profile length $\hat{y}_{max}$ at φ=55°. The non-dimensional eddy viscosity in azimuthal direction and the non-dimensional eddy diffusivities of heat are derived in the same way. As for central channels the eddy viscosities normal to the wall are slightly higher than the pipe data and are only a weak function of the azimuthal position.

The non-dimensional eddy diffusivities of heat in radial direction

$$\varepsilon_{hr}^{+} = \frac{-\overline{v\theta}}{\frac{\partial T}{\partial y}\hat{y}\, u_{\tau,av}} \tag{4}$$

presented in Fig. 23 are smaller than those of momentum, especially in the region next to the heated rod. It is not indicated to determine a radial eddy difusivity of heat in a reagion next to the unheated wall since both, the turbulent radial heat flux and the radial gradient of mean temperature tend to zero there. The non-dimensional eddy viscosity in azimuthal direction (Fig. 24) is defined by

$$\varepsilon_{ma}^{+} = \frac{-\overline{uw}}{\frac{1}{y}\frac{\partial U}{\partial \varphi}\hat{y}_{max} u_{\tau,av}}, \tag{5}$$

Because the gradient of mean velocity in azimuthal direction $\partial U / \partial \varphi$ is very small, reasonable values of ε_{ma}^{+} are available only at few positions and the scatter is quite large. The eddy viscosities in azimuthal direction are considerably higher than those normal to the walls, especially in the rod-to-wall gap region. The anisotropy, that is the ratio of the eddy diffusivities of momentum in azimuthal and radial direction is very high. Maximum values of about 30 are reached in the gap between rod and wall due to strong pulsations parallel to the wall. The non-dimensional eddy diffusivity of heat in azimuthal direction

$$\varepsilon_{ha}^{+} = \frac{-\overline{w\theta}}{\frac{1}{y}\frac{\partial T}{\partial \varphi}\hat{y}_{max} u_{\tau,av}}, \tag{6}$$

is plotted in Fig. 25. Like the azimuthal eddy viscosities, the eddy diffusivities of heat in azimuthal direction are much higher compared to the radial ones. The maximum values are reached at a position between 20° and 30° where also $\overline{w\theta}$ is very high. Again, there are some problems in evaluating ε_{ha}^{+} due to small gradients of mean temperature in azimuthal direction and the scatter of the computed data is expected to be quite large.

The radial turbulent Prandtl number, which is defined as the ratio between the eddy diffusivites of momentum and heat in radial direction takes values between 2 and 2.5 next to the heated rod. At longer distances from this rod the turbulent Prandtl number is close to unity, which is generally assumed for pipe flow. In regions where the azimuthal gradient of mean temperature is significant the turbulent Prandtl number parallel to the wall takes values between 1 and 2, similar to the radial turbulent Prandtl number. It is not indicated to determine an azimuthal turbulent Prandtl number in the rod-to-wall gap region and near the unheated wall, where $\partial T / \partial \varphi$ is close to zero.

3.7. Triple correlations

Triple correlations are a part of the diffusion term of the transport equations that are the basis of newer approaches to solve the closure problem of turbulence. All ten triple correlations that can be computed from the three velocity components were measured, but are not published in this paper due to limitations in space. Interested readers can get information about this topic from [19].

3.8. Frequency analysis

Auto- and cross-spectral power density functions of velocity and temperature fluctuations were measured at selected positions to characterize the large scale eddies. The auto-spectral power density functions of both, the velocity and temperature fluctuations (Fig. 26) show characteristic frequencies of quasi-periodic pulsations in the narrow rod-to-wall gap. The maxima of these, which are a function of the mean velocity and the dimensions of the gap, occur at frequencies of about 50 to 60 Hz. In the wider gap between two rods, the auto-spectral power density function of the azimuthal velocity component has its peak at a lower frequency of 30-40 Hz. Similar frequencies are also reflected by all cross-spectral power density functions. The appearance of similar frequencies in the spectra of both, velocity and temperature fluctuations, indicates the relationship between the involved transport processes.

4. Conclusion

Measurements of turbulence in a wall subchannel of a heated rod bundle were performed. The results compared to flow in heated central channels [13] and isothermal wall channels [14] of the same bundle indicate that:

(1) The wall shear stress, mean velocity and all velocity fluctuations show the same distribution previously measured in a wall channel in isothermal flow.
(2) The distribution of wall temperature at the heated rod varies over a wider range compared to a central channel. The highest temperatures are reached in the gap region between two heated rods.
(3) The intensities of the axial and azimuthal velocity fluctuations reach higher values and are more dependent on the angular position than in comparable central channels.
(4) The intensities of turbulent temperature fluctuations are larger than those measured in central channels. The maximum values are reached in the gap region between two heated rods.
(5) Values of the planar shear stress, measured for the first time in a 37-rod bundle, are very small compared to the other components of the Reynolds stress tensor.
(6) The turbulent heat fluxes in axial and in azimuthal direction are higher than in a central channel. The variation of the azimuthal heat flux along the perimeter of the wall is very large.
(7) The anisotropy, that is the difference between the eddy diffusivities in radial and in azimuthal direction is very large.
(8) The power-spectra of turbulent velocity and temperature fluctuations show characteristic frequencies of quasi-periodic pulsations through the gaps.

5. Nomenclature

$D_{h,c}$	hydraulic diameter of the central channel [m],
$D_{h,w}$	hydraulic diameter of the wall channel [m],
D	rod diameter [m],
P	rod pitch, distance between rod centers [m],
W	distance between wall and rod plus D [m],
L	length of rod bundle [m],
k^+	relative kinetic energy of turbulence [-],
q_w	wall heat flux [W/m²],

Re	Reynolds number [-],
T	time mean fluid temperature [°C],
T^+	dimensionless temperature, $(T_w-T)/T_{\tau,av}$ [-],
$T_{\tau,av}$	average friction temperature, $q_w/\rho c_p u_{\tau,av}$ [°C],
T_w	local wall temperature [°C],
$T_{w,av}$	average wall temperature [°C],
U	time mean velocity in axial direction [ms^{-1}],
u^+	dimensionless velocity, U/u_τ [-],
u_τ	local friction velocity, $\sqrt{\tau_w/\rho}$ [ms^{-1}],
$u_{\tau,av}$	average friction velocity [ms^{-1}],
u	fluctuating velocity in axial direction [ms^{-1}],
v	fluctuating velocity in radial direction [ms^{-1}],
w	fluctuating velocity in azimuthal direction [ms^{-1}],
u',v',w'	$\sqrt{\overline{u^2}}$, $\sqrt{\overline{v^2}}$, $\sqrt{\overline{w^2}}$ [ms^{-1}],
y	distance normal to the wall [m],
$\hat{y}$	distance between wall and line of maximum velocity [m],
$\hat{y}_{max}$	maximum distance between wall and centerline at φ=55° [m],
y^+	dimensionless distance from the wall, yu_τ/ν [-],
ε_m	eddy diffusivity of momentum, Eq. (2) [m^2s^{-1}],
ε_h	eddy diffusivity of heat, Eq. (5) [m^2s^{-1}],
ε^+	dimensionless eddy diffusivity, Eq. (3) [-],
θ	temperature fluctuation [K],
θ'	$\sqrt{\overline{\theta^2}}$ [K],
ν	kinematic viscosity [m^2s^{-1}],
ρ	density of fluid (air) [kgm^{-3}],
τ_w	local wall shear stress [Nm^{-2}],
$\tau_{w,av}$	average wall shear stress [Nm^{-2}],
φ	angular coordinate with origin at the rod-to-wall gap [°],
z	azimuthal coordinate with origin at the rod-to-wall gap [m],
Φ_u, Φ_w	auto-spectral power density functions of velocity fluctuations [m^2s^{-1}],
Φ_θ	auto-spectral power density function of temperature fluctuations [K^2s],
Φ_{uw}	cross-spectral power density function of velocity fluctuations [m^2s^{-1}],
$\Phi_{w\theta}$	cross-spectral power density function of velocity and temperature fluctuations [Km].

5.1. Subscripts and superscripts

a	azimuthal,
b	bulk,
h	heat,
m	momentum,
r	radial,
w	wall,
-	time averaged quantities.

6. References

1. W. Zeggel and N. Neelen, Validation of a wall parallel eddy viscosity formulation, IAHR 5th Int. Meeting on Liquid Metal Thermal Hydraulics, Grenoble (1986).
2. K. Rehme, The structure of turbulent flow through rod bundles, Nuclear Engineering and Design 99, 141-154 (1987).
3. K. Rehme, Experimental Observations of Turbulent Flow Through Subchannels of Rod Bundles, Exp. Thermal and Fluid Sci., **2**, 341 - 349, 1989.
4. J. Hejna, and F.Mantlik, The Structure of Turbulent Flow in Finite Rod Bundles, Proc. 1st World Conf. Exp. Heat Transfer, Fluid Mech., and Thermodynamics, Edts. R.K. Shah, E.N. Ganic & K.T. Yang, Elsevier, 1712 - 1719, 1988.
5. X. Wu, and A.C. Trupp, Experimental Study on the Unusual Turbulence Intensity Distributions in Rod-to-Wall Gap Regions, Exp. Thermal and Fluid Sci., **6**(4), 360-370, 1993.
6. D.S. Rowe, Measurement of Turbulent Velocity, Intensity and Scale in Rod Bundle Flow Channels, BNWL-1736, Battelle Pacific Northwest Laboratories, Richland, Washington, 1973.
7. D.S. Rowe, B.M. Johnson and J.G. Knudsen, Implications Concerning Rod Bundle Crossflow Mixing Based on Measurements of Turbulent Flow Structure, Int. J. Heat Mass Transfer, 17, 407-419, (1974)
8. J.D. Hooper and K. Rehme, Large-scale Structural Effects in Developed Turbulent Flow Through closely-spaced Rod Arrays, J. Fluid Mech., **145**, 305 - 337, 1984.
9. S.V. Möller, On Phenomena of Turbulent Flow Through Rod Bundles, Exp. Thermal and Fluid Sci., **4**, 25 - 35, 1991.
10. S.V. Möller, Single-phase Turbulent Mixing in Rod Bundles, Exp. Thermal and Fluid Science, **5**, 26-33, 1992.
11. K. Rehme, The Structure of Turbulence in Rod Bundles and the Implications on Natural Mixing Between the Subchannels, Int. J. Heat Mass Transfer, **35**(2), 567-581, 1992.
12. L. Meyer and K. Rehme, Large Scale Turbulence Phenomena in Compound Rectangular Channels, Exp.Thermal Fluid Science, 8, 286-304 (1994)
13. L. Meyer, Measurements of Turbulent Velocity and Temperature in a Central Channel of a Heated Rod Bundle, Nucl. Engrg. Des. 146, 71-82 (1994)
14. L. Meyer and K. Rehme, Turbulente Strömung durch Wandkanäle von Stabbündeln (P/D = 1.12, W/D = 1.06), KfK-Rep. 5007 (1992). Kernforschungszentrum Karlsruhe, FRG.
15. R.M. Lueptow, K.S.Breuer and J.H.Haritonidis, Computer Aided Calibration of X-probes Using a Look-up Table, Exp. in Fluids 6, 115-118 (1988).
16. L. Meyer, Calibration of a Three-Wire-Probe for Measurements in Nonisothermal Flow, Exp.Thermal Fluid Sci. 5, 260-267 (1992)
17. A.D. Cutler, P. Bradshaw, A crossed hot-wire technique for complex turbulent flows, Exp. in Fluids 12, 17-22 (1991).
18. J.D. Hooper, Fully developed turbulent flow through a rod cluster, Ph.D. Thesis, School of Nuclear Engineering, University of New South Wales (1980).
19. T. Krauss and L. Meyer, Measurement of turbulent velocity and temperature in a wall channel of a heated rod bundle, to be published as FZKA-Report (1995).

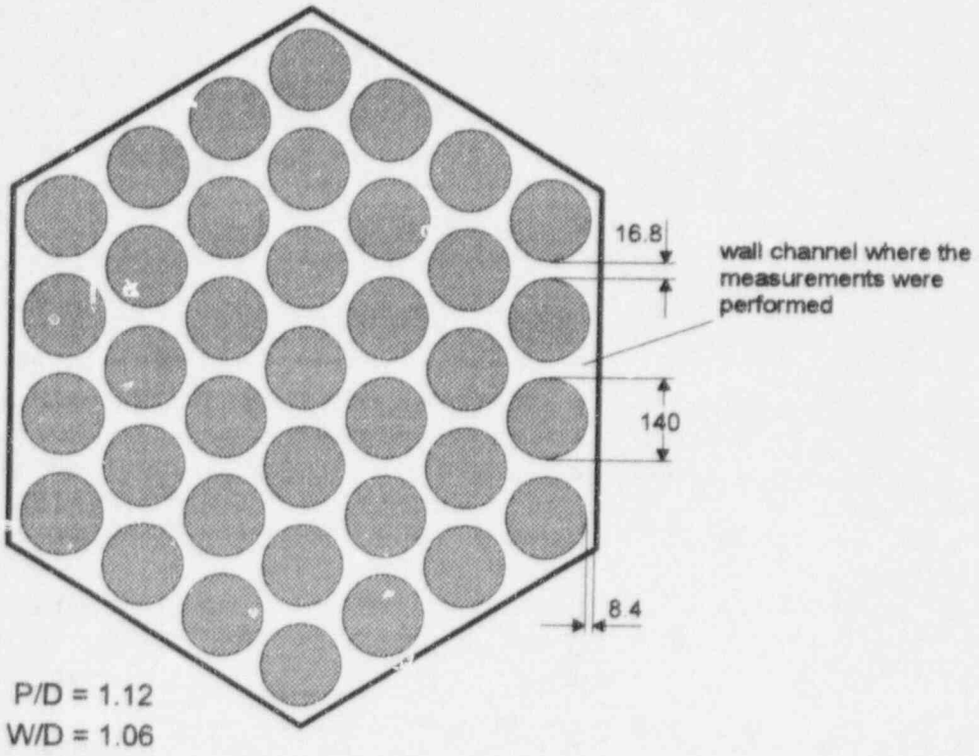

Fig. 1. Cross section of 37-rod bundle.

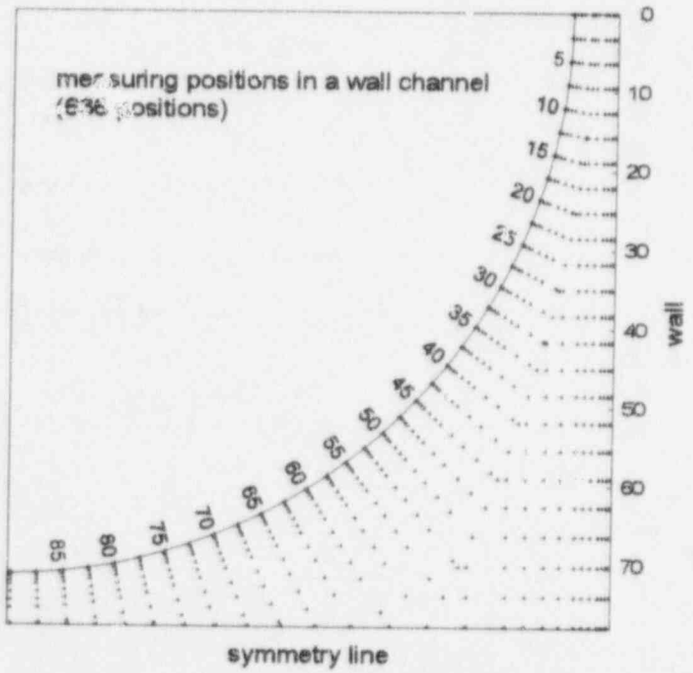

Fig. 2. Measuring positions in a wall channel.

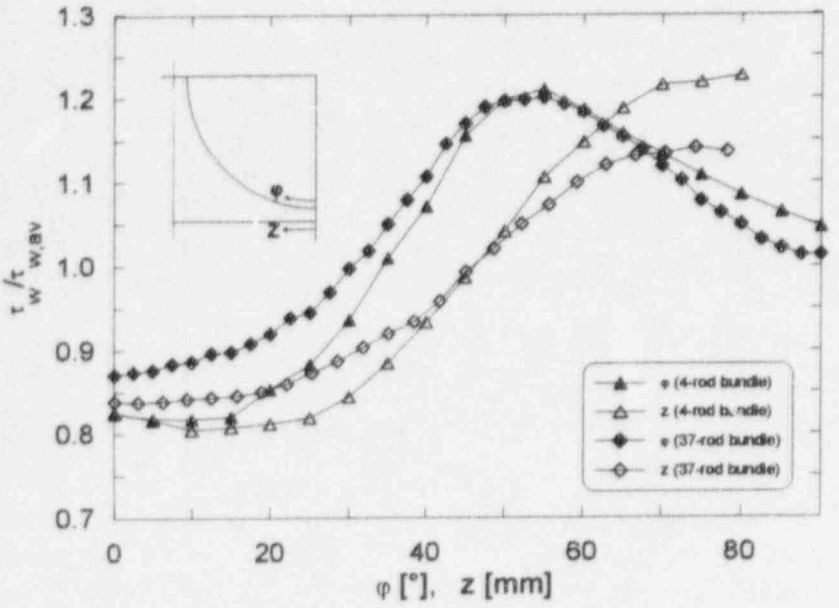

Fig. 3. Wall shear stress distribution.

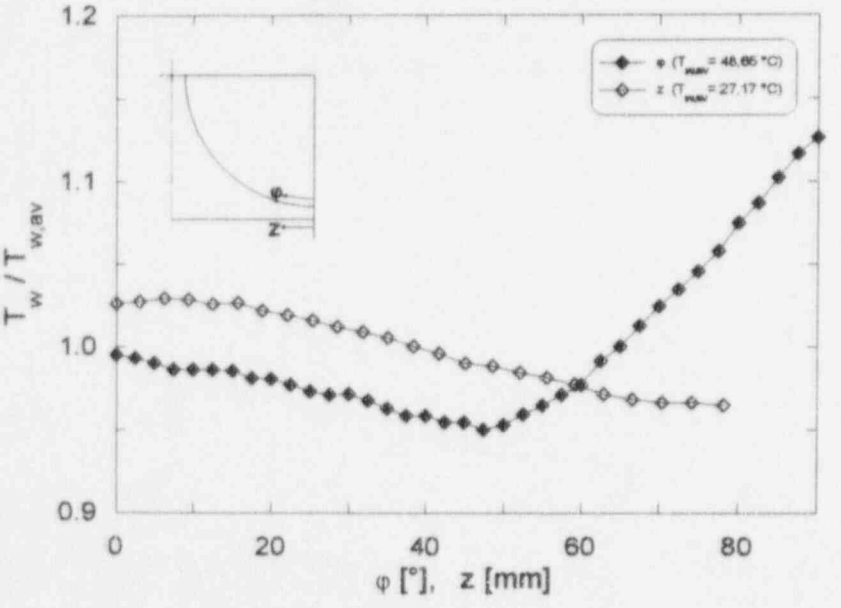

Fig. 4. Wall temperature distribution.

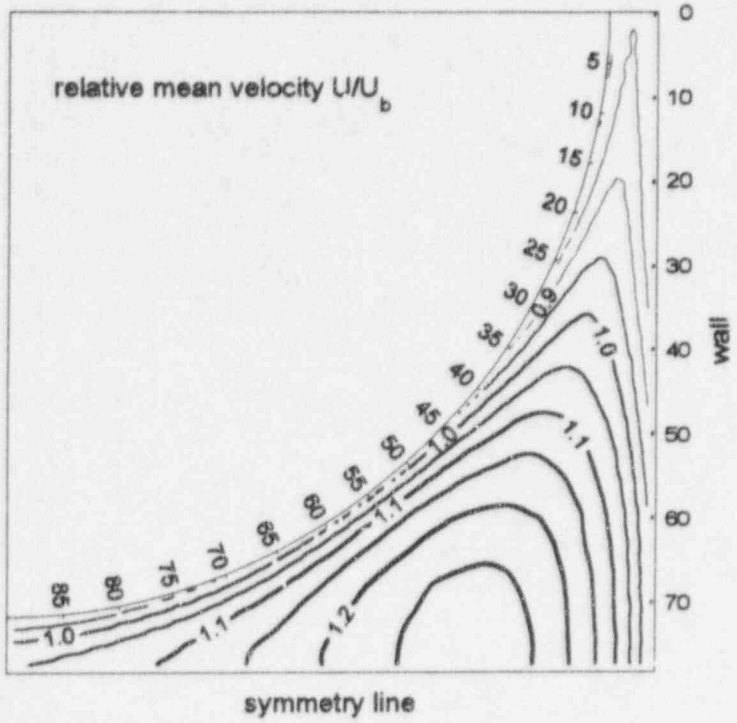

Fig. 5. Distribution of time mean velocity.

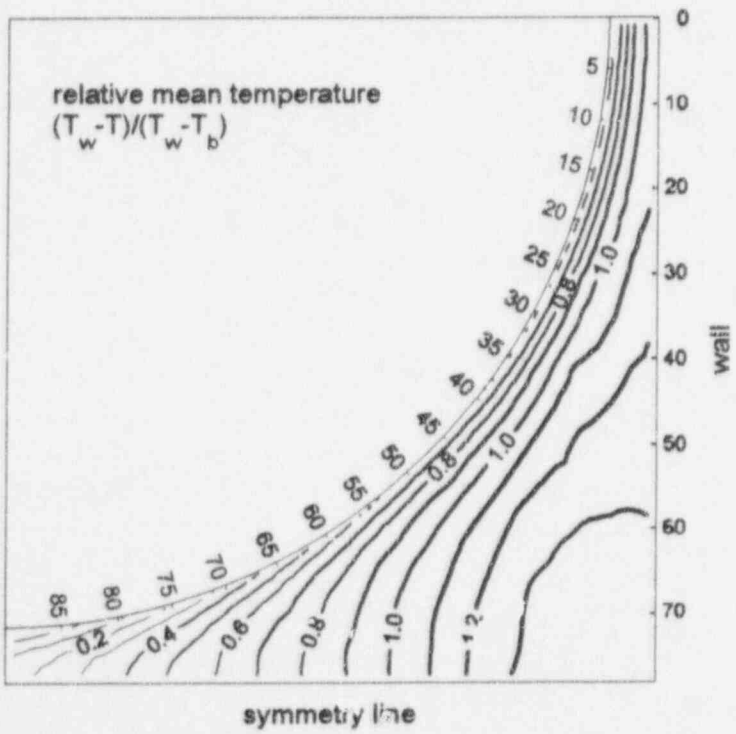

Fig. 6. Distribution of time mean temperature.

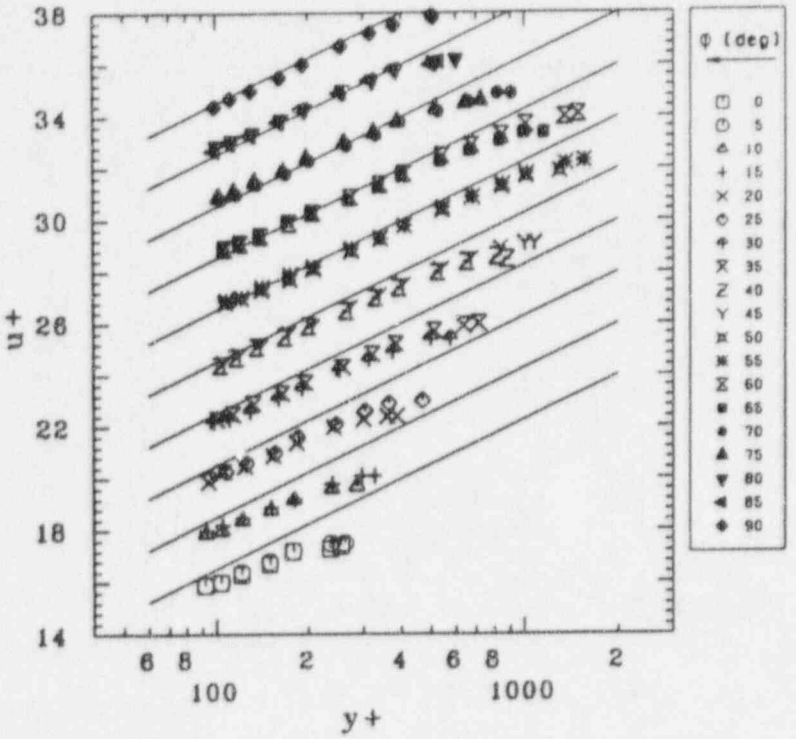

Fig. 7. Logarithmic profiles of the dimensionless velocity (rod).

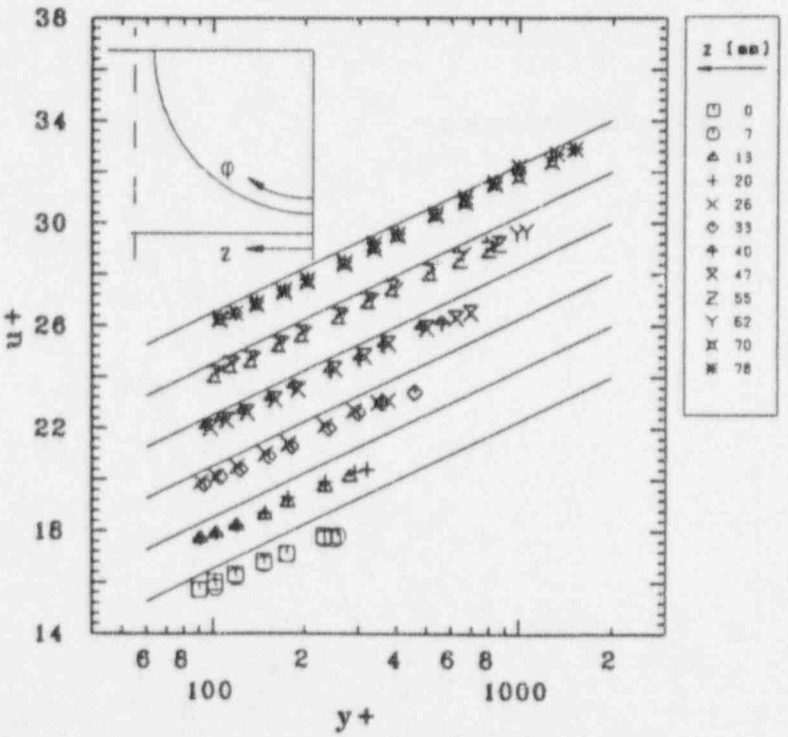

Fig. 8. Logarithmic profiles of the dimensionless velocity (wall).

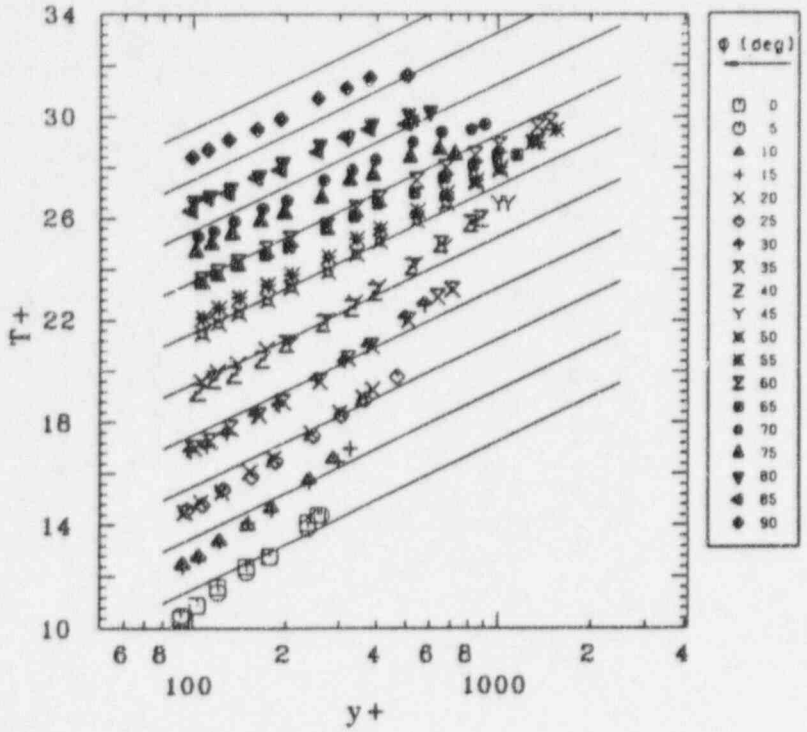

Fig. 9. Logarithmic profiles of the dimensionless temperature (local).

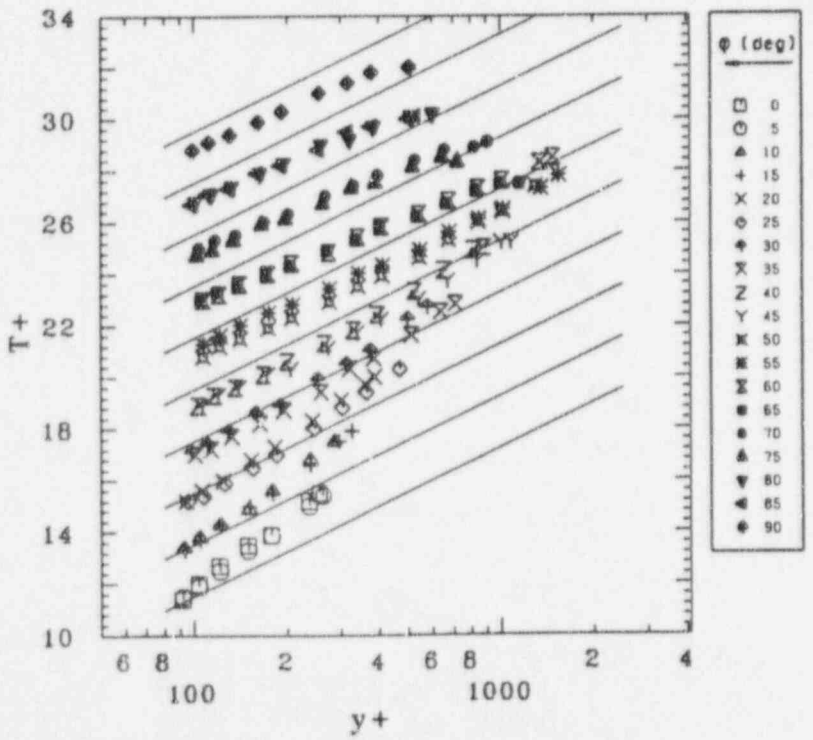

Fig. 10. Logarithmic profiles of the dimensionless temperature (average).

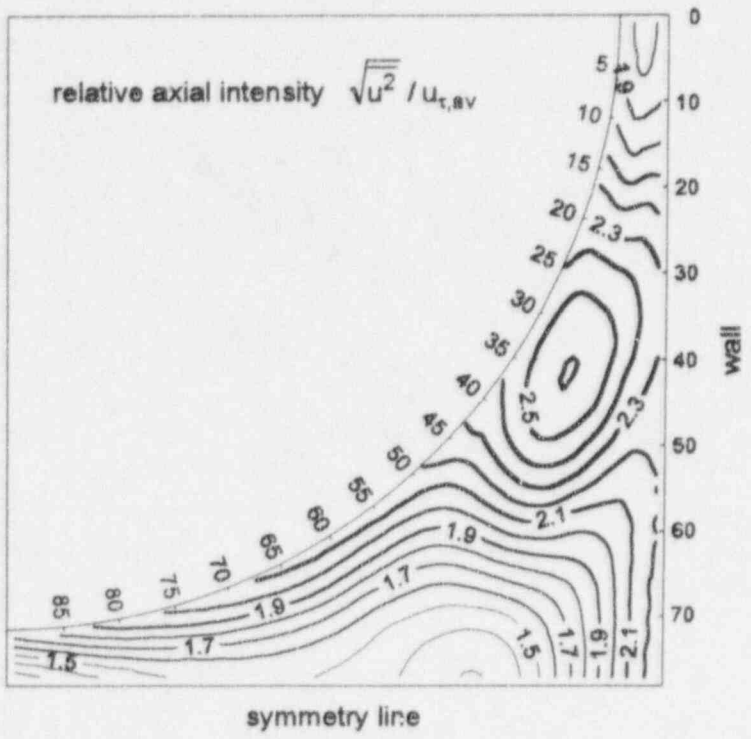

Fig. 11. Turbulent intensity of axial velocity.

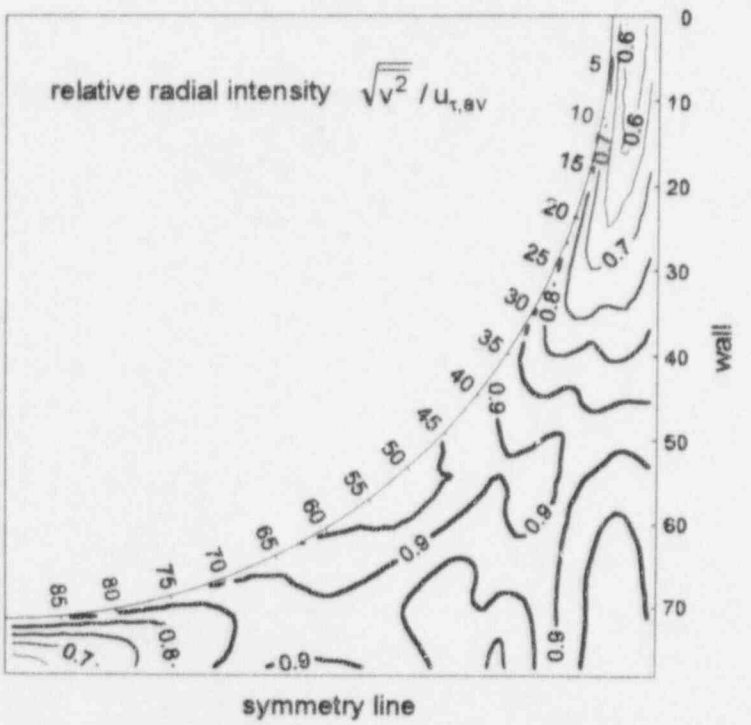

Fig. 12. Turbulent intensity of radial velocity.

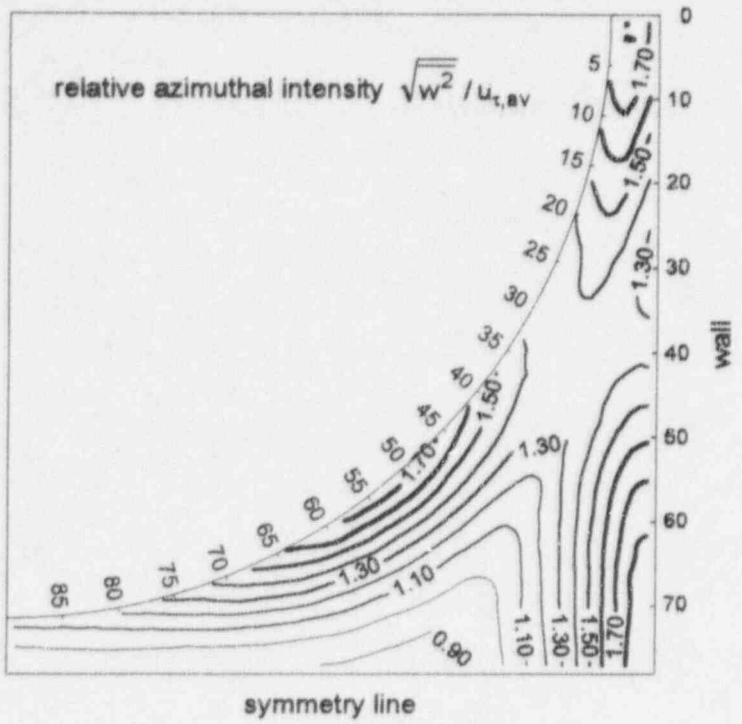

Fig. 13. Turbulent intensity of azimuthal velocity.

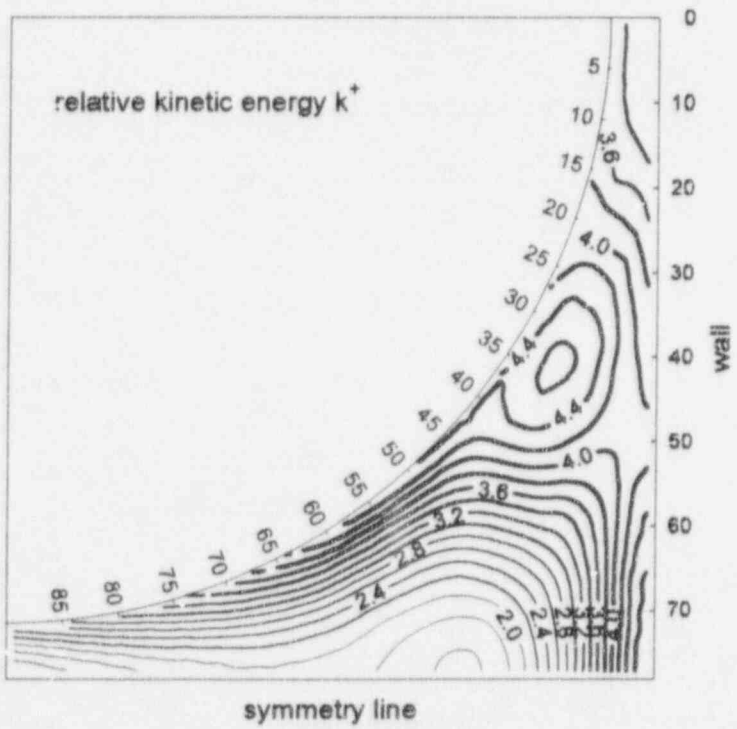

Fig. 14. Turbulent kinetic energy.

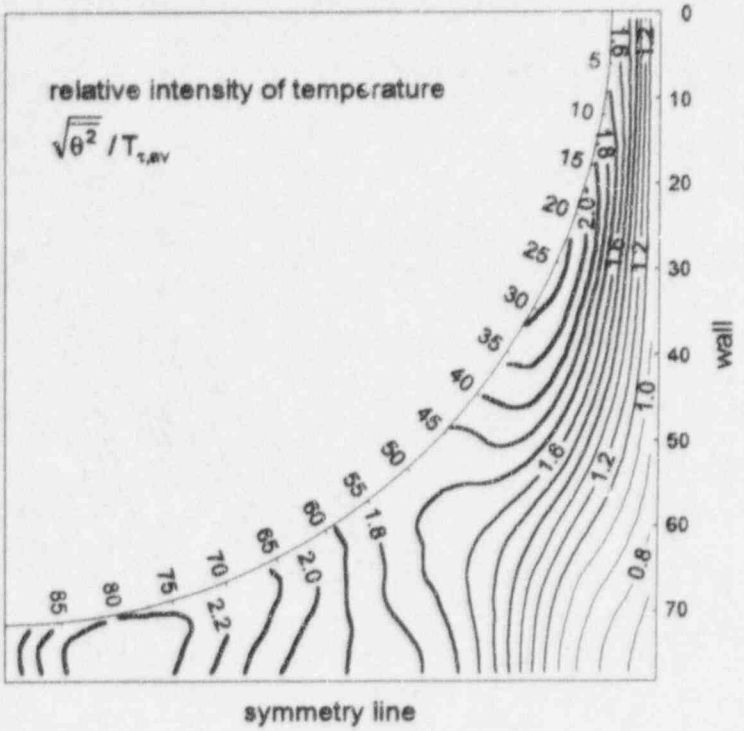

Fig. 15. Turbulent intensity of temperature.

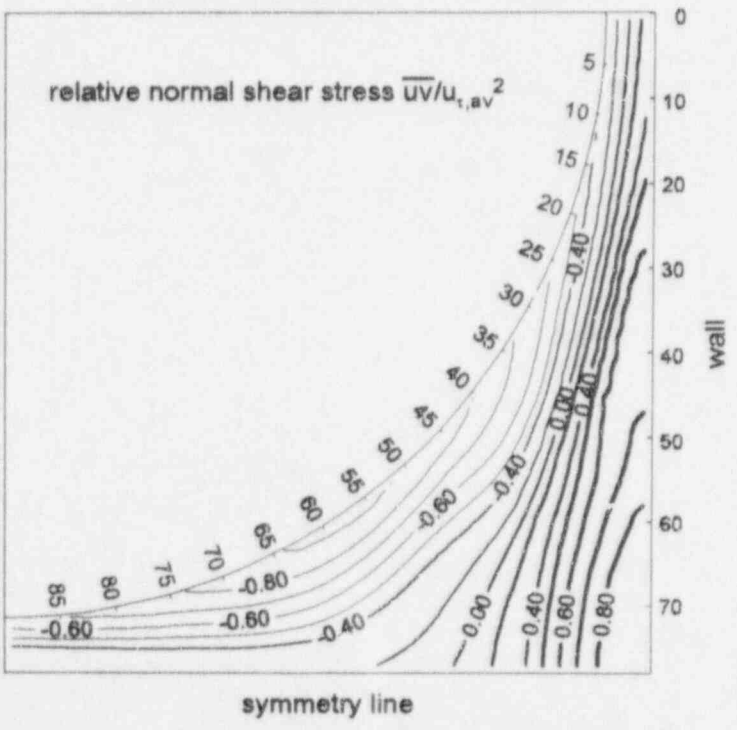

Fig. 16. Relative turbulent shear stress normal to the wall.

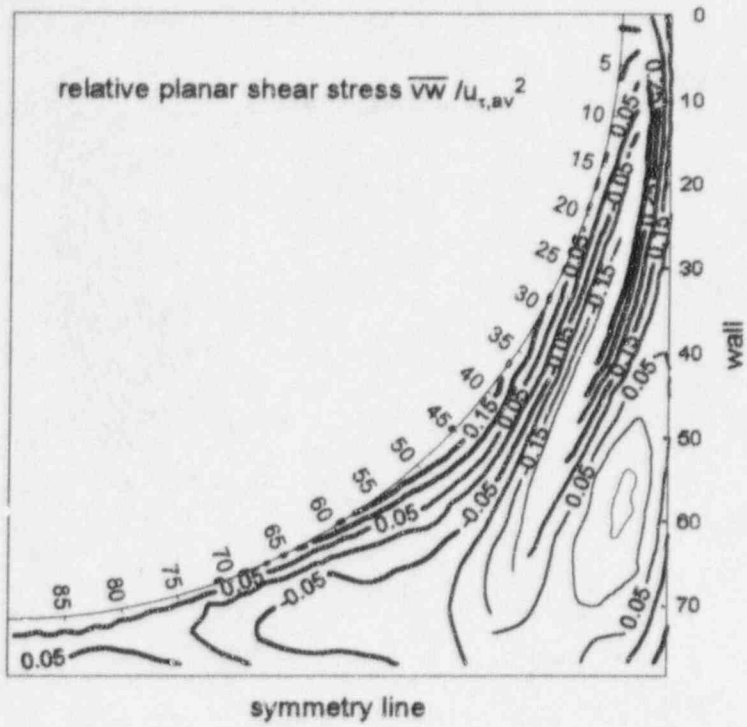

Fig. 17. Relative turbulent planar shear stress.

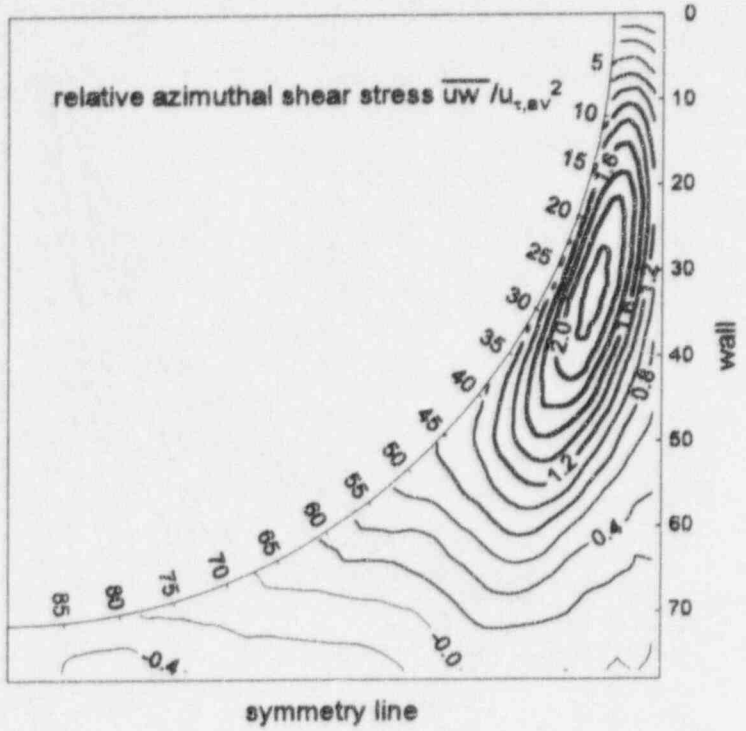

Fig. 18. Relative turbulent shear stress in azimuthal direction.

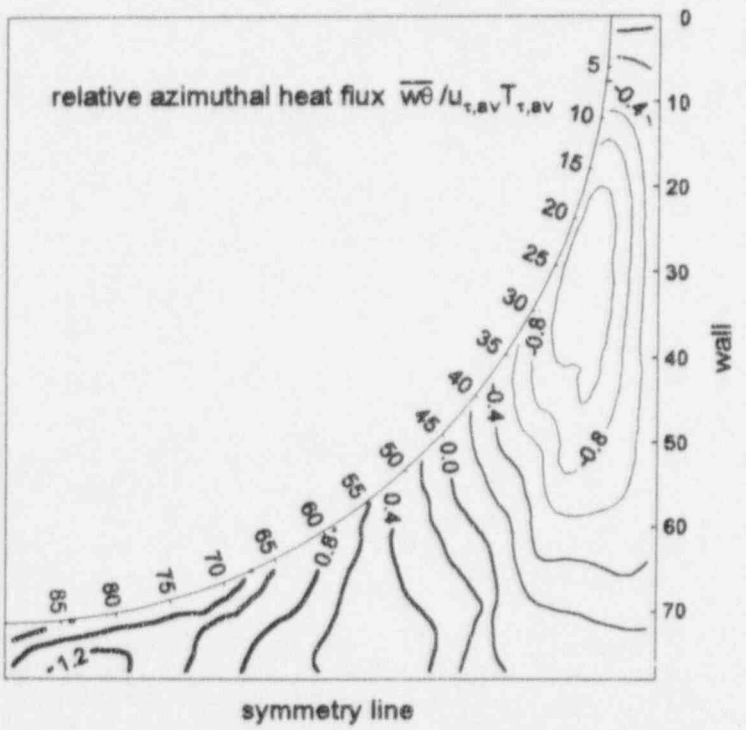

Fig. 19. Turbulent heat flux in azimuthal direction.

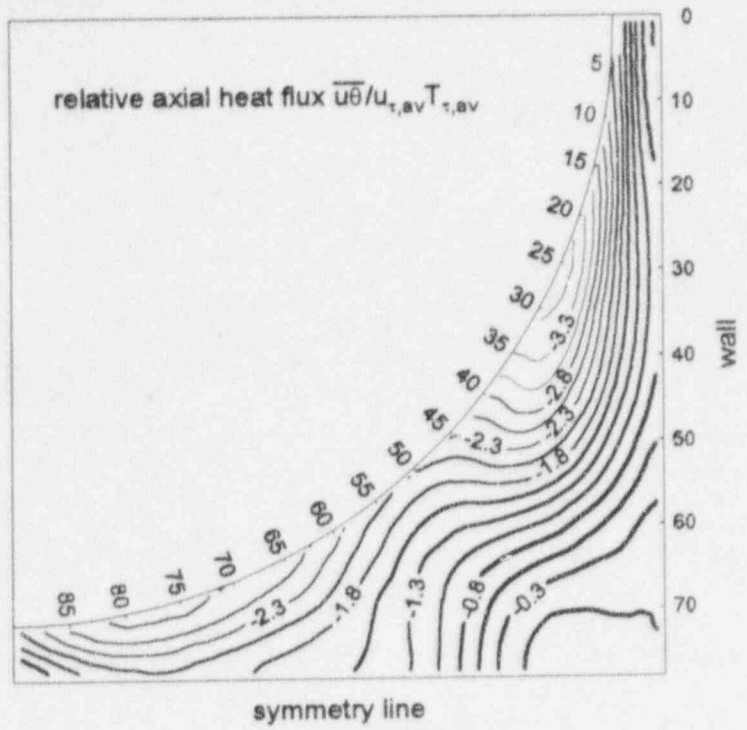

Fig. 20. Turbulent heat flux in axial direction.

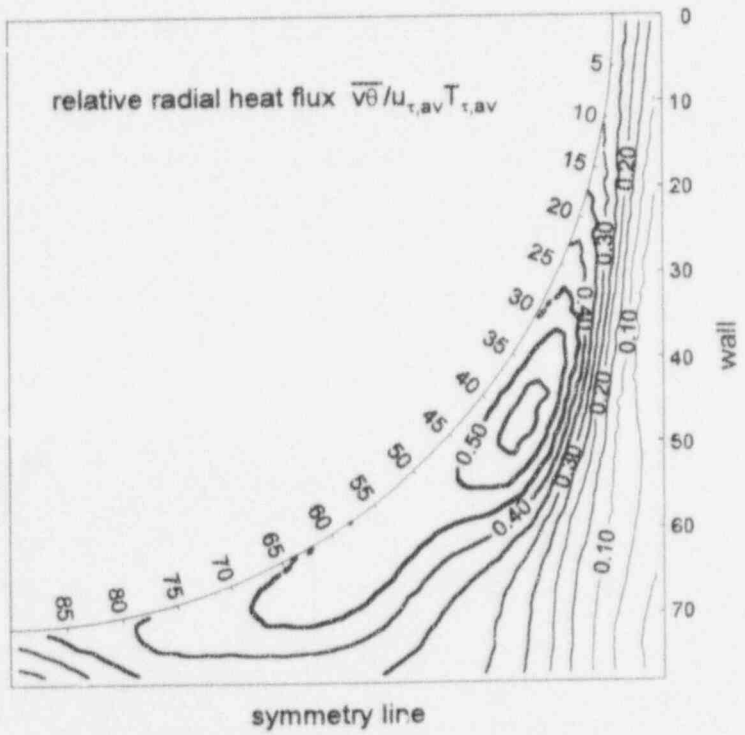

Fig. 21. Turbulent heat flux normal to the wall.

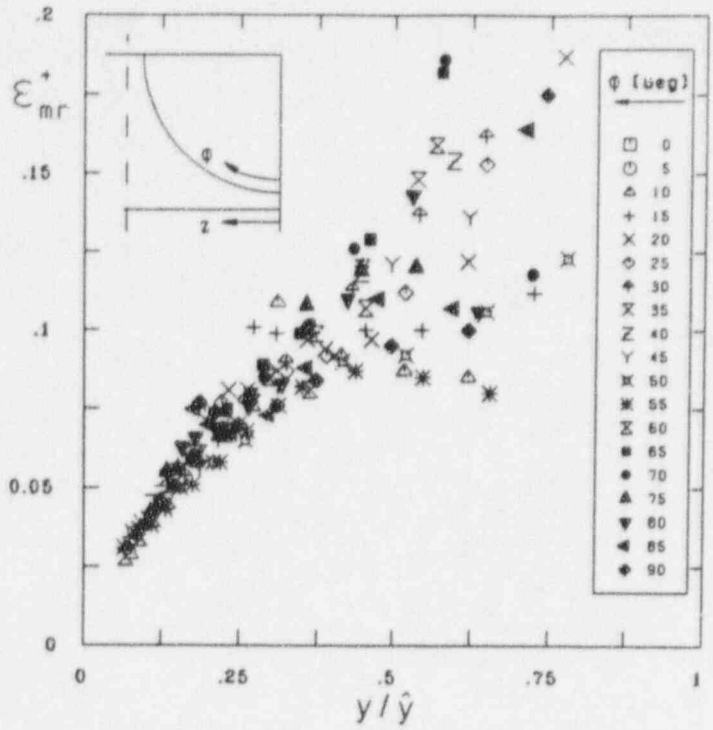

Fig. 22. Eddy viscosity normal to the wall.

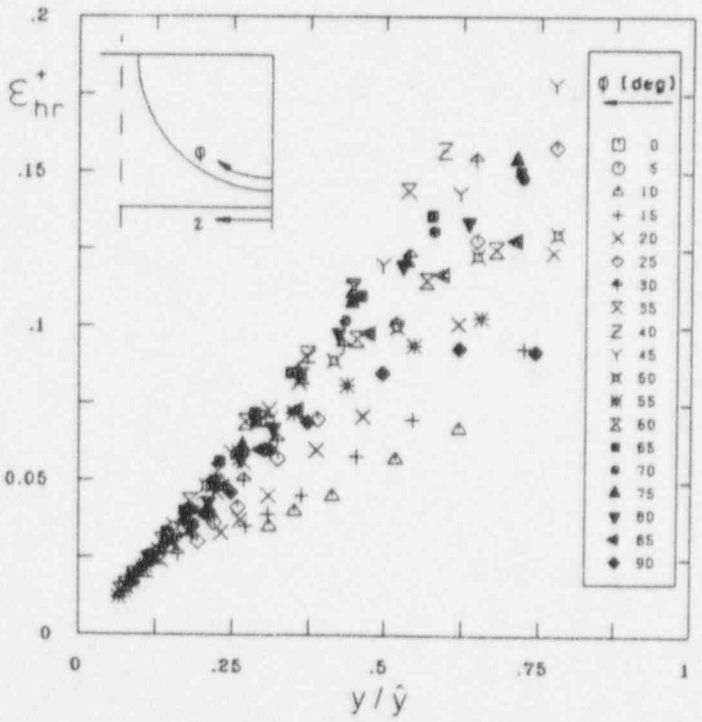

Fig. 23. Eddy diffusivity of heat normal to the wall.

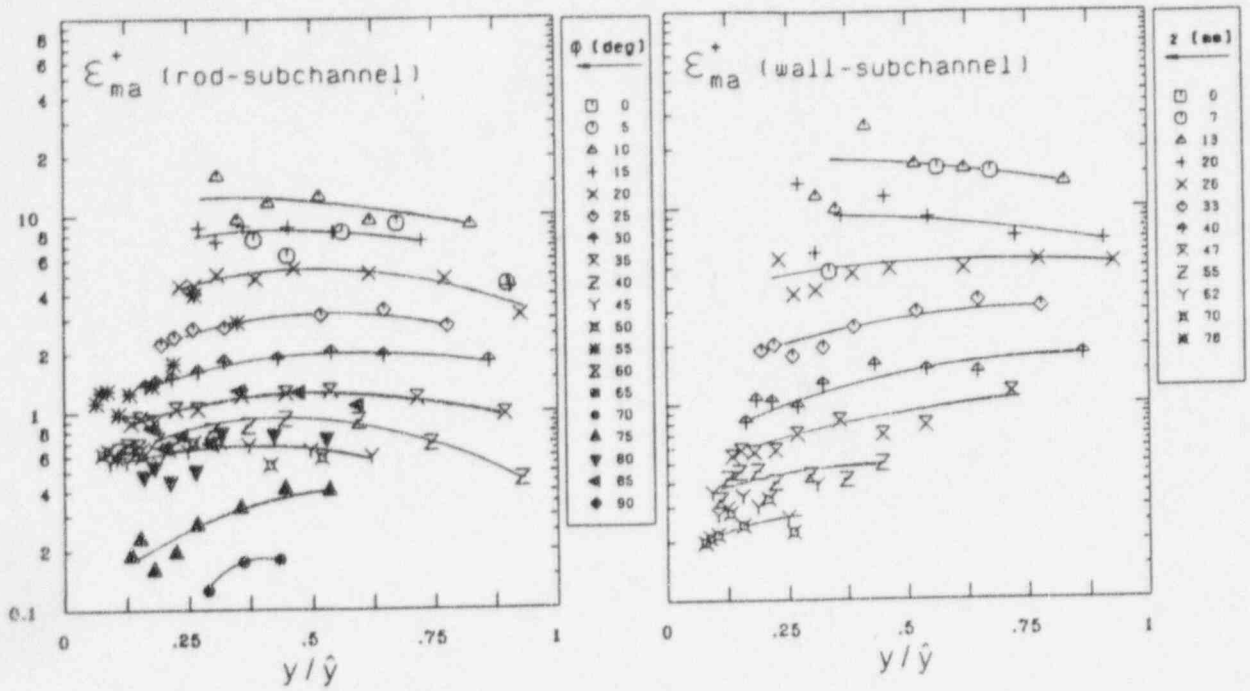

Fig. 24. Eddy viscosity parallel to the wall.

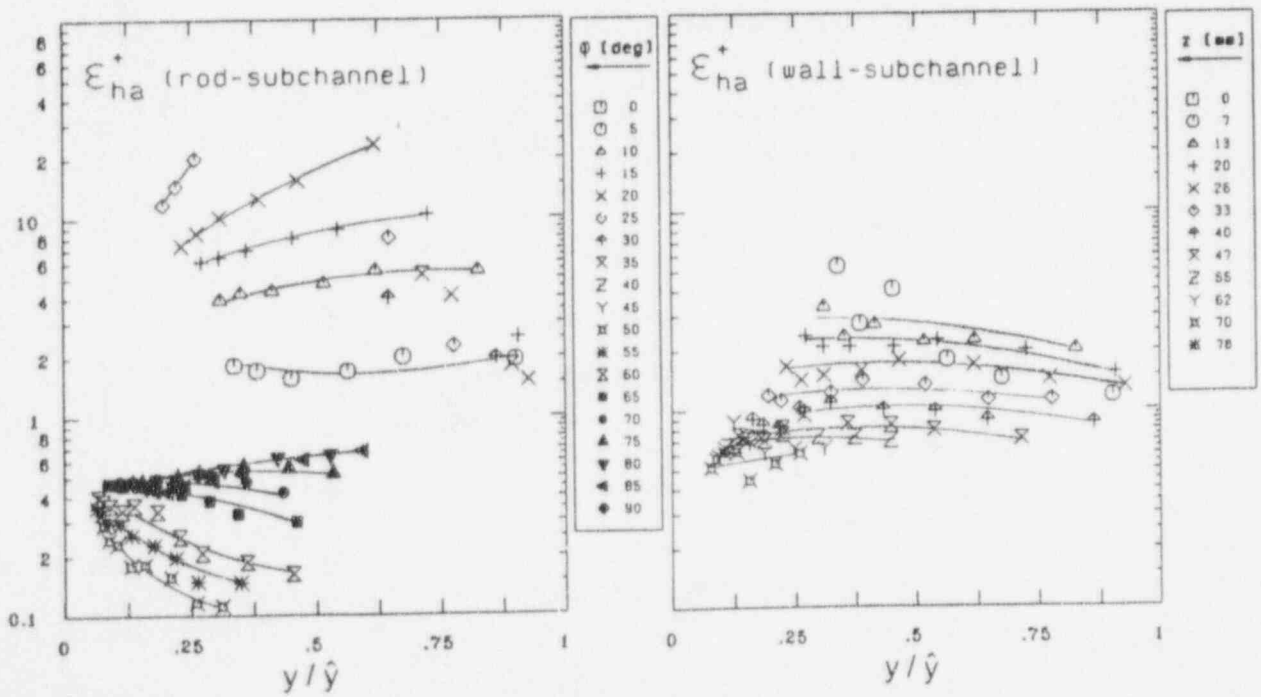

Fig. 25. Eddy diffusivity of heat parallel to the wall.

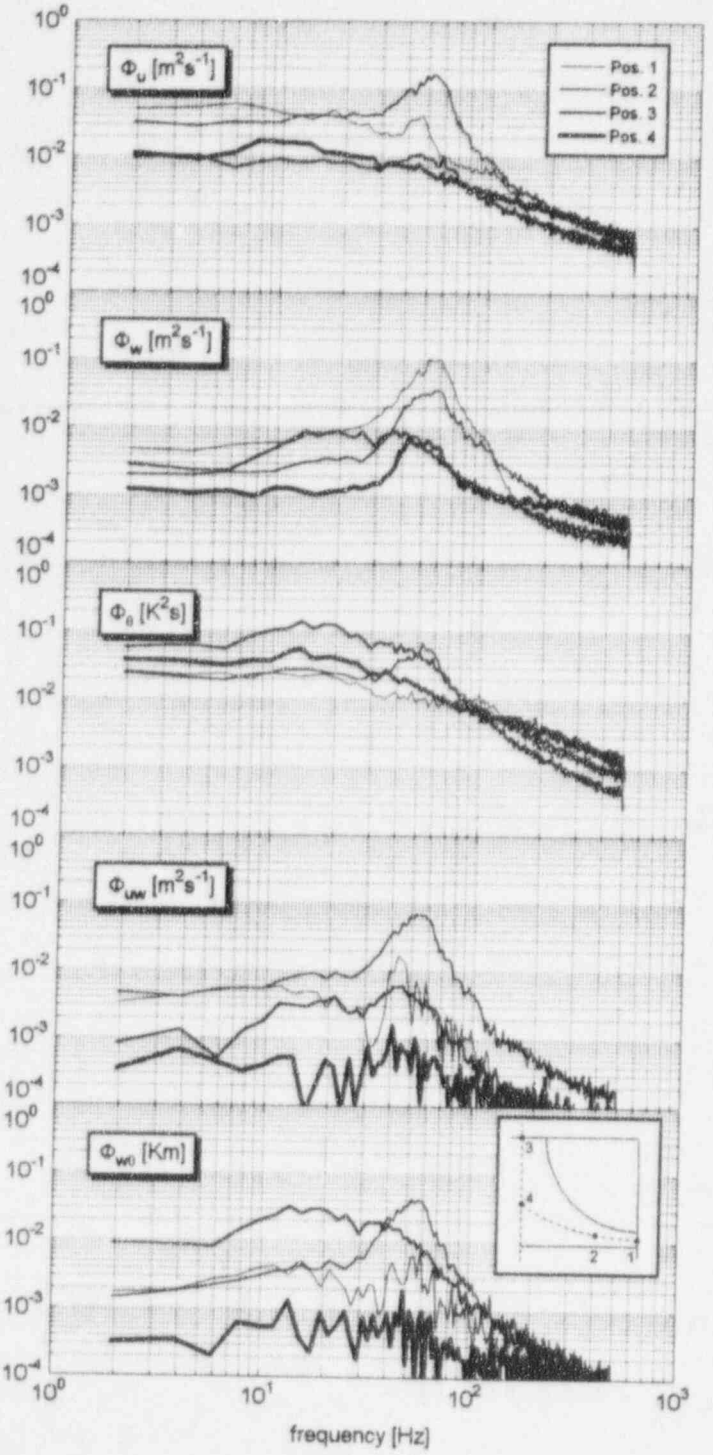

Fig. 26. Spectra of velocity and temperature fluctuations

THE COOLABILITY LIMITS OF A REACTOR PRESSURE VESSEL LOWER HEAD

T.G. Theofanous and S. Syri

Center for Risk Studies and Safety
Departments of Chemical & Nuclear and
Mechanical & Environmental Engineering
University of California, Santa Barbara, CA 93106

ABSTRACT

Configuration II of the ULPU experimental facility is described, and results from a comprehensive set of experiments are provided. The facility affords full-scale simulations of the boiling crisis phenomenon on the hemispherical lower head of a reactor pressure vessel submerged in water, and heated internally. Whereas Configuration I experiments (published previously) established the lower limits of coolability under low submergence, pool-boiling conditions, with Configuration II we investigate coolability under conditions more appropriate to practical interest in severe accident management; that is, heat flux shapes (as functions of angular position) representative of a core melt contained by the lower head, full submergence of the reactor pressure vessel, and natural circulation. Critical heat fluxes as a function of the angular position on the lower head are reported and related to the observed two-phase flow regimes.

1. INTRODUCTION

The purpose of this paper is to make available the first experimental data directly relevant to establishing the coolability limits (critical heat flux) of reactor-scale hemispheres submerged in water and heated internally. The situation arises in the management of severe accidents, and a relatively recent idea that the relocation of molten corium could be arrested, at the lower head of a reactor pressure vessel, by external flooding, as illustrated in Figure 1 (Theofanous et al., 1994a). For this idea to work, it is necessary that the thermal load created by natural convection of the heat-generating pool on the inside, be below what could cause a boiling crisis (BC) on the outside. The key features of the problem can be seen with the help of Figure 2, depicting the reactor-vessel-cavity configuration in the AP600 design, which is our main current interest (Theofanous et al., 1994c).

Considering first the "local" aspects, we will note that the downward-facing geometry lends itself to the formation of a two-phase boundary layer that is "squeezed" upon the heating surface by gravity forces. This "squeeze" is moderated by turbulent mixing (including interfacial instabilities and entrainment) as buoyancy drives the steam past the heating surface and the surrounding water. The balance between these two mechanisms is quite different in the various regions around the lower head. This gives rise to widely different two-phase flow regimes, and as a consequence, we can expect significant variations of the critical heat flux and perhaps even of the underlying mechanism(s) for it. For example, in the vicinity of the stagnation point ($\theta \sim 0°$) the vapor velocities are very low and the surface orientation, relative to the gravity

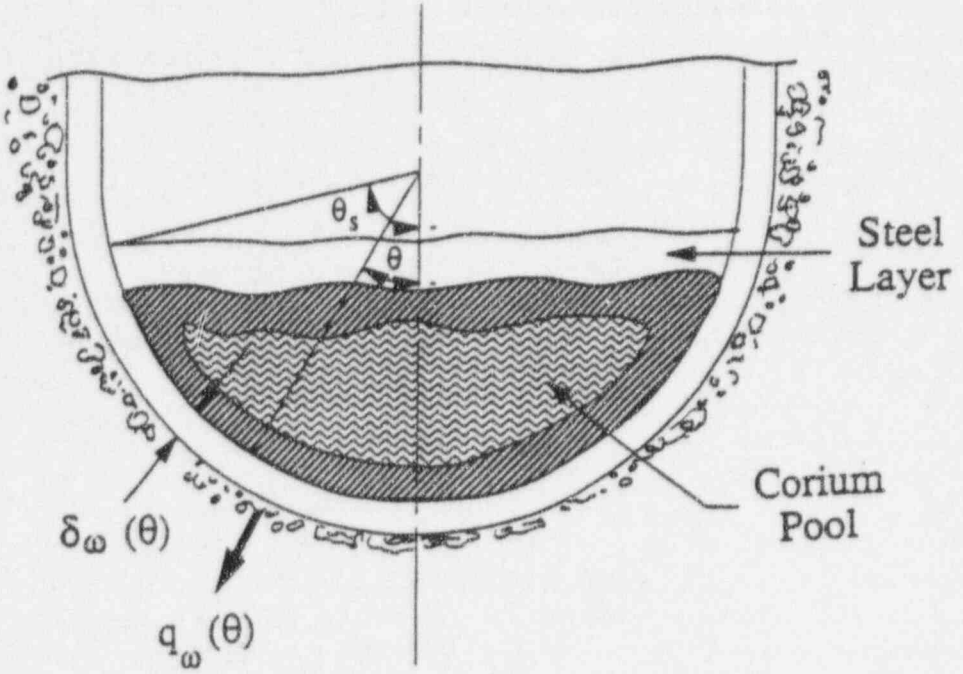

Figure 1. Schematic of the in-vessel retention phenomenology.

vector, drives the maximum phase separation with the vapor "squeezed" up against the wall. We expect periodic formation of relatively large bubbles, growth, and escape. Under such flow conditions we can expect that boiling crisis will occur if the underlying thin liquid film dries out, within one such period, **and if** the surface temperature rises to high enough levels to prevent rewetting when the liquid rushes back-in following bubble escape. As a consequence, surface wettability (controlling the behavior of the thin film), and wall thickness (controlling the rate of heatup following the dryout of this film) should be important. Aspects that could affect the behavior of these bubbles, including any convection in the free-stream water (see global behavior discussed below) and its subcooling, should also be important. On the other hand, near the equator of the lower head hemisphere ($\theta \sim 90°$), we expect that cumulative vapor generation from all the upstream positions will give rise to high vapor, and entrained liquid, flow velocities, and in addition, the vapor "squeeze" effect described above would be minimal in the near-parallel orientation of the surface to the gravity vector. As a consequence, we expect a highly turbulent two-phase flow within a relatively "diffuse" boundary layer. Correspondingly, the BC mechanism would be convection-dominated. However, phase separation and perhaps even capillarity may continue to have some bearing on the mechanism in this regime, as well. Evidently, intermediate (or mixed) mechanisms can be envisioned as we go from the stagnation region to the equator with the details of this transition region being strongly dependent upon the power (input) shape.

Let us turn next to the global aspects. In a fully-flooded cavity, as indicated in Figure 2, the gravity head would be ~7 meters, which corresponds to ~14 °C subcooling with saturated water at the top. The supply of this subcooled water to the cavity depends on any flow restrictions on the flow path, and on the gravity head developed due to the two-phase flow in the riser. Moreover, the availability of any subcooled water in the immediate vicinity of the heating surface would depend on the **local** mixing and flow patterns as described above. This coupling of the local to the global behavior is quite important in that it indicates a truly conjugate behavior. The key

mechanism is void drift in the riser, and the void fraction distribution depends on the power input (including shape), the subcooling, and on the flow losses along the natural circulation path—especially on any inlet or outlet restrictions. The following clarifications need to be made: (a) power is also supplied along the riser section, it being the radiative heat flow conducted through the side wall of the reactor vessel; (b) our present interest is in wide open paths into the reactor cavity, as in Figure 2; and (c) key aspects of the flow geometry would be dictated by the thermal insulation design (not shown in Figure 2), which is a reactor specific feature—here we concentrate on a basically unimpeded geometry, which in principle is a feasible design option (it is in the AP600). In addition, the dynamics of the natural circulation loop, such as flow and pressure oscillations may be important (i.e., loop elasticity), especially on the bubble regime discussed above.

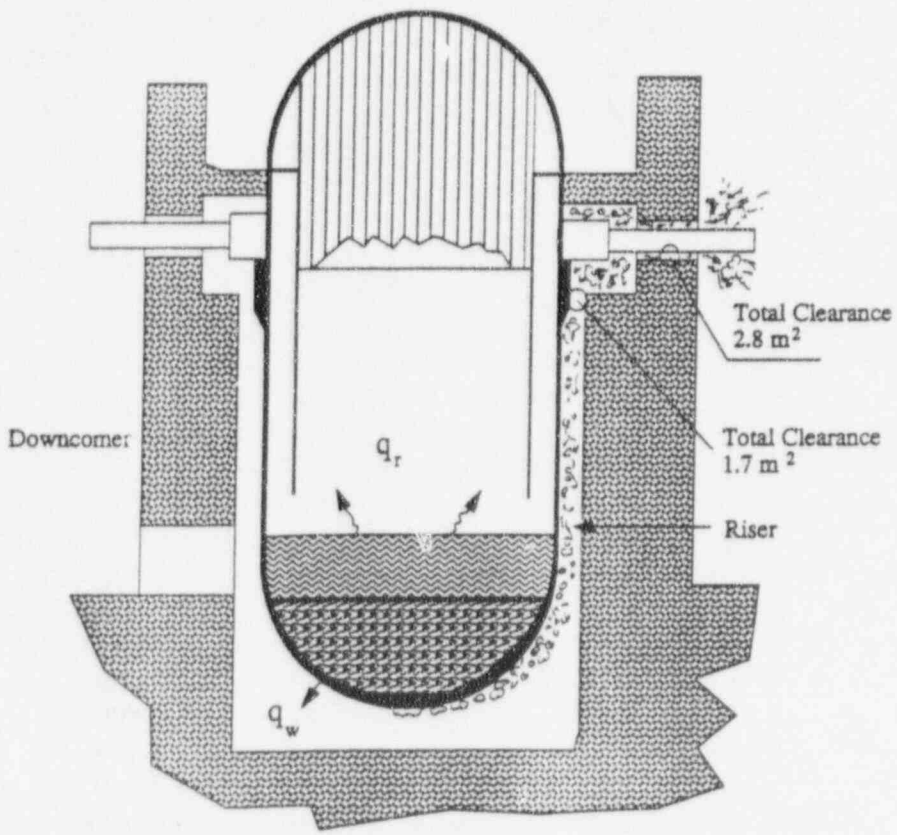

Figure 2. Key geometric features of cavity flooding and venting paths. Illustration of the two-phase boundary layer on the lower head. Thermal insulation not shown.

Mechanistically, these are behaviors unlike any CHF situations considered previously. Considering also the status of fundamental understanding in the extensively investigated problem of BC on a horizontal, upwards facing plate (Lienhard, 1994), we chose to pursue an experimental approach **that faithfully simulates the reactor in all the key aspects of the phenomena involved**. Based on the above discussion, these key aspects include:

1. **Heater length scale and shape**. To properly represent the two-phase boundary layer behavior, especially in the intermediate region, we need a full-length geometry, including the correct curvature.

2. **Heating surface thermal inertia**. In the reactor, the lower head thickness could vary from its initial value of 15 cm (for most of the region), to a low value of a few centimeters due to thinning by melt attack near the equator (Theofanous et al., 1994c). Therefore, a minimum of a few centimeters in heated thickness is needed to properly represent the thermal inertia.

3. **Power shape**. In conjunction with the above item 1, a correct power history in the upstream region is necessary to represent the two-phase boundary layer conditions in the reactor. In addition, the total power shape, including that in the riser, must be represented to simulate void distribution and flow behavior.

4. **Heating surface wetability**. The reactor lower head is designed to be made of forged carbon steel (SA 508), machined to 200 r.m.s. mean roughness. Even though it is to be painted in situ, the paint is expected to flake off in boiling water, and the exposed steel surface to be well-wetted. This surface condition must be confirmed and matched experimentally.

5. **Loop length scale and hydraulic diameter**. To properly represent subcooling due to gravity head we need a full-length loop ($\sim$7 m). The annular gap in the reactor is $\sim$20 cm, and a similarly large cross sectional length scale (diameter) is needed in a one-dimensional geometry to allow proper simulation of the vapor drift.

The ULPU facility was built to embody all of the above key characteristics, allowing, therefore, a full-scale simulation capability. The experimental approach is evolving gradually from overall parametric studies and simulations (of the reactor conditions of interest), to detailed investigation of local phenomena, and thus eventually to identification of the crisis mechanism and to an analytical model. The emphasis on simulations in the early part of this program derives from two reasons. One is to afford an early identification and focus on the particular flow and heat transfer regimes relevant to the problem of practical interest. The other, and perhaps more important one, is that the practical need for reasonably robust estimates of CHF is imminent as reactor-specific accident management schemes are now up against key decision points and regulatory scrutiny (AP600 and Loviisa---see Theofanous et al., 1994a). The results presented in this paper are intended to fulfill this immediate need. In addition, these results provide an initial perspective on mechanisms as a starting point for the more detailed investigations of the phenomena at the local level. It should also be noted that both of these reactors have lower heads with no penetrations, so the effects of such complications in geometry are left for future studies.

The experiment concept is based on what we call the "power shaping principle" (Theofanous et al., 1994b). Briefly, it allows us to determine the power shape on a two-dimensional test section (representing a "slice" of the lower head) needed to create the correct hydrodynamic conditions (matching those in the reactor) at any angular position for which the critical heat flux is sought. The experimet involves three distinct configurations as illustrated in Figures 3 and 4.

Configuration I is for studying saturated, pool boiling in $-30° < \theta < 30°$, and especially in the region around $\theta \sim 0°$, which is not as well represented in the other configurations. Configuration II is for simulating the complete geometry (a one-quarter circle) under loop flow (including the effects of subcooling) conditions. As seen in Figure 4, this configuration is to represent an open-to-the-cavity geometry. A channel geometry, as it might arise from particular thermal insulation designs with an inlet at the very bottom ($\theta \sim 0°$), can be created by introducing a baffle, as illustrated in Figure 4, to obtain Configuration III. In this paper we present data from Configuration II only. The results for Configuration I have been presented previously (Theofanous et al., 1994b), and Configuration III will be addressed for specific reactor and thermal insulation

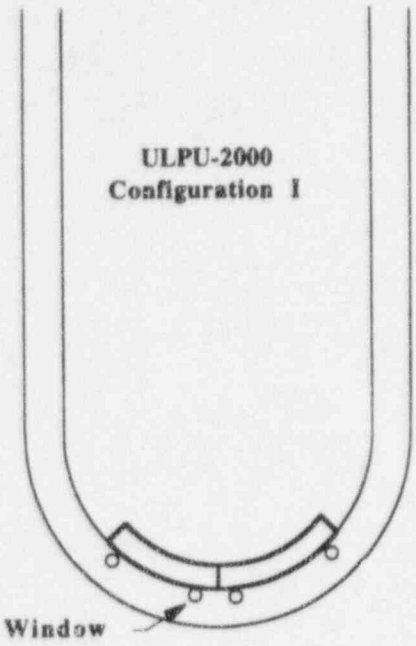

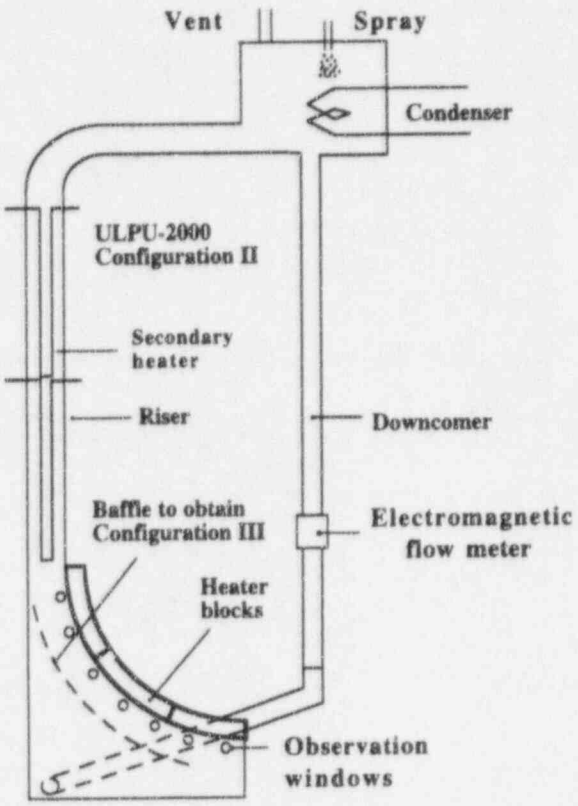

Figure 3. Schematic of Configuration I in ULPU-2000. The heater blocks extend over the region $-30° < \theta < 30°$.

Figure 4. Schematic of Configurations II and III in ULPU-2000. The heater blocks extend over the region $0° < \theta < 90°$.

designs, as needed. Up to and including the present work, the heater blocks were made out of copper and the data were obtained with the surface of it aged. Item 4 from the above-specified similarity requirements wil be fully satisfied with a heater block made of steel (the AP600 vessel wall material composition), and handled and painted according to AP600 specifications. This has been recently installed in ULPU, and results will be reported in the near future.

2. DESCRIPTION OF THE CONFIGURATION II FACILITY

The overall geometry of the experiment and related terminology are shown in Figure 4. There are three heater blocks (the primary heater, to be described shortly below) fit on top of a two-dimensional chamber (15 cm wide) with a shape (in the other two dimensions) as shown. This chamber simulates an open lower cavity geometry (no reactor vessel insulation); it is 2 m wide (at the base) and 0.5 m in height at the short end. The chamber is made of stainless steel sheet, 2.5 mm thick, and it is reinforced externally over the flat areas to sustain the substantial hydrostatic forces without any significant distortion. This test section stands bolted on shock absorbers capable of carrying 3000 kg, which in turn are anchored to the floor. The riser and downcomer are assembled from glass piping 6 m long and 15.2 cm and 7.6 cm in diameter respectively. The riser is equipped with a cable heater (referred to as the secondary heater)

extending essentially over the whole length, and operating at a fixed power level of 24 kW. The purpose of this heater is to simulate the radiative power from the melt delivered through the wall of the reactor pressure vessel to the water in the annular space between the cavity wall and the reactor vessel. (The riser in the experiment corresponds to this space.) Finally, the condensor unit at the top is to minimize coolant losses and allow operation with saturated water at the inlet to the downcomer. In Configuration II runs this was accomplished by direct contact condensation; that is, a fine spray of demineralized, room temperature water injected at rates sufficient to make up the steam loss to the environment (let out through a permanently open vent line). The condenser was also equipped with a safety relief valve which, however, did not ever have to energize.

The whole facility, in operation, is shown in Figures 5 and 6.

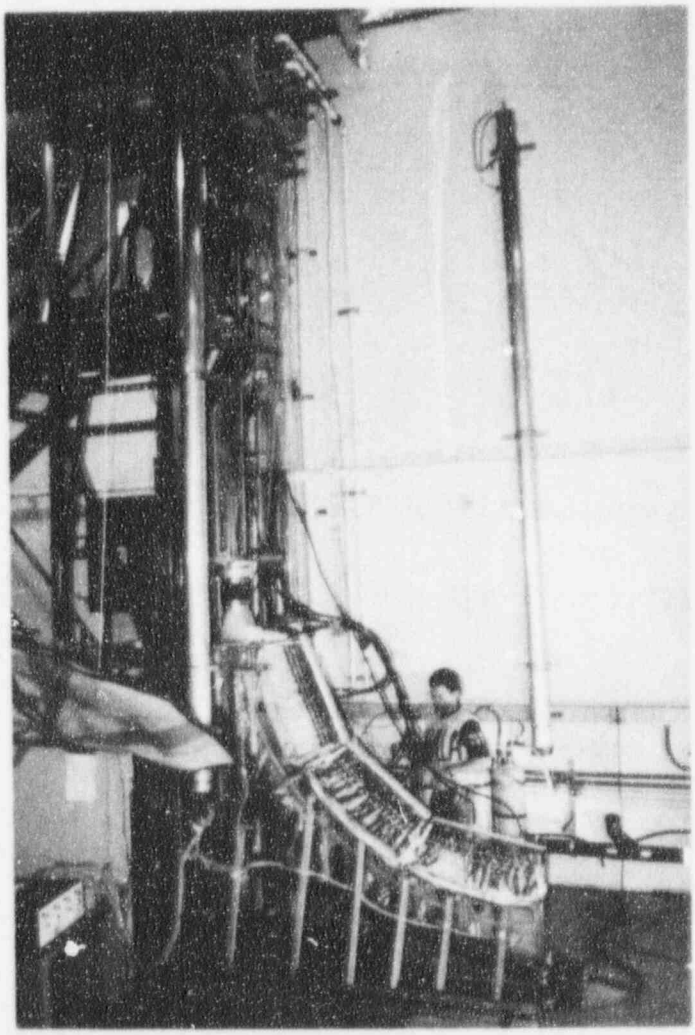

Figure 5. The ULPU-2000 Configuration II in operation.

The three heater blocks were built, each covering, nominally, a 30° arc of a circle, with a radius of curvature of 1.76 m, which is well within the range of typical reactor dimensions. The actual arc is 27°, with a length of 0.83 m. The block height and width were chosen as 7.6 cm and 15 cm, respectively, such as to ensure sufficient thermal inertia and to minimize side-wall

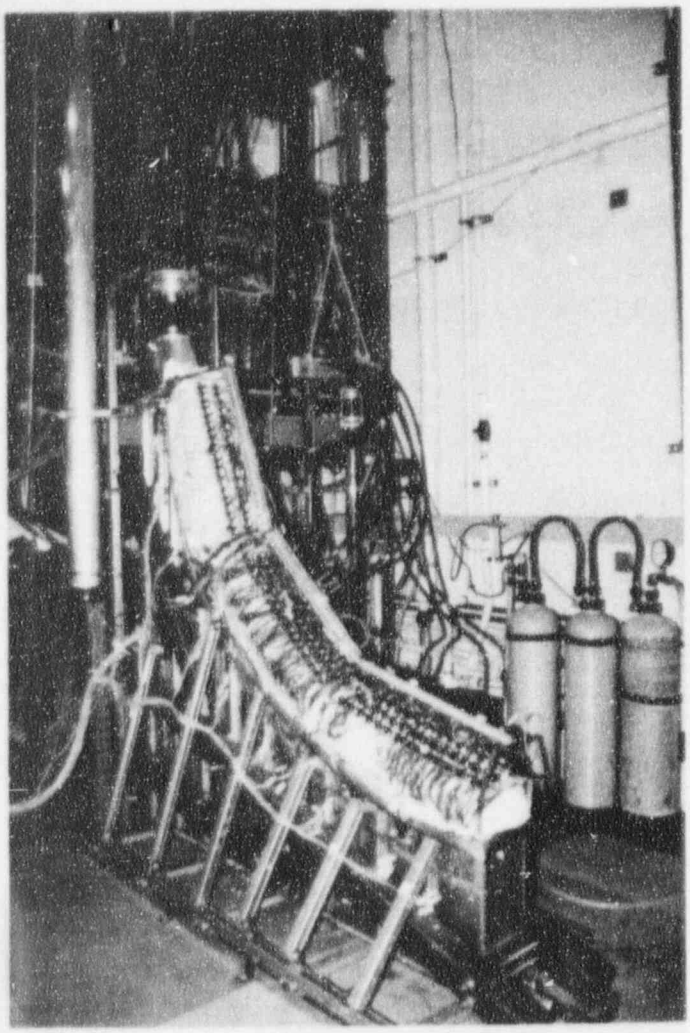

Figure 6. The ULPU-2000 Configuration II test section.

effects. One such block, just prior to assembly, is shown in Figure 7. The holes are 9.5 mm in diameter and allow two cartridge heaters (per hole) to be inserted, one from each side. The "fit" must be very good, while precision machining is also required in the accurate positioning of the holes, the 1.5 mm in diameter holes needed for the thermocouples, and the forming the smooth, curved faces. Copper stock was selected as the raw material. Voltage (217 V) is supplied to the cartridge heaters through 32 relays which are individually computer controlled to cycle in the "on-off" positions so as to obtain any desired power distribution on the heater block.[1] In the runs reported here we grouped the relay-cardridge connection such as to create eight individually controlled heating zones per heater block (3.375° arc each, for a total of 24 zones). The heating blocks can deliver up to 2,000 kW/m^2 (hence the name ULPU-2000), and a total power of 500 kW. The total power obtained by summing the calculated power of each cartridge (from the voltage applied, the known resistivity, and the fractional "on"-time), agreed to within 1% of the total power supplied by the power generator. Temperatures are measured at eight corresponding positions along the length of each block, as illustrated in Figure 8.

[1] In all experiments the cycling time was 3.52 s, which is small when compared to the conduction time constant of the copper block (51 s). The transient conduction simulation of the heater block shows that the heat flux variation on the surface is less than 0.1%

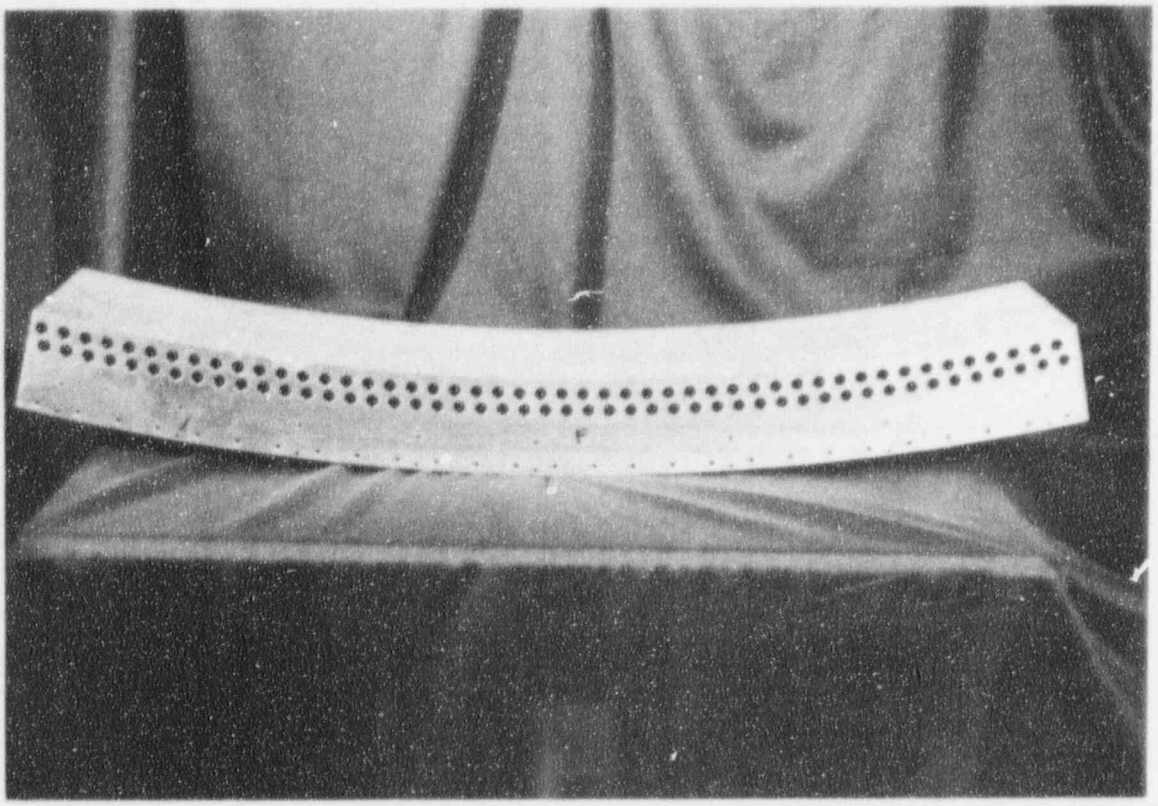

Figure 7. One of the heater blocks immediately after machining.

On the sides, the blocks overlap with the 2.5 mm stainless steel "chamber" walls (see Figure 4), by approximately 13 mm, with a rubber gasket in between. Absence of steep temperature gradients in this region (under nucleate boiling conditions the surface superheat is below ~40 °C) assures that any "bypass" losses to water are also negligible.

The flow regimes could be observed through the windows illustrated in Figure 4, and normal as well as high speed video recordings were made for a more detailed study. Water temperatures were measured at the inlet and outlet of the test section, and at several angular positions as a function of distance from the heater surface (using thermocouple trees). There are thermocouples also at the "back side" of the heater blocks—they are monitored during operation, on-line, together with the surface thermocouples as the critical safety parameters. Void fractions in the riser were measured, in the lower and upper halves of it, using differential pressure measurement. Boiling/condensation-induced vibration were obtained from a pressure tranducer mounted on the short end of the test section "chamber". Finally, the loop flow rate was obtained from an electromagnetic flow meter installed around the middle of the downcomer section. Data from all these instruments were continuously recorded during operation. Heat losses were evaluated, both analytically and experimentally, and found to be negligible.

3. OVERVIEW OF THE TEST PROGRAM

All runs in Configuration II were carried out with sufficient water in the loop to close the natural circulation path. Thus, there were a relatively strong flow, depending on the total power level (typically ~ 120 gpm), and subcooling at the base, corresponding to the gravity head (~10 K). Although the flow regimes near the heater surface in these runs were qualitatively similar to those observed in Configuration I, here the BC would occur typically within a few

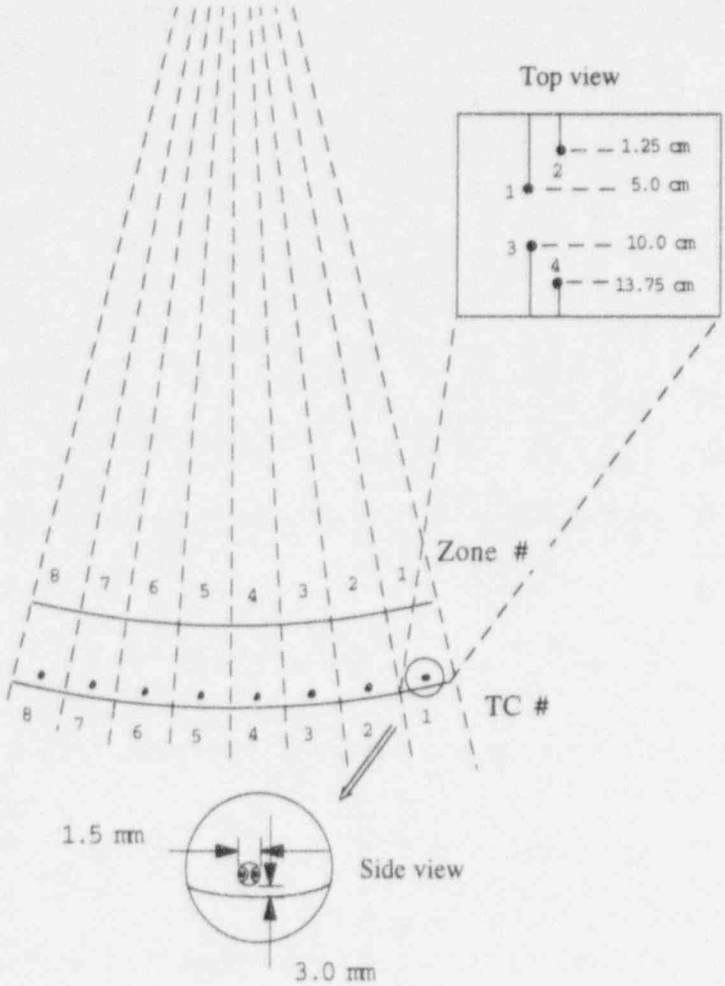

Figure 8. The heating zones and thermocouple positions on a heating block. Over the 3 heater blocks there is a total of 24 zones. Zone #1 is at $\theta \sim 90°$ and zone #24 is at $\theta \sim 0°$.

minutes or not at all. It appears that the present conditions (flow, subcooling) do not favor a BC-delay-time behavior, as found in Configuration I. Thus, zeroing in the CHF was now much easier; starting from the high end, the power was reduced after successive occurrences of boiling crisis (each of those runs being only a few minutes long), until the last reduction (typically by a few percent) where the heater remained in nucleate boiling. Once it was established that the delay time was not a significant factor here, this nucleate boiling condition was allowed to continue, for most runs, for 10 to 30 minutes. A grouping of several successive BCs and a final period in nucleate boiling is referred to as **one** experimental run.

Regarding the power shape, two types of runs were carried out: "uniform flux" (UF) runs, involving a number of zones around $\theta = 0°$ at a uniform power (that is, simulating heat flux at $\theta \sim 0°$) while the remaining two blocks were powered according to the power shaping principle; and "shaped flux" (SF) runs, powered according to the power shaping principle, to simulate BC at specific locations ($\theta \neq 0°$) along the test section. The reference power shape used here is the same as that employed in Configuration I, and it is shown in Figure 9. However, certain modifiers from these general descriptions are necessary:

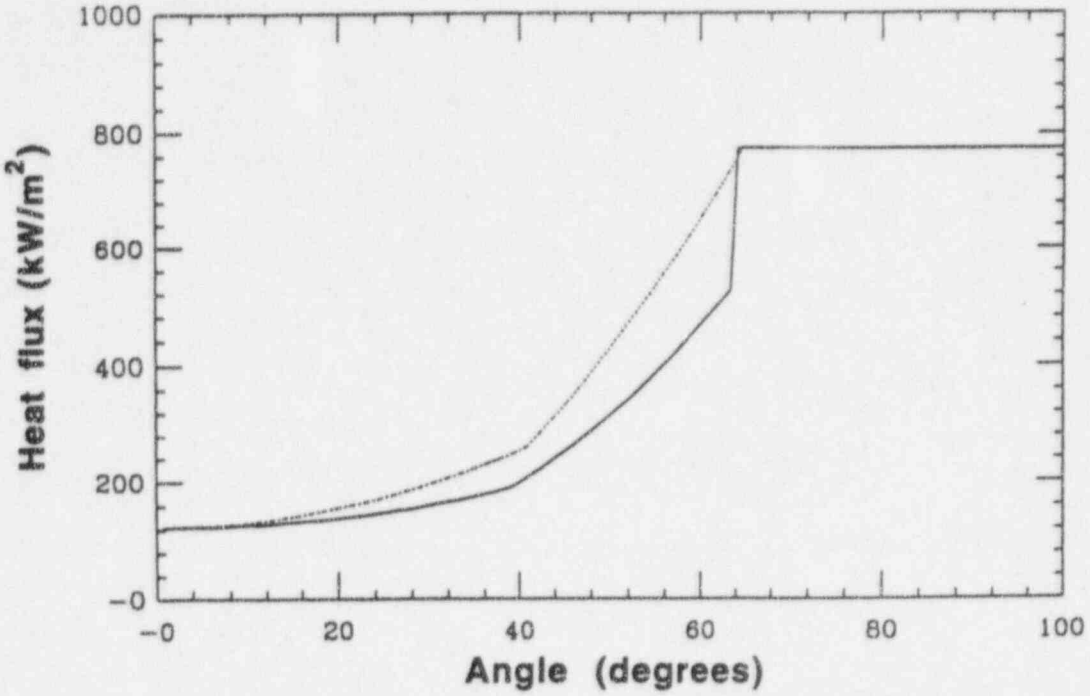

Figure 9. The reference reactor heat flux shape (——) (from Theofanous et al., 1994a), and the shape used in the simulations (. . . . .).

(a) Because of the strong peaking in the reference shape, the use of power shaping principle for $\theta \sim 0°$ always produces BC at $\theta = 90°$; that is, under reactor conditions, the position $\theta \sim 90°$ is by far more limiting than the very bottom of the lower head. Thus, to obtain the BC at $\theta \sim 0°$ we had to reduce the downstream power very significantly below that required by the power shaping principle. This was done, up to whatever degree was necessary, while maintaining the shape, however. That is, the highest power in the downstream (to the uniform flux section) region is still at 90°. [This power level was denoted in the run identification number as a percentage of the uniform flux level, imposed at $\theta = 0°$.] An example of what has been described above is given in Figure 10.

(b) For SF runs, the same "compromise," for the same reason described above, was necessary for forcing BC anywhere on the lower block ($0 < \theta < 30°$).

(c) For BC in the upper block ($60° < \theta < 90°$), an essentially exact simulation could be obtained for the lower end of it ($\theta \simeq 67.5°$); but in order to force BC at 90°, the upstream power profile within the third block had to be reduced somewhat. The reason for this is that in this upper region the reactor flux is rather flat, which translates to a rather uniform shape also according to the power shaping principle, thus yielding BC at $\theta < 90°$.

About naming, we follow the same procedure employed in Configuration I. That is, we use a prefix, UF or SF, to denote uniform and shaped flux respectively. Following this there is a numerical index that for UF runs indicates the number of zones subject to the uniform flux, while for SF runs indicates the zone at which BC is simulated. Uniform flux runs are only employed to simulate BC at the bottom end of the test section ($\theta \simeq 0°$). Then, there is a third numerical index for UF runs only, indicating the percentage of increase in power at the upper end of the

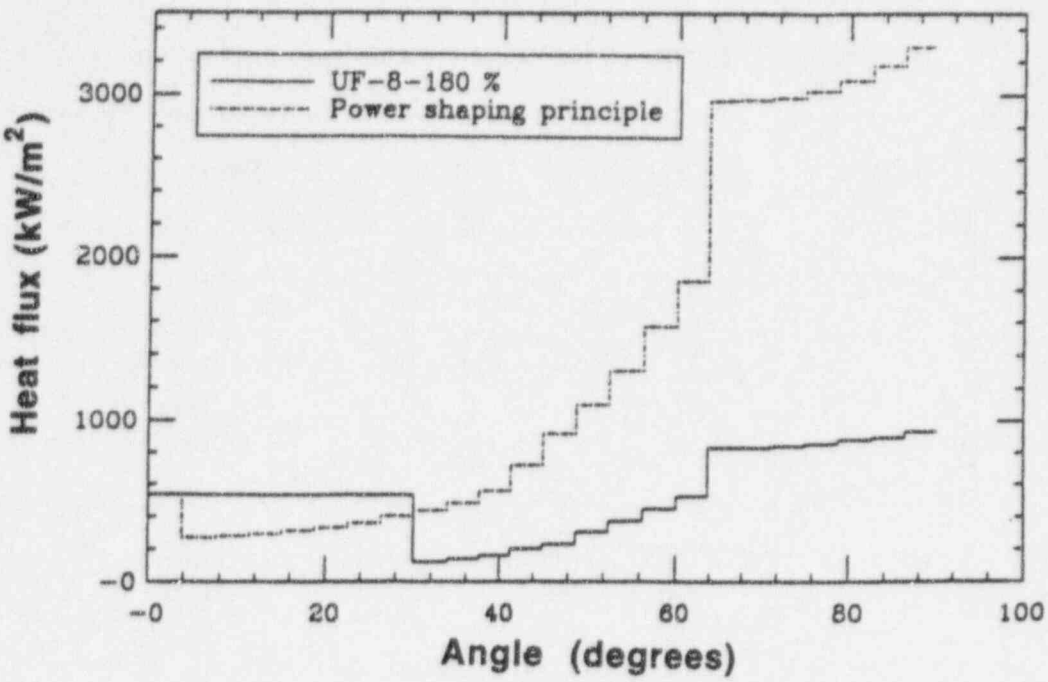

Figure 10. Illustration of the power shape "compromise" necessary to force BC at $\theta = 0°$.

test section ($\theta = 90°$) in relation to that on the uniform flux portion. Finally, the number in parenthesis at the end indicates the order in which repeat runs (if any) were performed; however, repeat runs were not run consecutively, but rather were intermingled among the various runs.

To illustrate the above, UF-8-145%(2) means: (a) a uniform flux run, simulating BC at $\theta \sim 0°$, with all 8 zones of the lower block (i.e., zones 17 to 24) at the same power; (b)middle and upper blocks powered according to the power shaping principle (as discussed above) and such that the power level at the upper end (90°) is 145% of that at $\theta = 0°$; and (c) this is the second run carried out under these conditions. On the other hand, SF-7(4) means: (a) run with a heat flux distribution according to the power shaping principle; (b) a run simulating BC in zone #7 ($\theta \sim 67°$); and (c) this is the fourth run carried out under these conditions.

A listing of all runs carried out in Configuration II is given in Table 1. The flux shapes employed in all UF runs are shown in Figure 11. The flux shapes employed in all SF runs are shown in relation to the shapes dictated by the power shaping principle in Figures 12(a) through 15(a). The effect of axial conduction in smoothing the delivered (step-wise) fluxes is shown in Figures 12(b) through 15(b), and the implied flux "corrections" at the points of boiling crisis are summarized in Table 2. These corrections have been applied already to the data reported. This type of correction for all UF runs is negligible.

Table 1. Listing of Runs Carried Out in Configuration II		
Group	Subgroup	Remarks
SF	SF–1 SF–7 SF–13 SF–17 SF–21	3 Tests 3 Tests 1 Test 4 Tests 2 Tests
UF	UF–3–180% UF–3–220% UF–8–145% UF–8–180%	1 Test 1 Test 2 Tests 1 Test

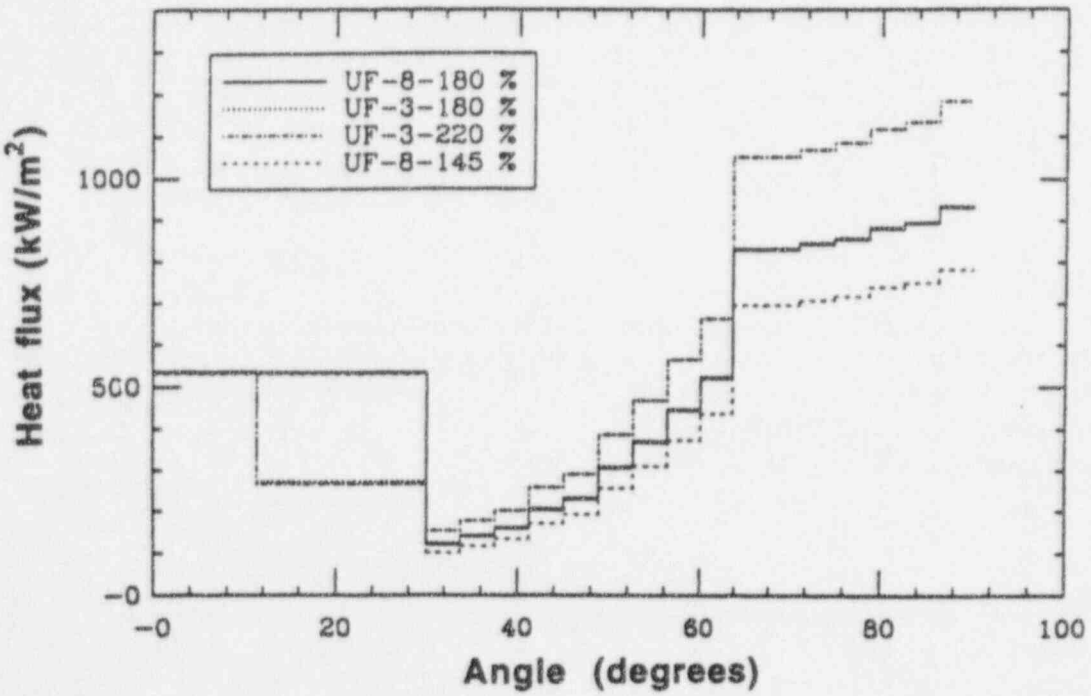

Figure 11. Heat flux profiles imposed on UF-type runs. The shape required for "simulation" for these runs is shown in Figure 10.

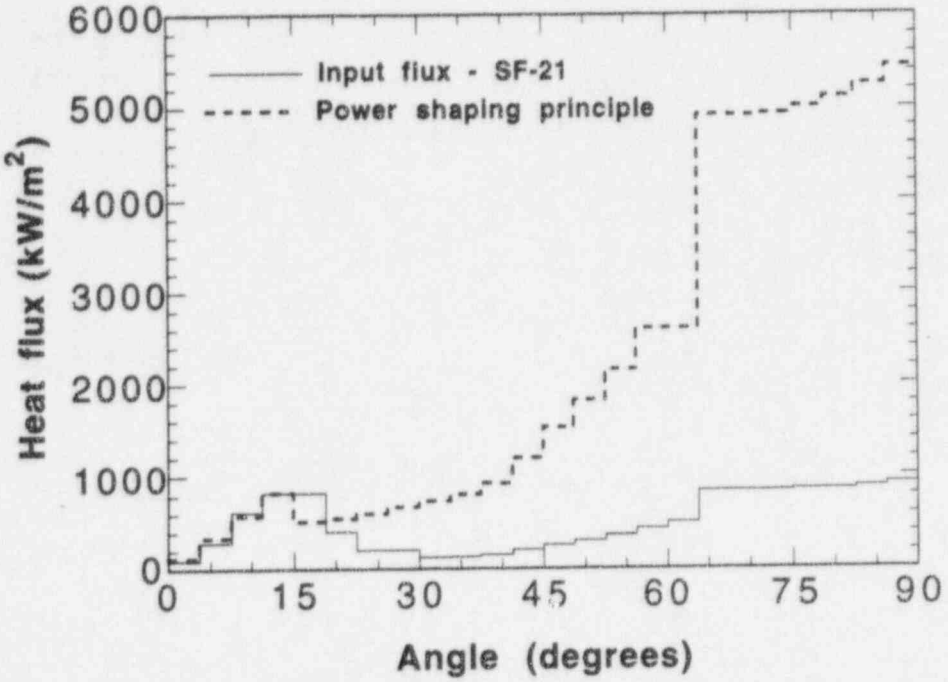

Figure 12(a). The actual power shape for run SF-21 compared to that derived from the power shaping principle.

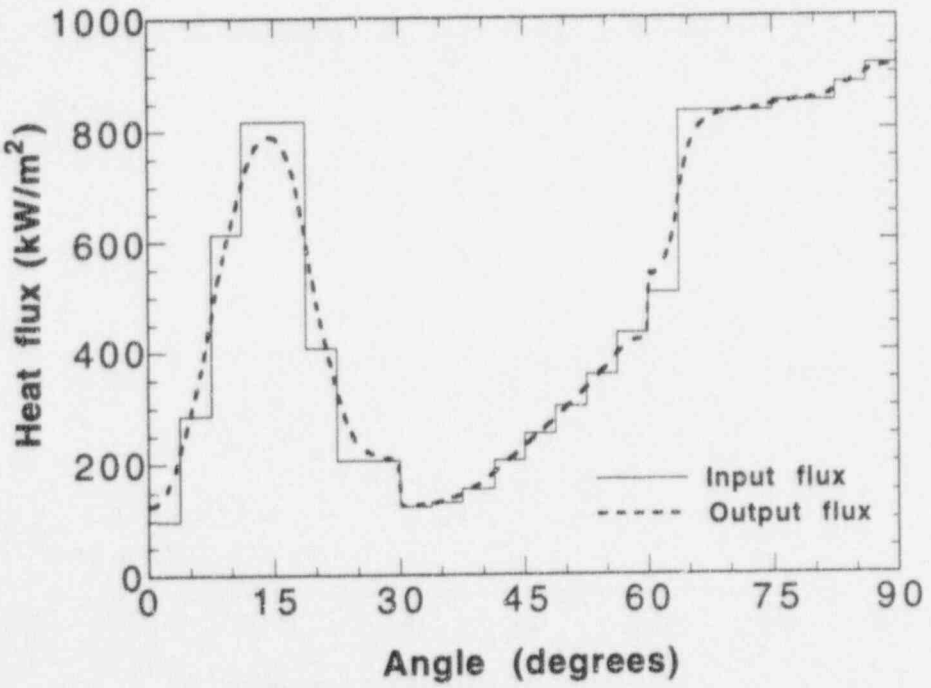

Figure 12(b). The effect of axial conduction in the heater block in modifying the input flux shape for run SF-21.

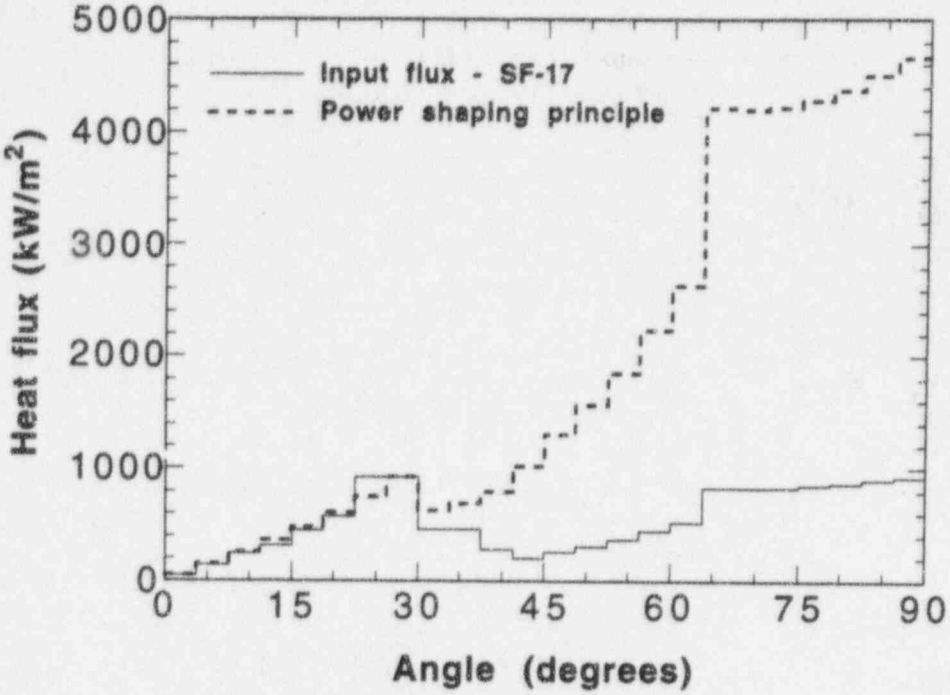

Figure 13(a). The actual power shape for run SF-17 compared to that derived from the power shaping principle.

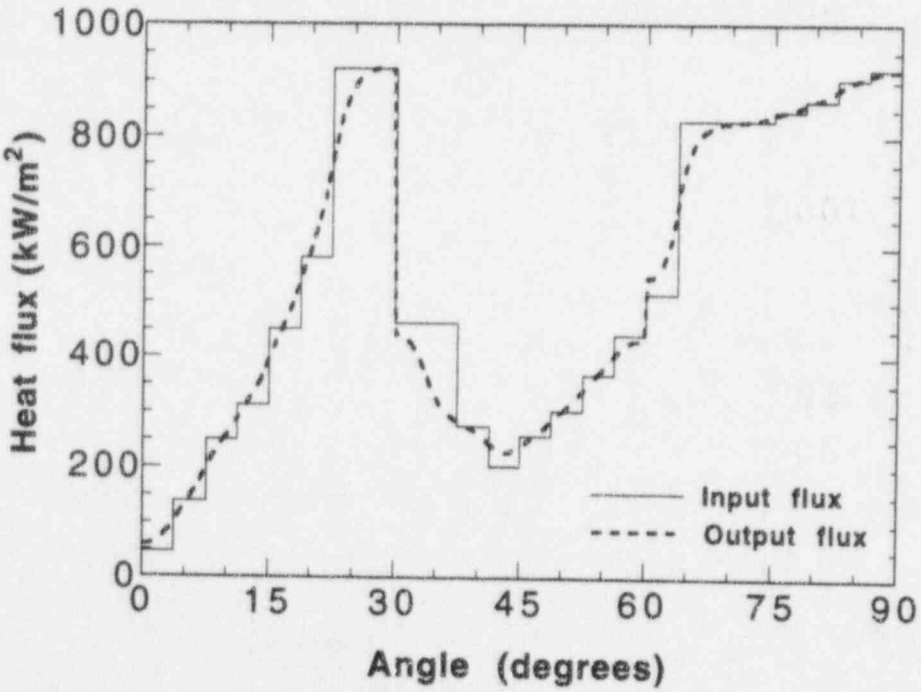

Figure 13(b). The effect of axial conduction in the heater block in modifying the input flux shape for run SF-17.

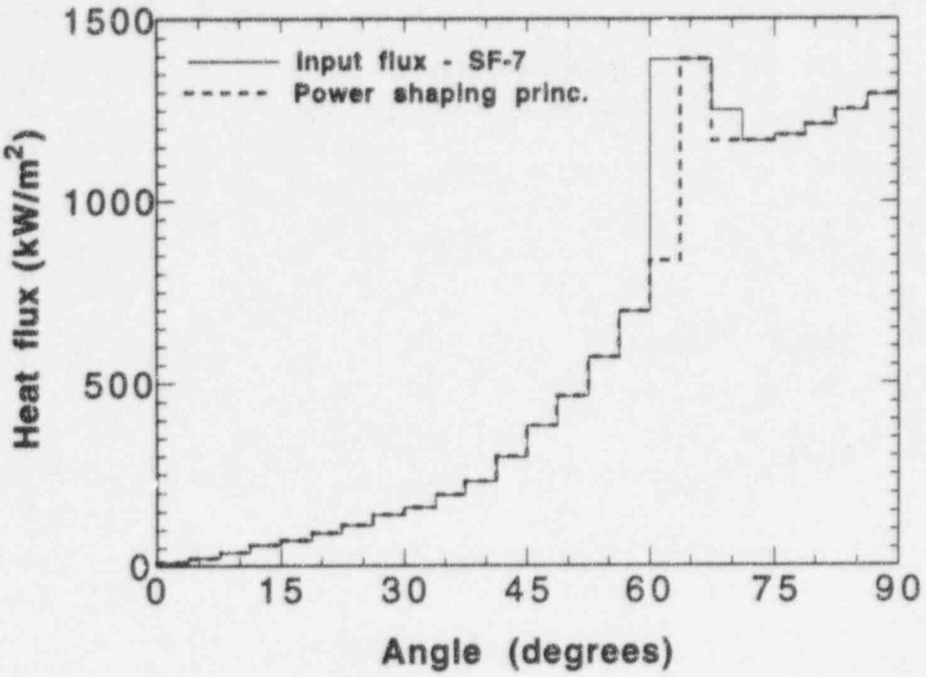

Figure14(a). The actual power shape for run SF-7 compared to that derived from the power shaping principle.

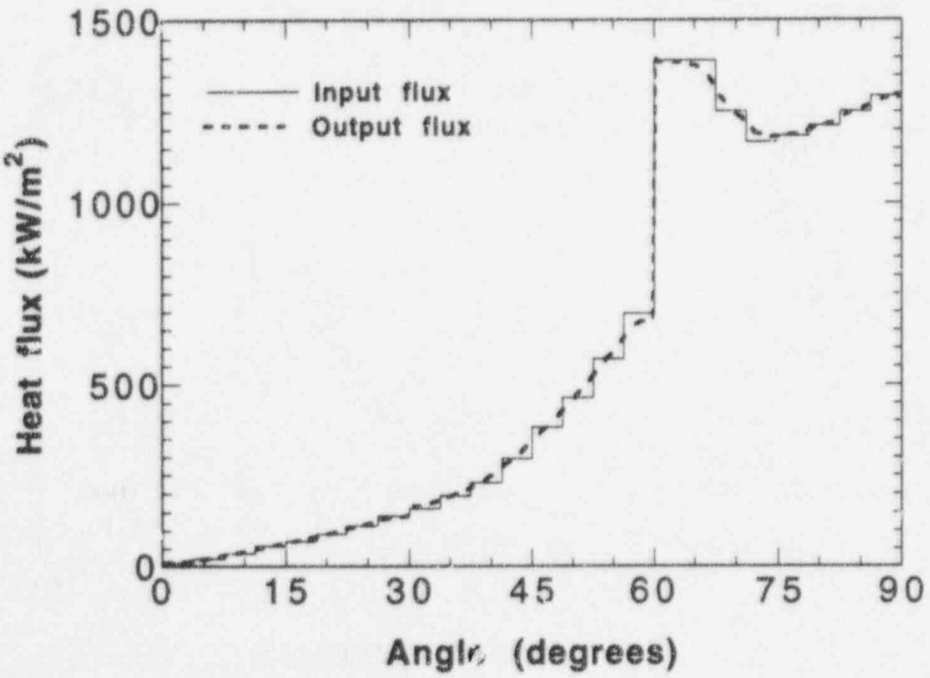

Figure 14(b). The input flux shape used for run SF-7, and the actual shape obtained (output flux) accounting for axial conduction.

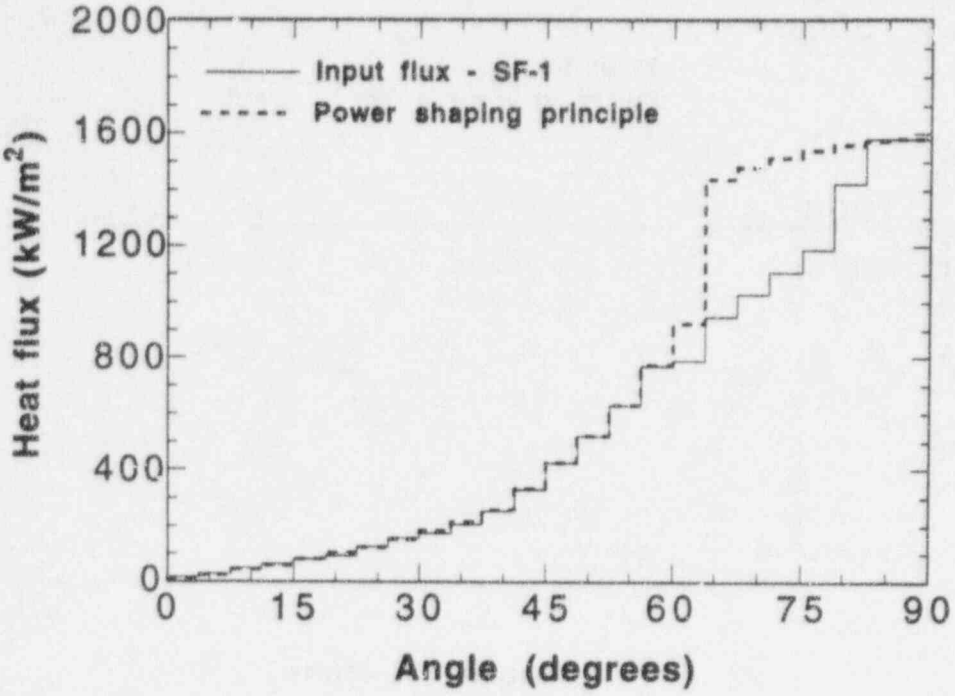

Figure 15(a). The actual power shape for run SF-1 compared to that derived from the power shaping principle.

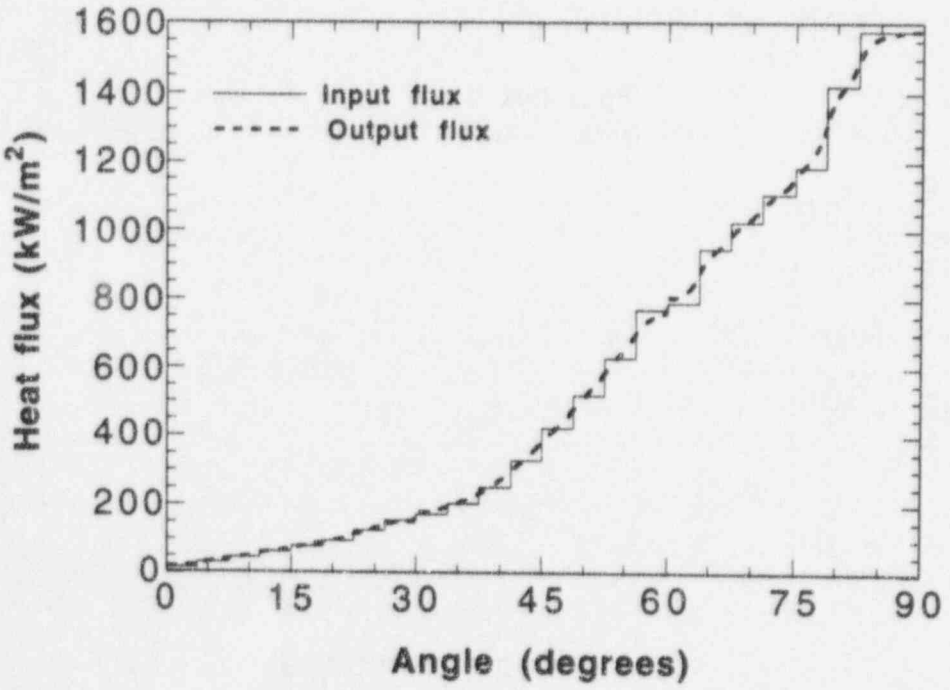

Figure 15(b). The effect of axial conduction in the heater block in modifying the input flux shape for run SF-1.

Table 2. Heat Flux Correction to the Input Flux due to Axial Conduction		
Run #	CHF Position	Correction Factor
All UF	0°	1
SF-21	15°	0.965
SF-17	30°	0.992
SF-13	45°	0.94
SF-7	67.5°	0.962
SF-1	90°	0.998

4. EXPERIMENTAL RESULTS AND DISCUSSION

A rough idea of the surface aging effect on CHF is given in Figure 16. In it, we see that the effect is measurable even after ~4 hours of operation, but it is clearly leveled out, compared to the very initial value of 450 kW/m^2. Also, for $\theta = 90°$, the initial value was ~1.2 MW/m^2, as compared to the fully-aged value of ~1.6 MW/m^2. As noted already, this work is focused on the fully-aged surface condition, and these are the results reported and discussed below.

The results from all experimental runs are shown in Figure 17, and in tabular form in Table 3. In Figure 17, we also show the results from Configuration I. The following observations and comments can be made:

1. Configuration II exhibits a significantly higher tolerance to boiling crisis as compared to Configuration I. These are clearly the effects of flow and subcooling, and they amount to about 50% increase.

2. For Configuration II, the variation of CHF with angular position seems to be composed of two, remarkably linear, regions. We believe these to be reflective of the significantly different flow regimes observed in the respective regions (see discussion in the introduction section).

3. The CHF level at the upper end (~1.6 MW/m^2) is remarkably higher than the "conventional wisdom value" for a horizontal, upward facing, flat plate in pool boiling, which for 10 °C subcooling is 1.3 MW/m^2. Clearly flow and orientation are important.

Further, it should be noted that in Table 3 we find three runs in which BC occurred rather late compared to a few minutes; however, note that all three cases were for the lowermost region ($0° < \theta < 15°$), and that the differences were rather small (2–4%). This again is another indication, or symptom, of a different mechanism in the lower region identified in the data trends (Figure 17). The lower envelope for the Configuration II data in Figure 17 can be expressed by:

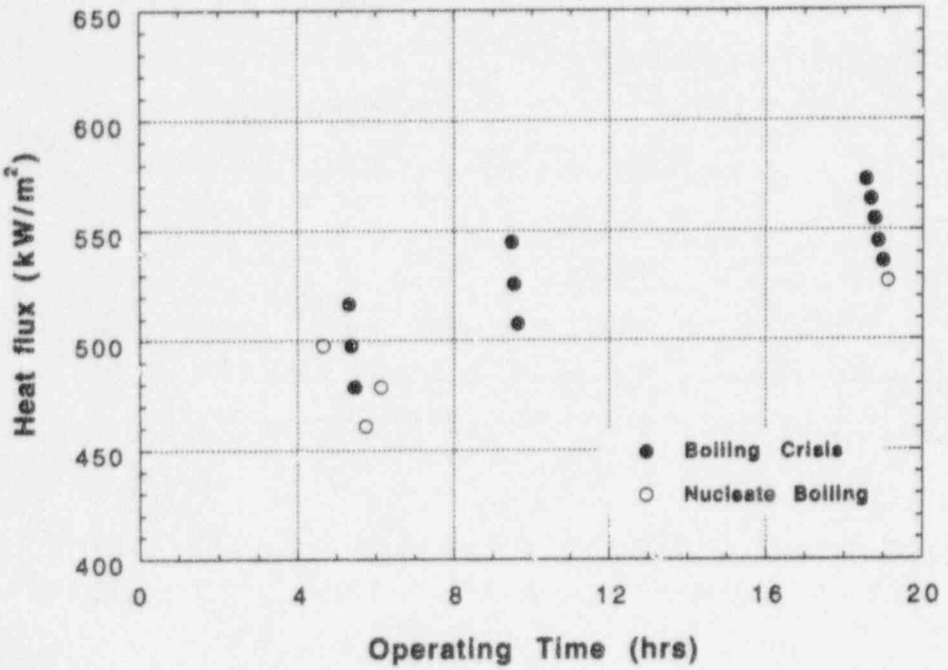

Figure 16. Illustration of the surface aging effect in Configuration II, for times greater than 4 hrs. [Data for earlier times are not shown.] All data refer to boiling crisis at $\theta = 0°$.

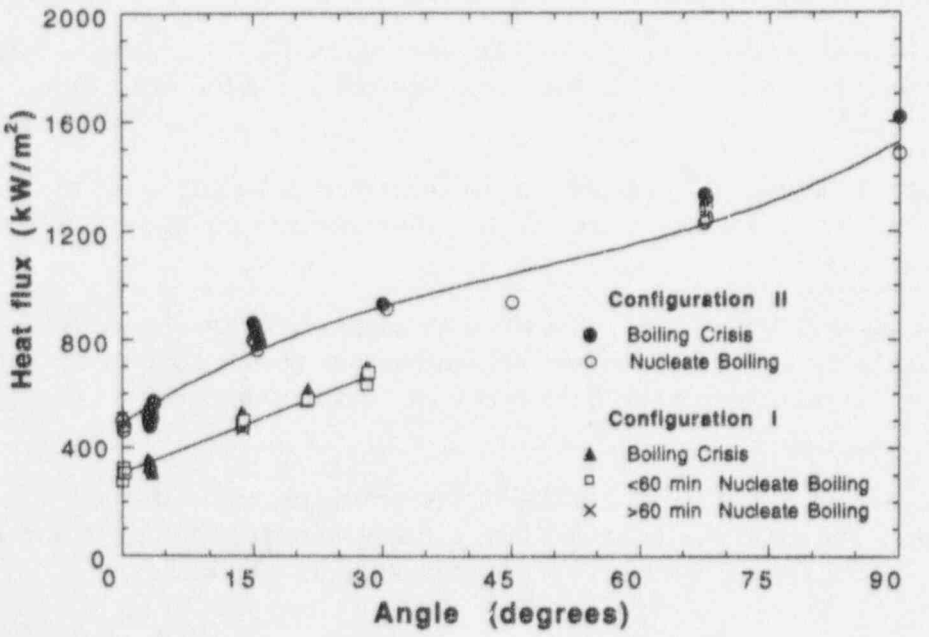

Figure 17. Collective presentation of all critical heat flux data in both Configuration I and Configuration II experiments in ULPU-2000. The line shown for Configuration II is Eq. (3). The BC points at $\theta \sim 0°$ have been displaced to the right for clarity of presentation.

Table 3. Listing of the Experimental Runs Performed in ULPU-2000 Configuration II, Heat Fluxes, and Respective Waiting Times.

Test	Nucleate Boiling		CHF	B.C Time
	Flux (kW/m^2)	Time (min)	(kW/m^2)	(min)
UF–3–180%	461	15	517	2.5
			498	3.5
			479	14
UF–3–220%	479	15		
UF–8–145% (1)			545	1.5
			526	3.5
			508	47
UF–8–145% (2)	527	120	573	1.5
			564	1
			555	2
			536	3
UF–8–180%	498	15		
SF–1 (1)	1485	10		
SF–1 (2)	1504	30	1617	1
			1579	2
SF–1 (3)	1579	10	1617	2.5
SF–7 (1)	1231	30		
SF–7 (2)	1246	30		
SF–7 (3)	1282	10		
SF–7 (4)	1299	60	1335	2
			1317	1.5
			1335	1
SF–13	932	30		
SF–17 (1)	932	10		
SF–17 (2)	914	30	932	2.5
SF–17 (3)	914	30		
SF–21 (1)	789	30	862	1
			843	2
			816	2
SF–21 (2)	762	30	789	13

$$q_{cr}(\theta) = 500 + 13.3\theta \ \text{kW/m}^2 \quad \text{for} \quad \theta < 15^\circ \tag{1}$$

$$q_{cr}(\theta) = 540 + 10.7\theta \ \text{kW/m}^2 \quad \text{for} \quad 15^\circ < \theta < 90^\circ \tag{2}$$

However, the data can be fit equally well with one equation:

$$q_{cr}(\theta) = 490 + 30.2\theta - 8.88 \cdot 10^{-1}\theta^2 + 1.35 \cdot 10^{-2}\theta^3 - 6.65 \cdot 10^{-5}\theta^4 \ \text{kW/m}^2 \tag{3}$$

This line is shown in Figure 17.

The undertainty in these results is very small compared to available margins in the case of AP600 (Theofanous et al., 1994c) as well as in comparison to other uncertainties that normally enter such assessments. Basically, there are three reasons for this: (1) small measurement error in cartridge power (~2%), (b) negligible heat losses from the heating blocks, and (c) convenience for back-to-back runs and easy recovery from BC. As noted already, the small measurement error is confirmed by finding cumulative power of cartridge heaters to be within 1% of the total power supplied (independently measured). The easy recovery from BC is because of the high thermal inertia of the heater block. Back-to-back experiments allow the approach to the true BC limit by successive fine-step approximations. As seen in Figure 17 and Table 3, the data show that this could be done within a few percent.

5. CONCLUSIONS

With the completion of the Configuration II experiments reported here, we have established a firm estimate for the coolability limits of the lower head of a reactor vessel submerged in water and heated internally. The scale of the experiment, and the power shaping principle, ensure that these data, and resulting correlation, are directly applicable to the reactor. The correlation reveals a two region behavior [Eqs. (1) and (2)] which has been related to the different flow regimes observed in the two-phase boundary layer in the respective regions.

6. ACKNOWLEDGMENTS

This work was funded by IVO International Ltd. (supporting S. Syri) and the U.S. Department of Energy's Advanced Reactor Severe Accident Program (ARSAP) through ANL subcontract No. 23572401. We are also grateful to Sergio Angelini, Tony Salmassi, and Mitch Frey, for help with design and construction of Configuration II, and to Jeff Smith and Charlie Liu, for helping with the construction, running of the latest portion of the experiments, and helping with the data reductions. Messrs. Steven Sorrell (DOE) and Stephen Additon (TENERA) played a key role in programmatically supporting this project.

7. REFERENCES

1. Lienhard, J.H. (1994) "Snares of Pool Boiling Research: Putting Our History to Use," Proc. Tenth International Heat Transfer Conference, Brighton, UK. Vol. 1, Keynote Papers, (G.F. Hewitt, ed.) London: Chameleon Press, Ltd., GK-11, pp 333-348.

2. Theofanous, T.G., C. Liu, S. Angelini, O. Kymäläinen, H. Tuomisto and S. Additon (1994a) "Experience from the First Two Integrated Approaches to In-Vessel Retention Through External Cooling," OECD/CSNI/NEA Workshop on Large Molten Pool Heat Transfer, Grenoble, France, March 9-11.

3. Theofanous, T.G., Sanna Syri, Tony Salmassi, Olli Kymäläinen and Harri Tuomisto (1994b) "Critical Heat Flux Through Curved, Downward Facing, Thick Walls," Nucl. Eng. and Des. **151**, 247–258.

4. Theofanous, T.G., C. Liu, S. Additon, S. Angelini, O. Kymäläinen, and T. Salmassi (1994c) "In-Vessel Coolability and Retention of a Core Melt," DOE/ID-10460, November 1994 Peer Review Version.

Numerical Simulation of Multi-Dimensional Two-Phase Flow Based on Flux Vector Splitting [1]

H. Städtke, G. Franchello, B. Worth
Commission of the European Communities
Joint Research Centre - Ispra Establishment
I-21020 Ispra (Varese) Italy

Abstract

This paper describes a new approach to the numerical simulation of transient, multi-dimensional two- phase flow. The development is based on a fully hyperbolic two-fluid model of two-phase flow using separated conservation equations for the two phases. Features of the new model include the existence of real eigenvalues, and a complete set of independent eigenvectors which can be expressed algebraically in terms of the major dependent flow parameters. This facilitates the application of numerical techniques specifically developed for high speed single-phase gas flows which combine signal propagation along characteristic lines with the conservation property with respect to mass, momentum and energy. Advantages of the new model for the numerical simulation of one- and two-dimensional two-phase flow are discussed.

1. Introduction

A serious limitation of all 'best estimate' thermohydraulic systems codes, like RELAP5, TRAC, CATHARE and ATHLET, is the inability to accurately predict local flow parameters characterised by strong thermal and mechanical non-equilibrium effects. The safety of LWRs under accident and off-normal conditions is therefore jeopardised by fundamental inadequacies in the basic modelling approach and outdated numerical methods used in these codes. Major problems therefore arise when attempting to predict local flow phenomena dominated by strong spatial gradients or quasi-discontinuities: e.g. the formation and tracking of two-phase mixture levels, direct contact condensation during ECC injection of subcooled liquid, quench front propagation in the case of reflooding an uncovered core, tracking of boron dilution fronts, and two-phase critical flow conditions.

Code deficiencies are often related to our present rather limited understanding of local heat, mass, and momentum exchange processes at the (continuously varying) interface and therefore considerable effort has been focused on developing improved correlations for these processes. However, this seems to be only one part of the problem. There is certainly also a number of more basic limitations in existing codes which might be identified as follows: (1) the generally non-hyperbolic character of the governing equations

[1] Paper submitted for the 7th International Meeting on Nuclear Thermal Hydraulics Saratoga Springs, NY USA, September 10-15, 1995.

represent an 'ill-posed' initial-boundary value problem which requires specific numerical damping terms in order to obtain stable results, (2) the use of numerical methods based on staggered grid discretization and donor-cell techniques introduces a large amount of numerical diffusion, thus hindering the introduction of real physical viscosity effects, and (3) the general use of numerical schemes which are only first-order accurate in space.

As an alternative to the approach commonly used in all the presently available codes, a new model for inhomogeneous two-phase flow has been developed at the JRC-Ispra based on a single-pressure two-fluid approach (six equation model). By introducing appropriate formulations for the interfacial coupling between the two separated momentum equations (including space and time derivatives of phasic velocities, void fraction and phasic densities), a completely hyperbolic system of equations has been obtained. An important feature of the new model, (as demonstrated in refs. [1], [2], [3]), is that the eigenvalues (characteristic velocities) and the corresponding eigenvectors of the coefficient matrix of the governing equations can be expressed analytically as algebraic functions of the major dependent flow parameters. This allows the application of more advanced numerical techniques which make explicit use of the characteristic directions of the flow field. In this context the use of 'flux vector splitting' techniques can significantly reduce numerical diffusion and unphysical viscosity effects which dominate in nearly all present methods based on staggered grid and donor cell approaches.

2. Hyperbolic Model for 2-Dimensional Inhomogeneous Non-equilibrium Two-Phase Flow

The new model, originally developed for purely one- dimensional two-phase flow has been described elsewhere in some detail, e.g. [1], [2], [3]. The present paper concentrates on the extension of the physical model and the related numerical method to multi-dimensional flow processes.

2.1 Two-Fluid Model of Two-Phase Flow

The present two-phase flow model is based on a 'macroscopic' description of two-phase flow using time and volume averaged values for all state and flow parameters. This leads to what is often called the 'two- fluid model' of two-phase flow with separate balance equations for mass, momentum and energy for both liquid and vapour phase. The systematic derivation of the governing equations for the two fluid model is largely attributed to the work of Ishii [4], Bouré [5], Delhaye & Achard [6], and Drew & Lahey [7]. The general form of the conservation equations for multi-dimensional two-phase flow are given in Appendix A1.

A major difficulty in applying the two-fluid approach arises from the fact that, even when the balance equations are complemented by the state equations for the two phases and by additional correlations for the right-hand side coupling terms, the resulting set of relationships contains more unknown dependent variables than the number of available equations. The most common procedure to close the system of equations has been to postulate a local pressure equilibrium between the two phases. Phasic pressure

differences arising from the curvature of the liquid-vapour interface (surface tension effects) in different flow regimes are thereby neglected.

For the simplified case of equal pressure values for the two phases, the separated balance equations for two- dimensional flow conditions are used (Appendix A2). These formulations are the result of space/time averaging procedures and simplifying assumptions like the neglection of internal diffusive effects (bulk viscosity and heat conduction). The much larger influence of fluid friction, heat transfer and pressure forces at the phasic interface dominate all interfacial exchange processes and are thus included in the constitutive relations for the interfacial transport of mass, momentum and energy.

Also for reasons of simplicity, entropy is introduced as a major dependent variable in the following characteristic analysis. It can be shown, however, that this is not a restriction of generality and that the model can be extended to any other form of the energy equations. The balance equations for the phasic entropies can be readily obtained from the energy equations, removing the mechanical energy terms with the help of the two momentum equations. The only additional assumption is that all flow parameters remain continuously differentiable. Non-conservation of entropy is clearly permissible via equation (A1.8) in keeping with the Second Law of Thermodynamics.

In most practical applications of the two-fluid model, it is assumed that all source terms on the right-hand sides of equations (A2-1) to (A2-8) are algebraic functions of the flow and state parameters of the two phases, which leads to the 'Wallis Model' for inhomogeneous two-phase flow.

The basic equations of the 'Wallis Model' are known to yield two complex conjugate eigenvalues, which means that the system of governing equations is non-hyperbolic. This has several undesirable consequences: (1) the model does not represent a 'well posed' initial-boundary value problem; (2) high wave-number instabilities can result which require specific damping terms in the numerical algorithm and add significant artificial (numerical) diffusion to the governing system of equations; (3) the model does not correctly describe pressure wave propagation phenomena, and for this reason it is not able to provide realistic critical flow predictions; (4) numerical techniques which make explicit use of the hyperbolic character of the flow equations cannot be applied. The new two-phase flow model presented here overcomes all of these limitations.

2.2 Interfacial Momentum Coupling Terms

As can be seen from Appendix A2, the total interfacial forces in x- and y-directions have been split into viscous and non-viscous parts

$$\left.\begin{aligned}\left(F_g^{int}\right)_{x,y} &= \left(F_g^{v}\right)_{x,y} + \left(F_g^{nv}\right)_{x,y}\\ \left(F_f^{int}\right)_{x,y} &= \left(F_f^{v}\right)_{x,y} + \left(F_f^{nv}\right)_{x,y}\end{aligned}\right\} \tag{1}$$

The 'viscous' part, F_i^v, is assumed to represent the interfacial drag forces which are usually described by algebraic expressions of the form

$$\left(F_i^v\right)_{x,y} = c_{drag}\varrho_{cont}\left(v_g - v_f\right)^2_{x,y}, \tag{2}$$

with the density of the continuous phase, ϱ_{cont}, and an empirical flow regime-dependent interfacial friction factor c_{drag} (c.f. equation (42), section 3).

The 'non-viscous' part, F_i^{nv}, has been introduced in order to compensate for information lost in the averaging procedure. This term contains only space and time derivatives of major dependent parameters, including phasic velocities, void fraction and the phasic densities.

The criteria which have been used to determine an expression for the non-viscous part of the interfacial forces are [1]:

- the non-viscous interfacial friction terms should not affect the sum of the momentum equations
- the non-viscous interfacial terms should not contribute to the dissipation of mechanical energy and thus should not act as an entropy source
- the coefficient matrix should have only real eigenvalues which represent physically meaningful characteristic velocities
- the coefficient matrix should have a complete set of independent eigenvectors
- the system of equations should yield, as limiting cases, the single phase flow of gas/vapour ($\alpha_g \to 1$), liquid ($\alpha_f \to 1$), and homogeneous flow ($v_g = v_f$)
- the model should provide algebraic formulations for two-phase sound velocity which are in agreement with existing experimental data
- the system of equations should implicitly provide realistic values for critical mass flow without the need of additional modelling assumptions.

As a result of a comprehensive and thorough investigation, [1], [2], the following formulations for the non-viscous interfacial friction terms have been introduced:

$$\begin{aligned}
\left(F_g^{nv}\right)_x &= -\alpha_g\alpha_f\varrho\left[k\left(\frac{d^f v_g}{dt} - \frac{d^g v_f}{dt}\right) - \frac{\alpha_g\varrho_f - \alpha_f\varrho_g}{\varrho}(v_g - v_f)_x\left(\frac{\partial v_g}{\partial x} - \frac{\partial v_f}{\partial x}\right)\right] \\
&\quad -\alpha_g\alpha_f(\varrho_g + \varrho_f)(v_g - v_f)_x^2\frac{\partial \alpha_g}{\partial x} \\
&\quad -\alpha_g\alpha_f(\varrho_g + \varrho_f)(v_g - v_f)_x\left[\frac{\alpha_g}{\varrho_g}\frac{d_x^g\varrho_g}{dt} + \frac{\alpha_f}{\varrho_f}\frac{d_x^f\varrho_f}{dt}\right] \qquad (3)
\end{aligned}$$

$$\begin{aligned}
\left(F_g^{nv}\right)_y &= -\alpha_g\alpha_f\varrho\left[k\left(\frac{d^f v_g}{dt} - \frac{d^g v_f}{dt}\right) - \frac{\alpha_g\varrho_f - \alpha_f\varrho_g}{\varrho}(v_g - v_f)_y\left(\frac{\partial v_g}{\partial y} - \frac{\partial v_f}{\partial y}\right)\right] \\
&\quad -\alpha_g\alpha_f(\varrho_g + \varrho_f)(v_g - v_f)_y^2\frac{\partial \alpha_g}{\partial y} \\
&\quad -\alpha_g\alpha_f(\varrho_g + \varrho_f)(v_g - v_f)_y\left[\frac{\alpha_g}{\varrho_g}\frac{d_y^g\varrho_g}{dt} + \frac{\alpha_f}{\varrho_f}\frac{d_y^f\varrho_f}{dt}\right] \qquad (4)
\end{aligned}$$

with the total derivatives

$$\frac{d_x^i}{dt} = \frac{\partial}{\partial t} + (v_i)_x \frac{\partial}{\partial x}, \qquad \frac{d_y^i}{dt} = \frac{\partial}{\partial t} + (v_i)_y \frac{\partial}{\partial y} \tag{5}$$

and the following conditions for the total conservation of momentum

$$\left(F_f^{mv}\right)_x = -\left(F_g^{mv}\right)_x, \qquad \left(F_f^{mv}\right)_y = -\left(F_g^{mv}\right)_y \tag{6}$$

The first term in each of equations (3) and (4) might be seen as a generalisation of the 'virtual mass force' in the 'objective' form as proposed by Drew et al [7]. The open parameter k in front of the virtual mass acceleration term, which is known to have a strong influence on the two-phase sound velocity, can be used to adjust the model for different flow regimes [2]. The remaining terms in equations (3) and (4) include space and time derivatives for the void fraction and phasic densities. These terms are necessary in order to obtain the characteristics of the model as summarised in the following.

Introducing the 'non-viscous' terms of the interfacial forces, the set of governing equations (A2-1) to (A2-8) can be combined in matrix form, thus

$$\frac{\partial \mathbf{U}}{\partial t} + [\mathbf{G_x}]\frac{\partial \mathbf{U}}{\partial x} + [\mathbf{G_y}]\frac{\partial \mathbf{U}}{\partial y} = \mathbf{D} \tag{7}$$

with the state vector

$$\mathbf{U} = \begin{bmatrix} p \\ (v_g)_x \\ (v_f)_x \\ (v_g)_y \\ (v_f)_y \\ \alpha_g \\ s_g \\ s_f \end{bmatrix} \tag{8}$$

and the source term vector $\mathbf{D}$. The coefficient matrices, $[\mathbf{G_x}]$ and $[\mathbf{G_y}]$ are a straightforward extension of those for the one-dimensional case as explicitly given in [1], [11].

2.3 Characteristic Analysis of the Governing Flow Equations

The eigenvalues of coefficient matrices $[\mathbf{G_x}]$ and $[\mathbf{G_y}]$ are the characteristic velocities:

$$[\mathbf{G_x}]: \begin{cases} \lambda_1 = (v_g)_x \\ \lambda_2 = (v_f)_x \\ \lambda_3 = v_x + a_x \\ \lambda_4 = v_x - a_x \\ \lambda_5 = (v)_x \\ \lambda_6 = (v)_x \\ \lambda_7 = (v_g)_x \\ \lambda_8 = (v_f)_x \end{cases} \qquad [\mathbf{G_y}]: \begin{cases} \lambda_1 = (v_g)_y \\ \lambda_2 = (v_f)_y \\ \lambda_3 = v_y + a_y \\ \lambda_4 = v_y - a_y \\ \lambda_5 = (v)_y \\ \lambda_6 = (v)_y \\ \lambda_7 = (v_g)_y \\ \lambda_8 = (v_f)_y \end{cases} \tag{9}$$

[2] For the sample calculations included here, a value of $k = 0.5$ was used throughout.

The mixture velocities which appear in the eigenvalues λ_3 and λ_4 are defined as a weighting between the volumetric mixture velocity v_1 and mixture mass velocity v_2

$$v_\xi = \frac{(v_1)_\xi + k\frac{\varrho^2}{\varrho_g\varrho_f}(v_2)_\xi}{1 + k\frac{\varrho^2}{\varrho_g\varrho_f}}, \qquad \xi = x, y \tag{10}$$

with

$$v_1 = \alpha_g v_g + \alpha_f v_f, \qquad v_2 = \frac{\alpha_f\varrho_g v_g + \alpha_f\varrho_g v_g}{\alpha_f\varrho_g + \alpha_f\varrho_f}. \tag{11}$$

The mixture sound velocity in λ_3 and λ_4 can be expressed as

$$(a_\xi)^2 = (\tilde{a}_\xi)^2 - (\Delta a_\xi)^2, \qquad \xi = x, y \tag{12}$$

where the first term is governed by the 'frozen' sound velocity a_0. The second term in equation (12) might be seen as a correction which accounts for the direct influence of the mechanical disequilibrium between phases on the propagation of sound waves.

$$\left.\begin{aligned} \tilde{a}^2 &= \frac{\alpha_g\varrho_f + \alpha_f\varrho_g}{\frac{\alpha_g\varrho_f}{a_g^2} + \frac{\alpha_f\varrho_g}{a_f^2}} \frac{1 + k\frac{\alpha_g\varrho_g + \alpha_f\varrho_f}{\alpha_g\varrho_f + \alpha_f\varrho_g}}{1 + k\frac{\varrho^2}{\varrho_g\varrho_f}} \\ \Delta\,(a_\xi)^2 &= \alpha_g\alpha_f\varrho_g\varrho_f(v_g - v_f)_\xi^2 \frac{(\varrho_f + k\varrho)(\varrho_g + k\varrho)}{(\varrho_g\varrho_f + k\varrho^2)^2} \end{aligned}\right\} \tag{13}$$

The physical interpretation of the characteristic velocities have been given in some detail in [1], [2] which will be summarised in the following.

The first two eigenvalues λ_1 and λ_2 describe the propagation of void-pressure waves which have no analogy in single-phase gas-dynamics. That the two phasic velocities appear here might not be in agreement with all current proposals on this subject, however our present knowledge in this area is still insufficiently mature (and often contradictory) that a definitive judgement is not yet possible. In this sense, the present model seems to be the best compromise for a practicable model so long as one stays with the assumption of equal pressure values for the two phases.

The eigenvalues λ_3 and λ_4 describe the propagation of pressure/density waves. Since an equal phasic pressure is assumed, these values have the form $v \pm a$. Predicted values for the sound velocity are in good agreement with experimental data as is shown in [1], [2]. The two-phase sound velocity is strongly influenced by the 'virtual mass' coefficient k which describes the non-algebraic momentum coupling between the two phases. Some interesting limiting values for the two-phase sound velocity over a range of possible k values are discussed further in [2].

The four remaining eigenvalues $\lambda_{5,6}$ and $\lambda_{7,8}$ are not influenced by additional 'non-viscous' terms in the model and would appear in the same form also in the 'Wallis'

model. The values λ_5 and λ_6 represent the propagation of the transverse momentum and λ_7 and λ_8 can be interpreted as the propagation of entropy/temperature waves within the two phase mixture.

The existence of only real eigenvalues is a necessary but in itself insufficient condition for the existence of a 'well-posed' hyperbolic system of partial differential equations. A further requirement is the existence of a complete set of independent eigenvectors. That this is the case for the present model has been demonstrated in [2]. Here it was shown in addition that both the left-side and the right-side eigenvectors can be expressed algebraically as functions of the major flow parameters, and in addition that the governing equations can be transformed into the 'characteristic' form. This is a prerequisite for the proper application of a number of advanced numerical techniques which make explicit use of the hyperbolic nature of the governing field equations.

2.4 Conservative Form of the Governing Flow Equations

Introducing the following state vector of conservative variables, $\mathbf{V}$, and the corresponding flux vectors in x- and y-directions, $\mathbf{F_x}$ and $\mathbf{F_y}$, respectively

$$\mathbf{V} = \begin{bmatrix} \alpha_g \varrho_g \\ \alpha_f \varrho_f \\ \alpha_g \varrho_g (v_g)_x \\ \alpha_f \varrho_f (v_f)_x \\ \alpha_g \varrho_g (v_g)_y \\ \alpha_f \varrho_f (v_f)_y \\ \alpha_g \varrho_g s_g \\ \alpha_f \varrho_f s_f \end{bmatrix}, \quad \mathbf{F_x} = \begin{bmatrix} \alpha_g \varrho_g (v_g)_x \\ \alpha_f \varrho_f (v_f)_x \\ \alpha_g \varrho_g (v_g)_x^2 + \alpha_g p \\ \alpha_f \varrho_f (v_f)_x^2 + \alpha_f p \\ \alpha_g \varrho_g (v_g)_x (v_g)_y \\ \alpha_f \varrho_f (v_f)_x (v_f)_y \\ \alpha_g \varrho_g (v_g)_x s_g \\ \alpha_f \varrho_f (v_f)_x s_f \end{bmatrix}, \quad \mathbf{F_y} = \begin{bmatrix} \alpha_g \varrho_g (v_g)_y \\ \alpha_f \varrho_f (v_f)_y \\ \alpha_g \varrho_g (v_g)_y (v_g)_x \\ \alpha_f \varrho_f (v_f)_y (v_f)_x \\ \alpha_g \varrho_g (v_g)_y^2 + \alpha_g p \\ \alpha_f \varrho_f (v_f)_y^2 + \alpha_f p \\ \alpha_g \varrho_g (v_g)_y s_g \\ \alpha_f \varrho_f (v_f)_y s_f \end{bmatrix} \tag{14}$$

the matrix form of the conservation equations becomes

$$\frac{\partial \mathbf{V}}{\partial t} + \frac{\partial \mathbf{F_x}}{\partial x} + \frac{\partial \mathbf{F_y}}{\partial y} + [\mathbf{H_x}]^{nc} \frac{\partial \mathbf{F_x}}{\partial x} + [\mathbf{H_y}]^{nc} \frac{\partial \mathbf{F_y}}{\partial y} = \mathbf{E} \tag{15}$$

with the 'non-conservative' parts of the coefficient matrices in x and y-directions

$$[\mathbf{H}_\xi]^{nc} = ([\mathbf{J}][\mathbf{G}_\xi] - [\mathbf{K}_\xi])\,[\mathbf{K}_\xi]^{-1}, \qquad \xi = x, y \tag{16}$$

and the Jacobian matrices

$$[\mathbf{J}] = \frac{\partial \mathbf{V}}{\partial \mathbf{U}}, \qquad [\mathbf{K}_\xi] = \frac{\partial \mathbf{F}_\xi}{\partial \mathbf{U}}, \qquad \xi = x, y \tag{17}$$

The 'non-conservative' matrix $[\mathbf{H}_\xi]^{nc}$, which concerns only the two separated momentum equations, requires some specific treatment in the numerical solution procedure. However, this does not change the conservation of the overall momentum of the two-phase mixture [3].

[3] Similar 'non-conservative' terms appear also in the separated momentum equations for the 'Wallis model' of two-phase flow.

For an equally-spaced two-dimensional Cartesian grid, equation (15) can be written in a 'finite volume' form (see Fig. 1)

$$\begin{aligned}
\mathbf{V}_i^{n+1} = \mathbf{V}_i^n \; &- \; \frac{\Delta t}{\Delta x}\left\{(\hat{\mathbf{F}}_x)_{i+1/2,j} - (\hat{\mathbf{F}}_x)_{i-1/2,j}\right\}^n \\
&- \; \frac{\Delta t}{\Delta x}\left([\mathbf{H}_x]^{nc}\right)_{i,j}^n \left\{(\hat{\mathbf{F}}_x)_{i+1/2,j} - (\hat{\mathbf{F}}_x)_{i-1/2,j}\right\}^n \\
&- \; \frac{\Delta t}{\Delta y}\left\{(\hat{\mathbf{F}}_y)_{i,j+1/2} - (\hat{\mathbf{F}}_y)_{i,j-1/2}\right\}^n \\
&- \; \frac{\Delta t}{\Delta y}\left([\mathbf{H}_y]^{nc}\right)_{i,j}^n \left\{(\hat{\mathbf{F}}_y)_{i,j+1/2} - (\hat{\mathbf{F}}_y)_{i,j-1/2}\right\}^n + \mathbf{E}_{i,j}{}^{n+1}\Delta t \qquad (18)
\end{aligned}$$

where $(\hat{\mathbf{F}}_x)_{i\pm1/2,j}$ and $(\hat{\mathbf{F}}_y)_{i,j\pm1/2}$ represent the fluxes at cell-to-cell interfaces.

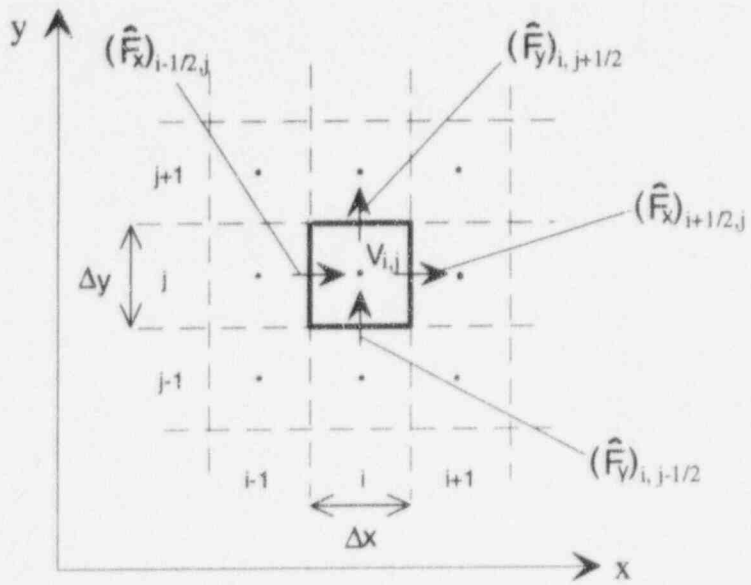

Fig. 1: Space discretization on a two-dimensional Cartesian grid

The balance equations in finite volume form (18) can be generalised for unstructured grids, (Fig. 2), as follows:

$$\begin{aligned}
\mathbf{V}_i^{n+1} = \mathbf{V}_i^n \; &- \; \frac{\Delta t}{A_i}\sum_1^s \left\{S_s(\hat{\mathbf{F}}_i)_s\right\}^n \\
&- \; \frac{\Delta t}{A_i}\sum_1^s \left\{S_s([\hat{\mathbf{H}}_i]^{nc})_s(\hat{\mathbf{F}}_i)_s\right\}^n \\
&+ \; \mathbf{E}_i{}^{n+1}\Delta t \qquad (19)
\end{aligned}$$

where $(\hat{\mathbf{F}}_i)_s$ represents the projection of the flux vector $\mathbf{F}$ normal to each individual section s of the compu' ational cell i.

Figure 2 shows the spatial discretization of the unstructured grid with respect to the normal Cartesian axes, made up from irregular polygons of arbitrary segment length S_s, and with a cell-centre located at the geometric centre-of-gravity of the polygon.

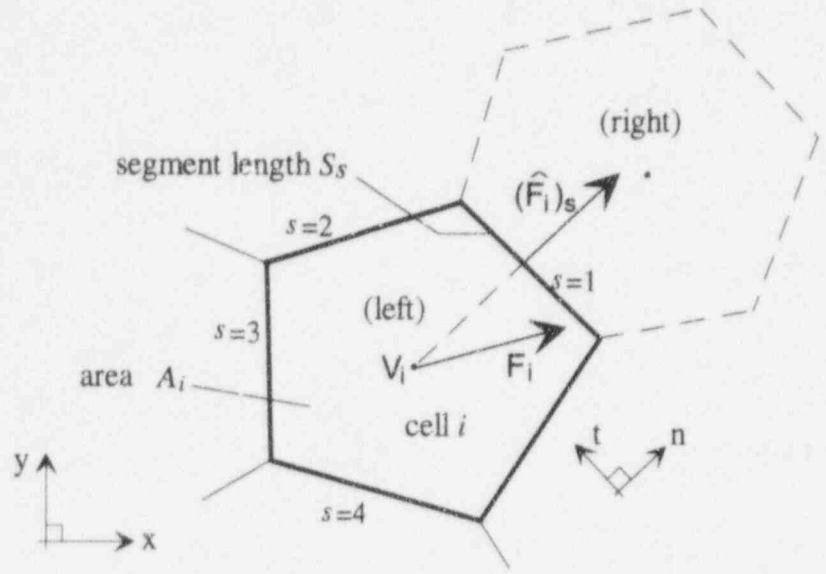

Fig. 2: Space discretization for an unstructured grid

2.5 Transformation of Governing Equations normal to the Boundary Section of the Computational Cell

The fluxes normal to the cell-to-cell interfaces, $(\hat{\mathbf{F}}_i)_s$, are calculated from a series of quasi one-dimensional Riemann problems normal to the specific boundary section of the computational cell. For this purpose, the basic equations (7) are projected normal to the cell boundary:

$$\frac{\partial \mathbf{U}}{\partial t} + [\mathbf{G_s}] \frac{\partial \mathbf{U}}{\partial n} = \mathbf{D}, \tag{20}$$

with the state vector of 'primitive' variables

$$\mathbf{U} = \begin{bmatrix} p \\ (v_g)_n \\ (v_f)_n \\ (v_g)_t \\ (v_f)_t \\ \alpha_g \\ s_g \\ s_f \end{bmatrix} \tag{21}$$

where the indices n and t denote velocity components normal and tangential to the particular boundary sections of the computational cell. The characteristic velocities are now:

pressure/void waves:

$$\lambda_1 = (v_g)_n, \qquad \lambda_2 = (v_f)_n \tag{22}$$

pressure/density waves:

$$\lambda_3 = v_n + a_n, \qquad \lambda_4 = v_n - a_n \tag{23}$$

propagation of transverse momentum:

$$\lambda_5 = (v_g)_n, \qquad \lambda_6 = (v_f)_n \tag{24}$$

temperature/entropy waves:

$$\lambda_7 = (v_g)_n, \qquad \lambda_8 = (v_f)_n \tag{25}$$

with the definition of the two-phase mixture flow velocity v, and the two-phase mixture 'sound' velocity a corresponding to equations (10) and (12).

For the eight real eigenvalues, a complete set of independent eigenvectors can be derived, a necessary condition for the existence of a hyperbolic system of equations. This allows a similarity transformation resulting in the characteristic form of the flow equations:

$$[\mathbf{T_s}]^{-1}\frac{\partial \mathbf{U}}{\partial t} + [\mathbf{\Lambda_s}][\mathbf{T_s}]^{-1}\frac{\partial \mathbf{U}}{\partial n} = [\mathbf{T_\varepsilon}]^{-1}\mathbf{D_s} \tag{26}$$

with the diagonal matrix of the eigenvalues

$$[\mathbf{\Lambda_s}] = [\mathbf{T_s}]^{-1}[\mathbf{G_s}][\mathbf{T_s}]. \tag{27}$$

The columns of the transformation matrix $[\mathbf{T_s}]$ are the right eigenvectors of the coefficient matrix $[\mathbf{G_s}]$:

$$[\mathbf{T_s}] = [\mathbf{V_s}]_R^T \tag{28}$$

The rows of the inverse of $[\mathbf{T_s}]$ are, up to a common factor, the left eigenvectors of $[\mathbf{G_s}]$:

$$[\mathbf{T_s}]^{-1} = [\mathbf{V_s}]_L \tag{29}$$

With respect to the individual characteristic velocities (eigenvalues), the coefficient matrix $[\mathbf{G_s}]$ is split into elementary parts related to each of the eigenvalues

$$[\mathbf{G_s}] = \sum_{k=1}^{8}[\mathbf{G_s}]_k \tag{30}$$

with

$$[\mathbf{G_s}]_k = [\mathbf{T_s}][\mathbf{\Lambda_s}]_k[\mathbf{T}]^{-1} \tag{31}$$

where the diagonal matrix $[\mathbf{\Lambda_s}]_k$ includes only the k_{th} eigenvalues.

2.6 Flux Vectors at Cell-to-Cell Interfaces

In order to derive an expression for the cell-to-cell interfaces, the system of balance equations (20) is transformed using the fluxes as major dependent parameters:

$$\frac{\partial \mathbf{F}}{\partial t} + [\mathbf{R_s}]\frac{\partial \mathbf{F}}{\partial n} = [\mathbf{K}]\ \mathbf{D}, \tag{32}$$

with the new coefficient matrix

$$[\mathbf{R_s}] = [\mathbf{K}][\mathbf{G_s}][\mathbf{K}]^{-1}, \tag{33}$$

and the Jacobian

$$[\mathbf{K_s}] = \frac{\partial \mathbf{F_s}}{\partial \mathbf{U}}. \tag{34}$$

Such a 'similarity' transformation does not change the eigenvalues of the governing system of equations. Thus the eigenvalues of $[\mathbf{R_s}]$ are the same as those for $[\mathbf{G_s}]$ based on the primitive parameters given in equations (22) to (25). Equivalent to equation (26), a characteristic form of the governing equations can be obtained also for the fluxes as major dependent parameters

$$[\mathbf{T_s^*}]^{-1}\frac{\partial \mathbf{F}}{\partial t} + [\mathbf{\Lambda_s}][\mathbf{T_s^*}]^{-1}\frac{\partial \mathbf{F}}{\partial n} = [\mathbf{T_s^*}]^{-1}\mathbf{E_s} \tag{35}$$

where the matrix of right eigenvectors transforms as

$$[\mathbf{T_s^*}] = [\mathbf{K}][\mathbf{T_s}]. \tag{36}$$

From a linearized form of equation (35), the following expression for the numerical fluxes at the cell-to-cell boundaries as a function of the corresponding 'left-' and 'right-side' values can be derived

$$(\hat{\mathbf{F}})_s = \sum_{k,\lambda_k>0} ([\tilde{\mathbf{R}}]_k)_s(\mathbf{F})_l + \sum_{k,\lambda_k<0} ([\tilde{\mathbf{R}}]_k)_s(\mathbf{F})_r. \tag{37}$$

The matrix $([\tilde{\mathbf{R}}]_k)_s$ represents the 'reduced' coefficient matrix based on average conditions at the cell-to-cell interface,

$$([\tilde{\mathbf{R}}]_k)_s = \frac{1}{\lambda_k}([\mathbf{R}]_k)_s \tag{38}$$

with

$$([\mathbf{R}]_k)_s = \left([\mathbf{K}]([\mathbf{G}]_k)[\mathbf{K}]^{-1}\right)_s. \tag{39}$$

Here the $[\mathbf{G}]_k$ are the split matrices introduced for the 'primitive' state vector as introduced by equation (30).

Equation (37) can be interpreted as a 'weighting procedure' for the upstream and downstream fluxes based on the sign of the different eigenvalues. Figure 3 indicates how the

left- and right-side flux vectors contribute to the weighted-average flux at the cell boundary in the so-called Approximate Riemann Solver. This illustrates also the difference from the simpler donor cell technique where the intercell (junction) state parameters are taken only from the upstream (donor) cell based on the sign of the phasic velocities whilst disregarding the signal propagation properties along characteristic lines.

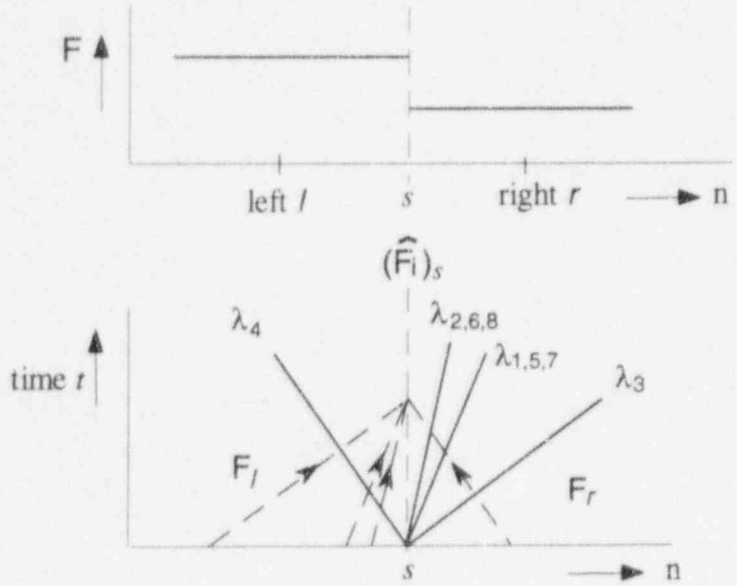

Fig. 3: Approximate Riemann Solver for two-phase flow

3. Interfacial Transfer Processes for Mass, Momentum and Energy described by Algebraic Expressions

All the derivations presented so far are independent of the specific expressions for the interfacial transport processes for mass, momentum and energy, assuming that they can be formulated as algebraic functions of the major flow parameters. These 'closure laws', which form the elements of the source term vectors in the balance equations, have a large influence on the final quality of the predicted results. The 'closure laws' are strongly influenced by the specific two-phase flow regime as characterised by the void distribution in time and space and by the local interfacial area concentration. Since the correlations describing interfacial transport processes often have very small time constants, the source term vectors require a strictly implicit treatment with respect to the time discretization.

For the purpose of the verification of the present two- phase flow model and the related numerical methods, relatively 'simple' correlations are used for the representation of mass, momentum and energy exchange between the two phases as summarised in the following.

For the interfacial mass, momentum and energy coupling between the phases the following correlations are used at present:

mass exchange due to evaporation/ condensation

$$\sigma_g^M = -\sigma_f^M = \frac{\alpha_g \alpha_f}{h_g^s - h_f^s} \left(C_1 \, C_f^p \, \varrho_f \, [T_f - T_s] + C_2 \, C_g^p \varrho_g \, [T_g - T_s] \right) \tag{40}$$

heat exchange associated with evaporation/condensation

$$\sigma_g^Q = -\sigma_f^Q = \frac{\alpha_g \alpha_f}{h_g^s - h_f^s} C_1 \, C_g^p \, \varrho_g \, [T_g - T_s] \tag{41}$$

interfacial friction

$$F_g^v = -F_f^v = C_3 \, \alpha_g \, \alpha_f \, \varrho \, (v_g - v_f)^2 \tag{42}$$

with the mixture density

$$\varrho = \alpha_g \varrho_g + \alpha_f \varrho_f \tag{43}$$

The open parameters C_1 to C_3 have been determined in order to give 'reasonable' results for the examples which follow [4]. This semi-empirical approach permits constant values to be used to correlate experimentally-derived flow regime parameters which (it is commonly agreed) cannot be determined from first principles. More detailed formulations for the interfacial exchange processes, taking into account the transport property of the interfacial area concentration as well as the dynamics of flow regime transitions, are under development.

4. Numerical Examples for One- and Two-Dimensional Flow Conditions

In order to check the prediction capability of the present two-phase model and the selected numerical approach, various classical benchmark calculations have been made using the flux vector splitting technique described above. For some of the examples, a second-order accurate scheme was used. All the predictions were performed with a rather coarse grid. This was done primarily for economic reasons (cpu-time), however, it has been found also that any deficiencies in the predictions become much more evident in the case of less detailed space discretization.

4.1 Oscillating Manometer Problem (Figs.1.1 and 1.2)

This 1-dimensional benchmark problem was originally proposed (by V. Ransom) in order to check whether a particular model can describe a moving liquid level, possibly with some phase separation, and to assess the magnitude of any artificial (numerical) viscosity present in the numerical method used. The beauty of this test case is that, in the absence of wall friction, the analytical solution is known, assuming that the liquid column oscillates as a rigid body.

With the present model, the tracking of the liquid level at the liquid/vapour interface, where the void fraction changes from 0.0 to 1.0, is achieved with a resolution smeared

[4] Constant values of $C_1 = 100.0$, $C_2 = 300.0$, $C_3 = 10.0$ have been used throughout, based on available experimental data.

over just two cells. The predicted frequency is in excellent agreement with the undamped analytical solution. Any inherent numerical damping is extremely small and may be attributed to the slight energy dissipation caused by small slip velocities between the phases in the vicinity of the exposed liquid surface.

4.2 Edward's Pipe Blowdown (Figs.2.1 to 2.4)

A classical test case for transient two-phase codes has been the prediction of the blowdown of a quantity of initially subcooled liquid from a pipe of nearly 4 m length, also known as CSNI standard problem No. 1 (Edward's pipe). The water in the pipe had an initial pressure of 7.0 MPa and a temperature T = 502 K which corresponded to a subcooling of 56.8 K. The new calculations presented here consider the jet downstream of the pipe outlet as a 2-dimensional expansion, obtained by using a more realistic boundary condition at the exit plane.

The transient was initiated by the rupture of a bursting disk at time zero. The back pressure from the environment was atmospheric pressure. Calculated results for pressure and void fraction along the pipe length at different times are shown in Figs. 2.1 to 2.2.

The first 10 ms of the transient are characterised by the propagation of a rarefaction wave from the open end into the pipe, the reflection of the wave at the closed end, and the onset of flashing of the initially subcooled liquid. After a fast depressurization and a distinct undershoot of pressure at the closed end of the pipe, the pressure is held close to 2.9 MPa, corresponding to the saturation pressure for the initial temperature.

The ensuing blowdown is controlled by the two-phase discharge from the pipe and the continuous evaporation (flashing) of the liquid. The phasic velocities continuously increase after the rarefaction wave has passed, where the value for the heavier liquid phase is always below the velocity of the gas phase. From a closer examination of the void profile in the very early phase of the transient, it is interesting to note that at the closed end of the pipe the evaporation rate is temporarily greater than in the middle section. This is the result of the strong pressure decrease following the reflection of the rarefaction wave.

A comparison between measured and predicted values is shown in Figs. 2.3 and 2.4 for the pressure at the open end and the void fraction in the middle section of the pipe.

4.3 Blowdown from a horizontal pipe with an Abrupt Area Change at the Exit (Figs. 3.1, 3.2)

The blowdown of a horizontal pipe is often modelled as a 1-dimensional process with constant boundary conditions at the exit simulating the downstream atmospheric conditions. However, the process is certainly more complex due to the formation of an expanding two-phase jet at the pipe exit and the continuation of incomplete evaporation of the superheated liquid. This process, which has a feedback effect with respect to the upstream critical flow conditions at the pipe exit, is of a strictly multi-dimensional nature. At least some of these aspects are shown in Fig. 3.1 (early stage of jet development) and Fig. 3.2 (later stage). Both figures show the predicted void distribution

downstream of the discharge line, with superimposed velocity fields for the vapour and liquid phases of the expanding two-phase jet. Figure 3.1shows the mainly liquid core just emerging from the exit plane, whereas Fig. 3.2 shows the jet break-up process with significantly decoupled phasic velocities resulting from the strong evaporation and local pressure gradients. Although no measured data are available for direct comparison, the predicted results provide at least an intuitively correct description of the complex two-phase flow expansion.

4.4 Blowdown of a partially filled Pressure Vessel through a Horizontal Discharge line (Figs. 4.1, 4.2)

This test case concerns the idealised 'blowdown' of a 2-dimensional pressure vessel through a horizontal discharge line. The vessel is assumed initially 50 per cent filled with saturated water at an initial pressure of 50 bar. The transient is initiated by the instantaneous opening of a discharge line to the atmosphere.

The transient is characterised by a fast depressurization of the vessel contents and the corresponding strong evaporation of the liquid phase ('flashing'), and a rapid swelling of the two-phase mixture level within the vessel which is controlled by critical two-phase flow conditions in the discharge nozzle. This behaviour is qualitatively represented in Fig. 4.1 by the predicted void fraction distribution in the pressure vessel and discharge line for six different time values. The figure also indicates a significant amount of liquid hold-up in the upper region of the pressure vessel after the two-phase mixture level has exceeded the elevation of the discharge line connection. The predicted velocity fields for the vapour and liquid phases, shown in Fig. 4.2 at two different times (0.00363 s and 0.0288 s), indicate a distinct two-dimensional flow pattern in the vessel upstream of the discharge line connection resulting in strong phase separation processes which could not be predicted by a one-dimensional flow model. Again, sufficiently accurate measured data of the complex flow field are lacking for proper model evaluation, despite much (limited) data from integral experiments.

5. Summary and Outlook

Based on a 6-equation two-fluid approach, a new model for multi-dimensional inhomogeneous non-equilibrium two- phase flow has been developed using separated conservation equations for mass, momentum and energy (entropy) for the two phases. Introducing an appropriate formulation for the non- viscous, interfacial forces, a hyperbolic system of equations has been derived, characterised by the existence of only real eigenvalues and a complete set of independent eigenvectors. Both sets of eigenvalues and eigenvectors can be expressed algebraically as functions of the major dependent flow parameters permitting a complete characteristic analysis of the governing flow equations.

The new model allows the application of Flux Vector Splitting (FVS) techniques for the numerical integration of the flow equations. This technique combines preservation of the signal propagation along characteristic lines with the property of accurate conservation of mass, momentum and energy. The main prediction capabilities which the

new approach offers for the simulation of transient two-phase flow are demonstrated by a number of calculations for various 1- and 2-dimensional test cases.

Error estimation has not been attempted and at present is of little practical value. All the numerical results were obtained with a (nearly) second-order accuracy in space, assuming a linear distribution of the respective flow parameters over the computational cells in connection with slope limiters based on the Monotonic Upwind Scheme for Conservation Laws (MUSCL) as introduced by Van Leer [10].

Further extensions to the present model will include an additional balance equation for the interfacial area concentration. This is of specific interest for the dynamic description of flow regime transitions and the improvement of the prediction of interfacial transport processes for mass, momentum and energy. A further extension envisaged is the inclusion of energy dissipation processes due to bulk viscosity effects. An obvious extension to fully 3-dimensional flow is foreseen, with inclusion of dynamic mesh refinement methods and their application to unstructured grids.

Nomenclature

Variables

a	sound velocity
A	flow cross sectional area; area of cell
c	coefficient in non- viscous interfacial friction forces
C_p	specific heat at constant pressure
d	coefficient in non- viscous interfacial friction forces
F	force per unit volume
h	enthalpy
k	'virtual mass' coefficient
m	mass flow density
n	space co-ordinate
p	pressure
Q	volumetric energy source
s	entropy
S	cell-to-cell segment length
t	time
T	temperature
$\bar{\mathbf{T}}$	viscosity tensor
u	internal energy
v	flow velocity
x	space co-ordinate
X	vapour quality
α	volumetric phase concentration, void fraction
λ	eigenvalue of a matrix

F	numerical flux function at cell interfaces
ϱ	density
σ^M	volumetric source term for mass, from interfacial exchange processes
σ^Q	volumetric source term for heat, from interfacial exchange processes
σ^S	volumetric source term for entropy, from interfacial exchange processes
$\mathbf{C}, \mathbf{D}, \mathbf{E}$	source term vectors
$\mathbf{F}$	flux vector
$\mathbf{U}, \mathbf{V}$	state vector
$[\mathbf{A}], [\mathbf{B}], [\mathbf{G}]$	coefficient matrices
$[\mathbf{H}], [\mathbf{R}]$	coefficient matrices
$[\mathbf{I}]$	identity matrix
$[\mathbf{J}], [\mathbf{K}]$	Jacobian matrices
$[\mathbf{T}]$	transformation matrix
$[\mathbf{V}]_R$	matrix of right eigenvectors
$[\mathbf{V}]_L$	matrix of left eigenvectors
$[\mathbf{\Lambda}]$	diagonal matrix of eigenvalues

Subscripts

f	liquid
g	gas or vapour
i, j	cell number
k	k_{th} eigenvalue
l	'left-side' value
n	current time level; also normal component
r	'right-side' value
s	cell boundary segment
t	tangential component

Superscripts

ex	quantity exchanged between the phases
ext	external
int	quantity at interface
nv	non-viscous
v	viscous
s	saturated condition
T	transpose of a matrix
-1	inverse of a matrix

References

[1] H. Städtke, R. Holtbecker, *Hyperbolic Model for Inhomogeneous Two-Phase Flow*, Int. Conf. on Multiphase Flows, Sept. 24-27, 1991, University of Tsukuba, Japan.

[2] H. Städtke, R. Holtbecker, *Hyperbolic Model for One-dimensional Inhomogeneous Two-Phase Flow*, 29th Mtg. of European Two-Phase Flow Group, June 2-3, 1992 Stockholm, Sweden.

[3] H. Städtke, R. Holtbecker, *Numerical Simulation of Two-Phase Flow Based on Hyperbolic Flow Equations*, 6th Int. Topical Mtg. on Nuclear Reactor Thermal Hydraulics, NURETH-6, Oct. 5-8, 1993, Grenoble, France.

[4] M. Ishii, *Thermodynamics of Two-Phase Flow*, Eyrolles, Paris, 1975.

[5] J. A. Bouré, *On a Unified Presentation of the Non- Equilibrium Two-Phase Flow Models*, Proc. of ASME Symp., New York, 1975.

[6] J. M. Delhaye, J. L. Achard, *On the Averaging Operators Introduced in Two-Phase Flow Modelling* , Proc. CSNI Specialist Mtg. on Transient Two-Phase Flow, Toronto, 1976.

[7] D. A. Drew, R. T. Lahey, *Application of General Constitutive Principles to the Derivation of Multidimensional Two Phase Flow Equations*, Int. J. Multiphase Flow 5, 243-264, 1979.

[8] D. Drew, I. Cheng, R. T. Lahey, *The Analysis of Virtual Mass Effects in Two-phase Flow*, Int. J. Multiphase Flow 5, No. 4, 233-242, 1979.

[9] S. K. Godunow, *A Finite Difference Method for the Numerical Computation of Discontinuous Solution of the Equations of Fluid Dynamics*, Mat. Sbornik, 47, 271-290, 1959.

[10] Van Leer B., *Towards the Ultimate Conservative Difference Scheme, a Second-Order Sequel to Godunow's Method*, J. Comp. Physics, Vol. 32, pp. 101-13€, 1979.

[11] H. Städtke, G. Franchello, B. Worth, *Numerical Simulation of Multi-Dimensional Two-Phase Flow based on Hyperbolic Flow Equations*, 31st Mtg. of European Two-Phase Flow Group, June 6-8, 1994, Piacenza, Italy.

Appendix A1

General Form of Conservation Equations for Multi- Dimensional Two-Phase Flow

$i = g$ (vapour or gas), $i = f$ (liquid)

mass:

$$\frac{\partial}{\partial t}\left(\alpha_i \varrho_i\right) + \nabla \cdot \left(\alpha_i \varrho_i \vec{v}_i\right) = \sigma_i^M \tag{A1-1}$$

$$\sum_{i=g,f} \sigma_i^M = 0 \tag{A1-2}$$

momentum:

$$\begin{aligned}\frac{\partial}{\partial t}\left(\alpha_i \varrho_i \vec{v}_i\right) + \nabla \cdot \left(\alpha_i \varrho_i \vec{v}_i \vec{v}_i\right) + \alpha_i \nabla p_i + \left(p_i - p_i^{int}\right) \nabla \alpha_i \\ = \vec{F}_i^{int} + \vec{F}_i^{ext} + \sigma_i^M \vec{v}_i^{ex} + \nabla \cdot \left(\alpha_i \bar{\mathbf{T}}_i\right)\end{aligned} \tag{A1-3}$$

$$\sum_{i=g,f} \vec{F}_i^{int} = 0 \tag{A1-4}$$

energy:

$$\begin{aligned}\frac{\partial}{\partial t}\left[\alpha_i \varrho_i \left(u_i + \frac{v_i^2}{2}\right)\right] + \nabla \cdot \left[\alpha_i \varrho_i \vec{v}_i \left(h_i + \frac{v_i^2}{2}\right)\right] + \nabla\left(\alpha_i \vec{q}_i\right) - p_i^{int} \frac{\partial \alpha_i}{\partial t} - \nabla\left(\alpha_i \bar{\mathbf{T}}_i\right) \\ = \sigma_i^M \left(h + \frac{v^2}{2}\right)^{ex} + \sigma_i^Q + \vec{F}^{ext} \cdot v_i + \vec{F}^{int} \cdot v_i^{Fi}\end{aligned} \tag{A1-5}$$

$$\sum_{i=g,f} \sigma_i^Q = 0 \tag{A1-6}$$

entropy:

$$\begin{aligned}\frac{\partial}{\partial t}(\alpha_i \varrho_i s_i) + \nabla \cdot (\alpha_i \varrho_i \vec{v}_i s_i) = \frac{\sigma_i^Q}{T_i} + \frac{Q_i^{ext}}{T_i} + \frac{F_i^{int}}{T_i}(v^{int} - v_i) \\ + \frac{\sigma_i^M}{T_i}\left[h^{ex} - h_i + \frac{1}{2}(v^{ex} - v_i)^2\right] + \sigma_i^M s_i = \sigma_i^S\end{aligned} \tag{A1-7}$$

$$\sum_{i=g,f} \sigma_i^S \geq 0 \tag{A1-8}$$

Appendix A2

Balance Equations for Two-dimensional Two-Phase Flow (equal phasic pressures)

mass:

$$\alpha_g \frac{\partial \varrho_g}{\partial t} + \varrho_g \frac{\partial \alpha_g}{\partial t} + \alpha_g (v_g)_x \frac{\partial \varrho_g}{\partial x} + \alpha_g (v_g)_y \frac{\partial \varrho_g}{\partial y} + \varrho_g (v_g)_x \frac{\partial \alpha_g}{\partial x} + \varrho_g (v_g)_y \frac{\partial \alpha_g}{\partial y} + \alpha_g \varrho_g \frac{\partial (v_g)_x}{\partial x} + \alpha_g \varrho_g \frac{\partial (v_g)_y}{\partial y} = \sigma_g^M \tag{A2-1}$$

$$\alpha_f \frac{\partial \varrho_f}{\partial t} + \varrho_f \frac{\partial \alpha_f}{\partial t} + \alpha_f (v_f)_x \frac{\partial \varrho_f}{\partial x} + \alpha_f (v_f)_y \frac{\partial \varrho_f}{\partial y} + \varrho_f (v_f)_x \frac{\partial \alpha_f}{\partial x} + \varrho_f (v_f)_y \frac{\partial \alpha_f}{\partial y} + \alpha_f \varrho_f \frac{\partial (v_f)_x}{\partial x} + \alpha_f \varrho_f \frac{\partial (v_f)_y}{\partial y} = \sigma_f^M \tag{A2-2}$$

momentum x-direction:

$$\alpha_g \varrho_g \frac{\partial (v_g)_x}{\partial t} + \alpha_g \varrho_g (v_g)_x \frac{\partial (v_g)_x}{\partial x} + \alpha_g \varrho_g (v_g)_y \frac{\partial (v_g)_x}{\partial y} + \alpha_g \frac{\partial p}{\partial x} = (F_g^v)_x + (F_g^{nv})_x + (F_g^{ex})_x + \sigma_g^M (v^{ex})_x \tag{A2-3}$$

$$\alpha_f \varrho_f \frac{\partial (v_f)_x}{\partial t} + \alpha_f \varrho_f (v_f)_x \frac{\partial (v_f)_x}{\partial x} + \alpha_f \varrho_f (v_f)_y \frac{\partial (v_f)_x}{\partial y} + \alpha_f \frac{\partial p}{\partial x} = (F_f^v)_x + (F_f^{nv})_x + (F_f^{ex})_x + \sigma_f^M (v^{ex})_x \tag{A2-4}$$

momentum y-direction:

$$\alpha_g \varrho_g \frac{\partial (v_g)_y}{\partial t} + \alpha_g \varrho_g (v_g)_x \frac{\partial (v_g)_y}{\partial x} + \alpha_g \varrho_g (v_g)_y \frac{\partial (v_g)_y}{\partial y} + \alpha_g \frac{\partial p}{\partial y} = (F_g^v)_y + (F_g^{nv})_y + (F_g^{ex})_y + \sigma_g^M (v^{ex})_y \tag{A2-5}$$

$$\alpha_f \varrho_f \frac{\partial (v_f)_y}{\partial t} + \alpha_f \varrho_f (v_f)_x \frac{\partial (v_f)_y}{\partial x} + \alpha_f \varrho_f (v_f)_y \frac{\partial (v_f)_y}{\partial y} + \alpha_f \frac{\partial p}{\partial y} = (F_f^v)_y + (F_f^{nv})_y + (F_f^{ex})_y + \sigma_f^M (v^{ex})_y \tag{A2-6}$$

entropy:

$$\alpha_g \varrho_g \frac{\partial s_g}{\partial t} + \alpha_g \varrho_g (v_g)_x \frac{\partial s_g}{\partial x} + \alpha_g \varrho_g (v_g)_y \frac{\partial s_g}{\partial y} = \sigma_g^S \tag{A2-7}$$

$$\alpha_f \varrho_f \frac{\partial s_f}{\partial t} + \alpha_f \varrho_f (v_f)_x \frac{\partial s_f}{\partial x} + \alpha_f \varrho_f (v_g)_y \frac{\partial s_f}{\partial y} = \sigma_f^S \tag{A2-8}$$

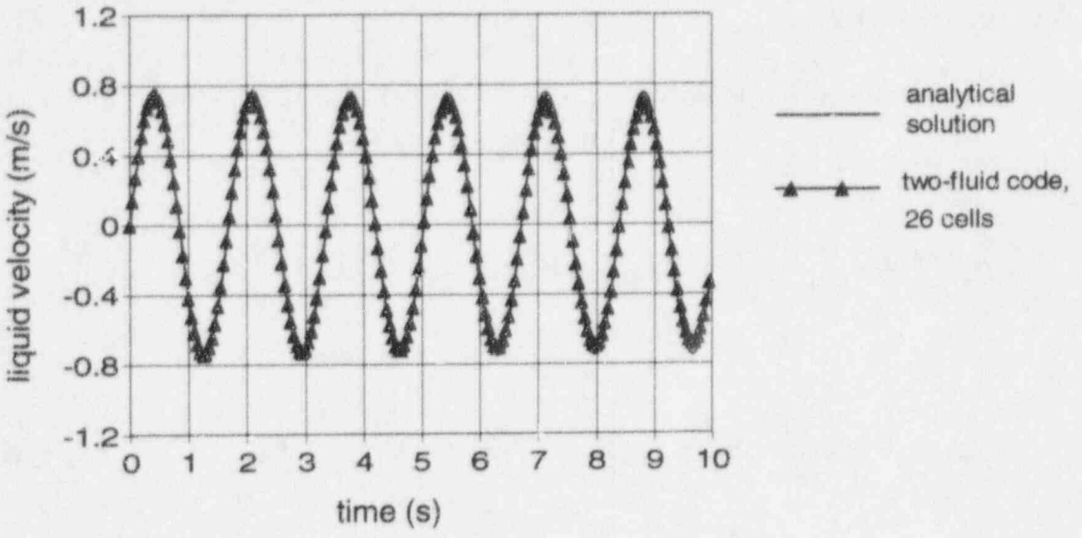

Fig.1.1: Oscillating manometer problem, Liquid velocity at bottom of U-tube.

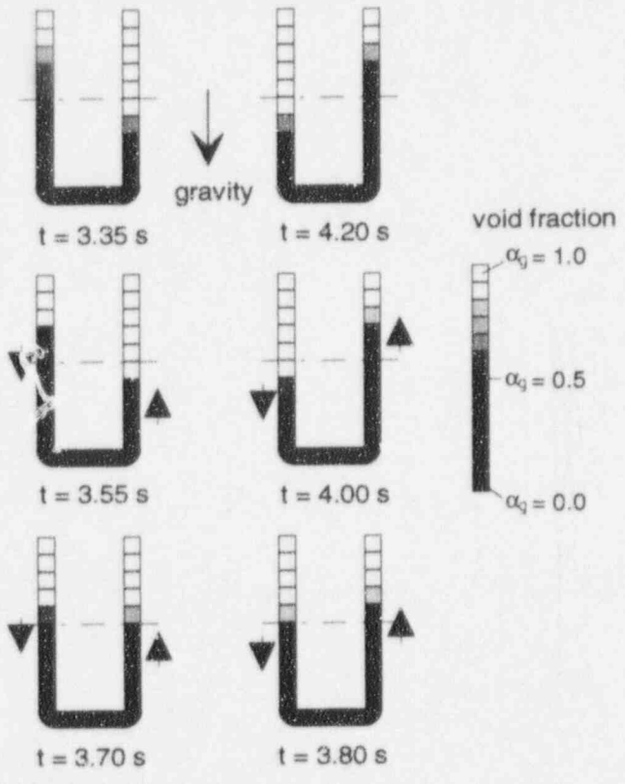

Fig. 1.2: Oscillating manometer problem, Void distribution during 1/2 period; vapour/liquid density ratio: 1:1000

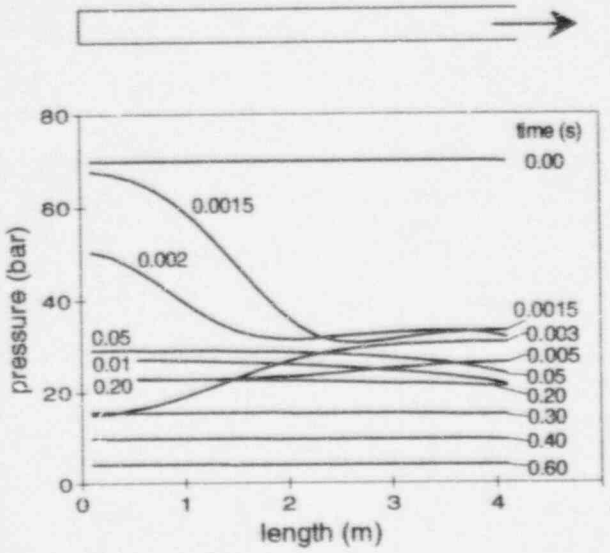

Fig. 2.1: Edward's pipe, pressure variation along pipe length.

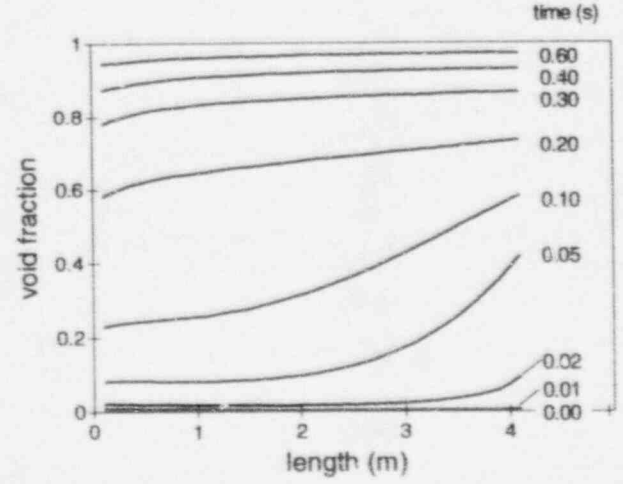

Fig. 2.2: Edward's pipe, void fraction along pipe length.

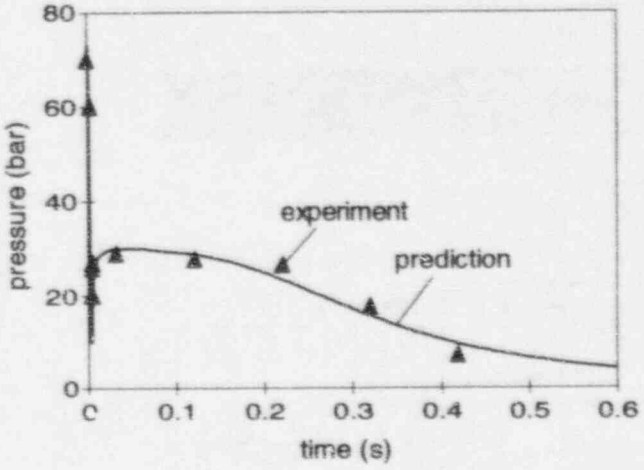

Fig.2.3: Edward's pipe, pressure at pipe end

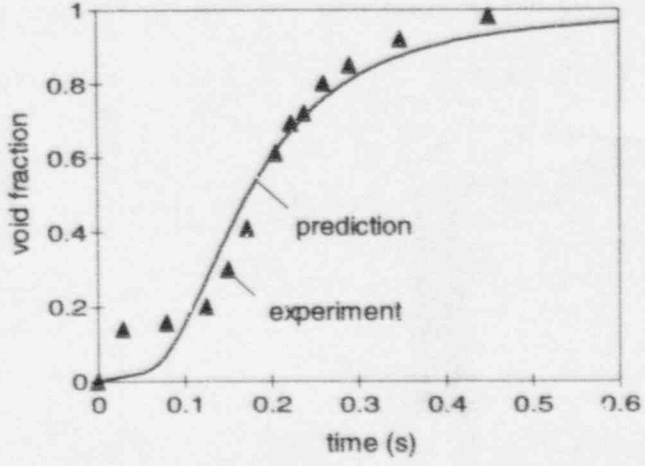

Fig.2.4: Edward's pipe, void fraction at pipe mid-section

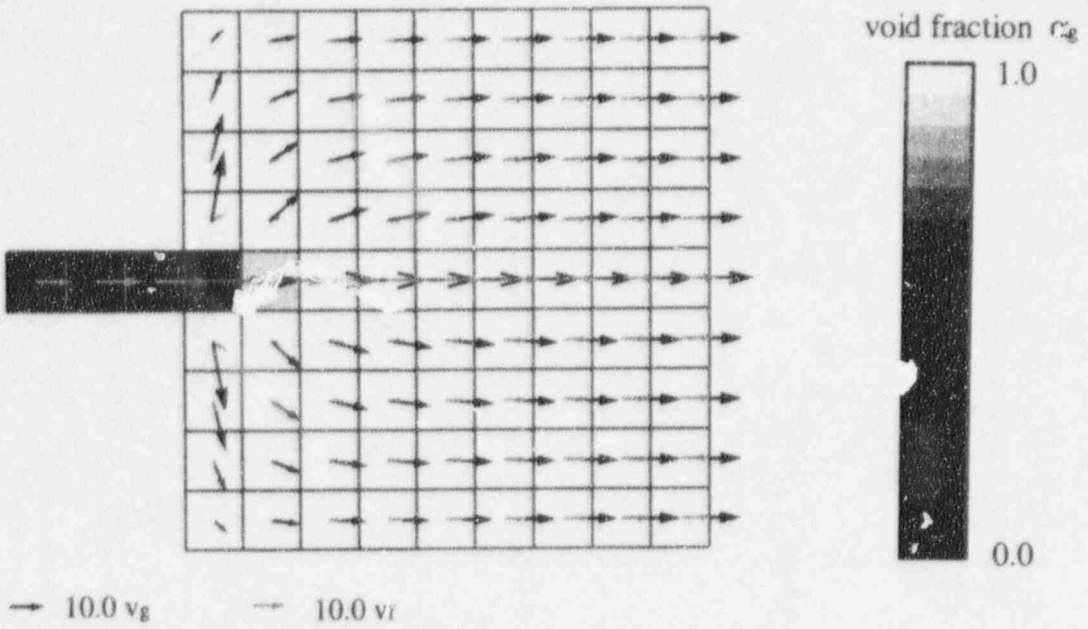

Fig. 3.1: Edward's pipe blowdown with an abrupt area change. Void fraction distribution and liquid and vapour velocity fields downstream of pipe outlet at time t = 0.0105 s.

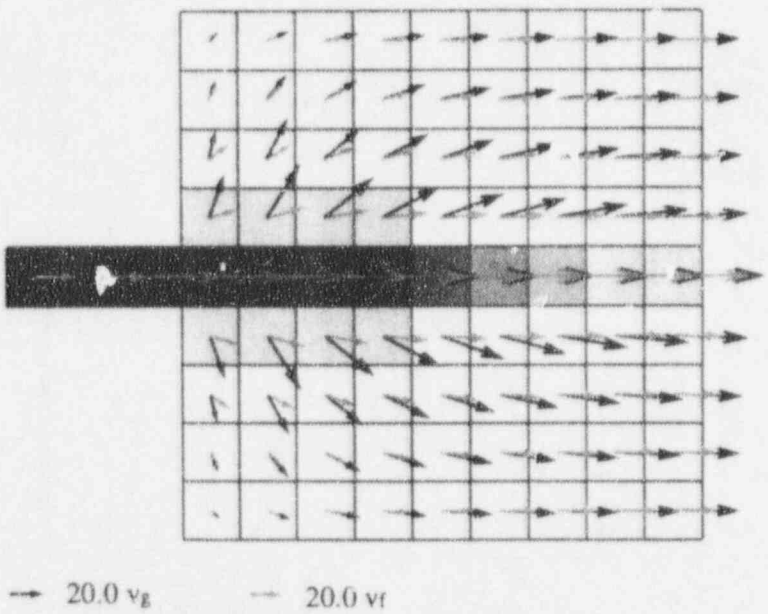

Fig. 3.2: Edward's pipe blowdown with an abrupt area change. Void fraction distribution and liquid and vapour velocity fields downstream of pipe outlet at time t = 0.0303 s.

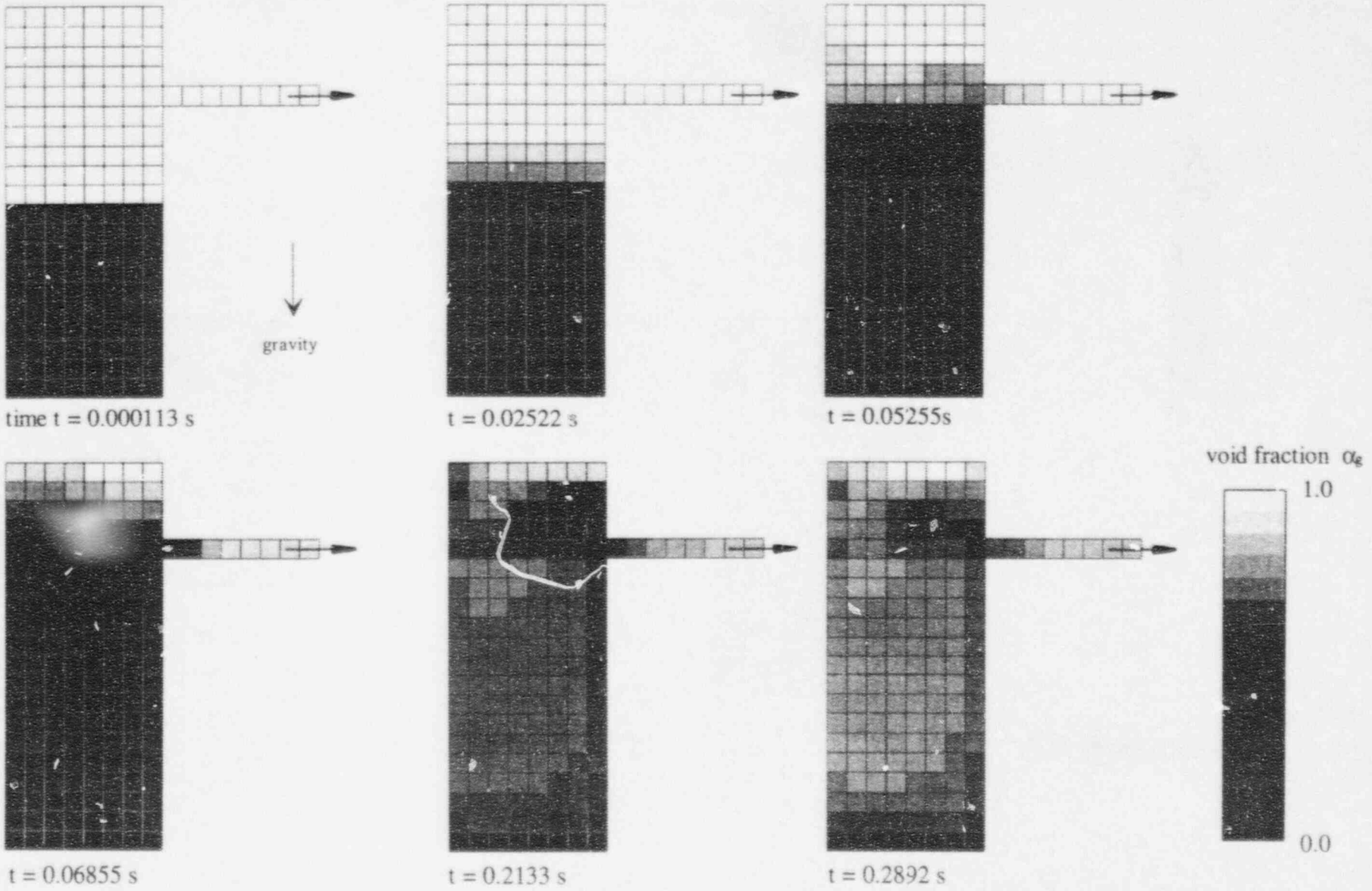

Fig. 4.1: Blowdown of a vertical vessel with a horizontal discharge line. Void distribution at various times.

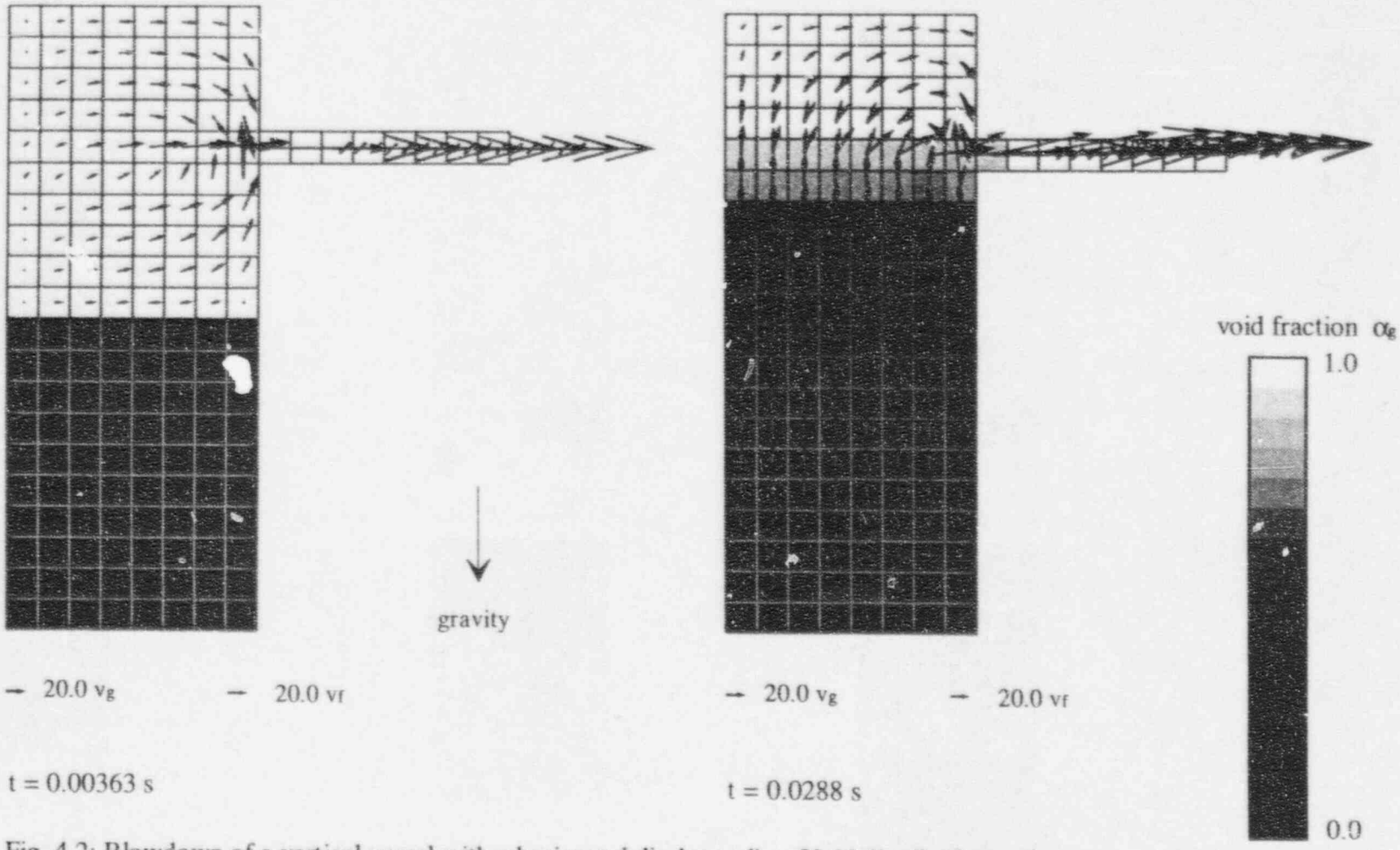

Fig. 4.2: Blowdown of a vertical vessel with a horizontal discharge line. Void distribution and vapour and liquid velocity fields (m/s) at two different times.

CFD PREDICTION OF FLOW AND PHASE DISTRIBUTION IN FUEL ASSEMBLIES WITH SPACERS

H. Anglart and O. Nylund
ABB Atom AB
Vasteras, Sweden

N. Kurul and M. Z. Podowski
Rensselaer Polytechnic Institute
Troy, NY 12180, USA

ABSTRACT

This paper is concerned with the modeling and computation of multi-dimensional two-phase flows in BWR fuel assemblies. The modeling principles are presented based on using a two-fluid model in which lateral interfacial effects are accounted for. This model has been used to evaluate the velocity fields of both vapor and liquid phases, as well as phase distribution, between fuel elements in geometries similar to BWR fuel bundles. Furthermore, this model has been used to predict, in a detailed mechanistic manner, the effects of spacers on flow and phase distribution between, and pressure drop along, fuel elements. The related numerical simulations have been performed using a CFD computer code, CFDS-FLOW3D.

1. INTRODUCTION

Flow and heat transfer calculations for reactor fuel assemblies are typically based on either one-dimensional models for individual subchannels or models of interconnected subchannels in which cross flows are accounted for in a simplified manner. The recent progress in CFD methods has provided opportunities for using mechanistic multidimensional models reflecting the actual geometry of the assembly. Whereas such multidimensional calculations are quite feasible and yield good results for single-phase flows, the combined modeling complexity and numerical difficulties have considerably limited so far the application of CFD-based models to two-phase flows inside fuel canisters of boiling water reactors.

If the development of mechanistic models and methods for flows along fuel elements enclosed inside typical BWR channel boxes has encountered difficulties, the modeling of local effects due to spacers moves the overall issue to a much higher level of complexity. The presence of spacers in BWR fuel assemblies affects various thermal-hydraulic characteristics of the reactor core. The effect which is usually accounted for using empirical correlations is the increased channel pressure drop. Whereas for single-phase flows, the pressure drop across spacers can be quantified with a reasonable accuracy using geometry-dependent local loss coefficients, the situation gets much more

complicated in the case of boiling channels. Since our understanding of the mechanisms governing two-phase pressure drop is still not fully satisfactory even for flows in smooth channels, the complexity of spacer geometry makes it even more difficult to predict the related local pressure losses. This is mainly because the overall loss coefficients may vary with flow conditions, including parameters such as mass flux, superficial velocities of each phase, void fraction, etc. In fact, the pressure drop across spacers will be affected not only by changes in the area-averaged parameters but also by changes in their lateral distributions in the near-spacer region.

In addition to the increased irreversible pressure losses, spacers may also change the void distribution along the channel. The combined flow acceleration/deceleration of each phase may affect local distributions of both phasic velocities and concentrations, thus resulting in a different axial void distribution. This is particularly important in nuclear reactors, where small changes in the core-average void directly affect, through the void reactivity feedback, the axial power distribution in the core.

The objectives of this paper are two fold. First, it has been demonstrated that using multidimensional models of two-phase flow, local distributions of flow fields and concentrations for both phases can be predicted for actual BWR geometries. Secondly, it has been shown for the first time that such models can also be used to evaluate in a mechanistic manner the effect of spacers on local pressure drop and other two-phase flow parameters around the spacers.

The two-phase models used in the predictions have been numerically implemented using the CFDS-FLOW3D computer code as a solver of the governing two-phase flow equations.

2. AN EVALUATION OF LATERAL FLOW AND PHASE DISTRIBUTIONS IN A FRIGG LOOP ASSEMBLY

The present analysis used the FT-6a assembly of the early FRIGG Loop Project as a reference geometry. A cross-sectional view of the FT-6a assembly is shown in Fig. 2-1. The test section consisted of six electrically heated rods, placed in a cylindrical pressure vessel. The heated length of the test section was 4.22 m, the vessel internal diameter was 71 mm, and the heated rod diameter was 13.8 mm. The void fraction was measured both in axial and lateral directions using the gamma ray attenuation system. The lateral void distribution was measured in three zones, as indicated in Fig. 2-1. A more detailed description of the geometry and measurements can be found in [13].

2-1. Model Description

The ensemble-averaged balance equations of mass, momentum and energy, which govern each phase, can be written as ([4], [5]),

$$\frac{\partial}{\partial t}(\alpha_k \rho_k) + \nabla \bullet (\alpha_k \rho_k \mathbf{U}_k) = \Gamma_k \qquad (2\text{-}1)$$

$$\frac{\partial}{\partial t}(\alpha_k \rho_k \mathbf{U}_k) + \nabla \bullet (\alpha_k \rho_k \mathbf{U}_k \mathbf{U}_k) = \nabla \bullet \left[\alpha_k \mu_k^e \left(\nabla \mathbf{U}_k + (\nabla \mathbf{U}_k)^T\right)\right] - \alpha_k \nabla p_k + \alpha_k \rho_k \mathbf{g} + \mathbf{U}_{ki} \Gamma_k + \mathbf{M}_k \tag{2-2}$$

$$\frac{\partial}{\partial t}(\alpha_k \rho_k H_k) + \nabla \bullet (\alpha_k \rho_k \mathbf{U}_k H_k - \alpha_k \lambda_k^e \nabla T_k) = \frac{\partial}{\partial t}(\alpha_k p_k) + Q_k + H_{ki} \Gamma_k + E_k \tag{2-3}$$

where $\alpha_k, \rho_k, p_k, \mathbf{U}_k, T_k$ and H_k are the volume fraction, density, pressure, velocity, temperature and enthalpy of phase k, respectively (the subscript i denotes the value at the interface). $\Gamma_k, \mathbf{M}_k, E_k$ are the rates of transfer (per unit volume), of mass, momentum, and energy, respectively, and μ_k^e, λ_k^e are the effective viscosity and thermal conductivity of phase k, respectively. Additional terms present in the governing equations are $\mathbf{g}$ - the acceleration of gravity, and Q_k - the heat source to phase k.

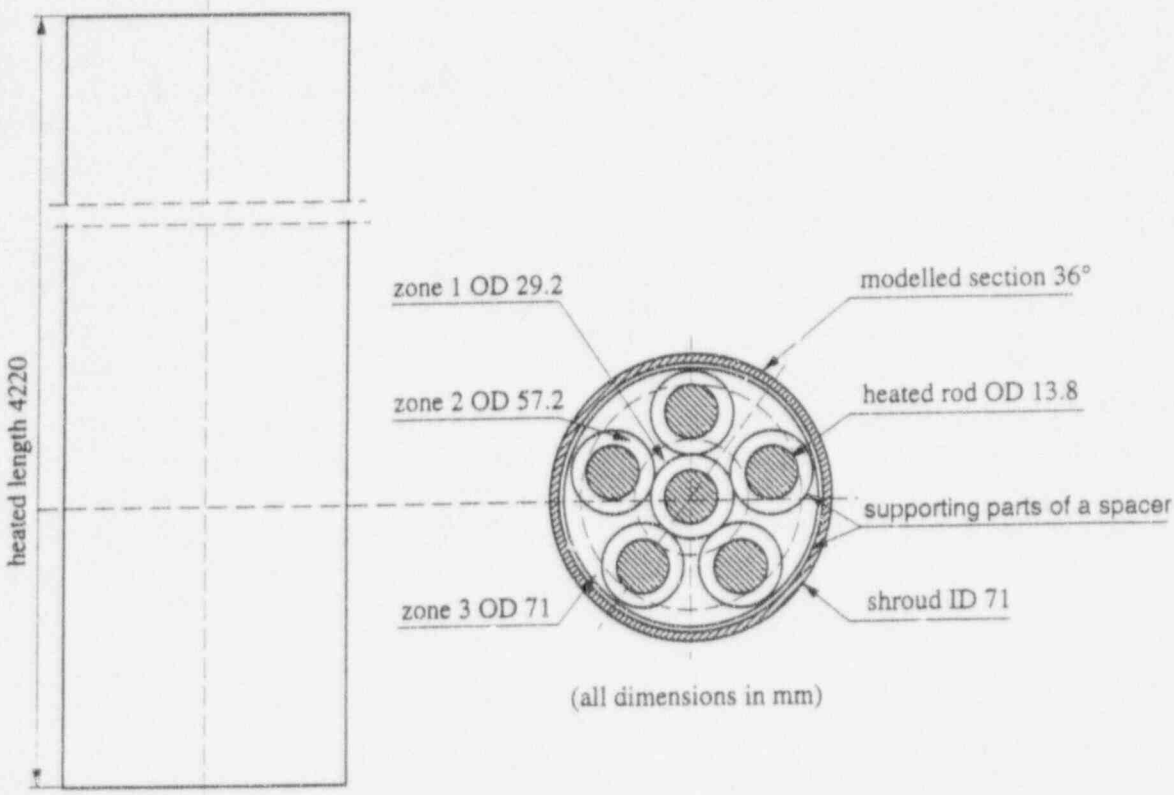

Figure 2-1. Test section FT-6a of the early FRIGG Loop project.

The three-dimensional model of unsteady, multiphase flow given by (2-1) through (2-3) must be supplemented with additional relationships (equations of state, constitutive equations, boundary and initial conditions) to achieve the closure. The key issue in accurate modelling of multiphase flows is to specify correctly the constitutive terms which include the phase interaction terms ($\Gamma_k, \mathbf{M}_k, E_k$), and self-interaction terms (μ_k^e, λ_k^e) as functions of the state variables.

2-2. Closure relationships

The closure relationships used in the present model refer to two-phase bubbly flow, with continuous liquid phase and disperse gas phase.

2-2-1. Interfacial effects

As already mentioned, the phase interaction terms which supplement equations (2-1), (2-2) and (2-3) are the interfacial mass transfer term, Γ_k, interfacial momentum transfer term, $\mathbf{M}_k$, and interfacial energy transfer term, E_k.

Interfacial momentum transfer

The total interfacial force can be expressed as a superposition of terms representing different physical mechanisms. Specifically,

$$\mathbf{M}_k = \mathbf{M}_k^d + \mathbf{M}_k^{vm} + \mathbf{M}_k^L + \mathbf{M}_k^{Lw} + \mathbf{M}_k^{TD} \tag{2-4}$$

where the individual terms on the right hand side of equation (2-4) are, respectively, the drag force, virtual mass force, lift force, "lubrication" force and, turbulent dispersion force.

The drag force is expressed as,

$$\mathbf{M}_l^d = -\mathbf{M}_g^d = \frac{1}{8} C_D A^{'''} \rho_l \left|\mathbf{U}_g - \mathbf{U}_l\right| \left(\mathbf{U}_g - \mathbf{U}_l\right) \tag{2-5}$$

where C_D and $A^{'''}$ are the drag force coefficient and the interfacial area density, respectively. Equation (2-5) shows, that the drag force exerted by the gas phase (bubbles) on the liquid phase is a vector directed along the relative velocity of the gas phase. The drag force coefficient is flow-regime-dependent, and can be calculated from the following correlations [8],

$$C_D = \begin{cases} 24\dfrac{1+0.1\mathrm{Re}_b^{0.75}}{\mathrm{Re}_b} & for \quad 0 < \alpha_g \le 0.10 \\ \dfrac{2}{3} d_b \sqrt{\dfrac{g\Delta\rho}{\sigma}} \left[\dfrac{1+17.67(1-\alpha_g)^{1.238}}{18.67(1-\alpha_g)^{1.5}}\right]^2 & for \quad 0.10 < \alpha_g \le 0.25 \\ 9.8(1-\alpha_g) & for \quad 0.25 < \alpha_g \end{cases} \tag{2-6}$$

The interfacial area density can be determined for large range of the gas volume fraction from the Ishii and Mishima correlation, [7],

$$A^{'''} = \frac{4.5}{D} \frac{\alpha_g - \alpha_{gs}}{1-\alpha_{gs}} + \frac{6\alpha_{gs}}{d_b} \frac{1-\alpha_g}{1-\alpha_{gs}} \tag{2-7}$$

where α_{gs} is the void fraction in the small bubble region, and $\alpha_{gs} = \alpha_g$ for spherical bubbles. In the present model the expression recommended by Kurul and Podowski [10] has been used for α_{gs},

$$\alpha_{gs} = \begin{cases} \alpha_g & for \quad \alpha_g < 0.25 \\ 0.3929 - 0.5714\alpha_g & for \quad 0.25 \le \alpha_g < 0.6 \\ 0.05 & for \quad 0.6 \le \alpha_g \end{cases} \tag{2-8}$$

Since the void fraction in the present calculations did not exceed 0.4, the first term on the RHS of this equation (applicable to slug flows only) has been ignored.

The second term in equation (2-4) represents the virtual mass force, which comes into play when one phase is accelerating relative to the other one. In case of a bubble accelerating in a continuous liquid phase, this force can be described by the following expression,

$$\mathbf{M}_l^{vm} = -\mathbf{M}_g^{vm} = C_{vm}\alpha_g\rho_l\left[\frac{D_l\mathbf{U}_l}{Dt} - \frac{D_g\mathbf{U}_g}{Dt}\right] \tag{2-9}$$

where C_{vm} is the virtual mass coefficient, which for a spherical particle is equal to 0.5, [5].

The third term in equation (2-4) is the lift force, which arises from a velocity gradient of the continuous phase in the lateral direction. Drew and Lahey derived the following expression, [6],

$$\mathbf{M}_l^L = -\mathbf{M}_e^L = C_L\rho_l\alpha_g\left(\mathbf{U}_g - \mathbf{U}_l\right)\times\left(\nabla\times\mathbf{U}_l\right) \tag{2-10}$$

where C_L is the lift force coefficient, which for shear flow around a spherical bubble is equal to 0.5, [6].

The term $\mathbf{M}_k^{Lw}$ in equation (2-4) represents the "lubrication" force, and is expressed as,

$$\mathbf{M}_l^{Lw} = -\mathbf{M}_g^{Lw} = C_{Lub}\alpha_g\rho_l\frac{\left|\mathbf{U}_g - \mathbf{U}_l\right|^2}{d_b}\mathbf{n}_w \tag{2-11}$$

where the coefficient C_{Lub} has been used as given by Antal et al. [3],

$$C_{Lub} = \max\left(0, C_{w1} + C_{w2}\frac{d_b}{y_w}\right) \tag{2-12}$$

The last term in equation (2-4) accounts for the effect of the dispersion of bubbles in the turbulent liquid flow. In the present model, the expression proposed by Lopez de Bertodano has been used, [12],

$$\mathbf{M}_l^{TD} = -\mathbf{M}_g^{TD} = C_{TD}\rho_l k_l \nabla \alpha_g \tag{2-13}$$

where, in [11] the value for the turbulent dispersion force coefficient, C_{TD} , for bubbly two-phase flow was 0.1.

Interfacial mass and energy transfer

It is assumed, that the difference in the kinetic energy between phases is negligible compared to the latent heat, and the surface tension effects can be neglected. Moreover, the phases are assumed to be saturated at the interface, which leads to,

$$E_k = 0 \tag{2-14}$$

The vapour generation rate at the wall in the nucleate boiling region can be modelled in a mechanistic way by deriving an equation for the total mass of bubbles detaching from a heated wall,

$$\Gamma_g'' = \frac{\pi d_{bw}^3}{6}\rho_g f N'' \tag{2-15}$$

where Γ_g'' is the evaporation rate per unit heated area, d_{bw} is the bubble diameter at detachment, f is the detachment frequency, and N'' is the number of nucleation sites per unit heated area. Having expressions for the bubble detachment diameter, the detachment frequency and the number of nucleation sites per unit heated area, one can find the vapour phase generation rate from equation (2-15). For the modelling of the subcooled boiling heat transfer, a model proposed by Kurul [9] has been used. In case of saturated boiling, the vapour generation rate is calculated as,

$$\Gamma_g'' = \frac{q_w''}{h_{fg}} \tag{2-16}$$

where q_w'' is the wall heat flux.

In the bulk of subcooled water, the vapour phase is condensing at the bubble surface. Wolfert et al. [19] proposed the following correlation for the heat transfer coefficient at the bubble-liquid interface,

$$h = \rho_l c_{pl} \sqrt{\frac{\pi}{4}\frac{\left|\mathbf{U}_g - \mathbf{U}_l\right|}{d_b}\frac{\lambda_l}{\rho_l c_{pl}}\frac{1}{1+\frac{\lambda_l'}{\lambda_l}}} \tag{2-17}$$

where d_b is the bubble diameter. Since the temperature is very close to the saturation temperature, the condensation rate can be determined from,

$$\Gamma_l = \frac{h(T_{sat} - T_l)}{h_{fg}} \tag{2-18}$$

2-2-2. Turbulence modelling

The effective viscosity of the liquid phase is found as a sum of the molecular viscosity μ_l and the turbulent viscosity, μ_l', where, the turbulent viscosity of the continuous phase in the bubbly two-phase flow is calculated from the following equation,

$$\mu_l' = \rho_l C_\mu \frac{k_l^2}{\varepsilon_l} + C_{\mu b} \frac{d_b}{2} \alpha_g \left| \mathbf{U}_g - \mathbf{U}_l \right| \tag{2-19}$$

in which the first term on the right-hand-side represents the shear-induced turbulent viscosity, and the second term represents the bubble-induced turbulent viscosity of the liquid phase. The kinetic energy (k_l) and the turbulent dissipation (ε_l) are determined from the classical $k-\varepsilon$ model [15], and the following values of the coefficients are used $C_\mu = 0.09$, $C_{\mu b} = 1.2$ [16].

2-2-3. Bubble diameter

The bubble size is modelled as a function of a local water subcooling from the following equation [9],

$$d_b = \begin{cases} 0.00015 & for \quad \Delta T_{sub} > 13.5K \\ -10^{-4}\Delta T_{sub} + 0.0015 & for \quad 0 < \Delta T_{sub} \le 13.5K \\ 0.0015 & for \quad \Delta T_{sub} \le 0K \end{cases} \tag{2-20}$$

where $\Delta T_{sub} = T_{sat} - T_l$ is the liquid phase subcooling.

3. AN ANALYSIS OF LOCAL VOID DISTRIBUTION IN THE FT-6A TEST SECTION

The model described in the previous section has been extensively tested and validated against experimental data. The model of the subcooled boiling has been validated against measurements of temperature and void distribution in a pipe 15.4 mm ID, with a constant heat flux of 5.7 10^5 W/m^2, inlet water subcooling 60 K, water mass flux 900 kg/m^{2}s at pressure 4.5 MPa. The results presented in Refs. [9] and [1] show good agreement with the measured data. The model was also used for prediction of adiabatic air-water flow in rectangular channels, and good agreement with the experiment was observed, as shown in Ref. [2].

In this paper, the model has been used for prediction of void distribution in diabatic, bubbly two-phase flow in rod bundle geometry. Measurements of hydrodynamic characteristics, instability thresholds and burnout limits in such geometries were performed in FRÖJA and FRIGG projects [13].

Only $^1/_{10}$ of the test section has been modelled, utilizing the symmetry of the assembly. The modelled part is indicated in Fig. 2-1, and the computational mesh used is shown in Fig. 3-1. The modelled segment was divided into 8550 computational cells with the lateral size range of ~0.7 ÷ 1.0 mm and 40 mm long in the axial direction. Special care was taken to specify equal-sized and regular cells close to walls, since this helps to avoid numerical problems in modelling close-to-wall effects. Because the present model is mainly applicable to bubbly two-phase flows, the modelled part comprises the first 1 m from the inlet, where the void fraction is within the range corresponding to this flow regime.

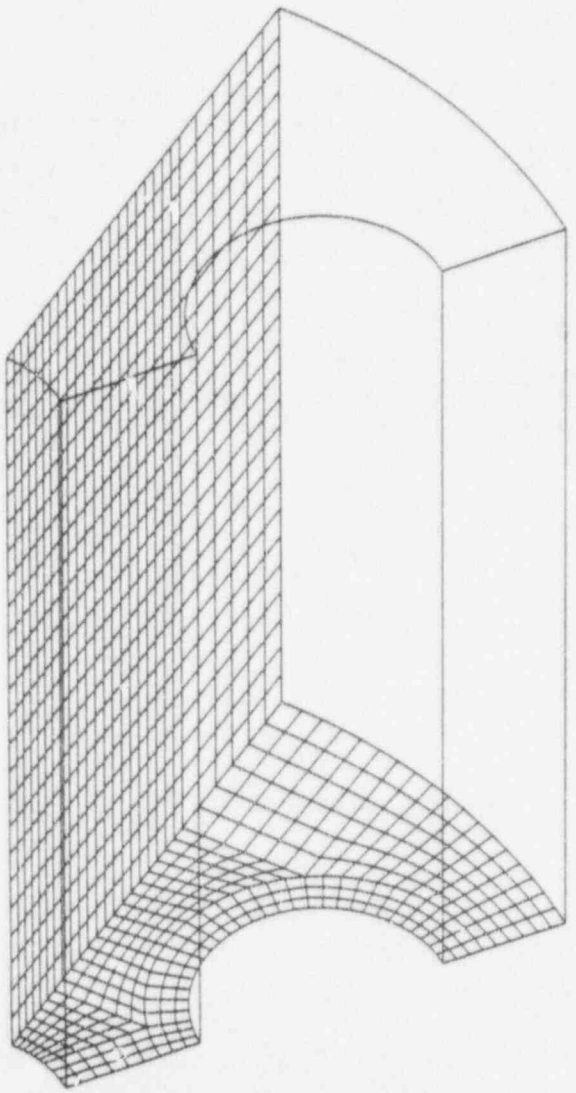

Figure 3-1. Computational mesh used for modelling of void distribution in test section FT-6a.

The following operating conditions have been used in the calculations: the water mass flux 1163 kg/m^{2}s, inlet subcooling 4.5 K, system pressure 50 bar, and heat flux 522 kW/m^2.

The calculated axial void distribution has been averaged in each zone; these zones were exactly the same as the zones used in the FRIGG loop tests. The comparisons between the axial distribution of the computed and measured void fraction in each zone are shown in Fig. 3-2. The calculated lateral distributions of void fraction at different distances from the inlet along the first 1.2 meter of the test section are shown in Fig. 3-3. As can be seen, the predictions are in good agreement with the measurements. Only the void fraction in zone 1 is slightly overpredicted, which results in overestimating the mean void fraction along the test section.

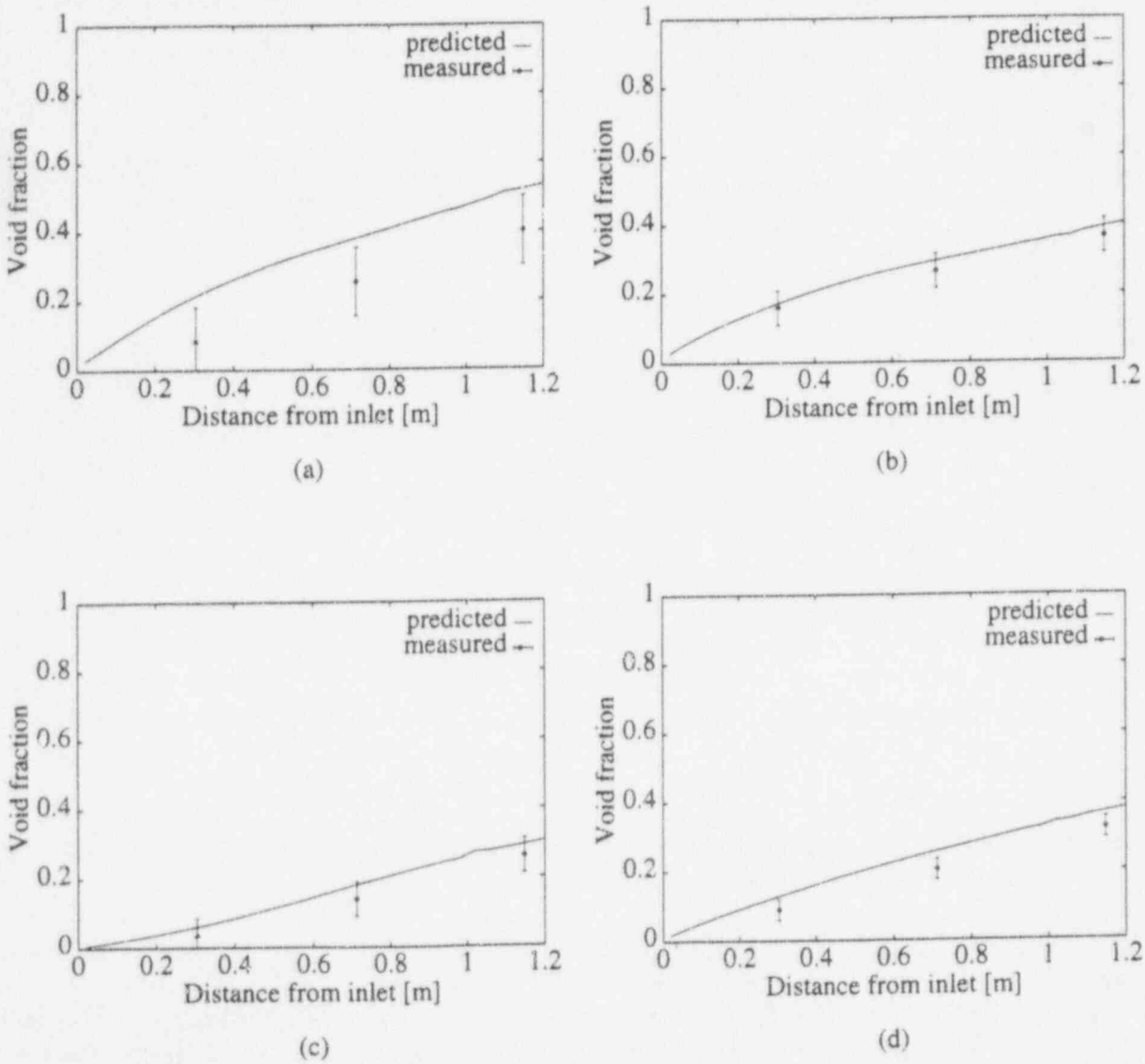

Figure 3-2. Axial void distributions along the test section FT-6a; (a) - zone 1, (b) - zone 2, (c) - zone 3, (d) - mean in test section

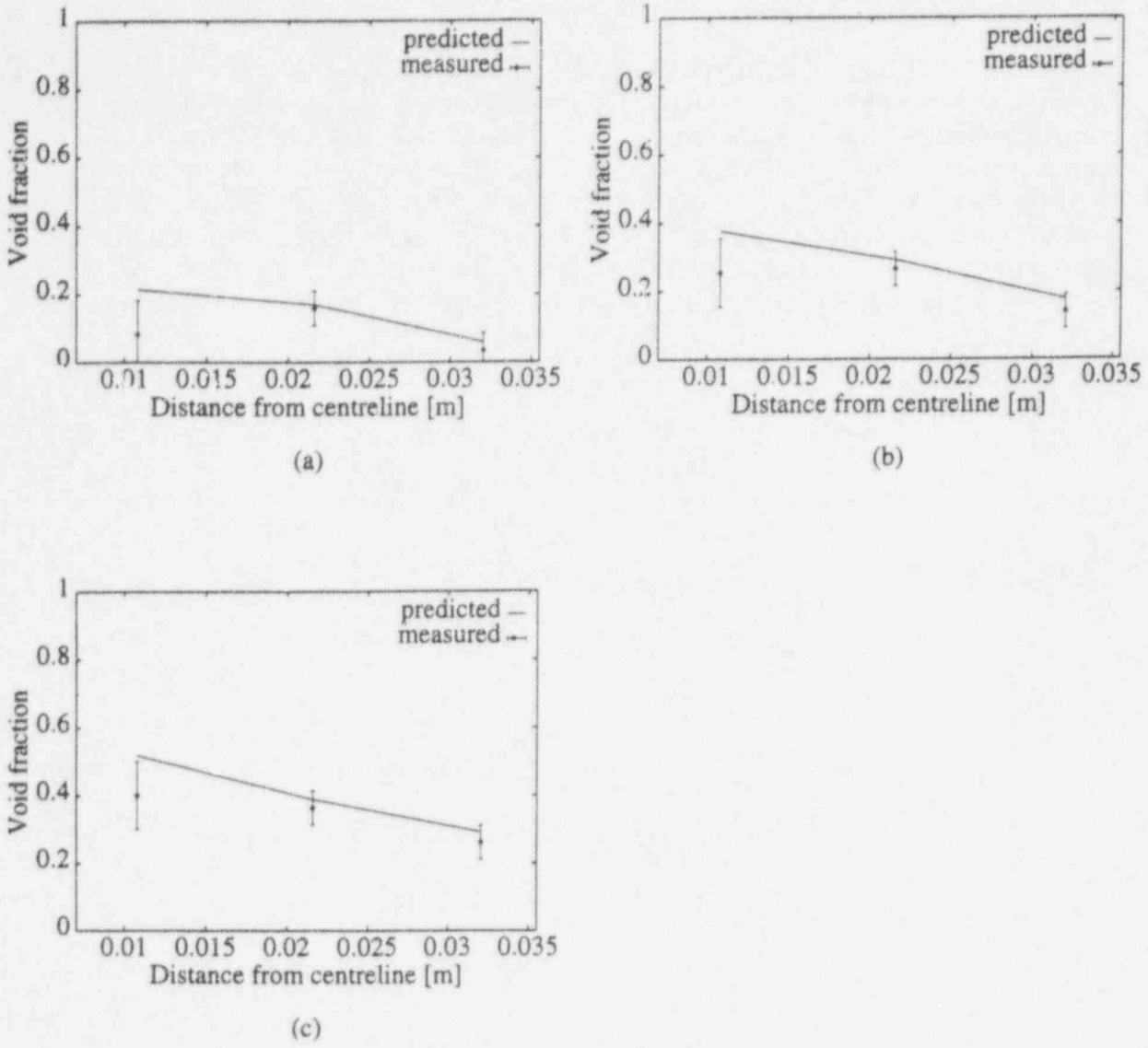

Figure 3-3. Lateral void distributions in the test section FT-6a at different locations from the inlet; (a) at 304mm, (b) at 713mm, (c) at 1148mm.

4. AN ANALYSIS OF THE EFFECT OF SPACERS ON LOCAL PRESSURE AND VOID DISTRIBUTIONS

Since multichannel assemblies typically employ several grid spacers at various axial locations, it was important to investigate the effect of spacers on local conditions in two-phase flows. The analysis was performed also for the FT-6a test section. The main objective of this study was to analyze the effects of the thickness and lateral location of the spacers on the local phase and velocity distributions, and on the resultant additional pressure drop. For this purpose, three geometrical configurations have been considered. The first case uses an

equivalent geometry approach, in which the assembly is replaced by an equivalent parallel-plate channel and the actual spacers are replaced by two inserts of equal thickness preserving the actual area contraction ratio. This is shown in Fig. 4-1. Naturally, the length of both inserts corresponds to the length of the spacers. Next the geometry of two sections of the spacers has been simulated: a spacer section between the central rod and one of the five peripheral rods, and a section between a peripheral fuel rod and the channel wall (see Fig. 4-2).

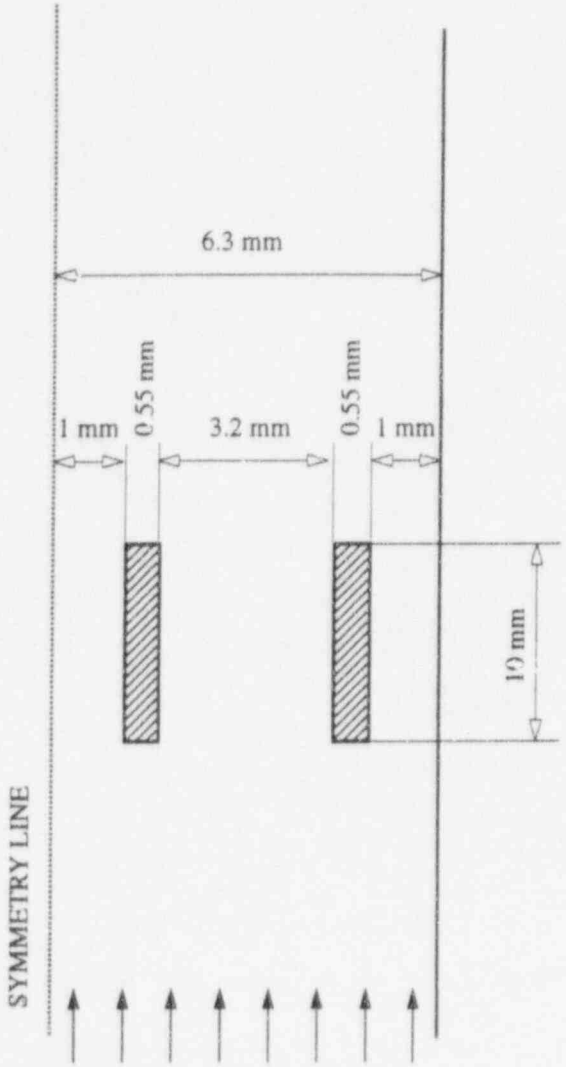

Figure 4-1. The equivalent parallel plate geometry representing the FT-6a assembly with spacers.

Two series of test calculations have been performed. The first series was aimed at evaluating the effective flow resistance of the spacers in single-phase flows. The equivalent parallel-plate geometry was used for this purpose. The channel section used in the calculations was 0.4 m long and the spacer was located at 0.09 m from the inlet. The simulations were performed for liquid water over a wide range of mass fluxes, from 500 kg/m2-s to 2000 kg/m2-s. A typical pressure distribution around the spacers is shown in Fig. 4-3.

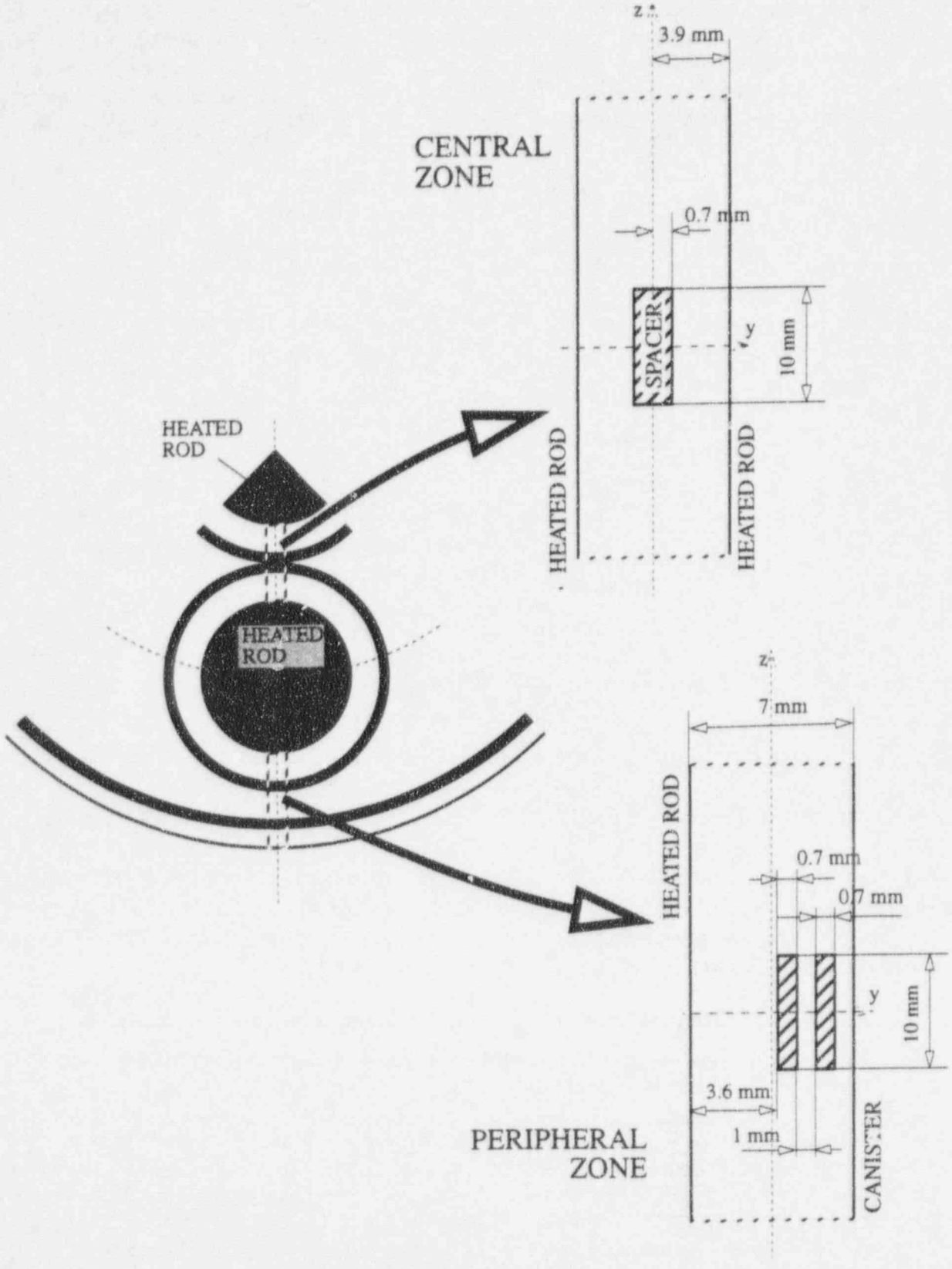

Figure 4-2. The sections of the FT-6a assembly and corresponding computational geometry used in the present simulations.

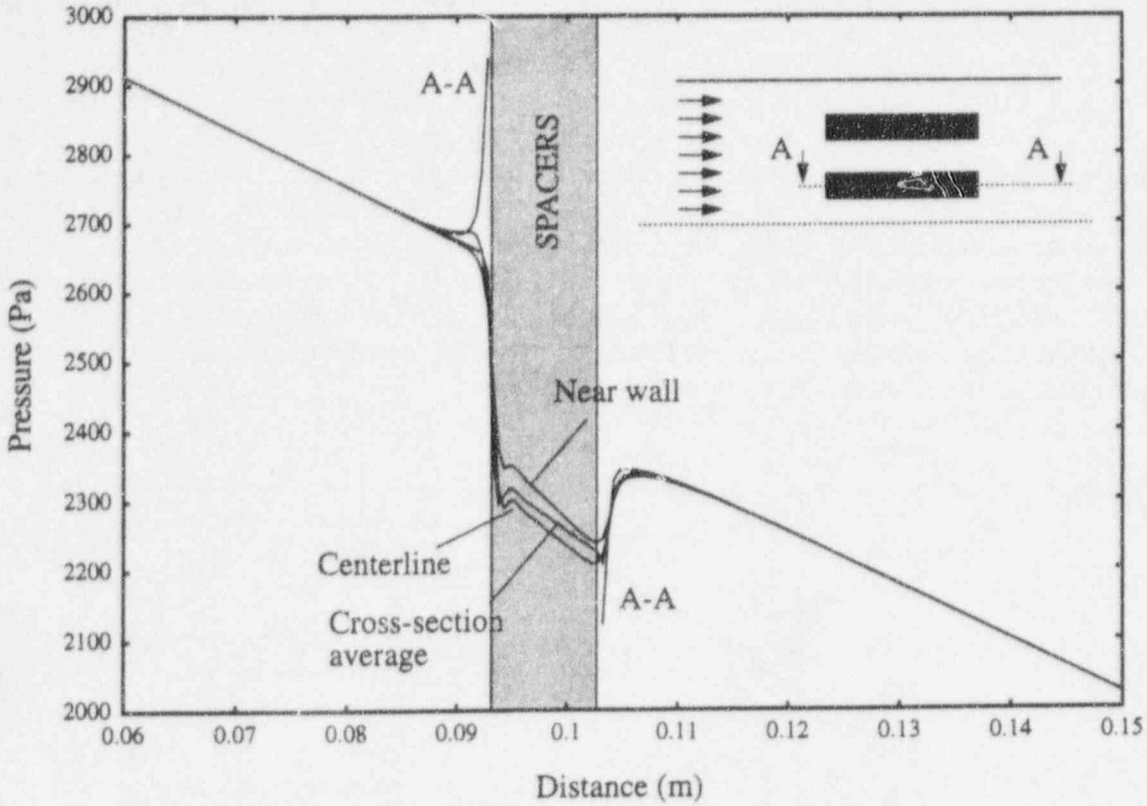

Figure 4-3. The calculated pressure drop in single phase flow for the equivalent geometry, shown in Fig. 4-1, G=861 kg/m^2 s.

The calculations for various flow conditions have been performed to deduce the effective spacer loss coefficient. The results are shown in Table 4-1. As can be seen, the predicted K_{sp} decreases slightly, as expected. Moreover, the obtained average value of K_{sp} agrees very well with the experimental data reported in Ref. [13] for the same spacer-to-channel area ratio, A_{sp}/A_{ch} = 0.177. Specifically, the value measured in Ref. [13] was K_{sp} = 0.29 for Re = 2.10^5. This agreement confirms that the area ratio is the major geometrical factor affecting the loss coefficient of spacers with sharp corners.

Table 4-1: The predicted local loss coefficients in single phase flow

G (kg/m2 s)	Re (based on D_h)	Local loss coefficient
600	1.51 10^5	0.3398
861	2.16 10^5	0.3300
1200	3.01 10^5	0.3080
1500	3.76 10^5	0.3165
2000	5.02 10^5	0.3191

The simulations of two-phase flows around spacers have been performed for the same geometry to estimate the two-phase pressure drop multiplier using a fully-developed flow solution as boundary condition at the inlet to the channel section containing the spacer. The pressure drop across the spacer was evaluated using the same channel/spacer geometry as that for single-phase simulations. Since the fully developed flow for the equivalent geometry differs from that for the actual geometry, the effect of phase distribution on the local pressure drop becomes an issue. In order to determine the effect of phase distribution, the cross-section averaged pressure distributions obtained for two different inlet conditions were compared as shown in Fig. 4-4. In both cases, the velocity distributions were of fully developed flow. As can be seen in Fig. 4-4, the cross-section averaged pressure distribution remain unaffected whether the inlet phase distribution is uniform or fully developed.

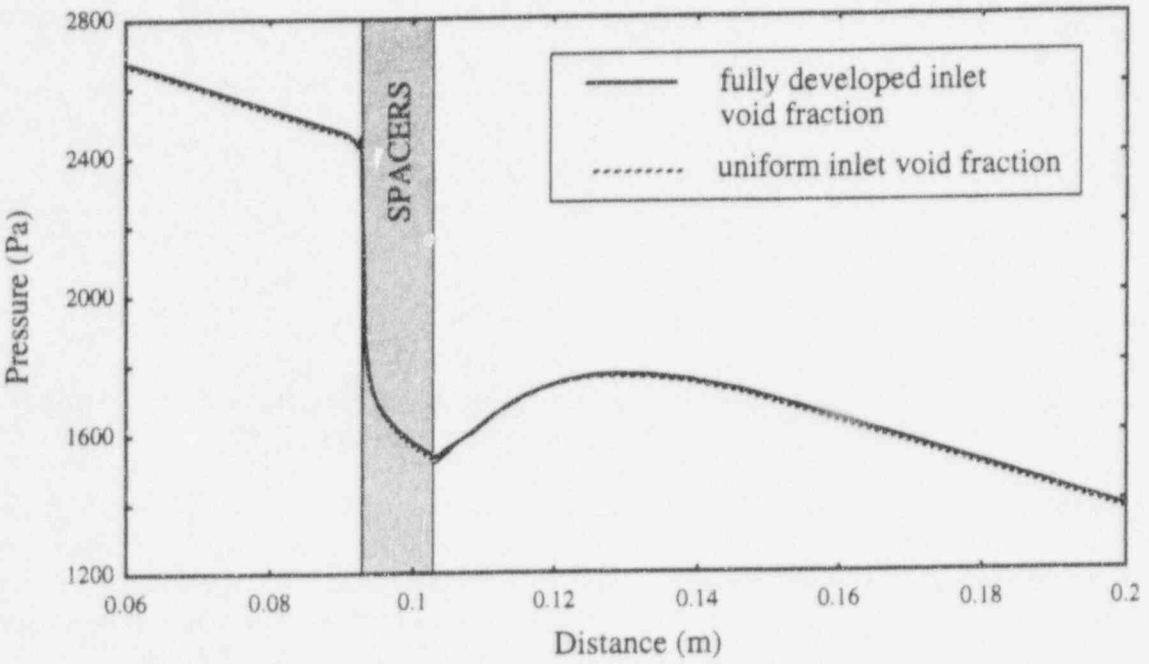

Figure 4-4. Effect of inlet phase distribution on the local pressure drop. G=1162 kg/m^2 s, α=20%.

In order to determine the local pressure drop due to the spacers, a series of test cases were considered for two mass fluxes and for void fractions ranging from 5% to 30%. The predicted pressure distributions are shown in Fig. 4-5. By comparing these results against the single-phase loss coefficient of the spacer, a local two-phase flow multiplier has been deduced for various flow conditions. The results are shown in Fig. 4-6. As can be seen, for average void fractions below 10% the two-phase flow multiplier of the spacer changes only slightly, and increases to about 1.2-1.3 as the average void fraction upstream from the spacer approaches 30%. These results agree well with the experimental data reported in Refs. [14] and [17]. The effect of mass flux on the two-phase flow multiplier is also shown in Fig. 4-6. Specifically, an increase in the flow rate by a factor of two

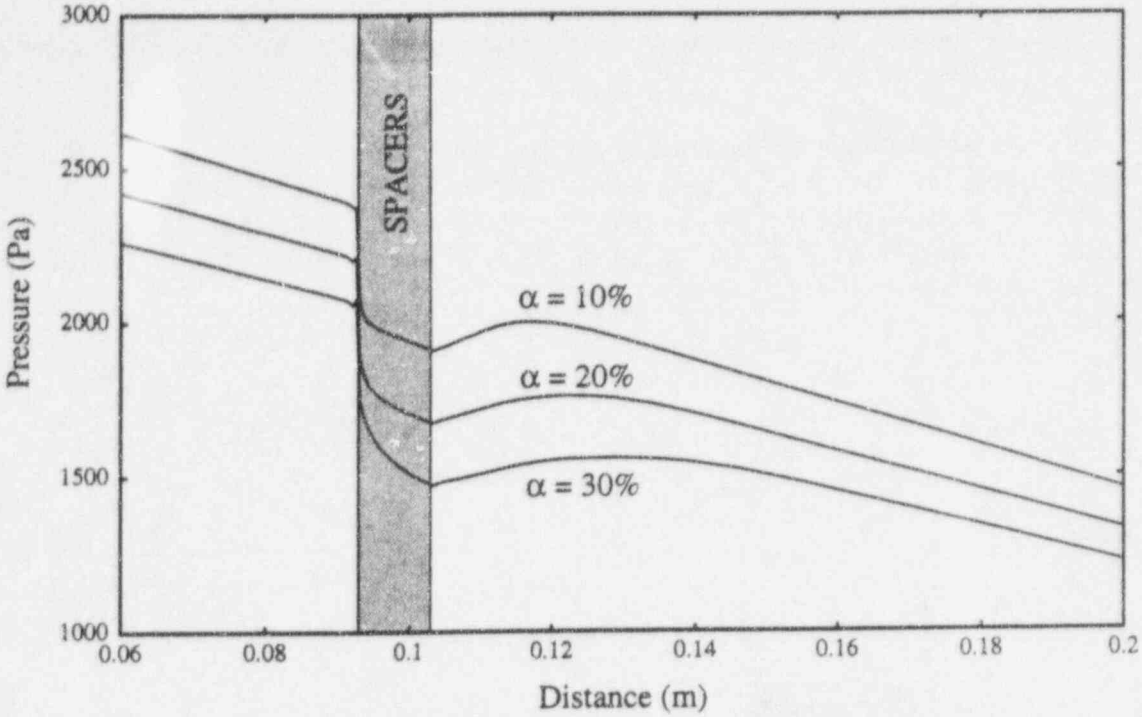

Figure 4-5. The cross-section averaged two-phase pressure drops for various inlet void fractions, G=861 kg/m^2 s.

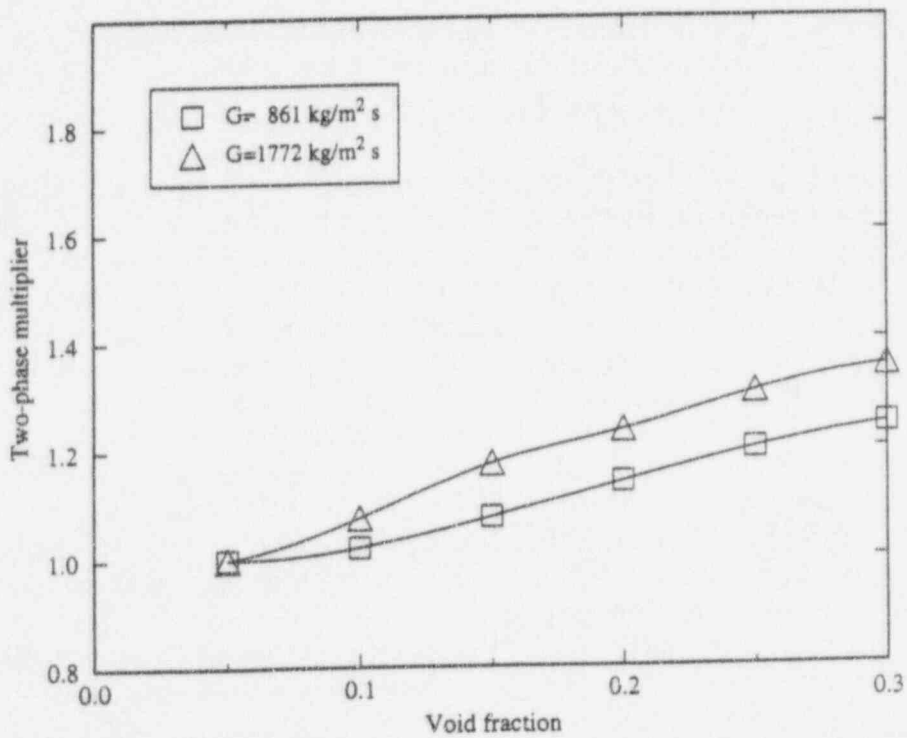

Figure 4-6. The calculated two-phase multiplier for the local pressure loss due to spacers.

changes the local two-phase flow multiplier by about 8% if the average void fraction is 30%.

In order to study the local void distributions around various sections of the spacers used in the FT-6a test section, two cases have been considered as indicated before. The results for the geometry simulating the central region (see Fig. 4-2) are shown in Fig. 4-7 and 4-8. Similar results for the peripheral region are shown in Figs. 4-9 and 4-10.

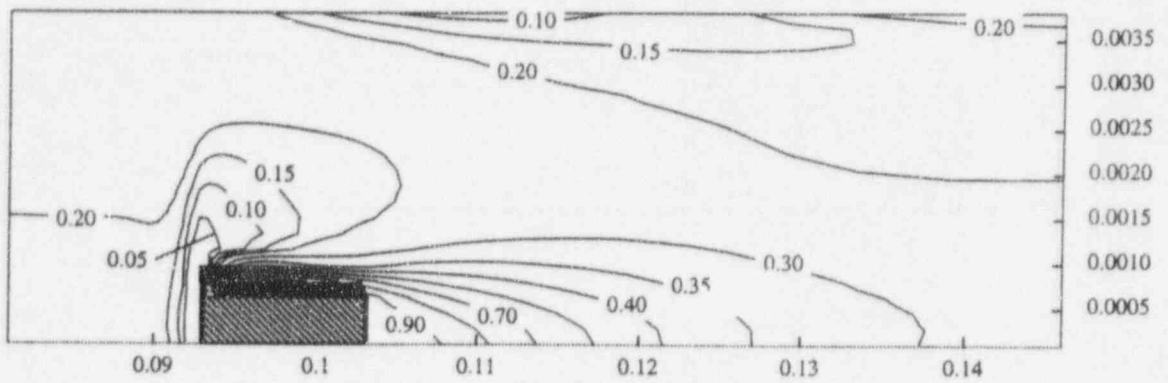

Figure 4-7. The calculated constant void fraction lines in the central zone; inlet conditions ob' ained from 3-D calculations.
G=1162 kg/m2 s, = 21% (see Fig. 4-2 for the geometry).

The inlet conditions for both regions were obtained from the three-dimensional computations presented in the first part of the paper at hand. Specifically, the velocity and void fraction distributions used in Figs. 4-7 through 4-8 were obtained from the fields where the average void fraction was 21%. These results indicate that the upstream face of the spacers is covered almost entirely by liquid, whereas vapor accumulates near the downstream side of the spacers forming a vapor packet. This is mainly due to the low inertia of the vapor (relative to the liquid phase), which facilitates the flow of the incoming vapor around the spacer, and pushes the vapor into the region directly downstream from the spacer. These predictions are in accordance with the experimental observations reported in Refs.[14] and [17]. On the other hand, the void fraction along the wall does not indicate high vapor concentrations. This can be observed more clearly in Fig. 4-11. At both high and low vapor contents, the void fraction along the wall increases slightly just upstream of the spacer, followed by a significant decrease.

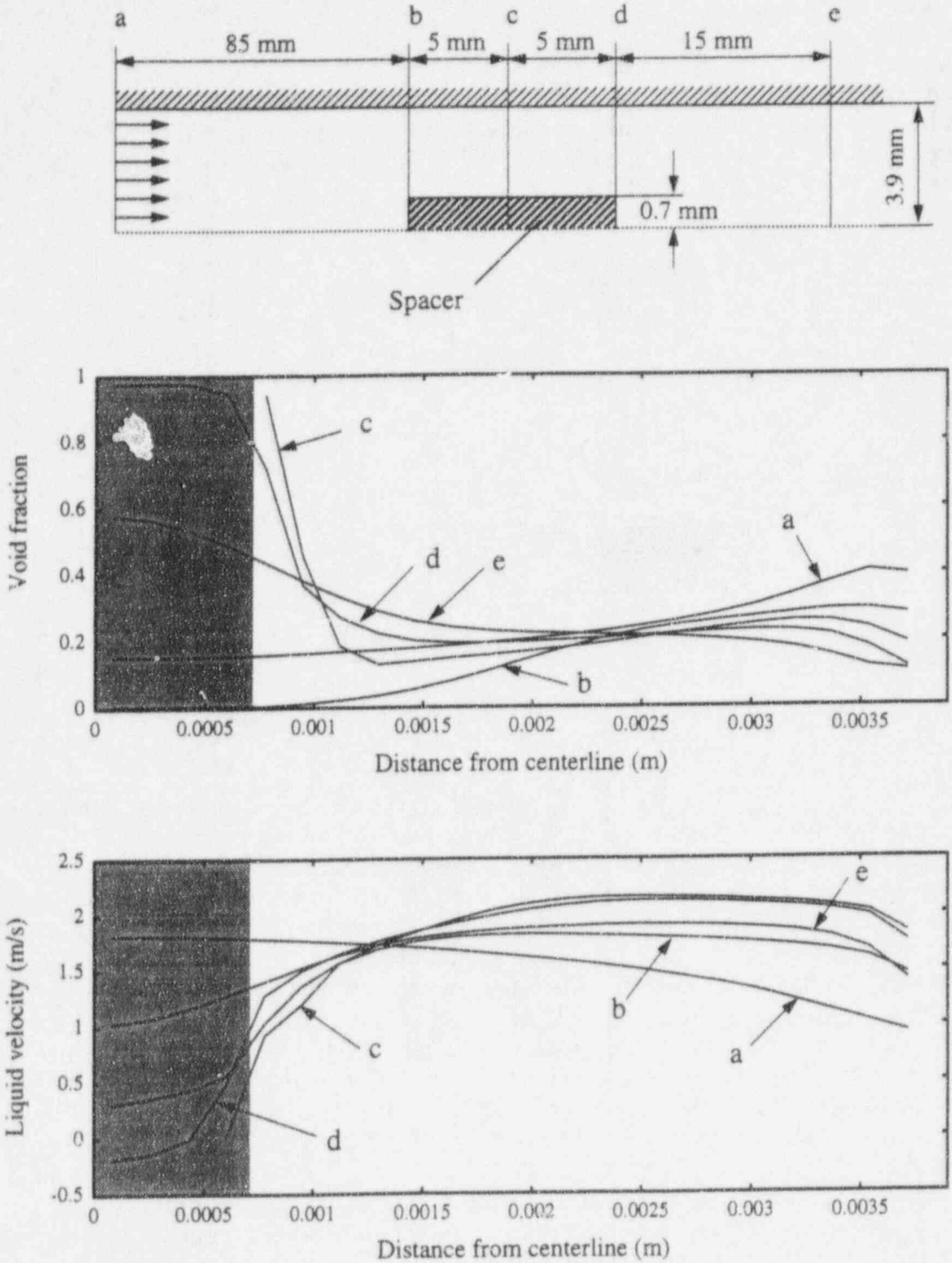

Figure 4-8. The calculated void fraction distributions at several cross sections in the central zone; inlet conditions obtained from 3-D calculations. G=1162 kg/m^2 s, α = 21% (see Fig. 4-2 for the geometry).

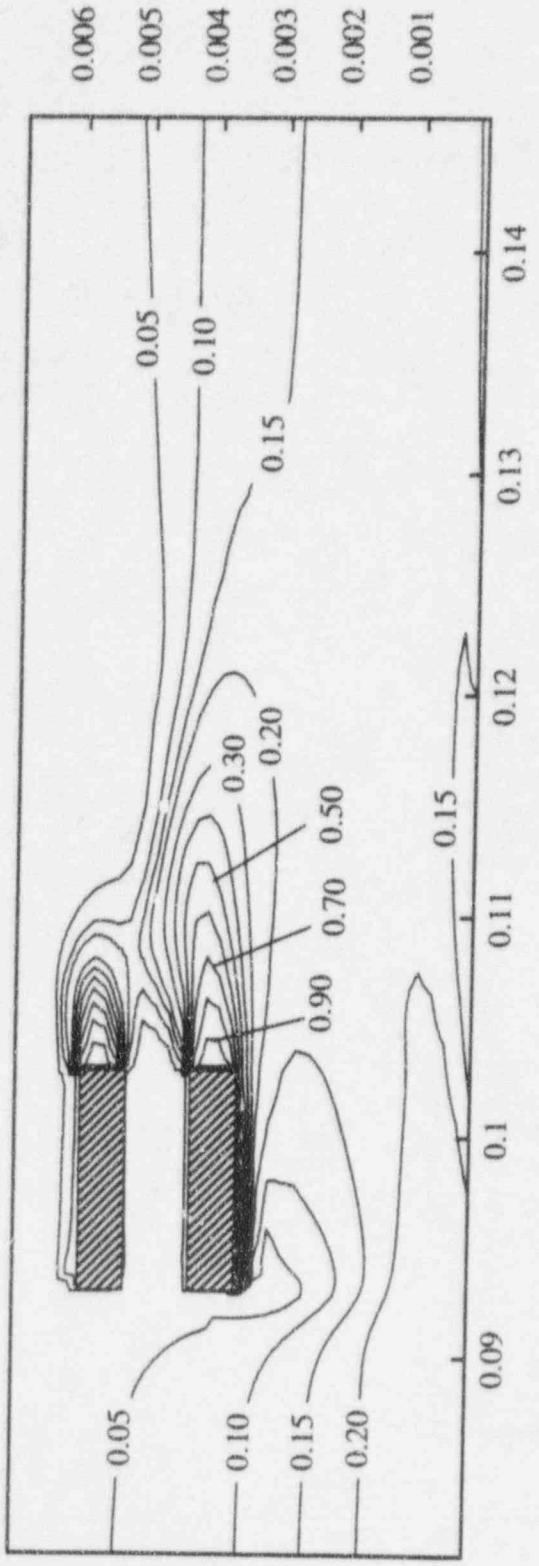

Figure 4-9. The calculated constant void fraction lines in the peripheral zone; inlet conditions obtained from 3-D calculations. G=1162 kg/m^2 s, α = 13% (see Fig. 4-2 for the geometry).

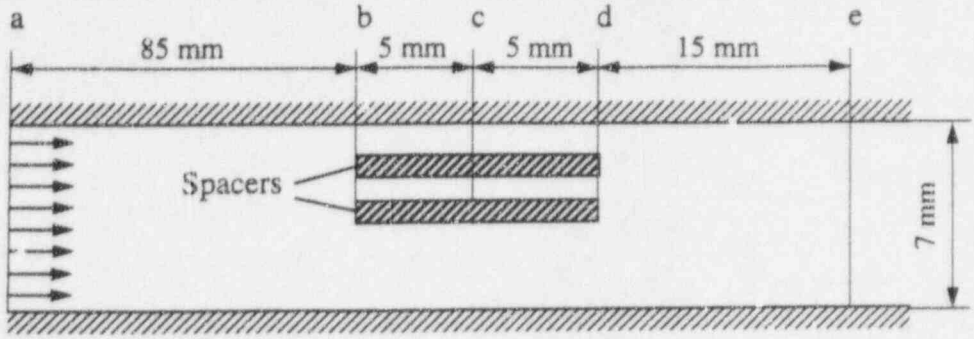

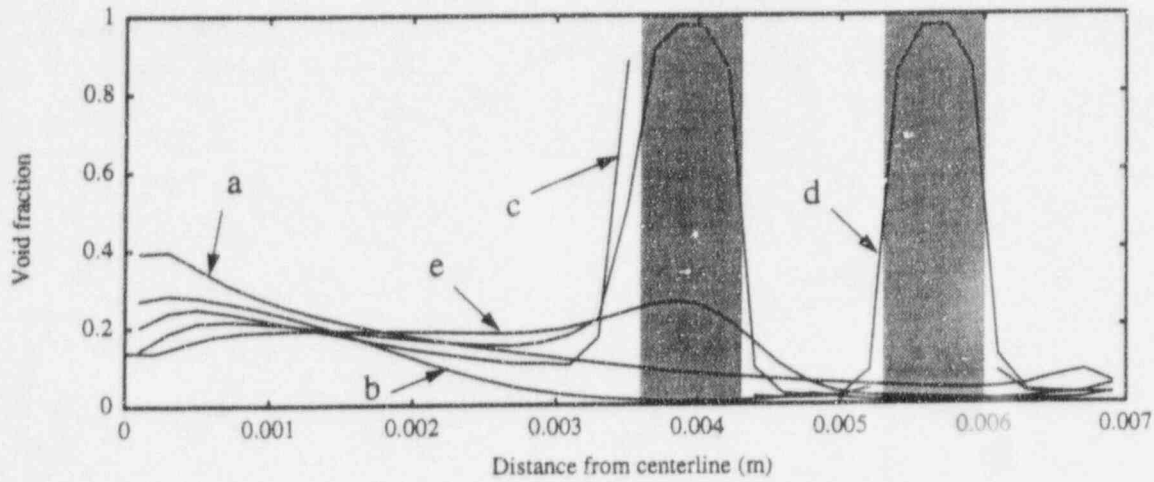

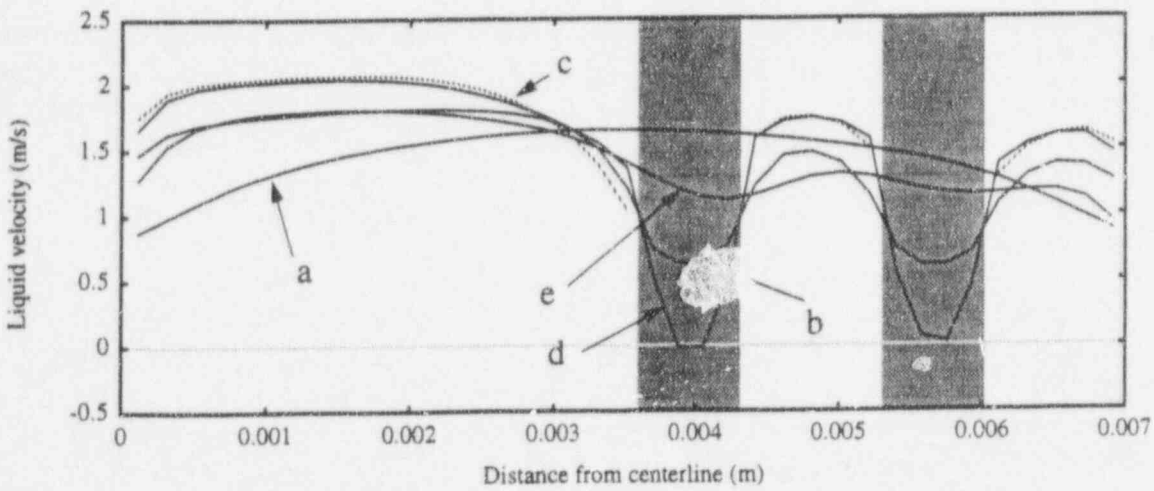

Figure 4-10. The calculated void fraction distributions at several cross sections in the peripheral zone; inlet conditions obtained from 3-D calculations. G=1162 kg/m^2 s, α = 13%, (see Fig. 4-2 for the geometry).

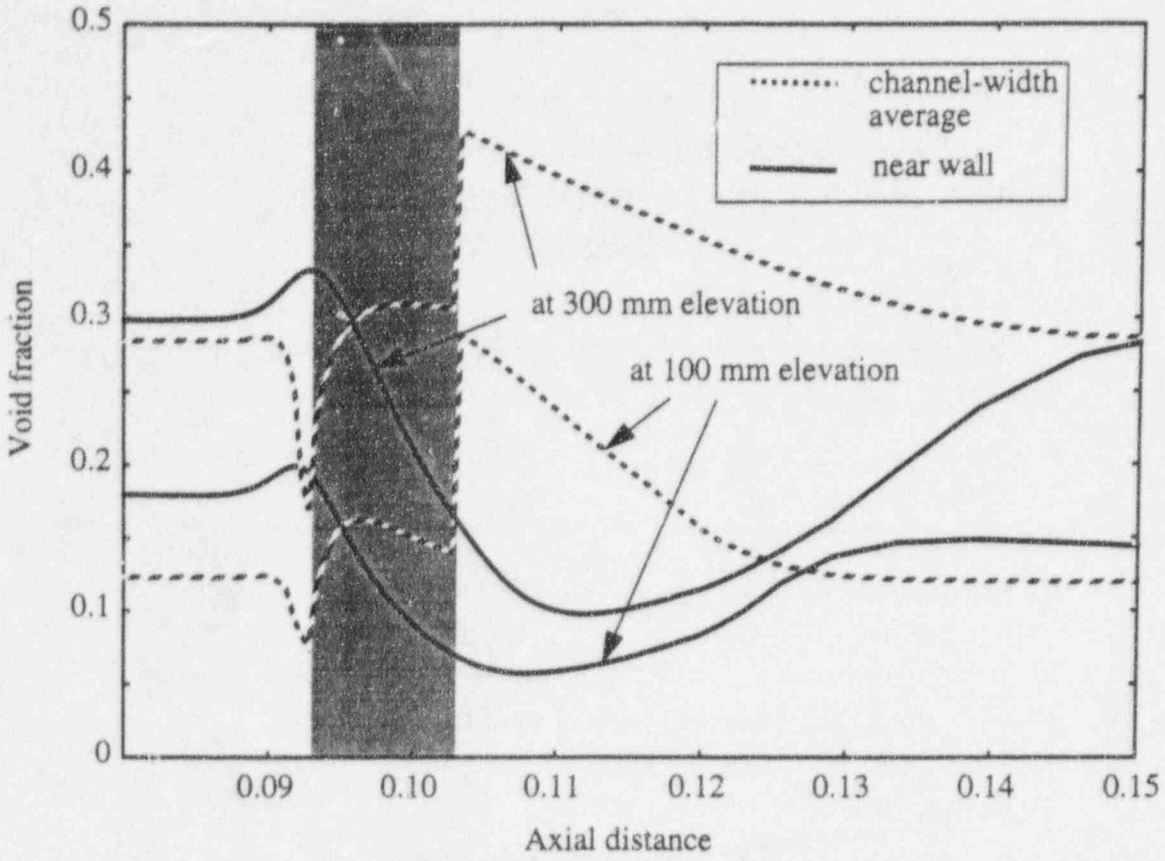

Figure 4-11. Axial void fraction distributions in the vicinity of the spacers in the central zone, for different inlet void fraction, and G=1162 kg/m^2 s.

5. CONCLUSIONS

Numerical simulations have been performed aimed at studying multidimensional effects for two-phase flows in multi-rod assemblies. The model developed for this analysis has been numerically implemented using CFDS-FLOW3D as a solver of the governing conservation equations. The issues which have been investigated included the predictions of lateral void distribution between cylindrical rods and the effect of spacers on both local phase distribution and pressure drop along the assembly.
It has been shown that the proposed model properly predicts the basic physics of two-phase flows in the complex geometries of BWR fuel assemblies. Furthermore, several specific results of the calculations have been compared against experimental data, showing very good agreement.

NOMENCLATURE

A''' - Interfacial area density
$C_\mu, C_{\mu b}$ - constants in equation (2-19)
C_D - drag force coefficient defined in equation (2-6)
C_L - lift force coefficient

C_{Lub} - "lubrication" force coefficient defined in equation (2-12)
C_{vm} - virtual mass coefficient
C_{w1}, C_{w2} - coefficients in equation (2-12)
C_{TD} - turbulent dispersion force coefficient
D - channel equivalent diameter
E_k - energy transfer to phase k.
H_k - enthalpy of phase k
$\mathbf{M}_k$ - interfacial force per unit volume for phase k
$\mathbf{M}_k^d$ - drag force
$\mathbf{M}_k^{vm}$ - virtual mass force
$\mathbf{M}_k^L$ - lift force
$\mathbf{M}_k^{Lw}$ - "lubrication" force
$\mathbf{M}_k^{TD}$ - turbulent dispersion force
N'' - number of nucleation sites per unit area
Q_k - heat source to phase k
T_k, T_l, T_{sat} - temperature of phase k, liquid and saturation, respectively
$\mathbf{U}_k, \mathbf{U}_l, \mathbf{U}_g$ - velocity of phase k, liquid and gas, respectively
c_{pl} - heat capacity of liquid phase
d_b - bubble diameter
d_{bw} - bubble diameter at the moment of detachment from a wall
f - bubble detachment frequency
$\mathbf{g}$ - gravity
h - heat transfer coefficient
h_{fg} - latent heat
k_l - turbulent kinetic energy
$\mathbf{n}_w$ - unit vector normal to a wall
P_k - pressure
q_w'' - wall heat flux
t - time
y_w - distance to a wall
Γ_k - interfacial mass transfer for phase k
Γ_g'' - evaporation rate per unit heated area
Γ_l - condensation rate
α_k, α_g - volume fraction of phase k and gas, respectively
α_{gs} - void fraction of small bubble region, equation (2-8)
ε_l - dissipation of turbulent kinetic energy
μ_l^t - turbulent viscosity of liquid
μ_l - molecular viscosity of liquid
μ_k^e - effective viscosity of phase k
λ_l - thermal conductivity of liquid
λ_k^e - effective conductivity of phase k

λ_l' - turbulent conductivity of liquid

ρ_k, ρ_l, ρ_g - density of phase k, liquid and gas, respectively

$\Delta\rho = \rho_l - \rho_g$ - phase density difference

σ - surface tension

REFERENCES

[1] Anglart, H., Modelling of Vapour Generation at Wall in Subcooled Boiling Two-Phase Flow, 1st CFDS Int. User Conference 6-7 May 1993, Eynsham Hall, Oxford, UK.

[2] Anglart, H., Andersson, S., Podowski, M.Z. and Kurul, N., An Analysis of Multidimensional Void Distribution in Two-Phase Flows, Proc of the 6-th Int Topical Meeting on Nuclear Reactor Thermal Hydraulics - NURETH-6, Grenoble, October 5-8, 1993, Vol I, 139-153.

[3] Antal, S.P., Lahey, R.T. Jr. and Flaherty, J.E., Analysis of Phase Distribution In Fully Developed Laminar Bubbly Two-Phase Flow, Int. J. Multiphase Flow, Vol. 17, (1991), pp. 635-652.

[4] CFDS-FLOW3D User Guide, Computational Fluid Dynamics Services, Harwell Laboratory, UK, 1994.

[5] Drew, D.A., Analytical Modeling of Multiphase Flows, in Boiling Heat Transfer - Modern Developments and Advances, R.T. Lahey, Jr. Ed., Elsevier Science Publishers, 1992.

[6] Drew, D. and Lahey, R.T. Jr., Application of General Constitutive Principles to the Derivation of Multidimensional Two-Phase Flow Equations, Int. J. Moltiphase Flow, Vol. 7, (1979), pp. 243-264.

[7] Ishii, M. and Mishima, K., Study of Two-Fluid Model and Interfacial Area, ANL-80-111, (1981).

[8] Ishii, M. and Zuber, N., Drag Coefficient and Relative Velocity in Bubbly, Droplet or Particulate Flows, AIChE Journal, 25, (1979), 843-855.

[9] Kurul, N., Multidimensional Effects in Two-Phase Flow Including Phase Change, PhD Thesis, Rensselaer Polytechnic Institute, (1990).

[10] Kurul, N. and Podowski, M.Z., On the Modeling of Multidimensional Effects in Boiling Channels, ANS Proc., 1991 National Heat Transfer Conference, Minneapolis, MN, (1991).

[11] Lahey, R.T., Jr., Lopez de Bertodano, M. and Jones, O.C., Phase Distribution in Complex geometry conduits, Nuc. Engrg. Des. 141 (1993), pp. 177-201.

[12] Lopez de Bertodano, M., Turbulent Bubbly Two-Phase Flow in a Triangular Duct, PhD Thesis, Rensselaer Polytechnic Institute, (1992).

[13] Nylund, O., Becker, K.M., Eklund, R., Gelius, O., Haga, I., Hansson, P.T., Hernborg, G. and Åkerhielm, F., Measurements of hydrodynamics chracteristics, instability thresholds, and burnout limits for 6-rod clusters in natural and forced circulation, FRIGG-1 report, ASEA and AB Atomenergi, Sweden, 1967.

[14] Nylund, O., Full-scale loop studies of BHWR and BWR fuel assemblies, ASEA RESEARCH, Vol. 10, 1969.

[15] Rodi, W., Turbulence Models and Their Applications in Hydraulics, IAHR/AIRH Monograph, 1984.

[16] Sato, Y., Sadatomi, M. and Sekoguchi, K., Momentum and heat transfer in two-phase bubbly flow-I, Int. J. Multiphase Flow Vol. 7, No. 2, (1981), pp. 167-178.

[17] Tapucu, A., Teyssedou, A., Trochen, N., and Merilo, M., "Pressure Losses Caused by Area Changes in a Single-Channel Flow Under Two-Phase Flow Conditions," Int. J. Multiphase Flow, Vol. 15, No. 1, pp. 51-64.

[18] Wang, S.K., Lee, S.J., Jones, O.C. and Lahey, R.T., Jr., 3-D Turbulence Structure and Phase Distribution Measurements in Bubbly Two-Phase Flows, Int. J. Multiphase Flow, Vol. 13, (1987), pp. 327-343.

[19] Wolfert, K., Burwell, M.J. and Enix, D., Non-Equilibrium Mass Transfer Between Liquid and Vapour Phases During Depressurization Process in Transient Two-Phase Flow, Proc. 2nd CSNI Specialists Meeting, Paris, Vol. 2, (1978), 1377-1387.

COMPUTATIONAL FLUID DYNAMIC ANALYSIS OF A CLOSURE HEAD PENETRATION IN A PRESSURIZED WATER REACTOR

D. R. Forsyth and R. E. Schwirian
Westinghouse Electric Corporation
Nuclear Technology Division
P.O. Box 355
Pittsburgh, Pennsylvania 15230-0355

ABSTRACT

ALLOY 600 has been used typically for penetrations through the closure head in pressurized water reactors because of its thermal compatibility with carbon steel, superior resistance to chloride attack and higher strength than the austenitic stainless steels. Recent plant operating experience with this alloy has indicated that this material may be susceptible to degradation. One of the major parameters relating to degradation of the head penetrations are the operational temperatures and stress levels in the penetration.

To determine the temperatures in the penetrations, a conjugate heat transfer analysis of the penetration fluid and metal was performed using Computational Fluid Dynamics (CFD) techniques. The analysis considered the fluid mass, momentum and energy conservation equations together with energy conservation in the structure using finite element numerical analysis techniques. The analysis utilized a "k-epsilon" turbulence model which defines the eddy viscosity in terms of "k", the turbulence energy, and "epsilon", the turbulent dissipation. The technique utilized to assure convergence is presented. Also included is a discussion of the discretization of the model and the impact of boundary condition variations on the solution.

The solution results indicated that two recirculation regions develop within the penetration. The uppermost circulation cell has hotter fluid rising along the centerline of the penetration. The lower circulation cell has hotter fluid rising along the inside diameter of the penetration and cooler fluid traveling downward along the centerline of the penetration. Thus, the top and bottom circulation cells rotate in opposite directions. This effect could clearly not have been evaluated via conventional thermal/hydraulic analytical tools. The CFD temperature results could then be used, in conjunction with the penetration stress distribution, to predict time to crack initiation and the crack growth rate in the penetrations.

INTRODUCTION

The primary function of the reactor vessel closure head penetrations, in conjunction with the reactor internal guide tube assembly, is to provide a straight, low friction path for control rod insertion and withdrawal from the fuel assemblies. Another function of the closure head penetrations is to provide conduits for instrumentation or for safety injection into the upper head region of the reactor. Some of the locations in the closure head have "spare" penetrations, that is. the penetrations are capped off with a head adapter plug. This type of capped reactor vessel head penetration is presented in Figure 1.

One of the important factors relative to potential Alloy 600 degradation in vessel head penetrations is the material temperature. The material temperature effect on crack growth for a postulated axial surface flaw has been presented in Reference [1] which indicated that significantly reduced crack growth occurs with reduced material temperatures on the order of 20-30°C for a given material and stress level. The temperature distribution in the penetration will be primarily influenced by:

a) the environmental conditions around the penetration above the closure head insulation blanket and

b) the free convection flow dynamics in the upper head and within the inside diameter of the penetration.

Figure 1

Schematic of the Capped Reactor Vessel Head Penetrations

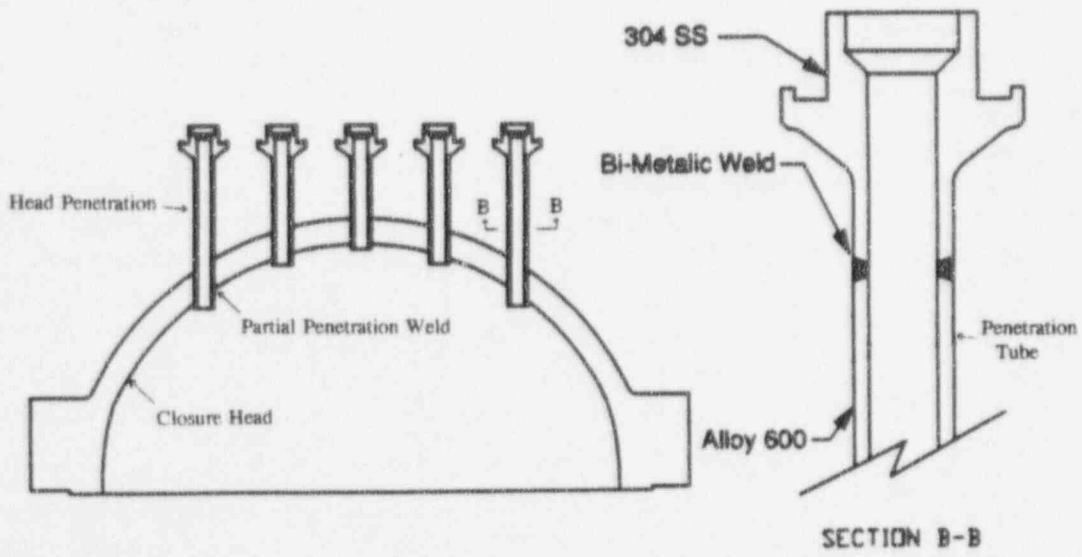

Recently, indications of cracking have been observed on certain "spare" penetrations with a head adapter plug installed at the top of the penetration. These indications have occurred in the vicinity of the partial penetration weld and up to the bi-metallic weld between the Alloy 600 and 304 stainless steel penetration tube. This paper provides a summary of the thermal/hydraulic calculations which were performed to determine the fluid velocities and temperatures within the capped penetration as well as the penetration structural temperature profiles at steady state full power conditions.

ANALYSIS MODEL

The capped closure head penetration, shown in Figure 2, consists of a penetration tube with a thickness of 1.5875 cm (0.625 inches) and an outside diameter of 5.08 cm (2.0 inches). Since the length of the tube varies depending upon its location on the closure head (See Figure 1), two models were developed representing either a peripheral or inner location. The only difference in these models was the axial length of the tube. The length of the tube (dimension "C" in Figure 2) was set to 104.22 cm (41.03125 inches) for peripheral locations and for the second model, the length was 71.28 cm (28.0625 inches) for inner locations, i.e. close to the centerline of the reactor vessel. A transition weld between the 304 stainless steel and Alloy 600 exists at approximately 31.75 cm (12.5 inches) from the top of the penetrations. A 8.255 cm (3.25 inch) insulation blanket is layered over the top surface of the closure head to reduce the heat loss off the closure head.

To determine the penetration temperature distribution a CFD analysis of the penetration was performed using the ANSYS and FLOTRAN (References [2] and [3]) computer codes. This analysis considered the fluid mass, momentum and energy conservation equations together with energy conservation in the structure using finite element numerical analysis techniques. Close agreement between this CFD approach and benchmark solutions can be found in Reference [4] for buoyancy driven flows within a square cavity with differential heating to the vertical sides. The benchmark solution, against which FLOTRAN results were compared, was derived using a stream function-vorticity formulation with a Boussinesq approximation for the density variations in Reference [5].

Figure 2

Capped Reactor Vessel Head Penetration Geometry

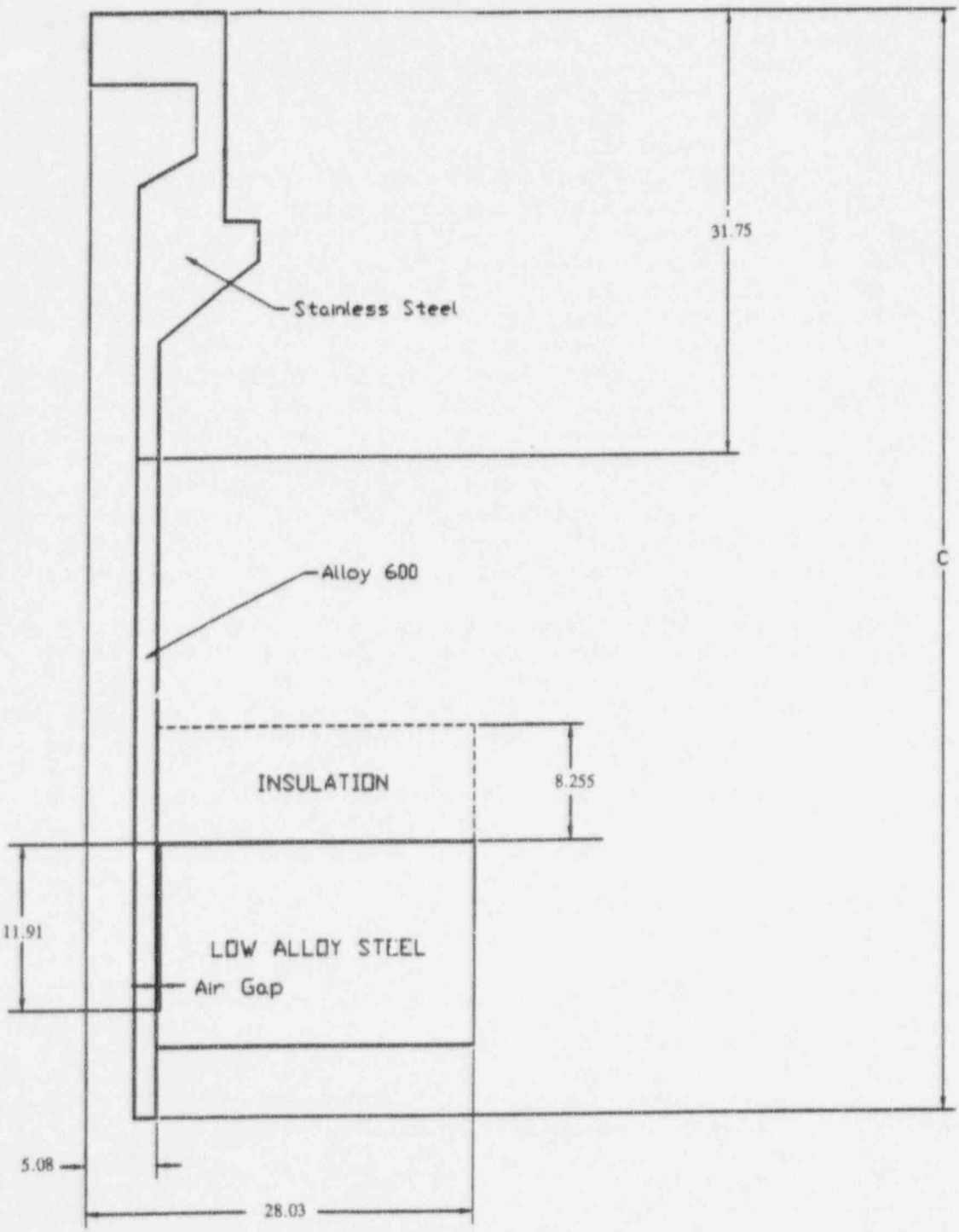

Two-dimensional axisymmetric finite element models of the capped inner and peripheral penetrations were created using the ANSYS computer code. The penetration analysis model, as shown in Figure 3 for the inner penetration, consisted of approximately 3700 elements and was discretized with sufficient detail to simulate the flow profiles in the critical regions and to determine the temperature gradients within the penetration. Note that a portion of the upper head region was also included in the modeling. Moreover, care was taken to create a detailed mesh near the inside surface of the penetration tube and the closure head. This was done to ensure an appropriate modelling of the heat transfer along these surfaces.

An adjusted heat transfer coefficient of 5.85×10^{-5} watts/cm^2-°C was applied to the upper surface of the closure head to account for the insulation blanket above the closure head and the convective heat transfer to the reactor cavity above the closure head. The heat transfer coefficient applied to the outside surface of the penetration above the insulation was 2.54×10^{-3} watts/cm^2-°C. The impact of the air gap between the closure head and penetration tube above the partial penetration weld was also included in the model. Modeling this extremely small air gap between the closure head and penetration tube above the partial penetration weld would have resulted in an undesirable aspect ratio for the finite elements. As a result, the gap size was increased and the material properties of those elements were adjusted to ensure that the appropriate heat transfer characteristics were modeled. A fluid velocity boundary condition, of relatively small magnitude, was utilized to ensure that the bulk upper head fluid temperature condition at the bottom of the model could be maintained at a value of 294.9°C (562.8°F) for all cases. The temperature boundary condition for the penetration outside surface above the insulation blanket on the closure head is a function of the heat losses from the control rod drive mechanisms and the containment cooling system. As a result, two cases were considered to determine the sensitivity of the impact of head cooling air temperature variations on the solution. Case #1 assumed the closure head cooling temperature was 21.1°C (70°F). Case #2 was performed assuming an air temperature of 35°C (95°F).

SOLUTION APPROACH

The Schmidt number may be considered the ratio of turbulent transport for momentum to the turbulent transport for energy (temperature). For all the FLOTRAN calculations performed in this study, a Schmidt number of 1.0 was utilized. In order to promote FLOTRAN convergence, the following technique was followed:

Figure 3

Capped Reactor Vessel Head Inner Penetration Analysis Model

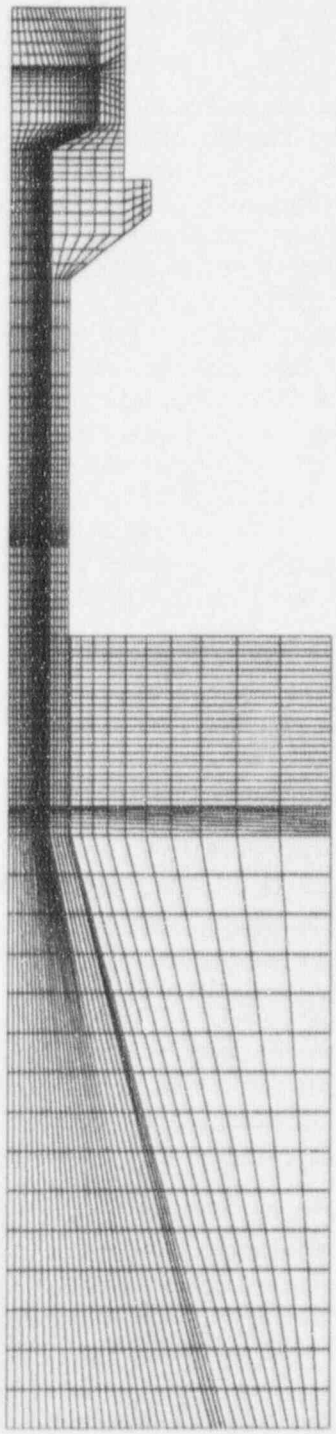

a. The first step in the solution approach was to use a value of laminar viscosity high enough to obtain a stable solution. During these iterations, the "k-epsilon" turbulence equations were turned off.

b. After monitoring the solution for a number of iterations, the laminar viscosity was reduced. Each reduction of viscosity was followed by a sufficient number of iterations to confirm convergence, and the cycle was then repeated.

c. At a laminar viscosity 1/2 to 1/5 of the original value used, the "k-epsilon" turbulence equations were turned on to establish a turbulence field. To retain solution stability the eddy viscosity calculated from this field was not used initially in the fluid momentum equations.

d. Once a stable "k-epsilon" field was established, the calculated eddy viscosity was added to the laminar viscosity and the resultant used in the fluid momentum equations. Initially, the relaxation parameter for viscosity was set to a very small value; that is, only a small amount of eddy viscosity was introduced. After a sufficient number of iterations, the relaxation parameter was increased to normal values.

e. Using this procedure, the laminar viscosity was eventually reduced to its' correct value and a converged flow field was obtained.

RESULTS

The results from the ANSYS/FLOTRAN analysis of the capped penetrations indicated that, during steady state 100% full power operation, two recirculation regions develop within the penetrations at both inner and peripheral locations. The uppermost circulation cell pattern, shown in Figure 4, has hotter fluid rising along the centerline of the penetration and cooler fluid traveling downward along the inside diameter surface of the penetration. However, the lower circulation cell (See Figure 5) has hotter fluid rising along the inside diameter of the penetration and fluid traveling downward along the centerline of the penetration. Therefore, the top and bottom circulation cells rotate in opposite directions. Figure 6 presents the streamlines of the two cells. The presence of these counter-rotational cells are a result of the bottom cell being heated whereas the top cell is being cooled.

Figure 4

Fluid Circulation Pattern in Upper Portion of the Capped Reactor Vessel Head Penetration at a Peripheral Location

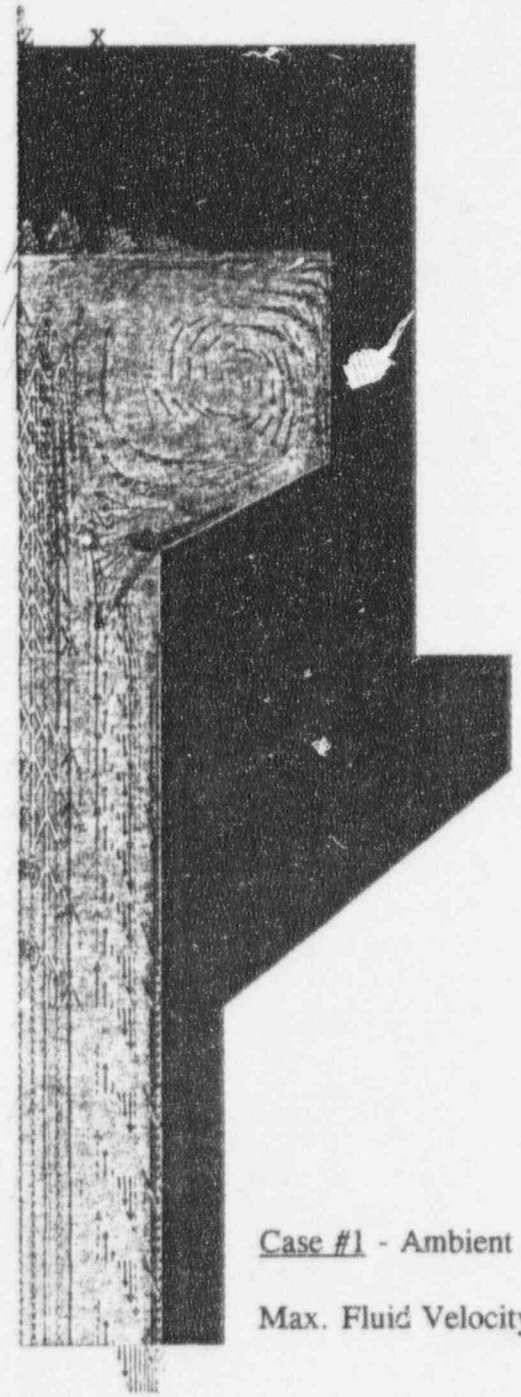

Case #1 - Ambient Air Temp. = 21.1 °C

Max. Fluid Velocity = 3.7 cm/sec

Figure 5

Counter Rotational Fluid Circulation Patterns in the Lower Portion of the Capped Reactor Vessel Head Penetration at a Peripheral Location

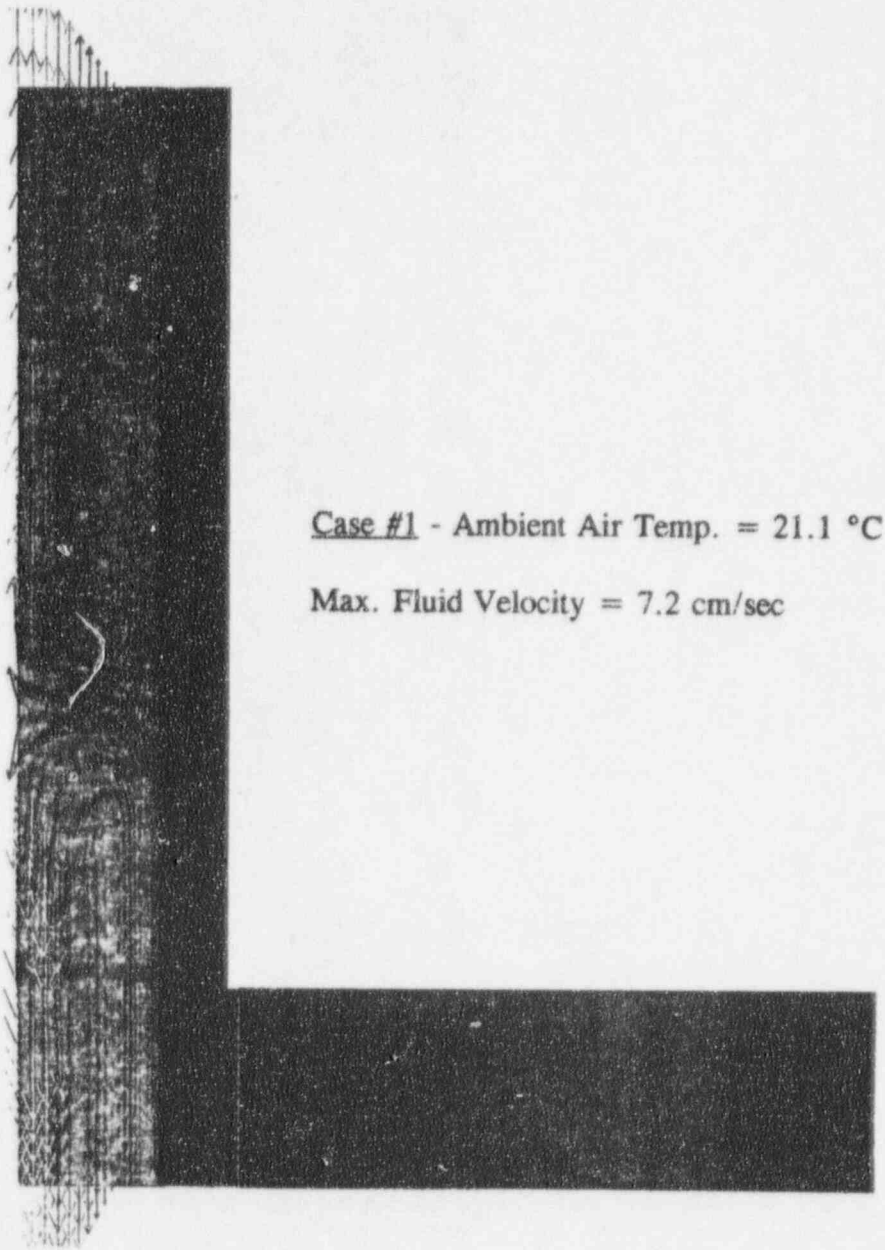

Case #1 - Ambient Air Temp. = 21.1 °C

Max. Fluid Velocity = 7.2 cm/sec

Figure 6

Counter Rotational Fluid Circulation Streamline Patterns

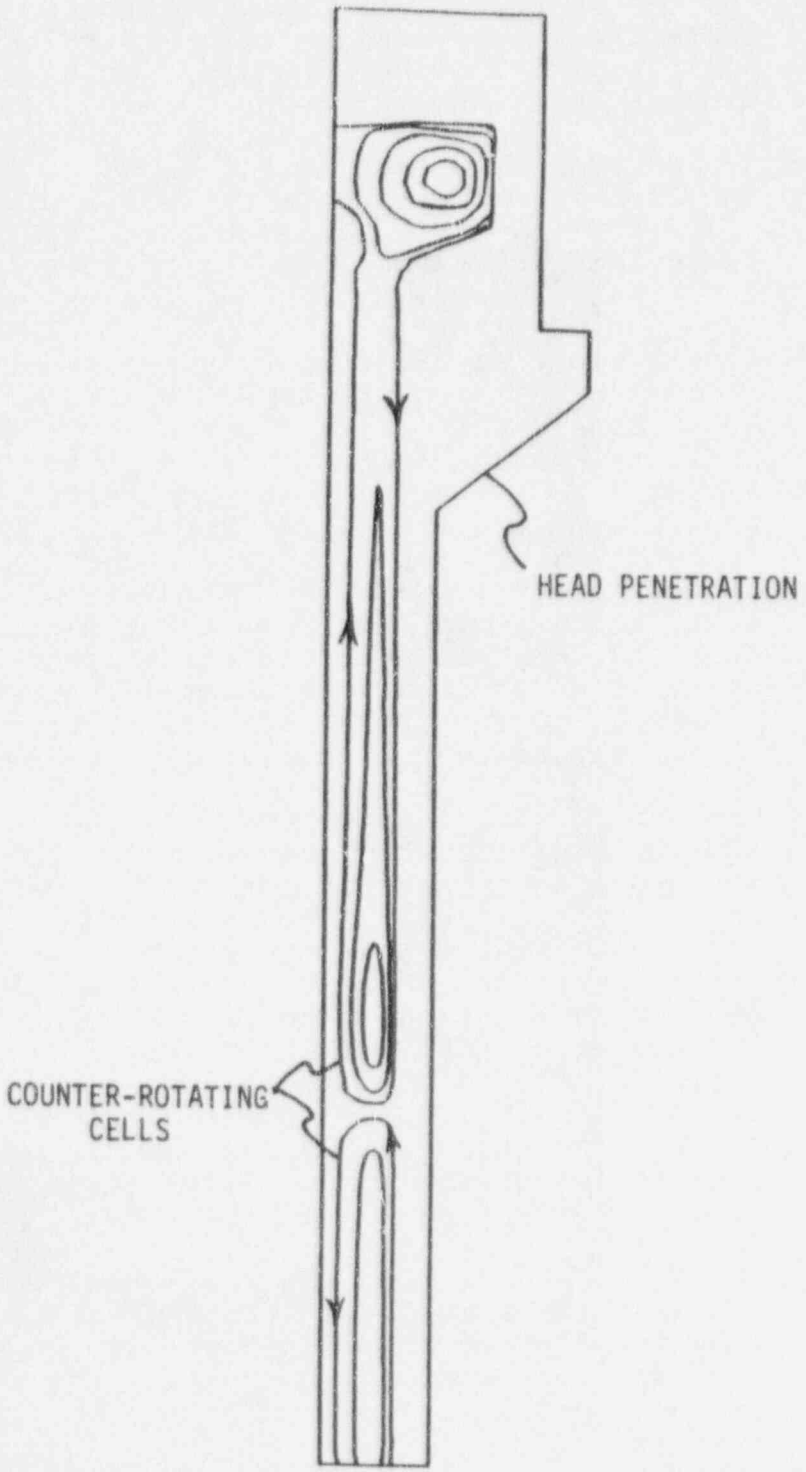

Comparing the ANSYS/FLOTRAN results for the analyzed cases indicates that:

1) changing the ambient temperature of the air surrounding the penetration above the closure head insulation blanket from 21.1°C to 35°C (70°F to 95°F) did not significantly change the axial interface location of the two recirculation cells within the penetration. Therefore, the predominant parameter relative to the axial position of the interface is believed to be the closure head insulation design (e.g. thickness).

2) the ambient air temperature change of 13.9°C (25°F) resulted in a temperature reduction of approximately 4.4°C (8°F) at the partial penetration attachment weld which located at the interface between the penetration and the lower surface of the closure head.

3) a comparison of the temperature contour profiles in the fluid and metal in the upper portion of the penetration is presented in Figures 7 and 8. These figures indicate that an ambient air temperature reduction of 13.9°C (25°F) results in a temperature reduction of approximately 6.1°C (11°F) for the minimum penetration temperature and a temperature reduction of approximately 4°C (7°F) at the outside surface of the penetration and at the bimetallic penetration weld. As expected, the variation in the ambient air temperatures had less of an impact on the metal penetration temperatures for those portions of the penetration closer to the reactor vessel closure head.

4) the ambient air temperature reduction of 13.9°C (25°F) did not significantly change the fluid velocities in the upper recirculation cell. However, the strength of the upper recirculation cell was substantially increased for the inner penetration relative to the strength of the upper recirculation cell for the peripheral location. The velocity in the upper recirculation cell increased from 3.8 cm/sec (for the peripheral locations) to 4.9 cm/sec for the inner penetration locations. It is not clear precisely why the recirculation velocities are higher for the inner penetrations. One possibility is the lower frictional drag of the upper cell in the inner penetrations.

5) the interface between the recirculation cells moved somewhat lower in the inner penetration relative to that location of the interface for the peripheral penetrations, possibly because of the greater strength of the upper cell.

6) the average radial heat flux along the inside diameter of the penetration above the insulation blanket was determined to be 0.65 watts/cm^2 with an ambient air temperature of 35°C (95°F). The impact of the ambient air temperature reduction of 13.9°C (25°F) was determined to result in an average radial heat flux of 0.69 watts/cm^2. Note that the average radial heat flux along the inside diameter of the penetration for the inner penetration was not significantly different than the value for the peripheral penetration.

7) the average heat transfer film coefficient along the inside diameter of the penetration above the insulation blanket, which could be extracted from the FLOTRAN results, was determined to be 3.524 x 10^{-3} watts/cm^2-°C for the ambient temperature of 35°C (95°F) case. As expected, the impact of the ambient air temperature reduction of 13.9°C (25°F) did not significantly change the average heat transfer film coefficient along the inside diameter of the penetration especially in the region below the insulation blanket. Moreover, the film coefficient for the inner penetration along the inside diameter of the penetration was also not significantly different than the value obtained for the peripheral penetration.

CONCLUSIONS

A computational fluid dynamic analysis of two types of capped reactor vessel closure head penetrations have been performed. This analysis determined the fluid velocity and temperature profiles within the penetration and the temperature distribution in the penetration at steady state full power operation for two values of air temperatures above the closure head. In addition, the sensitivity on the change in penetration axial length was also evaluated. For all cases considered, two circulation cells were found to be developed within the penetration fluid at steady state full power conditions. Moreover, these circulation cells within the penetration were found to rotate in opposite directions since the bottom cell is being heated whereas the top cell is being cooled. Also, the strength of the upper circulation cell was found to be greater for the inner penetrations relative to that found in the peripheral locations. One possibility for this phenomena is the lower frictional drag of the upper cell for the inner penetrations.

Figure 7

Temperature Contours in the Upper Portion of the Capped Reactor Vessel Head Penetration at a Peripheral Location

Case #1 - Ambient Air Temp. = 21.1 °C

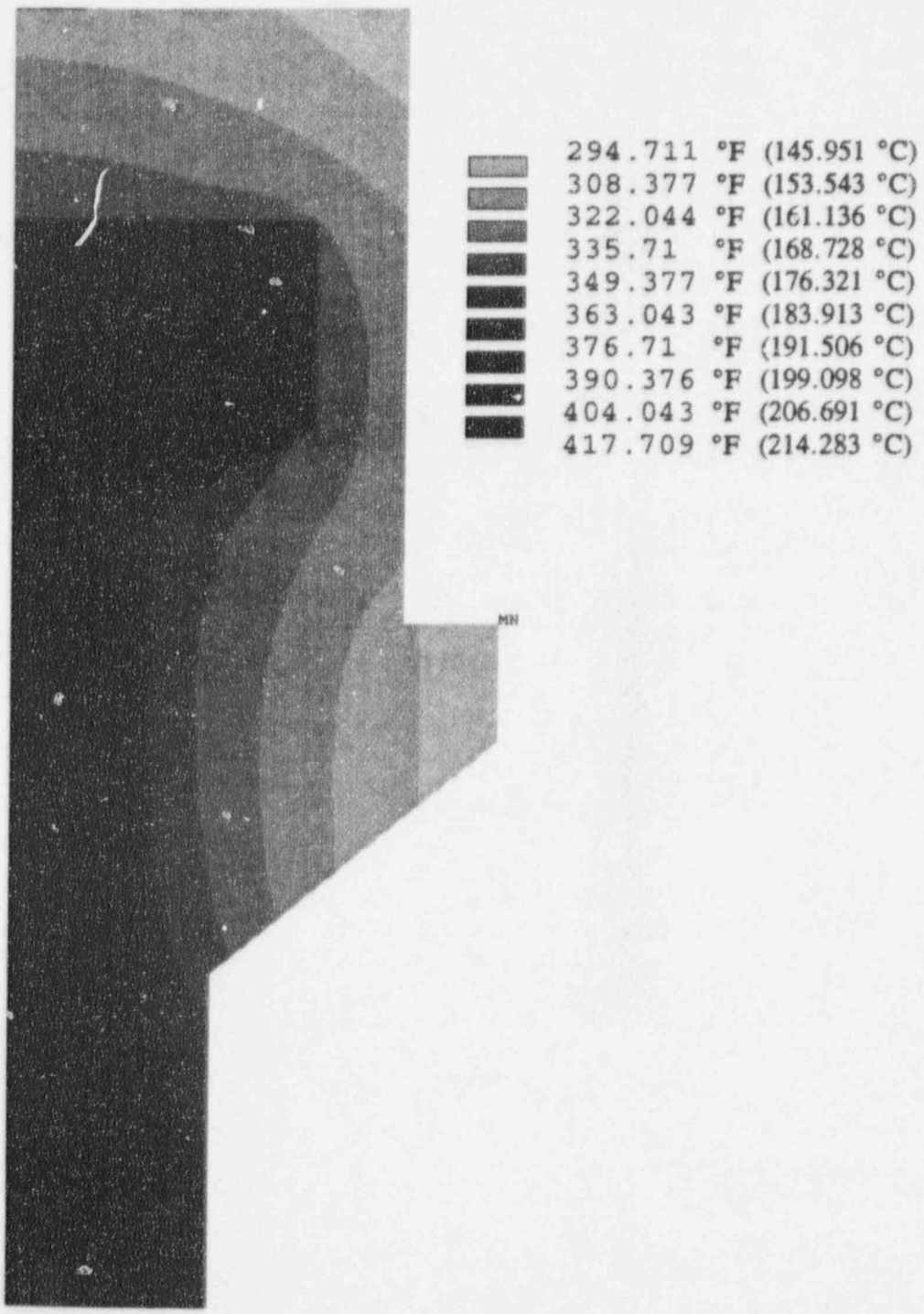

Figure 8

Temperature Contours in the Upper Portion of the Capped Reactor Vessel Head Penetration at a Peripheral Location

Case #2 - Ambient Air Temp. = 35 °C

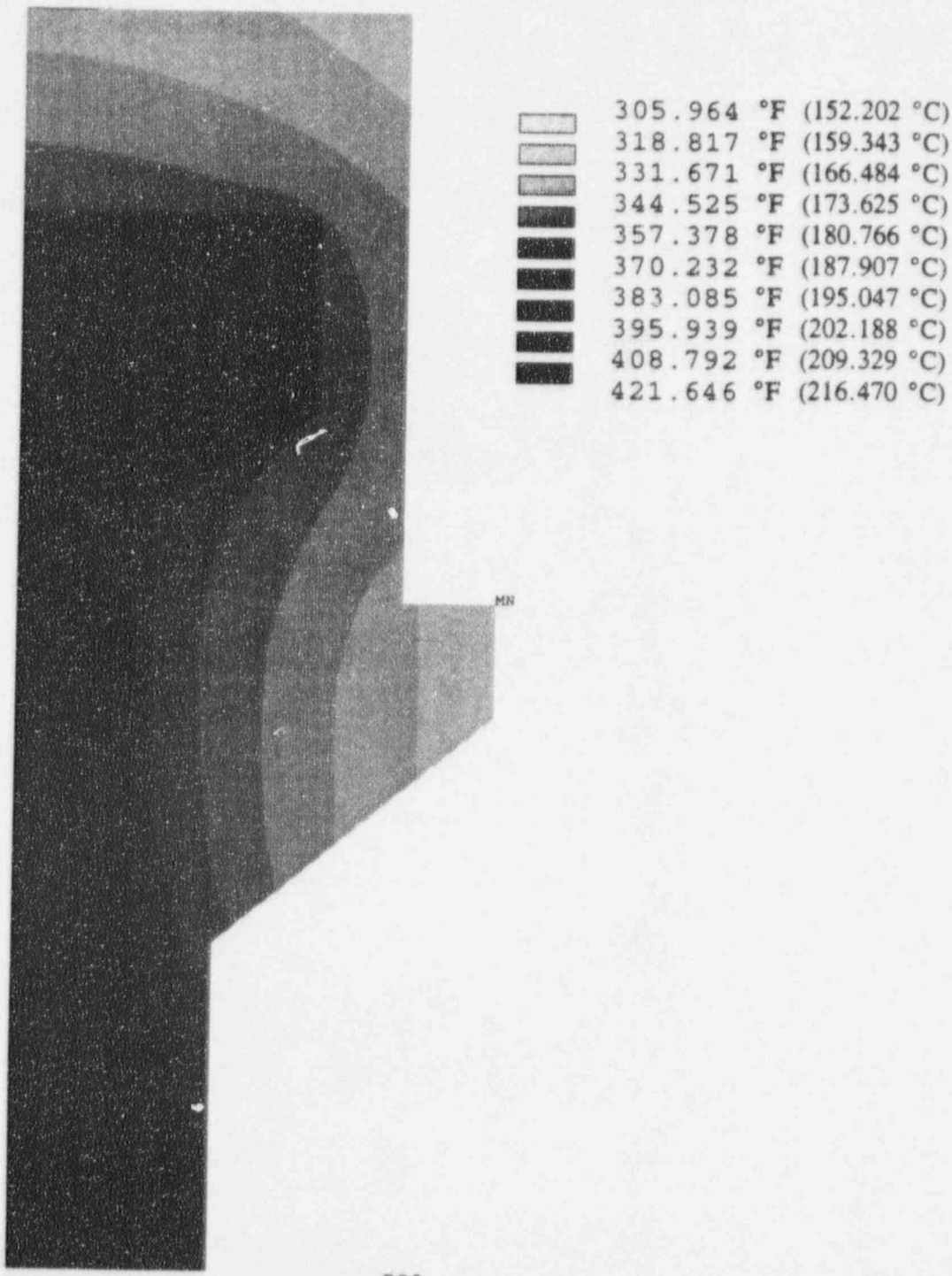

REFERENCES

[1] W. H. Bamford, et. al., "An Integrated Industry Approach to the Issue of Head Penetration Cracking for the USA", PVP-Vol. 288 Service Experience and Reliability Improvement: Nuclear, Fossil, and Petrochemical Plants, Presented at the 1994 Pressure Vessels and Piping Conference, Minneapolis, Minnesota, June, 1994.

[2] "ANSYS User's Manual for Revision 5.0, DN-R300: 50-1 to 50-4", Swanson Analysis Systems, Incorporated, December 23, 1992.

[3] COMPUFLO Inc., "FLOTRAN User's Manual, Release 2.1", June, 1992.

[4] COMPUFLO Inc., "FLOTRAN Benchmark Manual, First Edition, 1991.

[5] G. DeVahl Davis, "Natural Convection of Air in a Square Cavity: A Bench Mark Numerical Solution", International J. Numerical Methods Fluids, Vol. 3 249-264, (1983).

THEHYCO-3DT: THERMAL HYDRODYNAMIC CODE FOR THE 3 DIMENSIONAL TRANSIENT CALCULATION OF ADVANCED LMFBR CORE

S.G. Vitruk[1], A.S. Korsun[1], P.A. Ushakov[2], B.N. Gabrianovich[2]

E-mail: root@thehy.mephi.msk.su
[1]Moscow Engineering Physics Institute, Kashirskoe shosse 31, Moscow, 115409, Russia
[2]Institute of Physics and Power Engineering, Obninsk, 249020, Russia

Abstract.

The multilevel mathematical model of neutron thermal hydrodynamic processes in a passive safety core without assemblies duct walls and appropriate computer code SKETCH, consisted of thermal hydrodynamic module THEHYCO-3DT and neutron one, are described.

A new effective discretization technique for energy, momentum and mass conservation equations is applied in hexagonal - z geometry.

The model adequacy and applicability are presented. The results of the calculations show that the model and the computer code could be used in conceptual design of advanced reactors.

1. Introduction.

The continuously increasing requirements to safety standards of nuclear power plants result in appearance of nuclear reactor projects of new generation. Such projects need an analysis of transient events ranging from normal operational states to catastrophic accident excursions. These events demand multiple, three-dimensional, time dependent calculations. These calculations can be very expensive because of multiple unknowns involved. Due to these situations, the efficient algorithms for mathematical modelling have been created in Moscow Engineering Physics Institute [7,8,9]. In particular computer code named **SKETCH** (**S**pace **K**inetic and **T**hermal **H**ydrodynamic) with thermal hydrodynamic module **THEHYCO-3DT** (**THE**rmal **HY**drodynamic **CO**de - **3** **D**imensional **T**ransient) has been developed for analysing of transient events. This report is mainly concerned with thermal and hydrodynamic three-dimensional transient processes in passive safety core without assemblies duct walls. The core may consist of arbitrary type fuel elements and one phase coolant. The thermal hydrodynamic core problems have been solved in approximation of the porous media model. Thus the code, written for LMFBR, can be used to analyse the complex safety problems related to different reactor types.

The computer code may be used to obtain some optimal parameters of core by means of various calculations and predicts temperature and velocity fields in the following processes:

- top or bottom blockages of core;
- local or global changes of nuclear power or coolant flow;
- et al.

2. Mathematical model.

The multilevel mathematical model of core thermohydrodynamics is used in computer code THEHYCO-3DT for complex calculation.

At the "CORE" level, conservation equations, state equation and boundary conditions for viscous compressible fluid are written in approximation of the porous media model as

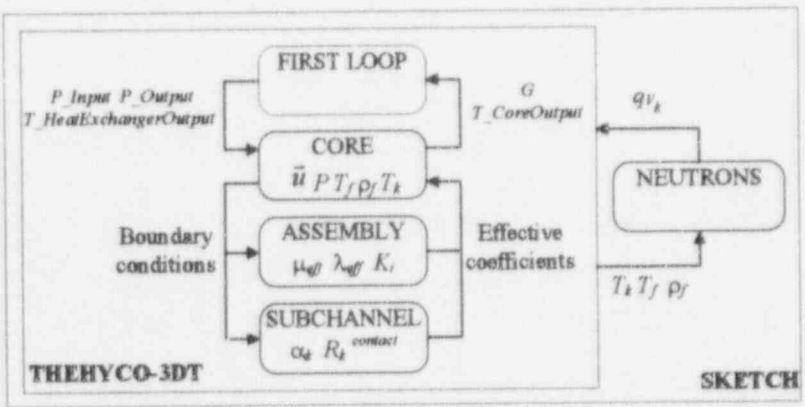

Figure 1. The core multilevel model, realised in computer code SKETCH.

- mass conservation:

$$\frac{\partial\left(\varepsilon_f \rho_f\right)}{\partial \tau} + div\left(\varepsilon_f \rho_f \vec{u}\right) = 0; \tag{1}$$

- momentum conservation ($i = x, y, z$):

$$\frac{\partial\left(\varepsilon_f \rho_f u_i\right)}{\partial \tau} + div\left(\varepsilon_f \rho_f \vec{u} u_i\right) = \left(div\left(\vec{\vec{\sigma}}\right) + \varepsilon_f gradP + \varepsilon_f \rho_f \vec{g}\right) \cdot \vec{e}_i - K_f \rho_f |\vec{u}| u_i, \tag{2}$$

- energy conservation:

$$c_f\left(\frac{\partial\left(\varepsilon_f \rho_f T_f\right)}{\partial \tau} + div\left(\varepsilon_f \rho_f \vec{u} T_f\right)\right) = -div\left(\vec{q}\right) + \sum_{k=1}^{type} s_k \alpha_k \left(T_k|_\Gamma - T_f\right); \tag{3}$$

- state equation:

$$\rho_f = \rho_f\left(P, T_f\right). \tag{4}$$

- On the free boundary, velocity $\vec{u}(x,y,z,\tau)$ is assigned and pressure $P(x,y,z,\tau)$ is defined from Neyman condition for eq.(2). On the duct boundary, normal velocity $u_\perp$ is equal zero and longitudinal velocity $u_|$ is defined from

$$\vec{e}_n \cdot grad\, u_| + u_| / l_{eff} = 0,$$

where $\vec{e}_n$ - normal vector and l_{eff} - extrapolated addition to boundary [1]. On the free boundary, temperature $T_f(x, y, z, \tau)$ is defined from condition of full mixing on the outside and the duct boundary is adiabatic.

In anisotropic porous media, heat flux vector $\vec{q}$ have the expression $q_i = -\lambda_{ij} \partial T_f / \partial x_j$. In general case six components of symmetric tensor λ_{ij} have been evaluated by A.S. Korsun. We simplify $\vec{q}$ in eq. (3) to $-\lambda_{eff} gradT_f$, where λ_{eff} is effective thermal conductivity in cross directions under longitudinal flowing of rod bundles. According to estimations the above assumption decries effective diffusion heat transfer. In approximation of incompressible fluid and steadiness of μ_{eff}, we simplify $div\left(\vec{\vec{\sigma}}\right) \cdot \vec{e}_i$ in eq. (2) to $\mu_{eff} div\left(grad\, u_i\right)$.

We complicate the equations of energy conservation for k-type fuel elements in porous media approximation. At the same time in every point of fluid the following equations for $T_{k,x,y,z}(r, \tau)$ are solved (in axial geometry, for example)

$$\left[\rho c \frac{\partial T}{\partial \tau} = \frac{1}{r}\frac{\partial}{\partial r}\left(r\lambda \frac{\partial T}{\partial r}\right)\right]_k + \begin{bmatrix} q_{Vk}, \text{if fuel} \\ 0, \quad \text{if clad} \end{bmatrix}, \tag{5}$$

with boundary condition between fuel and cladding

$$\left[-\left[\lambda \frac{\partial T}{\partial r}\right]^{fuel} = \frac{1}{R^{contact}}\left(T^{clad} - T^{fuel}\right)\right]_k, \tag{6}$$

with boundary condition between cladding and fluid

$$-\lambda_k \frac{\partial T_k^{clad}}{\partial r} = \alpha_k \left(T_f - T_k^{clad} \right), \tag{7}$$

where $k = 1 \ldots type$.

At the "ASSEMBLY" level, the effective viscosity μ_{eff}, the effective thermal conductivity λ_{eff} and the resistance-form force coefficients K_i are evaluated from experiments or preliminary calculation by channel model based code such as COBRA-IV, SABRE et cetera [2]. These codes may be used in code THEHYCO-3DT as submodules. The experimental data [3,4] are used in the code release version.

For example, in the porous media, consisted of rod bundles, effective coefficients are defined as

$$K_i = \varepsilon_f \frac{\xi_i}{2 d_G}; \tag{8}$$

$$\lambda_{eff} = \varepsilon_f \rho c |u_z| \frac{l_c}{d} \frac{A}{l/d - 1} \mu^T$$

$$\mu_{eff} = \varepsilon_f \rho |u_z| \frac{l_c}{d} \frac{A}{l/d - 1} \mu^G \tag{9}$$

where ξ_i - friction factor along i direction [3], μ^T, μ^G - coefficients of inter channel exchange of energy and momentum (1/m) [4], d_G - hydraulic diameter (m), d - fuel rod diameter (m), l_c - distance between centres of adjacent channels (m), l - distance between centres of fuel rods (m), A - area of channel cross section (m^2).

At the "SUBCHANNEL" level the contact thermal resistance $R_k^{contact}$ is defined from simple model of thermal expansion without internal stress and quasi state heat transfer coefficient α_k from the experimental data [3].

At the "FIRST LOOP" level (fig. 1), the core is modelling as point hydraulic resistance and power injection. The bottom (*P_input*) and top (*P_Output*) collector pressures and the outlet heat exchanger temperature (*T_HeatExchangerOutput*) are calculated from this model. At each time step, *T_HeatExchangerOutput*, *P_input* and *P_Output* are passed as core boundary conditions from the "FIRST LOOP" level to the "CORE" level. The top collector temperature (*T_CoreOutput*) and the flow rate G are obtained from core calculation results. At each time step, *T_CoreOutput* and G are passed back from the "CORE" level to the "FIRST LOOP" level.

At the "NEUTRONS" level, three-dimensional transient distribution of the neutron flux is described by few - group space - time dependent neutron kinetics equations in diffusion approximation and equations for the generation of the delayed neutron precursors [7,8,9]. The model has the following characteristics:

- diffusion approximation;
- one mesh point per hexagonal assembly in each horizontal plane;
- arbitrary axial mesh points for three-dimensional calculations;
- six groups of delayed neutrons;
- arbitrary energy groups (depend on the kind of modelled transient and computer resources).

The power density in k-type fuel elements $q_{V,k}$ is obtained from the "NEUTRONS" level to the "FUEL ELEMENTS" level. The temperature distributions in k-type fuel element T_k, fluid temperature T_f and density ρ_f are passed back (fig. 1).

3. Numerical solution.

At the "CORE" level, the idea of F.H. Harlow & J.E. Welsh method [5] is used for solving transient three - dimensional equations (1)-(4) for viscous incompressible fluid with space - time dependent coefficients and complex feedback. Instead of the mass conservation equation (1) the Poisson equation for pressure is considered. The discrete analogy of the Poisson equation is linear combination of the initial equations (1-2) discrete analogies. It should be pointed out, that discrete analogy obtained directly from differential Poisson equation isn't compatible with the initial equations (1-2) discrete analogies.

The special displaced meshes allow to use correctly this method, only. Until now, the method was applied on the Cartesian coordinate system. The authors extended the method applicability to hex-z geometry (fig. 2).

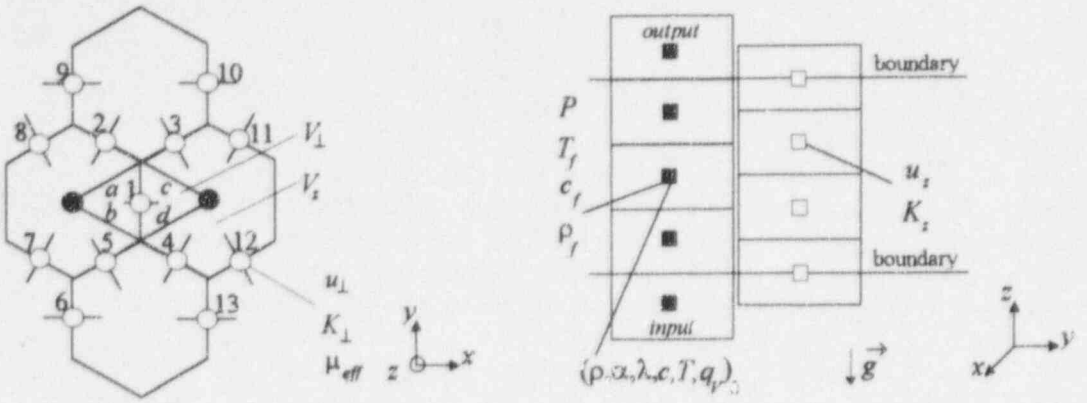

Figure 2. The special displaced meshes in hex-z geometry for description mass, energy and momentum (13-points pattern) transfer.

In the first, the normal components of velocity vector are defined on the a, b, c, d bounds of control volume (c.v.) N 1:

- $u_a=(u_3+u_8+u_5)/3$, $u_b=(u_4+u_7+u_2)/3$, $u_c=(u_{11}+u_2+u_4)/3$, $u_d=(u_5+u_{12}+u_3)/3$.

In the second, if normal component of velocity vector is outside of c.v. N 1, the momentum difference δ is proportional

- $\delta_a \approx u_a\, u_1$, $\delta_b \approx u_b\, u_1$, $\delta_c \approx u_c\, u_1$, $\delta_d \approx u_d\, u_1$,

else

- $\delta_a \approx u_a\, (u_1+u_9)/2$; $\delta_b \approx u_b\, (u_1+u_6)/2$; $\delta_c \approx u_c\, (u_1+u_{10})/2$; $\delta_d \approx u_d\, (u_1+u_{13})/2$.

All equation discrete analogies are constructed by the control volume integrating method and on the displacement meshes in hex-z geometry (fig. 2). The upwind difference scheme is used for the approximation of convection terms and the central difference scheme - for the diffusion ones. The fully implicit time technique is applied.

The discrete analogy of the equations (1) is

$$\varepsilon_f \frac{\rho_f^{\tau+\delta_\tau} - \rho_f^{\tau}}{\delta_\tau} + \frac{1}{V_z}\left[\sum_{l=1}^{8}\left(\rho_f \vec{u}_l \left(\varepsilon_f \vec{S}\right)_l\right)\right]^{\tau+\delta_\tau} = 0. \qquad (10)$$

The equation of momentum conservation (2) is solved in terms of normal projections to the surface of pressure control volume:

$$\varepsilon_f \frac{\left(\rho_f u_z\right)^{\tau+\delta_\tau} - \left(\rho_f u_z\right)^{\tau}}{\delta_\tau} =$$

$$\left[\frac{1}{V_z}\left(-\sum_{l=1}^{8}\rho_f \vec{u} u_z \left(\varepsilon_f S\right)_l\Big|_{\vec{n}_l} + \sum_{l=1}^{6}\mu_{eff}\, grad\, u_z\, S_l\Big|_{\vec{n}_l}\right) - K_z \rho_f |\vec{u}| u_z - \varepsilon_f \frac{\delta P}{\delta_z} - \varepsilon_f \rho g\right]^{\tau+\delta_\tau}; \qquad (11)$$

$$\varepsilon_f \frac{\left(\rho_f u_\perp\right)^{\tau+\delta_\tau} - \left(\rho_f u_\perp\right)^{\tau}}{\delta_\tau} = \left[-\frac{1}{V_\perp}\sum_{l=1}^{4}\rho_f \vec{u} u_\perp \left(\varepsilon_f S\right)_l\Big|_{\vec{n}_l} - K_\perp \rho_f |\vec{u}| u_\perp - \varepsilon_f \frac{\delta P}{\delta_\perp}\right]^{\tau+\delta_\tau}. \qquad (11a)$$

The discrete analogy of equations (3) is

$$c_f \varepsilon_f \frac{\left(\rho_f T_f\right)^{\tau+\delta_\tau} - \left(\rho_f T_f u_z\right)^{\tau}}{\delta_\tau} =$$

$$\left[\frac{1}{V_z}\left(-\sum_{l=1}^{8}\rho_f \vec{u} T_f \left(\varepsilon_f S\right)_l\Big|_{\vec{n}_l} + \sum_{l=1}^{6}\lambda_{eff}\, grad\, T_f S_l\Big|_{\vec{n}_l}\right) + \sum_{k=1}^{type} s_k \alpha_k \left(T_k\Big|_\Gamma - T_f\right)\right]^{\tau+\delta_\tau} \qquad (12)$$

In all required point of porous media the same discrete analogy has been constructed for the eq.(5), too. The equations system (1-5) with boundary conditions are solved by fully implicit iteration technique along all directions [6].

In approximation, neither z direction nor x, y directions of coolant motion are preferred, and in the calculation area, no assumptions about the pressure field are made. All mentioned above allow to calculate the arbitrary coolant flows without time step limitation.

4. Model adequacy.

Each module of thermal hydrodynamic code THEHYCO-3DT has been tested separately, but complex experiment is still required. The hydrodynamic module is the most significant one. For this module P.A. Ushakov, B.N. Gabrionovich have carried out the experiment on assembly, flowed by air.

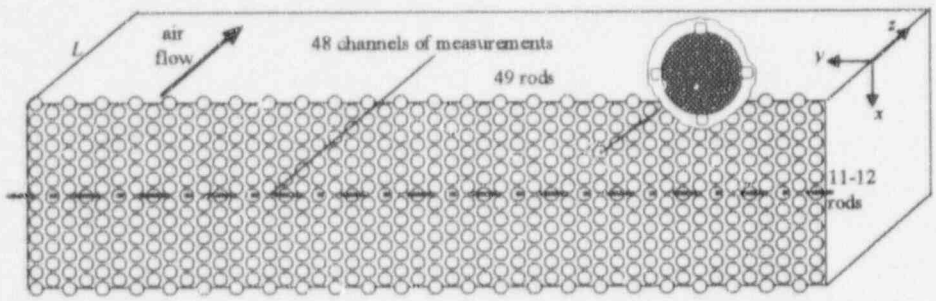

Figure 3. Experimental assembly (d=15mm, L/d=84, T/d=62, s/d=1.13, Re=7900).

The assembly consisted of 563 wire wrap rods ([11+12] rows × 49 columns). In the Fig.3, the experimental assembly is shown (d - rod diameter, L - assembly length, T - period of wire wrap, s-distance between centres of adjacent channels). The velocity field has been measured inside the assembly under the conditions of 37% input or/and output blockages

- the central blockage of input

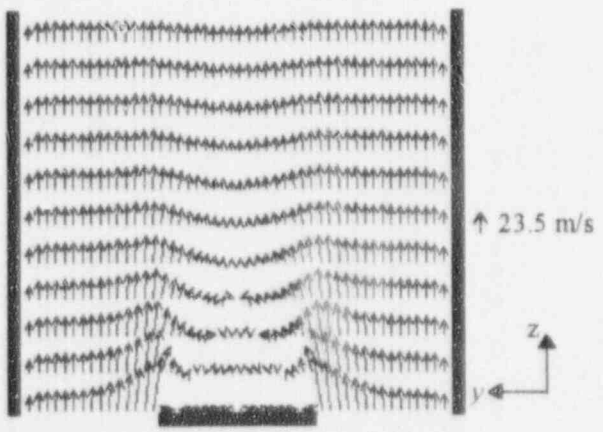

Figure 4. Velocity field.

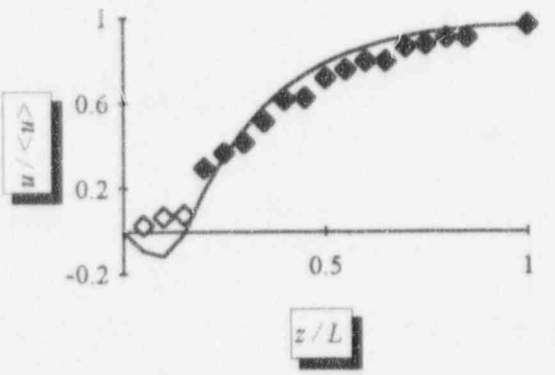

(- calculation, ♦ experiment, ◊ accuracy loss)
Figure 5. Axial velocity in central channel.

- the wall-adjacent blockage of input

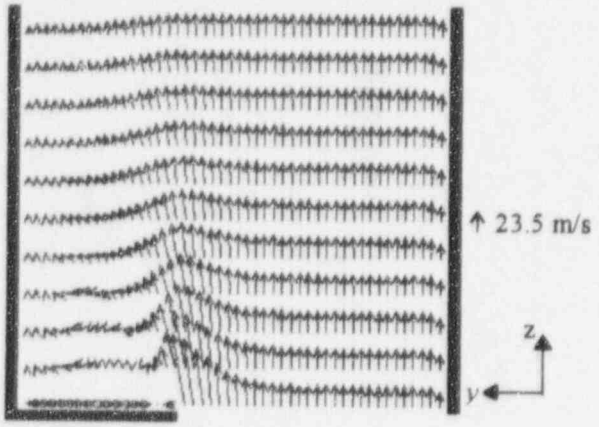

Figure 6. Velocity field.

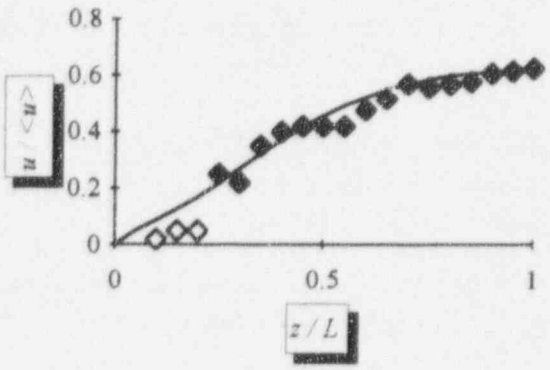

(- calculation, ♦ experiment, ◊ accuracy loss)
Figure 7. Axial velocity in wall-adjacent channel.

- the central blockage of output

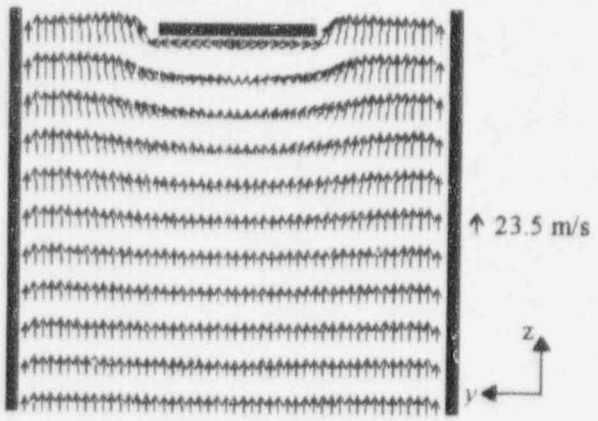

Figure 8. Velocity field.

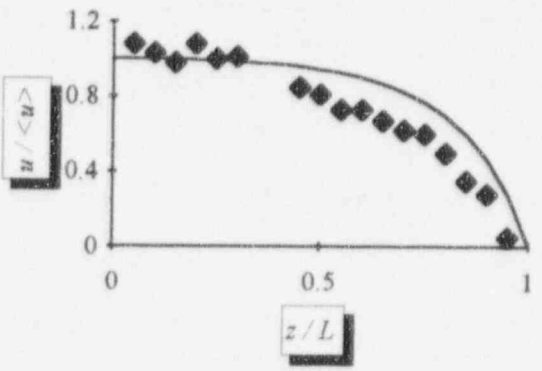

(- calculation, ♦ experiment)
Figure 9. Axial velocity in central channel.

- the wall-adjacent blockage of output

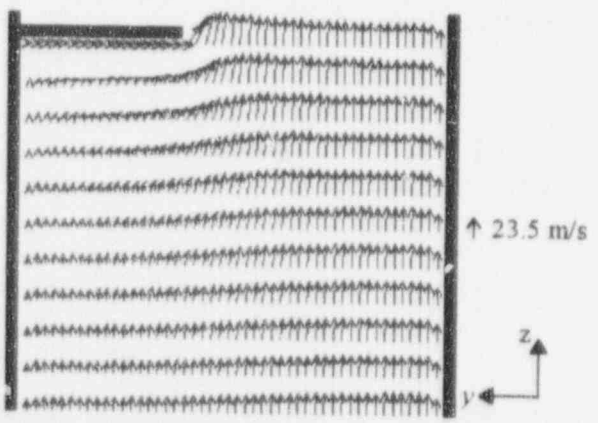

Figure 10. Velocity field.

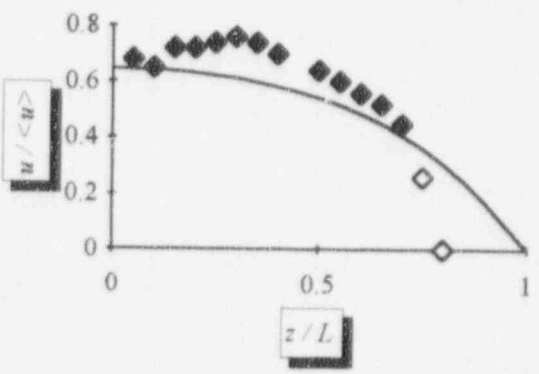

(- calculation, ♦ experiment, ◊ accuracy loss)
Figure 11. Axial velocity in wall-adjacent channel.

- the wall-adjacent blockage of input and output

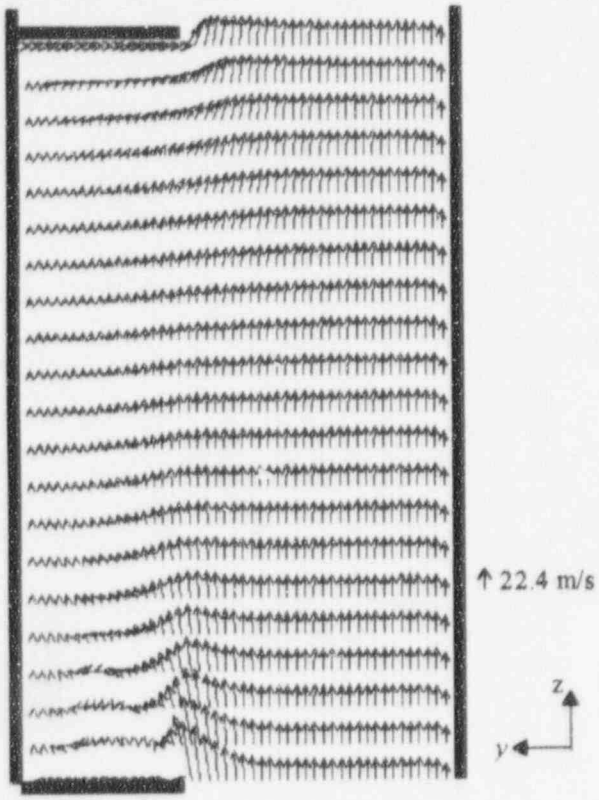

Figure 10. Velocity field.

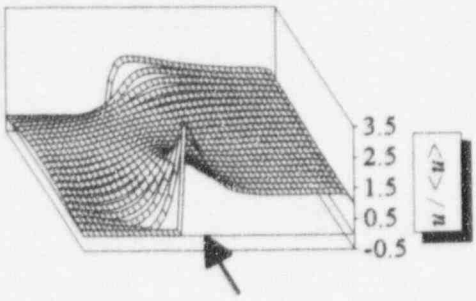

Figure 11. Axial velocity.

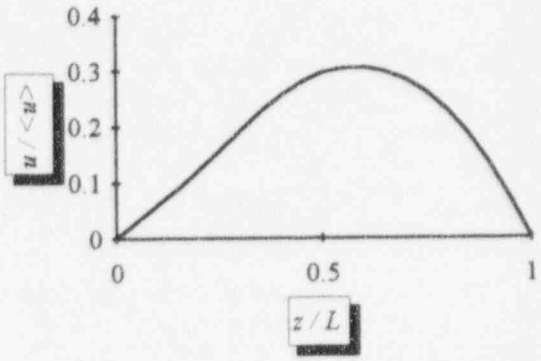

(- calculation, experiment data are impossible)
Figure 12. Axial velocity in wall-adjacent channel.

5. Model applicability for LMFBR.

To demonstrate the SKETCH code operation capability, the calculations have been done [8,9] for accidents caused by control rod self-moving without scram - TOP WS and loss of flow without scram - LOF WS in advanced fast reactor with liquid lead coolant [10]. Here, the LOF WS accident caused by blocking a core input is presented. The core consist of 211 assemblies without duct walls. The wall-adjacent input blockage overlaps the 36 assemblies. The calculations up to 80 sec. have been carried by SKETCH (Fig. 14).

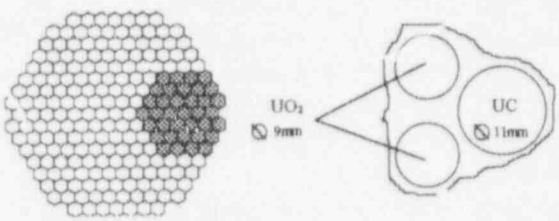

Figure 13. Core and subchannel (*type* = 2).

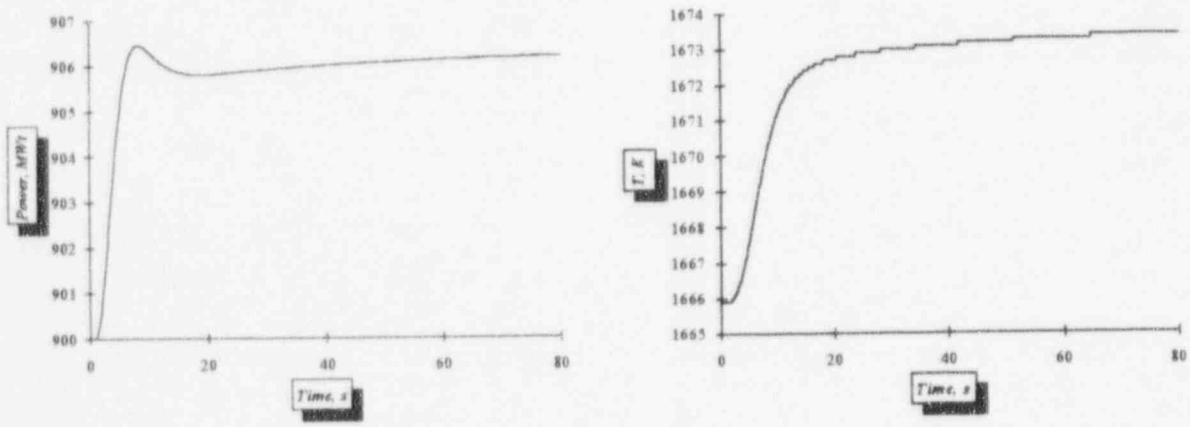

Figure 14. Reactor power and fuel (UO_2) temperature.

Following figures demonstrate calculated values in the first cross section of core behind the blockage:

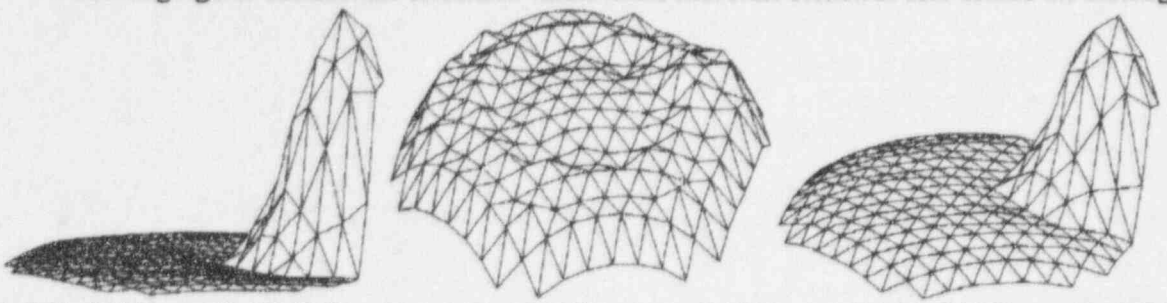

a) ($\min T_f$=664 K, $\max T_f$=1045 K) b) ($\min T_k$=1145 K, $\max T_k$=1815 K) c) ($\min T_k$=707 K, $\max T_k$=965 K)

Figure 15. The lead coolant (a), UO_2 fuel (b) and UC fuel (c) temperature (τ=5 s).

Conclusions.

The physical consistency of the results allows to conclude that THEHYCO-3DT (SKETCH) computer code has operational capability. The accuracy and speed of the model and the code suggest that they might be valuable for conceptual design of new generation high safety liquid metal reactor. It should be pointed out that further liquid metal experimental data are required for code validation.

The porous media model, used in THEHYCO-3DT, is universal approach. That is why code works in core as well as in assembly. But for any intended code application the effective coefficients must be corectly defined.

The code requires 486DX o^r higher processor and about 4 Mb of memory, only.

Table of Nomenclature.

Symbol	Quantity	SI unit
$\vec{\vec{\sigma}}$	stress tensor (without pressure)	kg/ms^2
$\vec{q}$	heat flux	W/m^2
μ_{eff}	effective dynamic viscosity	kg/m s
λ_{eff}	effective thermal conductivity of fluid	W/m K
K_i	coefficients of resistance-form force	1/m
ε_f	porosity	-
Γ	boundary between fluid and fuel element	-
T	temperature	K
ρ	density	kg/m^3
c	specific heat capacity	J/kg K
$\vec{u}$	velocity vector	m/s
P	pressure	Pa
s_k	surface area per volume unit	1/m
α_k	heat transfer coefficient	W/m^2 K
$R_k^{contact}$	contact thermal resistance	m^2 K/ W
q_{Vk}	power density	W/m^3
$\vec{g}$	acceleration vector of gravity	m/s^2
$\vec{n}$	normal vector	-
$\vec{e}_i$	unit vector	-
S_l	area of c.v. l surfase	m^2
V	value of control volume	m^3
	Subscripts and superscripts	
$(\,)_k$	k-type fuel elements	
$(\,)_f$	fluid	
$(\,)_i$	i coordinate	
$(\,)^{clad}$	cladding	
$(\,)^{fuel}$	fuel	

References.

[1] A.S. Korsun, M.S. Sokolova, "Boundary condition for porous media model", Proceedings of the First Russian National Conference on Heat Exchange, Moscow, Russia, vol. 7, pp. 112-118, (1994).
[2] F.E. Dunn, D.J. Malloy and O.Mohr, "Computer Code Abstract. Liquid-Metal-Cooled Reactor Thermal-Hydraulic Calculations in the United States," Nuclear Science and Engineering 100, 558-563 (1988).
[3] P.L. Kirillov and other, Thermohydraulic Calculation Handbook (Nuclear Reactor, Heat Exchanger, Vapour Generator), Moscow (1990).
[4] A.V. Zhukov and other, Thermohydraulic Calculation of Fast Reactor with Liquid Metal Coolant, Moscow (1985).
[5] F.H. Harlow and J.E. Welsh. Phys. Fluids 8, 2182-2189, (1965).
[6] A.S. Korsun and S.G. Vitruk. "A two-level mathematical model and computer code for calculation of transient, thermal-hydraulic nuclear core regime," //1992 Annual Report by Moscow Engineering Physics Institute, Moscow, Russia, pp. 54-62.
[7] N.V. Schukin, A.S. Korsun, S.G. Vitruk, V.G. Zimin, S.D. Romanin, "Mathematical model and computer code for the analysis of advanced fast reactor dynamics", Proceedings of the Joint International Conference on Mathematical Methods and Supercomputing in Nuclear Application, M&C+SNA'93: Congress and Exhibition Centre Karlsruhe, Germany, Volume 1, (April 19-23, 1993).
[8] N.V. Schukin, V.G. Zimin, S.D. Romanin, S.G. Vitruk, A.S. Korsun, D.M. Baturin, "Validation and Verification of Computer Code SKETCH for the Analysis of Advanced Fast Reactor Dynamics", Proc. of 1994 Topical Meeting on Advances in Reactor Physics, Knoxville, USA, vol. 2, pp. 313-323, (April 11-15, 1994).
[9] N.V. Schukin, V.G. Zimin, S.D. Romanin, S.G. Vitruk, A.S. Korsun, D.M. Baturin, "The code SKETCH for space dynamic modelling of enhanced fast reactor", Issues of Nuclear Science and Design, Moscow, Russian, (will be published in 1995).
[10] P.N. Alekseev, Yu.A. Zverkov, A.G. Morozov, "Concept of the New Generation High Safety Liquid Metal Reactor", Proc. of Int. Conf. on Safety of New Generation Power Reactor, May 1988, Seattle, USA pp. 742-746.

TRANSITION TO CHAOS IN A SQUARE ENCLOSURE CONTAINING INTERNAL HEAT SOURCES

A.Cihat BAYTAŞ
Istanbul Technical University
Institute For Nuclear Energy
80626 MASLAK-ISTANBUL-TURKEY

Tel: 90-212-285 3945; Fax: 90-212-285 3884
e-Mail: NEBAYTAS@TRITU

Abstract

A numerical investigation is performed to study the transition from steady to chaotic flow of a fluid confined in a two-dimensional square cavity. The cavity has rigid walls of constant temperature containing uniformly distributed internal heat source. Effects of the Rayleigh number of flow and heat transfer rates are studied. In addition to, same problem is solved for sinusoidally changing internal heat source to show its effect on the flow model and heat transfer of the enclosures. Details of oscillatory solutions and flow bifurcations are presented.

I.INTRODUCTION

Thermal convection in a fluid with internal energy sources is of major interest in nuclear reactor safety analysis. In severe nuclear reactor accidents, heat is generated in the core debris strictly as a result of radioactive decay. The augmentation of decay heating of core debris by exoergic reactions especially with metallic constituents of core debris is a critical aspect of reactor accident analysis.

A number of studies have been conducted on natural convection in fluids with internal energy sources. Bejan [1] and Yang [2] give a comprehensive overview of this important area in heat transfer. Baker et al. [3] and Faw et al. [4] were interested in natural convection in a fluid with internal energy sources for nuclear reactor safety. A laboratory experiment using an inclined square enclosure containing internal energy sources whose all walls were maintained at constant temperature was presented by Lee and Goldstein [5]. Dependable numerical studies of two-dimensional convection in porous medium do, however, show periodic, quasi-periodic and chaotic oscillations, Kimura et. al. [6]. May [7] completed a computational study on natural convection in a square enclosure containing internal heat sources. There was a comparison in May's [7] study with experimental result of ref [5].

This paper investigated buoyancy-driven flow in an enclosure bounded by four rigid walls of constant temperature containing uniformly distributed constant internal source and additionally internal source strength is changed sinusoidally. The purpose of the direct numerical analysis is to study the transitions to various time-dependent flows. All study is repeated for $Pr = 7$ and $Pr = 0.73$. This choice for $Pr = 0.73$ corresponds to air, it also approximates the Prandtl number value for molten mixed-oxide nuclear fuel, $(U_{0.8}\ PU_{0.2})\ O_2$ [8]. With increasing Rayleigh number transition to chaotic flow is calculated for a cavity having an aspect ratio of one. The obtained results are shown that for $Ra = 10^6$, $Pr = 0.73$ and for $Ra = 10^7$, $Pr = 7$ the flow becomes chaotic. In addition to, the secondary aims of this paper is to report on oscillatory convection in an enclosure which has an internal heat source changing sinusoidally with time. The obtained result for $Ra = 10^6$ showed that the flow becomes chaotic from a quasi-periodic pattern for dimensionless source amplitude $A = 0.5$ and period $P = 0.05$. If the debris is perturbeted by any external heat source during the accident, the flow model and heat transfer mechanism of debris will be changed. The power spectral density of the time series of stream function is calculated using the Cooley-Tukey [9] fast Fourier Transform algorithm.

II. MATHEMATICAL FORMULATION

The two-dimensional square enclosure ($H/D = 1$) model is presented in Fig.1. The fluid is treated as Newtonian and Boussinesq-incompressible, with constant transport properties and

coefficient of thermal expansion. The enclosure is initially occupied by motionless fluid, the temperature of which is uniform and all walls are considered isothermal (the rigid conducting walls) ($T = Tw$ or $\theta = 0$). The internal source (q_o''') is distributed uniformly over the cavity.

The conservation of mass, momentum, and energy, with the two-dimensional unsteady laminar assumption, gives rise to a system of equations consisting of the continuity , the Navier-Stokes, and the energy equations. Three-dimensional effects are neglected here. To aid in the numerical solution of the governing equations we first introduce the dimensionless stream function, Ψ , and dimensionless vorticity, Ω, into the two momentum equations, eliminate the pressure gradient terms and obtain a single vorticity equation. A system of dimensionless equations in the stream function-vorticity formulation is obtained. In conservative form, this is written as

Vorticity Transport Equation

$$\frac{\partial \Omega}{\partial \tau} + \frac{\partial (U\Omega)}{\partial X} + \frac{\partial (V\Omega)}{\partial Y} = Pr \nabla^2 \Omega + 8 Ra Pr \frac{\partial \theta}{\partial X} \tag{1}$$

Stream Function Vorticity Equation

$$\frac{\partial^2 \Psi}{\partial X^2} + \frac{\partial^2 \Psi}{\partial Y^2} = -\Omega \tag{2}$$

Energy Equation

$$\frac{\partial \theta}{\partial \tau} + \frac{\partial (U\theta)}{\partial X} + \frac{\partial (V\theta)}{\partial Y} = \nabla^2 \theta + 8 \tag{3}$$

Velocity Equations

$$U = \frac{\partial \Psi}{\partial Y} \; ; \; V = -\frac{\partial \Psi}{\partial X} \tag{4}$$

All symbols have been defined in the Nomenclature. The non-dimensionalization was carried out using the following dimensionless variables:

$$(X,Y) = \frac{x,y}{D} \quad ; \quad (U,V) = \frac{u,v}{(\alpha/D)} \quad ; \quad \theta = \frac{T - T_w}{\Delta T}$$

$$\Omega = \frac{\omega D^2}{\alpha} \quad ; \quad \Psi = \frac{\psi}{\alpha} \quad ; \quad \tau = \frac{t\alpha}{D^2} \qquad Pr = \frac{\nu}{\alpha}$$

$$Ra = \frac{g.\beta}{\alpha \nu} \left(\frac{D}{2}\right)^3 \frac{q_o''' D^2}{8k} \quad ; \quad \Delta T = \frac{q_o''' D^2}{8k} \tag{5}$$

Pure conduction heat transfer characteristic length in the definition of Rayleigh number and reference temperature difference (ΔT) was chosen (D/2) of the region with unstable temperature gradient [5, 7, 10].

Initial and boundary conditions.

$\tau = 0 \quad U = V = \theta = \Psi = 0$ (6)

$\tau > 0 \quad U = V = \theta = \Psi = 0$ for $X = 0,1$ and $Y = 0,1$. (7)

$\Omega = \Omega_w$ for $X = 0,1$ and $Y = 0,1$. (8)

The boundary vorticity Ω_w is evaluated using the following third-order polynomial interpolation [11] for Ψ near the solid wall:

$$\Omega_w = \frac{7\psi_w - 8\psi_{w+1} + \psi_{w+2}}{2(\Delta n)^2} + O(\Delta n)^2 \tag{9}$$

where w shows the grid point lying on the wall, w + 1 the point adjacent to the wall, and Δn the grid size in the direction normal to the wall, either ΔX or ΔY.

III. SOLUTION PROCEDURE

The control volume approach was used for the discretization since it guarantees the conservation of mass, momentum, and energy not only in each volume, but also globally, over the whole domain [12]. For the present investigation the computational domain is divided into a number of staggered rectangular control volumes around each grid point. The staggered grid procedure was used in primitive variables with a power-law differencing scheme and a fully implicit scheme for evaluating the time derivatives as described by Patarkar [12]. The coupled equations (Eg.(1) and Eg.(3)) are solved by using the Alternating Direction Implicit (A.D.I.) method developed by Douglas and Peaceman [13]. Being an implicit method, ADI allows larger time steps compared with the explicit methods. In addition, it leads to tridiagonal systems of simultaneous equations that are much easier to solve [12] than the pentadiagonal systems that arise when fully implicit methods are used. These tridiagonal systems of simultaneous equations can be solved with the Thomas algorithm, or tridiagonal matrix algorithm (TDMA) [12]. The stream function Equation (2) is solved by chosing the Successive Overrelaxation (SOR) procedure [1]. At each time step and after the vorticity equation has been solved until a convergence criterion of the form

$$\sum_{i,j} \left| \phi_{i,j}^{l+1} - \phi_{i,j}^{l} \right| / \sum_{i,j} \left| \phi_{i,j}^{l+1} \right| \leq \varepsilon \tag{10}$$

is satisfied. Here ε is a convergence parameter, and the value $\epsilon = 10^{-5}$ was found to be adequate. In this study, it was found that the optimum overrelaxation parameter for Eg.(2) was 1.86.

Relaxation was used to aid the convergence in solving the vorticity equation ($\lambda = 0.4$), although it was not needed in the solution of the energy equation. Here, the value of convergence parameter (10^{-5}) was found to be adequate, since a further reduction in it did not significantly effect the results and did increase the computational effort.

1. Grid dependency studies and model validation

It was impossible to obtain a stable steady solution for Pr = 7 and for a Rayleigh number of 5.2×10^4 or greater and in addition for Pr = 0.73 and for a $Ra = 5 \times 10^4$ or greater. Different grid sizes and time steps were tried in order to examine the grid dependency. The present solution are compared with Mays's [7] results as shown in Table 1. Results in Table 1 indicate that 41x41 grid size is adequate for Pr = 7 and $Ra = 10^5$ and also up to a Rayhleigh number of 10^7. All results up to $Ra = 10^7$ are not shown here for brevity. The dependence of the results on the time step have been tested and the suitable dimensionless time step is found to be 5×10^{-6} in this investigation.

Further validation of the present model has been done by comparing the present solutions with numerical work of May [7] and experimental work of Lee and Goldstein [5] for the case of natural convection in an enclosure (Table 2). Excellent agreement has been obtained between the two results.

2. Heat Transfer

The average Nusselt number are defined the same way as in the references [5,7,10]
Average Nusselt number:

$$Nu_a = \frac{1}{2}\int_0^1 \left.\frac{\partial\theta}{\partial n}\right|_{wall} dn \tag{11}$$

where n denotes the x- or y- direction.

IV. RESULTS AND DISCUSSION

To reduce the numerical effort, the problem was studied for a square enclosure. Furthermore, to understand the heat transfer mechanism and transition to chaos for Pr = 0.73 and Pr = 7 for different Ra numbers.

Two examples of how oscillations proliferate as Ra increases at constant Pr are displayed in Fig.2. In Fig.2(a) and (b), an interesting effect is the dependence of the oscillatory convection on the Prandtl number; the oscillatory convection heat transfer increases on the top wall of enclosure as Pr increases. This effect is explained by the fact that, as the Pr number is greater than 1.0, thermal effects are expected to play an important role compared to inertial effects.

At sufficiently low Rayleigh numbers (until Ra $\approx 10^4$) the flow is laminar and steady as shown in Fig.2. As the Ra number is increased $Ra \geq 5.0\times10^4$ for Pr = 0.73, and $Ra \geq 5.2\times10^4$ for Pr = 7, the solutions are oscillating and the time dependency begins with a bifurcation from the steady state to an oscillatory periodic flow. The flow is oscillating for $Ra = 10^5$, Pr = 7 and its solution can be shown in Fig. 8(a) from reference [7]. Also, the flow is oscillating for $Ra = 10^5$, Pr = 0.73. Its solution is not shown here for brevity. To understand the phenomenon further, the phase portraits and power spectra of the solutions have been obtained for different Ra. Power spectra have been computed from the time series of stream function using well-known Cooley-Tukey [9]. Fast Fourier Transform algorithm. The time history of the stream function and temperature have been generated at a point near the top left corner (0.25, 0.875). Figures 3 and 4 show the power spectra and the temperature θ against stream function at the location (x = 0.25, y = 0.875) of the cavity. The phase portrait and power, spectrum show a period-doubling in Fig. 3(a).

Fig. 3(b) and (c) illustrates the phase portrait and frequency spectra of stream function. Fig. 3(b) and (c) shows that the flow is chaotic. In these cases, the Fourier spectrum has a continuous nature. The phase portrait shows a limit cycle behaviour in Fig.4(a) and quasi-periodic behaviour in Fig. 4(b). Phase plane behaviour and power spectra for a chaotic solution is shown in Fig.4 (c). The last part of Fig.2(b) for $Ra = 10^6$ is shown in Fig.5. Fig.5 shows the variation of $Nu_{a\tau}$ with time for the $Ra = 10^6$, Pr = 7 for one cycle of oscillation. The corresponding isotherms and streamline patterns are shown in Fig.6 and Fig.7, respectively. In the beginning at $\tau = \tau_1$ a small temperature trough is situated near the upper-right portion of the cavity in Fig.6. Then the beginning of a new temperature trough is situated near the upper-left portion of the cavity at time $\tau = \tau_4$. Temperature trough is advanced to right side of upper wall and at the same time, a secondary temperature trough is appeared at $\tau = \tau_5$. At $\tau = \tau_7$ a new upper temperature trough appears again at the upper-right portion of cavity and from $\tau = \tau_7$ the whole procedure repeats itself until its starting point, which completes one period of the oscillation. Flow patterns during one period of oscillation is shown in Fig.7. The strong roll is situated near the upper-right of top wall of the cavity at $\tau = \tau_1$. The strong roll is destroyed (τ_2, τ_3). The strong roll appears again at $\tau = \tau_5$ and than a pair of strong rolls is situated near the upper-right portion of cavity. From $\tau = \tau_7$, the whole phenomena is repeated until its starting point.

In addition to this investigation, it is thought that any zirconium cladding around the fuel rods would be completely oxidized to ZrO_2 during core degradation, and admission of the zirconium oxide promptly initiates dramatic rises in the melt temperature. Reflecting on this observation, the internal source will be changed sinusoidally with time about a mean value (q_o'''), with amplitude (a) and period (p) for $Ra = 10^5$ in order to simulate the dramatic changes caused by the heat source of debris bed by inclusion of the zirconium oxide.

In this situation, new internal heat source of enclosure will be defined the following manner:

$$q''' = q_o''' + a\ Sin(2\pi t/p) \tag{12}$$

and the new dimensionless energy equation is like below

$$\frac{\partial\theta}{\partial\tau} + \frac{\partial(U\theta)}{\partial X} + \frac{\partial(V\theta)}{\partial Y} = \nabla^2\theta + 8[1 + A\ Sin(2\pi\tau/P)] \tag{13}$$

where the dimensionless variables for new heat source are as follows.

$$A = \frac{a}{q_o'''} \quad , \quad P = \frac{p\alpha}{D^2} \tag{14}$$

The new governing equations (Eq.1, 2, 4 and 13) were solved for $Ra = 10^5$, $Pr = 7$ and the dimensionless amplitude $A = 0.5$, the dimensionless period $P = 0.05$ to simulate the effects of the heat source of debris bed. Fig.8(a) shows the variation of $Nu_{\theta T}$ versus the dimensionless time for $Ra = 10^5$ and $Pr = 7$, Fig.8(a) is given by May [7] and for $A = 0$. Fig.8(b) shows the $Nu_{\theta T}$ variation versus the dimensionless time for $Ra = 10^6$, $Pr = 7$, $A = 0.5$ and $P = 0.05$. When Fig.8(a) and Fig.8(b) are compared, the solution is obviously oscillating in Fig.8(a) but the solution becomes chaotic in Fig.8(b). In the case of Fig.8(b), convection heat transfer is more dominant then the solution in Fig.8(a) and the convection heat transfer is increased if heat source oscillates with determinated period and amplitude. At the same time, the corresponding phase plane behaviour of the dimensionless temperature versus stream function and power spectrum are shown in Fig.9. The phase portrait shows a chaotic behaviour, and the flow can not be described by a small number of well-defined characteristic frequencies. Namely, the flow is described as chaotic or weakly turbulent. All different sinusoidal results are not shown here for brevity.

V.CONCLUSIONS

The problem of natural convection in an enclosure has been studied numerically for the case in which all solid walls are cooled and it has a uniformly distributed internal heat source. Unsteady-state solutions have been obtained depending on the parameters of Ra and Pr. Steady-state solutions could be obtained in the Rayleigh number until 10^4 for $Pr = 0.73$ and $Pr = 7$. The oscillatory convection solutions could be obtained for $Ra \geq 5 \times 10^4$ and $Pr = 0.73$ and for $Ra \geq 5.2 \times 10^4$ and $Pr = 7$. Results obtained using an unsteady model indicated that successive flow bifurcations take place from these threshold Ra numbers up to $Ra = 10^6$ for $Pr = 0{,}73$ and $Ra = 10^7$ for $Pr = 7$. As Rayleigh number increases further, the flow becomes chaotic. In order to simulate the dramatic effects with time of the heat source of debris bed by admission of the zirconium oxide, constant internal heat source was replaced with a source oscillating with time about a mean value (q_o'''), with dimensionless amplitude $A = 0.5$ and dimensionless period $P = 0.05$ for $Ra = 10^5$, $Pr = 7$. In this case, the convection heat transfer was increased and flow became chaotic when the flow was quasi periodic for $Ra = 10^5$, $Pr = 7$ and $A = 0$, namely heat source was constant.

NOMENCLATURE

A	dimensionless amplitude
a	amplitude, w/m^3
D	horizontal length of cavity, m
g	gravitational acceleration, m/s^2
H	vertical height of cavity, m

k	thermal conductivity of fluid, W/mK
Nu_a	average Nusselt number [Eq.11]
n	direction normal to the wall
P	dimensionless period
p	period, s
Pr	Prandtl number
q_o'''	the mean internal energy source, W/m^3
Ra	Rayleigh number
t	physical time, s
T	local temperature, K
u,v	velocity components in the x and y dire· s, m/s
U,V	dimensionless velocity components in the X and Y directions
x,y	cartesian coordinates, m
X,Y	dimensionless coordinates
α	thermal diffusivity of fluid, m^2/s
β	coefficient of thermal expansion of fluid, K^{-1}
ε	prescribed error
ΔT	reference temperature
Θ	dimensionless temperature
λ	relaxation parameter
ν	kinematic viscosity of fluid, m^2/s
ρ	density of fluid, kg/m^3
τ	dimensionless time
ψ,Ψ	dimensional and dimensionless stream function
ω,Ω	dimensional and dimensionless vorticity

Subscripts

i,j	grid point indices
T	top wall
w	value on wall

REFERENCES

[1] A.Bejan, Convection heat transfer. Wiley, New York (1984).

[2] K.T.Yang, Natural Convection in Enclosures. In Handbook of Single-phase Convective Heat Transfer (Edited by S.Kakaç, R.Shah and W.Aung), chap 13. Wiley, New York (1987)

[3] L.Baker, Jr., R.E. Faw, and F.A.Kulacki, Postaccidental heat removal-partI: heat transfer within an internally heated nonboiling liquid layer', Nuc.Sci.Eng., 61, 222-230 (1976).

[4] R.E.Faw, L.Baker, Jr., Postaccidental heat removal - Part II: Heat transfer from an internally heated liquid to a melting solid, Nuc.Sci. Engrg., 61, 231-238 (1976).

[5] J.H. Lee, R.J. Goldstein, "An experimental study on natural convection heat transfer in an inclined square enclosure containing internal energy sources", ASME J. of Heat Transfer, 110, 345-349 (1988).

[6] S.Kimura, G.Schubert, "Route to Chaos in Porous-medium Thermal Convection", J.Fluid Mech., 166, 305-324 (1986).

[7] H.O.May, "A numerical study on natural convection in an inclined square enclosure containing internal heat sources", Int. J.Heat Mass Transfer, 34, 919-928 (1991).

[8] S.Acharya, R.J.Goldstein, "Natural convection in an externally heated vertical or inclined square box containing inter al energy sources", ASME J.of Heat Transfer, 107, 855-866 (1985).

[9] N.C. Geçkinli, D.Yavuz, Discrete Fourier transformation and its applications to power spectra estimation, Elsevier Scientific Publishing Company, New York, (1983).

[10] F.A.Kulacki, R.J.Goldstein, "Thermal convection in A horizontal fluid layer with uniform volumetric energy sources", J.Fluid Mech., 55, part 2, 271-287 (1972).

[11] J.O.Wilkes and S.W. Churchill, "The finite difference computation of natural convection in a rectangular enclosure", AIChE Journal, 12, 161-166 (1966).

[12] S.V. Patankar, Numerical heat transfer and fluid flow, Hemisphere, Washington, D.C. (1980).

[13] J.Jr. Douglas and D.W. Peaceman, "Numerical solution of two dimensional heat flow problems", AIChE Journal, 1, 502-512 (1955).

Table 1. Grid dependency for unseady and steady solution.

Grid Size	t_{oscill}	May [7]	Presented	
		θ_{min} X=Y=0.5	θ_{min} X=Y=0.5	Nu_{eT}
21x21	0.318	0.170	0.1697	1.380
41x41	0.363	0.181	0.1772	1.330
61x61	0.376	0.183	0.1814	1.324

Table 2. Comparison of present numerical solutions with experimental data (θ_{max}) of Lee and Goldstein [5] and with computational work of May [7].

Ra	Lee et al. [5]	May [7]	Presented
	experimental	numerical (A.D.I.)	numerical (A.D.I.)
$1x10^4$	0.3866	0.382	0.375
$5x10^4$	0.293	0.270	0.275
$1x10^5$	0.256	0.235	0.2357

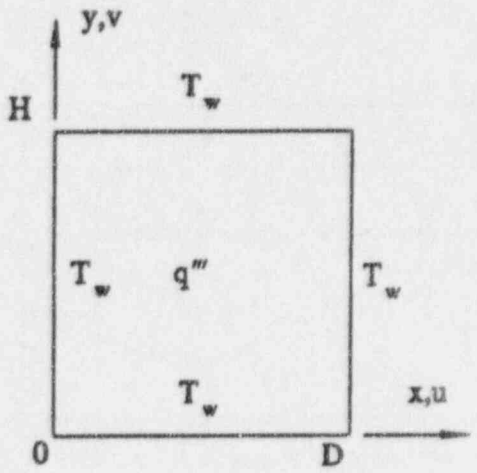

Fig.1. Shematic diagram of the physical situation.

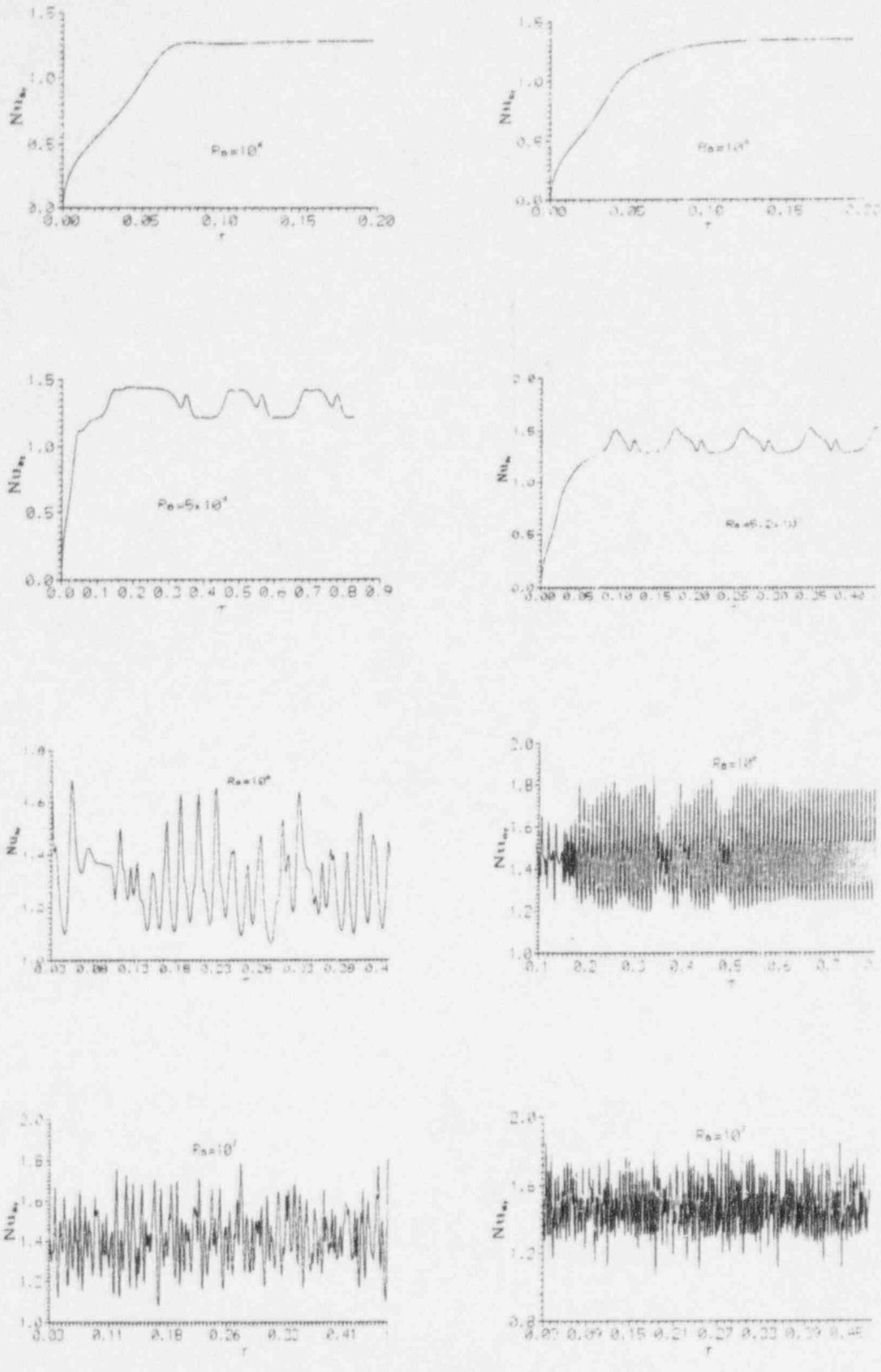

(a) (b)

Fig.2. The effect of Pr and Ra on the Nu_{aT} oscillations
(a) Pr=0.73. (b) Pr=7

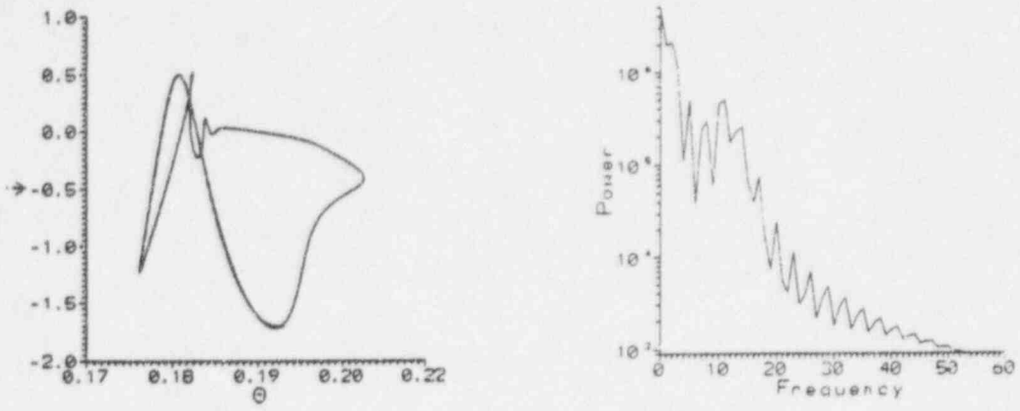

(a)

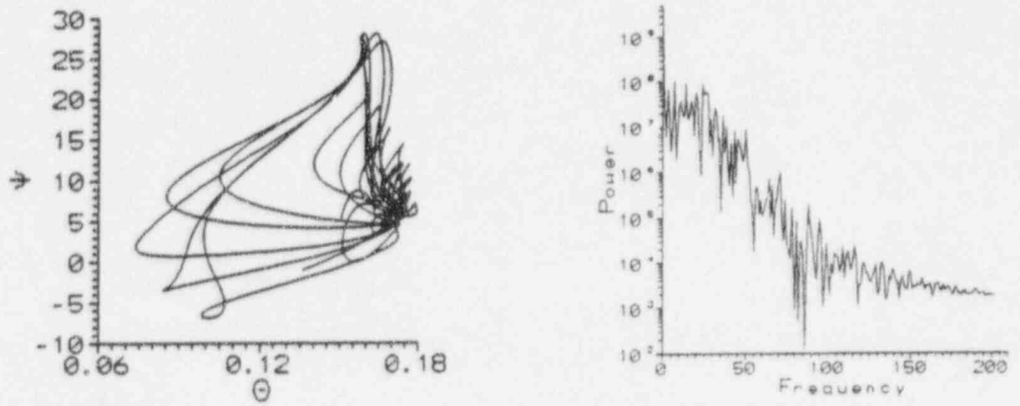

(b)

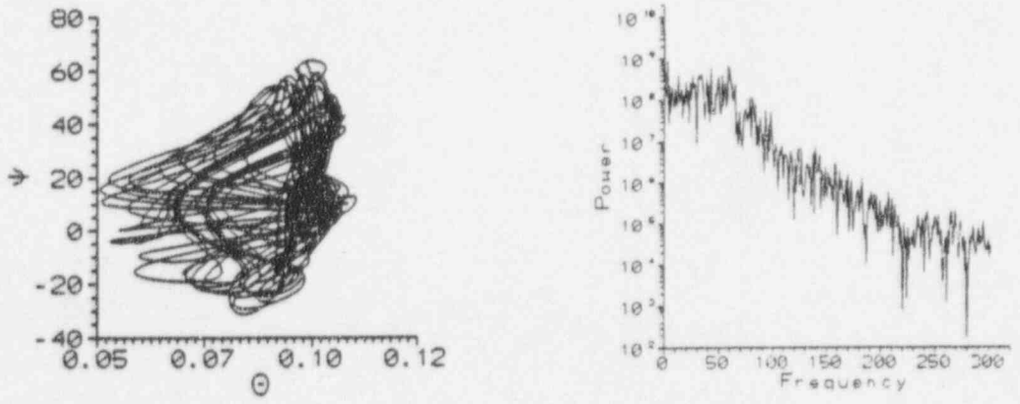

(c)

Fig.3. Phase portraits (Ψ versus θ) and normalized power spectra (Ψ) at the point (0.25, 0.875) for Pr=0.73: (a) Ra=5×10^4, (b) Ra=10^6, (c) Ra=10^7.

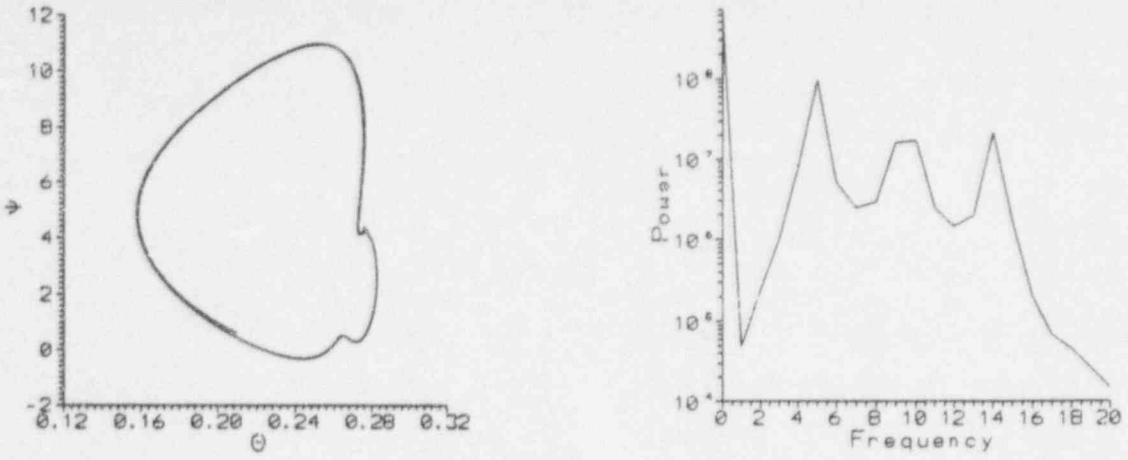

(a)

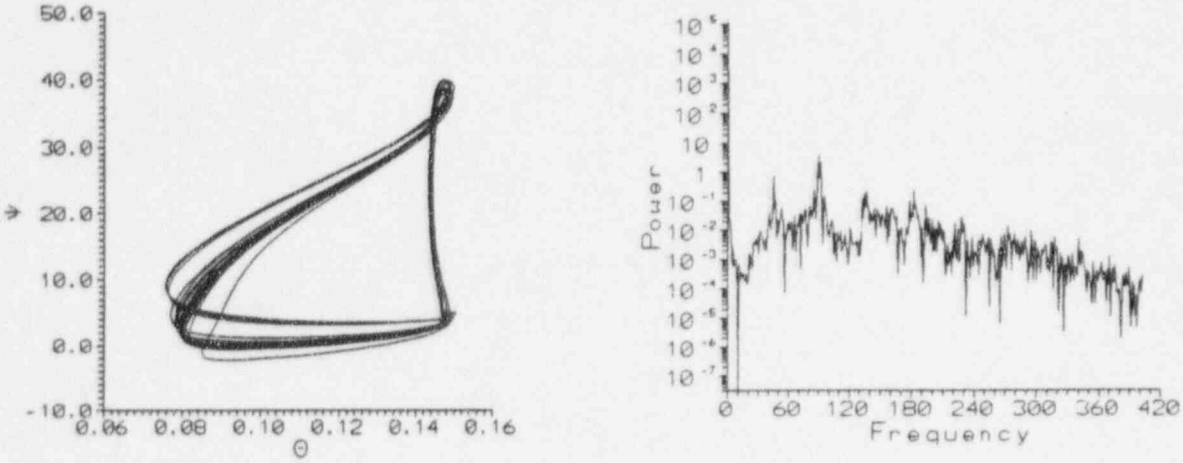

(b)

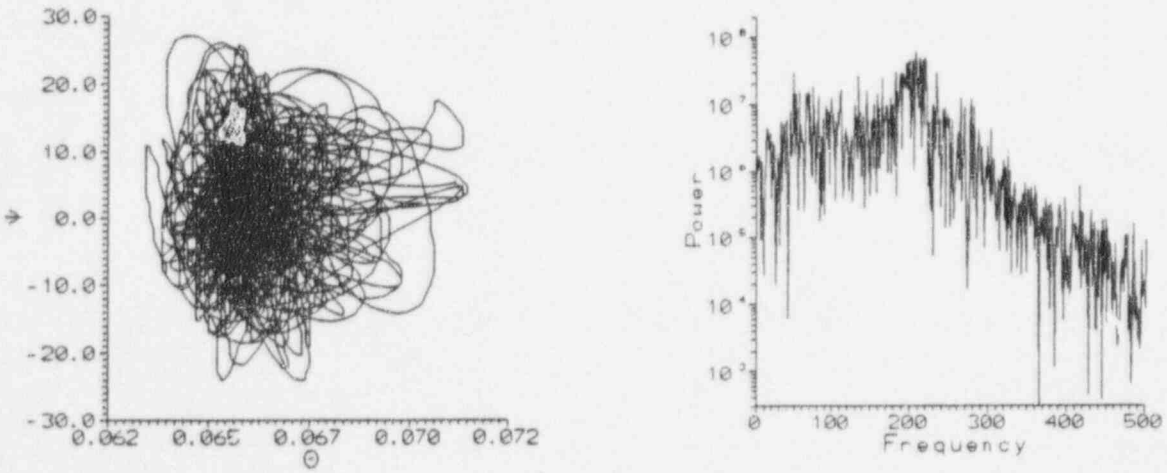

(c)

Fig.4. Phase portraits (Ψ versus θ) and normalized power spectra (Ψ) at the point (0.25, 0.875) for Pr = 7: (a) Ra = 5.2×10^4, (b) Ra = 10^6, (c) Ra = 10^7.

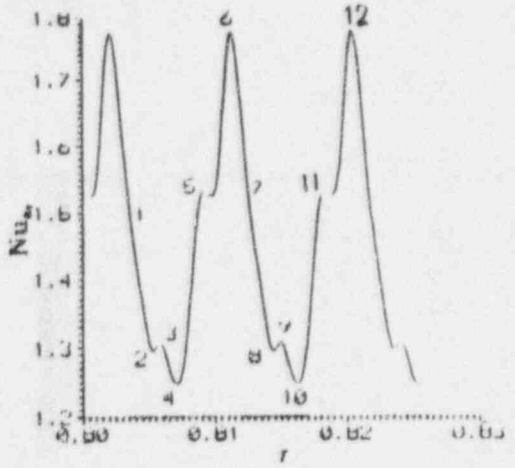

Fig.5. $Nu_{\delta T}$ as a function of time for $Ra = 10^6$, $Pr = 7$ and one period of oscillation.

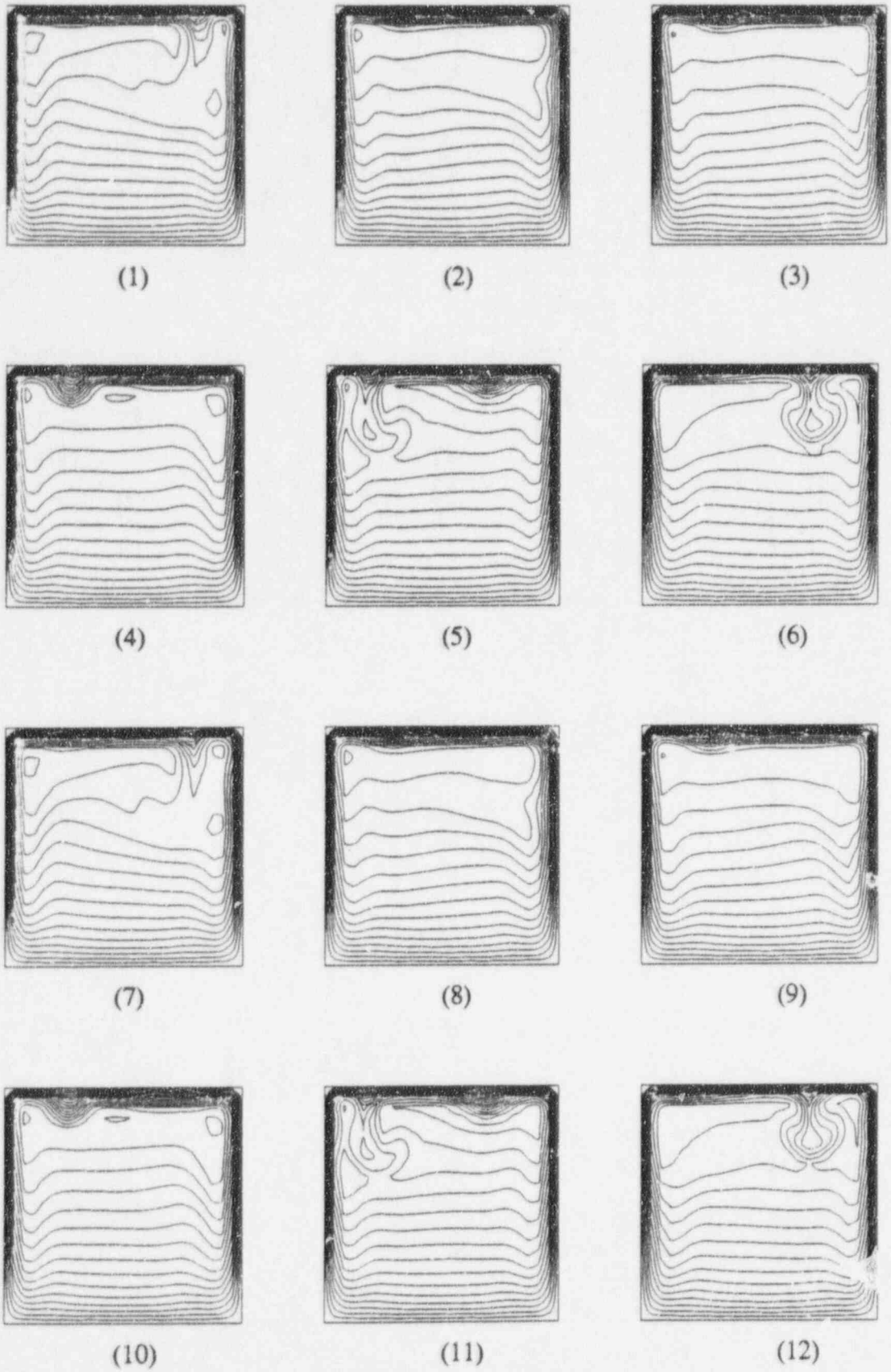

Fig.6. Isotherms during one period of oscillation.

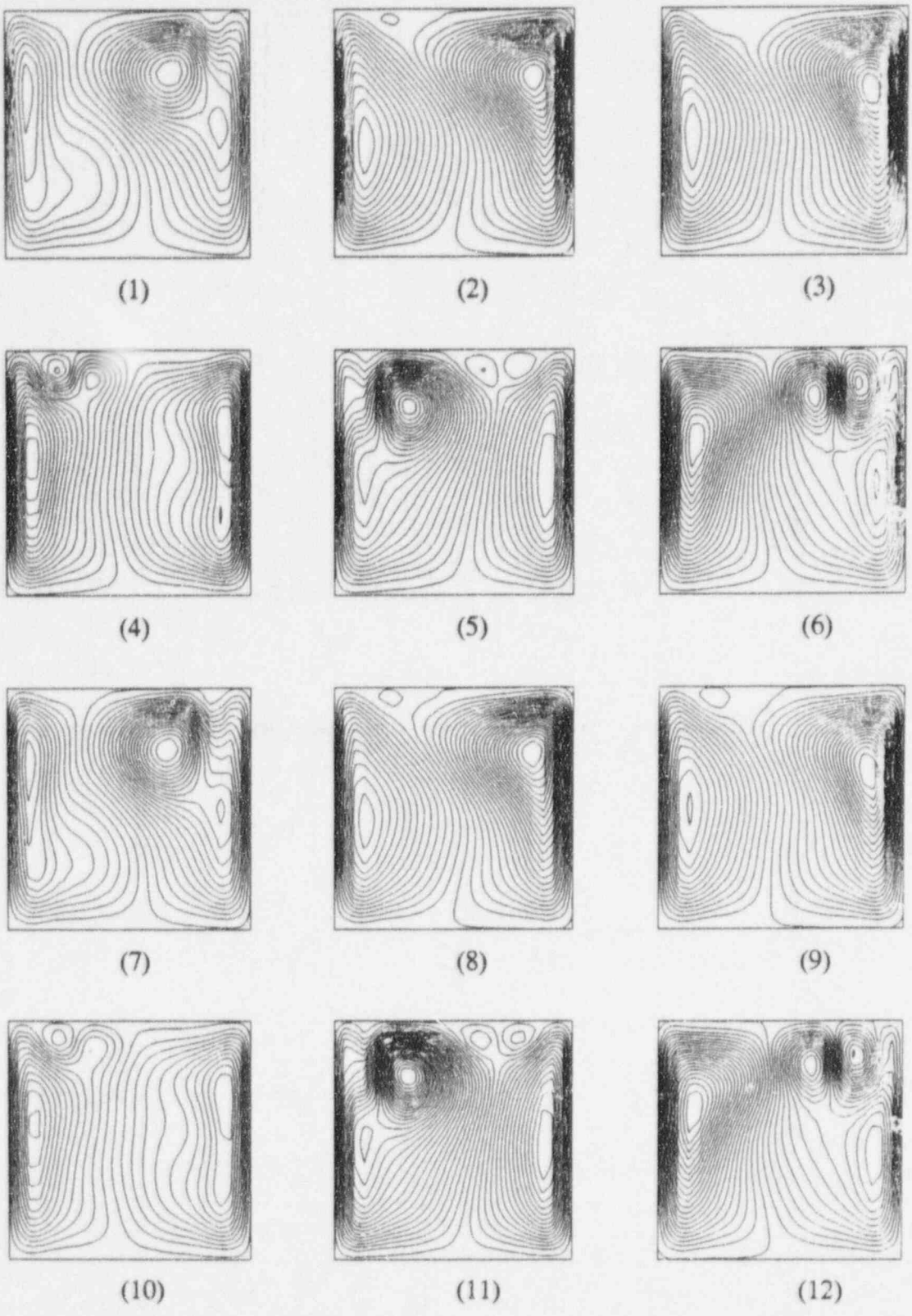

Fig.7. Flow patterns during one period of oscillation.

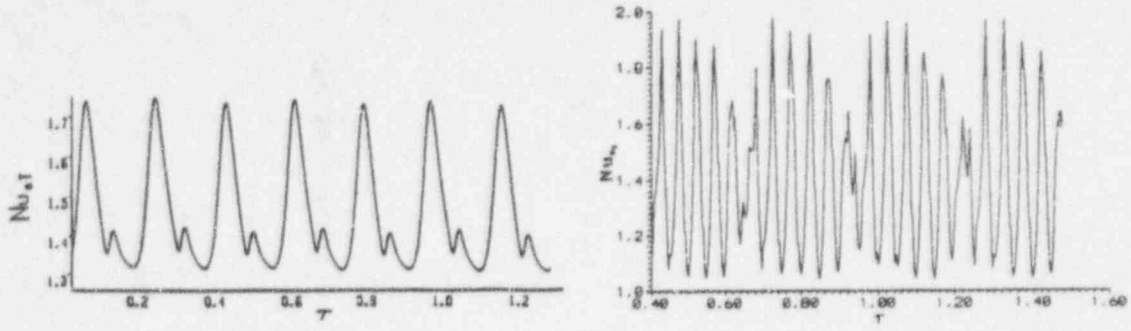

(a) (b)

Fig.8. $Nu_{\delta T}$ as a function of time for $Ra = 10^5$, $Pr = 7$.
(a) the solution of May [7] ($A = 0$),
(b) present solution for $A = 0.5$, $P = 0.05$

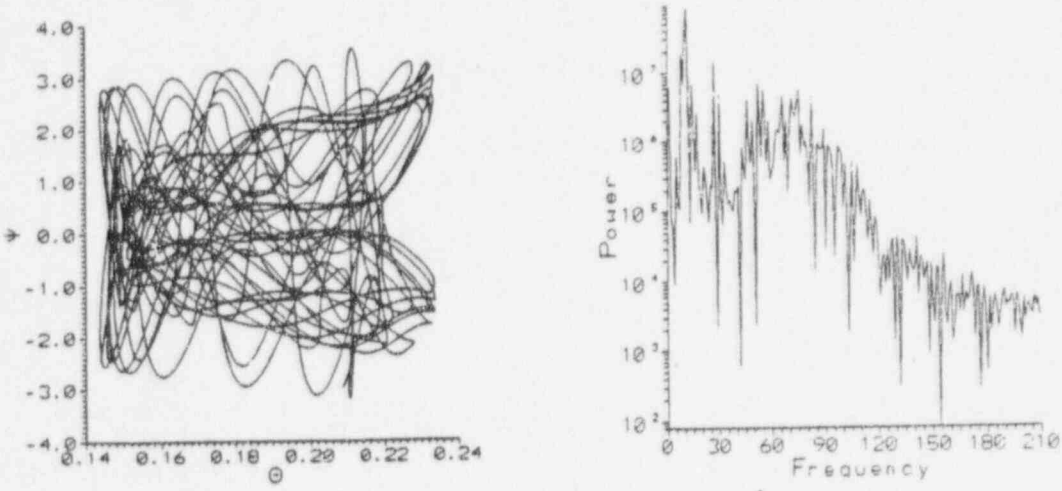

Fig.9. Phase space trajectory of Ψ versus θ at the point (0.25, 0.875) and power spectra of Ψ for $A = 0.5$, $P = 0.05$ and $Ra = 10^6$, $Pr = 7$.

ASTRID : a 3D eulerian software for subcooled boiling modelling - Comparison with experimental results in tubes and annuli.

Brière E., Larrauri D., Olive J.
Electricité de France. Direction des Etudes et Recherches.
6, Quai Watier. 78400 Chatou. France.
e-mail : Etienne.Briere@der.edf.fr

ABSTRACT

For about four years, Electricité de France has been developing a 3-D computer code for the Eulerian simulation of two-phase flows. This code, named ASTRID, is based on the six-equation two-fluid model. Boiling water flows, such as those encountered in nuclear reactors, are among the main applications of ASTRID.

In order to provide ASTRID with closure laws and boundary conditions suitable for boiling flows, a boiling model has been developed by EDF and the Institut de Mécanique des Fluides de Toulouse. In the fluid, the heat and mass transfer between a bubble and the liquid is being modelled. At the heating wall, the incipient boiling point is determined according to Hsu's criterion and the boiling heat flux is split into three additive terms : a convective term, a quenching term and a vaporisation term. This model uses several correlations.

EDF's program in boiling two-phase flows also includes experimental studies, some of which are performed in collaboration with other laboratories.

Refrigerant subcooled boiling both in tubular (DEBORA experiment, CEN Grenoble) and in annular geometry (Arizona State University Experiment) have been computed with ASTRID.

The simulations show the satisfactory results already obtained on void fraction and liquid temperature. Ways of improvement of the model are drawn especially on the dynamical part.

INTRODUCTION

Two-phase flow has always been a large field of research in the nuclear industry. Electricité de France is involved in this research and has a strong interest in steam water flow modelling connected to safety studies. The development of a CFD code for 3D local analyses is considered as a very useful contribution to this research, with potential applications to the understanding of the "Departure from Nucleate Boiling" phenomenon, or to complementing safety codes (1D or subchannel types) for local problems in complex geometries. This paper presents the stage reached in the development of the ASTRID code and its validation in simple geometries.

THE ASTRID CODE

The ASTRID code is being developed by Electricité de France, Research & Development Division. ASTRID is a 3-D, 2-fluid computer code for the Eulerian simulation of two-phase flows (Thai Van, [1]).

The numerical method is based on finite difference and finite volume discretization, and an incremental version of the fractional step method.

CONSERVATION EQUATIONS

Six equations are written : these are the averaged conservation equations for mass, momentum and energy in each phase (k=1 or 2) :

- Mass Equation

$$\frac{\partial}{\partial t}\alpha_k \rho_k + \frac{\partial}{\partial x_j}\alpha_k \rho_k U_{kj} = \Gamma_k \quad (1)$$

with the condition at the interface

$$\sum_{k=1}^{2} \Gamma_k = 0 \quad (1bis)$$

- Momentum Equation

$$\alpha_k \rho_k \frac{\partial}{\partial t} U_{ki} + \alpha_k \rho_k U_{kj} \frac{\partial}{\partial x_j} U_{ki} = -\alpha_k \frac{\partial P}{\partial x_i} + \alpha_k \rho_k g_i - \frac{\partial}{\partial x_j}\alpha_k \left\langle \rho u_i'' u_j'' \right\rangle_k + I_{ki} - U_{ki}\Gamma_k \quad (2)$$

with the condition at the interface

$$I_{ki} = I'_{ki} + U_{\sigma i}\Gamma_k$$

$$\sum_{k=1}^{2} \Gamma'_{ki} = 0 \quad (2bis)$$

- Energy Equation (using the enthalpy variable H)

$$\alpha_k \rho_k \frac{\partial}{\partial t} H_k + \alpha_k \rho_k U_{kj} \frac{\partial}{\partial x_j} H_k = -\frac{\partial}{\partial x_j} \alpha_k \left\langle \rho h'' u''_j \right\rangle_k + \Pi_k - H_k \Gamma_k \quad (3)$$

with the condition at the interface

$$\sum_{k=1}^{2} \Pi_k = 0 \quad (3bis)$$

α is the volumetric phase fraction, ρ the density, P the pressure of the continuous phase, g the gravitation force per unit mass and U the mean velocity.

$\langle\rangle_k$ is the averaging operator associated to phase k.

For any variable X, x'' is its fluctuating part.

Γ, Γ' and Π are the interphase transfer terms for mass, momentum and energy respectively.

CLOSURE LAWS

These six equations do not constitute a closed system, so that closure laws must be specified for :

- the turbulence terms (i.e. the terms containing the average of fluctuation products in the above equations).
- the interphase transfer terms (Γ, Γ' and Π).

Closure relations are an important, however difficult, part of two-fluid modelling : the closure laws vary from problem to problem (since there exists no universal acknowledged expression). Thus, the ASTRID user must specify these laws, in order to adapt them to the physical phenomena involved in the flow to be simulated.

The closure relations allowed by ASTRID always assume that one phase (k=1) is dominant and continuous, while the other phase (k=2) is composed of dispersed inclusions. For instance, this allows the simulation of a bubbly flow, with vapour bubbles dispersed in the continuous liquid.

Turbulence Modelling

Turbulence is predicted using the eddy viscosity concept.

- For the continuous phase, a standard k-ε model is used. Additional terms take into account the interfacial turbulent momentum transfer.
- For the dispersed phase, an extension of the Tchen's theory related to the dispersion of discrete particles is used : the turbulence of the dispersed phase is given as a function of the turbulence of the continuous phase (Simonin, [2]).

Interfacial momentum transfer

This term is written as follows :

$$\Gamma'_{2,i} = -\Gamma'_{1,i} = \alpha_2 \left\langle \frac{\partial \sigma'_{1,ij}}{\partial x_j} \right\rangle_2 + \alpha_2 \left\langle f_{r,i} \right\rangle_2 \quad (4)$$

where the first term on the right hand is the turbulent part of the stress applied on the particle by the undisturbed surrounding fluid flow which would occur if the particle were withdrawn and the second term corresponds to the interfacial transfer induced by the flow disturbance due to the inclusions.

The latter term consists of a combination of the drag, added mass, and lift forces, each of which has to be modelled. In the present article, Basset and lift forces are neglected. The practical form is obtained by averaging the resulting force on the dispersed phase volume.

$$\alpha_2 \langle f_{r,i} \rangle_2 = -\alpha_2 \rho_1 F_D V_{r,i} - \alpha_2 \rho_1 C_A \left[\frac{\partial V_{r,i}}{\partial t} + U_{2,j} \frac{\partial V_{r,i}}{\partial x_j} \right] - \frac{\partial}{\partial x_j} \alpha_2 \rho_1 C_A \langle u''_{2,j} v''_{r,i} \rangle_2 \quad (5)$$

where the added-mass coefficient C_A is taken as 0.5, so as the lift coefficient C_L.

The average drag coefficient F_D is written in terms of the local mean particle Reynolds number :

$$F_D = \frac{3}{4} \frac{C_D}{\bar{d}} \left\langle \left| \vec{v}_r \right| \right\rangle \quad (6)$$

with

$$\left\langle \left| \vec{v}_r \right| \right\rangle = \sqrt{V_{r,i} V_{r,i} + \langle v''_{r,i} v''_{r,i} \rangle_2}$$

$$C_D = \frac{24}{Re} \left(1 + 0.15 \, Re^{0.687} \right) \alpha_1^{-1.7} \qquad Re < 1000$$

$$C_D = 0.44 \qquad Re > 1000$$

$$Re = \frac{\alpha_1 \rho_1 \left| \vec{v}_r \right| \bar{d}}{\mu_1}$$

$V_{r,i}$, the average of the local relative velocity $v_{r,i}$ between each inclusion and the surrounding fluid, can be expressed as a function of the total relative mean velocity $\Delta U_i = U_{2,i} - U_{1,i}$ and a drifting velocity $V_{d,i}$ due to the

correlation between the instantaneous distribution of particles and large-scale turbulent fluid motions (Simonin, [3]) :

$$V_{r,i} = \left[U_{2,i} - U_{1,i}\right] - V_{d,i} \qquad (7)$$

$$V_{d,i} = \left\langle u_{1,i} \right\rangle_2 - U_{1,i} = \left\langle u''_{1,i} \right\rangle_2$$

The drifting velocity $V_{d,i}$ takes into account the dispersion of particles due to transport by turbulent fluid motion and reduces to the single turbulent correlation between the volumetric fraction of the dispersed phase and the velocity of the continuous phase for the tracer-particle limit case when the particles have sufficiently small inertia to follow fluid motion precisely. According to the theoretical case of discrete particles suspended in homogeneous turbulence (Deutsch, [4]), the velocity $V_{d,i}$ is written as follows :

$$V_{d,i} = -D'_{12,ij}\left[\frac{1}{\alpha_2}\frac{\partial \alpha_2}{\partial x_j} - \frac{1}{\alpha_1}\frac{\partial \alpha_1}{\partial x_j}\right] \qquad (8)$$

where the fluid-particle turbulent dispersion tensor $D'_{12,ij}$ is expressed in terms of the turbulent characteristics of the two phases, i.e. the covariance tensor between the turbulent velocity fluctuations of the two phases $q_{12} = < u''_{1,i} u''_{2,i} >_2$ and a fluid-particle turbulent characteristic time τ'_{12}:

$$D'_{12,ij} = \tau'_{12} < u''_{1,i} u''_{2,i} >_2 \qquad (9)$$

For practical calculations, the fluid-particle dispersion tensor is limited to its diagonal part :

$$D'_{12,ij} = \tau'_{12}\frac{1}{3} q_{12}\,\delta_{ij} \qquad q_{12} = < u''_{1,i} u''_{2,i} >_2 \quad (9^{\text{bis}})$$

In first approximation, the first term in equation (4) represents the correlation between the local instantaneous distribution of the inclusions and the fluid turbulent pressure gradient and is written as follows (Bel F'Dhila, [5]) :

$$\alpha_2 \left\langle \frac{\partial \sigma'_{1,ij}}{\partial x_j} \right\rangle_2 = \rho_1 < u''_{1,i} u''_{2,j} >_2 \frac{\partial \alpha_2}{\partial x_i} + \alpha_2 \rho_1 \frac{\partial}{\partial x_j}\left[< u''_{1,i} u''_{2,j} >_2 - < u''_{1,i} u''_{1,j} >_1 \right] \qquad (10)$$

Modelling heat and mass transfer between phases

Heat transfer between phases is calculated as follows :

- the interface between the bubble and the liquid is assumed to be at the saturation temperature,
- heat transfer between the bubble and the interface is instantaneous,
- a thermal boundary layer surrounds the bubble, so that the heat transfer between the liquid and the interface occurs through this boundary layer.

Thanks to these hypothesis, the mass transfer between phases is calculated using the equivalence between the heat received by the interface and latent energy of vaporisation (condensation if negative) :

$$\Gamma_2 = \frac{1}{L}\left[h\left(T_1 - T_{sat}\right) + \frac{\alpha_2 \rho_2 Cp_2}{\delta t}\left(T_2 - T_{sat}\right)\right]$$

Since then, a thermal coefficient is needed. We write that the Nusselt number is a function of the Reynolds number, the liquid Prandtl number, the Peclet number and the Jacob number, where the Jacob number is based on the liquid superheat ΔT_l and the Reynolds and Peclet numbers are based on the relative velocity between phases U_r :

$$Ja = \frac{\rho_l C_{pl} \Delta T_l}{\rho_v L} \quad \text{and} \quad Nu = \frac{2R}{\lambda_l} h$$

$$Re = \frac{2R U_r}{\nu_l} \quad \text{and} \quad Pe = \frac{2R U_r}{a_l}$$

where L is the latent energy of vaporisation, R is the bubble radius, ρ_l is the liquid density, C_{pl} is the liquid specific heat, ν_l is the liquid viscosity and a_l is the liquid diffusivity.

$$\begin{cases} \text{If } (Ja < 0) \quad \text{then} \quad Nu = 2 + 0.6\,Re^{0.5} Pr^{0.33} \\ \text{If } (Ja > 0 \text{ and } Pe < \frac{36}{\pi} Ja^2) \quad \text{then} \quad Nu = \frac{12}{\pi} Ja \\ \text{If } (Ja > 0 \text{ and } Pe > \frac{36}{\pi} Ja^2) \quad \text{then} \quad Nu = \frac{2}{\sqrt{\pi}}\sqrt{Pe} \end{cases} \qquad (11)$$

The first relation (Ja < 0) is a classical one for a non-boiling situation. The second one is obtained by calculating the heat exchange through a thin boundary layer surrounding a motionless bubble. The third one corresponds to the case where heat transfer is controlled by the relative velocity rather than the liquid superheat.

BOUNDARY CONDITIONS

The system obtained from the conservation equations and the closure laws given above can be solved only if appropriate boundary conditions are given.

Boundary conditions at the inlets and outlets of the domain bring no modelling difficulty. However, they are seldom known accurately, and assumptions must be made on the main variable profiles.

The dynamic boundary conditions at the walls are written as for single-phase flows : a laminar and a turbulent sub-layers are assumed to be present. They apply only to the continuous phase ; the conditions for the dispersed phase are derived from those for the continuous phase.

The thermal boundary conditions at heating walls, in the case of nucleate flow boiling, are detailed below.

Modelling heat transfer at the wall

Modelling the boiling heat transfer is presently a real challenge for researchers. Indeed, boiling involves complex phenomena and a lot of research work is still needed before reaching a satisfactory understanding of the process.

In this context, a first model must rely on a simplification of the basic physical mechanisms which control the strong increase of heat flux during the nucleate boiling process. These mechanisms depend on local interaction between the wall and the fluid, in particular the wall site activity, that is to say the life of isolated bubbles (growth, collapse or departure) in a given thermal-hydraulic state and the spatial distribution of active sites.

In the absence of any global understanding of the processes involved, our aim here is to provide ASTRID with a first model of the wall heat transfer mechanisms. Closures involving the parameters, namely the mean bubble frequency, the mean waiting time between bubble departures, the mean bubble maximum equivalent diameter and the active site spatial density, must be given by the ASTRID user, in relation with his particular problem.

The two steps of this model are presented below :

- the condition for boiling incipience,
- the heat flux calculation.

Incipient boiling condition

In order to obtain satisfactory results, the incipient boiling point in a forced flow has to be determined accurately. We have chosen the widely used Hsu's criterion (Hsu, [6]). According to this criterion, a bubble will grow from a vapour embryo occupying a cavity if the liquid temperature at the tip of the embryo is at least equal to the saturation temperature corresponding to the bubble pressure.

Using the single phase temperature profile in viscous sub-layer, the following relations are obtained :

- if cavities of all sizes containing vapour embryo are available (which means that even the largest cavities contain vapour embryo), the wall superheat at boiling incipience $(\theta_w - \theta_{sat})$ and the wall heat flux q are related by :

$$\theta_w - \theta_{sat} = \theta_{crit1} = \left[\frac{8\sigma\theta_{sat}}{L\rho_{sat}} \frac{q}{\lambda_l} \right]^{1/2} \quad (12)$$

while the activated cavity radius r_{c1} is :

$$r_{c1} = \frac{\lambda_l}{2q} \theta_{crit1}$$

When the wall temperature reaches the critical value, the cavities of radius equal to r_{c1} are activated. Then, as the temperature still increases, smaller cavities are activated too.

- if the radius r_{cmax} of the largest cavity available (allowed to contain vapour embryo) on the surface is smaller than r_{c1}, the required wall superheat is higher :

$$\theta_w - \theta_{sat} = \theta_{crit2} = \frac{q}{\lambda_l} r_{cmax} + \frac{2\sigma\theta_{sat}}{L\rho_{sat}} \frac{1}{r_{cmax}} \quad (13)$$

In the three above equations, θ is a temperature (in K), σ the surface tension, L the latent energy of vaporisation, q the heat flux density from the wall, ρ_{sat} the volumic mass of the saturated vapour and λ_l the conductivity of the liquid phase.

If we refer to the well documented experimental study of Hino & Ueda [7][8], these relations are connected with the observed hysteresis phenomenon.

Boiling heat flux

In a first simplified approach, and following the analysis of Del Valle & Kenning [9] and Kurul & Podowski [10], the boiling heat flux is split into three terms :

- a "single phase flow" convective heat flux q_c at the fraction of the wall area unaffected by the presence of bubbles.

- a "quenching" heat flux q_Q where bubble departures bring cold water in contact with the wall periodically.
- a "vaporisation" heat flux q_v needed to form the vapour phase.

The wall surface unit is split into two parts : an area influenced by bubble departure A_b and a "single phase flow area" A_c with the relation : $A_c + A_b = 1$

A_b is the sum of the area of influence of each bubble over the unit surface. Neglecting the overlapping areas of influence between adjacent bubbles, A_b is written :

$$A_b = \mathrm{Min}\left(1 \ , \ n\pi D_i^2 / 4\right) \quad (14)$$

where n is the active site density.

D_i is the diameter of the area of influence. D_i is proportional to the bubble maximum diameter D. According to [10], $D_i = 2D$.

A classical law of single phase flow heat transfer at the wall is used to predict the flux q_c from the local Stanton number St_δ :

$$q_c = A_c \rho_l C_{pl} (\theta_w - \theta_\delta) U_\delta St_\delta \quad (15)$$

where δ is a point in the inertial sub-layer, U_δ the liquid velocity at point δ and C_{pl} the liquid specific heat.

Following [9], the quenching heat flux is modelled as the mean value of a transient conductive heat flux supplied to a semi infinite medium at external temperature θ_δ, during the waiting period t_w between the departure of a bubble and the beginning of growth of the following one.

$$q_Q = A_b t_w f \frac{2\lambda_l (\theta_w - \theta_\delta)}{\sqrt{\pi a_l t_w}} \quad (16)$$

a_l is the liquid thermal diffusivity :

$$a_l = \frac{\lambda_l}{\rho_l C_{pl}}$$

f is the bubble departure frequency,

$t_w f$ is the time fraction during which quenching occurs.

The use of a pure conductive process to model quenching is not well established, since the external convective heat flux often has a time scale comparable to it.

The vaporisation heat flux q_v is assumed to be proportional to the volume V of the bubble :

$$q_v = nf \rho_v L V \quad (17)$$

where $V = \frac{\pi}{6} D^3$.

It means that the net heat flux used to form vapour is supposed to arise from the wall. This approximation is well adapted for subcooled boiling, while for saturated boiling, energy is also received at the upper part of the bubbles.

Provided coherent closure relations for n, D, f and t_w are given, and the radius r_{cmax} is estimated, we have a closed model of the on-off boiling conditions associated with a given heat flux.

Correlations

The following correlations have been used in this study :

- For the density of active sites n [10] :

$$n = \left[210(\theta_w - \theta_{sat})\right]^{1.8} \quad (18)$$

- For the frequency f [10] :

$$f\sqrt{D} = \sqrt{\frac{4}{3}\frac{g(\rho_l - \rho_v)}{\rho_l}} \quad (19)$$

- For the time tw [9] :

$$t_w = 1/f$$

(the time of bubble growth is neglected).

- For the bubble diameter D (Unal , [11]) :

$$D = 2{,}42.10^{-5} . p^{0{,}709} . \frac{a}{\sqrt{b\Psi}} \quad (20)$$

with : p = pressure in Pa.

$$a = \frac{(\theta_w - \theta_{sat})\lambda_s}{2\rho_v L\sqrt{\pi a_s}} \quad b = \frac{(\theta_{sat} - \theta_\delta)}{2\left(1 - \rho_v/\rho_l\right)} \quad (21)$$

$$\Psi = \max\left(1 , \left(\frac{U}{U_0}\right)^{0,47}\right) \quad (22)$$

where s refers to the solid wall, δ to a point in the fluid turbulent sub-layer, and $U_0 = 0,61$ m/s. This correlation has been determined in subcooled water flows. We shall notice that Unal's correlation for bubble departure diameter has been developed for water flows, due to the lack of any other law we use it for other fluids.

NUMERICAL METHODS

Space discretization is based on structured meshes with collocated arrangements of the velocity components. It uses cartesian or curvilinear coordinates. For a better description of complex geometries which are typical of industrial situations, slanted boundary elements are defined.

ASTRID uses a mixed finite difference-finite volume method based upon an incremental version of a fractional step process to calculate main flow parameters (Simonin, [12]) ; (Hérard, [13]). As a matter of fact, like most of the two-fluid Eulerian models, ASTRID does not allow a completely conservative form.

To ensure discrete consistency of the separate phase mass balance equations, pressure as well as volumetric fraction of the dispersed phase are located at the center of each cell of the so-called velocity grid ; a second grid -called pressure grid- is then defined (see figure 1). Finite volume formulation is retained to solve mass conservation equations. The other equations will be solved with a finite difference method, the associated variables being non conservative (located on the velocity grid).

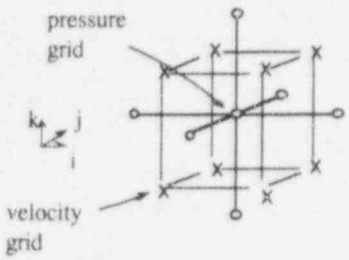

Figure 1: Staggered grids.

In principle, the fractional step method splits transport equations into elementary partial differential equations. This includes the following steps, each of which uses a specific numerical method :

- mass fraction for the dispersed phase is first predicted with a finite volume solver,
- (hyperbolic) advection step for all variables in each phase is solved using a three-dimensional method of characteristics with third order interpolation (optional treatment of variables by advection with finite volume solver is also available) ;
- (parabolic) diffusion step in each phase after taking into account the source terms ; alternate directions implicit methods are used in this part,
- (elliptic) step for pressure correction deduced from a combination of both the dispersed and continuous phase mass equations which is computed using a finite volume approach,
- continuous q^2 and ε source and diffusion step,
- prediction of particle fluctuating motions.

This method allows to solve equations (1), (2) and (3) with the temporal derivatives, steady state computation will be obtained with constant boundary limits and simulation time long enough to reach the steady state.

EXPERIMENTS TO VALIDATE THE MODELLING

In order to have experimental data to compare ASTRID results with, and to improve the physical modelling, EDF has developed some experimental studies of its own, and collaborates in some others :

- the Dedale experiment has been designed to investigate the dynamic of water-air bubbly flows in a vertical tube, at low void fractions first, then at higher void fractions, up to the transition to slug flows (Grossetête, [14]),
- the Poseidon experiment will allow us to study a boiling R12 flow around three heating rods, in a configuration close to those encountered in PWR nuclear reactors, and even up to the critical heat flux,
- the Debora experiment is carried out at the CENG (Grenoble, France), with the collaboration of EDF and Framatome. A boiling R12 flow in a tube is being studied up to the critical heat flux (Garnier, [15]),
- EDF and the Institut de Mécanique des Fluides de Toulouse (IMFT) are collaborating in an experiment designed to investigate the behaviour of boundary layers with nucleation at a wall. The experiment is an horizontal rectangular channel in which water flows and air is injected through a porous medium,

- an experimental study of a subcooled boiling R113 flow in a vertical annulus with a heated inner rod is carried on at the Arizona State University -ASU- [(Roy, 16]). EDF and EPRI collaborate in this study.

Note that Poseidon and Debora are both "PWR-like-condition" experiments, while the IMFT experiment is a more fundamental study, designed to investigate physical phenomena at a smaller scale.

Of course, we will also use the well documented experimental data available in the literature.

FIRST 1-D SIMULATION OF AN EXPERIMENT

A first comparison of the wall heat and mass transfer model with existing data was performed before implementation of this model in ASTRID (Borée, [17]).

The experimental results given by Hino & Ueda [7][8] were simulated : this was a R113 flow in an annular geometry, heated from the inner rod.

The results were correct in 1-D, except that the point of boiling incipience was found to be very sensitive to the value of the r_{cmax} parameter (the maximum radius of wall cavities that are useful for boiling incipience), which is difficult to know accurately.

SIMULATION OF ASU BOILING R113 FLOW IN ANNULAR GEOMETRY

The experiment

Turbulent subcooled boiling flows were investigated in this experiment. The test section is a vertical annular channel. The inner diameter is 15.9 mm, the outer diameter is 38.1 mm, and the measurement plane is located 1.94 m downstream of the beginning of the heated length (only the inner wall is heated).

The fluid is R113 under a pressure of 277 kPa. Only subcooled boiling is studied : the inlet temperature is about 30°C under the saturation temperature (T_{sat}=81.2°C).

Measured variables

Vapour phase fraction, bubble diameter and bubble axial velocity were measured by a dual-sensor fibre-optic probe. It was possible to make measurements at a distance of 0.4 mm from the wall [16].

The heated wall temperature was measured by thermocouples welded on the inner surface of the heating tube with the help of heat conduction calculations.

Liquid and vapour temperatures were obtained through a fluid temperature measurement achieved by a micro-thermocouple.

ASTRID calculations

We used ASTRID to simulate this boiling R113 flow. Note that although ASTRID is a 3-D code, this simulation is basically 2-D but solved on a 3-D grid with curvilinear coordinates. The first point of the mesh is located 0.4 mm from the heating wall, about the same distance as the closest measurement point. The radial discretization of the annulus uses 13 points (the mesh is non-uniform), the axial discretization uses 111 meshes $3.\ 10^{-2}$ meter long.

All the present calculations have been run with a constant bubble diameter. As vapour is produced at the heating wall and condenses in the subcooled liquid flow, this is equivalent to causing coalescence to happen (the number of bubbles decreases, rather than each bubble's diameter). This is a simplification : in fact, the model should include a decreasing diameter effect due to vapour condensation and an increasing diameter effect due to coalescence, as observed in the experiment. So, a bubble coalescence model should be included in the global boiling model. For the present calculations, we have set the diameter to 1 mm which is a value close to experimental measurements and coherent with bubble departure diameter given by Unal's correlation [11].

We simulated 4 different configurations :

	Heat flux (W/m^2)	Mass velocity ($kg/m^2/s$)	Inlet temperature (°C)
conf. 1	79400	568	50.2
conf. 2	94950	785	50.2
conf. 3	115725	785	50.2
conf. 4	126000	785	50.2

As mentioned above, though temporal derivatives are included in the equation solved, no temporal variation of the parameters is imposed and simulations reproduce steady state flows. We used the following boundary conditions :

At the inlet constant velocity, turbulent kinetic energy equals 0.05 m^2/s^2, dissipation rate equals 0.5 m^2/s^3 and void fraction is set to an arbitrary low value, 0.001.

In the different simulations, before comparing numerical and experimental results, we verified the conservation of mass and energy and obtain the following results :

	mass conservation (%)	energy conservation (%)
conf. 1	- 0.005	+ 0 93
conf. 2	+ 0.035	+ 1.77
conf. 3	- 0.018	+ 1.03
conf. 4	+0.024	+ 1.38

Mass conservation is very good and energy conservation is acceptable with a finite difference scheme and allows us to compare numerical results with experimental ones.

For the 4 configurations, the ASTRID simulations have been performed using the standard modelling (as described previously).

The comparison between experimental and computed results (see figure 2 to figure 13) concerns void fraction, bubble velocity, liquid temperature profiles along a dimensionless radius. The figures in which each variable is plotted are listed in the following table :

	void fraction	temperature	bubble velocity
conf. 1	fig. 2	fig. 3	fig. 4
conf. 2	fig. 5	fig. 6	fig. 7
conf. 3	fig. 8	fig. 9	fig. 10
conf. 4	fig. 11	fig. 12	fig. 13

In these figures, zero abscissa is at the surface of the inner heating rod, while abscissa 1 is at the surface of the outer tube. On the four configurations, the same trends are observed :

- the numerical model under estimates void fraction (fig. 2, 5, 8, 11), but the good agreement on the slope of the profile indicates the consistency of the modelling of the rate of condensation. Moreover, the point where no vapour remains is fairly well evaluated.
- The numerical results obtained on liquid temperature (fig. 3, 6, 9, 12) are also quite good, the difference between computation and measurement is always less than 2 K. As for the void, the code under estimates the liquid temperature. Those trends can be explained by the results obtained on bubble velocity.
- Indeed, the bubble velocity results (fig. 4, 7, 10, 13) are not completely satisfactory : the average value is overestimated, though radial profile isn't too bad. This over prediction can explain the discrepancies observed on void fraction and liquid temperature.

SIMULATION OF DEBORA BOILING R12 FLOW IN A TUBE

The Debora experiment is carried out at the CENG (Grenoble, France), with the collaboration of EDF and Framatome [15].

The experiment

Debora uses Refrigerant 12 to study boiling phenomena in a vertical tube of 19.2 mm internal diameter and 3.5 m heated length. Pressure can vary from 1.4 to 2.6 MPa, mass velocity from 2000 to 5000 kg/m^2/s, heat flux from 74 to 190 kW/m^2. Debora simulates the flow conditions encountered in PWR nuclear reactors.

Measured variables

Void fraction is measured by means of an optical fibre probe from subcooled boiling until critical heat flux conditions.

ASTRID calculations

We used ASTRID to simulate the R12 flow in the Debora geometry, with a pressure of 2.6 MPa (and thus a saturation temperature of 86.5 °C), in 4 different configurations :

	Heat flux (W/m^2)	Mass velocity (kg/m^2/s)	Inlet temperature (°C)	void fraction profiles
conf. 1	74000	2000	60	fig. 14
conf. 2	74000	2000	63	fig. 15
conf. 3	74000	2000	65	fig. 16
conf. 4	74000	2000	70	fig. 17

For these calculations, the radial discretization of the tubes uses 11 points (the mesh is uniform), the axial discretization uses 221 regular meshes. As for ASU simulation, all the present calculations have been run with a constant bubble diameter : according to Unal's correlation and measured diameter, we set the diameter to 0.3 mm. The comparison between experimental and computed results (see figure 14 to figure 17) concerns only void fraction. In all these figures, abscissa is the non dimensional radius (0 at the centre, 1 at the outer heating wall).

At the inlet constant velocity, turbulent kinetic energy equals 0.05 m^2/s^2, dissipation rate equals 0.5 m^2/s^3 and void fraction is set to an arbitrary low value, 0.001.

In these simulations, mass conservation is still very good but a very good energy conservation could not be achieved, because the grid mesh includes very distorted computing cells.

Discussion

The discussion is limited by the lack of experimental results which allow comparisons only on void fraction. The general physical results are quite good ; the rate of condensation is well predicted in the four configurations, but the prediction of void fraction at the wall is better for higher subcooled conditions.

CONCLUSION

3D modelling of boiling flows with ASTRID has already given very encouraging results : we have shown that the simulation of subcooled boiling flows with the two-fluid model 3D ASTRID code is possible and can lead to sound results.

The results obtained on void fraction are satisfactory in a wide range of conditions : different fluids, heat fluxes, mass flow rates and subcooling levels. It is important to underline that all the numerical results presented are obtained with the same physical model. The only differences are, of course, the physical properties of the two different fluids and the average diameter of the bubbles, set to 1 mm for Arizona cases and to 0.3 mm for Debora cases ; these two values are coherent with the measurements performed in each case, and with the bubble departure diameter given by Unal's correlation [11].

The results obtained on bubble velocity underline the improvements which have to be performed in dynamic model :

- improvement of the interfacial momentum transfer model. For that purpose we have set up an experimental program on void profile development in a vertical cylindrical pipe in air/water flow [14],
- introduction of a boundary condition on radial bubble velocity at the heating wall,
- improvement of the wall condition for liquid velocity by development of wall law adapted to nucleation situation [16],
- development of a coalescence-fragmentation model.

We shall also perform simulations of other literature experiments in order to enlarge the qualification basis of the code.

Thus, providing the code with appropriate physical models and boundary conditions remains a big challenge and will be an important field of studies for the next years.

NOTATION

Latin letters

a_σ	thermal diffusivity of the solid
ak	thermal diffusivity of phase k
A_b	sum of the area of influence of each bubble over the unit surface
A_c	single phase flow area
C_A	added-mass coefficient
C_L	lift force coefficient
C_L	drag force coefficient
C_{pl}	liquid specific heat
d	average bubble diameter
D_i	diameter of the area of influence
D	bubble max diameter
$D^i_{12,ii}$	the fluid-inclusion turbulent dispersion tensor
f	bubble detachment frequency
F_D	the average drag coefficient
$f_{t,i}$	interfacial transfer induced by the flow disturbance due to the inclusions
g_i	the i-component gravity
H_k	the mean enthalpy respectively for the continuous (k=1) and dispersed (k=2) phases
$I_{k,i}$	the part of the interfacial momentum transfer rate between phases which remains after substraction of the mean pressure contribution
Γ_{ki}	the part of the interfacial momentum transfer rate between phases independant of mass transfer
J_a	Jacob number

k	turbulent kinetic energy of continuous phase
L	latent energy of vaporisation
n	density of active sites
Nu	Nusselt number
P	the mean pressure of the continuous phase
Pe	Peclet number
q_{12}	the covariance between the turbulent velocity fluctuations of the two phases (eq. (9 bis)
q_c	part of the heat flux due to the single phase flow transfer (eq. 15)
q_Q	part of the heat flux due to the quenching (eq. 16)
q_v	part of the heat flux due to the evaporation (eq. 17)
r_{cl}	radius related to the critical temperature θ_{crit1}
r_{cmax}	radius of largest cavity available on the surface
Re	local mean particle Reynolds number
R	bubble radius
St_δ	Stanton number at a point δ in the inertial sub-layer
t_w	waiting period during nucleation
Tin	inlet temperature of the liquid
T	temperature
$U_{k,i}$	the mean velocity i-component respectively for the continuous (k=1) and dispersed (k=2) phases
$u''_{k,i}$	the corresponding velocity fluctuation i-component
U	average velocity
U_θ	velocity used in boiling mode
U_δ	average liquid velocity at point δ
U_r	average relative velocity between phases
$U_{\sigma,i}$	average relative velocity i-component between phases
$<u''_{1,i}\, u''_{1,j}>_1$	the turbulent Reynolds stress tensor
$<u''_{2,i}\, u''_{2,j}>_2$	the kinetic part of the granular stress tensor
$<u''_{2i}\, v''_n>_2$	the covariance tensor between the turbulent fluctuations of the two phases
V	volume of the bubble
v''_n	fluctuating part of the local instantaneous relative velocity between each particle and the surrounding fluid
$V_{r,i}$	average of the local instantaneous relative velocity between each particle and the surrounding fluid
$V_{d,i}$	fluid eddy-particle drifting velocity
Greek letters	
α_k	the volumetric fraction of the phase k
Γ_k	the interfacial mass transfer rate between phases
Π_k	the interfacial heat transfer rate between phases
ρ_k	the mean density of the phase k
δ_{ij}	Kronecker symbol
ε	dissipation rate of turbulent kinetic energy
ν_k	dynamic viscosity of phase k
λ_k	conductivity of phase k
μ_k	cinematic viscosity of phase k
σ	surface tension of the liquid (eq. (12), (13))
$\sigma'_{1,ij}$	turbulent part of the stress applied on the particle (eq. (4) and (10)
θ_{crit1}	first overheat of the wall in the incipient boiling model
θ_{crit2}	second overheat of the wall in the incipient boiling model
θ_w	temperature at the wall surface
θ_{sat}	saturation temperature of the liquid
θ_δ	liquid temperaure at point δ
τ'_{12}	turbulent tensor
ψ	coefficient used in the boiling model
indexes	
l	liquid
v	vapour
d	relative to the point δ
operators	
$<\,.\,>_k$	the averaging operator associated to the phase k

REFERENCES

[1] Thai Van D. et al., "Multi-Dimensional Two-fluid Model Computation of Turbulent Dispersed Two-Phase Flows", Proc. of the 1994 ASME Fluids Engineering Division Summer meeting, Lake Tahoe, Nevada, June 19-23, pp 277-290 (1994)

[2] Simonin O. & Viollet P.L. 1989, "Numerical Study on Phase Dispersion Mechanisms in Turbulent Bubbly Flows", International Conference on Mechanics of Two-Phase Flows, Taipei, Taiwan (1989)

[3] Simonin, O., Viollet, P.L., 1990, "Modelling of Turbulent Two-Phase Jets loaded with Discrete Particles", Phase-Interface Phenomena in Multiphase Flow, Hemisphere Publ. Corp., edited by F.G. Hewitt et al., pp. 259-269 (1990)

[4] Deutsch, E., Simonin, O., "Large Eddy Simulation Applied to the Modelling of Particulate Transport Coefficients in Turbulent Two-Phase Flows", Proc. 8th Int. Symp. on Turbulent Shear Flows, Munich, Germany (1991)

[5] Bel F'Dhila, R., Simonin, O., "Eulerian Prediction of a Turbulent Bubbly Flow Downstream of a Sudden Pipe Expansion", Proc. 6th Workshop on Two-Phase Flow Predictions, Erlangen, Germany, March 30-April 2 (1992)

[6] Hsu Y.Y.,"On the Size Range of Active Nucleation Cavities on a Heating Surface"
J. of Heat Transfer, 84, 207-216 (1962)

[7] Hino R. & Ueda T., "Studies on Heat Transfer and Flow Characteristics in Subcooled Flow Boiling. Part 1. Boiling Characteristics", Int. J. Multiphase Flow, 11, 269-281.(1985)

[8] Hino R. & Ueda T, "Studies on Heat Transfer and Flow Characteristics in Subcooled Flow Boiling. Part 2. Flow Characteristics", Int. J. Multiphase Flow, 11, 283-297 (1985)

[9] Del Valle M.V.H. & Kenning D.B.R., "Subcooled Flow Boiling at High Heat Flux"
Int. J. Heat Mass Transfer, 28, 1907-1920 (1985)

[10] Kurul N. & Podowski M.Z., "Multidimensional Effects in Forced Convection Subcooled Boiling"
Conference on heat and mass transfer, Jerusalem (1991)

[11] Unal H.C., "Maximum Bubble Diameter, Maximum Bubble Growth Time and Bubble Growth Rate during Subcooled Nucleate Flow Boiling of Water up to 17.7 MN/m2", Int. J. Heat Mass Transfer, 19, 643-649 (1976)

[12] Simonin O., Viollet, P.L., "Prediction of an Oxygen Droplet Pulverisation in a Compressible Subsonic Co-flowing Hydrogen Flow", Numerical Methods for Multiphase Flows, ASME FED, Vol. 91, pp. 73-82.(1990)

[13] Hérard J.M., Simonin, O., "Numerical Modelling of Turbulent Two-Phase Flows", Engineering Turbulence Modelling and Experiments, W. Rodi and E.N. Ganic, ed. Elsevier Science Publishers B.V., pp. 887-896 (1990)

[14] Grossetête C., "Experimental Investigation and Preliminary Numerical Simulations of Void Profile Development in a Vertical Cylindrical Pipe", Proc. Second International Conference on Multiphase Flow, '95-Kyoto (1995)

[15] Garnier J., "Measurements of Local Thermal Hydraulic Parameters in R12 Simulating PWR conditions from One-Phase Flow until Critical Heat Flux Conditions", European Two-Phase Flow Group Meeting, Hannover (1993)

[16] Roy R.P. & al., "Local Measurements in the Two-Phase Region of Turbulent Subcooled Boiling Flow", ASME J. of Heat Transfer.(1993)

[17] Borée J., Freydier Ph. et al., "Boiling Water Flows. A Local Wall Heat Transfer Model for use in an Eulerian 3-D Computer Code", Second ASME-JSME International Conference on Nuclear Engineering, San Francisco (1993)

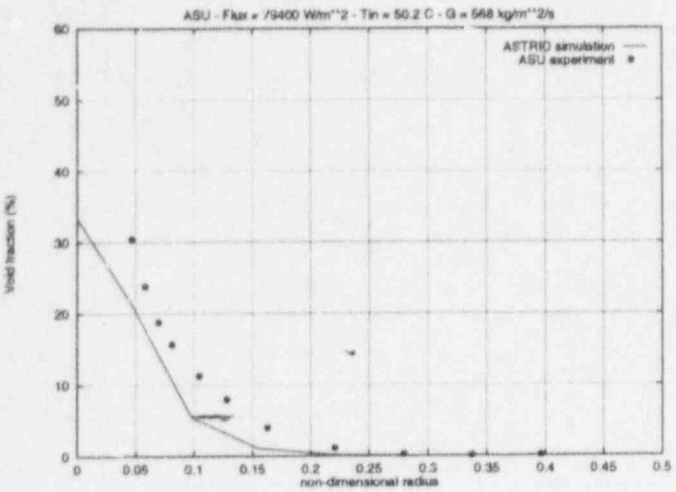

fig. 2 : void fraction - configuration 1

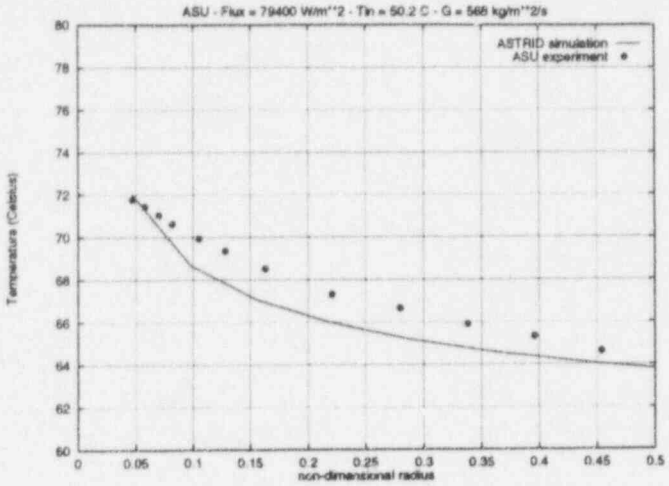

fig. 3 : liquid temperature - configuration 1

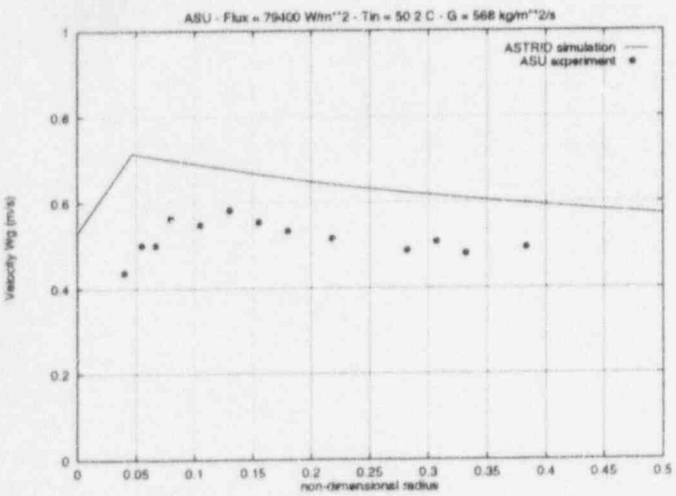

fig. 4 : bubble velocity - configuration 1

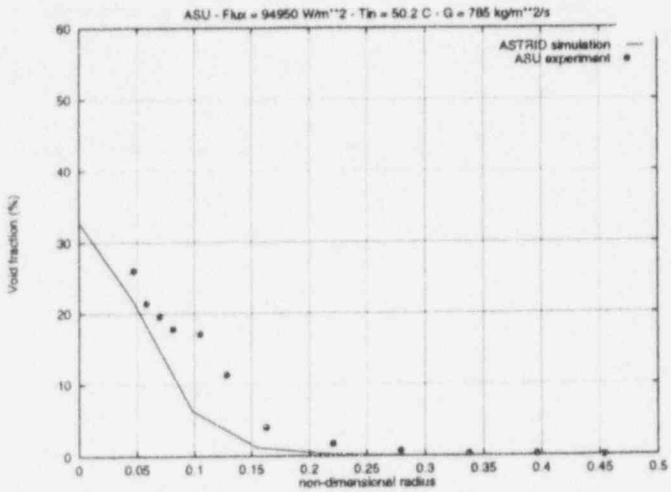

fig. 5 : void fraction - configuration 2

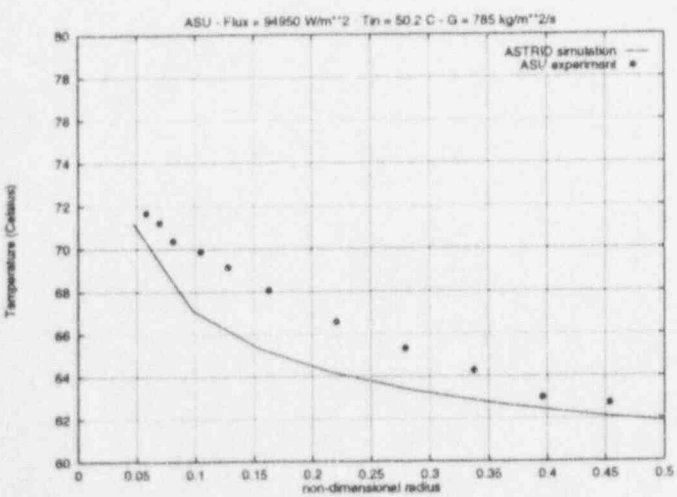

fig. 6 : liquid temperature - configuration 2

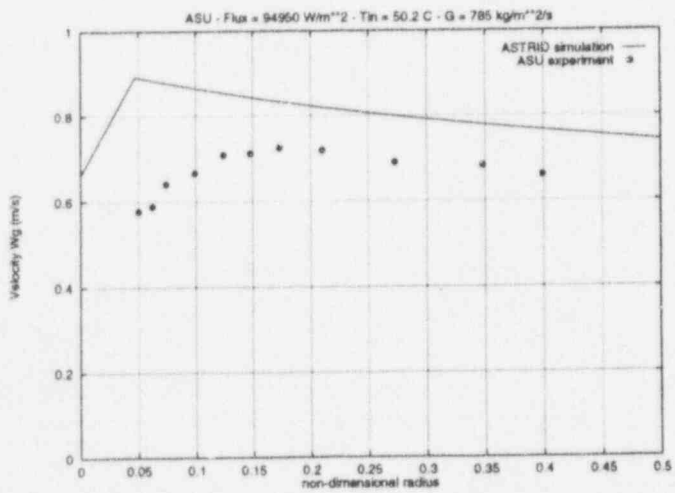

fig. 7 : bubble velocity - configuration 2

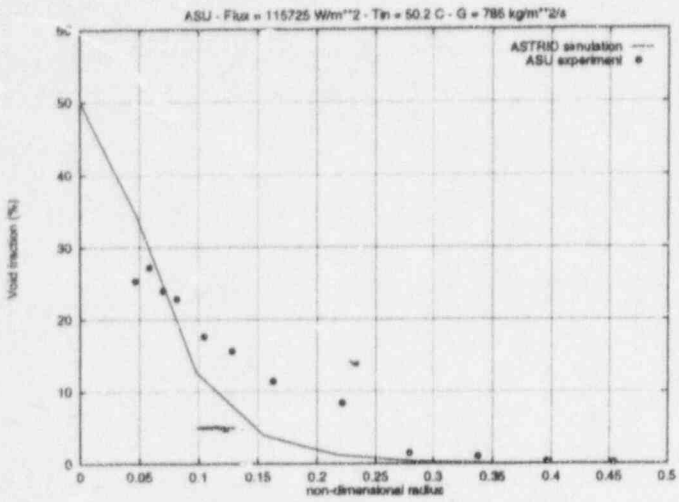

fig. 8 : void fraction - configuration 3

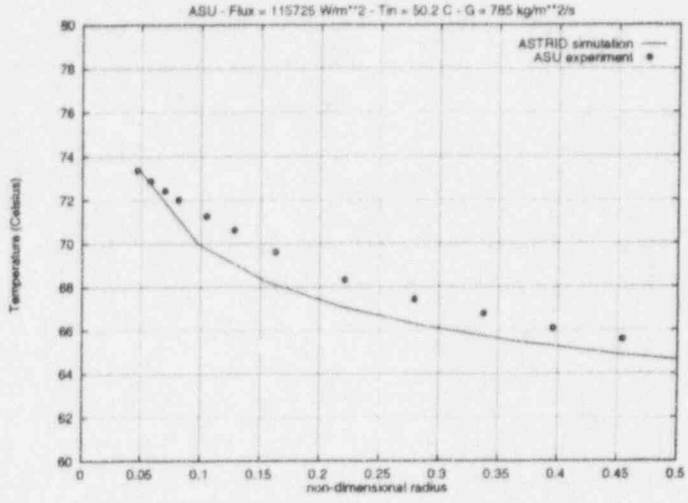

fig. 9 : liquid temperature - configuration 3

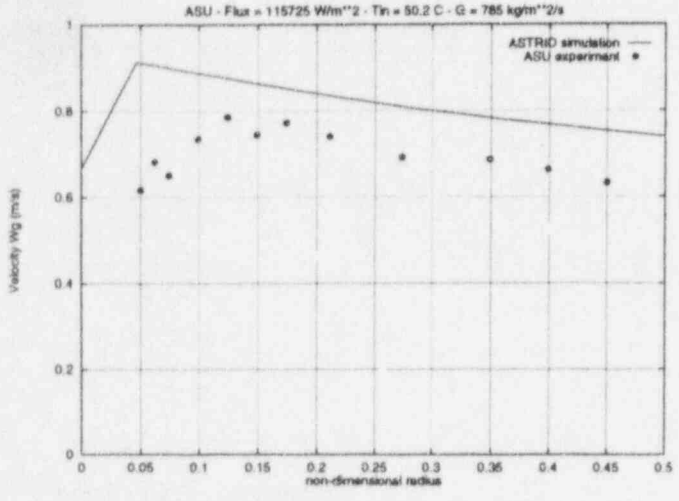

fig. 10 : bubble velocity - configuration 3

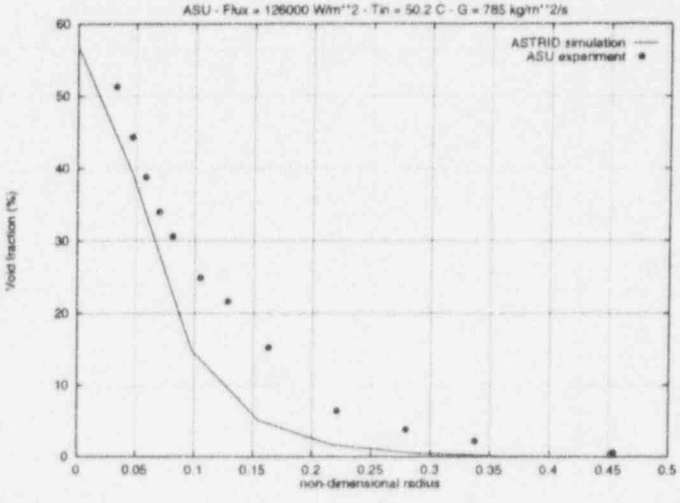

fig. 11 : void fraction - configuration 4

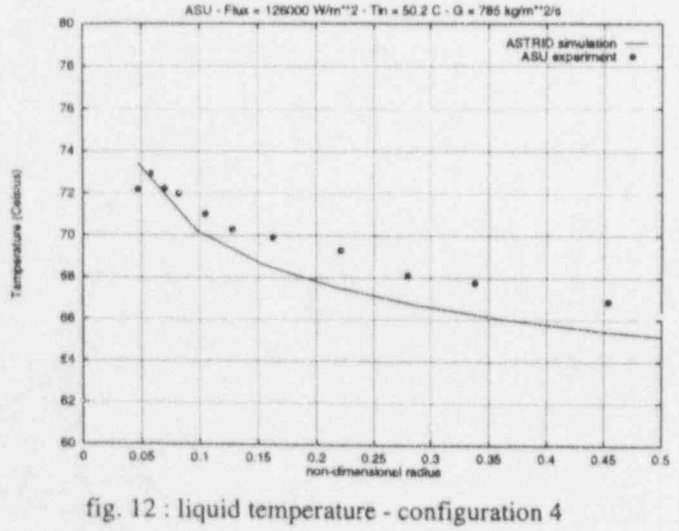

fig. 12 : liquid temperature - configuration 4

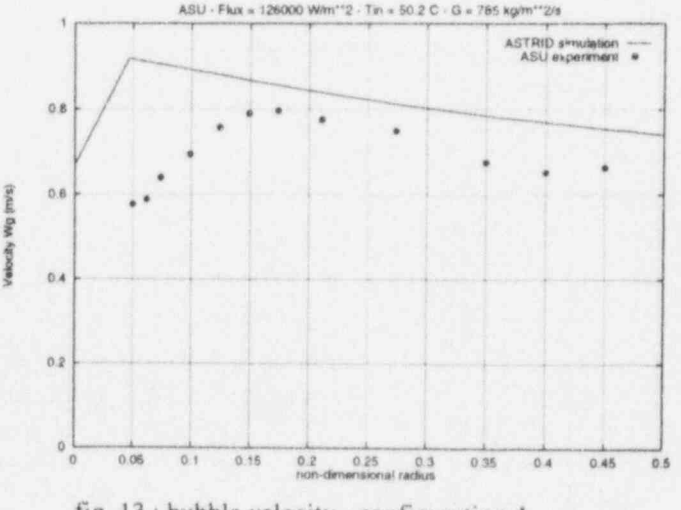

fig. 13 : bubble velocity - configuration 4

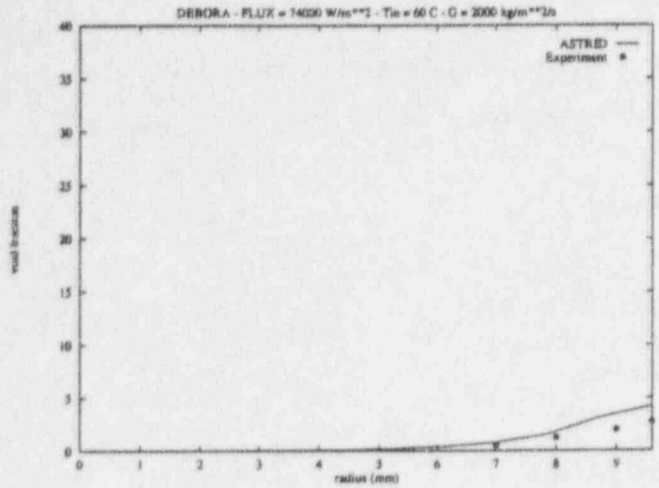

figure 14 : Debora Configuration 1 - void fraction

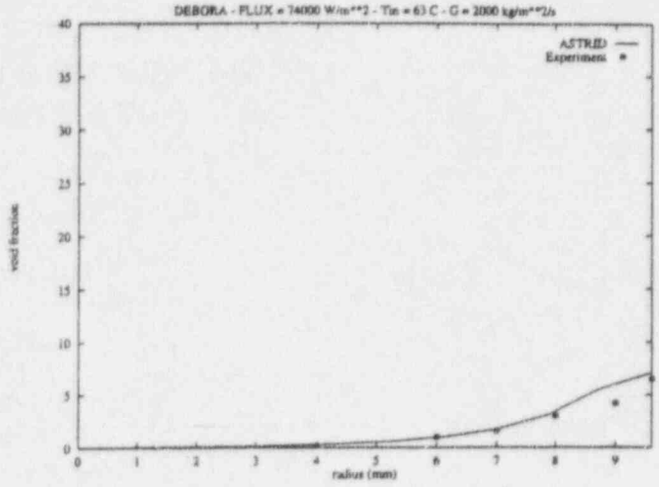

figure 15 : Debora Configuration 2 - void fraction

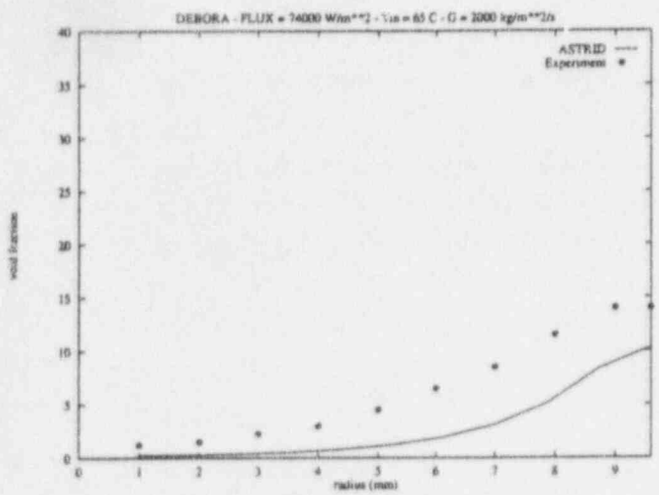

figure 16 : Debora Configuration 3 - void fraction

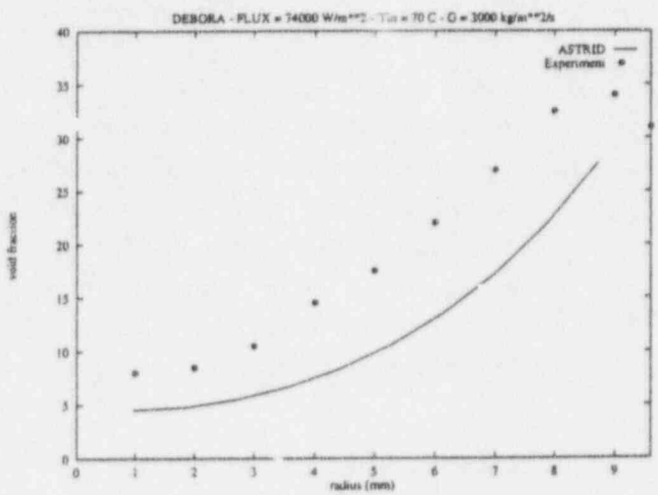

figure 17 : Debora Configuration 4 - void fraction

THE MULTI-DIMENSIONAL MODULE OF CATHARE 2 DESCRIPTION AND APPLICATION

F.Barré, I.Dor, C.Sun
French Atomic Energy Comission (C.E.A.)
Centre d'Etudes Nucleaires de Grenoble
DRN/DTP/STR-LML
85 X 38041 GRENOBLE CEDEX
FRANCE
Tel. (33) 76884904, Fax (33)76885177
E-mail: barre@ventoux.alpes.cea.fr

SUMMARY

In this paper, the three-dimensional module of CATHARE 2 is presented. It is based on a two-phase-flow six-equation model.
A predictor/corrector multistep method, with an implicit behaviour, is used to discretize the equations. Blowdown and boil-off analytical tests are used for an initial validation of the module. UPTF downcomer refill tests simulating the refill phase of a large-break loss-of-coolant accident are calculated.
Additional models, including molecular and turbulent diffusion, are added in order to perform containment calculations.

1. INTRODUCTION

CATHARE is the safety code developed by EdF (the French utility), Framatome (the French vendor) and the safety authority (CEA-IPSN). It is based on a six-equation two-fluid model with 4 additional equations for non-condensable gases [**1**] . Additional equations can be also used for transportation of boron and activity. Several hydraulical models are available:

*A one-dimensional model, with fully implicit time discretization

*A three-dimensional model, with a multistep method for time discretization, ensuring implicit behaviour. Its description is the subject of this paper.

*A tee model, boundary conditions (including source, sink and pump models) and various components useful to describe an industrial device.

Additional models are present in the code to take into account thermal conduction in the heat structures, mechanics in the fuel pins, cladding oxydation, neutronics and reflooding. The coupling of these models with the thermal-hydraulic models is implicit.

The aim of the three-dimensional module is mainly to describe either the pressure vessel

of a PWR during a Large Break LOCA or a severe accident, or the behaviour of the containment building or any other components where 3D-effects are important. The objectives are:

* to provide a robust two-phase-flow three-dimensional module,
* to add the models nescessary to describe large cavities with diffusion of gases,
* to have a flexible module to be used in any geometries and to be connected to a standard CATHARE circuit.

The three-dimensional module is based on the two-fluid six-equation model to ensure correct modelling of two-phase flow. The scalar equations (mass equations, energy equations, non-condensable gas equations) are integrated inside a volume with either six faces (in rectangular coordinates) or five or six faces (in cylindrical coordinates). Two momentum equations (one for each phase) are centered on each of the five (or six) faces to define the liquid and gas velocities. In this basic version, neither the molecular diffusion nor the turbulent diffusion are taken into account. The constitutive relationships are those of the one-dimensional module [2]. Heat structures and the fuel module (taking into account mechanics and oxydation) are connected to this module. The reflooding module of CATHARE, using a two-dimensional heat conduction model in the fuel pins has been implemented. In a first step, qualification is performed using separate effect tests from the qualification of CATHARE 2, in order to verify that this module, with its particularities, gives the same quality of results asthe one-dimensional module, when the flow is essentially one-dimensionnal. In a second step, typical experiments involving multidimensional effects are used for qualification.

For describing long term transients in a containment building, an option has been introduced where mass and energy diffusion terms have been implemented in the equation of each phase. Another option allowsa turbulence model to be used on each phase. These options are qualified in single phase conditions by using the results of the TRIO-VF code [3].

In the basic module, the equations are discretized using a first order finite difference scheme with staggered spatial mesh and a donor-cell method. A second order scheme has been implemented in the mass and energy fluxes to be able to take into account the propagation of fronts.

2. TWO PHASE FLOW THREE-DIMENSIONAL MODEL

2.1 Six equation model with non-condensable gases

An extension of the six equation two fluid model derived by Delhaye and al.[4] is used. this model is presented on table 1. For each phase mass equation, energy equation and momentum equations in each direction are written.

2.2 Spatial discretization

The data management and the numbering of the volumes and the faces are not described by (i,j,k) coordinates but by indirect addresses in order to avoid defining the empty parts of the geometry and in a further approach to plan development of non-structured meshing. A scalar point is denoted as **I** (Figure 1) and, for example in the direction x, the neighbour scalars are denoted as ISX+(I) and ISX-(I). The neighbouring faces are called IVX+(I), IVX-(I). In the same way, the face number IF perpendicular to the X-axis (Figure 2) is located between the scalar points denoted IAX-(IF) and IAX+(IF) .

Table 1 : CATHARE three dimensional two fluid model

Mass equation for the phase k:

$$\frac{\partial}{\partial t}\left(\alpha_k \rho_k\right) + \mathrm{div}\left(\alpha_k \rho_k \vec{V}_k\right) = (-1)^k \Gamma_k \qquad (1)$$

Energy equation for the phase k:

$$\frac{\partial}{\partial t}\left(A\alpha_k \rho_k e_k\right) + \mathrm{div}\left(A\alpha_k \rho_k e_k \vec{V}_k\right) + p\left[A\frac{\partial}{\partial t}(\alpha_k) + \mathrm{div}\left(A\alpha_k \vec{V}_k\right)\right] = \qquad (2)$$

$$(-1)^k \cdot \Gamma_k h_k + (-1)^k q_{ke} + q_{kw}$$

Momentum equation for phase k:

$$\alpha_k \rho_k \left[\frac{\partial \vec{V}_k}{\partial t} + \left(\vec{V}_k \cdot \vec{\nabla}\right) \cdot \vec{V}_k\right] + \alpha_k \cdot \vec{\nabla P} + p_i \cdot \vec{\nabla \alpha_k} = (-1)^k \cdot \vec{\tau}_i - \vec{F}_k + \vec{\alpha_k \rho_k g} \qquad (3)$$

Non-condensable gas transport equation (i=1,4)

$$\frac{\partial}{\partial t}(\alpha_g \rho_g X_i) + \mathrm{div}\left(\alpha_g \rho_g X_i \vec{V}_g\right) = S_i \qquad (4)$$

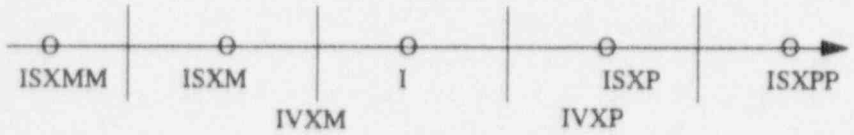

Figure 1
Definition of the neighboured faces and volumes of the volume I
O: center of the volumes | : faces in the x-direction

2.3 Time discretization

Since the beginning of CATHARE development in 1979, a fully implicit scheme (interphase exchanges, pressure propagation and convection terms are implicitly evaluated) has been used to achieve the largest possible time step with no CFL limit. In the case of a three-dimensional module, a fully implicit method would be highly time consuming on account of having to solve large Jacobian matrices. It was decided to keep implicit behaviour by developing a quasi-implicit multistep method with a high level of implicitness.

In the first step (predictor step), the level of implicitness is higher in CATHARE than in other similar codes. In the scalar equations (mass, energy and non-condensable gas transport), the sources terms (in particular the transfer between phases) are implicitly evaluated. The convective terms are implicitly evaluated if the fluid exits the integration volume and explicitly evaluated if it

enters. The momentum equations are projected on the three axes. Discretization is similar for each of the projection. In the momentum equations, the closure terms (e.g. the interfacial friction τ_i, the phasic wall friction τ_{kw}, etc) are implicitly calculated. The pressure and the velocity components on the projection axis are implicit. The two other components are explicit.

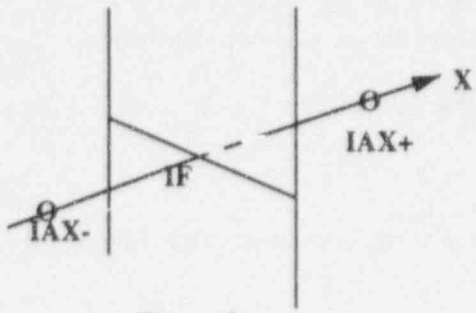

Figure 2

Definition of the scalar points beside a face IF

The second step (corrector step) ensures correct mass and energy balance. In this step, the momentum equations are not used: the pressure field and the phasic velocity map are not changed and the solution of the predictor step is considered. In the scalar equations the source terms are those calculated with the solution of the predictor step. Only the convective terms are re-evaluated to have a correct distribution of the energy and of the phases.

A final step is nescessary to calculate the main variables, (i.e. liquid or gas temperatures, void fraction, gas concentrations).

2.4 Discretized equations (predictor step)

The discretized scalar equations are presented on table 2.

For the phase mass equations, it may be noted that all the terms of this equation, including the mass transfer between phases, are implicitly evaluated, excepted the scalar donor cell values of the void fraction and the density: $\tilde{\alpha}_k$, $\tilde{\rho}_k$, which are taken as being implicit if the fluid exits the cell or explicit if the fluid enters the cell. For example:

$$(\tilde{\alpha}_k \cdot \tilde{\rho}_k)_{ivxp} =$$

$$\begin{cases} \text{either } \alpha_k(I) \cdot \rho_k(I) & \text{if } u_k(ivxp) > 0 \\ \text{or } \alpha_k^*(isxp) \cdot \rho^*_k(isxp) & \text{if } u_k(ivxp) < 0 \end{cases}$$

$$(\tilde{\alpha}_k \cdot \tilde{\rho}_k)_{ivxm} =$$

$$\begin{cases} \text{either } \alpha_k(I) \cdot \rho_k(I) & \text{if } u_k(ivxm) < 0 \\ \text{or } \alpha_k^*(isxm) \cdot \rho^*_k(isxm) & \text{if } u_k(ivxm) > 0 \end{cases}$$

For the phase energy equation, the scalar donor cell terms are taken as being either implicit if the fluid exits the cell or explicit if it enters. All the other terms, including the source terms (heat exchange between phases q_{ke}, heat exchange between heat structure and phase 'k' q_{kv}, and heat exchange due to mass transfer Γh_k^0) are taken as being implicit.

$h_k^0 =$ either hl for the liquid energy equation (k=l)
or hv for the gas energy equation (k=g).

For the non-condensable gas equations the discretization is similar to the phase mass equations.

The projection upon the x-axis of the discretized momentum equation, perpendicular to the face IF, is presented on table 3.

In this momentum equation, the implicit variables are P and u_k, including in the interfacial friction $\tau_{i,x}$ and the wall friction $F_{k,x}$. The other scalar variables and the other velocitiy components v_k and w_k are explicitly evaluated.

$$\Delta u_k(IF) =$$

$$\text{either } u_k(IF) - u_k(ivxm(iaxm)) \text{ if } u_k(IF) > 0$$

$$\text{or } u_k(ivxp(iaxp)) - u_k(IF) \text{ if } u_k(IF) \le 0$$

2.5 Discretized equations (corrector step)

In the mass and energy equations, the balances are not conservative because the mass and energy fluxes are taken as being either implicit or explicit. The corrector step ensures a correct mass and energy balance. In this step, the pressure field and velocities, which are the results of the predictor step, are not re-evaluated. The momentum equations are therefore not recalculated. The source terms, in particular the transfer between phases, are calculated with the scalar and vector variables which are the solution of the predictor step. In conclusion, in this step only the phase distribution and the temperature field are re-evaluated.

In that way, the equations of the corrector step are linear and the jacobian matrix has the same shape, on the one hand for the mass and energy equation of the liquid phase and on the other hand for the mass, energy and gas transport for the gas phase. These equations are presented on tables 4 and 5.

2.6 The solving of the system

In CATHARE, the system of non-linear equations is solved using a Newton-Ralphson iterative method. In each time step, the general solving of the 3D-module is similar to the techniques used for the other modules of the code, using the principle of domain reductions:

Table 2 : Discretized scalar equations

Mass equation for phase k written in the integration volume I (5)

$$VOL \cdot \alpha_k \cdot \rho_k(I) - VOL \cdot \alpha_k^* \cdot \rho^*_k(I) +$$
$$(\Delta t \cdot A_y \cdot \tilde{\alpha}_k \cdot \tilde{\rho}_k \cdot u_k)_{ivxp} - (\Delta t \cdot A_x \cdot \tilde{\alpha}_k \cdot \tilde{\rho}_k \cdot u_k)_{ivxm}$$
$$+ (\Delta t \cdot A_y \cdot \tilde{\alpha}_k \cdot \tilde{\rho}_k \cdot v_k)_{ivyp} - (\Delta t \cdot A_y \cdot \tilde{\alpha}_k \cdot \tilde{\rho}_k \cdot v_k)_{ivym} +$$
$$(\Delta t \cdot A_z \cdot \tilde{\alpha}_k \cdot \tilde{\rho}_k \cdot w_k)_{ivzp} - (\Delta t \cdot A_z \cdot \tilde{\alpha}_k \cdot \tilde{\rho}_k \cdot w_k)_{ivzm} = (-1)^k \Delta t \cdot VOL \cdot \Gamma(I)$$

Energy equation for phase k written in the integration volume I (6)

$$VOL \cdot \alpha_k \cdot \rho_k \cdot e_k(I) - VOL \cdot \alpha_k^* \cdot \rho_k^* \cdot e_k^*(I)$$
$$+ (\Delta t \cdot A_x \cdot \tilde{\alpha}_k \cdot \tilde{\rho}_k \cdot \tilde{e}_k \cdot u_k)_{ivxp} - (\Delta t \cdot A_x \cdot \tilde{\alpha}_k \cdot \tilde{\rho}_k \cdot \tilde{e}_k \cdot u_k)_{ivxm}$$
$$+ (\Delta t \cdot A_y \cdot \tilde{\alpha}_k \cdot \tilde{\rho}_k \cdot \tilde{e}_k \cdot v_k)_{ivyp} - (\Delta t \cdot A_y \cdot \tilde{\alpha}_k \cdot \tilde{\rho}_k \cdot \tilde{e}_k \cdot v_k)_{ivym} +$$
$$(\Delta t \cdot A_z \cdot \tilde{\alpha}_k \cdot \tilde{\rho}_k \cdot \tilde{e}_k \cdot w_k)_{ivzp} - (\Delta t \cdot A_z \cdot \tilde{\alpha}_k \cdot \tilde{\rho}_k \cdot \tilde{e}_k \cdot w_k)_{ivzm}$$
$$+ [(A_x \cdot \tilde{\alpha}_k \cdot u_k)_{ivxp} - (A_x \cdot \tilde{\alpha}_k \cdot u_k)_{ivxm} + (A_y \cdot \tilde{\alpha}_k \cdot v_k)_{ivyp} - (A_y \cdot \tilde{\alpha}_k \cdot v_k)_{ivym} +$$
$$(A_z \cdot \tilde{\alpha}_k \cdot w_k)_{ivzp} - (A_z \cdot \tilde{\alpha}_k \cdot w_k)_{ivzp}] \cdot \Delta t \cdot P(I)$$
$$+ P(I) \cdot (VOL \cdot \alpha_k(I) - VOL \cdot \alpha_k^*(I)) =$$
$$\Delta t \cdot VOL(I) \cdot (\Gamma \cdot h_k^\circ + (-1)^k q_{ke})(I) + \Delta t \cdot S_{exch} \cdot q_{kw}(I)$$

Transport equation for the gas i (i=1,4) is written in the integration volume I: (7)

$$VOL \cdot \alpha_g \cdot \rho_g \cdot x_i(I) - VOL \cdot \alpha_g^* \cdot \rho^*_g \cdot x_i^*(I)$$
$$+ (\Delta t \cdot A_x \cdot \tilde{\alpha}_g \cdot \tilde{\rho}_g \cdot \tilde{x}_i \cdot u_g)_{ivxp} - (\Delta t \cdot A_x \cdot \tilde{\alpha}_g \cdot \tilde{\rho}_g \cdot \tilde{x}_i \cdot u_g)_{ivxm} +$$
$$(\Delta t \cdot A_y \cdot \tilde{\alpha}_g \cdot \tilde{\rho}_g \cdot \tilde{x}_i \cdot v_g)_{ivyp} - (\Delta t \cdot A_y \cdot \tilde{\alpha}_g \cdot \tilde{\rho}_g \cdot \tilde{x}_i \cdot v_g)_{ivym}$$
$$+ (\Delta t \cdot A_z \cdot \tilde{\alpha}_g \cdot \tilde{\rho}_g \cdot \tilde{x}_i \cdot w_g)_{ivzp} - (\Delta t \cdot A_z \cdot \tilde{\alpha}_g \cdot \tilde{\rho}_g \cdot \tilde{x}_i \cdot w_g)_{ivzm} =$$
$$(-1)^k \Delta t \cdot S_i(I) \cdot \Gamma(I)$$

Table 3 : Discretization of the momentum equations

The projection upon the x-axis of the discretized momentum equation, perpendicular to the face IF: (8)

$$\left(\alpha^m_{x,k}(IF) \cdot \rho^m_{x,k}(IF) \cdot (u_k(IF) - u_k^*(IF))\right)/(\Delta t)$$
$$+ \alpha^v_{x,k} \cdot \rho^m_{x,k} \cdot u_k \cdot \Delta u_k(IF) + \alpha^m_{x,k} \cdot \rho^m_{x,k} \cdot \overline{v_k} \cdot \Delta u_k(IF) + \alpha^m_{x,k} \cdot \rho^m_{x,k} \cdot \overline{w_k} \cdot \Delta u_k(IF) +$$
$$\alpha^m_{x,k} \cdot \rho^m_{x,k} \cdot g_x(IF) + \left(\alpha^m_{x,k}(IF) \cdot (P(iaxp) - P(iaxm))\right)/\Delta t$$
$$+ p_i \cdot (\alpha_k(iaxm) - \alpha_k(iaxp))/(\Delta z) + (-1)^k \cdot \tau_{i,x} + F_{k,x} = 0$$

Table 4 : Discretized equations used for the corrector step

$$
\begin{aligned}
&VOL(I)\cdot s_k(I) - VOL(I)\cdot s_k^*(I)\\
&+ (\Delta t\cdot A_x\cdot u_k\cdot \tilde{s}_k)_{ivxp} - (\Delta t\cdot A_x\cdot u_k\cdot \tilde{s}_k)_{ivxm}\\
&+ (\Delta t\cdot A_y\cdot v_k\cdot \tilde{s}_k)_{ivyp} - (\Delta t\cdot A_y\cdot v_k\cdot \tilde{s}_k)_{ivym}\\
&+ (\Delta t\cdot A_z\cdot w_k\cdot \tilde{s}_k)_{ivzp} - (\Delta t\cdot A_z\cdot u_k\cdot \tilde{s}_k)_{ivzm} = S_k
\end{aligned}
$$

Table 5 : Values of s_k

Equation:	Mass balance	Energy balance
Liquid phase	$s_1 = \alpha_l\cdot\rho_l$	$s_2 = \alpha_l\cdot\rho_l\cdot e_l$
Gas phase	$s_3 = \alpha_g\cdot\rho_g$	$s_4 = \alpha_g\cdot\rho_g\cdot e_g$
Non condensable gas (i=1,4)	$s_{4+i} = \alpha_g\cdot\rho_g\cdot x_i$	

For each iteration of the time step:

-1- Elimination of the internal equations as a function of the connections with the other modules using the predictor step. The result of this operation is the contribution of the 3D module to the general matrix of the system.

-2- After solving the system equation, regeneration of the connection variables.

-3- Regeneration of the internal variables.

If the time step has converged, correction of internal phase separation and of the temperature distribution, using the corrector step, is carried out.

2.6.1 Solver for the predictor.

The internal variable elimination step using the equations of the predictor step is performed in three steps. By using the momentum equations, simple arithmetic manipulation eliminates the velocities. In the scalar equations, the enthalpies, void fraction and gas qualities are eliminated as a function of the pressure. Then the velocities are eliminated using the results of the momentum equation manipulation. It reduces the system leaving only the pressure as an unknown. This reduction leads to a highly sparse Jacobian linear system matrix, with 7 diagonals or 9 diagonals, depending on the choice of coordinate sytem. Then, by adding the equations of the connections, the internal pressure is eliminated as a function of the main variables of these boundaries. This step leads to the inversion of the large Jacobian matrix. It is performed using either a direct solver or a bi-conjugate gradient technique for a non-symetrical matrix.

2.6.2 Solver for the corrector.

The solving of the corrector step is achieved by inversion of a 7 or 9 diagonal matrix similar to the pressure matrix of the predictor step. The same solvers already used for the predictor can be used here because the band matrix has exactly the same structure in both steps.

3. QUALIFICATION OF THE 3-D TWO PHASE FLOW MODEL

3.1 Introduction

Numerical qualification of the module has been intensively performed. In particular, the stability of the numerical scheme has been proved. Mass and energy balance has been systematically verified. It has been already presented.

Physical assessment of this module has been started using comparison with simple two-phase flow analytical experiments, used in the assessment of the 1D-module [5], in order to be sure of discretization. Then, experiments devoted to multidimensional problems are used.

3.2 Tapioca experiment

The TAPIOCA blowdown experiment was conducted at the CEA in Cadarache, France [6]. The test section consists of a tube with a 0.32m internal diameter and a 2.6m length. The volume to depressurize is 0.33m^3. At the beginning of the test, the tube is filled with pressurized water at 280C and 15 MPa.The available measurements are: absolute pressure, differential pressure at six levels, fluid temperature and wall temperature. The break can be located at four positions (top of the test section and three different lateral positions). Different sizes of the break are also available. In this paper, typical results obtained with the three-dimensionnal module, modelling a test with a 20mm-diameter lateral break, are presented. An experiment with lateral break has been selected because the three dimensional behaviour of the blowdown is more relevant than in other test. The test section is modelled with 782 meshes with the 3-dimensional module. The break nozzle is modelled by a 1D-module. The critical flow is performed using the one dimensional model and the characteristic method to evaluate the sonic velocities. Mass inventory, pressure and void fraction profiles are compared. Good agreement is shown between experiment, calculation with the 1D-module and calculation with the 3D module(figures 3 and 4).

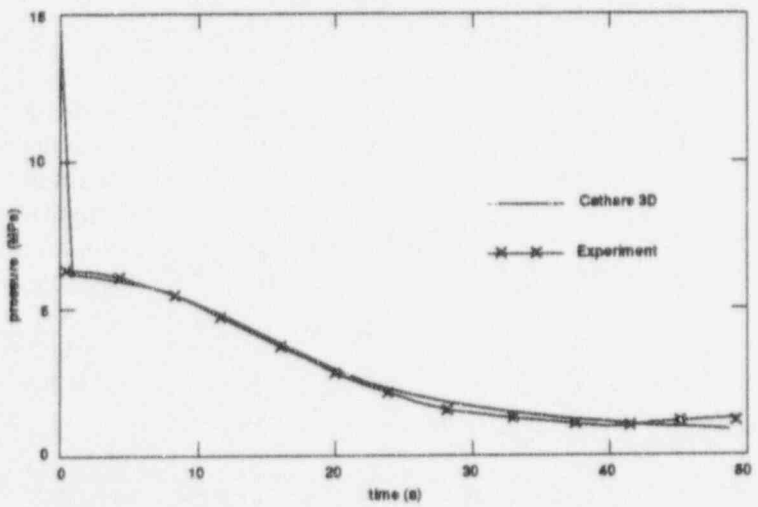

Figure 3
Tapioca experiment
Measured and predicted pressure.

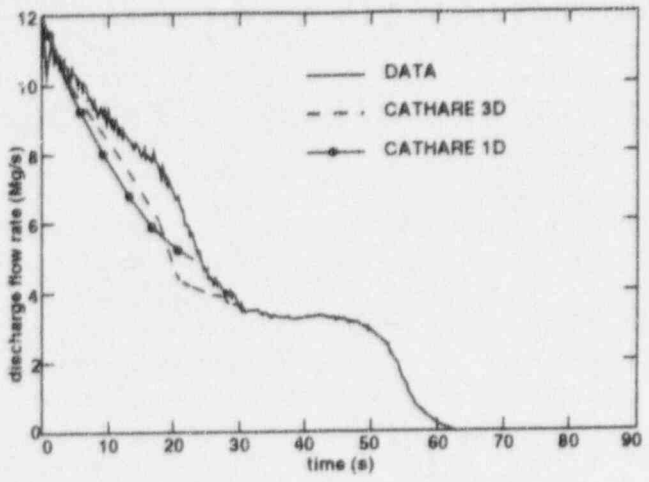

Figure 4: Tapioca experiment
Comparison between predicted and measured break flow

3.2 Marviken experiment

The MARVIKEN critical flow tests were conducted at the Marviken power station in Sweden [7]. The four major components of the facility are a vessel, a discharge pipe, connected at the bottom of the vessel, a test nozzle with the minimum flow area of the assembly and a rupture disk to model a break. The total height of the vessel is 24.55m. The vessel diameter is 5.22m. The total volume of the vessel is 421.m^3. The pressure is measured at the top and at the the bottom. The temperatures are measured at different elevations. In the instrumentation ring of the break, pressure, temperature and void fraction over three chords are measured. Results are presented here for a run initialised at 4.96MPa and 233.5C and with a 0.5m diameter and 0.166m length nozzle. Comparisons between the experiment, the 3-D calculation and the 1-D calculation are presented for pressure and void fraction profile on figures 5 and 6.

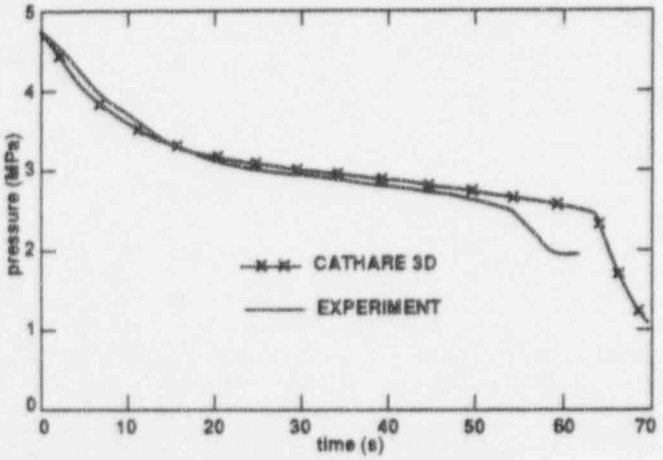

Figure 5: Marviken experiment
Comparison between predicted and measured pressure

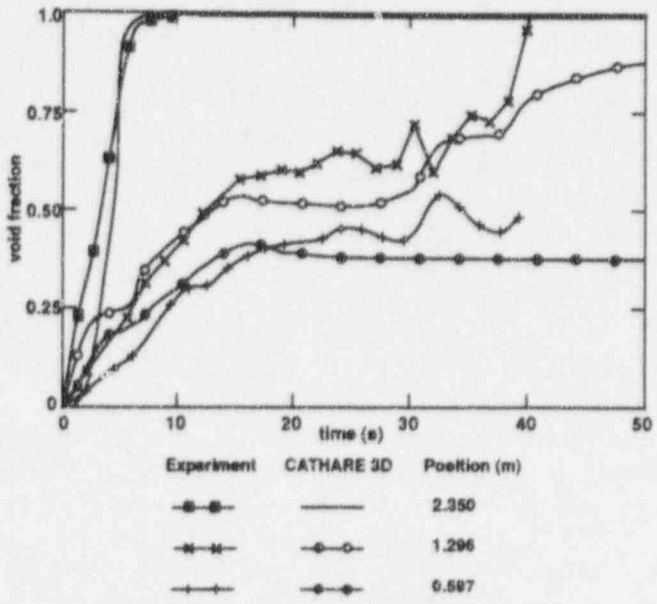

Figure 6: Marviken experiment
Comparison between predicted and measured void faction profile

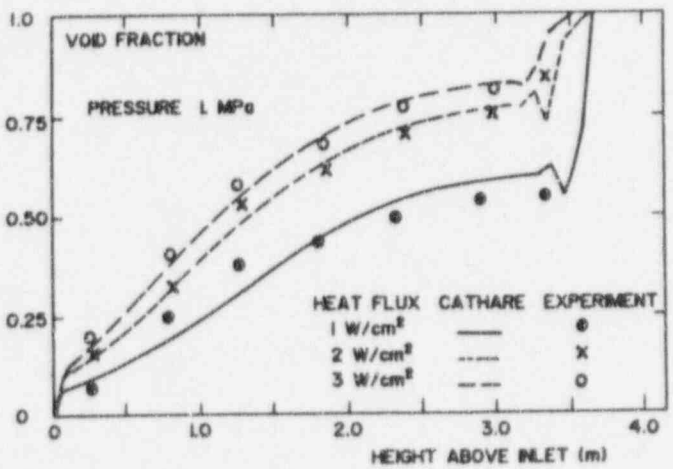

Figure 7: Pericles experiment
Comparison between predicted and measured void fraction profile

3.3 PERICLES boil-off tests.

The PERICLES experiment was conducted by CEA in GRENOBLE, France [5]. This experiment was devoted to reactor core physics. Boil off tests and low and high pressure reflooding tests were run in two test sections. The cylindrical test section consists of 368 electrical rods and 25 guide tubes in a 17x17 assembly. The rectangular test section consists of three 7x17 heated rod assemblies: it is devoted to the study of multi-dimensional effects during reflooding.

Rod and guide tube wall temperatures are measured with thermocouples. 124 electrical

rods, with 6 thermocouples each, are instrumented allowing temperature measurements at 41 elevations. Fluid temperature is measured with three thermocouples at the end of the test section. Eight pressure taps are located along the test section. Inlet and outlet mass flow rates and generated power are measured.

In a first attempt, only boil off tests were calculated with the three-dimensional module. Comparisons of void fraction profile between 3D-module and experiment are presented. In the near future, reflooding tests will be performed.

3.4 UPTF tests.

The objective of the UPTF test programme [8] is the full-scale investigation of the 3D two-phase-flow behaviour in the primary system of a PWR during the end of blowdown, refill, and reflood phases of a loss-of-coolant accident (LOCA). Separate effect tests and integral tests are performed to study thermal hydraulic phenomena across the upper tie plate, in the upper plenum, in the hot and cold legs and in the downcomer of the primary system.

In a first attempt, the model was qualified against downcomer refill tests. In a previous

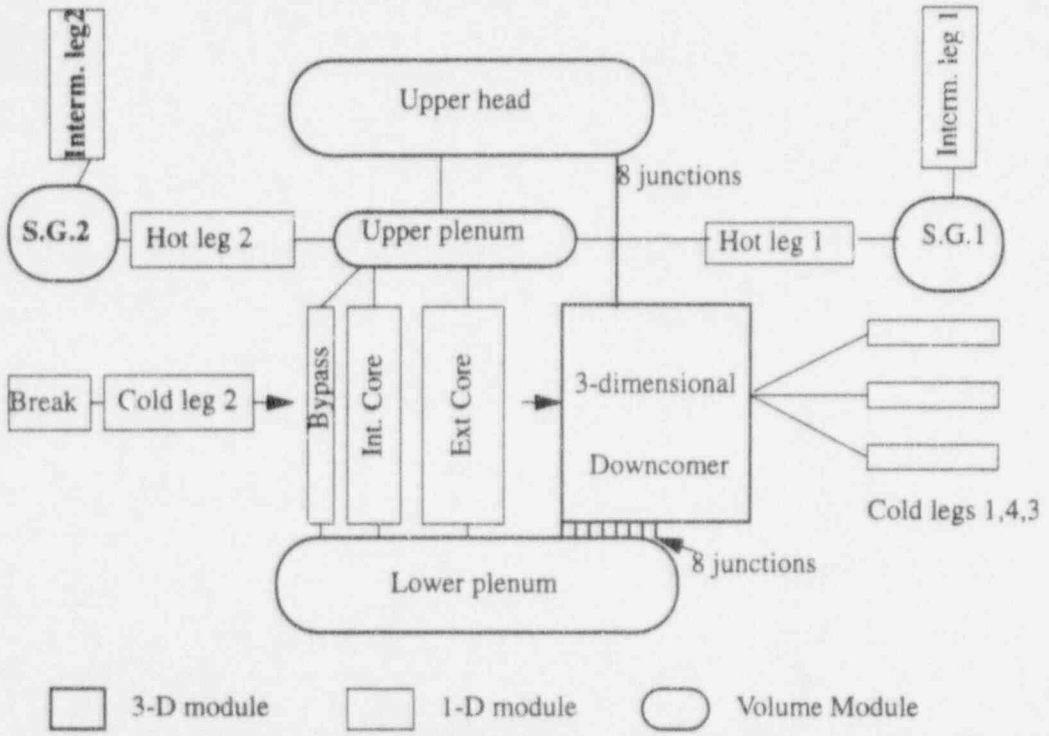

Figure 8
UPTF Cathare modelling

paper [9], some weakness of a one-dimensional modelling were highlighted due to the particular multidimensional nature of the flow in the upper part of the downcomer and it was demonstrated that a multidimensional model was necessary. Investigation of tests with a low rate of subcooling of the injected water was performed first. It permitted the study of the mechanical effects without the thermal problems caused by the condensation.

The test presented here is a transient which tends to represent the conditions at the end of the de pressurization phase of a large break LOCA. The pressure is still decreasing rapidly due to the break discharge. Accumulators discharge ECC water. The vapour which condenses on this subcooled ECC water is created by flashing of the saturated water which remains from the primary coolant. In this test, an initial saturated water level is present in the lower part of the pressure vessel. The accumulator discharge is intiated before opening the break. Thus in the first phase, pressure variations are controlled by condensation. In the CATHARE calculation the whole circuit is repesented. A 1x8x8 mesh has been choosen for the 3D module.

The CATHARE calculation has good numerical behaviour (figures 9,10,11). The physical results show that depressurization is well predicted as is the refilling phase. But the pressure variations suggest an under-estimation of condensation.

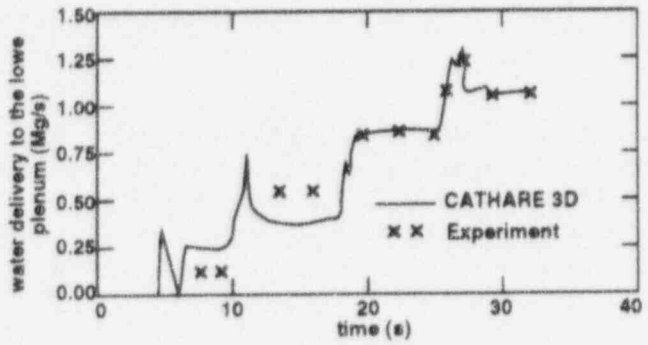

Figure 9: UPTF experiment

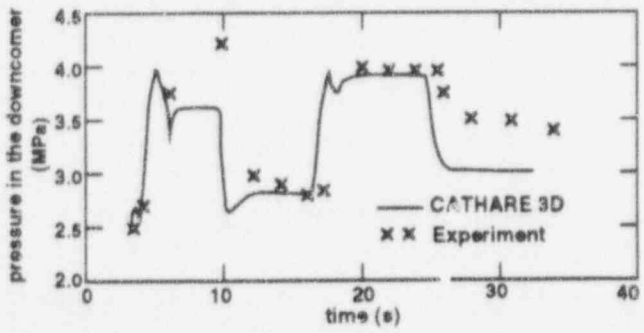

Figure 10: UPTF experiment

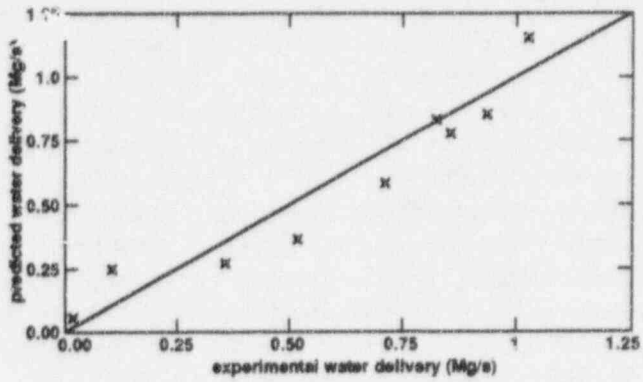

Figure 11: UPTF experiment

4. DIFFUSION AND TURBULENCE MODELS

4.1 Introduction

For containment building investigations, extensions of the previous models were necessary. Generally, at the beginning of the calculation of a sequence of accidents, the building is filled with air. Then vapour can enter it and later other gases such as nitrogen from the ECC or hydrogen from the oxydation reaction due to the action of water on superheated fuel cladding. Thus it is necessary to calculate the diffusion of gas inside this building, the condensation rate, etc. For this application, further development work is required.

4.2 Implementation of mass and energy diffusion terms.

In the models previously discussed, no diffusion terms are taken into account in the equations of the three-dimensional module. Numerical diffusion exists due to the staggered mesh and the donor cell method. But in some physical situations, as in the containment calculations, it is important to evaluate the diffusion of gas and energy is important. Molecular diffusion has been added in the equations.

The diffusion of one gas in another one is taken into account in the non-condensable gas equations:

$$\frac{\partial}{\partial t}(\alpha_g \rho_g X_i) + \mathrm{div}\left(\alpha_g \rho_g X_i \vec{V}_g\right) - \mathrm{div}\left(D_i \alpha_g \rho_g \overrightarrow{\nabla X_i}\right) = S_i \qquad (10)$$

D_i is the diffusion coefficient. The temperature diffusion is taken into account in the phase energy equations:

$$\frac{\partial}{\partial t}\left(A\alpha_k\rho_k e_k \right) + \mathrm{div}\left(A\alpha_k\rho_k e_k \vec{V}_k \right) - \mathrm{div}\left(\lambda_k\rho_k\alpha_k \overrightarrow{\nabla T_k} \right) \qquad (11)$$
$$+ p\left[A\frac{\partial}{\partial t}(\alpha_k) + \mathrm{div}\left(A\alpha_k \vec{V}_k \right) \right] =$$
$$(-1)^k \Gamma_k h_k + (-i)^k q_{ke} + q_{kw}$$

4.3 Implementation of turbulent diffusion terms in the two-phase flow model.

Investigation of the turbulence model can be necessary. The equations described below are averaged and filter the turbulent fluctuations. They thus describe the evolution of the main flow variations. The turbulence model implemented here is based on the approximation of an eddy viscosity computed with a k-ε model. The turbulent exchanges between phases are not taken into account. Development work is still underway on that subject. The correlations of velocity fluctuations are written for each k phase. The averaged phase velocity $\vec{V}_k$ in the equations of §2 is replaced here by the sum of this averaged velocity and the fluctuation: $\vec{V}_k + \vec{V}'_k$. The three components are written: $(u_k + u'_k, v_k + v'_k, w_k + w'_k)$. The momentum equation projected on the x-axis is written:

$$\alpha_k\rho_k\left[\frac{\partial u_k}{\partial t} + \left(\vec{V}_k \cdot \vec{\nabla} \right) \cdot u_k \right] + \alpha_k \cdot \frac{\partial P}{\partial x} + p_i \cdot \frac{\partial \alpha_k}{\partial x} \qquad (12)$$
$$+ Dt - \frac{\partial}{\partial x}\alpha_k \cdot T^k_{x,x} - \frac{\partial}{\partial y}\alpha_k \cdot T^k_{x,y} - \frac{\partial}{\partial z}\alpha_k \cdot T^k_{x,x}$$
$$= (-1)^k \cdot \tau_{i,x} - F_{k,x} + \alpha_k\rho_k g_x$$

With the very classical Boussinesq hypothesis, it can be written:

$$Dt = -2\frac{\partial}{\partial x}\left(\alpha_k\rho_k \nu^t_k \frac{\partial u_k}{\partial x} \right) + \frac{2}{3}\frac{\partial}{\partial x}(\alpha_k\rho_k K_k) + \qquad (13)$$
$$\frac{2}{3}\frac{\partial}{\partial x}\left(\alpha_k\rho_k \nu^t_k \left(\frac{\partial u_k}{\partial x} + \frac{\partial v_k}{\partial y} + \frac{\partial w_k}{\partial z} \right) \right)$$
$$-\frac{\partial}{\partial y}\left(\alpha_k\rho_k \nu^t_k \left(\frac{\partial u_k}{\partial y} + \frac{\partial v_k}{\partial x} \right) \right) - \frac{\partial}{\partial z}\left(\alpha_k\rho_k \nu^t_k \left(\frac{\partial u_k}{\partial z} + \frac{\partial w_k}{\partial x} \right) \right)$$

In the phase energy equation, additional term appears:

$$\mathrm{div}\left(\langle \alpha_k\rho_k e_k \vec{V}_k \rangle \right) = -\frac{\nu^t_k}{P_{rt}}\alpha_k\rho_k \nabla e_k \qquad (14)$$

$$\text{with } \nu^t_k = C_{\mu,k}\frac{K_k^2}{\varepsilon_k} \qquad (15)$$

These equations introduce for each phase the kinetic turbulent energy K_k and the dissipa-

$$\frac{\partial}{\partial t}\left(A\alpha_k\rho_k e_k\right) + \mathrm{div}\left(A\alpha_k\rho_k e_k \vec{V}_k\right) - \mathrm{div}\left(\lambda_k\rho_k\alpha_k\overrightarrow{\nabla T_k}\right) \qquad (11)$$
$$+ p\left[A\frac{\partial}{\partial t}(\alpha_k) + \mathrm{div}\left(A\alpha_k\vec{V}_k\right)\right] =$$
$$(-1)^k\Gamma_k h_k + (-1)^k q_{ke} + q_{kw}$$

4.3 Implementation of turbulent diffusion terms in the two-phase flow model.

Investigation of the turbulence model can be necessary. The equations described below are averaged and filter the turbulent fluctuations. They thus describe the evolution of the main flow variations. The turbulence model implemented here is based on the approximation of an eddy viscosity computed with a k-ε model. The turbulent exchanges between phases are not taken into account. Development work is still underway on that subject. The correlations of velocity fluctuations are written for each k phase. The averaged phase velocity $\vec{V}_k$ in the equations of §2 is replaced here by the sum of this averaged velocity and the fluctuation: $\vec{V}_k + \vec{V}'_k$. The three components are written: $(u_k + u'_k, v_k + v'_k, w_k + w'_k)$. The momentum equation projected on the x-axis is written:

$$\alpha_k\rho_k\left[\frac{\partial u_k}{\partial t} + \left(\vec{V}_k \cdot \vec{\nabla}\right)\cdot u_k\right] + \alpha_k \cdot \frac{\partial P}{\partial x} + p_i \cdot \frac{\partial \alpha_k}{\partial x} \qquad (12)$$
$$+ Dt - \frac{\partial}{\partial x}\alpha_k \cdot T^k{}_{x,x} - \frac{\partial}{\partial y}\alpha_k \cdot T^k{}_{x,y} - \frac{\partial}{\partial z}\alpha_k \cdot T^k{}_{x,x}$$
$$= (-1)^k \cdot \tau_{i,x} - F_{k,x} + \alpha_k\rho_k g_x$$

With the very classical Boussinesq hypothesis, it can be written:

$$Dt = -2\frac{\partial}{\partial x}\left(\alpha_k\rho_k\nu^t{}_k\frac{\partial u_k}{\partial x}\right) + \frac{2}{3}\frac{\partial}{\partial x}(\alpha_k\rho_k K_k) + \qquad (13)$$
$$\frac{2}{3}\frac{\partial}{\partial x}\left(\alpha_k\rho_k\nu^t{}_k\left(\frac{\partial u_k}{\partial x} + \frac{\partial v_k}{\partial y} + \frac{\partial w_k}{\partial z}\right)\right)$$
$$\frac{\partial}{\partial y}\left(\alpha_k\rho_k\nu^t{}_k\left(\frac{\partial u_k}{\partial y} + \frac{\partial v_k}{\partial x}\right)\right) - \frac{\partial}{\partial z}\left(\alpha_k\rho_k\nu^t{}_k\left(\frac{\partial u_k}{\partial z} + \frac{\partial w_k}{\partial x}\right)\right)$$

In the phase energy equation, additional term appears:

$$\mathrm{div}\left(\langle\alpha_k\rho_k e_k\vec{V}_k\rangle\right) = -\frac{\nu^t{}_k}{P_{rt}}\alpha_k\rho_k\nabla e_k \qquad (14)$$

$$\text{with } \nu^t{}_k = C_{\mu,k}\frac{K_k^2}{\varepsilon_k} \qquad (15)$$

These equations introduce for each phase the kinetic turbulent energy K_k and the dissipation rate ε_k which in the well known k,ε model are solutions of transport equations.

4.4 Validation

Validation of these models has been performed by comparisons with experiments and also by comparison with the TRIO-VF code [3] which is well qualified for these problems. As an example, a test of helium stratification in a reactor containment [10] filled with air is presented. At the beginning of this test, the containment is totally filled with Nitrogen. The transient is initiated with the onset of helium injection at the bottom of the dome. Helium volumic concentration at different times along the vertical centerline of the dome is presented by comparison with TRIO-VF code on figure 12. both codes give same results, especially for the final concentration and the time to get it. Calculation without turbulent diffusion has been performed with CATHARE and shows that it was nescessary to introduce these models. Without turbulent diffusion, the Helium gas is accumulated at the top of the jet near the outlet . With turbulent diffusion, the concentration of helium in the containment (Figure 13) is approximately constant.

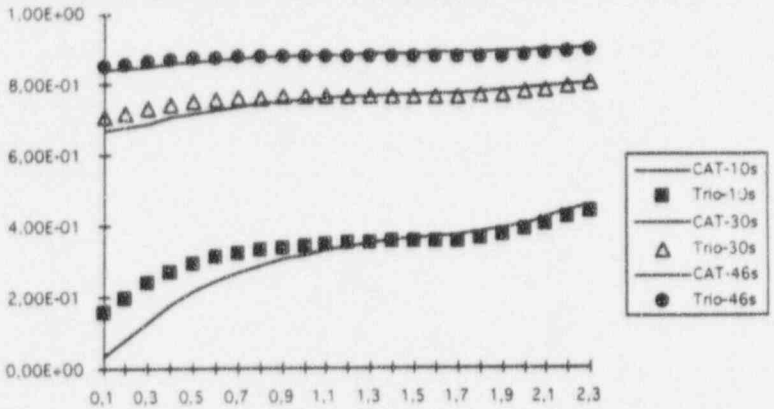

Figure 12
Helium concentration profile along z-axis; comparison between CATHARE and TRIO-VF

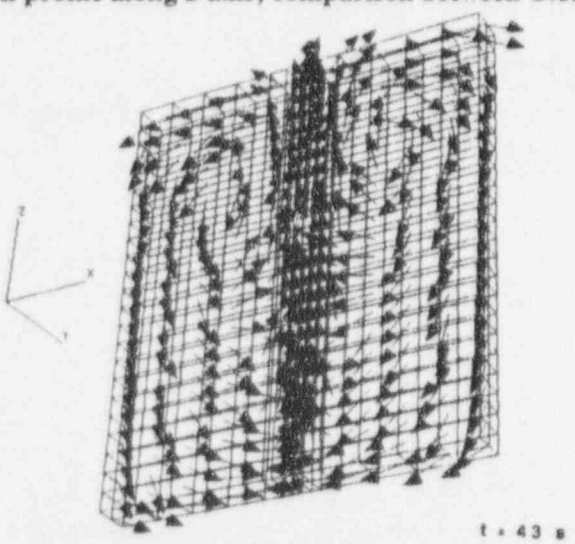

Figure 13
Gas velocity in the containment

4.5 Containment Calculation

The aim of this calculation was to demonstrate the capability of a system code as CATHARE to be use for containment analysis.. The three dimensional module with 756 meshes in cylindrical coordinate is used to model the dome and twelve volume modules to describe the different boxes (figure 14). In the presented transient (figures 15, 16) the containment is filled with air.Vapour is injected from the primary circuit. During this phase vapour condenses on the cold wall of the contaiment. Later on, Hydrogen is injected from the primary circuit. At the end cold water aspersion is initiated.The results are on Figures 17 to 19. The cold liquid droplets are falling down. The vapour is dragged by the liquid and sucked by condensation. The pressure is decreasing at the end of this transient due to condensation. A stratification of Hydrogen concentration is noticed. Hydrogen is also falling down to the lowest boxes.Further analysis of this calculation and sensitivity studies are underway.

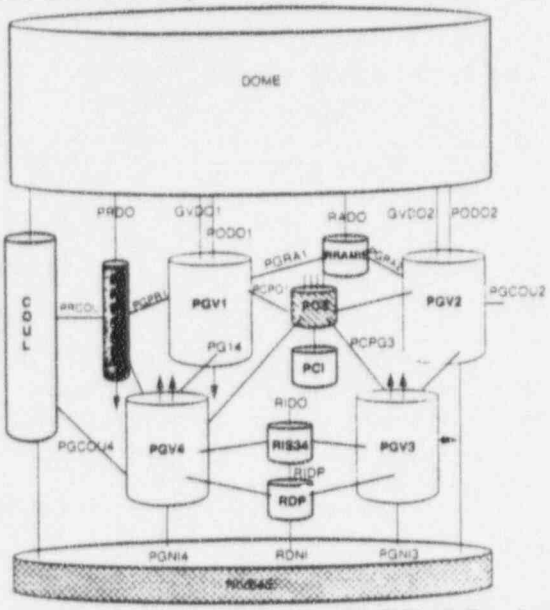

Figure 14 Containment modelling for CATHARE calculation

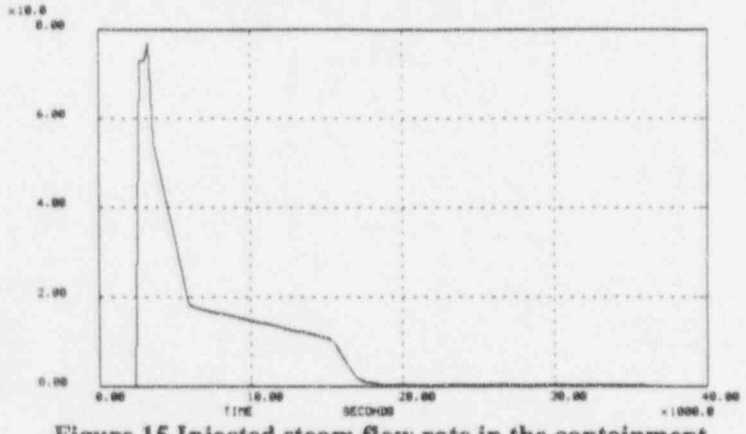

Figure 15 Injected steam flow rate in the containment

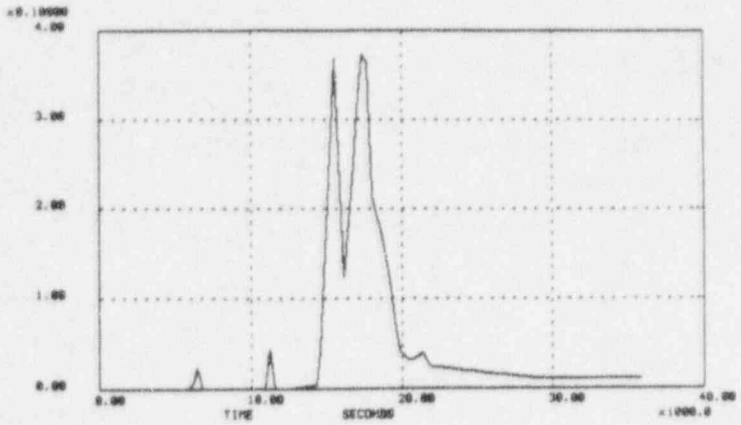

Figure 16 Injected hydrogen in the containment

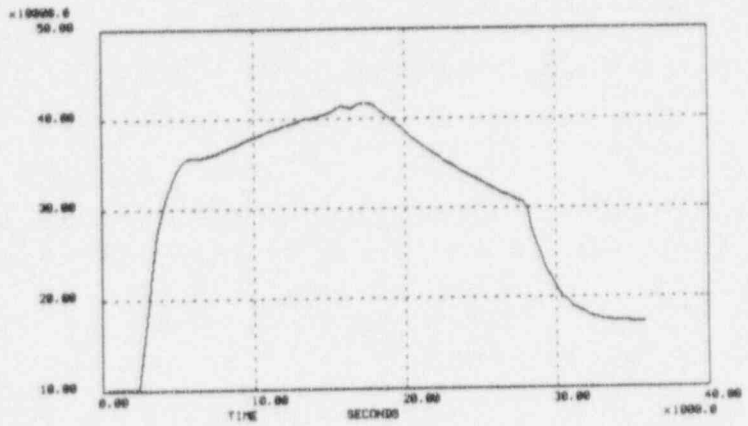

Figure 17 Evolution of the pressure in the dome

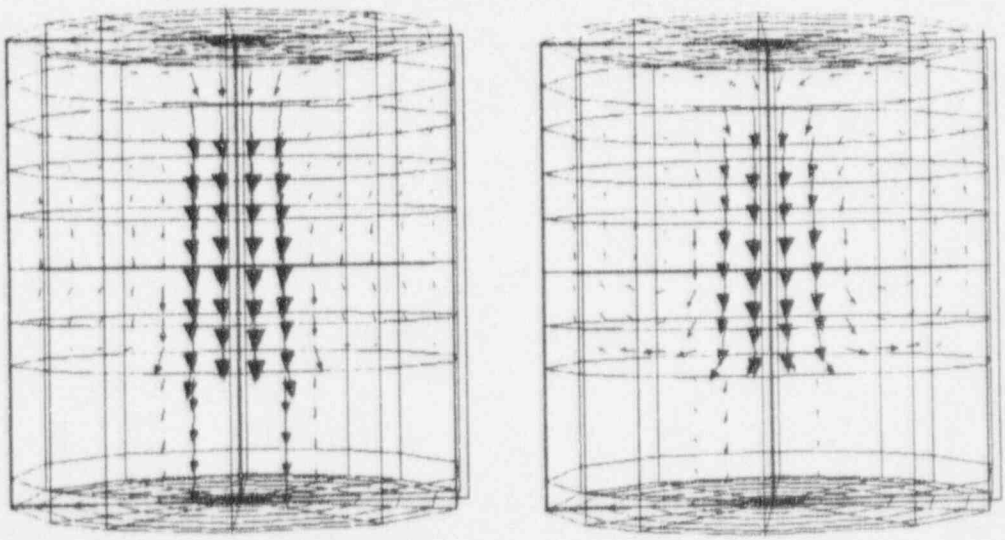

Figure 18 Profile of liquid (left) and gas (right) velocities in the 3D dome

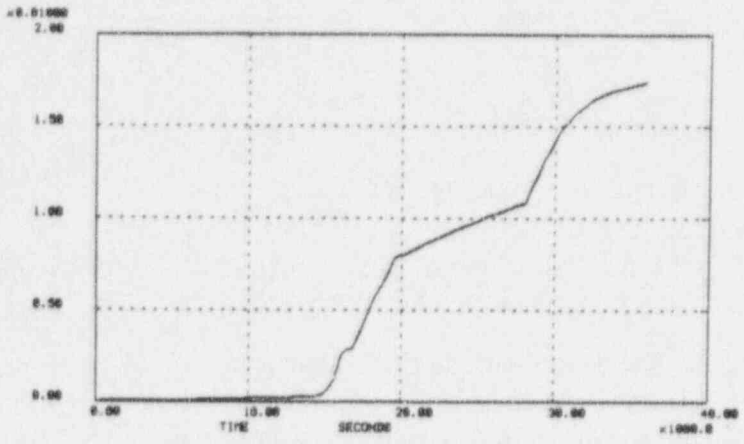

Figure 19 Hydrogen concentration in the lowest box

6. CONCLUSIONS

The new multidimensional module of CATHARE has proved its numerical efficiency. It is convenient to use for a large range of applications covering the two-phase flow phenomena in nuclear reactor primary circuits, the turbulent gas flow in power plant containments, etc.

Qualification against simple analytical two phase flow experiments has been performed to check the suitability of the two phase flow model.

Analysis of UPTF downcomer tests has started with this new module. It shows that a methodology for using and adjusting this module has to be defined for its use for safety problems. In particular, modifications are needed for the momentum equations. These improvements are under development.

In the near future new fields of investigation are planned for the qualification of this module, including 3D-reflooding problems, CCFL, wall film condensation in containment and turbulent gas diffusion.

Numerical developments are in progress, on the one hand to accelerate solvers, by using parallel computing, and, on the other hand, to implement non-structured meshing.

REFERENCES

[1] **F.BARRE et al.:** New developments in the CATHARE 2 code. NURETH 6, Grenoble, France, October 5-8, 1993.

[2] **D.BESTION:** The physical closure laws in the Cathare code, Nucl. Engrg. Des. 124 (1990) 229-245

[3] **D.GRAND, J.P.MAGNAUD, J.R.PAGES, M.VILLAND:** "Three dimensional computa-

tions of thermal-hydraulics phenomena in reactor vessels". Advances in Mathematics, Computations and Reactor Physics,Pittsburgh, April 28th - May 1st, 1991

[4] **A.E.BERGLES, J.G.COLLIER, J.M.DELHAYE, G.F.HEWITT, F.MAYINGER:** Two-phase flow and heat transfer in the power and process industries. Hemisphere Publishing Corporation,1981.

[5] **F.BARRE, M.BERNARD:** The CATHARE code strategy and assessment,Nucl. Engrg. Des. 124 (1990) 257-284

[6] **M.LAVAUX:** Report FRAMATOME TP/CT/DC.494,1989

[7] **MARVIKEN:** The Marviken full scale critical flow tests report, MXC-301, 1982

[8] **H.GLAESER:** Analysis of downcomer and tie plate countercurrent flow in the upper tie plate test facility (UPTF), Proc. Fourth Int. topical meeting on Nuclear Reactor thermalhydraulics, Karlsruhe, October 1989.

[9] **I.DOR:** Analysis of UPTF downcomert tests with the CATHARE multidimensional model,Nucl. Engrg. Des. 149 (1994) 129-140

[10] **V.BARTHEL, D.GRAND, M.VILLAND:** Three dimensional numerical simulation of hydrogen distribution and mixing in containment, Proceeding of a workshop held in Brussels (Belgium) on hydrogen behaviour and mitigation in water-cooled nuclear power reactors, March 4th-8th, 1991.

REFLOODING AND BOIL-OFF EXPERIMENTS IN A VVER-440 LIKE ROD BUNDLE AND ANALYSES WITH THE CATHARE CODE

Virpi Korteniemi, Timo Haapalehto
Lappeenranta University of Technology
Department of Energy Technology
LAPPEENRANTA, FINLAND

Markku Puustinen
VTT Energy
Nuclear Energy
LAPPEENRANTA, FINLAND

ABSTRACT

Several experiments were performed with the VEERA facility to simulate reflooding and boil-off phenomena in a VVER-440 like rod bundle. The objective of these experiments was to get experience of a full-scale bundle behaviour and to create a database for verification of VVER type core models used with modern thermal-hydraulic codes. The VEERA facility used in the experiments is a scaled-down model of the Russian VVER-440 type pressurized water reactors used in Loviisa, Finland. The test section of the facility consists of one full-scale copy of a VVER-440 reactor rod bundle with 126 full-length electrically heated rod simulators. Bottom and top-down reflooding, different modes of emergency core cooling (ECC) injection and the effect of ECC water subcooling and flow rate were studied in the reflood experiments. In the boil-off experiments the effect of heating power on the heat-up of the rods was studied. In this paper the results of calculations simulating two reflood and one boil-off experiment with the French CATHARE2 thermal-hydraulic code are also presented. Especially the performance of the recently implemented top-down reflood model of the code was studied.

1. INTRODUCTION

In nuclear power plants fuel pellets, cladding of fuel rods, the primary cooling circuit and containment are the barriers to prevent radioactive fission product releases into the environment. Several assisting and emergency systems cool down the reactor and hinder radioactive releases during accidental situations.

A large break loss-of-coolant accident (LBLOCA) is one of the accidental situations which might lead to overheating and breaking of the fuel rods. To recover the coolability of the core and to continue the effective removal of the decay heat ECC water is injected into the downcomer and/or upper plenum. During the LBLOCA reflooding phase the ECC water starts to propagate between the hot fuel rods. When the local cladding temperature of a fuel rod falls below the quenching temperature, the liquid wets the surface of the cladding. This quenching of a hot surface is the transition from vapor heat transfer regime to liquid heat transfer regime. A very large variation of the thermal-hydraulic conditions occur in the immediate vicinity of the quench front. This reflooding phenomenon is studied here.

The other field of interest in this study is the boil-off situation. A small break loss-of-coolant accident (SBLOCA) may result in the drying out of a reactor core by boiling off the coolant. Low primary flow and intermediate or low pressure transients may sequentially lead to an uncovery, overheating and damage of the core. Especially, the use of thermal-hydraulic codes requires assessment in order to predict also this situation correctly.

Both reflooding and boil-off phenomena have been widely studied on many facilities simulating western type pressurized water reactors (PWR), but only on few facilities simulating Russian designed pressurized water reactors (VVER) which have rod bundle and ECC system configurations different from those of the PWRs. Especially experiments with a full scale VVER-440 like rod bundle have been so far even more uncommon. Some experiments with smaller facilities modelling parts of the VVER bundle have been reported, for example experiments on the 19 rod REWET-II facility by Kervinen et al. [1], [2].

To widen the experimental data base under various conditions expected to appear in the VVER-440 core, a series of reflooding and boil-off experiments were conducted with the scaled-down VEERA facility. The test section of the facility includes one electrically heated full-scale copy of a VVER-440 reactor 126 rod bundle. Owing to the full size rod bundle the facility gives a good opportunity to study different phenomena occurring during the reflooding and boil-off processes in the postulated loss-of-coolant accident (LOCA) in a larger scale than which the previous studies with the REWET-II facility dealt with. Areas of interest include bottom and top-down reflooding, different modes of ECC injection, the effect of ECC water temperature and flow rate, as well as the effect of heating power on the heat-up in the boil-off situation. With the facility, over 30 experiments were carried out with different parameter values, from which three were chosen for simulation with the French CATHARE2 thermal-hydraulic code. This set of experiments includes two reflood experiments with either upper plenum or downcomer ECC injection and one boil-off experiment.

This paper describes the VEERA facility and the experimental arrangements, and presents some of the results gained with the experiments, as well as with the code calculations. The main objective of the code calculations was to test the new top-down reflood model of the CATHARE2 code.

2. TEST DESCRIPTION

2.1. VEERA facility

The VEERA facility was constructed in 1987 by Lappeenranta University of Technology (LTKK), VTT Energy and Imatran Voima Power Company (IVO). Originally, VEERA was used for experiments that simulate soluble neutron poison (boric acid) behavior in a PWR during the long-term cooling period of LOCAs as it is presented by Tuunanen et al. [3] and Raussi et al. [4]. The reference reactor of the VEERA facility is the modified Russian VVER-440 design of the Loviisa power plant in Finland. The main design principle of the facility is the accurate simulation of the rod bundle geometry. The reactor vessel is simulated by a stainless steel U-tube structure consisting of a downcomer, lower plenum, core, core outlet nozzle and upper plenum, Fig. 1.

All the elevations in the reactor vessel simulator below the hot leg connection are scaled 1:1. The scale of the volumes and flow areas is 1:349, referring to the number of fuel rod assemblies in the facility and the number of fuel assemblies in the reference reactor. The primary loops with horizontal steam generators are not simulated in the facility. The exhaust steam line consists of a moisture separator and a condenser. Simulation of the main circulation pumps, pressurizer and auxiliary systems has not been considered necessary in the intended experiments. ECC injection nozzles are located in the upper plenum, lower plenum and downcomer. Cooling water can be preheated up to 100 °C in the ECC tank. A pump is used for injecting water into the facility. The major design characteristics of the VEERA facility are given in Table 1.

The test section includes one full-scale copy of a VVER-440 reactor hexagonal rod bundle. It consists of 126 full-length electrically heated rod simulators and an unheated cold center rod, which replaces the support tube of the actual fuel bundle. The bundle is enclosed in a thermally insulated hexagonal shroud. The heated rod simulators have heating coils inside stainless steel cladding in a magnesium oxide insulation. The heated length, the outer diameter and the lattice pitch of the fuel rod simulators, as well as the number and construction of the rod bundle spacers, are the same as in the reference reactor. In order to simulate better the actual power profile of the reference reactor, a nine-step chopped cosine axial power distribution is adopted. Viewing windows on the side walls of the shroud can be used for visual observation of the quench front propagation and the behavior of thermocouples attached on the outer surface of the rods.

The structures below the core are not simulated exactly due to the electric connections to the rod simulators, whereas the structure right above the core bundle, i.e. the core outlet nozzle, is accurately simulated (Fig. 1). The flow area of the perforated plate inside the core outlet nozzle corresponds to that of the upper tie plate of the reference reactor. In the steam line the moisture separator consists of 10 lamellae. The condenser is made of two pipes, one inside the other, where cold water flows in the shell side and hot water in the tube side.

Sheathed electrical heaters with a power range from 200 to 2500 W have been attached, by means of metal bands, to the outer surface of the downcomer, lower plenum, hexagonal shroud and upper plenum walls to heat up the structures and thus reach suitable initial conditions and avoid unwanted condensation. The whole facility housing, except the viewing windows, is thermally insulated with 100 mm thick mineral wool.

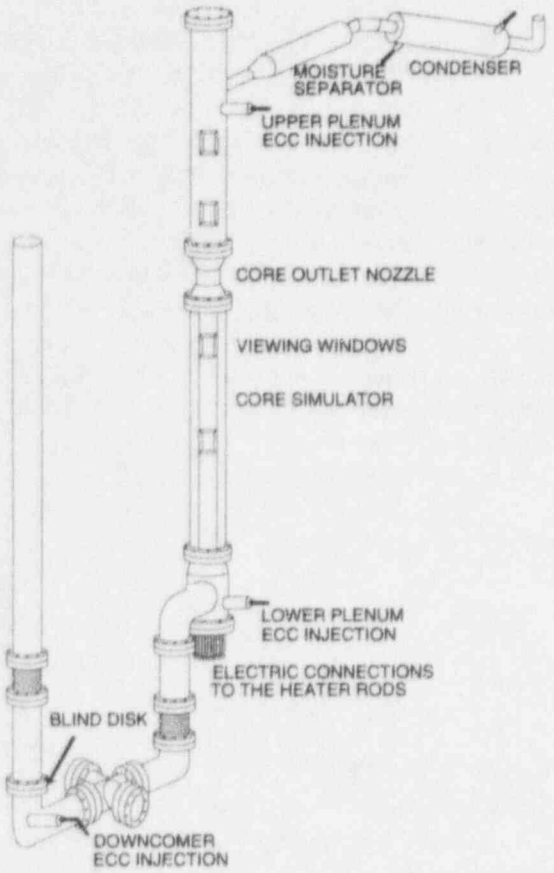

Fig. 1. Schematic view of VEERA facility.

Table 1. VEERA facility characteristics.

Reference reactor	VVER-440
System design pressure	0.5 MPa
Fuel rod simulators:	
heated length	2420 mm
outer diameter	9.1 mm
cladding thickness	1 mm
axial peaking factor	1.4
power distribution	nine-step cosine
averaged linear heating power	20 W/cm
maximum clad temperature	900 °C
insulator material	MgO
Rod bundle:	
number of rods in bundle	126
rod arrangement	triangular
bundle geometry	hexagonal
lattice pitch	12.2 mm
flow area in bundle	86.0 cm^2
heating power	0 - 100 kW
number of spacer grids	11

2.2. Instrumentation and data acquisition system

The main measurements in the experiments are coolant and cladding temperatures, system pressure, pressure differences and heating power. Thermocouples are used for temperature measurements. Most of them are in the rod bundle at different radial and axial locations. They are either spot welded or tied onto the rod cladding, Fig 2. Thermocouples measuring coolant and cladding temperatures are of the NiCr-Ni type with a 0.5 mm diameter. Wall temperatures are usually measured with 1.0 mm or 1.5 mm diameter thermocouples. The cladding, coolant and wall temperatures are measured with 28, 20 and 7 thermocouples respectively. The vertical sectional view of the bundle, shown in Fig. 3, gives the axial positions of the eleven grid spacers as well as the measurement levels of the cladding and coolant temperatures. In Fig. 3 the black filled boxes show some particular cladding temperature measurement points. These points are referred to in the figures of chapter 4 in this paper to show the elevations and locations of measurements that are the basis of the experimental data curves in those figures.

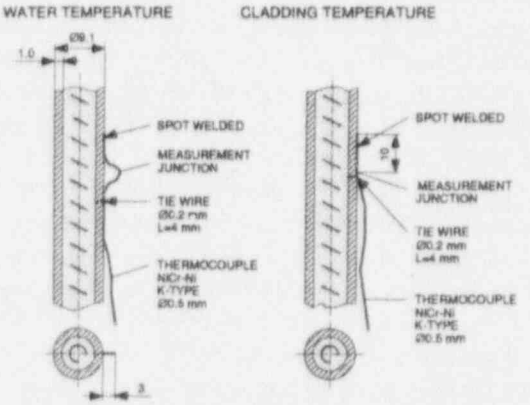

Fig. 2. Attachment of thermocouples on rod cladding.

The system pressure is measured with a sensor in the upper plenum. The pressure difference measurements are used for level indication and local pressure loss evaluation. The total number of the pressure and differential pressure transducers is eight. The ECC flow rate is measured with a magnetic flow meter. The heating power to the test section is determined from the electric current and voltage measurements by an ac/dc power analyzer.

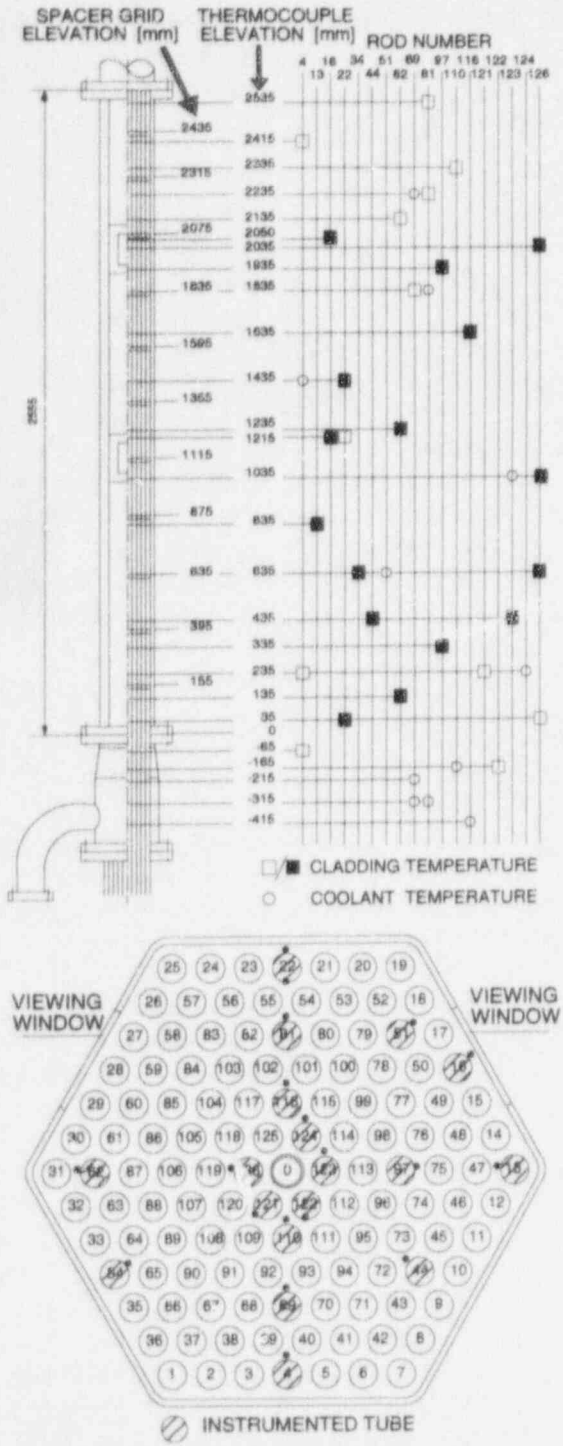

Fig. 3. Locations of thermocouples and grid spacers in rod bundle.

Table 2. Range of parameters in reflood and boil-off experiments.

Core power	50 - 95 kW
Fraction of nominal power	1.1 - 2.2 %
Average linear heat rating	1.6 - 3.1 W/cm
ECC mass flux	20 - 160 kg/m^{2}s
System pressure	0.1 MPa
Max initial clad temperature	700 °C
ECC water temperature	25 - 90 °C
Initial wall temperatures	100 - 250 °C
Initial water level	
- reflood experiments	3700 mm
- boil-off experiments	6550 mm

The data acquisition system of the nearby PACTEL facility [5] is used in the reflood and boil-off experiments. The system consists of a data acquisition unit, a controller and a workstation. A disc and tape drive are used for the mass storage of experimental data. Data from approximately 60 channels are recorded during the experiments.

Most of the sensors used in the VEERA facility are K-type thermocouples with an overall accuracy better than ±2 °C. The pressure difference measurements are the most problematic as regards experimental accuracy. Accordingly, at the start of each test series, a calibration, based on hydrostatic pressure differences, is carried out. A large portion of inaccuracy encountered in the pressure difference measurements can be avoided by making sure that water in the pressure tabs is at the right temperature, i.e. it does not warm up considerably during the experiments. For the absolute pressure measurement, an inaccuracy less than ±2 %, obtained with normal calibration before installing the sensor, is well within the needs of the experiments in question. The inaccuracy of the power analyzer is ±1 %.

2.3. Test conditions

It is important to consider a sufficiently broad variation of the thermal hydraulic parameters for the reflood and boil-off experiments. This ensures that the local conditions during reflooding and boil-off in an actual PWR are covered and provides an adequate data base for model development. Keeping in mind the limitations set by the facility characteristics and its instrumentation, the range of the main parameters and thermal-hydraulic conditions of the reflood and boil-off experiments with the VEERA facility were determined to be as listed in Table 2.

All these experiments were carried out without the downcomer side of the facility. This was accomplished by installing a blind disk to the lower part of the downcomer, Fig. 1. The reason for this was to reduce the impact of U-tube oscillations. This would have disturbed the forced reflood phenomena under investigation. As regards the reflood experiments, two ECC injection points were used, that is either the downcomer or the upper plenum injection point. All the experiments were done under 0,1 MPa atmospheric pressure.

2.4. Experimental arrangements

The preparation of the facility for a reflood experiment was carried out as follows. All pressure difference lines were purged and filled with cold water to reduce measurement errors due to voids or warm up of water in the lines during the experiments. As monitoring of the measurements was started, readings of the temperature measurements were checked over. Initially the facility was filled with air and vapor, except for the lower plenum, the lower part of the downcomer and the ECC tank, which were filled with water. Water in the ECC tank was heated up to a temperature of 25 - 90 °C depending on the test parameters. The shroud and the upper plenum walls were preheated by means of electrical heaters attached onto the outer surface of the structures to avoid undesired condensation. The heat-up of the rods was also started by applying partial test power. ECC flow rate was adjusted by using a bypass line. When the structures had reached the desired temperature (typically from saturation temperature to 250 °C), the heater rods were powered for the desired heat flux. The full power had to be set several seconds before the desired initial rod surface temperature was reached, so that the radial temperature profile within each heater rod was developed appropriately. The data acquisition system was then started to record all measurements. When the temperatures of the rods reached a predetermined value (typically 500-700 °C), ECC injection was initiated by opening the valve which guides the water flow from the bypass line into the facility. As water started to accumulate in the core region, the simulator rods first cooled down and finally quenched rapidly. After the quenching of the whole test bundle, the experiment was terminated by cutting off the power from the heater rods and by stopping the coolant water flow into the test section.

In a boil-off experiment practically the same kind of preparations as explained above were used. The facility was initially filled with water to the top of the core region. When the upper plenum walls had reached the desired initial temperature, full test power was set. As the water boiled off and the swell level in the core decreased, the upper parts of the heater rods started to get revealed and heat up. The experiment was terminated by cutting off the heating power, when the temperatures of the rods approached 500 - 600 °C

For testing the overall performance of the facility and also the various experimental procedures, several reproducible experiments were carried out. The results of these experiments showed good agreement with each other. In terms of rewetting times at the axial bundle midpoint, for example, the differences were less than 5%.

3. CATHARE CODE AND CODE MODEL FOR VEERA FACILITY

3.1. CATHARE code

The computer code used in the calculations presented in this study was the French thermal-hydraulic code CATHARE. The CATHARE code was developed in Grenoble by Electricité de France, FRAMATOME and the French Atomic Energy Commission (CEA) as described by Barre and Bernard [6]. The CATHARE2 code is based on a two-fluid, six-equation model for best-estimate simulation of PWR's LOCAs and operational transients.

The version of the code used in the simulations was CATHARE2 V1.3E with modification concerning the calculation of the reflooding. The scale of reflooding is usually much smaller than the characteristic scale of the calculation used in the two-fluid code models. The basic version CATHARE2 V1.3E includes a specific calculation model for only bottom quench front propagation. In this study, also a top-down reflood model was implemented into the version CATHARE2 V1.3E of the code. Hence, the modified version of the code was able to calculate both bottom and top-down quench front propagations simultaneously. Both specific reflood models are two-dimensional heat transfer models solved on a local fine mesh, which is moving along the wall with the quench front velocity. This method has been presented by Bartak and Haapalehto [7].

3.2. VEERA facility model

Three of the experiments were simulated with the modified version of the CATHARE2 V1.3E code, Table 3. All the calculations presented in this study were done by using an IBM RS6000 work station. The nodalization scheme used in the CATHARE calculations is shown in Fig. 4. The geometrical model consisted of seven basic components: three axial pipe elements, two volumes and two boundary conditions. The hydraulic axial pipe element of the core was divided into 10 nodes according to the power distribution of the rods, and each of these nodes was divided into four subnodes. Hence, the measurement points of the facility did not differ more than 30 mm from the corresponding code model points. The spacer grids were described as small flow resistances. The shroud was not modelled in the reflood calculations, because the code is able to calculate the quenching of only one wall, i.e. the heating rods. In the boil-off calculation the shroud was modelled.

The reflood calculations included the description of the geometrical data of the facility and the initial hydraulic conditions. After this initialization, the heating of the rods to the required initial cladding temperature was performed. Finally, the ECC injection was started and the bottom and top-down reflood calculations were initiated. The boil-off calculation included the corresponding geometrical data and the initial conditions. The actual calculation part dealt with the heating and boiling of the water and the temperature rise of the rods.

Three different input models (*Base case, Case I, Case II*) were used in the reflood calculations. In *Case I* the material properties of the insulator material (magnesium oxide) given by the rod manufacturer were used instead of the values included in the code. The included values were used in *Base case*. Differing from *Case I*, the wetted perimeter value in the core region and in the core outlet nozzle was decreased in *Case II*. In the CATHARE2 code the wetted perimeter is used to calculate CCFL.

In the boil-off calculations the above mentioned changes to the accurate geometry simulation of the *Base case* input model had no noticeable effect. Changes in the flow area of the core outlet nozzle and flow resistances at the locations of the nozzle plates (referred to as *Case III*) had an effect on the fluid distribution in the facility. The basis for using the *Case III* model comes from the recommendation for CATHARE2 users presented by

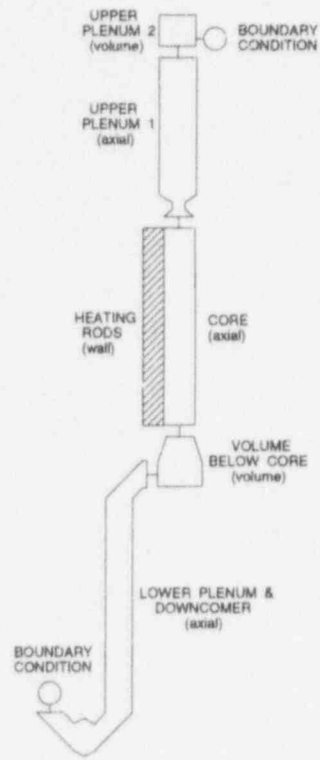

Fig. 4. CATHARE2 nodalization scheme for VEERA facility.

Table 3. Parameters of three experiments calculated with CATHARE2 code.

EXPERIMENT NUMBER	EXPERIMENT TYPE	HEATING POWER (kW)	INITIAL CLADDING TEMPERATURE (°C)	ECC WATER TEMPERATURE (°C)	ECC FLOW RATE (kg/s)
RF_DCB010	REFLOOD (downcomer inj.)	90	600	90	0.3
RF_UP025	REFLOOD (upper plenum inj.)	50	500	90	0.25
BLO_027	BOIL-OFF	50	-	-	-

Farvaque [8]. The recommendation is that instead of using accurate modelling of sudden changes in cross section, one should use smoother geometry along with flow resistances to express pressure differences.

4. RESULTS

4.1. Reflood experiments and calculations

The downcomer ECC injection experiments showed far more effective cooling of the core than the upper plenum ECC injection experiments, provided that other experimental parameters were the same. Fig. 5 shows the quench front propagation in these two cases. In Fig. 5 (as well as in the other figures in this chapter), the elevations and locations of these quenching points against time have been taken from cladding temperature curves measured with thermocouples shown as black filled boxes in Fig. 3. The quenching time in the bundle midplane can be even ten times longer in the upper plenum injection experiment than in the corresponding downcomer injection experiment. The reason for worse cooling in the upper plenum injection experiments is the vapor generated in the bundle, which prevents the water from penetrating to the core.

Also the injection water flow rate affects considerably the quenching times, especially in the case of the downcomer injection, Fig. 6 (see elevations in Fig. 3). In the bundle midplane the quenching times behave quite linearly, i.e. with a four times bigger ECC flow rate, the quenching time drops to one quarter of the original.

In all reflooding experiments the bottom and top parts of the bundle quench in the early stage of the reflooding phase. This is due to the spacer grid effect and the condensation of vapor in the tight core outlet nozzle and upper plenum. The falling film and droplets start to quench some parts of the rods before the main quench front reaches them. The quenching times in the experiments seem to vary a lot in different rods in lateral direction near the core midplane, i.e. between around one and two meter elevations. As an example of this multidimensional behaviour Fig. 7 shows cladding temperature measurements between one and two meter heights in one downcomer injection experiment (rod numbers and elevations refer to Fig. 3). This multidimensional quenching is caused by non-uniform coolant flow distribution in the test section. The cladding temperatures in the centre rods seem to decrease more rapidly than the temperatures at the edge rods.

The effect of the injection water temperature, the initial cladding temperature and the heating power of the rods on the reflooding was also studied in the downcomer injection experiments. Not so significant changes in the quenching times were found as with different flow rates. Typical cladding temperature curves at different bundle elevations in one downcomer and upper plenum injection experiment are shown in Fig. 7 and 8 (see elevations and locations in Fig. 3). The cladding temperature curves in the downcomer injection experiments are smoother than in the upper plenum injection experiments, where temperature measurement points may quench and heat up several times before the final cool-down.

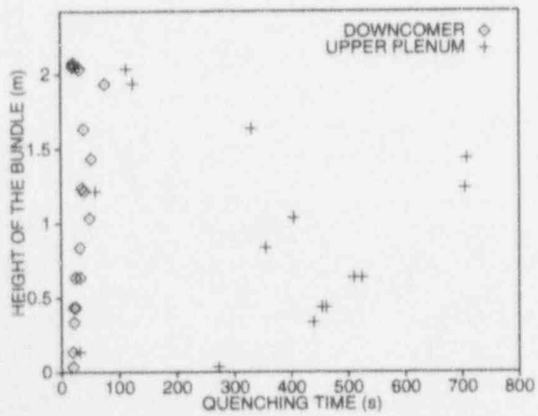

Fig. 5. Quench front propagation in downcomer and upper plenum injection experiments.

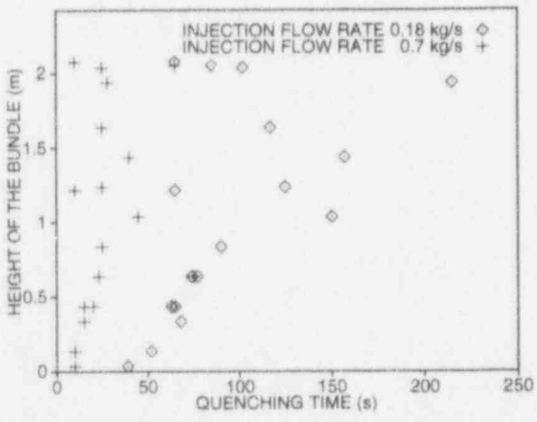

Fig. 6. Effect of injection water flow rate on quenching times in downcomer injection experiments.

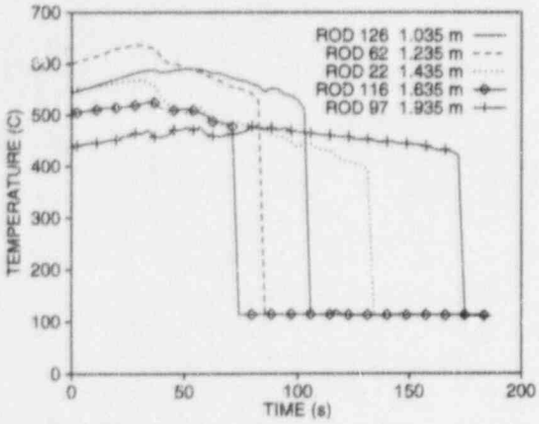

Fig. 7. Typical cladding temperature curves in downcomer injection experiment.

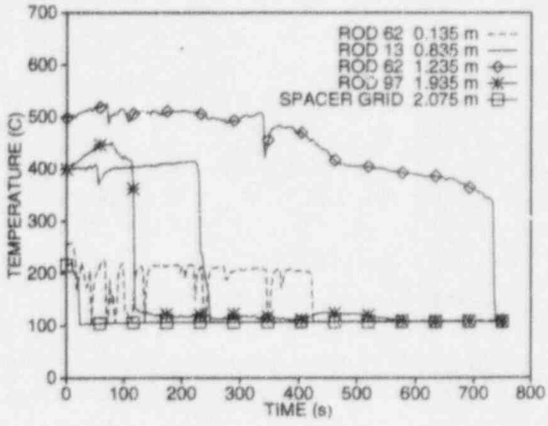

Fig. 8. Typical cladding temperature curves in upper plenum injection experiment.

The downcomer injection experiment (RF_DCB010) was calculated with the CATHARE2 code. The quenching times in the experiment (see elevations in Fig. 3) and in the CATHARE2 calculations (*Base case*, *Case I*, *Case II*) are presented in Fig. 9. The code seems to be capable of calculating two simultaneously propagating quench fronts, as was the case in the experiments. The best results are obtained with modified insulator material and wetted perimeter values *(Case II)*. Fig. 10 presents cladding temperature measurements in the experiment (see elevations and locations in Fig. 3) and in the three versions of the code calculations at two different elevations. The quenching temperatures calculated by the code are too low and the quenching times too long in the lower part of the core. In the upper part of the core the situation is better, especially in *Case II*, where the quenching temperatures differ from the experimental values less than 30 °C and the quenching times about 10 seconds.

The quenching times in the upper plenum experiment (RF_UP025) and in the corresponding code calculations are shown in Fig. 11. The bottom quench front did not start to rise in the *Base case* and *Case I* calculations like in the experiments. Pressure differences over the core bundle (collapsed levels) in the experiment and in these two calculations differ from each other considerably after 350 seconds of transient time, Fig. 12. The reason for this is that water accumulates in the upper plenum region in the CATHARE2 calculation. Only in *Case II* the code calculates the rise of the bottom quench front, even though the quenching is too rapid compared to the experimental result (Figs. 11 and 12; see elevations in Fig. 3).

The problems in the code simulations seem to be due to incorrect calculation of the CCFL phenomenon, which has an essential impact on coolant inventories in different parts of the facility, especially in the upper plenum

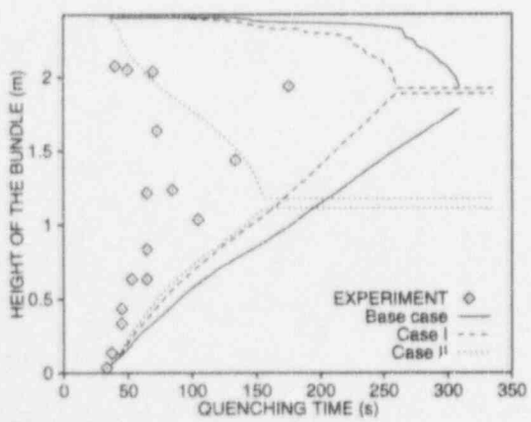

Fig. 9. Quenching times in downcomer injection experiment and CATHARE2 calculations.

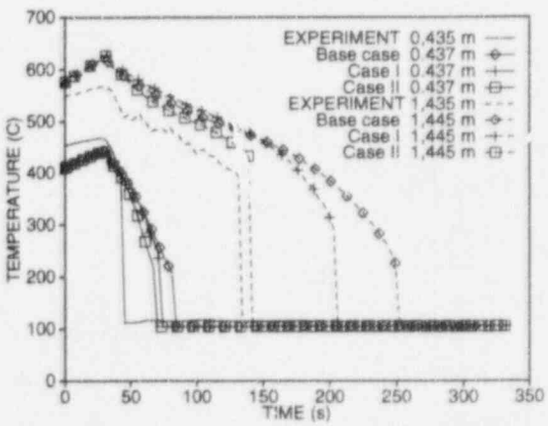

Fig. 10. Cladding temperatures at two different elevations in downcomer injection experiment and CATHARE2 calculations.

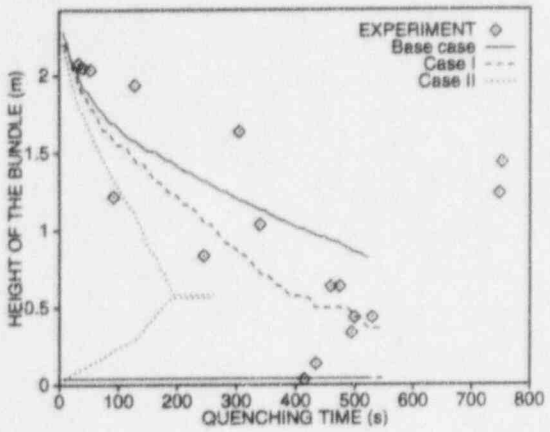

Fig. 11. Quenching times in upper plenum injection experiment and CATHARE2 calculations.

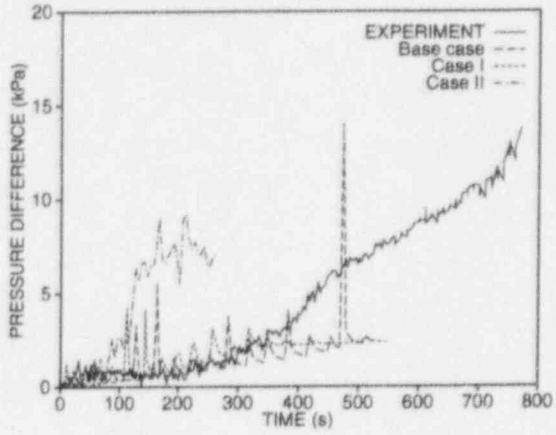

Fig. 12. Pressure differences in upper plenum injection experiment and CATHARE2 calculations.

injection situation. The calculations show that by changing the hydraulic diameter in the upper core region, the CCFL model of the code is effected and more water is allowed to enter in the core region. Also one fundamental reason for discrepancies between the calculations and the experimental results is that a one-dimensional model cannot accurately describe multidimensional phenomena. The non-uniform flow within different parts of the core region, i.e. centre or edge rods, is impossible to simulate with a one-dimensional code.

4.2. Boil-off experiments and calculations

The boil-off experiments were performed especially to get comparison data for the CATHARE2 calculations. Altogether three experiments were performed. The effect of the heating power on the heat-up of the rods was studied, i.e. three different power levels were used in the experiments, Fig. 13. The collapsed level corresponding to a certain swell level was smaller when the core power was higher. This means that with the higher core power more water is evaporated before the core heat-up.

The experiment modelled with CATHARE2 was the one with 50 kW heating power (BLO_027). The *Case III* calculation with decreased core outlet nozzle wetted perimeter and with the increased flow area and flow resistances gave better results than the *Base case* calculation. Fig. 14 shows the pressure differences in the experiment and in the two calculation cases. The changes in the core outlet nozzle flow area have a very significant effect on the

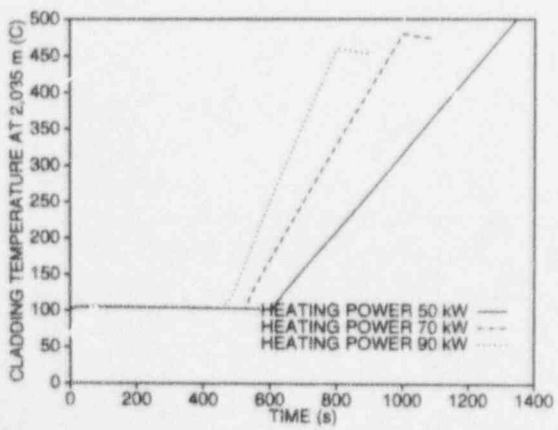

Fig. 13. Effect of heating power on heat up of rods in boil-off experiments.

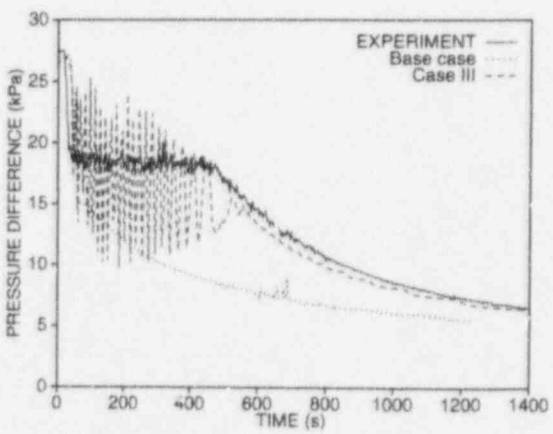

Fig. 14. Pressure differences in boil-off experiment and CATHARE2 calculations.

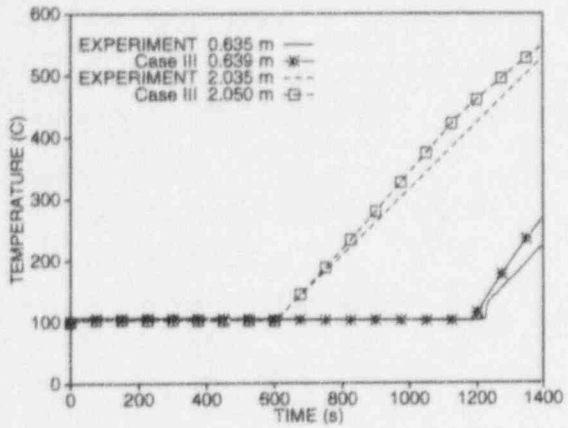

Fig. 15. Cladding temperatures of rods in boil-off experiment and CATHARE2 calculation.

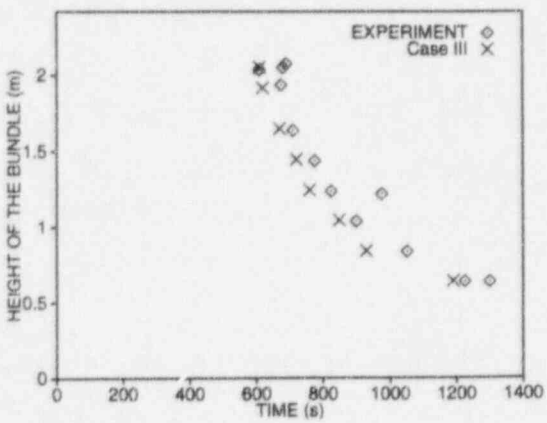

Fig. 16. Swell level in boil-off experiment and CATHARE2 calculation.

behavior of the pressure differences, as can be seen in Fig. 14. When this flow area is increased (*Case III*) the calculated pressure difference compares well with the measured curve, but large oscillations appear during the first 500 seconds of the transient. These oscillations can be avoided with the correct nozzle flow area modelling (*Base case*), but then the right pressure difference behavior is lost. In Figs 15 and 16 the cladding temperatures and height of the swell level in the experiment and in the *Case III* calculation are presented. The heat up of the rods is calculated correctly (Fig. 15), although the swell level drops slightly faster in the calculation than in the experiment, Fig. 16.

5. CONCLUSIONS

In order to produce comparison data for the best-estimate thermal-hydraulic code CATHARE2, over 30 reflood and boil-off experiments were performed under typical conditions on the VEERA facility. The VEERA facility is a scaled-down model of the Russian type VVER-440 reactor. Investigating the results from experiments and code calculations, the following has been concluded:

Experiments

(1) More effective cooling of the rod bundle was obtained with downcomer than with upper plenum ECC injection. Probably a vapor bed is generated in the middle part of the bundle preventing the water from penetrating to the core. ECC water flow rate has also a moderate influence on the quenching times of the rods. The effect of the injection water temperature, the initial cladding temperature and the heating power was only minor compared with the injection location and flow rate. Multidimensional quenching in all reflood experiments was noticed near the bundle midplane.

(2) The collapsed level corresponding to a certain swell level was smaller when the core power was higher.

Calculations

(3) The CATHARE2 code predicts the propagation of both quench fronts (bottom and top-down) satisfactorily in the case of downcomer injection. Especially in the upper plenum injection case the simulation of the CCFL phenomenon is dominating the top-down quench front propagation, but the CATHARE2 model seems to give reasonable results.

(4) The prediction of dropping collapsed level and core heat up in the boil-off situation succeeds well, if the flow area of the core outlet nozzle is increased. The swell level drops slightly faster in the CATHARE2 calculation than in the experiment, but the heat-up of the rods is calculated correctly.

REFERENCES

[1] T. Kervinen,"Reflood Experiments with Simultaneous Upper and Lower Plenum Injection in the REWET-II Rod Bundle Facility", International Meeting on Thermal Nuclear Reactor Safety, ANS/ENS/JAES, Chicago, 1982.

[2] T. Kervinen, H. Purhonen, H. Kalli, "REWET-II Experiments to determine the Effects of Spacer Grids on the Reflooding Process", Fifth International Meeting on Thermal Nuclear Reactor Safety at Karlsruhe, September 9 - 13, 1984.

[3] J. Tuunanen, T. Kervinen, H. Kalli, H. Tuomisto, M. Komsi and E. Markkanen, "Long-Term Emergency Cooling Experiments with Aqueous Boric Acid Solution with the REWET-II and VEERA Facilities", Proceedings of International ENS/ANS Conference on Thermal Reactor Safety, Avignon, Vol. 4, pp. 1428 - 1436 (1988).

[4] P. Raussi, R. Munther, H. Kalli, J. Kouhia and M. Puustinen, "Experimental VVER safety studies in Finland", Transactions of ENC '94, International Nuclear Congress - Atoms for Energy, Lyon, October 2 - 6, 1994, Vol. II, pp. 222 - 225.

[5] H. Purhonen, J. Miettinen, "PACTEL - Parallel Channel Test Loop, General Description for ISP", Proceedings of the ISP 33 First Workshop 18 - 19.2. 1992, Lappeenranta, Finland.

[6] F. Barre and M. Bernard, "The CATHARE Code Strategy and Assessment", Nuclear Engineering and Design, Vol. 124 (1990), pp. 257 - 284.

[7] J. Bartak and T. Haapalehto, "Simultaneous bottom and top-down rewetting calculations with the Cathare code", Nuclear Technology Vol. 106 April 1994, p. 46 - 59.

[8] M. Farvaque, "User's Manual of CATHARE2 V1.3E", Report STR/LML/EM/91-61, Grenoble, France, November, 1992.

COUNTER–CURRENT FLOW IN A VERTICAL TO HORIZONTAL TUBE WITH OBSTRUCTIONS

P. Tye,[1] *A. Matuszkiewicz,*[1] *A. Teyssedou,*[1]
A. Tapucu,[1] and *W. Midvidy*[2]

(1) Institut de Génie Nucléaire
École Polytechnique de Montréal
Montréal, Québec, Canada H3C 3A7
(2) Ontario Hydro

1. ABSTRACT

This paper presents experimental results on counter–current flow and flooding in an elbow between a vertical and a horizontal run. The experimental technique used allowed not only the flooding limit to be determined, but also the entire partial delivery region to be studied as well. The influence that various size orifices placed in the horizontal run have on both the delivered liquid flow rates and on the flooding limits is also examined. It is observed that both the flooding limits and the delivered liquid flow rates decrease with decreasing orifice size. Further, it is also observed that the mechanisms that govern the partial delivery of the liquid are significantly different when an orifice is present in the horizontal leg as compared to the case when no orifice is present.

2. INTRODUCTION

Counter–Current Flow (CCF) in general and the Counter–Current Flooding Limit (CCFL) in particular are of great importance in the area of nuclear reactor safety analysis. In CANDU reactors, during a postulated loss of coolant accident (LOCA), the water coming from the inlet and outlet headers enters the fuel channels through the feeder pipes. These pipes consist of vertical and horizontal runs. In some feeders, orifices and/or venturi type flow obstructions are installed for flow adjustments and measurements. Steam produced in the feeders and/or in the fuel channels may flow in the direction opposite to that of the water, thereby creating vertical and horizontal counter–current two–phase flows in the feeder pipes. Under these conditions, the rate at which cooling water can enter the fuel channels may be limited by the flooding phenomena. During flooding, the liquid is partly entrained in the same direction as the steam flow. The liquid delivery is greatly affected by the geometry of the feeder pipes, shape and number of fittings, flow area restrictions and the way the feeder pipe is connected to the header and to the end–fitting. Thus, knowledge of the flooding phenomena in a geometry similar to the header–feeder system in a CANDU reactor is of prime importance in the safety analysis of nuclear reactors in order to improve the prediction of the time required for the emergency cooling injection system to refill the fuel channels. The objectives of this research are to study the influence of a 90° elbow between a vertical and a horizontal run and the affects of its interaction

with an orifice on the entire range of counter–current flow phenomena from the onset of flooding up to the zero penetration limit.

3. PREVIOUS WORK

Over the last 30 years a great deal of experimental and analytical work has been done on the determination of the flooding point in vertical counter–current two–phase flows. The same cannot, however, be said for counter–current two–phase flows occuring in an elbow between a vertical and a horizontal tube where the amount of information available in the open literature is quite limited. Similarly, while the influence of an obstruction on the flooding point in vertical counter–current two–phase flows has been studied by a number of different researchers the amount of information available on this subject under horizontal flow conditions is rather scarce. Nevertheless, we will examine what information is available regarding the influence of obstructions on the flooding phenomena under both vertical and horizontal counter–current flow conditions as well as that available on the influence of an elbow between a vertical and a horizontal tube.

For vertical flows Celata *et al.* [1] examined the influence of orifices on the delivered liquid flow rate under counter–current flow conditions. They carried out their experiments in a 20 mm I.D. test section without an obstruction and with orifices having β ratios ($\beta = D_{orif}/D_{tube}$) of 0.60, 0.70, 0.75, 0.80, 0.85, 0.90, and 0.95. For a given orifice they observed that the delivered liquid flow rate was only a function of the gas flow rate and did not depend on the inlet liquid flow rate. They also found that for a given gas flow rate the delivered liquid flow rate decreased with decreasing orifice size. They also observed, that for a given β ratio, the zero penetration point, the point where the delivered liquid flow rate is zero, was the same for all the liquid flow rates used during the experiments. Tye *et al.* [2] carried out experiments for the determination of the flooding point in a 19 mm I.D. test section without an obstruction and with orifices having β ratios of 0.66, 0.72, 0.83, and 0.90. They found that the presence of the orifice significantly reduced the gas flow rate required to initiate flooding for a given liquid flow rate. Further, they found that this influence became more pronouced for smaller β ratios. Tye *et al.* [3] carried out similar experiments in a 63.5 mm I.D. vertical test section for the characterization of the entire partial delivery region of counter–current flow from the point of onset of entrainment (flooding limit) up to the zero liquid penetration point. It was again found that the presence of the orifice significantly reduced the gas flow rate required to initiate flooding for a given liquid flow rate. Further, they observed that for each of the orifices the delivered liquid flow rate was only a function of the gas flow rate and was independent of the liquid flow rate. They also found that the inlet gas flow rate at the zero penetration point was a constant for each of the orifices studied.

Krolewski [4] carried out flooding experiments for vertical to horizontal and inclined to horizontal flows. The test facility consisted of a 51 mm I.D. 584 mm long horizontal leg connected to a vertical or inclined leg by either a 90° or a 45° elbow. Air and water at atmospheric conditions were used as the working fluids. The point of onset of flooding was

determined to be the point at which a sudden increase in the pressure drop across the test section occured. Data were reported for a number of different geometrical configurations. For the one most closely resembling the test facility used in the present study, the author's results indicate that there is a significant decrease in the gas flow rate required to provoke flooding as compared to that which would be required for the same tube diameter under vertical flow conditions.

Siddiqui *et al.* [5] carried out flooding experiments in a vertical to horizontal 90° elbow for various pipe diameters, lenghts and radii of curvature of the elbow. The authors found that at high liquid flow rates a hydraulic jump formed in the horizontal leg close to the bend and that flooding was caused by slugging which occured at this point. At low liquid flow rates, for the range of tube diameters that were studied, it was found that the hydraulic jump was very small and difficult to observe. The authors also observed that the flooding limit was dependent on the tube diameter, the lenght of the test section as well as the radius of curvature of the bend. The results indicate that for all the liquid flow rates studied the gas flow rates at the flooding point were much smaller than those corresponding to flooding in a vertical pipe. The authors also found that for the range of tube diameters studied, the square root of the non-dimensional superficial gas velocity at the zero penetration point was constant.

Wan [6] studied the counter-current flow of steam and water in an upright 90° elbow. Qualitatively the results were quite similar to those of Siddiqui *et al.* [5]. The author, however, identified three distinct flow patterns occuring in the experiments. These patterns were: 1) steady counter-current flow with no slugging, 2) slugging with liquid carryover, and 3) slugging with an oscillating water column in the vertical leg and no liquid carryover.

Kawaji *et al.* [7] studied the counter-current flooding limit in vertical and vertical to horizontal and downwardly inclined 51 mm I.D. pipes. For the horizontal pipes the experiments were carried out using two different lenghts of the horizontal run: 2.54 m and 0.1 m. For the longer of the two sections and for low liquid flow rates the authors also observed the formation of a hydraulic jump in the horizontal leg downstream of the elbow. Under these conditions the flooding was observed to be due to the hydraulic jump. Furthermore, the flooding was found to occur at lower gas velocities than those observed with the vertical runs only. At higher liquid flow rates the flooding mechanism changed and it was observed to occur due to slugging near the exit of the horizontal leg.

Kawaji *et al.* [8] carried out experiments to determine the flooding limit in a 51 mm I.D. test section with multiple elbows and orifices having β ratios of 0.550, 0.670 and 0.865. Three different geometrical configurations were studied: double-vertical elbow in which the second and third elbow are in the vertical plane, double-horizontal elbow in which the second and third elbow are in the horizontal plane, and double-inclined elbow in which the second and third elbow are at 45° to the vertical plane. Although there are some differences in the results for the three different geometries studied, qualitative observations can be made as to the effects of the orifice size on the flooding point. The

authors found that the orifice having the largest β ratio had very little effect on the flooding point as compared to the results without the orifice. For the two smaller orifices it was found that, for a given liquid flow rate, the flooding gas velocities were much smaller than those observed with the largest orifice and in the no orifice case. Further, the flooding gas velocity was found to decrease with decreasing orifice β ratio.

Tye *et al.* [3] presented preliminary results of partial delivery experiments in a 63.5 mm I.D. vertical to horizontal tube without an orifice and with various sized orifices placed in the horizontal leg. They found that for a given inlet liquid flow rate subject to a given counter–current gas flow the delivered liquid flow rate decreased with decreasing β ratio. They also found that the gas flow rate at the zero penetration point was unique for each of the orifices used as well as for the unobstructed tube and did not depend on the inlet liquid flow rate.

4. TEST FACILITY AND INSTRUMENTATION

The CCF test facility shown in Figure 1 is capable of supporting vertical test sections as well as test sections containing both vertical and horizontal legs. Water and air at close to atmospheric conditions are used as the working fluids. The water is supplied to the test section by a pump connected to a constant head water tank. The liquid flow rate is controlled in two steps: the coarse control is done using a set of valves and a by–pass circuit at the pump outlet, and the fine control is done using a set of two different size parallel needle valves located next to the test section. The temperature of the inlet water is held constant at $20 \pm 0.5^{\circ} C$. The air is supplied by the mains of the laboratory.

4.1 CCF test section containing vertical and horizontal runs

Figure 2 shows a schematic diagram of the test section containing both vertical and horizontal runs. It is constructed of 63.5 mm I.D. clear plexiglass tubes to allow flow visualization. The vertical run is supported by an aluminum I–beam and the test section is positioned vertically using 3 adjustable supports. The horizontal run is also supported by an aluminum I–beam structure, it is positioned horizontally using 6 adjustable supports of the same type as those used to position the vertical run. The angle of the test section from the horizontal can be varied as required. For the experiments presented in this paper an angle of 90° was used between the vertical and the horizontal run. The major components of the test facility are:

- the upper plenum which serves as a collector/seperator for any liquid hold up during CCF and CCFL experiments,
- the porous wall water injector which consists of a 63.5 mm I.D. tube with 800 1 mm holes in the wall,

- the tubular test section consists of a 2022 mm long vertical section and a 3327 mm long horizontal run. The L/D ratio of the horizontal leg is 52. Both the vertical and horizontal runs contain flanges in which an orifice may be placed. The vertical and horizontal runs are connected by a 90° PVC elbow. The horizontal and vertical runs are centered in the elbow by two plexiglass collars and are sealed using O-rings.

- the lower plenum which contains the liquid outlet including a water level control system and the air inlet system. The level control system consists of a 3.45 kPa (0.5 psid) pressure transducer used as a liquid level transducer. The signal produced by this transducer is used as the process variable input of an electronic level controler. The level control system is capable of maintaining the water level in the lower plenum constant throughout the entire range of liquid flow rates, i.e., from full delivery up to the zero liquid penetration point.

The flow area restrictions (orifices) are installed in the test sections by means of the flanges designed for this purpose. The positions of these flanges are shown in Figure 2. For the present study the orifice was placed in the horizontal run only. The orifices are made of 1.5 mm thick stainless steel plates without a chamfered edge. The β ratios ($\beta = D_{orif}/D_{tube}$) of the orifices used in this research are 0.90, 0.83, 0.77 , 0.72, 0.66, and 0.55.

4.2 Instrumentation

The test facility is instrumented to measure liquid and gas flow rates, inlet flow temperatures, and absolute pressures.

- Liquid Flow Rate: The liquid flow rate is measured using "Flow Technology" turbine flowmeters; which cover the range from 0.05 to 4.54 m^3/h with an accuracy of better than 1% of full scale.

- Gas Flow Rate: The gas flow rate is measured using a set of five "Brooks" rotameters; covering the range from 0.085 to 132.5 m^3/h at an inlet pressure of 2 bars. The accuracy of the rotameters is ±1% of full scale.

- Absolute Pressure: The absolute pressure in the lower plenum is measured using a "Sensotec" pressure transducer; the range of the absolute pressure covered is from 0 to 0.14 bars with an accuracy of ±0.25% of full scale.

- Temperature: The temperature of the gas is measured with a thermocouple having an accuracy of ±0.5 $°C$ which is installed in the air delivery line. The temperature of the liquid is measured with an RTD having an accuracy of ±0.5 $°C$.

5. EXPERIMENTAL PROCEDURE

In the past, several different physical phenomena have been used to characterize the flooding point. Some authors identified it as liquid bridging, surface wave instabilities, inception of droplet entrainment, etc. However, none of these phenomena necessarily leads to a net upward liquid flow. The liquid that is entrained above the liquid inlet may subsequently flow downward. As described by Tien *et al.* [9], three criteria have been used by different authors for the characterization of the CCFL: a) point of inception of liquid entrainment; b) inception of liquid film upflow; and c) zero liquid penetration. However, for a given liquid flow rate these events occur at significantly different gas flow rates. Thus, it is obvious that a lack of clarity and consistency in the definition of flooding will significantly affect the experimental results as well as their interpretaton.

For the above reason, we will clearly state the definition of flooding and the experimental criterion that we will be using in this research. The standard definition of the counter-current flooding limit, and the one used in these experiments, is (Bankoff & Lee [10]): *"for a given downward liquid flow the maximum upward gas flow rate for which full liquid delivery out the bottom of the tube is maintained, corresponds to the counter-current flooding limit."* It is important to note that the counter-current flooding limit is just a limit for the gas flow rate beyond which only partial liquid delivery out of the lower end of the test section will occur. This point corresponds to the maximum gas flow rate for which full liquid delivery still exists, and it is the most widely accepted experimental criterion for the point of flooding (Bankoff & Lee [10], and Dukler, *et. al.* [11]). Having defined our criterion for the experimental detection of the flooding point we will now describe the experimental procedure.

The first point that could be studied for each liquid flow rate was determined by fixing the required inlet liquid flow then slowly increasing the gas flow until the point where a measurable amount of entrainment was obtained. The subsequent experiments beyond this initial point were carried out by fixing the liquid and gas flow rates and collecting and weighing the entrained liquid using the collection system located in the upper plenum. In this manner the entire range of CCF phenomena from the point of inception of entrainment to the zero penetration point was studied for each liquid flow rate. In order to minimize the scattering in the data, on average 20 kg of entrained liquid was collected for each run. The time required to collect this amount of liquid ranged from approximately 2 minutes for the highest entrained liquid flow rates up to 30 minutes for the lowest entrained liquid flow rates that were studied. To further minimize the scattering in the data, for the largest inlet liquid flow rates when an orifice was present in the horizontal leg the collection was repeated up to three times and the results were averaged. For the experiments presented in this paper the inlet liquid flow rates range from 0.1 m^3/h to 3.0 m^3/h.

6. EXPERIMENTAL RESULTS

The experimental results obtained in the course of this work will now be presented. The reults obtained for the entire parial delivery region and those for the flooding point only will be presented seperately.

6.1 Partial Delivery Results

Figures 3a–c show the delivered liquid superficial velocity, $J_{\ell\ delivered}$, vs. the gas superficial velocity, J_g, for the present tests; seven different cases were studied. They are the no orifice case and the cases for orifices having β ratios of 0.90, 0.83, 0.77 0.72, 0.66, and 0.55.

The results for the case without an orifice, $\beta = 1$ in Figure 3a, show that the delivered liquid superficial velocities decrease smoothly with increasing gas superficial velocity. As opposed to what was observed by Siddiqui *et al.* [5], in the present experiments the hydraulic jump was not seen to play a role in the flooding mechanism. For the case without an orifice a hydraulic jump was observed to occur in the horizontal leg. As the gas flow rate was increased the hydraulic jump was seen to travel back towards the elbow and eventually enter it. As the gas flow rate was increased beyond that required to drive the hydraulic jump into the elbow, entrained droplets were observed in the gas stream in the vertical leg just above the elbow, these droplets did not, however, necessarily lead to the onset of flooding as they were frequently seen to be redeposited into the liquid film only a few centimeters above the elbow. In this region, it was observed that the flow was in the form of an annular film with entrained droplets in the gas core, shown schematically in Figure 4. A further increase in the gas flow rate was necessary to provoke flooding. As the gas flow rate was increased an increasing number of droplets, which could not reach the upper plenum, were visible in the gas core just above the elbow. At the flooding point, the flow pattern was seen to change from a stable counter–current annular flow with entrained droplets, to counter–current churn flow. This churn flow was in the form of a pulsating column in the vertical leg. This pulsating column caused large amplitude waves to form in the horizontal leg that were subsequently driven back into the elbow by the counter–current gas flow and upward to the collection system. The results shown in Figures 3a–c are similar to those of Kawaji *et al.* [8] in that largest orifice used in these experiments had almost no influence on the delivered liquid flow rate as compared to the unobstructed case ($\beta = 1$ in Figure 3a and $\beta = 0.90$ in Figure 3b). Further, our results show that this observation can be extented from the flooding limit studied by Kawaji *et al.* [8], through the entire partial delivery region right up to the zero penetration point.

The results for the largest orifice studied ($\beta = 0.90$) shown in Figure 3b are very similar to those observed for the case without an orifice described above. However, for the cases with an orifice placed in the horizontal run no hydraulic jump was observed. It can be seen that for this case the delivered liquid superficial velocities decrease smoothly with increasing gas superficial velocity as observed in the case without an orifice. For

the case having an orifice of $\beta = 0.83$ (Figure 3a) at superficial gas velocities greater than 1 m/s the results are quite similar to the results for $\beta = 0.90$ in that the delivered liquid superficial velocities decrease smoothly with increasing gas superficial velocity. For largest inlet liquid superficial velocities and for gas superficial velocities between 0.5 and 1.0 m/s it can be seen that a plateau region is reached in the delivered liquid superficial velocity. For gas superficial velocities less than 0.5 m/s it can be seen that the delivered liquid superficial velocity decreases very rapidly with increasing gas superficial velocity. For the smaller orifices ($\beta = 0.77$ to $\beta = 0.55$) the results are clearly different than those observed for the cases of $\beta = 1.0$ and $\beta = 0.90$. At very low gas superficial velocities and high inlet liquid superficial velocities the delivered liquid superficial velocity decreases very rapidly with increasing gas superficial velocity. It was visually observed that in this region a very densely packed bubble column, with the occasional Taylor bubble rising through it, was formed in the vertical leg. This is shown in Figure 5. The liquid upflow was mostly due to entrainment in this bubble column. The passage of the Taylor bubbles caused periodic increases in the liquid upflow. In the horizontal leg large slow moving plugs carried the gas into the elbow. At gas superficial velocities between approximately 0.5 and 3.5 (m/s) (see Figures 3b and 3c) it can be seen that a plateau is reached in the delivered liquid superficial velocity and that the liquid delivery is almost independent of the gas superficial velocity. The size of this plateau seems to increase with decreasing β ratios (i.e., increasing blockage severity). In this region it was visually observed that the liquid upflow was mostly in the form of very fast moving slugs. It was further observed that the slugging frequency decreased with increasing gas superficial velocity. This region is qualitatively similar to region 2 identified by Wan [6]. At even higher gas superficial velocities, the delivered liquid superficial velocity was seen to decrease quite smoothly with increasing gas superficial velocity. In this region a wavy stratified flow existed in the horizontal leg, the waves were seen to travel in the direction of the gas flow, while the liquid substrate travelled in the opposite direction. The liquid level of this stratified flow decreased with increasing distance from the elbow. It appears that the case having an orifice of $\beta = 0.83$ is a transition between two distinct regions of flow behaviour. At high gas superficial velocities the results for $\beta = 0.83$ are similar to those of $\beta = 1.0$ and $\beta = 0.90$, while at lower gas superficial velocities there are a number of similarities with the results for $\beta = 0.77$ to $\beta = 0.55$ described above. It is also interesting to note that in the region were the transition takes place, gas superficial velocities between (0.4 *to* 1.0 m/s), the results for this orifice exhibit more experimental scatter than any of the other cases studied.

For all the cases studied it was visually observed that the disturbance that lead to partial liquid delivery always formed in the elbow. A pulsating column was formed in the vertical leg which caused large amplitude waves to form in the horizontal leg that were subsequently driven back into the elbow by the counter-current gas flow. For the experiments with an orifice installed in the horizontal leg the mechanism was similar to that observed in the case without the orifice. The major difference was that the wave produced by the pulsating column was seen to be reflected by the orifice and travelled back towards the elbow; it was then possible for this wave to interfere constructively with those waves

generated by the pulsating column above the elbow. If the height of the wave resulting from the meeting of the incident and reflected waves was sufficient to bridge the tube, a liquid slug resulted which was then blown violently back into the elbow and into the vertical leg. This sequence of events is shown in Figures (6a and b). Figure 6a shows the incident and reflected waves traveling towards each other. The slug formed by the interference of these waves is shown in Figure 6b. For smaller orifices the height of the liquid film in the horizontal leg and the size of the wave reflected from the orifice both increased. This resulted in more frequent and more violent slugging behaviour being observed for the smaller orifice. For the experiments with the $\beta = 0.90$ orifice no reflection of the wave by the orifice was seen to occur. At higher gas superficial velocities a region was reached where the liquid level in the horizontal leg was insufficient to allow bridging to occur and a region of steady counter–current flow without slugging but with liquid carryover (similar to region 1 of Wan [6]) was established. Another observation is that the gas superficial velocity corresponding to the point of zero liquid penetration for a given orifice as well as for the no orifice case is the same for all the inlet liquid superficial velocities. A similar observation for results without an orifice was made by Siddiqui *et al.* [5]. A further point of interest is that, while by strict definition, as soon as J_ℓ delivered is less than J_ℓ injected the flooding limit has been reached, however, Figures 3a–c show that a large increase in the gas superficial velocity is still required to reach the point of zero liquid penetration. This is an important point for the refilling of a nuclear reactor following a LOCA.

6.2 Flooding Results

It is important to point out that Figures 3a–c represent the locus partial delivery for all the cases studied and **not** the flooding limits. The relationship between the partial delivery and the flooding limit is illustrated for a given orifice, in this case $\beta = 0.77$, in Figure 7. The insert in this figure shows the flooding limit as well as the partial delivery results for one particular inlet liquid superficial velocity ($0.12\ m/s$). It can be seen that for this orifice the locus of flooding points lies considerably above the locus of partial delivery points for most of the range of gas superficial velocities covered. The two curves approach each other at the extremes of very low and very high inlet liquid superficial velocities. As the orifice β ratios increased and for the no orifice case the locus of flooding limits was seen to approach the locus of partial delivery points. In examining Figure 7 it is important to recall that the flooding limit corresponds to the maximum gas flow rate for which full liquid delivery still exists. From the insert we can see that as the superficial velocity of the gas is increased the delivered liquid superficial velocity remains constant at its inlet value until a particular gas superficial velocity is reached; at this point the delivered liquid superficial velocity drops suddenly. The maximum gas superficial velocity for which the delivered liquid superficial velocity retains its inlet value corresponds to the flooding limit. The abrupt transition from full to partial delivery may be related to the hysteresis effect observed by many other researchers. The partial delivery region below the flooding point with decreasing gas flow rates will be studied in the near future. The mechanisms governing the transition from full to partial liquid delivery have been described in detail in the previous section.

The flooding limits were obtained in the manner described above for all of the inlet liquid superficial velocities and for all of the cases studied. The results for the flooding limits only are presented in Figures 8a and 8b in terms of the square root of the non dimensional superficial velocies, $J_g^{*\frac{1}{2}}$ and $J_\ell^{*\frac{1}{2}}$, where $J_k^{*\frac{1}{2}}$ is defined as:

$$J_k^{*\frac{1}{2}} = \left\{ \frac{\rho_k^{\frac{1}{2}} J_k}{[gD(\rho_f - \rho_g)]^{\frac{1}{2}}} \right\}^{\frac{1}{2}} \quad . \tag{1}$$

Examining Figures 8a and 8b it can be seen that the flooding limits decrease with decreasing β ratios. For the case with no orifice in the horizontal leg (Figure 8a) the results are quite similar to those of Siddiqui *et al.* [5]. Further, it can be seen that the largest orifice used ($\beta = 0.90$) had almost no effect on the flooding limit as compared to the case without an orifice, a fit of the ($\beta = 1.0$) data has been added to Figure 8b for reference purposes. The same observation can be made about the next largest orifice ($\beta = 0.83$) at values of $J_\ell^{*\frac{1}{2}}$ less than 0.4. For the other orifices ($\beta < 0.83$) that were studied it is quite clear from both Figures 8a and 8b that for a given value of $J_\ell^{*\frac{1}{2}}$ a decrease in the β ratio leads to a decrease in the the value of $J_g^{*\frac{1}{2}}$ at the flooding limit. This result is qualitativly similar to the observations of both Celata *et al.* [1] and Tye *et al.* [2 & 3] for vertical pipes. Further, the flooding limits are well below those obtained by Tye *et al.* [3] for vertical flow in a test section of the same diameter over the same range of orifice β ratios.

6.3 Comparison of Flooding Results

The flooding results obtained in the present study will be compared to other experimental results obtained on geometrically similar test facilities. They will also be compared to the one model available in the literature which is able to predict the flooding point for this type of geometry. For the cases where an orifice is installed in the horizontal leg, the present results will only be compared to other experimental results due to the fact that, as yet, no model exists which is able to predict the flooding behaviour due to the interactions of an elbow between a vertical and a horizontal run, and an orifice.

6.3.1 Comparison with Other Experimental Results: No Orifice

Figure 9 shows a comparison of our experimental results for the case without an orifice with the results of Krolewski [4], Siddiqui *et al.* [5], Kawaji *et al.* [7], and Wongwises [12]. The geometric arrangements of their various test sections are also shown in the same figure. In all these cases the various authors studied the influence of different parameters, i.e., the radius of curvature of the elbow, the L/D ratio of the horizontal leg, the influence of the tube diameter, and the influence of the angle of inclination of the lower leg from the horizontal. It should be noted that no ıe of the test facilities of the other researchers who's data have been used for this comparison is identical in all respects to the one used in the

present study. However, for the comparisons the results of each author obtained on the test section having the geometry most similar to the one in the present study were used. At the lower values of $J_\ell^{*1/2}$ the results of Krolewski [4], Siddiqui *et al.* [5] and Kawaji *et al.* [7] are in reasonably good agreement with our results. At values of $J_\ell^{*1/2} > 0.4$ the results of Krolewski [4] and those of Kawaji *et al.* [7] start to diverge from ours. This divergence could be due to the influence of parameters that differ between the various test facilities. The results of Wongwises [12] are in disagreement with all the other available data for the flooding in a test section containing a vertical and a horizontal leg connected by an elbow.

6.3.2 Comparison with Other Experimental Results: Orifice

Figure 10 shows a comparison of the present flooding results with those of Kawaji *et al.* [8]. A schematic of the test facility used by Kawaji *et al.* [8] is also shown in the same figure. It consists of a 1 m long vertical leg connected to a 1.5 m long horizontal leg containing and orifice 1.1 m downstream, with respect to the liquid flow, of the first elbow. The horizontal leg was connected to a second 1 m long vertical leg which was in turn connected to a third 1 m long horizontal leg. At high values of $J_\ell^{*1/2}$ Kawaji *et al.* [8] reported that flooding occured in the second vertical leg of the test facility. Since the geometrical arrangement used by Kawaji *et al.* [8] is different than the one used in the present study the data reflecting the occurence of the flooding in the second vertical leg were not used for comparison. In the region where Kawaji *et al.* [8] reported that the flooding occured as a result of the orifice their data are in very good agreement with that obtained in the present study. In general both sets of results indicate that the gas superficial velocity required to provoke flooding for a given gas flow rate, decrease with decreasing orifice β ratio.

6.3.3 Comparison with Correlation: No Orifice

The only correlation available for the prediction of the flooding in an elbow between a vertical and a horizontal leg is that of Ardron & Banerjee [13]. It is given by the following relation:

$$J_g^{*\frac{1}{2}} = 1.444 - 0.004\lambda - \cosh(\lambda^p K^q (J_\ell^{*\frac{1}{2}})^r) \quad . \tag{2}$$

where,

$$\lambda = \frac{L(Re^{*-n})}{D} \quad ,$$

$$Re^* = \frac{D}{\nu_g}\sqrt{\frac{gD(\rho_\ell - \rho_g)}{\rho_g}} \quad ,$$

$$K = \frac{\nu_g}{\nu_\ell}\sqrt{\frac{\rho_g}{\rho_\ell}} \quad ,$$

and the constants have the following values: $n = 0.2$, $p = 0.057$, $q = -0.020$, and $r = 0.70$.

Figure 11 shows the results of a comparison of the above flooding correlation with the experimental flooding limits obtained in this study for the no orifice case. We can see that the correlation is in reasonably good agreement with the experimental results over most of the range of $J_\ell^{*\frac{1}{2}}$ studied but begins to diverge from the experimental results for $J_\ell^{*\frac{1}{2}} > 0.5$.

This correlation is not applicable to the cases having an orifice in the horizontal leg and to the best of the authors knowledge no correlations exist which were developed to predict flooding behaviour due to the interactions of an elbow between a vertical and a horizontal run, and an orifice.

7. CONCLUSIONS

Experiments were carried out to study the entire regime of counter-current flow from the point of onset of entrainment up to the zero penetration point in a test section containing a vertical and a horizontal run both with and without orifices. It was observed that a significant change occured in the flooding mechanism for the smaller orifices. The delivered liquid flow rate was controlled by a mechanism of wave production due to a pulsating column in the vertical leg and wave reflection due to the presence of the orifice. It was further observed that for all the orifices studied the zero penetration point was only a function of the orifice β ratio and of the gas flow rate and was independent of the inlet liquid flow rate.

The experimental results, for the flooding point only, obtained in the present study have been compared to the results of other researchers. In spite of the fact, that none of the test facilities used by the other researchers are identical to the one used in the present study, the results of the other researchers are in good agreement with the present results. The Ardron & Banerjee [13] correlation was found to do a reasonably good job of predicting our experimental flooding results in the no orifice case.

No comparisons are presented for the experimental results which study the entire partial delivery region from the onset of entrainment up to the zero penetration point. This is due to the fact that, to the best of the authors knowledge, no other experiments of this type have ever been performed in a test section containing an elbow between a vertical and

a horizontal. Furthermore, other than the present results, no data on the partial delivery region in which the interaction between an elbow and an orifice was studied, are known to exist.

ACKNOWLEDGEMENTS

This work has been funded by COG (CANDU Owners Group) under contract number WPIR 1513, Safety and Thermalhydraulics, Working Party #5.

REFERENCES

[1] Celata G.P., N. Cumo G.E., Farello & Setaro T.; "The Influence of Flow Obstructions on the Flooding Phenomenon in Vertical Channels." Int. J. Multiphase Flow, Vol. 15, No. 2, pp. 227–239, (1989).

[2] Tye P., Davidson M., Teyssedou A., Tapucu A., Matuszkiewicz A., & Midvidy W.; "The Counter–Current Flooding Limit in Vertical Tubes with and without Orifices," CNS 4th Int. Conf. on Sim. Meth. in Nucl. Engng. Montréal, Vol. 2, Session 5C, Pub. Canadian Nuclear Socitey, (1993).

[3] Tye P., Matuszkiewicz A., Teyssedou A., Tapucu A., Davidson M., Midvidy W., & Huynh, H.; "The Influence of Flow Obstructions on Counter–Current Flow and Flooding in Vertical and Horizontal Tubes," CNA / CNS Annual Conf. Montréal, Vol. 1, Session 3A, Pub. Canadian Nuclear Socitey, (1994).

[4] Krolewski, S.M.; "Flooding in a Simulated Nuclear Reactor Hot Leg." Bachelor's Thesis, MIT, (1980).

[5] Siddiqui H., Banerjee S., Ardron K.H.; "Flooding in an Elbow Between a Vertical and a Horizontal or Near–Horizontal Pipe. Part I: Experiments" Int. J. Multiphase Flow, Vol. 12, No. 4, pp. 531–541, (1986).

[6] Wan, P.T., "Countercurrent Steam–Water Flow in an Upright 90° Elbow," 8th Int. Heat Transfer Conf. San Francisco Ca. USA, pp. 2313–2318, (1986).

[7] Kawaji M., Thomson L.A. & Krishnan V.S.; "Countercurrent Flooding in Vertical–to–Inclined Pipes." Exp. Heat Transfer, Vol. 4, pp.95–110, (1991).

[8] Kawaji M., Lotocki P.A. & Krishnan V.S.; "Countercurrent Flooding in Pipes Containing Multiple Elbows and an Orifice." JSME, Ser. B, Vol. 36, No. 3. pp.95–110, (1993).

[9] Tien C.L. & Liu C.P.; "Survey on Vertical Two–Phase Counter–Current Flooding," EPRI Report No. NP–984, (1979).

[10] Bankoff S.G. & Lee S.C.; "A Critical Review of the Flooding Literature," Multiphase Science and Technology (G.F. Hewitt, J.M. Delaye and N. Zuber *Eds.*), Vol. 2, Chapter 2. Hemisphere Publishing Co., N.Y., (1986).

[11] Dukler A.E., L. Smith & Chopra A.; "Flooding and Upward Film Flow in Tubes–I." Int. J. Multiphase Flow, Vol. 10, No. 5, pp. 585–597, (1984).

[12] Wongwises, S. "Experimental Investigation of Two–Phase Countercurrent Flow Limitation in a Bend Between Horizontal and Inclined Pipes," Exp. Thermal and Fluid Science, Vol. 8, pp. 245–259, (1994).

[13] Ardron K.H. & Banerjee S.; "Flooding in an Elbow Between a Vertical and a Horizontal or Near–Horizontal Pipe. Part II: Theory" Int. J. Multiphase Flow, Vol. 12, No. 4, pp. 543–558, (1986).

NOMENCLATURE

A	Cross sectional area (m^2).
D	Diameter (m).
g	Acceleration due to gravity (m/s^2).
J	Superficial velocity (m/s).
L	Length (m).
β	Orifice ratio $(= D_{orifice}/D_{tube})$.
ν	Kinematic viscosity (m^2/s).
ρ	Density (kg/m^3).

Subscripts and Superscripts

ℓ	liquid.
g	gas.
$*$	non dimensional quantity.

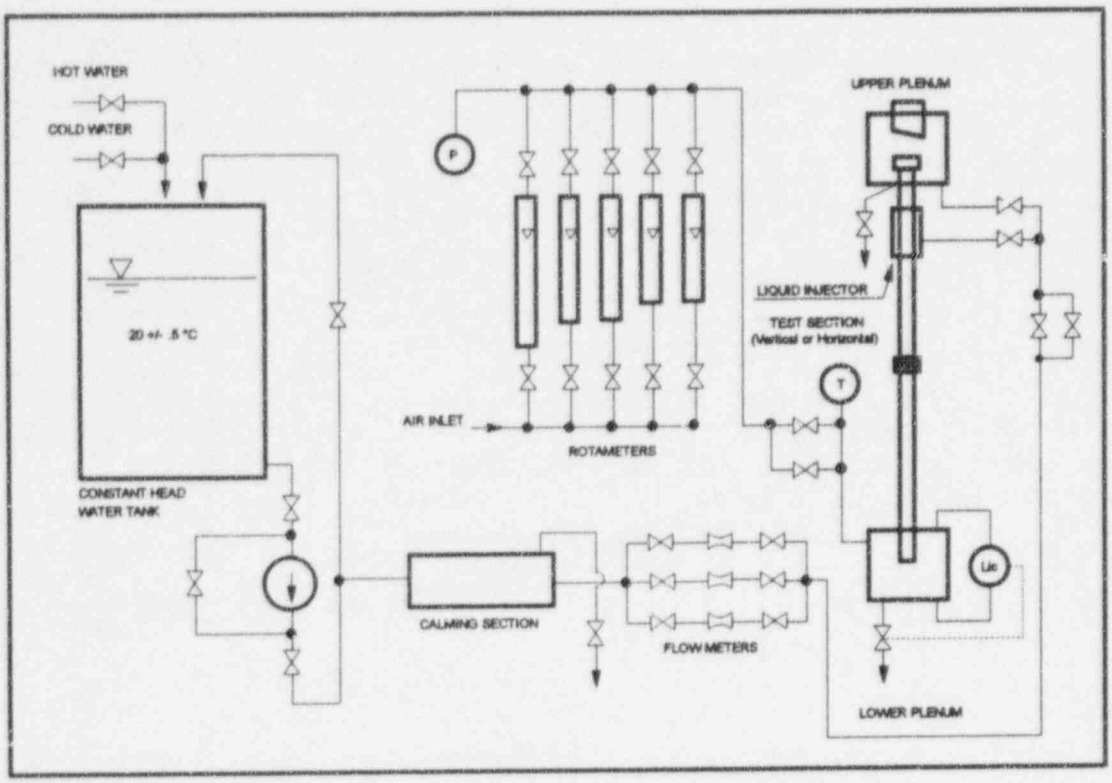

FIGURE 1. CCF Test Facility.

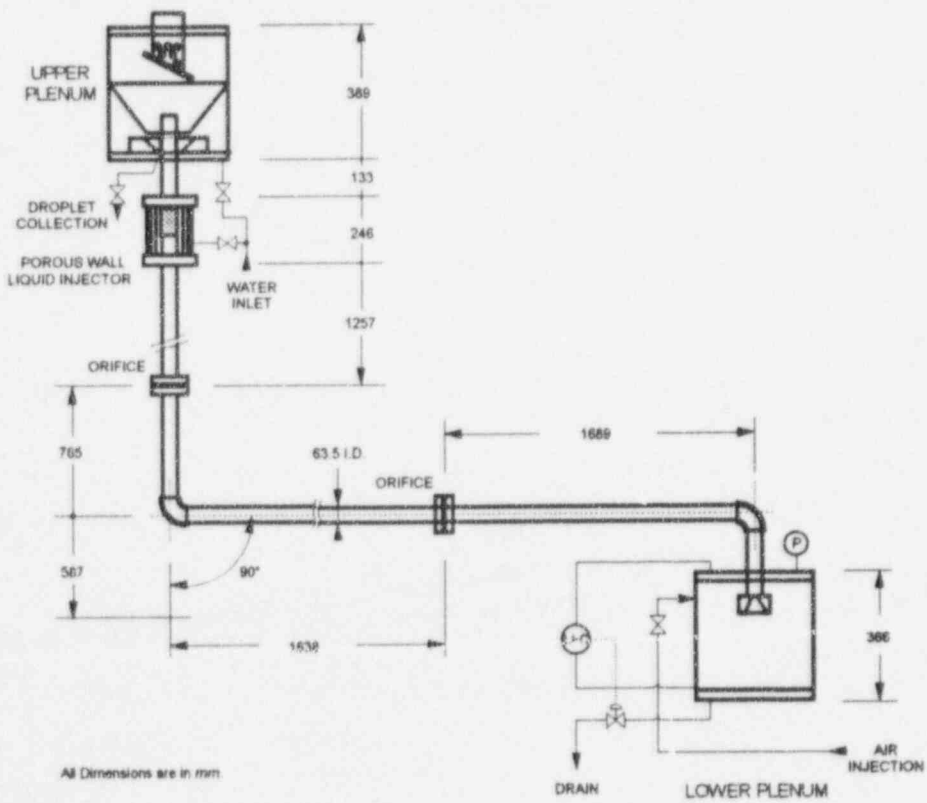

FIGURE 2. Test Section With Vertical and Horizontal Runs.

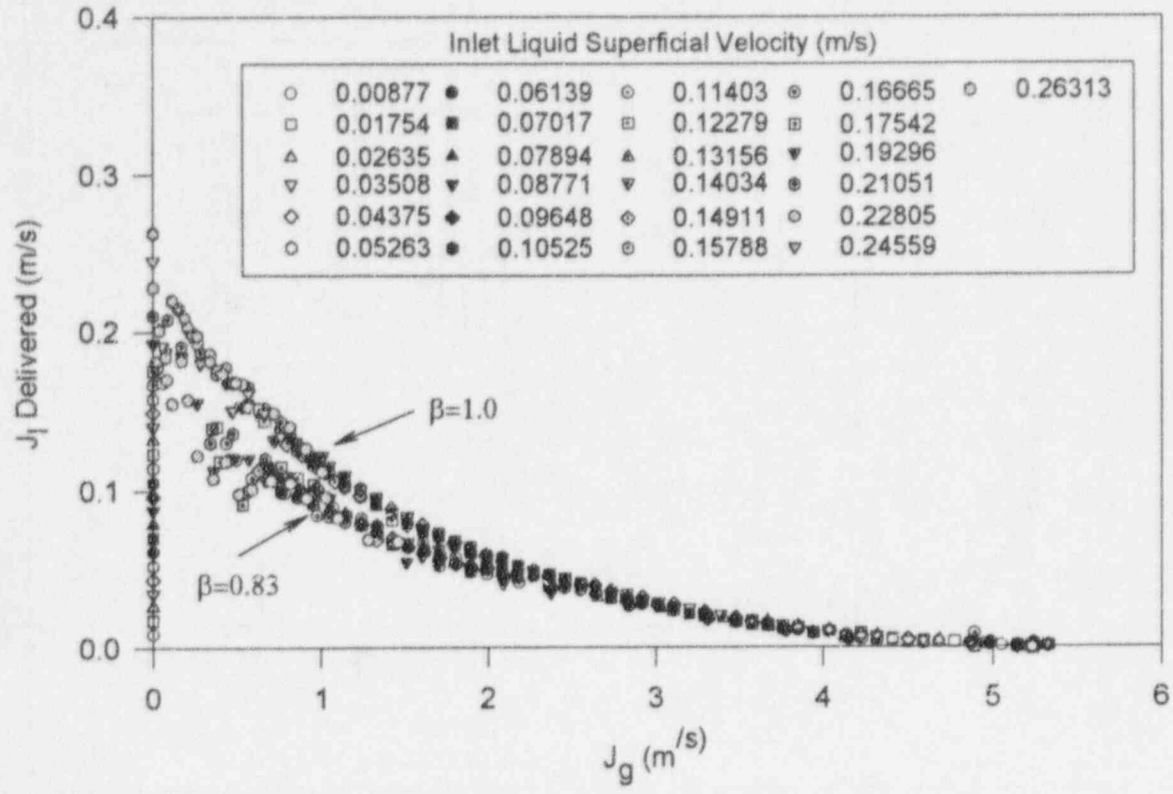

FIGURE 3a. J_ℓ Delivered v.s. J_g.

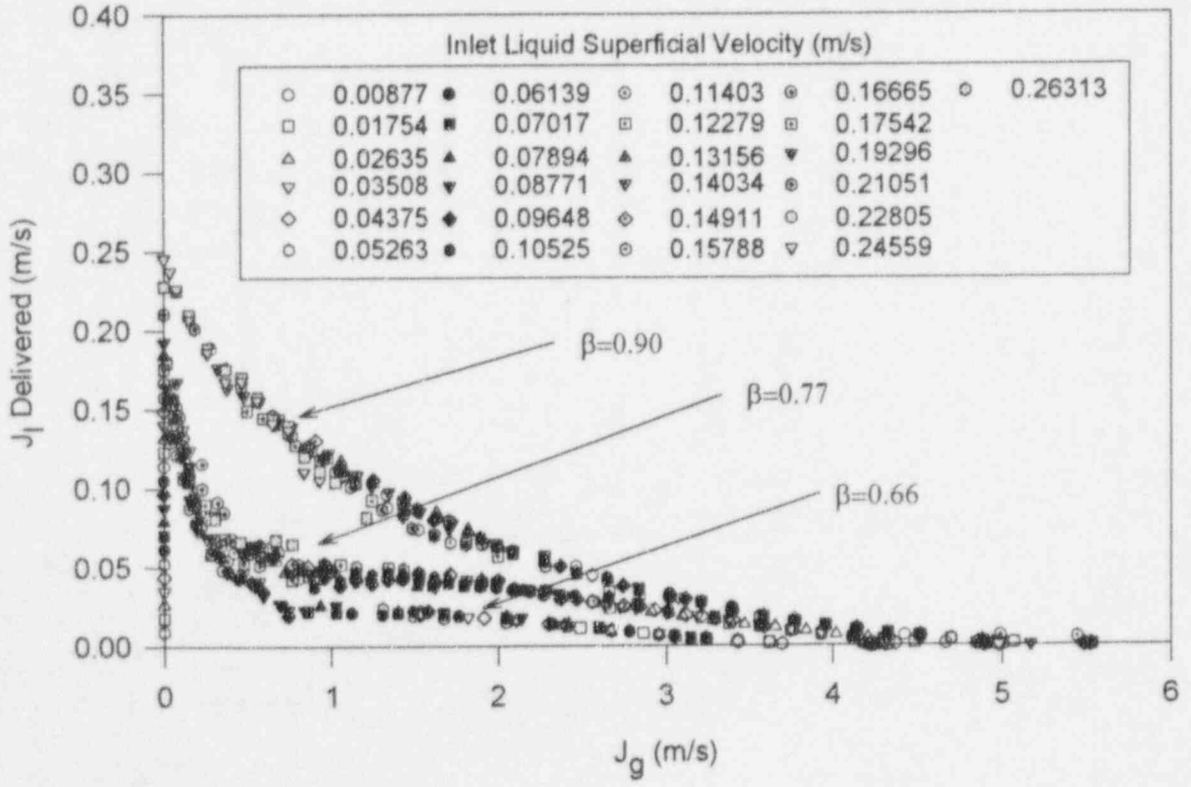

FIGURE 3b. J_ℓ Delivered v.s. J_g (Cont.).

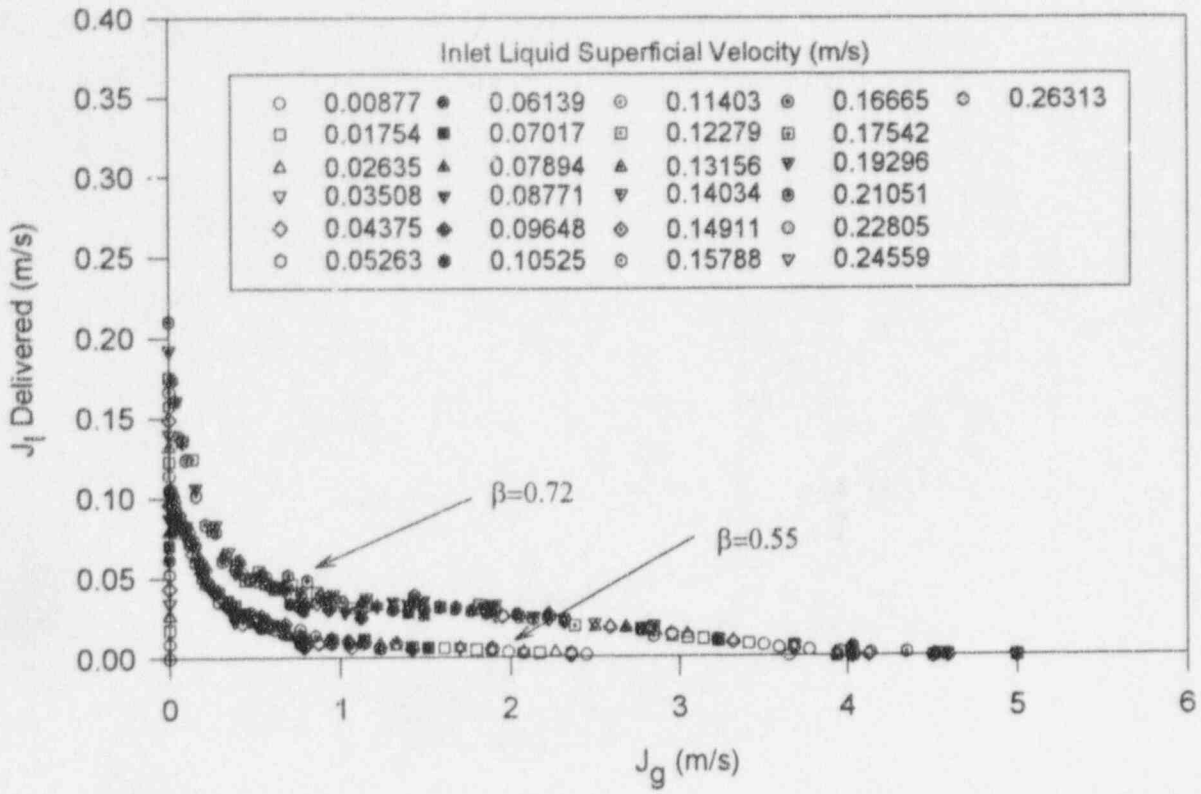

FIGURE 3c. J_ℓ Delivered v.s. J_g (Cont.).

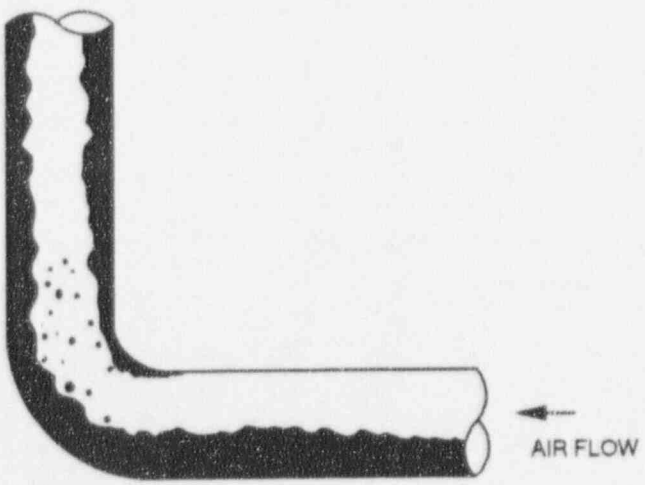

FIGURE 4. Entrainment and Deposition Above Elbow.

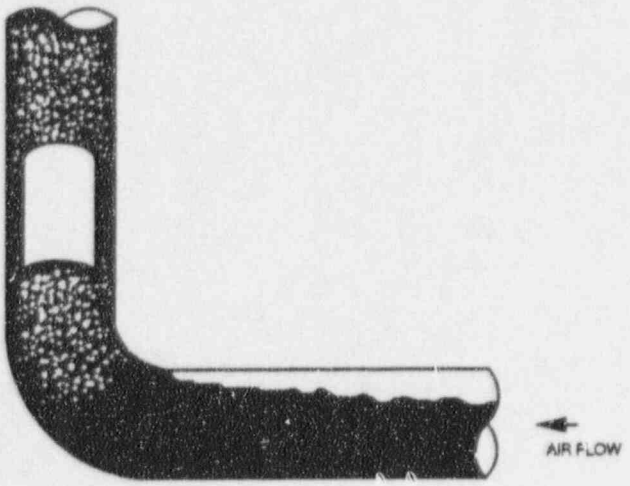

FIGURE 5. Bubble Column and Taylor Bubble in Vertical Leg.

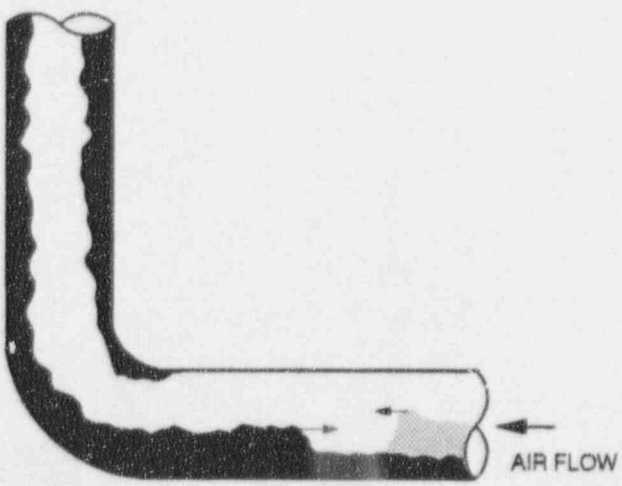

FIGURE 6a. Wave Generated by Pulsating Column and Reflected by Orifice.

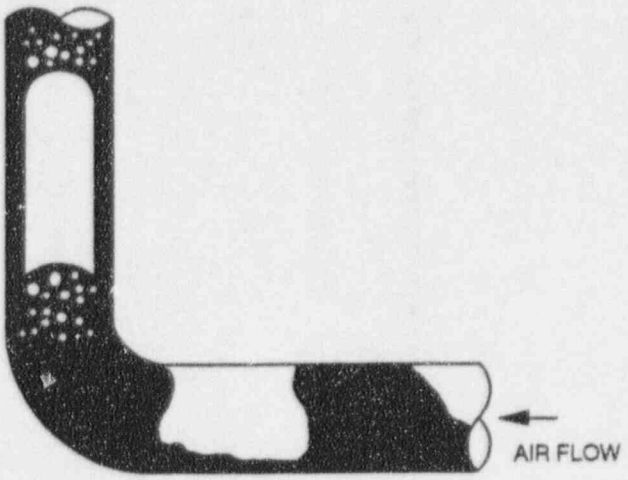

FIGURE 6b. Slug Caused by Interference of Incident and Reflected Wave.

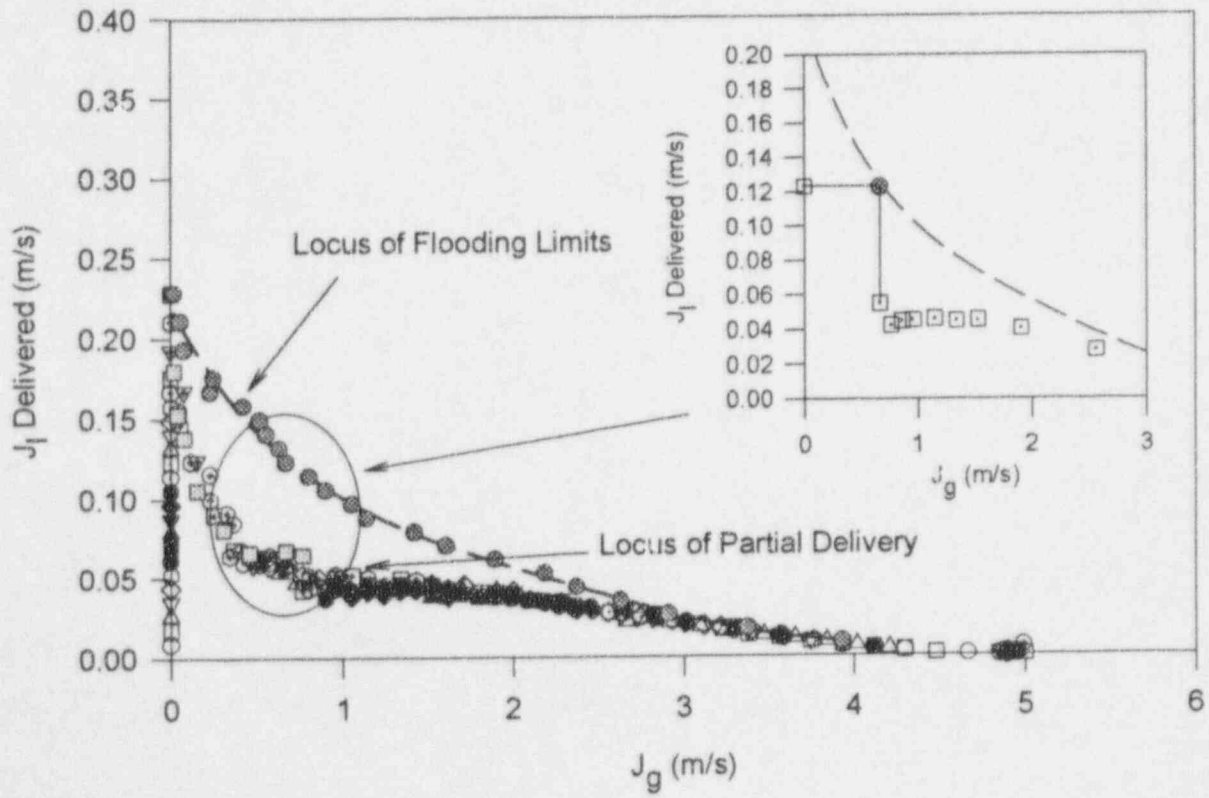

FIGURE 7. Determination of Flooding Limit.

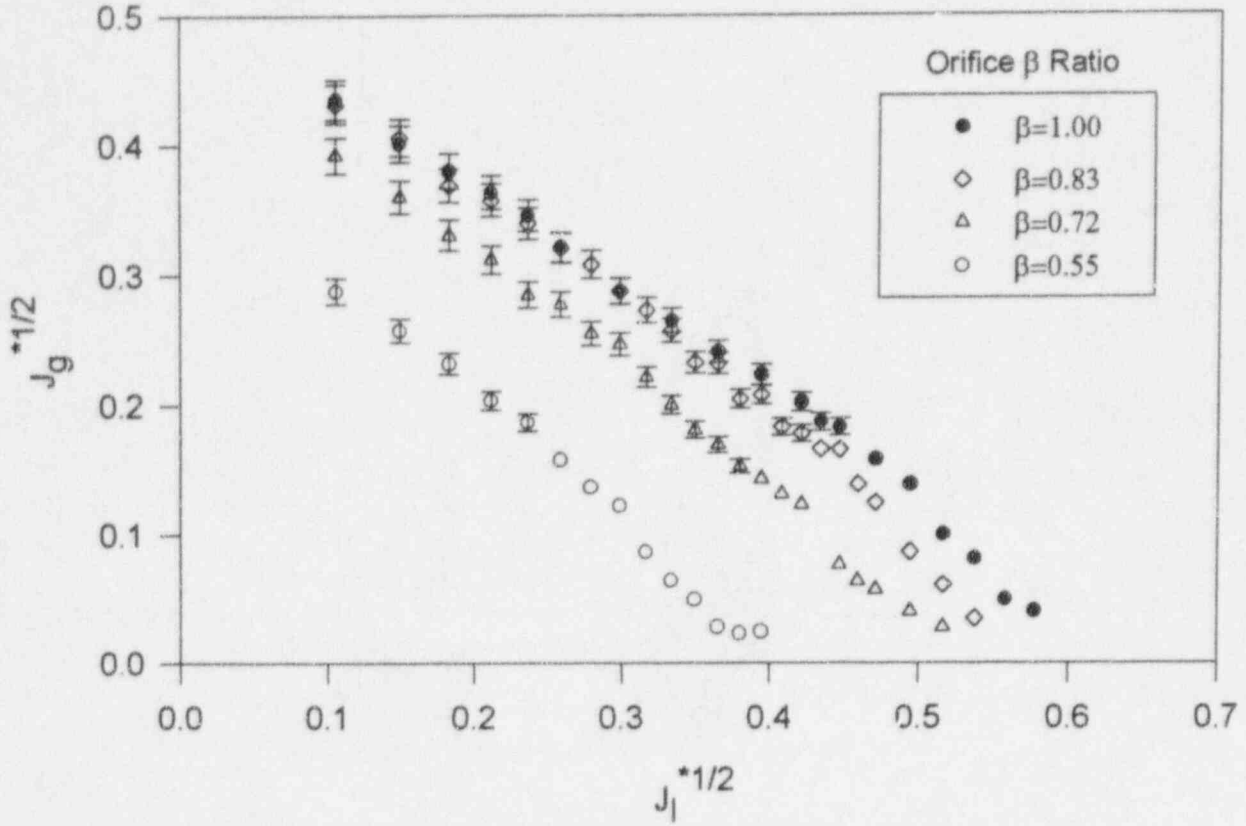

FIGURE 8a. Flooding Limits Horizontal Test Section.

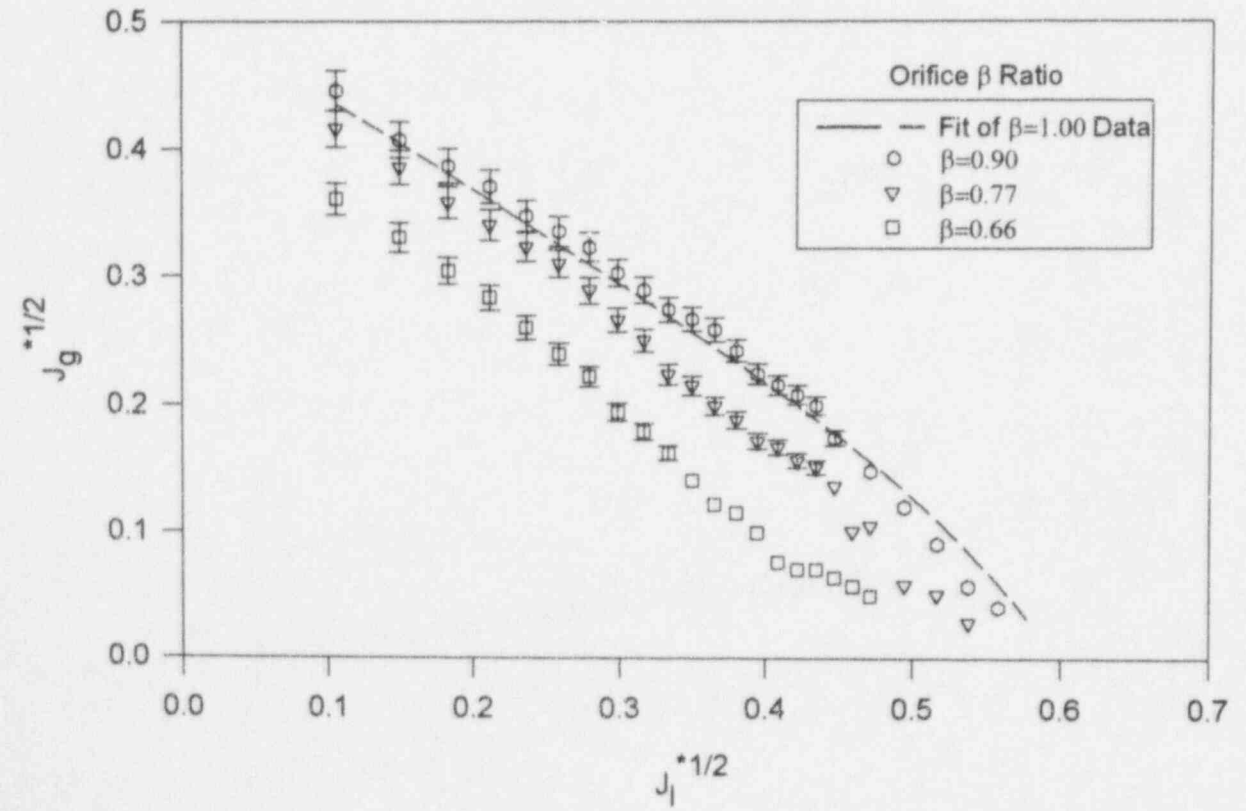

FIGURE 8b. Flooding Limits Horizontal Test Section (Cont.).

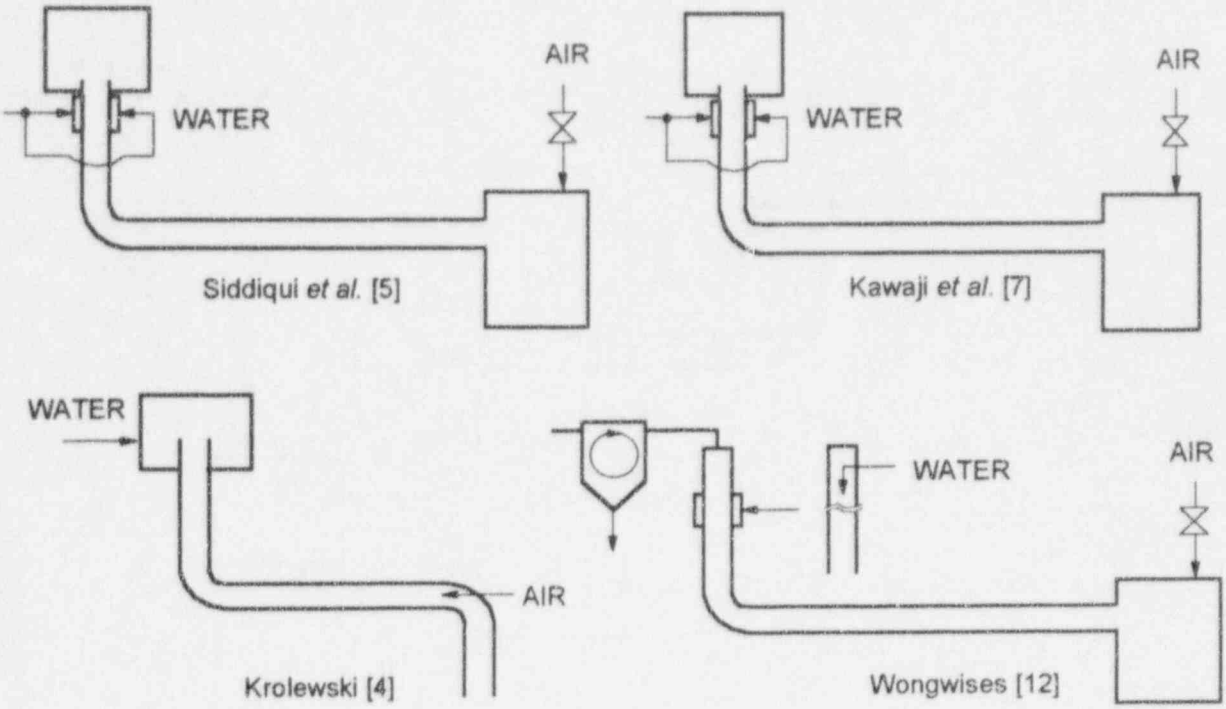

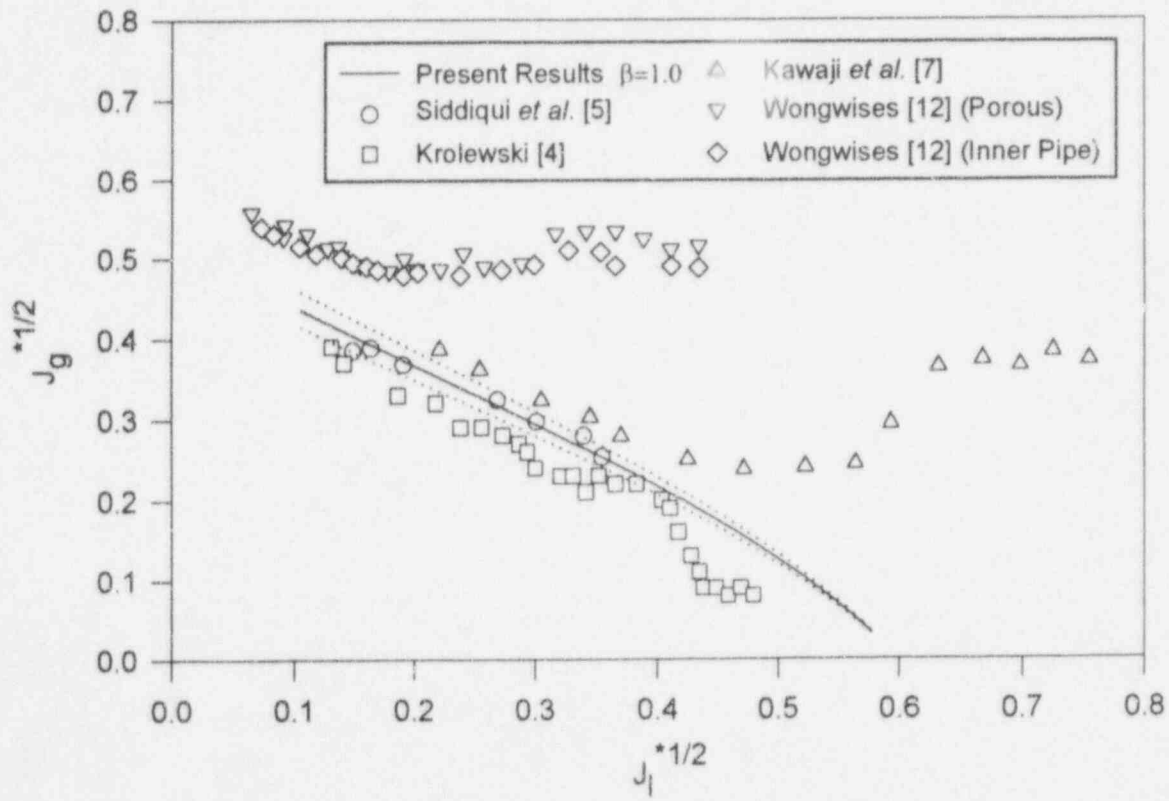

FIGURE 9. Comparison of Flooding Data with other Researchers (No Orifice).

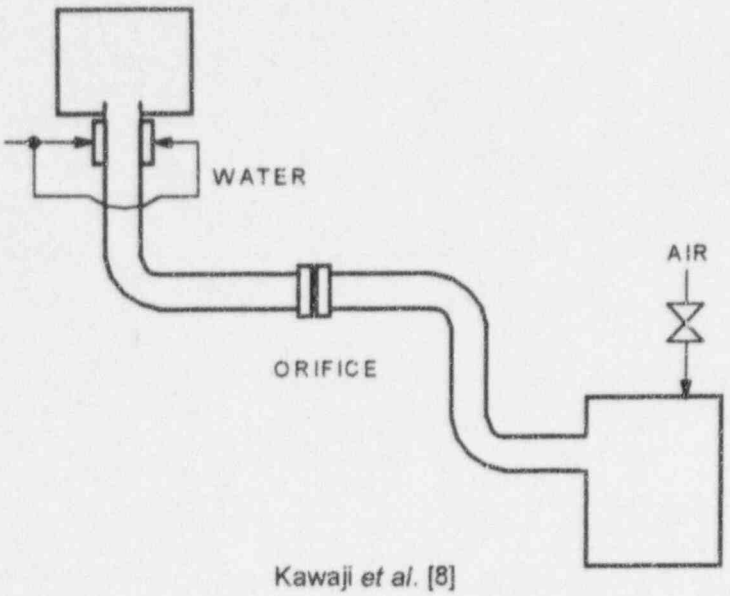

Kawaji *et al.* [8]

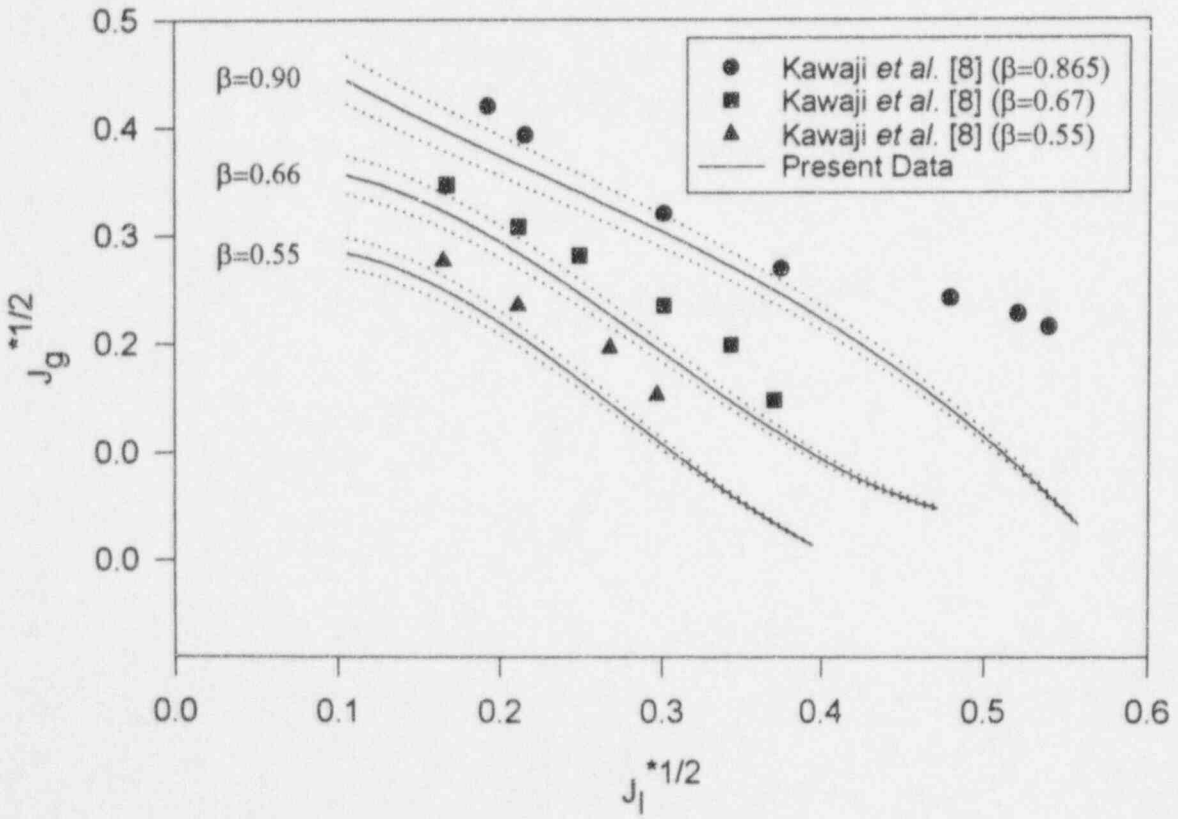

FIGURE 10. Comparison of Flooding Data with Data of Kawaji [8] (Orifice).

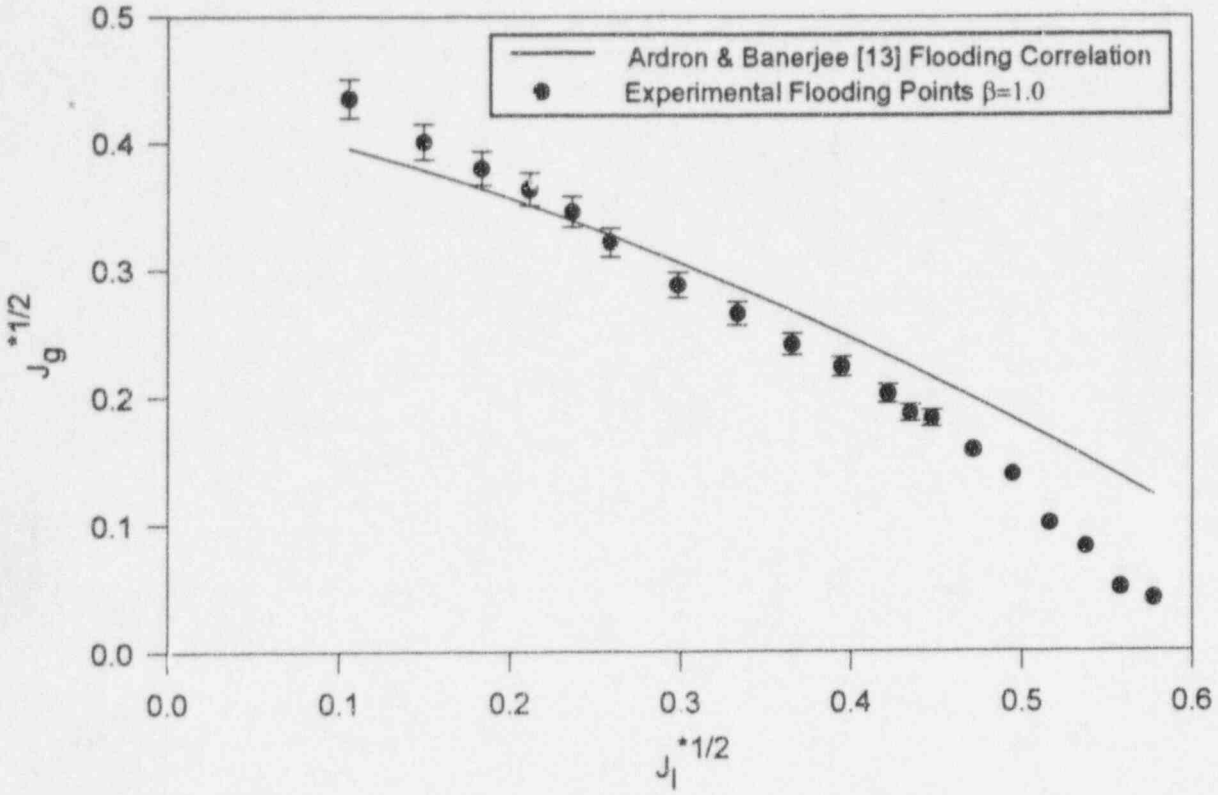

FIGURE 11. Comparison of Flooding Data with Ardron & Banerjee Correlation.

Flooding Characteristics of Gas-Liquid Two-Phase Flow in a Horizontal U Bend Pipe

T. Sakaguchi, S. Hosokawa, and Y. Fujii
Faculty of Engineering, Kobe University
1-1 Rokkodai, Nada, Kobe 657 Japan

Hisato Minagawa
Faculty of Engineering, Shiga Prefectural University,
Shiga 522 Japan

Nobuo Nakamori and Takashi Ueno
Mitsubishi Heavy Industries, Ltd.
2-1-1 Shinhama, Arai, Takasago 676 Japan

Junichiro Kodama
Koryo engineering, Co. Ltd.
Takasago 676 Japan

ABSTRACT

For next-generation nuclear reactors, hybrid safety systems which consist of active and passive safety systems have been planned. Steam generators with horizontal U bend pipelines will be used as one of the passive safety systems. It is required to clarify flow characteristics, especially the onset of flooding, in the horizontal U bend pipelines in order to examine their safety.

Flooding in vertical pipes has been studied extensively. However, there is little study on flooding in the horizontal U bend pipelines. It is supposed that the onset of flooding in the horizontal U bend pipelines is different from that in vertical pipes. On the other hand, liquid is generated due to condensation of steam in pipes of the horizontal steam generators at the loss of coolant accident because the steam generators will be used as a condenser or a cooling system of steam from the reactor. It is necessary to simulate this situation by the supply of water at the middle of horizontal pipe.

In the present paper, experiments were carried out using a horizontal U bend pipeline with a liquid supply section in the midway of pipeline. The onset of flooding in the horizontal U bend pipeline was measured. Effects of the length of horizontal pipe and the radius of U bend on the onset of flooding were discussed.

NOMENCLATURE

C	coefficient of Wallis' formula	[-]
D	inner diameter of pipeline	[m]
h_G	width of air passage	[m]
h_L	liquid height	[m]
ID	index of deviation	[%]
$\langle J_G \rangle$	gas volumetric flux	[m/s]
$\langle J_L \rangle$	liquid volumetric flux	[m/s]
J_G^*	nondimensional gas volumetric flux	[-]
J_L^*	nondimensional liquid volumetric flux	[-]
L_D	length between water supply section and U bend	[m]
L_T	total length of horizontal pipe	[m]
L_V	length between water supply section and lower tank	[m]
m	coefficient of Wallis' formula	[-]
N	total sample number	[-]
R	radius of U bend pipe	[mm]
T	time	[s]
V_G	average gas velocity	[m/s]
V_L	average liquid velocity	[m/s]
X	length from lower tank	[mm]
g	acceleration of gravity	[m/s^2]
ρ_G	gas density	[kg/m^3]
ρ_L	liquid density	[kg/m^3]
σ	standard deviation	[-]

Subscripts

cal	calculation
exp	experiments
G	gas
L	liquid

1. INTRODUCTION

A part of liquid phase flows upward when gas flow rate reaches a limit value in countercurrent gas-liquid two-phase flow in a vertical pipe. This limit is called the "onset of flooding". Understanding of the onset of flooding is required for safety evaluation of loss-of-coolant accidents (LOCAs) in nuclear reactors.

Hybrid safety systems which consist of active and passive safety systems have been planned for next-generation nuclear reactors. Steam generators using horizontal U bend pipelines will be used as one of the passive safety systems. Liquid is generated due to condensation and flows into both directions in the horizontal U bend pipeline. To evaluate safety for this type of steam generator, it is required to understand flow characteristics in a horizontal U bend pipeline, especially, limit conditions in which whole liquid phase flow into gas outlet or gas inlet. It is supposed that the limit condition is related with flow direction of liquid phase in a horizontal pipe and in a vertical part of U bend. In the other word, the limits are related with the onset of flooding in a horizontal and a vertical pipe.

Flooding in a vertical pipe[1-5] has been studied extensively because of its importance for nuclear reactors and for chemical industries. Many empirical correlations have been proposed in literature to predict the onset of flooding[1-5]. However, each correlation is limited to narrow ranges of operating conditions, fluid properties, tube geometry and entry configurations on which the correlation was constructed. Bankoff and Lee [6-7] reviewed flooding models and concluded that additional systematic work on condensing flow was recommended to investigate condensing effect. They also indicated that most models incorporated a tube diameter effect, but the effect of the tube length was not elucidated yet. These researches indicated that flooding was closely related with test section geometry and inlet geometry. Several studies[8-9] have been done to understand flooding characteristics in countercurrent flow in horizontal pipes or inclined pipes. Siddiqui and Banerjee[10] studied on flooding in a pipeline with an elbow between a horizontal and a vertical pipe. In their study, the flooding was observed in the vertical pipe part. These studies on flooding in vertical or in horizontal pipes give us fundamental knowledge on flooding in horizontal U bend pipelines. However, there are few studies using a horizontal U bend pipeline. Thus, relations of flooding characteristics among a horizontal U bend pipeline, a horizontal pipeline and a vertical pipeline are not clarified.

Flow characteristics in a U bend pipeline or a serpentine tube[11-17] have been studied. Flow pattern[11-15], pressure drop[15-16] and phase distribution[16-17] in a U bend pipeline or a serpentine tube were investigated in these studies. Usui et al.[12], and Farukhi and Parker [13] described flooding in U bend pipeline. The flows in these studies were cocurrent two-phase flows. Therefore, they referred to a reverse flow in U bend as "flooding". Liquids were supplied compulsively from end of pipes in these studies. However, liquid is generated in a horizontal pipe of cooling system due to condensation of steam in pipes. It is supposed that flooding characteristics in this type of flow loop were different from that in other cooling systems. For understanding of flooding characteristics in our cooling system, it is required to understand the onset of flooding in the horizontal U bend pipeline in which liquid is supplied at the midway of pipeline.

The purpose of the present study is to investigate the onset of flooding in the horizontal U bend pipeline which has water supply section at the midway of pipeline. Effects of the length of the horizontal pipe and the radius of the U bend on the onset of flooding were elucidated. The present experimental results are compared with previous formulas and discussed.

2. EXPERIMENTAL APPARATUS

Schematic diagram of experimental apparatus is shown in Fig. 1. Main parts of a flow loop are an air supply section with a lower tank (LT is an abbreviation for it), a water supply section (WS) and a test section. The test section is formed by a lower and an upper horizontal pipe (LH and UH, respectively). LH part is installed just under UH part. They are connected by a U bend (U). The test section is positioned in a vertical plane. The test section is made of acrylic resin in order to observe flow pattern in the test section. The inner diameter (D) of the test section is 17.3 mm. Liquid was generated due to condensation of steam in pipes in cooling systems. Water is supplied at the middle part of horizontal pipe in order to simulate the condensation. The length (L_D) between WS and U was changed from 1.27m to 6.27m. The length (L_U) between WS and LT was also changed from 0.83m to 5.83m. In order to understand effects of the radius of U bend, experiments were done using three types of the U bend, whose radius (R) was 94.5 mm, 300 mm or 600 mm.

Air and water under room temperature and atmospheric pressure were used for gas phase and liquid phase, respectively. A Mohno pump (HEISIN-SOBI, 2NE20PA) was used to keep liquid flow rate constant. Its flow rate was measured by float type flow meters (NIHON FLOW SELL, ST-4). Furthermore, the liquid flow rate

was confirmed by the measurement using graduated cylinders. A cooler was used to keep the temperature of the water constant. Filters were also used to remove dusts in the water. A porous pipe (pore diameter: 100μm, porosity: 36%, polymethyl-meta acrylate) was used at the center of LH to supply water in the midway of the lower horizontal pipe. The water supply section is shown in Fig. 2. This porous pipe has same inner diameter with the test section and its length is 50 mm. The air was supplied by a compressor (HITACHI, 7.50U-7V6, Pressure: 6.8×10^5 Pa). Its flow rate was controlled and measured by critical flow nozzles and pressure gauges. The air was supplied to the test section through LT. The air passed through the test section and flowed out from the end of UH. A cooler (HITACHI, AC-90F) was used to keep temperature of air constant, and a filter was also used to remove dusts in the air.

Three parameters of the geometry of test section, which are the length between the water supply section and the U bend (L_D: 1.27, 2.27, 4.27, 6.27 m), the length between the water supply section and the lower tank (L_U: 0.83, 1.83, 3.83, 5.83 m) and the radius of U bend (R: 94.5, 300, 600 mm), were changed to understand the effects of the geometry on the flooding and the carry-up characteristics. Experimental range of liquid volumetric flux ($<J_L>$) was changed from 0.00591 m/s to 0.414 m/s and the gas volumetric flux ($<J_G>$) was from 0.113 m/s to 2.36 m/s in the present experiments. The flow behavior was visually observed and recorded using video cameras.

3. DEFINITIONS OF FLOODING AND CARRY-UP

Flooding in a horizontal U bend pipeline is different from that in a vertical pipe. In a countercurrent gas-liquid two-phase flow in a vertical pipeline, a part of liquid phase flows upward when gas flow rate reaches a limit value. This flow reversal is referred as "flooding". In the horizontal U bend pipeline, the water supplied from the WS flows to both directions even under the condition of $<J_G>=0$. This condition corresponds to the flooding in the vertical pipe. This condition is not called "flooding" in the present study. In the present paper, the condition, under which a part of the liquid phase is carried into the UH part, is referred as "flooding".

When the gas volumetric flux is zero, the water flows into both upstream and downstream directions in the LH part (LH_U and LH_D are abbreviations for them, respectably). The liquid height gradually increases to a certain value. Part of the water flows into the LT. Wave was not observed on the gas-liquid interface under this condition. The gas-liquid interface is sloped in the LH_U part. The liquid height, however, is almost constant in the LH_D part. With increasing gas flow rate, the liquid height in the LH_D part becomes higher due to a shear force on the gas-liquid interface. The flow in the LH_U part is countercurrent gas-liquid stratified flow under this condition. There is a liquid film in LH_D part, (we call it stratiform stagnation). A circulation of liquid in the liquid film occurs due to the shear force on the gas-liquid interface. There is no liquid phase in the UH part and the U part.

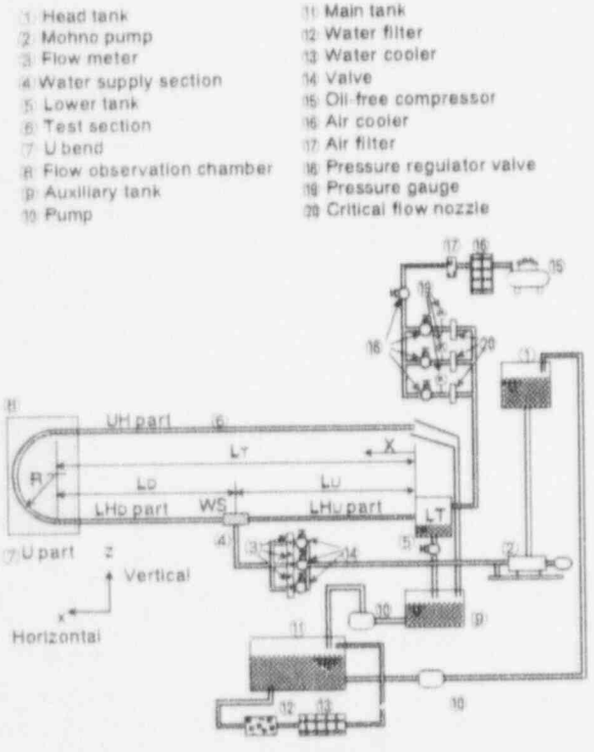

Fig. 1 Schematic diagram of experimental apparatus.

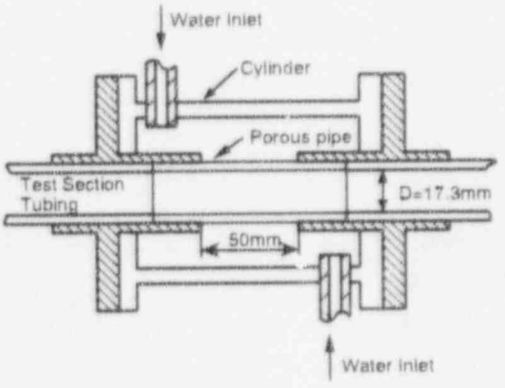

Fig. 2 Water supply section.

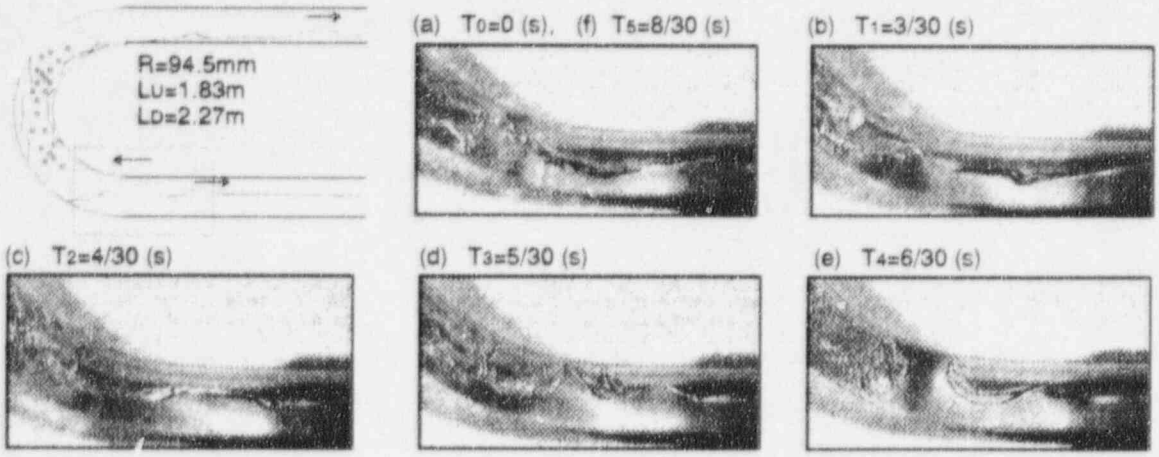

Fig.3 Slugging.

The liquid height in the LH part becomes higher with further increasing gas flow rate. Part of liquid surface grows its height and a triangular wave appears on the gas-liquid interface at U inlet. This wave instantly reaches to the upper wall and generates a short liquid slug. The short liquid slug is pushed up to the upper region of U part by the air. This is an onset of liquid slug. When this short liquid slug climbs U part, the liquid slug is broken up (Fig. 3 (a)). The liquid phase flows back to U inlet (Fig. 3 (b)). The onset of "flooding" occurs with this onset of liquid slug in the region of present experimental conditions. Namely, a part of liquid phase caused by the breakup of liquid slug reaches into the UH part under every condition of present experiments. This backward flow causes the rising of liquid height and the waves (Fig. 3 (c)). One of crests among waves reaches to the upper wall (Fig. 3 (d)). A short liquid slug is generated (Fig. 3(e)). The flow situation returns to the condition shown in Fig. 3(a), namely Fig. 3(f). This process of flow pattern was cyclically repeated as shown in Fig. 3. This flow pattern is called a "slugging". The liquid slug is not observed in UH part because of the breakdown of the liquid slug in the U bend part. The fluctuation of gas-liquid interface was observed in the U inlet as mentioned above. This fluctuation induces waves, which travel to the WS part and disappear soon. The liquid slug was not observed in LH_D part, because the liquid height is low in the LH part. The gas-liquid interface is smooth and slopes gently in the LH_U part.

The slugging in U bend part becomes violently under the condition of higher gas volumetric flux. The liquid flow rate carried up to the UH part increases due to the increase of the shear force on the gas-liquid interface. The liquid slugs break up in the midway of U part. The wavy flow is observed in the UH part. Namely, the liquid phase does not flow into the LT in the high gas flow rate. Whole of liquid phase flows to the exit of the test section passing through the U part and the UH part. This limit condition is referred as "carry-up".

4. EXPERIMENTAL RESULTS

The flooding and the carry-up limits were measured in the present study. In this section, the effects of the three parameters of test section geometry, L_D, L_U and R, on the flooding and the carry-up limits are discussed.

4.1 Effects of length between water supply section and U bend on flooding and carry-up limits

The length (L_D) between the water supply section and the U bend was changed in order to understand its effects on the flooding and the carry-up limits. The experimental results were shown in Figs. 4 and 5. Lines are drawn based on the least square method. The standard deviations (σ) and the index of deviations (ID) of the experimental data from these lines are shown in each figure. ID is defined by next formula.

$$ID=\sqrt{\frac{1}{N}\sum\left(\frac{J^{*}_{G\,cal}-J^{*}_{G\,exp}}{J^{*}_{G\,exp}}\right)^{2}}\times 100 \qquad (1)$$

J_G^* and J_L^* are defined by equations (3) and (4) in next section. The gas volumetric flux at the onset of flooding decreases with increasing value of L_D. When J_G^* is zero, J_L^* is 0.42 in different value of L_D. This indicates that the flooding occurs even in J_G^* is zero when J_L^* is larger than this limit value, and that this limit value does not change with the value of L_D. The liquid heights along the lower horizontal pipe just before the onset of flooding were shown in Fig. 6. The liquid heights near the U bend inlet are almost the same value except the case of L_D=1.27 m in which the conductance probe was installed not near the U bend inlet. The gradient of liquid surface increases with the value of $\langle J_G \rangle$ and decreasing the value of L_D. This means that the gradient of gas-liquid interface is closely related with shear force on it.

On the other hand, the carry-up limits little change in different value of L_D. The effect of the length between the water supply section and the U bend on the carry-up limit is little. This is explained as follows; the carry-up limit is deeply related with the liquid height at the inlet of test section, which is controlled by the liquid flow condition between the water supply section and the lower tank. The liquid heights at the inlet of test section take almost the same value in the condition of the same liquid flow rate and the same length L_U as shown in Fig. 6. This means that the carry-up limit is controlled not by the length L_D but by the liquid flow rate and the length L_U.

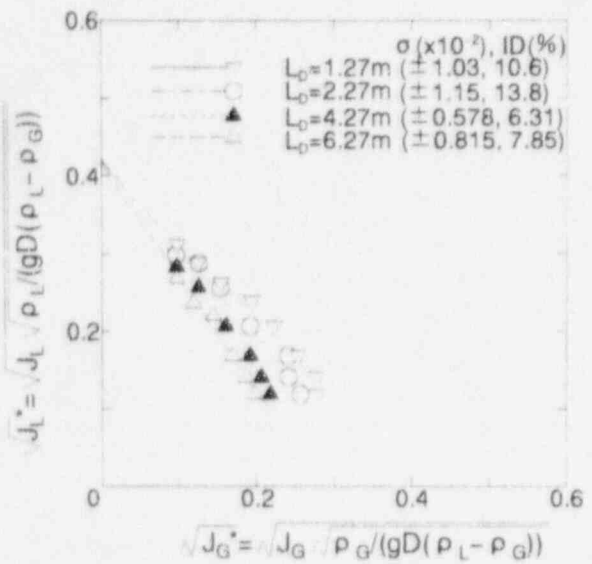

Fig. 4 Effects of length of L_D on flooding limits. (R=300 mm, L_U=1.83 m).

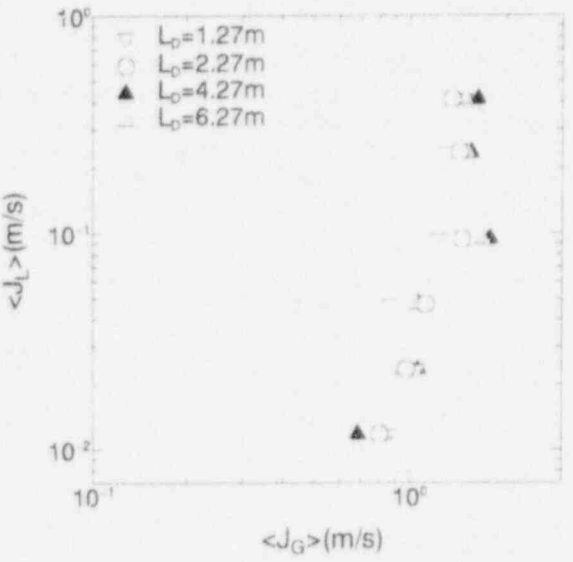

Fig. 5 Effects of length of L_D on carry-up limits. (R=300 mm, L_U=1.83 m).

	Position of conductance probe X(mm)							
▽ L_D=1.27m	250	1500	1250	1500	2360	2760		
○ L_D=2.27m	250	750	1000	1500	2500	3360	3760	
▲ L_D=4.27m	250	750	1250	1500	2500	3500	4500	5760
△ L_D=6.27m	250	750	1250	1500	2500	3500	6500	7760

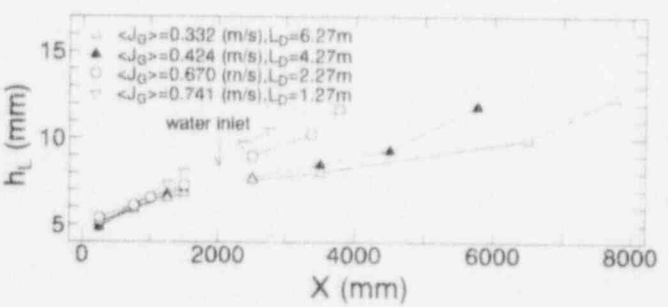

Fig. 6 Effects of length of L_D on liquid height just before flooding. ($\langle J_L \rangle$=0.0118 m/s, R=300 mm, L_U=1.83m).

4.2 Effects of length between water supply section and lower tank on flooding and carry-up limits

The flooding and the carry-up limits in the different length (L_U) between the water inlet and the lower tank were shown in Figs. 7 and 8, respectively. In the case of the larger value of L_U, flooding occurs in the lower both volumetric fluxes. The carry-up occurs in the lower gas volumetric flux with increasing the value of L_U. The liquid heights just before flooding were measured and shown in Fig. 9. The liquid height near the U bend inlet is almost the same except the case of the smaller value of L_U. The gradients of gas-liquid interface are slightly decrease with increasing the value of L_U. The shape and the slope of liquid surface in the region between the water supply section and the U bend also slightly decrease with increasing the value of L_U.

For the carry-up limits, the limit lines shift to the lower gas flow rate with increasing value of L_U. The water between the water supply section and the lower tank was pushed to the water supply section by the gas flow under the condition of the carry-up. The surface area of gas-liquid interface between the water supply section and the lower tank is closely related with the total shear force which draws the water to the water supply section. This area increases with L_U, so the total shear force becomes large. When L_U is large, the carry-up occurs in the condition of low gas flow rate. The carry-up limits are controlled by the length(L_U) between the water supply section and the lower tank.

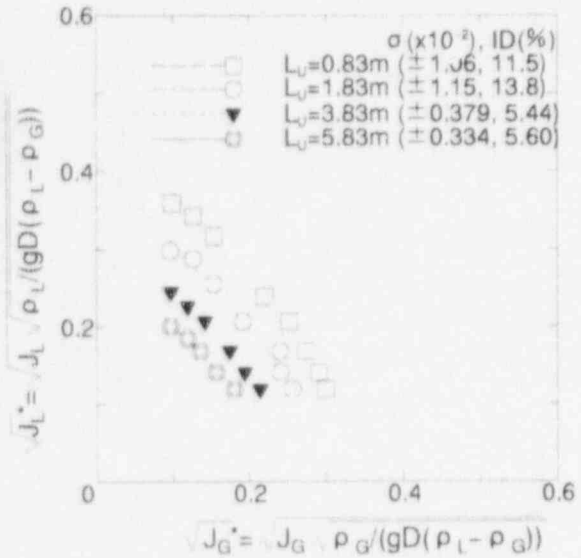

Fig. 7 Effects of length of L_U on flooding limits. (R=300 mm, L_D=2.27 m).

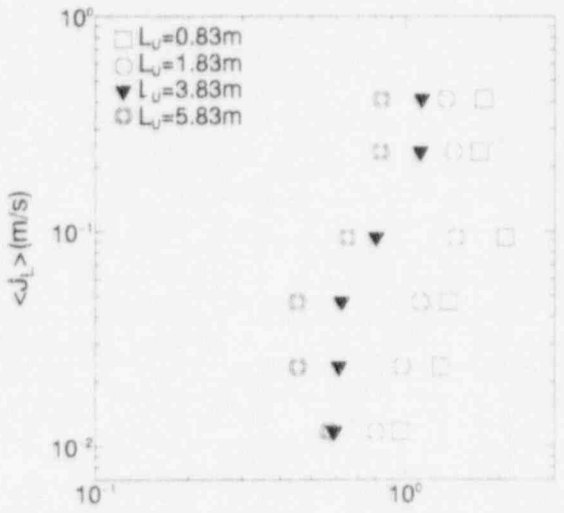

Fig. 8 Effects of length of L_U on carry-up limits. (R=300 mm, L_D=2.27 m).

	Position of conductance probe X(mm)							
Lu=0.83m	250	500	1500	2000	2500			
Lu=1.83m	250	750	1000	1500	2500	3360	3760	
Lu=3.83m	250	750	1250	1500	2160	3160	4500	5760
Lu=5.83m	250	750	1250	1500	2160	3160	6500	7760

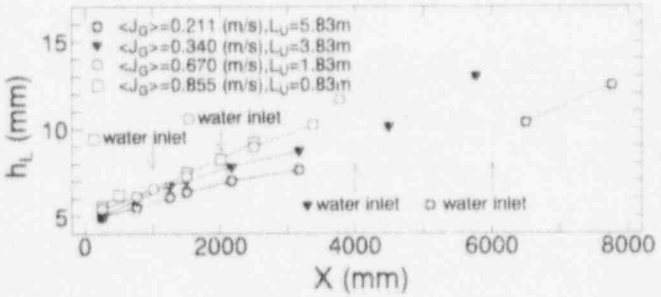

Fig. 9 Effects of length of L_U on liquid height just before flooding. ($<J_L>$=0.0118 m/s, R=300 mm, L_D=2.27m).

4.3 Effects of radius of U bend on flooding and carry-up limits

The flooding and the carry-up limits in the different radius of the U bend were shown in Figs. 10 and 11, respectively. The flooding limits do not change in different radius. This indicates that the flooding limit is little related with the radius of U bend in the present experimental conditions. The liquid heights little change in different radius of U bend as shown in Fig. 12. These results are different from Siddiqui's experimental results[10] using L bend pipes. This suggests that the flooding in the U bend pipeline with smaller value of R do not depend on the flow situation in the U bend part but depend on the flow situation near the U bend inlet in the horizontal pipe.

The carry-up limits little change in different value of radius under the condition of higher liquid volumetric flux. However, the carry up limits shift to the lower gas volumetric flux with increasing value of radius at the lower liquid volumetric flux. The flow pattern in this condition is slugging when the radius of U bend is 94.5 mm [11]. However, the flow patterns are slugging and slug flow in the case of R=300 and 600 mm.

5. Discussions

The present flooding data are compared with results of the previous studies and discussed in this section. At first, the present results are compared with Wallis' formula in a vertical pipe. Next, the onset of liquid slug is discussed and compared with Mishima-Ishii's formula since the flooding is always observed when the slugging initiates at the inlet of U bend.

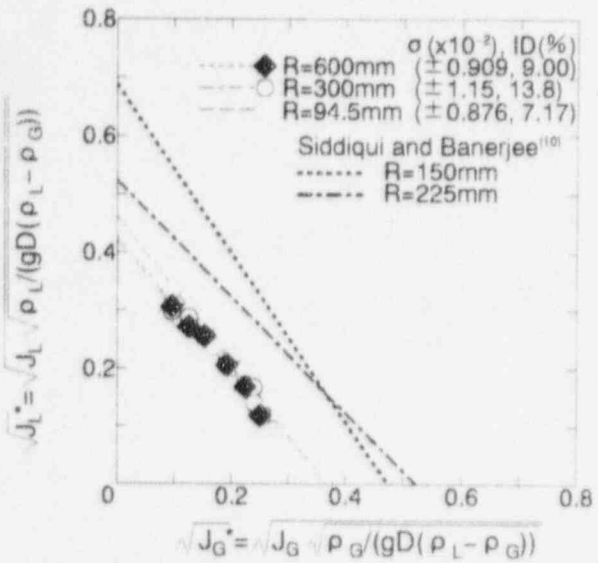

Fig. 10 Effects of radius of U bend on flooding limits. (L_U=1.83 m, L_D=2.27 m).

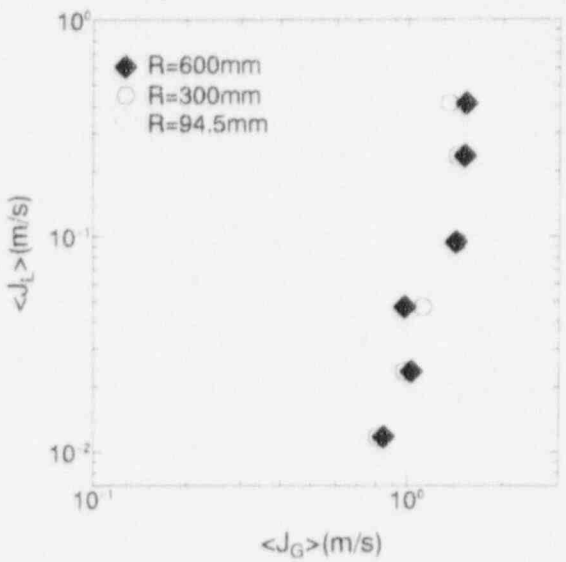

Fig. 11 Effects of radius of U bend on carry-up limits. (L_U=1.83 m, L_D=2.27 m).

	Position of conductance probe X(mm)								
R=94.5mm	250	500	750	1000	1250	1500	2500	3000	3500
R=300mm	250	750	1000	1500	2500	3360	3760		
R=600mm	250	750	1250	1500	2500	3000	3500		

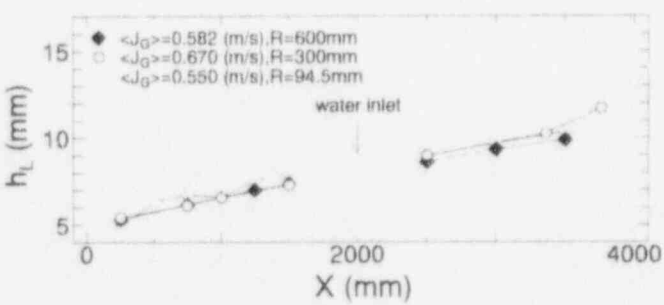

Fig. 12 Effects of radius of U bend on liquid height just before flooding. ($<J_L>$=0.0118 m/s, L_U=1.83 m, L_D=2.27 m).

5.1 Comparison with flooding limit in a vertical pipe

The results of flooding limit compared with those in a vertical pipe are shown in Fig. 13. The flooding limit in a vertical pipe was calculated using following formula proposed by Wallis[1].

$$\sqrt{J_G^*} + m\sqrt{J_L^*} = C \qquad (2)$$

where

$$J_L^* = J_L \sqrt{\frac{\rho_L}{gD(\rho_L - \rho_G)}} \qquad (3)$$

$$J_G^* = J_G \sqrt{\frac{\rho_G}{gD(\rho_L - \rho_G)}} \qquad (4)$$

C is a constant which is related with the conditions of the inlet and the outlet of test section. The flooding limit for a vertical pipe in Fig. 13 was calculated by C=0.88. The other constant m is a nondimensional constant due to the pipe geometry. This value is 1 except the case using high viscosity fluid in the vertical circular pipe.

It is assumed that there is a liner correlation between J_G^* and J_L^* in the present results. The Wallis' formula is useful in this case. The flooding in the horizontal U bend pipeline occurs in the lower flow rates than those in the vertical pipe. The two constants (m, C) in the Wallis' formula were derived from the present data. They are shown in Figs. 14 and 15 as functions of L_D/L_T (= 1 - L_U/L_T) and R/L_T, respectively. There are liner correlations between m and L_D/L_T and between C and L_D/L_T. The value of m decreases with increasing values of L_D/L_T. When the value of L_U is constant, the value of C also decreases with increasing value of L_D/L_T. However, the value of C increase with the value of L_U/L_T when the value of L_D is constant. The values of C and m little change in different value of R/L_T. Then, the correlations between m, C, L_D/L_T and L_U/L_T were expressed by equations (5) and (6).

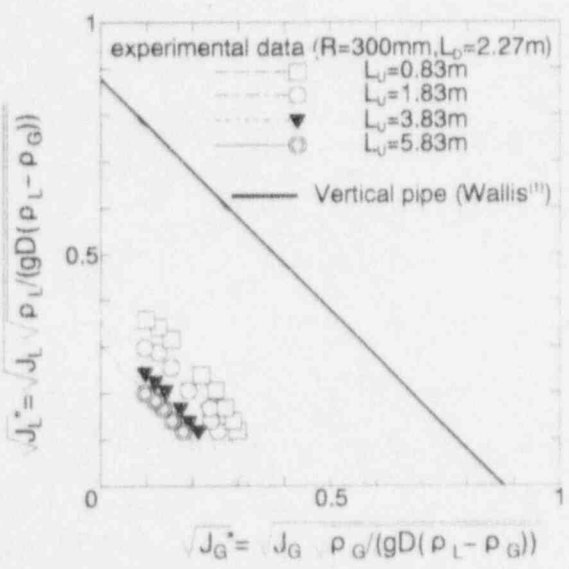

Fig. 13 Flooding limits in a U bend pipe and a vertical pipe.

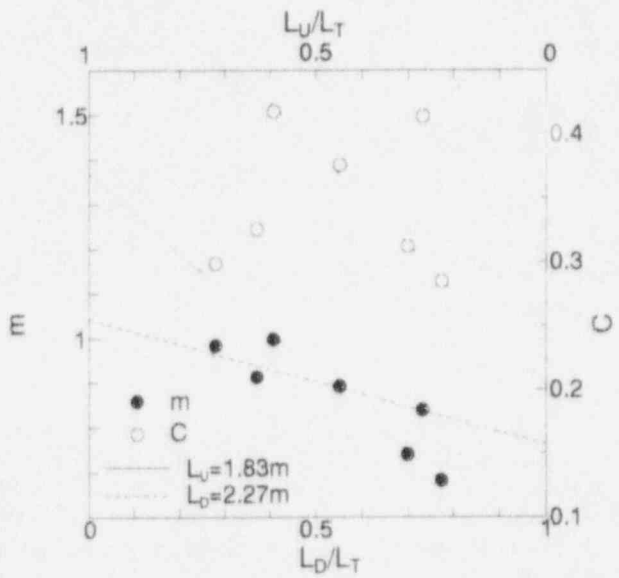

Fig. 14 Effects of L_D/L_T on the constants m and C. (R=300 mm).

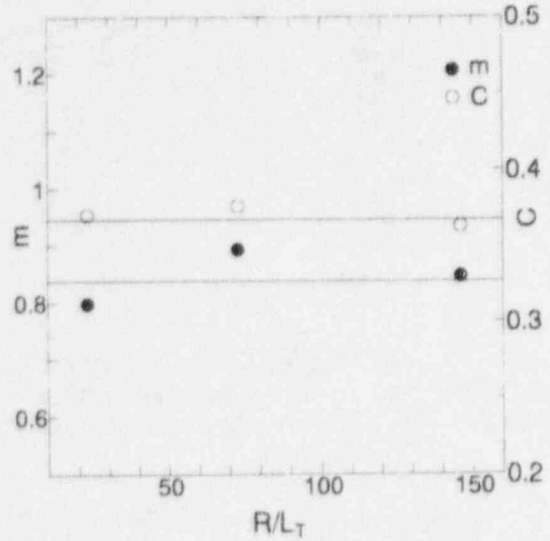

Fig. 15 Effects of radius of U bend on the constants m and C. (L_U=1.83 m, L_D=2.27 m).

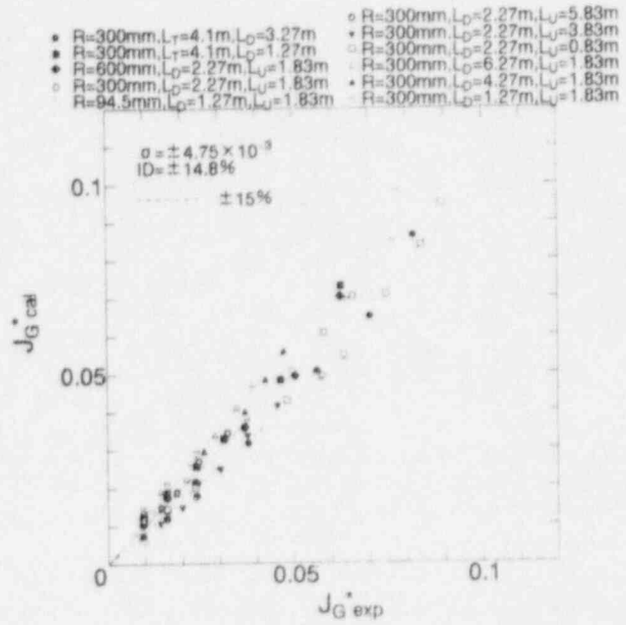

Fig. 16 Calculated results compared with experimental data.

$$C = -0.371\frac{L_D}{L_T} + \frac{84.4}{\frac{L_U}{D}+136} + 0.227 \qquad (5)$$

$$m = -0.888\frac{L_D}{L_T} + \frac{39.9}{\frac{L_U}{D}+59.5} + 1.12 \qquad (6)$$

The coefficients were derived from the present data. These applicable ranges are limited in the present experimental condition. The values of J_G^* calculated from equations (2), (5) and (6) are compared with the present results in Fig. 16. The standard deviation between the calculated value and the present results is about ± 15%. This is mainly caused by the assumption that the experimental results of J_L^* and J_G^* is expressed by a linear correlation

5.2 Comparison of onset of liquid slug in a horizontal pipe

A liquid slug is generated at the U inlet in the horizontal U bend pipeline. This liquid slug climbs up the U part, and the liquid phase flows into the UH part. This is the process of "flooding". The flooding is always observed when a liquid slug is generated at the U inlet in the present experiment. Then, the flooding limits in the horizontal U bend pipeline are compared with the onset of liquid slug in a horizontal pipe.

Many studies have been carried out on the onset of liquid slug. Mishima and Ishii [19] supposed that a wave called "most dangerous wave" due to Kelvin-Helmholtz instability grows into a liquid slug. They derived theoretically the criterion of slug formation using wavelength and proposed the following formula.

$$V_G - V_L \geq 0.487\sqrt{\frac{gh_G\rho_L}{\rho_G}} \qquad (7)$$

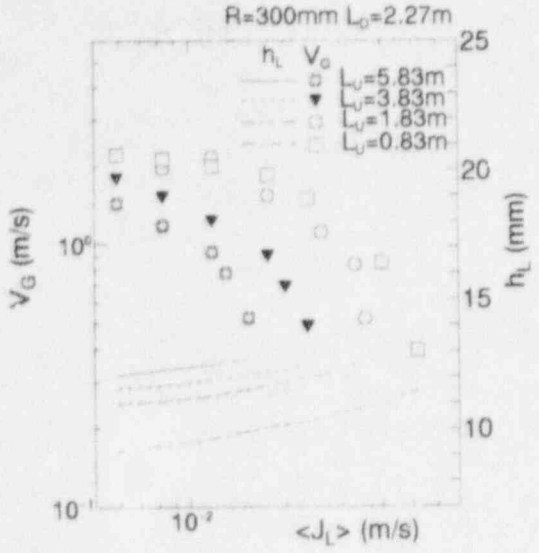

Fig. 17 Comparison of average air velocity and liquid height. (correspond to Fig. 7).

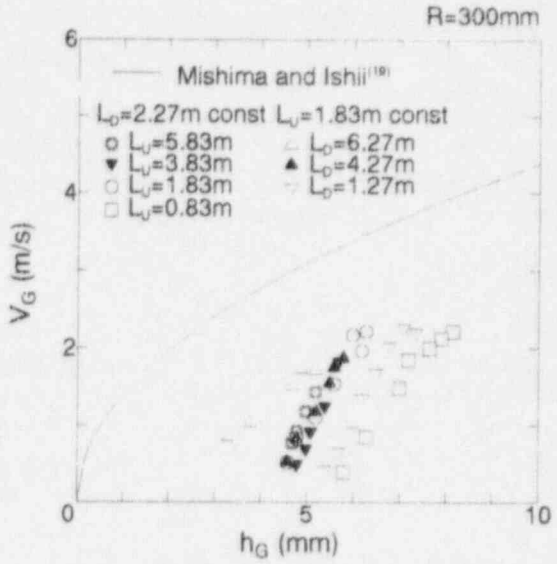

Fig. 18 Comparison of experimental data to Mishima and Ishii's theory. (Effect of length of L_U and L_D).

Equation (7) shows a relation between the average gas velocity (V_G), the average liquid velocity (V_L) and the air depth (h_G) at the onset of liquid slug. Figure 17 shows the liquid height (h_L) and the average gas velocity just before the flooding near the U inlet. The liquid height becomes low and the gas average velocity at the onset of flooding becomes high with decreasing value of $<J_L>$. The flooding occurs also in the lower value of V_G when the value of L_U is large.

Figures 18 and 19 show the comparison of present experimental data and the value calculated by equation (7). The liquid does not flow before the flooding in the LH_D part in the present study. So we assumed V_L=0. The relation between the V_G and the h_G of the experimental results is similar to that by equation (7). That is, the liquid slug is generated at the higher value of V_G when the height of gas depth h_G is large. In the horizontal U bend pipeline, the liquid slug is generated in the lower value of V_G than that in the horizontal pipeline. This is because the liquid phase is dammed up at the U bend inlet and this process enhances the increase of liquid height and the generation of liquid slug.

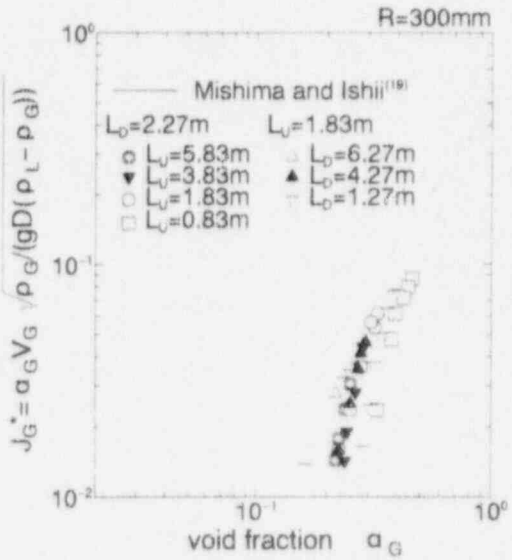

Fig. 19 Comparison of experimental data to Mishima and Ishii's theory. (Effect of length of L_U and L_D)

6. CONCLUSION

The flooding and the carry-up limit in the horizontal U bend pipelines were measured. The effects of the length of horizontal pipe and the radius of U bend on the flooding and the carry-up limits were elucidated. The following conclusions are obtained in the present experimental apparatus and conditions.

(1) The both volumetric fluxes at the flooding limit decrease with increasing value of L_D. The carry-up limits little change with increasing value of L_D.
(2) The both volumetric fluxes at the flooding limit decrease with decreasing value of L_U. The carry-up limits shift to the lower gas volumetric flux with increasing value of L_U.
(3) The radius of U bend is little related with the flooding and the carry-up limits.
(4) The flooding in the horizontal U bend pipeline occurred in lower both flow rates than those in a vertical pipe.
(5) The constants m and C in the Wallis' formula are expressed by L_D/L_T and L_U/L_T.
(6) The relation between V_G and h_G in the onset of flooding in the horizontal U bend pipelines is similar to that in the onset of liquid slug in a horizontal pipe.

REFERENCES

[1] Wallis, G.B., One-dimensional Two-Phase Flow, McGraw-Hill, 339 (1969).
[2] Lacy, C.E., and Dukler, A.E., Int. J. Multiphase Flow, Vol. 20, No. 2, pp. 219-233 (1994).
[3] Lacy, C.E., and Dukler, A.E., Int. J. Multiphase Flow, Vol. 20, No. 2, pp. 235-247 (1994).
[4] Centinbudaklar, A.G. and Jameson, G.J., Chemical Engineering Science, Vol. 24, pp. 1669-1680 (1969).
[5] Katto, Y., Int. J. Multiphase Flow, Vol. 20, No. 1, pp. 45-61 (1994).
[6] Bankoff, S.G., and Lee, S.C., Multiphase Science and Technology, Hemisphere, pp. 95-180 (1986).
[7] Bankoff, S.G., and Lee, S.C., NATO ASI Series E, No. 64, Hemisphere, PP. 745-780 (1983).
[8] Gardner, G.C., Int. J. Multiphase Flow, Vol. 9, No. 4, pp. 367-382 (1983).
[9] Lee, S.C., and Bankoff, S.G., ASME;J. of Heat Transfer, Vol. 105, pp. 713-719 (1983).
[10] Siddiqui, H., et al., Int. J. Multiphase Flow, Vol. 12, No. 4, pp. 531-541 (1986).
[11] Sakaguchi, T., et al., International Conference on Multiphase Flow '95 Kyoto, Vol. 3, FT1-9 (1995).
[12] Usui, K, et al., J. of Nuclear Science and Technology, Vol. 17, No. 12, pp. 875-887 (1980).
[13] Farukhi, M.N., and Parker, J.D., Proc. of Int. Heat Transfer Conf., Vol. 5th, No. 4, pp. 205-209 (1974).
[14] Oshinowa, T., and Charles, M.E., The Canadian Journal of Chemical Engineering, Vol. 52, pp. 25-35 (1974).
[15] Alves, G.E., Chemical Engineering Progress, Vol. 50, No. 9, pp. 449-456 (1954).
[16] Usui, K., et al., J. Nuclear Science and Technology, Vol. 18, No. 3, pp. 179-190 (1981).
[17] Usui, K., et al., J. Nuclear Science and Technology, Vol. 20, No. 11, pp. 915-928 (1983).
[18] Fisher, S.A., and Yu, S.K.W., Int. J. Multiphase Flow, Vol. 1, pp. 771-791(1975).
[19] Mishima, K. and Ishii, M., Trans. ASME, J. Fluid Engng., Vol. 102, pp. 441-445 (1980).

CCFL IN HOT LEGS AND STEAM GENERATORS AND ITS PREDICTION WITH THE CATHARE CODE

G.Geffraye, P.Bazin, P.Pichon, A.Bengaouer

CEA/DRN/STR
17 rue des Martyrs
38054 GRENOBLE cedex 9 - FR

ABSTRACT

This paper presents a study about the Counter-Current Flow Limitation (CCFL) prediction in hot legs and steam generators (SG) in both system test facilities and pressurized water reactors.

Experimental data are analysed, particularly the recent MHYRESA test data. Geometrical and scale effects on the flooding behavior are shown.

The CATHARE code modelling problems concerning the CCFL prediction are discussed. A method which gives the user the possibility of controlling the flooding limit at a given location is developed. In order to minimize the user effect, a methodology is proposed to the user in case of a calculation with a counter-current flow between the upper plenum and the SG U-tubes. The following questions have to be made clear for the user : when to use the CATHARE CCFL option, which correlation to use, and where to locate the flooding limit .

1- INTRODUCTION

In a Pressurized Water Reactor (PWR), during emergency core cooling conditions following a loss-of-coolant accident, a counter-current flow of steam and water may occur between the core and the SG. Two important hydrodynamic limitations, the onset of flooding and the zero liquid penetration, may take place either at the upper core region , hot leg bend, SG inlet plenum or U tubes entrance.

In order to well understand all the parameters which may influence the CCFL, an analytical experiment MHYRESA has been carried out at CEA-CEN Grenoble. The various test sections - 2 types of hot leg geometry, 3 diameters from .075 to .351 m - allow to investigate scale and geometrical effects on the flooding behavior particularly at the SG entrance and at the hot leg bend. The test results are compared to other experimental data including the large scale UPTF data, and to existing correlations.

CATHARE is a system code for nuclear reactor thermal hydraulics jointly developed by the French Atomic Energy Commission (CEA/DRN and CEA/IPSN), EDF (French utility) and FRAMATOME (French vendor). Previous assessment calculations have shown that the code could not predict correctly the flooding limit in complex geometry [1,2]. A method has been developed which gives the user the possibility of controlling the flooding limit at a given location of the meshing corresponding to a geometrical singularity, flow restriction, flow enlargement, pipe bend...Wallis type or Kutateladze type correlations can be used. The MHYRESA tests are here interpreted using this new capability.

A correct use of the CCFL option requires :

- the knowledge of the limitation location
- the knowledge of the appropriate flooding limit

In order to minimize the user effect, precise recommendations must be given. A methodology to use the CCFL option in case of a reactor calculation or a system test facility calculation is developed.

2- THE MHYRESA EXPERIMENTAL PROGRAM

The MHYRESA experimental program has been carried out at CEA-CEN Grenoble.

Four different test sections are used to study the flooding phenomenon in the hot leg and SG inlet plenum. The effects of the size and of the scaling criteria on the CCFL behavior are investigated.

All the tests series are conducted in ambient air-water conditions with plexiglass test section to focus on mechanical behavior without thermal exchanges and to allow the visualisation of the flow pattern .

a - A schematic of the experimental rig

Fig.1 shows a schematic of the experimental rig. It is composed of

- a pipe representing the hot leg. The experimental tube is connected to
- a tank representing the upper plenum. Its capacity remains the same for all the test sections; it amounts to 3 m^3.
- and to the SG inlet plenum whose geometry depends on the scaling. It is surmounted by a separator tank.

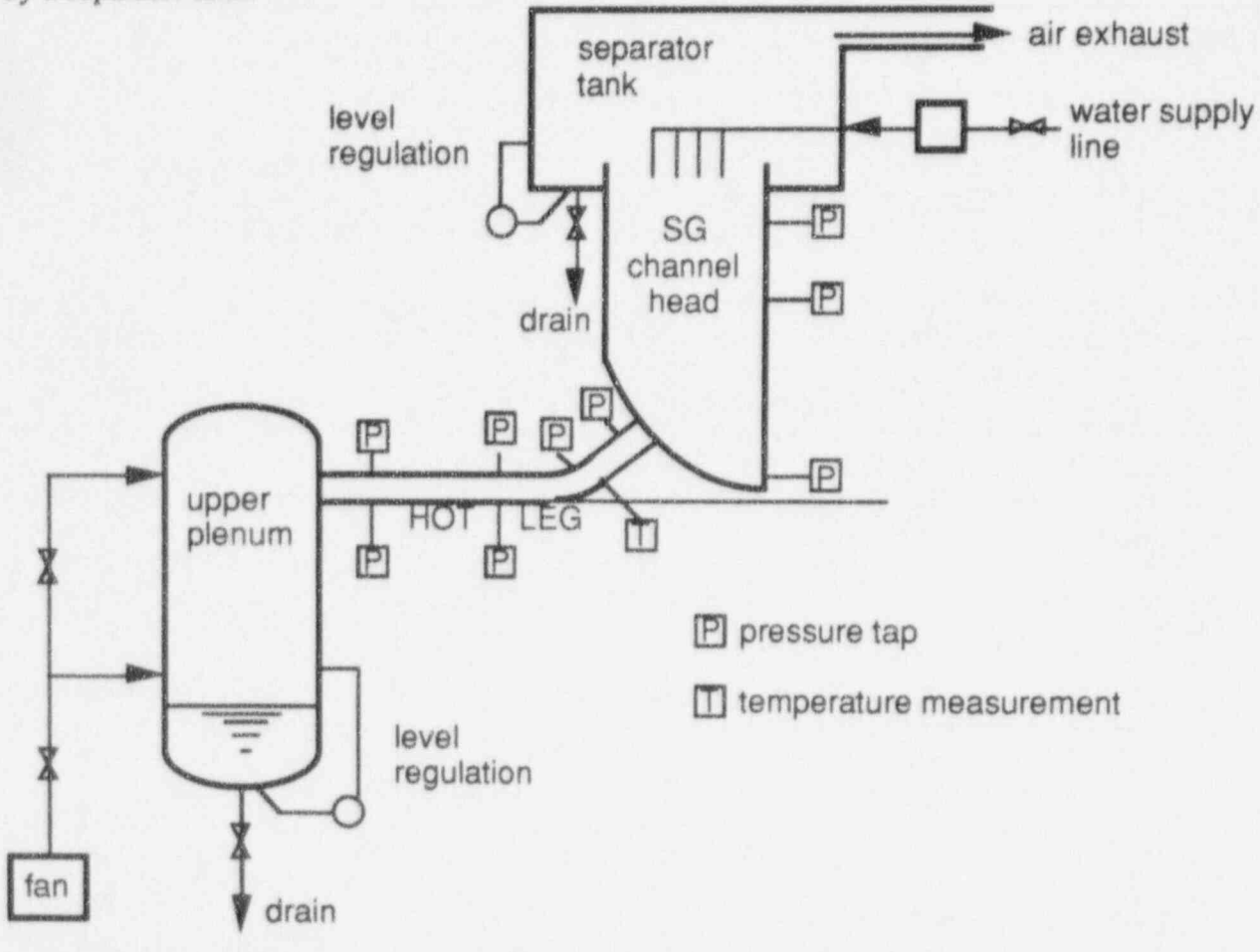

Fig.1 : Schematic diagram of the experimental rig

Air circuit

Air is injected from a fan through regulation valves and flow meters in the upper plenum. The air injection pipe of 0.350m diameter can be attached at level 0.5m or level 2.750m from the upper plenum bottom.

The top of the separator tank is opened to the atmosphere.

Water circuit

Water is injected at the top of the SG channel head through injectors whose diameter correspond to the ID of a SG tube (0.01968 m). Their number vary with the test section.

The liquid down-flow as well as the liquid carry-up is collected into capacities where the level is kept constant by means of valves, and then drained and measured.

b - The test sections

Four test sections (see table 1 and fig.2) represent the hot leg and the SG inlet plenum with two volume scaling factor (1/100 and 0.22) and two geometrical scaling criteria. These latter correspond to :

- on the one hand a geometrical similarity of the french PWR with two diameters 0.075 and 0.351 m (called respectively R75 and R351).
- on the other hand the BETHSY geometry . BETHSY is a 1/100 scaled down model of a french 3-loop PWR. The horizontal piping diameter is scaled keeping the Froude number. The SG plenum is represented by a vertical tubular part and a capacity in order to preserve the scaled volume and the elevations, avoiding too significant geometrical distortions.Two diameters are used : 0.118m for the Froude similarity and 0.075m corresponding to the geometrical similarity. They are respectively noted B118 and B75.

All the test sections respect the elevation between the hot leg axis and the underside of the SG tubesheet.

test section	Similarity of the hot leg diameter	scale volume	scale elevation	diameter in mm
B118	Froude	1/100	1/1	118
B75	geometrical	1/100	1/1	75
R75	geometrical	1/100	1/1	75
R351	geometrical	22.7/100	1/1	351

Table 1 : Characteristics of the four Mhyresa test sections

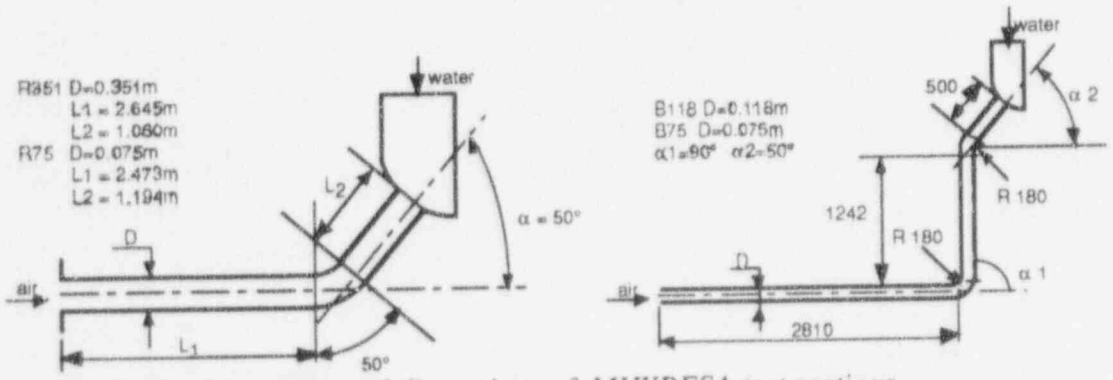

Fig.2 : Schematic and dimensions of MHYRESA test sections

c- Experimental procedure

Two kinds of experimental procedure are performed :

• for a given value of the feedwater liquid flowrate, the gas flowrate is smoothly increased until the liquid starts to accumulate. The onset of flooding is determined when the pressure drop above the CCFL location shows a sudden increase.
This procedure is not possible on the large scale test section (R351) because the change in the pressure drop is smooth and does not give a clear criterion for the flooding determination.

• A steady state is established with constant values of both liquid feedwater and gas flowrates. The flooding conditions are given by the mean values of the liquid down-flow (which is smaller than the feedwater flow) and of the gas up-flow.

The zero liquid penetration corresponds to the particular case with only few drops flowing down.

Only this second kind of experimental results obtained on MHYRESA is discussed hereafter.

3- EXPERIMENTAL RESULTS AND ANALYSIS

On MHYRESA, the visual observations and the pressure drop measurements allow to locate the flooding phenomenon in the bend in the small scale test sections (0.075 and 0.118 m in diameter), whereas limitations are observed in the hot leg in the large scale test section (R351). It is important to notice that CCF limitations never take place at the SG inlet plenum.

Selected MHYRESA experimental data are plotted fig.3, using the classical Wallis parameter, $J^*_k{}^{1/2} = J_k{}^{1/2} (\rho_k / g \Delta\rho D)^{1/4}$ (see nomenclature). It represents the ratio of inertial forces to gravity forces, the length scale being the tube diameter D.

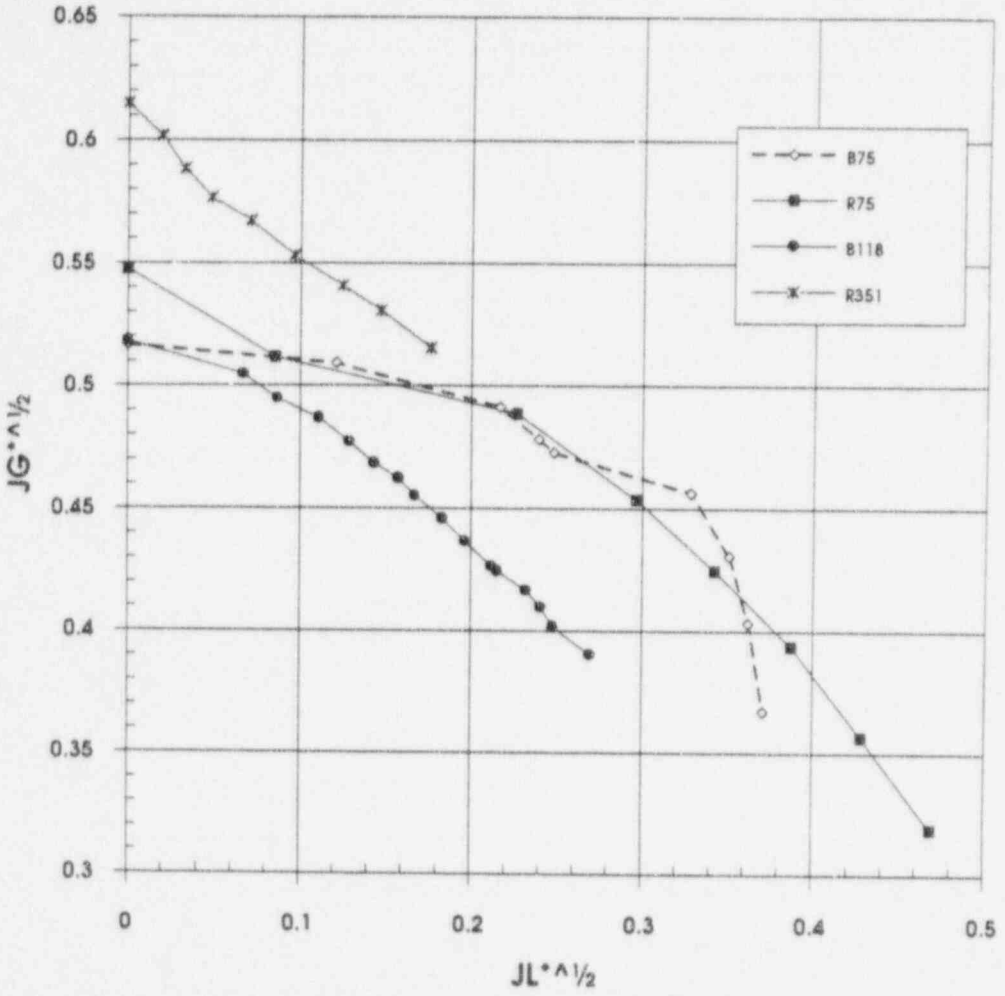

Fig.3 : MHYRESA test data

In both 0.075m diameter test sections, rather strong oscillations of the liquid amount in the bend and in the SG inlet plenum are observed and the experimental flooding limits are spread and dependent on the liquid feedwater flowrate. Data of Fig.3 and table 2 represent a particular case corresponding to a high value of the injected liquid flowrate. This oscillatory behavior can be attributed to a low pressure range, a small diameter and a large upper plenum which creates particular system effects. The rather large upper plenum volume associated with a very low density of the gas phase leads to conditions where it is difficult to keep a gas volume flowrate constant in the hot leg. In such extreme conditions, the CCFL behavior is not only a local

phenomenon but it is strongly influenced by system effects. Sensitivity calculations with the CATHARE code show that more stable conditions are obtained when a higher pressure or a smaller upper plenum volume is used. The unstable conditions are encountered in the experiment which is characterized by an open circuit, low pressure air-water conditions without phase change. It is not evident that the same system effects may exist in a closed loop with steam-water conditions. As a consequence, the data analysis will be focussed on the larger scale B118 and R351 test series.

In the BETHSY geometry (B118) these phenomena are not observed and there is no scattering in the flooding points.

In the large scale test section (R351), only a small effect of the feedwater liquid flowrate is seen on the flooding data.

Among these results, a simple Wallis type law [3] :

$J^*_g{}^{1/2} + M\, J^*_l{}^{1/2} = C$, M and C being constant (eq.1)

agrees reasonably well with experimental data only for the large scale case (R351). For the other test sections there is no clear linear trend in the frame $J^*_g{}^{1/2}$ versus $J^*_l{}^{1/2}$.

The zero liquid penetration corresponding to no liquid flowing down - $(J^*_g{}^{1/2})_0$ - is smaller in case of B118 compared to R351 (see table 2). One can suspect that the presence of a vertical part modifies the CCFL by reducing the flooding limit.

The MHYRESA data are compared to some other experimental correlations [4,5,6,7,8].

The attention is focussed on the zero liquid penetration point. The comparison is made using the Wallis and the Kutateladze coefficients. Here, Ku^*_k $(= J_k\, (\rho_k{}^2 / g\, \Delta\rho\, \sigma)^{1/4})$ is the Kutateladze parameter which has been proposed as one of the typical parameters for CCFL, as well as Wallis parameter. The difference between them is a geometrical dependency for the Wallis number, but not for the Kutateladze number. Richter [9] showed that they correlate the experimental data over different range of Bond (Bo) number . For Bond number less than approximately 40, the Wallis number seemed to be more appropriate. Nevertheless while considering the following experimental data (table 2), the scattering on the Wallis parameters is evaluated around 50%, whereas the scattering on the Kutateladze parameters is around 300%. The CCFL point seems to be rather better described by the Froude similarity for a range of diameters from 0.0254 to 0.75 m than by the Kutateladze one.

	D (m)	Vertical part in hot leg	Pressure (bar)	Bond number	$(J^*_g{}^{1/2})_0$	$(Ku^*_g{}^{1/2})_0$
ECTHOR	0.250	no	1	85	0.58	1.76
MHYRESA R351	0.351	no	1	129	0.61	2.06
UPTF D= 0.75 A= πR^2	0.750	no	15 3	355 311	0.57	2.47 2.39
UPTF Dh Ah	0.640	no	15 3	303 266	0.7	2.92 2.83
RICHTER	0.203	no			0.7	
OHNUKI	0.0254	no	1	9	0.56	0.98
MHYRESA R75	0.075	no	1	31	0.52	1.23
KROLEWSKI	0.058	yes			0.5	
MHYRESA B75	0.075	yes	1	24	0.52	1.19
MHYRESA B118	0.118	yes	1	43	0.52	1.33

Table 2: Flooding characteristics

The UPTF data can be correlated with a Wallis type correlation (eq.1) in two different ways:

• If the section A and the diameter D of the hot leg is used, a first set of constants M and C is obtained.

• Considering that the limitation is located at the region of the so called "Hutze", Weiss and al [4] propose to use the reduced cross section Ah and local hydraulic diameters Dh corresponding to the "Hutze" area.

Both correlations are presented in table 2.

It is not clear which one of these correlations is the most appropriate for a reactor geometry without the "Hutze". If one compares the UPTF data with ECTHOR and MHYRESA R351 tests which use a similar geometry without "Hutze", it seems that the first choice can better correlate data in the range $0.25<D<0.75$m as the constant $C=(J^*_g{}^{1/2})_0$ remains in a narrow range $0.57<C<0.61$. However no general trend can be found when looking to the smaller scale data. Richter data (D=0.203m) agree better with UPTF data when using the second type of UPTF correlations.

Several authors propose flooding correlations established from different data base. None of the correlation can agree with all the data of table 2. It is likely that many parameters may have an influence : scale, presence of vertical section or inclined section, geometry of the bend, length of the hot leg, fluid (air-water, steam-water), test procedure, experimental facility system effects. In the absence of a precise knowledge about all the possible effects, no universal flooding correlation has been developed for data of table 2. It seems more reasonable to accept that the CCFL in a hot leg will remain a phenomenon which cannot be predicted with a high accuracy, and code uncertainty evaluation method should take this into account. Moreover, as it will be seen later, according to the design of many reactor or system test facilities, the hot leg does not seem to be the most limiting component between the core and the SGs.

However, some limited observations can be noticed :

• the Froude similarity is more appropriate than the Kutateladze similarity even for large diameters.

• keeping in mind all the above mentioned reservations, one can note :

- the value of $(J^*_g{}^{1/2})_0$ - corresponding to the zero penetration point - for all data with a vertical part in the hot leg is 0.51 ± 0.01

- the value $(J^*_g{}^{1/2})_0$ for test data without vertical part and with $D\geq0.25$m is 0.59 ± 0.02

4 - CATHARE CCFL PREDICTION

An analysis of the CCFL and the flooding phenomena shows that the buoyancy, the interfacial friction, the liquid acceleration, and the form losses are the most important forces playing a role in this process. Provided that the interfacial friction and the singular pressure drops are well correlated, then any 1-D two-fluid code should be able to predict the CCFL phenomenon and a flooding limit. In practice, in systems such as reactors or integral loops, two-fluid codes predict the qualitative behavior but are never very accurate.

Looking at the validation of the CATHARE code on system tests, it was observed that a frequent source of errors was indeed associated to the CCFL prediction in complex geometries such as the upper tie plate of the core, the hot leg bend, the entrance of the steam generator channel head or the inlet of the SG U-tubes. The analysis of the physical and numerical problems revealed three main difficulties :

- The interfacial friction correlations are developed for established or quasi-established flows and are not valid in these perturbated flows occuring in complex geometries.

- At the location where the limitation occurs, there is a high void fraction gradient due to the liquid accumulation above. The numerical scheme using the staggered mesh and a weighted average of two void fractions in the momentum equations induces a high sensitivity to the meshing in the flooding prediction.

- Due to the local 3-D effects the liquid acceleration term of the momentum equation cannot be correctly estimated.This term plays an important role in the prediction and participates to the high sensitivity to the mesh size [10].

It is then proposed to use a specific modelling of the momentum equations in such complex geometries. The principles are the following :

- The mixture momentum equations - sum of the classical CATHARE phasic equations [11] - remains unchanged. The cross-momentum equation (CME) is obtained by elimination of the pressure gradient from the two momentum equations. It is then written in a simplified form, as the equilibrium between the buoyancy force, a "singular interfacial friction" and the time acceleration terms. The " singular" term is a correlation for the combined effects of the interfacial friction, wall friction and singular head losses. Moreover the CME must be calculated with a local void fraction different from the average void fraction of the mesh. This local void fraction must also be correlated.

- The simplified CME controls the flooding limit. A general method is used to translate any flooding correlation in terms of a " singular interfacial friction" and a "limit void fraction". Wallis type or Kutateladze type correlations can be written in the following general form [12]:

$$J_G^{*1/2}\ B_o^{\varepsilon/4} + M_n\ J_L^{*1/2}\ B_o^{*\varepsilon/4} = C_n \qquad \text{(eq.2)}$$

where Bo is the Bond number (see nomenclature).
M_n and C_n are constant.
ε is a parameter; ε equal to 0 in eq.2 corresponds to the Wallis model, ε equal to 1 in eq.2 corresponds to the Kutateladze model.
It has been demonstrated by R.FREITAS [12] that it corresponds to the following "singular interfacial friction" τ_{is} (eq.3):

$$\tau_{is} = \alpha\left(1-\alpha\right)\frac{B_o^{\varepsilon}}{C_n^4\, d}\left[\sqrt{\rho_G} + M_n^2\left(1-\alpha\right)\sqrt{\rho_L}\right]^2\left[\left(V_G - V_L\right)^2\right] \qquad \text{(eq.3)}$$

when the following *"limit void fraction"* α_F (eq.4) is used: $\alpha_F = \dfrac{R\sqrt{\tilde{J}_G}}{\left(R-1\right)\sqrt{\tilde{J}_G} + 1}$ (eq.4)

with $\tilde{J}_G = \dfrac{J_G}{J_o}$, $J_o = C_n^2\left[\dfrac{g\,\Delta\rho\, d}{\rho_G\, B_o^{\varepsilon}}\right]^{1/2}$

and $R = M_n^2\left(\dfrac{\rho_L}{\rho_G}\right)^{1/2}$

According to the envelope theory, α_F gives the highest liquid downflow for a given gas upflow.

CATHARE writes the momentum equations on a vector node surrounded by two scalar nodes. The modified momentum equation is used on option at a given vector node and is calculated using the limit void fraction except in two cases. The void fraction calculated at the scalar node below is used when it is lower than α_F and the void fraction calculated above is used when it is higher than α_F. These two cases correspond to counter-current flows below the flooding curve.

This new specific CCFL treatment has been implemented in CATHARE 2 version V1.3 and operationality (validation, verification and qualification) tests have been performed. They include the Hannover experimental tests simulating the upper tie plate of a PWR core presented in [12]. It is also tested for the PWR SG tubes (see §5). CATHARE can follow exactly the chosen experimental flooding correlations. It must be mentioned that the use of the CCFL option at a given node will not be efficient if the intrinsic limit of the code is more severe upstream or downstream of this node.

5 - MODELLING WITH THE CATHARE CCFL OPTION

The use of the CATHARE CCFL option presented in §4 requires some guidelines. The user has to know :

- where the flooding limit may occur between the SG tubes and the core.
- when it is necessary to use the CCFL option
- and if necessary which correlation to assign to the CCFL option.

Two cases are considered : the Bethsy system loop and the scale one 3-loop French reactor .

During a small break loss-of-coolant accident, the SGs are expected to operate in a reflux-condensation mode. In some conditions the CCFL may occur at the SG U-tubes entrance. In this framework, a survey of the various correlations proposed in the bibliography is made.

According to R.TREWIN [13], the CCFL correlation [3] based on the Wallis parameter: $J^*_g{}^{1/2} + M\, J^*_l{}^{1/2} = C$, where M=1 and C=0.88,
is applicable for the U-tubes in the PKL facility.

An accurate analysis of BETHSY loop experimental data in the context of counter-current flow limitation in the SG U-tubes has been made by P.BAZIN [14] .The data points cover a quite wide range of liquid flowrates - corresponding to Jl* from 0.01 to 0.16 - whereas the PKL data concern a more restricted range of water flowrates. Neither PKL nor BETHSY provide data for the zero penetration conditions. The available partial delivery points of both test facilities are in rather good agreement. The PKL data were correlated assuming M=1 giving C=0.88. Whereas a best fit of Bethsy data results in M=0.5 and C=0.75 (correlation A) . In the framework of the experimental MHYRESA program, a detailed study on counter-current flow in a single tube is underwork. It includes sensitivity tests on tube entrance geometry. A set of correlations will be derived.

The flooding curve in the BETHSY hot leg is extrapolated from the MHYRESA B118 data (fig.3), using a Wallis description with M= 0.55 and C=0.55 (correlation B). The constant C=0.55 is different from $(J^*_g{}^{1/2})_0$ of table 2 as it results from a best fit of all B118 test data.

In the following study, the flooding curve in the french reactor hot leg is established using the UPTF correlation (§ 3) with M=1 and C=0.57 (correlation C). This correlation has been chosen as it corresponds to the most severe limitation in the hot leg, compared with the other UPTF correlation and with a possible correlation of MHYRESA R351 data (fig.3).

The above correlations are used to calculate the extrapolated zero penetration conditions : correlation A for the SG U-tubes, B for the Bethsy type hot leg, and C for the reactor type hot leg. They are expressed in terms of limiting steam mass flowrate for each case and for different pressures. Looking at the table 3, one can conclude that the limitation systematically occurs in the SG U-tubes.

	Bethsy loop			French 3-loop PWR		
Pressure(bar)	3	15	70	3	15	70
	Steam Mass Flowrates (kg/s)					
SG U-tubes	0.10	0.21	0.41	9.81	20.22	40.16
Hot leg	0.14	0.29	0.57	14.57	30.04	59.66

Table 3: Extrapolated zero penetration conditions

It appears interesting to underline that the flooding curve in the SG U-tubes is, in both cases, below the flooding curve in the hot leg. They are expressed in terms of mass flowrate. The comparison is limited to the experimentally investigated range of parameters (see fig.4). Considering the reactor case and for the highest liquid flowrates, one can notice that the flooding

curves intersect. One must keep in mind that the most limiting correlation has been chosen to represent the flooding limit in the hot leg.

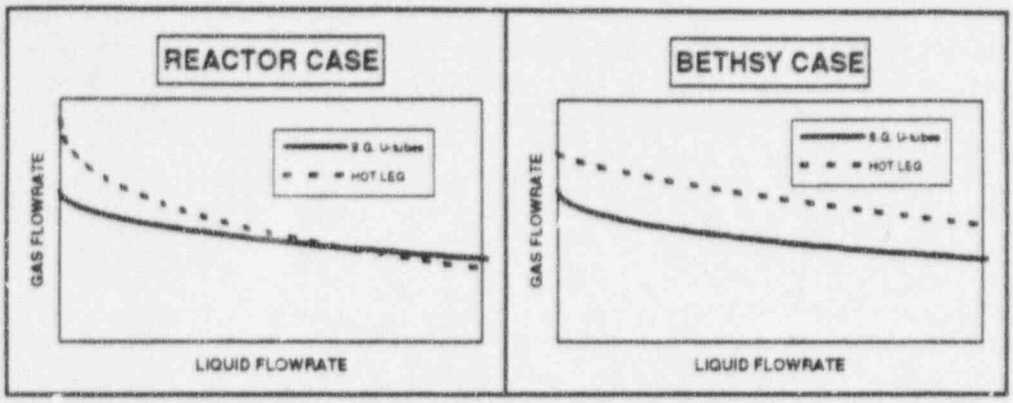

Fig.4 : Flooding curves at two different locations

CATHARE 2 Version V1.3 calculations have been conducted . The SG U-tubes, the SG channel head, the hot leg and the upper plenum are modelled. A constant water flowrate is injected at the top of the SG tubes . Vapor is injected at 70 bar in the upper plenum. The gas flowrate is first chosen high enough to prevent the liquid from flowing down. It is then slowly decreased until all the liquid falls down. In both cases, CATHARE predicts a counter-current limitation in the hot leg and not in the SGs. This is opposite to the above conclusions.

The CCFL option is assigned at the tubes entrance using the above correlation (A). The limitation occurs in the U-tubes, the flooding curve is perfectly described. When the CCFL model is used at the SG tubes entrance, the code does not predict a more severe limitation in the hot leg.

The figure 5 illustrates the calculation for the french 3-loop reactor. The injected liquid flowrate corresponds to a J^*_l of 0.185. As long as the J^*g is greater than 0.562 ($=0.75^2$), the liquid down-flow is zero. After decreasing the gas flowrate, the calculated J_l^* (thin line) follows the prescribed correlation (thick line). Then, when all the water accumulated in the tubes is emptied the predicted J_l^* decreases to the injection value.

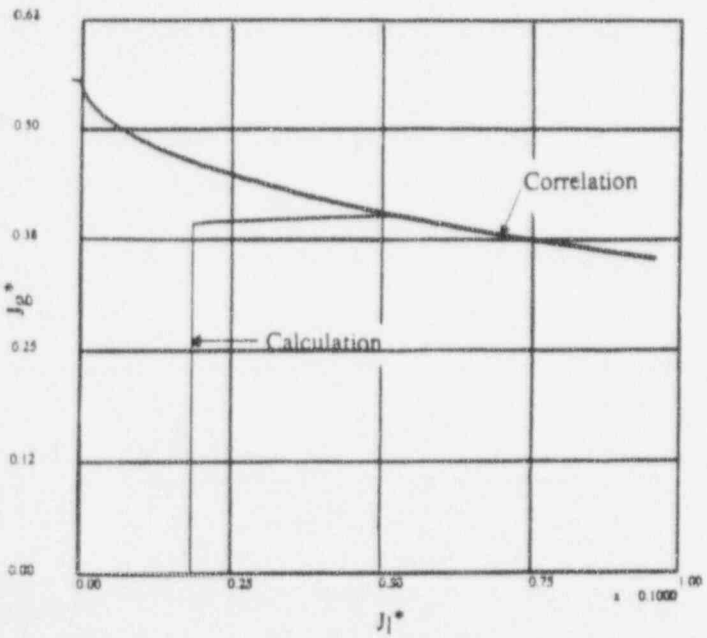

Fig.5 : CATHARE 2 version V1.3 with the CCFL option CCFL in the SG U-tubes - Reactor case

Considering all the situations of counter-current flow between the upper plenum and the SGs which can be encountered in a reactor calculation or in an integral tests calculation, it is observed that :

• The user must first determine the component where the limitation is the most severe. The data discussed here can provide the information for this purpose.

• The entrance of the SG U-tubes is the most limiting component, at least for both 3-loop french reactor and Bethsy test facility.

• The CATHARE user should use the CCFL option at the SG tubes entrance. It was also shown [12] that the CCFL option is necessary to control the flooding limit at the top of the core. These two locations correspond to "singular geometries" characterized by local flow restriction.

As a problem of second order importance, one considers a potential counter-current flow limitation occuring between the upper plenum and the inlet SG channel head. This corresponds to cases where the SG tubes are empty (no more exchanges between the primary and the secondary sides) but where water hold-up is maintained either in the hot leg or in the SG inlet plenum. Experiments show that the limitation is never located at the entrance of the SG inlet plenum. It was observed in the horizontal part of the hot leg for both UPTF tests and Mhyresa R351. It was located at the hot leg bend for the B118 test section. These cases are not characterized by strong geometrical singularity at CCFL location. One can expect that the standard momentum equations with the standard interfacial friction model are able to describe the counter-current flow behavior rather well.

Both reactor and Bethsy cases are calculated with water injection in the SG inlet plenum. (the injected water flowrate for the reactor is 6kg/s; for Bethsy it is 1kg/s). The predicted flooding limits are compared to the correlations (B) and (C) in figures 6 and 7. They represent the liquid flowrate down to the upper plenum function of time for a decreasing steam flowrate. They correspond to a steam-water flow at 70 bar.

In both cases the zero liquid penetration point is obtained for a too low J^*_{g0}. Sensitivity tests show that the interfacial friction correlation for stratified flow controls the predicted limit. The development of a better correlation is required to reduce the remaining discrepancy. However the use of the CCFL option would not be efficient as the present limit is too severe.

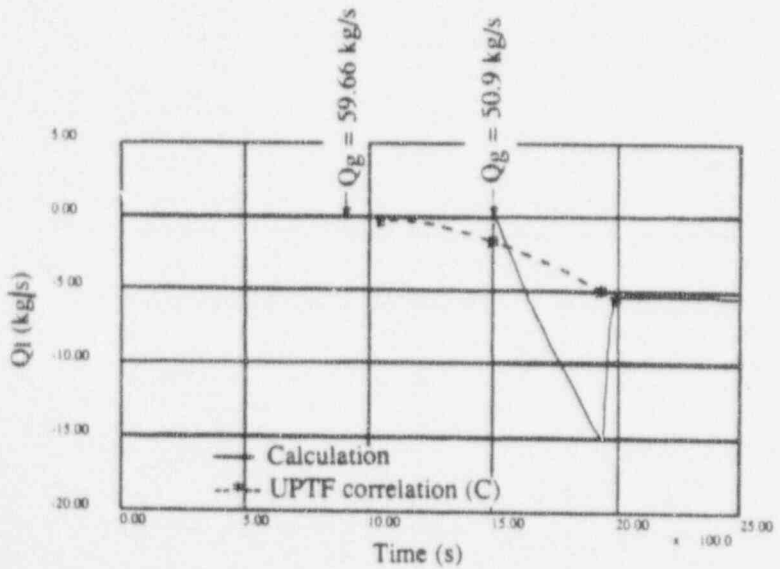

Fig.6 : Reactor case - CATHARE 2 version V1.3
Liquid mass flowrate down-flow

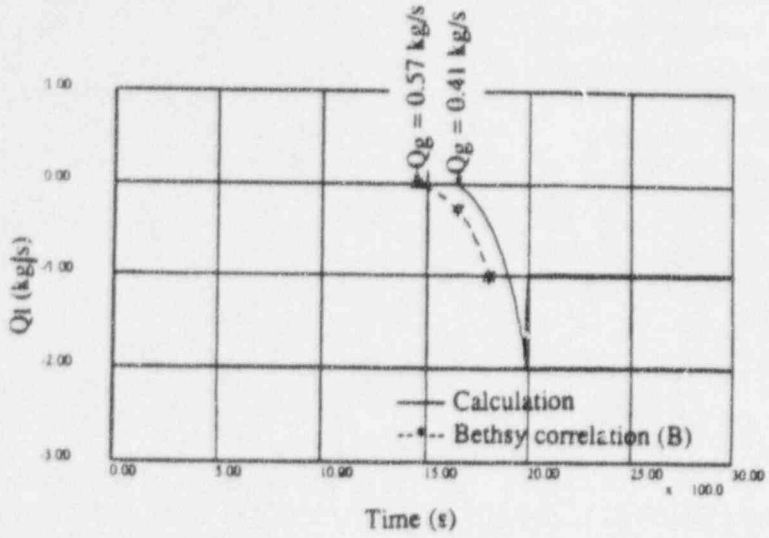

Fig.7: Bethsy case - CATHARE 2 version V1.3
Liquid mass flowrate down-flow

6 - CONCLUSION

The CCFL prediction in hot leg and SG for reactor calculations and system tests calculations is investigated. A new specific CCFL treatment is tested in CATHARE 2 version V1.3.U : the user has the possibility to control the CCFL at a given location.

For a good use of this model, a methodology has been developed and applied to the BETHSY loop and to a french type reactor. It could also be applied for a different type of geometry. Experimental data from MHYRESA tests and other experiments (such as the UPTF tests) are used to determine the location of the limitation and to estimate the quantitative flooding limits in both studied cases. The most severe limit is found at the inlet of the SG U-tubes. A CATHARE calculation without the CCFL option does not predict the same behavior. The CCFL option used at the SG tubes entrance is able to predict the appropriate limit.

In reflux-condensation situation, the CATHARE code provided with the CCFL option is able to predict correctly the liquid down-flow to the core function of the steam up-flow.

An other problem is the prediction of the liquid hold-up in the hot leg which may occur also in situations without CCFL in SG tubes. It requires a good prediction of the flooding limit in the horizontal part of the hot leg or in the hot leg bend where no general correlation describing all existing data could be found. This should be controlled by standard momentum equations without CCFL option. For the CATHARE code a better prediction of the phenomenon requires a better interfacial friction correlation for stratified flows.

Anyway the use of the CCFL option is limited to cases where the limitation occurs in a "singular geometry" and it is recommended for the upper tie plate and the SG tubes inlet for which correlations are available.

Nomenclature

$J^*_{k\ 1/2}$	Wallis number for phase k
J_k	superficial velocity for phase k, m/s
ρ_k	density of phase k, kg/m^3
g	gravitational acceleration, m/s^2

$\Delta\rho$	density difference ($\rho l - \rho g$), kg/m^3
D	hot leg diameter, m
A	cross section corresponding to the diameter D,m^2
Dh	hot leg diameter at the level of UPTF hutze,m
Ah	cross section corresponding to the diameter Dh,m^2
M,C	Flooding parameters
M_n,C_n	Flooding parameters for a general flooding correlation
Ku^*_k	Kutateladze number for phase k
σ	surface tension, N/m
$(J^*_g{}^{1/2})_0$	Wallis number for gas at CCFL point
$(Ku^*_g{}^{1/2})_0$	Kutateladze number for gas at CCFL point
Bo	Bond number, $(D^2 g \Delta\rho / \sigma)^{1/2}$
τ_{is}	Singular interfacial friction
α_F	Singular void fraction

References

[1] - F. BARRE and M.BERNARD, "The Cathare code strategy and assessment", Nucl.Engrg.Des;124,257-284(1990).

[2] - D.BESTION," Analysis of experiments of the University of Hannover with the Cathare code on fluid dynamic effects in the fuel elements top nozzle area during refilling and reflooding", Report EUR 12528 EN. 1989.

[3] - G.B WALLIS, "One-dimensional two-phase flow", Mc-Graw-Hill, INC, 1965.

[4] - P.WEISS, R.EMMERLING, R.HERTLEIN, J.LIEBERT "UPTF experiment - Two-phase flow experiments in full-scale to extend knowledge of PWR LOCA thermal-hydraulics", National Heat Transfer Conf., Proceed. vol.6, San Diego, (1992).

[5] - A.OHNUKI, H.ADACHI, Y.MURAO "Scale effects on countercurrent gas-liquid flow in a horizontal tube connected to an inclined riser",Nucl.Engrg.Des;107,283-294(1988)

[6] - H.J.RICHTER, G.B.WALLIS, K.H.CARTER and S.L.MURPHY, "Deentrainenment and counter-current air-water flow in a model of PWR Hot leg", Thayer School of Ebgineering, Sept.1978.

[7] - ECTHOR : Program PSW 2.3 Small Size Break ; Final Report EP/TA/DC.533

[8] - S.M.KROLEWSKI, "Flooding limits in a simulated Nuclear Reactor Hot Leg", Massachusetts Institute of Technology, Submission as Part of requiremqnt for a B.Sc., 1980.

[9] - H.J.RICHTER, "Flooding in tubes and annuli", Int.J. Multiphase flow, Vol.7, N°6,pp.647-658.

[10] - R.FREITAS and D.BESTION, "Qualification report. Hannover experiments on upper tie plate flooding limit. CATHARE 2 - Version V1.3 - Revision 5", CEA/STR/LML/EM/92-121,1992.

[11] - D.BESTION, "The physical closure laws in the Cathare code", Nucl.Engrg.Des,124,229-245,1990.

[12] - R.FREITAS and D.BESTION, "On the prediction of flooding phenomenon with the CATHARE code",NURETH 6th, October 1993.

[13] - R.TREWIN, P.WEBER, R.MANDL, K.UMMINGER, " Countercurrent flow limitation and liquid entrainment in the steam generator U-tubes of a PWR",

[14] - P.BAZIN , " BETHSY test facility - Study of Counter-current flow limitation in the steam generator U-tubes", Report CEA/STR/LES/93-125, 1993.

AUTHORS INDEX

A

Abdelmessih, A.H. 264
Addabbo, C. 2159
Adomaitis, E. 3083
Akagawe, K. 2994
Akiyama, M. 1653
Aksan, N. 2079, 2280, 2303
Aksan, S. N. 2904
Aksenova, A.E. 865
Aktas, B. 2035
Alemberti, A. 2869
Al-Falahi, S. 2263
Almenas, K. 1418
Allison, C.M. 1851
Analytis, G.Th., 2011, 2067, 2079, 2654
Anderson, M. 1519
Andersson, N. G. 2895
Andreani, M. 1249, 2079
Angelini, S. 1754
Anghaie, S. 1997
Anglart, H. 673
Annunziato, A. 2159
Araya, F. 1169
Arnoux-Guisse, F. 2250
Aritomi, M. 875

B

Babelli, I. 947, 1272
Bacchiani, M. 2869
Balasubramaniam, V. 1380
Balino, J. 462
Banas, A.O. 284
Banati, J. 1116
Bang, K.H. 1677
Banerjee, S. 434
Baratta, A.J. 978
Barthel, V. 1456
Bartkus, G. 3083
Bartsoen, L. 2704
Barre, F., 750, 2045
Baytas, A.C. 720
Bazin, P. 815
Beckjord, E. 1
Belov, V. A. 1555
Benet, L. V. 1443
Bengaouer, A. 815
Bertrand, C. 2250
Bertodano, M.L. 1272
Bestion, D. 2222
Blinkov, V.N. 967
Boatwright, W.J. 1083
Bobkov, V.P. 2539
Boldyrev, A. V 1914
Bonnet, J. M. 1958
Bonnin, O 2250
Boyack, B.E., 1100, 1153
Boyer, B. D. 2185
Brauner, N. 192
Briere, E. 736
Brockmeir, U. 1830
Brown, N.W. 2470
Brun, P. 1351
Bui, V.A. 1809

C

Camelo, E. 111
Caroli, C. 1443
Carpentino, F.L. 21
Carrica, P. 462, 2453, 3218
Caruso, A. 1489
Carver, M.B. 284
Centner, B. 2704
Chae, H. T. 2786
Chaigne, G. 1351
Chang, J.S. 574
Chang, S. K. 2428
Chen, G. 1997
Chen, N. C. J. 2335
Chen, X. 1586
Chen, X.M. 377, 933

Cheng, X. 846
Cheng, S.C. 2583
Cheng, Z. 3093
Cherbonnel, C. 1489
Chetal, S. C. 1361, 1380
Chiang, J-H 875
Cho, J.H. 336
Choe, W.G. 1083
Chu, C. C. 2359
Chudanov, V.V. 865
Chun, M.-H. 93
Chung, B. J. 1477
Chung, M.K. 986
Cizek, J. 2112. 2636
Clausse, A. 231, 2453, 2762, 3218, 3232
Coddington, P. 1249
Cognet, G. 1797
Conway, L.E. 2869
Cornet, P. 1443
Corradini, M.L. 1501, 1519, 1637, 1728, 1743, 1779, 2240
Coste, P. 1456, 2222
Coulon, N. 1443

D

Dasaradhi, S. 2924
Daubert, O. 2250
D'Auria, F. 2146, 2303, 2904
Davis, K.L. 1851
Dehbi, A. 402
de Cachard, F. 166
de Crecy, F., 2045, 2480
Deguchi, A. 2721
Delgadino, G. 462
Delmastro, D.F. 3232
Deryugin, A. I. 1914
Deslandes, H. 1456
DeVore, C.V. 1083
DiMarco, P. 3218
Dinh, T.N. 827, 1809
Doerffer, S. 2583
Domoradov, A. 1090
Dor, I. 750
Dorning, J.J. 2677
Doubek, M. 2815
Dougherty, T.J. 3197
Dowlati, R. 1272
Driscoll, M.J. 1224
Durin, M. 1574

E

El-Genk, M.S. 353
Elkassabgi, Y. 2924
Elia, Jr., F.A. 336
Erbacher, F.J. 846
Ezsol, Gy. 2102

F

Fakory, M.R. 1982
Falkov, A. A. 2384
Farahani, A.A. 1728, 1779
Feltus, M.A. 1127
Finjakin, A. 1090
Firnhaber, M. 1830
Flour, I. 1489
Forsyth, D.R. 696
Fox, R. J. 1501
Franchello, G. 648
Fraser, D.W.H. 264
Frogheri, M. 2146
Frohlich, G. 1607
Fukahori, T. 2994
Fuketa, T. 2957
Fukuda, K. 554
Fujii, Y. 804, 1663
Furuya, M. 923

G

Gabrianovich, B.N. 711
Gango, P. 1535, 3120
Garnier, J. 2519
Gautier, G.M. 1196
Gauvain, J. 1574
Geffraye, G. 815
Georgevich, V. 2957, 2977, 3028, 3052
Glaeser, H. 2203, 2303, 2904
Glebov, A.G. 353

Gracyalny, E. 2240
Grassi, W. 3218
Green, J. 1418
Groeneveld, D.C. 2583
Gu, C-Y 3153
Guentay, S. 402
Guellouz, M.S. 2738
Guido-Lavalle, G. , 231, 2762

H

Haapelehto, T. 770, 2806
Hadaller, G.I. 2608
Hagen, S. 1830
Hama, K. 1333
Hamaguchi, H. 212
Han, J.T. 1272
Hanninen, M. 2263
Harkins, C.K. 2003
Harmony, S.C. 1100
Harrison, J.F. 1083
Harvel, G.D. 574
Hassan, Y.A. 434, 497, 591, 3073
Hata, K. 1333
Hayes, R.C. 2608
Hecker, M. 2250
Hejzlar, P. 1224
Hemstrom, B. 2895
Henderson, P. 1797
Herer, C. 2519
Herrero, V.A. 2762
Hiltbrand, D.W. 1083
Hochreiter, L.E. 43
Hofmann, F. 2250
Hofmann, P. 1830
Hohmann, H. 1688, 1712
Hohorst, J.K. 1851
Hongisto, O. 1535
Hori, K. 574
Hosokawa, S. 804
Huang, H. C. 2428
Huhtiniemi, I.K. 1712
Hwang, S. T. 2169

I

Ibrahim, W. A. 3073
Ieda, Y. 1313
Ikeda, T. 1972
Inada, F. 923
Inoue, A. 1663
Ishida, N. 487
Ishii, M. 947, 1272
Ishijima, K. 2957
Iwamura, T. 1169
Iwashige, K. 1972

J

Jacob, M.C. 21
Jacobson, S. 2895
Jafri, T. 3197
Juanico, L.E. 3232
Juhel, D. 2480
Jun, B. J. 2786

K

Kainulainen, S. 854
Kajiwara, H. 2021
Kalli, H. 299, 2146, 2834
Kamide, H. 1313
Kang, C. S. 1477
Kao, S. P. 2428
Karasulu, M. 911
Karlsson, R. 2895
Karoutas, Z. 3153
Karve, A.A. 2677
Karwat, H. 248
Kasinathan, N. 1361
Kawahara, A. 2721
Kawaji, M. 478
Kawanishi, K. 574
Kelly, A.E. 2003
Khodjaev, I.D. 1139
Kim, H. 2786
Kim, M.H. 1677
Kim, S. 2773
Kim, S.H. 2957, 2977, 3028, 3052
Kim, S.W. 1889

Kim, Y.-S. 93
Kiso, Y. 2994
Kisselev, A.E. 1914
Kirillov, P.L. 2558, 2916
Klingenfus, J. 1069
Klingenfus, J.A. 2410
Knebel, J. U. 1407
Kobayashi, J. 1313
Kodama, J. 804
Kodaira, T. 2957
Kok, H. V. 2884
Kondo, S. 1302
Korsun, A.S. 711
Korteniemi, V. 770
Kouhia, J. 299, 854, 2806, 2834
Kozina, N.V. 2539
Kramerov, A.J. 967
Krauss, T., 603
Kuhn, S.Z. 312
Kurul, N. 673, 1889
Kuul, V. S. 2384

L

Lahey, Jr., R.T. 49, 1889, 1930
Larrauri, D. 736
Laugier, E. 2119
Laurinat, J.E. 514
Leduc, C. 1456
Lee, B.-R. 93
Lee, J. B. 2786
Lee, K-W 2489
Lee, S. J. 1863
Lee, S-Y 2489
Lemekha, A.V. 1914
Lemonnier, H. 111
Leonardi, M. 2146
Lepekhin, A.N. 2384
Levin, A.E. (2) 1231, 1291
Lider, S. 978
Lillington, J. 2904
Lime, J.F., 1100, 1153
Linca, A. 1607
Lischer, D.J. 336
Lombardi, C. 2506
Lorencez, C. 478
Lu, D. 1302
Lucas, A. T. 2941
Lundstrom, P. 1535

Mc

McDonald, J.M. 532
McDuffey, J. 131
McPherson, G.D. 1291

M

Macian, R. 2669
Madni, I. K. 2349
Magallon, D. 1688, 1712
Magnaud, J. P. 1443
Mahaffy, J.H. 2035, 2669
Majed, M. 2608
Maron, D.M. 192
Marshall, T.D. 532
Masson, V. 3218
Matsui, G. 3142
Matuszkiewicz, A. 781
Matsuzaki, M. 1663
Medich, C. 2841, 2869
Menant, B. 1324
Menna, J.D. 514
Melnikov, V. 508
Meyer, L., 603
Midvidy, W. 781
Miettinen, A. 2146
Minagawa, H. 804
Monji, H. 3142
Moreau, G. -M. 1881
Moraga, F. 1930
Mori, M. 875
Morii, T. 1653
Moskalev, A. 1090
Mudde, R. F. 2884
Muftuoglu, A.K. 1127
Munther, R. 299
Murao, Y., 478, 1169

N

Nair, S 947

Nakamori, N. 804
Nam, H.-Y. 93
Neitzel, H.J. 846
Nguyen, T. Q. 2112
Nigmatulin, B.I. 508, 967, 1555
Nigmatulin, R.I., 49, 141
Nik, N. 911
Nimokata, H. 1398
Ninokata, H. 2721
Nithianandan, C.K. 2410
No, H.C. 986
Noe, H. 1324
Norback, G. 2608
Nourbakhsh, H.P. 3093
Nourgaliev, R.R. 827, 1809
Nylund, O. 673

O

Ochterbeck, J. 111
Ogura, K. 2021
Ohashi, H. 1653
Okamoto, K 497, 591
Ohshima, H. 1313
Okkonen, T. 1809
Olive, J. 736
Ousaka, A.
Ozawa, M. 487

P

Palagin, A.V. 1914
Palazov, V.V. 423
Park, G-C 2169, 2773
Park, H.S. 1743
Park, J.-W. 76
Park, R.J. 1863
Parlatan, Y. 2185
Perneczky, L. 2102
Pernsteiner, A.P. 1501
Parrish, K.R. 1046
Paul, P.K. 514
Pernica, R. 2636
Perret, C. 2045
Pershukov, V.A. 1555
Peterson, P.F., 312, 933, 1501
Petit, M. 1574
Petry, A. 1090
Pichon, P. 815
Pigny, S. 1881
Piplica, E.J. 43
Philip, O.G. 497, 591
Po, L-C 2438
Pochard, R. 2303, 2904
Podowski, M.Z. 673, 1003, 1889, 1930
Pokharna, H. 1272
Pokusaev, B.G. 1032
Polyansky, G.N. 2384
Porkholm, K. 2263
Poskas, P. 3083
Pribaturin, N.A 1032
Puihonen, H. 2146, 2834
Puustinen, M. 770

Q

R

Radet, J. 2119
Rajakumar, A. 1361
Rajan, S.R. 911
Ransom, V.H. 1272
Raussi, P. 854
Raymond, P. 2621
Refling, J.G. 978
Reilly, S.S. 2410
Revankar, S.T. 1272
Richards, C. 2303
Rigamonti, M. 2869
Ris, V.V. 1555
Ritterbusch, S.E. 21
Rizwan-uddin 2677
Robinson, G.E. 978
Rohatgi, U.S. 2185
Rosa, M. 1003
Rouge, S. 1949
Rovinsky, Y. 192
Ruan, Y.Q. 248
Ruggles, A.E. 131, 2470

S

Saarenpaa, T. 2438
Sakaguchi, T. 212, 804
Sakurai, A. 554, 1333
Samoilov, O.B. 2384
Sanz, D. 231
Saphier, D. 2621
Sawada, T. 1398
Schindler, M. 1607
Schmidl, W.D. 497, 591
Schmitt, B. 1022
Schneider, R.E. 21
Schoen, B. 2856
Scholin, B. 3153
Schrock, V.E. 312, 377, 933
Schwirian, R.E. 696
Sehgal, B.R. 827
Seo, J.K. 2169
Selmer-Olsen, S. 111
Selivanov, Y.F. 2916
Sencar, M. 2280
Shamoun, B.I. 1637
Shimizu, A. 1398
Shiotsu, M. 554, 1333
Shoukri, M. 3175
Sidenkov D.V. 1555
Siefken, L.J. 1851
Sienicki, J. J. 2359
Sim, S. K. 1863
Simoneau, J. P. 1324
Simonin, O. 1489
Sjoberg, A. 2303, 2904
Smirnov, E.M. 1555
Smith, R.J. 2003
Smogalev, I.P. 2558
Souyri, A. 2519
Solvik, G.C. 2185
Song, C.H. 986
Sonnenburg, H.G. [illegible]
Soyama, K. 2957
Spencer, B.W. 2359
Spindler, B. 1881
Stadtke, H. 648
Steiner, J.L. 1100
Steinhoff, F. 2203
Stekelenburg, A.J.C. 2785
Stern, F. 2608
Strizhov, V.F. 865
Stumpf, H.J. 1100
Sulfredge, C.D. 3003
Sun, C. 750
Sung, Y. 2112
Syri, .S. 627
Szabados, L. 2102

T

Tabata, H. 875
Takaguchi, M. 3142
Takahashi, M. 1663
Takemoto, T. 875
Takeuchi, Y. 1333
Takizawa, A. 1302, 2021
Taleyarkhan, R.P. 2957, 2977, 3028, 3052
Tapucu, A. 781
Tavoularis, S. 2738
Tarantini, M. 2841
Teresaka, H. 2021
Teschendorff, V. 2203
Teyssedou, A. 781
Theofanous, T.G. 627, 1535, 1586, 1754
Tikhonenko, L.K. 967
Tirkkonen, H. 2438
Todreas, N.E. 1224
Trambauer, K. 1830
Tsiklauri, G. 1022
Tucker, R. F. 2924
Tuomisto, H. 1535
Tuunanen, J. 423
Tye, P. 781
Tyler, T.N. 2669

U

Ubra, O. 2815
Ueda, H. 2021
Ueno, T. 804
Umekawa, H. 487
Umminger, K. J. 2856
Unrau, D. 284

Ushakov, P.A. 711

V

Vabishchevich, P.N. 865
Vaidyanathan, G. 1361, 1380
Valenti, S. N. 2957, 2977, 3028, 3052
Valentin, B. 1351
Vanhoenacker, L. 2704
van der Hagen, T.H.J.J. 2785, 2884
Van Hove, W. 2704
Van Laeken, K. 2704
Vasil'ev, A.D. 2470
Velusamy, K. 1380
Vescovi, O. 2869
Veshchunov, M.S. 1914
Vilemas, J. 3083
Vinberg, A.A. 1555
Vinogradov, V.N. 2539
Virtanen, E. 2806
Viskanta, R. 1272
Vitruk, S.G. 711
Volchek, A M. 1914

W

Weber, P. 2856
Wang, W. 1272
Watson, R.D. 532
Wendel, M.W. 2335, 2470
Williams, P.T. 2941
Wiman, P. 2608
Wissinger, G. 1069
Worth, B. 648

X

Xiang, J. Y. 2977

Y

Yacout, A.M. 2394
Yamshchikov, N.Y. 1914
Yang, B.W. 3197
Yang, Y.H. 1653
Yang J.Y. 2169
Yang, W.S. 2394
Yasuo, A. 923
Yefanov, A.D. 2916
Yegorova, L. 1830
Yoder, G.L. 2335, 2924
Yoo, K. J. 1863
Yoshino, M. 2994
Youchison, D.L. 532
Yuann, R.Y. 377
Yuen, W.W. 1586, 1754

Z

Zaichik, L.I. 1555
Zabiego, M. 1797
Zeitoun, O. 3173
Zhou, Z. 888
Zyatnina, A.O. 2539

NRC FORM 335 (2-89) NRCM 1102, 3201, 3202

U.S. NUCLEAR REGULATORY COMMISSION

BIBLIOGRAPHIC DATA SHEET

(See instructions on the reverse)

1. REPORT NUMBER (Assigned by NRC. Add Vol., Supp., Rev., and Addendum Numbers, if any.)
NUREG/CP-0142
Vol. 1

2. TITLE AND SUBTITLE
Proceedings of the 7th International Meeting on Nuclear Reactor Thermal-Hydraulics
NURETH-7

Sessions 1 - 5

3. DATE REPORT PUBLISHED
MONTH: September | YEAR: 1995

4. FIN OR GRANT NUMBER

5. AUTHOR(S)
Compiled by R. C. Block and F. Feiner, Northeastern New York Chapter, American Nuclear Society

6. TYPE OF REPORT
Conference Proceedings

7. PERIOD COVERED *(Inclusive Dates)*

8. PERFORMING ORGANIZATION – NAME AND ADDRESS *(If NRC, provide Division, Office or Region, U.S. Nuclear Regulatory Commission, and mailing address; if contractor, provide name and mailing address.)*
Compiled by Northeastern New York Chapter, American Nuclear Society

9. SPONSORING ORGANIZATION – NAME AND ADDRESS *(If NRC, type "Same as above"; if contractor, provide NRC Division, Office or Region, U.S. Nuclear Regulatory Commission, and mailing address.)*

American Nuclear Society
555 N. Kensington Avenue
La Grange Park, IL 60525

American Institute of Chemical Engineers
345 East 47th Street
New York, NY 10017-2392

American Society of Mechanical Engineers
345 East 47th Street
New York, NY 10017-2392

Canadian Nuclear Society
144 Front Street West
Suite 725
Toronto, Ontario, Canada M5J2L7

European Nuclear Society
Secretariat: Monbijoustrasse 5
P.O. Box 5032
CH-3001 Berne, Switzerland

Atomic Energy Society of Japan
No. 1-13, 1-chome
Shimbashi, Minato-ku
Tokyo 105, Japan

Japan Society of Multiphase Flow
Prof. Akimi Serizawa
Department of Nuclear Engineering
Yoshida, Sakyo, Kycto 606-01
Japan

Division of Systems Technology
Office of Nuclear Regulatory Research
U.S. Nuclear Regulatory Commission
Washington, DC 20555-0001

10. SUPPLEMENTARY NOTES

11. ABSTRACT *(200 words or less)*

This volume includes papers presented at the 7th International Meeting on Nuclear Reactor Thermal-Hydraulics (NURETH-7) September 10-15, 1995 at Saratoga Springs, N.Y. The following subjects are discussed: progress in analytical and experimental work on the fundamentals of nuclear thermal-hydraulics, the development of advanced mathematical and numerical methods, and the application of advancements in the field in the development of novel reactor concepts. Also combined issues of thermal-hydraulics and reactor/power-plant safety, core neutronics and/or radiation.

12. KEY WORDS/DESCRIPTORS *(List words or phrases that will assist researchers in locating the report.)*
thermal-hydraulics, reactor/power-plant safety, core neutronics and/or radiation

13. AVAILABILITY STATEMENT
unlimited

14. SECURITY CLASSIFICATION
(This Page)
unclassified
(This Report)
unclassified

15. NUMBER OF PAGES

16. PRICE

Federal Recycling Program

UNITED STATES
NUCLEAR REGULATORY COMMISSION
WASHINGTON, D.C. 20555-0001

OFFICIAL BUSINESS
PENALTY FOR PRIVATE USE, $300

120555139531 1 1AN
US NRC-OADM
DIV FOIA & PUBLICATIONS SVCS
TPS-PDR-NUREG
2WFN-6E7
WASHINGTON DC 20555

SPECIAL FOURTH CLASS RATE
POSTAGE AND FEES PAID
USNRC
PERMIT NO. G-67